

PROCEEDINGS

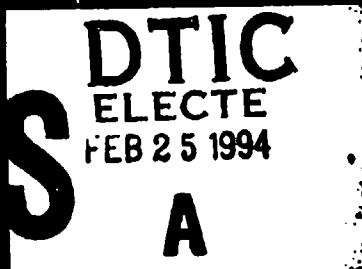
②

AD-A276 372



FOURTH TUNNEL DETECTION SYMPOSIUM ON

Subsurface Exploration Technology

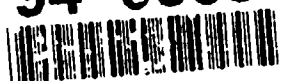


This document has been approved
for public release and sale; its
distribution is unlimited.

*Looking for a
Needle in a Haystack*

plates: All DTIC reproductions
will be in black and
white.

94-06038

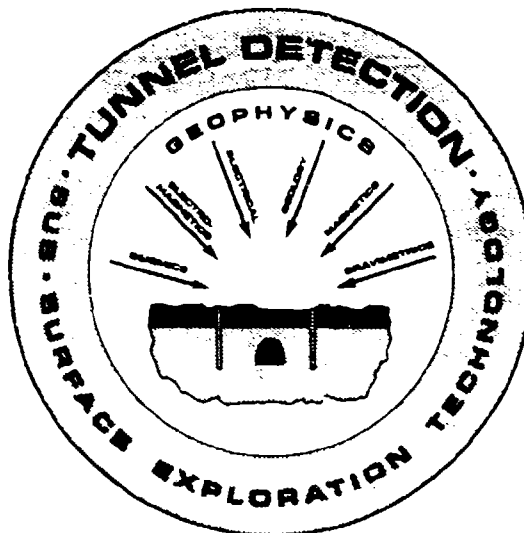


94 2 24 001

April 26-29, 1993
Golden, Colorado, USA

Fourth Tunnel Detection Symposium on **Subsurface Exploration Technology**

April 26-29, 1993
Golden, Colorado, USA



Accession For	
NTIS CRA&I	<input checked="" type="checkbox"/>
DTIC TAB	<input type="checkbox"/>
Unannounced	<input type="checkbox"/>
Justification	
By	
Distribution /	
Availability Codes	
Dist	Avail and/or Special
A-1	

Sponsored by:

DTIC GOVERNMENT 3

Combat Engineering Directorate,
U.S. Army Belvoir Research,
Development, and Engineering Center



In cooperation with:

Colorado School of Mines -
Office of Continuing Education
Department of Geophysics
Department of Mining Engineering



The Belvoir Research, Development and Engineering Center

The Center employs over 900 military and civilian personnel and is located at Fort Belvoir, Virginia, about 15 miles south of Washington, DC. The Center's mission is to do the research, development, and engineering to provide material and technical capabilities to the U.S. Army in the field for Combat Support (combat engineer equipment) and Combat Service Support (logistics equipment). It also provides for all ground equipment fuels and lubricants for the Department of Defense, and is responsible for a large number of complex and diverse fields of endeavor to enhance the mobility and survivability of friendly forces.

The Colorado School of Mines

Located in Golden, Colorado, about 15 miles west of Denver, the Colorado School of Mines ranks as the largest institution in the United States dedicated to science and engineering education related to minerals, energy, and materials. For more than 100 years, the School has maintained its dedication to quality education, research and public service. The School's 2950 graduate and undergraduate students represent all 50 states and 67 foreign countries. CSM alumni serve in industry, government, and education in all parts of the world.

The School offers undergraduate and graduate degrees in ten disciplines, and graduate degrees only in an additional three.

REPORT DOCUMENTATION PAGE

Form Approved
OMB No. 0704-0188

Public reporting burden for this collection of information is estimated to average 1 hour per response, including the time for reviewing instructions, searching existing data sources, gathering and maintaining the data needed, and completing and reviewing the collection of information. Send comments regarding this burden estimate or any other aspect of this collection of information, including suggestions for reducing this burden, to Washington Headquarters Services, Directorate for Information Operations and Reports, 1215 Jefferson Davis Highway, Suite 1204, Arlington, VA 22202-4302, and to the Office of Management and Budget, Paperwork Reduction Project (0704-0188), Washington, DC 20503.

1. AGENCY USE ONLY (Leave blank)		2. REPORT DATE 30 Sep 93	3. REPORT TYPE AND DATES COVERED Symposium Proceedings, 26-29 Apr 93	
4. TITLE AND SUBTITLE Fourth Tunnel Detection Symposium on Subsurface Exploration Technology			5. FUNDING NUMBERS DAAK70-92-C-0015	
6. AUTHOR(S) Dr. R.M. Miller, CSM Mr. R.F. Dennis, BRDEC				
7. PERFORMING ORGANIZATION NAME(S) AND ADDRESS(ES) Colorado School of Mines (CSM) Office of Continuing Education Department of Geophysics Department of Mining Engineering Golden, CO 80401			8. PERFORMING ORGANIZATION REPORT NUMBER	
9. SPONSORING/MONITORING AGENCY NAME(S) AND ADDRESS(ES) Combat Engineering Directorate, U.S. Army Belvoir Research, Development and Engineering Center (BRDEC) Fort Belvoir, VA 22060-5818			10. SPONSORING/MONITORING AGENCY REPORT NUMBER	
11. SUPPLEMENTARY NOTES CSM Editors: Shirley Ashlock; Jim Proud BRDEC Editors: Colleen Cosgriff; Sherry Krebs				
12a. DISTRIBUTION/AVAILABILITY STATEMENT Approved for Public Release; Distribution is Unlimited			12b. DISTRIBUTION CODE	
13. ABSTRACT (Maximum 200 words) These Proceedings document the 47 technical papers delivered during the Fourth Tunnel Detection Symposium on Subsurface Exploration Technology held 26-29 April 1993 in Golden, Colorado. The objective of the Symposium was the exchange of technical information on the most recent advances in subsurface exploration technology. Previous series of symposia on this subject (1981, 1984 and 1988) were focused on the application of detecting and locating deep tunnels (to 300 meters) in hard rock geological environments. The scope of this symposium was expanded to include a wider variety of subsurface applications, viz., shallow tunnels (to 30 meters), natural cavities, historical, archaeological and other underground structures, buried utilities, environmental clean-up etc. Subjects discussed included field methods and experimentation, instrumentation, methods for analysis of field data and interpretation, field problems, application of theories of subsurface exploration, mathematical and scale modeling, and related subjects.				
14. SUBJECT TERMS 1. Tunnel Detection 2. Geophysical Methods 3. Subsurface Sensing 4. Sensors			15. NUMBER OF PAGES	
			16. PRICE CODE	
17. SECURITY CLASSIFICATION OF REPORT UNCLASSIFIED	18. SECURITY CLASSIFICATION OF THIS PAGE UNCLASSIFIED	19. SECURITY CLASSIFICATION OF ABSTRACT UNCLASSIFIED	20. LIMITATION OF ABSTRACT SAR	

GENERAL INSTRUCTIONS FOR COMPLETING SF 298

The Report Documentation Page (RDP) is used in announcing and cataloging reports. It is important that this information be consistent with the rest of the report, particularly the cover and title page. Instructions for filling in each block of the form follow. It is important to stay *within the lines* to meet optical scanning requirements.

Block 1. Agency Use Only (Leave blank).

Block 2. Report Date. Full publication date including day, month, and year, if available (e.g. 1 Jan 88). Must cite at least the year.

Block 3. Type of Report and Dates Covered. State whether report is interim, final, etc. If applicable, enter inclusive report dates (e.g. 10 Jun 87 - 30 Jun 88).

Block 4. Title and Subtitle. A title is taken from the part of the report that provides the most meaningful and complete information. When a report is prepared in more than one volume, repeat the primary title, add volume number, and include subtitle for the specific volume. On classified documents enter the title classification in parentheses.

Block 5. Funding Numbers. To include contract and grant numbers; may include program element number(s), project number(s), task number(s), and work unit number(s). Use the following labels:

C - Contract	PR - Project
G - Grant	TA - Task
PE - Program Element	WU - Work Unit Accession No.

Block 6. Author(s). Name(s) of person(s) responsible for writing the report, performing the research, or credited with the content of the report. If editor or compiler, this should follow the name(s).

Block 7. Performing Organization Name(s) and Address(es). Self-explanatory.

Block 8. Performing Organization Report Number. Enter the unique alphanumeric report number(s) assigned by the organization performing the report.

Block 9. Sponsoring/Monitoring Agency Name(s) and Address(es). Self-explanatory.

Block 10. Sponsoring/Monitoring Agency Report Number. (If known)

Block 11. Supplementary Notes. Enter information not included elsewhere such as: Prepared in cooperation with...; Trans. of...; To be published in... When a report is revised, include a statement whether the new report supersedes or supplements the older report.

Block 12a. Distribution/Availability Statement. Denotes public availability or limitations. Cite any availability to the public. Enter additional limitations or special markings in all capitals (e.g. NOFORN, REL, ITAR).

DOD - See DoDD 5230.24, "Distribution Statements on Technical Documents."
DOE - See authorities.
NASA - See Handbook NHB 2200.2.
NTIS - Leave blank.

Block 12b. Distribution Code.

DOD - Leave blank.
DOE - Enter DOE distribution categories from the Standard Distribution for Unclassified Scientific and Technical Reports.
NASA - Leave blank.
NTIS - Leave blank.

Block 13. Abstract. Include a brief (Maximum 200 words) factual summary of the most significant information contained in the report.

Block 14. Subject Terms. Keywords or phrases identifying major subjects in the report.

Block 15. Number of Pages. Enter the total number of pages.

Block 16. Price Code. Enter appropriate price code (NTIS only).

Blocks 17. - 19. Security Classifications. Self-explanatory. Enter U.S. Security Classification in accordance with U.S. Security Regulations (i.e., UNCLASSIFIED). If form contains classified information, stamp classification on the top and bottom of the page.

Block 20. Limitation of Abstract. This block must be completed to assign a limitation to the abstract. Enter either UL (unlimited) or SAR (same as report). An entry in this block is necessary if the abstract is to be limited. If blank, the abstract is assumed to be unlimited.

FOREWORD

The Fourth Tunnel Detection Symposium on Subsurface Exploration Technology was held 26 - 29 April 1993 at the Denver Marriott West in Golden, Colorado. The Symposium was sponsored and conducted by the Combat Engineering Directorate, U.S. Army Belvoir Research, Development and Engineering Center (BRDEC) in cooperation with the Colorado School of Mines (CSM) Office of Continuing Education and the Departments of Geophysics and Mining Engineering. The objective of the Symposium was the exchange of technical information on the most recent advances in subsurface exploration technology. Previous series of symposia on this subject (1981, 1984 and 1988) were solely focused on the application of detecting and locating deep tunnels (to 300 meters) in hard rock geological environments. The scope of this Symposium was expanded to include a wider variety of subsurface applications, viz., shallow tunnels (to 30 meters), natural cavities, historical, archaeological and other underground structures, buried utilities, environmental clean-up, etc. Subjects discussed included field methods and experimentation, instrumentation, methods for analysis of field data and interpretation, field problems, application of theories of subsurface exploration, mathematical and scale modeling and related subjects. The expanding interest in this technology was evidenced by a record number of papers as well as attendees. The Symposium was characterized by excellent presentations, vigorous discussion during and outside the formal sessions, and endurance, with essentially full attendance right up through the closing session. A field trip was also included on the last day to the nearby BRDEC Tunnel Detection Test Site, where several subsurface exploration systems were demonstrated to a large number of attendees.

Welcoming remarks were offered by Mr. Ray Dennis, BRDEC, whose office has sponsored all four of these symposia and has spearheaded the technology search efforts in this area for the U.S. Army since 1976. He reviewed briefly the history of the program and highlighted the past interest and significant contributions from the industrial, academic and government communities where, ultimately, the technical expertise resided. It was with regret that he reported a Department of Defense (DOD) decision and announcement of last month to disestablish BRDEC and concurrently to eliminate the Army's Tunnel Detection Business Area as part of the 1993 Base Realignment and Closure (BRAC 93) package (See APPENDIX C). He asked all attendees to accept his sincere thanks and appreciation for their past interest and efforts which had contributed to many past successes under the Army's Tunnel Detection program and wished them continued success in their future work. Despite this announcement, the mood of attendees remained enthusiastic with several of the presenters identifying alternative military and civilian applications of tunnel detection technology. It was also universally agreed that the interchange of knowledge represented by this series of symposia should be continued under other sponsors.

Both the Colorado School of Mines and the Belvoir Research, Development and Engineering Center would again like to thank the attendees and authors of the papers for their contributions to the success of this Fourth Symposium. Sincere appreciation is also extended to the Organizing Committee, Session Chairs, and other personnel at Colorado School of Mines for their efforts in making this Symposium a success. It is hoped that readers will benefit from the information brought together in these proceedings, and that they find it useful for their own efforts or applications in subsurface exploration.

Russell J. Miller
Symposium Chairman

Table of Contents

	<u>Page</u>
Foreword	- i -
Program Committee Members	- ix -
Session Chairpersons	- x -
Opening Remarks <i>Phillip R. Romig</i>	1
The Dragon Head Method For Tunnel Detection And Using PEMSS Data For Determining Geology <i>Frank Ruskey</i>	5
Afterthoughts On Anticipating Problems And Nuturing Opportunity In Geophysical Searches <i>Frank Ruskey</i>	10
Session 1: Ground Penetrating Radar	17
PEMSS Response Of Rock Tunnels To "In-Axis" And Other Nonperpendicular Antennae Orientations <i>Alleman, T.J., Cameron, C.P., and Mac Lean, H.D.</i>	19
PEMSS Characterization Of Metamorphic Environments In The Central Korean Peninsula <i>Cameron, C.P., Mitchell, K.D., Shin, K.C., and Walker, B.W.</i>	45
Sixteen Channel Ground-Probing Radar Detection And Imaging Of Tunnels And Other Sub-Surface Features <i>Chignell, R.J.</i>	65
Radar Waveforms From A Three Dimensional Tunnel <i>Moran, M.L., and Greenfield, R.J.</i>	71
Pulsed GPR Detection Of Voids In Layered Geologic Materials <i>Roggen then, W.M.</i>	85

Session 2: Seismic Methods	93
Source Signature - An Experimental Approach <i>Descour, J.M.</i>	95
Seismic Location Of Small Explosions And Shot Hole Drilling At The Colorado School Of Mines' Edgar Mine, Idaho Springs, Colorado <i>Lewis, R.D., Koester, J., Sykora, D., and Greenfield, R.J.</i>	115
Cross-Borehole Seismic Signatures Of Tunnels <i>Rechtien, R.D., Greenfield, R.J., and Ballard, Jr., R.F.</i>	131
Location Of A Tunnel Boring Machine (TBM) Using Seismic Wavefield Analyses <i>Silva, W., Stark, C. and Ruskey, F.</i>	147
Seismic Tomography At The WIPP Site <i>Andersen, H.T., and Skokan, C.K.</i>	179
Session 3: Data Processing	183
Prestack Imaging And Tomographic Inversion Of Seismic Cross-Borehole Data <i>Balch, A.H., and Karazincir, M.H.</i>	185
Digitizing Analog Radar Data <i>Beasley, Jr., G.C.</i>	197
Electromagnetic Data Evaluation Using A Neural Network: Initial Investigation - Underground Storage Tanks <i>Cisar, D., Dickerson, J., and Novotny, T.</i>	207
Time-Frequency Representations Applied To Analysis Of Hole-To-Hole Electromagnetic Data <i>Duff, B.M., and Zook, B.J.</i>	221
The Role Of Cross Borehole Radar In The Discovery of "Fourth Tunnel" At The Korea DMZ <i>Kim, S-Y., and Ra, J-W.</i>	253

Waveform Modeling Of Electromagnetic Tunnel Signatures For Integral Equation TE And TM Mode <i>Greenfield, R.J.</i>	259
High-Speed Digital Radar Systems and Applications To Subsurface Exploration <i>Wright, D.L., Olhoeft, G.R., Grover, T.P., and Bradley, J.A.</i>	275
Session 4: Cross-Hole Tomography	289
Cross Well Acoustic Tomography To Delineate Abandoned Underground Mine Workings <i>Killoran, L.K., Munson, R.D., and Rich, T.T.</i>	291
Cross-Hole Tomography Using Improved Born Inversion <i>Kim, J-H., Kim, S-G., and Ra, J-W.</i>	299
Velocity, Attenuation, Dispersion and Diffraction Hole-to-Hole Radar Processing <i>Olhoeft, G.R.</i>	307
Cross-Borehole Measurement Of Dipole Array Patterns In A Dissipative Medium: A Laboratory Scale Model Study <i>Peden, I.C., and Kipp, R.</i>	321
Cross-borehole Seismic Tomographs Of Tunnels <i>Rechtien, R.D., and Ballard, R.F.</i>	333
Diffraction Tomographic Signal Processing Algorithms For Tunnel Detection <i>Witten, A.J., Schatzberg, A., and Devaney, A.J.</i>	345
Tunnel Imaging Employing Pseudo-Attenuation Of High-Frequency Seismic Waves <i>Wong, J., Wright, J., and Block, L.</i>	357
Session 5: Models	377
Efforts To Generate Guided S-Waves In Rock <i>Descour, J.M., and Miller, R.J.</i>	379

Development Of A Wide-Band Amplitude And Phase Measurement System For Underground Imaging <i>Ha, T-S., Yun, J-S., Kang, J-S., and Ra, J-W.</i>	391
Forward Modeling Of Electromagnetic Wave Propagation In Layered Media: Implications For Cross-Borehole Radio-Wave Detection Of Voids In Coal Measure Rocks <i>Jackson, M., Wedepohl, E., Friedel, M., and Hauser, K.</i>	399
Near-Field Diffraction Pattern By A Trapezoidal Cylindrical Air Cavity <i>Lee, T-K, Kang, J-S., and Ra, J-W.</i>	413
Laboratory Investigations Of The Seismo-Electric Effect <i>Skokan, C.K., and Chi, D.</i>	425
Gradiometer Antennas For Detection Of Tunnels By Scattered Electromagnetic Waves <i>Stolarczyk, L.G., and Allen, J.</i>	435
Decision Aids For Subsurface Exploration <i>Weisinger, J.R.</i>	447
Session 6: Other Methods	459
The Application Of Coal And Rock Thickness Measurement Technology To Tunnel Detection <i>Chufu, R.L.</i>	461
Gradiometer Antennas For Tunnel Detection <i>Hill, D.A.</i>	479
Tunnel Detection Without The Use Of Boreholes: What Are Our Capabilities And What Improvements Can Be Made? <i>Kemerait, R.C.</i>	497
Electromagnetic Detection Of Buried Dielectric Targets In Low Loss Media <i>Peden, I.C., Schneider, J.B., and Brew, J.</i>	517
Considerations For Geophysical Survey Design And Data Interpretation <i>Romig, P.R., and Wilson, D.</i>	537

Resistivity Changes Over Time Related To Modeled Fluid Flow In Room-Q Of The Waste Isolation Pilot Plant <i>Truskowski, M.G., and Andersen, H T.</i>	545
Detection Of Deeply Buried Tunnels With Electrical Conductors <i>Stolarczyk, L.G., and Allen, J.</i>	561
Session 7: Case Studies	573
Surface Geophysical Methods Applied To The Detection Of Shallow Tunnels And Buried Objects <i>Allen, J.W.</i>	575
Exploration Case History And Engineering Geology of "Tunnel-4", Northern Punchbowl Sector, Korean Demilitarized Zone <i>Cameron, C.P.</i>	595
Geophysical Techniques Applied To Cavity Detection At The Wharf Mine, Lead, South Dakota <i>Hauser, K.L., and Friedel, M.J.</i>	617
Stealth Tunneling Using Trenchless Technology <i>Coss, T.R.</i>	637
Borehole Radar Tunnel Detection At Gjovik, Norway <i>Kong, F.N., Westerdahl, H., and By, T.L.</i>	649
Mining Through Underground ¹ Workings At Wharf Resources' Open Pit Gold Mine, Black Hills, South Dakota, USA <i>Hammond, A.D., and Loomis, T.A.</i>	659
APPENDIX A: Index To Authors	671
APPENDIX B: Symposium Attendees	675
APPENDIX C: BRDEC News Release on BRAC 93	685

Symposium Chairman

Russell J. Miller
Colorado School of Mines

Program Committee

Fred Alger
U.S. Bureau of Mines

Christopher P. Cameron
University of Southern Mississippi

Peter Chamberlain
U.S. Bureau of Mines

David A. Hill
NIST

Dennis Lachel
Lachel & Associates

Gary Olhoeft
U.S. Geological Survey

Roy Greenfield
Pennsylvania State University

Jerry Wright
U.S. Bureau of Reclamation

Session Chairpersons

Session 1 Ground Penetrating Radar

Gary R. Olhoeft
U.S. Geological Survey

W. Doug Steele
Geotech

Session 2 Seismic Methods

Robert C. Kemerait
ENSCO, Inc.

R. Kent Young
U.S. Army BRDEC

Session 3 Data Processing

David A. Hill
U.S. Department of Commerce

D.C. George
Chem Nuclear Geotech

Session 4 Cross-Hole Tomography

Roy J. Greenfield
Pennsylvania State University

J-W. Ra
Korea Advanced Institute of Science and Technology

Session 5
Models

Robert M. Duff
Southwest Research Institute

Walter J. Silva
Pacific Engineering and Analysis

Session 6
Other Methods

Christopher P. Cameron
University of Southern Mississippi

Ken Hauser
U.S. Bureau of Mines

Session 7
Case Studies

Richard Lewis
U.S. Army Waterways Engineer Experiment Station

Jerry Wright
U.S. Bureau of Reclamation

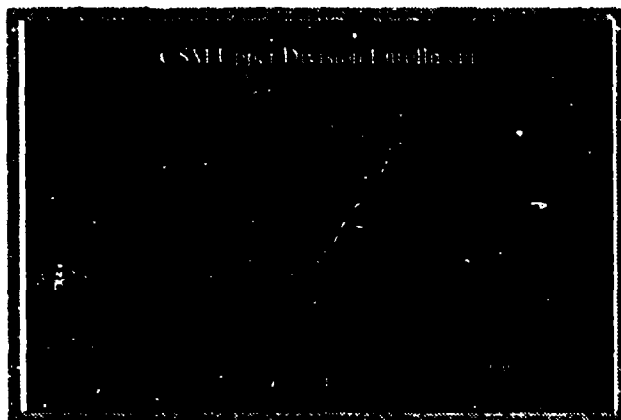
OPENING REMARKS

1993 TUNNEL DETECTION CONFERENCE

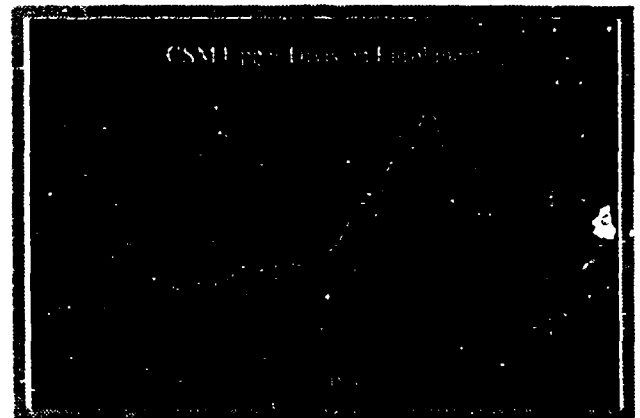
Phillip R. Romig
Department of Geophysics
Colorado School of Mines
April 26, 1993

Good morning, ladies and gentlemen, and may I add my warmest welcome to you. Perhaps it's fitting that these remarks should follow immediately on the heels of Ray Dennis' rather depressing announcement of the termination of the U.S. Army's Tunnel Detection Program after nearly two decades. My message is that, as we look to the future, this is not so much a time for gloom as it is a time for optimism on the part of those foresighted enough to recognize and adapt to the changes that are occurring.

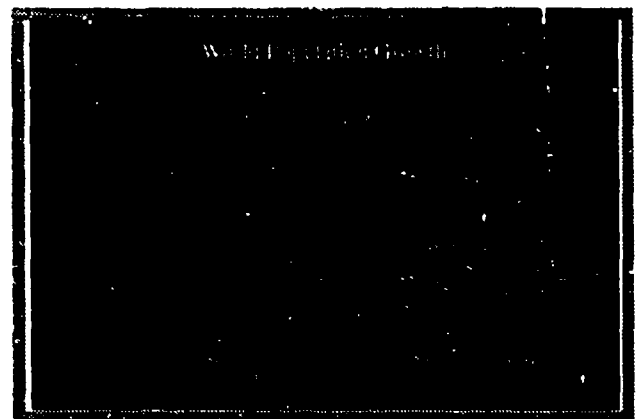
STRATEGIC ISSUES



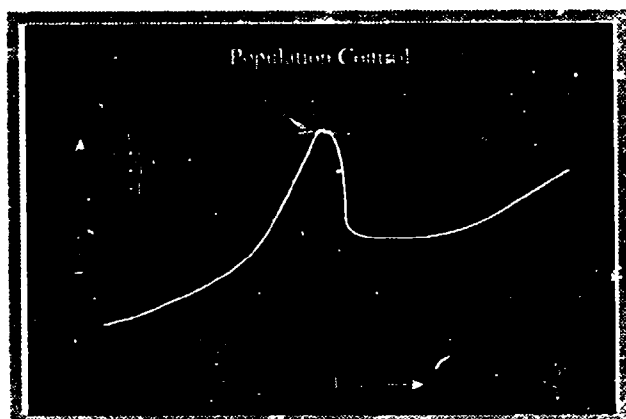
Let me start by trying to persuade you of the hazards of trying to predict the future by extrapolating the past. In order not to embarrass anyone else, I'll pick on our own department. This figure shows the enrollment in geophysics between 1963 and 1983, along with a statement from our 1983 annual report. As you can see, the future seemed one of endless growth and prosperity.



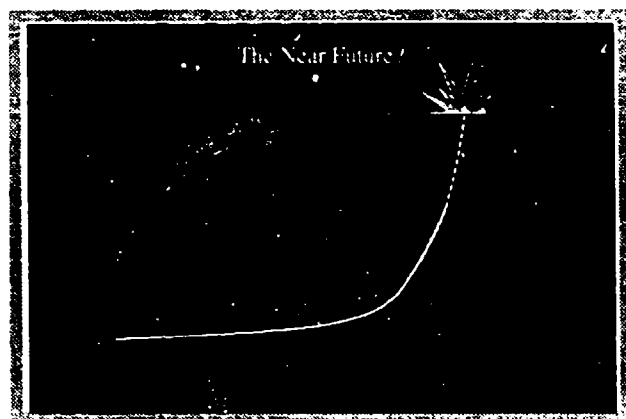
Now look at what happened in the ensuing ten years. Not only was the future not as bright as we hoped, but our enrollment hit one of the lowest points ever. Just as the past did not predict the future ten years ago, so it should not be assumed to predict the future today. How, then, should we plan for the future?



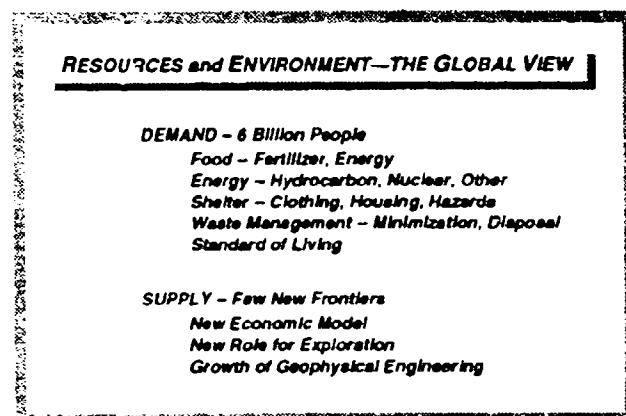
Universities must base their plans on projections of the condition of the world at least ten years into the future -- it takes that long for curricular decisions to begin having an impact on industry and society. If we look that far into the future, then it seems clear to me that one global issue dominates everything else: population. This figure from the AAPG Explorer illustrates graphically what has been happening to the world's population in the century.



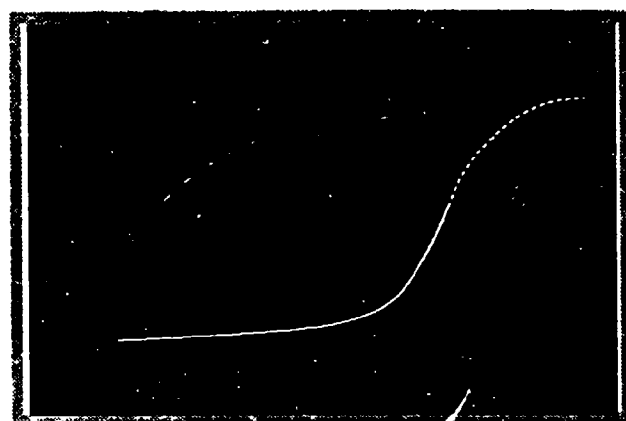
To grasp the significance of the population issue, you also have to include the concept of carrying capacity. There are many examples of what happens when a local population exceeds carrying capacity: for example, the black plague in the 1300s killed 1/3 of the population of Europe.



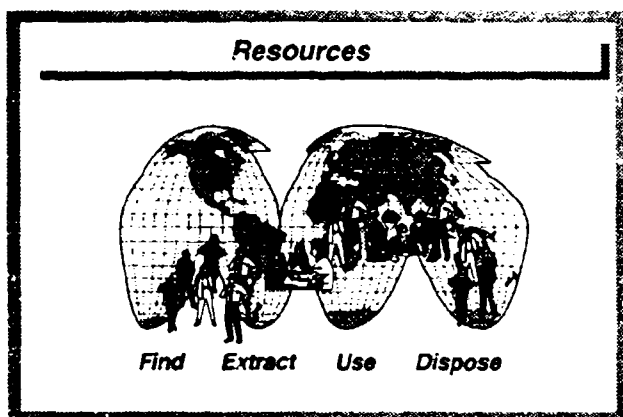
What is fundamentally different about the situation today is that, for the first time in history, we're approaching carrying capacity on a global scale. Always before there has been a "new frontier." 100 years ago, when the eastern U.S. became more crowded, Horace Greeley advised; "Go west, young man." (Of course, the legend conveniently ignores the fact that Greeley was promoting a land development scheme, but that would detract from the story.) When the dust bowl hit the midwest in the 1930s, the farmers and their families moved on to California. Today, however, there is no new frontier to absorb our growing population.



It's not difficult to define what will become the dominant global issues as population approaches carrying capacity. The question for us is: "What role shall we play?"



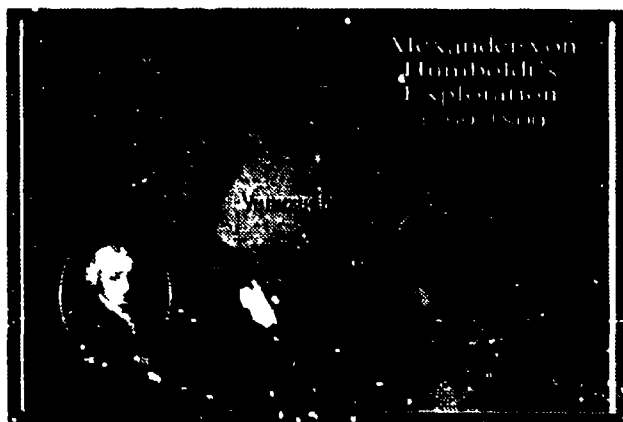
Clearly there are two parts to the solution. The social scientists must find ways to bring the earth's population growth under control. For us, as earth and physical scientists and engineers, the challenge is deceptively simple: either we find ways to increase the carrying capacity of the earth in the short term (i.e. approximately 100 years) and buy time for the population control efforts of the social scientists to take effect, or our global society will suffer disasters of unimaginable proportions.



This, then, is the basis for my statement that the future is one of unlimited opportunity. The greatest challenge -- and obligation -- facing earth scientists will be to find, extract and use the earth's resources to provide a reasonable standard of living for a burgeoning global population without poisoning the air we breath, the water we drink and the food we eat.

TACTICAL ISSUES

Now let's focus on the role of earth-science research, including what you all have been doing for the last two decades in the tunnel detection program. Once again, to do this, we need to consider the fundamental issues involved. In this case, it's necessary to start with some understanding of the history of research.

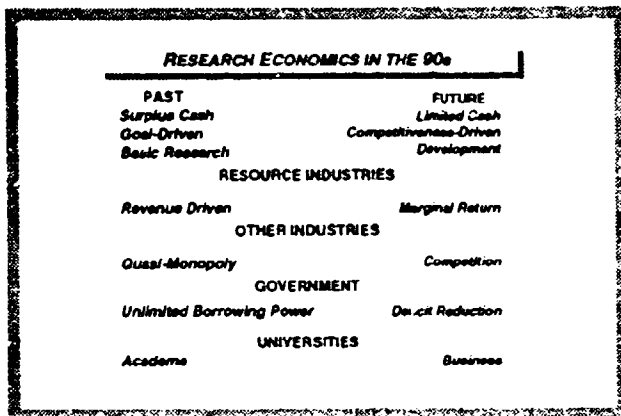


With this slide, it may appear that I'm completely

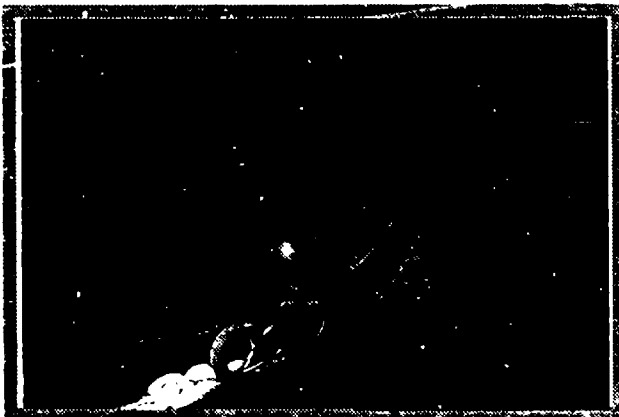
changing the subject, but bear with me for a minute. In addressing the research issue, I need to start back a couple hundred years. This slides illustrates one of the most impressive exploratory expeditions in the history of humanity. In 1799, Alexander Von Humboldt began an epic journey to the new world. During the next few years he explored approximately 24,000 miles of rivers and coastal areas in Venezuela and neighboring countries; he collected 60,000 samples of flora and fauna, and he spent the next 25 years of his life analyzing and reporting the results of that expedition. As impressive as his achievement was, the point of including it in this discussion is that he was able to do it because his parents died and left him independently wealthy. At the tender age of 24, he found himself with virtually unlimited funds and no obligations for the use of his time. This gave him the freedom to choose to explore the new world.



Humboldt was not alone. If you read the history of science, you find that most of the great scientists either were independently wealthy or had a wealthy patron. For a millennium, this has been a basic premise: good research requires the money and the time to stroll leisurely through the forest of life, exploring the side roads and carefully evaluating the obstacles ahead.

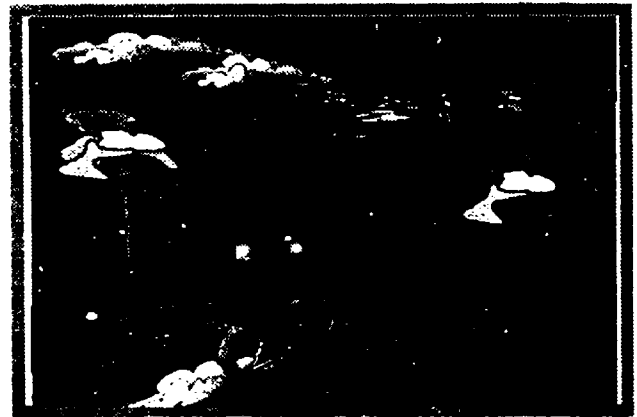


More recently, that money and time were provided by institutions that were able to build excess cash into their budget structures: oil companies had what sometimes have been referred to as "excess profits"; companies such as AT&T and IBM were either de-jure or de-facto monopolies and could build the cost of research into their rate structure, and many governments had unlimited borrowing power. University faculty often had the luxury of free time, which is the equivalent of excess cash.



Unfortunately, today all of this has changed. Just as the driver of a speeding motorcycle must focus intently on the road immediately ahead, so these traditional sources of research funding have been forced by competitive pressures to focus on short-term return. The oil industry has become a marginal-return business where cost control is as important as revenue generation. Bell Labs and Watson Labs have become more concentrated on

technical services rather than basic research. The message of the last election in the U.S. was that deficit reduction is the top priority. The university environment today is every bit as competitive as industry, and university faculty, pre-occupied with generating money and managing workloads, no longer have free time in which to think great thoughts or make revolutionary breakthroughs.



These pressures are changing the fundamental structure of the university and the role of the university in research and development. We need to develop a new kind of partnership between industry, government and the universities that will ensure that we focus on the road ahead and meet the immediate demands of an increasingly competitive world while at the same time providing the passengers who can still be watching for the interesting side roads and warning us of obstacles in the road ahead.

CONCLUSION

My message, then, is that this Workshop is about looking forward, finding solutions to global needs of the 21st century, not looking back at our accomplishments in tunnel detection. For the earth to support 6 billion people in 2000, 7 billion in 2035 and 8 billion by 2050, we are going to have to go underground for more and more of our activities. Doing that will depend on seeing inside the earth, which is precisely what you have been trying to do for the last twenty years. The need for your technology is greater than ever, and I wish you a productive and fruitful conference.

THE DRAGON HEAD METHOD FOR TUNNEL DETECTION AND USING PEMSS DATA FOR DETERMINING GEOLOGY

Frank Ruskey
Research Geophysicist

Text for talk presented at the BRDEC Fourth Tunnel Detection Symposium
Denver, Colorado, April, 1993

ABSTRACT

Often overlooked in the development of innovative geophysical procedures and data analysis techniques is the day-to-day set of circumstances stimulating fruition. These factors are a story in themselves that should be brought out for historical learning. For even though the technology itself is of value and the goal important, ancillary events have a place that is worthy of consideration. Much can be learned from looking at the ancillary aspects of any new idea. Thomas S. Kuhn, in his excellent book, "The Structure of Scientific Revolutions", describes paths of development that were akin to those found in the evolution of the Dragon Head Method and in the use of PEMSS data for determining geology. The Dragon Head Method, originally suggested for the Korea tunnel program by the JASON Committee in 1987, lay dormant for over three years until re-conceived in a moment of inspiration by the on-site technical supervisor, Frank Ruskey. The phenomena itself had been seen by Bureau of Mines researchers as an aberration to their GPR field data about ten years earlier. Gary Olhoeft's suggested use of PEMSS data for determining geology lay dormant for over four years until it eventually became the topic in a related brainstorming session, Korea. The creative geophysics value of these techniques and their development is brought out. These examples show that both the technological aspects and the human nuance aspects of innovative development are fraternal twins and mutually essential. It behooves us to also learn to fine tune these elements in any comprehensive geophysical program.

When Russ Miller asked me last week to give several talks at this symposium, I felt that I should talk about the development of innovative geophysics at least once. Such seems germane at these times of transition in geophysics. It also seems appropriate in light of Phil Romig's excellent talk earlier this morning on the future of geophysics in the twentieth century. Phil's talk was not only good, parts of it reminded me of our own experience over twenty years ago when he, Al Balch, and I first explored the concept of shallow seismics. "Impossible", was the expert advice of those times. "Ground roll will eat your lunch", they cautioned. But the three of us went out and did it anyway. Today we find a growing industry developing around shallow seismics that also holds promise for jobs of the future. There are often breakthroughs resulting when geophysicists and scientists refuse to be inhibited by the man-made constraints of what appears to be the physical world. Thomas S. Kuhn highlights this well in his book on breakthroughs in science. He points out that nearly all new concepts in any technology will inevitably be beset by initial disdain. Kuhn's book is the classic on the topic.

John A. Wheeler, Professor Emeritus at both Princeton and the University of Texas at Austin, has been one of my heroes because of his wisdom, wit and practicality. I'm impressed by his correlating information theory with the act of observation, the quantum, and the ensuing tie to entropy. Entropy, often defined as disorder, or randomness, or "shuffledness" or Chaos Theory, holds promise for being one of the best of today's thought forums for understanding the physical world. Interestingly, and the reason I bring it up, is that it also ties to the mundane such as in creative breakthroughs for geophysics - and any discipline. John's thesis is that entropy, like a quantum event, is tied to the state of mind of the observer. Arising from this is the idea that the potential for any new idea is proportional to one's lack of understanding, and so therefore is the entropy, or apparent chaos of the system. Quantum entropy or chaos can also be found in "The Emperor's New Mind" by the eminent mathematician, Penrose. In his book, Penrose makes the interesting observation, on an out-growth from quantum physics, that for every thought one has there are perhaps millions of parallel thoughts occurring simultaneously with it. At any time we merely focus in on the thought that moment to moment is appropriate for us. I like to think that some of these factors were imbedded in the development scenarios for Dragon Head techniques and for using PEMSS to define geology.

Appropriately, another excellent book of recent vintage by P. Ranganath Nayak and John M. Ketteringham titled, "Breakthroughs!" is recommended reading for the times. Actually for any time, and for any technology. In their book, the authors trace the development of many of today's innovations such as microwave cooking, stick-on labels, walkman tape players and many other useful products that rose to fruition in spite of early rejection and adversity. Managerial and peer disdain, and the concept of not-invented-here, beset each of these breakthroughs. Yet ultimately they succeeded and their promoters, although sometimes lost to history, are always to be emulated. For any new, innovative technology will always be beset by the establishment and the naysayers. So it was in the tunnel detection program, Korea, over the Dragon Head Method, and the use of PEMSS to determine geology.

In his paper this morning, Dave MacLean brought up the excellent work performed by Tim Alleman, Dave himself, and others, on the results of in-line-axis cross bore-hole radar studies, in Korea. Interestingly, I was the initiator of that enterprise. And Col. Kim, ROKA, dubbed it "Dragon Head Method". When I first brought up the concept to Tim and others of our CONUS staff, the idea was summarily rejected as not being feasible. At those early times Tim himself acquiesced to participate in tests on the concept to prove that the idea wouldn't work. The physics of radar propagation would not permit it. Feedback from our experts, in spite of the JASON recommendation, were that the idea was not in conformity with known radar physics. From my recollection of former Bureau of Mines work at Marshall and Gold Hill, Colorado in 1978, I had seen the phenomena occur several times as an aberration in our data. At Marshall we attributed it to the air wave reflecting from a nearby cliff face. Although in retrospect the numbers wouldn't support that. Later at Gold Hill in 1979, while performing a series of radar antenna tests with Tom Lander, Bob Lerner and Royce Brown from MIT, who were under contract from BRDEC, we observed the phenomena increasingly build as we brought our test antennas closer to the test adit opening. The adit went several hundred feet into the side of a hill sloping about thirty degrees and we progressively brought it out to observe attenuation changes at decreasing source to receiver depths. Tom Lander at the time made the remark: "Oh hell, the air wave through the tunnel and back up the slope is masking our through rock transmission results". At the time, for neither of these incidents did we connect with the idea that this air wave transmission could someday be useful. Although totally unrelated to these tests above, I now recall that Larry Stolarczyk developed for the Bureau of Mines a radio communication technique that utilized low frequency transmission through coal mine labyrinths. Ken Stokic also defined the concept in his Ph.D Thesis in the mid 70's. Many clues, many contributors. In any event it all came together for me in a moment of personal inspiration in the middle of the night. I knew it would work and would be useful for tunnel detection, Korea, and elsewhere.

Consequently Tim went up to one of the test sites with the ROKA PEMSS system and I went up to an active site with the TNT PEMSS system. As Tim conducted his tests he observed there was an air wave component transmitting through the tunnel under some separations. Encouraged by this - we kept in touch with each other by telephone for the sites were some twenty miles separated - I observed what appeared to be similar results in my data. I drew the erroneous conclusion that we had indeed found a tunnel. Unfortunately I was basing my judgement on some data that was of the wrong scale and I was fooled by transmission through a considerable section of quartz in the geology. Chris Cameron will appreciate the significance of this. Lessons to be learned in light of my talk theme of creativity in geophysics, and breakthroughs in technology, were that new concepts always work eventually. And secondarily, as it seems to so frequently happen in a new enterprise, the enthusiasm of the moment can sometimes be misleading. But not to be discouraged. Such seems to be the inevitable chaos-like pattern as new concepts emerge. In the early stages of any new technique there will always be a melding of success and disconcerting factors.

In his paper Dave MacLean showed the results of the work by Tim et al. As a first step in the development of the technique the frequencies used and the transmitter to

receiver separations may be conservative and perhaps not optimum, but do provide a proof of concept that is valuable. Lower frequencies such as used by Dr. Ra, KAIST, or by Larry Stolarczyk, in their systems have yet to be used. These lower frequencies may provide the breakthrough impetus for the method that will bring it into full fruition. As always many persons contribute their expertise to creativity in geophysics - or any venture. Dr. Ra, nice to see you made it to this symposium all the way from Korea. You may recall when I gave a talk to your student body in December, 1991, a student asked me what contributions I had been making to geophysics over the past four years. Dragon Head was one of them, but at the time the topic was not discussed in open forum. I'm sure you will understand this now. Further, I hope you will have occasion to try the procedure during some of your tests with your new and promising Wide-Band Phase-Measuring System. Time to wind up tunnel detection at the DMZ. You can be the one to do it.

While the Dragon Head Method and its development represents one form of breakthrough nuance, another was found in Korea that, for many subjective reasons, fell prey to the "not-invented-here" syndrome. I speak here of the potential for determining geology sufficiently from PEMSS (cross bore-hole radar) data using Gary Olhoeft's analysis and presentation method. Chris Cameron will never acknowledge this - will you Chris (?) - but we really needed only a smattering of geology for the man-made tunnel detection program. From the talk this morning by Chris Cameron (et al) we note that awareness of the value of using PEMSS for geologic interpretation has come to fruition. Finally. As with many technological enterprises, it has come into the rightful place as part of an overall melding of various methods for determining geology. Sometimes useful concepts occur through back-door development. Chris' paper highlights this nicely.

From the day Gary first brought up the concept at least four years ago till now, we could have had all the detailed geologic coverage we needed for the problem at hand, with very little additional interpretation effort. As with the radar air-wave we observed back in 1979 and labeled noise, a striking element of Gary's data presentation charts was that they were replete with hole-to-hole geologic information which we ignored or, with arm waving, cast aside since it showed too much geology. Early on we disdained the use of Gary's analysis method because it was, at times, too difficult to interpret in terms of tunnel location. Yet it did describe the geology beautifully. Gary's method is completely described in his paper for the Third Tunnel Detection Symposium in 1988.

In the later days of the program we reverted to the geophysical age-old method of merely interpreting our squiggle traces for tunnel characteristics. Yet at the same time, we emphasized our field geology element and brought in E-logging so that we could develop a comprehensive geologic picture of the DMZ. Not necessary. The eyeball squiggle trace interpretation was excellent in itself, but could have been effectively supplemented by obtaining all the geologic coverage we needed for free from PEMSS. In hindsight, although the issue was brought up several times during 1991 and 1992, the creative aspects of determining geology from PEMSS were deemed inappropriate and subdued. I'm glad to see the results and conclusions of Chris' efforts.

Thus it always seems to be when bringing worthy technology to fruition. The literature cited above highlights this by showing the value of learning to stand back and re-appraise a venture at any time. We can, and should, always re-examine our methodology in context with our avowed goals, especially if we hope to optimize our geophysics for the challenges of the next decade. Phil Romig in his talk this morning provided us with many insights into this process and raised the challenge for us to fine tune our profession and technology development.

Hopefully, we all can learn something by being cognizant of these few historical incidents from the Tunnel Detection Program in Korea. And, in addressing the challenges of the future, we must learn to trust our humanity.

AFTERTHOUGHTS ON ANTICIPATING PROBLEMS AND NURTURING OPPORTUNITY IN GEOPHYSICAL SEARCHES

Frank Ruskey
Research Geophysicist

Text for talk presented at the BRDEC Fourth Tunnel Detection Symposium
Denver, Colorado, April, 1993

ABSTRACT

Anticipating problems and nurturing opportunities is a business concept applicable to tunnel detection and geophysics in general. Geophysical managers who heed this concept are less likely to suffer from "not-invented-here" myopia". The short-sighted pitfall here is one of managerial focusing on existing equipment and techniques rather than on the underlying needs the techniques should satisfy. An important truth in geophysical exploration is that techniques grow and prosper when they satisfy the basic goal of finding the sought-for target; in our case man-made tunnels. Basic goals should be affirmed and re-affirmed.

Geophysical operations managers often develop emotional attachments to equipment and old ways of doing things and are reluctant to drop them. The abandonment of an old procedure, or equipment, is a decision that can too easily be put off until later. An often heard rationalization for not dropping old procedures is that they may make a contribution to something (database archiving, for instance) and thus they should be retained. This argument is valid only if the contribution is significant and cannot be obtained by other means; or, if the assets cannot be diverted to other, more productive uses. Another common rationalization is that an old procedure is needed in order to have a "full-line" of techniques and thus support interesting aspects of the program. In fact, procedures that are not significant contributors to the program goal may actually detract from needed effort on essential techniques.

Some typical examples are presented such as the marginal value of total E-logging and geologic information as it pertains to the sought-for target. While such information may be pertinent to many applications, it may not necessarily be useful, beyond a certain point, for locating man-made tunnels, as operational history in Korea showed. A man-made infiltration tunnel is not geologically dependent! Unlike the case for oil, gas, minerals, etc., the clandestine tunnel is there not because of the geology, but in spite of the geology.

Generally, when you attend a conference of this type, there will be two talks that you will remember in six months, a year, or several years hence. One is your own. Another, thinking in retrospect on this conference, might be one of Phil Romig's thought-provoking talks of the past few days. You may remember a third.

When Russ Miller called me a week or so ago and asked me to give this talk, I was somewhat hard-pressed to know what to speak about. As many of you who have known me over the years recall, I like to talk on such things as human enterprise in science and technology or Chaos Theory applied to both technology and humanity. Over the years I have discovered that there is an intrinsic validity to both of these topics as related to geophysical search. For fundamentally we are human beings with many human characteristics that should not be intellectually subdued but rather, fully exploited. Perhaps, at times, we may be shortchanging our enterprise(s) by not being cognizant of, and using, our human capacity - beyond merely our five senses - supplemented by our technologies as tools of the trade. Merely tools. At times, I believe we raise these tools to heights beyond what is intrinsically of value.

And so I wanted to talk about all these things relating the human elements of "us" that we often forget. "Don't do it, Ruskey," they told me, "give them nuts and bolts. What geophysicists and scientists want to hear about are nuts and bolts". But I wanted to talk about ideas that compare human operations analogously with the computer, wherein the computer keyboard and monitor are comparable to our attributes of speech and logic. While at the same time we neglect or subdue that part of ourselves, again using the computer analogy, that compares with the CPU. I often wonder how effective we could be in solving the geophysical quandaries alluded to by Phil Romig in his fine talks over the past few days, if we were to learn to use more fully, and thus to exploit, our CPU human-capacity characteristics such as intuition, telepathy, ESP, PSI, subconscious creativity and the like. "Don't do it Ruskey," they told me, "give them nuts and bolts."

Nuts and bolts such as the observation that E-logging, beyond a certain point, was not necessary for the enterprise in Korea. E-logging was always of marginal value to the program in the search for man-made tunnels. It aided our understanding of the geology beyond any useful point and sometimes clarified PEMSS interpretation. When the equipment was working, which wasn't very often until the 10th hour days of the search, the information merely abetted our understanding of the geology - which we really didn't need. And, as I brought out in my talk on Monday, we could have had geologic information for free from the PEMSS data with very little additional effort. Plus we would have had a useful zone of interrogation of twenty meters between holes rather than only a meter at most from the logging. (But who in those days wanted to listen to the wisdom of Gary Olhoeft?) While E-logging information may be pertinent to many applications, it may not be necessarily useful, beyond a certain limited point, for locating man-made tunnels. Operational history in Korea over the years has shown this. We should have been aware that our target goal of a man-made infiltration tunnel is not geologically dependent! About the only value we obtained at times from the E-logging data was to confirm that, indeed, those areas where PEMSS responses were distorted were, indeed, areas of high conductivity and the like. So? While in these days some may want to use it for garbage locating, etc., the

tunnel is there, if I may repeat myself, not because of the geology but in spite of the geology. Besides, although subdued, there was a possible health and safety issue that is a story in itself - but not for this talk.

What I had wanted to do in my talk was to try to paint a Chaos Theory, Mandelbrot-like, picture in which the unfolding image, in its final presentation, is the goal rather than the individual fractals. This may be achieved anyway - at least the chaos! Many times Chris Cameron and I tried to get a handle on combining both human capacity and our technologies during various discussions, both CONUS and OCONUS. I know we made some progress in our mutual understanding for both geology, (See, Chris, I really do like some geology!), and human nuances applied to science and technology. Hence, I really wanted to talk about the idea that we are not limited to our five senses of sight, sound, touch, taste, and smell. We have many other unexploited human capacities, some previously named, that we should learn to bring to bear on our geophysics and other technologies. "Don't talk about that, Ruskey," they said, "geophysicists and scientists want to hear only about nuts and bolts."

Such as the idea that, at times, the equipment development of our enterprise became the focus of our endeavor and resulted in many wonderful systems. Some of them great cadillac-like technological marvels. I'm reminded of the SLS and the BITS systems. Both excellent systems, but not practical for the tunnel search problem at hand. Good for college research. They were too complicated and required a near-PhD to run and maintain them rather than just a sharp field technician. And, of course, never a GI - either army. The SLS came overseas during the mid days of the program. Visualize a large five-ton truck with power generator in tow. Whenever reports of below-ground noises were reported either by ROK soldiers or with DSLD readings, up on the hill would go this big behemoth for all to see. Undoubtedly the North Koreans saw it too in all its glory, watched it's personnel scurry about laying out geophone sensor arrays, mounting radio link antennas, and the like. Being at least as smart as we were, the North undoubtedly stopped their drill and blast tunneling until the behemoth was pulled off-line. We had again lost sight of the fact that, unlike in a mineral or oil search, we were dealing with human beings down there who could, and would, countermeasure any of our technological attempts whenever possible.

In his special show-and-tell meeting last night, Chris Cameron showed us some interesting yet disconcerting things about our technological beliefs with PEMSS, our prime tool. Not to steal your thunder, Chris, but what you showed us seems so appropriate for this moment. Chris was able to show us PEMSS data taken at one of our test sites that demonstrated how readily geology, voids, and system setup could thwart our best efforts and equipment responses such that we interpreters could be fooled again and again. Many of our bore-hole pairs could have been across a tunnel yet we could have missed it. What a revelation at this 11th hour of the program!

I see Warren Andrews in the audience. Warren is a good friend and compatriot of twenty years ago when we were both in Toastmasters. Warren, you will remember even then I had the reputation of being an iconoclast in Toastmasters. Yet I was voted in three years in a row as Club President, and later was chosen Area Governor. Someone out there must

have listened to and liked the message. So when Russ asked me to give a talk, I really wanted to talk about such things as what we sometimes call the Real World or Reality. Over the years what I have noticed is that when people, geophysicists and scientists included, talk about Reality they usually are talking about a nebulous, perhaps mystical, Mother Nature. Who, I often ask, is this Mother Nature we give subservience to? Do we not also use the word reality, not really knowing what it is, as a shield of sorts or as a claim to total rightness? When what we are really, and merely, talking about is the world as we personally see it or the world as our group sees it, etc. I'm convinced that if we could learn to be more scientific and objective when using either Real World or Mother Nature in our thinking and scientific talk that we could derive substantive results in trying to address the issues of the twentieth century mentioned in Phil Romig's talks. "Give them nuts and bolts. Ruskey," they cautioned me, "not this other stuff. What they want to hear about is the wisdom of pulling DSLD's off the line when it became obvious that there was no longer active drilling and blasting along the DMZ."

You may recall the DSLD's were a non-manned passive seismic event-recording device. Usually it was set in place where tunneling was suspected to record drill and blast operations twenty-four hours a day. The units were A/C line powered with battery backup. They recorded a sixteen second strong-motion event on tape and awaited other events or the arrival of a civilian technician and military driver to retrieve the tapes once a week or so. The tapes were then taken to the ADP Center for dumping to paper for visual interpretation. Good operational and managerial wisdom dictated that the DSLD's days were probably over for some time. Except for database building and historical record purposes, many recognized there was no longer tunnel search value here. For some reason, we were not always able to apply the same criterion to other aspects of our data gathering as we did for the more obvious DSLD's. When Kent Young of Ft. Belvoir developed these five to eight years ago, they had an operational need and the technology was straightforward. Further, the units can now be modified for other on-going tunnel detection applications. Sure hope the powers that be don't surplus out all of these units. Such a step could indeed be couched as tunnel vision. No pun intended. In any event, this scenario highlighted the operational folly elsewhere of not stopping when we were just gathering data for data's sake. Such continuation of data gathering was not productive for the customer's need for finding tunnels. "That's it, Ruskey, give them nuts and bolts," they said. But I really wanted to talk about other things outside of the realms so appropriate to geophysicists just talking to geophysicists.

For example, I wanted to talk about topics such as visualization and positive thinking, or the concept of self-fulfilling prophecy. In these days of geophysical transition, instead of seeing our future in the noble enterprise of searching for minerals and oil, for instance, we now find ourselves satisfied with searching for and delineating the world's garbage accumulations. Seems like such a comedown for what used to be a frontier occupation at the forefront of practical science applications. If we see our future as being one of locating the world's garbage, we may find our usefulness and technology in just that boat. The law of self-fulfilling prophecy will prevail. Surely there is something better out there for our future. Can we not learn, in quiet moments, to visualize ourselves providing for our industry and the world a revolutionary set of concepts that melds human capacity, technology,

science, earth targets of any type, and economics that will be both useful and inspiring to future generations? Why not? Is not the control of ourselves, our industry, our contribution to life, in our hands?

In one of his excellent talks this week, Phil Romig spoke of a comparison between our technology and value to the world as being similar to that of the medical industry. A good point. The medical world searches out and ferrets out the nuances of the human body. Geophysicists search out the nuances of the earth. The comparison between ourselves and the medical industry may be more all-encompassing than we realize. While it is true that portions of our technology were derived from the medical industry - the time series analysis and tomography come to mind - the other side of the coin may be there too. The medical industry, because of its current propensity to develop technology for technology's sake, often lost sight of its avowed goal to devote itself to curing the ills of humans. (Akin to garbage location processes for geophysics?) The net outcome of this over the years is that the medical industry is often looked upon as an all powerful enemy - to be avoided whenever possible - yet having a hold on us that is out of control. Will we not be looked upon similarly - if we may not already be? In one of my recent experiences with the medical industry let me relate the following: Last year I broke my ankle due to falling from a ladder. I went in for medical attention. X-rays were prescribed and when the results came out I was set down in a chair in a hallway while the doctor, off to the side and out of earshot, looked at the X-rays and explained their nuances with great aplomb to several of his aspiring neophytes. The vibrant conversation they held, with arm waving, was not unlike groups of us at TNT, Korea, looking at and voicing opinions about PEMSS data. A great show and experience for them and their mystical technology while I sat uncomfortably off in the hallway. Finally, the doctor came over and said, "You broke your ankle." I hope we, as a noble industry, can avoid falling into the same technologically-focused trap. We must learn to include the human capacity elements into our science and technology.

But they cautioned, "Don't talk about such things, Ruskey. Give them nuts and bolts. That's what geophysicists and scientists want to hear about." But I wondered if such was perhaps tunnel-like vision, with no intended pun, leading to self-fulfilling prophecy fruition. Which way do we want to go?

"Tell them about database accumulation and the development of the latest in ADP processing as a major thrust rather than concentrating on the avowed goal of finding tunnels." Herein lies an appropriate story in itself. While I always have, and always will, promote and respect the usefulness and power of our ADP tools, I remain convinced that a focusing on such devices as a major goal neither helps the location of tunnels, in our instance, nor does it necessarily meet the best interests of the sponsor. Although not openly defined, a major philosophy we operated under was to acquire the latest available ADP equipment and database programs so that a neat package of information was on readily accessible file and, most importantly, so that our people, when the program terminated, would now be well trained, at the customer's expense, for other company jobs. Is this fair to the sponsor? As events showed, it certainly did not locate any tunnels. While in Korea, I recall waiting for weeks to have processing performed on field data I was interested in, only to be told that delays were inevitable while the new database programs were brought

on-line and massaged. The cart before the horse, I often thought. The search for tunnels, unlike searches for oil, minerals, waste contamination(s), etc., is a chase process - especially when the tunnel makers are still in their creations and are determined to avoid detection. Time is of the essence in a chase program. Database nuances are a luxury to be addressed after the primary goal is satiated. We all had much to learn.

Another strange procedure, from a geophysical prospect-evaluation point of view, we indulged in was to incorporate a military modus-operandi of "tidying up the front". This was based on the wisdom of General Montgomery of World War II fame. Tidying up the front meant using a process of elimination, no pun intended, wherein each subject site was studied - not necessarily to find a tunnel there, although that would be acceptable - but to work at wiping off each site progressively until what remained would surely be the prime site(s). Try selling that to a customer in a search for oil or minerals.

Interestingly, as Chris Cameron's illuminating presentation last evening highlighted, not one tunnel was ever "found" with any of our technologies. Verified but not found. Not one. For in actuality neither tunnels, nor commercial oil and minerals are ever found with geophysical technology or geology. Clues as to likelihood perhaps, but never the find. The only way a tunnel is found is to drill a hole into it and then to send down a bore-hole camera to look around. There is no other way, regardless of what we like to think. Drilling is the essential technique for locating tunnels, such as found in Korea, yet we traditionally gave this procedure short shift in favor of all our special technologies. We missed the boat by dwelling too long on these elements of, often, personal interest. We looked down on the drillers, and their contribution was something of an afterthought.

Hanging on the wall at TNT, Korea, is a classical picture of we experts at our last Panel of Experts gathering. In the picture can be seen the group of us at the DMZ leaning over a vehicle hood with maps - all deeply engrossed in expounding on our personal wisdom of how to use our technologies to find a tunnel. In the background are several ROK Army drills and their drilling personnel busily at work. Here was the final key to the success of our endeavors yet no one went over to talk to the drillers and give them a few words of recognition or encouragement. Not anyone. We experts from the United States could have done much to raise their stature to its essential posture.

In Korea, the drillers are just GI drillers. Judged in their performance by how much hole they make in a given day. Consequently, they push steel for all they are worth with maximum bit pressure regardless of what series of geological formation(s) they are in. (See Chris, I do recognize that geology has a role.) The result is a series of drill holes along the DMZ with unbelievable deviations - some with as much as 60 meters in a 300 meter hole. Besides missing tunnel locations with PEMSS we no doubt missed many with sheer sloppy drilling. Of course, this matter was often discussed over a beer, and we eventually sent over a geologist with one of our drilling experts. Because of his excellent expertise in drilling he was generally aghast at the methods of the ROK drillers - and even referred to them in casual conversation as Gooks - drawing, no doubt, from earlier Korean war terminology. No wonder they were unable to perform professionally. To the Korean driller the geologist was merely another device to keep tabs on their performance, when it could have

been a means for fine tuning drilling. Admittedly with our expert's help drilling did improve and deviations were minimized. But the geologist himself wound up "being in the way" and was later found along the side of the road. Naturally.

By contrast, stateside, I recall from some of my oil patch experience, drillers were accorded high respect. They basked in that and performed accordingly. One time I was sitting on a well helping the geologist - he was not as good as you, Chris. In the background we could noticeably hear the drill rig humming a constant rrrrrr hour after hour. Then suddenly the tone changed slightly. We both jumped up, raced to the rig, and asked the cigar-chomping, grizzled driller if he caught it. Sure enough he had marked his depth chart to show where the change in tone occurred. We waited a while, the tone changed back to the steady rrrrrr, and the depth location was again marked by the driller on his chart. After completing the string we authorized pulling steel, setting a packer and performing a drill-stem test at the recorded interval. And sure enough, we found an oil producing horizon. Basically, the driller found it.

What does this all mean? In view of Phil's talks on the challenges for geophysics in the twentieth century, I contend we have much to ponder. While our professionalism and technologies are great and will evolve incrementally over the years, we will short-change ourselves if we lose sight of the CPU side of our humanity and the dormant inherent capacity therein that should knowingly be developed together with our tools. The quest should be both: "How to build better mouse traps", and "How to completely integrate ourselves with the physical processes at hand". It is not a casual remark to speak of being one with Mother Nature. We are Mother Nature.

Session 1

Ground Penetrating Radar

PEMSS Response of Rock Tunnels to "In-Axis" and Other Nonperpendicular Antennae Orientations

T. J. Alleman
Consultant, Delcambre, LA

C. P. Cameron
The University of Southern Mississippi
Hattiesburg, MS

H. D. Mac Lean
Chem-Nuclear Geotech, Inc.
Grand Junction, CO

Prepared for
Fourth Tunnel Detection Symposium on
Subsurface Exploration Technology
Colorado School of Mines
Golden, CO

April 26-29, 1993

Prepared for U.S. Department of Energy
Grand Junction Projects Office

Prepared by Chem-Nuclear Geotech, Inc.
Grand Junction, CO

Work Performed Under DOE Contract No. DE-AC04-86ID12584 for the U.S. Department of Energy

Abstract

Results of pulsed-electromagnetic search system (PEMSS) experiments conducted at the Tunnel Two Test Pad, Korea, provide proof of concept that the more acute the angle between a tunnel and a borehole pair straddling its axis, the greater the magnitude and the prominence of the PEMSS arrival-time anomaly. These results validate the longitudinal or "in-axis" tunnel detection scheme proposed by J. F. Vesechy, W. A. Nierenberg, and A. M. Despain.

The in-axis tunnel search method deploys cross-borehole radar antennae essentially parallel to the tunnel axis. A series of experiments at the Tunnel Two Test Pad evaluated the effect of the angular relationship between the alignment of a pair of PEMSS boreholes and a known tunnel axis and established that a large PEMSS arrival-time anomaly is sometimes seen using this method. However, an anomaly is observed only if the boreholes are close to the tunnel. Other parameters examined included the effects of (1) the distance of the boreholes to the tunnel wall and (2) the angle between the tunnel axis and the PEMSS borehole alignment that varied from perpendicular to subparallel.

Experiments were conducted with boreholes aligned nearly parallel to the tunnel axis to evaluate the operational feasibility of the longitudinal or in-axis method of PEMSS search and to establish the range of PEMSS signals in typical intrusive granitic types of rock that are indigenous to this part of Korea. PEMSS signals were shown to penetrate as much as 170 meters of granitic rock; however, this figure is highly variable and dependent on site-specific geological conditions.

The presence or absence of PEMSS signals on in-axis PEMSS data records at any given depth is as much a function of local rock mass parameters as is the presence of a tunnel. Careful analysis of any in-axis PEMSS anomaly or feature must be conducted to determine the most likely cause of any observed signal on the PEMSS data record.

The in-axis method is useful primarily as a means of confirming that a void is actually related to a tunnel and for determining the alignment of a tunnel. These experiments established that use of the in-axis method must be restricted to boreholes located within 1 to 5 meters of the tunnel walls. Accordingly, the drill hole spacings in each of two parallel borehole strings must be significantly closer to accommodate a search campaign. In addition, the measuring process is time consuming because of the many combinations of boreholes required to cover a range of tunnel-axis orientations. The method is operationally difficult to execute if adverse terrain and surface conditions are encountered between a pair of widely separated boreholes.

1.0 Introduction

Tests at Countertunnel Three conducted during the first quarter of 1991 stimulated interest in pulsed-electromagnetic search system (PEMSS) results with the antennae oriented at acute angles to a tunnel axis. PEMSS runs over Countertunnel Three were performed to characterize a tunnel signature in the complex, layered Precambrian metamorphic series that underlies substantial portions of the Demilitarized Zone (DMZ) between North and South Korea.

Borehole pair DT-14 to 91-2 crossed the Countertunnel at an acute angle and produced a pronounced arrival time anomaly of about 20 nanoseconds (see Figure 1). This prominent PEMSS response prompted an interest in investigating the effect of the angle between the PEMSS antennae alignment and the tunnel axis and in the special case where antennae alignments are essentially parallel to the tunnel axis. This special case characterizes the "in-axis" or longitudinal detection method first suggested by Vesechy et al. (1980). These authors were prompted by the results and theoretical considerations of Waite and Hill (1977), who described the use of tunnels as electromagnetic (EM) waveguides for communication purposes.

PEMSS experiments with antennae aligned at angles ranging from perpendicular to parallel to the tunnel axis were conducted at the Tunnel Two Test Pad in Korea during August 1991. The numerous boreholes that flank the tunnel at the Test Pad (see Figure 2) permitted experiments that could address three specific issues related to abnormal antennae alignment situations:

- The limiting effect on tunnel detectability of an acute or critical angle existing between the tunnel axis and the line joining PEMSS boreholes.
- The determination of the detectability range of PEMSS signals in granitic types of rock typical of the Korean DMZ.
- The operational feasibility of searching for tunnels using the in-axis method when the PEMSS borehole pair is aligned essentially parallel or at an acute angle to the tunnel axis.

Experiments with the antennae aligned perpendicular to the tunnel axis documented the normal PEMSS response to a tunnel; experiments with the antennae aligned at acute or parallel angles to the tunnel axis provided insights into the responses that could be expected under abnormal alignment situations.

The Tunnel Two Test Pad (Figure 2) is well suited to the performance of PEMSS experiments designed to resolve these issues. A string of closely spaced boreholes along the road leading to the Test Pad provides an ideal situation to determine the range of PEMSS signals in rock. Because of the numerous boreholes at this site, PEMSS antennae/tunnel axis alignments are possible in virtually any desired configuration. The geology of the site is well documented; rock mass characteristics are typical of the intrusive granitic rock mass that underlies portions of the central Korean Peninsula (Goodnight 1986).

The existence of a "critical angle" beyond which all PEMSS energy would be reflected away from a tunnel had not been demonstrated previously but was assumed from considerations of raypath geometry. For the interface between air and rocks typically existing in Korea, this angle is about 20°. However, raypath theory can be applied to EM wave propagation only if the wavelength is substantially smaller than the dimensions of the illuminated surface and if relatively insignificant losses occur in the transmission medium. Neither of these conditions holds for an air-filled tunnel in rock.

The appropriate theoretical model for PEMSS energy transmission in rock is not central to the issues addressed in this discussion, and no particular model is proposed. The purpose in conducting this work is to resolve the critical-angle issue because the existence of an extinction angle would significantly affect cross-borehole radar system deployments. Borehole deviation can result in antennae alignments with suspected tunnel axes that range from moderately acute to almost parallel. The experiments described in this report were intended to provide the desired empirical evidence that would confirm or deny the existence of this extinction angle.

Results obtained from experiments at Countertunnel Three were not sufficiently comprehensive to systematically describe an extinction angle. However, the results aroused suspicion that an extinction angle did not exist and provided the incentive to thoroughly review historical records to further investigate this issue. A review of the PEMSS borehole logs in the Tunnel Neutralization Team (TNT)* files revealed no definitive field examples that might demonstrate the "critical angle" phenomenon.

*The Tunnel Neutralization Team is part of the Tunnel Detection Program of the U.S. Army and is funded by the U.S. Army's Belvoir Research, Development and Engineering Center.

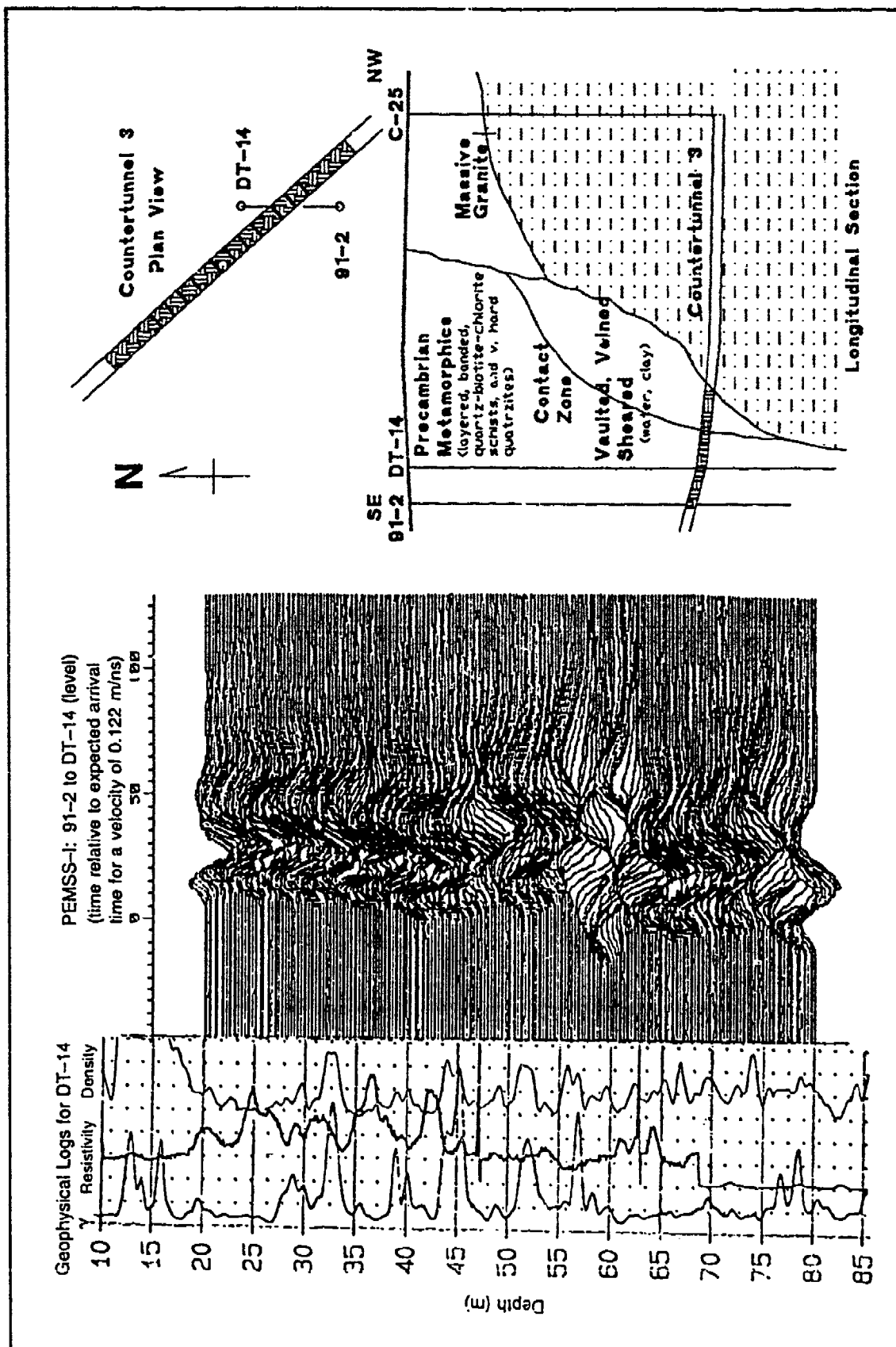


Figure 1. Geophysical Log of Borehole DT-14; PEMSS Data Record for Borehole Pair 91-2 and DT-14; and Plan and Longitudinal Section of Counter Tunnel Three

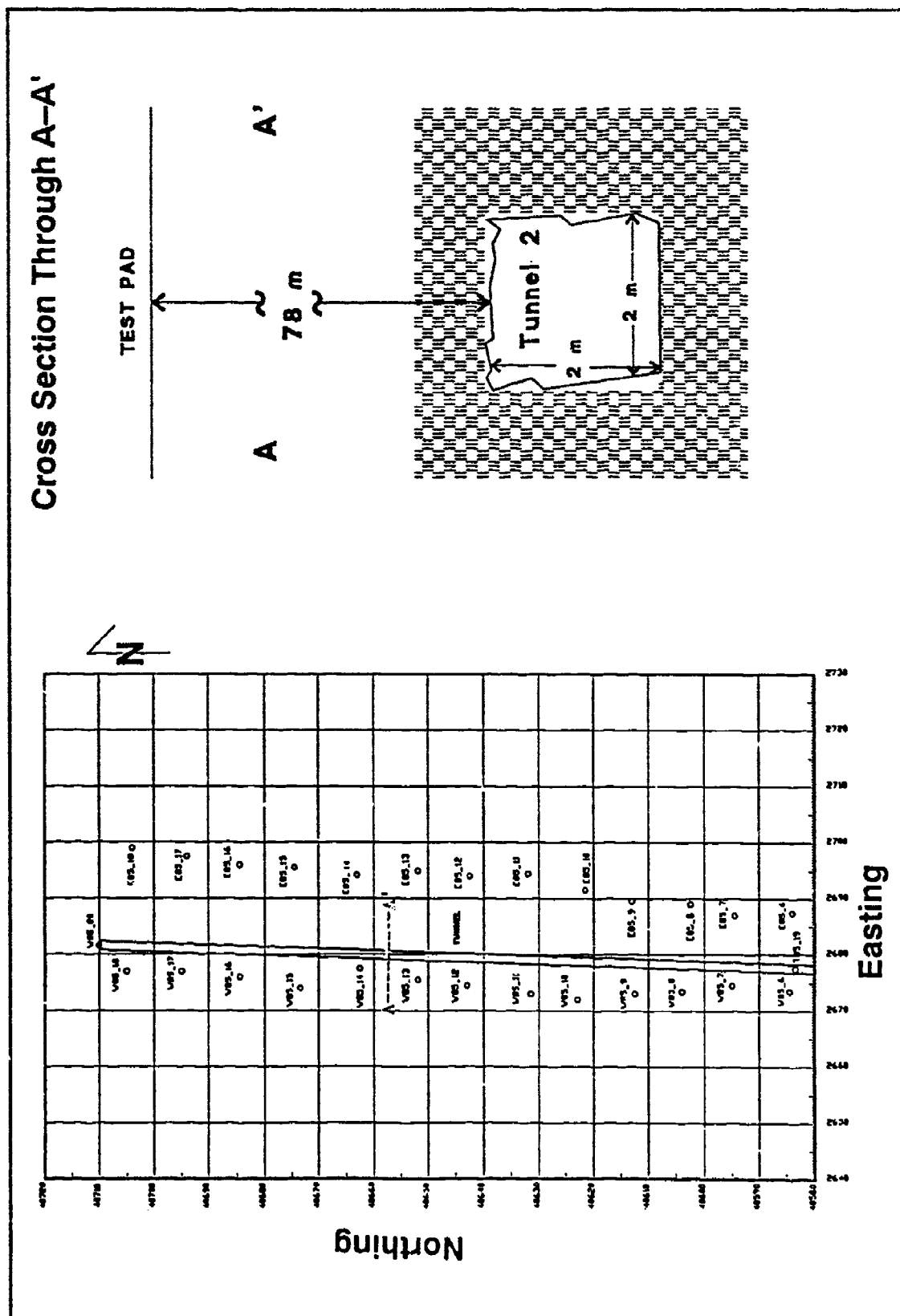


Figure 2. Borehole Locations at Tunnel Two Test Pad and Cross Section A-A'

One example of a PEMSS record taken with the antennae aligned at a substantial angle to the tunnel axis is available in data from the extensive surveys conducted at Tunnel Four. PEMSS surveys at this site in the boreholes shown in Figure 3 provided PEMSS data records for borehole/tunnel axis alignments that vary from perpendicular to acute. The normal or expected tunnel response at the Tunnel Four site is shown in the PEMSS data record from Boreholes 80-14-4 to 80-14-3, shown in Figure 4. These two boreholes are oriented roughly perpendicular to Countertunnel Three. The PEMSS data record for

Boreholes 80-14-5 to 80-14-4, which are aligned at 40° to the tunnel axis, is shown in Figure 5. A much larger arrival time anomaly can be observed on this record (20 versus 9 nanoseconds [ns]). As was observed in a similar situation at Countertunnel Three, the angle of incidence of the raypath between these two boreholes and the tunnel axis certainly exceeds the critical angle for a hard rock/air interface, yet an arrival-time anomaly not only is apparent but exceeds the anomaly observed with the conventional borehole-to-tunnel axis alignment.

2.0 Experimental Method

The effect on the PEMSS records was observed for four variables: (1) distance from the borehole,

(2) incident angle, (3) total separation, and (4) other factors such as tunnel wall and cell conditions. The

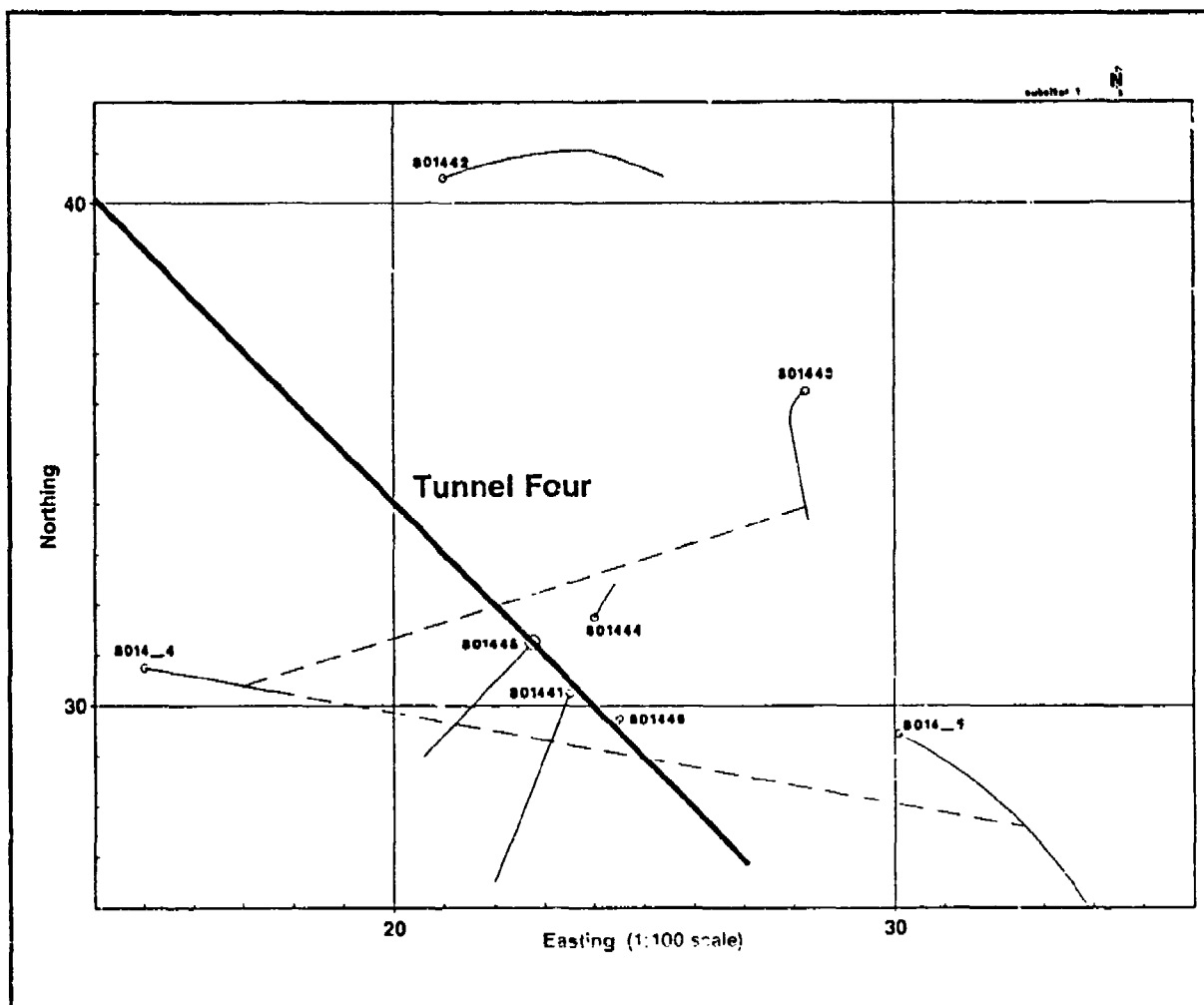


Figure 3. Borehole Locations at Tunnel Four Site

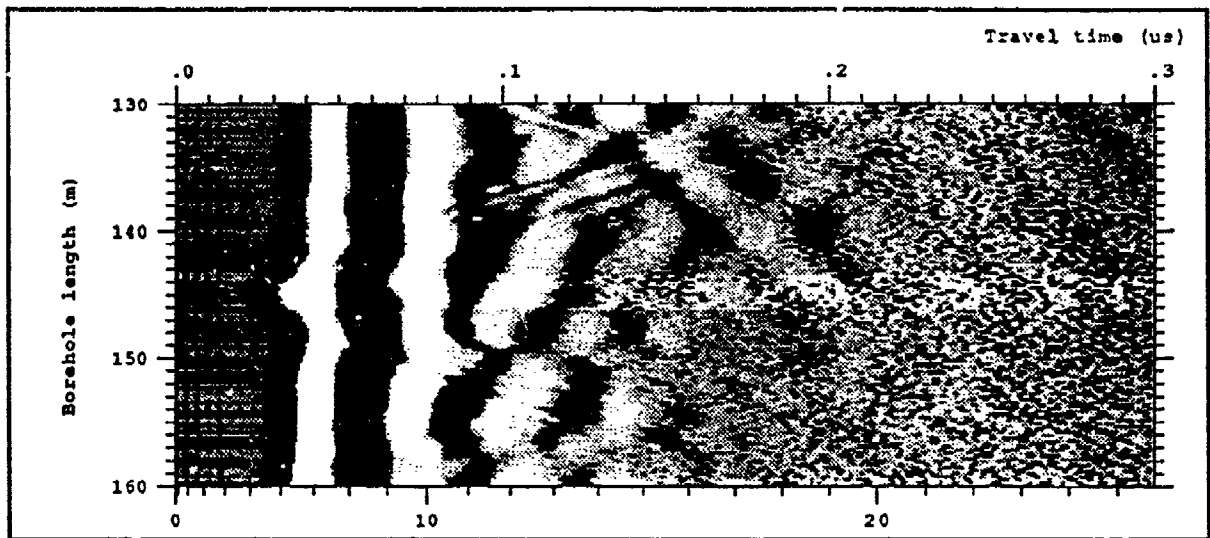


Figure 4. Tunnel Four PEMSS Data Record for Boreholes 80-14-4 to 80-14-3

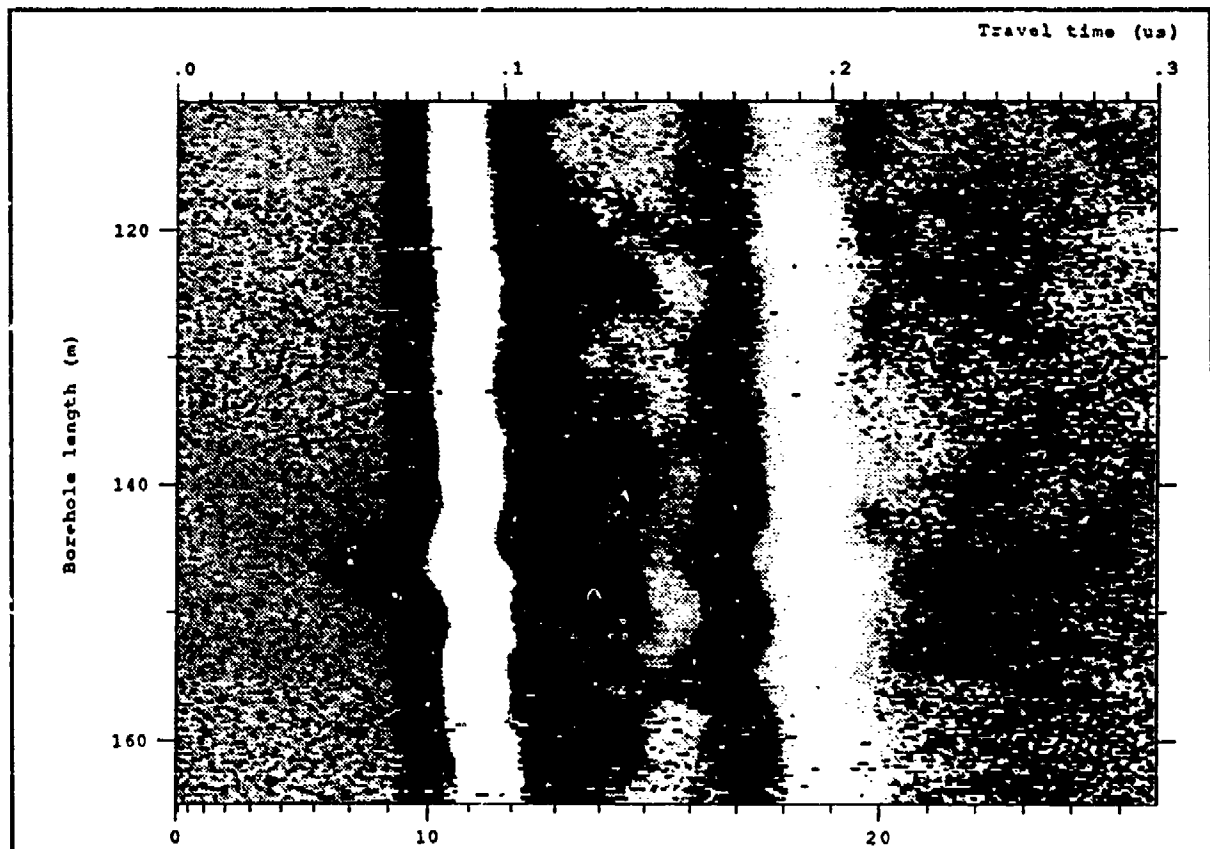


Figure 5. Tunnel Four PEMSS Data Record for Boreholes 80-14-4 to 80-14-5

combinations of raypath/tunnel-axis alignment ensured the inclusion of raypaths subparallel to the tunnel alignment for which the transmitter and the receiver alternately were relatively close to and far from the tunnel wall.

2.1 Effect on Tunnel Detectability of Acute Angles Between Borehole Pair and Tunnel Axis

To observe the effect on the PEMSS anomaly as the PEMSS path crosses the tunnel axis at various angles, PEMSS data were collected for various combinations of boreholes in an area where the tunnel is unobstructed by fill material. Table 1 presents the borehole pairs used and the applicable angle between the incident raypath and the tunnel alignments.

2.2 PEMSS Borehole Alignments Subparallel to Tunnel Axis

Tests were conducted using borehole pairs that did not cross the tunnel axis and were aligned almost parallel to the tunnel axis (see Table 2), as in the longitudinal or in-axis method described by Vesecky et al. (1980). Tests with the antennae relatively far from

the tunnel wall were conducted using boreholes on the east side of the tunnel that are 13 to 18 meters (m) from the tunnel wall. Tests with the antennae relatively close to the tunnel wall used boreholes on the west side of the tunnel that are only 3 to 9 m from the tunnel wall (see Figure 2).

Borehole W85-20 at the Test Pad is of special interest because it is not offset from the axis but actually penetrates the tunnel. This borehole provides an opportunity to observe directly a PEMSS signal passing along a raypath that includes a length of air-filled tunnel with only one segment of the raypath undergoing refraction. The receiver was operated in Borehole W85-20, and the transmitter was placed in Borehole W85-13, located approximately 50 m to the south and adjacent to the tunnel wall. Figure 6 presents the PEMSS data record for this test.

2.3 Range of PEMSS Signals in Rock

The PEMSS range in intrusive granite was determined experimentally using a string of boreholes situated along the road leading to the Test Pad. The PEMSS antennae were separated by a short distance, and the system gain was adjusted so that a signal of

Table 1. Hole Pairs Crossing Tunnel Axis

Transmitter	Receiver	Collar Separation (m)	Axial Distance (m) ^a	Distance to Tunnel (m)		Angle to Tunnel (°) ^b
				Transmitter	Receiver	
W85-18	E85-18	23.7	.3	4.0	17.7	89.3
W85-18	E85-17	24.5	11.9	4.0	15.4	61.0
W85-18	E85-16	29.2	21.9	4.0	13.3	41.5
W85-18	E85-15	36.8	31.5	4.0	13.0	31.2
W85-18	E85-14	46.8	42.4	4.0	13.7	25.0
E85-14	W85-18	46.8	42.4	13.7	4.0	25.0
W85-18	E85-12	67.0	63.9	4.0	14.0	17.4
W85-18	E85-11	74.5	72.1	4.0	12.7	14.6
W85-18	E85-10	86.6	84.5	4.0	12.9	12.6
W85-17	E85-18	25.2	9.1	3.8	17.7	68.9
W85-16	E85-18	33.5	23.0	4.6	17.7	46.6
W85-15	E85-18	39.5	31.3	4.3	17.7	37.5
W85-14	E85-18	47.1	41.2	3.2	17.7	29.1
E85-18	W85-14	47.1	41.2	17.7	3.2	29.1
W85-13	E85-18	59.1	53.4	5.5	17.7	25.3
W85-12	E85-18	68.8	63.6	6.4	17.7	22.4
W85-11	E85-18	79.0	73.8	8.6	17.7	21.0

^aThe distance along the tunnel axis that falls between intercepts of the normals extended from the boreholes to the tunnel axis.

^bThe angle between the line joining the antennae and the tunnel axis.

Table 2. Hole Pairs Subparallel to Tunnel Axis

Transmitter	Receiver	Distance (m)	Axial Distance (m)	Distance to Tunnel (m)		Angle to Tunnel (°)
				Transmitter	Receiver	
E85-18	E85-17	11.8	11.6	17.7	15.4	11.1
E85-18	E85-16	22.0	21.6	17.7	13.3	11.5
E85-15	E85-18	31.5	31.1	13.0	17.7	8.6
E85-14	E85-18	42.3	42.1	13.7	17.7	5.4
E85-12	E85-18	63.8	63.7	14.0	17.7	3.4
E85-18	E85-12	63.8	63.7	17.7	14.0	3.4
E85-11	E85-18	72.0	71.8	12.7	17.7	4.0
E85-18	E85-10	84.3	84.2	17.7	12.9	3.3
W85-17	W85-18	9.4	9.4	3.8	4.0	1.1
W85-16	W85-18	23.3	23.3	4.6	4.0	1.5
W85-15	W85-18	31.6	31.6	4.3	4.0	.5
W85-14	W85-18	41.5	41.5	3.2	4.0	1.1
W85-13	W85-18	53.8	53.8	5.5	4.0	1.6
W85-18	W85-13	53.8	53.8	4.0	5.5	1.6
W85-18	W85-12	64.0	64.0	4.0	6.4	2.2
W85-18	W85-11	74.2	74.1	4.0	8.6	3.5
W85-18	W85-10	83.4	83.4	4.0	4.9	.6
W85-13	W85-20	57.7	57.3	.6	6.9	5.3

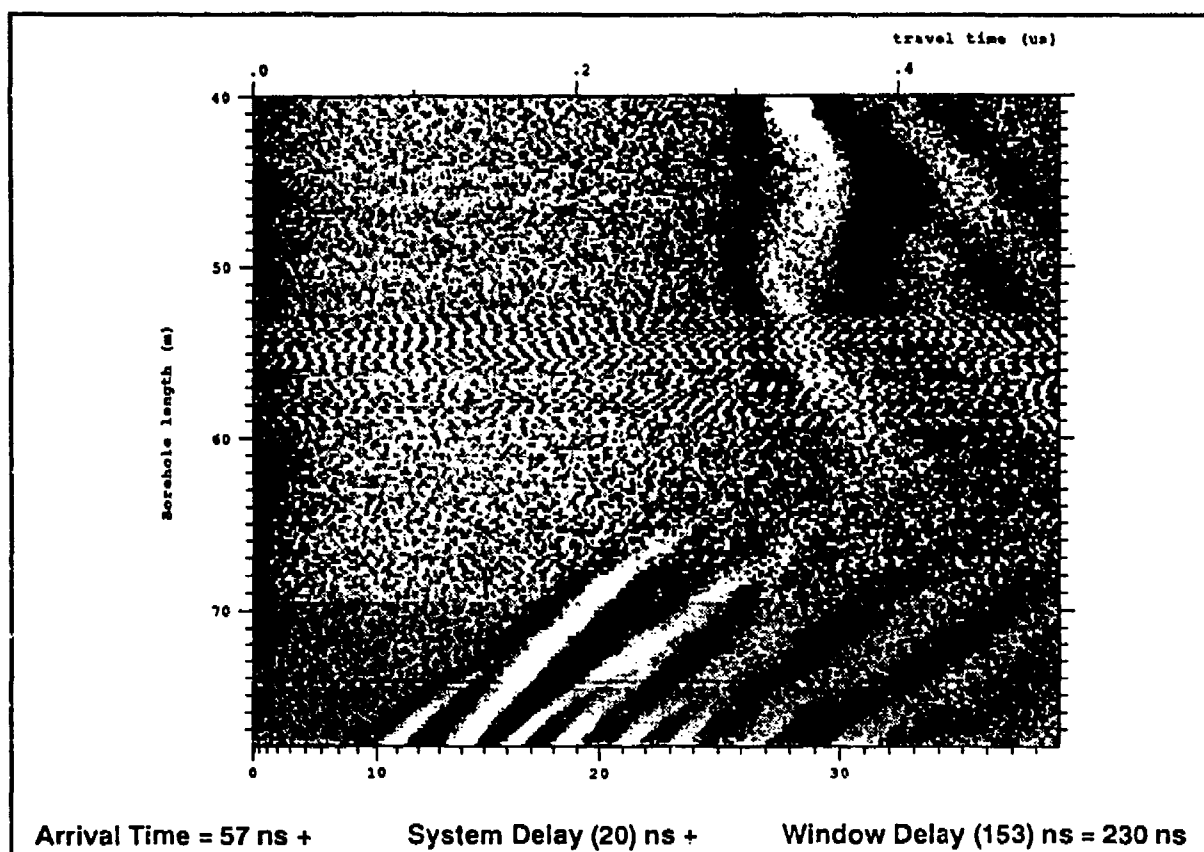


Figure 6. PEMSS Test Pad Data Record for Boreholes W85-13 to W85-20

"standard" amplitude was displayed. For each subsequent increase in antennae separation, the system gain was adjusted to reproduce the same signal amplitude. Thus, the system gain is an inverse indicator of the total signal attenuation. The ultimate range of a PEMSS signal in rock was determined by extrapolating

the separation at which the PEMSS signal would be undetectable. Table 3 presents the separation and signal attenuation in decibels (dB), which are inferred from the system gain, for the borehole pairs used in this experiment.

Table 3. PEMSS Signal Attenuation Test

Transmitter	Receiver	Separation (m)	Attenuation (dB)
88-40	88-39	22.8	-18
88-40	88-37	61.4	10
88-40	88-36	78.8	20
88-40	88-35	97.5	40
88-40	88-32	136.6	73

3.0 Discussion of Results

3.1 Effect of Acute Angles Between PEMSS Raypath and Tunnel Axis Alignment on Tunnel Detectability

PEMSS records were made with the antennae located on opposite sides of the tunnel at angles ranging from normal to acute, as shown in Figure 7. The PEMSS data records for these experiments are shown in Figures 8a through 8d. A complete set of PEMSS data records for all of the borehole combinations listed in Table 4 are in Alleman et al. (in preparation), which describes these tests in detail. Significant results summarized in Table 4 show

- The arrival time anomaly increases with increasingly acute incidence angles.
- The largest arrival time anomalies are observed at the highest incidence angle.

The PEMSS signal transit time can be calculated for this model using typical rock velocities and the simple refraction and reflection previously described; algorithms to calculate PEMSS signal travel times for these models are in Appendix A. Table 4 presents PEMSS signal travel times calculated for simple reflection and refraction models.

Analyses of the arrival-time anomalies listed in Table 4 also suggest that the raypath followed by the PEMSS signal is not a simple refraction at the tunnel wall as shown in Figure 9. For at least the lower

incident angles, the PEMSS signal appears to follow a longer path and is reflected alternately from the tunnel walls as shown in Figure 10. Using an angle of reflection of 55°, the path length of each reflected segment is about 3.5 meters (m). For a tunnel cross section of 2 m, the wave just fits in the tunnel. The frequency of this signal is 43 megahertz (MHz), which is consistent with the PEMSS operating frequency.

The PEMSS data record for the runs made with one of the PEMSS antennae located in the tunnel (W85-13 to W85-20) is shown in Figure 6. The time of flight of the signal indicated by the arrival time of 230 ns is inconsistent with the calculated arrival time of 285 ns for a ray that follows the simple refraction model. A more complex path involving multiple reflections off the tunnel wall is suggested.

The observed travel indicates that the tunnel is acting as a waveguide. The PEMSS signal enters the tunnel and is propagated within the tunnel as a standing wave. Nodes of the wave energy lie on the tunnel wall, thus minimizing attenuation. This signal is then more readily detected by the receiver than signals that follow other raypaths. The raypath followed by the signal that is recognized as the first arrival at the receiver depends as much on the strength of the signal as on the minimum time path. The path of the first arrival signal that is recorded at the receiver can be inferred for other geometries by comparing observed arrival times with the calculated transit time for the simple refraction and guided wave models.

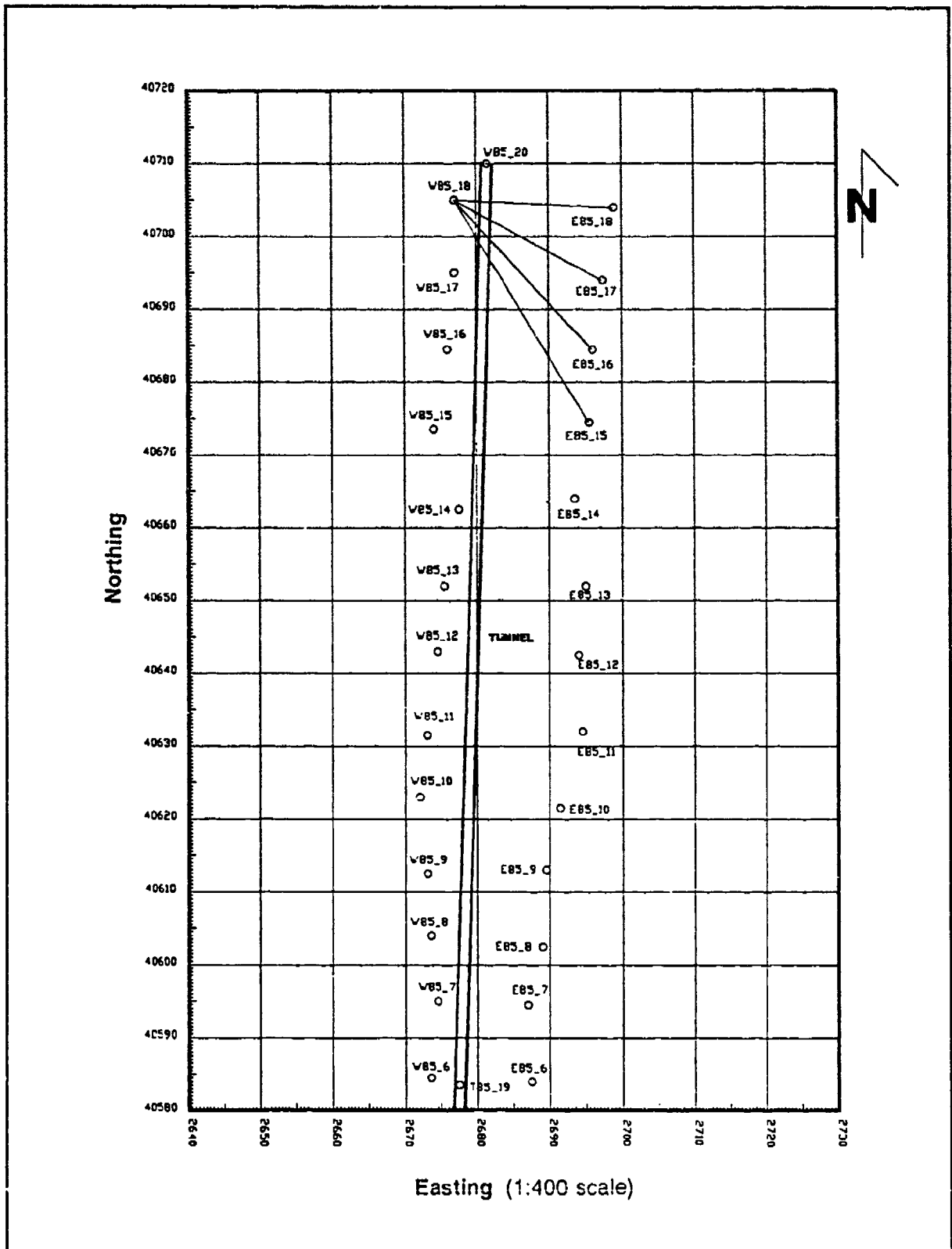


Figure 7. Cross-Borehole PEMSS Surveys Made at Test Pad To Evaluate Effects of an Acute Angle Between Line Joining PEMSS Antennae and Tunnel Axis

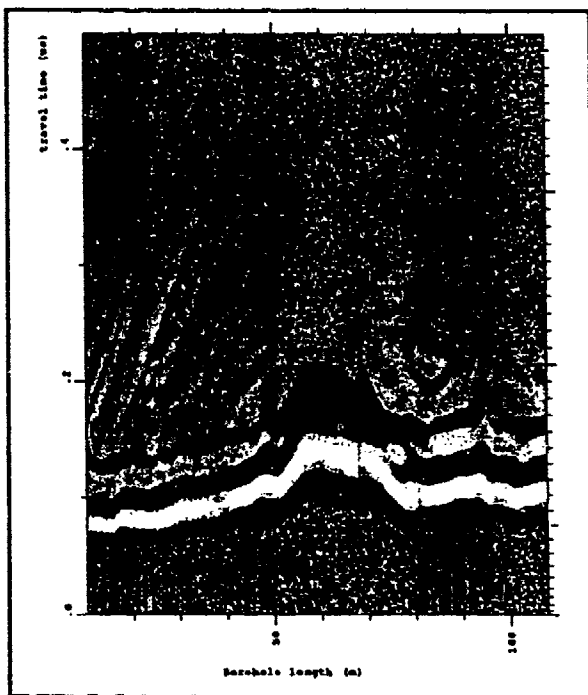


Figure 8a. PEMSS Test Pad Data Record;
Boreholes W85-18 to E85-18

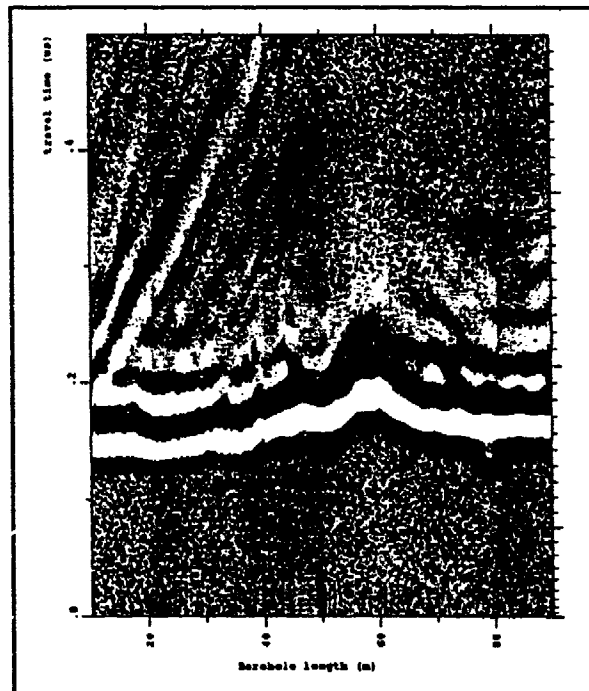


Figure 8b. PEMSS Test Pad Data Record;
Boreholes W85-18 to E85-17

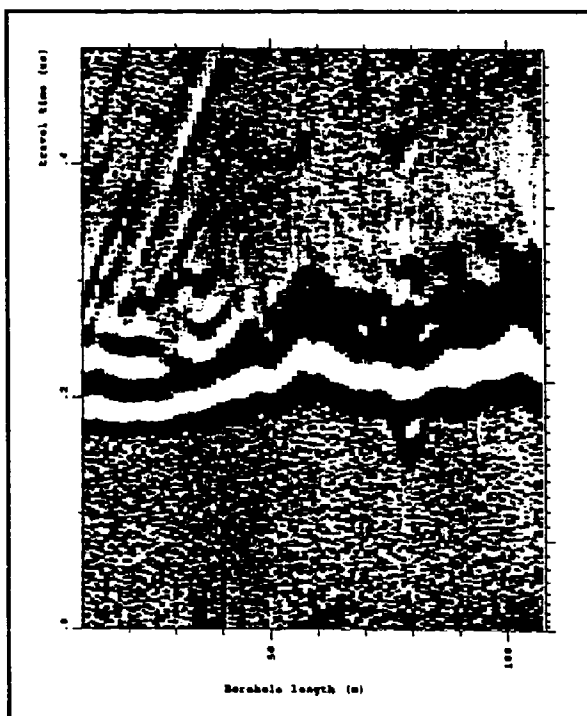


Figure 8c. PEMSS Test Pad Data Record;
Boreholes W85-18 to E85-16

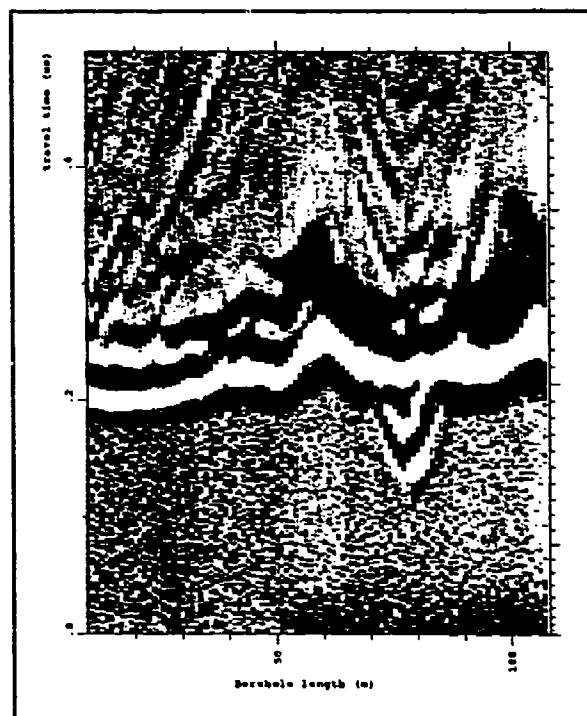


Figure 8d. PEMSS Test Pad Data Record;
Boreholes W85-18 to E85-15

Table 4. Observed and Calculated PEMSS Arrival Times for Refraction and Multiple Reflection Transmission Modes

Transmitter	Receiver	Separation (m)	Angle to Tunnel (°)	Observed Anomaly (ns)	Predicted Anomaly (ns)	
					Waveguide	Refraction
Hole Pairs Crossing Tunnel Axis						
W85-18	E85-18	24	89	12	NA	11
W85-18	E85-17	25	61	19	17	17
W85-18	E85-16	29	42	48	35	44
W85-18	E85-15	37	31	85	64	82
W85-18	E85-14	47	25	124	102	130
W85-18	E85-12	67	17	182	190	236
W85-18	E85-11	75	15	238	238	286
W85-18	E85-10	87	13	255 ^a	296	351
W85-17	E85-18	25	69	14	16	13
W85-16	E85-18	34	47	18	28	37
W85-15	E85-18	40	38	21	46	66
W85-14	E85-18	47	29	50	81	110
W85-13	E85-18	59	25	^b	120	157
W85-12	E85-18	69	22	124 ^a	163	203
W85-11	E85-18	79	21	117 ^a	192	241
Hole Pairs Subparallel to Tunnel Axis						
E85-18	E85-17	12	11	^c	^c	^c
E85-18	E85-16	22	12	^c	^c	^c
E85-15	E85-18	32	9	^c	^c	^c
E85-14	E85-18	42	5	^c	^c	^c
E85-12	E85-18	64	3	^c	57	95
E85-11	E85-18	72	4	^c	104	152
E85-18	E85-10	84	3	^c	163	219
W85-17	W85-18	9	1	^c	^c	^c
W85-16	W85-18	23	2	42	41	59
W85-15	W85-18	32	1	100	87	108
W85-14	W85-18	42	1	156	142	173
W85-13	W85-18	54	2	182	184	222
W85-18	W85-12	64	2	229	224	272
W85-18	W85-11	74	4	260	261	311
W85-18	W85-10	83	1	327 ^a	334	393
W85-9	W85-18	92	0	350 ^a	383	452

^aTimes picked are uncertain; low signal-to-noise ratio.

^bAnomaly seen but signal-to-noise ratio is too low to pick times.

^cObserved anomaly—no anomaly seen. Predicted anomaly—tunnel arrival is later than rock arrival.

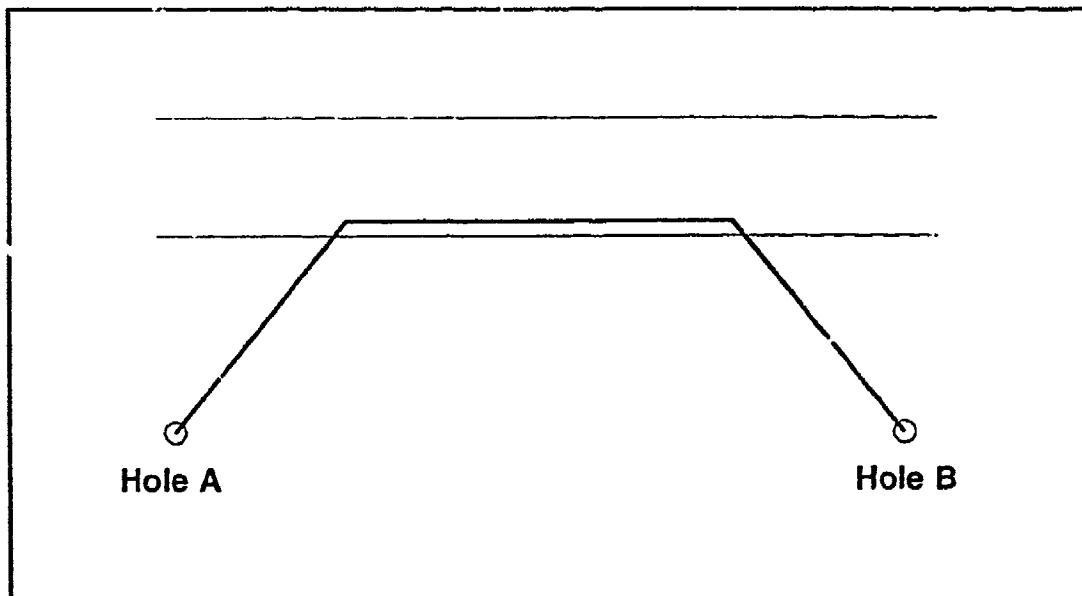


Figure 9. PEMSS Signal Transmittal by Simple Refraction

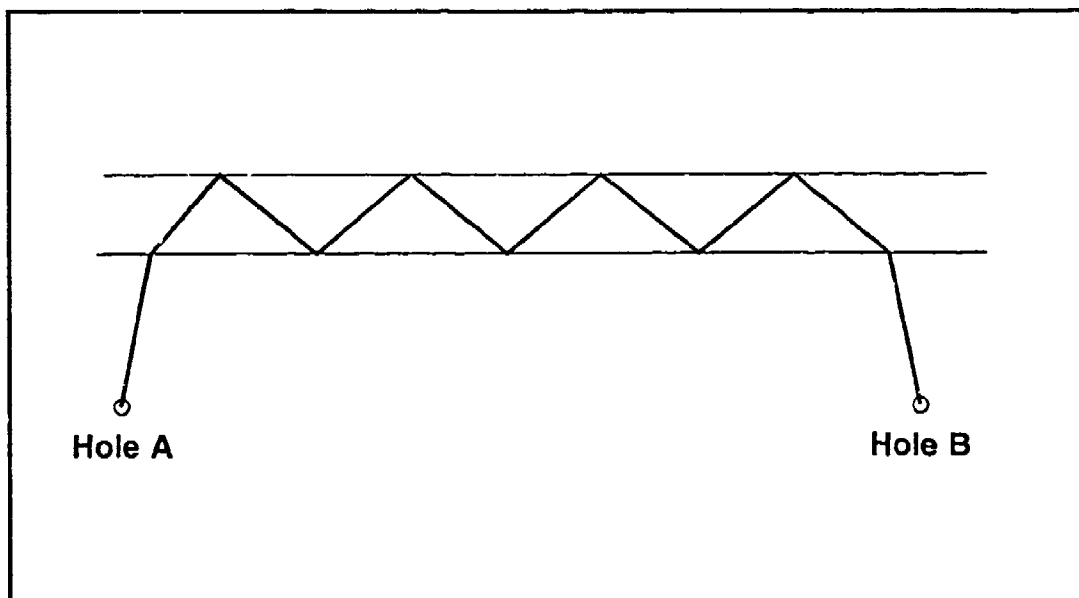


Figure 10. PEMSS Signal Transmittal by Multiple Reflections

PEMSS signal transit times and predicted arrival time anomalies calculated for single refraction and multiple reflection transmission models are given in Table 4. Comparison of observed arrival times with the calculated times for various transmission models provides empirical evidence to support the actual mode of PEMSS signal transmission in the tunnel.

Study of Table 4 indicates that for high angles between the borehole alignment and the tunnel axis (low-incident angles), the observed PEMSS arrival times and the calculated time for a simple refraction raypath are in reasonable agreement. However, as this angle gets smaller (angle of incidence increases), the travel time calculated for the waveguide models appears to better conform to the observed travel times. The waveguide travel path fits the observed arrival times when the angle between the boreholes and the tunnel axis is 17° or less. Stated in another way, the PEMSS signal follows a simple refracted raypath if the incident ray angle is 73° or less; the waveguide model appears to be more appropriate for incident angles greater than 73° . In all probability, signals following both raypaths are present at the receiver for all configurations. The signal recognized as the first arrival will be whichever signal is significantly above the noise level for a particular geometry.

3.2 Evaluation of In-Axis Method; Hole Pairs Subparallel to Tunnel Axis

None of the data records from boreholes on the east side of the tunnel (15 to 17 m from the axis) show a discernable arrival-time anomaly. Representative data records from surveys conducted on the east side of the tunnel were extracted from Alleman et al. (in preparation) and are presented in Figure 11. However, prominent arrival-time anomalies at tunnel depth can be seen in the PEMSS data records of hole pairs situated on the west side of the tunnel; significant examples are shown in Figure 12. All of these boreholes are located 2 to 5 m from the tunnel wall. Clearly, the arrival time anomaly associated with the tunnel increases as the distance between the boreholes and the tunnel decreases.

3.3 Range of PEMSS Signals in Rock

The range of PEMSS signals in the type of rock (granite) that is characteristic of the Test Pad area was measured by incrementally increasing the

transmitter-to-receiver separation in a string of boreholes drilled along the road used to access the Test Pad. The maximum range was estimated by extrapolating the separation at which the attenuated PEMSS signal was no longer detectable. In practice, this occurs at the point where the signal gain is elevated to the point where noise dominates the PEMSS record and no coherent signal can be detected.

The signal attenuation expressed in terms of the gain required to recognize a coherent PEMSS signal is noted in Table 1 for each antenna separation used in the PEMSS range test. The relationship between distance and attenuation is semilogarithmic. Therefore, if separation is plotted in meters and the attenuation in decibels, the relationship should be nearly linear. The separation and attenuation information tabulated in Table 1 are plotted in Figure 13. A linear relationship between the PEMSS signal strength or attenuation and the path length in rock is obvious. The two lines on the figure represent an envelope that includes all attenuation measurements made during these experiments.

PEMSS operators generally accept that the maximum signal gain that can be employed before the records are dominated by noise is 60 to 70 dB for most of the rock mass of the Korean DMZ. For signal gains in excess of 60 dB, the signal response must be averaged (stacked). The upper limit for stacking the signal is 100 dB. By projecting the interpreted attenuation to 100 dB for the hard, homogeneous granite rock mass at Tunnel Two, 170 m is the maximum thickness of this rock through which PEMSS signals can penetrate.

Analyses of the amplitudes of the PEMSS data records and those shown in Figure 13 reveal that the signal which follows the tunnel alignment has about the same, or only slightly greater, strength than the signal that propagates directly through rock. However, a small portion of the wave energy traveling along a tunnel will be lost because of interaction with the tunnel wall. The reasonable expectation is that the attenuation of PEMSS signals traveling along an air-filled tunnel is nearly constant at all tunnel sites. This attenuation will be approximately equal to the attenuation through an equal thickness of granite at the Test Pad. Further, it is apparent that the path length through this low porosity granite appears to be the maximum achievable path length in rock.

The attenuation of PEMSS signals traveling through other types of rock will vary over a wide range but will be greater than that observed in granite at the Test Pad, particularly in the layered gneisses and schists that are abundant in the widespread

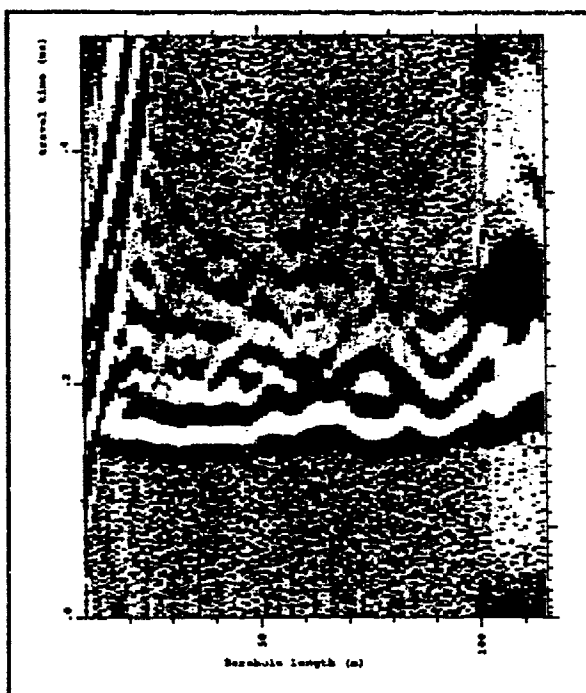


Figure 11a. PEMSS Test Pad Data Record;
Boreholes E85-15 to E85-18

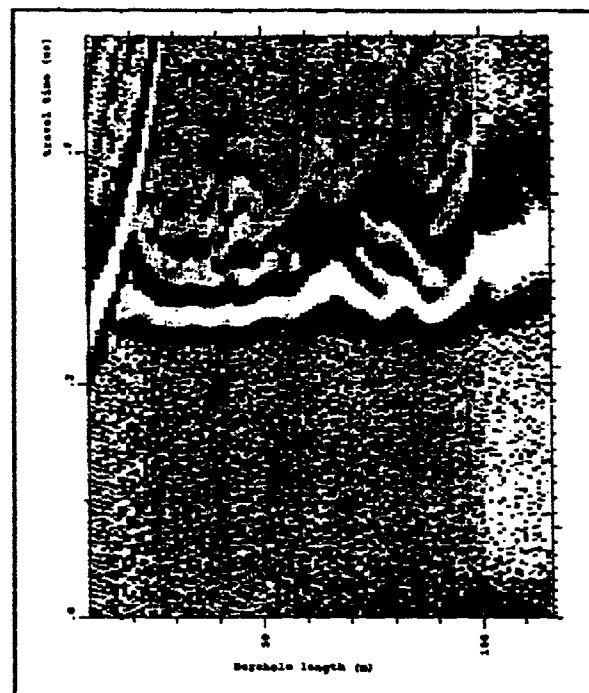


Figure 11b. PEMSS Test Pad Data Record;
Boreholes E85-14 to E85-18

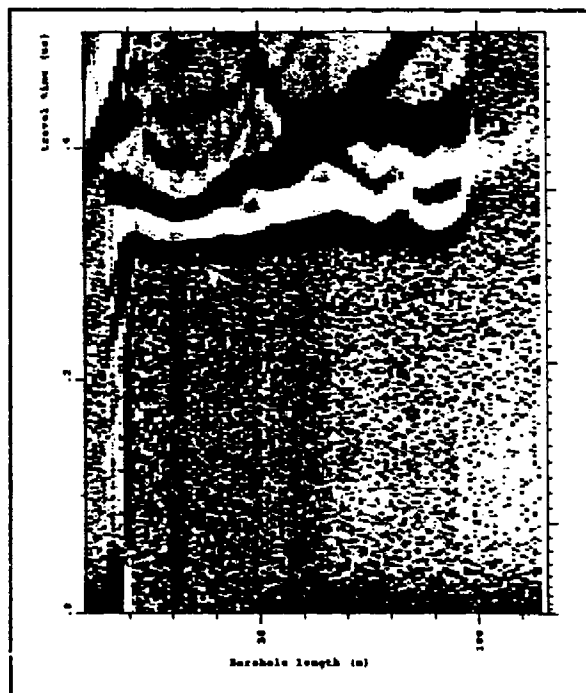


Figure 11c. PEMSS Test Pad Data Record;
Boreholes E85-12 to E85-18

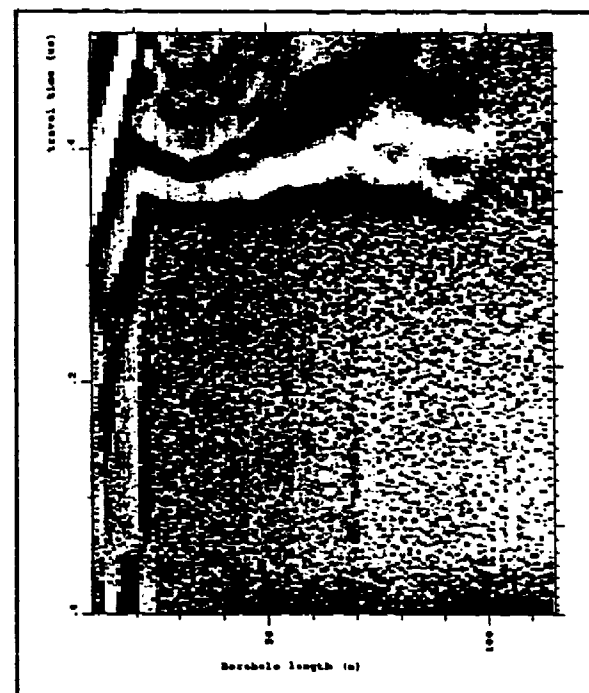


Figure 11d. PEMSS Test Pad Data Record;
Boreholes E85-11 to E85-18

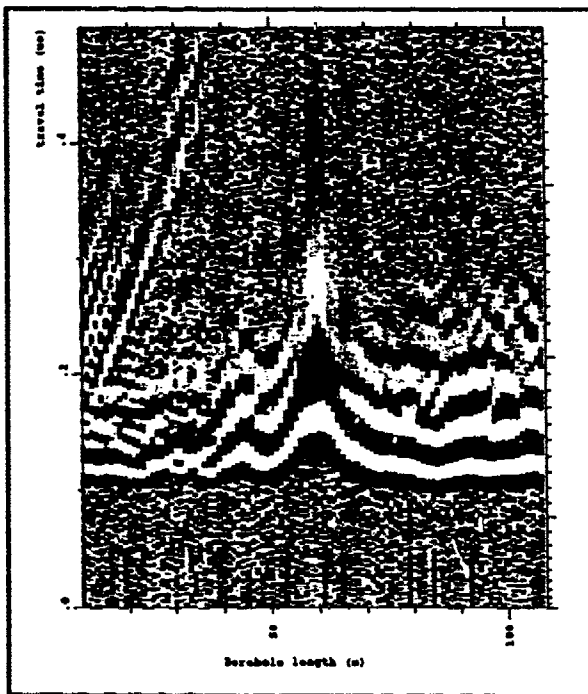


Figure 12a. PEMSS Test Pad Data Record;
Boreholes W85-17 to W85-18

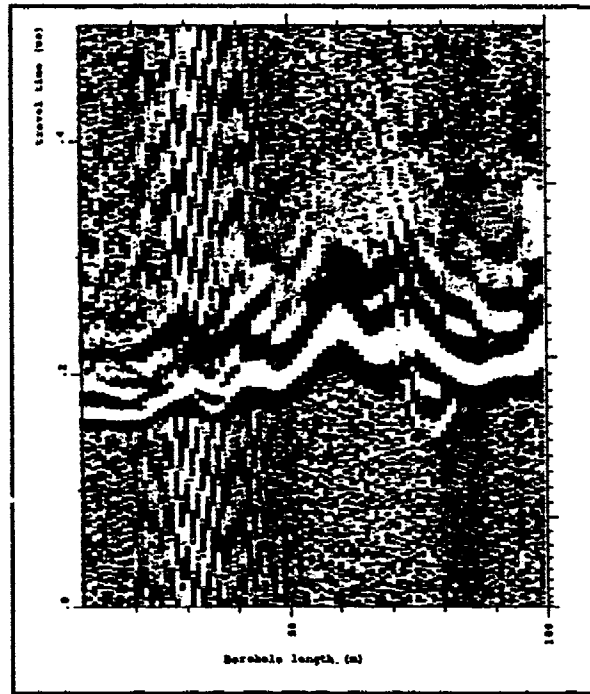


Figure 12b. PEMSS Test Pad Data Record;
Boreholes W85-16 to W85-18

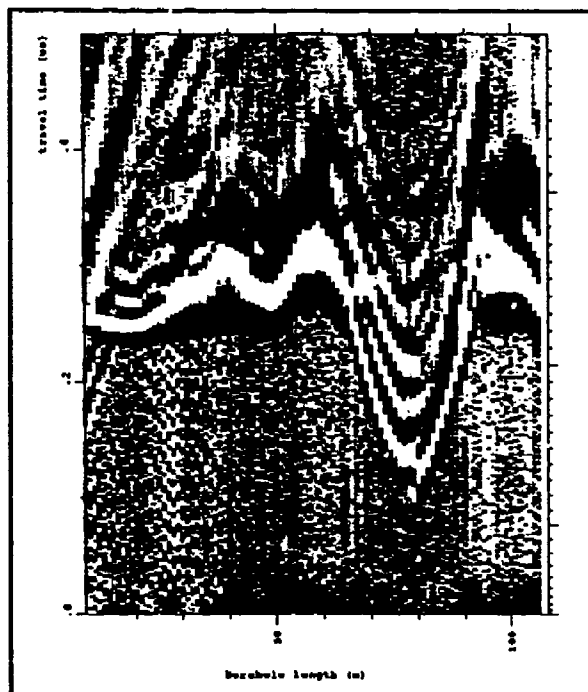


Figure 12c. PEMSS Test Pad Data Record;
Boreholes W85-14 to W85-18

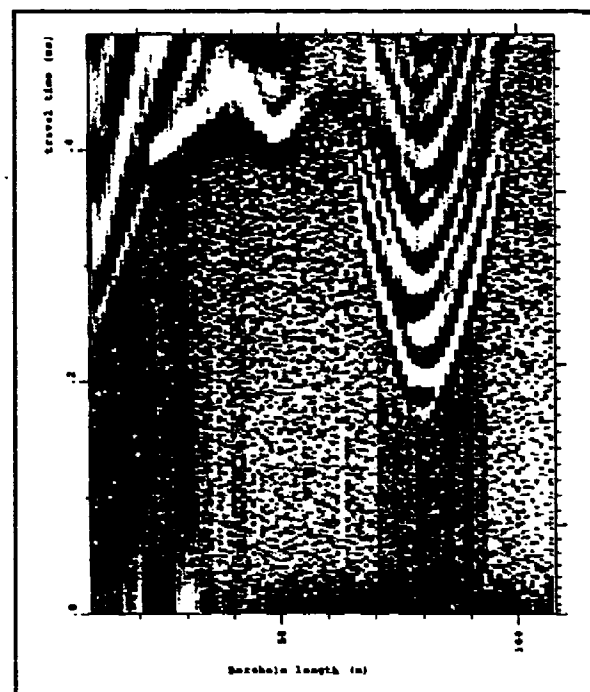


Figure 12d. PEMSS Test Pad Data Record;
Boreholes W85-18 to W85-12

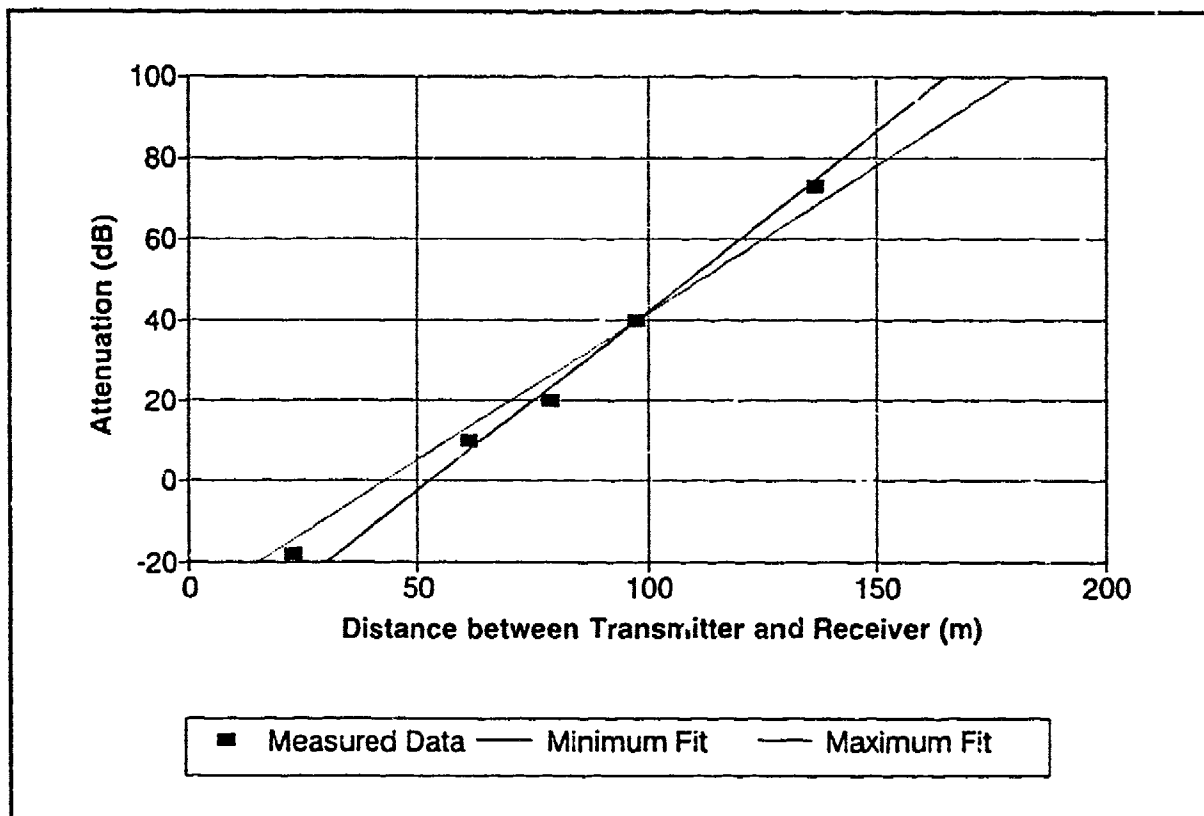


Figure 13. PEMSS Signal Range in Test Pad Granite

metamorphic terranes in this region. Accordingly, the 20-m hole spacing normally used for PEMSS searches would probably be inadequate to support the in-axis method at sites with layered gneisses and schists. The minimum separation of boreholes at other sites can be estimated from the relative attenuation at a given search site compared with the attenuation observed in the granite at the Test Pad. If the attenuation at a site is greater, the borehole spacing must be closer than the spacing that was effective at the Test Pad.

These PEMSS results suggest that the in-axis method of PEMSS search is viable in rocks similar to the granite at the Test Pad if the two borehole strings

are separated by about 50 m and the spacing between the boreholes is no more than 10 to 15 m. At many sites, especially where the target is at considerable depth, this spacing distance is an onerous restriction because it is difficult to maintain a constant borehole separation over a substantial depth range. Moreover, the in-axis method requires an additional parallel borehole string with the separation between adjacent boreholes at tunnel depth to be no greater than 10 to 15 m. Compared with a conventional cross-borehole search pattern, the number of boreholes drilled within a search site would have to be increased fourfold!

4.0 Conclusions

Recognition of a PEMSS signal that has apparently traversed 100 m or more in rock is not an indication that an air-filled tunnel was included in the PEMSS signal raypath. Data from the experiments described in this report indicate that PEMSS signals can penetrate through as much as 170 m of hard, homogeneous

granite, but this figure is highly variable and dependent on site-specific geological conditions.

These experiments show that the PEMSS arrival-time anomaly increases as the angle between the borehole alignment and tunnel axis decreases. The largest arrival-time anomalies are observed when the

angle between the line joining two PEMSS boreholes and the tunnel axis alignment is very acute.

Use of the in-axis search method produces substantial arrival-time anomalies, but only when both the transmitter and receiver antennae are close to the tunnel. To produce these anomalies, the cumulative distance of both boreholes from the tunnel wall must be less than 10 to 15 m.

The results of these experiments indicate that the in-axis search method offers significant potential as a means to verify that an indicated void is a tunnel and to determine the alignment of this tunnel. However, the method generally is not practical for use as a primary search method because of the requirement to drill two rows of closely spaced boreholes and the difficulty of operating the transmitter and receiver antennae at widely separated locations over rough terrain.

5.0 Acknowledgments

The successful completion of the tests described in this report was made possible by the enthusiastic encouragement and support provided by Mr. Frank Ruslavy, Tunnel Neutralization Team (TNT) Technical Supervisor. Mr. John Kielty merits equal gratitude. Mr. Kielty, TNT PEMSS operator and electronics technician, first brought the Countertunnel Three results to our attention and then provided long hours and arduous effort to produce the high-quality Tunnel Two field data referenced in this report. Appreciation is extended to Mr. Bruce Walker and to Mr. Keum Chul Shin of TNT for their efforts in the large amount of

data production needed for this study. Mr. James Allen of Chem-Nuclear Geotech, Inc., provided thoughtful reviews and helpful comments during manuscript and report preparation.

This work is part of the operations and research conducted by the Tunnel Detection Program of the U.S. Army and was performed under U.S. Department of Energy Contract No. DE-AC04-86ID12584 with funding provided by the U.S. Army Belvoir Research, Development and Engineering Center. The views of the authors do not purport to reflect the position of the U.S. Army or the Department of Defense.

6.0 Bibliography

- Alleman, T. J., 1989. *Experiments To Determine the Digitizing Rate and Time Delays for PEMSS II*, Eighth U.S. Army (EUSA) TNT-J2, Internal Report.
- Alleman, T. J., and C. P. Cameron (in preparation). *PEMSS Experiments for Paths at Various Angles to Tunnel Axis*, Chem-Nuclear Geotech, Inc., U.S. Department of Energy, Grand Junction Projects Office, Grand Junction, CO.
- Bronwell, B. A., and R. E. Beam, 1947. *Theory and Application of Microwaves*, McGraw Hill Book Co., Inc., New York.
- Clough, J. W., 1976. "Electromagnetic Lateral Waves Observed by Earth Sounding Radars," in *Geophysics*, Vol. 41, No. 6A, December 1976.
- Goodnight, C., 1986. *Geologic Characterization of TNT Test Pad*. Technical Note TN6, Prepared by the U.S. Department of Energy Grand Junction Projects Office for the U.S. Department of the Army, Belvoir Research, Development and Engineering Center, Ft. Belvoir, VA.
- Jasik, H., and R. C. Johnson, 1984. *Antenna Engineering Handbook*, McGraw-Hill, New York.
- Ulrissen, F. F., 1982. *Application of Impulse Radar to Civil Engineering*, Lund University of Technology, Department of Engineering Geology, Sweden.
- Vesechy, J. F., W. A. Nierenberg, and A. M. Despain, 1980. *Tunnel Detection*, Jason Technical Report JSR-79-11, SRI International, April 1980.
- Waite, J. R., and D. A. Hill, 1977. *Radio Frequency Transmission via a Trolley Wire in a Tunnel with Rail Return*, IEEE Transactions Antennas Propagation, Vol. AP-25, pp. 248-253.

Appendix A

Derivation of Travel Times for Theoretical PEMSS Raypaths

The following definitions are applicable to all equations in the appendix.

V_R = velocity in rock,

V_A = velocity in air,

θ_R = angle between p_1 and normal to tunnel,

θ_A = refracted angle in air,

p_1, p_2, p_3 = raypath lengths,

L = axial distance (indicated on figures),

L_1, L_2 = distance as indicated on figures,

d_1, d_2 = distance as indicated on figures,

W = tunnel width,

N = number of repetitions,

m = meters

p_{anom} = predicted anomaly in time,

T_{air} = travel time through air (in tunnel),

T_{rock} = travel time for p_1 and p_2 segments,

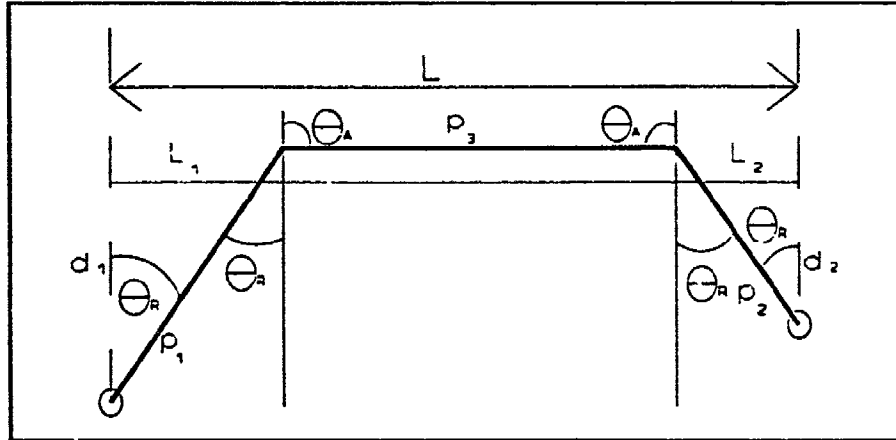
T_{srock} = travel time through rock along axial distance,

A_A = angle between p_3 and normal to tunnel, and

A_R = angle between p_1 and tunnel wall.

Part A

Antennae on Same Side of Tunnel



$$\sin\theta_R / \sin\theta_A = V_R / V_A; \quad \sin\theta_R = (V_R / V_A) \cdot \sin\theta_A$$

Both holes are on the same side of the tunnel:

$$\theta_A = 90^\circ; \quad \cos\theta_R = d_1 / p_1; \quad \sin\theta_R = V_R / V_A$$

$$\sin\theta_R = \sqrt{1 - \cos^2\theta_R} = \sqrt{1 - (d_1^2 / p_1^2)}$$

$$\sin^2\theta_R = 1 - (d_1^2 / p_1^2)$$

Since the $\sin 90 = 1$

$$\sin\theta_R = V_R / V_A; \quad d_1^2 / p_1^2 = 1 - \sin^2\theta_R; \quad p_1^2 = d_1^2 + L_1^2$$

and

$$p_1 = d_1 / \left[\sqrt{1 - \sin^2\theta_R} \right] = d_1 / \sqrt{1 - (V_R / V_A)^2}$$

$$p_2 = d_2 / \left(\sqrt{1 - (V_R / V_A)^2} \right); \quad L_1 = \sqrt{p_1^2 - d_1^2}; \quad p_3 = L - L_1 - L_2$$

$$p_3 = L - \sqrt{d_1^2 / (1 - \sin^2\theta_R) - d_1^2} - \sqrt{d_2^2 / (1 - \sin^2\theta_R) - d_2^2}$$

$$p_3 = L - (d_1 + d_2) \cdot \sqrt{1 / (1 - \sin^2\theta_R) - 1}$$

$$p_3 = L - (d_1 + d_2) \cdot \sqrt{[(\sin^2\theta_R) / (1 - \sin^2\theta_R) - 1]}$$

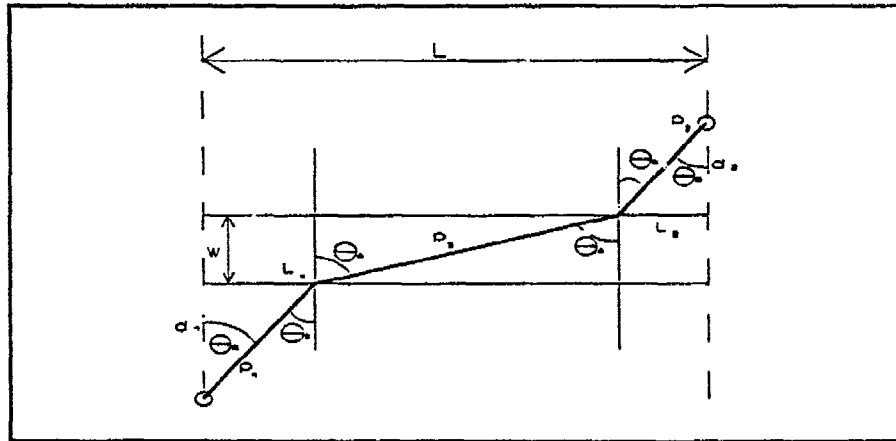
$$p_3 = L - (d_1 + d_2) \cdot \sin\theta_R \cdot \sqrt{1 / (1 - \sin^2\theta_R)}$$

$$p_3 = L - (d_1 + d_2) \cdot (V_R / V_A) \cdot \sqrt{1 / [1 - (V_R / V_A)^2]}$$

$$p_{\text{anom}} = p_3 / V_A + (p_1 + p_2 / V_R) - T_{\text{stock}}$$

Part B

Antennae on Opposite Sides of Tunnel



$$\sin\theta_R / \sin\theta_A = V_R / V_A$$

$$\cos\theta_R = d_1 / p_1$$

$$p_1 = d_1 / \cos\theta_R = d_1 / \sqrt{1 - \sin^2\theta_R}$$

$$p_2 = d_2 / \sqrt{1 - \sin^2\theta_R}$$

$$\sin\theta_R = L_1 / p_1 = (L_1 / d_1) \cdot \sqrt{1 - \sin^2\theta_R}$$

$$L_1 = p_1 \cdot \sin\theta_R = (d_1 \cdot \sin\theta_R) / \sqrt{1 - \sin^2\theta_R}$$

$$L_2 = p_2 \cdot \sin\theta_R$$

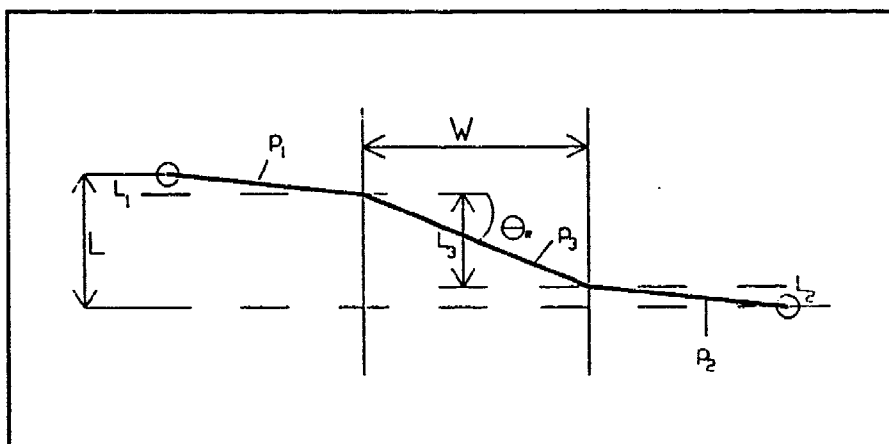
$$L_3 = L - L_1 - L_2 = L - (p_1 + p_2) \cdot \sin\theta_R$$

$$p_3 = \sqrt{L_3^2 + W^2}$$

$$p_{\text{anem}} = (T_{\text{air}} + T_{\text{rock}}) - T_{\text{srock}} = p_3 V_A + (p_1 + p_2 V_R) - T_{\text{srock}}$$

Part C

Antennae Alignment Nearly Perpendicular to Tunnel Axis



$$\sin \theta_R \approx (V_R / V_A) \cdot (L / W)$$

$$R_t \approx 1 / \sqrt{1 - \sin^2 \theta_R / V_R}$$

$$L_3 \approx L - (d_1 + d_2) \cdot (L / W) \cdot (V_R / V_A)$$

$$= L \cdot [1 - (d_1 + d_2) \cdot (V_R / W \cdot V_A)]$$

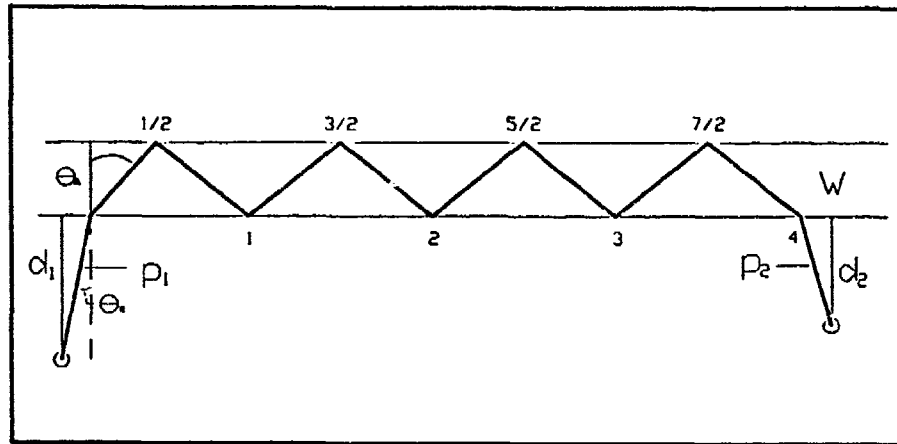
$$L = (d_1 + d_2) \cdot (V_R \cdot L_3) / (V_A \cdot W) + L_3$$

$$L = L_3 \cdot [1 + (d_1 + d_2) \cdot V_R / (V_A \cdot W)]$$

$$L_3 = L / [1 + (d_1 + d_2) \cdot V_R / (V_A \cdot W)]$$

Part D

Waveguide; Antennae on Same Side of Tunnel



$$\sin\theta_R / \sin\theta_A = V_R / V_A$$

$$p_1 = d_1 / \sqrt{1 - \sin^2\theta_R}$$

$$p_2 = d_2 / \sqrt{1 - \sin^2\theta_R}$$

$$L_3 = L - (p_1 + p_2) \cdot \sin\theta_R$$

$$\tan\theta_A = (L_3 / 2 \cdot N) / W$$

$$\theta_A = \tan^{-1} (L_3 / 2 \cdot N \cdot W)$$

$$\sin\theta_A = (L_3 / 2 \cdot N) / (p_3 / 2 \cdot N)$$

$$\text{Wavelength} \Rightarrow Wv$$

$$p_3 = L_3 / \sin\theta_A$$

$$\cos\theta_A = W / (Wv / 2) = 2 \cdot W / Wv$$

$$Wv = 2 \cdot W / \cos\theta_A$$

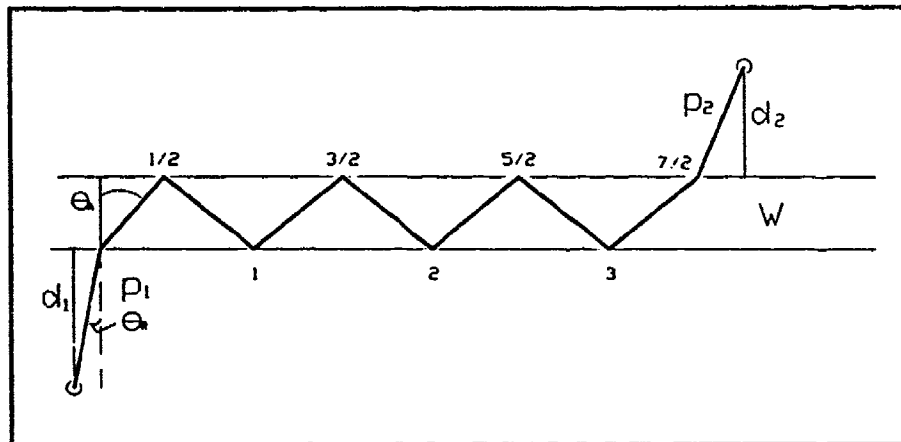
$$\text{frequency} \Rightarrow f$$

$$f = (3 \cdot 10^8 \text{ m/s}) / Wv(\text{m})$$

$$f_{\text{MHz}} = 300 / Wv \text{ MHz}$$

Part E

Waveguide; Antennae on Opposite Sides of Tunnel



$$\sin\theta_R / \sin\theta_A = V_R / V_A$$

$$p_1 = d_1 / \sqrt{1 - \sin^2\theta_R}$$

$$p_2 = d_2 / \sqrt{1 - \sin^2\theta_A}$$

$$L_3 = L - (p_1 + p_2) \cdot \sin\theta_R$$

$$\tan\theta_A = [L_3 / (2 \cdot N + 1)] / W$$

$$\theta_A = \tan^{-1} L_3 / \{[(2 \cdot N + 1) \cdot W]\}$$

$$\sin\theta_A = [L_3 / (2 \cdot N + 1)] / [p_3 / (2 \cdot N + 1)]$$

$$p_3 = L_3 / \sin\theta_A$$

**PEMSS CHARACTERIZATION OF METAMORPHIC ENVIRONMENTS
IN THE CENTRAL KOREAN PENINSULA**

by

**C. P. Cameron,
University of Southern Mississippi
Hattiesburg, MS**

and

**K. D. Mitchell, K. C. Shin, B. W. Walker
Chem-Nuclear Geotech, Inc.
Seoul, ROK**

Paper prepared for:

**Fourth Tunnel Detection Symposium on
Subsurface Exploration Technology
Colorado School of Mines
Golden, Colorado**

April 26-29, 1993

ABSTRACT

The Pulsed Electromagnetic Search System (PEMSS), developed by Southwest Research Inc., is a cross-hole ground probing radar instrument which operates in the 20 - 100 MHz range. At borehole separations 20 meters received signals usually exhibit maximum power in the 30-40 MHz range. In use as a primary instrument in the search for clandestine tunnels in intrusive igneous and complex metamorphic terranes of the Korean Demilitarized Zone (DMZ) since the early 1980's, the system has also performed (albeit inadvertently) as a rock mass characterization tool. PEMSS data are collected hole-to-hole, generally across 5 ray paths, at 0.2 meter intervals. The boreholes are generally drilled in linear alignments at average spacings of 15-20 meters and afford opportunities to indirectly characterize lithological and structural rock mass discontinuities.

The received signals are processed for velocity (arrival time), attenuation, and dispersion using wiggle-trace, tomographic and signature analysis techniques. When raw and processed PEMSS data are compared to conventional borehole geophysical logs, diamond drill core logs, and projections of surface geology, the capacity and limitations of the method to define structural discontinuities, (faults, shear zones, changes in fracture density), and lithologies, (quartz veins, amphibolites, quartzose gneisses), are apparent. The system also exhibits electromagnetic signal sensitivity to conductive mineral assemblages (especially graphite, clays, sulfides), and to hydrogeological conditions. Characteristics of certain features can be recognized by detailed examination of travel time, attenuation, and a measure of dispersion.

Generally, discrete ground features, (quartz vein accumulations, amphibolite bands, natural and man-made cavities), on the order of 2 meters can be detected if holes are no more than approximately 20 meters apart. Planar structures can generally be detected at greater transmitter-receiver separations. Both theoretical considerations and empirical evidence suggest that signal propagation range is limited by structural, mineralogical, and hydrogeological conditions in the rock mass. Propagation distances in central Korean terranes range from 10 meters or less in some cases to 100 meters or more in others. Tomographic inversion to characterize structural and lithological discontinuities with dimensions of one meter or less is also seriously affected by distance between boreholes. The orientation of the borehole antennae array relative to the solid geometry of subsurface features plays a significant role in terms of arrival times and signal character; and the use of offsets and tomographic interpretation is no less important to the correct interpretation of geologic features than their use in the search for air-filled cavities.

Results presented here suggest that rock mass characterization by PEMSS offers a valuable supplement to traditional ratings of Rock Quality Designation (RQD) as revealed by continuous core. Preliminary results by other workers suggest that cross-hole seismic data from these terranes will show similar results. With further advances in processing and interpretation techniques, combined cross-hole geophysical surveys should someday play a key role in many engineering site characterizations; providing the sort of 3-dimensional imaging of the subsurface not generally attainable solely with conventional borehole and surface information.

INTRODUCTION

The Pulsed Electromagnetic Search System (PEMSS), developed by Southwest Research Inc., is a time domain, short pluse (duration approximately 0.01 μ sec) radar system proven capable of detecting air filled cavities about 2 meters in diameter, constructed in intrusive granitic rock masses, between boreholes spaced at 15-20 meters. The system has been deployed as a primary exploration tool for clandestine tunnels in the Korean DMZ for over a decade. The development and deployment of the PEMSS provided impetus for several applied research efforts in the areas of the system's engineering, as well as studies related to its signal processing, modeling, and interpretation, (e.g. Owen, 1981; Kemerait et.al., 1988; Greenfield, 1988; and Olhoeft, 1988). Given the mission of the US Army's Tunnel Detection Program most of the cited work naturally concentrated on the PEMSS signal characteristics as they pertained to the anomaly typically caused by an air filled void in relatively homogeneous hard rock. Olhoeft, (1988) is something of an exception in this regard in that he recognizes and identifies geologic features that can seriously diminish the PEMSS signal-to-noise ratio as the wave propagates through the rock mass. In particular he cites the sensitivity of the system to conductive zones caused by anomalous water concentrations via enhanced fracture porosity, and accumulations of clay and graphite such as may be found in some faults and shear zones.

Despite the general recognition of the implications of PEMSS response to geologic complexity, attempts to systematically correlate PEMSS data records to changes in lithology, structural features, and conductive mineralization are relatively recent in terms of formal documentation. The correlation efforts thus far accomplished were made possible because of emphasis on detailed geological mapping wherever PEMSS is deployed, the acquisition of state-of-the-art conventional borehole geophysical logs on a routine basis, and the willingness to test suspect or interesting PEMSS events with continuous diamond drill core. The integration of this data on a case-by-case basis has led to new appreciation of the search environment and the potential of PEMSS to serve as a major tool for rock mass characterization in complex geological terrane. The examples discussed herein are part of a growing number of case histories along the DMZ which contain evidence that PEMSS maps rock quality (or "intactness") between boreholes. The "intactness" of a rock mass for civil engineering purposes such as tunneling and foundation characterization is most often evaluated by calculating the ratio of the summed length of core pieces greater than 10 cm in individual length, to the length of the total interval measured. The "Rock Quality Designation", or RQD, is expressed in percent and the rock mass classified as "Good", "Fair" etc based upon long-term observations and the empirical behavior of various rock masses after excavation in engineered works. Unfortunately, the rock mass is tested only over the generally small (76 mm or greater) diameter of the core, which yields very little information, if any, regarding the "condition of discontinuity. Any tool which offers promise with respect to better characterization of the rock mass between boreholes has the potential to affect appreciable savings and better define stability and safety factors in site characterization phases of civil engineering projects. For detailed definition and discussion of RQD the interested reader is referred to Murphy, (1985), and Deere, (1964).

This paper documents PEMSS response to some of the more commonly observed geologic features in the metamorphic sequences which make up a substantial portion of the central Korean Peninsula. Although these results are viewed as satisfactory at this stage, and give cause for some excitement with respect to the potential of this type of geophysical system, the scope of this work is still somewhat restricted given the restraints of time and other priorities. This work should therefore be viewed as a reasonable point of departure for substantially increasing

the number of correlation exercises necessary to further substantiate the data sets and conclusions offered here. Investigations into the physio-chemical and perhaps microscopic causes of the changes in PEMSS parametrics as a function of shifts in lithologic compositions (e.g. in particular the amphibolite phenomena) in these terranes also forms a research recommendation of this paper,

GEOLOGY

The rocks and structural situations described herein are part of a very ancient terrane, accounts of which document a 3.7 billion year record, most often incomplete, of repeated cycles of sedimentation, metamorphism, orogenesis, and igneous intrusion. The interested reader is referred to "Geology of Korea" (ed. Lee Dai-Sung, Geological Society of Korea, 1987), for a thorough and well-referenced summary of the geological evolution of the Korean Peninsula. What follows is a short summary of key aspects of the regional geologic framework of central Korea to provide a framework for the site specific characterizations discussed in later sections. Major elements of this summary are illustrated in the regional outline geologic map shown in Figure 1 and on Table 1.

Regional Geology and Tectonic Framework. The geology of this part of central Korea is dominated by the early Precambrian Kyonggi Gneiss Complex, a polymetamorphic terrane which contains age elements of both the Archean and Paleoproterozoic Eras (Kim, O. K., 1970, 1973; Sang H. O. and Hee, Y. C., 1984; Kim H. S., 1987; and Na, K. C., 1987). This basement complex is composed of foliated high-grade metasediment (i.e. schists and gneisses of sedimentary origin), as well as non-foliated (but often lineated) metamorphic rocks of apparent igneous origin.

The Kyonggi Gneiss Complex and the structural elements which deform it developed during at least five, and quite possibly six, orogenic (mountain building) episodes. Isotopic age dates of the oldest rocks of the complex tend to group in the 2500-2700 Ma and 1700-2200 Ma range (Fupingian and Wutaian Orogenies). These are the ages of major metamorphic episodes which transformed the rocks to (approximately) their present lithology and mineralogy. The Kyonggi metamorphic rocks were affected to a lesser extent by at least one, and quite possibly two, late Proterozoic orogenic movements. After a long period of relative stability and quiescence, the Kyonggi Complex was extensively intruded by granite stocks and batholiths during the Jurassic Period (Daebu Orogeny); and later still, the explosive volcanism that signalled the culmination of major uplifts in the Sino-Korean Paraplatform was followed by intrusion of late-kinematic granites during the Late Cretaceous Bulguksa Orogeny. Finally, a rifting event along portions of the Wonson - Seoul Fault in the central Peninsula resulted in the eruption of vesicular basalt and volcanic ash; an event which did not appreciably alter the older rocks of the basement to any appreciable amount.

The Kyonggi Gneiss Complex in the central portion of the Peninsula is cut by several major fault systems, most of which display a characteristic "Korean" (N-S) or "Sinian" (N10-30E) direction (Figure 1). One of these faults, the Wonson - Seoul Fault is probably a fundamental tectonic element, part of a crustal fracture system which splits the entire Korean Peninsula, (Figure 1). Severely tectonized rock extends outward for 300 meters to 2 kilometers from the fault zones which form this system.

Lithology. The Kyonggi Gneiss Complex is comprised of high rank metasediments and granitized derivatives such as banded gneisses, porphyroblastic garnet-bearing gneisses,

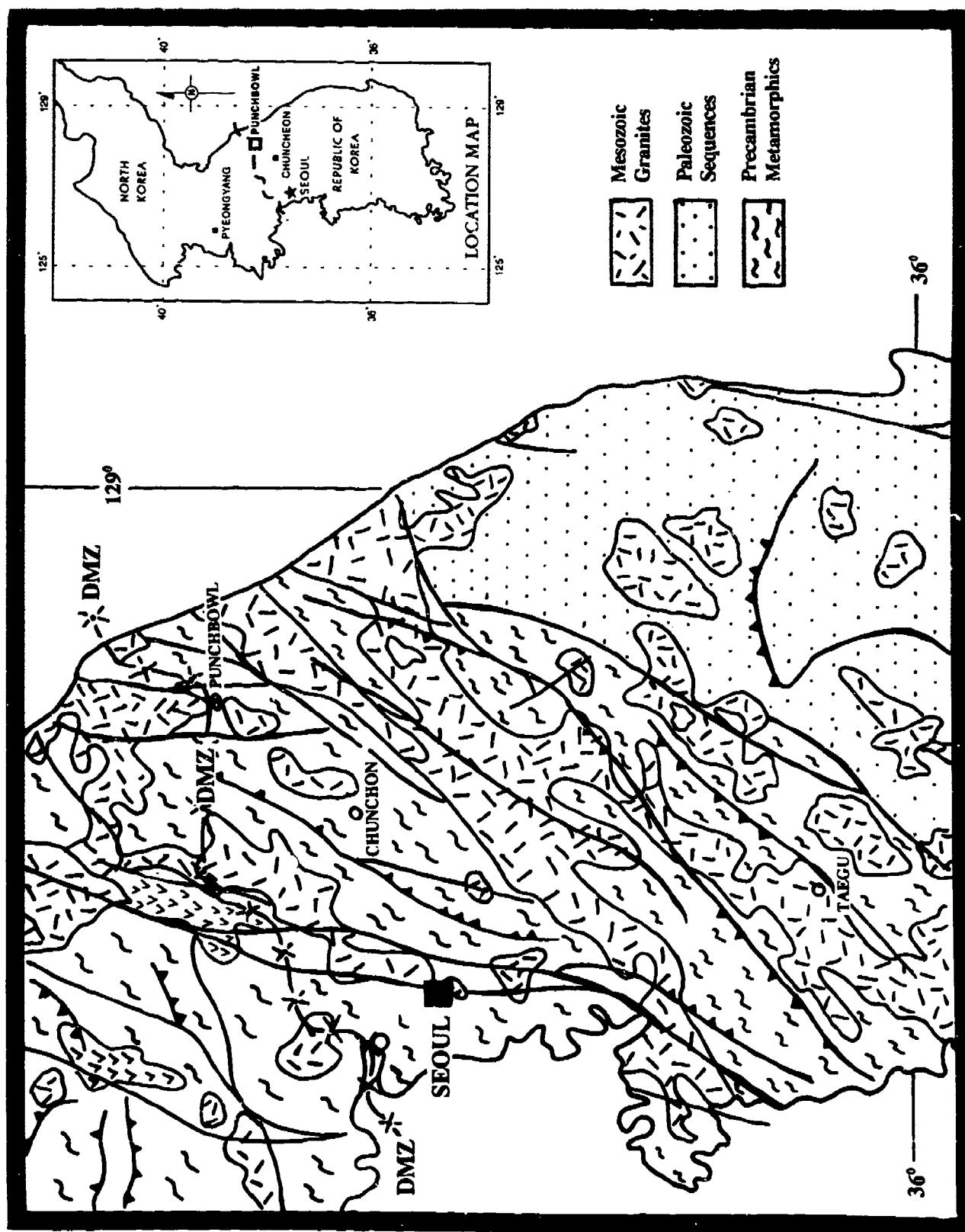


Figure 1. Outline Geological Map of the Central Korean Peninsula.

migmatitic gneiss, and granitic gneiss. Quartz-mica and biotite-chlorite schists are common in western portions of central Korea as are interbedded and intercalated quartzites, crystalline limestones and dolomite, calc-silicates, and marbles. Often graphitic with occasional zones of disseminated sulfides, the schists are phyllonitized where they have been affected by faulting. In fault and shear zones original foliation planes are severely disrupted and dilated by shearing. Very hard, quartzose gneisses, quartz-garnet gneiss, and quartz-biotite-garnet migmatites (mixed rock) are all common in the eastern mountains of Korea. Quartz accumulations in sinuous pods are common in these lithologies; having formed as a function of metamorphic differentiation and or partial melting during early Precambrian orogenic culminations.

Foliated and lineated amphibolites are dark, fine-grained rocks, rich in iron-magnesium minerals. The amphibolites have both concordant and discordant contact relationships with host gneisses and are assumed to be the product of the volcanism and mafic intrusion during the early Precambrian orogenic event(s).

Table 1.

Major Stratigraphic Units of the Central Korean Peninsula
(Demilitarized Zone Sector)

Quaternary	Chugaryeong Rift Valley Volcanics ¹	100,000 -300,000 BP
Cretaceous	Intrusive Granites and Explosive Volcanics	Bulgugsa (70-90 Ma)
Jurassic	Intrusive Granites	Daebo (140-230 Ma)
Neoproterozoic	Sadang-u Series ²	Chengkiangian (700-850 Ma)
Neo- and Mesoproterozoic	Yonchon Group ³ Metasediments	Chenkiangian - Chinningian (700-1400 Ma)
Paleoproterozoic	Ch'unchon Supergroup ³	Szepaoan (1400 Ma) Luliangian (1800 - 1950 Ma) Wutaian (2000 - 2100 Ma)
Archeozoic	Kyonggi Gneiss Complex	Fupingian (2400 - 2500, 2700 Ma) Sangkan (3100 - 3400 Ma)

Where gneisses, schists, or amphibolites have been affected by faulting, a gouge zone of

¹Chorwan Valley and the Banks of the Pukhan Gang.

²As a large calc-silicate and skarn roof pendant on Mesozoic Granite in the Kumwha Sector (NNW of Ch'unchon); not shown in Figure 1.

³Between the Kumwha Area and the Pukhan Gang, (north of Ch'unchon; not differentiated from other Precambrian metamorphics in this paper.

variable thickness is generally present, usually with substantially increased fracture density via rock cleavage. The lithological and mineralogical composition of the gouge is largely dependant upon the nature of the adjacent rocks and upon the chemistry of the groundwaters which have entered the system and reacted with the rocks of the fault zone over time. Many local faults and shear zones were formed in foliated (very thin-bedded to laminated in a stratigraphic sense) quartz-mica schists and gneisses; probably because these lithologies are weaker, particularly along planes of foliation, than the compact banded (thin to very thick-bedded) porphyroblastic gneiss and massive granitic gneiss. The quartz mica schists and gneisses commonly contain graphite, a mineral whose very low resistance to deformation, particularly shearing, results in its behavior as a fault plane "lubricant". Thus the faults displacing quartz-mica schists and gneisses generally have phyllonitic gouge zones composed of finely crushed, smeared, and macerated rock fragments, biotite, clays (especially chlorite, sericite, graphite, and sulfides (esp pyrite). Quartz vein accumulations are not uncommon in these zones; some are part of igneous hydrothermal systems sourced from significant depths⁴ during Mesozoic granite intrusions, others are fracture fillings developed during later epochs.

Some of the harder, more compact, banded gneisses and massive granitic gneisses tend to be recrystallized where disturbed by faulting; the fault zones generally mylonitized or cataclastized. Complex networks of quartz veins which highlight filled fracture systems served to "heal" the rock mass to the point that it often retains a considerable proportion of its original strength.

SITE SPECIFIC PEMSS CHARACTERIZATIONS

That cross-hole radar's response to geologic features in the metamorphic rock mass of the DMZ is often dramatic is a fact well known to geophysicists of the Eighth US Army's Tunnel Neutralization Team (EUSA-TNT), the Republic of Korea Army Tunnel Direction Directorate (ROKA-TDD), and their respective Panels of Experts. That the PEMSS is proven capable of illuminating an air filled cavity in the homogeneous intrusive granites of the DMZ is well-documented in the previously cited literature, and in Alleman, et. al. (1993, this volume). The latter paper demonstrates that, under at least some circumstances, PEMSS is capable of detecting air-filled cavities in complex layered metamorphic rock sequences; based on the result from the Countertunnel-3 Test Pad shown here in Figure 2.

The sites chosen to demonstrate PEMSS capability to characterize specific geologic situation in metamorphic terranes are illustrated on the borehole plan maps shown in Figure 3. These data may be taken as representative in that at least twice as many characterizations have been informally documented for various other sites than are discussed here; for reasons of preparation time and length restrictions. All of the features highlighted by the characterizations discussed in this paper have been duplicated at least once (and usually several times) in similar

⁴The Korean Peninsula is known by economic geologists and mining engineers worldwide for the "Korean-type" gold deposit; i.e. gold-bearing hydrothermal quartz veins with a mineral paragenesis of quartz and pyrrhotite followed by later pyrite and (often) free gold. This situation fit the "Mesothermal" hydrothermal classification of Lindgren, (1933). These deposits are thought to form in the "intermediate" zone of metamorphism; in the temperature range of 3-500°C; as deep as 10-17 km.

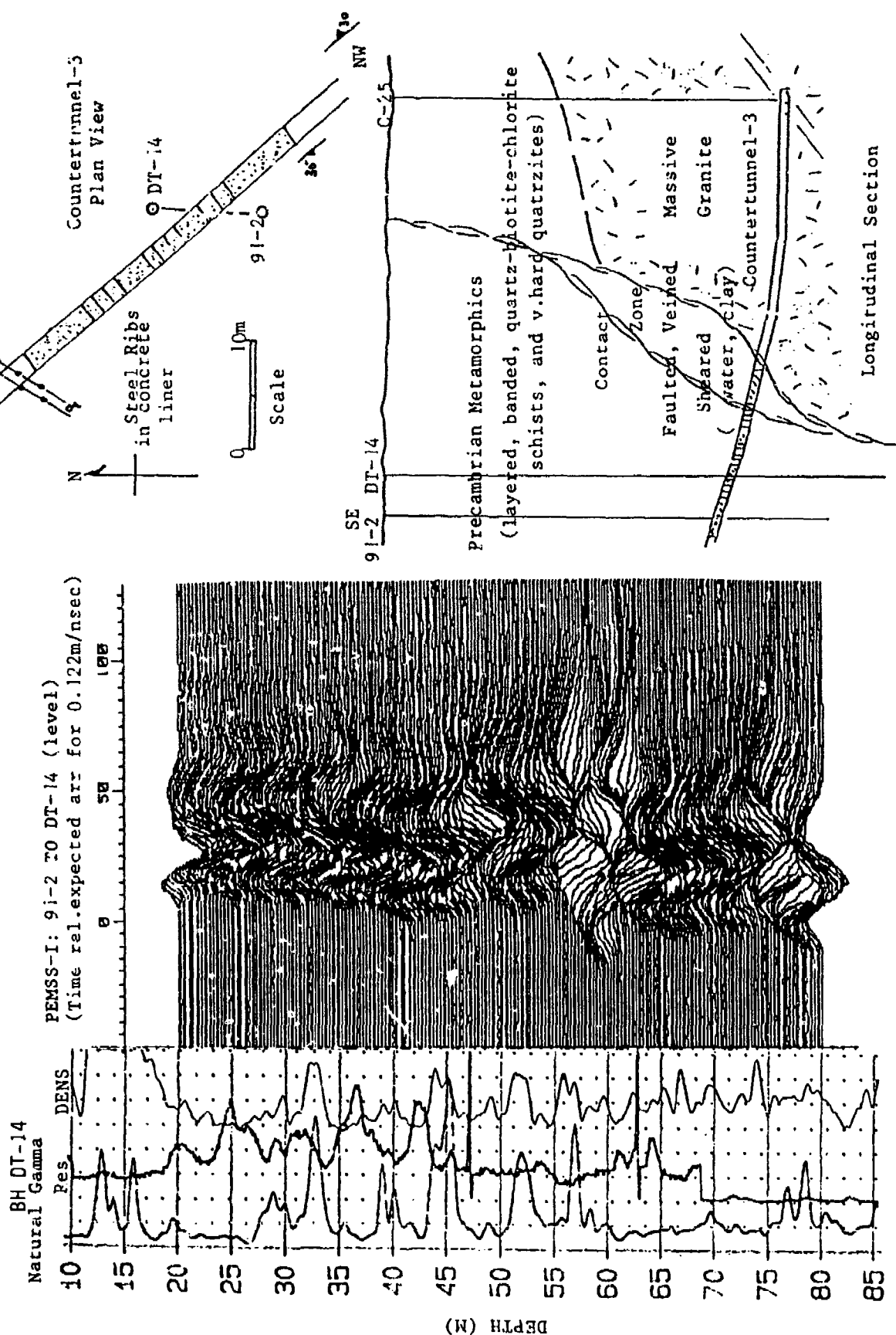


Figure 2. Conventional Geophysical Logs, PEMSS 1 Level Run Data Record, and Index Map and Longitudinal Section for part of the Countertunnel-3 Test Pad.

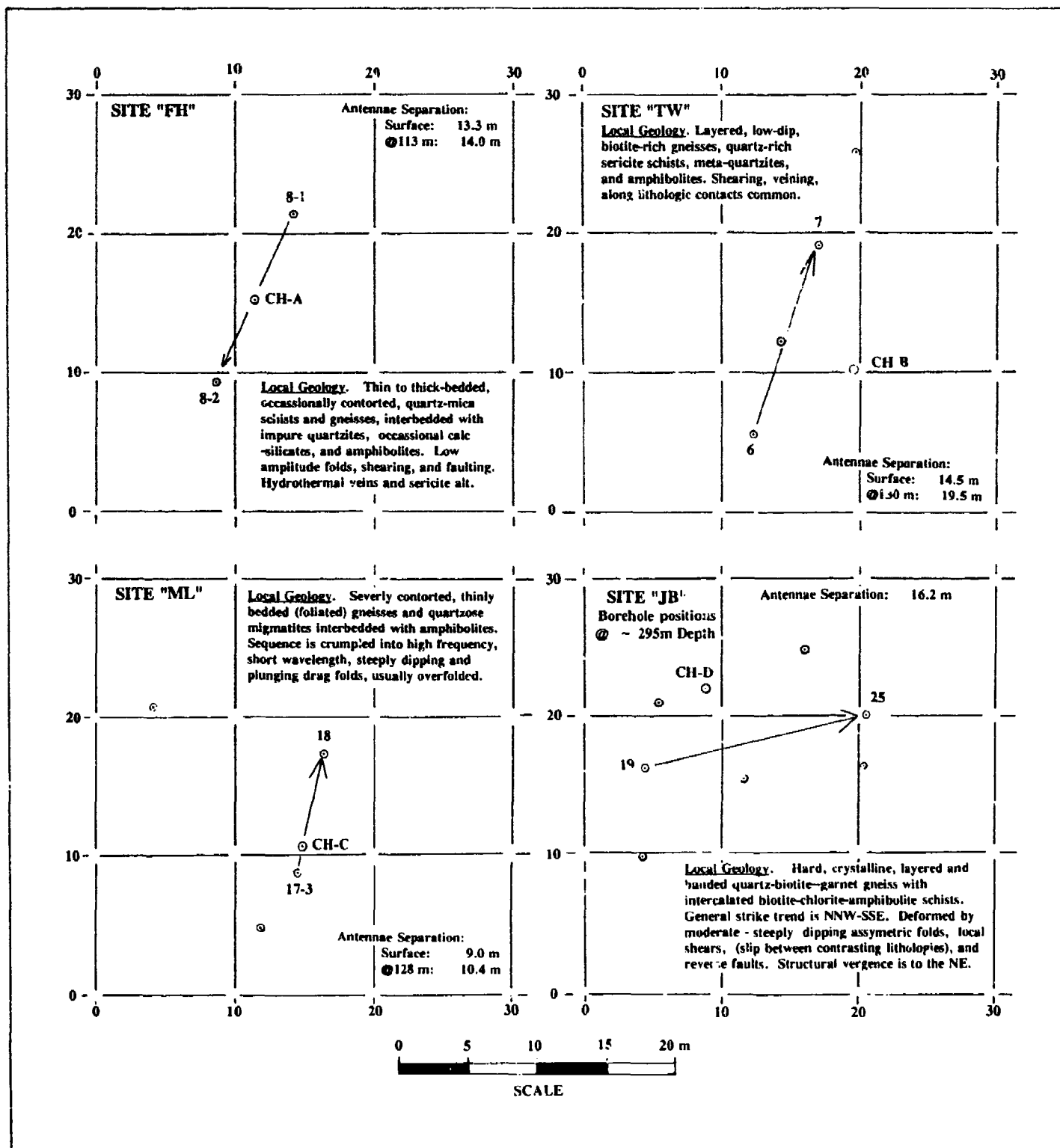


Figure 3. Borehole Plan Maps for PEMSS Characterization Areas

circumstances at other sites.

Site "FH" (PEMSS-1, Level Run, Figures 4 and 5)

General Setting. The site is in a generally flat terrain broken occasionally by low hills. This area is underlain by low-dip, gently folded, quartz-mica schists and gneisses, interbedded with impure quartzites, occasional calc-silicates, and amphibolites. The low-amplitude folds are broken by faults of regional dimension; a circumstance which results in severe contortion, drag-folding, shearing, rock mass brecciation, and chemical alteration in the displaced zone. Regional hydrothermal alteration, perhaps related to granite intrusion at depth, resulted in a pervasive sericitization which affects as much as 60% of the rock mass; although granite was not encountered in the surface or subsurface during regional and local mapping of the immediate area of this site.

Core Lithology, Structure, and RQD. Examination of continuous diamond drill core from CH-A revealed an alternating section of moderate and low-dip (foliation) quartzose biotite gneiss, biotite garnet gneiss, chlorite schists, and quartzites. The quartzites and some of the quartzose gneisses appear to have responded more readily than some of the other lithologies to brittle fracture; they are generally more highly veined with quartz (often healed). A significant zone of faulting, corresponding with very sharp loss of rock quality (as measured by the RQD) occurs between 27 - 35 meters depth, (Figure 4). A very pronounced, intact, hydrothermal quartz vein, with up to 1% sulfide in the form of pyrite and pyrrhotite, dips at 30° to the core between 89-91 meters depth; cutting across gently dipping quartz-biotite-garnet gneiss.

Geophysical Logs. Conventional geophysical logs are not yet available for this site.

PEMSS Data Record. A total or near total loss of signal occurs between 27.5 meters and 28 meters as the PEMSS antennae transit the fault zone. However, it is notable that a progressive delay in arrival time characterizes a 2 - 3 meter envelope around the main fault zone. The loss of signal, shown by its very pronounced attenuation and dispersion, is due to the high conductivity of this zone; resulting from a combination of high water flow, graphite, and clay accumulation. Use of the stacking capability of the PEMSS-2 or PEMSS-3 might improve definition of the faulted zone. Use of offsets would be necessary to estimate the apparent fault orientation.

The quartz vein between 89-91 meters depth is highlighted by a pronounced PEMSS early arrival event which is complimented by concomitant attenuation and dispersion anomalies, a faint but recognizable signal diffraction. This is a highly characteristic signature for small (2-6 meter) quartz vein pods. The correct interpretation of the orientation (apparent strike and dip) of these veins again depends on the use of offset data.

Other PEMSS events observed on this record are not as pronounced as those discussed above; their occurrence and interpretation are noted on the data record shown in Figures 4 and 5. However, the small event which occurs at about 43-44 meters is of some interest because it is not recognized at all in the core lithology or RQD. The progressive arrival time delay surrounding the zone of drastically diminished signal to noise ratio, combined with increased signal attenuation, is typical of a small zone of increased conductivity; most likely caused by increased fracture-controlled porosity and clay accumulation via foliation slip and shear along lithologic contacts.

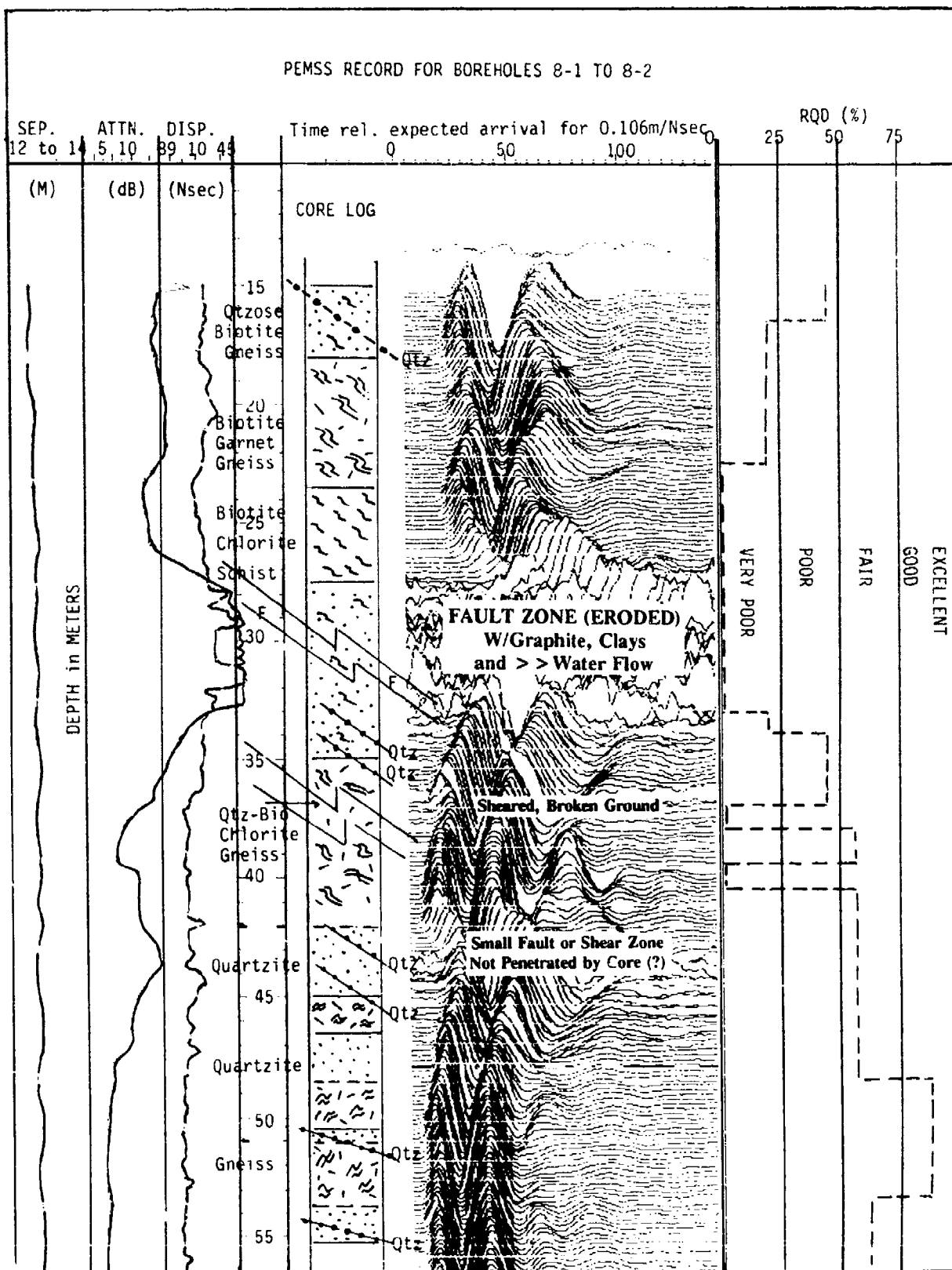


Figure 4. PEMSS Response Correlation Chart for Borehole Pair 8-1 to 8-2; Depth Range 15 - 55 Meters.

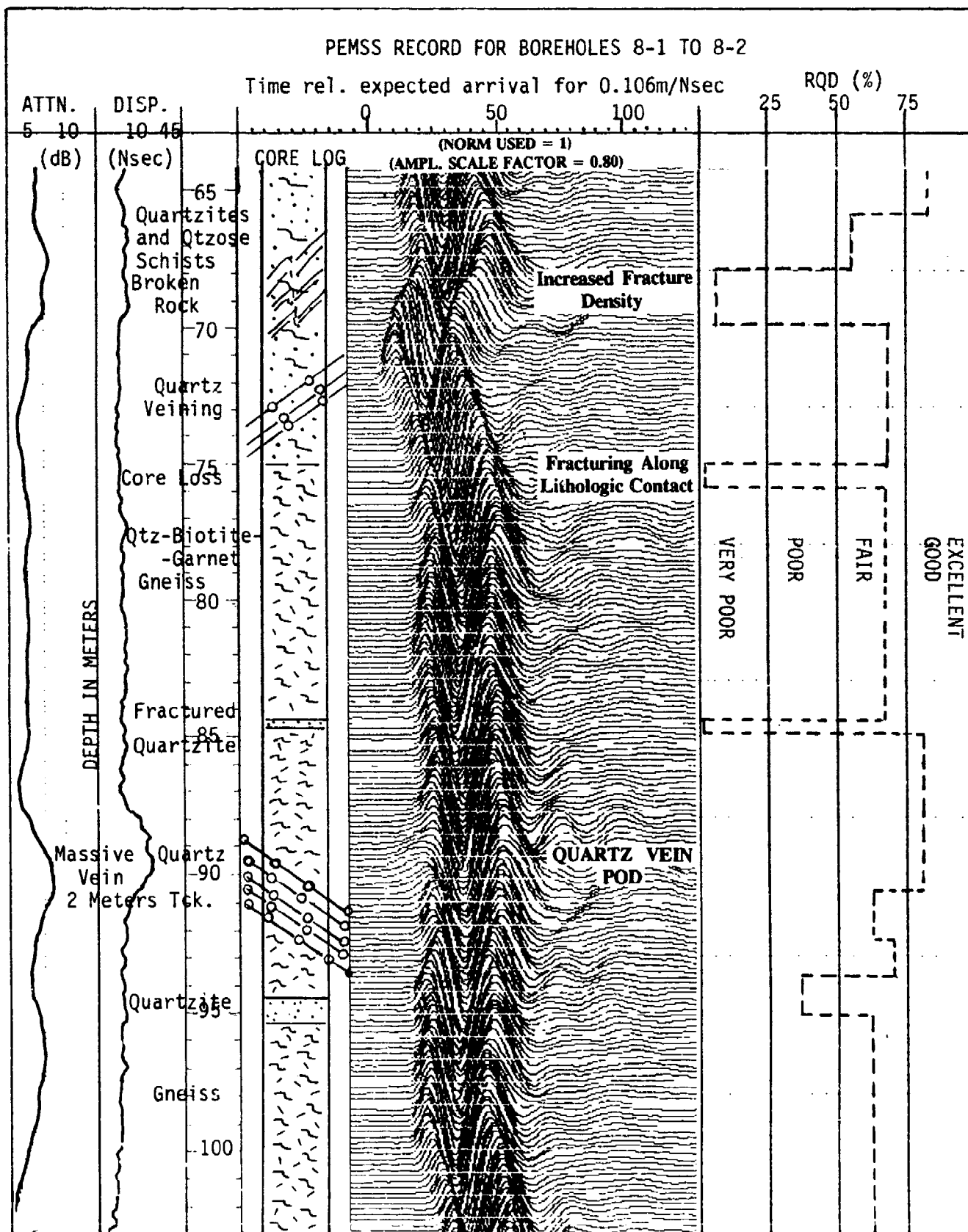


Figure 5. PEMSS Response Correlation Chart for Borehole Pair 8-1 to 8-2; Depth Range 65 - 103 Meters.

Site "TW", (PEMSS-2, Level-Run, Figure 6)

General Setting. This area is situated in a generally low and rolling terrain which is underlain by an evenly layered sequence of biotite-rich gneiss, quartz-rich sericite schists, metaquartzite, and amphibolites. The section is only locally contorted; most deformation occurs along the low-dip foliation planes as a function of slip shear between and along lithologic units. Some biotite-schists are chloritized, suggesting the hydrothermal effect of a nearby granite.

Core Lithology, Structure, and RQD. The core lithology comprises a shallow to moderately dipping sequence of alternating quartzo-feldspathic gneiss, metaquartzite, and amphibolite. Faulting, with clay accumulation occurs at 95 and 114 meters with concomitant loss of RQD. A zone of poor RQD also occurs at 40 meters but appears to be related to rock cleavage; the healed, and veined (quartz) intersecting fractures at about 45 meters is suggestive of local shearing or faulting.

Geophysical Log. The natural gamma ray log obtained from Borehole-7 shows general co-variance with lithology; gamma radiation being somewhat higher throughout zones of quartzite and quartzo-feldspathic gneiss, and lower in zones of amphibolite occurrence, with sharp peaks probably representing small fracture zones.

PEMSS Data Record. The PEMSS signal is responding with marked change in arrival time (delays of 9-15 Nsec) in response to lithologic variations between metaquartzite and amphibolite; the latter unit having an obviously lower transmission velocity than the former. These changes in signal arrival time, best seen on Figure 6 at 57 - 67 meters, and at 103 - 114 meters, are complimented by significant attenuation and dispersion events, particularly at the 103 - 114 event zone. A decrease in the amount of intact rock as measured by the RQD is also apparent in this zone.

The marked shifts in arrival time coupled with increases in attenuation and dispersion in the zones highlighted by the occurrence of amphibolite, is striking. As the three-way correlation between the natural gamma ray log, the core lithologic log, and the PEMSS data record clearly indicates, the PEMSS appears to map the amphibolite. However this record is somewhat ambiguous in that the effect of the diminished rock quality, related to shearing and faulting (with clay accumulation), might also account for at least part of the PEMSS response in the 103 - 114 meter depth zone.

Site "ML", (PEMSS-2, Level Run, Figure 7)

General Setting. Characterization Site "ML", with a surface formed of rolling hills and gentle swales, is underlain by severely contorted, thinly bedded (foliated) metasedimentary gneiss and quartzose migmatite, interbedded with generally concordant amphibolites. The sequence at this site is crumpled into high frequency, short wavelength, steeply dipping and plunging asymmetric drag folds, usually overfolded.

Core Lithology, Structure, and RQD. Detailed logging of the continuous core revealed a relatively intact sequence of alternating gneiss, migmatite, and amphibolite. The foliation is very steep in the upper part of the core, but gradually flattens to sub-horizontal at a depth of 110 meters; indicating that the core sampled a limb and axial portion of a tight synclinal fold. The RQD, (not shown) ranged from "good" to "fair" with only a few zones of poor, non-intact rock mass indicated. Of interest, is the thick amphibolite which occurs between 85 - 105 meters

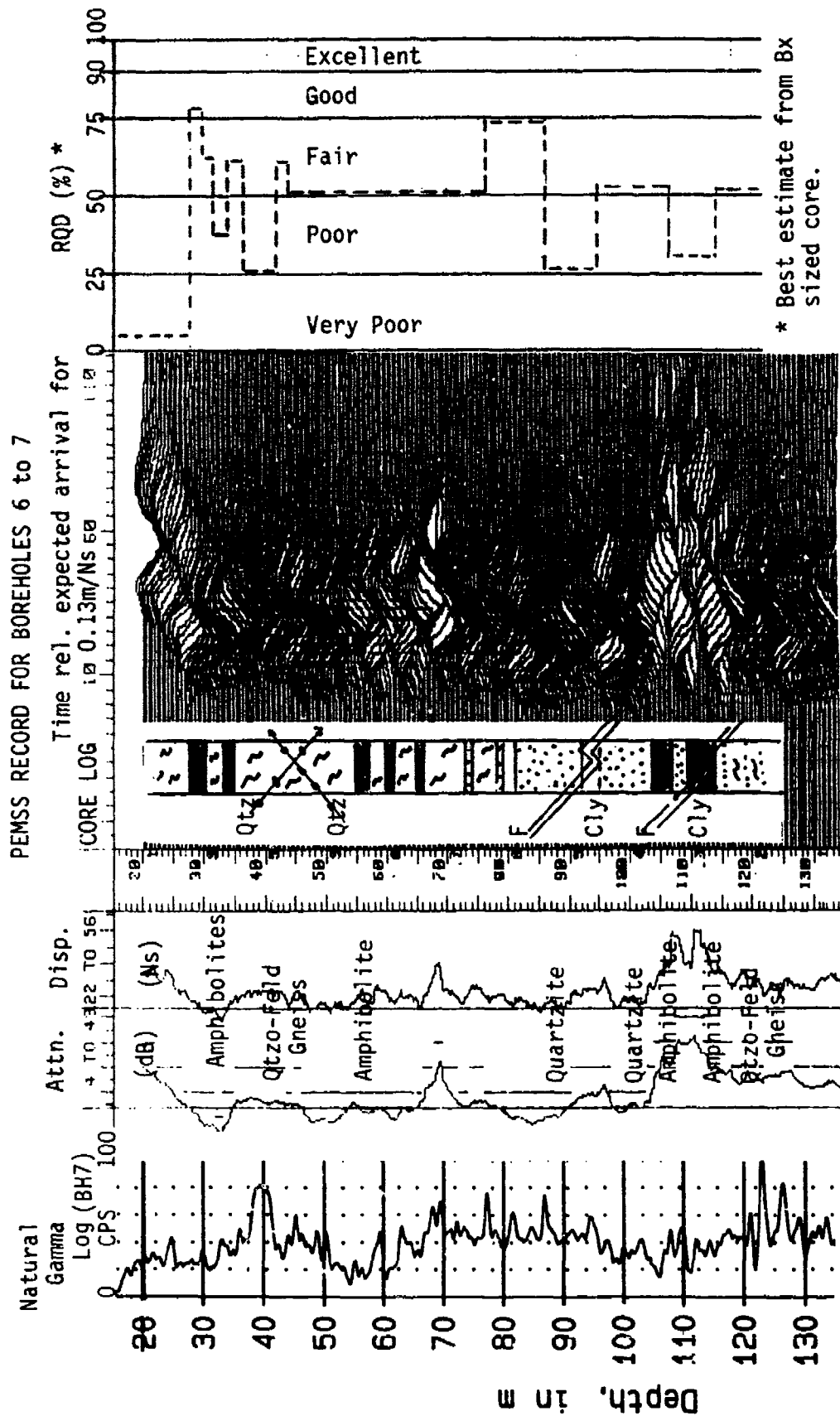


Figure 6. PEMSS Response Correlation Chart for Borehole Pair 6 to 7.

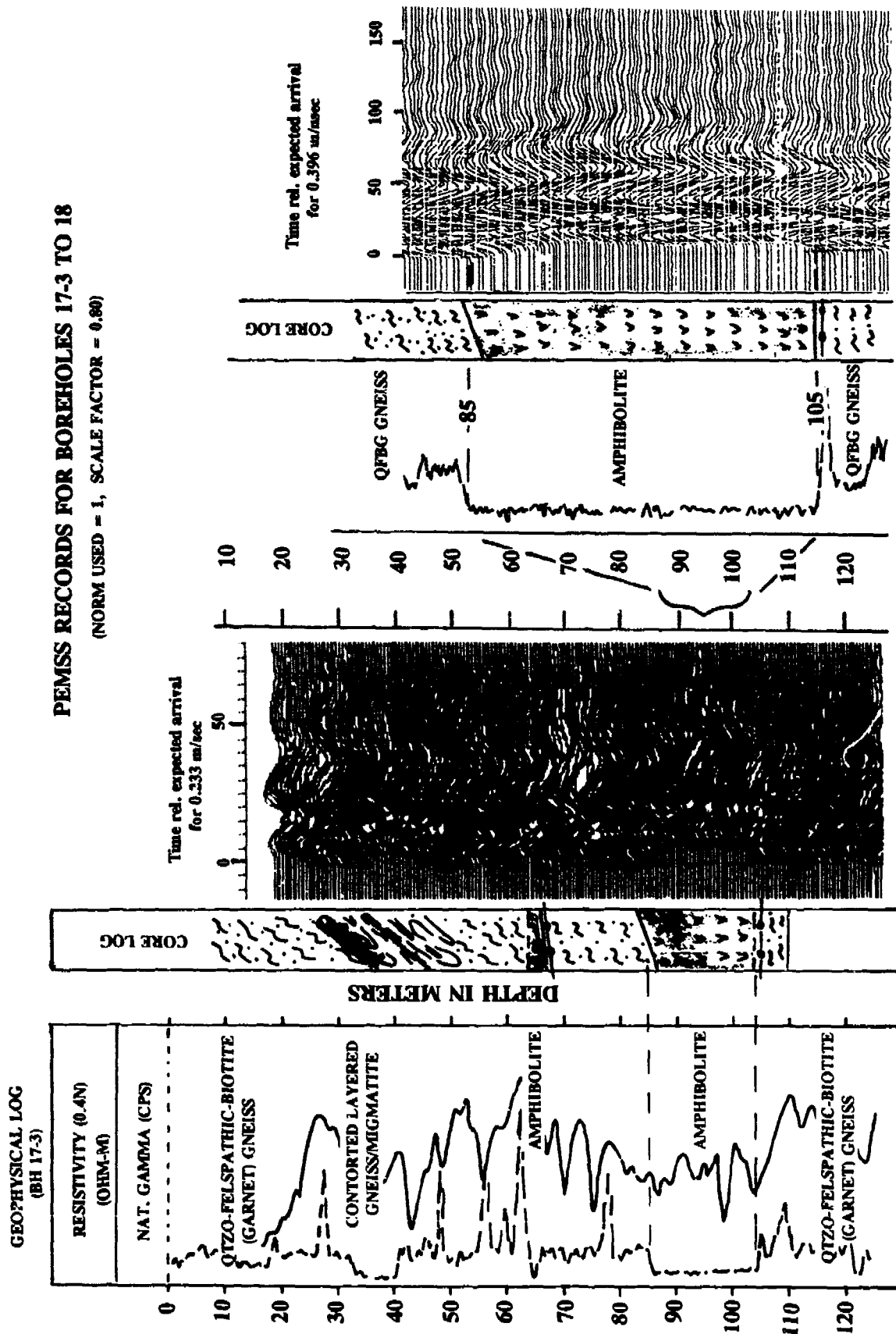


Figure 7. PEMSS Response Correlation Chart for Borehole Pair 17-3 to 18.

depth; and the response of this unit to conventional borehole geophysical logs and the PEMSS.

Geophysical logs. The natural gamma ray log for borehole 17-3, located only three meters from diamond drill hole CH-3 shows outstanding correspondence to lithology. As is clearly indicated in Figure 7, gamma radiation is consistently low in depth intervals occupied by amphibolites, and relatively high in those intervals described as quartzo-feldspathic-biotite (garnet) gneiss.

PEMSS Data Record. PEMSS is unambiguously mapping the low-transmission velocity amphibolites; and is unhampered in this by such complicating factors as shearing or faulting. A close inspection of this record clearly shows a 10 Nsec delay in signal arrival throughout the interval 85 - 105, and other intervals of amphibolite show similar arrival time shifts. Interestingly, no significant shifts in attenuation or dispersion are associated with the amphibolite interval per se; the small effects observed being at the veined lower contacts. This aspect deserves further attention and analysis, however.

If the three-way correlation between core lithology, gamma radiation change, and PEMSS arrival time is quite clear at this site, the reason for the PEMSS time shift is not. The physio-chemical and (perhaps) microscopic studies necessary to determine why amphibolite has an apparently slower transmission velocity than other metamorphic lithologies in this terrane have not yet been accomplished.

Site "JB", (PEMSS-3, Level Run and +/- 5 Meter Offsets, Figures 8 and 9)

General Setting. Characterization Site "JB" is situated in rugged, steep and broken mountain terrain. The site is underlain by alternating units of hard, layered and banded quartz-biotite-garnet gneiss and biotite-chlorite-amphibolite schists. General strike trend is NNW-SSE. The metamorphic sequence is deformed by moderate - steeply dipping asymmetric folds, generally overturned, local shears which generally reflect slip-strain between contrasting lithologies, and reverse faults, some of which appear to have formed as a function of failure along the steeply dipping axes of the aforementioned folds. Structural vergence in the area is pronounced to the NE.

Core Lithology, Structure, and RQD. Examination of continuous core recovered from CH-D revealed that a sequence of intact quartz-biotite-garnet gneiss with generally "excellent" rock quality as measured by RQD, is broken by faulting (repeated episodes) in the interval 290 - 300 meters. The fault zone is characterized by zones of hard ground which alternates with broken, veined (quartz), gneiss with high water flow (dissolution pits in secondary quartz), and considerable clay. The RQD ranges from "Fair" to "Very Poor" in the faulted interval.

Geophysical Logs. The guard (focused) and 0.4 Meter (Normal) resistivity logs for the corehole CH-D both showed correspondence with lithology in the upper and middle portions of the interval tested by coring. The hard, intact, gneisses of the "hanging wall" are significantly more resistive than the broken, clay and water-bearing, rocks which are faulted. The contact between intact and non-intact rock at about 290 meters is especially well-defined by the geophysical logs.

PEMSS Data Records and Tomographic Interpretation. Close examination of the parameters shown in Figures 8 and 9 reveals that the PEMSS is not only mapping the faulted ground as defined by the core lithologic log and the geophysical logs, but is also tracking the

PEMSS RECORDS FOR BOREHOLES 19 TO 25

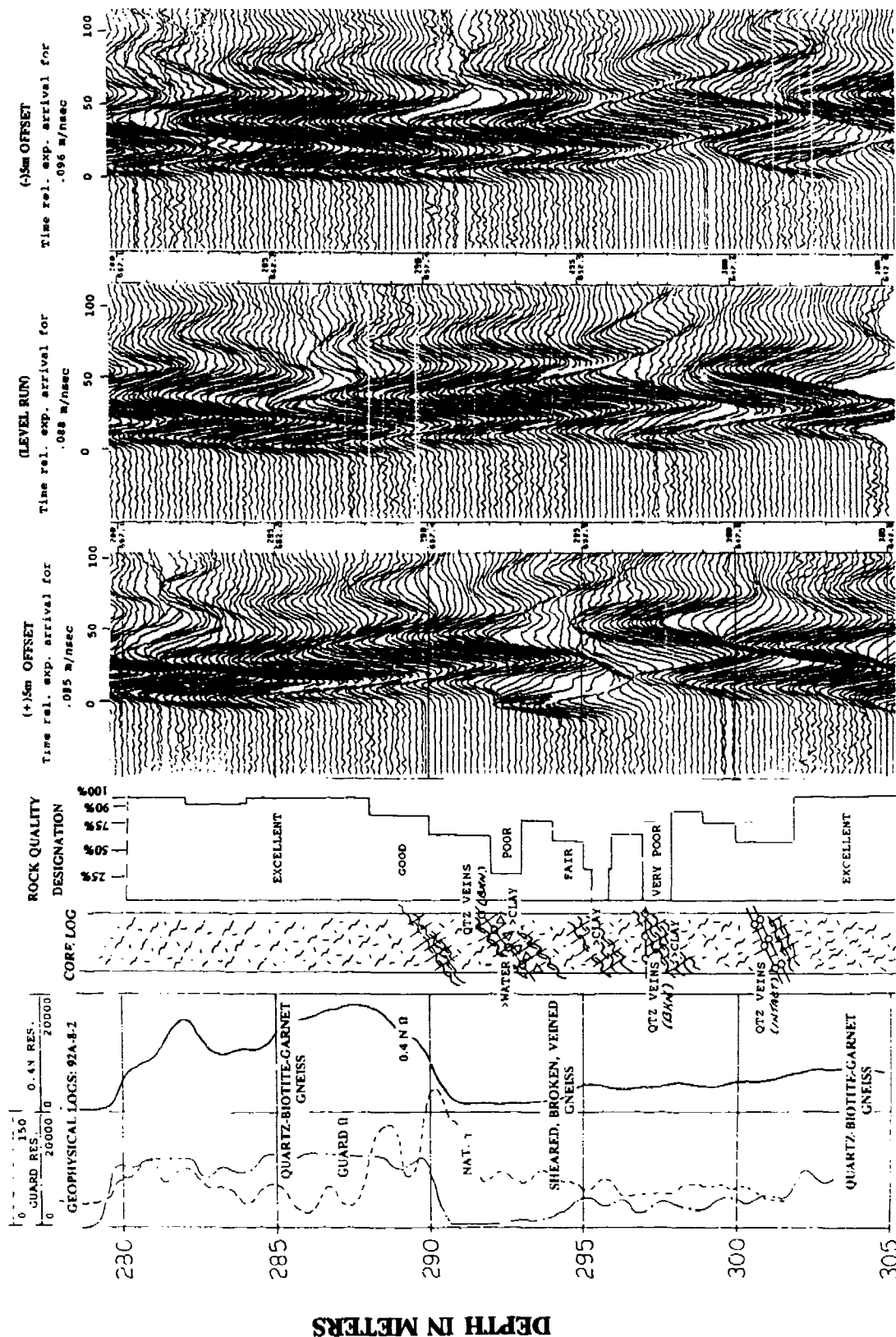


Figure 8. PEMSS Response Correlation Chart for Borehole Pair 19 to 25.

USGS TOMOGRAPHIC INTERPRETATION OF PEMSS-3 DATA
BOREHOLES 19 TO 25 - AREA "A"
MAXIMUM HOLE SEPERATION IS 19.3 METERS

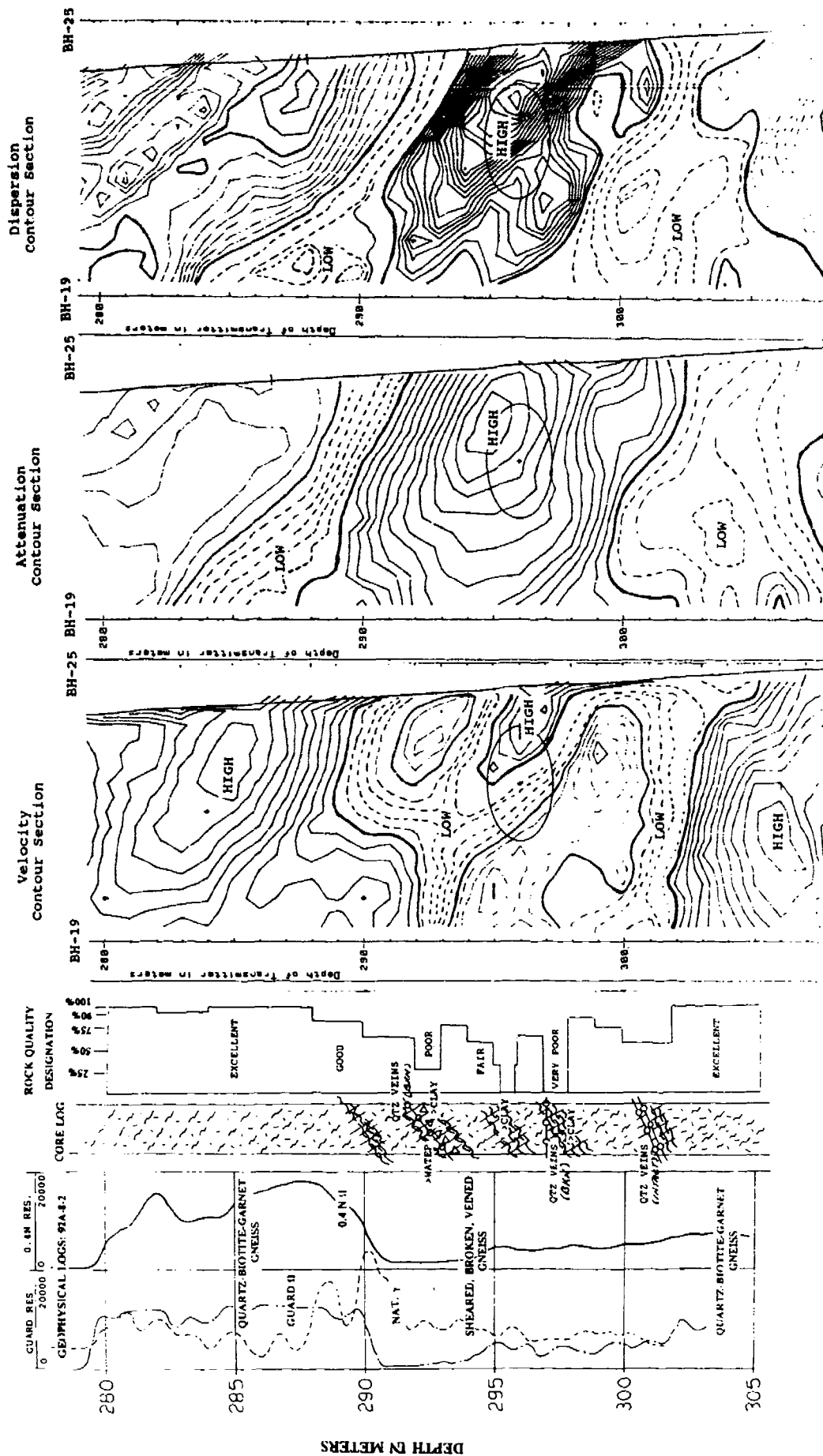


Figure 9. USGS Tomographic Interpretation and Correlation Chart of PEMSS Data from Borehole Pair 19 to 25.

RQD to a surprisingly accurate degree. These charts also demonstrate the effectiveness of the use of offsets in the analysis. The early-late-early-late-early variations in arrival times are best seen on the offsets which show an apparent dip of the feature in the direction of borehole 25. The complex shifts in velocity, accompanied by corresponding attenuation and dispersion events, are considerably enhanced and sharpened by the use of the USGS Tomographic Interpretation plots shown in Figure 9. Similar analyses of PEMSS surveys of borehole pairs to the north and south of the 19 to 25 pair, show that the fault feature strikes to the NNW and dips to the ENE (at about 30°).

CONCLUSIONS

- o When properly calibrated with drilling core and conventional borehole geophysical logs PEMSS can define structural features, (faults, shear zones, changes in fracture density), and lithologies, (quartz veins, amphibolite, quartzose gneiss, etc), in complex metamorphic terranes.

- o Within a specific structural or lithological environment the PEMSS system also exhibits signal sensitivity to conductive minerals (graphite, clays, sulfides), and hydrogeological conditions.

- o The geometry of the borehole array relative to the attitude of subsurface features plays a significant role in terms of PEMSS arrival times and signal character; use of offset data is essential and no less important to the correct interpretation of geologic features than their use in the search for air-filled clandestine tunnels.

- o Rock mass characterization by PEMSS offers a valuable supplement to traditional ratings of Rock Quality Designation (RQD) as revealed by continuous core. With improved data processing and interpretation techniques, and combined with borehole seismic methods, cross-hole EM characterization may someday largely replace conventional coring for the purposes of measuring RQD and strength of rock in metamorphic terranes.

FUTURE WORK

Future work must focus on substantially increasing the number of integrated data sets formally compiled; with efforts to maintain a consistent format in the graphic Response Correlation Charts. Obviously it would be most advantageous to integrate the data sets with the results of the Continuous Wave (KAIST) System and those of cross-hole seismic systems (BITS and JODEX). Equally interesting will be the physio-chemical and microscopic examinations required to explain the amphibolite "effect".

REFERENCES

Alleman, T. J., C. P. Cameron, and H. D. Maclean, 1989, "PEMSS Response of Rock Tunnels to "In-Axis" and Other Non-Perpendicular Antennae Orientations", in Proceedings: Fourth Tunnel Detection Symposium on Subsurface Exploration Technology, Colorado School of Mines, Golden, CO., April 26-29, 1993, this volume.

Deere, D. U., 1964, "Technical Description of Rock Cores for Engineering Purposes," Rock Mechanics and Engineering Geology, Vol.1, No.1, pp. 17-22.

Greenfield, R. J., 1988, "Modeling of Electromagnetic Propagation Between Boreholes", in Third Technical Symposium on Tunnel Detection Proceedings, Colorado School of Mines, Golden, CO., January 12-15, 1988, pp. 156-175.

Kemerait, R. C., J. N. Griffin, J. L. Meade, G. D. Kraft, and G. W. Pound, 1988, "Signal Processing Applied to Tunnel Detection by Borehole Radar", in Third Technical Symposium on Tunnel Detection Proceedings, Colorado School of Mines, Golden, CO., January 12-15, 1988, pp. 593-615.

Lingren, W., 1933, Mineral Deposits, 4th edition, pp 207-212, McGraw-Hill Book Company, New York.

Murphy, W. L., 1985, "Geotechnical Descriptions of Rock and Rock Masses," Technical Report GL-85-3, US Army Engineer Waterways Experiment Station, Vicksburg, Miss.

Olhoeft, G. R., 1988, "Interpretation of Hole-to-Hole Radar Measurements", in Third Technical Symposium on Tunnel Detection Proceedings, Colorado School of Mines, Golden, CO., January 12-15, 1988, pp. 617-629.

Qwen, T. R., 1981, "Cavity Detection using VHF Hole-to-Hole Electromagnetic Techniques", in Symposium on Tunnel Detection Proceedings, Colorado School of Mines, Golden, Colorado, July 21-23, 1981, U. S. Army MERADCOM, Ft. Belvoir, VA., pp. 126-141.

ACKNOWLEDGEMENTS

This work is part of the operations and research conducted under the Tunnel Detection Program of the United States Army. Funding for this mission is provided by the U.S. Army Belvoir Research, Development, and Engineering Center (BRDEC). C. P. Cameron's participation is funded by a Broad Agency Grant Contract (DACA39-90-K-0029) from the US Army Engineer Waterways Experiment Station (WES). His sincere appreciation is extend to Mr. Ray Dennis (BRDEC) and to Mr. Bob Ballard (WES) for their long-term support and encouragement during the course of this work.

This paper benefitted substantially by discussions over a long period of time with various members of the Tunnel Detection Panel of Experts, in particular Mr. H. Dave MacLean, Mr. Dave George, and Dr. Bob Duff. However, the views expressed herein do not purport to necessarily reflect their views nor the position of the Department of the Army or the Department of Defense.

SIXTEEN CHANNEL GROUND-PROBING RADAR DETECTION AND IMAGING OF TUNNELS AND OTHER SUB-SURFACE FEATURES

Dr R. J. Chignell

EMRAD Limited, Guildford, England

INTRODUCTION AND BACKGROUND

The team at EMRAD have been involved with the development of a series of novel ground-probing radar systems over the last few years. The objective of this paper is to present some of the latest developments in which a multi-channel radar has been used for the detection and mapping of tunnels. The work to be described is a natural extension of earlier activities, including the development of a real time Pipe Locator system. The system is also a civil extension of the work carried out at the time of "Desert Storm" in which, in a few weeks, a multi-channel real time system was constructed and demonstrated as a Concept Demonstrator hand held Mine Detector.

The civil development of the multi-channel approach has been pursued, both for shallow targets, for example in the imaging of sub-surface cracks in highways and for the deeper targets involved in tunnel detection and mapping to be described here. A major objective of the work is to automatically generate plan images of the area surveyed, to indicate the position and extent of the targets of interest. This represents a significant development, compared to the single cross-sectional views usually generated.

SYSTEM DESCRIPTION

The system essentially consists of four single channel radars, each with their own transmitter, receiver and antenna system, fully integrated to generate sixteen data channels. The system is usually mounted upon a simple trolley or cart, with the four antenna spread across the width of the swathe to be searched. Each time the radar is triggered, each transmitter is fired in turn, with all four receivers being employed with every transmitter. In this way, sixteen data channels are generated encoding much information about the underground environment, as shown in figure 1

The complete measurement sequence is triggered by a wheel sensor, which allows the measurement interval to be set electronically dependent upon the target sought. With the measurement interval set, the system is operated simply by being pushed along by the operator, typically at normal walking pace. The antenna spacing is set to search a swathe typically at least 2 m wide, in one pass of the system.

The survey cart is fully autonomous, incorporating either a small petrol generator or batteries. The data storage facilities are also included to store the large quantity of data generated. Each time the radar is triggered, sixteen waveforms of 512 points, each corresponding to 1 kByte of data are generated. Currently the high speed hard disc storage facilities are the slowest part of the system and limit the measurement speed. On site, only data recording and checking facilities are usually provided, with the signal processing available being limited to that required to further direct the survey. The radar hardware is, however, configured to allow subsequent real time operation, when all the signal processing options have been explored.

SIGNAL PROCESSING

Extensive signal processing is required to analyse and combine the data into the plan images sought. Figure 2 shows the overall schematic of the signal processing. The first steps involve the processing of individual waveforms to enhance the information encoded in each channel. Typically around eight individual algorithms may be applied sequentially to the channel data. The selection depends upon the information sought. Sometimes all the channels may be treated similarly, but on other occasions, for example the co-channels which transmit and receive on the same antenna, may be treated differently to the remainder.

When the individual waveforms have been processed, the information should be combined to generate the required plan image, or map formats of the buried objects. A number of schemes have been devised for this combination process, dependent upon the range of the measurements and the target characteristics. In combining the channels there are many issues to be addressed, including the mathematical formulation and considerations such as the gain equalisation between channels. As in other branches of geophysical surveying the combination of multi-channel data and the solution of the inverse scattering problem is a major topic in its own right.

Once the plan image has been generated, conventional image processing may be applied, to enhance particular features and perform functions such as edge detection. The plan images may then be integrated into other data handling systems. One approach that has been demonstrated, is to take a CAD drawing of the above ground features and use it as the basis of planning the radar survey. The data is then collected and processed to form the plan image. The edges of the target are then delineated to identify the extent of the target, and the edge information imported into the CAD system. A plan CAD drawing of the survey area is then generated, showing both the surface and sub-surface features.

RESULTS

With sixteen data channels and extensive signal processing and the limited length of the written paper, it is not possible to effectively track the progress of the data through the analysis. However, with the aid of colour images, the presentation will include a description of the differences between the channels and show how the data is employed to generate the plan images.

The experimental data presented will be taken from three sites. The first site is a Victorian brick sewer. This is the shallowest target, and the objective of the survey was to locate the path of the tunnel relative to a major highway and provide additional information on the presence of voids around the structure. At the second site, the position and condition of an old tramway tunnel under a highway had been lost, and it needed to be found as part of an assessment of the load becoming capability of the road. The third site is of major historical importance, although all the buildings were destroyed at least two hundred years ago. Access for the radar was severely limited by vegetation, but a number of tunnels were found that, with historical data, aided in understanding of the layout and use of the former structure.

Although throughout the signal processing analogue signals are employed once the plan image has been generated, it may be converted to the black and white format shown in figure 3, for the Victorian sewer. The edges of the structure may then be highlighted as shown in figure 4, so that the edge information may readily be translated to a CAD or other plan drawing of the site.

CONCLUSIONS

A multi-channel radar system and data analysis procedure has been demonstrated, that allows plan images of structures such as tunnels to be generated. On site, the system requires only one pass of the radar, typically at walking pace.

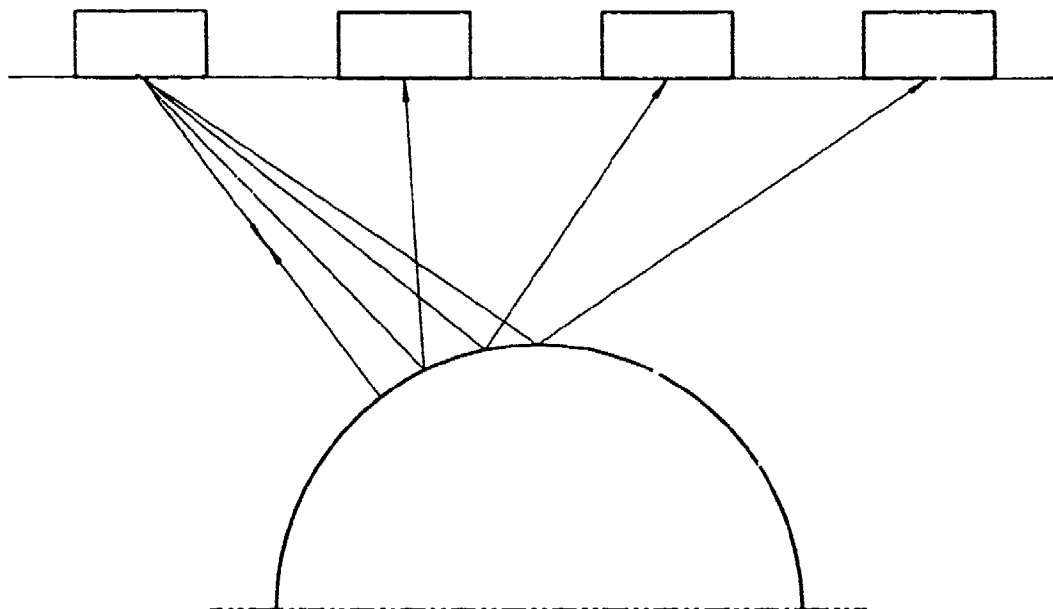


FIG. 1
 SHOWING THE DIFFERENT PATHS
 CHARACTERISED BY A MULTI-CHANNEL RADAR

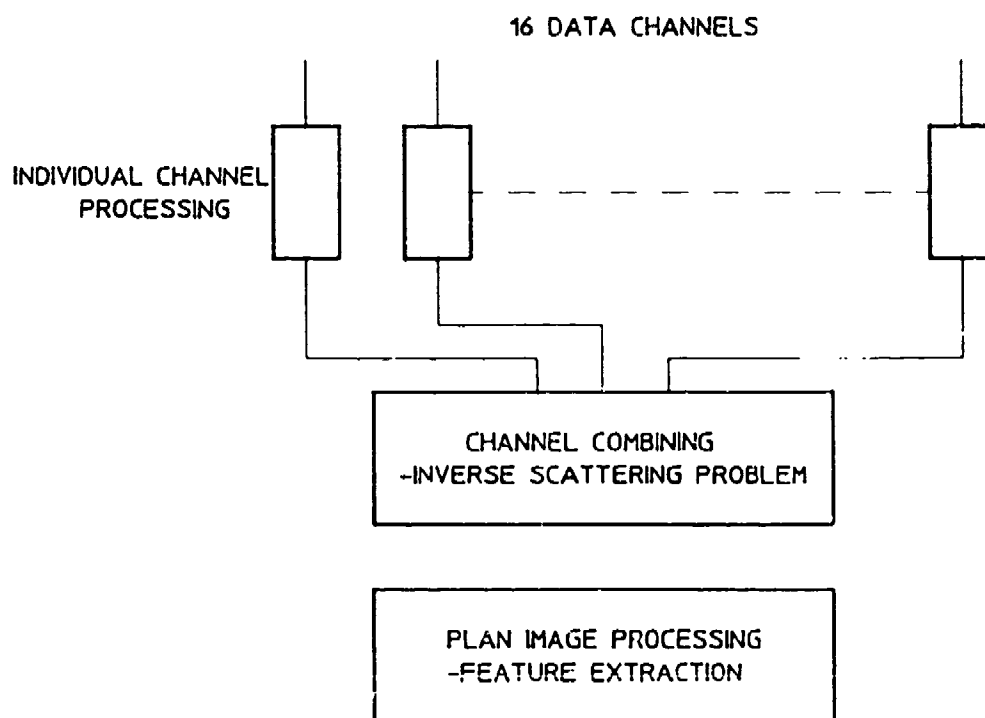


FIG. 2
 THE SIGNAL PROCESSING SCHEME

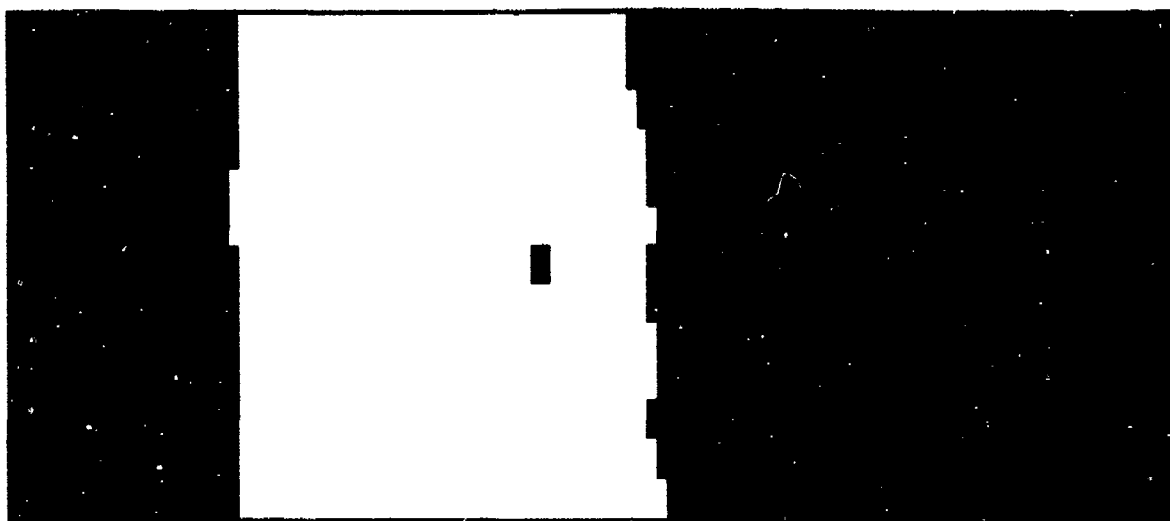


Fig. 3 Black and white plan image of Victorian Sewer

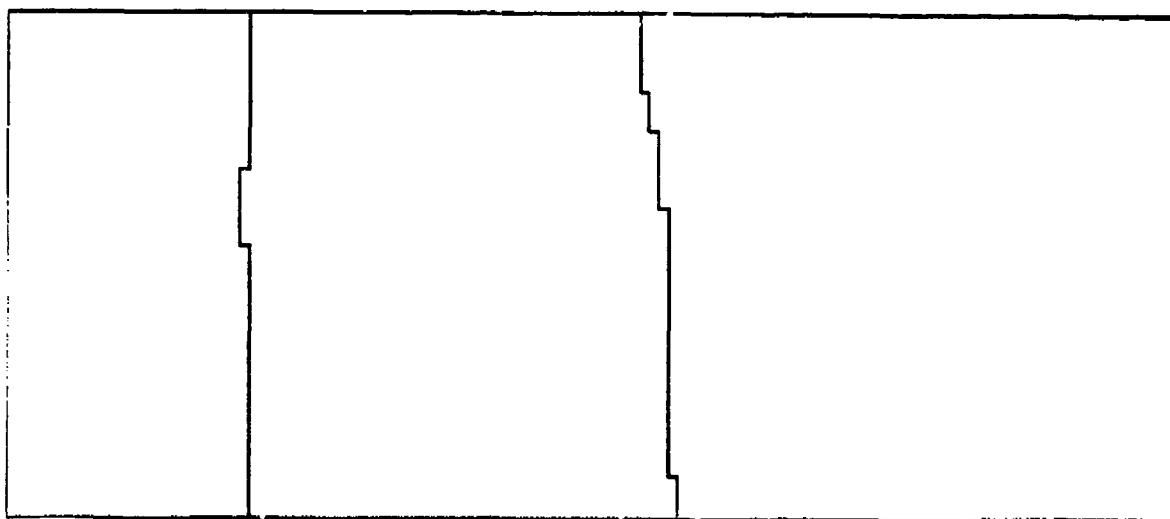


Fig. 4 Outline of Victorian Sewer fed to CAD System

Radar Waveforms From a Three Dimensional Tunnel

M.L. Moran* and R.J. Greenfield**

* Cold Regions Research and Engineering Lab, Hanover NH 03755-1290

** Dept. Geosciences Penn. State University, University Park PA 16802

ABSTRACT

Extensive use has been made of previously discovered tunnels to document the range of affects which may be observed in a cross borehole radar survey when a tunnel lies between the transmitter and receiver boreholes. These efforts have concentrated on the analysis of survey data collected when the source and receiver boreholes are located perpendicular to the tunnel axis. In a search for undiscovered tunnels it would be unlikely to encounter such an ideal geometry. The emphasis in this study is placed on investigating the signal response when the source and receiver boreholes are not perpendicular to the tunnel axis. To do this we developed a three-dimensional numerical model that produces time domain waveforms comparable to field data collected using the cross borehole PEMSS System (Pulsed Electromagnetic Sensing System, developed by South West Research Institute). The model uses an exact Green's function solution for a true vertically oriented, electric dipole.

The model results compare very well to PEMSS field data for both perpendicular (2D geometries) and obliquely incident ray paths (3D geometries). Field data and model simulations show that there is a marked difference in waveform appearance when ray paths strike the tunnel at oblique angles. Further model simulations for tunnels filled with air and water exhibit low amplitude shadow zones which extend along the entire length of the tunnel. This shadow zone is the most reliable indicator for the presence of a tunnel. Model results for air-filled tunnels in which the angle, α formed by a line normal to the tunnel axis and the line connecting the source and receiver is larger than 45° indicate that the tunnel is effectively opaque to incident radiation. Beyond angles of $\alpha=45^\circ$ arrivals in the shadow zone are dominated by energy which diffracts around the tunnel. Moderate tunnel dips for air-filled tunnels do not appreciably affect waveforms.

INTRODUCTION

Since ancient times defensive military positions have been threatened by tunnelling. In addition to the problem of man-made cavities there is a growing need to locate and characterize naturally occurring subsurface cavities such as those found in Karst terrains. One of the principal geophysical techniques applied to this problem is the cross borehole electromagnetic survey.

Extensive use has been made of previously discovered tunnels to document the range of waveform effects which may be observed when a tunnel lies between the transmitter and receiver boreholes [Greenfield 1988a-b; Olhoeft, 1988]. These efforts have concentrated on the analysis of survey data collected when the source and receiver boreholes are located perpendicular to the tunnel axis. In a search for undiscovered tunnels or cavities it would be unlikely to encounter such an ideal geometry. The emphasis in this study is placed on investigating the signal response when the source and receiver boreholes are not perpendicular to the tunnel axis.

To do this we developed a three-dimensional model capable of producing time domain waveforms comparable to field data collected using the cross borehole PEMSS System (Pulsed Electromagnetic Sensing System, developed by South West Research Institute) [Owen and Shuler 1980]. This system has a demonstrated capability of detecting tunnels and natural subsurface voids. The PEMSS system uses a vertically oriented electric dipole which emits a short pulse radar wave with peak power output centered around 30 MHz. The pulse width is approximately 0.1 micro second in duration. The transmitter and receiver are typically located in boreholes separated by approximately 30 m.

MODELING METHOD

The complete solution is found to the problem of a vertical electric diople in the vicinity of a infinite cylindrical tunnel (see Figure 1). Results are obtained in the frequency domain then transformed to the time domain to synthesize the short pulse radar signal. The time function for the electric dipole is obtained by deconvolving field data from depths away from the tunnel.

The frequency domain solution is found by expanding a dipole source field (primary signal) in a tunnel centered cylindrical coordinate system and then Fourier transforming into k_z space in the axial, z , direction. This approach is similar to that of Hill and Wait [1978], Wait [1953, 1955] and Lytle [1971] except that we obtain high frequency time domain results and no far field approximations are used. Boundary conditions at the surface of the cylinder give the reflection coefficients of the scattered wave fields. The scattered electric fields are then numerically integrated over k_z to transform back into three-dimensional space. In summary, the electric field integral equations for the scattered fields have the form,

$$E^{scat} = \int_{-\infty}^{\infty} \sum_{n=0}^{\infty} \{ (A_n K_n(\gamma \rho) n + \gamma_1 B_n K'_n(\gamma \rho)) \sin(n\phi) + (C_n K_n(\gamma \rho) n + \gamma_1 D_n K'_n(\gamma \rho)) \cos(n\phi) \} e^{ik_z z} dk_z \quad (1)$$

where A_n , B_n , C_n , D_n are the scattered wave coefficients that must be defined by matching the boundary conditions at the surface of the tunnel, ρ , ϕ , z are the cylindrical coordinates shown in Figure 1, γ is the product of the radial componet of wavenumber and $\sqrt{-1}$, k_z is the z componet of wavenumber, and $K_n(z)$ is a modified Bessel function of the second kind (analogous to e^{-z}). Since the rock has non-zero conductivity no singularities occur along the path of integration. Details of the solution and numerical methods may be found in Moran [1989].

RESULTS AND INTERPRETATION

There is a significant difference in waveforms for paths with $\alpha = 0^\circ$ compared to paths with α values greater than 30° . Figures 3a-b show field records for two borehole surveys which demonstrate this difference. The record sections are for a direct scan in which the transmitter and receiver are at the same height, D , above the center of the tunnel (see cross section and plan views shown in Figure 2). The amplitudes on the figures are relative to the primary signal, i.e. the signal when no tunnel is present to scatter energy. Notice the difference in the initial parts of the waveforms in the vicinity of the tunnel. The $\alpha = 0^\circ$ waveforms in Figure 3a exhibit a positive initial peak that arrives early relative to the primary signal. This early arrival is due to scattered field energy traveling through the high velocity air filled tunnel. In Figure 3b where $\alpha = 27^\circ$, waveforms in the vicinity of the tunnel do not exhibit the same initial arrival. In this case we observe only a very small negative peak which arrives only slightly earlier than the primary waveform. Both data sets show a 7 db peak-to-peak amplitude reduction around the depth of the tunnel. This reduced amplitude zone may be termed the tunnel shadow.

Comparisons of model results, for the $\alpha = 27^\circ$ PEMSS field data show good agreement (Figure 4). The path length was 23 m. The model tunnel radius, R , was 1.m. The tunnel's host media has a conductivity (σ_1), of .001 S/m and a relative dielectric constant (ϵ_1) of 8.0. These parameter values are representative of a damp granitic or metamorphic rock. The dominant tunnel effect is seen in the low amplitude early arrival which asserts itself in the interval between $D = -2.4$ and 2.4 m (at $D=0$ m the source and receiver are located at a height with respect to the center of the tunnel). Above and below this interval the waveform returns to the basic shape of the homogeneous media response (i.e. the primary wave). The synthetic waveforms

show good conformance with the field data. The minor differences between the simulated response and the field data are likely to be due to slightly different antenna waveforms, and or, geologic noise such as a fracture halo surrounding the tunnel which is unaccounted for in the simulation.

Figure 5 shows a suite of synthetic waveforms for an air filled tunnel at α angles ranging from 0° - 70° . The source receiver separation is 30 m, $R = 1$ m, $y_{SR} = 0$ m, and $D = 0$ m. This suite clearly shows the change in waveform that occurs as a function of α . The $\alpha = 60^\circ$ waveform is identical to the primary waveform, but is 7.1 db lower in amplitude. The 0 - 15° waveforms are characteristic of field data observed at small α angles. The $\alpha = 30^\circ$ waveform has the same wave shape seen in the field data shown above; for α greater than 55° the early arrival is completely gone. An amplitude reduction of approximately 7 db persists for all α angles. This shadow zone is present in all the air filled tunnels we have modeled. We have found that the shadow zone extends approximately 2 m above and below the tunnel center. Also of interest is a very small delay in arrival time (approximately .003 μ sec) for all waveforms with $\alpha > 60^\circ$.

Synthetics for tunnels with $R = 1.5$ m give similar results. There is a distorted waveform with an early arrival for all angles below $\alpha = 45^\circ$ with the waveforms changing smoothly with α . The amplitude in the shadow zone is approximately -11 db. The extent of the low amplitude zone is approximately 3 m above and below the tunnel axis. At depths 3-7 m above (or below) the center of the tunnel both the 1.5 m and 1 m radius tunnels exhibit a 1 to 2.4 db amplitude increase. This represents a region of constructive interference between the scattered and primary waves. For the $R=1.5$ m tunnel at $D=0$ m, $\alpha = 60^\circ$ a delay of approximately .007 μ sec is observed.

The physical explanation for the behavior of waveform dependance on α is as follows. At $D = 0$ m and $\alpha = 0^\circ$ the scattered wave is propagating through the air filled tunnel (the velocity of air is about 3 times that of the rock). As a consequence, this scattered energy arrives earlier than the energy that diffracts around the tunnel. The scattered and diffracted waves then interfere destructively to produce the observed shadow zone. An application of ray theory arguments shows that as α increases the scattered field energy that propagates through the tunnel is refracted towards the tunnel axis. Above about $\alpha = 50^\circ$ the energy is refracted critically and does not exit the side of the tunnel in the region of the receiver. In the field data shown in Figure 3h $\alpha = 27^\circ$. This gives an incident angle (θ) which is approaching the critical angle. In such a case only a small portion of the scattered energy will propagate through the tunnel and reach the receiver. Thus the total waveform observed is dominated by diffracted arrivals. Energy following such a curved diffraction path will retain the fundamental shape of the primary waveform but will have a substantially reduced amplitude, and a very slight arrival time delay relative to the time of the primary.

In Figure 6 we consider models in which the tunnel is filled with a mildly conducting material with the electrical properties of water ($\sigma_2 = 0.005$, $\epsilon_2 = 81$). Only three α angles, 0° , 30° , and 45° are considered. The waveforms showed several prominent features. First is the waveform alteration in the later half of the wavetrain which exhibits a move out and amplitude decay as the source and receiver are raised above the center of the water filled tunnel. Also prominent is a very late arrival which also exhibits move out and amplitude decay. These two effects are attributed to reverberation phenomenon which result from multiply reflected ray paths inside the tunnel. S. Low [1988] observes similar reverberations in a two-dimensional reflection mode radar simulation for a fluid filled cavity. Another interesting difference between the fluid filled and air-filled tunnel is the lack of significant amplitude enhancement at the higher y positions in the fluid filled models and the smaller peak to peak amplitude reduction of the $D=0$ traces. The only observable effect of varying α is a slightly darker (< 1 db) tunnel shadow at $D=0$ m. Otherwise, α variation does not seem to appreciably effect the received waveform for a fluid filled tunnel.

The next series of α models considered (Figure 7) are for a cylinder filled with a highly conducting material ($\sigma_2 = 10^{10}$, $\epsilon_2 = 8$). Three α angles will be considered, $\alpha = 0^\circ$, 15° , and 30° . The most striking result from these models is the lack of waveform alteration. They show very little indication of the presence of the cylinder. Of particular note is the lack of a shadow zone at the low y positions, only a .8 db amplitude deficit is observed as compared to the primary wave. A maximum amplitude reduction of 2 db is found in the interval of $D=2$ m to 2.4 m above the center of the tunnel.

In Figure 8 we look at the effect of tunnel dip (β) in addition to changes in α . Dip may be produced by either a truly dipping tunnel or by borehole deviation from vertical. We consider the effect of dip on an air-filled tunnel with a radius of $R=1$ m. Three increments in α were considered 0° , 15° and 30° . For each α we looked at two dips, $\beta = 10^\circ$, and 20° . The resulting waveforms were nearly identical with those observed for non-dipping air filled tunnels. The only observable difference between the dipping models and non-dipping cases was evident when we compare the $\alpha=30^\circ$, $\beta=20^\circ$ case with the non-dipping $\alpha=30^\circ$ model. In the dipping case we observe a slight difference in peak to peak amplitude profile. This amplitude difference is probably due to the fact that as the tunnel dips relative to the source and receiver boreholes the incident waves encounter an apparent "thickening" of the tunnel with increasing dip. At higher dips one would assume that this effect will become more pronounced. However dips much larger than $\beta = 20^\circ$ are unlikely in field situations. It is doubtful that even large dips would produce an anomaly which can be seen in field data. We conclude that moderately dipping tunnels and or deviant boreholes do not significantly alter the shape or amplitude of the received waveforms.

The last model study looks at the effect of tunnel dip (β) in addition to changes in α . Tunnel dip may be produced by either a truly dipping tunnel or an apparent tunnel dip due to borehole deviations from vertical. We consider the effect of dip on an air-filled tunnel in a rock host with $R=1$ m, and a source receiver separation of 30 m. The two models compared are shown in Figure 7a and 7b. The first model has $\alpha=30^\circ$ and $\beta=0^\circ$ and the other having $\alpha=30^\circ$ with $\beta = 20^\circ$. The only discernible difference is a slight persistence in the tunnel shadow at higher source receiver positions for the $\beta=20^\circ$ case. This amplitude difference probably results from an apparent thickening of the tunnel with the increased dip relative to the source and receiver boreholes. All modeling done to date with moderate β values has shown little sensitivity to this parameter. At β values greater than 20° one would assume that this effect will become a little more pronounced; however, dips larger than $\beta = 20^\circ$ are unlikely in field situations.

CONCLUSIONS

The results of this study reveal that the most reliable indicator of a tunnel's presence is the shadow zone which is observed when the tunnel is illuminated by radar. However, it should be recognized that amplitude anomalies can be produced by a variety of geologic structures unrelated to tunnels. Waveform alterations are seen, in the model studies, to be highly variable with changes in α and material properties. Model studies show that the lack of significant waveform alteration from a single set of field data should not be construed as definitive evidence that a tunnel is absent. Suspect targets should therefore be viewed from a variety of survey perspectives so as to maximize the probability of strong primary wave interaction with the suspected tunnel.

Additional field components need to be looked at. This study has focused exclusively on the vertical component of the electric field. Other components may prove to be more informative in the characterization of potential tunnel anomalies, particularly the radial electric field which will only exist if a scattering object obstructs the vertically polarized primary field. Variations in the magnetic fields in the presence of a tunnel may also prove of interest.

REFERENCES

- Greenfield, R. J.; 1988a, "Modeling of Electromagnetic Propagation Between Boreholes", Proceedings of the Third Technical Symposium on Tunnel Detection, Golden Colorado, pp. 156-172
- Greenfield, R. J.; 1988b, "Waveform Modeling Of Electromagnetic Waves Scattered By Tunnels, Expanded Abstracts 50th Annual SEG Meeting, Vol. 1, pp. 220-221.
- Hill, D.A.; Wait, J.R.; The Impedance of Dipoles in a circular Tunnel with an Axial Conductor; IEEE Trans. Geosc and Elect.; Vol GE-16, no. 2; pp. 118-125; 1978
- Low, S. P.; 1988, "The Response Of A Cylindrical Target: Implications For Ground Penetrating Radar", M.S. Thesis, Pennsylvania State University, 106 pg.

Moran, M. L.; 1989, "Time Domain Electromagnetic Scattering For A Three Dimensional Tunnel In The Presence Of A Vertically Oriented Electric Dipole", M.S. Thesis, Pennsylvania State University, 123 pg.

Owen T. E. ; Schler S. A. ; (1980), "Subsurface Void Detection Using Surface Resistivity And Borehole Electromagnetic Techniques", Geophysics, Vol. 46, No. 4, E-7.

Olhoeft, G.R. ; (1980), "Interpretation of Hole-To-Hole Radar, Proceedings of the Third Technical Symposium on Tunnel Detection, Golden Colorado, pp. 616-629

Wait, J.R.; (1953), "The Cylindrical Ore Body In The Presence Of A Cable Carrying An Oscillating Current", Geophysics, Vol. 17, No. 2, pp.378-386

Wait, J.R.; (1955), "Scattering Of A Plane Wave From A Circular Dielectric Cylinder At Oblique Incidence", Canadian Journal Of Physics, 33, pp.189-195

Lytle, R.J.; (1971), "Far-Field Patterns Of Point Sources Operated In The Presence Of Dielectric Circular Cylinders", IEEE Transactions On Antennas And Propagation, Vol. AP-19, No. 5, pp. 618-621

FIGURES

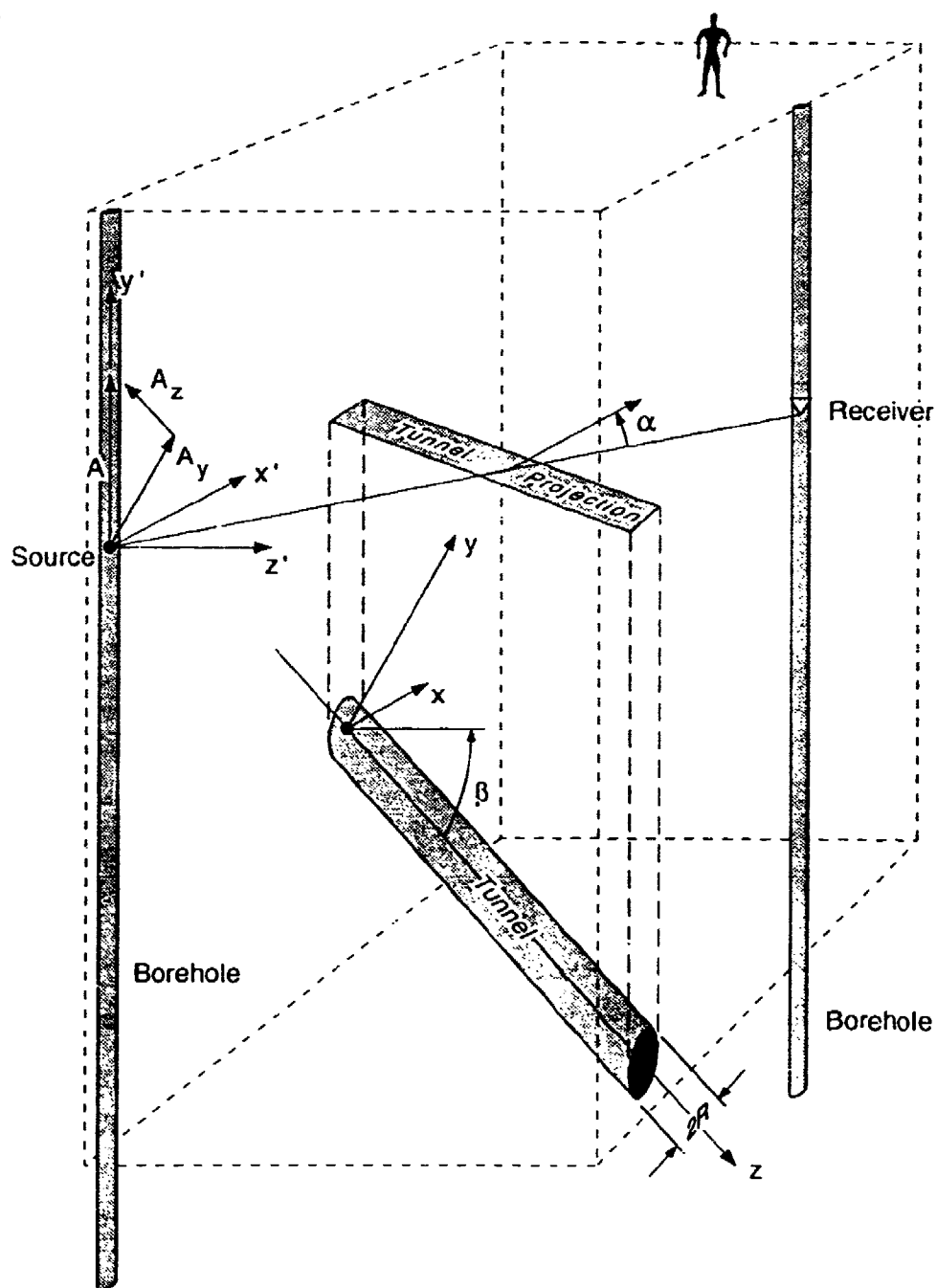


Figure 1 Three-dimensional tunnel/source-receiver perspective. The tunnel dips at an angle β below the earth's horizontal x' - z' plane and is obliquely rotated by an angle α measured between the x' axis and a line connecting the source and receiver positions. The tunnel diameter is $2R$.

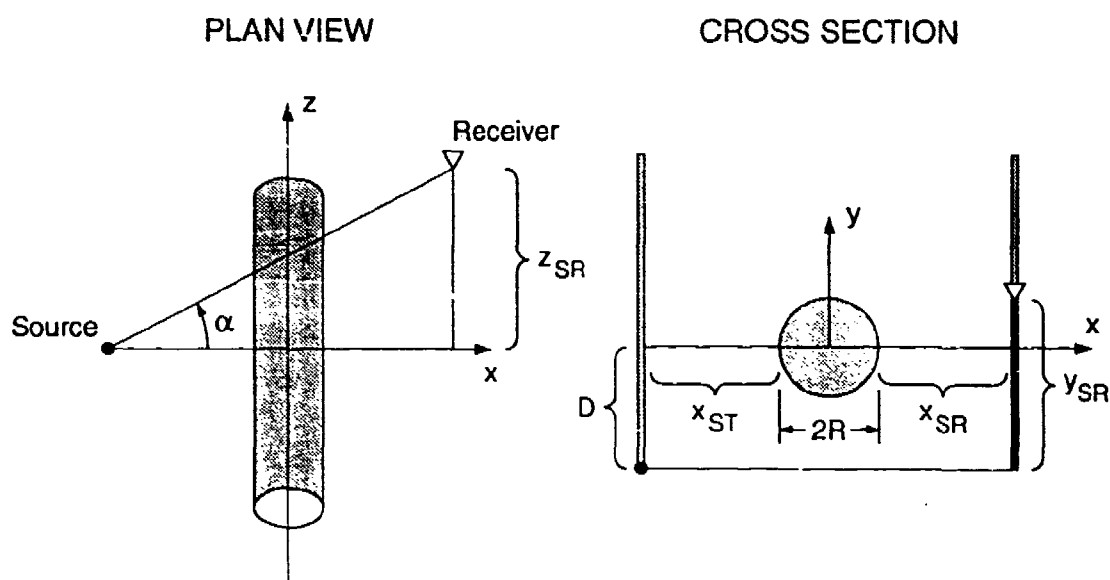


Figure 2 (a) Plan and (b) cross-sectional views of general source and receiver geometry. \bar{p} is the source to receiver separation, α defines the angle formed between \bar{p} and the x axis, Z_{SR} is the z axis separation between the source and receiver, X_{ST} , X_{RT} , and Y_{SR} are the x separation between the source and the tunnel's center, the x separation between the receiver and the tunnel's center and the y offset between the source and receiver. D is the source depth above or below the tunnel's center. The tunnel diameter is $2R$.

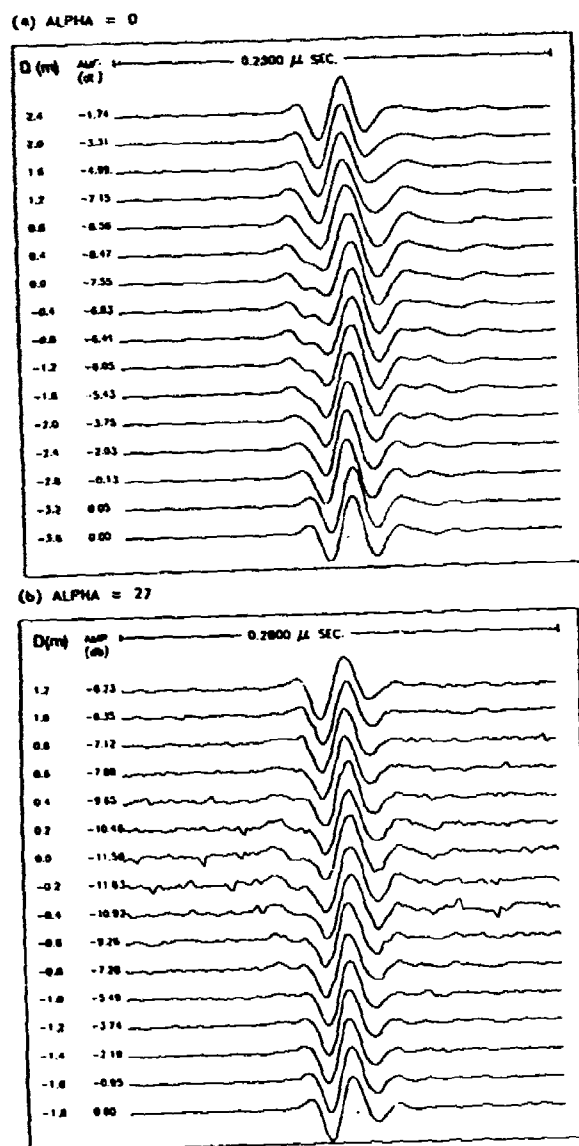


Figure 3 PEMSS field data. (a) Source and receiver have $\alpha=0^\circ$. (b) PEMSS field data with $\alpha=27^\circ$.

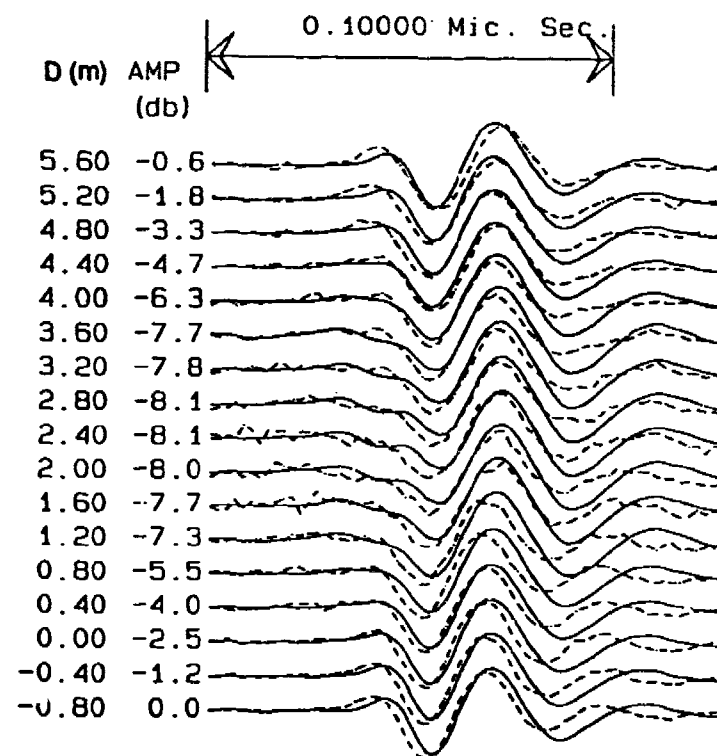


Figure 4 Overlay of model simulation and field data (dashed lines) from Figure 3b.

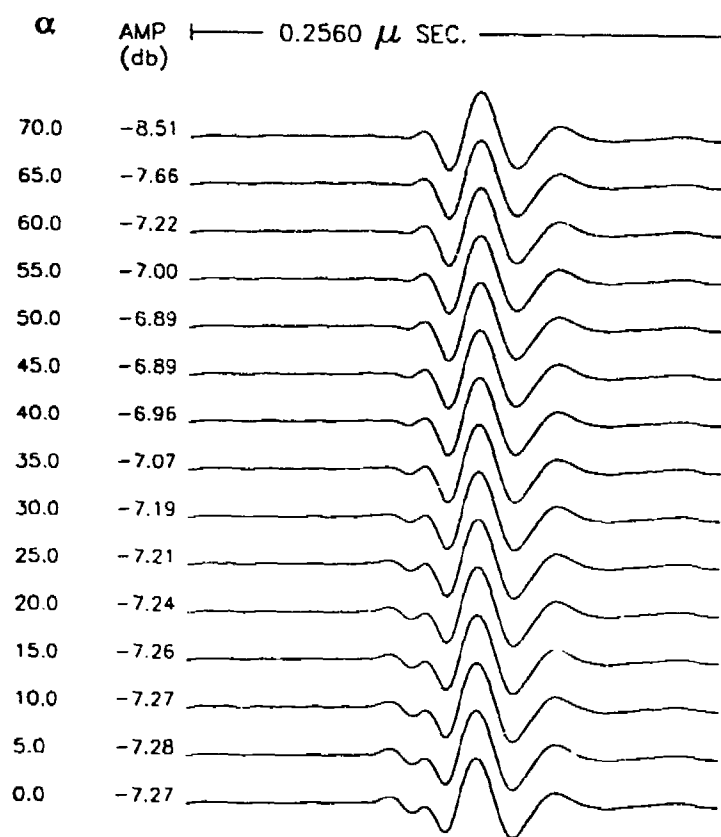


Figure 5 Composite suite of $D = 0$ traces for an air filled tunnel with $R = 1.m$, α ranges from 0° - 70° .

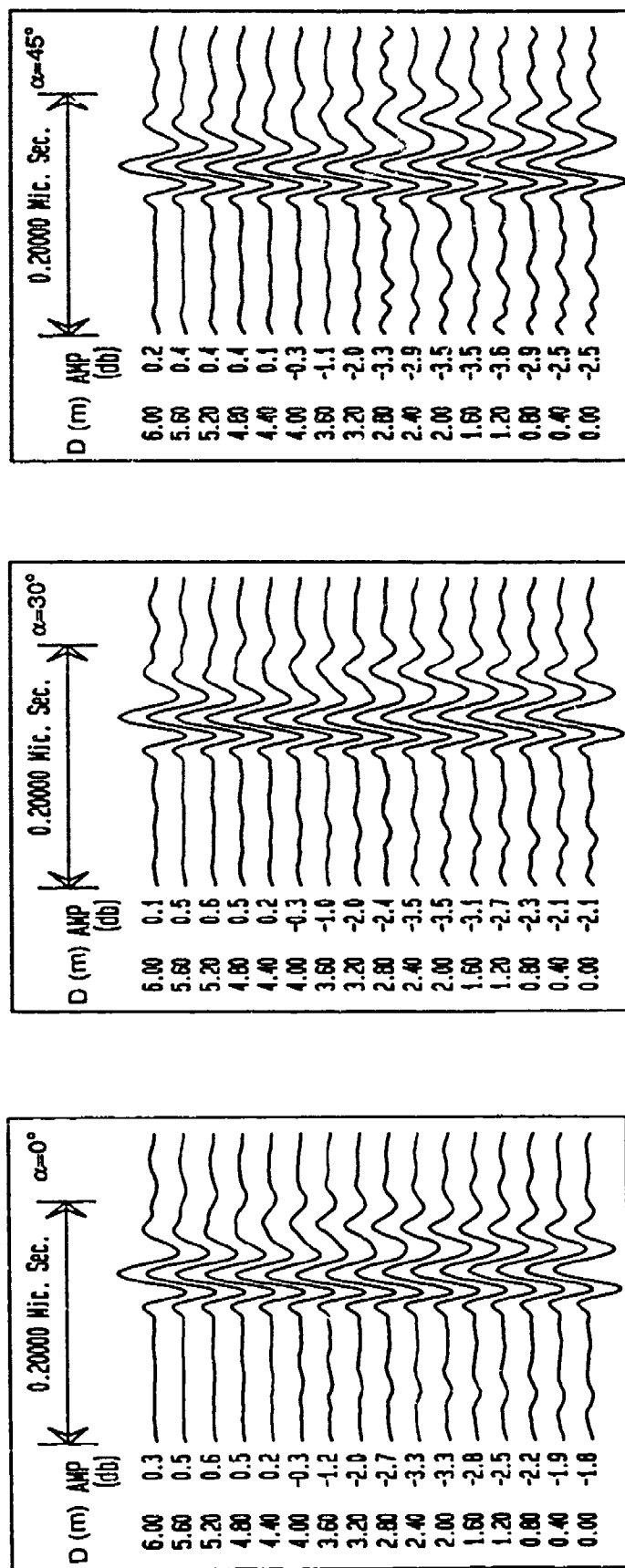


Figure 6 Series of models for water filled tunnels with $A=1.0$ meter and $\alpha=0, 30$, and 45 degrees.

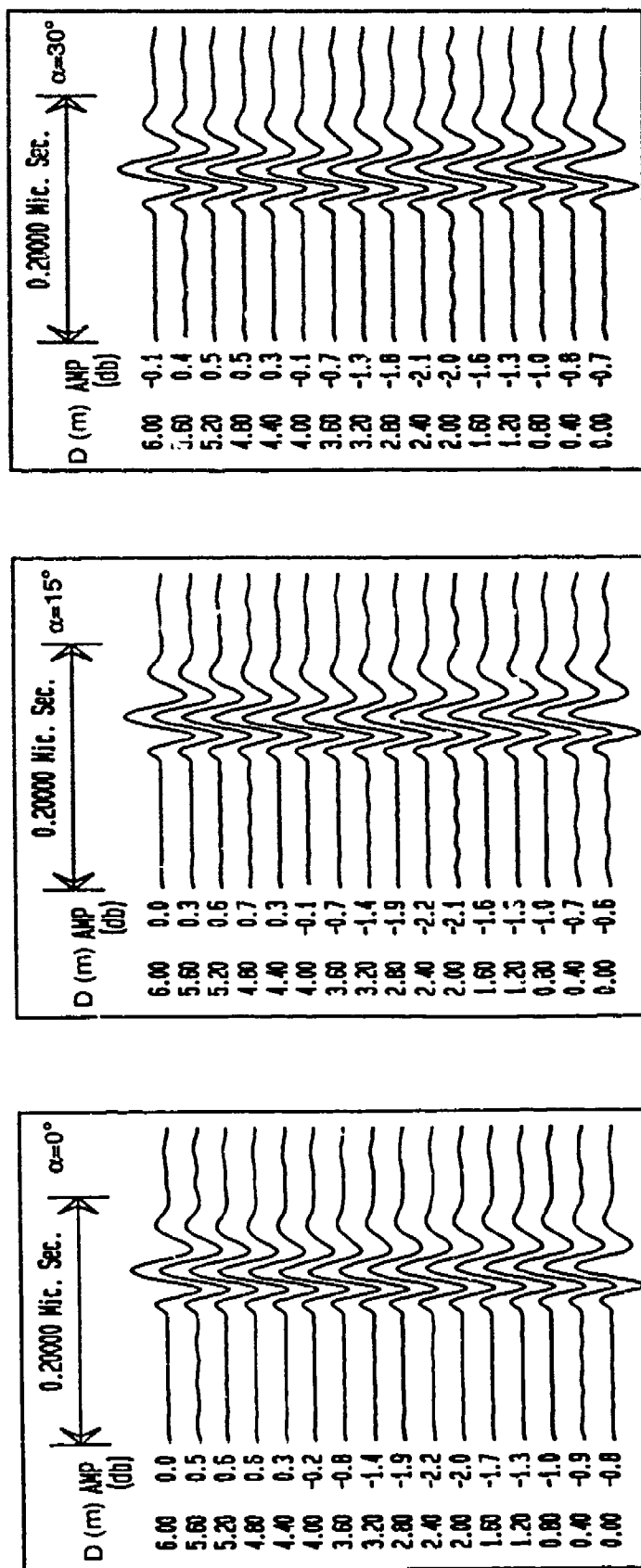


Figure 7. Series of models for a highly conducting tunnel with a radius of 1 m and $\alpha = 0^\circ$, 15° , and 30° .

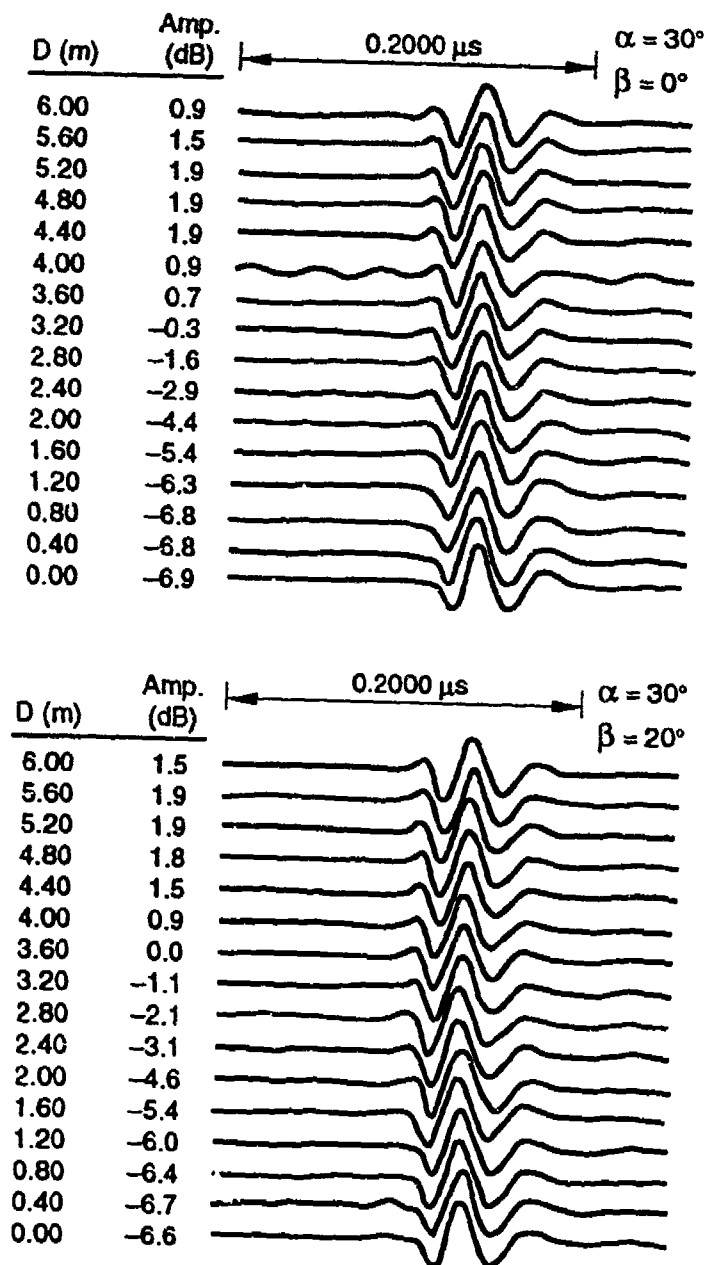


Figure 8. Model comparison between a non-dipping (a) air filled tunnel and (b) a tunnel which dips at $\beta=20^\circ$. Both simulated scans are at $\alpha=30^\circ$ with $R=10m$. Only a slight amplitude profile alteration is produced by the tunnel dip.

PULSED GPR DETECTION OF VOIDS IN LAYERED GEOLOGIC MATERIALS

W. M. Roggenthen

South Dakota School of Mines and Technology
Rapid City, South Dakota

ABSTRACT

Ground-probing radar (GPR) is a proven technology for the location of subsurface voids. Present research trends appear to concentrate on extending the useful depth of penetration and upon pattern recognition for location of those voids. The depth of penetration for pulsed radar applications has been improved by using higher-power transmitters and by using data acquisition techniques which involve point measurements and data stacking. These modifications have resulted in the acquisition of successful profiles in areas that previously were not amenable to GPR exploration which used lower-power transmitters and dynamic profiling methods. Pattern recognition is aided by the presence of artifacts that may sometimes also obscure or complicate the profiles and which include diffraction hyperbolas and reverberations. These distinctive features, although providing a more complex signature, provide clues for the identification of voids and their location. Examples from underground workings within Tertiary intrusives of Montana are compared to similar stopes and drifts within the Paleozoic sedimentary sequences of the Black Hills of South Dakota.

INTRODUCTION

The ability of pulsed ground-penetrating radar (GPR) to detect voids in the subsurface is derived from the sharp contrast in electrical properties between air or water filling a void and the surrounding host rock. The principles providing the foundation of the imaging techniques are well known (e.g. Ulriksen, 1982; Davis and Annan, 1989; Fisher and others, 1992). Although many new and exciting developments are in progress in terms of improved equipment (e.g. Douglas and others, 1992), for practical field applications we are constrained in most instances to use the equipment that is readily available. Therefore, most improvements in routine operations typically are achieved either through minor modifications in the equipment or through modification of the acquisition techniques. The following discussion deals exclusively with the optimum application of existing commercial technology.

Three examples will be used which are taken from data acquired in varying geologic environments and which represent a range of void detection problems. These situations range from the most geologically friendly situations, i.e. Tertiary silicic intrusions with minimal water content, to more difficult situations involving the shales and limestones of the Paleozoic. As is commonly understood, the primary obstacle to increased depth of penetration lies in the conductivity of the units being imaged (Olhoeft, 1987) although the ability to recognize the existence of applicable patterns is equally as important and depends upon the type of voids being imaged and the geologic character of the enclosing rock. In each instance a series of diagnostic target signatures or recognition criteria can be developed to distinguish the voids.

EXAMPLES

A number of features are distinctive in recognizing voids in the shallow subsurface including diffraction hyperbolas, associated deposits, and reverberations.

Diffraction Hyperbolas

Present day gold mining practices in Montana and South Dakota consist of open pit excavation involving drilling and blasting of benches followed by haulage by large wheeled vehicles. Many of these mining operations are located in areas that were previously mined by underground methods. The underground mining usually ceased shortly after the turn of the century although in some instances it may have operated into the 1950's. The existence of the underground stopes and drifts can represent a safety concern due to the potential for collapse as the benches are being developed by heavy equipment. Because the quality of the underground maps varies greatly from one operation to another, the exact location of the drifts and stopes is often not known.

Figure 1a shows field data taken across the boundary between a Tertiary silicic intrusive and a block of down-dropped shale in an open-pit gold mine in central Montana. As part of a safety program a series of the old stopes where underground development ceased during and prior to the 1950's were imaged using GPR in advance of heavy drilling and production equipment. A standard 100 MHz antenna (GSSI, Inc.) with monostatic geometry was used. The primary features are labeled in the diagram as shale (SH), Tertiary intrusive (Ti), and stopes or underground workings (A,B,C). The origin of the diagonal features plunging toward the left side of diagram is unknown but may be due to mineralized veins. This is probably the best situation for acquisition of GPR data that was encountered.

A number of techniques have been used to enhance the presentation of seismic data from the standpoint of interpretation and general appearance. These include digital filtering, both vertical or single trace filtering and horizontal filtering, and migration techniques. Vertical filtering typically accomplishes little in improving the data quality presentation because this is most useful in removing ambient receiver noise. This type of noise is typically subdued more effectively by stacking adjacent traces. Horizontal filtering is probably the most useful technique after the improvement achieved by stacking adjacent traces. All of the profiles in the following discussion were horizontally filtered with the exception of Figure 1a, which consists of raw field data only. Migration is an often-used technique taken from the tools of seismic interpretation and attempts to move the reflections back to where they originated as opposed to being plotted beneath the transceiver. In most instances, except perhaps during the very final stages of interpretation, it is often overused because it adds little to the location of the voids. An example of the migrated data from the field section of Figure 1a is shown in Figure 1b.

Several points can be made regarding the profile. First of all, good depth penetration was achieved due to the low conductivity of the intrusive rock although the ability to resolve targets, and probably to penetrate as well, was sharply curtailed when the metamorphosed shale was encountered. Secondly, the migrated data shown in Figure 1b did eliminate much of the geometric clutter associated with the stopes although most of the distinctive character of the profile was destroyed as well. Therefore, the relative amplitude of the void signature was enhanced at the expense of eliminating the geometric signature of the target. This emphasizes the point that the migration of profile data is really only useful during the final stages of interpretation as a means of clarifying the position of the anomaly after the identification of the anomaly has been established.

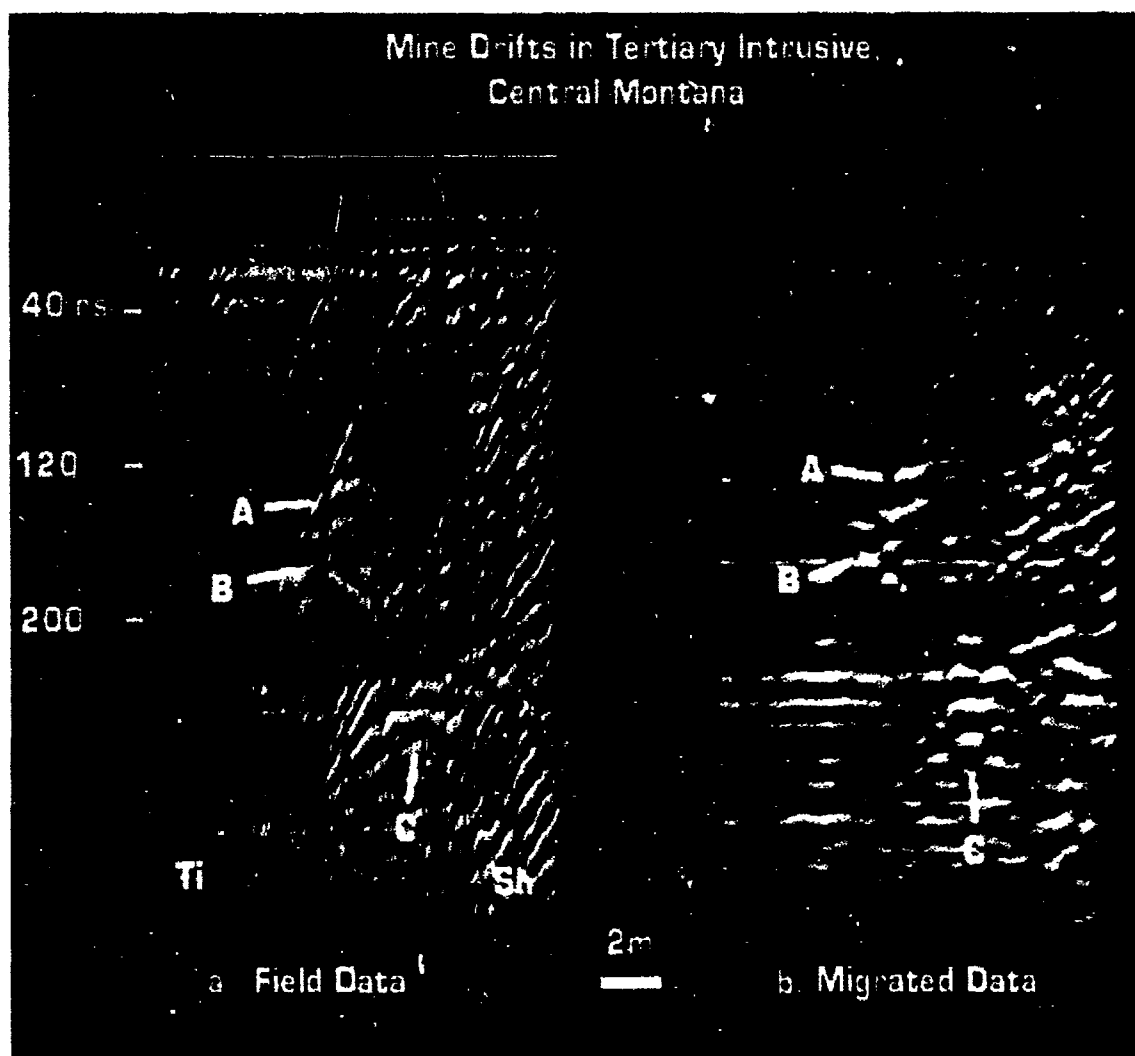


Figure 1. Old mine drifts and stopes in an area presently being mined by open pit methods. The relatively transparent area to the left consists of silicic Tertiary intrusive rock (Ti) whereas the more complicated areas to the right consists of a down-dropped block of Paleozoic shale (SH). A, B, and C in Figure 1a are identified as the old workings. The same points are shown in Figure 1b after the data has been migrated.

Associated Deposits

Jewel Cave National Monument is located in the southern Black Hills, SD. During planning for highway construction to the north of the present-day access to the monument, concern was expressed regarding the existence of shallow caves which might interfere with the construction. Preliminary assessment of the potential for GPR surveys to locate shallow caves using monostatic 100 MHz antennas showed that penetration was insufficient to investigate to the 6-10 meter depths required. One obvious way to increase the penetration was to increase the power of the signal being introduced into the subsurface.

The power being input into the ground is a function of several factors including antenna efficiency, antenna ground coupling and actual power furnished to the antenna. Of these factors increasing the power is probably the easiest to control in order to increase the depth of penetration. Therefore, a 100 MHz antenna (GSSI, Inc.) in a bistatic arrangement with a 5 kw transmitter was used. When the antennas were coupled directly by a coaxial cable to provide coordination between the transmitter and receiver, the configuration was unusable due to antenna cross talk between the receiving and transmitting antennas. To reduce this effect the transmit line was broken out of the 60 m data cable near the recording unit, and the transmit line was run as a separate coaxial cable to the receiving unit. Any antenna cross talk developing due to physical antenna linkage was forced to travel the 60 m up the transmitter cable from the transmitter antenna and back down the receiver cable to the receiving antenna. The net result of this elongated path was to: 1) delay the receipt of antenna cross-talk noise at the receiver antenna by approximately 400 ns and 2) attenuate the cross-talk noise by forcing it to travel a great distance through the cabling. This simple cabling alteration effectively eliminated the difficulties in using the high power transmitter in terms of noise generation.

A series of GPR profiles were collected using the arrangement described above wherein a high-power transmitter was used with the transmit cable being separated from the receive cable near the instrument recorder. This system resulted in the relatively noise-free data shown in Figure 2. Some noise, however, was generated due to cable movement. This generally happened either when the cables pulled under the transmitter/receiver or when the transmit cable was pulled rapidly when straightening it out. Although the increase in power should have resulted in dramatic increases in reflection strength, in practice it had the effect of increasing the workable depths by a factor of 2-3, which was still satisfactory in this instance.

The profile shows a number of interesting features which are located at the base of the Minnelusa Formation (Pennsylvanian) and near the top of the Madison Formation (Mississippian). The overall pattern shows that the nearly flat-lying limestones dip inwards (A in Figure 2) toward the center of a karst or cave. The development of this feature is probably associated with solution at the unconformity at the top of the Madison Formation (Yancey, 1978), but a more modern origin cannot be excluded. The higher amplitudes within the center of the profile may represent a region that contains some remnants of the voids representing the cave, but are more likely associated with material generated as a result of the cave formation. Drilling along the right side of the profile encountered red cave muds that immediately stuck the small-diameter drilling bit. In this instance, the voids or the remnants of voids are marked by the presence of materials that are characteristic of the formation of the voids themselves.

Reverberations

The profiles shown in Figure 3 were acquired at a mine located in the northern Black Hills of South Dakota along two parallel profiles that were separated by about four meters. Although the mineralization is similar in many ways to that mined at the property in Montana, the host for the ore consists of Lower Paleozoic sedimentary rocks of the Cambrian Deadwood Formation. A problem similar to that of the Montana gold mining operation exists in some of the areas being mined in that older drifts sometimes become unstable due to aging of the drifts.

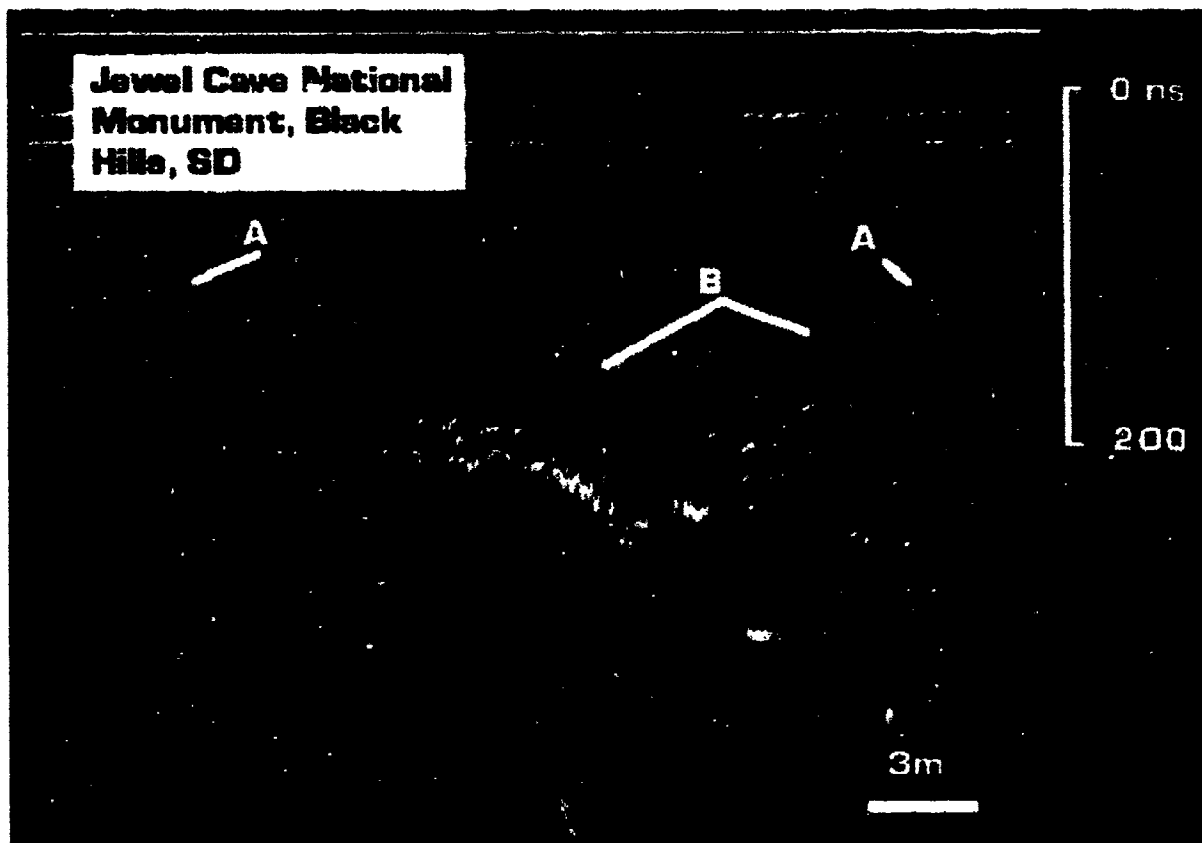


Figure 2. Profile of a solution feature at the boundary between the Mississippian Madison (Pahasapa) Formation and the Pennsylvanian Minnelusa Formation near Jewel Cave National Monument. The high amplitude anomaly marked as B probably consists of cave muds. The normally nearly horizontal reflectors of the lower Minnelusa appear to have sunk (A) into the center of the feature. Little, if any, void space is probably present.

Preliminary attempts at profiling using low-power transmitters were unsuccessful even though the conductivities at the site were not excessively high. The rocks consist of thin shales, sandstones, and some calcitic sandstones and all are above the water table at the present time. Some of the problems in penetration may have been due to the blasting practices at the mine. In order to provide material to grade the roadways during production, the benches are typically sub-blasted to depths of approximately one meter below the nominal bench level. This produces a highly disturbed zone at the top of the bench that

can be used as grading material but which also serves as a series of reflecting interfaces to reduce the energy being transmitted downwards.

The high-power transmitter provided the key to successfully imaging the old drifts, but collection of GPR data at individual points provided considerable improvement in the data, as well. For the purposes of the present discussion, this technique is referred to as "static" profiling. Although standard practice is to collect data while moving and then usually to stack the data, the somewhat slower static profiling technique is highly effective in improving data quality. Sampling every 5 cm is equivalent to stacking with a factor of four at typical dynamic profiling speeds of 0.2 m/s (0.7 ft/sec) using an acquisition rate of 16 scans/second. There is some indication that this method may be more effective than simple stacking because the antenna is allowed to remain at one position while collecting the data. Profiles using static profiling techniques and a high-power transmitter successfully imaged the stopes at depths in the 10-13 meter range.

The drifts shown in Figure 3 are marked by high amplitude reverberations that extend downwards beyond the times at which geologic reflections would normally be expected to occur. These features (D1 and D2) can be distinguished in both profiles. They lack the characteristic diffraction hyperbola probably because: 1) the signal strength received at the surface is much lower than that in Figure 1 and 2) the sharp corners that have been maintained in the Tertiary intrusive of Figure 1 may have been modified through collapse of the drifts in Figure 3. This aging process of underground openings has been well-established in bedded sedimentary rocks (Mraz, 1980), and the effective size of the void increases with time. Therefore, the voids tend to migrate upwards with time, and the GPR recognizes the void as being the top of the disturbed zone.

SUMMARY

Each of the examples shown above demonstrate the capability of GPR to image voids in a range of geologic materials that varies from the most easily managed materials to those characterized by higher degrees of attenuation such as the Paleozoic sedimentary sequences of the Black Hills. Although the pattern that is produced by the voids during a GPR survey are complicated by the presence of the initiating signal, this is not entirely detrimental to interpretation. The distinctive patterns associated with voids include the hyperbolas shed from diffracting corners and the repetitive ringing due to reverberations introduced into the cavity of the void or between highly reflecting interfaces associated with the void. Each of these signatures is dependent upon the material properties of the surrounding medium and the size of the cavity being imaged. In some instances, the associated features can give rise to distinctive signatures. In the case of the stratigraphic studies searching for shallow caves in the Jewel Cave area of South Dakota, cave muds yield distinctive signatures due to the strong contrast between the limestones and the muds.

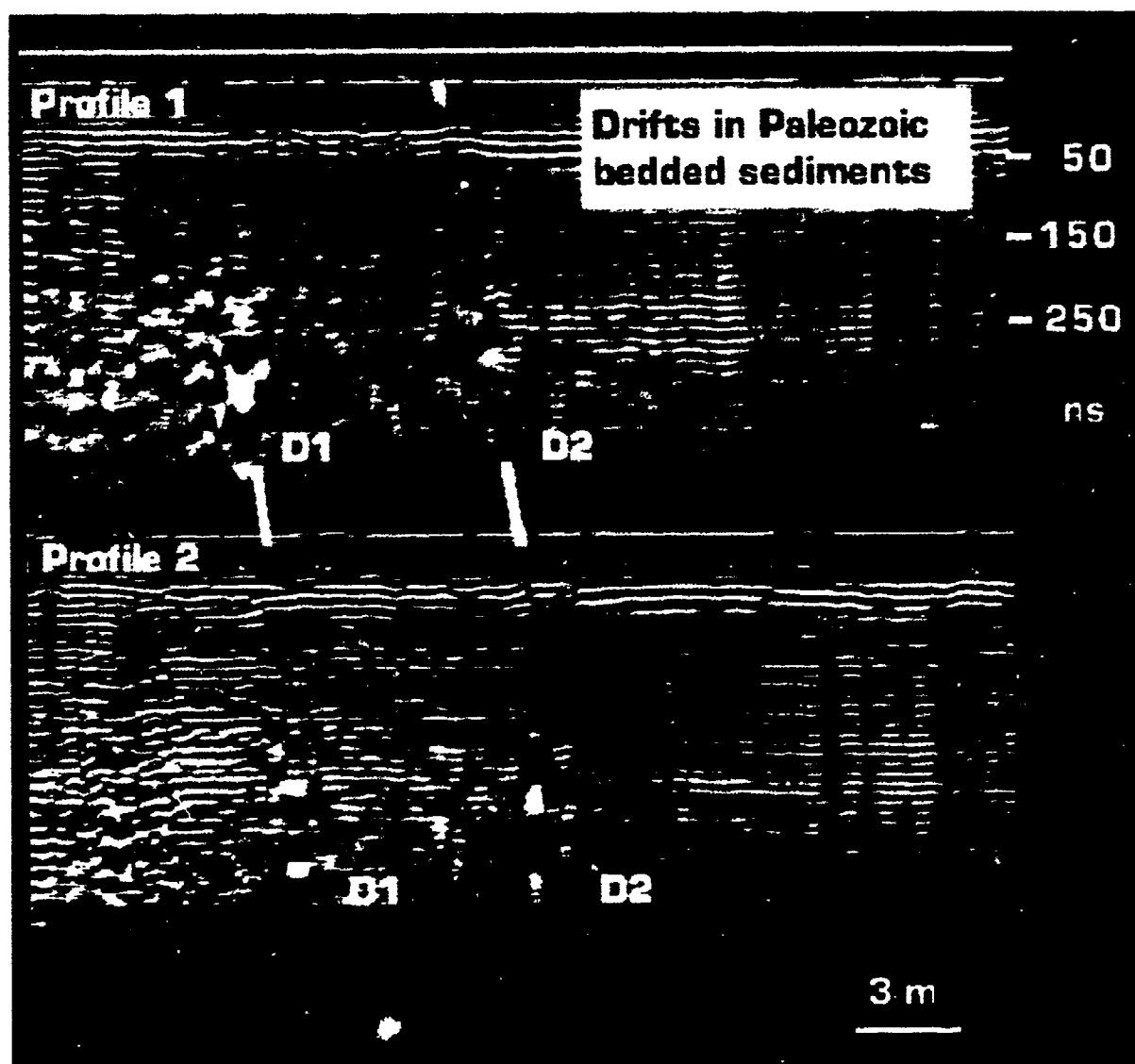


Figure 3. Drift and stopes in Paleozoic sedimentary rocks in the northern Black Hills, South Dakota. The two profiles are parallel and separated by about four meters. Reverberations clearly mark the voids, and the same features (D1 and D2), which appear to represent nearly parallel drifts, can be identified in both profiles.

REFERENCES

Davis, J.L. and A.P. Annan, 1989, "Ground-penetrating radar for high-resolution mapping of soil and rock stratigraphy," Geophysical Prospecting, Vol. 37, p. 531-551.

Douglas, D.G., A.A. Burns, C.L. Rino, and J.W. Maresca, Jr., A Study To Determine The Feasibility Of Using A Ground-Penetrating Radar For More Effective Remediation Of Subsurface Contamination, Environmental Protection Agency, EPA/600/R-92/089.

Fisher, E., G.A. McMechan, and A.P. Annan, 1992, "Acquisition and processing of wide-aperture ground-penetrating radar data," Geophysics, Vol. 57, p. 495-504.

Mraz, D., 1980, "Plastic behavior of salt rock utilized in designing a mining method," CIM Bulletin, Vol. 73, p. 11-123.

Olhoeft, G.R., 1987, "Electrical properties from 10^{-3} to 10^{+9} Hz -- physics and chemistry," in Physics and Chemistry of Porous Media II, AIP Conf. Proc. 154, J.R. Banavar, J. Koplik, and K.W. Winkler, eds., NY, Am. Inst. Physics, p. 281-298.

Ulriksen, P., 1982, Application of impulse radar to Civil Engineering (Ph.D. dissertation), Dept. of Engineering Geology, Lund University of Technology, Coden, Sweden, LUTVDGI (TVTG-1001)/1-175/1982.

Yancy, C.L., 1978, Geology and Elemental Distribution of the Mississippian Pahasapa Limestone - Pennsylvanian Minnelusa Formation Unconformity, Southwestern Black Hills, South Dakota, unpublished M.S. thesis, South Dakota School of Mines and Technology.

Session 2

Seismic Methods

SOURCE SIGNATURE -- AN EXPERIMENTAL APPROACH

Jozef M. Descour

Colorado School of Mines

Golden, Colorado 80401

ABSTRACT

An artificial rarefactional source was used in underground mine tunnels to investigate the relationship between the development of a simple seismic source, and the response in the rock. According to the investigation, the response (seismic signature) evolves with distance from source. The changes appear controlled by the source characteristics, and the stress distribution and the dispersion of seismic response in the rock along the wave path. The pattern appears universal for different sources. The study laid foundations for an improved technique to compensate for signature changes with distance and direction. The compensation for signature changes should allow to properly identify and locate seismic sources regardless of their origin and size.

INTRODUCTION

Typical seismic records for known sources and specific test site conditions are also referred to as seismic signatures of those sources. Seismic signatures acquired in selected test sites are stored in data banks for identifying the nature, and improving location of sources detected in similar conditions at other sites. The concept is based on finding a match for seismic signals detected in response to unknown sources. The rate of success for this approach can be significantly improved by focusing the investigation on elements in the seismic response adjacent to the source and common for different sources (original source signatures), and how that response changes with the direction and distance from the source.

A seismic source can be defined as a set of **varying** forces (driving forces), applied against the rock which result in proportional adjustments (deformations) in the adjacent rock. The adjustments are typically both dilatational and shear in nature, with proportions determined by the distribution of forces at the source (directional characteristics). Consequently, the original seismic signature can be characterized either by the driving forces, or by the adjustments, or both. The adjustments migrate through the rock as P- and S-waves respectively. For both waves, the interaction (convolution) with the rock properties along their wave paths result in a dispersion of the wave energy. The passage of seismic waves through selected points (seismic response), is measured by seismic sensors. Typically, seismic sensors are designed to measure velocities of the ground motions or their time derivatives (particle velocity or acceleration) in the rock. The response of seismic sensors to the ground motions is practically uniform for the same type

of sensors, but may differ between types. Also, the coupling of sensors to the rock can significantly alter the spectral response of individual sensors to seismic waves.

Concluding, the seismic response for any source in the rock should be considered a product of the original source signature and the transfer function between the source and an individual sensor. *Even for the same type of sensors and consistent coupling characteristics, and for the same type of seismic source and similar geometry of the array of sensors, the site specific rock conditions can result in significant differences between seismic response recorded at two different sites.* Consequently, the proper system to measure the rock conditions (transfer functions) for the test site where the model data were acquired, and for each search site, is desired.

The investigation was conducted in the Geophysical Test Bed at the Colorado School of Mines Experimental Mine, also called the Edgar mine, in Idaho Springs, Colorado. Figure 1 presents the locations of a number of seismic sources, and the array of sensors used to monitor seismic response to those sources. Initial efforts concentrated on characteristic features for different sources associated with mining activity. Each seismic record was considered a product of a convolution of two unknowns: the original source signature, and the transfer function in the rock between the source and the detection point. The signals for each source appeared quite complex and of unknown directional characteristics. Consequently, the attempts to deconvolve wave records obtained from six to eight detection points of the array appeared futile. The real progress became possible after developing a system to generate a simple seismic source by releasing a load applied at two opposite points of the tunnel's cross-section. The seismic records for this source were specific for an explicit and repeatable seismic response with well-developed directional characteristics.

TYPICAL SOURCES IN TUNNELS

Typical sources associated with the development or maintenance activities in underground tunnels are either impact sources, or alternating sources. The impact sources are characteristic of a pulse of a compressive force applied against the rock (fig. 2). The impact sources vary from single impact sources (hammer strike, single charge) (fig. 3), to quasi-periodic sources (drill action, knocking wheels at the track joints) (fig. 4), or to random swarms of sources (rounds of charges) (fig. 5). The alternating sources are characteristic of driving forces changing their signs a number of times which generate alternating responses in the rock. The forces are typically applied against the rock at one point, or at a number of randomly distributed points. The alternating sources are typically periodic sources with a period of alternating force significantly shorter than the duration of the source's activity. The typical alternating sources are: a fan (fig. 6), a sump-pump, or either stationary or moving piece of machinery such as a locomotive.

The work done by forces associated with impact sources result in stresses comparable with the strength of the rock. The stresses generated by forces associated with alternating sources are typically significantly below the strength of the rock. Consequently, the peak power of seismic response to any impact source in proximity to that source is usually a number of times higher than for an alternating source. At the same time, the power spectra for impact sources peak for higher frequency and cover

broader frequency range, typically above the frequency range for alternating sources. These differences can significantly alter the response to impact sources with distance compared to alternating sources.

The presented review summarizes the main features of source signatures for seismic sources monitored in the Edgar mine. Typically, the impact sources appeared complex in nature both in the time and frequency domains. Also, they appeared of poor repeatability and were difficult to control. A reliable detection of continuous/periodic sources was practically not possible at distances more than approximately 30 m from the source. Note that figures 3 through 6 present seismic records which were reprocessed based on the experience acquired from the investigation using a controlled load release as a source.

CONTROLLED LOAD RELEASE AS A SOURCE

Significant progress in the investigation on seismic signatures was made possible after introducing the specially designed system to generate seismic response by a sudden stress release (fig. 7). Originally, the system was developed to simulate seismic response to inelastic structural failures/elastic stress release events associated with mining. To generate a seismic source, a load on the order of 250 kN was applied gradually by the hydraulic prop between the two opposite points of the tunnel cross-section. The load produced an approximately symmetrical stress anomaly in the rock. The failure of a replaceable element in the loading system resulted in a sudden load release and an elastic adjustment/seismic response in the rock. The load changes were recorded along with seismic signals detected by the seismic array (fig. 8A). The load records provided detailed information about each source development (fig. 8B).

Large numbers of measurements were conducted in the Edgar mine with the prop installed consecutively at six locations (fig. 1), and with the load applied either vertically, or horizontally. The results confirmed an outstanding repeatability of the source for the same location, and for the same orientation of loading (fig. 9). The high repeatability rate made it easier to separate an elastic response characteristic for each source from random clusters of noise associated with the development of failure in the prop (fig. 10). The noise was of higher frequency than for the seismic response representing the whole source, and was detectable typically at distances less than 30 m from the source. A tendency for smaller failures/seismic sources to group in clusters prior to the occurrence of a larger event is known for failure developments in rock and other materials (Descour and Miller 1986, Hardy 1979, Leighton and Steblay 1972, Rao and Hardy 1989).

As described earlier, the development of an individual source was composed of a gradual build-up of a stress anomaly in the rock, and the sudden collapse of that anomaly from its center with the stress release migrating outward as seismic waves. The anomaly produced by the prop was predominately shear along the plane perpendicular to the load orientation at the source. Consequently, S-waves dominated the stress release along this direction (fig. 9). Significant levels of P-waves were observed along the direction of loading (fig. 11). The analysis focused on S-waves, which appeared to better represent the source development. A simple characteristic of the stress release produced simple seismic waveforms allowing a reliable tracing of characteristic wavelets at all detection points (fig.

9). In majority of seismic records a characteristic double wavelet could be identified (fig. 9). This property appears prevalent in seismic records from all impact sources (figs. 3,4,5), (Descour and Miller 1986). In general, all wavelets indicated a tendency to expand with distance from the source (fig. 12). A similar relationship was observed for the time shift between double wavelets (fig. 9). The relationship for double wavelets is a subject for further investigation. Also, the group velocity distribution demonstrated an explicit anomaly approximately symmetrical with respect to each source location (fig. 13), with the highest velocity adjacent to the source, and exponentially decreasing with distance.

An approximately linear relationship was found between the group velocity, and the dominant wave period (fig. 14) (Descour 1971 & 1991). The relationship appeared controlled by the dispersive properties and the elastic constants in the rock. Both groups of values were determined by the type of rock and the total of static and dynamic stresses along the wave paths. The wave velocity (V_s) and the dominant wave period (P_s) appeared related to the average diameter of the source (D_s) by the formula (Goldsmith and Allen 1955):

$$D_s = V_s * P_s / (2 * \pi)$$

The three-dimensional analysis of S-wavelets of the same origin indicated a general tendency for the ground motions associated with S-waves to remain parallel to the original load at the source (fig. 15).

Based on the results of the investigation (Descour and Miller 1986), the time shifts between consecutive seismic waveforms from a series of **comparable sources of the same location** should remain the same regardless of the location of the detection point (fig. 6). At the same time, the dispersion effect would result in an expansion of individual wavelets/compression of their spectra with distance from the source (figs. 6, 12). Consequently, beginning from distances at which half of the expanding dominate wave period would become comparable with the original time shifts between consecutive wavelets, the wavelets would have a tendency to overlap and irreversibly cancel one another (figs. 2,16). For those distances, the envelopes of the original wavelets would dominate the records. This model would partially explain the presence of high frequency signals in proximity to impact sources, and their abrupt disappearance at larger distances. Also, the phenomenon would contribute to velocity changes with distance, particularly strong in proximity to the source. The same rules appear to apply for continuous sources of periodic, even monochromatic signals (fig. 16).

CONCLUSIONS

The designed system using stress release as a seismic source should be applied at each search site to evaluate the local signal dispersion properties in order to modify seismic signature banks from the test site to approximate the search site conditions.

The relationship between the wave period and the wave velocity, and the size of the tunnel can be used to estimate the upper frequency range for monitoring seismic sources in tunnels of known dimensions, and in the known geological conditions (wave velocity).

For specific geological conditions and for a source of periodic seismic signals, the distance for possible source detection appears inversely proportional to the frequency of the signals.

Based on the relationship between the wave period, and the wave velocity, a significant variations in the duration of seismic wavelets for the same source can be expected between different detection points. This effect is controlled by the local dispersive properties in the rock, and depends on the type of source. Therefore, the attempts to directly correlate seismic records from different detection points, and/or from comparable geological sites can be useless or misleading.

The relationship between the dominant wave period, and the group velocity can be used to significantly improve location of sources by using dominant wave periods for the properly selected waveforms to modify their arrival times. This operation should approximate the constant velocity condition for the location (Descour 1991).

Three-dimensional recording may be useful for extracting S-waves from noisy signals based on their tendency to generate ground motions parallel to the load at the source.

ACKNOWLEDGMENTS

The results presented in this paper are derived from research conducted by the author for the project "Efforts in Support of Tunnel Detection (Geophysics) funded by the US Army, and for the project "Geophysics Applied to Abandoned Mined Lands" funded by the US Bureau of Mines.

REFERENCES

- Descour, J. M., 1991, "Use of Wave Spectra in Source Location -- An Integral Part of Source Characterization," Proceedings (in printing) of 5th Conference on Acoustic Emissions/Microseismic Activity in Geologic Structures and Materials, PA.
- Descour, J. M. and R. J. Miller, 1989, "Microseismic Monitoring of Engineering Structures," Proceedings of the Symposium on the Application of Geophysics to Engineering and Environmental Problems, CO, pp. 235-261.
- Descour, J. and R. J. Miller, 1986, "Coal Mine Bump Monitoring," (Contract J0245009), US Bureau of Mines OFR 32-88, 111 pp.
- Descour, J., 1972, "Results of Ultrasonic Tests on Samples Under Pressure as A Ground for Evaluation of Seismic Studies in Mines," (in Polish with English summary), Publications of the Institute of Geophysics, Polish Academy of Sciences, Vol. 47, Warsaw, pp. 185-198.
- Goldsmith, W., and W. A. Allen, 1955, "Graphical Representation of the Spherical Propagation of Explosive Pulses in Elastic Media," Journal of the Acoustic Society of America, pp. 47-55.

Hardy, H. R. Jr., 1985, "Application of Acoustic Emission Techniques to Rock and Rock Structures; A State-of-the-Art Review," Proceedings ASTM Conference on Acoustic Emissions in Geotechnical Engineering Practice, PA, pp. 4-92.

Hardy, H. R. Jr., 1972, "Application of Acoustic Emission Techniques to Rock Mechanics Research," ASTM Conference, ASTM STP 505, pp. 41-83.

Leighton, F. and B. Steblay, 1975, "Coal Mine Bounce and Roof Fall Research," Proceedings of NCA/BCR Coal Conference and Expo II, 16 pp.

Rao, M. V. M. S., Xiaoxing Sun, and H. R. Hardy Jr., 1989, "An Evaluation of the Amplitude Distribution of AE Activity in Rock Specimens Stressed to Failure," Balkema, Rotterdam ISBN 90 6191 8715, 8 pp.

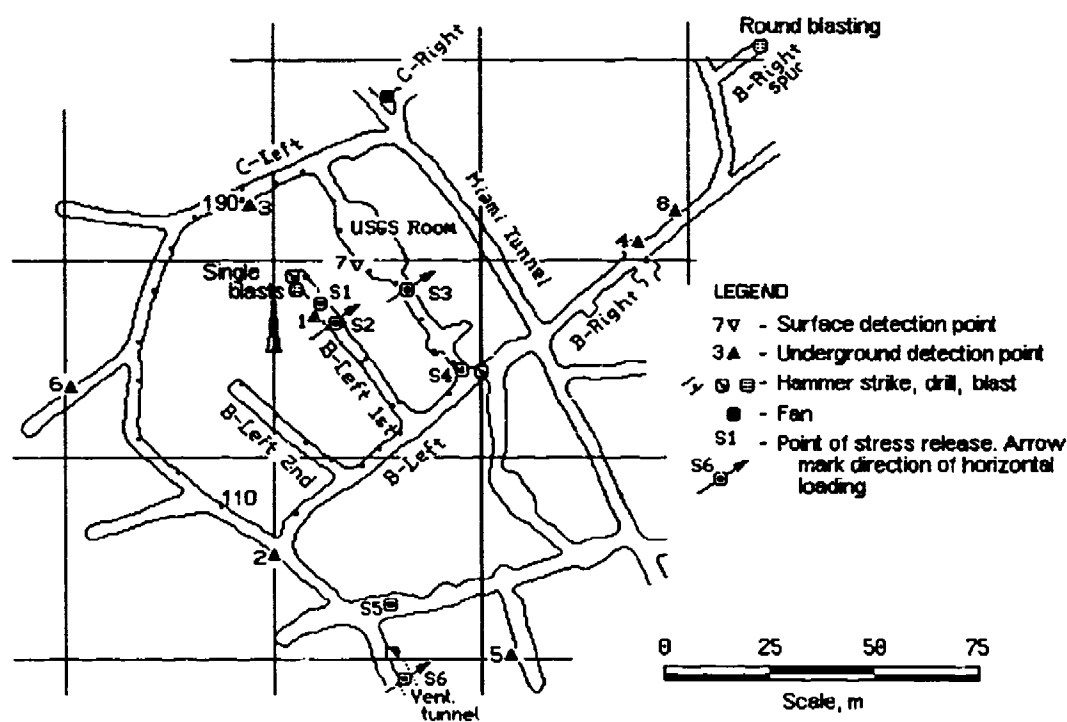


FIGURE 1. - Tunnels in the Edgar mine, location of monitored seismic sources, and the array of seismic detection points used for the investigation on seismic signatures.

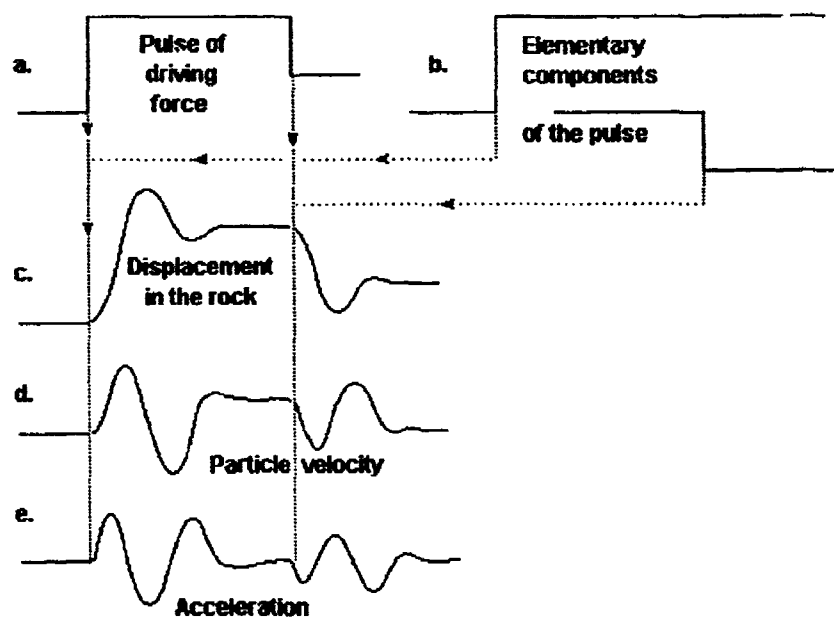


FIGURE 2. - A model of an impact source (a.) as a combination of two step functions (b.), an idealized displacement response in the rock (c.), and particle velocity (d.) and acceleration (e.) signals detected by seismic sensors.

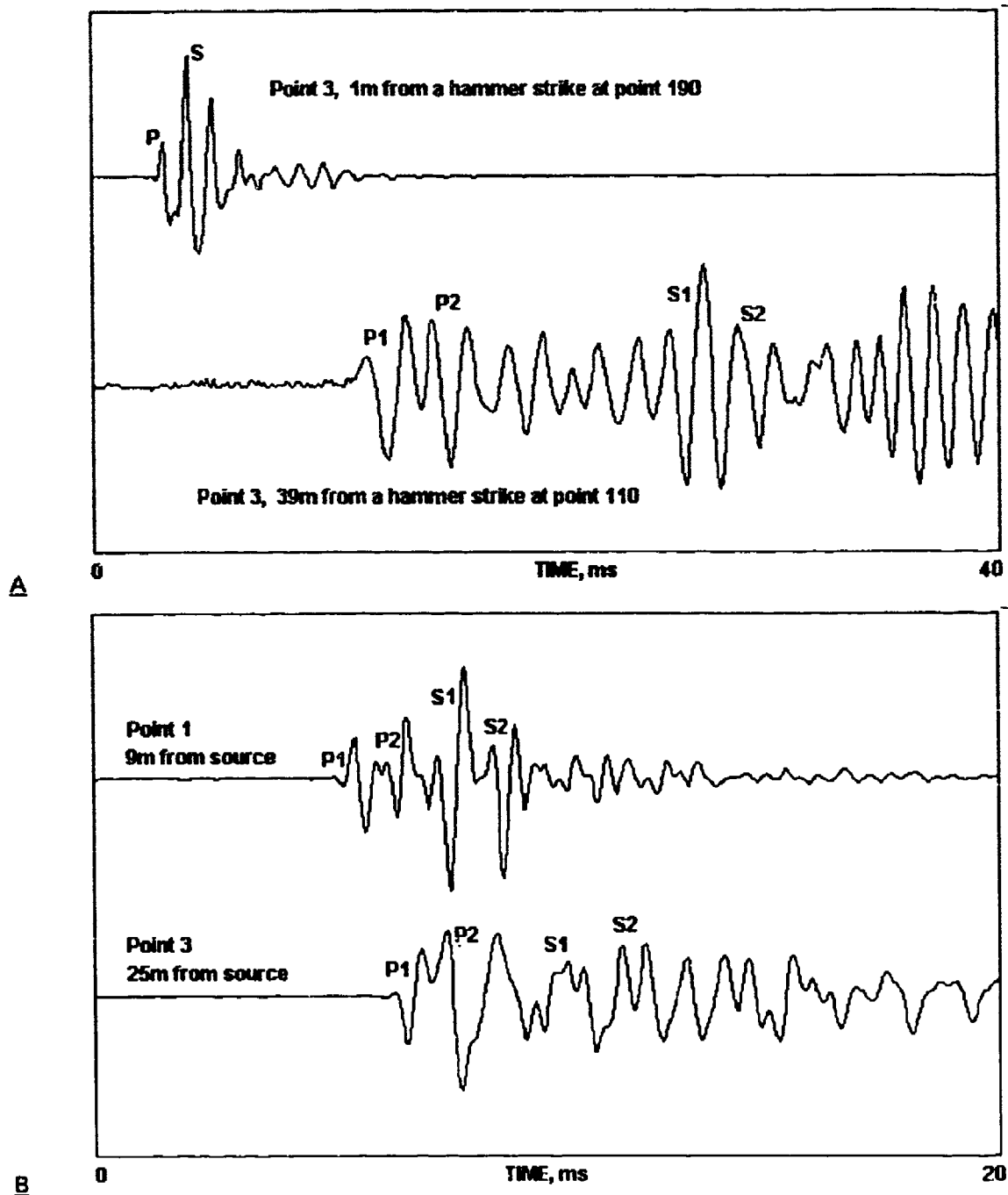


FIGURE 3. - Typical seismic waveforms detected at point 3 for hammer strikes at points 110 and 190 (A), and waveforms detected at points 1 and 3 for a 0.5-kg-dynamite blast in the rock in the front portion of B-Left 1st drift (B). Waveforms filtered using low-pass digital filter of 2.5 kHz cut-off frequency.

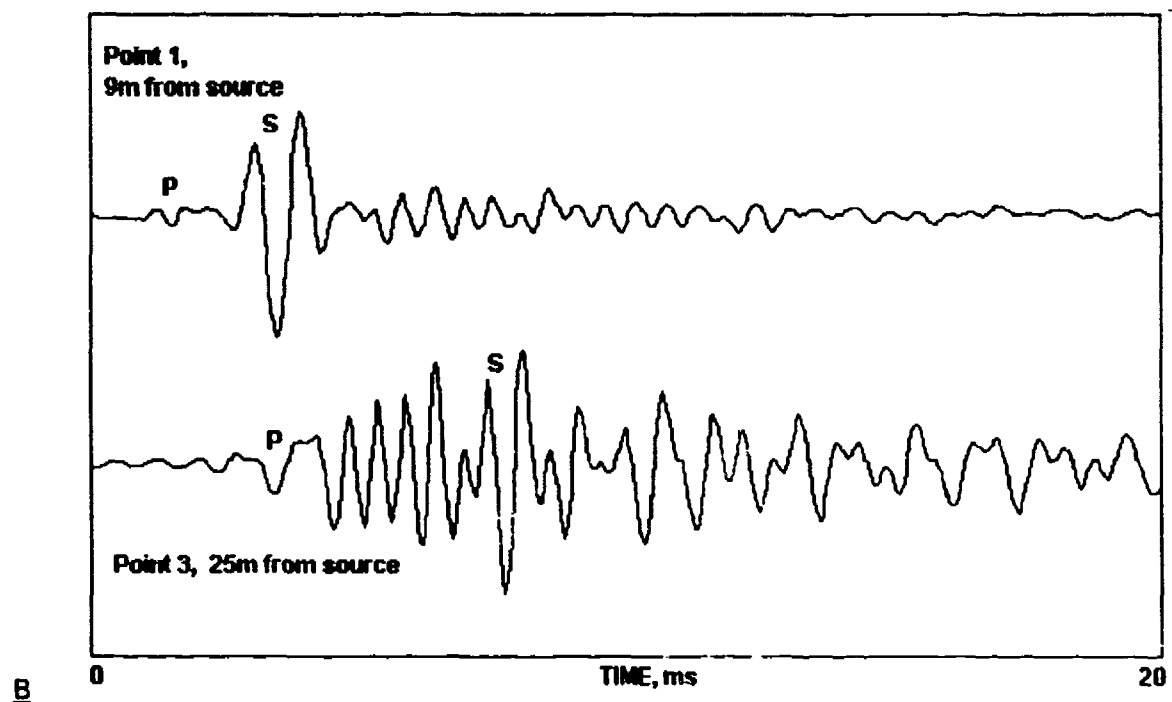
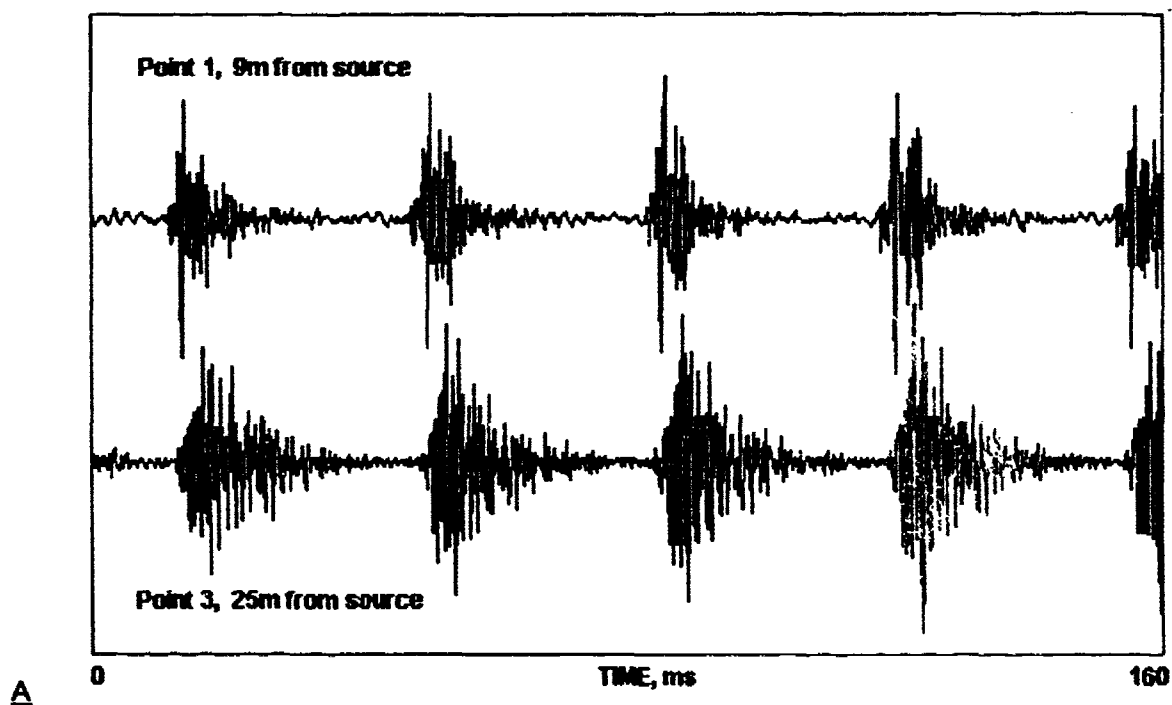


FIGURE 4. - Typical compressed records at points 1 and 3 for a jumbo-drill at the front portion of B-Left 1st drift (A), and expanded waveforms in response to one of the impacts. Waveforms filtered by 2.5 kHz low-pass digital filter.

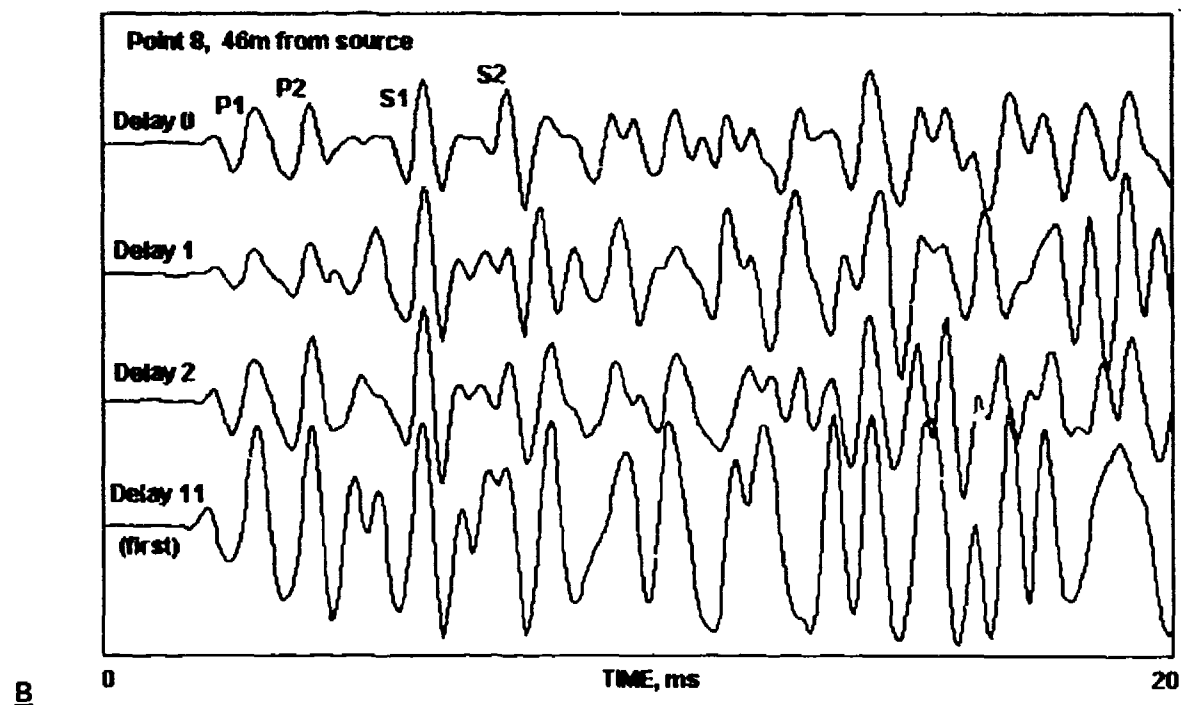
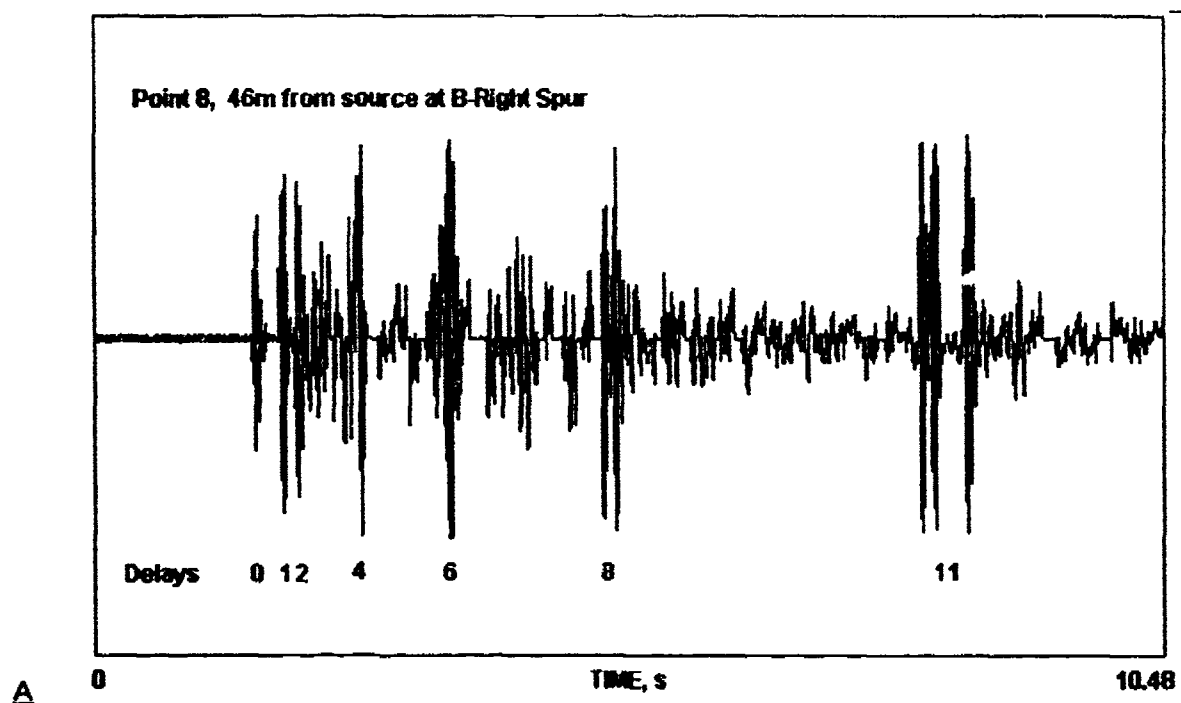


FIGURE 5. - A compressed seismic response detected at point 8 in B-Right for a round blasting at B-Left Spur (A), and expanded waveforms for delays 0, 1, 2, and 11 (B). Data processed using 1.25 kHz low-pass digital filter.

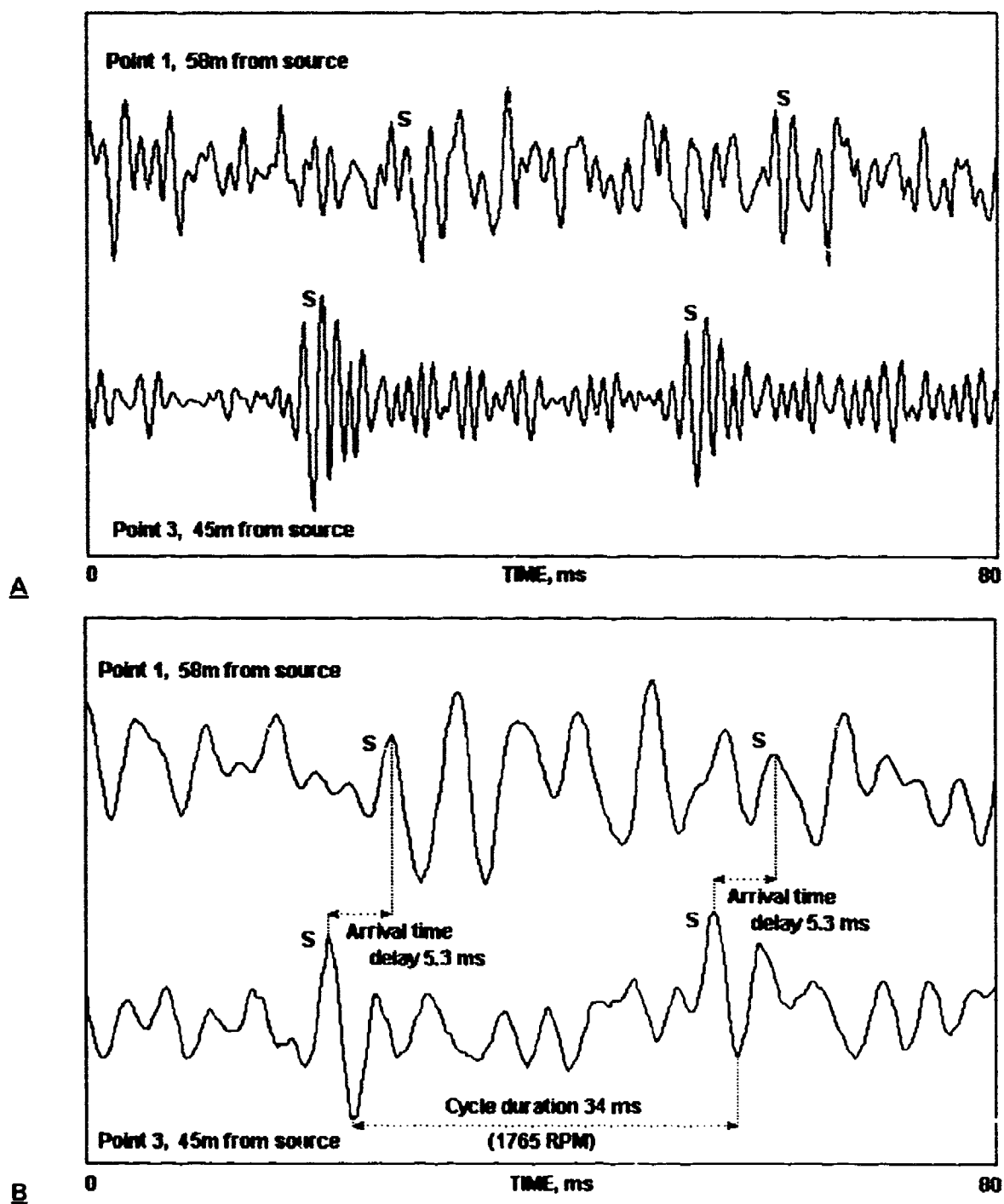


FIGURE 6. - Waveforms (S-waves) detected at points 1 and 3 for a centrifugal fan (nominal 1770 RPM) at C-Right drift, and processed using digital low-pass filters of cut-off frequency 1.25 kHz (A), and 0.5 kHz (B).



FIGURE 7. - The system (prop) used to generate seismic sources by a sudden stress release. The system positioned for the vertical loading.

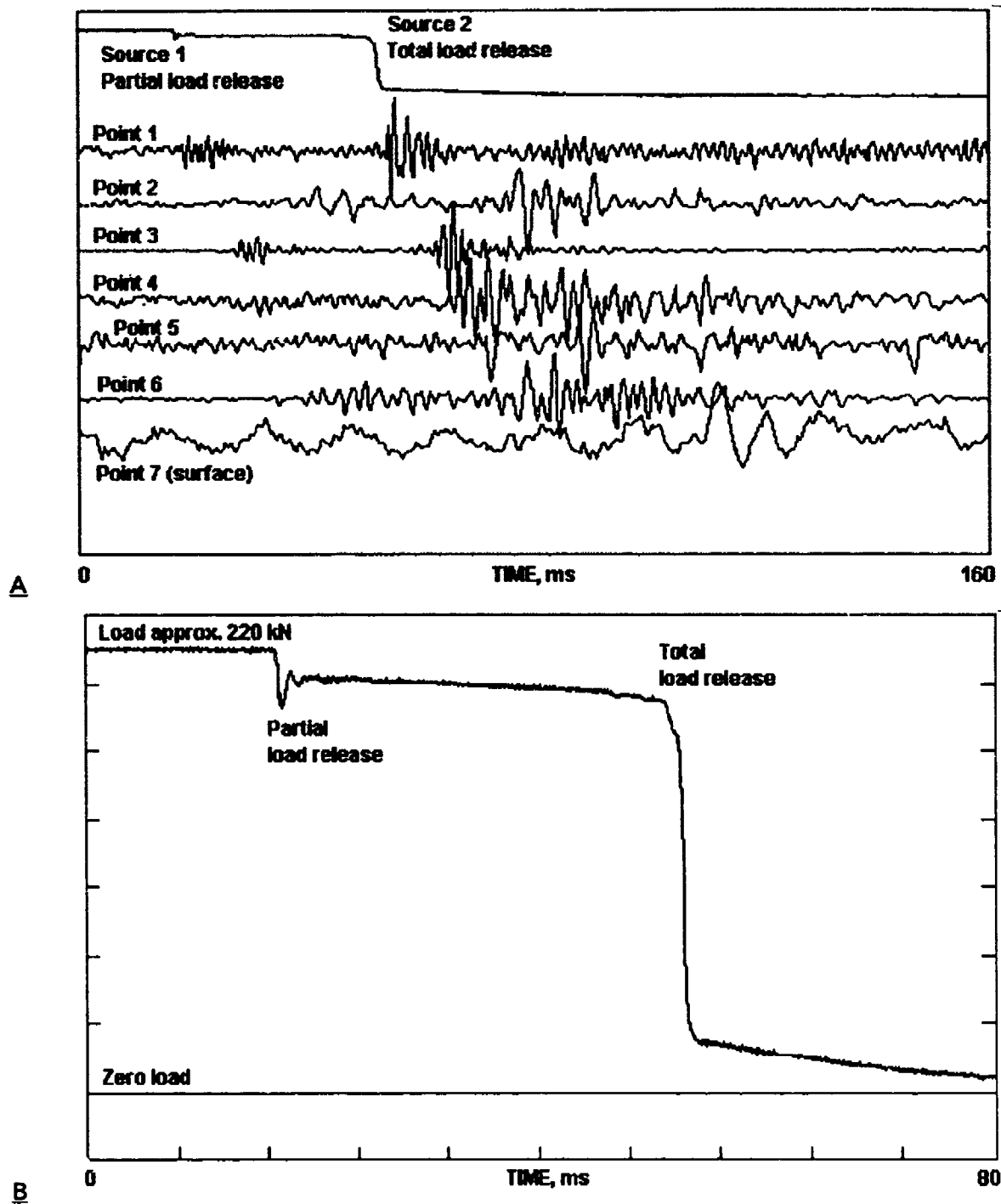
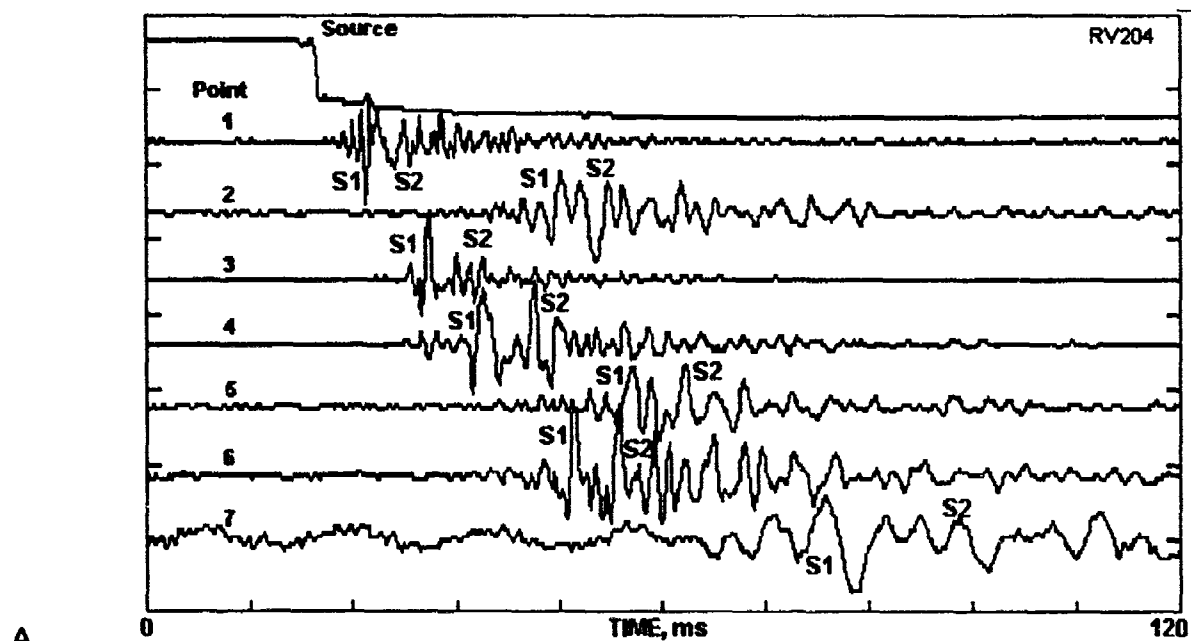
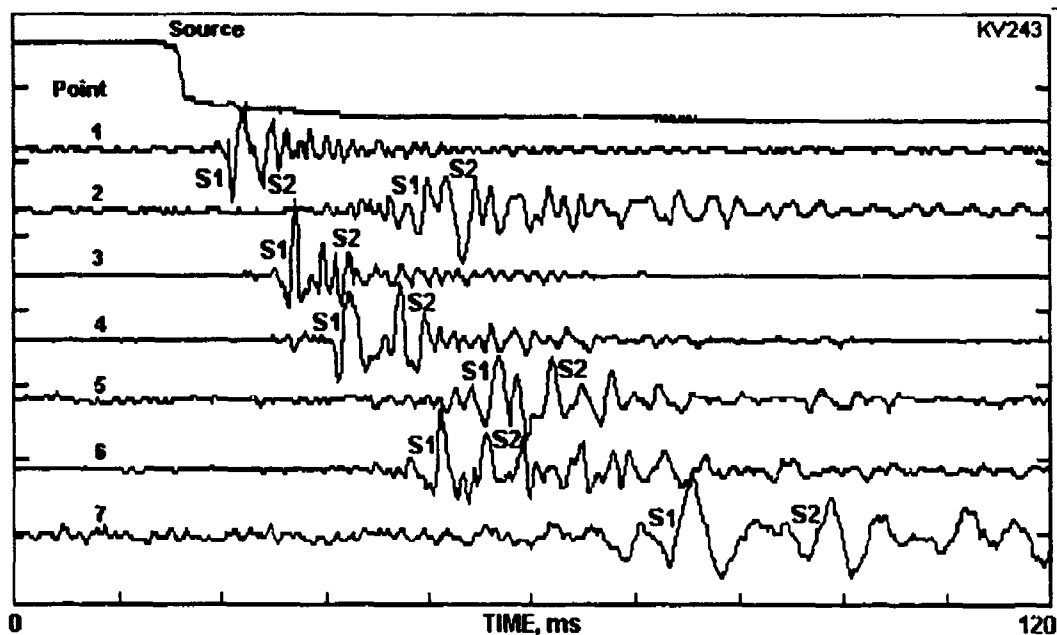


FIGURE 8. - Typical seismic records at points 1 through 7 for the horizontal load release at S2, combined with the load record from the prop (top) (A), and the expanded record of the load changes (hydraulic pressure) (B). Records were processed using 2 kHz digital low-pass filter.



A



B

FIGURE 9. - Comparison of two seismic records for the vertical load release at point S3, acquired at points 1 through 7 in August (A), and in November (B) 1990. Signals were processed using a digital low-pass filter of cut-off frequency 2 kHz. Note strong S-waves and practically no P-waves in each waveform.

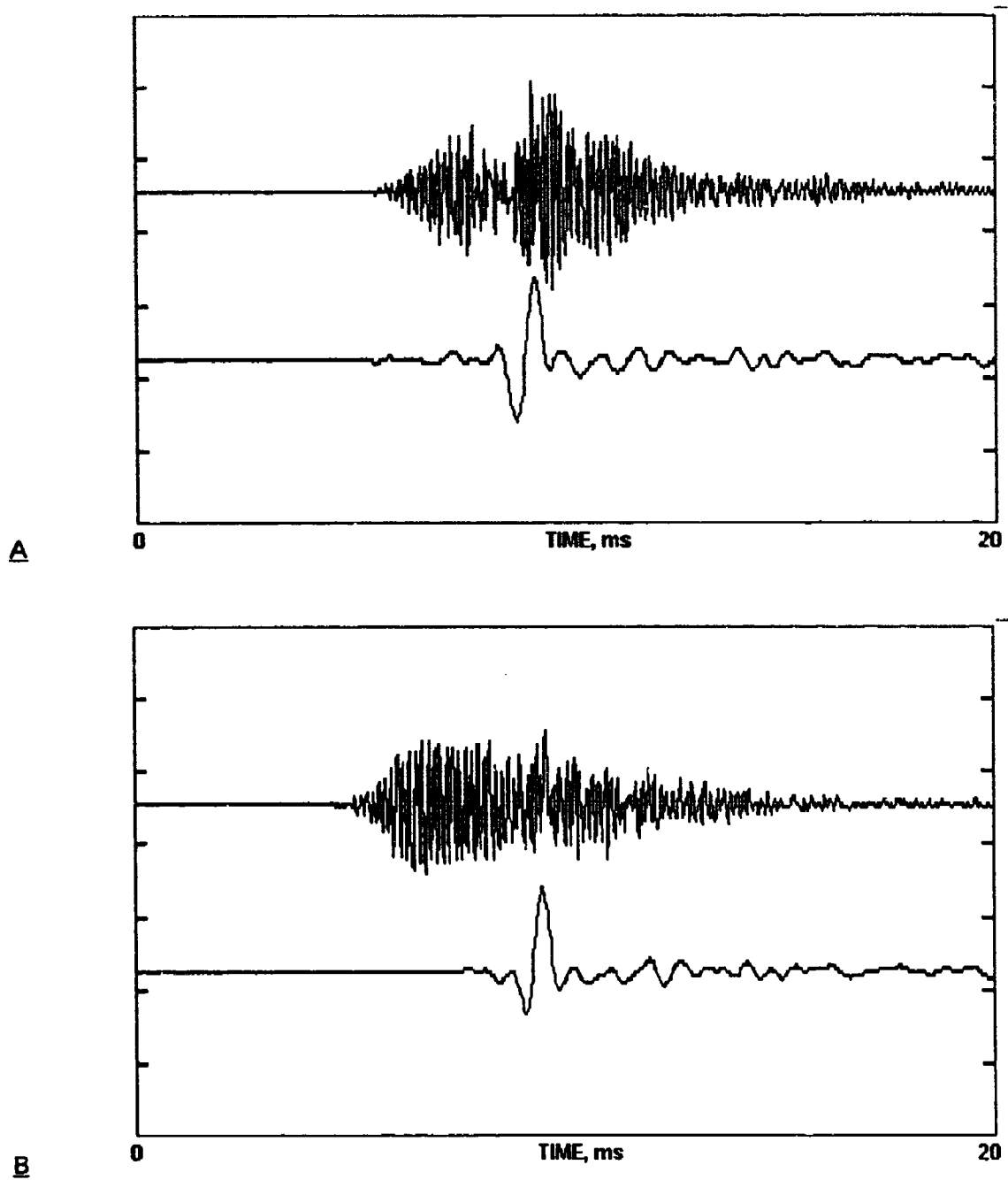


FIGURE 10. - Comparison of two seismic records at point 1 for two vertical load release events at point S3, with raw waveforms at the top of each pair, and the waveforms processed using 2 kHz low-pass filter at the bottom.

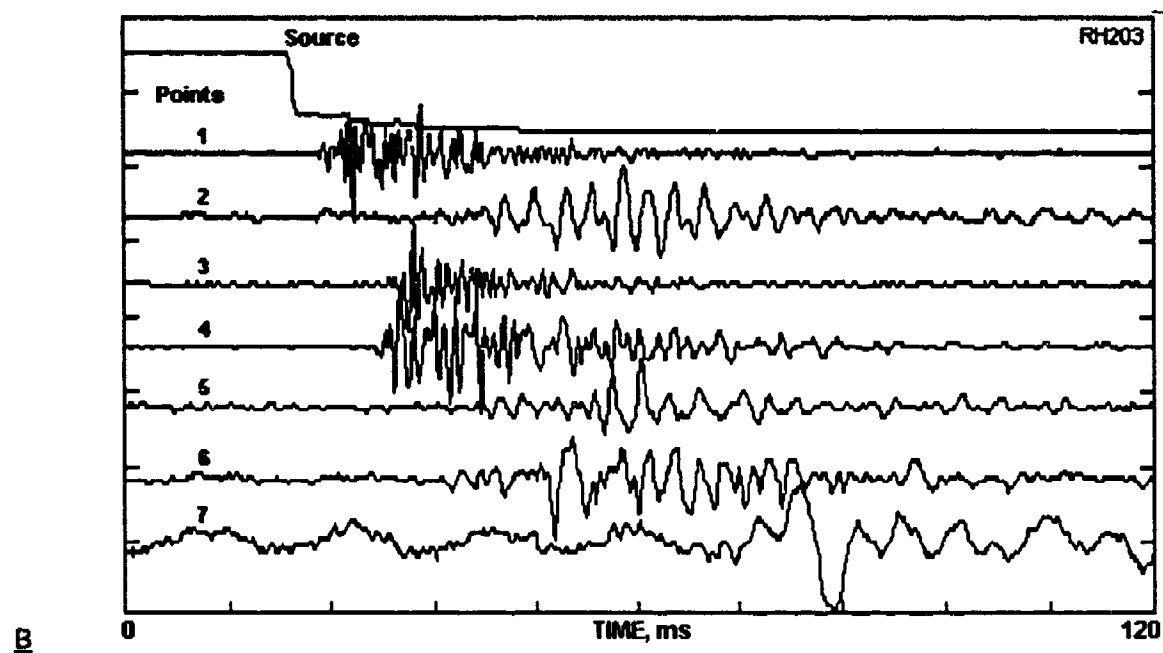
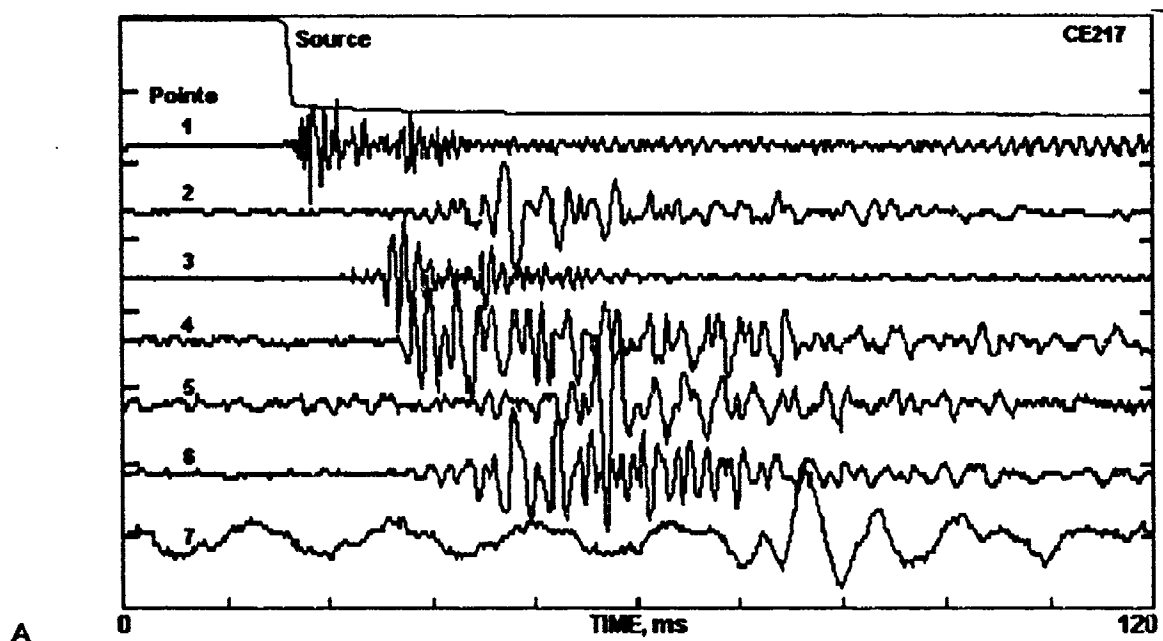


FIGURE 11. - Typical waveforms detected at points 1 through 6 underground, and at point 7 on the surface for the horizontal load release at points S2 (A), and S3 (B). Signals processed using 2 kHz low-pass filter.

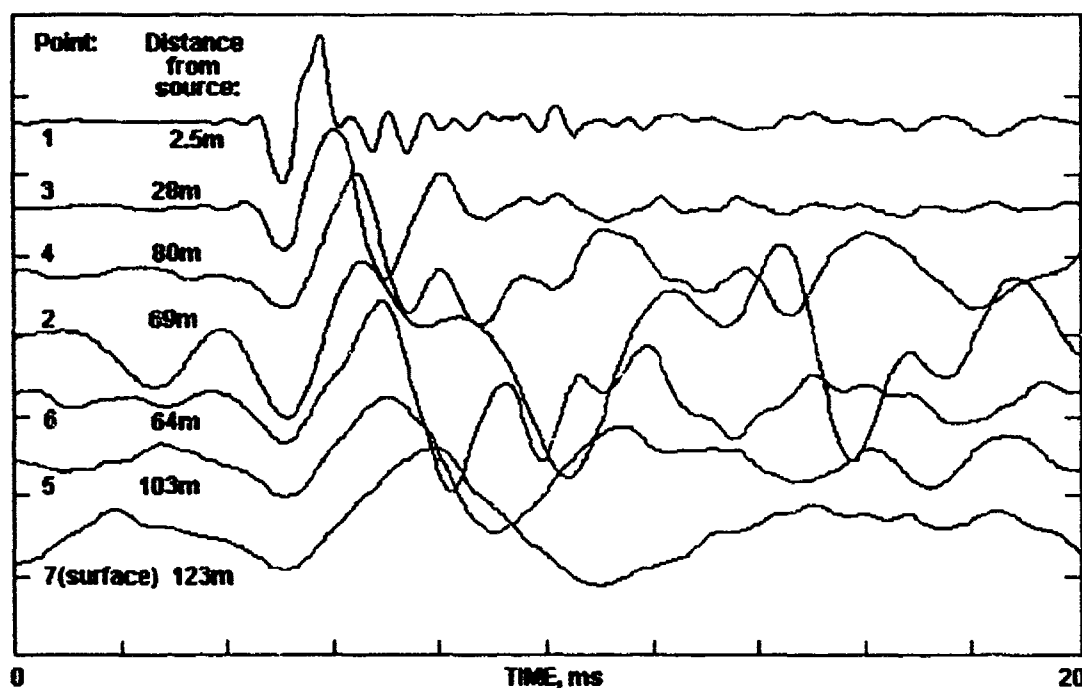


FIGURE 12. - Expansion with distance of S-wavelets generated in response to the vertical load-release event at point S1. Signals processed using 2 kHz low-pass filter.

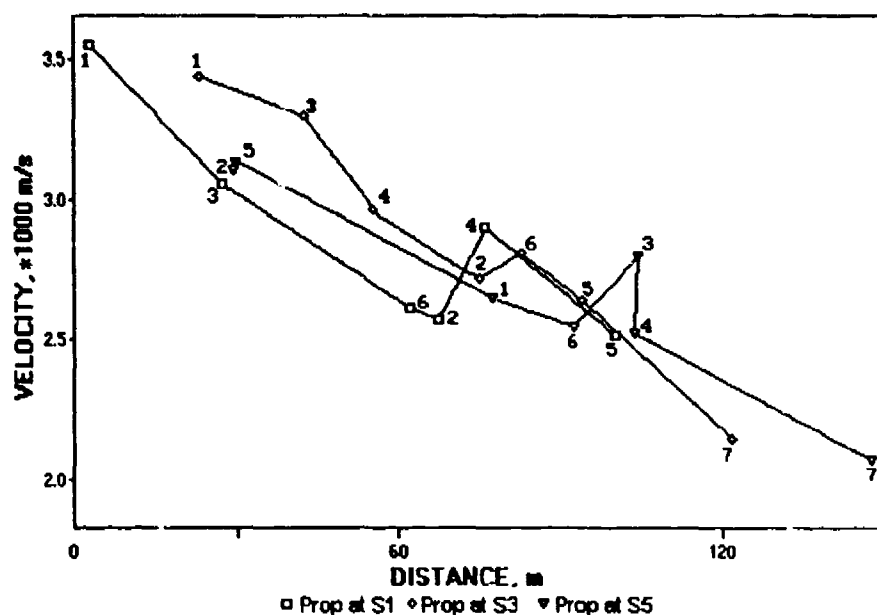


FIGURE 13. - The average group velocity decreasing with distance from source regardless of the source location.

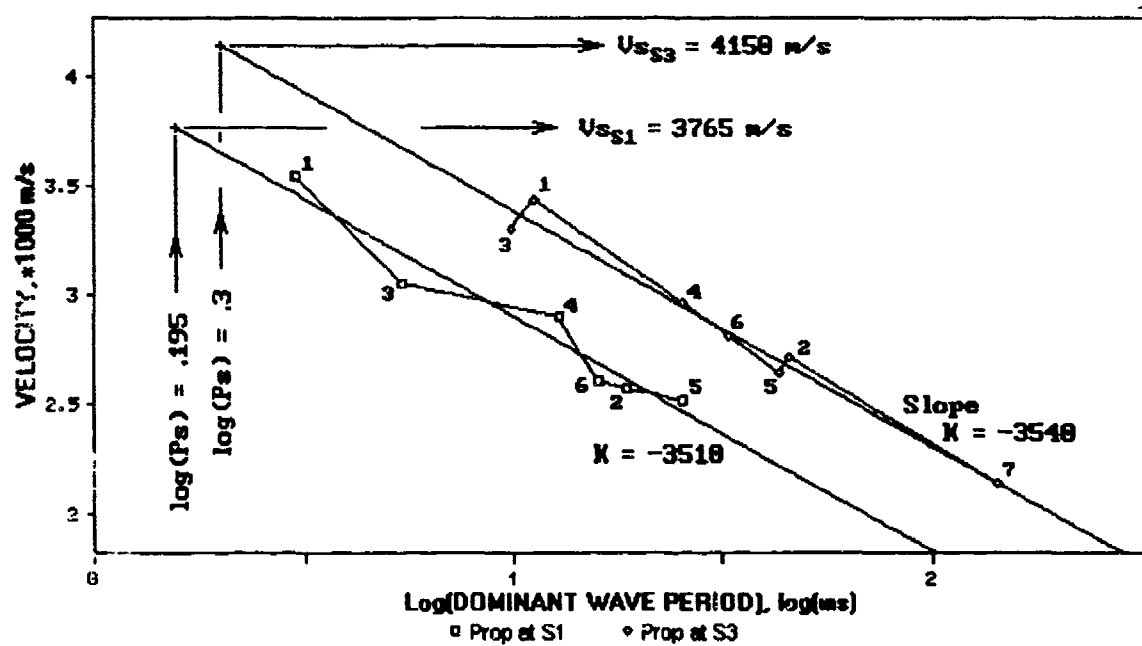


FIGURE 14. - The relationship between the average group velocity between the source and detection points, and the dominant wave period for S-waves measured at those points.

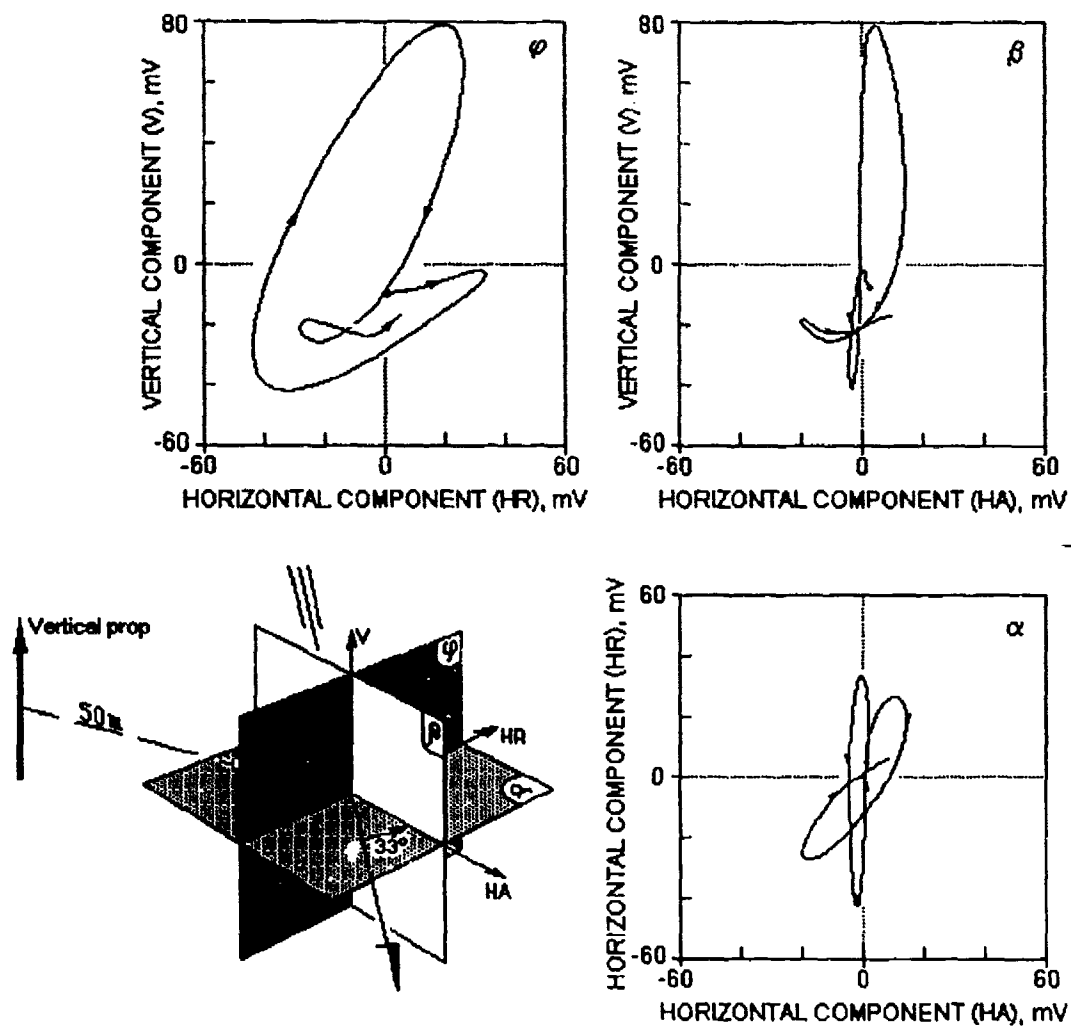


FIGURE 15. - Three-dimensional characteristics of ground motions caused by S-waves at point 3 for the vertical load release event at point S3.

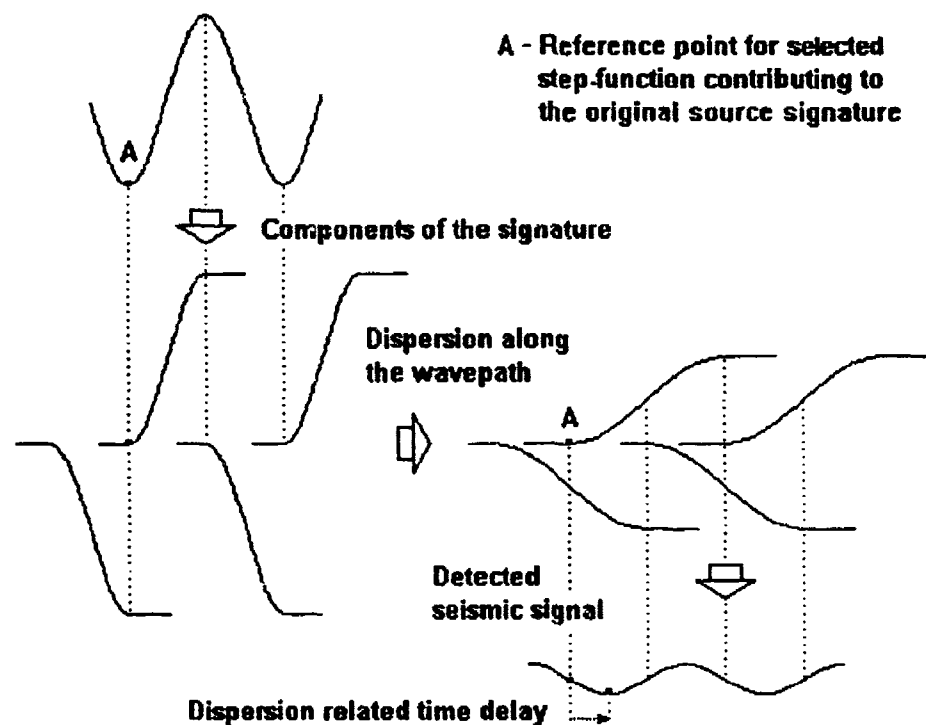


FIGURE 16. - An idealized model for seismic response in the rock (source signature) as a product of summation of rounded step ctions, and the dispersion related amplitude and velocity changes for that response with distance. The model applies for both periodic and impact sources (see fig. 2).

**Seismic Location of Small Explosions and Shot Hole Drilling
at the Colorado School of Mines' Edgar Mine,
Idaho Springs, Colorado**

Richard D. Lewis, Joseph Koester, and Dave Sykora
US Army Corps of Engineers, Waterways Experiment Station,
3909 Halls Ferry Road, Vicksburg, MS, 39187

Roy J. Greenfield
Pennsylvania State University, University Park, PA

Introduction: A field experiment was conducted at the Colorado School of Mines' Edgar Mine to assess methods of vectoring toward and locating small underground explosions and associated mining support machinery, (Lewis, 1991). A geometric array of geophones was placed on the surface and adjacent to the underground activity to record seismic waves generated by both impulsive (transient) sources and steady state (continuous) sources. The apparent direction from which the seismic wave train originates in relationship to the geophone array may be determined by either time domain (first break time picks) or frequency domain (Bartlett processing or array "steering") methods. Similar frequency domain signal processing is conducted on the data from the NORESS and like seismic arrays, which are operated for nuclear test treaty verification. It was determined that continuously operating machinery could be easily vectored if the seismic signal is sufficiently strong (about a 1-to-1 signal to noise ratio) and the site geology provides reasonable signal coherence at frequencies of interest. In addition, the apparent direction to the impulsive sources could be determined with approximately the same accuracy or precision with frequency domain methods as compared to time domain methods, but at 5 times lower signal-to-noise ratios.

Background: Frequency domain seismic array techniques have long been employed to determine locations to the source of transient events which have emergent first arrivals, i.e. where the time of arrival of the first motion cannot be clearly determined (Lacoss, Kelly, and Toksoz, 1969). They have also been applied to determine the source of steady state "background" signals. The data of interest in frequency domain method lies in the coherent phase differences of a particular chosen frequency in the signal collected by the geometric array of geophones, hence the need for a well-designed and patterned arrangement of geophones for data collection. The pattern shapes and array diameters are formulated in large part by using antenna design theory with important modifications due to the lower signal coherence, which is greatly dependent upon the local geology. See, Bibliography, "Frequency Domain Seismic Array Design".

Field Test: The Colorado School of Mines' Edgar Mine is located near Idaho Springs, Colorado. The local geology is dominated by deformed and highly fractured pre-Cambrian igneous and metamorphic rocks, generally of the Idaho Springs Formation, which is a meta-sedimentary granite or biotite gneiss, (Tweto, Ogden; and

Simms, 1963, Moench, Harrison and Sims, 1962). Intruding these are early Tertiary (Laramide) granitic and porphyritic rocks and associated breccia pipes, dikes, and irregular plugs,. The ore mineralization and extensive hydrothermal alteration at the test mine is a result of this activity, (Lovering and Goddard, 1950). The seismic array was fielded on a topographic knoll known locally as the "lower pad". Twelve 4.5 Hz natural period vertical geophones, damped 70% of critical were used in the geometric seismic array with a 40 foot outer diameter. Data were recorded on a FM tape recorder with a 40 dB dynamic range. Digitization was later conducted with a 12 bit A to D card at a channel sampling rate of 8,000 Hz for the impulses (explosions) and 2,500 Hz for the steady state (drilling) events. Shot hole boring was usually performed with a Gardner-Denver "feed-leg" type pneumatic drill. The holes were generally shot with 1 pound of dynamite. Slant ranges from the center of the seismic array to the shot point ranged from less than 400 to more than 1200 feet.

Source Spectra, Site Attenuation, and Signal to Noise Ratios: The predominant spectral energy, as determined by Fast Fourier Transform (FFT) analysis from the monitored dynamite blasts, occurred within a range of 80 to 220 Hz with the center frequency between 140 to 180 Hz, (Capon, 1969, Cooley and Tukey, 1965). The drill for shot hole boring produced a signal with a narrowband seismic signature with a predominate peak between 70 to 100 Hz, depending upon the driving air pressure for the equipment. Seismic wave attenuation investigations demonstrated the extreme anelastic properties of the site, which have also been generally noted in personal communications with previous investigators. The average seismic amplitude attenuation for P-waves was found to be $r^{-3.9}$ where r is the slant range. The attenuation from geometric spreading for P-waves should be $r^{-3.0}$. The nearly 1 order greater attenuation function, (-3.9 vs. -3.0) is clearly indicative of the greatly increased elastic wave absorption from the highly fractured and altered host rock. In addition to the large documented attenuation, significant forward scattering should be expected in the seismic wave train. This would result in a considerable decrease in seismic wave coherence, i.e. significant differences in the phase data for the same impulse, but measured at separate locations. The range that would be expected for a 1-to-1 signal-to-noise ratio for 1 pound blasts would be approximately 1200 feet. A similar signal level would be expected for the shot hole drilling at a distance of about 350 feet.

Directions to Explosions as Determined in the Time Domain: The first arrival time of the P-Wave at the geometric array could generally be determined within 0.1 milliseconds. A signal-to-noise ratio of 5-to-1 or slightly less was necessary to assure an acceptable first motion time. A least squares routine was used to regress a slope through the data using the spatial information (the geophone locations) and the first motion P-Wave arrival. This defined the apparent P-Wave velocities and the directions to the small dynamite explosions. Eight tests (1 pound dynamite explosions) collected at the geometric seismic array had sufficient

signal-to-noise for time domain analysis. The maximum range from source to receiver that could consistently produce useable data for this type of analysis was about 450 feet. The average absolute error between the determined direction and the true bearing toward the source was found to be 8.1° . The average apparent P-Wave velocity for the material under the 40 foot diameter geometric array was calculated to be 9240 ft/sec.

Frequency Domain Bartlett Beam Forming in K_x - K_y Space: The "two-dimensional power density" can be determined from the seismic data collected by a geometric array of geophones. This can be done for each discrete frequency in the seismic spectra, (Lacoss, Kelly, and Toksoz, 1969). The end result is usually a contoured estimate of the 2-dimensional seismic power at a chosen frequency, which also shows directional and propagation velocity of a seismic wave which traveled across the geometric array. For the Bartlett technique, the seismic power is computed, plotted and contoured in 2-dimensional wavenumber (K) space, using defined x and y directions, hence the terms K_x - K_y Space, and 2-D seismic power density. The computational process is often termed "beam forming" or "steering the array". To perform this operation, the spatial locations of each geophone along with the calculated spectral phase information at the chosen frequency are used as input data. The estimate of the apparent seismic power in this selected frequency band of a postulated elastic wave traveling across the geometric array is computed. Using the measured phase information, the seismic power estimate is calculated for generally hundreds of possible waves traveling at all azimuths across the array and for a large suite of velocities. Individual seismic power estimates for a set of propagational directions and velocities are then plotted in a K_x - K_y spatial diagram and contoured. The location of peak seismic power defines the most likely velocity (inverse of the wavenumber) and the source bearing (azimuth) of the elastic wave that traveled across the geometric array.

The great advantage of frequency domain beam forming is that much lower signal-to-noise ratios can be used to successfully determine the apparent direction to an impulsive elastic wave source. In addition, continuously operating sources such as compressors, pumps, drilling, etc. can also be vectored. Additional care must be used in this method in designing the geophone array and properly processing the data. Generally, the section of the spectra showing the greatest coherence provides the most favorable results, (Koopmans, 1974). This is to be expected, as the spatial coherence is a measure of the stability of the spectral phase with time. For this investigation it was determined that the first 0.04 seconds of the generally 0.1 second long elastic wave particle motion trace contained the greatest spatial coherency. The spectral portion from 90 to 160 Hz (effectively that portion of the spectra below the center frequency) was significantly more coherent than that from 160 to 230 Hz. A stronger tapering function in the computation of the Fourier spectral estimate, e.g., Hamming vs. Tukey, generally resulted in significantly greater accuracy determining the azimuth to the impulsive source.

Directions to Explosions as Determined in the Frequency Domain: Data from 11 explosions could be used for beam forming with the geometric seismic array. The lowest signal-to-noise ratio used was 1-to-1, which was also associated with the weakest signal collected. Other tests could not be processed due to clipped amplitudes in the recording process. The average absolute error from the determined direction and the true bearing toward the source was found to be 7.4° . The average apparent P-Wave velocity for the material under the 40 foot diameter geometric array was calculated to be 14,100 ft/sec. The determined azimuthal errors for the 1 pound dynamite explosions was approximately the same (7.4° vs. 8.1° for the frequency domain vs. time domain processing). The significant difference is that a 4 or 5 times lower signal-to-noise ratio could be utilized with the beam forming process.

Directions to Shot Hole Drilling as Determined in the Frequency Domain: Shot hole drilling was monitored at slant range of about 350 feet. A high confidence in the spectral coherence could be determined as long record lengths (about 15 seconds long) were obtainable. The average array coherence was determined by numerically averaging the spectral coherence as determined for all geophone pairs in the array. This was performed for an equal lengths of data collected immediately before the drilling started and during the operation. By examining the differences in these two plots of average array coherence, one may determine the most optimum frequency to use for the beam forming process to vector toward the drilling activity. It was generally possible to vector toward the drilling activity with less than a few degrees of error.

Conclusions: Frequency domain signal processing is a powerful method of locating low signal-to-noise impulsive or continuous seismic sources. In spite of very difficult geology which severely attenuated and degraded the signal coherence, extremely favorable results were obtained. When compared to time domain signal processing, similar location accuracy can be achieved with frequency domain processing using five times lower signal levels. This enormously increases the area which has been effectively monitored for a given signal level. It is also practical to locate both impulsive and continuous seismic sources with the same geometric array when using frequency domain passive seismic monitoring.

Acknowledgements: Support for this project was provided by the US Army Research, Development and Engineering Center, Ft. Belvoir, VA. Technical support was provided by the Instrumentation Services Division, US Army Corps of Engineers, Waterways Experiment Station, Vicksburg, MS. Permission was granted by the Chief of Engineers to publish this information.

REFERENCES

- Capon, J. 1969. "High-Resolution Frequency-Wavenumber Spectrum Analysis," Proc. IEEE, Vol 57, pp 1408-1418.
- Cooley, J.W., and Tukey, J.W. 1965. "An Algorithm for the Machine Calculation of Complex Fourier Series," Math. Comput., Vol 19, pp 297-301.
- Gupta, I.N., and Hartenberger, R.A., 1981. "Seismic Phases and Scaling Associated with Small High-Explosive Surface Shots," Bull. Seism. Soc. Am., Vol 71, pp 1731-1741.
- Koopmans, L.H., 1974. The Spectral Analysis of Time Series, Academic Press, New York, New York, 350 pp.
- Lacoss, R.T., Kelly, E.J., and Toksoz, M.N. 1969. "Estimation of Seismic Noise Structure using Arrays," Geophysics, Vol 34, pp 21-38.
- Lewis, R.D., 1991. "Seismic Location of Small Explosions and Shot Hole Drilling at the Colorado School of Mines' Edgar Mine, Idaho Springs, Colorado, US Army Corps of Engineers, Waterways Experiment Station, Vicksburg, MS, Technical Report GL-91-9, 189 pages.
- Lovering, T.S., and Goddard, E.N. 1950. "Geology and Ore Deposits of the Frount Range, Colorado," US Geol. Sur. Prof. Pap. 223, 319 pp.
- Moench, R.H., Harrison, J.E., and Sims, P.K. 1962. "Pre-cambrian folding in the Idaho Springs-Central City Area, Frount Range, Colorado," Geo. Soc. Am. Bull., Vol 73, pp 35-58.
- Tweto, O. and Sims, P.K., 1963. "Pre-cambrian Ancestry of the Colorado Mineral Belt," Geo. Soc. Am. Bull., Vol 74, pp 991-1014.

Bibliography

Frequency Domain Seismic Array Design

Advanced Research Projects Agency, 1972. "Seismic Array Design Handbook," NTIS AD-760 572.

AFTAC/VELA Seismological Center, 1967. "Relative Performance of Several Long Period Seismic Arrays," and "An Alternate Long Period Seismic Array Configuration for Installation in Norway," Tech. Note VSC-24A.

Blandford, R.R., and Clark, D.M. 1971. "Seismic Array Design," Advanced Research Projects Agency, NTIS AD-884-710.

Boverie, B., and Gregg, W.D., 1971. "A Signal Detectability Approach to Optimization of the Geometry of Distributed Aperture (Array) Receivers," IEEE Transactions on Antennas and Propagation, Vol AP-19, pp 22-30.

Capon, J., Greenfield, R.J., Lacoss, R.T., 1967. "Design of Seismic Arrays for Efficient On-Line Beamforming," Lincoln Lab. Tech. Note 1967-26.

Dowla, F. U., 1987. "Designing Arrays for Modern High-Resolution Methods," Lawrence Livermore National Lab. Report UCRL-96896.

Followill, F., and Harris, D., 1983. "Comments on Small Aperture Array Designs," Unpublished Report, Lawrence Livermore Lab., 62 pp.

Frosh, R.A., and Green, P.E., 1966. "The Concept of a Large Aperture Seismic Array," Proc. Royal Soc., A, Vol 290, pp 368-384.

Harris, D., and Dowla, F., 1986. "Seismic Arrays for Treaty Verification," Energy and Technology Review Lawrence Livermore Lab. UCRL-52000-86-8, pp 8-19.

Hartenberger, R.A. and Van Nostrand, R.G., 1970. "Influence of Number and Spacings of Sensors on the Effectiveness of Seismic Arrays," Geophys. Prospecting, Vol 20, pp 771-784.

Haubrich, R.A., 1968. "Array Design," Bull. Seis. Soc. Am., Vol 58, pp 977-991.

Hiebert-Dodd, K. L., Walck, M.C., Elbring, G. J., 1988. "ASSISTANT - A Hybrid Expert System for Assisting Seismologists in the Analysis of Seismic Array Performance," Sandia National Lab. Report SAND88-2971 UC-11.

Lacoss, R.T. 1965. "Geometry and Patterns of Large Aperture Seismic Arrays," Lincoln Lab. Tech. Note 1965-64.

Lacoss, R.T., Capon J., and Greenfield, R.J., 1968. "Preliminary Design of a Long-Period Seismic Array for Norway," Lincoln Lab. Tech. Note 1968-4.

Mraseh, C.P., Der, Z.A., Barker, B.W., and O'Donnel, A., 1980. "Seismic Array Design for Regional Phases," Geo-Tech-Teldyne, Alexandria, VA.

Mykkelveit, S., Astebol, K., Doornbos, P.J., and Husebye, E.S., 1983. "Seismic Array Configuration Optimalization," Bull. Seis. Soc. Am., Vol 73, pp 173-186.

Walck, M.C., Elbring, J.G., Hiebert-Dodd, K. L., 1988. "Seismic Array Performance Analysis Using a Hybrid Expert System," Sandia Report National Lab. Report SAND88-2410 UC-11.

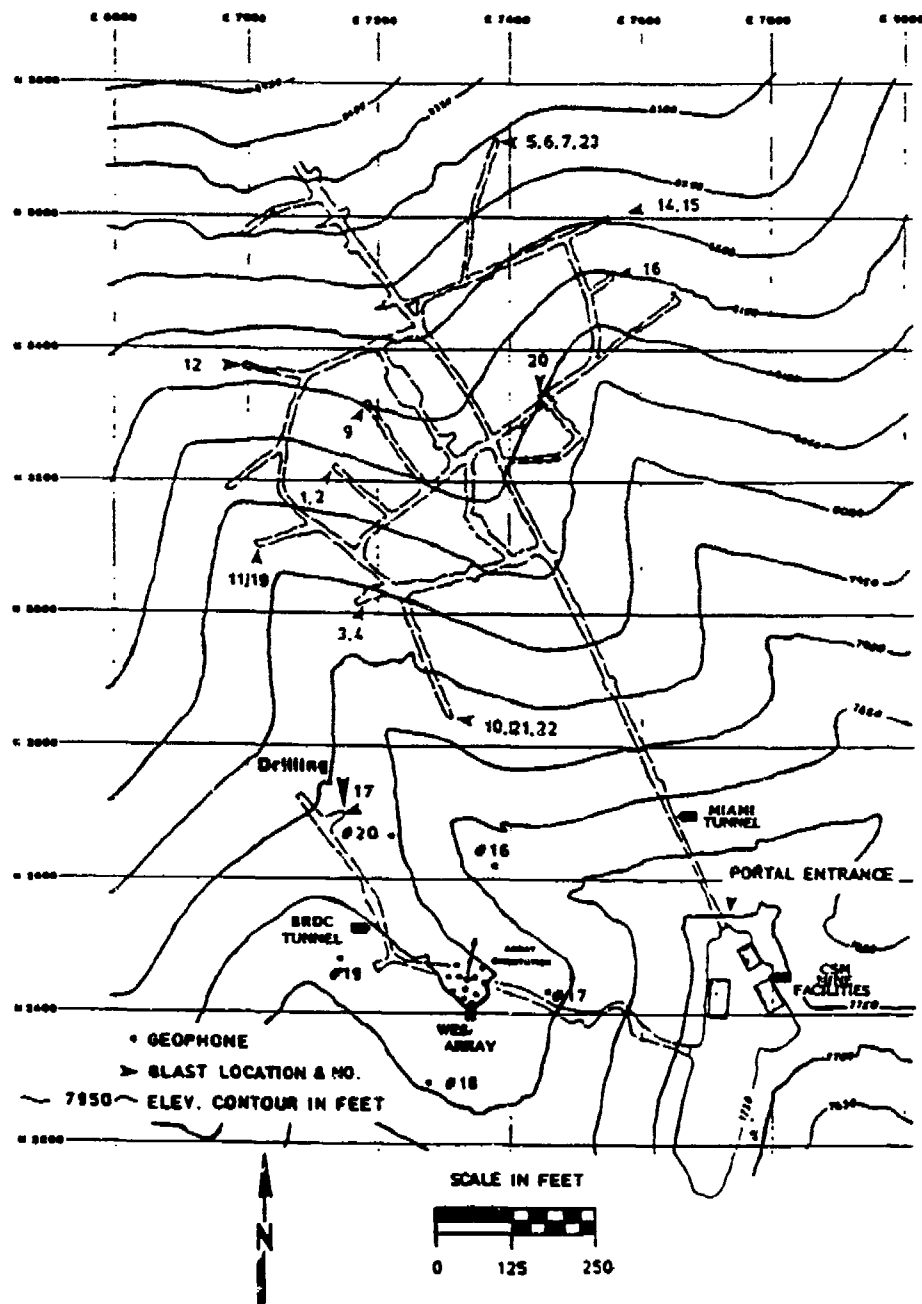


Figure 1. Generalized map showing surface contours and underground orientations of the Miami and BRDC tunnels of the CSM, Edgar test mine. Coordinates are in the CSM test mine coordinate system

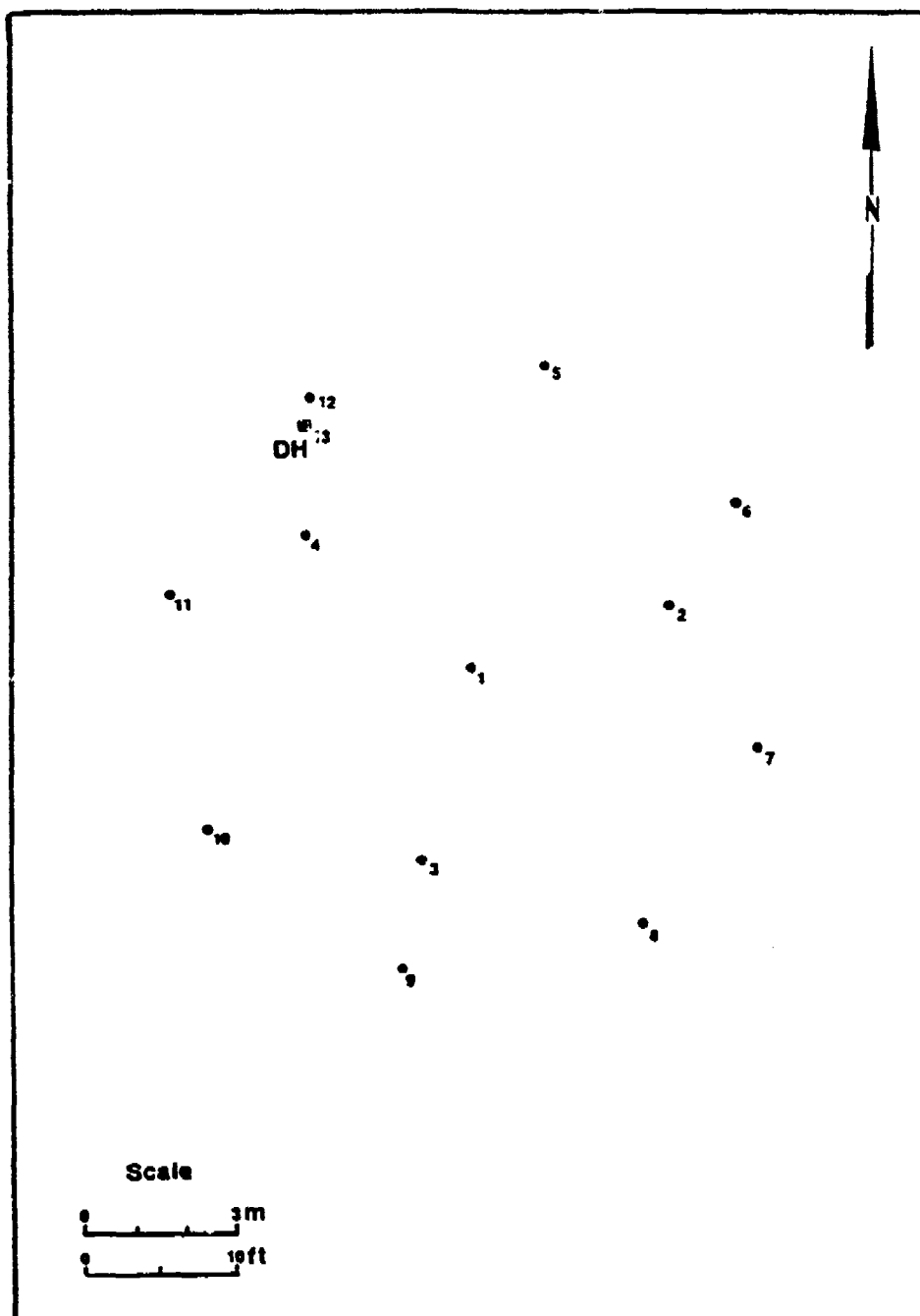


Figure 2. Surface geophone locations of the frequency domain array. Geophones 1 to 12 are the frequency domain array. Geophone 13 is a borehole triaxial geophone

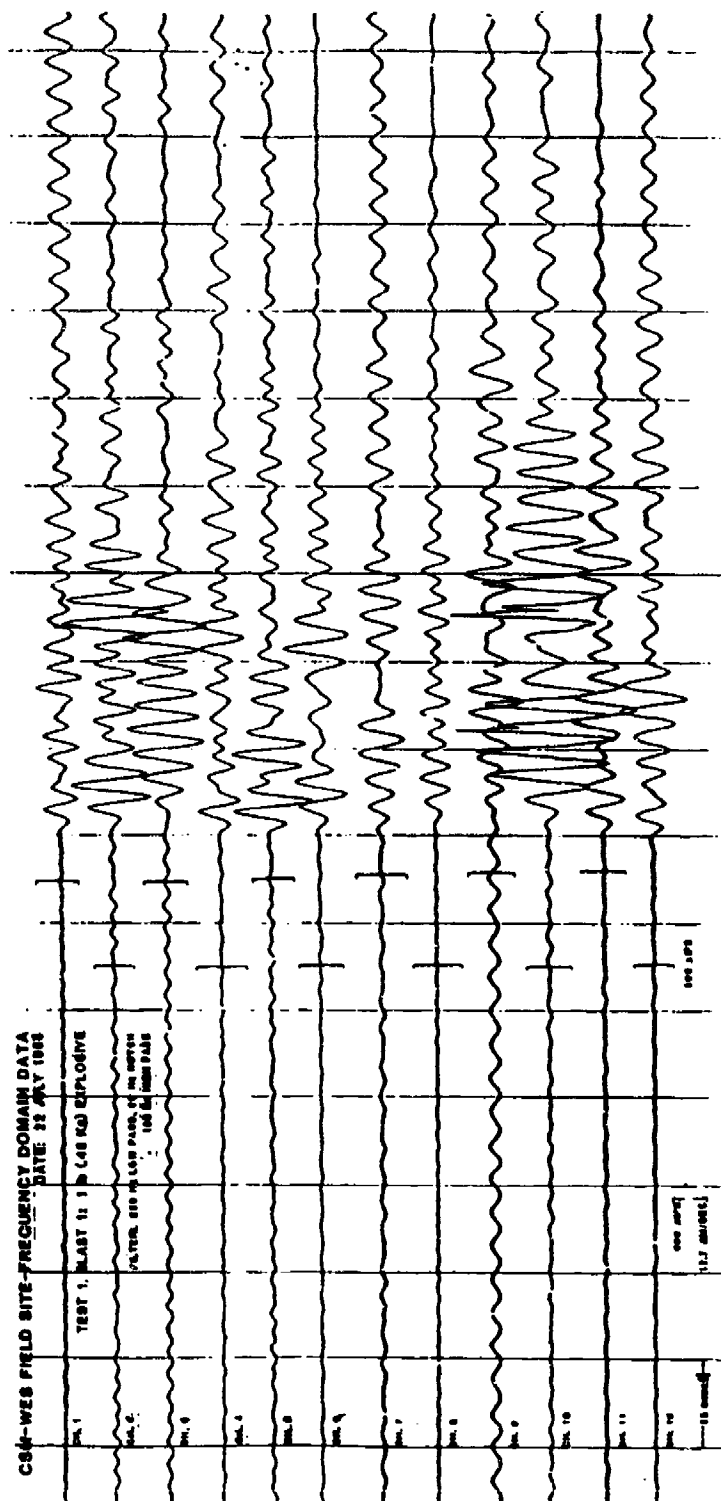


Figure 3. Time history trace of blast 1 as monitored at the frequency domain array. The particle velocity scales are 500×10^{-6} ips

BLAST 2

ANGLE TO SOURCE: 11.4 DEG. CCW FROM NORTH

APPEARANT VELOCITY: -10583.77 FT / SEC
-3225.933 M / SEC

LINE: $N = -10583.77 T + 28.0882$
CORRELATION COEFFICIENT: $R = -.9816867$

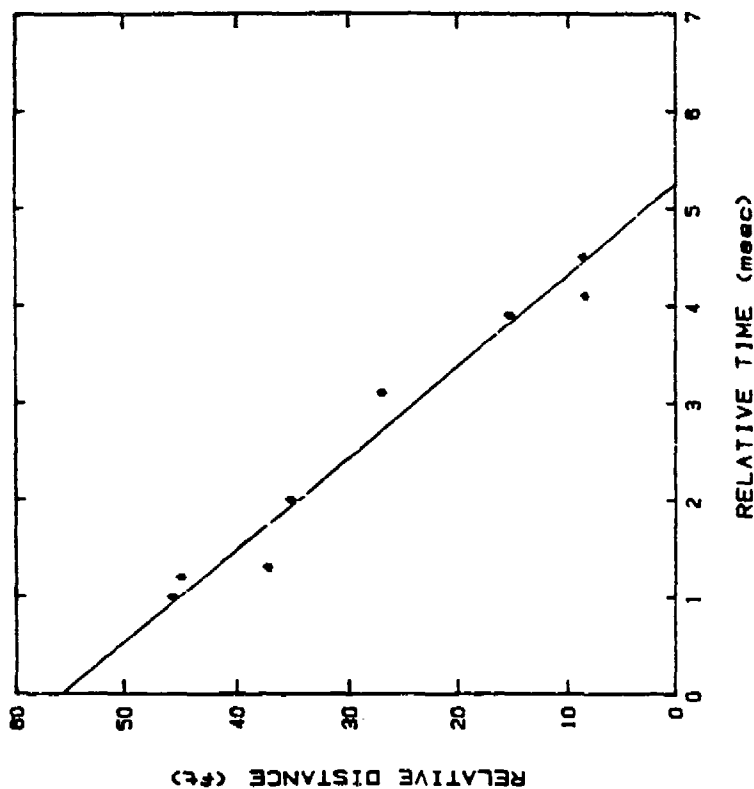


Figure 4. Least squares fit of the first particle motion time versus relative distance for each geophone in the frequency domain array when monitoring blast 2. Each geophone location is projected onto an axial line passing horizontally through the center of the array. The azimuth with the highest correlation coefficient is the steered direction. The slope of the regressed line determines the apparent P-wave velocity

CSM BLAST 11, Az=339°, Vel=8,840ft/sec, True Az=334°
 Incid Ang.=12° (2,690m/sec)
 3 blocks, 128 pts/block, 8000 samples/sec, 0.048sec,
 Tukey Window, $\Delta F=62.5$ Hz, Center 125 Hz

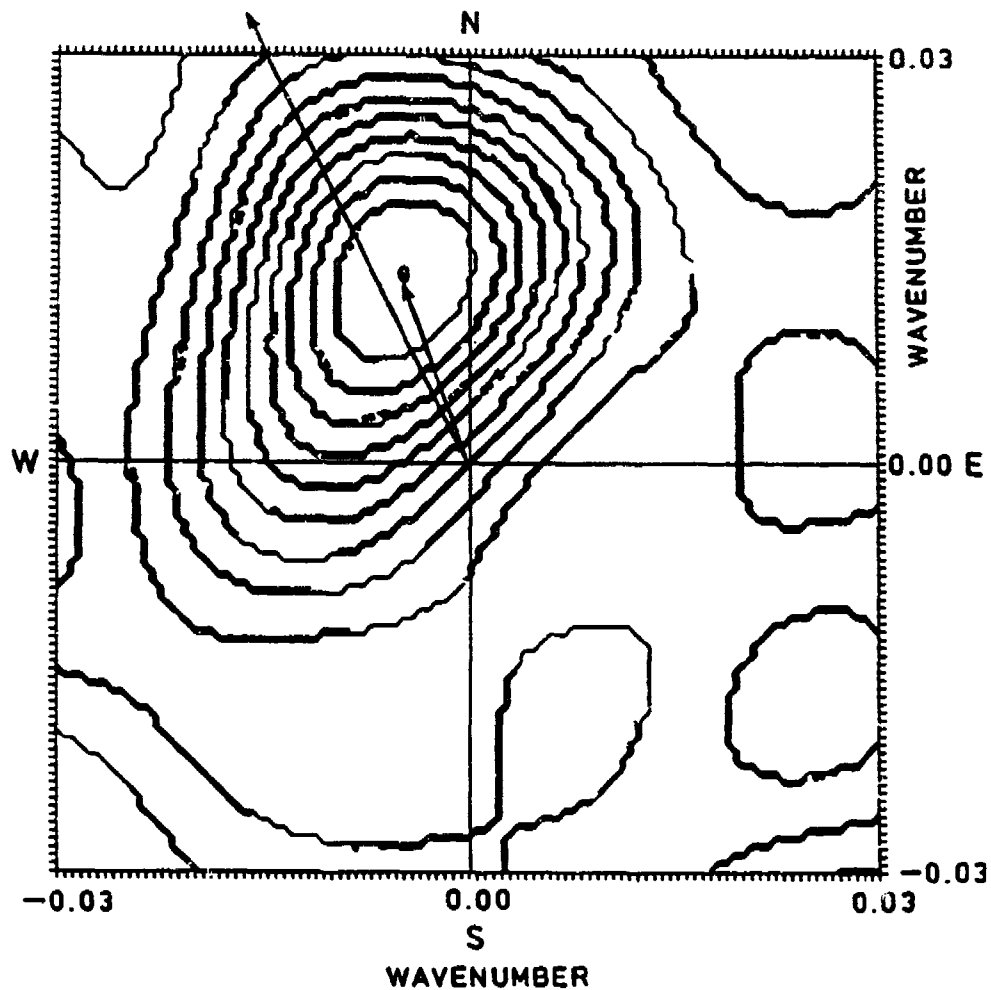
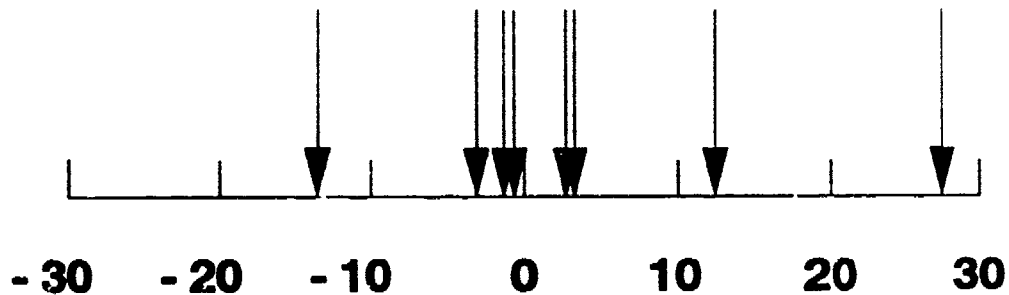


Figure 5. $K_x - K_y$ response of blast 11. The long arrow indicates the true azimuth to the blast location

Direction to Blast Azimuth Errors
Using First Arrival Times Collected
at the Frequency Domain Seismic Array

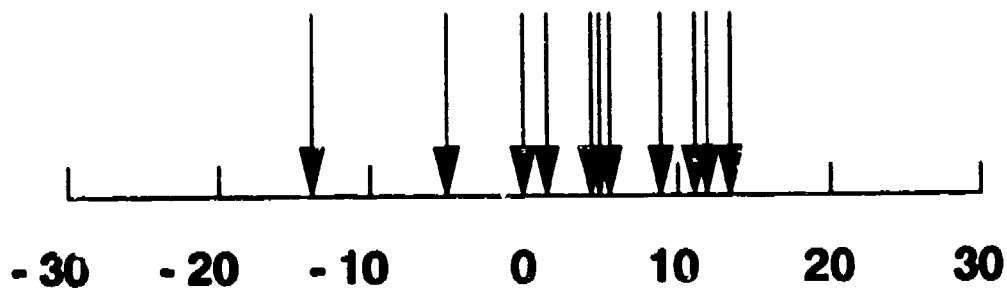
Average Absolute Error 8.1°



Blast Error Azimuths in Degrees

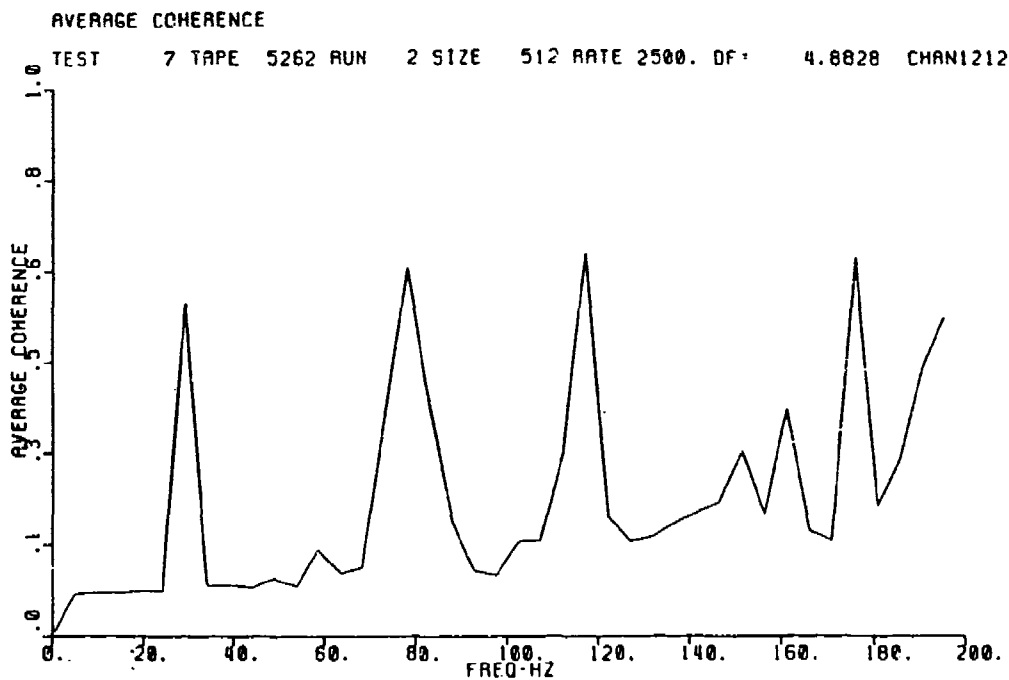
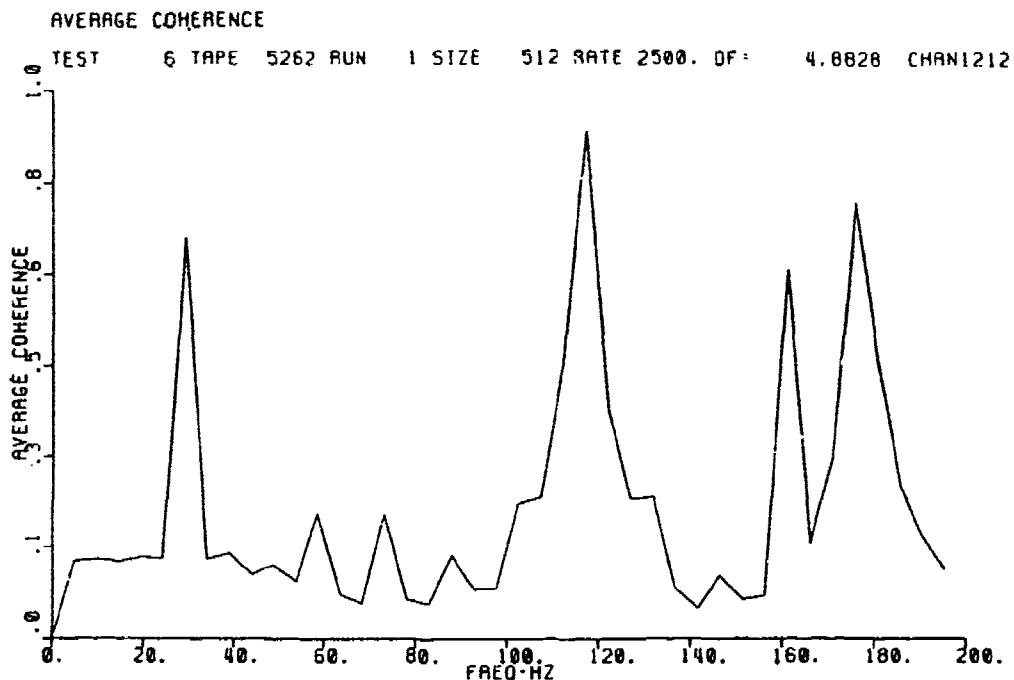
Direction to Blast Azimuth Errors
Using Bartlett Frequency Domain Processing
at the Frequency Domain Seismic Array

Average Absolute Error 7.4°



Blast Error Azimuths in Degrees

Figure 6. Comparison of Resulting Azimuth Errors to Small Dynamite Blasts with Time Domain Processing (Top) and Frequency Domain Processing (Bottom).



CSM Test 11/7 Drilling, Az = 326.5°, Vel = 4500 ft/sec True Az = 319.5°
 (1400 m/sec)
 73 blocks, 512 pts/block, 2500 samples/sec, 15.10 sec
 Tukey Window, $\Delta F = 4.88$ Hz, Center 78.1 Hz

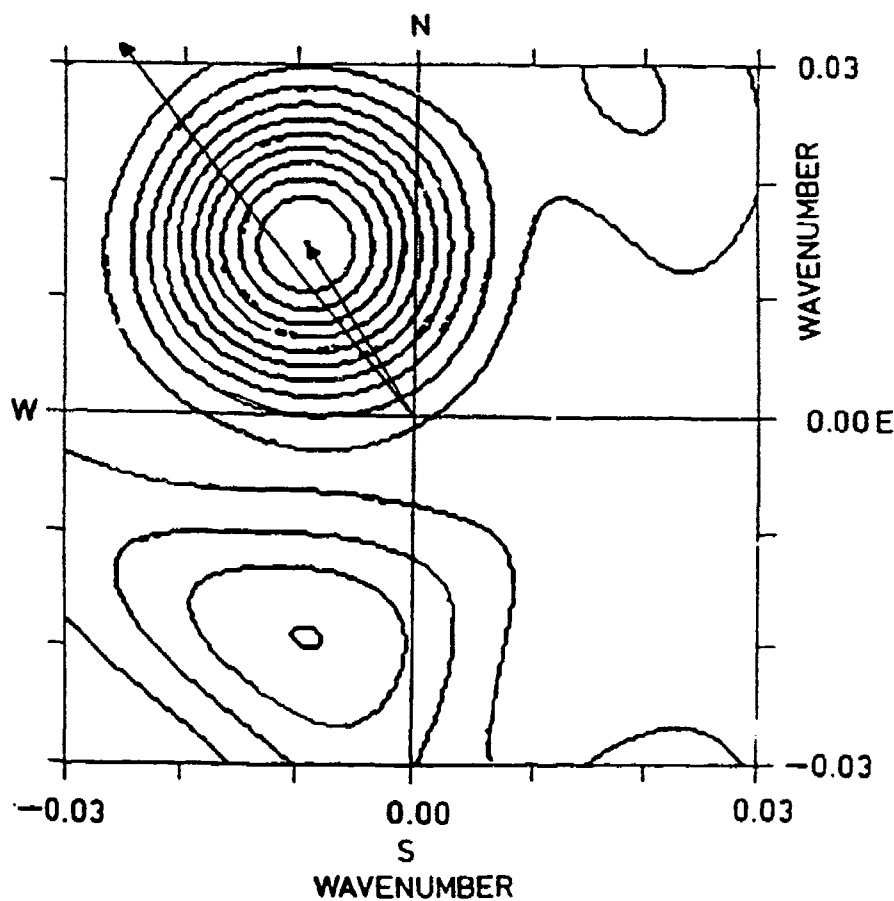


Figure 8. $K_x - K_y$ response for shot hole drilling monitored by the frequency domain array during test 11/7

CROSS-BOREHOLE SEISMIC SIGNATURES OF TUNNELS

Richard D. Rechten,
University of Missouri, Rolla, MO.

Roy J. Greenfield,
Penn. State University, University Park, PA.

Robert F. Ballard, Jr.,
U. S. Army Engineer
Waterways Experiment Station, Vicksburg, MS.

ABSTRACT

Seismic location of tunnels or voids with a cross-borehole survey is examined with field data and theory. The field data was taken at a site with a 2.2 m high by 2.7 m wide, roughly rectangular cross-section tunnel, using a newly developed 1 to 5 kHz system employing a P-wave sparker source. The synthetic records were obtained using a two-and-one-half-dimensional boundary valued solution for an explosive point source near a cylindrical void; the solution was evaluated with the method of steepest descent. The synthetic waveforms compared well to the field data; both showed a maximum reduction of amplitude in the tunnel shadow of 8 dB, and a maximum first arrival delay of 0.1 ms. Additional theoretical modeling was used to examine the variations of the received signals with tunnel size and frequency; amplitude reduction increased with frequency and tunnel size. Calculations showed that S-waves scattered from the tunnel are more than 20 dB smaller than the primary P-wave and so would be difficult to see in field data. The close comparison of synthetic waveforms to the field data indicate that the cylindrical model can be used to model data for roughly square cross-section tunnels or voids, as well as for circular cross-section tunnels, and thus is useful for data interpretation and survey planning.

INTRODUCTION

Cross-borehole seismic surveys have potential for finding tunnels

and underground cavities. In the cross-borehole seismic method, a source is placed in one borehole while the receiver is in a second borehole. Theoretical responses of tunnels and other structures aid in interpreting cross-borehole field data. Methods used previously to model two-dimensional tunnels include analog scale models (Schneider and Balch, 1991; Balch and Chang, 1991), boundary element methods (Kang et al., 1988), and finite element methods (Siggins and Stokes, 1987). Applying finite difference or finite element methods to elastic media where the separation of the boreholes is on the order of 10 wavelengths requires extensive computation. No methods are presently available to model seismic data when the path from source to receiver is not perpendicular to the tunnel axis.

In the present work, we develop a method to predict the waveforms for cross-borehole seismic signals. The path between boreholes can be at an arbitrary angle α to the tunnel axis. The source is a point explosive source; the model is a two-and-one-half-dimensional, homogeneous earth with a circular cross-sectional air-filled tunnel.

Data taken in a cross-borehole survey is compared to synthetic waveforms. Synthetic waveforms are then calculated for other tunnel sizes to show various effects of the tunnel on the waveform. Finally, the effects of water filling the tunnel is considered.

THEORY

A tunnel is represented as a void circular cylinder in an infinite whole space, as illustrated in Figure 1. The cylinder axis is oriented in the direction of the z -axis. A source and receiver are assumed to be located at a common depth, $y=D$, above (or below) the horizontal plane of the tunnel, $y=0$. A horizontal line connecting source and receiver boreholes makes an angle α with the x -axis. The

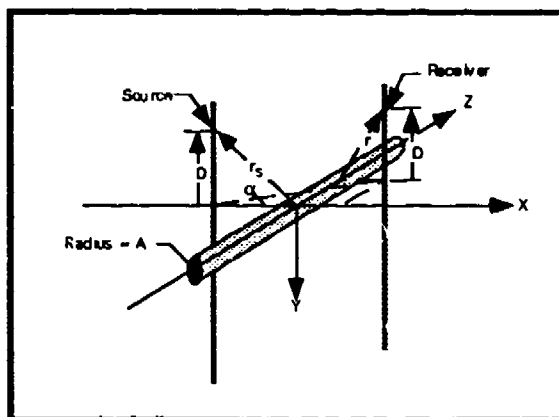


Figure 1. 3-D tunnel model for theoretical calculations. Both source and receiver are at the same elevation (D) above (or below) the axis of the tunnel.

source and receiver are located at cylindrical radii r_s and r , respectively, from the tunnel axis.

The model is what is often referred to as two-and-one-half-dimensional, where the medium is two-dimensional and the source is three-dimensional. The source is represented by a three-dimensional explosive point source. The total solution to the elastic wave equation is found in the frequency domain. The Green's function solution is in the form of an integral over k_z , the axial wavenumber, which is evaluated by the method of steepest descent. Source and receiver positions are arbitrary as long as the receiver is located in the far field.

The total waveforms are the sum of the incident (primary) P wave plus the P and S waves scattered from the cylinder. To arrive at a waveform, the frequency domain Green's function solution for the total wave field (including the tunnel scattered waves) is multiplied by the frequency domain representation of the source time function. This convolved result is then transformed back to the time domain. The three P and S displacement waveforms and the P pressure waveform are then calculated. The displacement waveforms include both the P- and S- wave contributions.

For comparison to field data the primary source time function is found by deconvolving an observed waveform (away from the tunnel). This procedure is carried out in the frequency domain by dividing the spectrum of the observed waveform by the infinite media Green's function (with no tunnel).

FIELD STUDY

System Description

The seismic energy source used during data acquisition was an electric-arc discharge device. Construction and performance aspects of this instrument, as well as a functional description of the data acquisition system, are given by Rechtien et al. (1993). The dominant frequency of the primary waveform generated by this device is in the neighborhood of 1.5 kHz, depending on borehole coupling and source-receiver distance, with a half-power bandwidth exceeding 1 kHz. The seismic field was sensed with a wide-band hydrophone having a 32 dB

downhole preamplifier. Received signals were passed through a high-pass filter set at 1 kHz (-3 dB point, -25 dB per octave) and an anti-alias, low-pass filter set at 7 kHz (-0.1 dB point, -94 dB per octave). These data were digitized with a 16-bit A/D converter at a sample interval of 10 μ s.

Geologic Setting

The test site is located in rugged, mountainous terrain which has about 250 m of relief. The site and surrounding 2 km area is on an exposed pluton, the composition of which ranges from granodiorite to granite. A man-made tunnel penetrates the pluton approximately 81 m beneath the ground surface. This tunnel, which is accessible for visual examination, is fenced on either side by a series of boreholes that provide unique opportunities for experimental investigations.

Geometry of Survey

The test configuration is shown in Figure 2. Source and receiver boreholes defined a plane perpendicular to the axis of the tunnel. These boreholes were separated by a horizontal distance of 20.3 m. The center of the tunnel was located approximately 4 m to the east of the receiver borehole. The geometric shape of the tunnel, which at any given position was determined to a large degree by existing joint patterns, is illustrated. The tunnel was approximately 2.7 m in width and 2.2 m in height.

Acquired data

Both source and receiver were lowered to depth positions 10 m below the center of the tunnel ($D=+10$) prior to initiation of the data acquisition run. Source and receiver

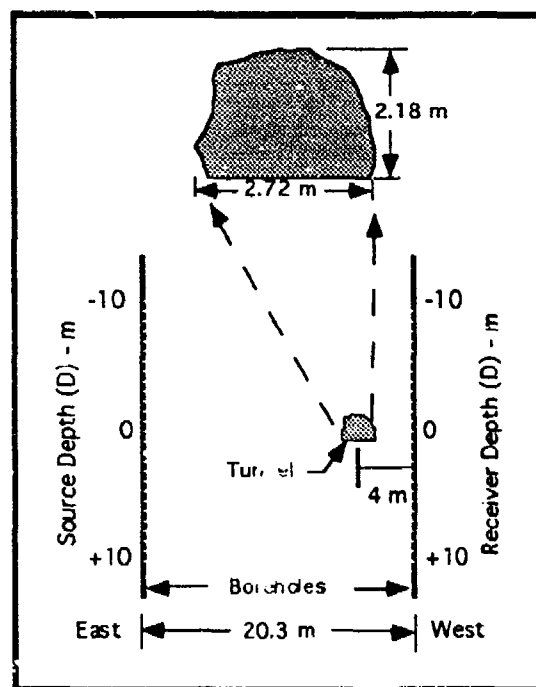


Figure 2. Field test configuration from a vantage point looking south. D designates the position of the source and receiver above or below tunnel depth.

were always kept at a common depth and simultaneously raised in increments of 0.2 m after each trace acquisition cycle. This run was completed at a depth of 10 m above the center of the tunnel ($D=10$), yielding a seismic section consisting of 101 traces. The hydrophone pressure seismogram thus acquired is shown in Figure 3. These data are presented in an amplitude normalized format; the amplitude of each trace was normalized to the amplitude value of the first positive peak.

Amplitude variation of first arrivals is illustrated in this figure as attenuation in dB relative to the maximum value of the data set comprised of first positive peak amplitudes.

Comparison of field data to synthetics

Figure 4 shows a comparison of field and synthetic pressure waveforms for a 7 m section centered around tunnel depth. All theoretical waveforms were calculated using a 1.5 m radius tunnel, $V_p = 5000$ m/s, $V_s = 2887$ m/s, and $\rho = 2000$ kg/m³. The borehole separation and the position of the tunnel in the modeling were the same as for the field data, which was shown in Figure 2. The field waveform approximately 4 m below the tunnel was used as the primary waveform in computing the synthetics. The spectral peak for field data in this borehole was around 1.6 kHz.

Arrival times for these waveforms were computer picked at the point where the amplitude exceeded .07 of the peak amplitude. As shown in Figure 5, arrival times for field data and the synthetic waveforms compare closely. The depth extent of the late arrivals is just under 3 m,

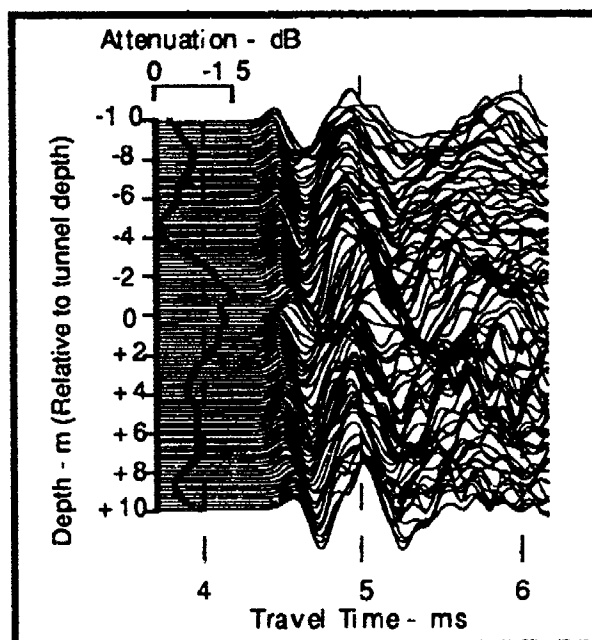


Figure 3. Common source/receiver depth section with mid-station at tunnel depth ($D=0$). Each trace is amplitude normalized to the value of the first positive peak. The trace interval is 0.2 m.

the diameter of the tunnel. Maximum delay caused by the tunnel near its center line is approximately 0.1 ms.

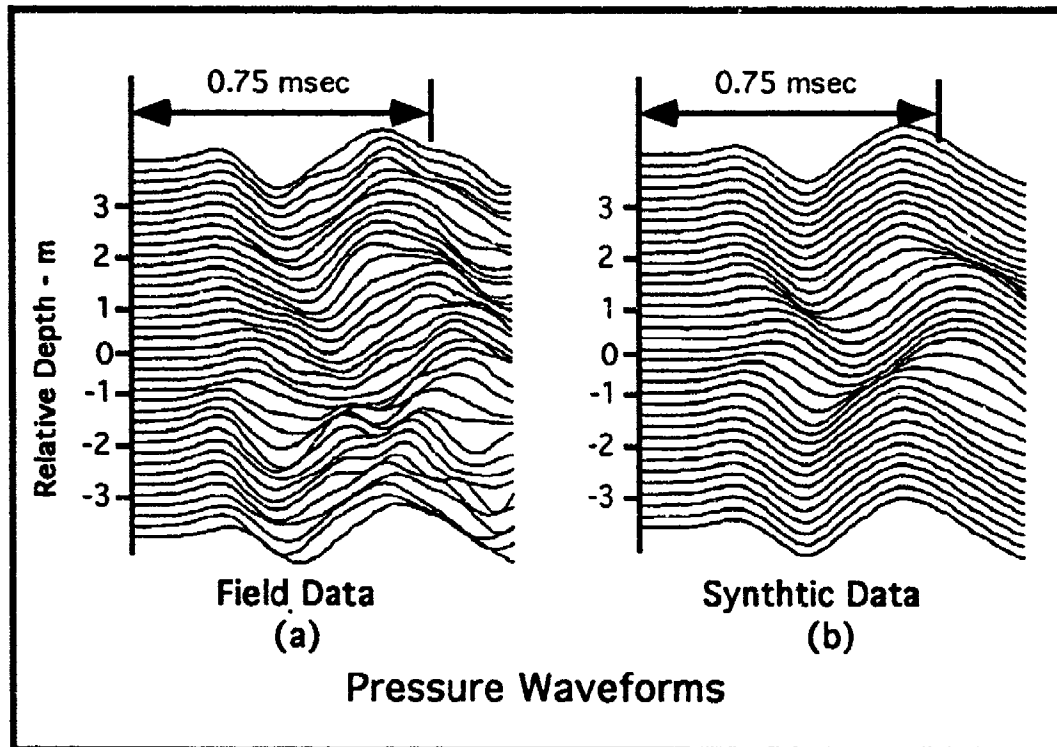


Figure 4. a). Expanded scale field pressure data above and below tunnel depth (Relative depth = 0). b). Synthetic data derived from theory. Each trace has been amplitude normalized to its own maximum peak-to-peak amplitude. True relative amplitude is presented in Figure 6.

A comparison was also made of the amplitude anomaly between the data and synthetics. The peak of the first small upward half-cycle was measured and is compared in Figure 6. The depth extent of the low amplitude zone and the basic amplitude anomaly of -8 dB agree well between field data and theory. In both the field data and the synthetic waveforms, the least amplitude does not occur precisely at the depth of the tunnel center. At this depth the amplitude is approximately 3 dB higher than at the points 0.8 m above and below the center. This amplitude effect was also seen on other examples of field data; its cause will be discussed in the next section.

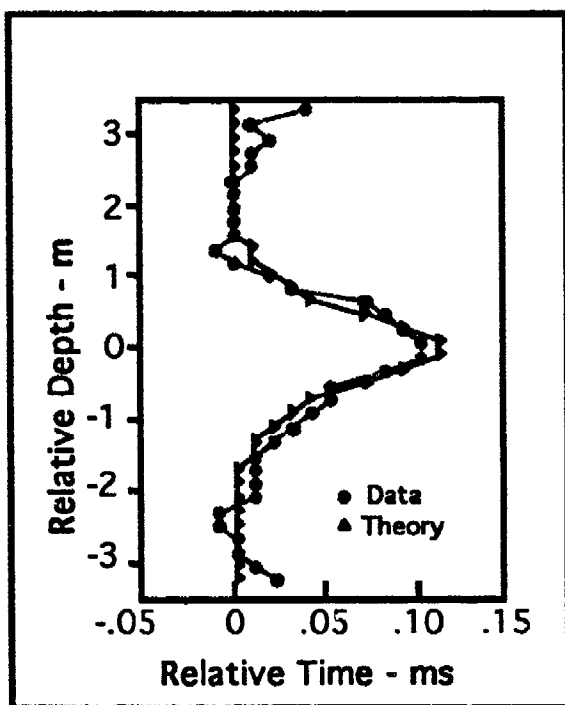


Figure 5. First arrival times.

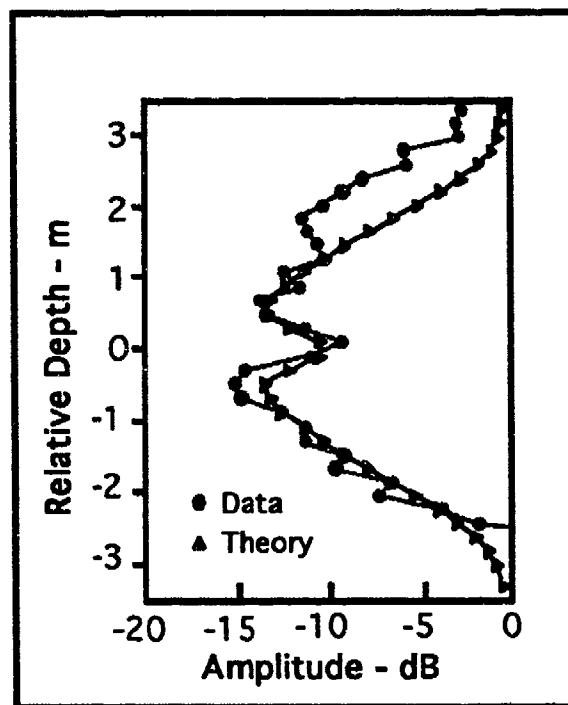


Figure 6. Amplitude of first positive peak.

A single adjustment in the ordinate of the theory curve shown in Figure 6 was made to match the theory with the data amplitude curve. This adjustment was made visually to give the best overall fit between the data and the theory curves. The adjustment was done because it was not possible to know exactly the amplitude to use for the primary waveform, since factors other than presence of a tunnel affect signal amplitude. Such factors are changes in rock velocity, the source radiation pattern, attenuation, and source and receiver coupling.

FURTHER SYNTHETIC RESULTS

Air-filled Tunnel

The following parameters were used in calculations presented below: a Poisson's solid with $V_p = 5000$ m/s, $V_s = 2887$ m/s and $\rho = 2000$ kg/m³ was used. Figure 1 was used as the geometrical model with $r_s = 10$ m, and $r = 15$ m for all cases. The borehole geometry used in the synthetic examples is different from the field data. This geometry was used for the synthetic example because many surveys are conducted with borehole

spacings of 15 to 30 m. Thus we adapted a reasonable average value for the distance between boreholes for the synthetic examples. The details of the features that will be examined are not very sensitive to the distance between boreholes or to the exact tunnel position.

To show the effect of the frequency content of the primary waveform, results were run for three primary waveforms having center frequencies of 5.0 kHz, 2.5 kHz, and 1.25 kHz. This range of frequencies covers those that are likely to be observed with cross borehole seismic systems. The 1.25 kHz and

2.5 kHz primaries were formed by appropriately stretching the time scale of the 5 kHz primary. Note that waveforms for the different frequency waveforms are plotted with different timescales. For the velocities given above, the P-wave wavelengths for these three center frequencies are 1, 2, and 4 m respectively. The S-wave wavelengths are 0.58, 1.15, and 2.31 m respectively.

Waveforms shown in Figure 7 show the interaction of the 5 kHz waveform with tunnels of varying sizes. All

waveforms are for $D = 0$ m. The primary 5 kHz waveform is the bottom trace for a designated tunnel radius of $A = 0$. Amplitudes are peak-to-peak relative to the primary. The plot shows that the arrival time delay increases as A increases, and shows how the amplitude of the signal decreases as A increases.

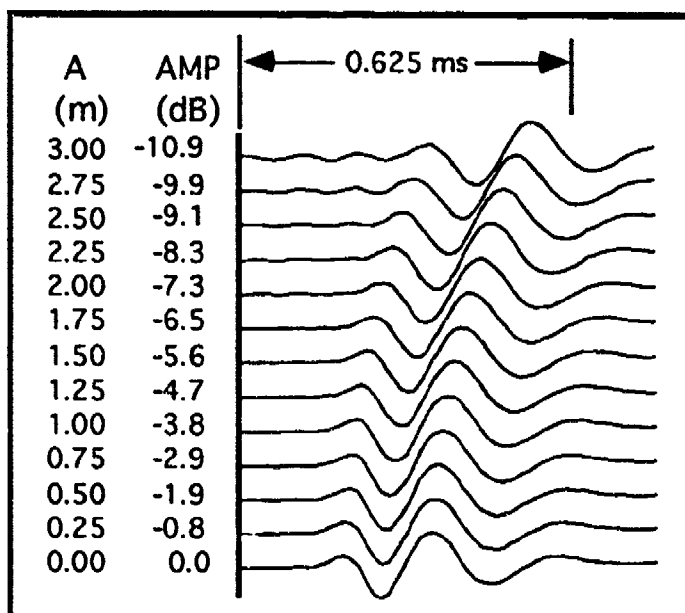


Figure 7. Synthetic waveforms for various tunnel radii (A). Bottom trace for $A=0$ is 5 kHz primary waveform. Amplitude is normalized to primary. $r_s=10$ m. $r=15$ m.

In Figure 8, the arrival time versus tunnel radius, A , are plotted for the 5, 2.5, and 1.25 kHz waveforms. Again $D = 0$ m. The curve labeled B in this figure is the ray theory time for the shortest path in the media. This

path traverses from the source to the tangent point on the tunnel, then follows the tunnel surface to the point of tangency for a line from the receiver.

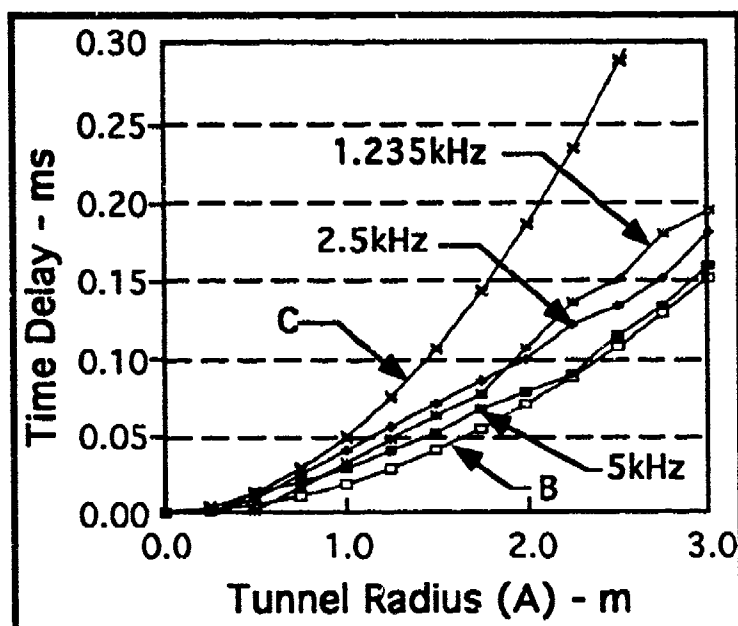


Figure 8. Variation of arrival time with tunnel radius for three different peak source frequencies. Curves B and C are discussed in text.

Times describing curve B assume a P-wave velocity for the entire path. The curve labeled C uses a Rayleigh wave velocity for that portion of the path on the tunnel surface. It is clear that curve B fits the times measured on the synthetic waveforms while curve C does not. Thus we may conclude that the first portion of the received waveform can be considered as a diffraction phenomena of the P-wave, and that this early energy does not travel around the tunnel in the form of a Rayleigh wave.

Amplitude of the first positive peak is plotted versus D for three tunnel sizes and the three different frequency primary waveforms and is presented in Figure 9. Note that for all cases the greatest amplitude decrease does not occur at the center of the tunnel -- rather, above (and below) the center. Three effects occur which are in agreement with the normal ideas of diffraction theory. First the D value of the most significant amplitude decrease goes up with decreasing frequency. Second the magnitude of the amplitude loss goes up with an increase in tunnel size. Third the magnitude of the amplitude loss goes up with an increase of frequency.

The scattered pressure waveforms for the 5 kHz primary waveform are shown in Figure 10. The amplitudes are peak-to-peak, normalized to the direct P-wave (or primary pressure waveform). A 5 kHz P-wavelength is 1 m, which is about 1/3 of the cylinder diameter. There are two pulses labeled as P1 and P2. We interpret the P1 pulses as the ones that are expected to be scattered from the top of the cylinder (see Figure 11). The pulses labeled P2 are interpreted as energy that has traveled around the bottom of the cylinder then re-radiated to the far field. Note that for D

above 2.8 m, where the P2 waveform has separated from the P1 waveform, the P2 Pulse is about 20 dB smaller than the primary pressure waveform.

The arrival times for the P2 pulses are consistent with the whole of the P2 path being traversed at P-wave velocity. The times are not consistent with propagation around the cylinder (dotted line in Figure 11) occurring at Rayleigh wave velocity. In additional simulations, the P-wave velocity was fixed at 5000 m/s while the S-wave velocity was varied. The arrival time of the P2 pulse did not change with V_s . However the amplitude ratio of P2/P1 was larger for the V_s of a Poisson solid than it was for V_s greater or less than the Poisson solid value.

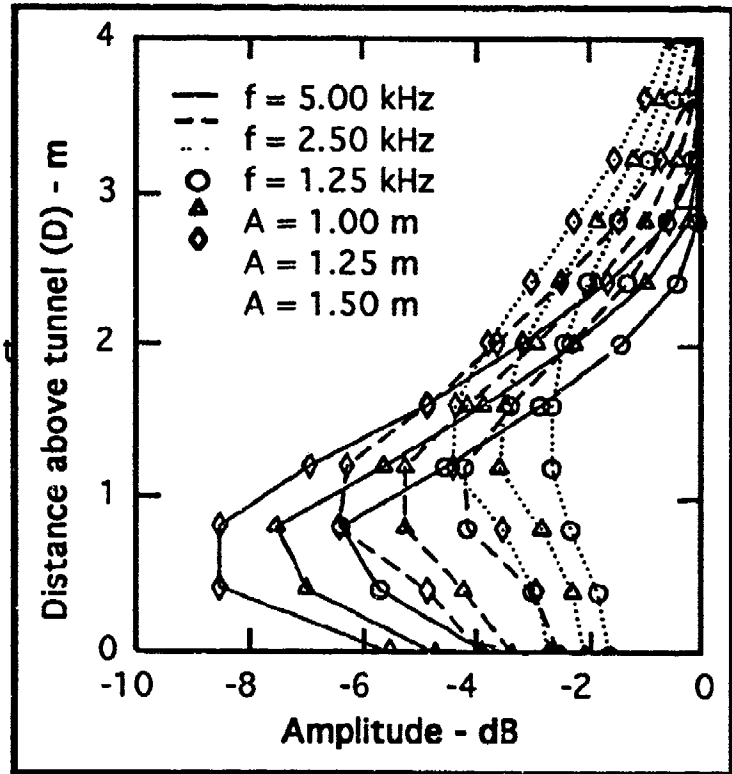


Figure 9. Amplitude versus D for three different frequency waveforms. Amplitude normalized to primary. Same geometry of Figure 7.

This result is in contrast with a result of Siggins and Stokes (1987) where they examined energy propagation around a hollow cylinder. For the problem of a line source on the cylinder surface they calculated far field (at 9.8 cavity radii) waveforms. The receiver was 180 degrees from the source. Their P-wave wavelength of the pulse was approximately equal to the cylinder diameter. The waveforms showed three pulses that were interpreted as having propagated around the cylinder surface as a pseudo-

Rayleigh waves. The time between their pulses was consistent with their Rayleigh wave interpretation. The cause of the difference in the present result from the Siggins and Stokes result is that in the present case both the source and receiver are away from the cylinder surface.

We believe that the reason for greatest decrease of the first peak

amplitude of Figure 6 not occurring at the center of the tunnel is that the P1 and P2 waveforms are in phase at this point, having traveled the same distance in diffracting around the tunnel. At points above (and below) the P1 and P2 pulses are not in phase.

Finally, we look at the P- to S-wave scattering due to presence of the tunnel. In Figure 12, the y (vertical) direction displacements are plotted for paths not perpendicular to the tunnel axis, i.e., $\alpha = 45^\circ$. Since the particle displacement is radial for the primary P-wave there it has 0 amplitude on the vertical displacement component.

However, the amplitudes on the plot are normalized to the amplitude of the radial displacement for the primary P-wave. Notice that the S-waves are larger than the vertical displacement component of the P1 and P2 wave but are approximately 20 dB below the radial component of the primary P-wave. The z displacement (horizontal S-wave, which is not shown) is on the order of 10 dB lower than the y (vertical) displacement S-waves. The source is a pure P-wave source so

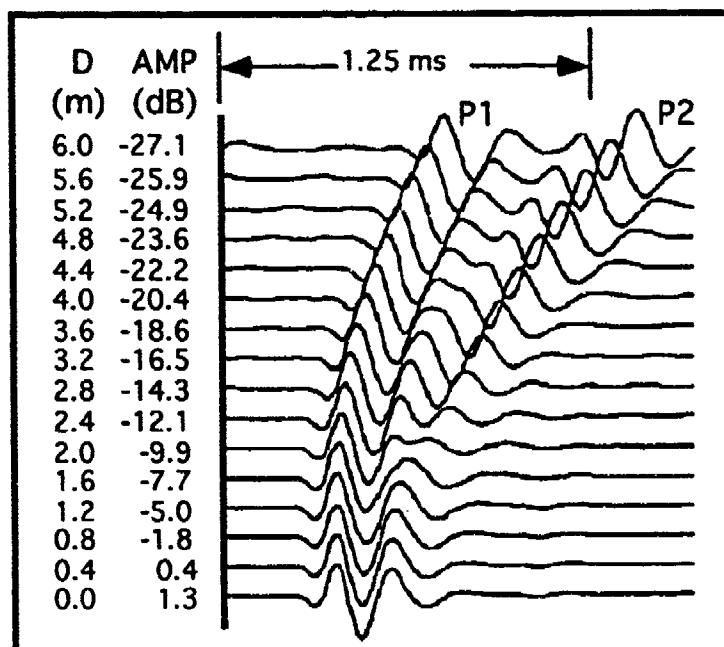


Figure 10. Synthetic scattered pressure waveforms. $A=1.5$, $\alpha=0$. Waveform is 5 kHz. P1 and P2 defined in text. Same geometry as Figure 7.

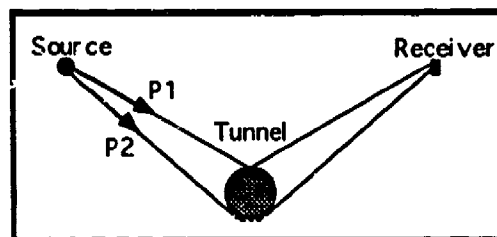


Figure 11. Ray interpretation of P1 and P2. Dotted line is portion of path around cylinder.

all the S-wave arrivals are generated by scattering by the cylinder.

Water-filled Tunnel

A model was developed for a two-dimensional, circular cross-section, fluid-filled tunnel. The model is shown in Figure 13. The source is, again, a point explosive source. Pressure waveforms are computed at the receiver. The primary signal used in this modeling had a central frequency of about 1.4 kHz.

Results were obtained for this specific model. In all cases the medium was a Poisson solid with $V_p = 5000$ m/s and $V_s = 2887$ m/s, and $\rho = 2200$ kg/m³.

Results were obtained for three different fillings. Model E20 had a water filling with $V_p = 1500$ m/s and density of 1000 kg/m³. Model E21 was for a tunnel filled with air. Model E22 had a fluid of $V_p = 3500$ m/s and a density of 2200 kg/m³; this model represents a fractured or low velocity rock. We used this third model since we do not presently have a computer program which will model a tunnel filled with an elastic solid. However neglecting the rigidity of the tunnel material in the third model should not effect the scattered waveform greatly.

The air-filled tunnel gave the normal result of a small arrival time delay of 0.06 ms for the $D = 0$ path. The waveforms are shown in Figure 14. This is the delay for the energy to go around the top and bottom of the tunnel. There is an amplitude decrease of as much as 8.5 dB.

For the water-filled tunnel the arrival time delays were the same as for the air-filled tunnel. The waveforms are shown in Figure 15. The

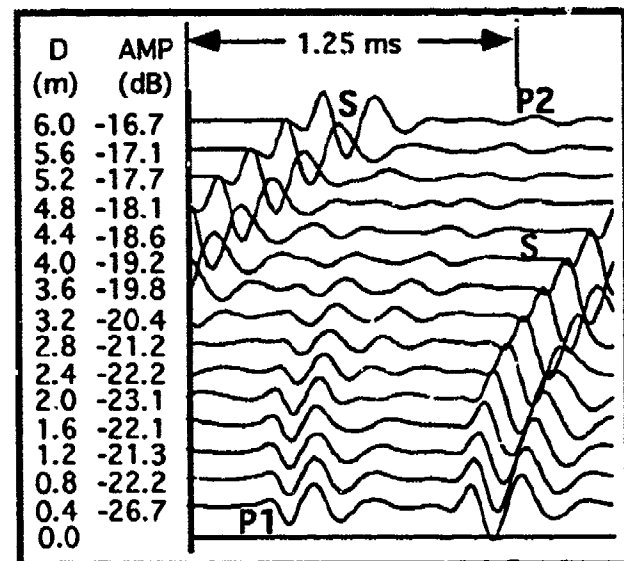


Figure 12. Displacement waveforms in vertical (y) direction. Scattered waves only. Both P and S waves included. $A = 1.5$ m. Waveform is 5 kHz. $\alpha = 45^\circ$. P1, P2 and S defined in text. Last 6 S-wave traces plotted in wrap-around format. Amplitude normalized to radial displacement of primary. $r_s = 10$ m, $r = 15$ m.

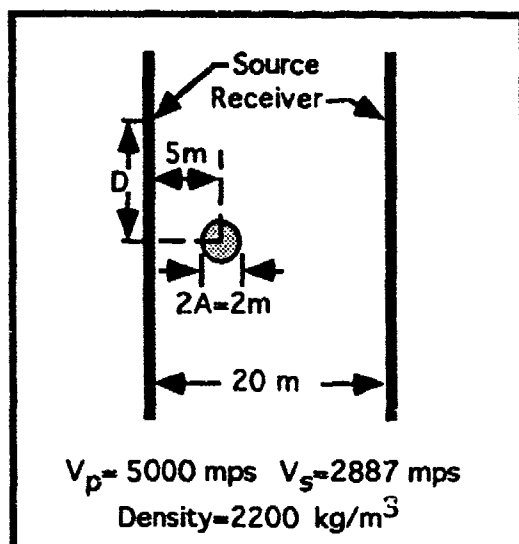


Figure 13. Two-dimensional, fluid-filled tunnel model. The source is a point explosion. Primary P-source is 1.4 kHz.

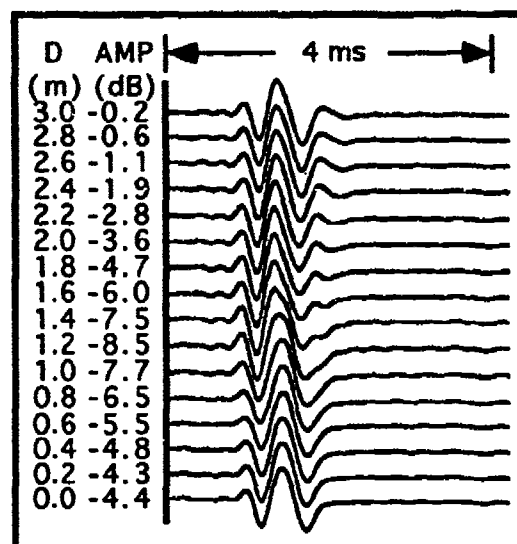


Figure 14. Air-filled tunnel. Maximum time delay was 0.6 ms for $D=0.0$.

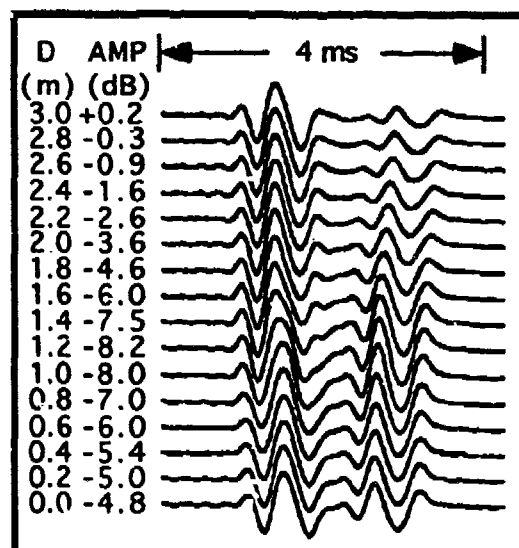


Figure 15. Water-filled tunnel, $V_p=1500 \text{ mps}$. Maximum time delay was 0.6 ms for $D=0.0$.

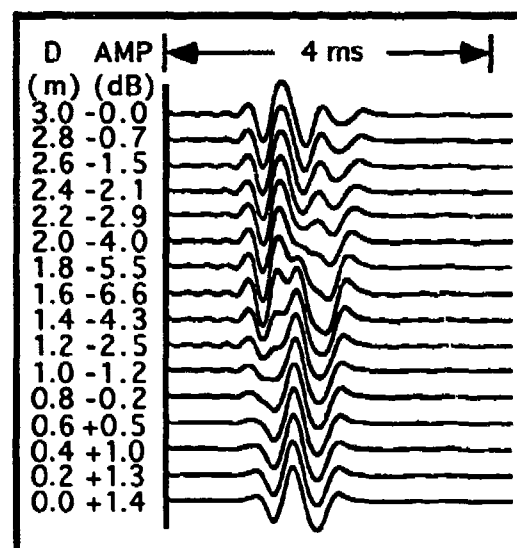


Figure 16. Heavy fluid-filled tunnel (fracture model). $V_p=3500 \text{ mps}$.

primary arrival is also energy that has been diffracted around the tunnel. There is a second arrival that has traveled through the water in the tunnel and arrives about 1.4 ms after the first arrival. This arrival is smaller than the first arrival for this geometry. The amplitudes of the first arriving pulse for this model are close to the amplitudes for the air-filled model.

For the model with the fluid velocity of 3500 m/s, for paths with D less than 1 m, the signal through the fluid and the arrival that has been diffracted around the tunnel arrive at about the same time. The waveforms are shown in Figure 16. These two arrivals together give an amplitude that is 1.5 dB above the primary signal for small D . However at $D = 1.6$ m the presence of the tunnel reduces the signal by 6.6 dB. For the range of $1 < D < 3$ m the signal waveform is distorted. This distorted waveform does not occur in the air-filled tunnel case.

DISCUSSION

The far field restriction could be removed by using numerical integration rather than the method of steepest descent to evaluate integrals in the solution. This was done for cross-borehole radar calculations by Moran (1989). The present close comparison of the synthetics to the field data indicates that the far field solution is satisfactory for a receiver within a few wavelengths of the tunnel.

The S-waves scattered at the tunnel by the primary P-wave are more than 20 dB lower than the primary P-waves for all the synthetic cases that we have examined. This probably explains why we have not seen S-wave arrivals in a number of field records taken near tunnels with the present system. In a geometry in which the receiver is far from the tunnel an S-wave arrival might be seen since the time delay between the P-wave and S-wave would be large and thus the P-wave coda might have time to decay to a level which allows the S-wave to be observed. However, for the present geometry, the use of scattered S-waves for tunnel or cavity detector or for dimension estimation does not appear to be very useful when a P-wave source is used. It might, however, be useful if an S-wave source was employed.

CONCLUSIONS

As a result of the successful comparisons of theoretical modeling to actual field data, we reached a number of conclusions. Crosshole seismic techniques are viable as diagnostics in detecting unknown air-filled cavities or tunnels. The waveform signature resulting from the presence of a tunnel can be calculated for arbitrary far-field sources and receiver locations using both P- and S-waves. The theory is useful in setting system requirements for tunnel or cavity detection systems and surveys and also as an aid in the interpretation of cluttered field data. The good fit to the data from the roughly square tunnel field data using the circular tunnel model indicates that small changes in tunnel cross-section do not significantly affect the received waveform. However changes in tunnel size do affect the amplitude and waveform. Theoretically calculated waveforms can be used for a variety of applications including conventional seismic reflection surveys for tunnels or voids.

ACKNOWLEDGMENTS

This research was supported by the USAE Waterways Experiment Station, Vicksburg, MS, and the Physical Security Equipment Division's Geophysics Team headed by Mr. Ray Dennis at the US Army Belvoir Research, Development and Engineering Center, Ft. Belvoir, VA. Permission was granted by the Chief of Engineers to publish this information. The views of the authors do not purport to reflect the position of the Department of the Army or the Department of Defense. The authors also wish to recognize the support of Dr. Donald Eccleshall, US Army Ballistic Research Laboratory, Aberdeen Proving Ground, MD. Appreciation is extended to US 8th Army Tunnel Neutralization Team, Seoul Korea, for their travel and logistical support of the field activities.

REFERENCES

- Abramowitz, M. and Stegun, I. A., 1968, Handbook of Mathematical Functions: Dover.
- Balch, A.H., And H. Chang, 1991, Seismic crosshole imaging of 2-D and 3-D physical elastic models using prestack reverse time migration: 61st Ann. Internat. Mtg., Soc. Expl. Geophys., Expanded Abstracts, 660-664.
- Ewing, W. M., Jardetzky, W. S., and Press, F., 1957, Elastic Waves in

Layered Media, McGraw-Hill.

Greenfield, R. J., 1978, seismic radiation from a point source on the surface of a cylindrical cavity: *Geophysics*, 43, 1071-1082.

Kang, Y. V., Roesset, J. M., And Stokoe, K. H., II, 1988, Tunnel detection using SH-waves: *Proc. 3rd International Symposium on Tunnel Detection*.

Moran, M.L., 1989, Time domain electromagnetic scattering for a three dimensional tunnel in the presence of a vertically oriented electric dipole: MS Thesis, The Pennsylvania State Univ.

Rechtien, R. D., Hambacker, K. L, Ballard, R. F., 1993, A high-frequency sparker source for the borehole environment: *Geophysics*, v. 58 no. 5 (in press)

Schneider, W.A., Jr., and A.H. Balch, 1991, Tomographic inversion as a tunnel detection tool: A three dimensional physical modeling feasibility study: 61st Ann. Internat. Mtg., Soc. Expl. Geophys., Expanded Abstracts, 656-659.

Siggins, A. F., And Stokes, A. N., 1987, Circumferential propagation of elastic, waves on boreholes and cylindrical cavities: *Geophysics*, 52, 514-529.[PB]

LOCATION OF A TUNNEL BORING MACHINE (TBM) USING SEISMIC WAVEFIELD ANALYSES

W. Silva, C. Stark, and F. Ruskey

Pacific Engineering and Analysis
El Cerrito, California

ABSTRACT

Often in the search for tunnels, emphasis is put on the development of new technologies. New and better signal sources and receivers are touted and the use of improved data processing is often emphasized.

While important, these objectives need not divert our attention from an inherent value in simple, basic equipment and its use. BRDEC digital seismic event recorders (DSLDD) and Sprengnether MEQ 800 smoked drum recorders fall into this latter category. The equipment is reliable, easy to deploy, and their data output is relatively simple to analyze and interpret.

The tests described in this report at Juam, South Korea were intended to demonstrate that it is possible to detect and locate a TBM in operation at depths of hundreds of meters and up to one kilometer away using simple off-the-shelf equipment and analysis procedures. The techniques used and developed for these tests are described for the reader who may eventually be interested in searches for TBMs or other continuous sources of seismic noise elsewhere.

INTRODUCTION

The general problem of detecting and locating the source of clandestine tunneling operations has a long and colorful history and has been of strategic importance on a number of occasions. Typical drill and blast tunnelling methods lend themselves quite naturally to all of the sophisticated detection and location techniques developed by the seismological community over the last 70 years. Numbers and types of instruments to deploy, areas to cover, and detection and location algorithms are components that have, and continue to be, exhaustively studied and pursued by earthquake seismologists.

Over the last 10 years, however, continuous tunneling techniques using tunnel boring machines (TBM) have become much more prevalent and, consequently, easier to obtain and implement by concerns with limited resources. As a result, the likelihood of using such sophisticated machinery for clandestine operations has increased and stimulated interest in detection and location capabilities using seismic methods (Greenfield, 1983; Greenfield et al., 1988). In 1985, the Belvoir Research, Development, and Engineering Center (BRDEC) sponsored the U.S. Army Engineers Waterways Experiment Station (WES) to construct a sophisticated computer driven system to detect and locate both impulsive and continuous tunneling activity (Greenfield et al., 1988). While this system was able to detect and locate continuous sources of seismic signals, BRDEC was also interested in determining the feasibility of a simpler approach using less sophisticated instrumentation and analyses and, most importantly, either off-the-shelf or BRDEC equipment.

To evaluate the utility of simple systems in identifying and locating a TBM, a series of tests were designed using MEQ-800 smoked drum recorders and two 8 channel digital event recorders (DSLDD, developed by BRDEC). These systems (MEQs and DSLDDs) are reliable and easy to deploy with output that is relatively simple to interpret and analyze. The tests were designed to address the following issues: 1) detect TBM seismic signatures, 2) discriminate these signatures against a noise background, 3) determine the detection range, and 4) evaluate the accuracy of several methods of source location. The results of such tests

would then provide important information on the usefulness of using MEQs and DSLDs for detection and location of TBM tunneling, provide useful procedural information for the implementation of those or similar systems to other applications, and to demonstrate that simple, reliable, and relatively inexpensive equipment and procedures can be successfully applied to new problems.

Description of the Site and TBM

The site is located at a reservoir project in South Korea, south of Seoul near the town of Juam. Metamorphic rocks typify the local geology which may be characterized as chaotic from the perspective of short wavelength seismic wave propagation. Additionally, the local topography is steep with a regolith of shallow clayey alluvium. The combination of a laterally heterogeneous medium and steep topography along with a shallow soil cover (several to tens of feet) certainly provide for the most challenging conditions for detection and location using seismic methods. The lateral heterogeneities and steep topography scatter wavefields and generate pseudo sources. An alluvium cover that is varying in thickness imparts a randomly varying amplification to seismic waves which can dramatically affect the signal amplitudes, negatively impacting the location accuracy based on signal strength. As a result, the Juam tests probably represent a severe test of the obtainable accuracy in TBM source location.

The TBM was commissioned to drive 6 km of a 8 km long tunnel through hard rock. Drill and blast methods were used from the opposite end to drive about 2 km and meet the TBM. The cutting head has a diameter of 4.5 m with 40 cutters and a 1.4 m stroke. The head rotates at 7.3 RPM. Nominal operation of the TBM runs about 15-20 hrs/day with about 1 1/2 hours per stroke (advance 1.4 m). After each stroke, rock cutting ceases for 20-30 minutes as the TBM repositions itself. These cycles are clearly observable in the recordings and are one of the signatures of typical TBM operations. The nominal driving rate is about 15 m/day through hard rock. Figure 1 (top) shows a plan view of the array of recorders along with the locations of the TBM at the beginning of the tests (6/7/88) and at the end (6/17/88) drawn on a local topo map. The bottom of Figure 1 shows a cross-section of the TBM tunnel and surface topography (courtesy of Dr. Chris Cameron). At the beginning of the tests (6/7/88) the TBM was at a depth of 364 m (76 m elevation) and 3.76 km from the portal.

INSTRUMENTATION

Experiment Design

The TBM was surrounded on the surface by 12 recording sites, occupied at various times during the tests. The idealized design of the array of stations is sketched in Figure 2. The stations were named according to the primary type of instrumentation installed.

Stations numbered one through eight are elements of the T-array, which consists of sites located in a line along the tunnel and two lines at right angles to it, giving it a T-shape. The T-array sites were instrumented with vertical DSLD (Digital Seismic Listening Device) velocity sensors with a corner frequency of 8 Hz. They were spaced a few hundred meters apart and were deployed for analysis of both time-domain and spectral characteristics of the TBM signal.

Sprengnether MEQ-800 recorders using 1 Hz vertical seismometers (Mark Products, L4-C) were used at 7 sites, 5 of which were in a line extending away from the TBM toward the south (stations 1, 7, B2, M3 and M4), one in front of the TBM to the west (DSLD station 2) and one far behind the TBM along the tunnel to the east (station MR1). These portable seismographs record analogue signals on smoked paper for visual analysis of waveforms. The stations extending away from the TBM were deployed to study the attenuation of signal amplitude with distance.

Two very closely-spaced arrays each using the 8 DSLD sensors were sited at stations 2 and B2. These arrays were designed for f-k beamsteering.

The instrumentation used in this experiment is summarized in Figure 3, which shows the actual station locations, having deviated from the idealized design due to rugged terrain and thick brush. Site locations are based on topo maps and are probably accurate to about 50 m.

Huddle Test

The DSLD instruments were tested in the field for uniformity of response by performing a huddle test. In this test, all geophones were installed adjacent to each other in a group (huddled) so they would record the same signal. They were all triggered to record at the same time so their spectral character could be compared relative to each other.

The Fourier amplitude spectra from recordings of the TBM signal at 256 samples/sec from all eight channels are shown in Figure 4. They have been smoothed with a 2 Hz triangular-weighted window and are plotted for frequencies above the instrument corner at 8 Hz. Seven out of the eight channels have spectra which are similar in character, following the same peaks and troughs out to about 60 Hz where they begin to show higher variability. Channel 6 was the outlier, with response above the others and seemed to have a problem with its gain level. This geophone/amplifier combination was replaced with another before the DSLD package was used.

MEQ-800 ANALYSES

Signal Identification

Seven sites were occupied by MEQ-800 instruments for recording at different times. Figure 5 is an example of a smoked drum record taken at site 1 (closest to the TBM) to show the character of the TBM signal. The predominant frequency is around 30 Hz, based on spectral analyses of the digital data shown in a later section. Some of the background noise is marked at the top of the figure and can be seen to be quite low and barely visible. The startup and shutdown cycles of the TBM are also pointed out. It starts up slowly and gradually, taking about a minute to gain full operation, whereas the signal stops more abruptly upon shutdown. While the machine is cutting rock, the signal is of fairly constant amplitude and is much larger than the background noise. The machine stops after each stroke (1.4 m) to be moved forward in the tunnel, after which it starts up again. This is a distinctive feature of the TBM signal and helps in its identification. This can be verified in Figure 5 where 15 hours are recorded, and 10 starts and stops occurred in that time period. One can see from this record that a few hours of recording with an MEQ would be sufficient to detect the TBM. Similar records were obtained at the other sites, and the signal could easily be distinguished from the noise at the farthest site (station M4) which is over one kilometer away.

Signal Attenuation with Distance

Five of the MEQ-800 seismographs were positioned to extend on a line away from the TBM source and were used in an analysis of the attenuation of wave amplitudes with distance from the TBM.

The records were inspected and an average peak-to-peak amplitude estimated by eye, which was converted to units of microns/sec. The amplitudes are displayed at their recording locations on Figure 6, where the MEQ-800 stations are marked with solid triangles. The recording at Station 2 to the west of the TBM has an anomalously low amplitude compared with an equal distance to the south. The five stations used for the attenuation analysis (Stations 1, 7, B2, M3, and M4) recorded amplitudes that decrease with distance continuously. The two crosses on Figure 6 indicate the positions of the TBM at the start and end of the total

recording experiment. The MEQ recordings were made during the middle of the time period, so distances from the sites were measured to the central point between the two TBM positions.

An estimate of the far-field amplitude (A) adjusted for geometrical spreading and neglecting intrinsic and scattering losses is given by

$$A = A_0 R^{-\alpha}$$

where R is the epicentral distance, A_0 is a constant, and the exponent α equals 1 for body waves and 1/2 for surface waves. These attenuation curves for body- and surface-waves are plotted as dashed lines in Figure 7, along with the amplitudes recorded which are represented by squares. The dotted lines are the estimated maximum and minimum noise levels on the recordings. The attenuation curves were constrained to pass through the closest amplitude recorded, at 75 m epicentral distance (to determine A_0). The body-wave curve fits the data quite well, whereas the surface-wave curve predicts much higher amplitudes. The recordings, being from a continuous source are most likely a combination of both surface and body waves, and probably contain local mode conversions but the geometrical attenuation of body waves seems to be the dominant mechanism of amplitude decay in this limited data set. Perhaps damping reduces the secondary scattered wavefields leaving the direct body waves (compressional and shear) as the primary components at these distances (tens of meters to about 1 km). While many more observations would be needed to properly constrain an attenuation relation, these results suggest that the TBM would be detectable on visible records out to distances of over 1 km, depending upon ambient noise conditions.

T-ARRAY ANALYSES

One TBM event and one background-noise event were selected from the digitally-recorded tapes of the T-array. These were analyzed for temporal and frequency characteristics of the TBM signature over the area covered by the array. The signal was sampled at 1024 samples/sec, and the manually-triggered events were 4 seconds long.

Time Series

The time series from all eight stations of the TBM and background-noise events are shown in Figure 8. From each of these plots, the average peak-to-peak amplitude in counts was estimated by eye. The MEQ amplitudes were combined with these T-array amplitudes by scaling the MEQ amplitudes using the two sites which recorded both on an MEQ and a DSLD. This combination extended the data set to the south and the values were contoured on a map, seen in Figure 9. The two crosses on the map are the positions of the TBM at the start and end of this experiment, and these recordings were made in approximately the middle of that time period. The distance from the center of the two TBM positions to the peak of the amplitude contours is about 80 m, with the peak to the east of the TBM. Given these station locations relative to the TBM, a fairly good location has been produced by using the temporal amplitudes.

A similar plot of the contoured noise amplitudes can be seen in Figure 10. No MEQ noise amplitudes were used. The background noise amplitudes do not bear much resemblance to the TBM signal amplitudes. The smoothed elevations are contoured in Figure 11. It is interesting that the hill at Station 6 and the valley at Station B2 both correlate with anomalously high TBM amplitudes, which suggests that there may be some topographic effects. This is not seen, however, in the noise amplitudes.

Spectra

Fourier amplitude spectra were computed for each of the time series in Figure 8, using a standard FFT algorithm and 5% cosine tapers at the beginning and end of each time series. The resulting spectra were smoothed over a 5 Hz triangular window and are shown in Figure 12 with the solid curves for the TBM

spectra and the dashed curves for the background noise.

The TBM spectra encounter the noise spectral levels on most channels beyond 50 Hz, with the minimum at 40 Hz on Channel 6. All TBM spectra have the dominant spectral peak at 33-35 Hz, which is not seen in most of the noise spectra. Channel 1 is the closest site to the TBM and thus the spectrum it produced is most representative of the TBM source. It contains the highest peak at 33 Hz, and other distinct peaks at 50, 75 and 115 Hz. These frequencies, especially at 33 and 50 Hz, seem to be characteristic of the source, and the f-k analysis in the following section supports this.

The spectral power at the largest peak (near 33 Hz) in each of the smoothed TBM spectra was contoured on a map, seen in Figure 13. The contour pattern is quite similar to that of the time-domain amplitudes (Figure 9) and the peak lies eastward of the TBM by about 125 m. The spectral power at 50 Hz was also contoured because that frequency produced the best results in the f-k beamsteer analysis (next section). Its power contours are very similar to the those of 33 Hz peaks.

BEAM ARRAY ANALYSES

Two small arrays recorded the seismic waves from the TBM. Beam 1 Array was located about 240 m west of the position of the TBM along the direction the tunnel was progressing (Station 2, Figure 3). Beam 2 Array was positioned to the southeast of the TBM at a distance of 555 m (Station B2, Figure 3). The arrays each consisted of eight closely- and randomly-spaced vertical DSLD geophones, with average separations of 4-5 m apart and not greater than 8 m. The positions of individual elements in each array are shown in Figure 14. The arrays were manually triggered to record a number of "events", including signal and TBM background noise samples. Recordings were made with a sampling rate of 245 samples/sec with record lengths of 16 seconds.

Methodology

Frequency-wavenumber (f-k) analysis is a method used on recordings from arrays to decompose the incident wavefield into a monochromatic plane wave with a propagation velocity in the horizontal plane (apparent velocity) and an azimuth of approach to the array. This is calculated separately for each frequency of interest, and the process is called beamsteering. The method has been described in detail in Capon (1973). The conventional method of estimation was used in this study.

Procedure and Results

For each of the Beam arrays, two events were chosen for analysis; one a recording of the TBM signal, the other background noise. The Fourier amplitude spectrum was calculated from each time series of 4096 points using a standard FFT algorithm with a 5% cosine taper at the beginning and end. The eight spectra were then averaged together for inspection. The averaged TBM and noise spectra thus obtained are presented in Figure 15. The spectra of the averaged noise in the plot have been multiplied by a factor of 5 and all spectra were smoothed with a triangular-weighted 1 Hz window for visual clarity. The gains at the two arrays were different, with Beam 1 instruments set at 85 dB and Beam 2 at 75 dB, so the averaged spectrum for the TBM recorded at Beam 1 was adjusted to 75 dB gain for direct comparison with the spectrum from Beam 2.

The averaged TBM spectra from the two arrays are similar in general characteristics, both containing many peaks and troughs and generally jagged appearances. The frequencies at which these peaks occur, however, are quite different in the two spectra. The Beam 1 spectrum has its largest peak out at 63 Hz, whereas the Beam 2 spectrum has very little energy at such high frequencies. They both have a large peak at around 20 Hz and around 50 Hz. Because of the diversity of spectral content between the two spectra, the

frequencies used in the f-k beamsters were selected by inspection of each average spectrum separately.

A 1-Hz window was utilized in the beamsters around each frequency, coinciding with the 1-Hz smoothing window used on the plots of average spectra from which frequency peaks for steering were chosen. The entire time series were used (4096 points), as we found this to produce better results than shorter time windows, presumably because the stationarity of the signal is improved in the longer record.

Initially, we chose the dominant peaks in the TBM average spectra for beamsteering on the assumption that the frequencies with the highest signal-to-noise ratio and the most power would be most representative of the source and produce the best steers. The results of these beamsters indicated that the source signal was not necessarily contained in the highest peaks, as explained later. Table 1 lists all the f-k analyses performed, with resulting azimuth and apparent velocity of the plane-wave fit to the wavefield. Also listed are the degrees away from the true direction of each result. The true direction from Beam 1 is 84° and from Beam 2 it is 330° azimuth, measured clockwise from north.

Figures 16 and 17 summarize the results of all beamsters for arrays Beam 1 and Beam 2, respectively. The frequencies chosen for analysis are indicated on the average spectra by arrows in the lower half of the figures, and their corresponding azimuths in the upper part of the figure, in degrees from the true direction. Points which fall on the center line are the best steers. It is evident that the size of the peak is not necessarily a good indicator of source frequency in this example, perhaps because the complex local geology is such that the waves are highly scattered by topography and weathered rocks near the surface. The farthest array, Beam 2, seems to do a better job of locating the proper direction of the source than Beam 1, especially at higher frequencies. This is expected, as the f-k method gives only horizontal direction and the Beam 1 Array epicentral distance is smaller than the depth of the tunnel, so the waves are coming up at a steep angle, making the steers less robust. Nevertheless, three frequencies in the Beam 1 spectrum did point toward the source.

To pinpoint the location of the TBM, both arrays must be used to provide an intersection of the two vectors from them at the azimuths in the beamster solutions and at the same or similar frequencies. Table 2 lists all combinations of frequencies and steers attempted and the distance of each vector intersection from the actual TBM. Many of the vectors did not intersect at all, as indicated in the table by an asterisk. The six best solutions are plotted in Figure 18. Each plot in Figure 18 lists the frequencies used at each array (B1 and B2) and the distance (r) from the TBM position at the time of recording (left cross). The best location of the source was found at 50 Hz, which puts it only 40 m away (Figure 18-E). The second-best steer combination was at 33.5 Hz, with a distance of 75 m (Figure 18-C). Both put the source to the southwest of its actual position. The f-k plots of contoured power for these two frequencies can be seen in Figure 19. The frequency used for the steer in Figure 18-A, which has an intersection at 245 m from the source, did not have a peak on the Beam 1 spectrum. The peak on the Beam 2 spectrum was so outstanding that a run was computed for the same frequency in the Beam 1 data as a test. The results are not ideal, but better than many others.

Figure 20 shows the spectra and beamster angles for both arrays together. The letter of each plot in Figure 18 is marked above the spectra in Figure 20 to point out which frequencies were used. A closer inspection reveals that the two best steers were at frequencies which had the same exact peak at both arrays, 50 and 33.5 Hz. No other peaks line up between the two spectra. Though some peaks steer toward the source from one of the arrays but not the other, the only frequencies that steer well from both arrays, thus giving a good solution where their vectors intersect, are those whose peaks are at the same frequency in both spectra. At 50 Hz, both spectra have high power, but certainly it does not stand out. At 33.5 Hz, Beam 1 has a large peak but the peak at Beam 2 is small. All 16 spectra, from both arrays, were averaged and plotted in Figure 21. The arrows point toward the best two steers. By averaging both arrays' spectra together, the peaks which are out of phase or existing in the spectra of only one array tend to decrease, and the aligning

peaks stand out more. Here it is seen that the 50-Hz peak, which steers the best, is more prominent. The highest energy is still in the 20-Hz range, and this does not do a good job of steering.

Also on Figure 21 is the noise averaged over the 16 spectra. The spectrum of background noise at a site often reveals the particular site response from topographic effects and resonance in soils or weathered rock. The microtremors will be amplified by the site geology in much the same way a stronger source would. The average noise spectrum at these sites has most of its energy in the frequency band of 10-28 Hz, which indicates that the TBM wavefield may also be amplified by the site in this band. A site resonance is not likely to produce a good plane-wave fit and steer well, because the waves are not coming directly from the source but instead are being trapped and reverberating in the soil column. If one were to judgementslly reduce the amplification of the spectrum in Figure 21 according to the amplitude of the noise, the spectrum would retain high levels in only the frequency bands of 28-35, 45-55 and 60-65 Hz. If one then steered at the five biggest frequency peaks left, at 30, 33.5, 48, 50 and 63 Hz, two of them would give good results, and the direct TBM source is fairly well represented in the averaged spectrum.

The 50 Hz signal at Beam 1 has an apparent velocity across the array of 10 km/sec (Table 1, Figure 19). This is the largest apparent velocity seen in any of the f-k runs and indicates that the plane wave is arriving at a very steep angle. We interpret this wave to be a body wave which came directly upward from the TBM source. As mentioned above, the epicentral distance of 240 m is smaller than the depth, which is 374 m plus the difference in elevation, making the elevation difference between the TBM and the Beam 1 Array 404 m. A simple exercise predicts the depth of the tunnel quite well using this 50 Hz wave. The angle of incidence (i) from vertical can estimated from

$$\sin i = \frac{V_p}{V_a}$$

Using a V_a (apparent velocity) of 10 km/sec and a V_p (P-wave velocity) of 5.0 km/sec (an average value for shallow granitic and metamorphic rocks in South Korea), the angle of incidence is 30 and therefore the angle from horizontal is 60°. The depth (z) is then calculated from geometry to be 416 m, which supports the idea that the steep 50 Hz wave is a P-wave directly from the source. The 33.5 Hz wave is of higher apparent velocity than most others, but is coming in at a much more horizontal angle and much slower than the 50-Hz wave.

Statistics

The 90% confidence interval for the conventional estimate of power (Capon and Goodman, 1970; Capon, 1971) is approximately equal to

$$\pm \frac{20}{(4M + 1)^{1/2}}$$

where M is the number of frequency points used in the frequency window for steering. In the 1 Hz windows we used, $M = 8$ and the 90% confidence is at ± 3.5 dB. On the f-k plots the innermost curve surrounding the peak power is at a level of 1 dB down from the peak, the second curve out is 2 dB down, and so on. The 90% confidence is therefore between the third and fourth contours, which encloses quite a large area on all the plots, and these statistics assert that we are 90% confident that the plane wave azimuth and slowness is within that boundary. If this were used as an indicator of how good the solutions are, they would seem quite poor, especially in some cases where the 3.5 dB contour completely encompasses the origin, or has 360° of possible azimuth. Despite these statistics, the azimuth of the peak itself has been proven in many uses to be accurate and the good beamsteers in this study support this.

CONCLUSIONS

The Juam TBM tests clearly demonstrated the usefulness of simple equipment and analysis procedures to detect and locate a source of continuous seismic noise. Both DSLD digital event recorders and MEQ-800 smoked drum recorders represent standard off-the-shelf instrumentation. The location techniques evaluated included time and frequency domain amplitudes as well as conventional beamsteering.

Signal Identification

Based on the observations and calculations made in this report, a previously unknown TBM signal should be easily recognizable both from time series and Fourier amplitude spectra. The spectra calculated from the known TBM all exhibit a characteristic peak at 33-35 Hz, even out to the distance of the farthest site, which was about 900 m away. The closest site (Station 1) recorded the best and most characteristic signal of the TBM, with spectral peaks not only at 33 Hz, but also at 50, 75 and 115 Hz (see Figure 12).

The time series provide an even easier and quicker identification of the signal. Smoked drum MEQ recordings over a few hours of TBM operation are sufficient to see the wave train which is characteristic of the TBM and the starts and stops of normal operation. The records can be analyzed immediately in the field, and therefore the use of these or similar portable analogue instruments is considered the easiest and most cost-effective method for identification. As seen in Figure 7, the MEQ records from this study had good signal-to-noise ratios out to over 1 km distance.

Source Location

Three techniques were tested for their ability to locate the known position of a TBM: time-series amplitudes, power-spectral amplitudes, and f-k beamsteering. The beamsteering analyses gave the best results; the location of the source using the 50 Hz steer was only 40 m from the true TBM's surface projection, and at 33.5 Hz it was 75 m away. Contours of the time-series average amplitudes placed the peak 80 m from the source, and the spectral power contoured peak at 125 m from it. The three solutions are summarized in Figure 22.

The beamsteer f-k analysis requires considerable time, technique, and skilled personnel. The time-series amplitudes, by comparison, are easy to measure, and simple analyses in the field may be sufficient for source location. Furthermore, based on our results, the location could probably be accomplished within a few days by one person and a single portable instrument, once the signal has been detected.

One may argue that the contour plot of time-series amplitudes depends entirely on the Station 1 record because it is the closest site and has the largest amplitudes, forcing the peak to be close by. If the stations were positioned around the TBM but none right over it, their contoured amplitudes would have looked like Figure 23 where we plotted the same amplitudes, omitting the Station 1 value. The general area of the signal would have been identified, and the next step would be to fill in the area where data are missing with more data points. One would notice the two peaks where the amplitudes are greatest and occupy sites around these, including the region where the actual source is. We believe this technique would quickly pin down the TBM location.

ACKNOWLEDGEMENTS

This work was supported by the U.S. Army Fort Belvoir Research, Development, and Engineering Center. The supervision of Ray Dennis is gratefully acknowledged. The authors express gratitude to field support provided by UNC Geotech under the direction of Dave MacLean. Special thanks to Susan Knutson and Bill Nelson for tireless field assistance under difficult conditions.

REFERENCES

Capon, J. (1973). "Signal processing and frequency-wavenumber spectrum analysis for a large aperture seismic array." Sponsored by Advanced Research Projects Agency of the Department of Defense, B. Alder, S. Fernbach, and M. Rotenberg, ed., Geophysics, vol. 13, Academic Press.

Greenfield, R.J., Ballard Jr., R.F., Sykora, D.W., Koester, J.P., Reed, B.E., and Savage Jr., M.B. (1988). "Development of a passive-seismic location system for detection of tunneling activities." Third Tech. Symp. on Tunnel Detection Proceedings, Belvoir Research, Development & Engineering Center.

Greenfield, R.J. (1983). "Seismic analysis of tunnel boring machine signals at Kerckhoff tunnel." U.S. Army Engineer Waterways Experiment Station, Vicksburg, MS., Misc. Paper GL-83-19.

Table 1. Summary of Beamsteers

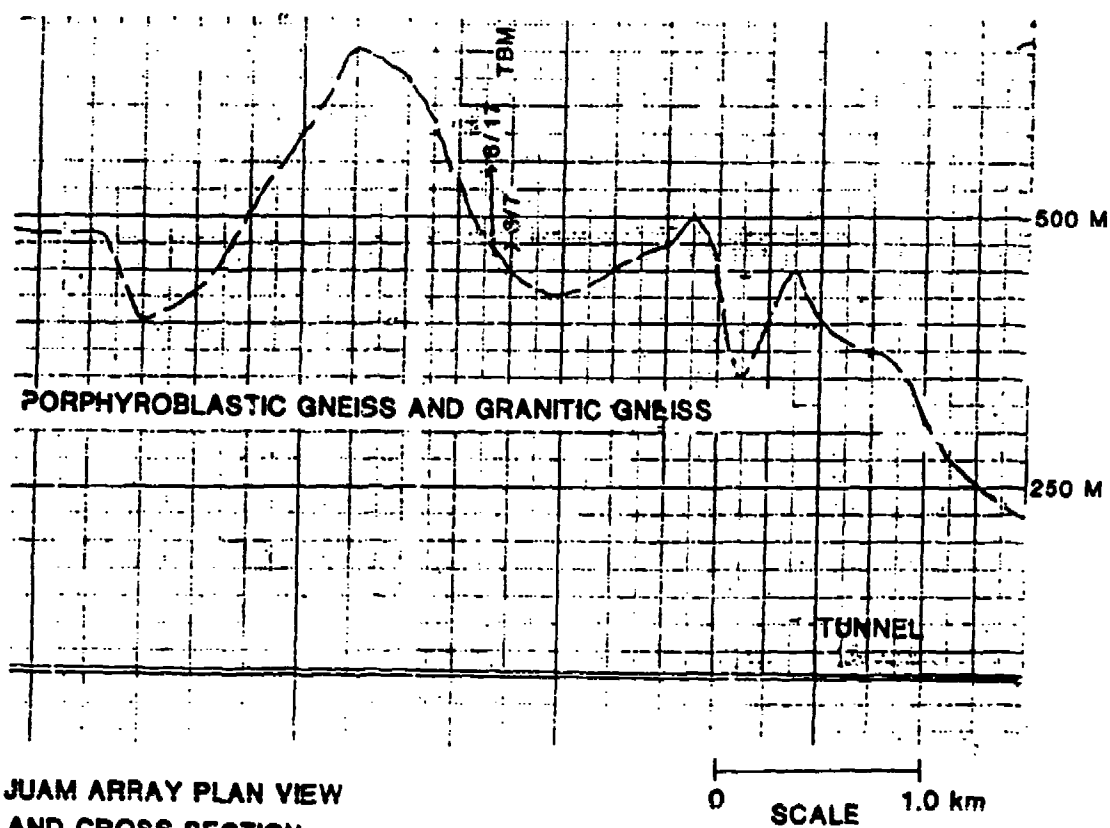
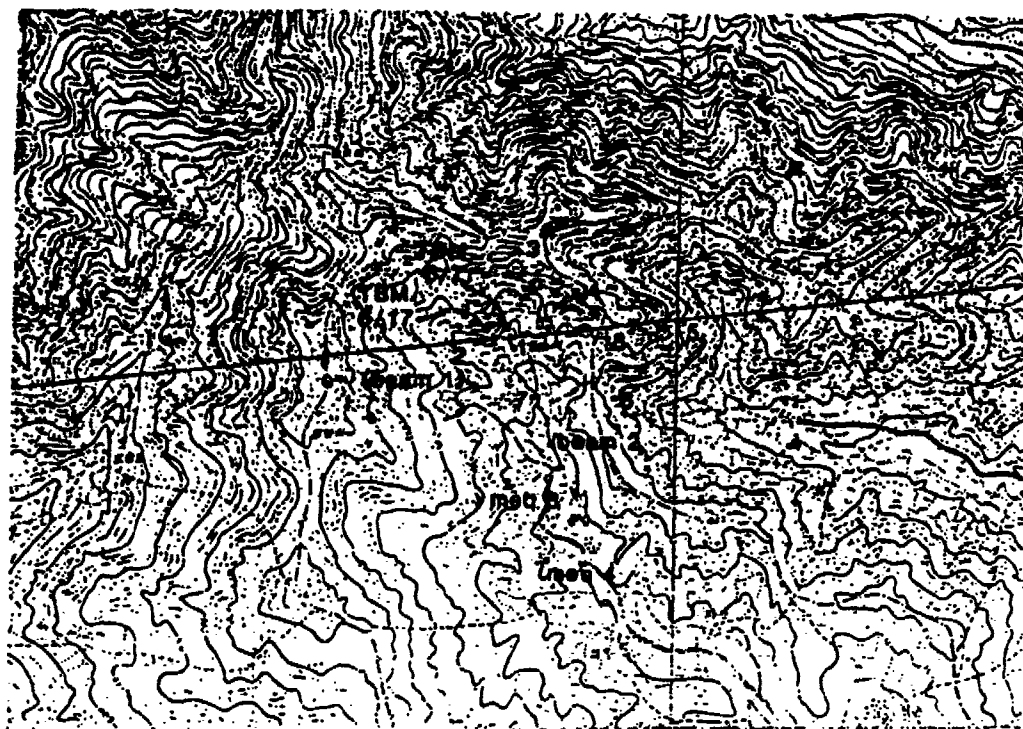
Array	Freq (Hz)	Azimuth (deg)	Peak (cnts-sec)	Va* (km/sec)	$\Delta\Phi$ (deg from true)
Beam 1	20.17	90	10951	10.0	4
	23.17	14	29478	1.2	-70
	28.25	243	17607	2.2	-101
	30.50	336	13989	0.4	-108
	33.50	79	21921	2.0	-5
	47.67	18	9564	3.2	-66
	50.00	90	13857	10.0	4
	51.83	270	11473	10.0	-176
	56.17	0	9815	10.0	-84
	63.00	18	36207	3.2	-66
	65.33	34	19219	2.8	-50
	67.50	27	20150	4.5	-57
Beam 2	20.17	354	3725	1.0	24
	25.00	134	893	0.4	164
	28.33	121	651	0.6	151
	30.00	297	955	0.4	-33
	33.50	324	326	1.2	-6
	39.67	309	1067	1.6	-21
	48.17	326	1400	2.8	-4
	50.00	326	1495	2.8	-4
	51.00	304	1682	2.8	-26
	58.67	330	567	1.2	0

*Apparent velocity.

Table 2. Beamsteering Pairs

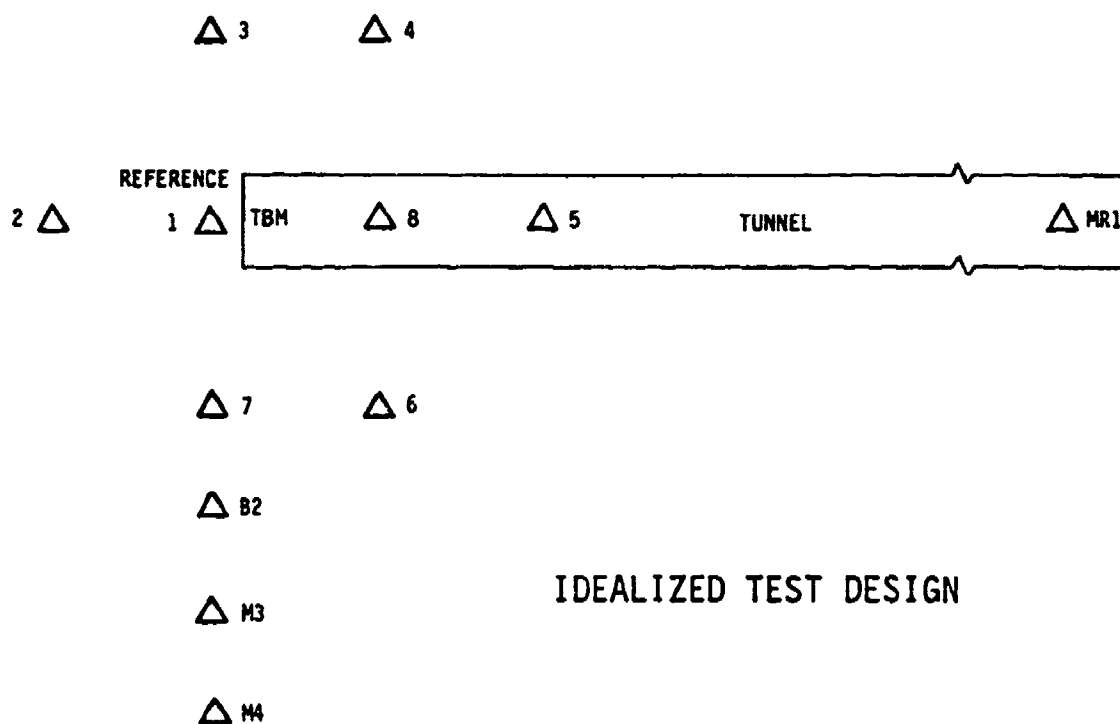
Array	Freq (Hz)	$\Delta\Phi(\text{deg})$	r (m)
Beam 1	20.17	4	245
Beam 2	20.17	24	
Beam 1	23.17	-70	1200
Beam 2	20.17	24	
Beam 1	23.17	-70	*
Beam 2	25.00	164	
Beam 1	28.25	-101	*
Beam 2	28.33	151	
Beam 1	30.50	-108	*
Beam 2	30.00	-33	
Beam 1	33.50	-5	*
Beam 2	28.33	151	
Beam 1	33.50	-5	*
Beam 2	30.00	-33	
Beam 1	33.50	-5	75
Beam 2	33.50	-6	
Beam 1	47.67	-66	215
Beam 2	48.17	-4	
Beam 1	50.00	4	40
Beam 2	50.00	-4	
Beam 1	51.83	-176	*
Beam 2	50.00	-4	
Beam 1	51.83	-176	*
Beam 2	51.00	-26	
Beam 1	56.17	-84	1375
Beam 2	55.25	11	
Beam 1	56.17	-84	405
Beam 2	58.67	0	

*Vectors do not intersect.



**JUAM ARRAY PLAN VIEW
AND CROSS SECTION**

Figure 1. Plan view of Juam TBM locations at beginning (6/7/88) and end (6/17/88) of the tests (top) and cross section showing topography and trace of tunnel (bottom).



IDEALIZED TEST DESIGN

Figure 2. Plan view of idealized station deployment. Sites 1-8 are distributed to examine time domain and power spectra characteristics while sites B2, M3, M4, and MR1 are primarily to study the attenuation of average amplitudes with distance.

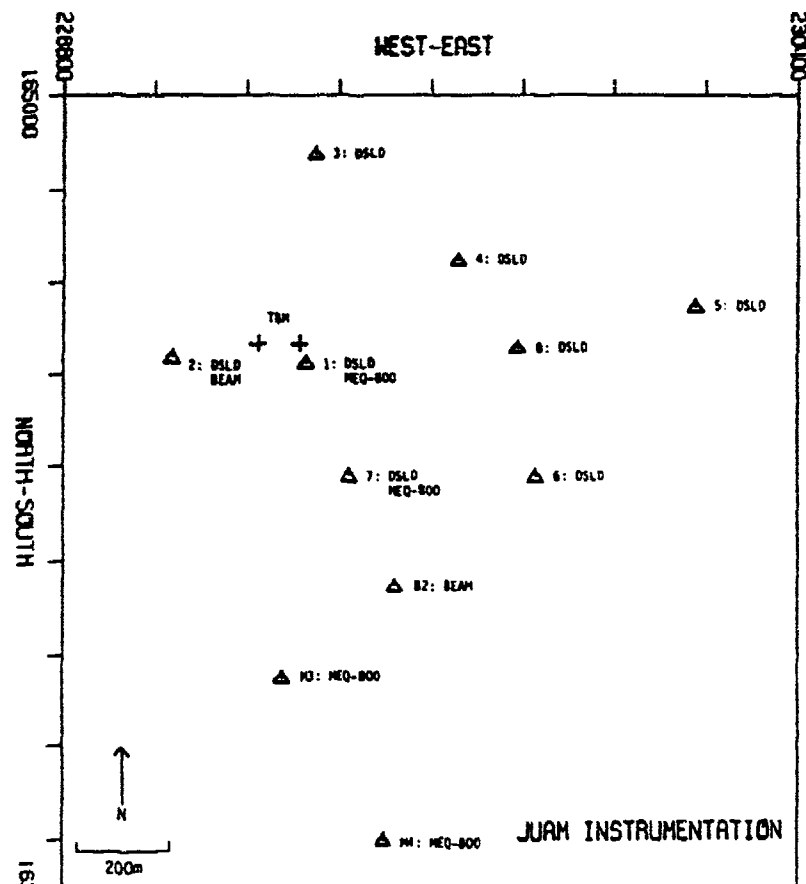


Figure 3. Plan view of actual site deployment. Local topography and thick brush necessitated some departures from the idealized distributions. Site locations are based on topo maps and are accurate to about 50 m.

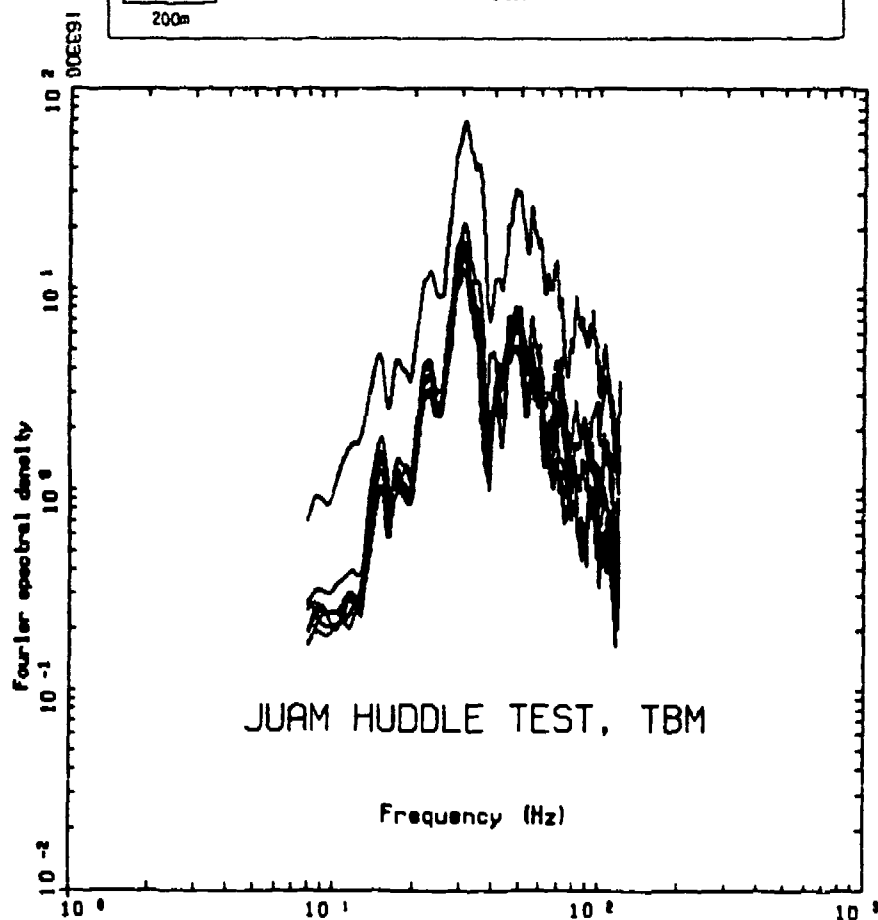


Figure 4. Plots of Fourier amplitude spectra from huddle test of the DSLD instruments using the TBM as a signal source. Location is at site 1, the closest site to the TBM. One sensor/amplifier set appears to have anomalously high gain and was replaced.

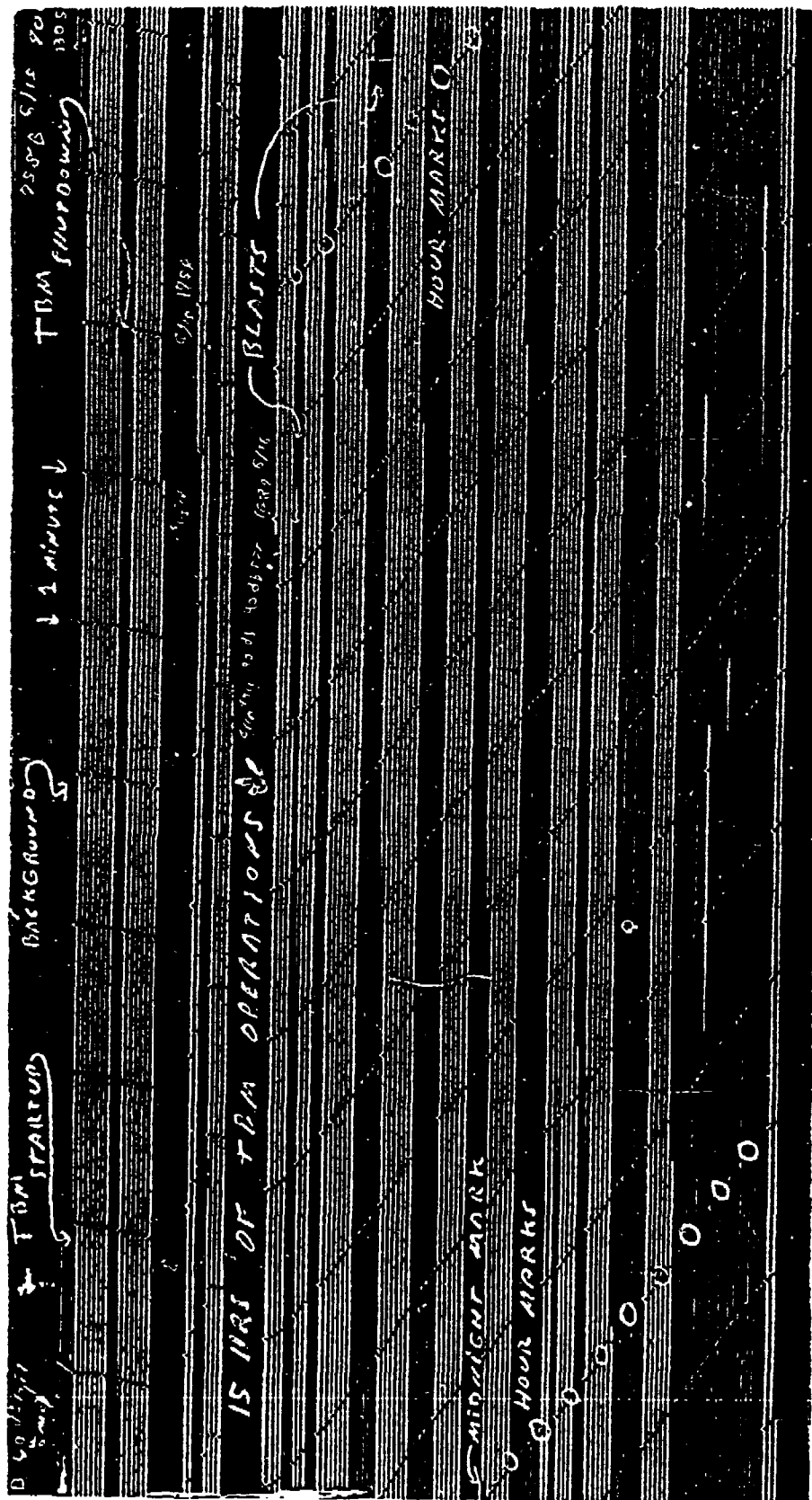


Figure 5. Example of MEQ-800 smoked drum recording of the TBM signal at site 1. The record is approximately 24 hours long and shows a block of about 15 hours of operation with typical starts and stops. Background noise is the barely visible light trace. Two blasts from the drill and blast excavation at the other portal were also recorded.

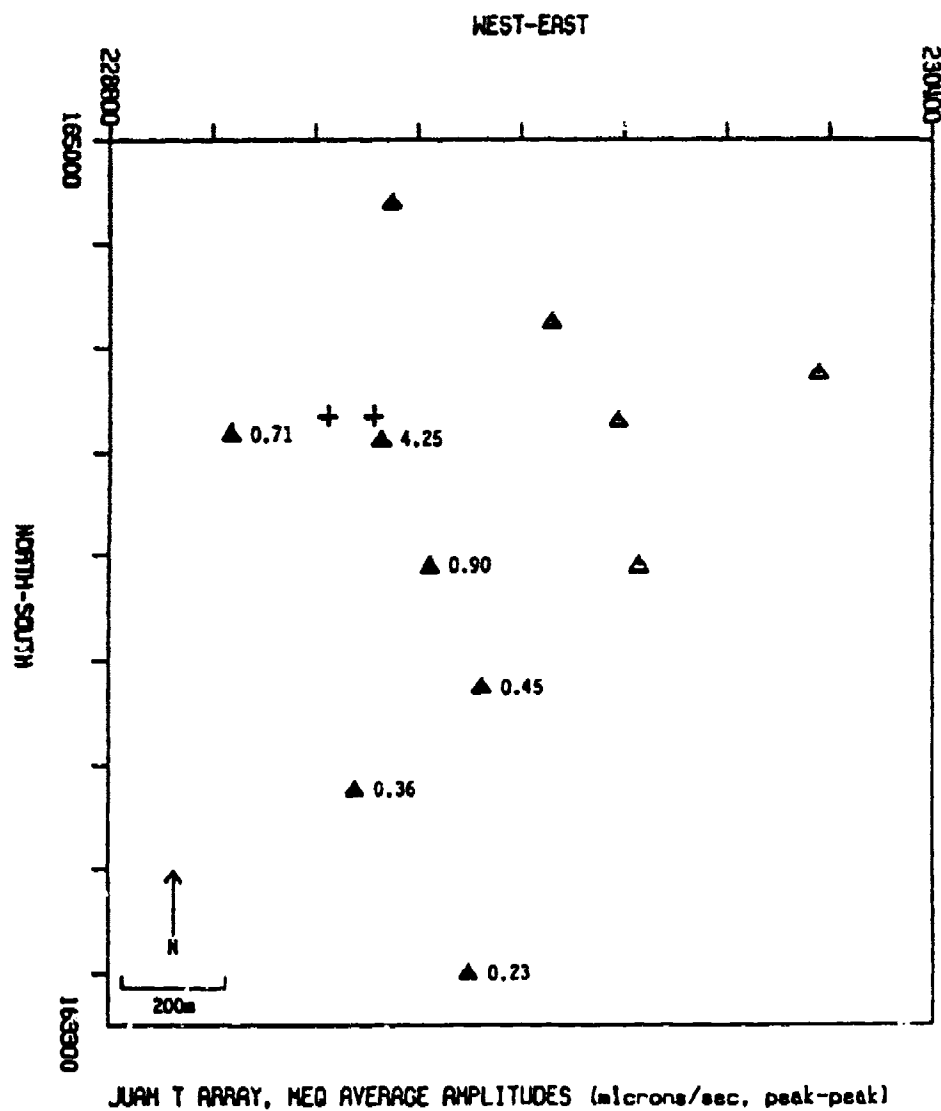
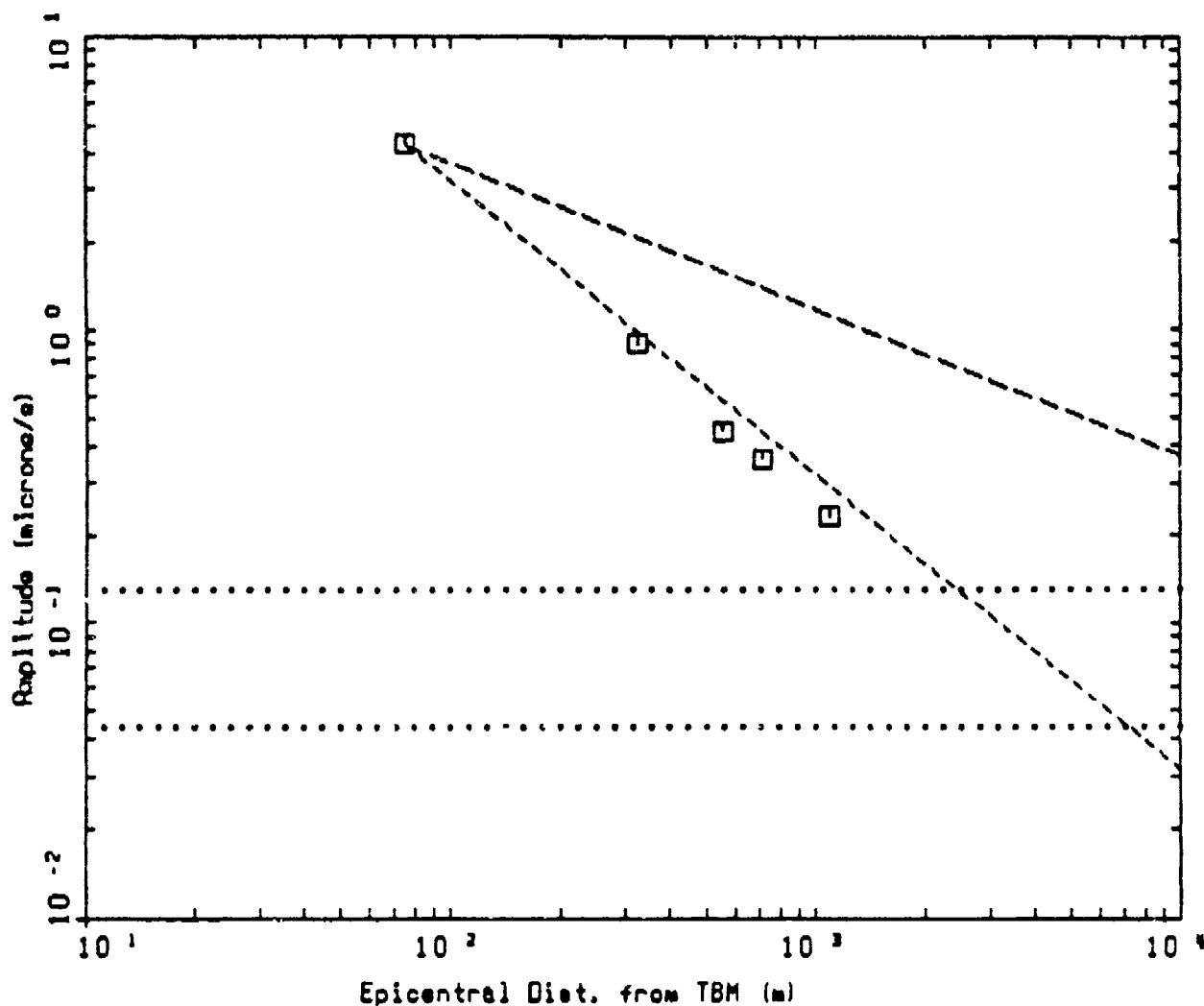


Figure 6. Plot of average MEQ amplitudes along the south limb showing the attenuation of signal with distance.



JUAM TBM ATTENUATION GEOMETRICAL

- LEGEND
- MEQ AVERAGE AMPLITUDES (peak-peak)
 - MEQ MAXIMUM NOISE LEVEL (peak-peak)
 - MEQ MINIMUM NOISE LEVEL (peak-peak)
 - BODY-WAVE ATTENUATION (1/R)
 - SURFACE-WAVE ATTENUATION (1/SQRT (R))

Figure 7. Plot of average peak-to-peak MEQ amplitudes with distance (squares). Straight dashed lines represent $1/R$ and $1/\sqrt{R}$ geometrical attenuation with $1/R$ falling off more rapidly with distance. Horizontal lines represent maximum and minimum average peak-to-peak noise levels.

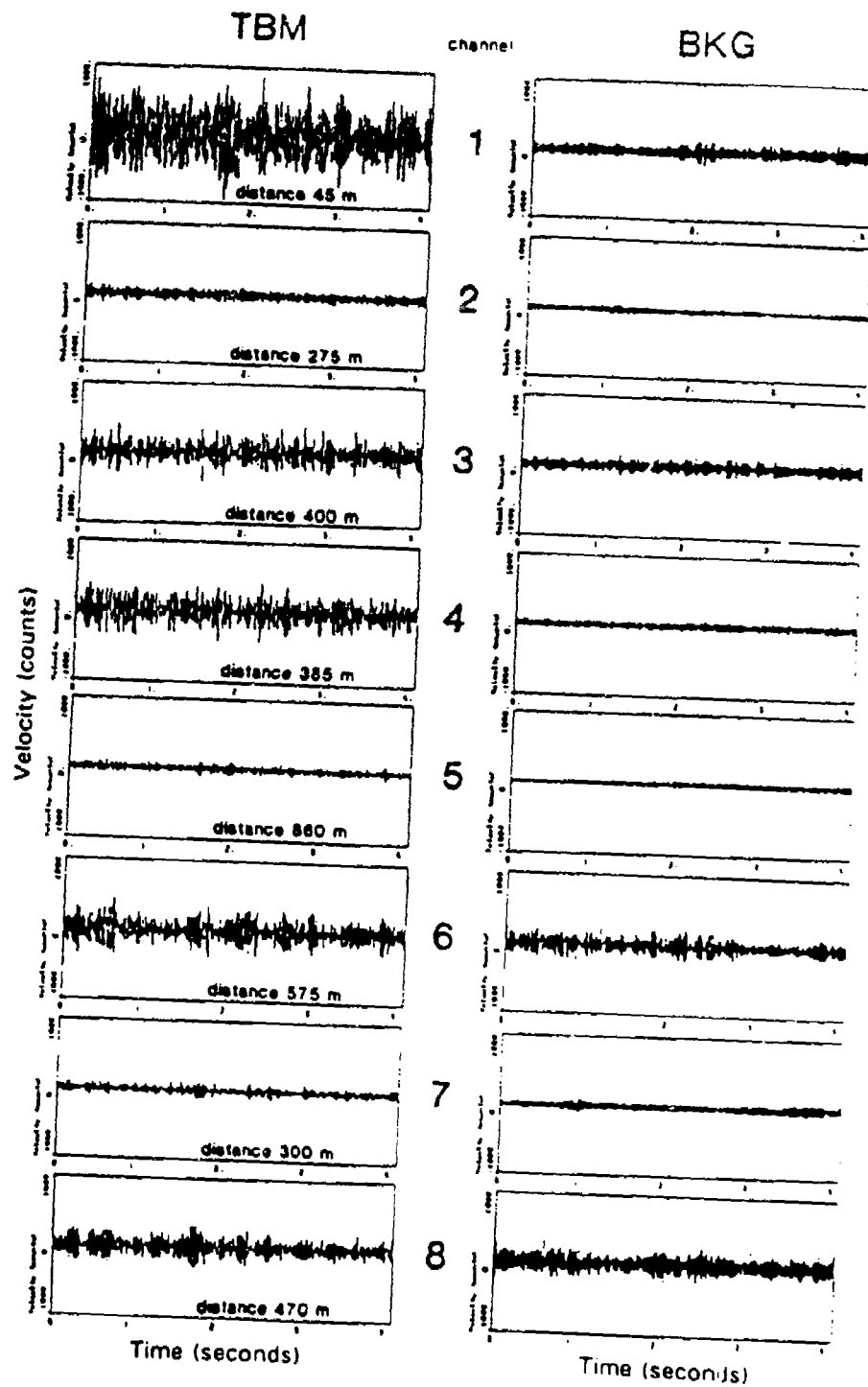
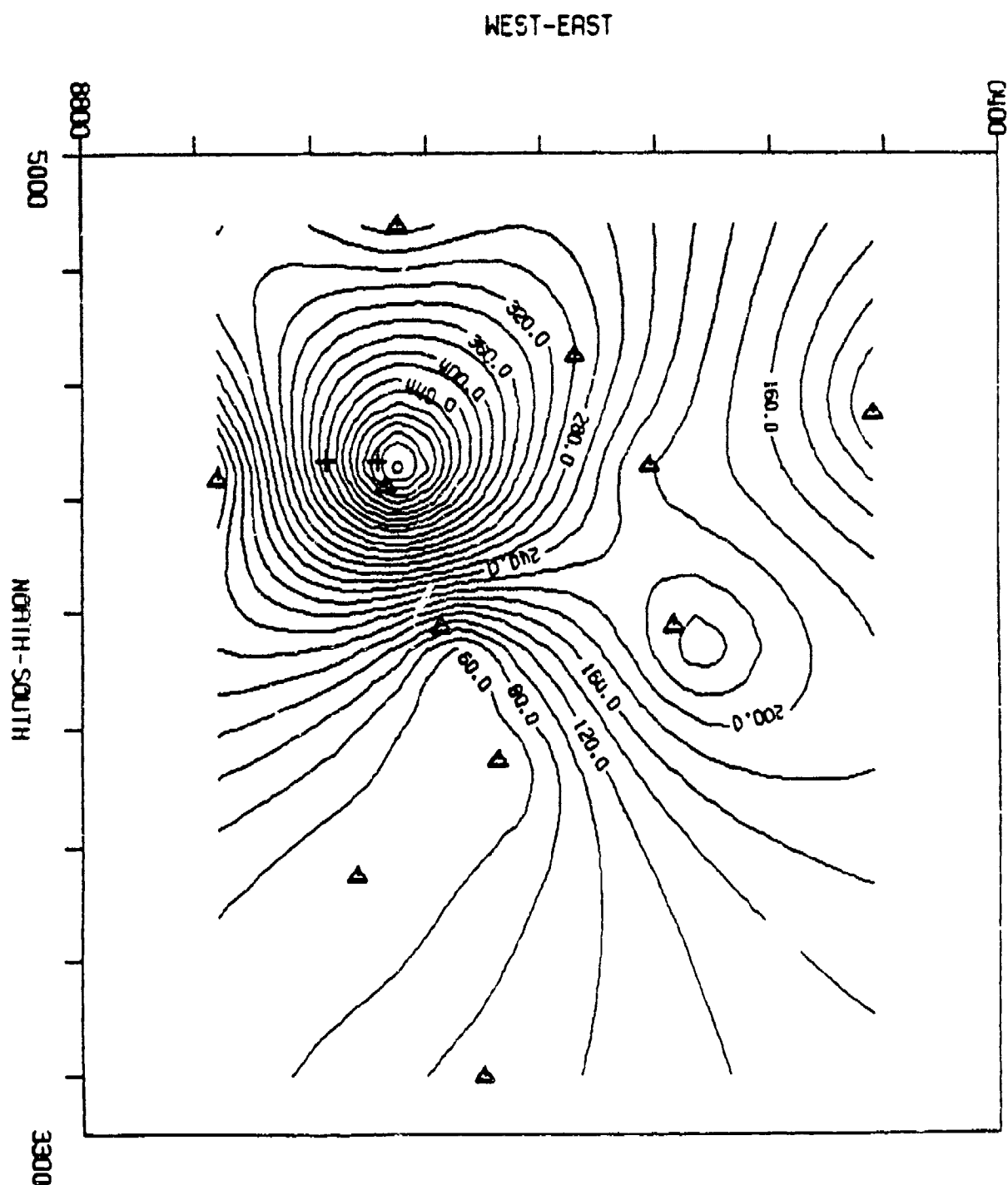
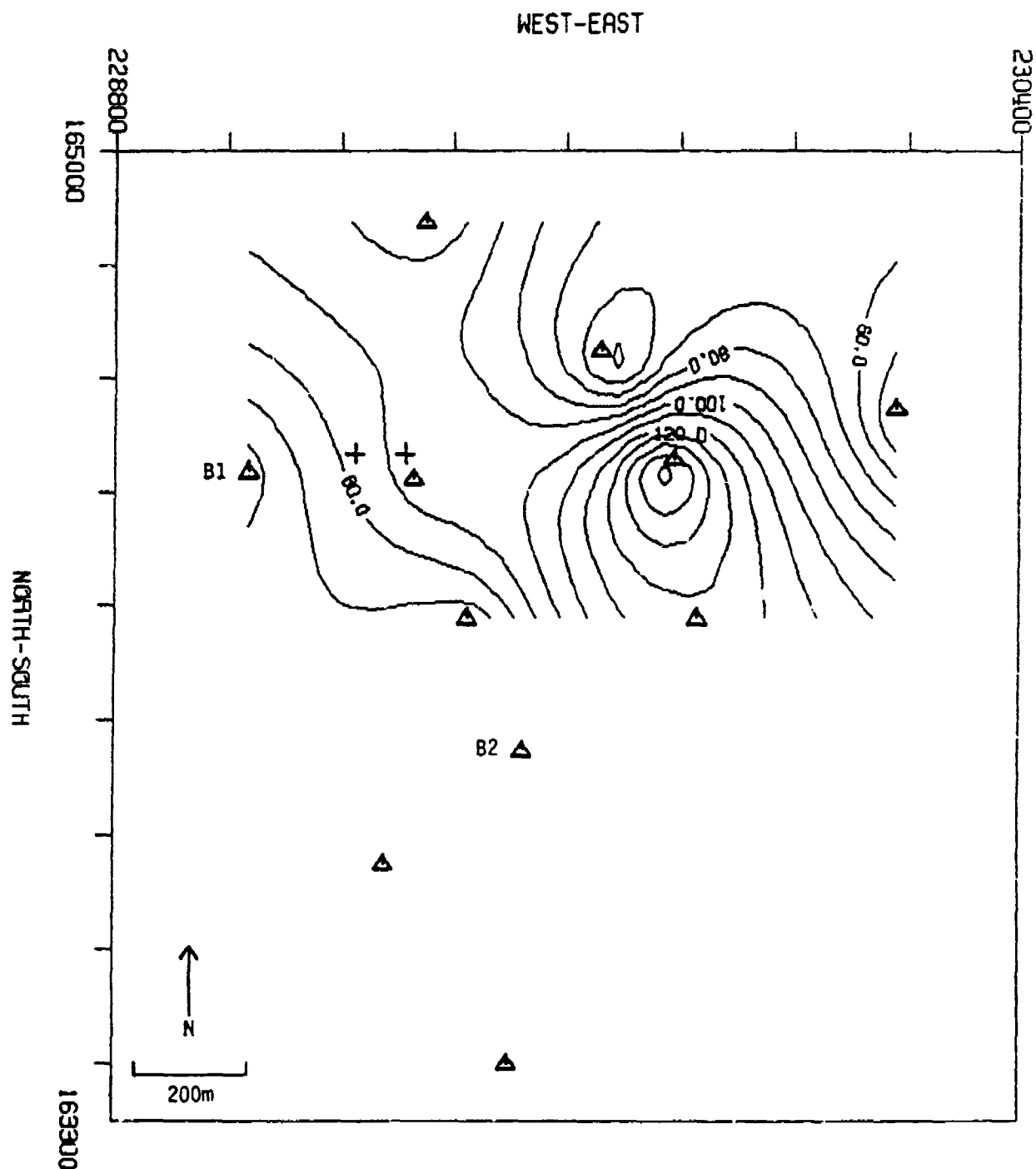


Figure 8. Plot of TBM signal (left) and background noise (right) recorded by the DSLD instruments at sites 1-8 (channel 1-8).



JUAM T ARRAY, AVERAGE TBM AMPLITUDE (Counts)

Figure 9. Contour plot of average amplitudes of the TBM signal recorded by both the DSLD and MEQ-800 instruments. The two crosses represent the starting (right) and final (left) position of the TBM.



JUAN T ARRAY, NOISE AMPLITUDE (Counts)

Figure 10. Contour plot of average amplitudes of background noise recorded by the DSLD instruments. The MEQ-800 data were not added since the background recordings were not done at exactly the same time.

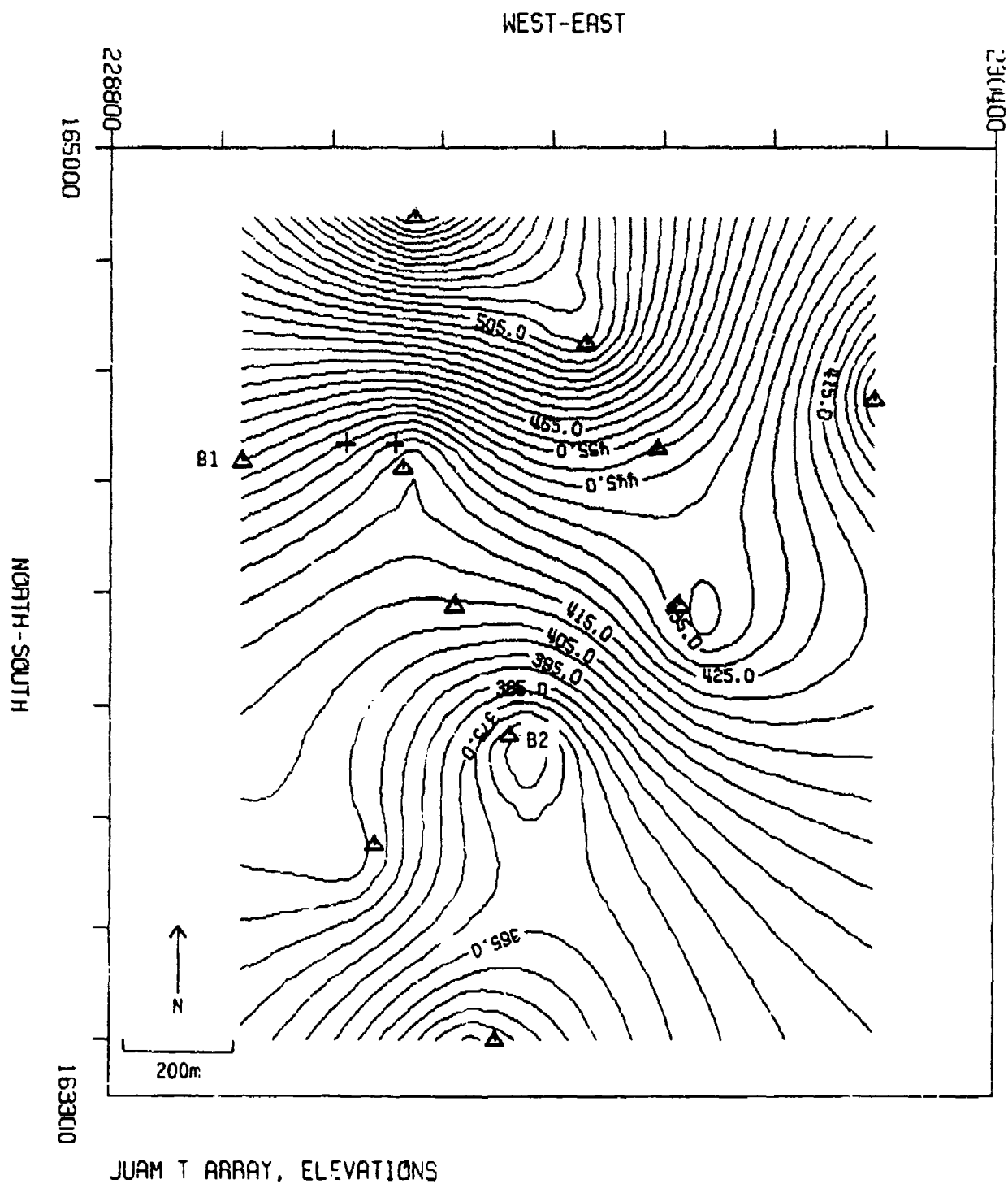


Figure 11. Contour plot of smoothed elevations of the site area.

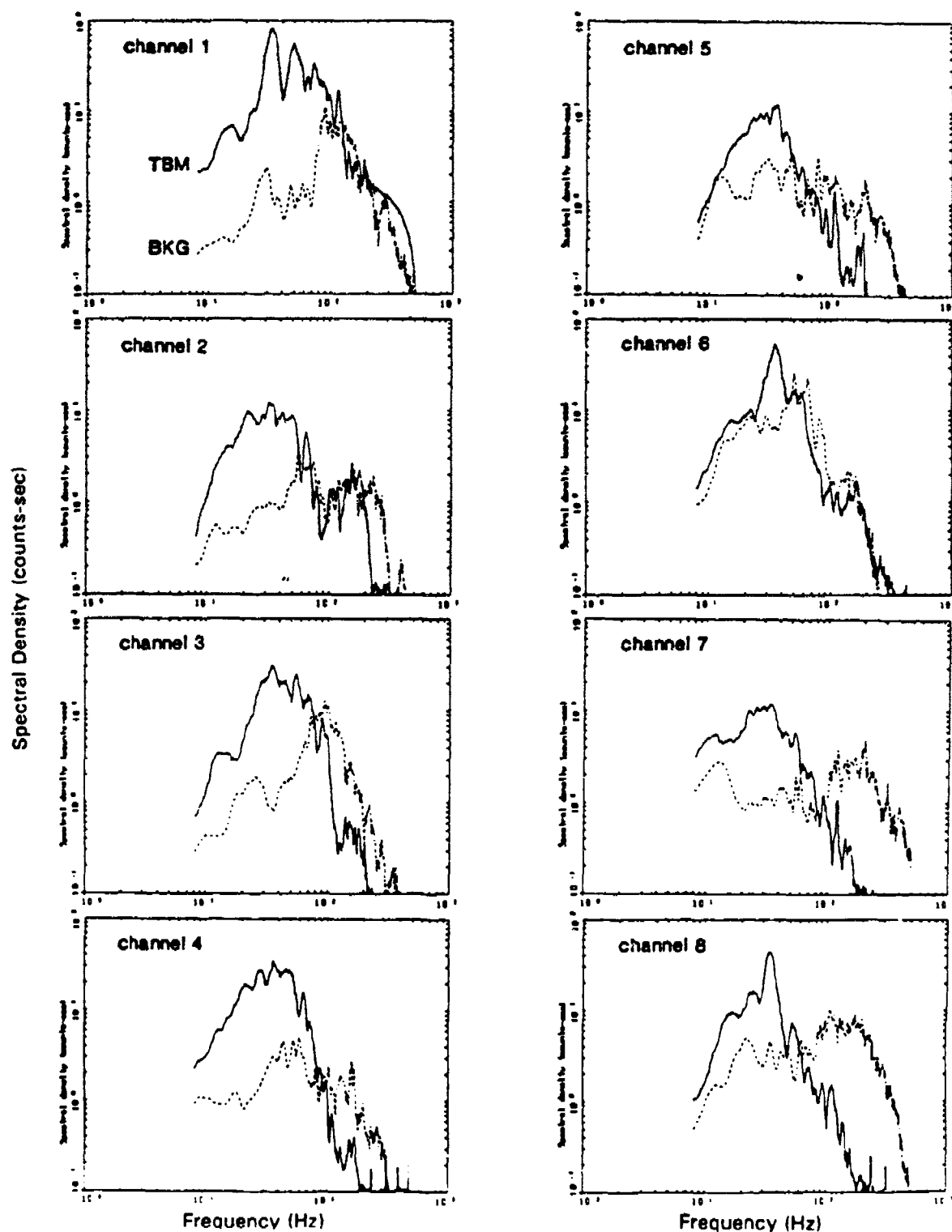
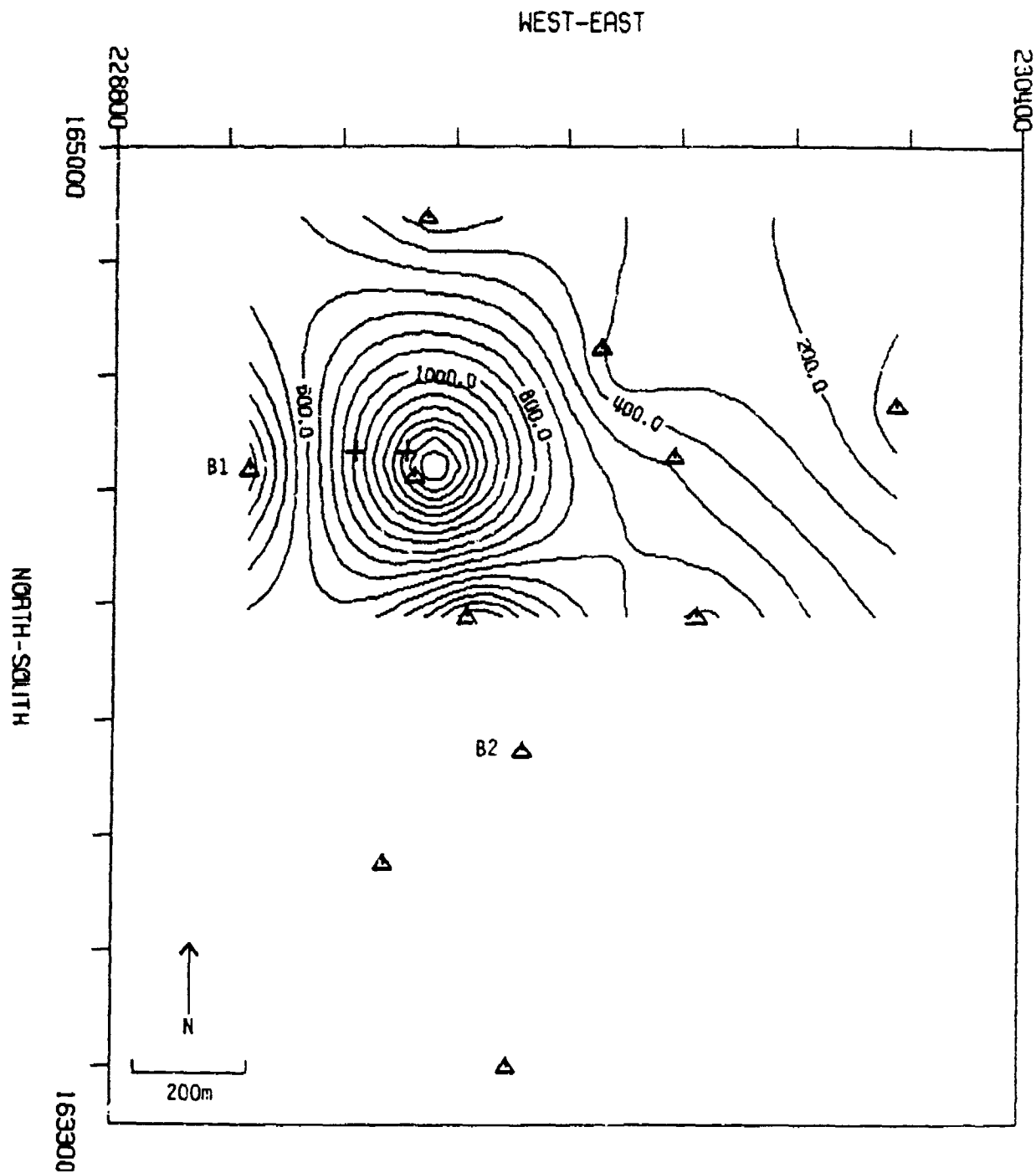
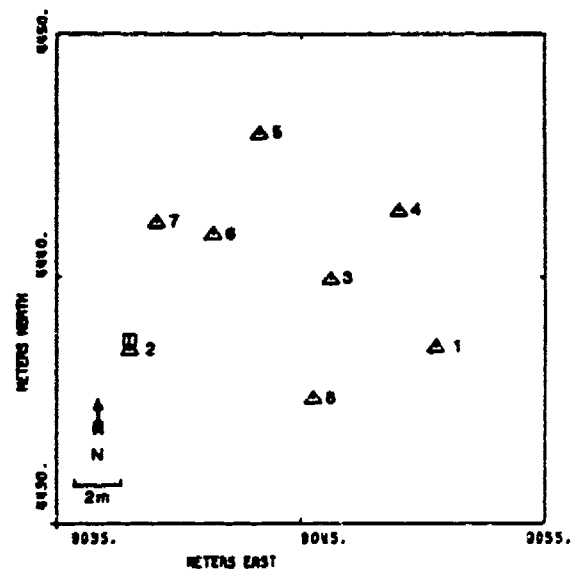


Figure 12. Plot of Fourier amplitude spectra of the TBM signal (solid lines) and background noise (dashed lines) recorded at the 8 DSLD sites. Time histories are shown in Figure 8.

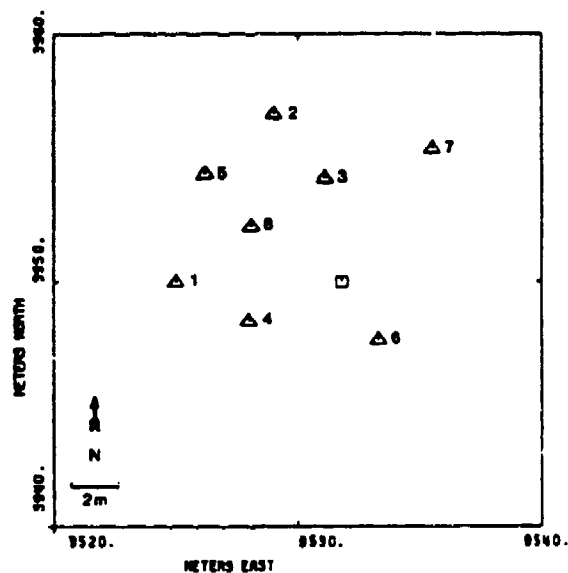


JUAM T ARRAY, POWER SPECTRA 30 HZ (Counts**2-sec)

Figure 13. Contour plot of spectral peak at 30 Hz for TBM signal recorded by the 8 DSLD sites. Spectra are shown in Figure 12.



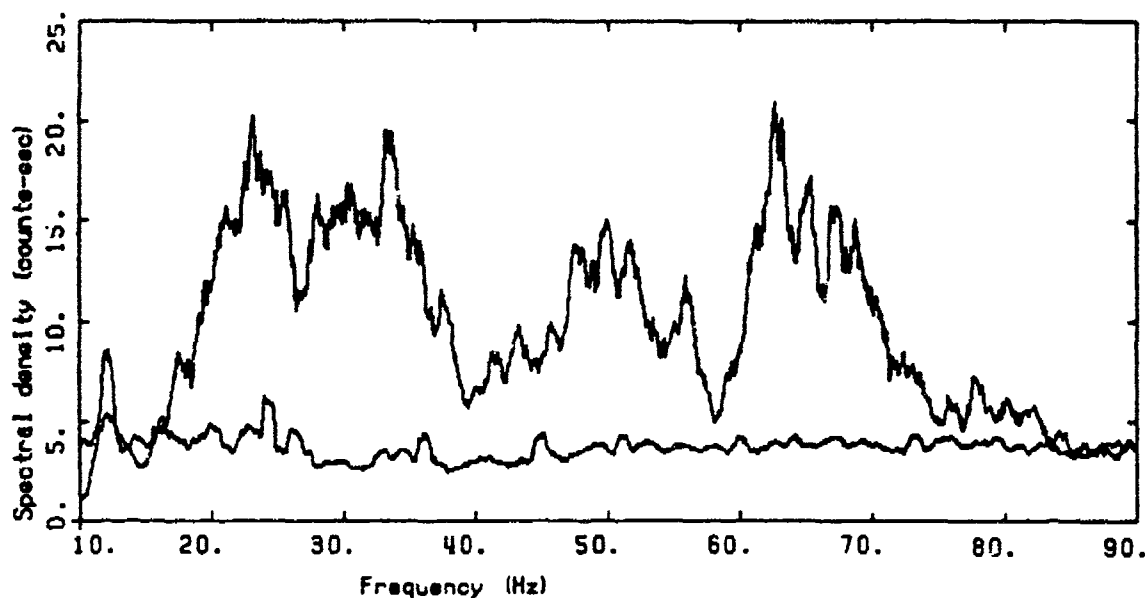
JUAN BEAM1 ARRAY



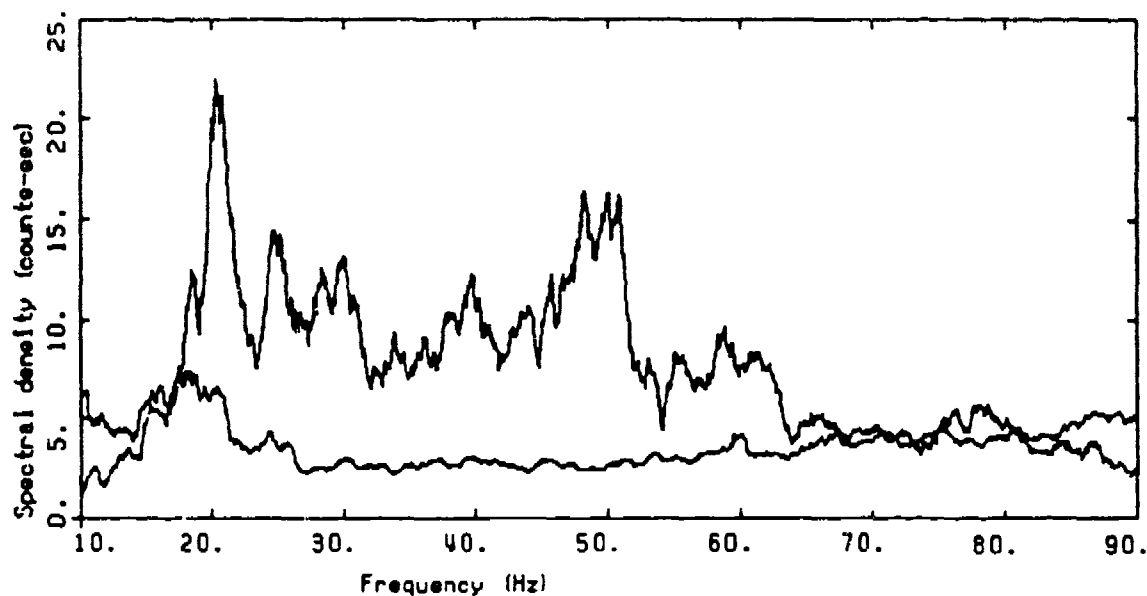
JUAN BEAM2 ARRAY

LEGEND
 △ LOCATIONS OF ARRAY ELEMENTS
 □ LOCATION OF MEQ-800

Figure 14. Station locations for the 8 channel beamsteer arrays (triangles). Sensors are randomly placed at about 2 m separations. Also shown are locations of the MEQ-800 sensors at these two sites (squares).



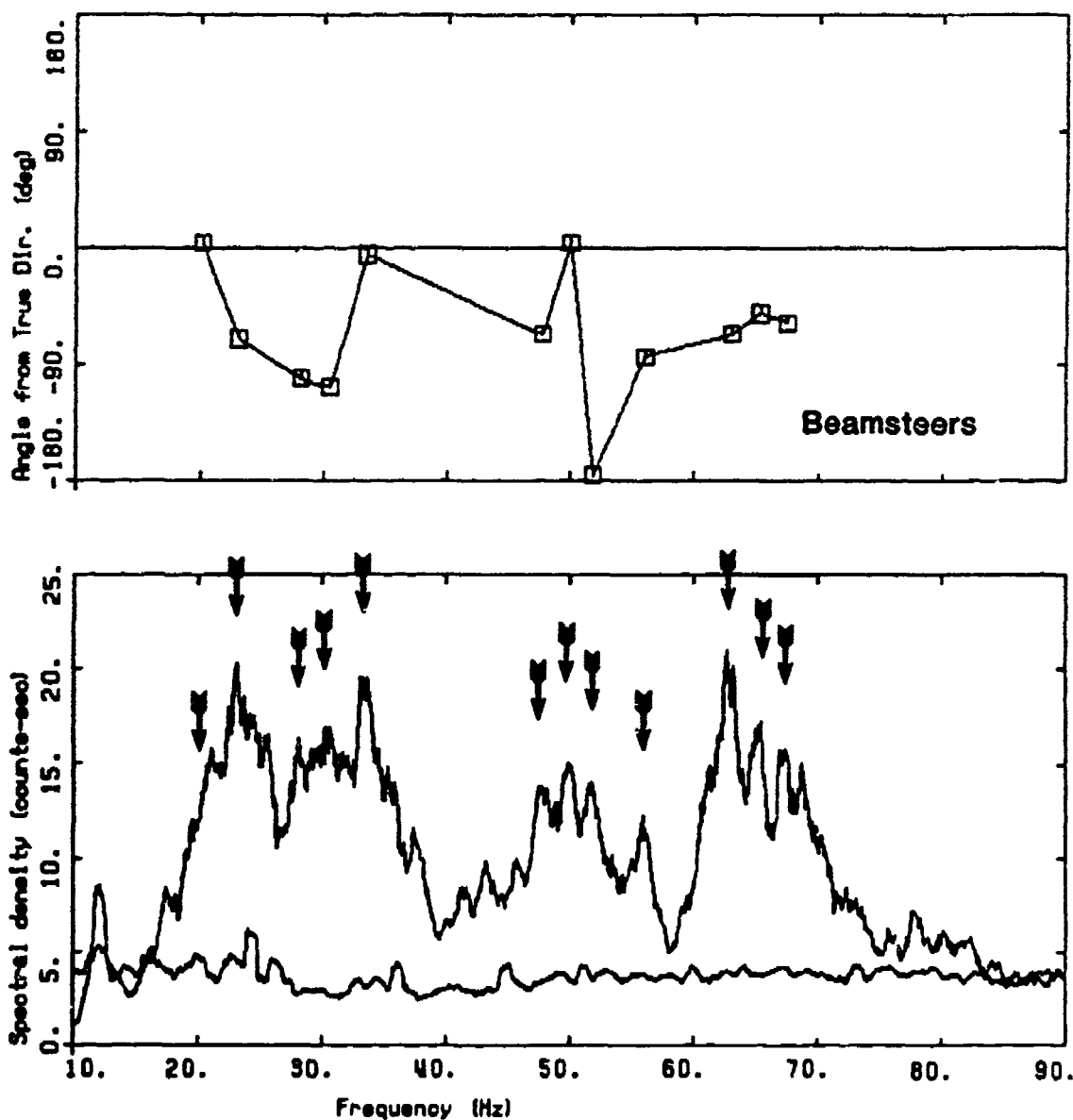
JUAM BEAM1 FOURIER SPECTRA



JUAM BEAM2 FOURIER SPECTRA

LEGEND
 — TBM, AVERAGE 8 STATIONS; 1 hz smoothing, 75 dB gain
 — NOISE = 5, AVERAGE 8 STATIONS; 1 hz smoothing, 75 dB gain

Figure 15. Plot of TBM signal and background noise (scaled up by a factor of 5) at each beamsteer site (Beam 1 and Beam 2) averaged over the 8 sensors. A 1 Hz wide triangular smoothing window has been applied.

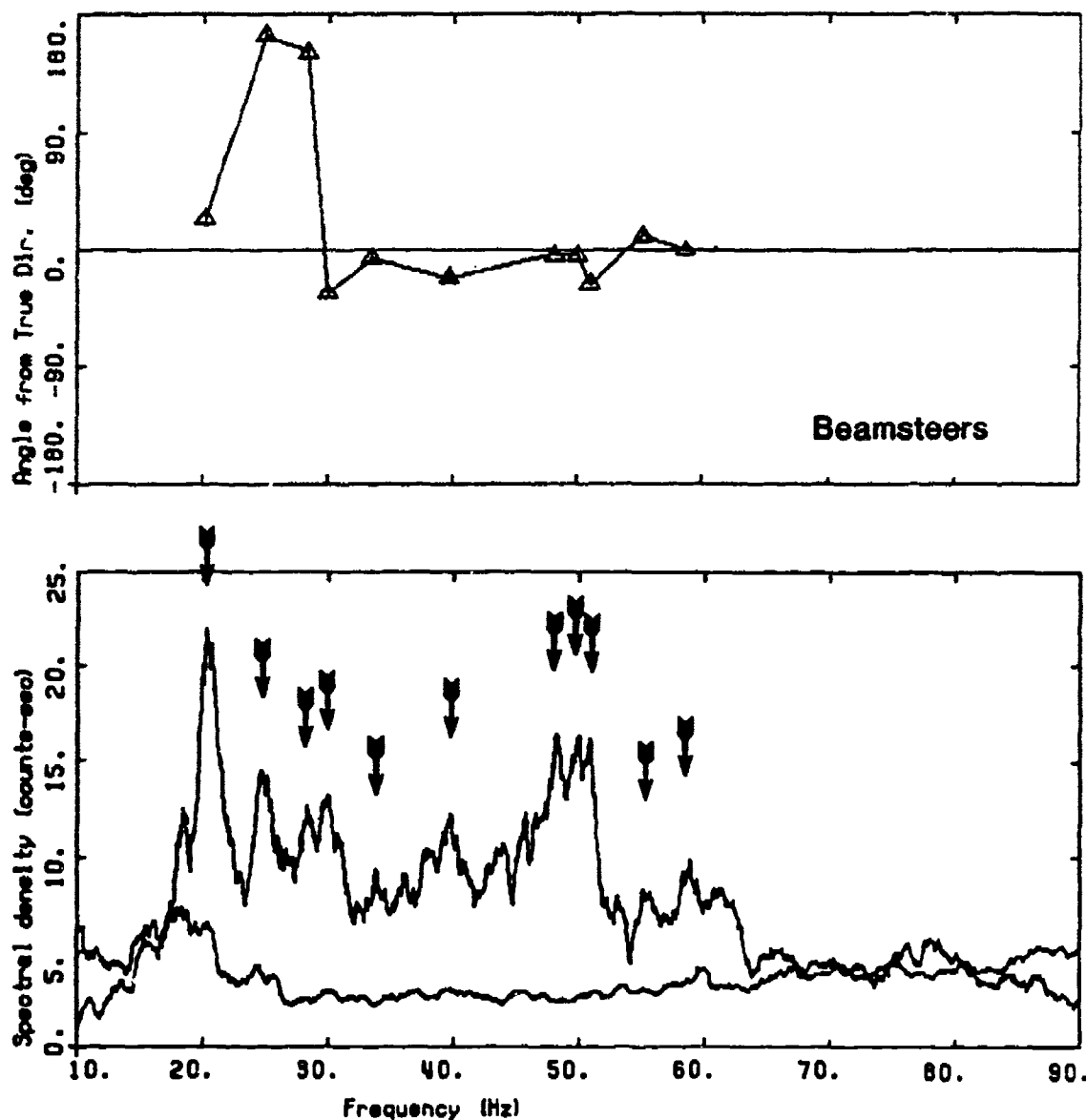


JUAM BEAM1 FOURIER SPECTRA

LEGEND

- TBM, AVERAGE 8 STATIONS; 1 hz smoothing, scaled to 75 dB gain
- NOISE = 5, AVERAGE 8 STATIONS; 1 hz smoothing, scaled to 75 dB gain

Figure 16. Results of the beamsteer analyses for site Beam 1. Top plot shows the deviation of the steer from the true azimuth for each frequency (arrows). Bottom plot shows Fourier amplitude spectra averaged over the 8 sensors (Figure 15).



JUAM BEAM2 FOURIER SPECTRA

LEGEND

TBM, AVERAGE 8 STATIONS; 1 hz smoothing, 75 dB gain
 NOISE = 5, AVERAGE 8 STATIONS; 1 hz smoothing, 75 dB gain

Figure 17. Results of the beamsteer analyses for site Beam 2. Top plot shows the deviation of the steer from the true azimuth for each frequency (arrows). Bottom plot shows Fourier amplitude spectra averaged over the 8 sensors (Figure 15).

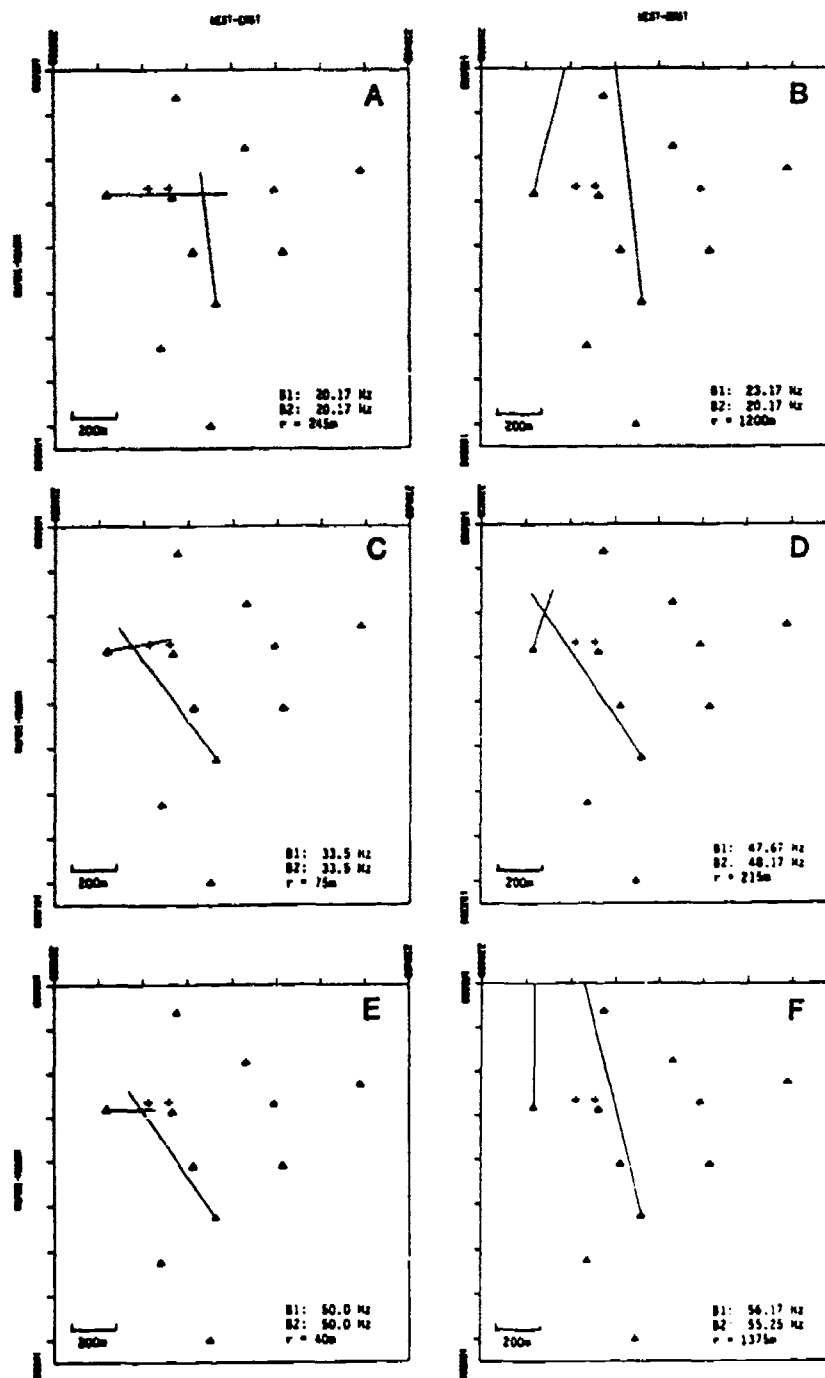
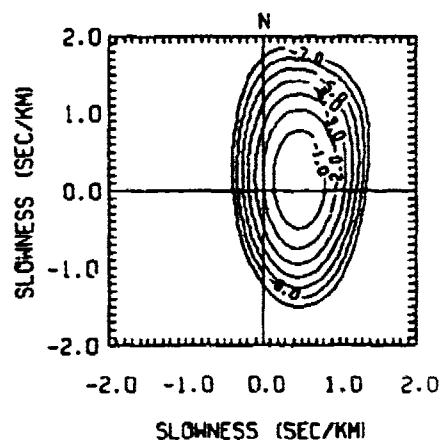


Figure 18. Plots of the six best beamsteer solutions (steers). Frequency of steer for each array is listed and r is the horizontal distance from the TBM to the intersection of the steers.

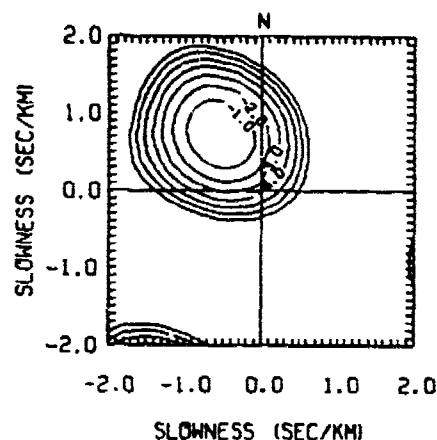
FK PLOTS OF BEST STEERS

33.5 Hz, 50.0 Hz

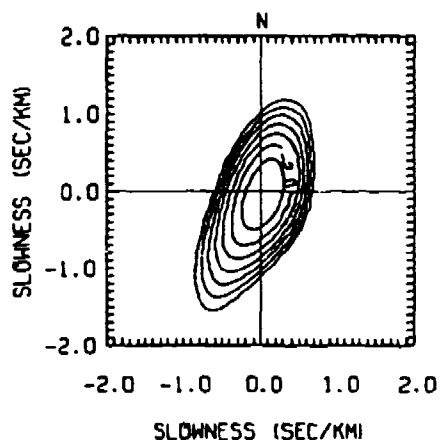
BEAM1 TBM: 33.5Hz 4096 1HW
AZIMUTH OF PEAK = 79
APPARENT VELOCITY (km/sec) = 2.0
MAXIMUM POWER (ct-sec) $\times 2 = 21921$



B2 TBM: 33.50 Hz 4096 1HW
AZIMUTH OF PEAK = 324
APPARENT VELOCITY (km/sec) = 1.2
MAXIMUM POWER (ct-sec) $\times 2 = 326$



BEAM1 TBM: 50.0 Hz 4096 1HW
AZIMUTH OF PEAK = 90
APPARENT VELOCITY (km/sec) = 10.0
MAXIMUM POWER (ct-sec) $\times 2 = 13857$



B2 TBM: 50.00 Hz 4096 1HW
AZIMUTH OF PEAK = 326
APPARENT VELOCITY (km/sec) = 2.8
MAXIMUM POWER (ct-sec) $\times 2 = 1495$

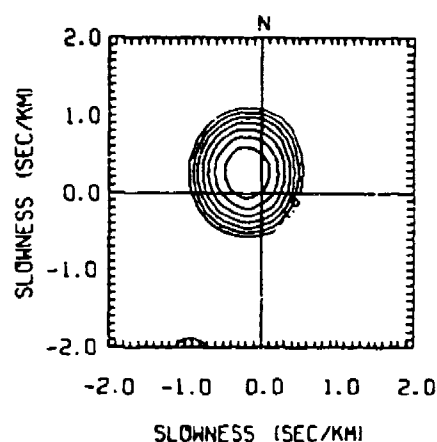
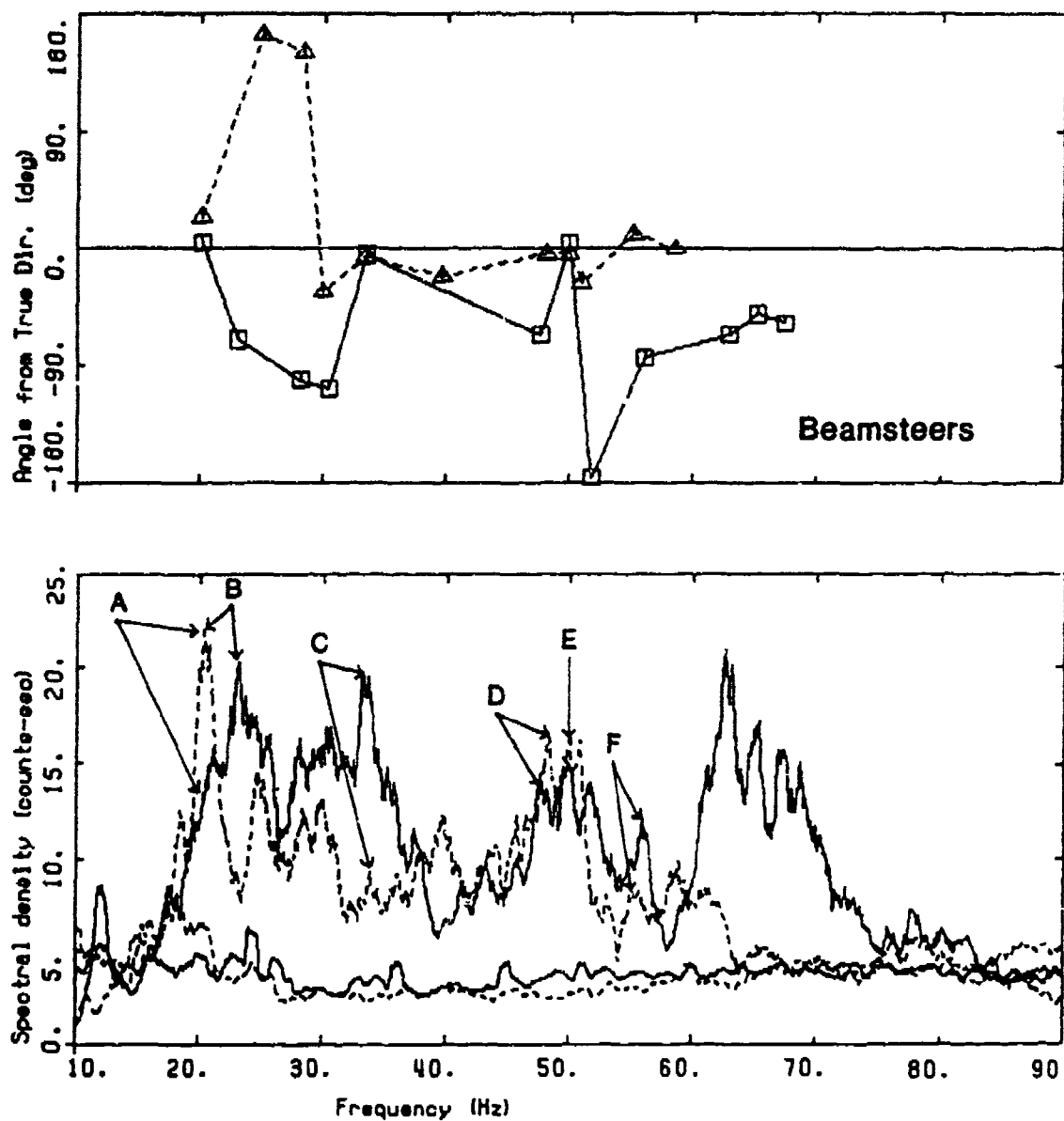


Figure 19. An example of the f-k plots of the best steers. The contours are in power and the azimuth from the origin to the peak power represents the azimuth of the steer. The slowness is the inverse of the horizontal propagation velocity (apparent velocity) of the steer.

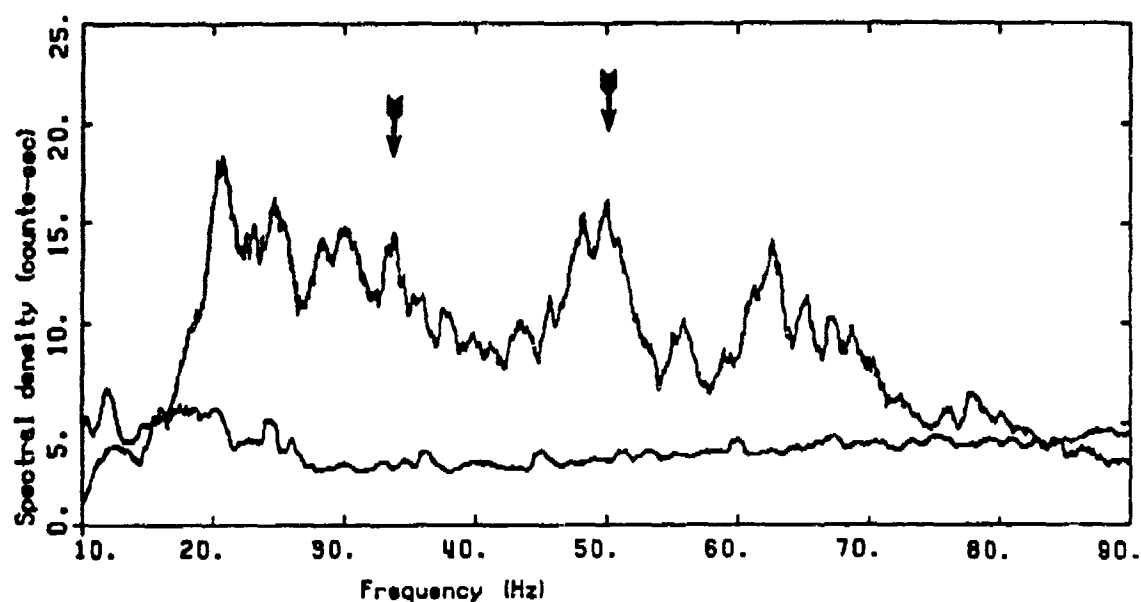


JUAM BEAM1, BEAM2 FOURIER SPECTRA

LEGEND

- BEAM1 TBM, AVERAGE 8 STATIONS: 1 hz smoothing
- BEAM 1 NOISE = 5, AVERAGE 8 STATIONS: 1 hz smoothing
- BEAM2 TBM, AVERAGE 8 STATIONS: 1 hz smoothing
- BEAM2 NOISE = 5, AVERAGE 8 STATIONS: 1 hz smoothing

Figure 20. Summary plot of the steers and average spectra for both beamsteer arrays. The letters correspond to the best steers shown in Figure 18.

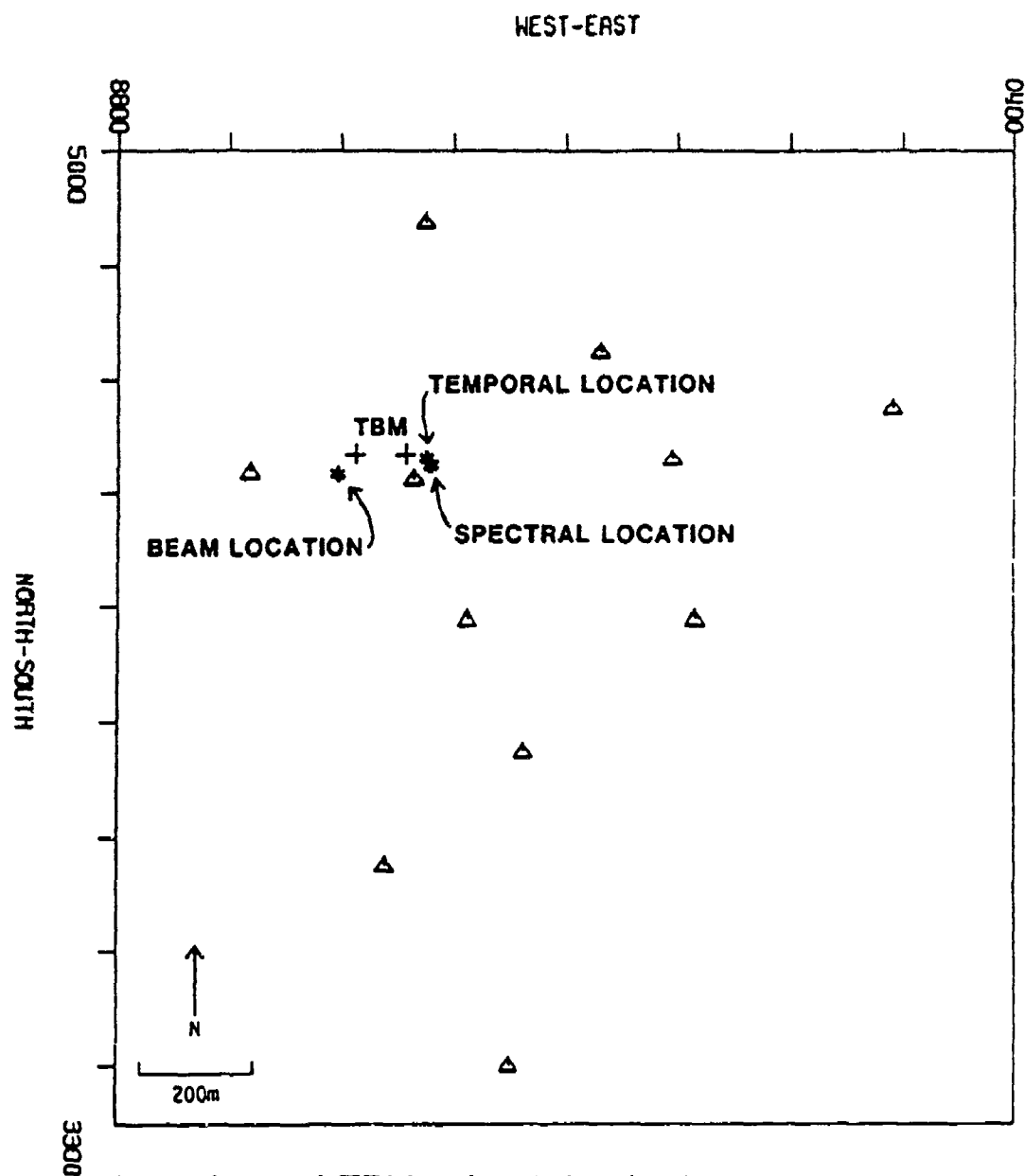


JUAM BEAM1 BEAM2

LEGEND

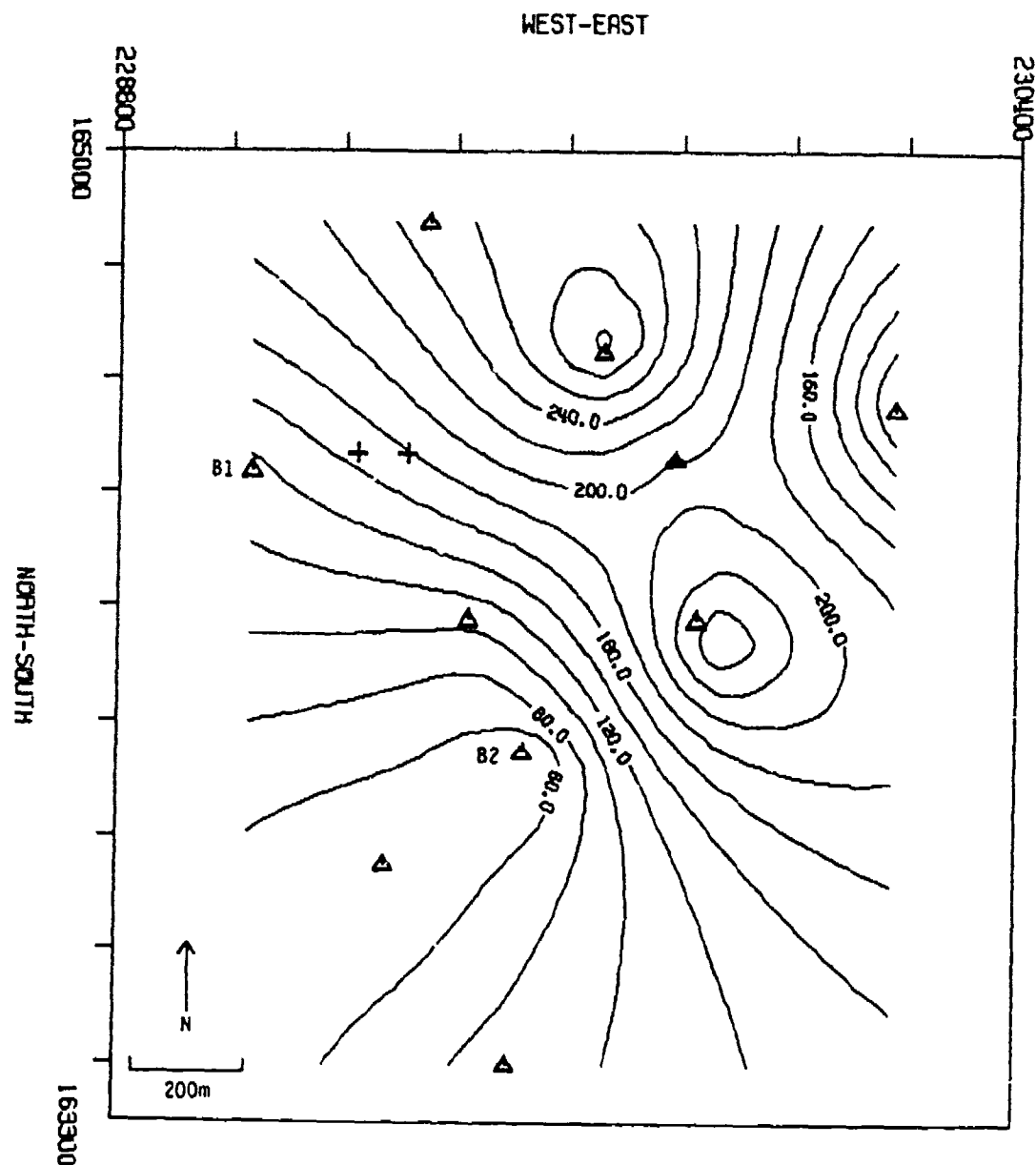
- TBM AVERAGE 16 STATIONS: 1 hz smoothing
- NOISE = 5, AVERAGE 16 STATIONS: 1 hz smoothing

Figure 21. Plot of Fourier amplitude spectra of the TBM signal and noise (scaled up by a factor of 5) averaged over both sites. The two best steers, at 33 and 50 Hz, have high peaks but are not the largest. Steering on the largest peak results in a very poor location (Figure 20).



Locations of TBM using 3 Methods

Figure 22. Summary plot showing locations of the recording sites and TBM (beginning and end of test period) and results of the three location techniques. Since most of the location analyses were done on data recorded around the middle of the test period, the midpoint of the TBM locations is taken as the TBM location.



JUAN T ARRAY, AVERAGE TBM AMPLITUDE (Cnts) WITHOUT STATION 1

Figure 23. Contour plot of average amplitudes of the TBM signal recorded by both the DSLD and MEQ-800 instruments with the closest site (site 1) deleted.

SEISMIC TOMOGRAPHY AT THE WIPP SITE

by

H.T. Andersen and C.K. Skokan

Department of Geophysics
Colorado School of Mines
1500 Illinois Street
Golden, Colorado 80401

ABSTRACT

A seismic tomography study was carried out at the WIPP site in southeast New Mexico, to determine the feasibility of using this technique to define and monitor the Disturbed Rock Zone (DRZ) around the underground excavations.

Several acoustic sources, sensors and methods of coupling to the rock face were tested. A pillar in the oldest part of the underground excavations was selected for a test, which consisted of 36 sources and 20 receiver positions. The resulting 720 P-wave travel times were inverted using the ART algorithm.

The test survey did not clearly define a Disturbed Rock Zone of generally lower acoustic velocity. However, the subtle response to local zones of damaged and disturbed rock showed that the technique can, with some refinements, be used to define and monitor the DRZ in an operational mining environment such as at WIPP.

INTRODUCTION

The WIPP site, located between the towns of Carlsbad and Hobbs in southeast New Mexico, was constructed to test the feasibility of transuranic waste storage in a bedded salt formation. The WIPP underground experimental and storage facility is in the Salado salt formation, approximately 2,150 feet beneath the surface.

An aspect of particular interest is the characterization of the Disturbed Rock Zone (DRZ) that develops in response to underground excavation. The development of this zone of disturbed, or mechanically altered, rock has significance in estimating the stability and ultimate duration of safe access to the underground storage rooms. As the DRZ is a result of dilatation and microfracturing, an associated generally lower seismic velocity can be expected. It should therefore be possible to determine the extent and character of the DRZ using seismic tomography.

DATA ACQUISITION

Several types of exploration and engineering geophones were tested, together with various methods of mounting the geophones to the rock face. Most of these acoustic sensors have their best response in the range of 4 to 100 Hz. However, from initial tests, it was found the velocity through the pillar was approximately 15,000 feet per second, and a large component of the information lay in the frequency range of 1,000 to 2,000 Hz. In addition, the underground environment during daily operations has a high noise level in the frequency range of approximately 10 to 300 Hz.

A Wilcoxon piezoelectric transducer, designed to monitor turbine vibrations, proved the most effective of the sensors tested. An added advantage was that the 10 microfarad coupling capacitor needed to match the Wilcoxon transducer output to the Geometrics ES-1210 engineering seismograph, served as an effective highpass filter, thus almost eliminating the background noise created by the mining operations.

A similar set of tests was carried out to determine the best method of mounting the transducers to the rock face so as to achieve adequate mechanical coupling. Probably due to the high frequencies involved and the poor mechanical strength of the rock face material, it was found necessary to use a 4 inch length of 1/4 inch diameter machine bolt cemented into a tightly fitting hole as a mount.

Due to simplicity, a 1 pound hammer source was chosen. As with the transducer mounts, it was found that a permanent rigidly attached strike plate was necessary to assure a consistent and repetitive impulse source. A 4 1/2 inch length of 5/16 inch diameter steel bolt cemented into a tightly fitting hole was used as a strike plate.

A pillar in the oldest part of the underground excavations was selected for the study, as it should have the greatest DRZ development. Reasonably easy access was available to all four sides of the pillar. A small test survey, consisting of 36 sources and 20 receiver locations on opposite ribs of the pillar between E-zero and E-140, and N-760 and N-1,100 drifts was carried out. Both the source and receiver arrays had stations and 5 foot intervals. An additional array of 12 source stations were located on the north rib, extending westward from the northeastern corner of the pillar. It was hoped that these arrays of sources and receivers would be adequate to map the extent of the mechanically altered rock clearly visible around the northeast corner of the pillar. A total of 720 P-wave travel times were determined.

CONCLUSIONS

The feasibility study showed that acoustic waves of sufficiently high frequency content can be transmitted and received through the bedded salt of the Salado Formation to resolve a tomographic image of the DRZ. Clear and consistent P-wave travel times can be measured in the WIPP underground environment during active mining operations. The test survey did not define a clear and continuous low velocity DRZ. However, the lower

velocities observed through the northeastern corner of the pillar show that with smaller station spacing in the receiver and source arrays together with a more accurate determination of the P-wave travel time, a DRZ of less than 5 feet can be measured and monitored.

SELECTED BIBLIOGRAPHY

- Albright, J.N., Johnson, P.A., Phillips, W.S., Bradley, C.R., and Rutledge, J.T., 1986, Crosswell acoustic surveying project: Los Alamos National Laboratories report. Prepared for DOE unconventional gas recovery research program.
- Barrows, L. and Fett, J., 1985, A high precision gravity survey in the Delaware Basin of southeastern New Mexico: Geophysics, v.50, n.5, pp. 825-833.
- Borns, D.J., Pfeifer, M.C., Skokan, C.K., Andersen, H.T., and Starrett, J.M., 1988, Geophysical methods to monitor the development of the disturbed rock zone around underground excavations in bedded salt: Published abstract SAGEEP March 1989.
- Bregman, N.D., Bailey, R.C., and Chapman, C.H., 1989, Crosshole seismic tomography: Geophysics, v.54, n.2, pp. 200-215.
- Butler, D.K., and Curro, J.R., 1981, Crosshole seismic testing - procedures and pitfalls: Geophysics, v.46, n.1, pp. 23-29.
- Devaney, A.J., 1984, Geophysical diffraction tomography: IEEE transactions on geoscience and remote sensing, v.GE-22, n.1, pp. 3-13.
- Dines, K.A. and Lytle, R.J., 1979, Computerized geophysical tomography: Proceedings of the IEEE, V.67, n.7, pp. 1065-1073.
- Herman, G.T., 1980, Image reconstruction from projections: The fundamentals of computerized tomography. Edited by Werner Rheinboldt, New York Academic Press.
- Hofland, G.S., 1987, The determination of an optimum convergence path for the algebraic reconstructive technique algorithm: Colorado School of Mines, unpublished paper.
- Ivansson, S., 1985, A study of methods for tomographic velocity estimation in the presence of low velocity zones: Geophysics, v. 50, n.6, pp. 969-988.
- Lytle, R.J. and Dines, K.A., 1980, Iterative ray tracing between boreholes for underground image reconstruction: IEEE transactions on geoscience and remote sensing, v.GE-18, n.3, pp. 234-240.

- Markiewicz, R.D., 1988, A seismic refraction on-site interpretation method: Colorado School of Mines, M.S. thesis T-3165.
- Mason, I.M., Buchanan, D.J., and Booer, A.K., 1983, Channel wave mapping of coal seams in the United Kingdom: Geophysics, v.45, pp. 1131-1143.
- Peterson, J.E., Paulsson, B.N.P., and McEvilly, T.V., 1985, Applications of algebraic reconstruction techniques to crosshole seismic data: Geophysics, v.50, n.10, pp. 1566-1580.
- Powers, M.H., 1986, A microcomputer tomographic inversion of acoustic crosshole data: Colorado School of Mines, M.S. thesis T-3095.
- Reeves, J., 1979, Investigations of seismic seam waves in US coals: Colorado School of Mines, M.S. thesis T-2148.
- Scudder, H.J., 1978, Introduction to computer aided tomography: Proceedings of the IEEE, v.66, pp. 628-637.
- Snodgrass, J.J., 1984, In-seam seismic surveys using controlled waveform source transducers: SME-AIME reprint 84-420, for presentation at Denver meeting, October 1984.
- Starrett, J.M., 1989, A feasibility study for using seismic tomography to monitor the integrity of salt pillars: Colorado School of Mines, M.S. thesis T-3587.
- Stewart, R.R., 1987, "Seismic Tomography": SEG continuing education course, copyright: Genix Tech., Ltd.
- Wong, J.N., Bregman, N., Hurley, P., and West, G.F., 1987, Crosshole seismic scanning and tomography: The Leading Edge, January 1987.
- Worthington, W.H., 1984, An introduction to geophysical tomography: First Break, November 1984, pp. 20-26.

Session 3

Data Processing

PRESTACK IMAGING AND TOMOGRAPHIC
INVERSION OF SEISMIC CROSS-BOREHOLE DATA
BY
A.H. BALCH AND M.H. KARAZINCIR

INTRODUCTION

Near surface geologic studies have usually been severely hampered by the investigators' inability to examine the near surface geology. Subsurface features of interest, including tunnels, are often hidden from view by the opaque earth. One can drill boreholes and examine subsurface materials directly, but this procedure is slow and expensive. An alternative is to use geophysical methods to delineate subsurface features. But the near surface geology is often complex, which makes geophysical data interpretation difficult or impossible. The geologic complexity often causes small anomalies caused by sought-after features to be obscured in complicated data sets.

In this paper we offer a partial solution to this problem: that of seismic reflection/diffraction imaging. We shall show that properly imaged reflections/diffractions can reveal subsurface features with remarkable clarity, even though these features are obscured from view and partially or totally obscured on the original raw data plate.

The results here are cast in a seismic context. Most of the principles used apply also to other wavefield geophysical techniques, for example pulsed electromagnetics.

We hope to demonstrate in this paper that seismic imaging, or migration, represents a big step forward in resolving ambiguities and other difficulties usually associated with near-surface seismic investigations.

THE METHOD

Figure 1 illustrates the problem to be solved and suggests a solution. A section of earth is under investigation, and we wish to know the presence and location of formation boundaries, voids, faults, and fracture zones in that slice of the earth. Our proposed solution is to straddle the section with two boreholes. A seismic source is energized at a multiplicity of locations in one borehole and a seismic detector(s) of some sort located in the other borehole measures the resultant wavefield. If acoustic discontinuities are associated with the geologic features mentioned, then these features will perturb the seismic wavefield. We may then be able to interpret the perturbed wavefield in terms of the geology.

Figure 1 also indicates that additional sources and/or detectors may be placed on the ground surface. The procedure may be called cross-borehole seismics, vertical seismic profiling or VSP, reverse VSP, or surface-surface seismics, depending on which source-receiver combination is used.

We shall demonstrate that this method succeeds if we acquire good quality data and then process these data to produce images of the geologic features. Except for the simplest cases, the observed wavefield is far too complex to interpret directly. In order to produce the desired images good quality data recordings are essential.

MODELING

To demonstrate the effectiveness of the technique, particularly that of cross-borehole seismics, and to develop imaging techniques and programs, we have constructed several scale physical elastic models.

These elastic models have many elements of realism not usually found in computer models, including arbitrary irregular boundaries; mode conversion; sources that emit both P- (compressional) and S- (shear) waves simultaneously; realistic, variable source waveforms; variable, non-reproducible source and receiver coupling; and spreading and attenuation losses.

A typical modeling setup is illustrated in Figure 2. A pulser energizes a source transducer, located on the physical elastic model, and also sends a synchronization pulse to a digitizing oscilloscope. The vector wavefield generated by the source is sensed by the detectors and sent to the oscilloscope via one or more amplifiers. The wavefield is observed on the oscilloscope, digitized, and off-loaded to a computer. Once in the computer the data are treated just as if they had been recorded in the field.

THE CROSS-BOREHOLE TUNNEL MODEL

A cross-borehole elastic model for tunnel detection is shown schematically in Figure 3, Balch, et al, (1991). Thirty-three source locations, in a vertical line along the left hand side (l.h.s.) of the model, represent a source borehole. Two hundred fifty-six two-component detector locations are arrayed in a line down the middle of the model, and represent a receiver borehole. The model itself consists of a 4' X 8' sheet of 1/4 inch Plexiglas. Two holes, representing tunnels, approximately 2/3 wavelength in diameter were drilled into the sheet. One hole is located between the "borehole arrays" and another is located outside this zone. There are five seismic "targets": the top and bottom of the sheet, the right-hand edge (r.h.s.), and the two holes.

The reflection/diffraction raypaths shown in Figure 3 actually represent four possible reflection events: P-P, P-S converted, S-P converted, and S-S. All four events were in fact observed and imaged. Note that, because of the location of the receiver array, three of the five targets yield inter-well reflections, and two produce intra-well reflections. This is an important distinction when it comes to imaging, and one that is often not considered in cross-borehole imaging. In the real earth either type of reflected event is possible.

A typical data set obtained from the model in Figure 3 is plotted in Figure 4. Nearly all the coherent events seen in the figure can be accounted for, since we know the model

exactly. However if we did not have that knowledge it would be difficult to deduce the nature of the model by visual inspection of the recorded data plots. Even in this simple case we need to use these data to create images of the reflecting horizons.

An appropriate data processing sequence is illustrated in Figure 5. Mode separation based on apparent velocity and polarization greatly simplifies the observed wavefield. Since there may be as much as 100,000 to one differences in amplitude amongst the observed events, some sort of automatic gain control is desirable. The physical model source wavelet is of relatively long duration; therefore it is helpful to apply some sort of deconvolution or inverse Q filtering in order to generate the data set we would have obtained if the source had been a short duration wavelet and passed through the medium unattenuated. The most important processing step shown in Figure 5 is that of (prestack) imaging, one image for each of the four modes from each common source gather. Finally these images are combined to produce final stacked images: one image for each of the four modes.

The final stacked images for each mode are shown in Figure 6. The targets show up with remarkable clarity, especially on the P-P image plot. The targets show up with varying degrees of clarity on the other mode plots. It is important to keep in mind that completely different reflected events recorded as raw data (Figure 4) were used to produce the four image plots shown in Figure 6. Reverse time migration, using a finite-difference solution to the scalar wave equation in a medium with a completely arbitrary distribution of velocities, was used to produce the Figure 6 image plots.

When scalar wave theory is used to image P-S converted wave reflections, ambiguities in the sign of the wave polarization can occur. These ambiguities can cause P-S reflector images to deteriorate when the partial images from the individual common source gathers are stacked, Erdemir and Balch (1992). By calculating P- wave incidence angles these ambiguities can be removed or compensated for. Figure 7 shows the result of the procedure when it is applied to the shear-mode reflections. A comparison of the images in Figure 7 with the P-S images in Figure 6 shows that this correction produces a spectacular improvement in the P-S images.

THE PEORIA STRATIGRAPHIC TRAP MODEL

A simplified cross-section through a portion of the Peoria oil field, in eastern Colorado is illustrated in Figure 8. A portion of the Cretaceous "J" sand is truncated, or pinched out, by a barrier bar from an ancient stream channel. This feature cuts off hydrocarbon flow to the well on the left, which is dry. The right hand well is productive. We wish to use cross-borehole imaging to demonstrate the feasibility of delineating the barrier bar, and consequently delineating the edge of the productive zone.

A two-dimensional physical elastic model based on this cross-section is shown in Figure 9. And a plot of a typical cross-borehole data set from the physical model is shown in Figure 10. Many of the coherent events seen in Figure 10 can be accounted for (especially since we know the nature of the model, Figure 9). However not even the most

optimistic seismic interpreter would claim to be able to delineate the pinch-out by visual inspection of the Figure 10 data plot.

In Figure 11 we see the result of multi-mode imaging, plus combining or stacking the four modes to generate a final image of the cross-section between source and receiver "boreholes". The image bears a remarkable resemblance to the model. In particular the pinch-out is imaged clearly and accurately.

A THREE-DIMENSIONAL TUNNEL MODEL STUDY

Our final example of cross-borehole imaging is based on a three-dimensional model of a tunnel, Figure 12. A horizontal hole, or tunnel, was drilled into a concrete block approximately 2'X6'X6'. A line of shear horizontal, SH, sources was arrayed vertically down one side of the block and a line of horizontal motion at transducers was arrayed vertically down the other side, as shown in the figure. The hole is between the vertical arrays. The shear wave polarization is parallel to the tunnel axis.

A partially processed common source gather is shown in Figure 13. Although SH diffractions/reflections from the hole can be seen (see arrows), it would be difficult to infer the presence of a hole, or its location, by visual inspection of the data plot.

In Figure 14 a plot of the imaged data is shown. The presence and location of the hole is easily determined.

TOMOGRAPHY

Acoustic tomography is an alternative approach to the imaging procedure just described. The difference between the methods is illustrated in Figure 15. Specifically, the tomographer uses the direct arrival (amplitude and/or arrival time), and usually ignores all other events. In diffraction imaging one ignores the direct arrivals and uses the reflected events. The methods are complementary.

A traveltome tomogram of a concrete block, comparable to the model shown in Figure 12, is shown in Figure 16. The tunnel shows up as a low velocity anomaly.

This example demonstrates that acoustic tomography is a viable method: the tunnel is clearly shown. The resolution is not as good as the diffraction image, Figure 14. Images of the top and bottom of the model cannot be obtained using tomography. Neither can tomography image extra-well features, such as those shown in Figures 6 and 7, because these features do not affect the direct arrival in any way.

CONCLUSIONS

Images computed from the reflected/diffracted wavefield generated by discontinuities in the earth, including tunnels, can be used to make a reliable unambiguous interpretation of the subsurface. These images can show the shape and location of reflectors/diffractors

with remarkable clarity. Visual inspection of plots of the wavefield itself are inadequate for this type of interpretation: the wavefield is far too complex to interpret in unimaged form. Traveltime and amplitude tomography are possible alternative ways of processing the recorded wavefield data. However, the images obtained by even very good tomograph inversions lack the resolution and clarity that is possible with diffraction imaging, and extra well features are never detected. In any case, tomography and diffraction imaging are complementary processes; tomography typically utilizes direct arrival amplitudes and time, diffraction imaging utilizes the reflected/diffracted and scattered wavefield, i.e., all events except the direct arrivals.

While much remains to be done in this discipline, especially to develop field procedures and equipment to map the subsurface routinely, our work and similar work by others has convinced us that seismic subsurface reflection/diffraction imaging can and will be used extensively in the future to detect geologic features and other targets of interest in the near surface: targets that are invisible to the investigator.

ACKNOWLEDGEMENT

The authors thank the Belvoir Research, Development, and Engineering Center, and especially Mr. Raymond f. Dennis of BRDEC for their generous financial support of this investigation and for providing the forum to present these results.

REFERENCES

Erdemir, Cemal, and Balch, A.H., 1992, Sign correction of P to S converted reflected waves by determining the angle of illumination: 54 *EAEG*, Paris, 1992

Balch, A.H., Chang, H., Hofland, G.S., Ranzinger, K.A., and Erdemir, C., 1991, The use of forward- and back- scattered P-, S-, and converted waves in cross-borehole imaging: *Geophysical Prospecting*, v. 39, pp 887-913.

FIGURES

- Figure 1. The subsurface investigation problem, and a possible solution.
- Figure 2. The physical elastic modeling setup
- Figure 3. Reflection/diffraction raypaths associated with the physical elastic model shown in Figure 2.
- Figure 4. Typical data set (common source gather) from the physical elastic modeling setup shown in Figure 2.
- Figure 5. Typical computer processing sequence for the data plotted in Figure 4.
- Figure 6. Final, stacked images for the physical elastic model, Figure 2, based on the data typified by Figure 4, after the processing sequence illustrated in Figure 5.
- Figure 7. P-S images of the model shown in Figure 2, with compensation for polarity change due to changes in illumination angle. Compare with P-S images in Figure 6.
- Figure 8: A simplified geologic cross-section through a portion of the Peoria Oil Field showing a "J" sand pinchout. It is desired to delineate the pinchout using seismic data from the two boreholes shown.
- Figure 9. Two-dimensional elastic physical model of the Peoria Field, based on the geologic model shown in Figure 8.
- Figure 10. Plot of typical cross-hole data set (common source gather) obtained from the model shown in Figure 9. It would not be possible to delineate the pinch-out by visual interpretation of these data.
- Figure 11. Multi-mode image of the physical elastic model shown in Figure 9, based on cross-borehole acoustic measurements typified by the data plot shown in Figure 10. The pinch-out is clearly delineated.
- Figure 12. Three-dimensional physical elastic tunnel model.
- Figure 13. Partially processed (common source gather) SH data plot obtained from the three-dimensional model shown in Figure 12. Tunnel diffractions are indicated by the arrows. It would be difficult to detect and locate the tunnel by direct interpretation of this plot.
- Figure 14. Imaged data. The tunnel is now unambiguously seen and located.

Figure 15. Illustration of the difference between tomography and diffraction imaging: tomography uses the direct arrival, diffraction imaging uses the reflections/diffractions. The methods are complementary since each method uses that portion of the data which the other ignores.

Figure 16. Traveltime tomogram from a three-dimensional model similar to that shown in Figure 12. compare with the diffraction image, Figure 14.

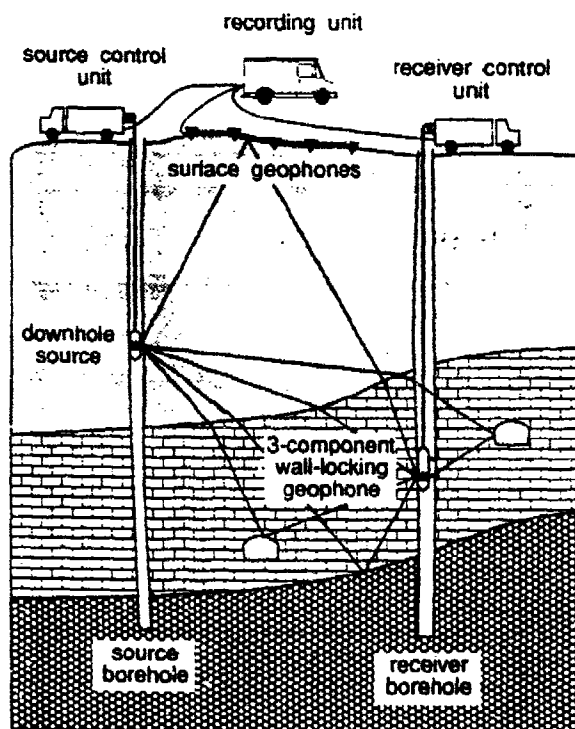


Figure 1.

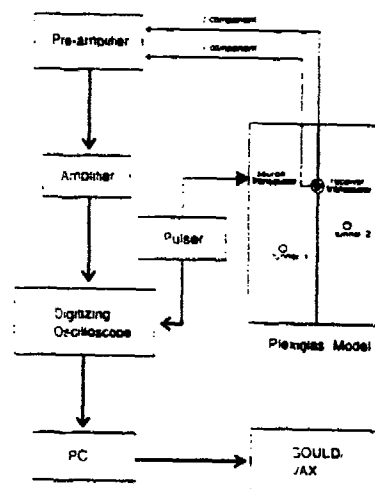


Figure 2.

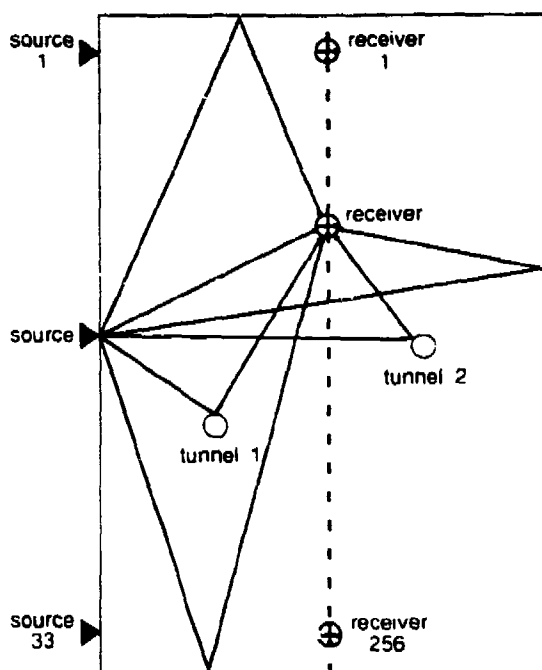


Figure 3.

COMMON SHOT GATHER - SOURCE = 33"
1-COMPONENT

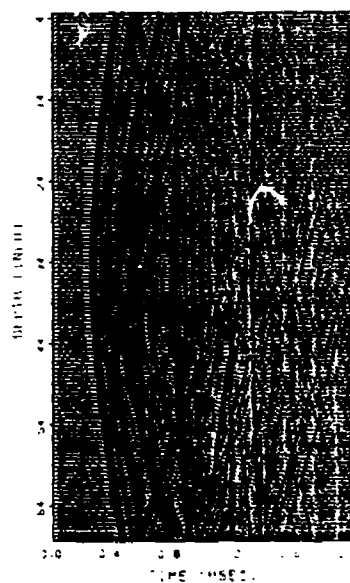


Figure 4.

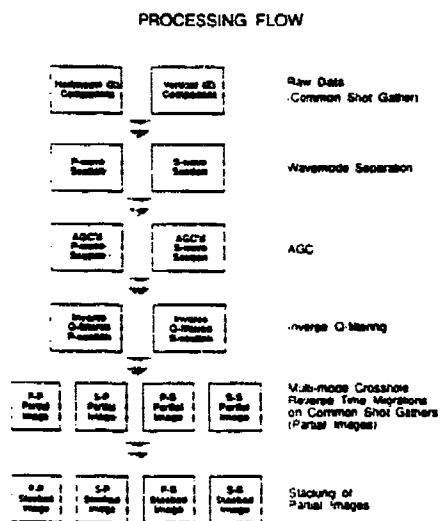


Figure 5.

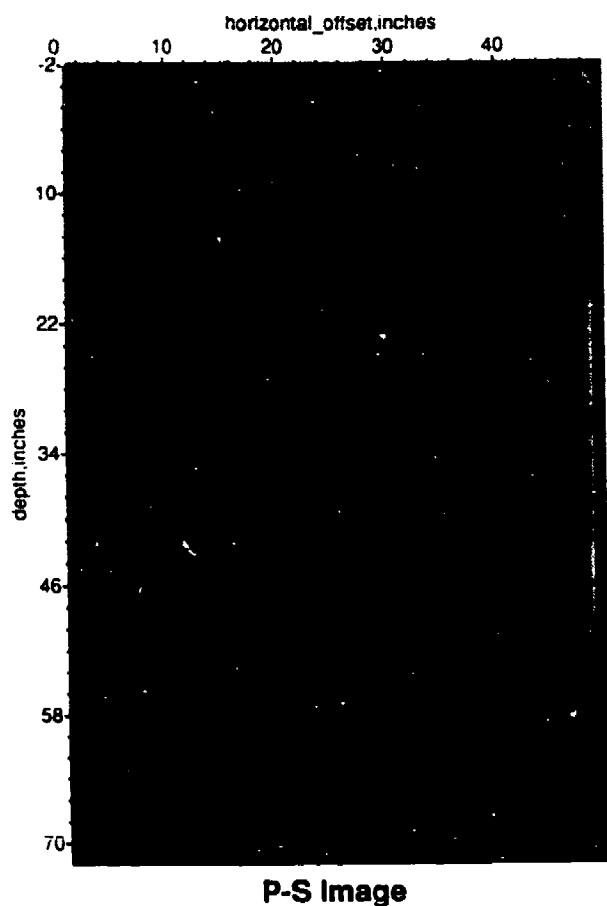


Figure 7.

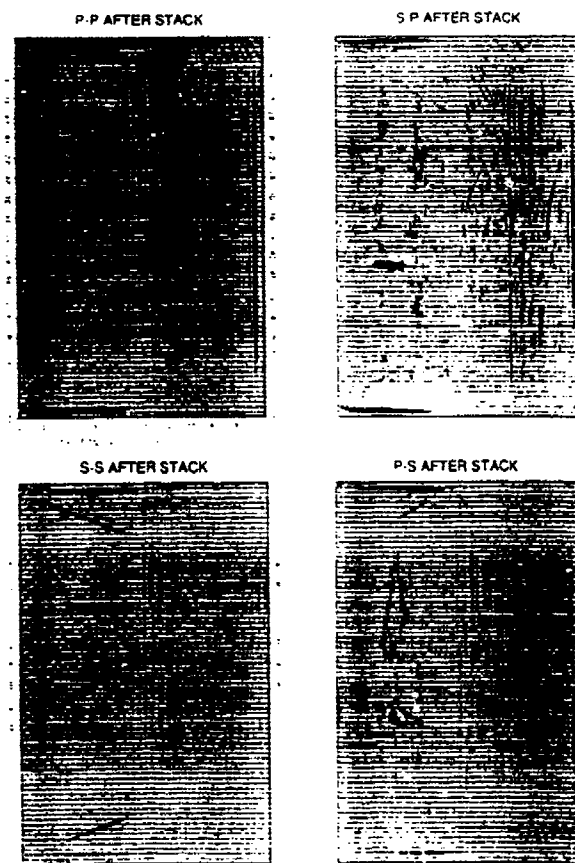


Figure 6.

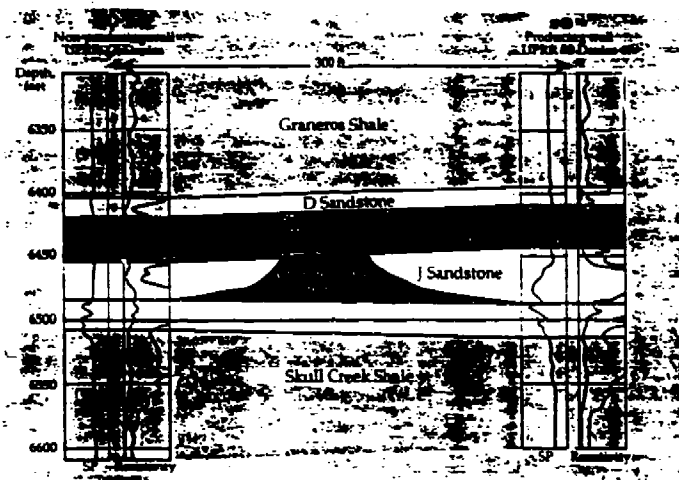


Figure 8:

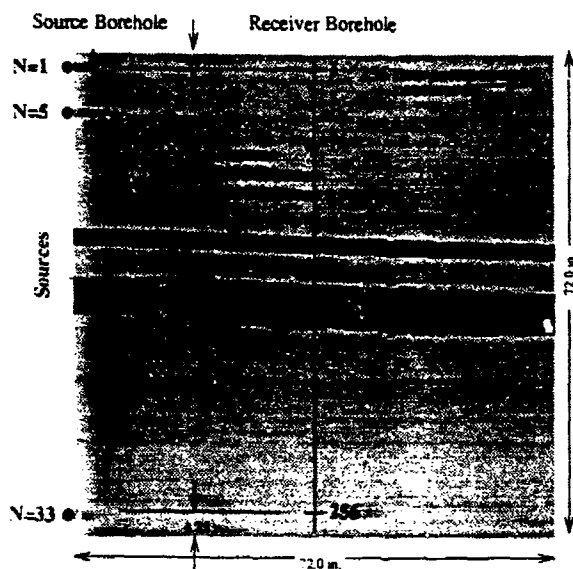


Figure 9.

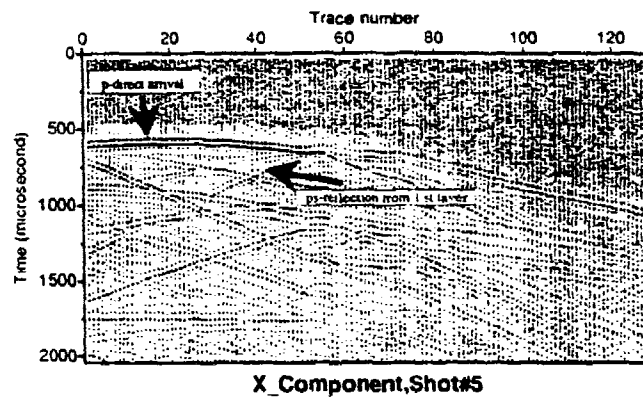


Figure 10.

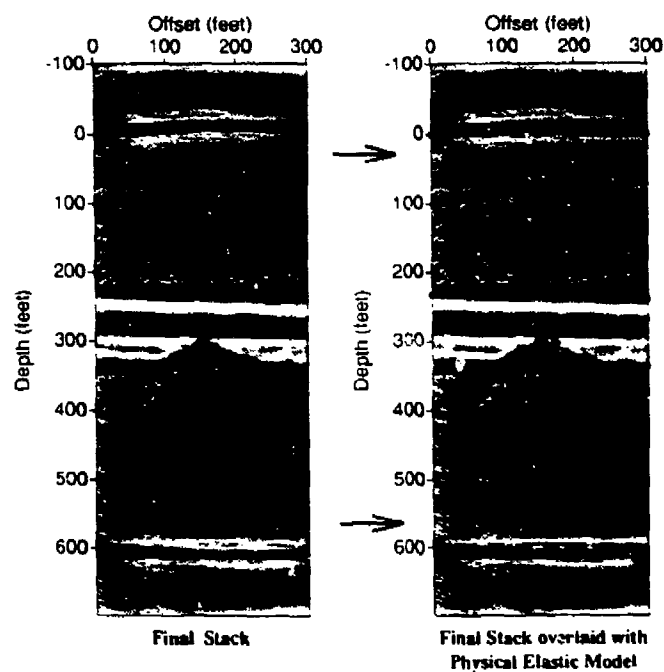


Figure 11.

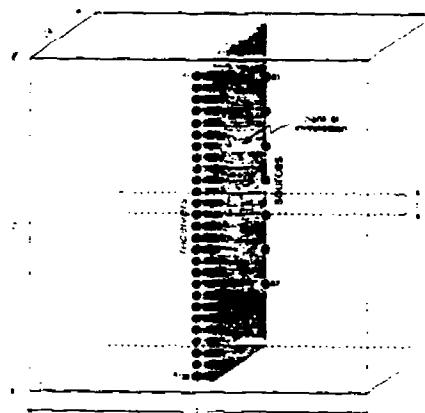


Figure 12.

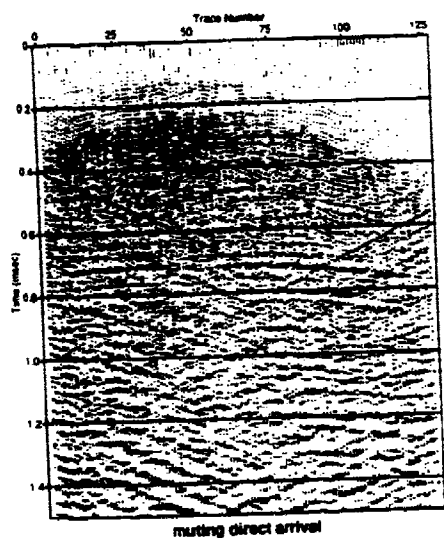


Figure 13.

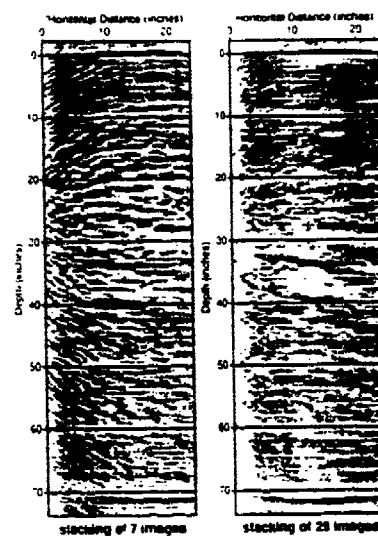


Figure 14.

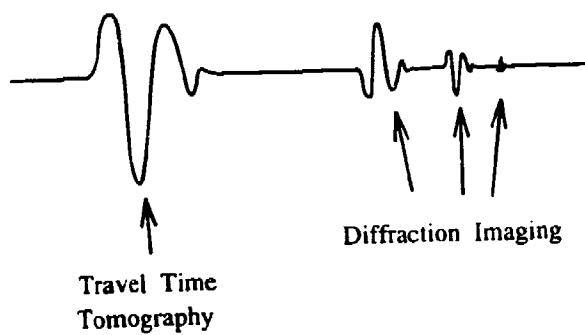


Figure 15.

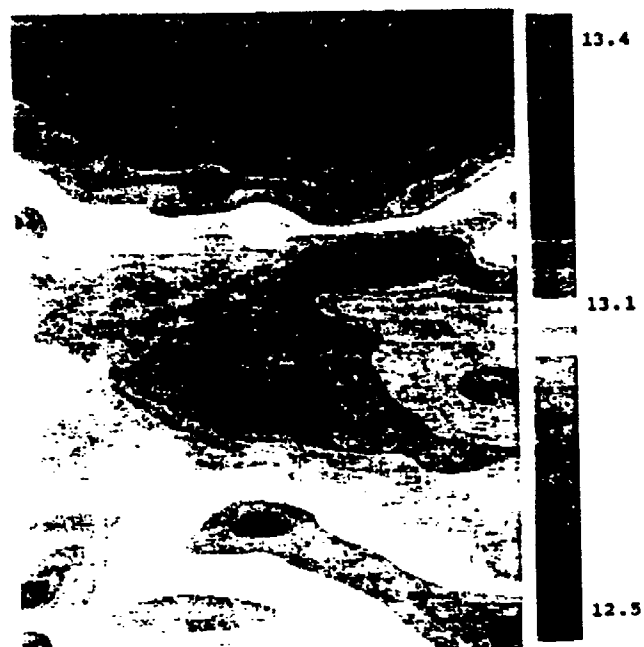


Figure 16.

Digitizing Analog Radar Data

George C. Beasley, Jr.

ENSCO Inc.

Abstract

A high resolution, large scale data storage and processing system for collecting, digitizing, and storing data provided by the GSSI SIR-8 GPR controller has been developed. This PC-based capability is relatively inexpensive, has a considerably more robust user interface, and provides a capability for wider dynamic range data and larger data storage capabilities than any available commercial unit. This system provides the basic data acquisition functionality for obtaining the high quality digital data required to apply today's steadily advancing digital signal processing techniques. It also improves the accuracy of, while greatly simplifying, the burdensome task of capturing the field survey parameters during data collection. Easily manipulated operator selections are provided for describing surveys spanning a diverse suite of GPR problems. Accurately and conveniently conveying the field survey parameters provides the GPR digital signal analyst with improved graphical representation of the data and other valuable information improving the overall efficiency of the analysis task.

Quality digital data and accurate survey information are the essential elements in providing interpretable GPR data. Both these elements were provided from integrating a modern PC-based computer and digitizing subsystem with specialized software generated from years of field data collection experience. The selection of the appropriate PC-based computing platform, including alphanumeric and graphical display capabilities, mass storage, and external input/output interfaces, as well as the analog to digital converter for transforming the analog GPR signals into digital values for storage within the PC's mass storage resources, was a crucial process. Proper specification of the type of operator display, data entry mechanism, and methods for powering the system are critical concerns for field operations. Selection of the A/D converter word size, data acquisition rates, and mass data storage devices and sizes were derived from the operating characteristics of the GSSI SIR-8 GPR controller. The current basic digital field acquisition capability could be easily adapted for application to another controller or to accommodate either more generic or specialized survey scenarios. The generation of such a capability provides the high resolution digital data and accurate survey descriptions needed for enhancing the overall precision and efficiency of the GPR survey process.

Introduction

This paper discusses the approach taken by ENSCO, Inc. to replace an aging, unreliable, and discontinued Geophysical Survey Systems, Inc. (GSSI) DT-6000 tape recorder that was required for digitizing and storing Ground Penetrating Radar (GPR) data from the GSSI Subsurface Interface Radar (SIR)-8 controller. The objectives of the replacement activity were to provide the required digitization of the SIR-8 output, storage for the digitized results, and input and storage of additional survey parametric data. This latter requirement allowed the generation of a new recording system exceeding the DT-6000 capabilities. The new recording system has improved the overall efficiency of field data collection activities and has helped to resolve some commonly recurring analysis problems.

Until the introduction of the system described herein, the DT-6000 was the primary means for acquiring SIR-8 GPR data in the field. Under a previous project, a SIR-8 digitizing capability had been generated using an HP 9000 based table top system with an Infotek Systems, AD200, internal 12-bit analog to digital (A/D) converter; however, this capability was only useful in the laboratory or for data collection activities where standard 115-volt, 60-hertz, AC power and some form of environmental control were readily available. The information gained during the HP-based project provided valuable information on the appropriate connections to the SIR-8 for a foreign digitizing system and also helped in determining the correct timing and sample rate requirements for accurate digitization of the SIR-8 output. This baseline information and the additional requirements for portability and semi-harsh environments provided the basis for the development of the PC-based capability to replace the DT-6000. The resultant system now provides a portable, field data collection system with significant processing power and a software system that can be tailored to a specific application for improving the overall efficiency of data collection.

Problem

To a field data collector, arriving at a survey site with an unreliable digitizing and recording system is worse than the battery power source going dead during a survey. At least, a dead battery provides a noticeable indication of an error and allows the operator to connect a fresh battery and to re-accomplish the survey. With an unreliable recorder, the results may not become apparent until an analysis of the collected data is begun. Unfortunately, at that point, re-accomplishment of the survey may not be an option.

The GSSI DT-6000, portable, quarter-inch cartridge (QIC), digital tape recorder normally used for acquiring and storing SIR-8 GPR data is costly to operate and to maintain in many respects. Ours had reached the point where it was completely unreliable, and had actually become a detriment rather than an asset to our survey capabilities. It had become difficult to predict when and where the next DT-6000 failure would occur. Also, the pre-formatted 65 Mbyte QIC tapes required by the DT-6000 are relatively expensive compared to today's Exabyte tapes (nearly 36 times more storage capacity at about one-third the cost). The physical format of the tapes

used by the DT-6000 is also incompatible with the format required by current data processing workstations. This requires time-consuming data downloads or transfers directly from the DT-6000 to the target analysis system.

Since the SIR-8 controller was still functioning reliably and the DT-6000 had become so unreliable, simple replacement of the DT-6000 seemed to be the only answer. However, our difficult decision to invest in a new DT-6000 was obviated when GSSI discontinued it from their product line. GSSI had already introduced its new and improved SIR-10 GPR system giving them cause to delete the failure prone DT-6000 as a part of the normal product evolution process. Also, the internal QIC tape drive assembly manufactured by 3M had been discontinued from the 3M product line nearly a year earlier.

What choice do owners of the old SIR-8 controller have when their DT-6000 dies? GSSI provides alternative recorders, but none provide improvements over the DT-6000's capabilities. They appear to be more cumbersome to use, and like the DT-6000, provide no means for digital recording of the data collection and site specific information with the collected data. Some SIR-8 owners may solve the problem by replacing their SIR-8 with a SIR-10. While this may be an attractive solution, it may be impossible for the SIR-8 owner faced with budgetary constraints. The SIR-10 does provide an integrated state-of-the-art Exabyte 8mm digital tape recorder which allows about 2.4 Gbytes of storage in the same enclosure with the controller and provides several other enhanced features, but none seem to justify the junking of a working SIR-8 controller.

The need existed to replace the DT-6000 recorder with a modern data acquisition and storage system. The requirements for portability and programmability were very important to the new system. However, there are other critical aspects during data collection related to conducting a proper analysis of GPR data. These aspects deal with recording the total suite of field data information. Field data collection consists of three major types of information. The most obvious of these is the actual GPR data, but information on the operational settings of the GPR controller and the other survey parameters are equally important. Information about the physical characteristics of the collection site is the third type of data required to conduct a proper analysis. Most field data collectors use only a written log to record these latter two types of data. Since they are not physically attached to the recorded data, written logs can become easily confused, misplaced, or totally lost. The inability to retrieve this basic information about the survey at analysis time renders the actual GPR data, by itself, useless. This is especially true if some time lapses between the collection and analysis periods or if the data collection and analysis are not performed by the same personnel.

During the design process of the DT-6000 replacement, strong consideration was given to generating the appropriate requirements for resolving field data annotation problems. The result was the incorporation of requirements for providing a screen oriented input mechanism and formatted storage space for equipment set-up

parameters, survey information, and site characteristics. This information was formatted and stored in a digital format along with the digitized GPR data.

All of these requirements were addressed during the development of a replacement for the old DT-6000 digital tape recorders. The ultimate objective of our DT-6000 replacement effort was to create a SIR-8 controller based GPR system that provided as much as possible of the SIR-10 functional utility with additional enhancements, for the collection and storage of equipment set-up, survey, and site information which are not provided by the SIR-10.

Solution

The solution for a DT-6000 replacement became a PC-based processing system equipped with the appropriate interfaces for accurately acquiring analog and storing digitized GPR data from the SIR-8 controller and for accepting and storing valuable parametric information entered by the operator, describing the survey and the site. This system needed the capability to supply these data to other computing systems for subsequent processing and analysis through direct downloading or by Digital Analog Tape (DAT). The PC-based capability created to fulfill these requirements consisted of two major components. The first was the appropriate hardware to provide the digitization, storage, display, and other interface and processing capabilities. The second was the software to provide the control of the digitizing and storage hardware and the human interfaces for data entry and display. These two components have been effectively integrated to maximize the return on investment of the development.

Hardware

The hardware was selected after careful consideration of the various options available in the current marketplace. An off-the-shelf PC compatible was selected rather than integrating a complete computing system from the board level. The currently available PC compatibles provided a very adequate, basic computing platform for supporting the other PC-bus standard, board level components. This tradeoff of using an off-the-shelf PC was made to allow application of most of the budget toward the development of extensive control software. Since most of the required capability of the new system comes from a PC-bus standard digitizer and portable MSDOS-based software, the actual computer these are incorporated into becomes a relatively independent part of the overall system. Essentially, any 80386 or higher PC-based computer with appropriate processing speed and interface board slots from laptop to tabletop units could provide the required processing functions. As shown in Figure 1, the selected system components for this development are quite robust. Although at first glance they seem expensive, the cost of this system is significantly less than that of creating a similarly capable system from an unpackaged back-plane and a board-level processor.

Dolch Portable Add-in Computer (P. A. C.), 486-33C
 8 Mbytes of Random Access Memory
 Sharp Thin Film Transistor (TFT) Flat Panel VGA Color Display
 VGA Display adapter
 Fujitsu M2624-FA, 513 Mbyte SCSI Hard Disk Drive
 1.44 Mbyte 3.5 inch Floppy Disk Drive
 Adaptec AHA-1542B SCSI and Floppy Disk Controller
 Hewlett Packard External, Portable Digital Analog Tape (DAT) Deck
 Analogic HSDAS-16 Analog to Digital Converter
 Ethernet Interface
 Multi-Function Parallel, Serial, and Game Port Card
 Track-ball Cursor Controller
 Mini 200-watt, 12-volt DC to 115-volt AC Inverter
 Portable 200-Amp-hour, 12-volt Battery System

Figure 1. List of System Hardware

Each of the hardware components was specifically selected to enhance the overall integrated system. The Dolch computer is a very compact system that also provides the physical enclosure for the 1.44 Mbyte, 3.5 inch floppy disk drive and the SCSI 513 Mbyte hard drive. Its internal two half-length and four full-length board slots provide the physical location for the VGA adapter, the multi-function parallel, serial, and game port, the SCSI and floppy disk controller, the A/D converter, and the Ethernet interface with one full-length slot to spare. The 8 Mbytes of RAM are mounted in sockets provided on the motherboard. The TFT flat panel VGA color display is permanently attached to the front of the lunch box style enclosure and is protected by the snap-on keyboard assembly during transit.

All connections to the SIR-8, external DAT tape unit, trackball, keyboard, and the Ethernet are made on the left side of the Dolch computer enclosure. Power is supplied to an AC connector at the back near the power switch. The complete computer assembly consumes less than 160 watts of 115-volt AC power which is easily supplied by the mini DC to AC inverter when in the field. Under field operation, the system, including the SIR-8 controller, consumes about 25 to 30 amps from the 12-volt DC source.

The DC source is a highly portable, dual 100 amp-hour battery system also developed by ENSCO. This battery system is mounted in a rugged shipping container and has the capability of being configured as a 200 amp-hour 12-volt DC supply, as 100 amp-hour plus and minus 12-volt DC supplies, or as a 100 amp-hour 24-volt

supply. A panel in the container provides the DC output connectors and two meters; one for monitoring voltage and the other for monitoring the output current of the selected battery. Each of the two batteries are monitored for a voltage level that can be set by the operator. When either battery drops below this level, a dual tone alarm sounds. This battery system has proved invaluable for powering the SIR-10 since the SIR-10 shuts down without warning and can lose valuable data when the input voltage drops below about 10.6 volts. The mini inverter used with the PC-based, DT-6000 replacement automatically provides a warning alarm before it shuts down due to low battery input voltage. This alarm allows an operator enough time to orderly exit the system, turn off the power, and replace the battery supply before continuing the survey. The only disadvantage of the current battery system is that it weighs nearly 170 pounds. However, this is a small inconvenience to have eight hours of data collection time available from a single rechargeable battery system.

The Sharp TFT, flat-panel, color display provides a striking color capability for the alphanumeric display parameters in the set-up menus and to the graphical display of waveform data as it is being collected. The ability to use colors when displaying data greatly improves the utility of the system. The colors provide quick recognition of control settings and data attributes. The display is very bright and has little persistence making it viewable in bright sunlight with minimal shading of the screen.

The Analogic HSDAS-16 A/D converter was selected for its reliability and the additional capabilities it could provide for more demanding A/D conversion requirements of potential future projects. This converter is capable of digitizing up to 16 channels. Internally, these 16 channels are connected to a sixteen-to-four multiplexing analog switch array. This array feeds four high-speed instrumentation amplifiers, each driving a 100 Khertz sampling A/D converter. Several modes provide various numbers of input channels at different maximum rates. The highest sampling rate for one channel operation is 400 Khertz, but the SIR-8 only requires about 51.2 Khertz for digitizing its raw data output. A second channel of the A/D could have been connected to the SIR-8 processed data output, but with the capabilities of the system there was no apparent need to acquire data from this source.

The A/D is essentially a self-contained data acquisition system. After programming the A/D with the appropriate commands and commanding a conversion to start, the A/D will wait for the Start of Scan signal from the SIR-8 and begin the digitization at the rate selected by the operator. The digitization rate changes according to the Scans per Second setting on the SIR-8.

The SIR-8, like most short-pulse GPRs, uses a down-sampling approach where the controller takes only one sample of the returned RF energy at the receiving antenna for each pulse transmitted. The timing for each of these samples is determined by the time-range set on the SIR-8 controller. This essentially provides a factor of 256 to 1024 reduction in the required sampling rate. The reduction is based on the number of samples that have been selected to compose a GF signal or scan. Without this approach, which is heavily dependent on the me-

target remaining in a stationary state, the sampling rates required to directly sample the RF energy could reach into the Ghertz for higher frequency antenna systems.

Since the SIR-8 does not automatically supply the recording system with information on the position of its Scans per Second control, the operator must provide this information to the recording system prior to initiating a data collection. The signal being digitized is actually the analog reproduction of the digitized samples the SIR-8 acquired during the down sampling process. The output from the SIR-8 is provided by an 8-bit D/A converter. This makes the 16-bit capability of the HSDAS-16 A/D converter seem like a considerable overkill; however, considering the potential of future uses for the new data acquisition system, the small additional investment in higher digitizer capacity for this application provides significant economy for future projects.

The portable Hewlett Packard DAT tape deck provides an excellent backup capability for the 513 Mbyte SCSI hard disk and provides an external path for the transfer of collected data. The deck is a SCSI device which is compatible with most of the current workstations used for data analysis. DAT tapes, depending on their physical length, can hold up to 2.4 Gbytes of data. This means that one tape can hold nearly five times the amount of data the internal SCSI disk can hold. During data collection, if the SCSI disk becomes full it can easily be dumped to the DAT tape while on site and the collection can continue.

The Ethernet interface allows data to be directly transferred from the hard disk in the Dolch computer via a coaxial cable network to an analysis workstation. The method currently used to transfer the data via Ethernet is through an FTP binary transfer. This method is relatively fast and accurate and maintains data file compatibility to any workstation on an Ethernet network.

Software

The software for controlling the digitization of the GPR controller output and for storing the resultant data on the large SCSI disk was written in the "C" programming language. The control program resides on the computer system as a single .EXE file and consists of three major parts. The first part is the A/D set-up and data collection routines. These were adapted from routines supplied by Analogic with the A/D converter. The second part is the graphical display routines. The third is the alphanumeric parameter input and display routines. When integrated, these parts are seen by the operator as three primary display screens. The first screen provides the interactive menu for establishing the current SIR-8 settings and for the entry of control information for the two graphical display screens used to display the collected GPR data. The second screen provides the display of a signal waveform immediately after acquisition from the SIR-8. This screen mimics the CRT on the SIR-8 and is very useful for setting the gain controls of the SIR-8 prior to data collection. The waveform display response is fast enough that the operator perceives no apparent delay between successive changes to the SIR-8 control inputs. This screen can also be used during data collection. The collected waveforms are displayed sequentially, one

at a time. The third screen provides a waterfall display of a complete data collection. It can be set to stack a predetermined number of scans and to display only the resultant stack or to display the actual raw data waveforms as acquired. For excessively long collections, the raw data display may become very crowded. A screen scrolling feature has not yet been implemented.

The data storage format emulates the current SIR-10 format. Files of this format are written directly to the hard disk. The SIR-10 format consists of a header block containing some of the equipment settings and a text field followed by the data block containing the actual waveform records. To implement this format, SIR-8 attributes which match those of the SIR-10 are placed in the appropriate positions of the header block and the collected scans are written to the data block. An additional parameter block was appended to the file. This block contains all the information entered by the operator that did not have a corresponding place in the header block. This latter block is the enhancement allowing information on the survey and site parameters to be included with the collected data. By following the SIR-10 format, all current analysis software that processes SIR-10 data should be able to process SIR-8 data acquired by the new system.

The software was developed on the Dolch computer to minimize the potential integration impact of porting the software from another development station. It was written modularly, considering the general requirements for GPR data collection, but it could be easily modified to implement any type of specialized data collection.

Conclusion

The replacement for the DT-6000 has provided new life to the SIR-8 and renewed consideration to applying it to various GPR survey problems. The current hardware and software have been integrated very effectively. The result is a highly effective replacement for the DT-6000 with significantly higher reliability and a system that is much easier to operate. Plans are being formalized to integrate the software of this system with a specialized set of Windows-based GPR analysis software currently under development. This new analysis package provides an extensive suite of GPR data processing and includes capabilities for stacking, filtering, hyperbolic move-out tracking, etc. With the merging of these two capabilities, an extremely portable, field deployable, PC-based GPR data collection and analysis capability will become available.

References

Adaptec Inc., 1990, AHA-1540B/1542B User's Manual, Milpitas, CA.

Analogic Corporation, 1990, PC-Based Data Acquisition Systems User's Manual, Wakefield, MA.

Dolch Computer Systems, 1991, P. A. C. Portable Add-in Computer Operating Manual, Milpitas, CA.

Fujitsu, Disk Drive Installation Guide, Revision 003.

Geophysical Survey Systems Inc., 1987, SIR System 8 Operation Manual, Hudson, NH.

Geophysical Survey Systems Inc., 1986, Model DT-6000 Tape Recorder with Model 200 Analog Interface Module Manual, Hudson, NH.

**Electromagnetic Data Evaluation Using a Neural Network:
Initial Investigation—Underground Storage Tanks**

**Darrin Cisar and John Dickerson,
Chem-Nuclear Geotech, Inc., Grand Junction, Colorado
and
Timothy Novotny, Mesa State College
Grand Junction, Colorado**

Abstract

Environmental and engineering studies utilize multiple methods of investigation with an *integrated geophysical approach*. This complicates data interpretation because while integrating data collected by a single method is no simple task, that of integrating multiple data types is even less so. Traditionally, simple analytical and numerical models have been used to interpret geophysical anomalies. However, interpretive models for the types of objects frequently encountered at environmental restoration sites have not been available. Simulating environmental targets as mineralized ore bodies has been our only available capability. This is neither cost- nor labor-effective and is wholly inappropriate for cultural artifacts.

Artificial intelligence neural network concepts can be applied to these processes of discriminating anomalies of interest from the host matrix. Neural networks are taught the defining response parameters for a particular archetype. The trained network is then used to interpret geophysical data anomalies relative to the response characteristics of the archetype.

For our investigation, frequency-domain electromagnetic (EM) data from known test configurations were used to train a neural network to discriminate underground storage tanks. The trained neural network was then used to "interpret" EM data collected at Hickam Air Force Base, Hawaii. The results were compared with known "ground truth" excavation information to determine the accuracy of the performance of the neural network.

The program demonstrated that artificial intelligence concepts can facilitate interpretation of geophysical anomalies. In addition, the neural network offers the potential of truly integrating collected data sets. The current state of the art of integrated interpretation is to overlay separate interpretations of the multiple methods employed and derive a "best fit" conclusion from this collage. The neural network provides a means of integrating the separate data sets in either a multiple (parallel) or a stepwise (serial) integral response.

Introduction

Traditionally, simple analytical models and more complicated numerical models have been used to interpret geophysical anomalies. However, interpretive models for slingram-type electromagnetic (EM) responses relevant to the types of objects that are frequently encountered during geophysical investigations at environmental restoration or other geotechnical sites are not available. A process of approximating EM relationships by simulating discrete environmental targets as large mineralized ore bodies has been our only current capability. This method is neither cost- nor labor-effective and is wholly inappropriate for cultural artifacts that are roughly the same dimensions as the EM arrays used to collect field data.

For environmental and engineering studies where the geophysical responses are derived from mixed target types, it is common to utilize multiple geophysical methods of investigation. These data are analyzed and interpreted through an *integrated geophysical approach*. This multi-technique approach compounds the problem of interpreting a large volume of data because the process of integrating the data collected by a single method is no simple task, and that of integrating multiple data types is even more difficult.

Interpretation of geophysical data is better accomplished through physical modeling of the expected response for a given anomaly source and computer-assisted comparison of the field data to numerical model responses. Microprocessor artificial intelligence concepts can be used to augment the interpretation of the complexly interrelated field data acquired during geophysical investigations through application of neural networks to the processes of discriminating anomalies of interest from the host matrix.

The neural network simulates the "learning" function of the human brain and is taught the response parameters for a particular target archetype by an iterative process of feedback. The trained network can then be used to interpret geophysical data anomalies relative to the response characteristics of the archetype. This use of a neural network offers the additional potential of truly integrating the collected data set. The current state of the art of integrated interpretation is to overlay separate interpretations of the multiple methods employed. A "best fit" conclusion is then derived from this collage. The neural network provides a means of actually integrating the separate data sets in either a multiple (parallel) or a stepwise (or serial) integral response.

Background of Neural Networking

The structural basis for artificial intelligence neural networks is the human brain. However, the information manipulation processes of the brain are mostly unmapped—information is processed through a network of dendrites, neurons, and axons. These work interactively to produce "learning." Inputs connected to millions of dendrites are in turn connected to millions of neurons. The neurons have only one axon (output), but that one axon could connect to another dendrite, which could connect back to the original neuron or to other dendrites and neurons.

The backpropagation and forward propagation operations of neural networks are analogous to the psychological Test-Operate-Test-Exit (TOTE) model of brain function use of feed back and feed forward. The bias portion of the model is simulated by a sigmoid function in the neural network that optimizes the information manipulation; the sigmoid transfer function is $1/(1 + e^{-L_{nn}})$. Figure 1 is a diagram of the modern TOTE model.

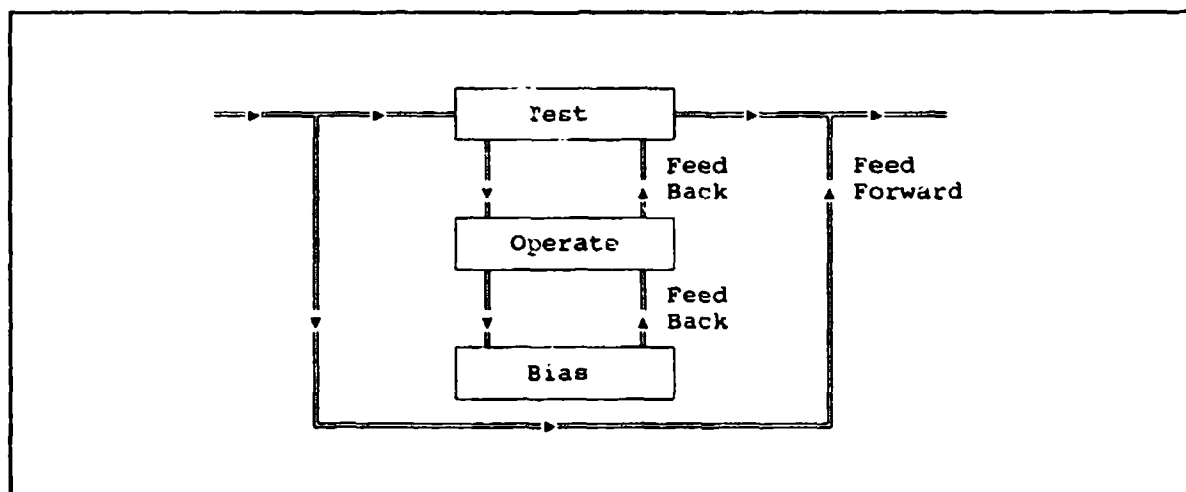


Figure 1. TOTE Model of Human Brain Functions

Neural networks replicate these brain processes by information layering. Neural networks generally have at least three layers: an input layer, a hidden layer, and an output layer (Figure 2). The number of layers can be increased by adding hidden layers. In each layer, there is a series of nodes that define information or the transfer of information. Extra nodes in the input and hidden layers allow one input and one hidden node to be always true, or equal to 1. The number of hidden nodes is usually half the number of input nodes.

Data are processed in a neural network by backpropagation and forward propagation operations. However, before backpropagation and forward propagation can be performed, training sets must be created. The sets of training points are the instructional media used to teach the neural network to discriminate a target response from the background field. These sets are a collection of data that are definitive for the target type. The number of training sets may vary, but in general, the more training sets there are, the more efficient the neural network will become.

Teaching is accomplished by an iterative random selection and backpropagation process. For each iteration, a sigmoid function generates and assigns a weighted value (w) to each training point (Figure 3). Subsequently, these weights are adjusted through a series of normalizing operations that set the training values between 0 and 1 each time the training set is randomly processed until the desired output efficiency is attained. The function produces a damping effect to allow values that are close to "correct" to remain relatively unchanged.

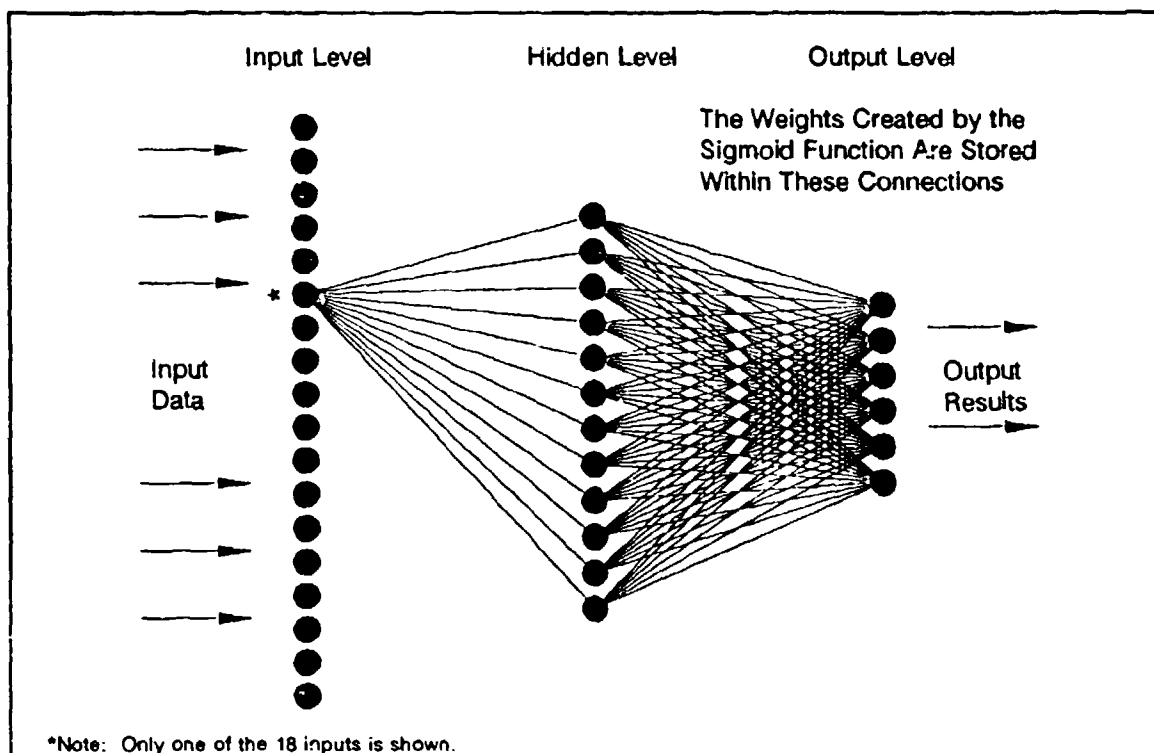


Figure 2. Information Flow Process for the Neural Network

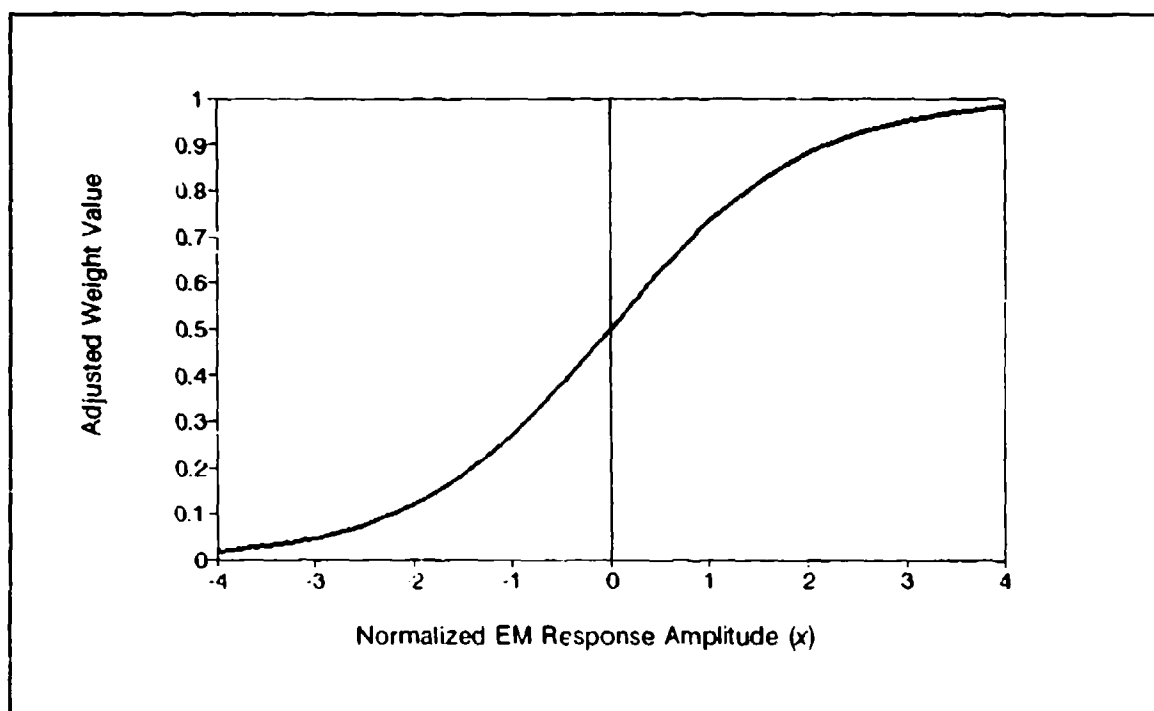


Figure 3. Sigmoid Transfer Function for the Neural Network

Forward propagation allows input data to flow through the network without changing the weighted values. Backpropagation compares the results produced by forward propagation with the optimized learned value (0 or 1, extremes) and adjusts the values positively or negatively to approach the correct value. The propagation methodology is

Input Level → Hidden Level

$$\Sigma(xw1) = x_1w1_{1,1} + x_2w1_{1,2} + \dots + x_nw1_{1,n}$$

$$f[\Sigma(xw1)] = H_i;$$

where

H_i = Hidden Node,
 x = Input Variable,
 $w1$ = Stored Weights, and
 $f[]$ == > Sigmoid Function.

Hidden Level → Output Level

$$\Sigma(Hw2) = H_1w2_{1,1} + H_2w2_{1,2} + \dots + H_nw2_{1,n}$$

$$f[\Sigma(Hw2)] = O_i;$$

where

O_i = Output Node,
 H = Hidden Node,
 $w2$ = Stored Weights, and
 $f[]$ == > Sigmoid Function.

The training process could take as few as 300 iterations or it could take as many as 6,000. The dependent variable is the required output reliability. A larger number of iterations does not necessarily mean the output will become more reliable. Selection of the best number of iterations for sufficiently training the neural network is arrived at by a heuristic approach. To determine neural network efficiency, a known data set is run through the network with the output displayed on a computer monitor. If the visual representation is correct when compared to the known information, then the neural network is considered to be "correctly" trained.

Before backpropagation can proceed, the values for input, hidden layers, output, and training level must be known. The training level is a value (η) between 0 and 1 that indicates the amount of damping that should occur within the sigmoid function. This allows the user to control the level of learning within the neural network. As η approaches 0, the output definition increases.

Setting η closer to 0, however, also increases the required training time. The goal is to set η at a "reasonable" level on the basis of how many input, hidden, and output nodes exist.

Once η is established, length of "training" can be interactively set (default is 10^6 epochs). An epoch is one complete iteration through the total number of training sets. For example, if there are 500 training sets, then one epoch equals 500 training sets. A "training set" is the collection of information points that relate to the response characteristics processed by the neural network.

Prior to propagation, the learning weights are randomly set to be between -0.5 and 0.5 and are stored within the network to maintain continuity prior to training. The training process continues until the desired number of epochs has been reached. The generated weights are saved to a file that will be used for data interpretation.

The training components include input nodes, hidden nodes, output nodes, η , propagation, backpropagation, a sigmoid function, and program procedures. The input nodes are information points that relate, one to one, with each of the training sets. Each input node connects to every hidden node. This connect structure is where weighted values are stored. The hidden nodes also connect to the output nodes (each hidden node connects to each output node). These connections are used in the same way as the connection between the input and hidden nodes (to store the calculated weights). The hidden nodes are not directly affected by input (or output) values but affect a bias in the input/output data manipulation.

Backpropagation changes the weighted values between the output nodes to the hidden nodes, and between hidden nodes to the input nodes. This is accomplished through a series of manipulations between the output node and the hidden node, and then between the hidden node and the input node.

In the first location, backpropagation is adjusting the weight set $w2_{ij}$. The formula for the adjustment of $w2_{ij}$ is

$$w2_{ij} = w2_{ij} + (\eta)(H_i)(D2_j),$$

where

$$D2_j = (O_j)(1 - O_j)(CO_j - O_j),$$

CO_j = the value assigned (0 or 1) by the program based on the key components of the desired learning object.

In the second location, the values are not acquired quite as easily, but notice that the value of $w2_{ij}$ does appear in both formula locations because there is a need to know what happened to $w2_{ij}$ to allow any adjustment to $w1_{ij}$. Therefore, $w2_{ij}$ must affect $w1_{ij}$, based on the output value from forward propagation.

D1, initially set equal to 0, becomes

$$D1_i = D1_i + (D2_j)(w2_{ij}).$$

Once $D1_i$ has been determined, the adjustment to $w1_{ij}$ can proceed. $w1_{ij}$ is manipulated through the equation

$$w1_{ij} = w1_{ij} + (\eta)(x_j)(D1_j).$$

Possible values for D1 and D2 are shown in Figure 4.

The output nodes are the final destination for data manipulation and connections that originate from the hidden nodes, with every hidden node connecting to each output node. Output values range between 0 and 1, with the largest value being the "best fit" for that location. This value is an indication from the neural network of how "true" it "thinks" the value should be considered.

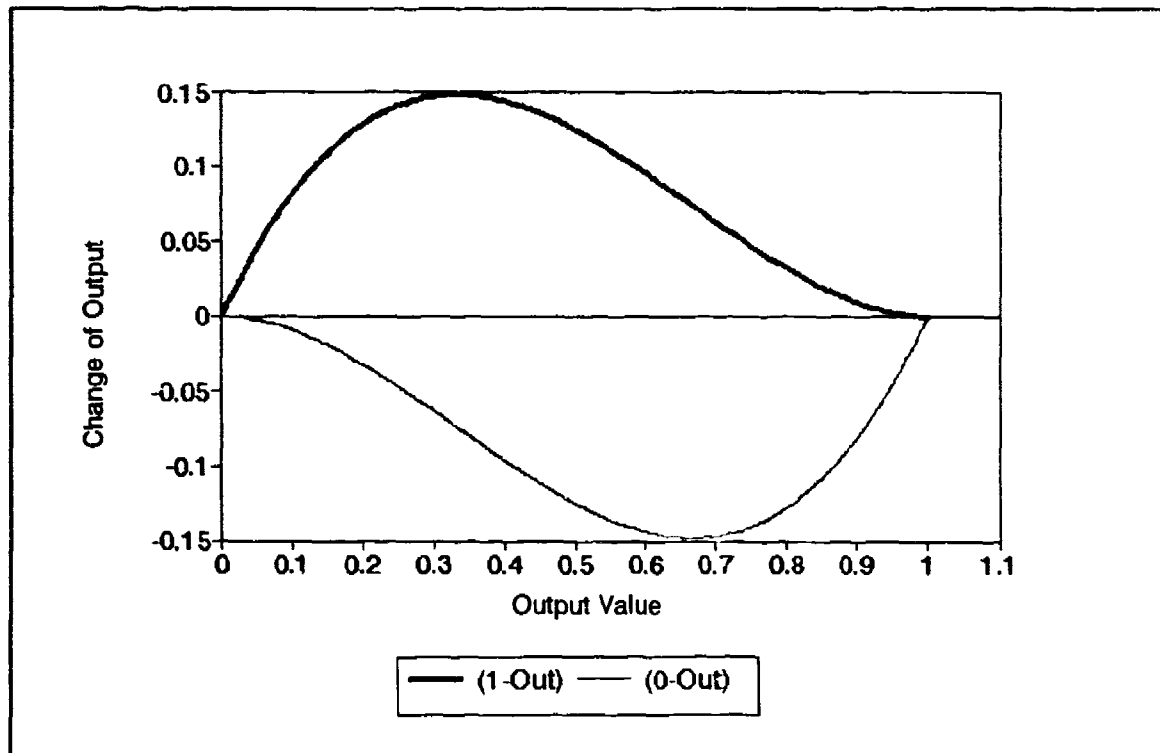


Figure 4. Possible Values of Output[i] from Backpropagation

Method of Investigation

A nonconductive gantry was used to collect slingram-type frequency-domain EM data in a free-space geometry that allowed geologic and cultural contributions to the instrument response to be mathematically removed. Each target of steel culvert pipe was drawn beneath a Geonics, Limited EM-31DL instrument mounted on the gantry. Readings were taken at three heights above the targets with the axes of the cylinders both parallel and orthogonal to the transmitter/receiver array. Measurements were made at 3-foot intervals over a "survey distance" of 96 feet as each target was pulled under the instrument.

The data consist of the conductivity (quadrature X constant) and inphase components of the EM response. The interrelationships of these data relative to target parameters and survey geometry suffice to define the EM anomaly attributable to the conductive cylinder. These data were used to create training sets for a neural network.

The initial training set consisted of quadrature and inphase measurements for both the vertical dipole (VQ and VI) and the horizontal dipole (HQ and HI) at three sequential measurement distances from the center of the instrument array. Each training set accordingly contained 12 measurements. For the 96-foot distance, there were 42 sets for each target/instrument array geometry when using a "6-foot survey interval." To illustrate, a training set could be described by

-48 ft HQ HI VQ VI
-42 ft HQ HI VQ VI
-36 ft HQ HI VQ VI.

The values

-42 ft HQ HI VQ VI
-36 ft HQ HI VQ VI
-30 ft HQ HI VQ VI

describe a subsequent (but not necessarily sequential) training set, as would

-45 ft HQ HI VQ VI
-39 ft HQ HI VQ VI
-33 ft HQ HI VQ VI.

Two target/instrument array orientations were used to collect the training set data: 1) cylinder axis and instrument parallel to "survey direction" and 2) cylinder axis parallel and instrument

array normal to survey direction. This resulted in 504 training points for each height above the target, with the number of input, hidden, and output nodes set at 12, 30, and 2, respectively.

The neural network was producing promising results with these initial settings for data collected at 2-meter spacings. To improve the output results, the number of outputs provided and the number of input parameters accepted were changed. The number of input nodes was increased to 18, the number of output nodes was increased to 6, and the number of hidden nodes was decreased to 12. These changes were prompted by efforts to add ratios of the conductivity and inphase responses for both the vertical and horizontal EM loops. Two additional information points were added to the three existing points in the input level. The input level is now in the form

VC	}	This is one point of three in the input level. (18 input nodes)
HC		
VI		
HI		
VC/VI		
HC/HI		

A second improvement to the neural network efficiency was accomplished by defining training sets on the basis of depth to target (Z). This change also required an increase in the number of training sets and output nodes. The increase in outputs allows better definition of the visual display. With better definition, the responses are visually more appealing and can be quantified with a "best fit" derived from the actual numeric output. The additional outputs provide displays for responses with the axes of the instrument array and the target parallel or perpendicular at $Z = \{4 \text{ feet}, 8 \text{ feet}\}$. These were added to the parallel and perpendicular axes displays for $Z = 2 \text{ meters}$. The result is greater resolution of the field data.

Changing the number of output nodes required a change in the number of training sets. The present number of training sets is now 126 for 2-meter survey spacings. These modifications necessitated re-examination of the efficiency in the number of hidden nodes. A trial-and-error strategy for finding an efficient neural network resulted in the adjustment of the number of hidden nodes from 30 to 12. The increased number of inputs to the neural network improved target discrimination while decreasing effects from geologic *and* cultural noise. The additional outputs provide an enhanced representation of the data and permit differences in target depths to be distinguished.

At present, the number of iterations, or the length of time the neural network is given to "study" the data, is arbitrarily selected. Visual presentation of field data is accomplished in four graphical displays that appear on the monitor.

The first three displays relate target probability and depth to a cubic icon. The program assigns a cubic icon with a dimensional value proportionate to weights assigned by the neural network.

As with the training of the neural network, this is a random iterative operation and the assigned weights are continually adjusted with each pass through the network. The icons are mapped to the computer video screen as three-dimensional blocks corresponding to the survey grid used to obtain the EM survey data. The blocks provide a weighted visual presentation of the anomalous responses. The fourth display represents the "best fit" with respect to the depth and direction. Each block represents a coordinate of the field data with program-assigned color that is based on the "best" output value. Within each block the best output value, depth, and direction are displayed numerically. The output value has an accuracy of three decimal places and is displayed without the decimal and all leading zeros.

Field Trials

During the summer of 1989, frequency-domain EM data were collected at Hickam Air Force Base, Hawaii, to determine if underground storage tanks were still in place at several sites on the base and, if in place, to map those locations. These data were used as the field trial data for the neural network. The data were reformatted and processed by the neural network program developed for our investigation. The program segregated the field data in "windows" comparable to the training set data used to instruct the neural network to discriminate underground storage tanks. Each segment was tested by the neural network to determine whether the data were associated with an EM response component measured with the survey array parallel or perpendicular to the long axis of an anomaly caused by a conductive cylinder.

Discussion of Results

Quadrature and inphase data collected at Hickam Air Force Base are shown contoured in Figures 5 and 6. Using these maps, an experienced observer should have no trouble in determining the presence and location of existing underground storage tanks. How does the neural network application compare with the processes and conclusions made by geophysicists? The iconograph produced by the neural network program is shown in Figure 7. This presentation agrees quite well with the visual interpretations made from the quadrature and inphase contour maps.

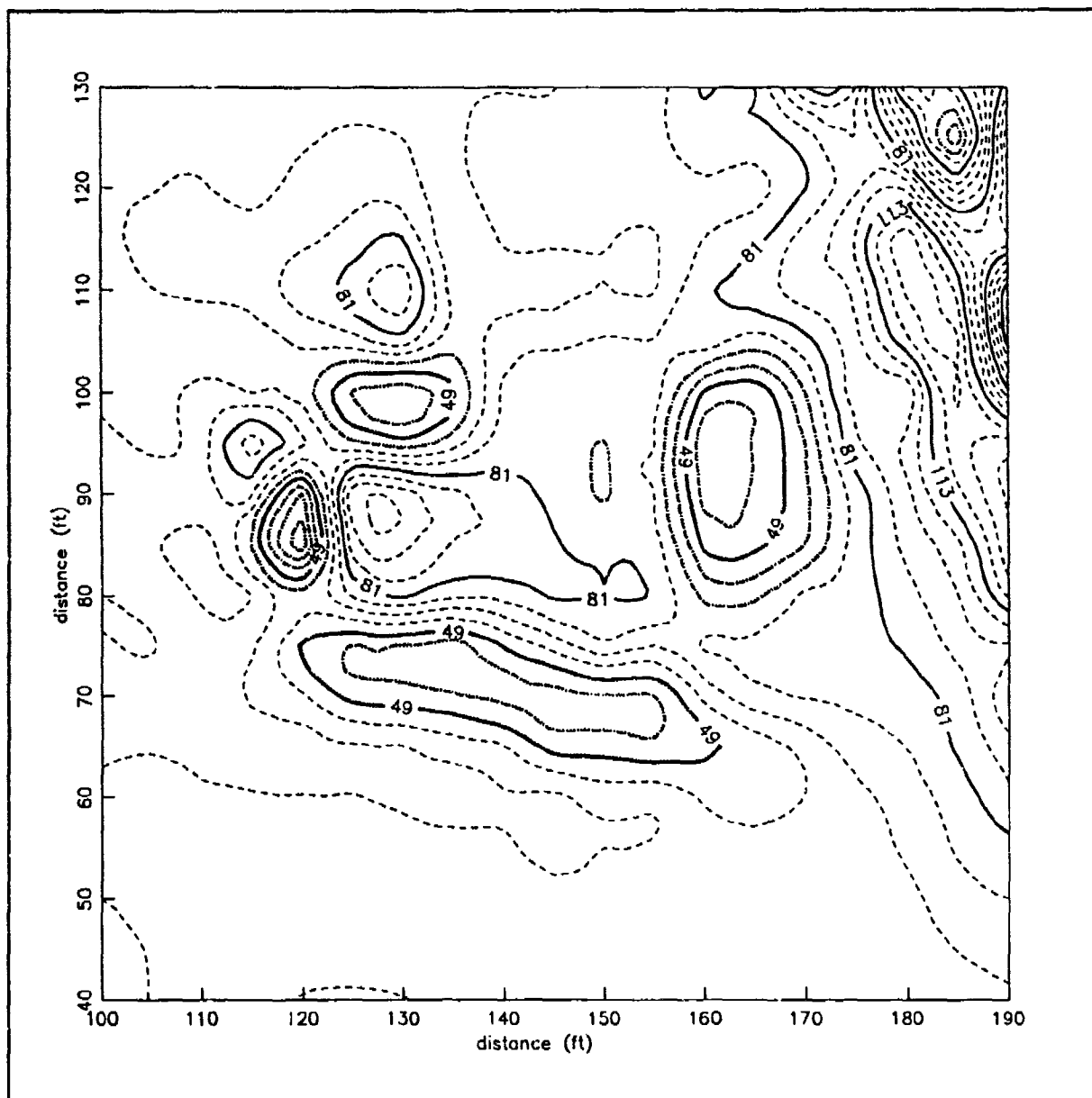


Figure 5. Conductivity Contour Map—Hickam Air Force Base, Hawaii (Contours in Millisiemens per Meter)

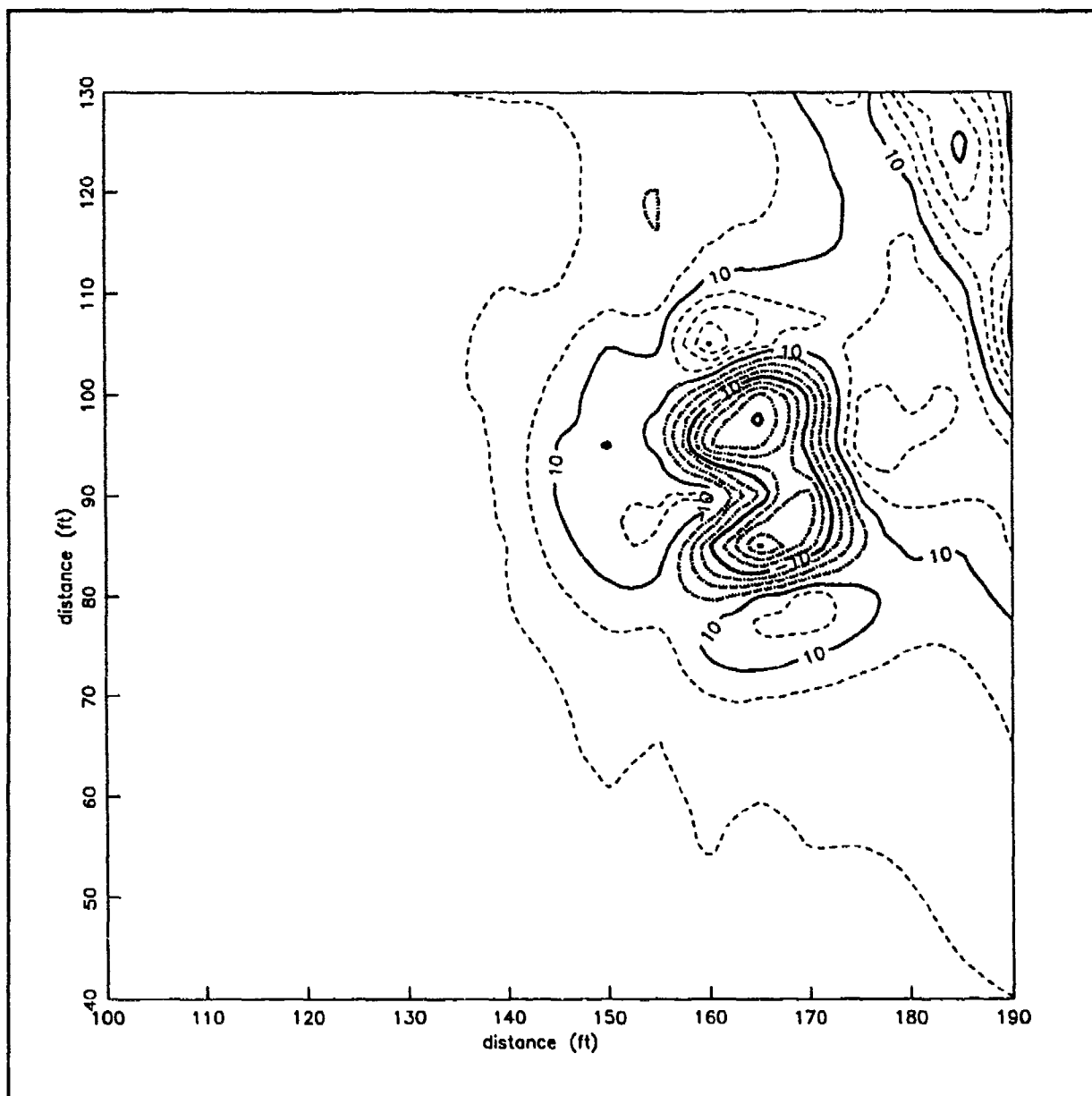


Figure 6. Inphase Contour Map—Hickam Air Force Base, Hawaii (Contours in Parts per Thousand)

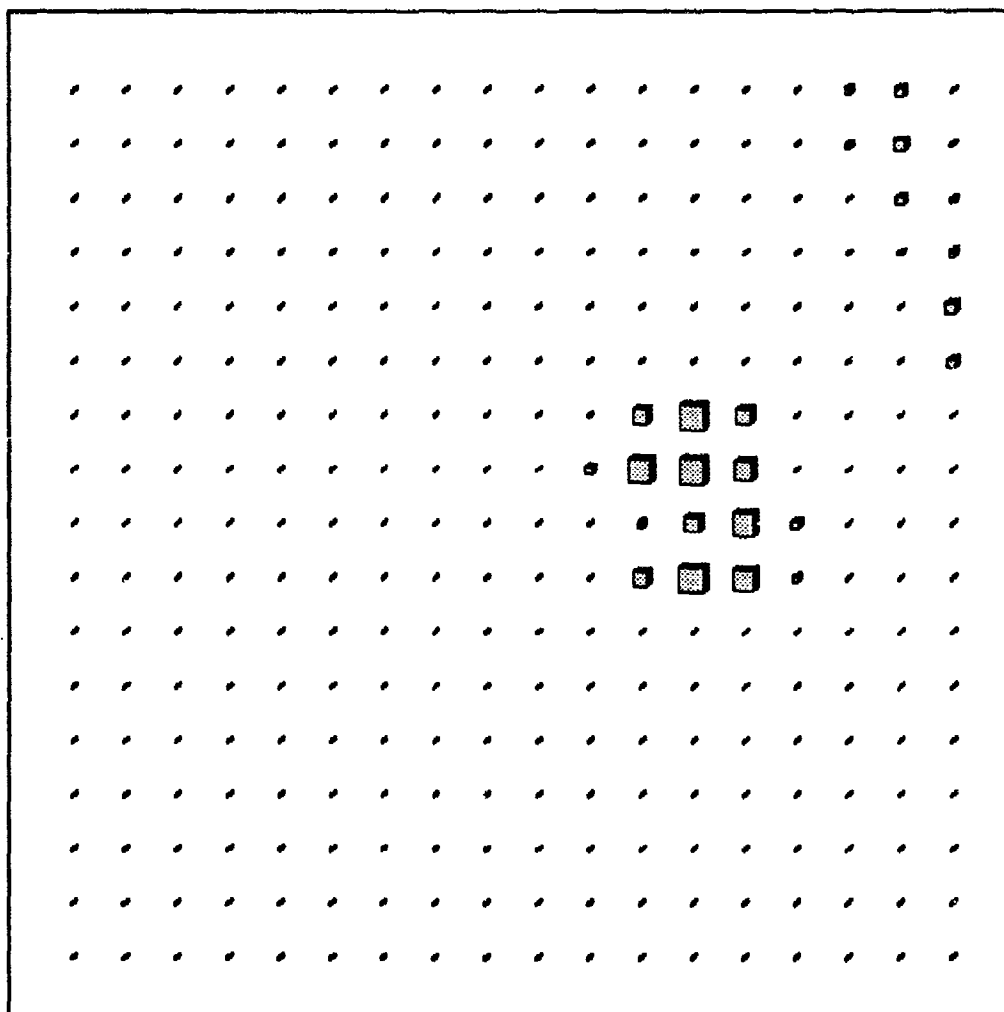


Figure 7. Iconograph Produced by the Neural Network Program

Conclusions

Artificial intelligence concepts do facilitate interpretation of geophysical anomalies. A properly trained neural network can be used to interpret geophysical data anomalies relative to the response characteristics of an archetype. The neural network can integrate data sets in either a multiple or stepwise integral response without requiring a visual collage. It can be a productive time-saver, and perhaps most significantly, the neural network is an expandable process.

To fully develop an automated neural network integration of several geophysical data types, the program should be modified to accept the additional input parameters. In addition to the separate EM response parameters used for this investigation, ratios between these data and other

data types can be integrated into the training set. The basis for such integration would be incorporation of the differing responses of several geophysical methodologies to a like set of physical parameters (e.g., survey geometry, target dimensions, target composition). Adding magnetic data would allow discrimination of ferromagnetic sources; adding time-domain data would increase the number of EM frequencies considered and could provide information regarding target depth and possibly target composition.

A statistical analysis of the neural network results remains to be performed. To accomplish this analysis, multiple sets of known field data will need to be processed through the neural network. The result of each run must be augmented with as much visual and numeric data as possible. A statistical analysis will yield a confidence interval for the neural network output, providing an evaluation of current program performance and direction for future neural network development.

Acknowledgements

We would like to thank the following Mesa State College students and professor for their participation and contributions: *Karl Castleton*, who contributed to the neural network programming; *Juli Stamm, John David, and Craig Jones*, for their assistance in editing and reviewing the work; *Norman Masters*, for his assistance in generating the graphics; and *Professor Tom Mourey*, who clarified the methods for use of neural networks for application to geophysical data sets.

This work was performed under the auspices of the U.S. Department of Energy, DOE Contract No. DE-AC04-86ID12584.

References

- Eberhart, R. and Dobbins, R., 1990, "Implementing a neural network in C: part 1 and 2," *The Micro Technical Journal Micro Cornucopia*, January-February 1990 and March-April 1990.
- Glees, P., 1988, *The human brain*, Cambridge University Press, Cambridge Mass.
- McClelland, J. L., Rumelhart, D. E., and the PDP Research Group, 1987, *Parallel distributed processing: Explorations in the microstructure of cognition volume 2: Psychological and biological models*, MIT Press, Cambridge, Mass.
- Pribram, K. H., 1971, *Languages of the brain: Experimental paradoxes and principles in neuropsychology*, Brooks/Cole Publishing Company, Inc.

TIME-FREQUENCY REPRESENTATIONS APPLIED TO ANALYSIS OF HOLE-TO-HOLE ELECTROMAGNETIC DATA

B.M. Duff and B.J. Zook
Southwest Research Institute

I. INTRODUCTION

PEMSS data is first analyzed by examination of the time domain representation of the received signal as a function of depth as shown in Figure 1. From this analysis the first time of arrival of the signal can be observed and this is often the most important piece of information. However we have learned to identify many other time domain features that are associated with the existence of tunnels. This variation of amplitude as a function of time will be designated as $x(t)$. When properly normalized the total energy of the signal is :

$$\int |x(t)|^2 dt$$

Another form of the data is the frequency domain representation, $X(f)$, obtained from the Fourier transform given by:

$$X(f) = \frac{1}{\sqrt{2\pi}} \int x(t) e^{j2\pi f t} dt$$

This representation of the data is called the spectrum and is a complex function. The total energy is also given by:

$$\int |X(f)|^2 df$$

The amplitude spectra of the data shown in Figure 1 is shown in Figure 2. Tunnel signatures have also been found in the spectra, the most obvious being an interference null in the 30MHz to 40 MHz region.

The two representations of the signal, time and frequency, have proved to be adequate for many analysis problems. However, our everyday experience tells us that a combination of the two representations is also important. Many signals are observed to change frequency with time. Most noteworthy is sound, in particular speech and music. The information content of these signals is very dependent on the way the frequency changes with time. When the frequency changes slowly it is relatively easy to observe. However, when the changes are rapid or hidden in a complex waveshape a two dimensional transform is needed.

II. TIME-FREQUENCY REPRESENTATIONS

The simplest and most direct approach to a time-frequency representation is to select only a small portion of the signal by multiplying by a window function. Obtain the Fourier transform of this part of the signal. Move the window to a slightly later portion of the signal and obtain the spectrum of that part. Repeat this process until the entire signal has been analyzed. This concept leads to the short-time Fourier transform (STFT) which is defined to be:

$$\text{STFT}(t, f) = \int x(t') w(t' - t) e^{-j2\pi f t'} dt'$$

where $w(t)$ is a window function. The analyses presented here use a Gaussian window. The most common presentation of the data is in the form of a spectrogram defined as:

$$\text{SPEC}(t, f) = |\text{STFT}(t, f)|^2$$

The problem with the STFT is that it gives poor resolution. To obtain high resolution in time the window function must be very narrow. However, a narrow window produces a very broad spectrum for each portion of the signal and hence poor resolution in frequency. Conversely a wide window gives good frequency resolution but poor time resolution.

The investigation of other time-frequency representations, or distributions, has been a very active research area in recent years. Only the Wigner-Ville distribution (WVD) has been applied to PEMSS data at this time. This distribution is defined by:

$$\text{WVD}(t, f) = \int z(t - t') z^*(t + t') e^{-j2\pi f t'} dt'$$

where $z(t)$ is the analytic signal derived from $x(t)$ by using the Hilbert transform.

Each of the time-frequency representations has some inherent tradeoffs. Although the STFT is easy to interpret it has poor resolution. The WVD introduces spurious responses caused by cross terms. For a review of several different distributions and their properties see Cohen¹.

III. DATA

PEMSS data from two different tunnel sites is presented. These are designated simply as tunnel A and Tunnel B. For each tunnel an analysis is presented for the waveforms recorded at several depths. The time domain, frequency domain, SPEC and WVD representations are presented for each depth.

¹Cohen, Leon, Time-Frequency Distributions - A Review, IEEE Proceedings, vol 77, no 7, July 1989, pp 941-981.

A. Tunnel A

The usual waterfall type of presentation of the time-domain data for tunnel A is shown in Figure 3.

1. 83 meter Depth

Figures 4, 5, and 6 show the time, frequency, SPEC, and WVD representations of the signal recorded at a depth of 83 meters. The SPEC is regular with a slight dispersion shift of energy from high frequency to low as time increases. The WVD shows features similar to the SPEC except that the contours above about 27 MHz are more compact and a second low magnitude contour appears to the right, (later time). This feature is believed to be associated with the reflection from the bottom of the tunnel.

2. 75.7 meters Depth

Figures 7, 8 and 9 show the data for the signal recorded near the bottom of the tunnel at a depth of 75.7 meters. The SPEC shows a shift of the peak energy to later times and lower frequencies while higher frequencies are maintained at early time. The WVD displays a concentration of the energy in the 20 MHz region. However, a finger extension of the contours to higher frequencies and earlier time is seen. This extension is flanked on both the right,(earlier time) and left (later time) by closed low magnitude contours.

3. 74.4 meters Depth

This depth is near the center of the tunnel and the data is shown in Figures 10, 11 and 12. Note the change in wave shape of the time-domain signal and the interference null of the frequency spectrum near 30 MHz. The SPEC shows an enhancement of the trends seen at the previous depth but now with a distinct high frequency, early time feature. The WVD also shows an enhancement of the features seen at the previous depth with now a strong packet of energy separated to the right at higher frequencies.

4. 73.3 meters Depth

This depth is near the top of the tunnel. Figures 13, 14 and 15 show a return to conditions seen below the tunnel. The separated contours seen at late time in the WVD may be associated with reflection from the top of the tunnel.

B. Tunnel B

PEMSS data for the second tunnel, designated as tunnel B, is shown in Figure 16.

1. 152.7 meter Depth

Figures 17, 18 and 19 show the data for tunnel B at a depth of 152.7 meters. This depth is seen to be well below the tunnel. Both the SPEC and WVD are seen to be very smooth and regular with indication of normal dispersion.

2. 148.3 meter Depth

The data recorded at 148.3 meters is below the tunnel but shows a very strong reflection from the bottom of the tunnel. The different representations are shown in Figures 20, 21 and 22. The effects of the reflection are found in all representations.

3. 144.2 meters Depth

This depth is near the center of the tunnel. Figure 23 shows the usual waveshape change in the time-domain and interference null in the frequency domain. The SPEC shown in Figure 24 shows similarities to that seen for tunnel A with a splitting of early and late time energy. The WVD seen in Figure 25 is more complex than seen for tunnel A. However similar features can be identified, namely the concentration of energy into near circular contours at about 25 MHz and separated early time/ high frequency contours.

4. 141.7 meters Depth

This depth is near the top of the tunnel and the data has returned to a regular form similar to that seen below the tunnel. This can be seen in the representations shown in Figures 26, 27 and 28.

IV. CONCLUSIONS

The ability to observe the variation of frequency content with time in a signal adds a potentially valuable tool in data analysis. In particular, this study has shown that the time-frequency representation reveals information about PEMSS signals that is not easily recognized from the time or frequency domains alone. In particular, there seems to be some unique features associated with the tunnel in both the SPEC and WVD representations. However, these observations must be considered preliminary. The technique is sufficiently for a more intensive study to be highly recommended.

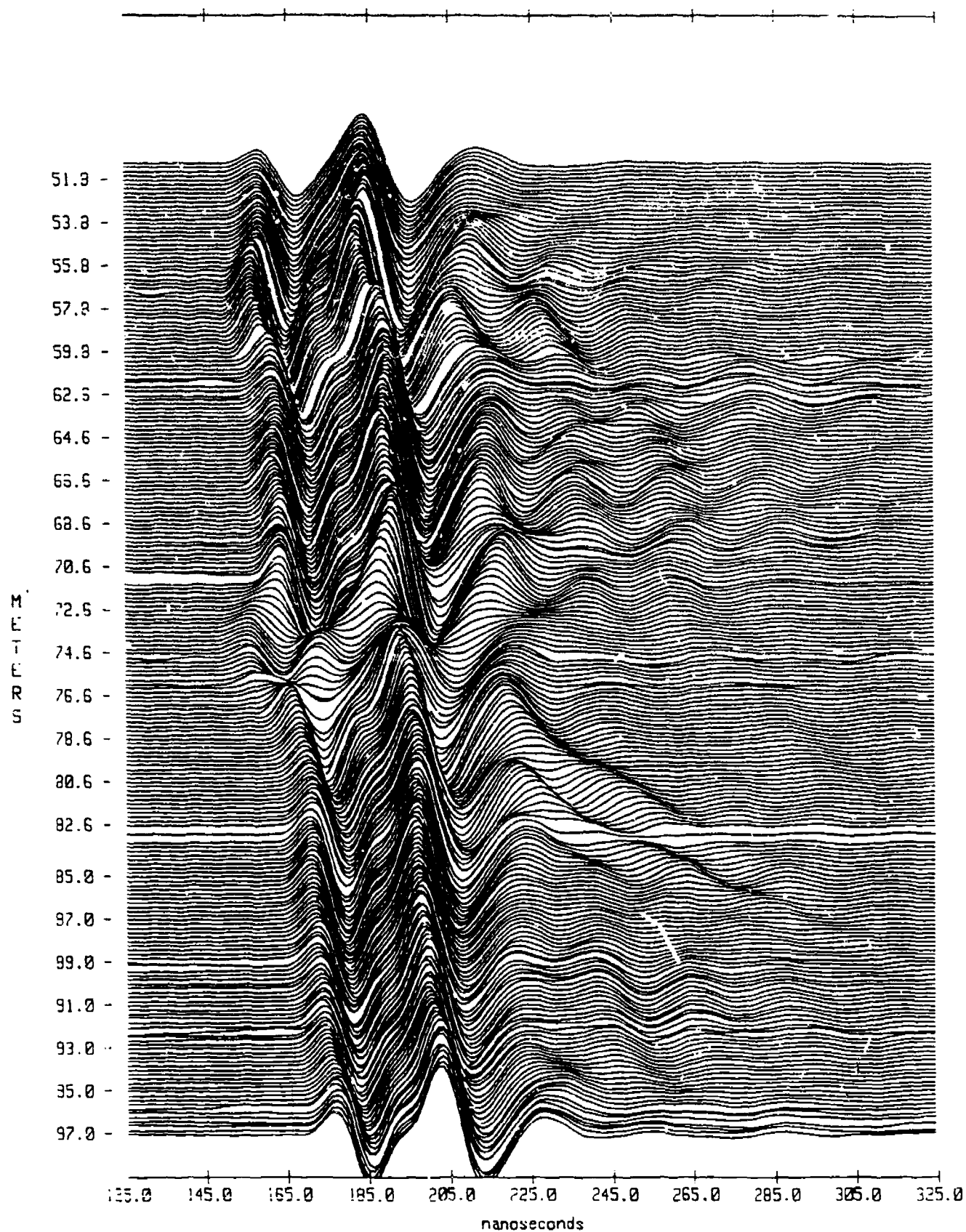


FIGURE 1. PEMSS TIME-DOMAIN

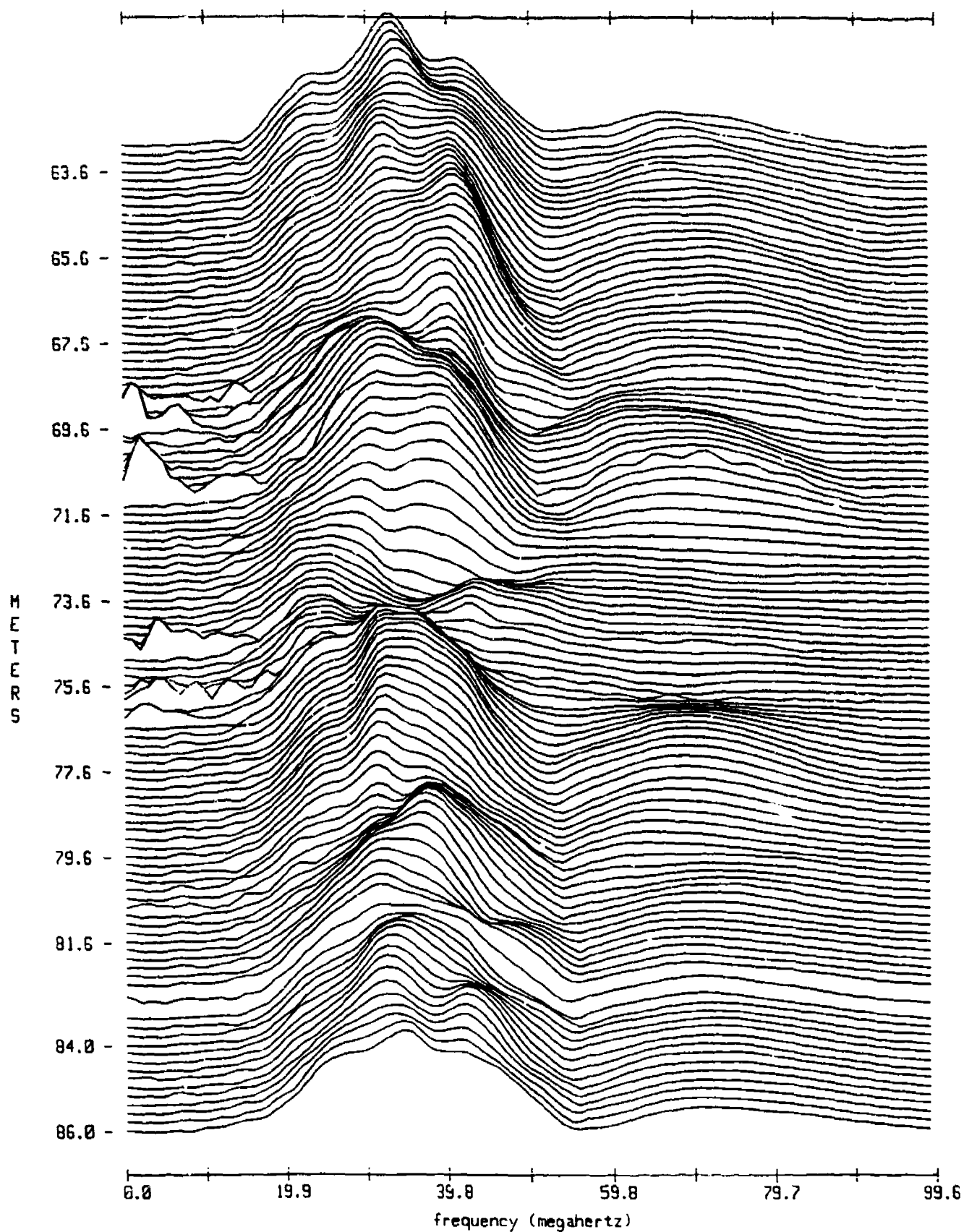


FIGURE 2. FREQUENCY-DOMAIN

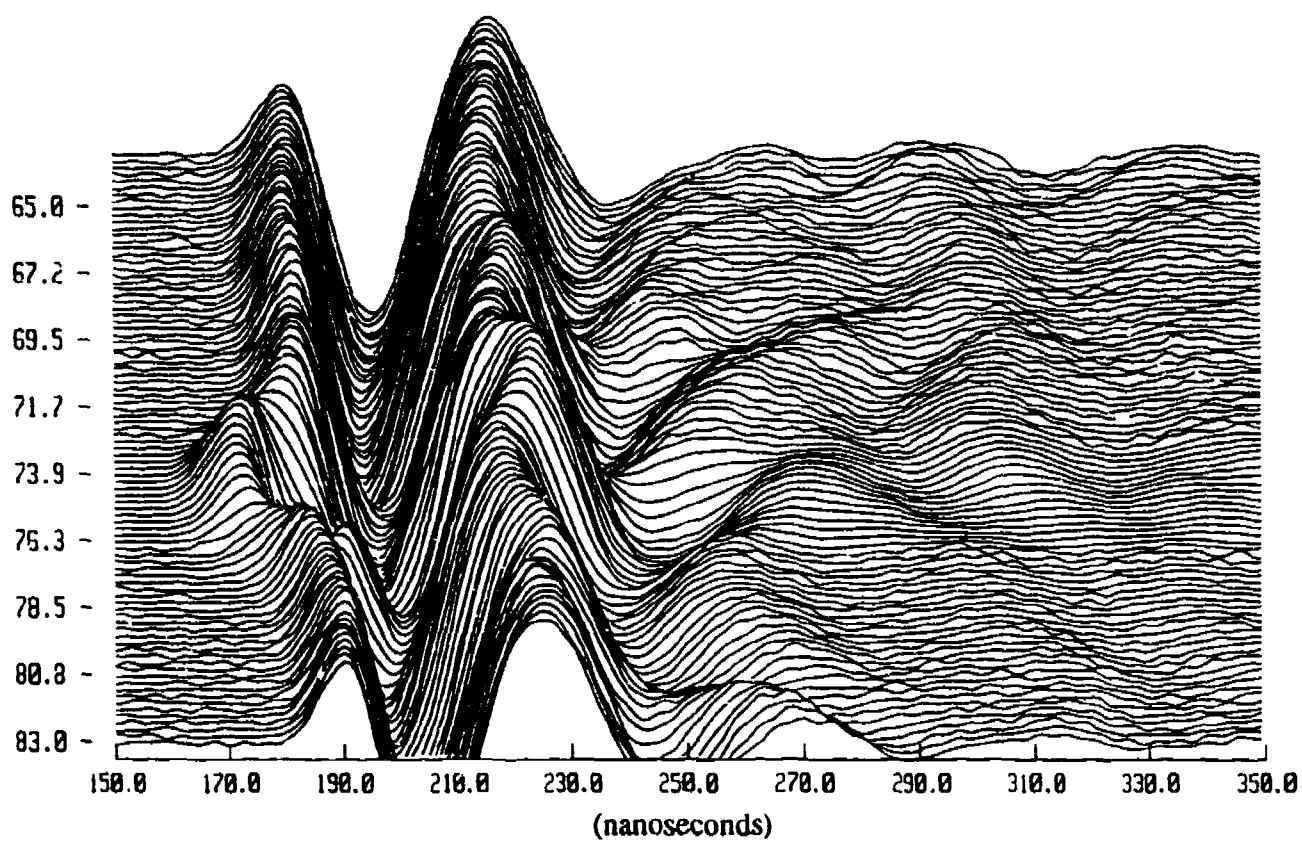


FIGURE 3. PEMSS DATA FOR TUNNEL A

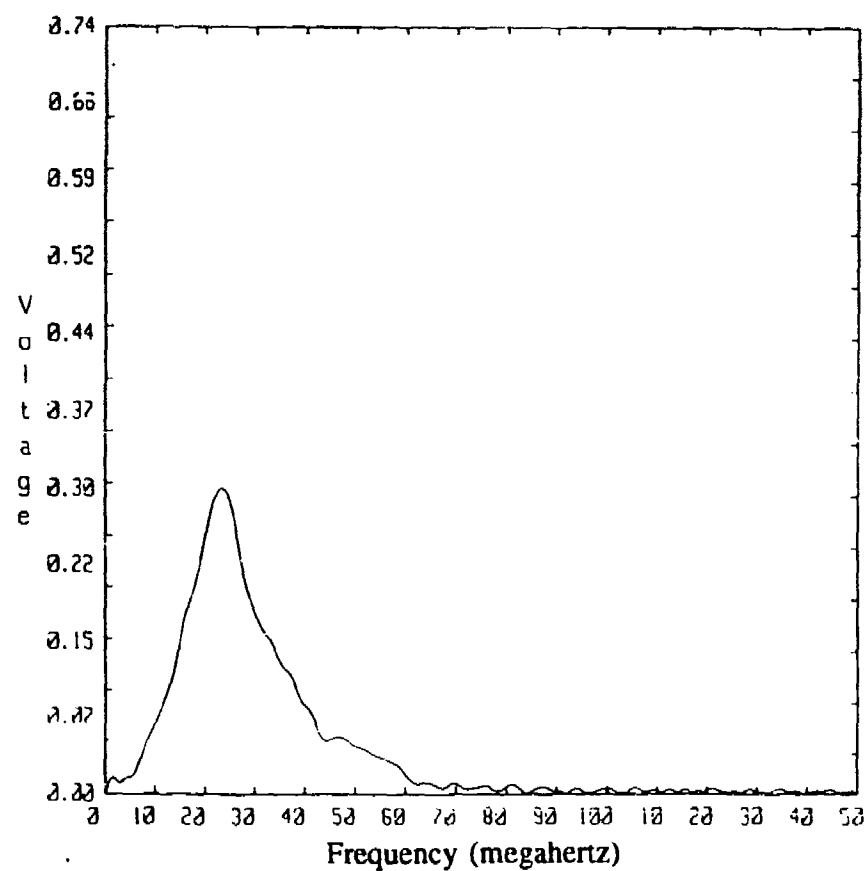
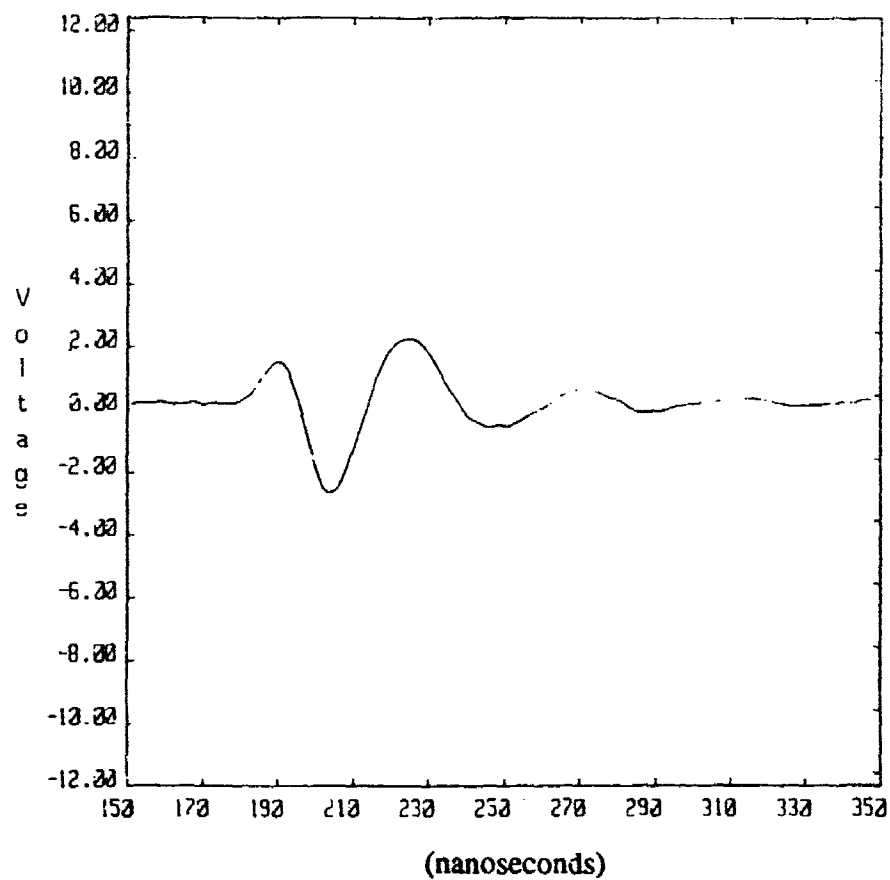


FIGURE 4. TIME-DOMAIN AND FREQUENCY-DOMAIN REPRESENTATIONS FOR TUNNEL A, 83.0 METERS DEPTH

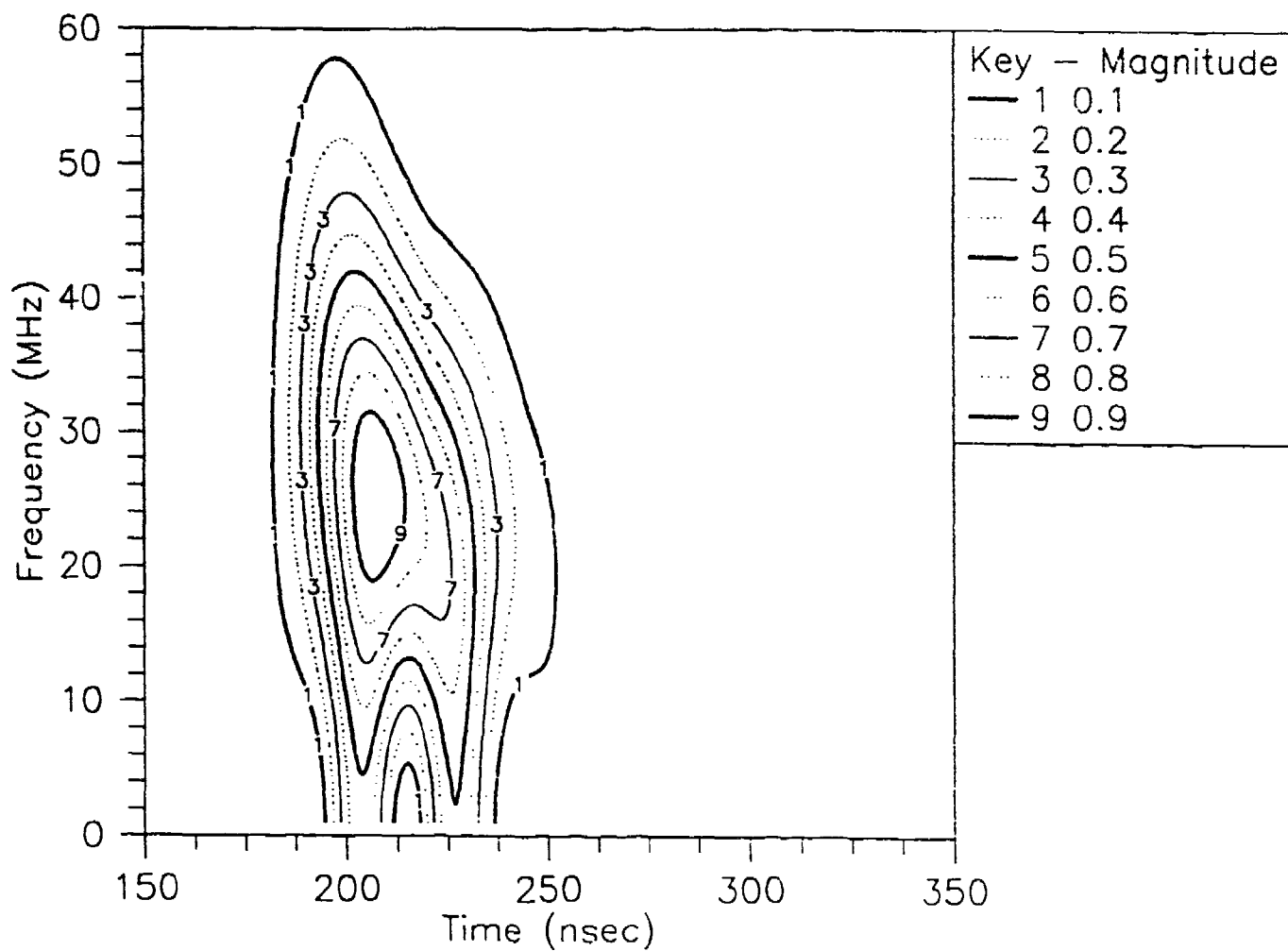


FIGURE 5. SPECTROGRAM FOR TUNNEL A, 83 METERS DEPTH

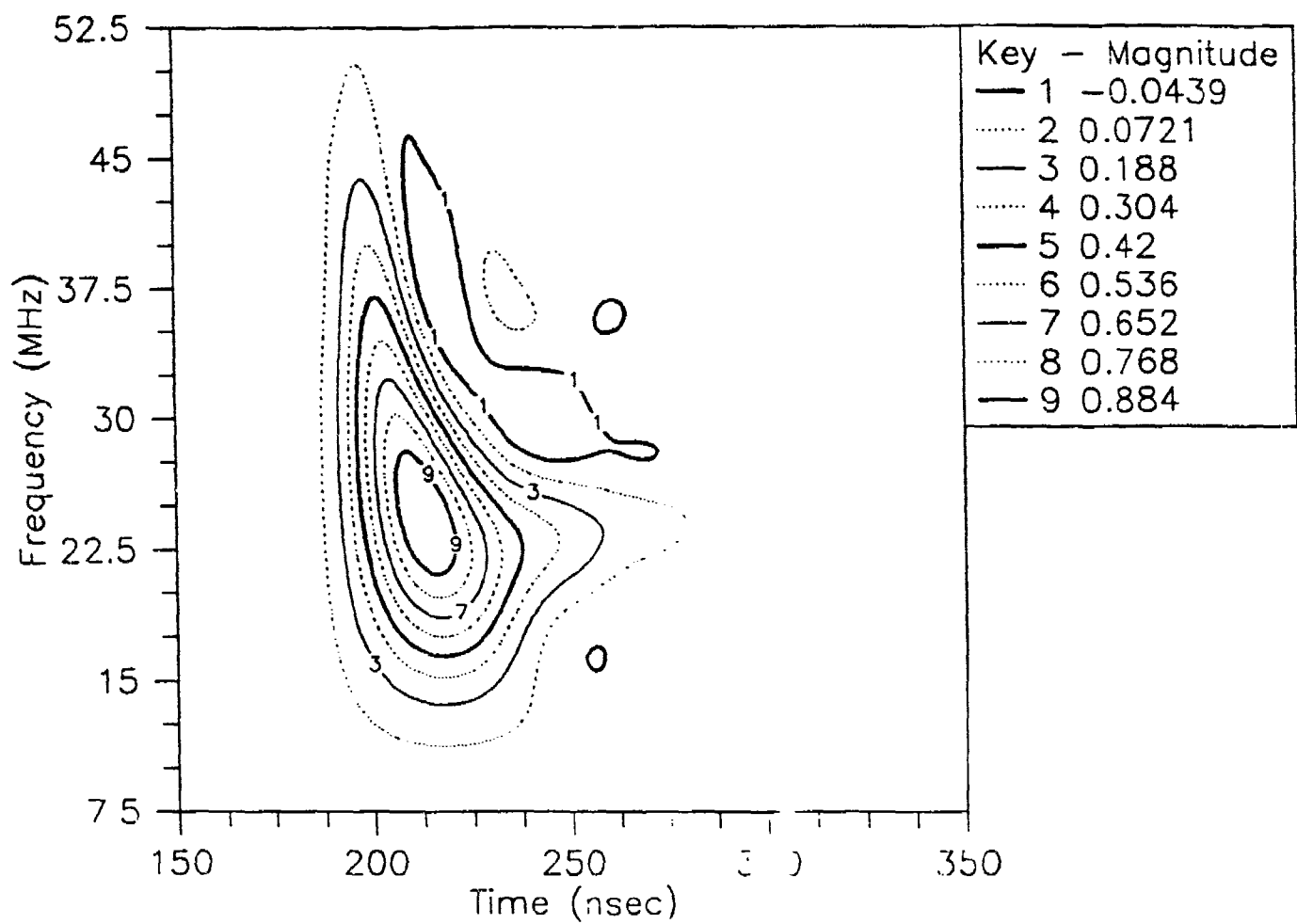


FIGURE 6. WIGNER-VILLE DISTRIBUTION FOR TUNNEL A, 83 METER DEPTH

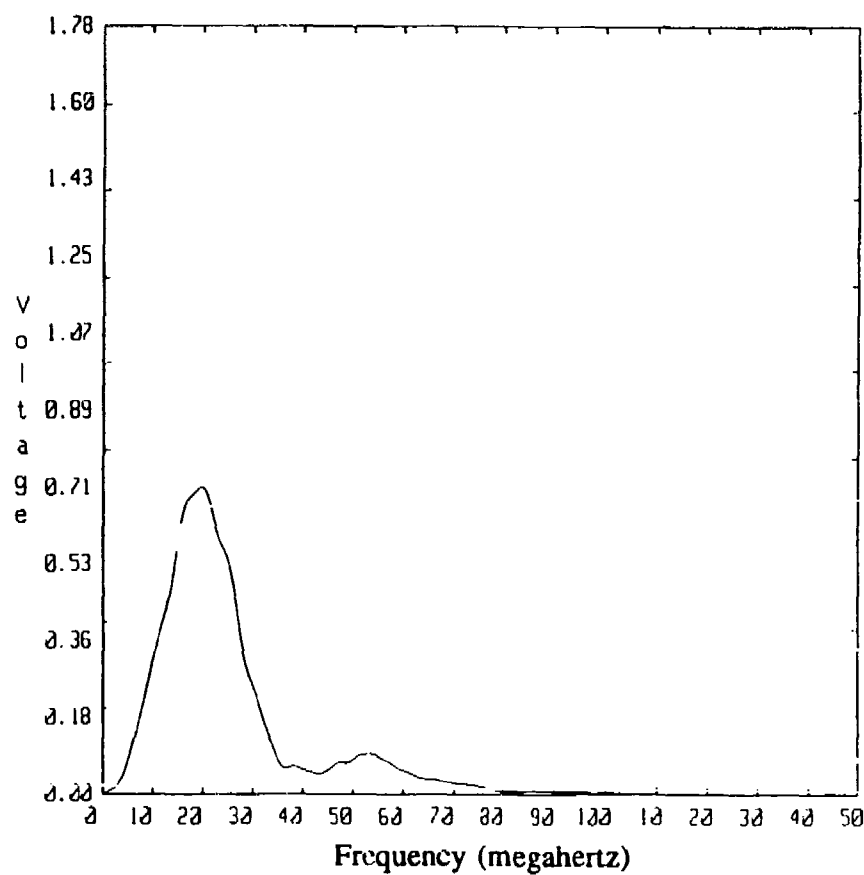
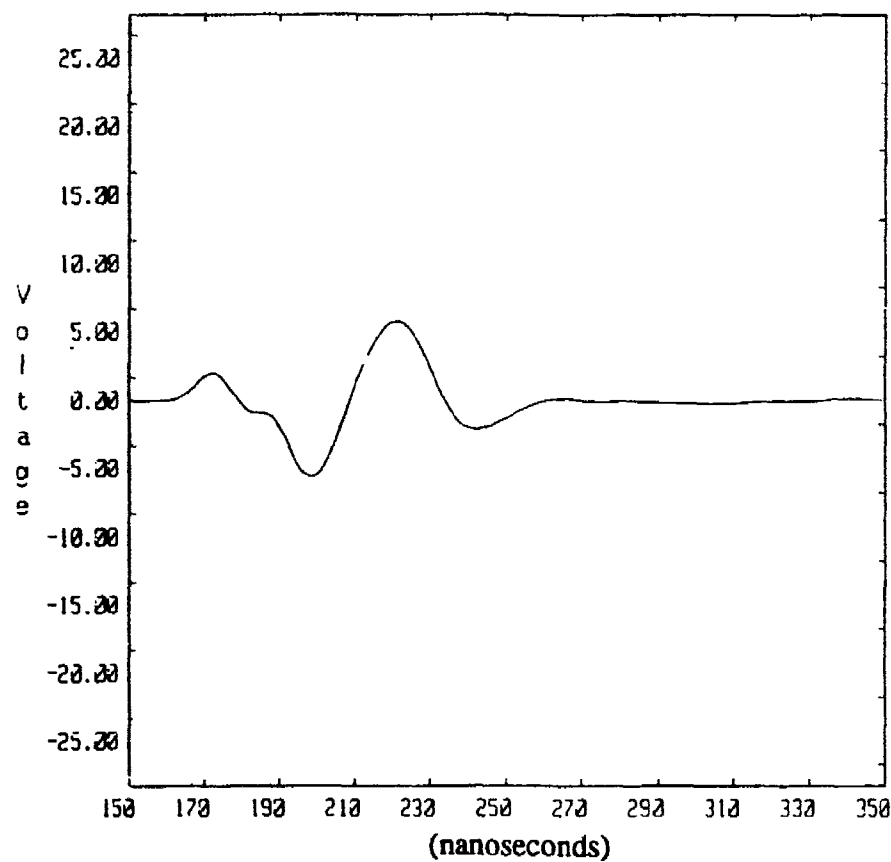


FIGURE 7. TIME-DOMAIN AND FREQUENCY-DOMAIN REPRESENTATIONS FOR TUNNEL A, 75.7 METER DEPTH

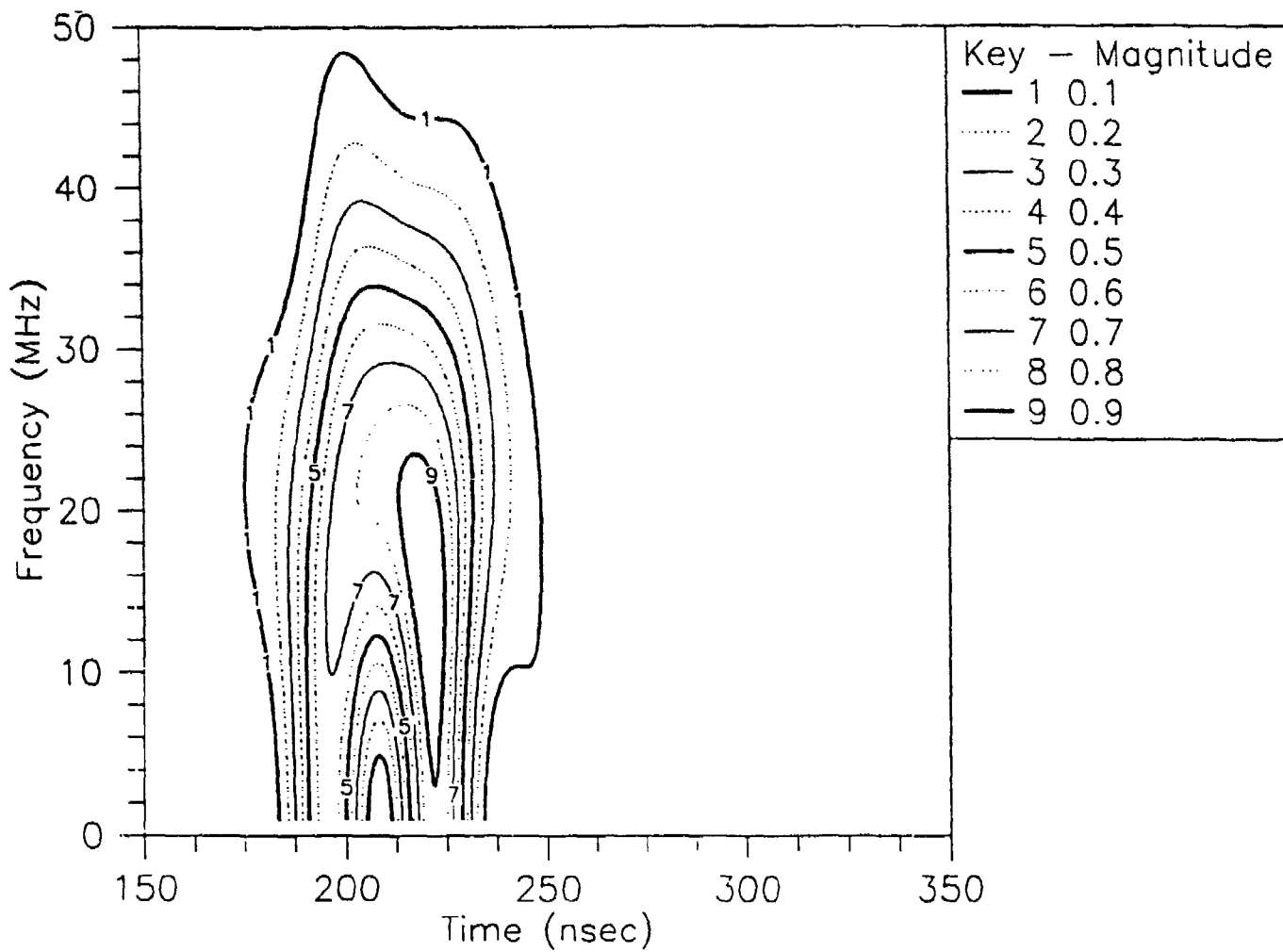


FIGURE 8. SPECTROGRAM FOR TUNNEL A, 75.7 METER DEPTH

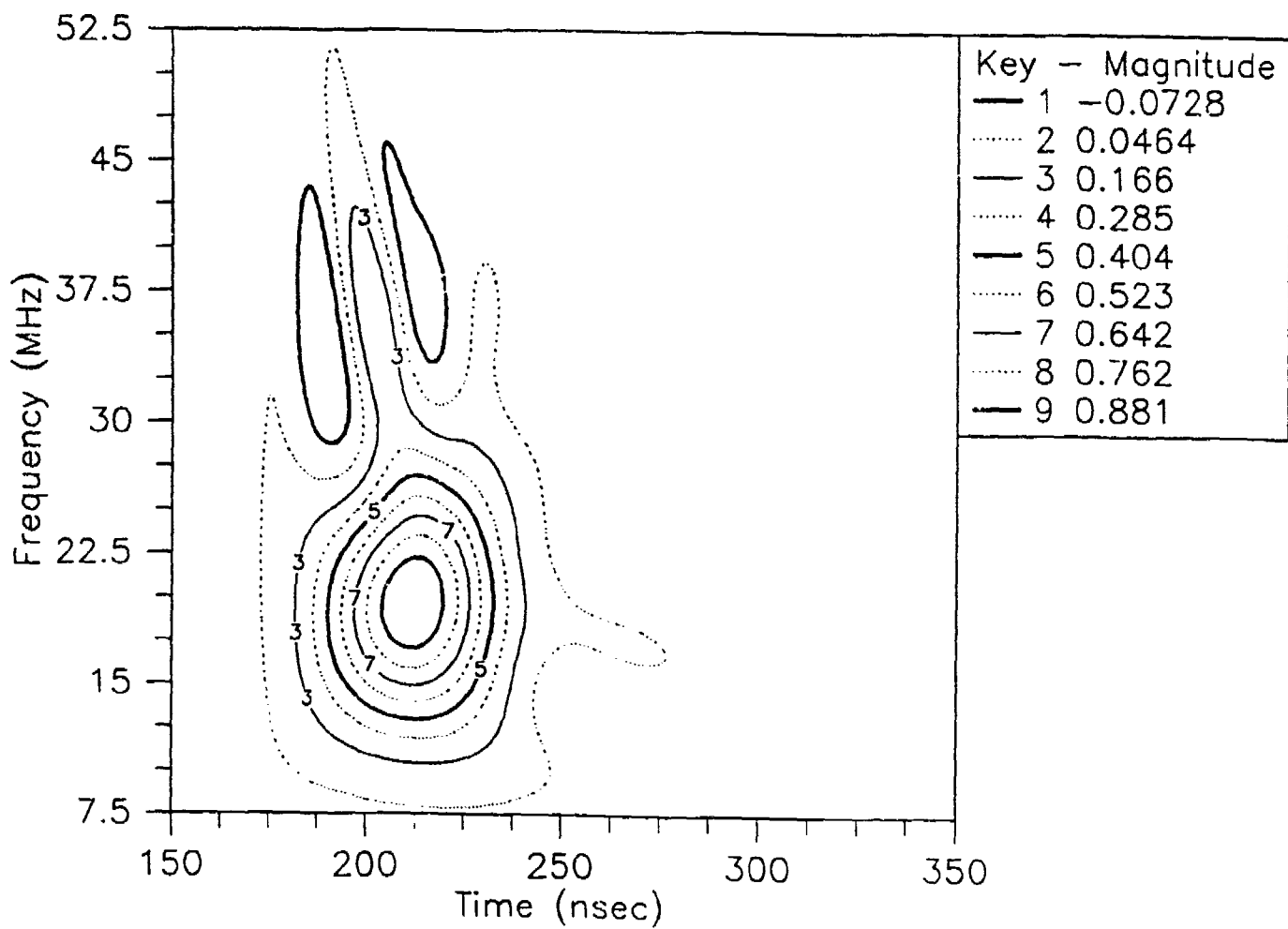


FIGURE 9. WIGNER-VILLE DISTRIBUTION FOR TUNNEL A, 75.7 METER DEPTH

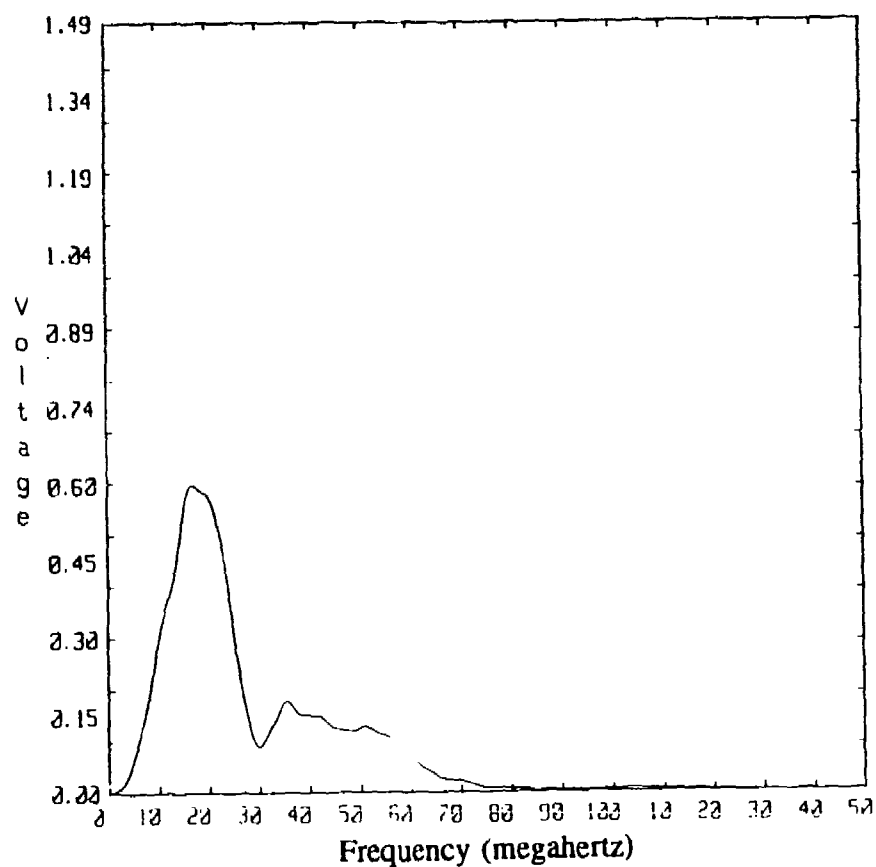
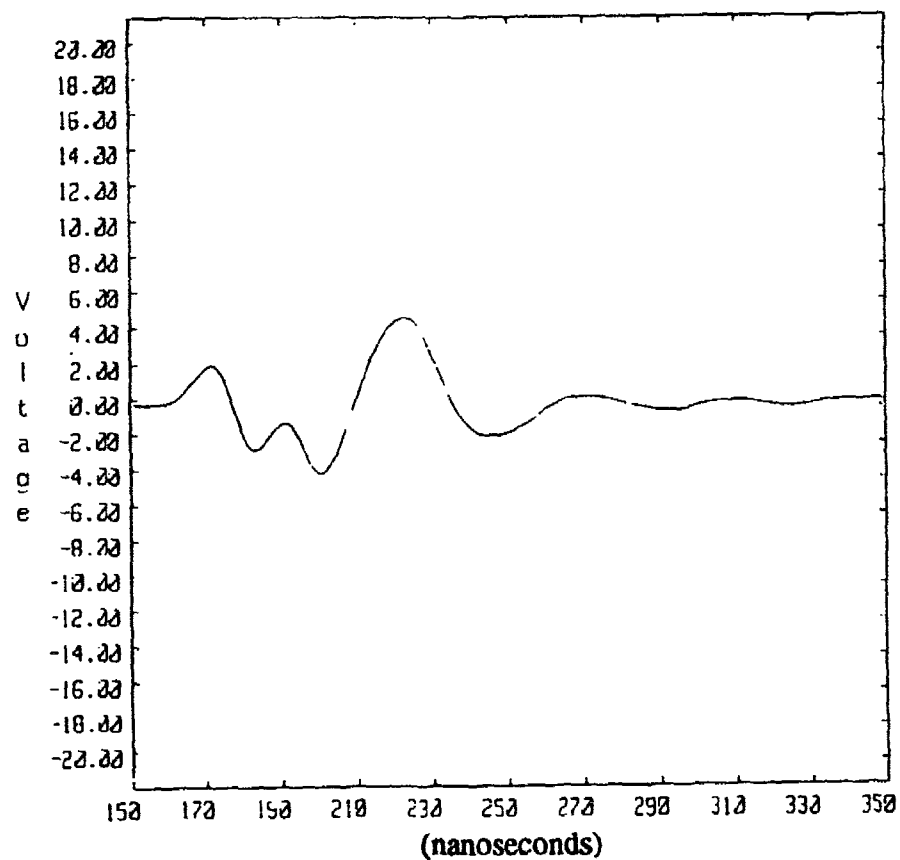


FIGURE 10. TIME-DOMAIN AND FREQUENCY-DOMAIN REPRESENTATIONS FOR TUNNEL A, 74.4 METER DEPTH

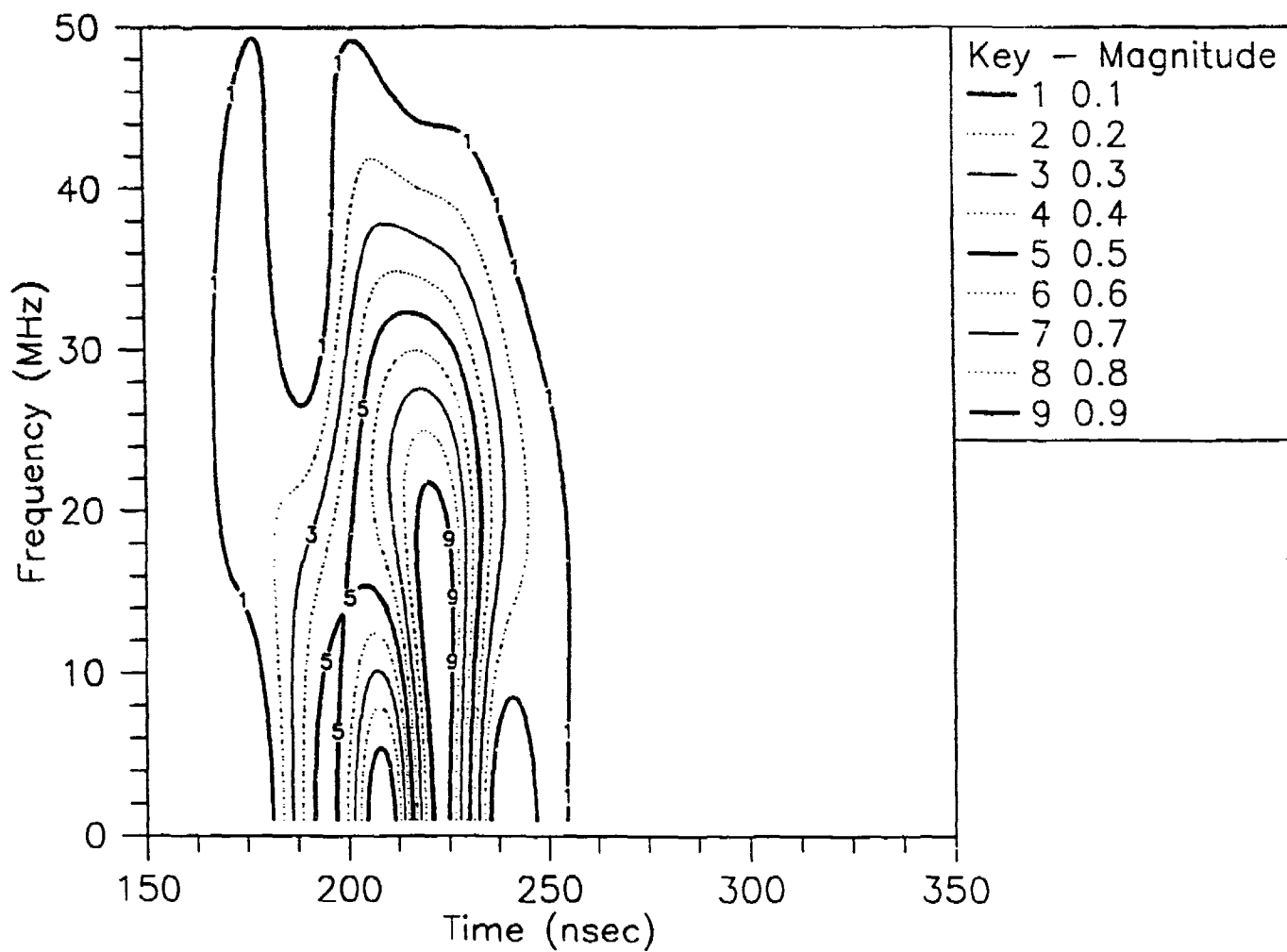


FIGURE 11. SPECTROGRAM FOR TUNNEL A, 74.4 METER DEPTH

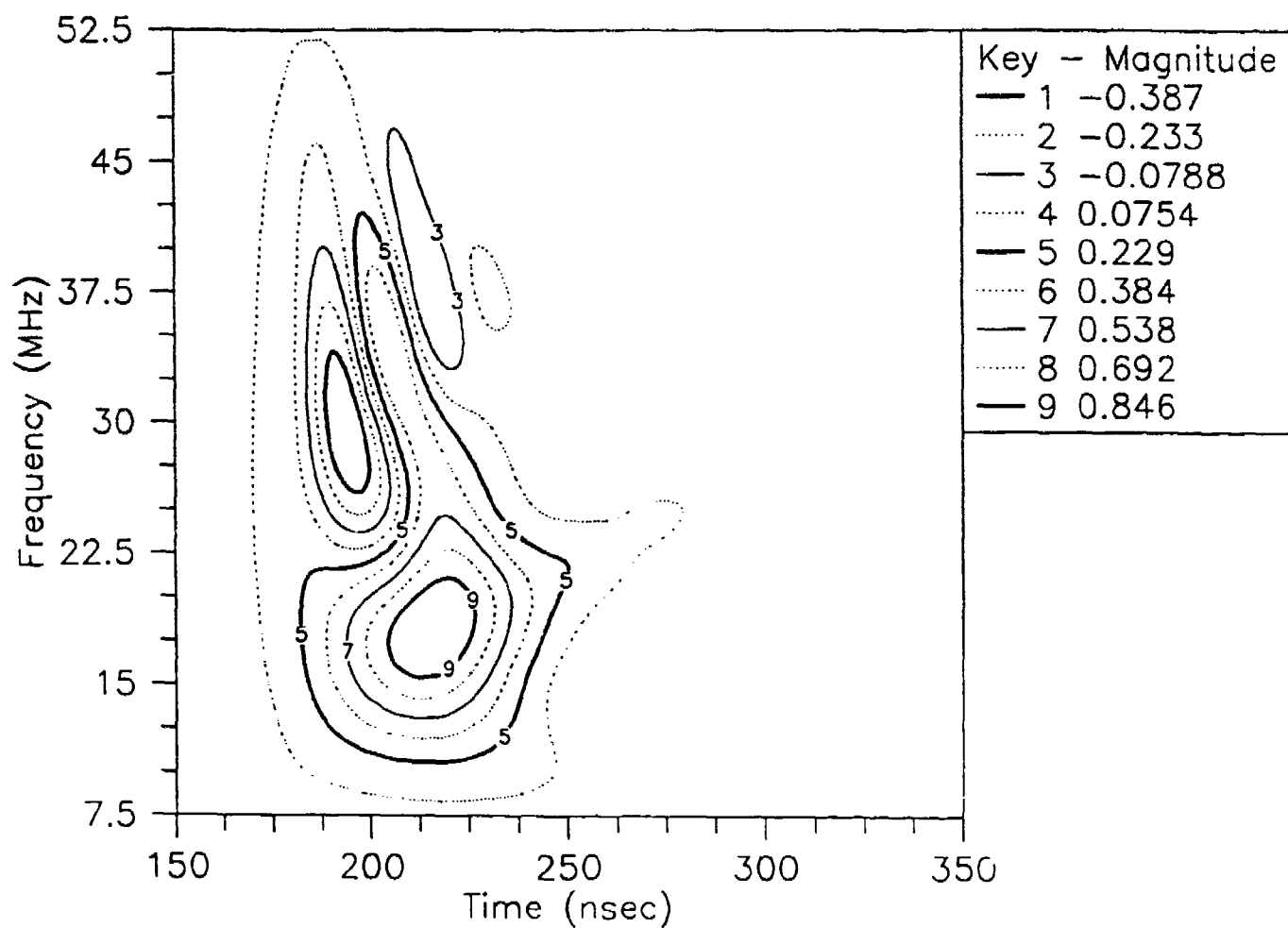


FIGURE 12. WIGNER-VILLE DISTRIBUTION FOR TUNNEL A, 74.4 METER DEPTH

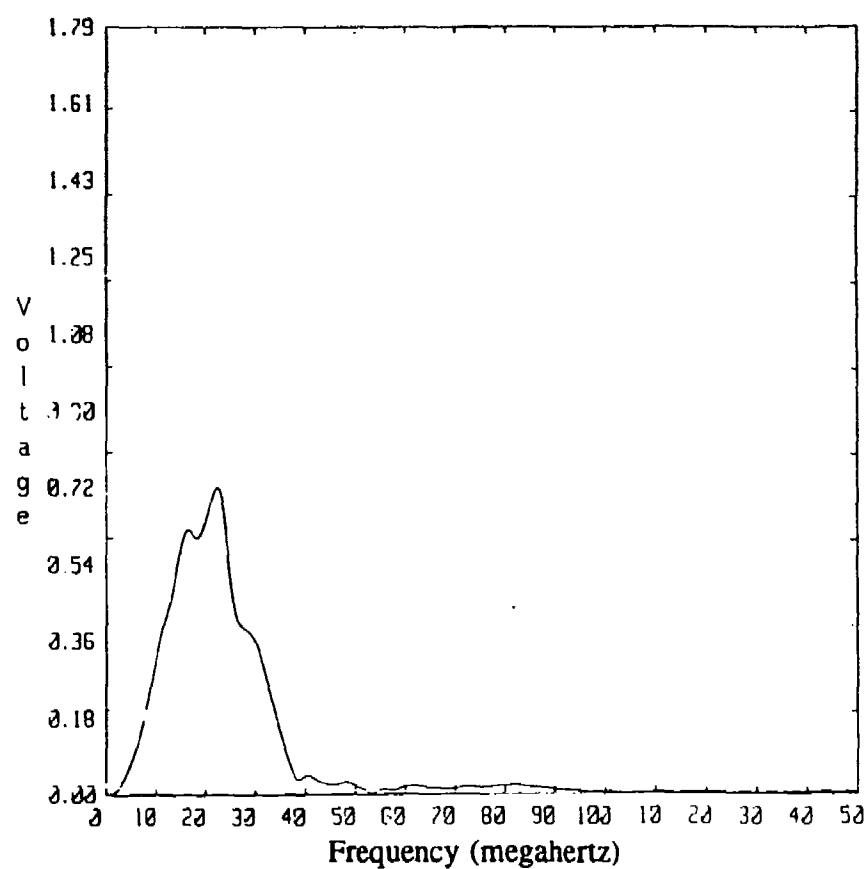
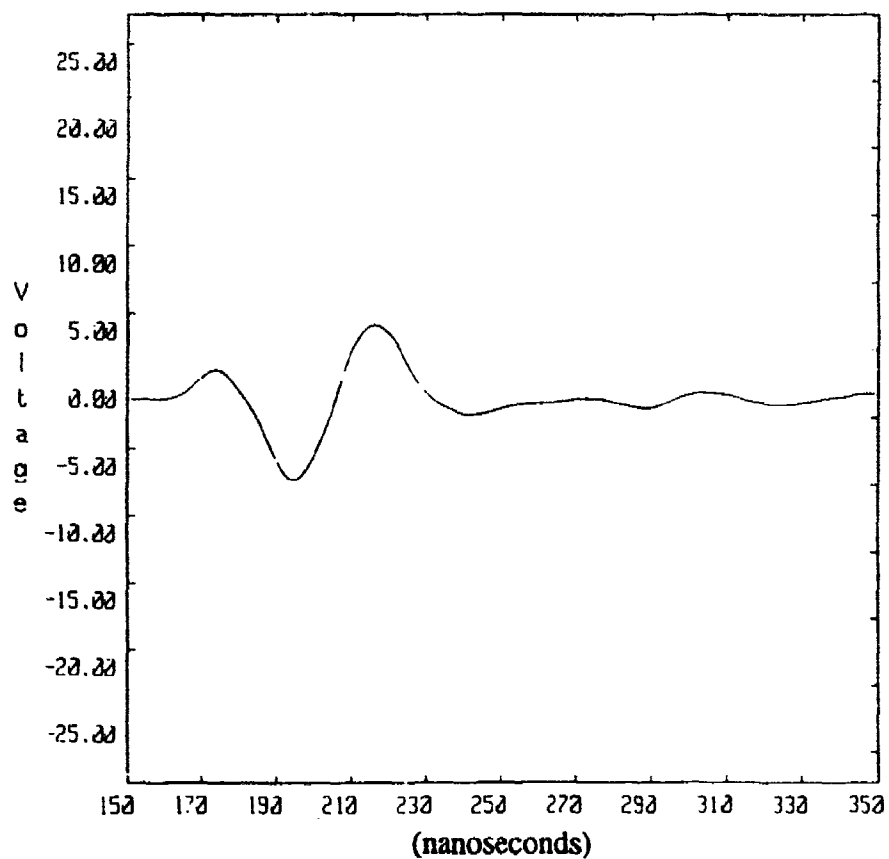


FIGURE 13. TIME-DOMAIN AND FREQUENCY-DOMAIN REPRESENTATIONS FOR TUNNEL A, 73.3 METER DEPTH

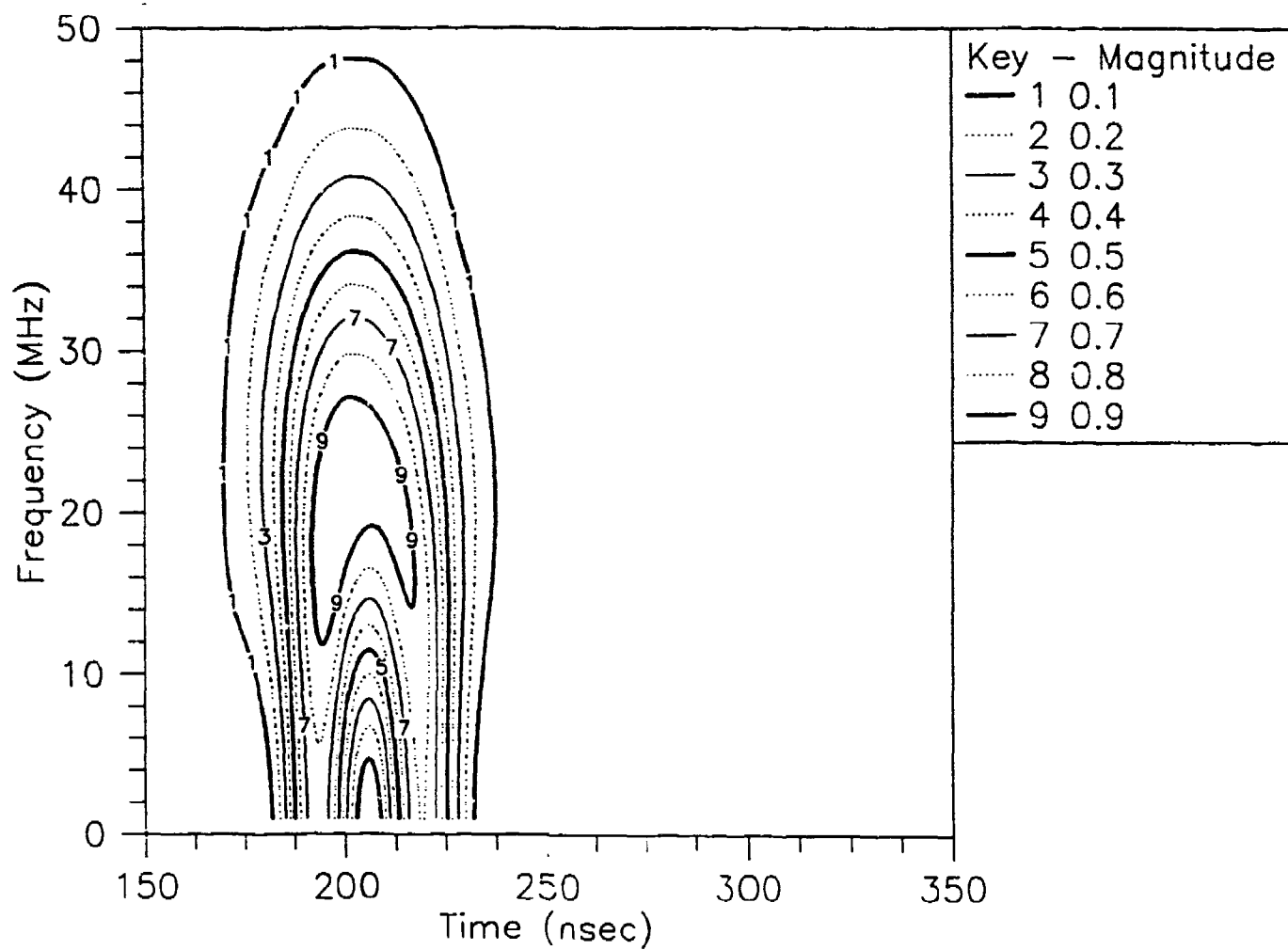


FIGURE 14. SPECTROGRAM FOR TUNNEL A, 73.3 METER DEPTH

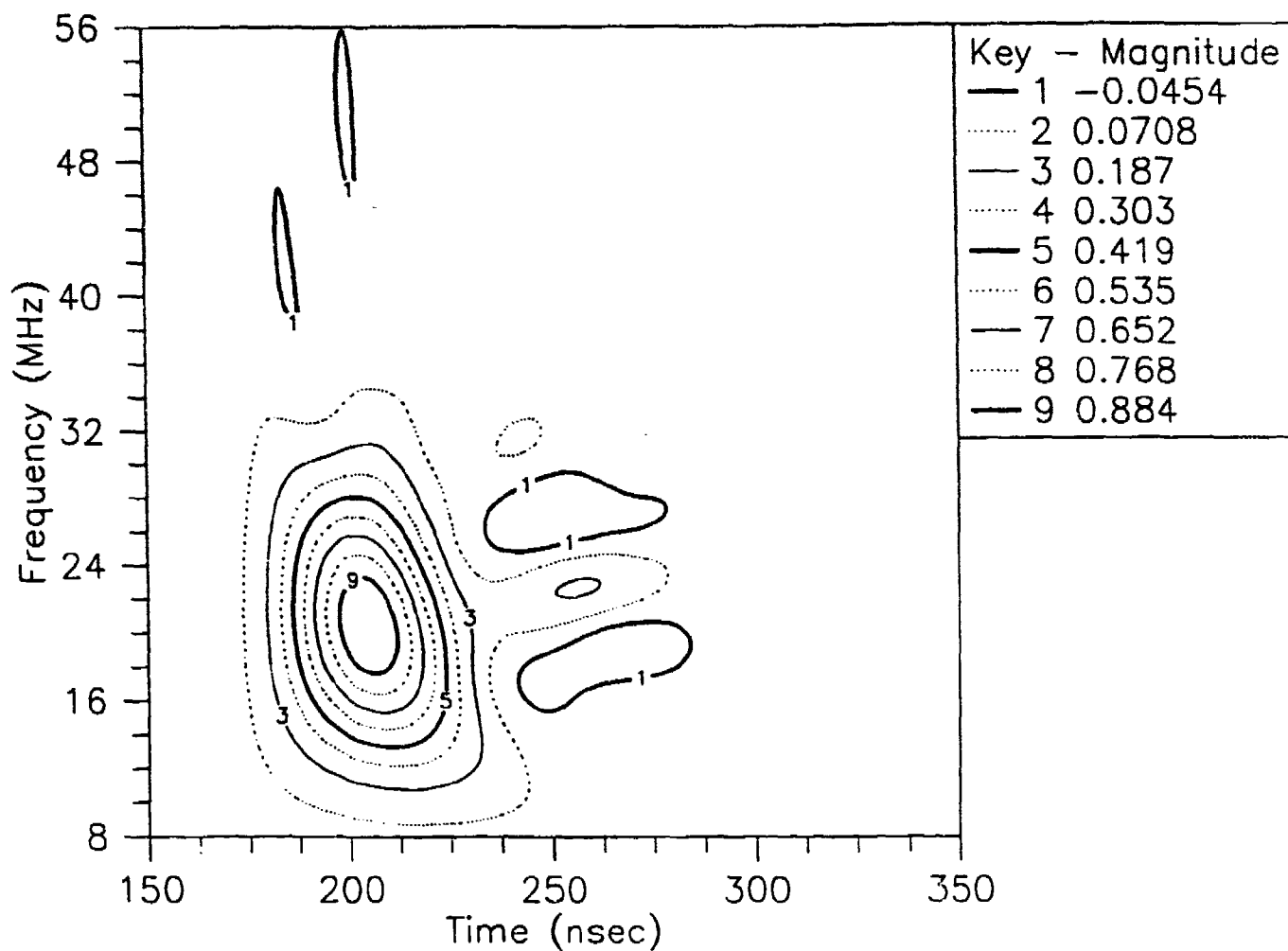


FIGURE 15. WIGNER-VILLE DISTRIBUTION FOR TUNNEL A, 73.3 METER DEPTH

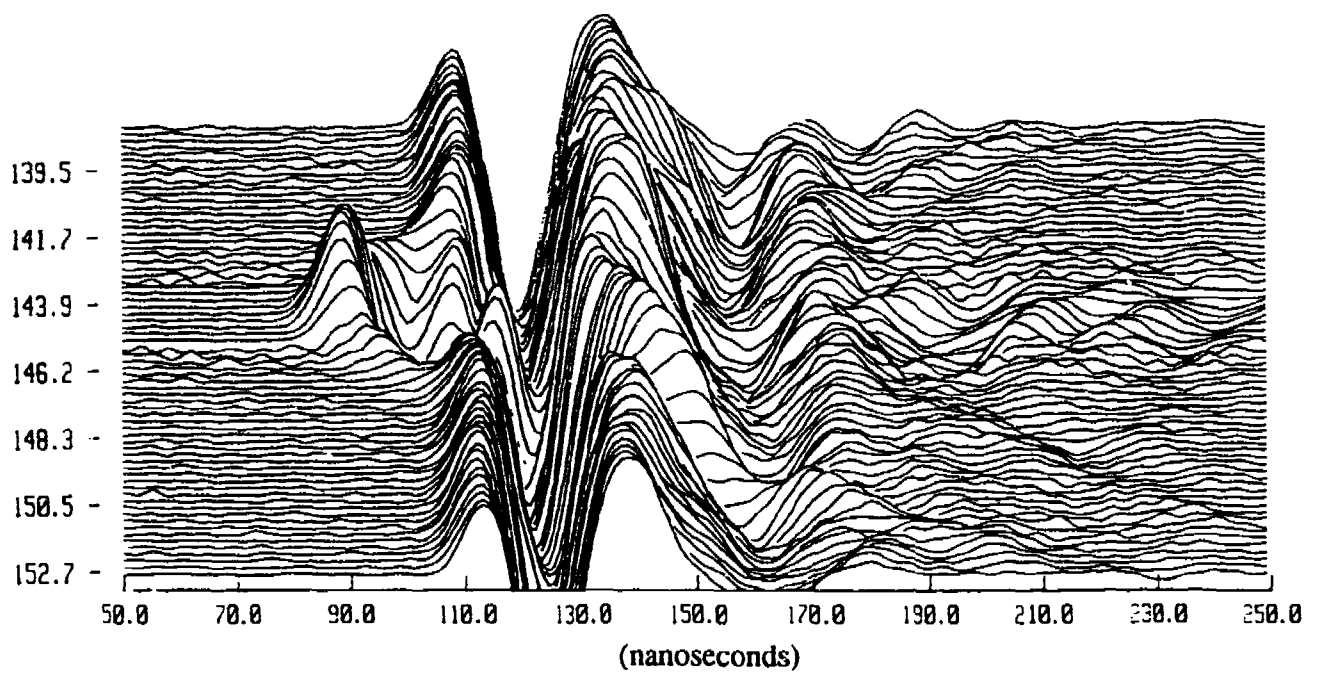


FIGURE 16. PEMSS DATA FOR TUNNEL B

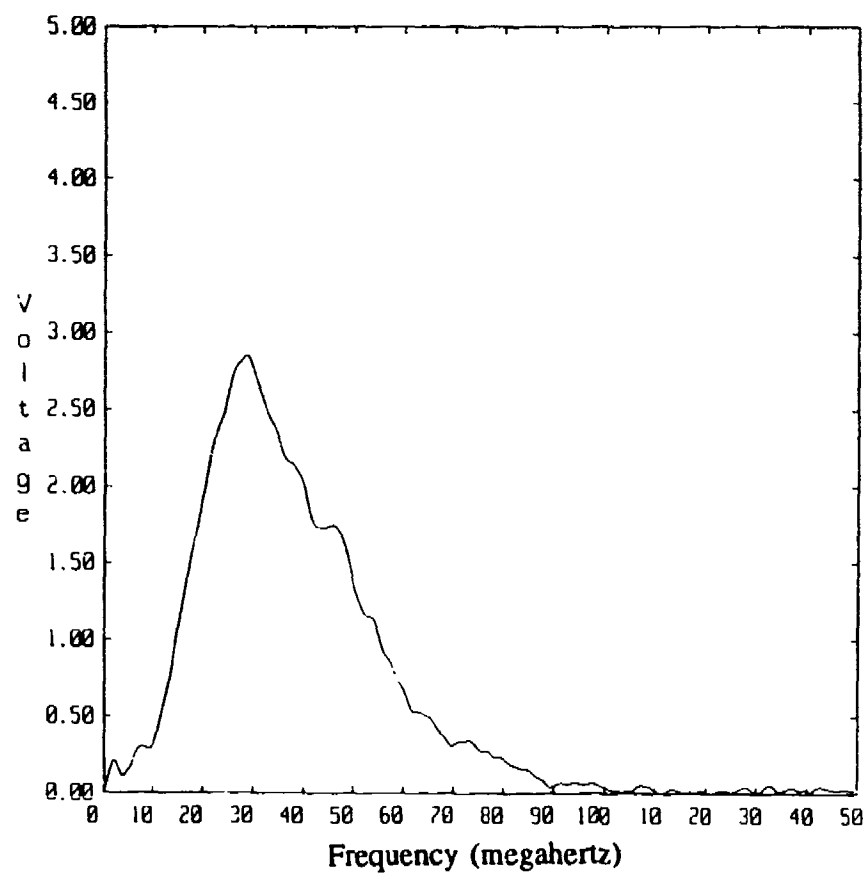
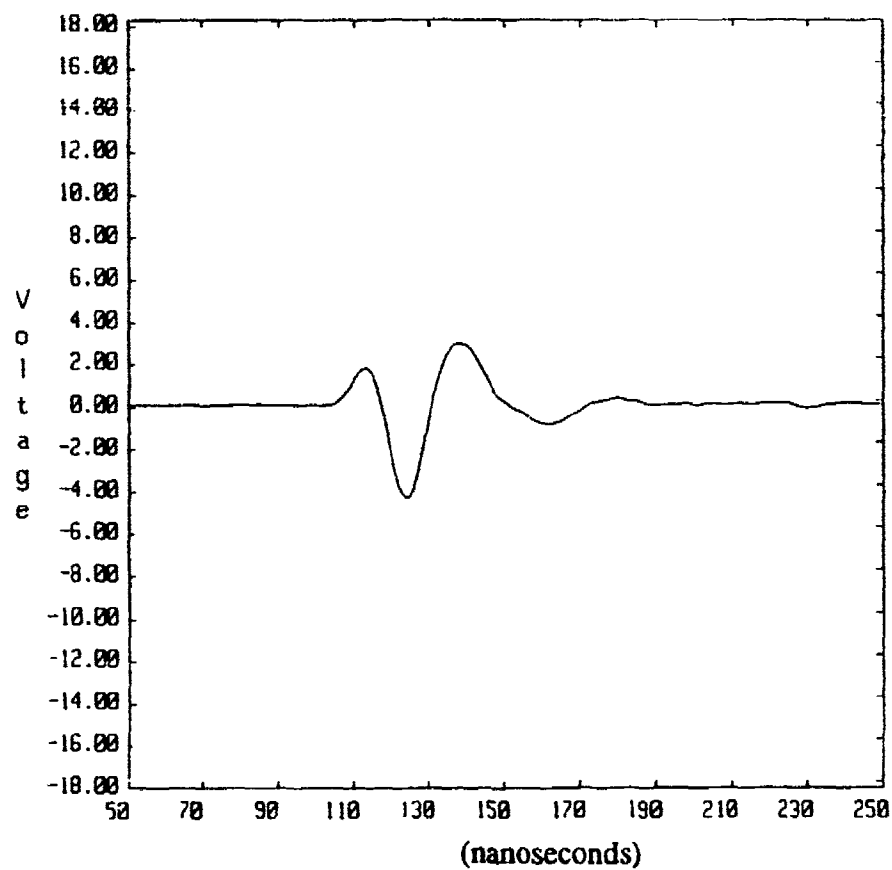


FIGURE 17. TIME-DOMAIN AND FREQUENCY-DOMAIN REPRESENTATIONS FOR TUNNEL B, 152.7 METER DEPTH

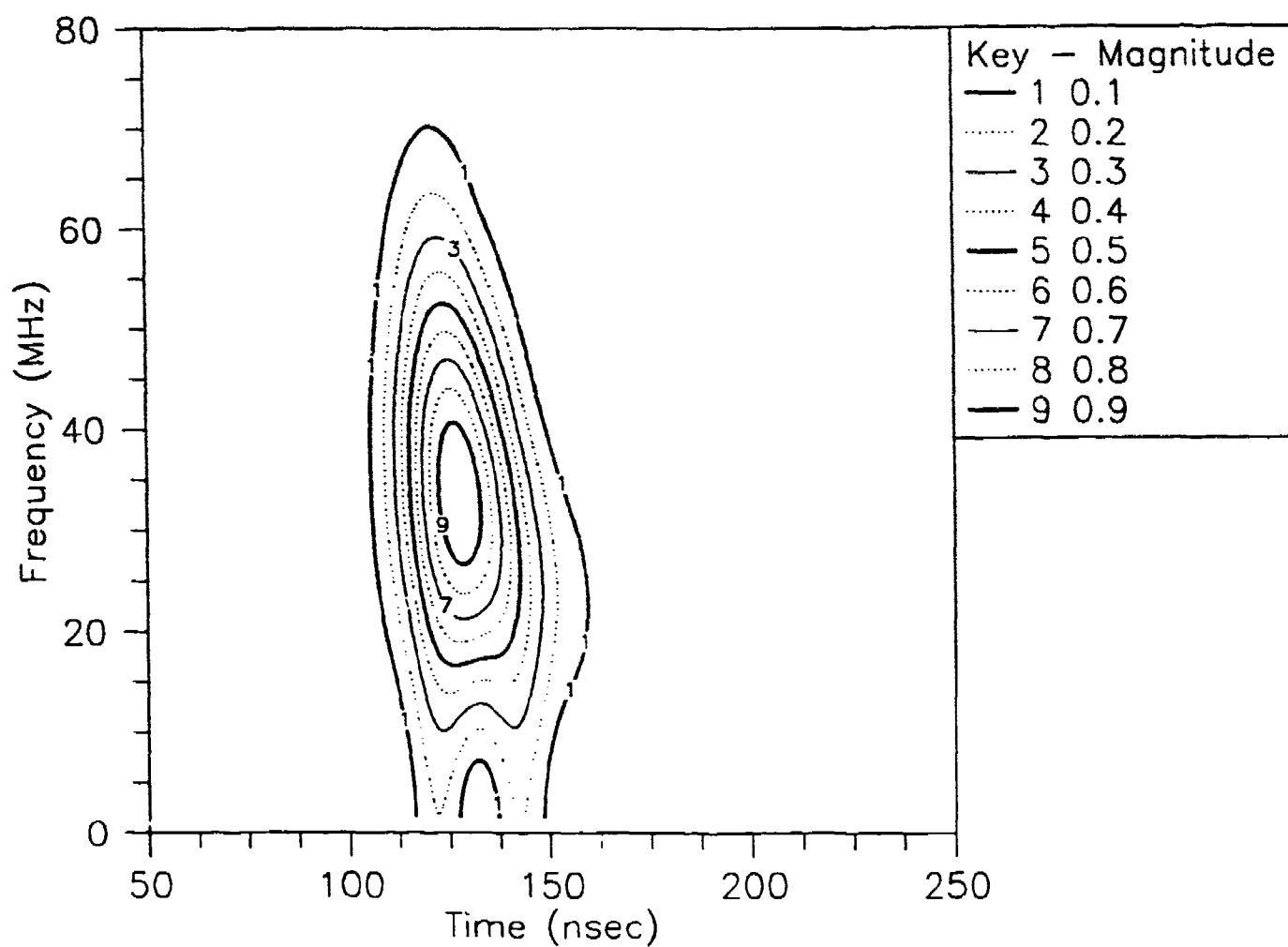


FIGURE 18. SPECTROGRAM FOR TUNNEL B, 152.7 METER DEPTH

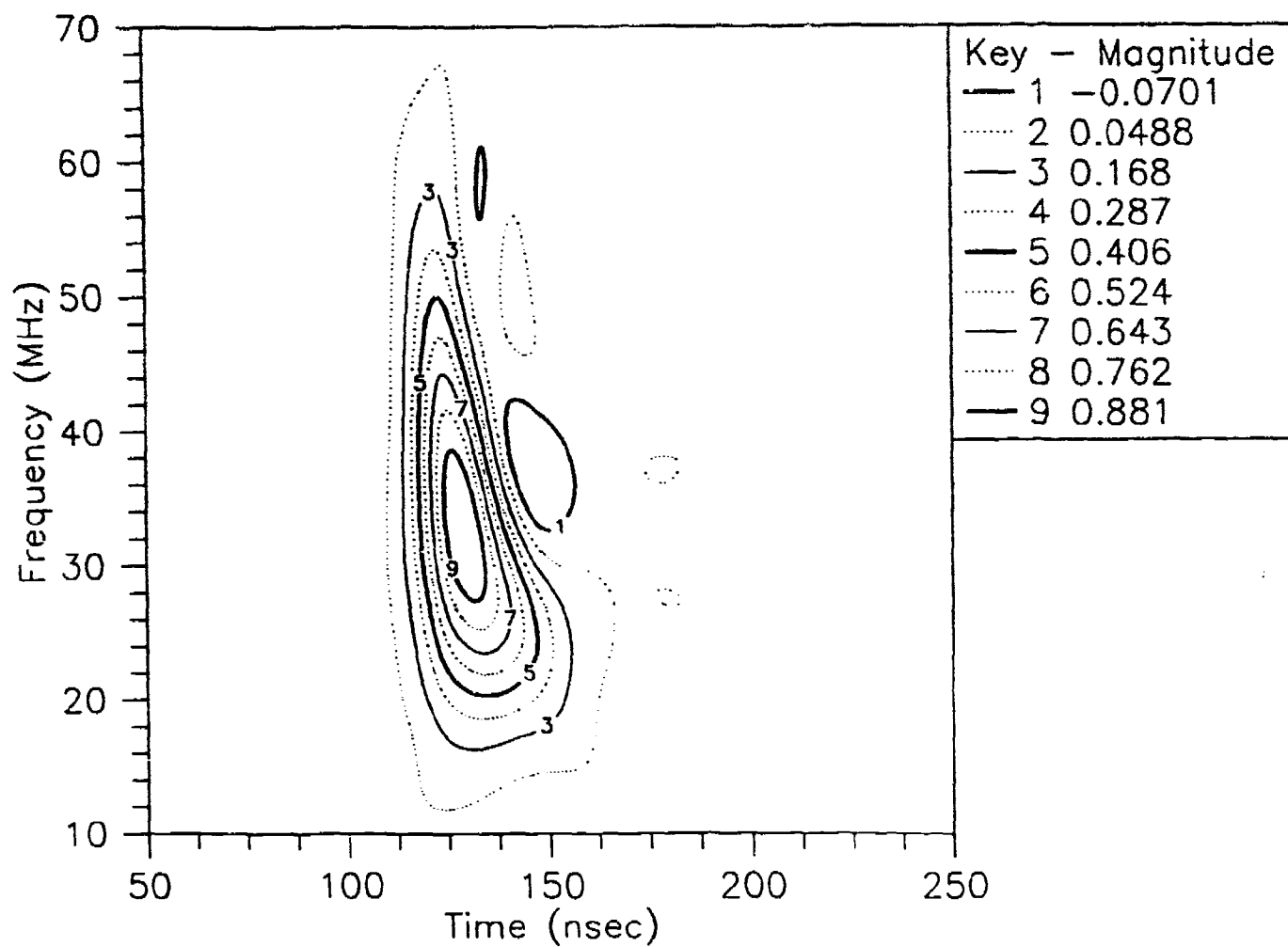


FIGURE 19. WIGNER-VILLE DISTRIBUTION FOR TUNNEL B, 152.7 METER DEPTH

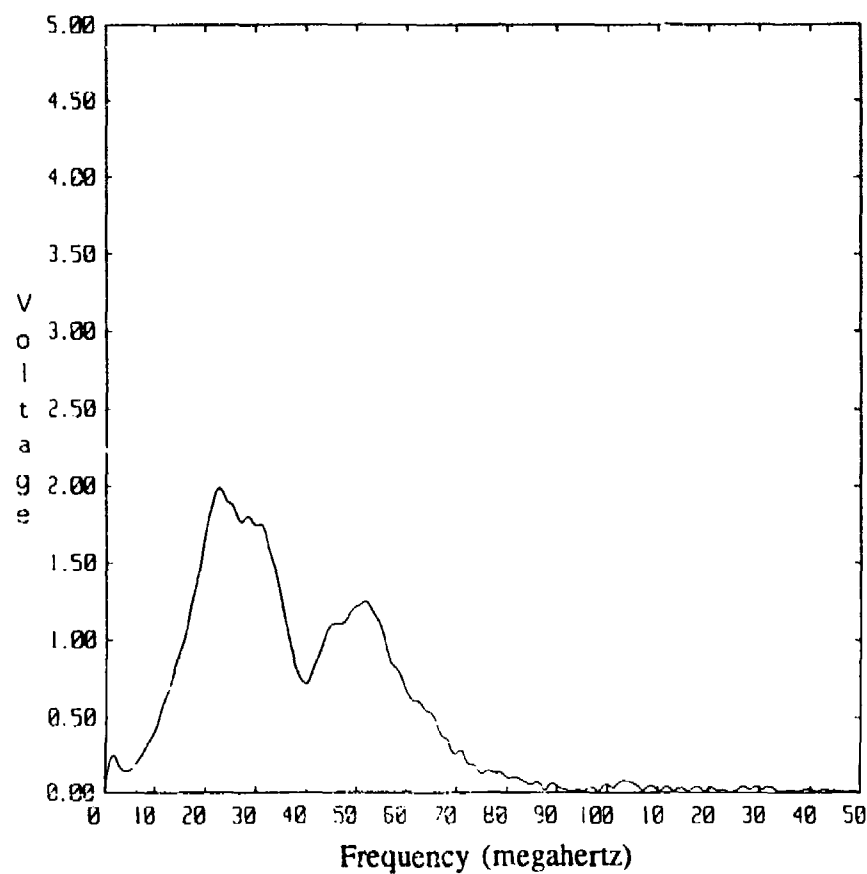
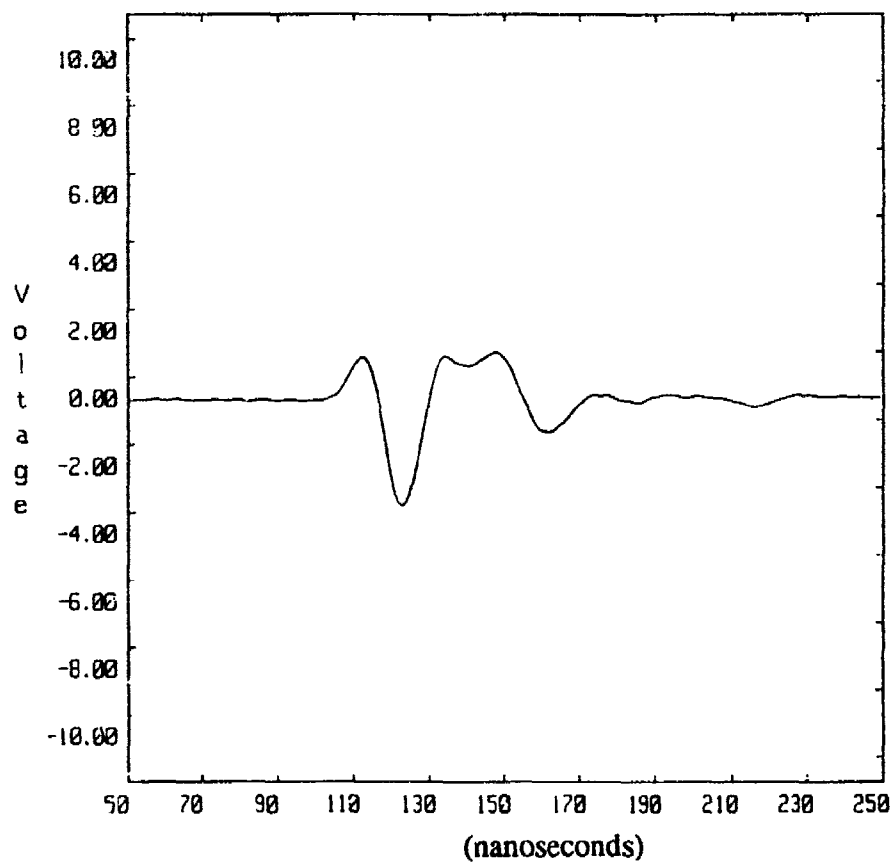


FIGURE 20. TIME-DOMAIN AND FREQUENCY-DOMAIN REPRESENTATIONS FOR TUNNEL B, 148.3 METER DEPTH

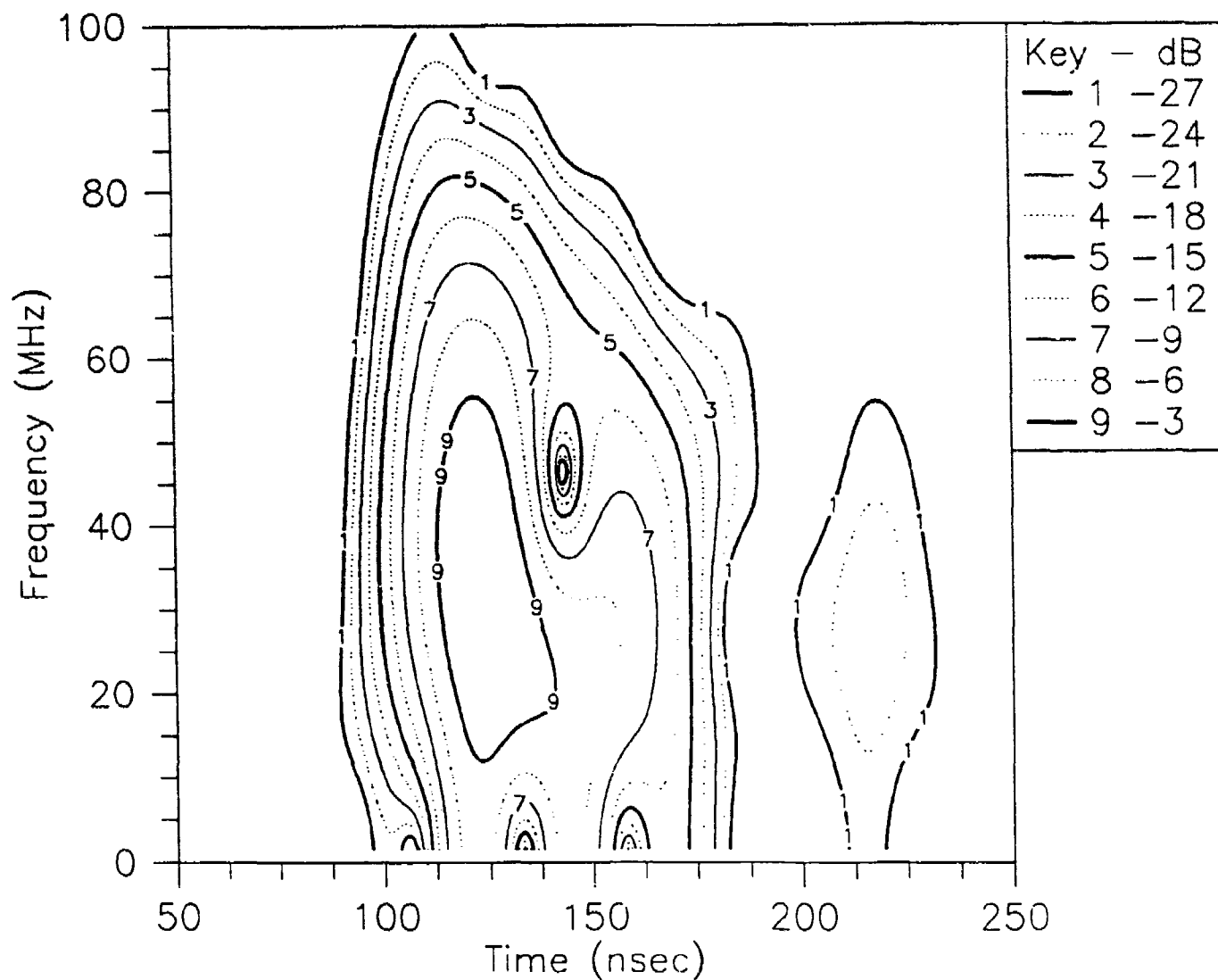


FIGURE 21. SPECTROGRAM FOR TUNNEL B, 148.3 METER DEPTH

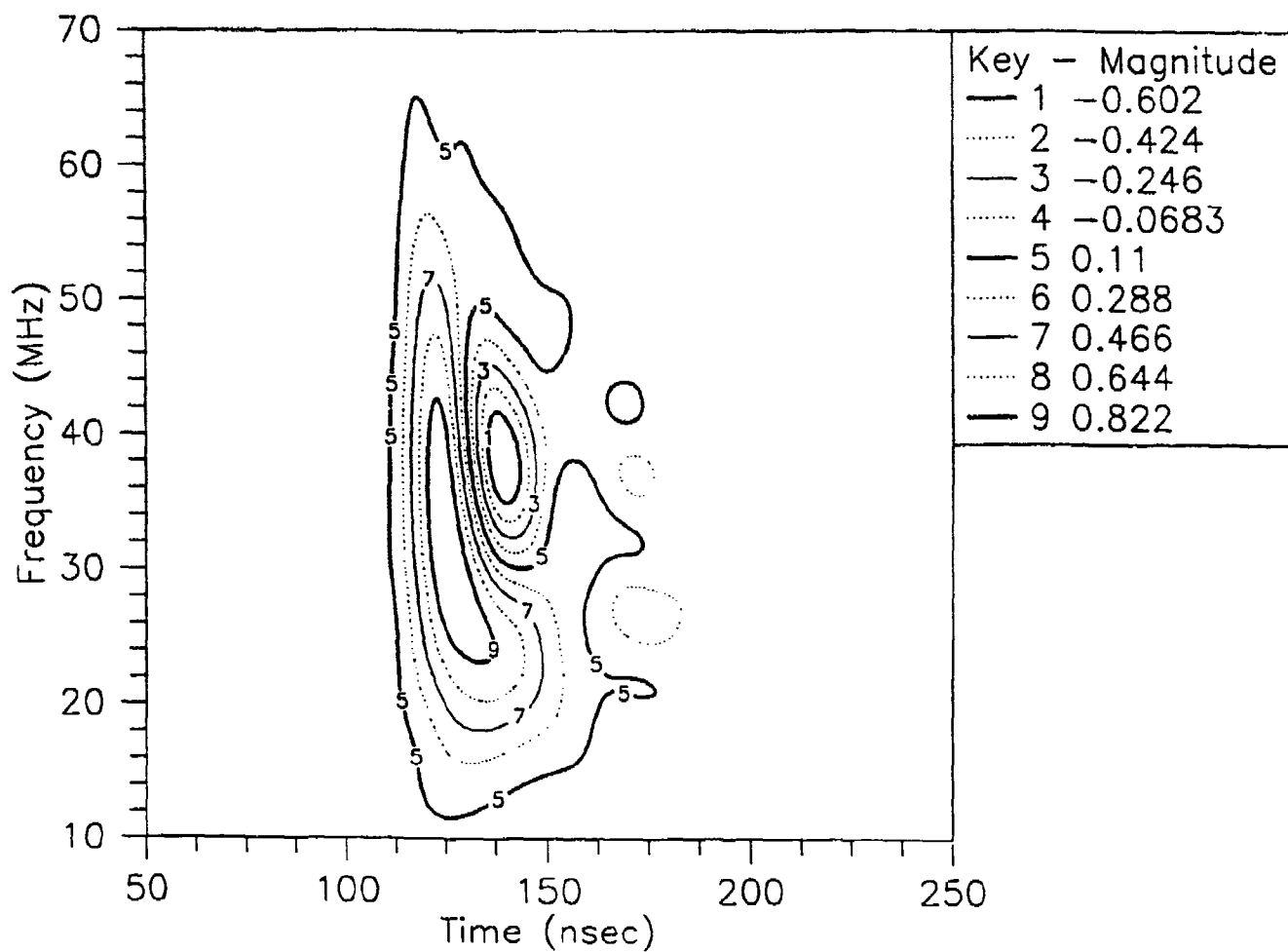


FIGURE 22. WIGNER-VILLE DISTRIBUTION FOR TUNNEL B, 148.3 METER DEPTH

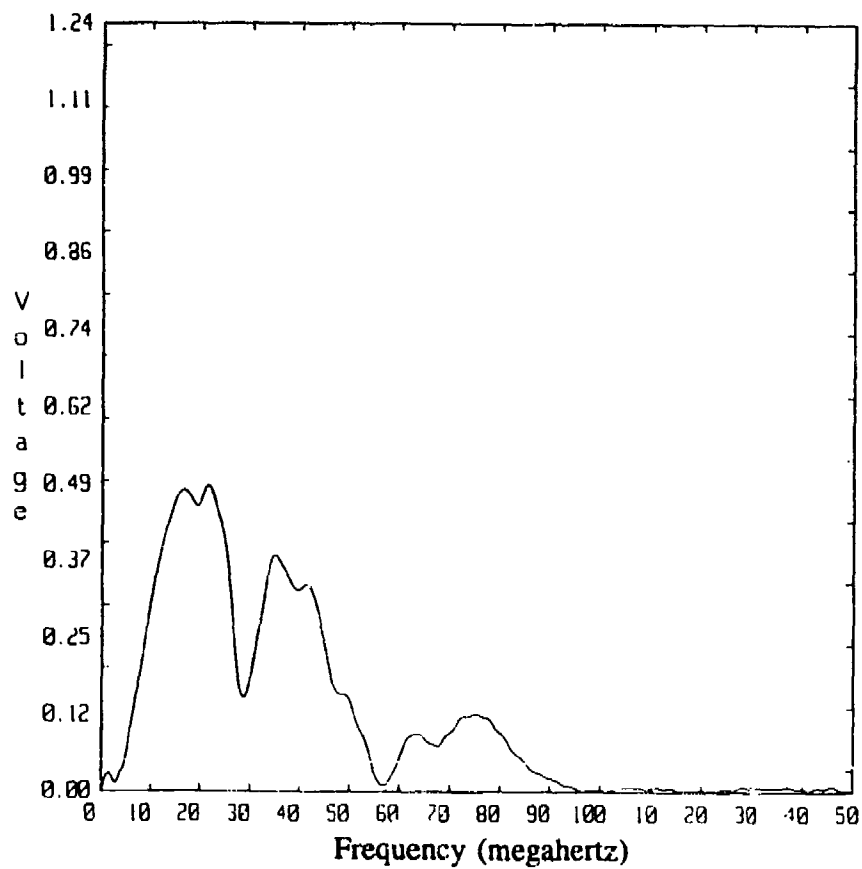
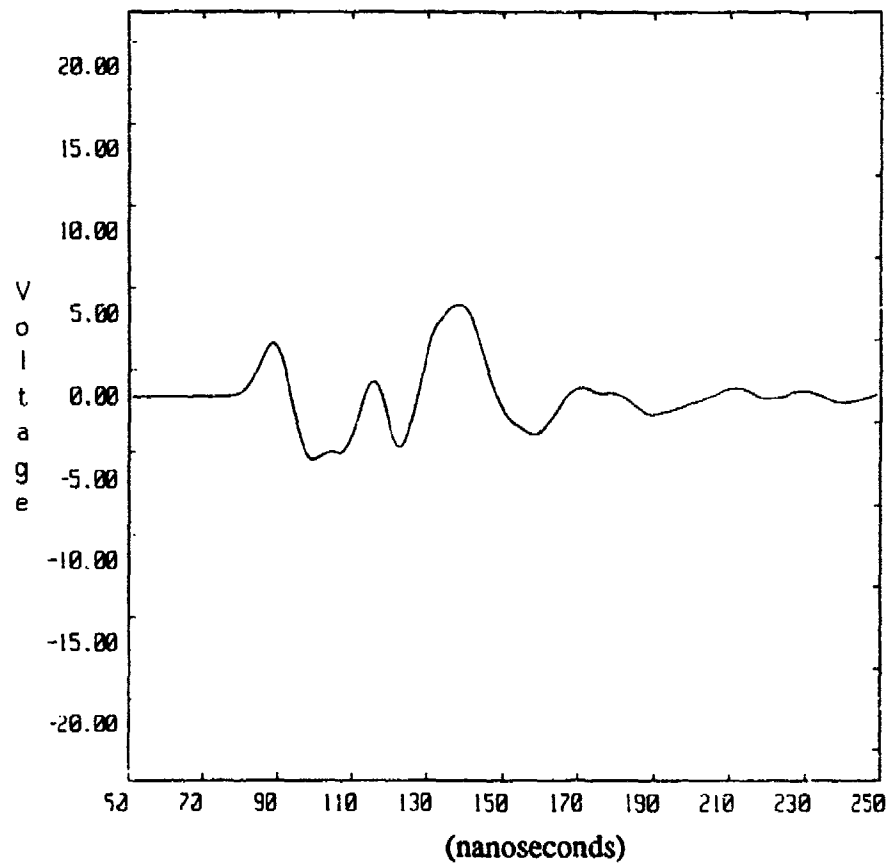


FIGURE 23. TIME-DOMAIN AND FREQUENCY-DOMAIN REPRESENTATIONS FOR
TUNNEL B, 144.2 METER DEPTH

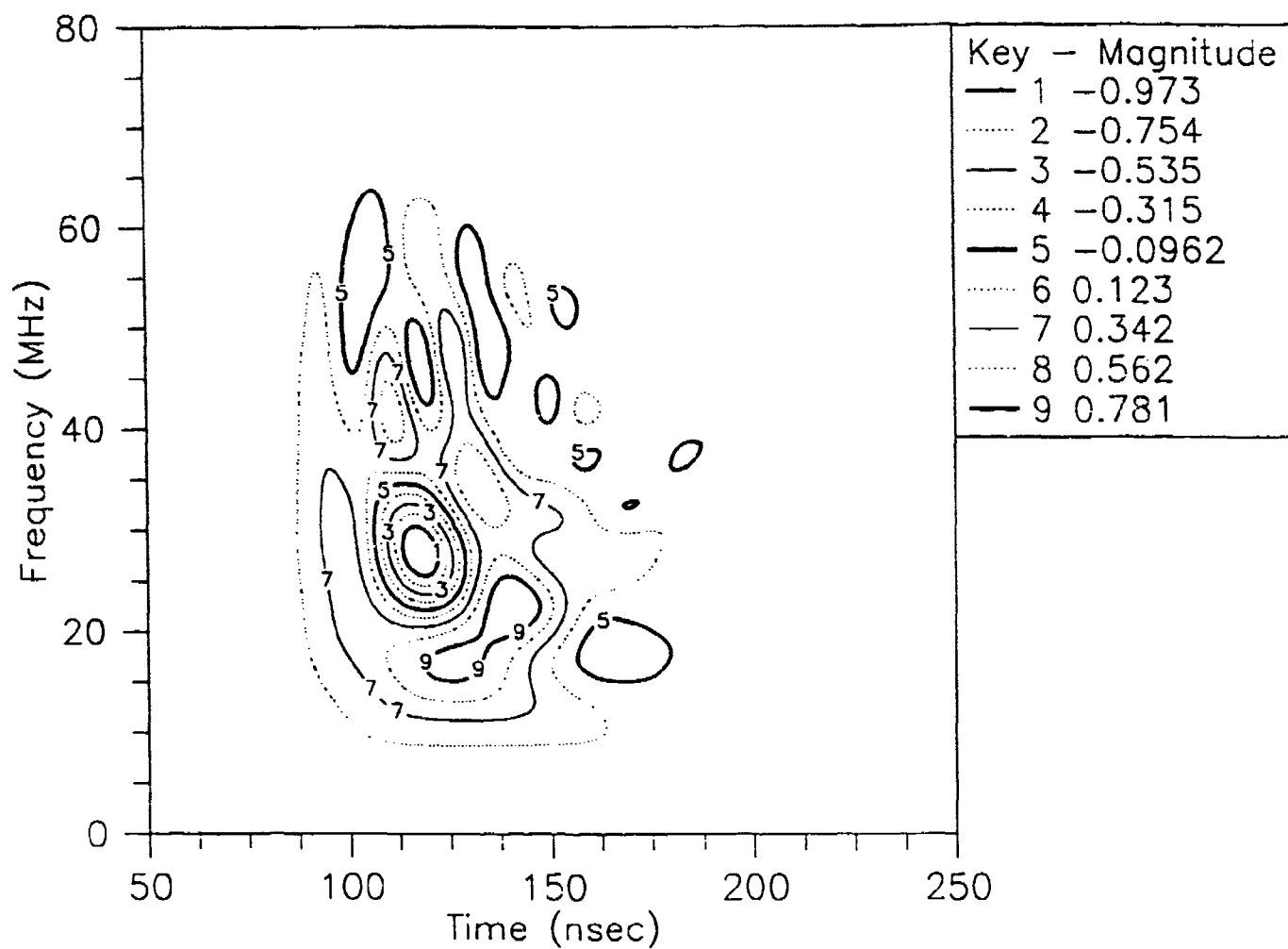


FIGURE 25. WIGNER-VILLE DISTRIBUTION FOR TUNNEL B, 144.2 METER DEPTH

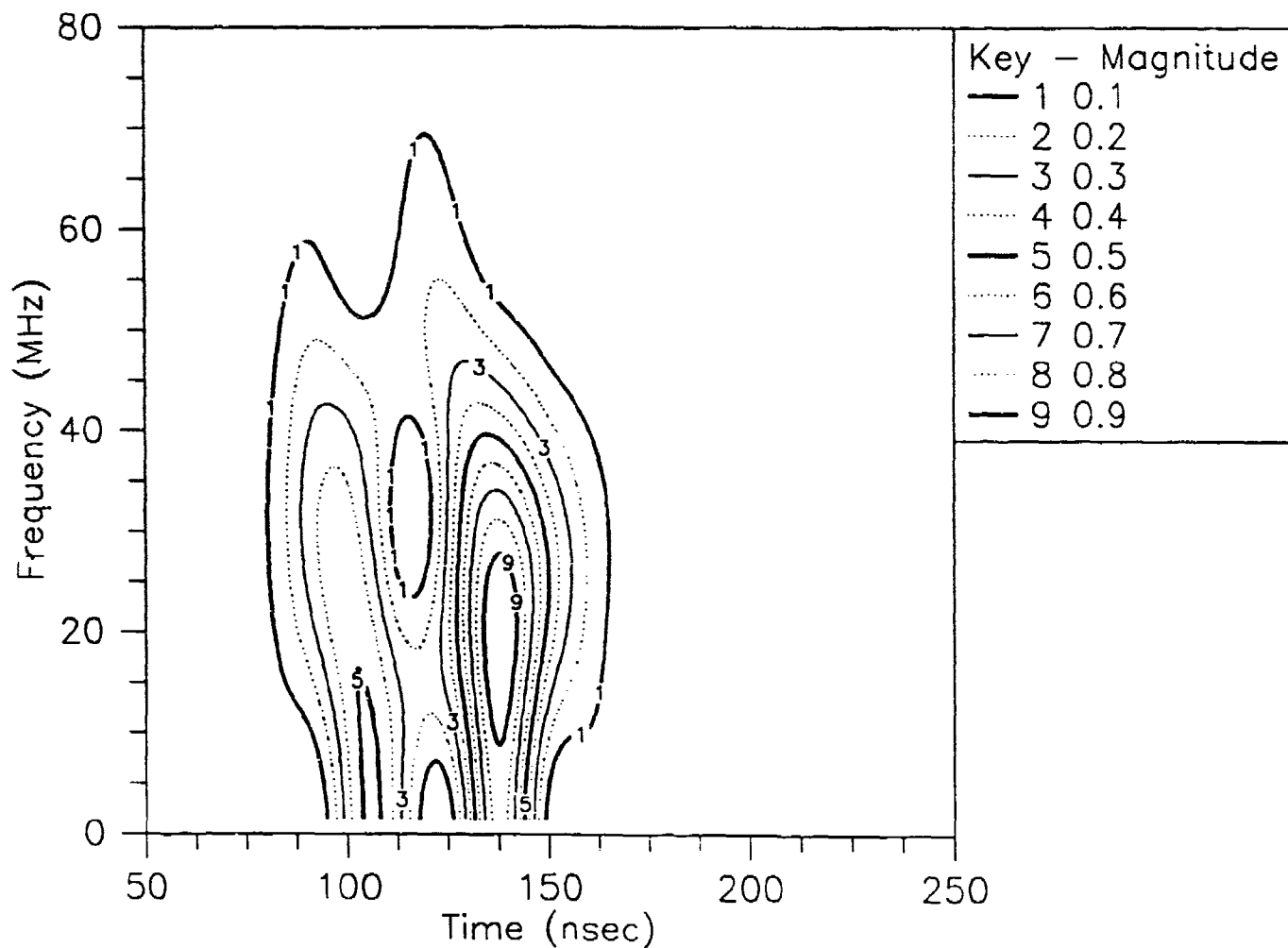


FIGURE 24. SPECTROGRAM FOR TUNNEL B, 144.2 METER DEPTH

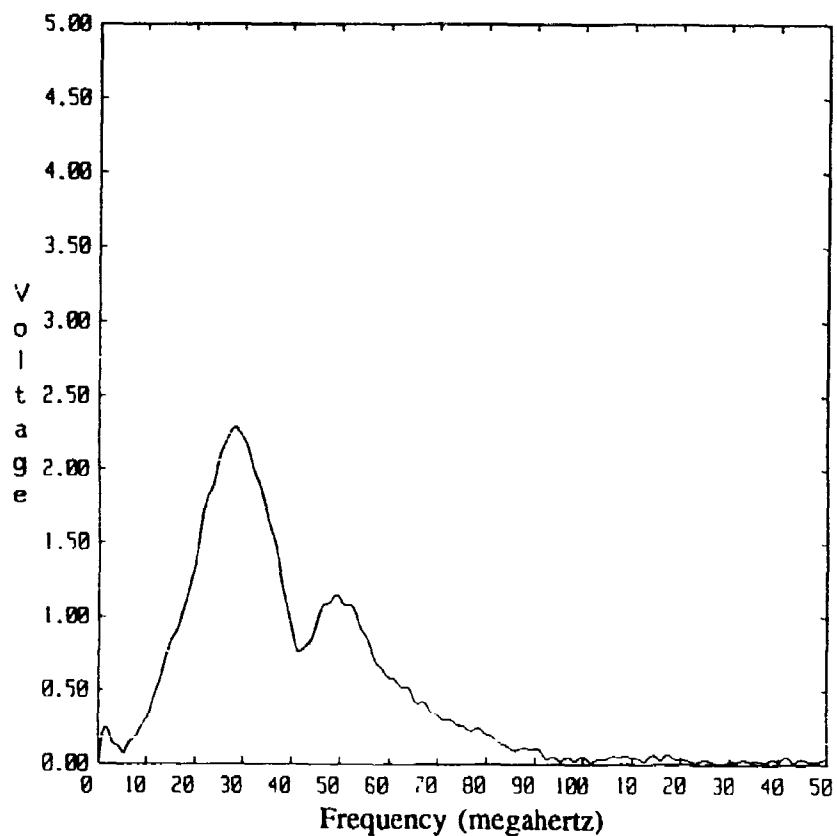
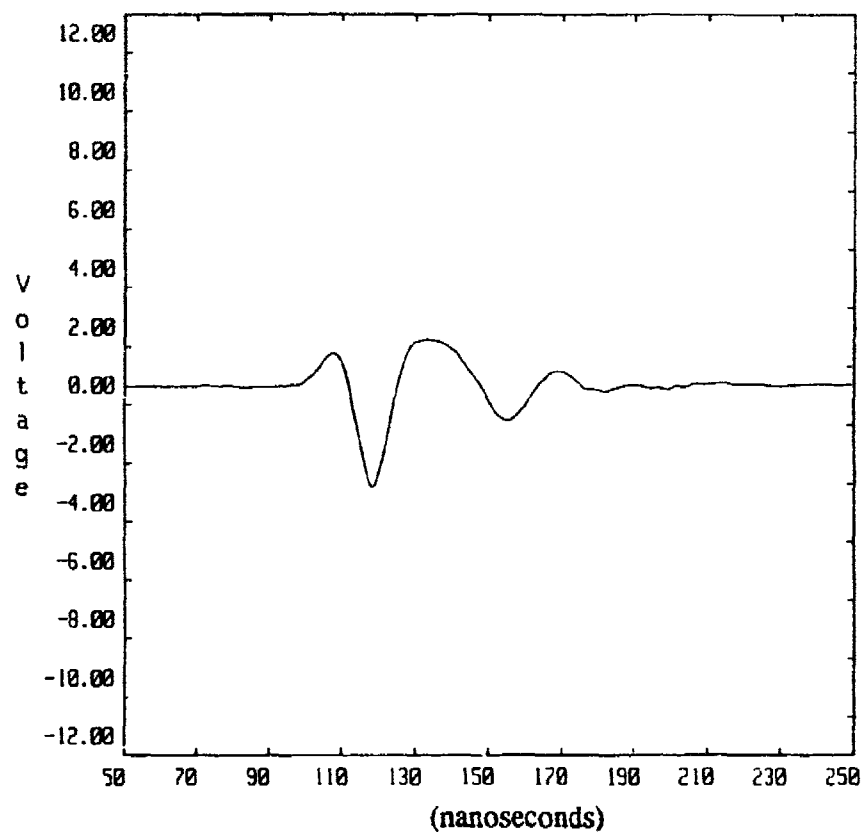


FIGURE 26. TIME-DOMAIN AND FREQUENCY-DOMAIN REPRESENTATIONS FOR TUNNEL B, 141.7 METER DEPTH

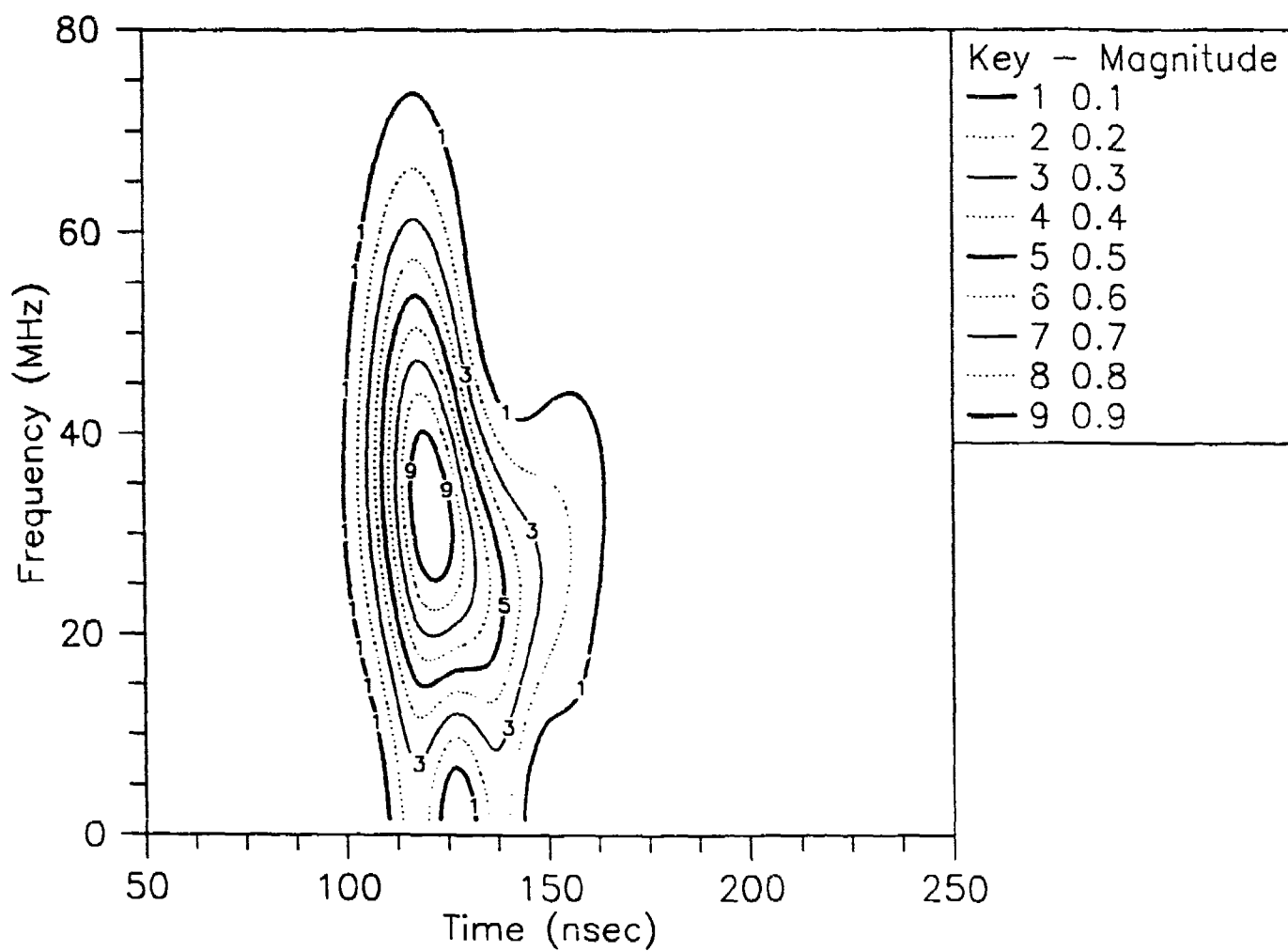


FIGURE 27. SPECTROGRAM FOR TUNNEL B, 141.7 METER DEPTH

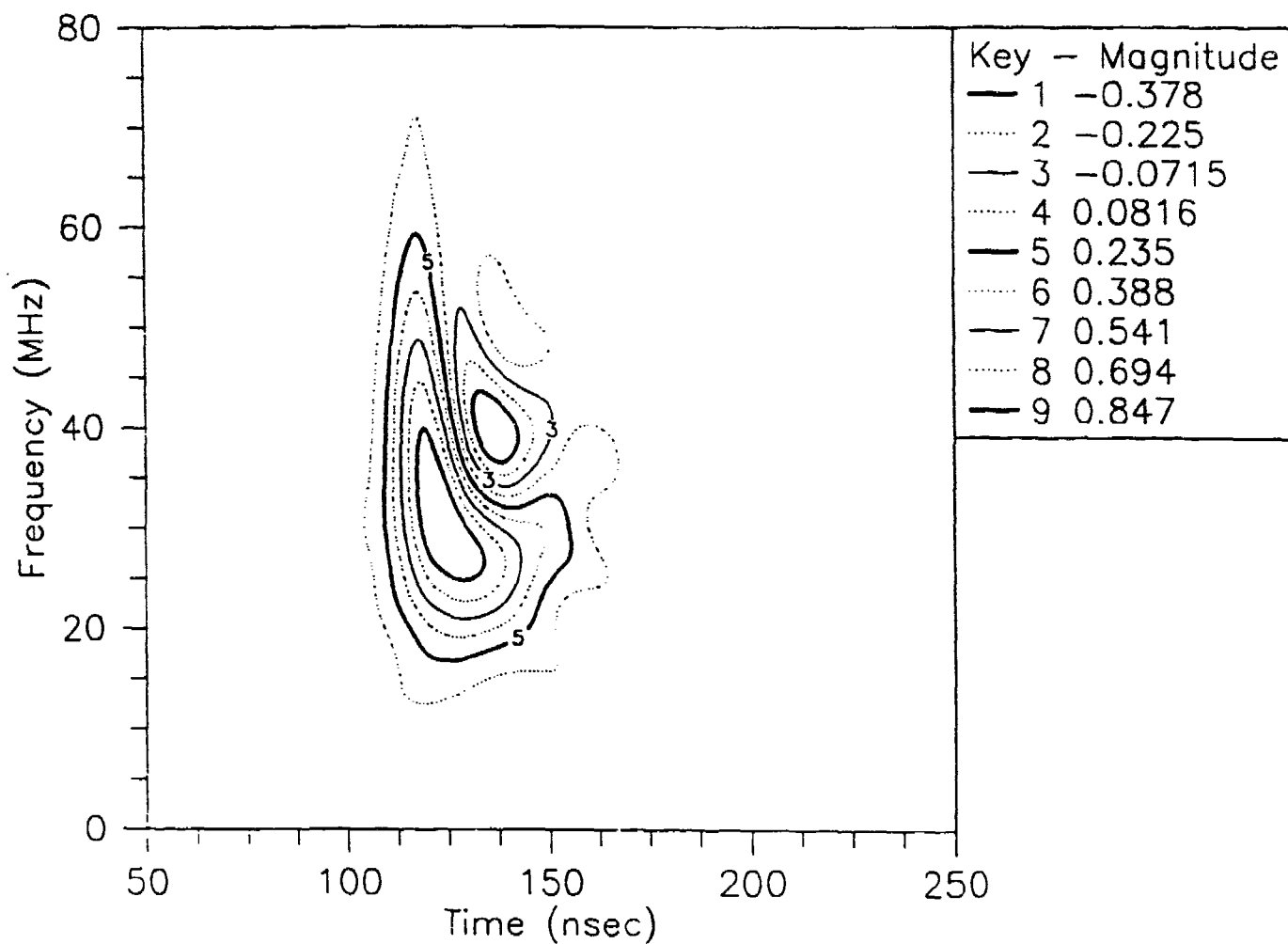


FIGURE 28. WIGNER-VILLE DISTRIBUTION FOR TUNNEL B, 141.7 METER DEPTH

THE ROLE OF CROSS BOREHOLE RADAR IN THE DISCOVERY OF "FOURTH TUNNEL" AT THE KOREA DMZ

Se-Yun, Kim

Div. of Appl. Phys. Elect.

Korea Institute of Science and Technology

P.O. Box 131 Cheongyangni, Seoul, Korea

Jung-Woong Ra

Department of Electrical Engineering

Korea Advanced Institute of Science and Technology

373-1, Kusung-dong, Yusung-gu, Taejon, Korea

ABSTRACT

Cross borehole radar was used to find and locate the Forth Tunnel at the Korean DMZ.

INTRODUCTION

A North Korean defector informed that he was a underground tunnel designer in the North and gave the direction as well as the depth of the 3rd DMZ tunnel, sometime in 1974. They soon started to dig boreholes around this area at the intervals of less than two meters, which is the tunnel size, but they could not find the tunnel. Many years later, they saw the water in one of the dug boreholes blated from which they found the 3rd tunnel.

This blasted borehole was found to shave the wall of the tunnel. Finding a underground tunnel in the depth of about 100 meters or more is very difficult with this kind of approach ever if they know the position of the tunnel, because the borehole is not straight and the end of the tunnel may not cross the plane of boreholes. It is well known that about 5 meters are deviated per every 100 meters in digging vertical boreholes. All of the underground tunnels in the Korean DMZ were found accidentally or by hearing the sound of the blasting TNT up to the 3rd tunnel.

Pulsed electromagnetic tunnel detection system [1] was introduced around 1979 in Korea and the interval of the boreholes were set by 20 meters for the hole-to-hole measurement of the tunnel. KAIST continuous electromagnetic wave system was developed around and UNC tested its capability in 1987. From this tested capabilities Korean Army gave about 4-months contract (August to December 1989) to use KAIST CW system in the Korean DMZ and found the 4th tunnel.

Role of the Cross Borehole Radar cross Borehole Radar

In order to find the tunnels, one needs to define the possible lines where these tunnels may penetrate from various information sources. Then the boreholes are dug to use various instruments in them. The role of the cross borehole radar such as KAIST CW system is to scan thoroughly the plane between boreholes whether there exists such tunnels or suspicious anomalies and their exact location if they exist.

After scanning so many boreholes by KAIST CW system, an interesting but very weak signatures were found in the newly dug northern boreholes between the borehole pairs 4 and 5 in Fig. 1. Since the amplitude pattern versus the depth with frequencies as a parameter was so weak, a painful human decision was needed to pursue further or to skip. It was suggested to confirm this area by digging one more borehole at 1 between 4 and 5. The deviation of the borehole is shown in the figure at the depth of 147 meters, where the small circle designates the surface position and the ended line of about 5 meters shows the deviation. From the careful measurement, one obtains the resonance signature similar to that in Fig. 2 between the boreholes of 1 and 5 at the depth of 146.2 meters but not between 1 and 4.

After this clear results, two additional boreholes 2 and 3 were asked to dig in order to check the direction of the tunnel. Measurements between all the pair of boreholes were made to find similar resonance patterns between borehole pairs of 1 and 3, 1 and 2, 4 and 3, and 4 and 2, but not between 2 and 3, 3 and 5, and 4 and 1. One may run the scanning measurement by the parallel alignment of the two antennas of transmitting and receiving and also an offset alignment with different depths and find the location of the tunnel by the back projection of the depths of the resonance like

the triangular survey. The same depth and the straight direction of the tunnel shown in Fig 1 suggest clearly that this is man-made tunnel.

The last job is to confirm that this is the man-made tunnel by digging borehole through the tunnel. Since the deviation of the boreholes, correction of the deviation by twice, the Forth Tunnel was hit at the 3rd digging.

It took all the patience and the attention. It was so lucky those northern end bore-hole crossed the tunnel. It was a luck to find one tunnel in such a short period of time about three months. But we were really assured by the capability of our machine.

References

- [1] Duff, R. 1988, "Short pulse hole-to-hole electromagnetic tunnel detection system and signal processing development," Proceedings of the Third Technical Symposium on Tunnel Detection, Golden, Colorado, Jan.

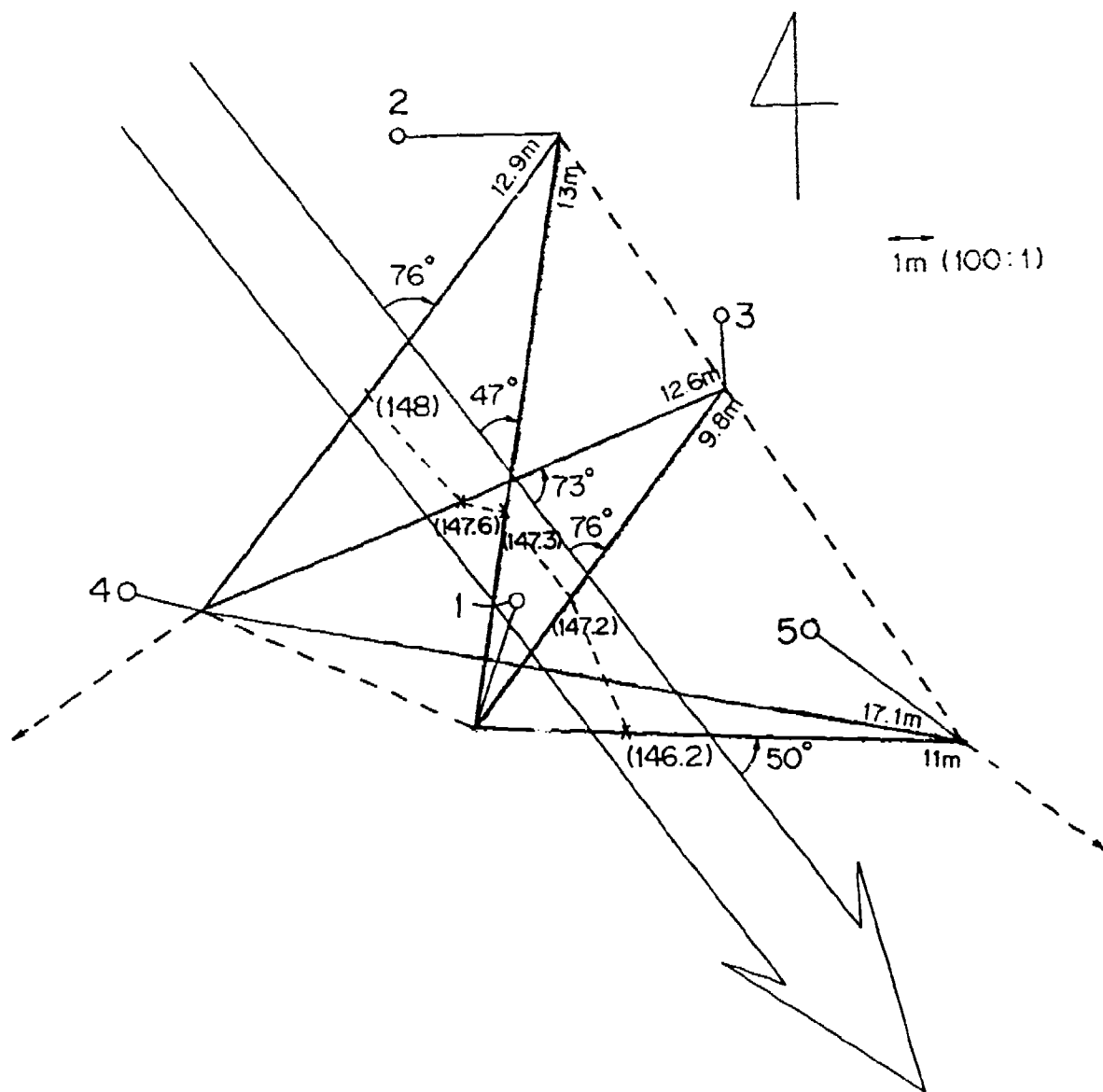


Figure 1. Location of bore-hole and tunnel

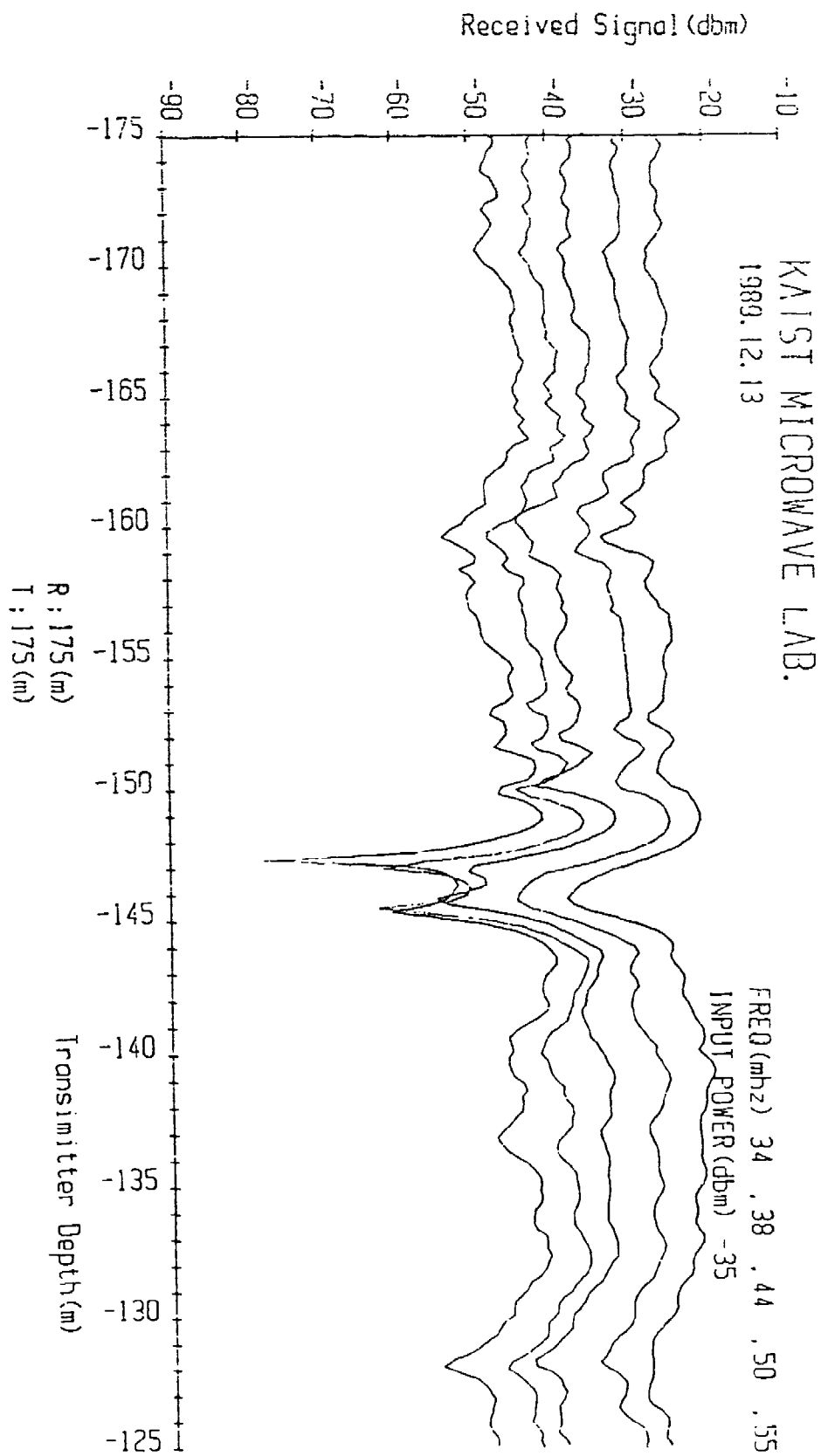


Figure 2. Amplitude pattern between bore-hole 1 and 3 at the Fourth Tunnel

WAVEFORM MODELING OF ELECTROMAGNETIC TUNNEL SIGNATURES FOR INTEGRAL EQUATION TE AND TM MODE

Roy J. Greenfield, Geosciences Dept., Penn. State Univ., Univ. Park, PA.

SUMMARY

A method has been implemented for generating synthetic two-dimensional TE and TM Mode waveforms for cross-borehole surveys for detection of tunnels, caverns, or anomalous material. Cross-borehole radar was initially used in the frequency-domain by Lytle et al (1979) to look for underground openings such as tunnels or caves. Owen and Schler (1980) developed a time-domain pulse system (PEMSS) for similar purposes. Both systems used vertical electric dipole transmitters and receivers. For a transmitter-to-receiver path perpendicular to the tunnel axis, the TE mode (magnetic field along tunnel axis, electric field transverse to the axis) is the propagation mode. It would also be possible to develop a system that relies on TM mode (electric field along the tunnel axis, magnetic field perpendicular to the axis) using wire loop sources and receivers.

Modeling is done for both TE and TM mode propagation, using integral equation solutions. This method is also known as the moment method. Frequency-domain solutions are convolved with source time functions obtained by deconvolution of field data. The result of the integral equation modeling was verified by comparing waveforms with series solutions for circular-cross-section tunnels. Synthetic waveforms are also compared to data from known tunnels.

Synthetic PEMSS waveforms (center frequency around 30 MHz) are given for a variety of tunnel shapes. The results show how waveforms are related to tunnel cross-section. For circular and square tunnels of the same cross-sectional area, the waveforms are quite similar. The waveforms are however quite sensitive to tunnel height and width for rectangular tunnels and to tunnel size. Results are also given for conductively lined tunnels. Data from a tunnel that appears to be partially filled with water compare well to synthetics. Data from a field example with a 9m-wide opening are compared with synthetic waveforms. The change in waveforms with tunnel configuration indicates that it may be possible to invert time-domain waveforms to get the general tunnel shapes. For 30 MHz waveforms, details in tunnel shape of less than about 0.5 m probably cannot be resolved.

The signal parameters arrival time, amplitude, and wave period were measured on synthetic waveforms, for different tunnel configurations, and plotted versus transmitter and receiver position. The plots showed that the arrival time and amplitude parameters developed by Olhoeft (1988) are generally useful for detecting tunnels, even when the tunnel shape departs from the 2-by-2 m tunnels for which they were developed. The period parameter however is not robust to changes in tunnel size.

INTRODUCTION

Cross-borehole radar was initially used in the frequency-domain by Lytle et al (1979) to look for underground openings such as tunnels or caves. Lytle et al used integral equation modeling to fit frequency-domain amplitude data. Owen and Schler (1980) developed a time-domain pulse system for similar purposes. The time-domain system has advantages over the frequency-domain system in terms of simplicity of interpretation and ability to discriminate against noise on the basis of arrival time.

Several methods of identifying tunnel signatures on time-domain records have been developed based on the properties of field data from tunnels with close to 2m-square cross-section tunnels (Olhoeft, 1988; Kemerait et al, 1988). Time-domain modeling using circular cross-section tunnels has been done and has produced a good fit to field data. This modeling used a series solution. (Greenfield, 1988; Moran and Greenfield, 1990; Moran, 1989). Examples of these waveform fits are shown in Figure 1. The amplitude variations with depth also agree.

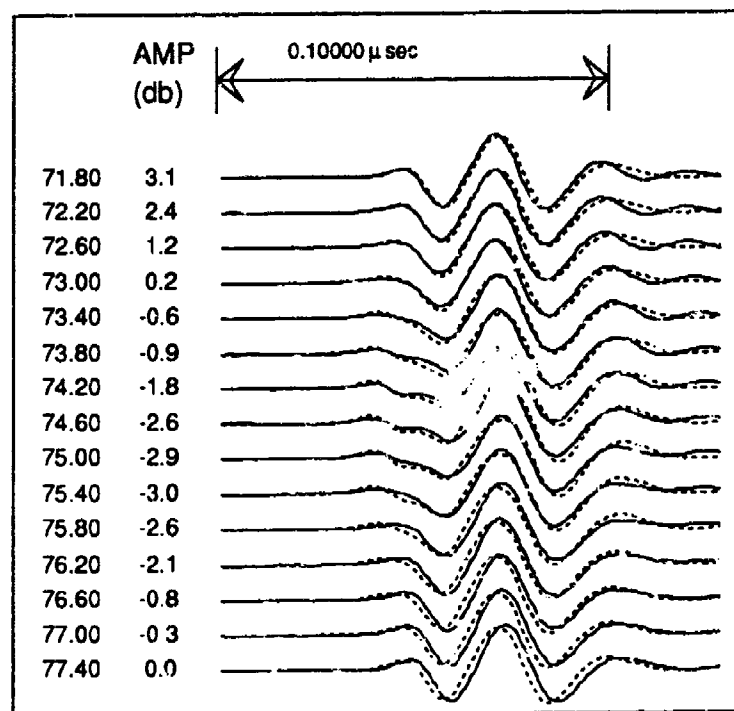


Figure 1. Fit of field data (solid line) at a tunnel with series solution synthetic waveforms (dashed lines). Path length was 25 m.

Both the Lytle et al system and the Owen and Schler system used vertical electric dipole transmitters and receivers. For a transmitter-to-receiver path

perpendicular to the tunnel axis, the TE mode (magnetic field along tunnel axis, electric field transverse to the axis) is the propagation mode. It is possible to develop a system which relies on TM mode (electric field along the tunnel axis, magnetic field perpendicular to the axis) using wire loop sources and receivers.

In this study, modeling is done for both TE and TM mode propagation, using integral equation solutions. Results are given for a variety of tunnel shapes as well as for tunnels with conducting floors and conducting crack halos above the roof.

THEORY

The integral equation method is used to obtain frequency-domain solutions for a unit source. All solutions are two-dimensional. The geometry is shown in Figure 2. The frequency-domain solutions are based on the work of Richmond (1965) for the TM mode and Richmond (1966) for the TE mode. The Richmond TE method was modified for a two-dimensional vertical electric dipole by Lytle et al (1979). Frank and Balanis (1983) and Howard and Kretzschmar (1986) have implemented the TM mode for line current sources. In the present work a vertical two-dimensional magnetic dipole source was used for the TM mode. The method was generalized slightly to allow the anomalous zone to be composed of more than one type of material. The material is defined by its dielectric constant, ϵ , and conductivity, σ . The free-space magnetic permeability is used for all materials.

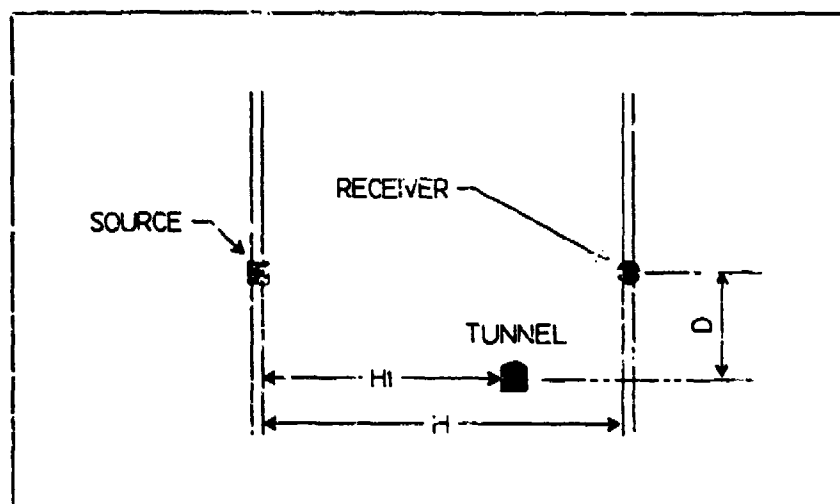


Figure 2. Geometry for integral equation modeling. Source and receiver at D above tunnel center

The frequency domain solution is convolved, in the frequency-domain, with a current source time function to give synthetic waveforms. An observed cross-borehole radar waveform is deconvolved to give the current source time function. The primary is centered around 30 MHz.

Confirmations Of The Calculations

To demonstrate the accuracy of the integral equation waveform calculation, a comparison is made between the Integral Equation method results and results with the series solution method for an air filled circular tunnel (Greenfield, 1990). Figure 3 shows that the waveforms given by the two methods are very close.

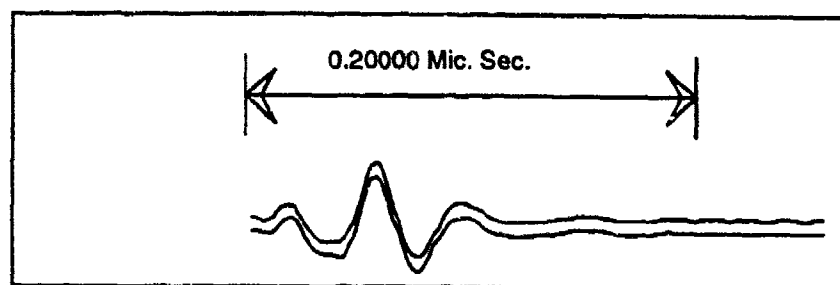


Figure 3. Waveform comparison between analytic (bottom waveform) and Integral Equation (top waveform) methods of calculation. Tunnel model is a 1 m radius circle. 80 blocks were used to form the Integral Equation model. TE mode. At $D = 0$ m.

RESULTS

Synthetic TE Waveforms For A Group Of Models

Eight of the models for tunnels that will be discussed are shown in Figure 4. In all models the rock and tunnel (air) materials have respectively relative dielectric constants, $\epsilon_r = 8$ and 1, and conductivity, $\sigma_r = .001$ and 0 s/m. at 30 MHz, the wavelengths in rock and air are 3.3 and 10 m respectively. Model A is a basic circular tunnel of radius 1.128 m which gives a cross-section area of 4 m². Model B is a 2-by-2 m square with the same area. Model C is a wide 3.2-by-2 m tunnel, Model D a high 2-by-3.2 m tunnel, and Model E a 2.6-by-2.6 square tunnel. Model F is close to the same shape as the square model, Model B, but is rotated 45°. Model G is a 2-by-2 m tunnel but has a 0.1 m thick conducting floor with $\sigma = .05$ s/m, $\epsilon = 20$. Model H represents a 2-by-2 m tunnel with a conductive fractured roof with $\sigma = .05$ s/m, $\epsilon = 20$.

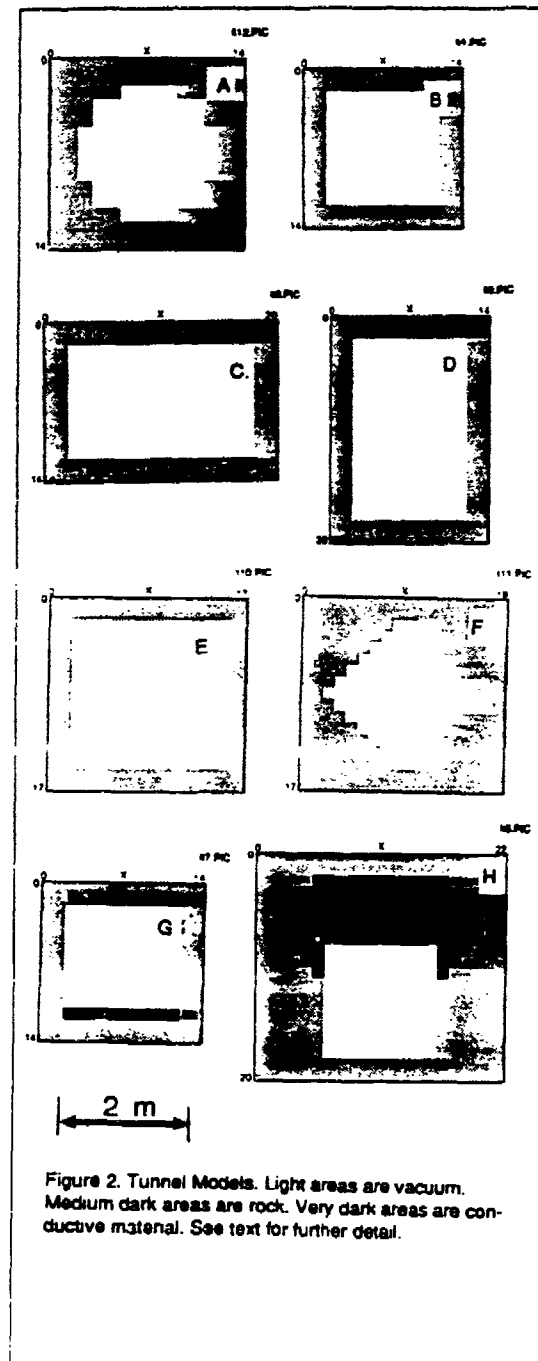


Figure 4. Tunnel Models. Light areas indicate vacuum. Medium dark areas are rock. Very dark areas are conductive material. See text for further details.

Figure 5 gives the TE waveforms for the Model B tunnel. The distance of the transmitter and receiver above the tunnel center, D , and the peak-to-peak amplitude is given for the waveforms. Spacing between waveforms is .4 m. This format is used for all waveforms shown. This set of waveforms is typical of those seen in field data for 2-by-2 m tunnels in metamorphic or igneous rock.

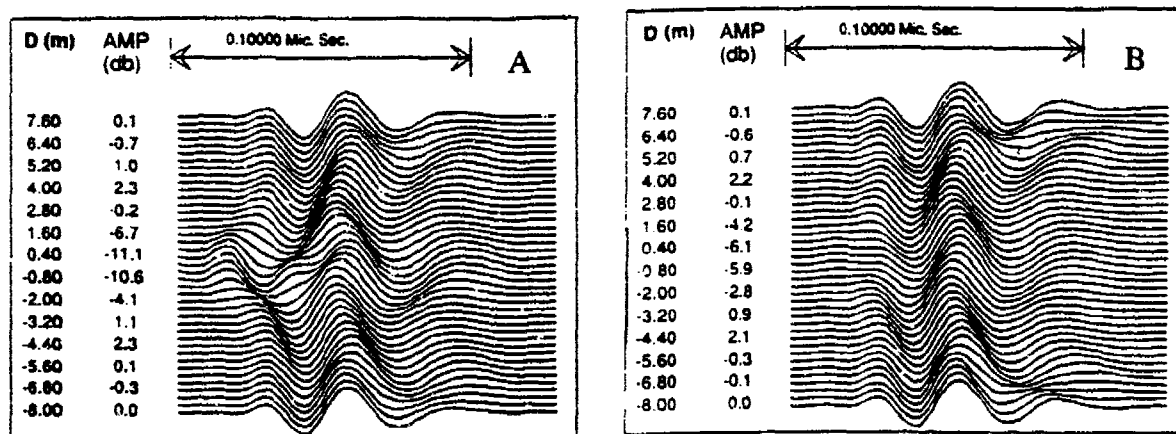


Figure 5. Waveforms for Model B. (A) TE mode. (B) TM mode. Amplitudes are peak-to-peak

Figure 6 shows a composite of TE waveforms for $D = 0$ m. Waveforms are shown for the primary waveform and for Models A to H. The waveforms for the circular tunnel (Model A), the 2-by-2 m tunnel (Model B) and the 2-by-2 tunnel with conducting floor (Model G) are very similar. The waveform for the diamond shaped tunnel (Model F) is also similar. The waveform for the wide tunnel (Model C) is more complicated than the other waveforms and has three positive peaks. The waveforms for Models D and E are also different from the circular tunnel waveform (Model A).

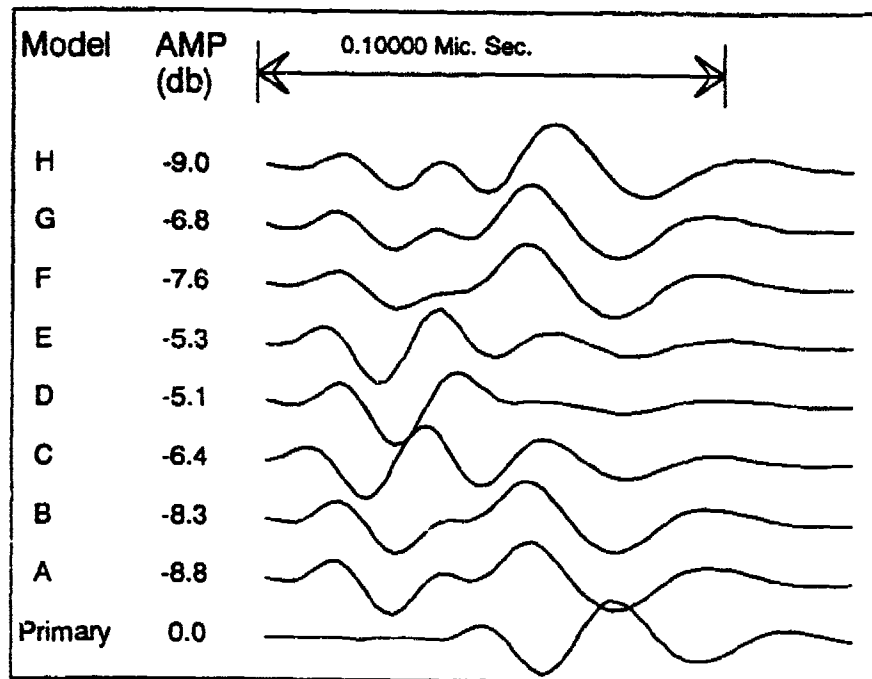


Figure 6. Composite TE waveforms for the primary waveform and 8 tunnel models. For $D = 0$ m.

Conductive Halo Model

Figure 7 shows the waveform set for the 2-by-2 m tunnel with the conductive roof halo (Model H). For this model some of the waveforms are quite distorted from the effects that occur for the square tunnel alone. Also the -15 db maximum of the amplitude anomaly is greater than for any of the other models. The parameter anomalies do not extend as far above the center of the tunnel as for the other tunnel models.

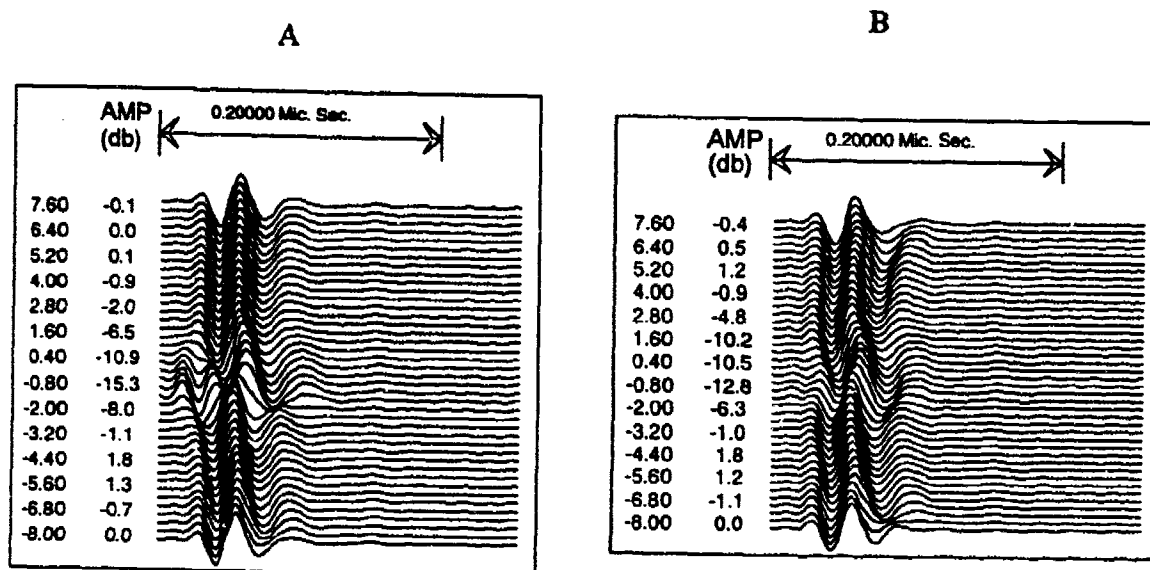


Figure 7. Synthetic waveforms for 2-by-2 m rectangular tunnel with conductive halo, Model H. (A) TE mode. (B) TM mode.

Identification Parameters

The typical indications of the tunnel are the early arrival times, the decrease in amplitude, and an increase in the period from the first positive peak to the second positive peak. Olhoeft (1988) defined three parameters, based on observations of data, to use in identifying tunnels. The first, termed "Velocity," was based on the arrival time of the first break. The second, termed "Attenuation" was based on the amplitude of the first peak in the waveform. The third, termed "Dispersion," was the period between the first and second positive peaks. In this paper similar parameters are denoted as Time Delay (arrival time of first break), Amplitude (amplitude of first positive peak), and Period (the period between the first and second positive peaks). These are measured on the synthetic waveforms. The definition of these parameters is shown in Figure 8.

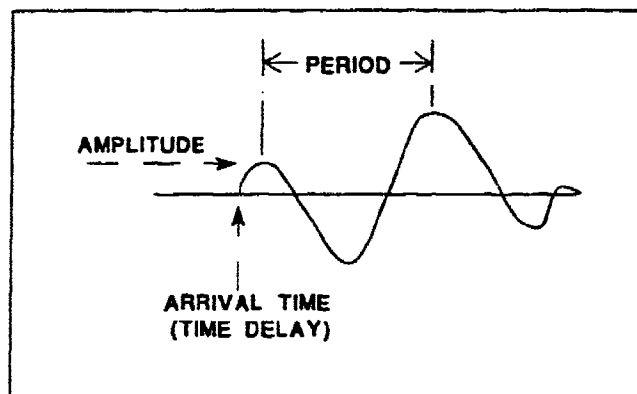


Figure 8. Definition of three waveform parameters.

Figure 9 gives plots of the three parameters versus D . Early arrivals occur for all models. A somewhat unexpected result is that the vertical extent of the early arrival is widest for Model C, not for Model D. The Model E time delay has the second greatest vertical extent. The amplitude parameter is consistent. It dips in the region of the tunnel for all models. All models do not have their smallest amplitude at $D = 0$, but rather have their smallest amplitudes at approximately 2 m above and below the tunnel axis. The period parameter shows a consistent increase around $D = 0$ for all models except for models C, D, and E. For these models the period increases from its primary waveform value of .026 ?? at $D = +2$ and -2 m. But near $D = 0$ the period is close to the .026 μ s primary waveform value.

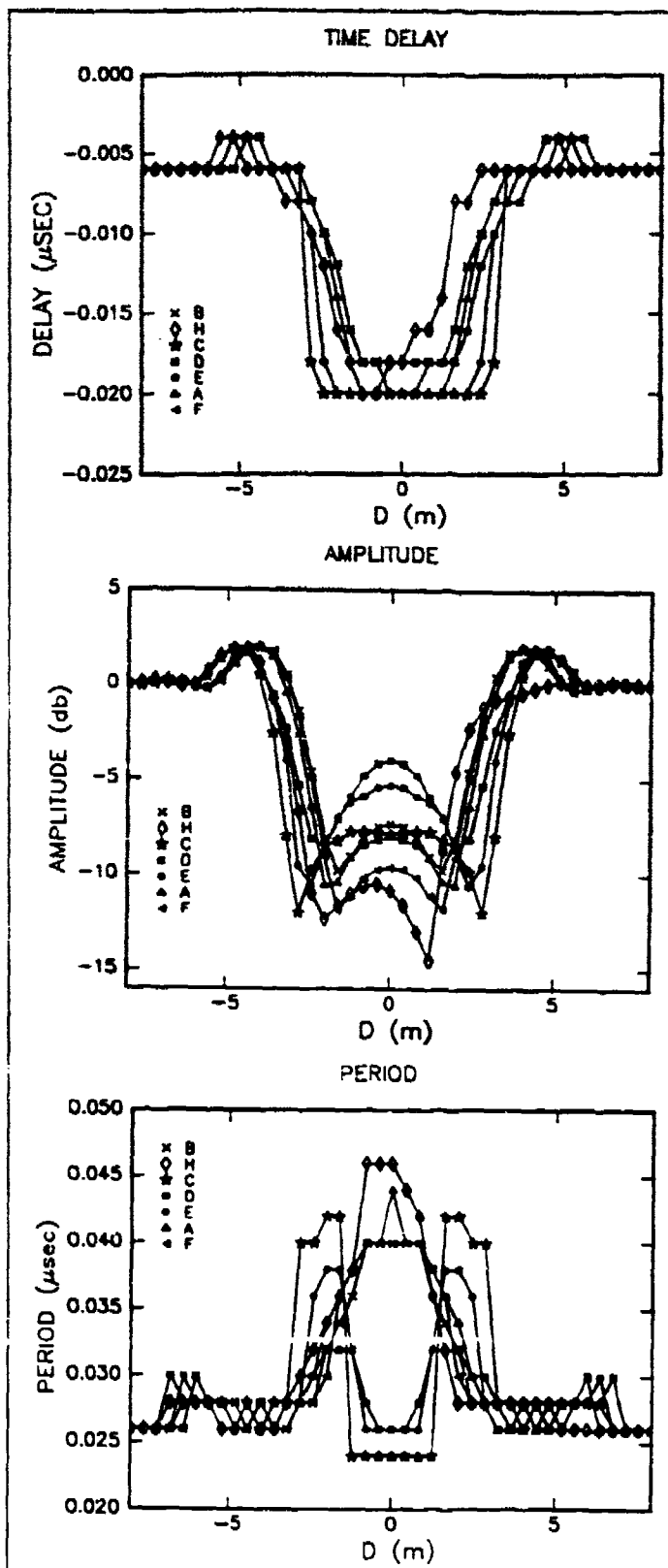


Figure 9. Plots of Delay Time, Amplitude of the first peak, and Period Parameters

Comparison Of TM With TE Waveforms

Figure 5 gives the TM waveforms for the square tunnel (Model B). The major features on the waveform are an amplitude anomaly of -6 db and the disappearance of the first positive peak. Thus, the early arrival due to energy propagating through the tunnel can not be seen. The TM mode tunnel signature for this empty tunnel model is not as clear as was the TE signature of Figure 5.

TM waveforms are shown in Figure 7 for Model H, the tunnel with the conductive halo. These waveforms showed a -15 db anomaly, and the arrival times appeared to be delayed. Thus for the model with the conductive area the TM mode signal shows a strong tunnel signature.

Partially Filled Tunnel Field Example

Data is available from a site, we denote as Site B, where a portion of a tunnel had been filled with rock rubble and water. An approximate cross-section of the filled tunnel is shown in Figure 10A. An alternative configuration for the tunnel is also shown. This field data is shown in the Figure 10B. Synthetic waveforms for the two tunnel configurations are also shown. The arrow in field data of Figure shows a slightly early arrival. This early arrival does not occur in the Figure 10C synthetic waveforms set.

This early arrival can be explained if the rock rubble and water did not reach to the top for the tunnel, but rather left an air space at the top. This model is shown in Figure 10A and the synthetic waveforms for this model are shown in Figure 10D. These synthetic waveforms show the early arrival seen in the field data.

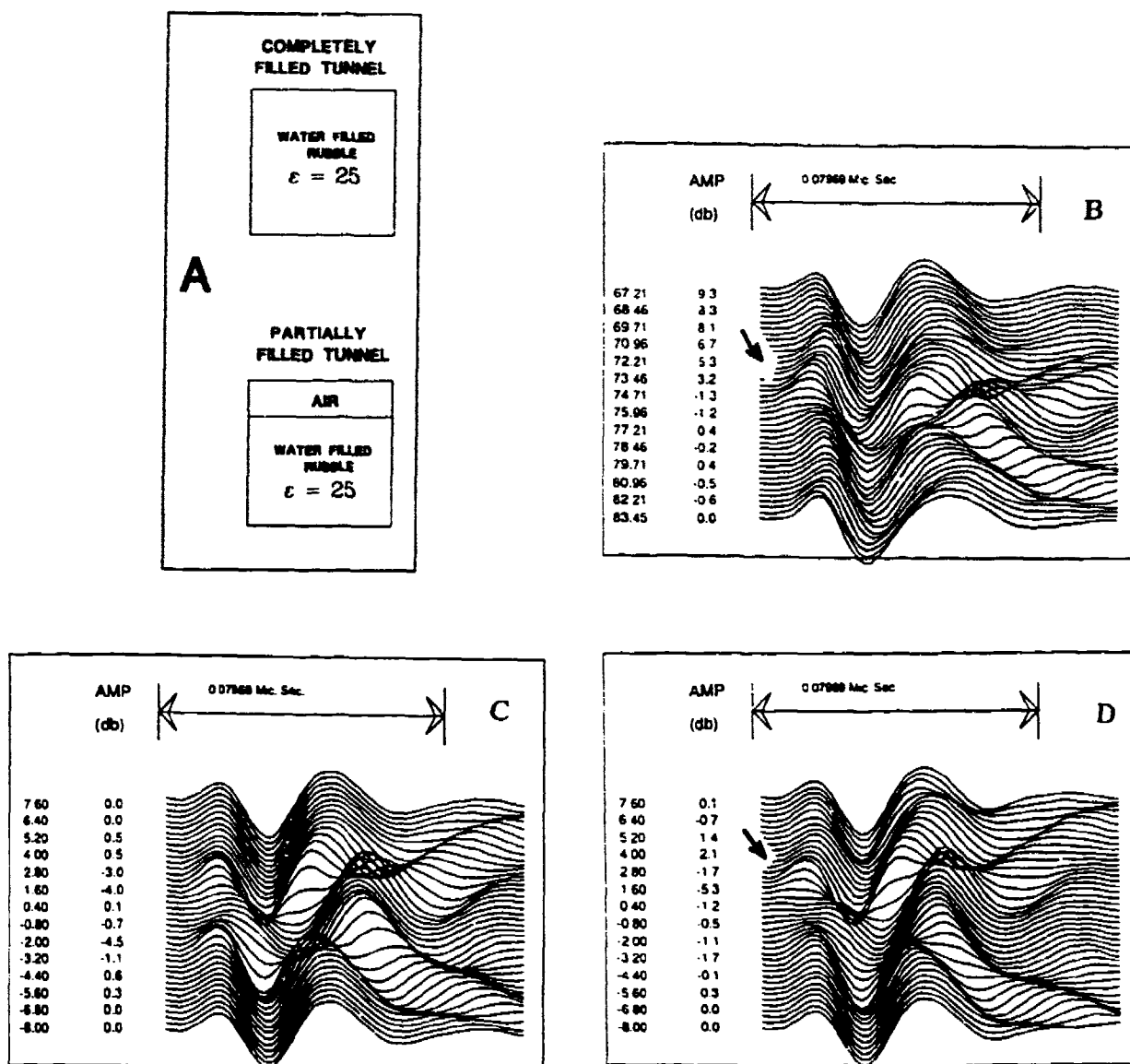


Figure 10. Tunnel configurations (A), field data (B), waveforms for completely filled tunnel (C), waveforms for partially filled tunnel (D).

Fit To Field Data At A Wide Mine

Several years ago data was taken with the PEMSS system at a mine. The path between one set of boreholes went through 9 m of air. The plan view of the experiment and the field data is shown in Figure 11. The peak energy of the signal was around 60 MHz. Only the hard copy record shown was available. The source receiver offset, D, was 0 m for this data.

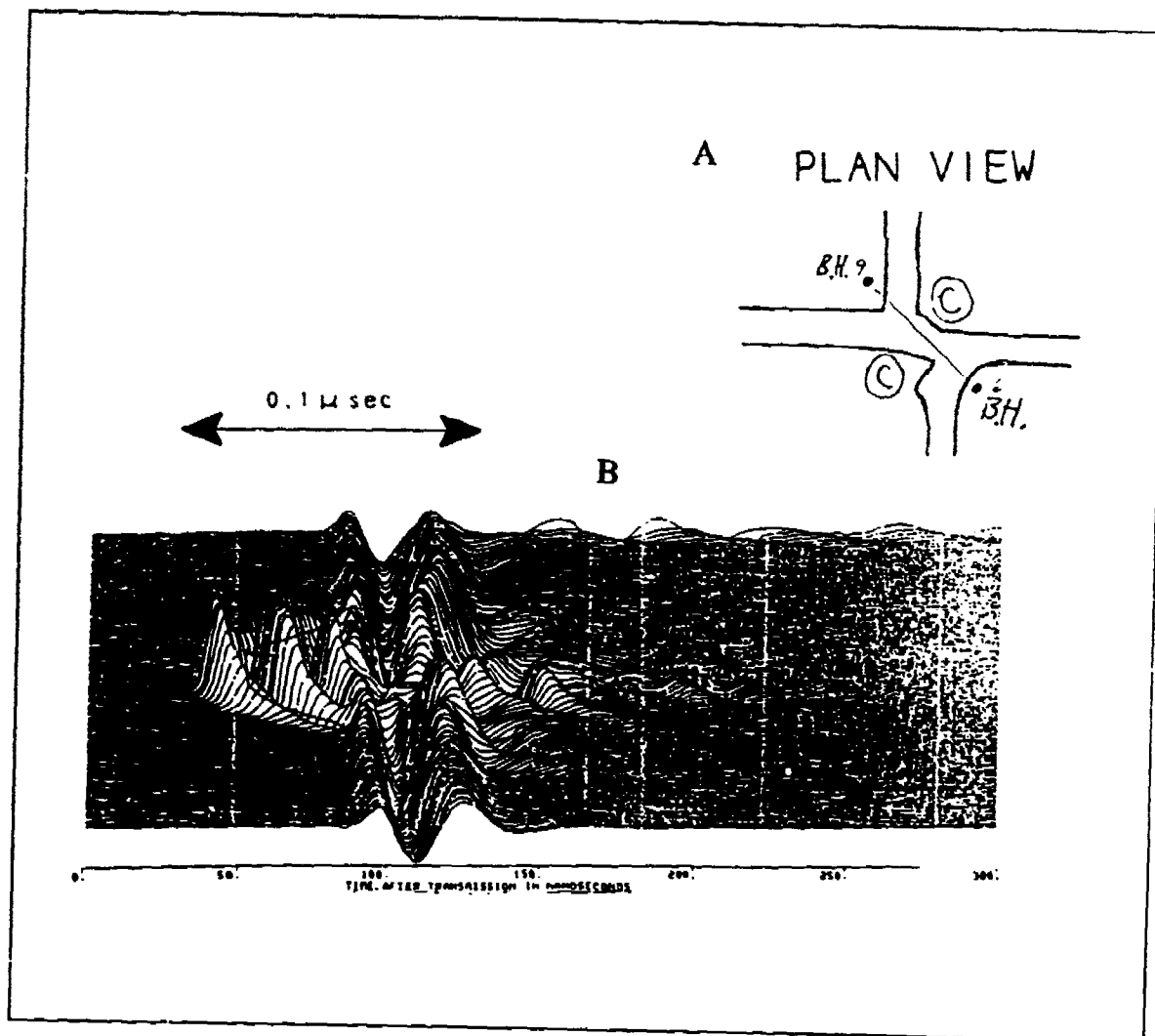


Figure 11. (A) Plan view of geometry for data taken at intersection of two tunnels. The part of the ray path in air is 9 m. Boreholes are separated by 11 m. (B) Field data. Note that peak frequency is approximately 60 MHz.

To model this data, the bottom trace of Figure 11 is digitized and is used as the primary signal. The two-dimensional model along with the resulting synthetic

waveforms is shown in Figure 12. The synthetic waveforms have several things in common with the field data. The tunnel causes the same early arrival (approximately $.05 \mu\text{s}$) in both field and synthetic waveforms. This is the theoretical value of the decrease in arrival time for a 9 m path in air compared to a 9 m path in rock. The first cycle of the waveforms near the mine depth also appears similar. However, there is a third positive peak on the field data that is not on the synthetic waveforms. I attribute this extra peak to energy that has reflected off the corners marked with C's on the Figure 11.

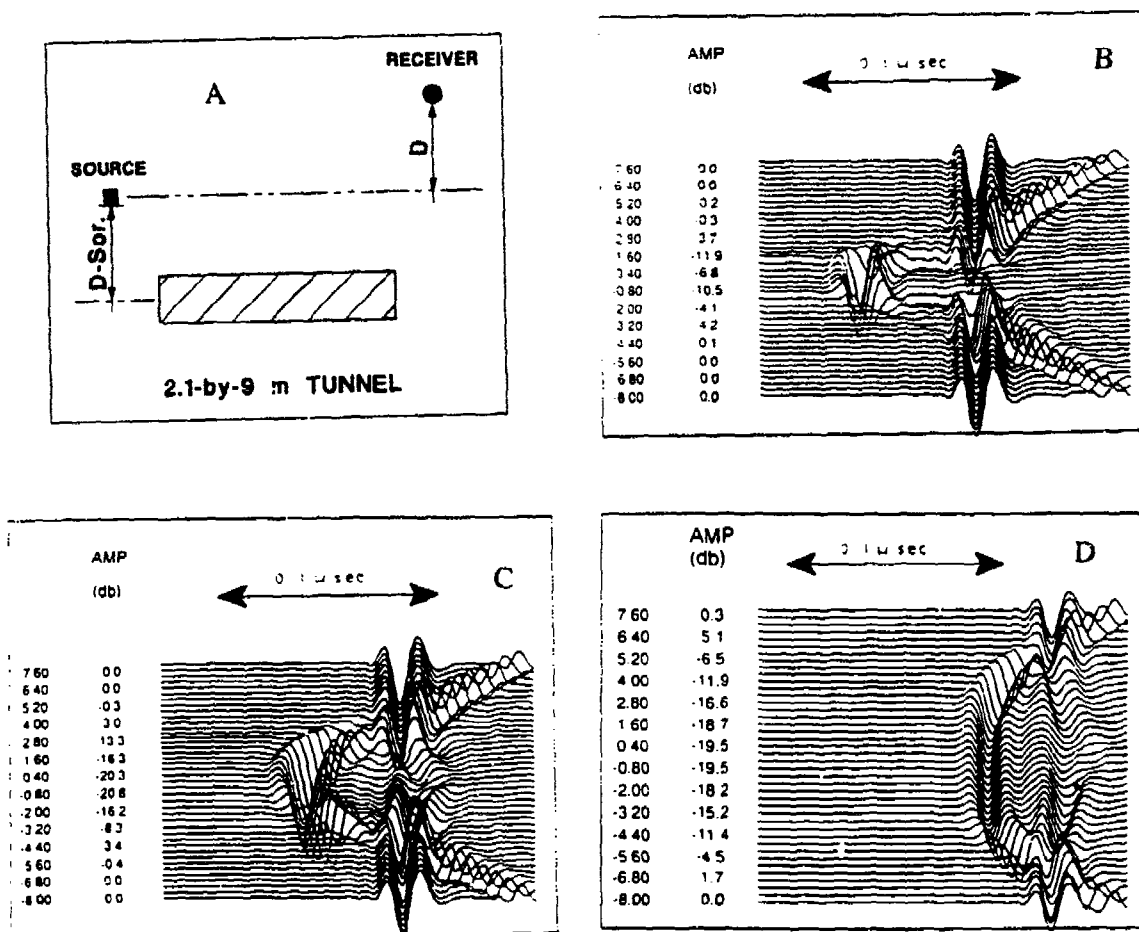


Figure 12. (A) Two-dimensional model to fit field data of Figure 11. Synthetic waveforms for three source-to-receiver offsets, D , are also shown. (B) $D = 0$ m. (C) $D = 5$ m. (D) $D = 10$ m.

Calculations are made of synthetic waveforms, or runs with the receiver offset above the transmitter; the results are shown in Figure 12. As expected the earliness of the arrival time is decreases with offset, D, since the length of the path through air decreases with offset.

CONCLUSIONS

The following conclusions were drawn from the work done in this study.

- a. Successful modeling can be achieved for both TE and TM modeling of cross-borehole data.
- b. Circular and square tunnels of the same cross-sectional area give waveforms that are quite similar.
- c. The waveforms are, however, sensitive to tunnel size.
- d. The change in waveforms with tunnel configuration indicates that it may be possible to invert time-domain waveforms to get the general tunnel shape.
- e. For 30 MHz waveforms, details in tunnel shape with a size scale of less than about 0.5m probably cannot be resolved.
- f. The amplitude and delay parameters developed by Olhoeft are generally useful for detecting tunnels, even when the tunnel shape departs from the 2-by-2 m tunnels for which they were developed. The period parameter can fail to indicate wide tunnels.

REFERENCES

- Frank, M. S., and Balanis, C. A., 1988, Electromagnetic tomography in tunnel detection: Proc. 3rd Technical Symposium on tunnel Detection, Golden, CO, 136-155.
- Greenfield, R. J., 1990, Electromagnetic, frequency-domain modeling of tunnel signatures, Final Rept. Contract Daca39-87-K0013, To Dept. of The Army, Wes, Vicksburg, Ms.
- Greenfield, R. J., 1988. Modeling of electromagnetic propagation between boreholes: Expanded Abstracts 50th Annual SEG Meeting, Anaheim, CA, 220-221.
- Howard, A. Q., Jr., and Kretschmar, J. L., 1986, Synthesis of EM geophysical tomographic data, IEEE Proc., 74, 353-360.

Kemerait, R. C., Griffin, J. N., Meade, J. C., Kraft, G. D., and Pound, G. W., 1988, Signal processing applied to tunnel detection by borehole radar, Proc. 3rd Technical Symposium on tunnel Detection, Golden, CO, 593-615.

Lytle, R. J., Lain, E. F., Lager, D. L., and Davis, D. T., 1979, Cross-borehole electromagnetic probing to locate high-contrast anomalies: *Geophys.*, 44, 1667-1676.

Moran, M. L., and Greenfield, R. J., 1990, Waveform analysis of electromagnetic scattering for a three-dimensional tunnel, Expanded abstracts, 60th Ann. Meeting, SEG, San Fran., CA, 414-417.

Moran, M. L., 1989, Time-domain analysis of electromagnetic scattering for a three-dimensional tunnel in the presence of a vertically oriented electric dipole, MS Thesis, Geosciences Dept., Penn. State Univ., Univ. Park, PA.

Olhoeft, G. R., 1988, Interpretation of hole-to-hole radar measurements, Proc. 3rd Technical Symposium on tunnel Detection, Golden, CO, 616-629.

Owen, T. E., and Schler, S. A., 1980, Subsurface void detection using surface resistivity and borehole electromagnetic techniques: Proc. 1980 National Meeting SEG, Houston, TX.

Richmond, J. H., 1965, Scattering by a dielectric cylinder of arbitrary cross-section shape: *IEEE Tran. on Ant. and Prop.*, 13, 334-341.

Richmond, J. H., 1966, TE-wave scattering by a dielectric cylinder of arbitrary cross-section shape: *IEEE Tran. on Ant. and Prop.*, 14, 460-464.

High-Speed Digital Radar Systems and Applications to Subsurface Exploration

David L. Wright, Gary R. Olhoeft, Thomas P. Grover, and Jerry A. Bradley

U.S. Geological Survey, MS 964
Box 25046, Federal Center
Denver, CO 80225

ABSTRACT

The U.S. Geological Survey has built several ground penetrating radar systems for geophysical and geotechnical applications where high-speed digital data acquisition, recording, and real-time data display are of critical importance. The current generation USGS system, unlike all commercial short-pulse radar systems, avoids analog equivalent-time signal sampling by using a high-speed, radio-frequency digitizer. The result is data rates 100 to 1000 times greater than for systems that use equivalent time sampling. The increase in data rates makes possible extended real-time stacking for enhancing signal-to-noise ratio with a digital stacking unit (DSU) designed and built by the USGS. It has an analog bandwidth of 100 MHz and digitizes at 100 Msamples/s at 8 bits. Time interleaving is used to achieve a 1 Gsample/s equivalent sample rate when necessary. Both sensitivity time control (time varying gain) in the radar receiver and summation averaging (stacking) by the DSU have been employed to increase the effective dynamic range and improve the signal-to-noise ratio of the radar system. The DSU can add any number of waveforms up to 65,536 (2^{16}) without overflow at rates as high as 33 Mpoints/s, and can dump stored data to a computer while simultaneously acquiring new data. The DSU can be used with any computer or work station equipped with the IEEE-488 interface.

The next-generation digital radar system will extend the analog bandwidth to 1 GHz and the single-shot digitizing rate to 1 or 2 Gsamples/s. With time interleaving the equivalent digitizing rate could be 20 Gsamples/s if needed. This system will have adequate speed and bandwidth to use antennas that radiate frequencies up to 1 GHz for high resolution ground penetrating radar (GPR) applications with fast signal stacking. A prototype DSU for this radar system has been tested in the laboratory.

Applications of the existing system include airborne subglacial topographic mapping in Greenland and Antarctica, single-hole radar and hole-to-hole tomography in Colorado, New Hampshire, and Texas for fracture mapping and tunnel detection. Velocity, attenuation and dispersion tomograms at Mirror Lake, New Hampshire illustrate the importance of using more than one measurement parameter for adequate interpretation in some field studies.

INTRODUCTION

High speed digital data acquisition systems have proven essential to the success of airborne and surface radar profiling and highly beneficial to hole-to-hole radar tomography. We have successfully mated commercially available high speed single-shot digitizers to very high speed hardware adders and memories in equipment that achieves exceptional data acquisition and averaging rates. This equipment has provided the digitally recorded data for hole-to-hole tomograms for fracture mapping at the Mirror Lake site, Grafton County, New Hampshire.

The Quest for Range

Every GPR is range limited. In some situations, for example where soil contains large quantities of clay minerals, the range may be too small to be of any practical use and alternative geophysical methods are indicated (Olhoeft, 1992). However, in environments where radar works, the data acquisition and display may be so fast and so revealing that radar becomes the method of choice. For this reason many attempts at extending the range have been and continue to be made. The range of any radar system in a particular environment can be calculated if the radar system, host medium electrical properties, and target parameters are known. The ratio of received signal to transmitted signal is described by the "radar equation" (Skolnik, 1962) which for a planar interface and vertical incidence takes the form of:

$$\frac{P_r}{P_t} = \frac{(G\eta\lambda\rho)^2}{4(4\pi)^2} \frac{e^{(-4\alpha R)}}{R^2} \quad (1)$$

where P_r is the received power, P_t is the transmitted power, G is the antenna gain, η is the antenna and feed system efficiency, λ is the wavelength, ρ is the electric field reflection coefficient at the interface, α is the attenuation in nepers/m, and R is the distance from the radar to the planar interface. Attenuation expressed in dB/m is related to α by:

$$\text{Attenuation(dB/m)} = 8.686\alpha \quad (2)$$

For any receiver of a given bandwidth, the minimum possible electronic noise level is given by the thermal noise as:

$$P_n = -114 \text{ dBm} + 10\log_{10}B + NF \quad (3)$$

where P_n is the noise level or the minimum amplifiable signal level, dBm is power in dB referenced to 1 mW, B is the bandwidth in MHz and NF is the noise figure of the amplifier. In actual use the noise is usually considerably higher than indicated in equation (3) due mainly to radio frequency (RF) signals from man-made sources and from system generated noise. If, in Equation (1), the calculated P_r does not exceed the noise level, no signal will be detected without additional information or processing.

One way to increase the system sensitivity (the ratio of the peak radiated power to the minimum detectable signal) is to increase the transmitter power, but there are practical limits on such increases, including the need to keep wide-bandwidth radiation down to levels that do not create interference with radio, television, other radar, and radiating communications systems. An alternative is to find some way to increase the effective signal-to-noise level in the receiver. For repetitive signals one way to accomplish an improvement is by signal averaging (stacking). The amount by which the signal-to-noise ratio (S/N) is improved if the noise is random and uncorrelated with the signal is given by

$$\frac{S}{N} \text{GAIN(dB)} = 10 \log_{10} N \quad (4)$$

where N is the number of waveforms coherently added. Almost all GPR's have some facility for adding waveforms.

As an illustration of the kind of range improvements that may be achieved by waveform addition, consider Figure 1. A family of curves is generated for attenuations of 0.0 dB/m to 7.20 dB/m. The slope of the 0.0 dB/m curve is due to the geometric ($1/R^2$) factor in a lossless medium. The 0.28 dB/m attenuation rate might be representative of high resistivity, largely unfractured granite in the 30 to 60 MHz frequency range. The 7.2 dB/m attenuation rate might be appropriate for certain welded tuffs. If clay minerals are present, attenuations in excess of 100 dB/m may occur. In Figure 1 it was assumed that the rock has a relative dielectric permittivity of 10, the wavelength was 3 m (corresponding to a 32 MHz frequency) in the rock, the antenna gain was 1.5, the antenna efficiency was 0.15 and the reflection coefficient was -0.52 where the "-" indicates that the reflected electric field is opposite in polarity to that of the incident electric field. An antenna efficiency of 0.15 could occur if the antennas were relatively heavily resistively loaded to reduce ringing. The low assumed antenna efficiency explains the vertical axis intercept of about -37 dB. If the interface were between rock and water the reflection coefficient would be 0.48 which is about the same magnitude as for the rock/air case, but the reflected electric field would have the same polarity as that of the incident electric field. If the system sensitivity is 120 dB without stacking (a relatively good system) the range for a given attenuation rate is the point at which that curve intersects the -120 dB level. If one adds 1000 waveforms, the range moves to the -150 dB line. If the initial system sensitivity is 150 dB without stacking

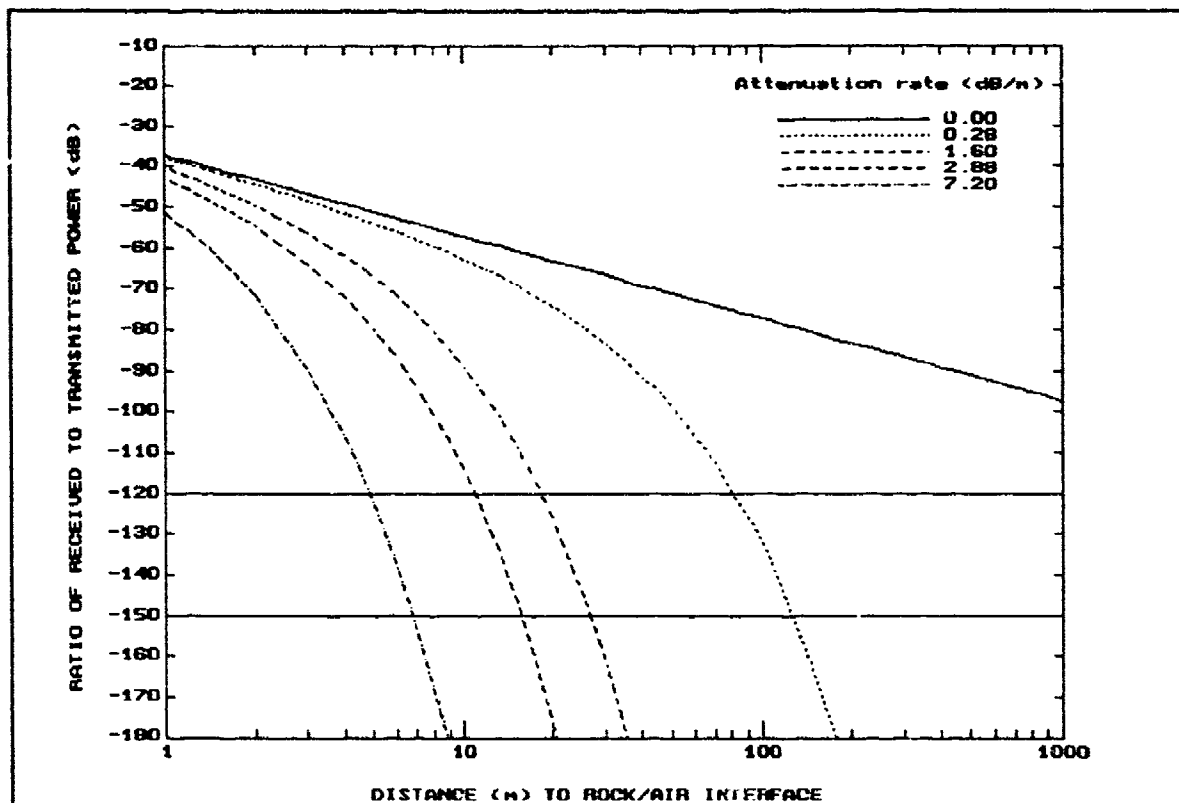


Figure 1. The ratio of received to transmitted power versus distance for various assumed attenuation rates.

(a very good system) and one adds 1000 waveforms, the limit moves to the -180 dB line. The increase in range is large for low attenuations and less for higher attenuations. The DSU that we built can theoretically improve the system sensitivity by up to 48 dB by adding 65,536 waveforms. We have, in Antarctica, added as many as 4096 waveforms while profiling, but as described below, there are practical reasons why one rarely would add as many as 65,536 waveforms.

The Need for Speed

Waveforms must remain in phase during coherent addition. This requirement sets an upper limit on the allowable motion of radar antennas during stacking. The practice that we generally follow is to allow the antennas to move no more than $\lambda/10$, where λ is the wavelength at the "center" frequency (i.e., the peak of the power spectrum of the pulse). For example, in granite at 60 MHz, λ is about 2 m. In such a case, typical of our borehole tomography fracture mapping operations, we do not allow our antennas to move more than 20 cm during stacking.

All commercial short-pulse GPR's use equivalent time sampling, a process in which one point is sampled from an entire waveform each time the transmitter fires (Figure 2).

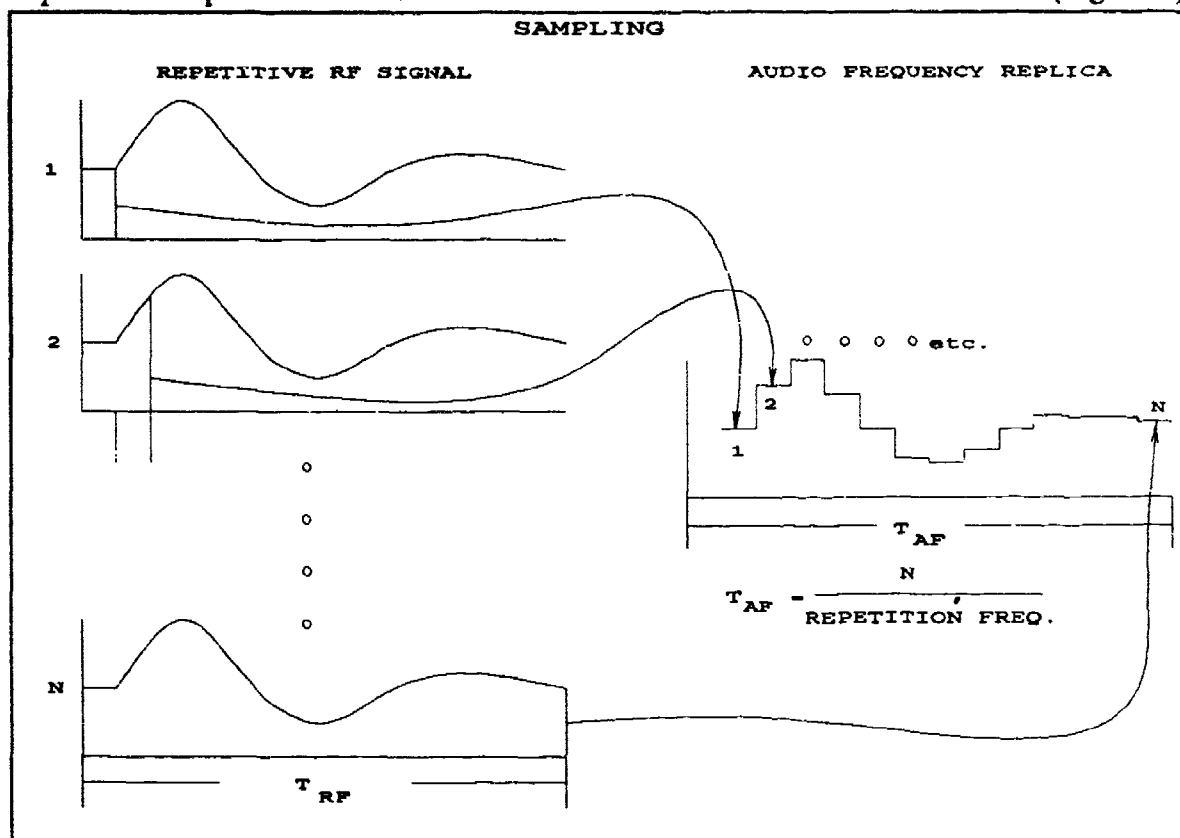


Figure 2. Schematic of sampling process. The audio frequency replica has a period given by the number of samples used to reconstruct the waveform divided by the pulser repetition frequency.

Thus it may take 100 to 1000 or more pulser firings to reconstruct one waveform and consequently the addition of 1000 waveforms may take at least 20 s for a typical commercial GPR. Some of the applications that we had in mind involved rapid surface and airborne profiling of the Greenland and Antarctic ice sheets so we began considering single-shot digitizers. The obvious advantage in going to a single-shot digitizer is that signals may be added, at least in theory, from perhaps 100 to 1000 or more times faster if it is possible to acquire an entire waveform instead of one sample of it in one shot. By the mid 1980's single-shot digitizers (Figure 3) that would digitize at 100 Msamples/s or faster were beginning to become widely available.

We examined a number of commercial systems described variously as digital waveform analyzers, signal analyzers, or digital oscilloscopes. The motivation for looking to single-shot digitizers was the desire to improve signal-to-noise ratio by rapid averaging

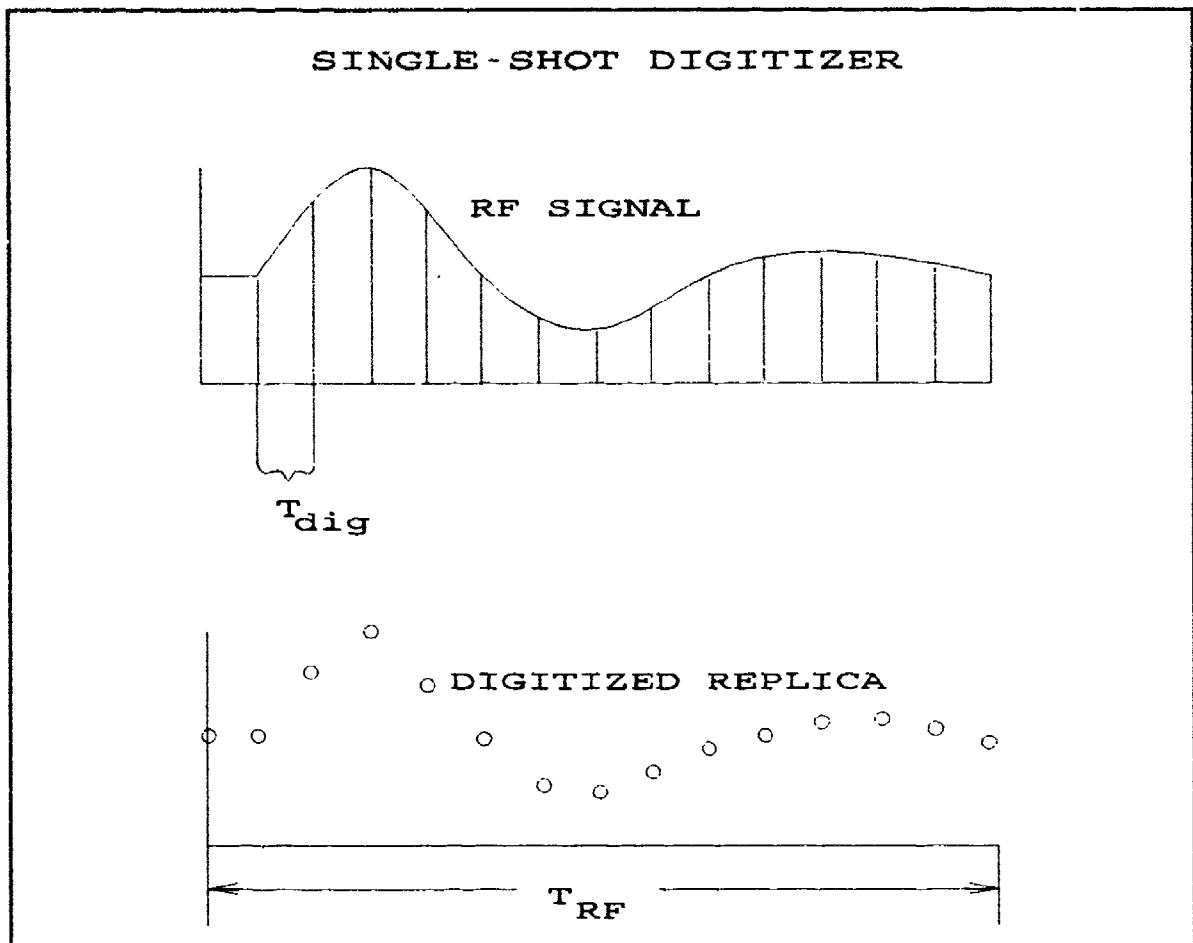


Figure 3. Schematic of single-shot digitizer. A digitized replica of an entire waveform is captured with every firing of the pulser. T_{dig} is the digitizer repetition period.

of signals while profiling. To our disappointment, we found that although there were commercial units available that would digitize very rapidly, they would not add waveforms nearly fast enough to keep up with the 50 kHz repetition frequency of typical GPR's. Therefore, we decided to design and build our own digitizer/stacker unit (DSU). This was accomplished in 1987 in time for field seasons in Greenland and Antarctica (Wright and others, 1989, Hodge and others, 1990, and Wright and others, 1990). Some of the specifications of the 1987 DSU are:

- Analog bandwidth of 100 MHz
- Single-shot digitizing rate of 100 megasamples/s at 8 bits.
- Digitize from 256 to 8192 points/waveform.
- Add any number of waveforms to 65536 (2^{16}).
- Add 50,000 waveforms/s at 256 points/waveform.

- Add 3000 waveforms/s at 8192 points/waveform.
- Transfer data without interruption of acquisition.
- Trigger external device with 1 ns delay interval.

Since the digitizer has only 8 bits, the question of dynamic range was addressed, in part, by implementing a receiver that had the ability to change gain by up to 60 dB in as little as 2 μ s (Wright and others, 1990). Although it may seem counter-intuitive, it is possible to record signals whose amplitudes are less than the threshold level of the least significant digitizer bit, and to attain more effective bits than are in the digitizer if one stacks and if there is sufficient noise that at least the least significant bit in the digitizer is randomized. With wide-band signals, having enough noise is seldom a problem. More information may be found in the references cited above. More recently the DSU has seen service in borehole radar and tomography applications described later. To date, four of the 1987 model DSU's have been built.

Despite the success of the 1987 DSU, there were limitations, primarily the analog bandwidth and digitizing rate, that prevented application in higher than 100 MHz GPR applications. We have therefore built a new modular DSU. Each module contains a digitizer, real-time memory, and adder memory. The existing prototype has two modules with the potential of doubling to four modules, and has the following characteristics:

- Analog bandwidth of 1 GHz.
- Single-shot digitizing rate of 1 Gsamples/s at 8 bits. (Could go to 2 Gsamples/s by doubling the number of modules from 2 to 4.)
- Digitize from 512 to 16,384 points/waveform with 2 modules. (Would be 1024 to 32,768 with 4 modules.)
- Real-time stack any number of waveforms up to 65,536 (2^{16}).
- Real-time stacking rate of 125 megapoints/s with 2 modules. The system could keep up with a 200 kHz radar pulser repetition rate at 512 points/waveform. At this rate it would take less than 330 ms to add 65,536 waveforms.
- Trigger output with 100 ps delay interval for time interleaving to 10 Gsamples/s.
- Useable with any computer or workstation equipped with IEEE-488 bus.

This modular DSU exists on the bench, but has not yet been incorporated into a digital radar system due to present lack of funds. If funds become available, we could implement a complete digital radar system with the above characteristics plus the following features, the first three of which already have been achieved:

- Real-time color data display using a graphic co-processor with minimum 1024 X 768 pixels by 256 colors resolution (24-bit per pixel also available).
- High speed, high density (minimum 500 Mbytes) optical erasable removable mass storage medium.
- Acquisition, playback, and processing software for in-the-field examination of data.

- Real time high speed DSP co-processor.
- System operating parameters controlled by acquisition software menu selection.
- In-field color hard copy.
- In-field tomography.
- Receiver gain change of at least 30 dB in 10 ns.

Fast receiver gain change is needed to offset the limited dynamic range of typical 8 bit single-shot digitizers, but significant gain changes in such short times have been difficult to achieve. However, we have recently built a prototype variable gain receiver including Gallium Arsenide attenuators that is showing great promise. The results of a bench test are shown in Figure 4. We have achieved a gain change of about 30 dB in about 10 ns. This should be fast enough for many GPR applications.

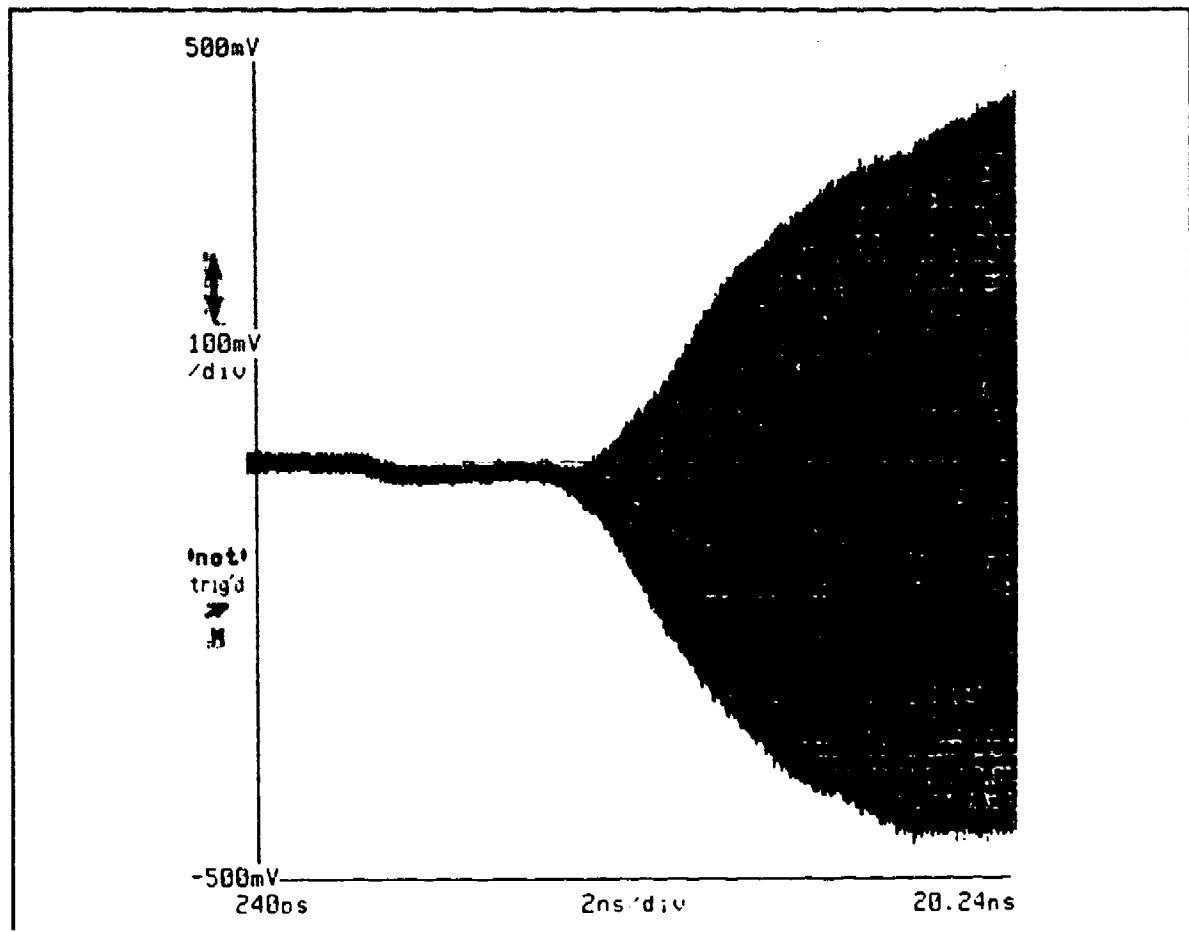


Figure 4. Tests of a prototype radar receiver with fast gain change capability. The gain changes by about 30 dB in about 10 ns.

The Fracture Picture

In addition to the Greenland and Antarctic airborne and surface profiling noted above, we have recently been participating in the Mirror Lake research project of the USGS Water Resources Division whose objective is to develop adequate 3D hydraulic flow models in fractured rock. The site is in central New Hampshire (Figure 5). The rock in the FSE

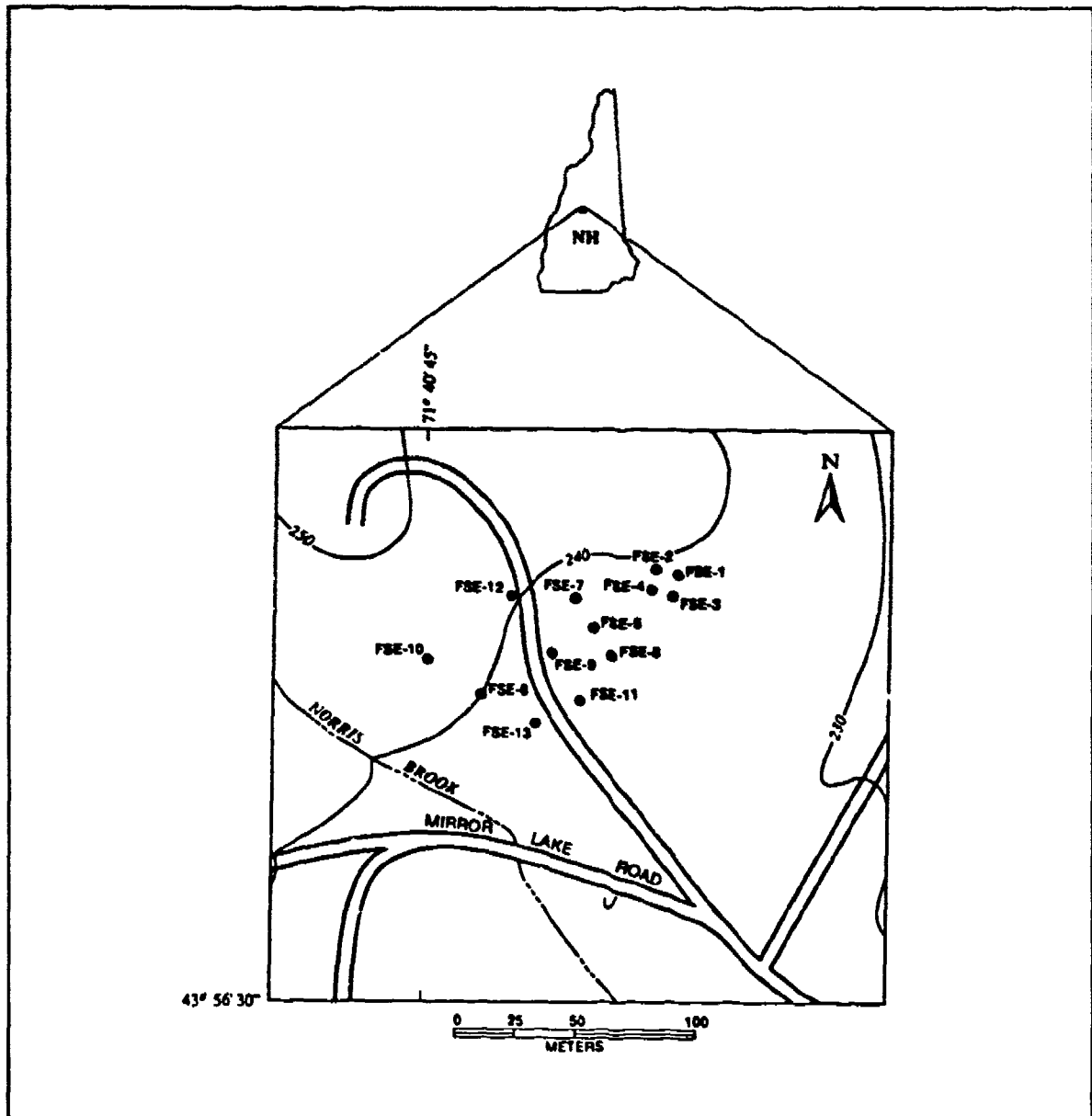


Figure 5. Location of the FSE well field in central New Hampshire. The tomograms in Figures 7 and 8 are derived from data between wells FSE-1, FSE-2, and FSE-4.

well field is largely granite, pegmatite, and schist. As part of the Mirror Lake project we are doing tomograms between a number of wells in the FSE well field.

The system consists of a short-pulse borehole transmitter and receiver (Figure 6) and the data acquisition system incorporates the 1987 DSU. We log pairs of wells with constant depth offsets (usually five offsets) between the transmitter and receiver at a logging speed of about 12 cm/s (25 ft/min). At this speed the system adds 512 waveforms, interleaves 10 times to achieve a 1 Gsample/s equivalent digitizing interval, does real-time graphics display, and records on magneto-optical disk at a spatial data density of less than

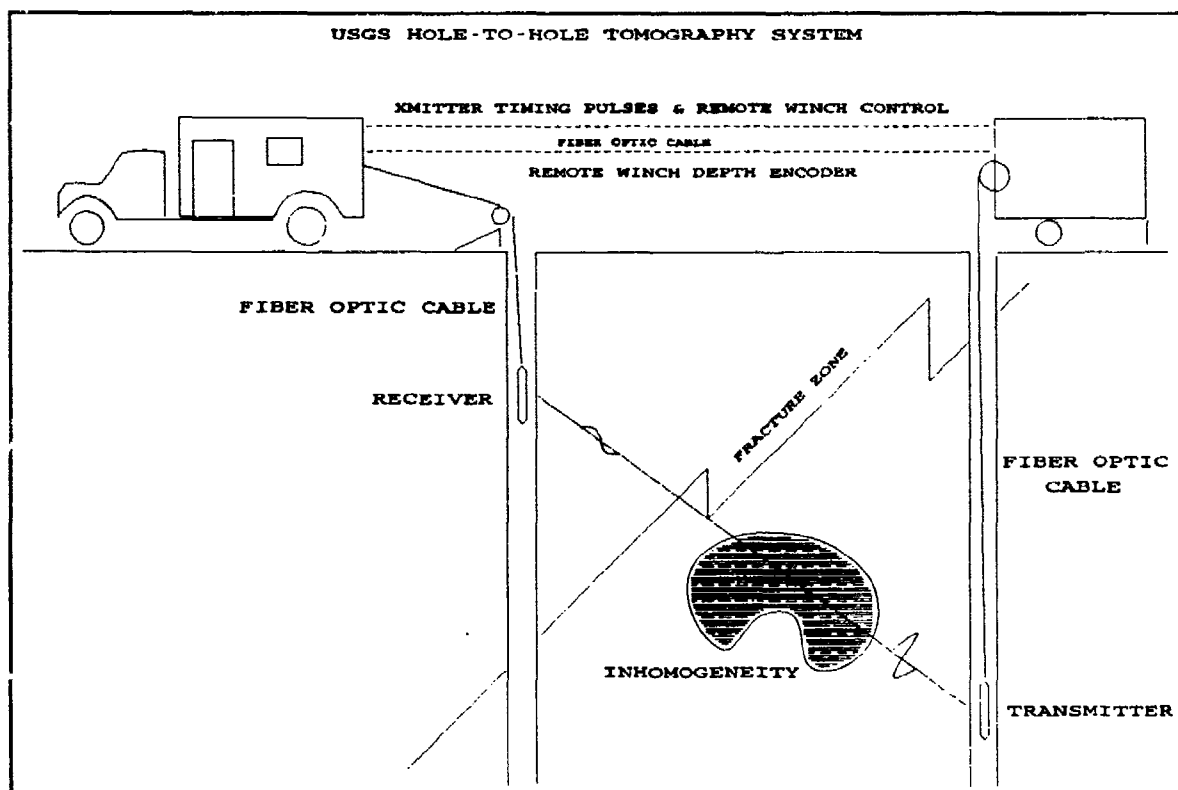


Figure 6. Schematic of the USGS hole-to-hole tomographic system. The transmitted pulse is delayed in time, attenuated in amplitude, and broadened. Each of these effects is diagnostic of the electrical properties of the media between the wells.

20 cm. We have a 30 MHz and a 60 MHz transmitter. In the granite at Mirror Lake at 60 MHz the wavelength is about 2 m. Full waveform data are recorded, and after automatic computer picking, the data are processed with software adapted from earlier tomographic processing software (Olhoeft, 1988) that was designed for tunnel detection applications. We usually produce three kinds of tomograms; one based on velocity (our standard processing assumes straight ray paths), one based on amplitude, and one based on dispersion.

Resulting tomograms can be viewed geometrically correctly in 3D. The tomograms can be rotated about vertical and horizontal axes and zoomed.

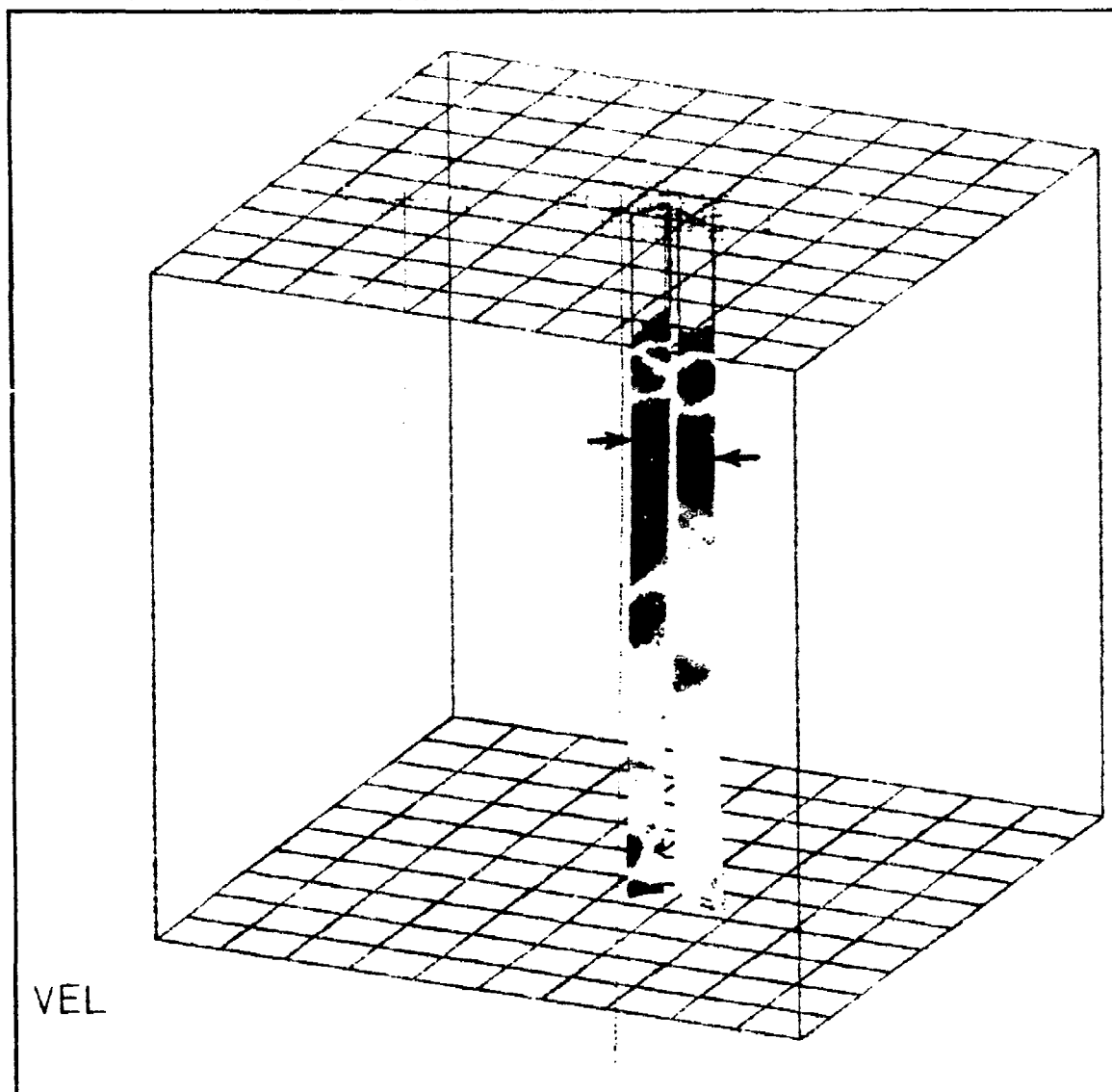


Figure 7. Velocity tomograms (red to blue = fast to slow) between wells FSE1-FSE2 and FSE2-FSE4. The arrows indicate a zone that is known to have hydraulically permeable fractures. The large cube is 100 m on a side and the grid is 10 m x 10 m.

Figure 7 shows a pair of velocity tomograms between wells FSE1-2 and FSE2-4. The arrows indicate the location of a hydraulically productive fracture zone.

Figure 8a presents a velocity tomogram between wells FSE1 and FSE4. Figure 8b

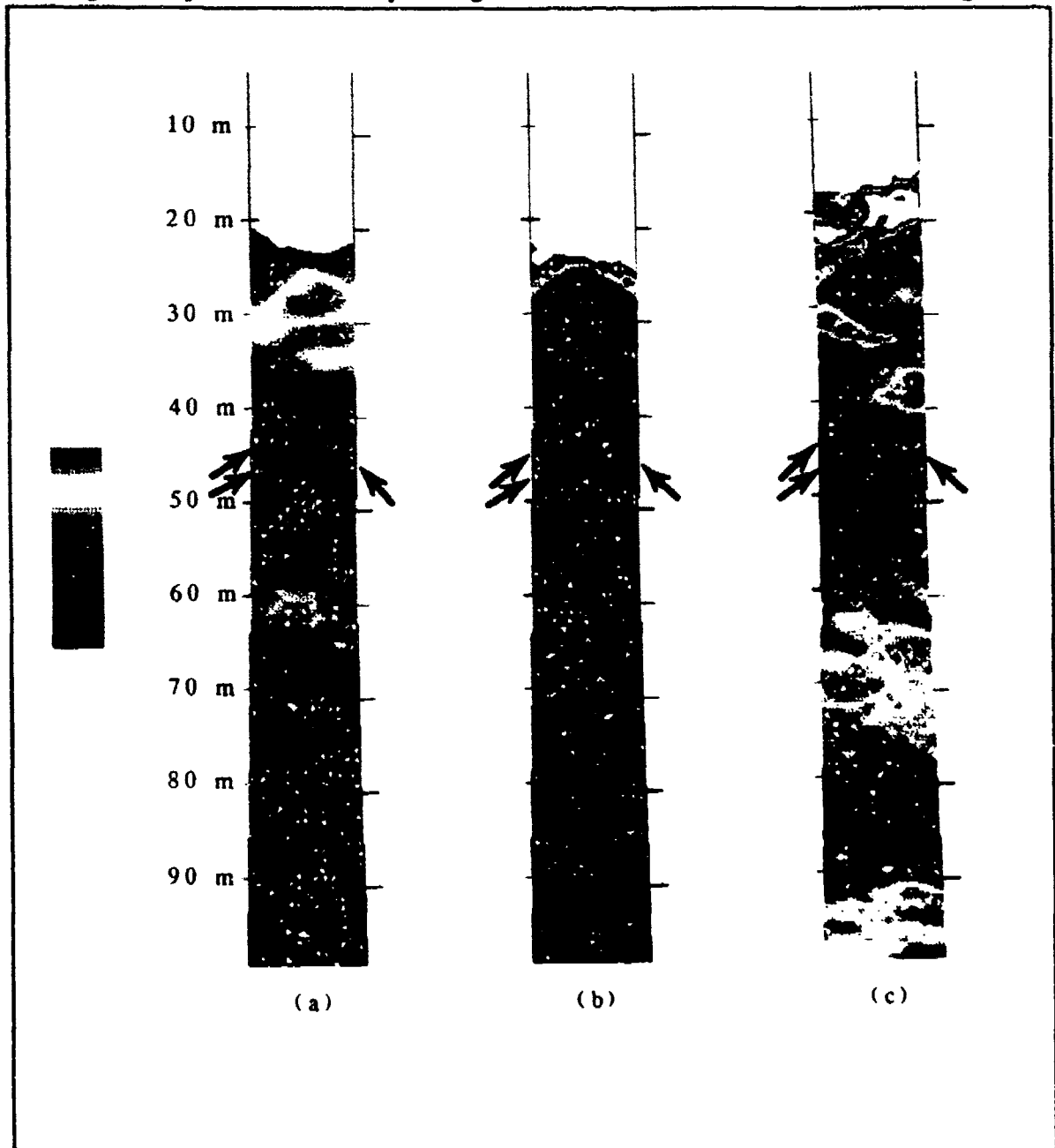


Figure 8. (a) Velocity tomogram, (b) Attenuation tomogram, and (c) Dispersion tomogram from data between wells FSE4 (left) and FSE1 (right). Fractures with high hydraulic transmissivity are marked at each borehole (Paillet, 1991).

is an amplitude tomogram of the same pair of wells, and Figure 8c is a dispersion

tomogram of the same pairs of wells. The color scale runs from blue (low) to red (high) in each case, but corresponds to different measurement units for the velocity, attenuation, and dispersion tomograms. The units and values are not essential to the objective of finding visual correlations to fractures. The algorithm used to produce these tomograms is a contouring algorithm rather than an area filling algorithm, and drew no contours through some small areas within each tomogram. These unfilled areas should be disregarded. The dispersion tomogram displayed here is produced from pulse width data. Alternative measures of dispersion exist and we are examining them (Olhoeft, 1993). We are examining dispersion tomography because it focuses on what happens to the high end of the received waveform spectrum which is expected to be more sensitive to small objects and edges that may scatter or diffract. The arrows on Figure 8 show locations in the wells that are known from packer and flow meter tests to be hydraulically producing and the slant of the arrows shows the approximate dip of the fractures as determined by acoustic televiewer logs (Paillet, 1991).

The tomograms image more than fractures, however, and we are just beginning the task of correlating the tomograms with acoustic televiewer images of the well walls, hydraulic packer and flowmeter tests, lithologic information, seismic tomography, and other sets of information as they become available. In many ways fracture mapping is more difficult even than tunnel detection because the characteristics of fractures are so varied that a "typical" fracture model may not exist except in some statistical sense.

Conclusions

Rapid stacking for signal-to-noise enhancement made possible by our DSU has much to recommend it, especially in cases where it is not possible or advisable to stop the physical motion of the system in order to stack.

The applications of our DSU and processing software to tomography in crystalline rock shows correlations with known hydrologic fractures, but the correlations are not one-to-one. Detailed correlation with other information, such as lithology and acoustic televiewer data is necessary for better interpretation. Higher frequencies and examination of the data to see whether diffraction tomographic processing is possible are being considered as possible means of improving the ability of tomograms to image fractures.

REFERENCES

- Hodge, S. M., and others, 1990, Determination of the surface and bed topography in central Greenland, by S. M., Hodge, D. L. Wright, J. A. Bradley, R. W. Jacobel, N. Skou, and B. H. Vaughn: *Journal of Glaciology*, v. 36, p. 17-30.
- Olhoeft, G. R., 1988, Interpretation of hole-to-hole radar measurements: in Third Technical Symposium on Tunnel Detection Proceedings, Jan., 12-15, 1988, Colorado School of Mines, Golden, CO, p. 616-629.
- Olhoeft, G. R., 1992, Geophysics Advisor Expert System Version 2.0, U.S.G.S. Open File Report 92-526.
- Olhoeft, G. R., 1993, Velocity, attenuation, dispersion and diffraction hole-to-hole radar processing: in Fourth Tunnel Detection Symposium on Subsurface Exploration Technology Proceedings, April 26-29, 1993, Colorado School of Mines, Golden, CO, this volume.
- Paillet, F. L., 1991, Comparing geophysical logs to core and cross-hole flow logging in the Mirror Lake drainage basin, in Mailard, G. E. and Aronson, D. A., (eds.), U.S. Geological Survey Toxic Substance Hydrology Program--Proceedings of the technical meeting, Monterey, Calif., March 11-15, 1991: U. S. Geological Survey Water Resources Investigation Report 91-4034, p. 162-171.
- Skolnik, M. I., 1962, Introduction to radar systems: New York, McGraw-Hill, 648 p.
- Wright, D. L., Bradley, J. A., and Hodge, S. M., 1989, Use of a new high-speed digital data acquisition system in airborne ice-sounding: Institute of Electrical and Electronics Engineers Transactions on Geoscience and Remote Sensing, v. GE-27, p. 561-567.
- Wright, D. L., and others, 1990, A digital low-frequency, surface-profiling ice radar system, by D. L. Wright, S. M., Hodge, J. A. Bradley, T. P. Grover, and R. W. Jacobel: *Journal of Glaciology* v. 36, p. 112-121.

Session 4

Cross-Hole Tomography

CROSS WELL ACOUSTIC TOMOGRAPHY TO DELINEATE ABANDONED UNDERGROUND MINE WORKINGS

L.K. Killoran, R.D. Munson, and T.T. Rich

U.S. Department of the Interior
Bureau of Mines, Denver Research Center
Denver, Colorado

ABSTRACT

The U.S. Bureau of Mines has developed a prototype cross well acoustic logging system under the Bureau's Abandoned Mined Lands Research Program. The cross well system was developed for the detection and delineation of abandoned underground mine workings and associated subsidence failure zones in relatively shallow environments. The logging system uses a piezoelectric, cylindrical bender as an acoustic source. A triaxial accelerometer assembly, designed to be rigidly locked in the borehole, is the receiver portion of the logging system. Both the source and receiver probes operate at high frequencies, thus providing short wavelengths capable of resolving small features in most rock types. A modified van with a dual-drum wireline winch, four-channel data acquisition system, power amplifiers, and waveform generator supports field operation of the logging system.

A field study was conducted on the lower pad at the Colorado School of Mines' Experimental Mine near Idaho Springs, CO, to demonstrate the cross well acoustic logging system. Compressional or P wave first-arrival travel times were used for the tomographic reconstruction of the velocity field in the two-dimensional cross section between the source and receiver boreholes. The resulting image identifies the location of the underground tunnel in the cross section and correlates well with geological and geophysical information for the mine site.

INTRODUCTION

The detection and delineation of abandoned underground mine workings and associated subsidence failure zones is difficult. Subsidence, directly or indirectly, causes millions of dollars in damage to property and may endanger public safety. Extensive drilling programs are employed each year in mining regions of the United States to locate abandoned underground voids. Except where surface subsidence features are evident, the drilling

programs are generally based on old mine maps of sometimes questionable accuracy, intuition of the drilling program leader, and topographic and cultural features. Generally, dense drilling patterns that are expensive, time-consuming, and have a limited statistical probability of success are required to locate the voids.

Cross well acoustic geophysical methods were initially developed for oil and mineral exploration to reconstruct the two-dimensional subsurface between boreholes. In these methods, acoustic energy is propagated from a source in one borehole to a receiver in another. In the oil industry, low-frequency systems (below 500 Hz) and large borehole separations (about 1,000 m) are typically used. Advances in hardware and software have expanded the application of these methods to mining by providing improved detail of the geological cross sections. One such application is the detection and delineation of abandoned underground mine workings and associated subsidence failure zones. The geologic structure of the overburden in an abandoned mine area affects the extent, severity, and timing of subsidence. Faults, joints, and other fractures provide planes or zones of instability in the overburden rock mass that can enhance the subsidence process and provide pathways for rock strata separation and downward movement. High-frequency, short-wavelength acoustic waves are required in order to resolve these small targets. However, high-frequency waves attenuate more rapidly than lower frequency waves, thus limiting the distance between boreholes. Wong, Bregman, West, and Hurley (1987) present a detailed overview of cross well acoustic acquisition and analysis.

Tunnel Detection Test Facility

In the late 1800's, the Edgar Mine produced high-grade silver, gold, lead, and copper. It is located about 0.4 km north of Idaho Springs, CO. The Colorado School of Mines (CSM) acquired a 99-year lease on the mine in 1921 for education and research. In 1976, the U.S. Army Belvoir Research and Development Center (BRADC), formerly the Mobility Equipment Research and Development Command (MERADCOM), tunnel was started at the site. This Tunnel Detection Test Facility was established for the purpose of evaluating technologies for tunnel detection in a relatively controlled environment. The U.S. Army developed, in cooperation with CSM, two surface test pads (lower and upper) with vertical drill holes configured to straddle the BRADC tunnel. Although the exact location of the tunnel is unknown, it is estimated that the tunnel lies beneath the lower pad at a depth of 45.7 m. The 3-m cross-sectional tunnel is dry for the most part. A number of geological and geophysical studies have been conducted to assist researchers in evaluating results (U.S. Army Corp of Engineers, 1988).

The Edgar Mine lies within the Colorado Front Range and is situated in the Front Range Mineral Belt which consists mainly of Precambrian gneisses and granitic rocks along with Laramide porphyritic intrusive igneous rocks. The Precambrian rocks in the Idaho Springs area are a series of high-grade metasedimentary felsic and biotite gneisses, metaigneous rock and igneous rocks of the Idaho Springs Formation. These rocks have undergone seven separate tectonic events of varying intensity from Precambrian through Tertiary. The wall rock of the tunnel is primarily interlayered gneisses, with varying amounts of biotite, pegmatites, and schists, and is generally stable except where weakened along faults and shear zones. These alterations occur throughout the tunnel in varying degrees of intensity. Amuedo and Ivey, Inc. (1984) give a detailed description of the geology in the BRADC tunnel.

Tunnel Detection Investigations

The U.S. Army Corps of Engineers conducted a geophysical investigation on the lower pad of the Tunnel Detection Test Facility (Ballard et al, 1984). A pneumatically chargeable, electrically fired Bolt D500 air gun was used as the acoustic source. The receiver was a triaxial geophone set equipped with a high-pressure inflatable bladder to provide coupling between the geophones and the borehole sidewall. Results of this study indicated that the depth to the center of the tunnel was 51.2 m. The background velocity (excluding the tunnel) was found to be 2.86 km/s and the tunnel location was indicated by a reduced velocity of 2.2 km/s.

The U.S. Bureau of Mines imaged the BRADC tunnel at a depth of about 50 m using cross well geophysics on the lower pad in 1986 and 1987 (Schneider and Peters, 1987). A low-frequency cross well system was developed for the Bureau under contract H0212006 by Southwest Research Institute (SWRI), San Antonio, TX. This system consists of an arc discharge sparker source and piezoelectric bender receiver. The operating frequency of this system ranges from 200 Hz to 2 kHz. The applicable borehole separation distance ranges from 20 m to 350 m (Peters, Owen, and Thill, 1985). The location of the tunnel was depicted by a calculated velocity of 2.1 km/s and the background velocity ranged from 2.7 km/s to 5 km/s. The tunnel was computed to be 2-m wide by 2-m high.

This paper discusses a new high-frequency cross well system developed through the Bureau's Denver Research Center. This system was used in May 1992 on the lower pad to delineate the BRADC tunnel. The prototype piezoelectric, cylindrical-bender source and wall-locking, triaxial receiver probes were developed under contract S0209037 by SWRI. This system operates at a

frequency range of 400 Hz to 5 kHz. Seismic data were acquired with a similar system for source and receiver separations in excess of 300 m (Balogh, Owen, and Harris, 1988). From this May 1992 study, the depth to the center of the tunnel was calculated to be 49 m. The velocities ranged from 2.3 km/s to 4.6 km/s, with a velocity of 2.4 km/s indicating the location of the tunnel. The dimensions of the tunnel were computed to be 3-m wide by 2-m high.

CROSS WELL LOGGING SYSTEM

The cross well acoustic logging system uses a prototype ceramic-piezoelectric, cylindrical-bender, transducer source capable of providing a waveform of a single frequency with selected number of cycles (burst), frequency sweeps, or a sweep frequency pulse (chirp). This probe is a free-hanging, impulsive source and is designed for application in relatively shallow environments (up to 600 m). It has a frequency range from 400 Hz to 5 kHz. The source consists of a hollow, piezoelectric cylinder rigidly bonded at the ends to the inside surface of a close-fitting outer steel cylinder. When excited, the ends of the piezoelectric cylinder remain stationary and the center of the cylinder expands or contracts depending upon the polarity of the excitation voltage applied. In a fluid-filled borehole, these radially oriented displacements produce acoustic waves that couple with the drilled formation to radiate repeatable seismic waves.

The prototype high-frequency acoustic receiver is a triaxial piezoelectric, accelerometer assembly designed to be rigidly locked in a shallow borehole (up to 600 m). This receiver design gives dry hole capability and minimizes sensitivity to tube waves. The clamping mechanism extends two rigid arms which provide for a multiple-point, high-force contact with the borehole. The borehole diameter range for the wall-lock mechanism is 100 mm to 200 mm. Three accelerometer sensors are mounted in a triaxial assembly. The output of each accelerometer is connected to a line-driving preamplifier located in the receiver probe. A sensor measures the magnetic azimuth to provide the directional orientation of the receiver.

A PC-based data acquisition system, waveform generator, power amplifiers, dual-drum wireline winch, up-hole band-pass filters and high-gain amplifiers support field operation of the cross well logging system. A curved ray tomographic reconstruction program written by Wattrus (1984) was used to process the acquired data. This program incorporates the simultaneous iterative reconstruction technique (SIRT) algorithm and the curved ray paths are computed using Snell's Law. Killoran (1992) provides a detailed description of the complete logging system.

CROSS WELL FIELD STUDY

A field study using the cross well logging system was conducted in May of 1992 on the lower pad of the CSM Experimental Mine. The objective of the study was to delineate the underground BRADC tunnel from cross well acoustic measurements. The test was conducted using vertical, water-filled boreholes. The boreholes were drilled to a depth of approximately 85.3 m, have a collar elevation of 2,450 m, a diameter of about 178 mm, and are uncased except for PVC pipe in the upper 3 m. The source was placed in borehole 7 (referenced by Ballard, Kean, Lewis, and Smith (1984) as G) and the receiver in borehole 6 (F). The boreholes are separated by a distance of 10.19 m. Acoustic signals were generated using a 2-cycle sine wave burst of 1.5 kHz frequency. Waveform frequency selection was based on the borehole separation distance, rock type, and the received signal amplitude and frequency. The receiver remained stationary while the source location varied. Ten fans of data were collected using a sampling rate of 15 kHz, and source and receiver depths ranging from 40 m to 58 m with a 2-m sampling interval. Over 130 ray traces were acquired.

ANALYSIS AND RESULTS

The tomographic reconstruction program written by Wattrus (1984) was applied to the seismic data acquired during the field study. Compressional or P wave first-arrival travel times were manually determined for each ray trace. The travel times, and source and receiver depths were input into the iterative program. The velocity profile, shown in figure 1, was computed in four iterations. The computed velocities vary from 2.3 km/s to 4.6 km/s. The resolution capability of the system operating at a frequency of 1.5 kHz, based on these computed velocities, ranges from 0.77 m to 1.53 m (Lytle and Portnoff, 1982).

The location of the tunnel is delineated in the tomogram in figure 1 as a low velocity (2.4 km/s) anomaly 3-m wide and 2-m high. The depth of the tunnel ranges from 48 m to 50 m and its distance from borehole 7 ranges from 3 m to 6 m. In general, the velocity variation in the tomogram can be attributed to the effects of stress caused by the tunnel, fracturing and weathering within the rock mass, as well as the different geologic materials within the cross section. The higher velocity zone (3.7 km/s to 4.6 km/s) above the tunnel indicates an area of more competent rock mass. However, the anomalies in the corners of the tomogram are due to edge effects resulting from the tomographic reconstruction. The following discussion will compare the results of this study with other geophysical investigations of the site.

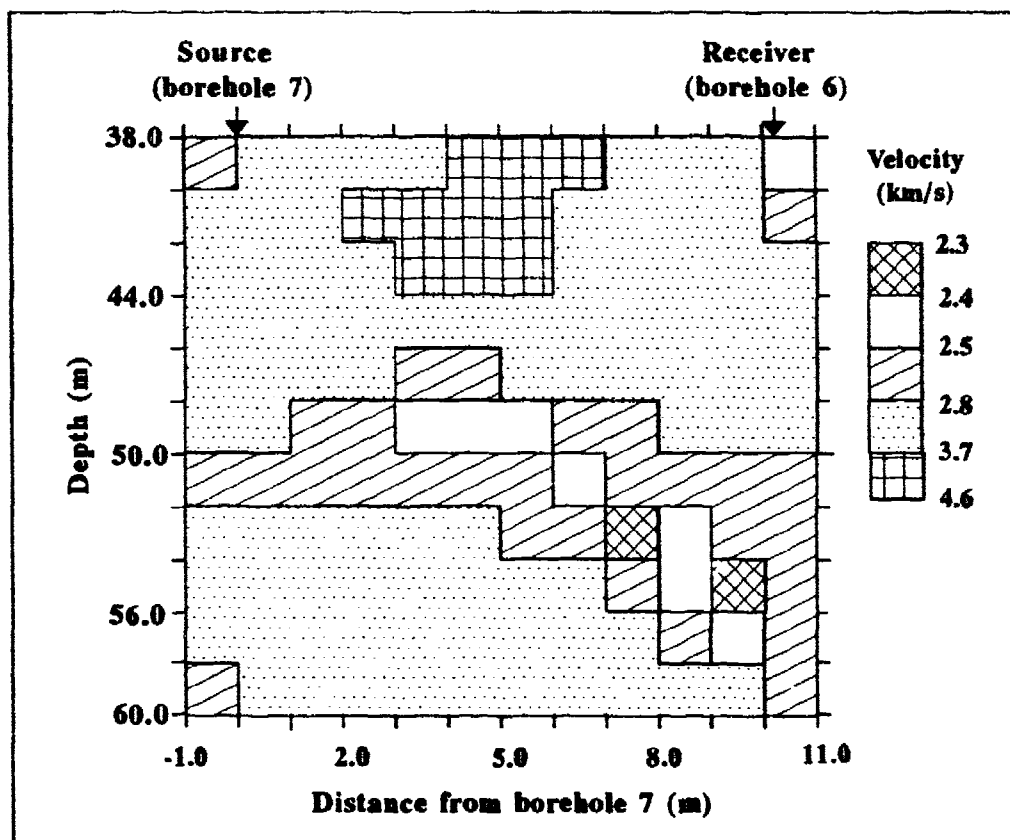


Figure 1. Tomogram of BRADC tunnel between boreholes 6 and 7 on the lower pad of the CSM Experimental Mine

A seismic refraction survey was conducted within the tunnel (U.S. Army Corp of Engineers, 1988). This survey indicated that the tunnel floor is disturbed (cracked) for a depth of about 0.61 m and has a velocity of about 0.83 km/s. Underlying that strata is granite which is badly weathered, faulted, and cracked and displays a lower than normal velocity. As depth increases, granite is less weathered and has a velocity of about 3.66 km/s. The tomogram shown in figure 1 correlates well with this seismic refraction survey. The highly fractured tunnel floor was not observed in the tomogram because its depth of 0.61 m is less than the resolution capability of 0.77 m. The area beneath the tunnel has a lower than normal velocity and beneath that, a velocity of 3.66 km/s corresponds well with that shown in the tomogram.

Daniels and Scott (1983) conducted a study to obtain a suite of nine geophysical well logs for the drill holes above the BRADC tunnel. Information concerning fracturing, mineralization, and general rock mineralogy were interpreted using these logs. The study found that the geophysical logs for borehole 7 indicated

fracturing at depths ranging from 50 m to 53 m, and the logs for borehole 6 revealed fracturing in the depth interval of 51 m to 55 m. The fracture zone in borehole 7 correlates well with the slightly decreased velocity in figure 1 in the depth range of 50 m to 52 m in the source borehole. In borehole 6, a reduced velocity is observed in the tomogram in the receiver borehole at depths ranging from 50 m to 58 m, which agrees well with the fracture interval previously stated.

The velocity profile computed by the tomographic reconstruction program produced an image that correlates well with the geological and geophysical data for the site. A tunnel 3-m wide and 2-m high was delineated in the cross section between the boreholes. A low velocity trend, indicating severe fracturing, can be observed from the bottom of the tunnel extending with depth toward the receiver borehole.

SUMMARY

The high-frequency prototype cross well acoustic logging system, using a piezoelectric, cylindrical-bender source and wall-locking, triaxial receiver, provided suitable waveforms for determining compressional or P wave first-arrival travel times. The curved ray tomographic reconstruction program computed an image of the two-dimensional cross section between the boreholes that correlates well with the geological and geophysical data at the Tunnel Detection Test Facility. The location of the BRADC tunnel was calculated to be at a depth of 48 m to 50 m. The computed tomogram also revealed a fracture zone beneath the tunnel.

REFERENCES

- Amuedo and Ivey, Inc., 1984. "Geology of the MERADCOM Tunnel, Edgar Mine Site, Clear Creek County, Colorado," (for the Colorado School of Mines under purchase order 47426), 12 pp.
- Ballard, R.F., T.B. Kean, R.D. Lewis, and G.E. Smith, 1984. "Active Detection of Tunnels by Induced Seismic Spectra," Dept of the Army Misc Paper GL-84-18, 71 pp.
- Balogh, W.T., T.E. Owen, and J.M. Harris, 1988. "A New Piezoelectric Transducer for Hole-to-Hole Seismic Applications," 58th Annl Intl Meeting for the Society of Exploration Geophysicists, Anaheim, CA, Oct, 8 pp.
- Daniels, J.J. and J.H. Scott, 1983. "Geophysical Well Logs for Eleven Drill Holes at the Colorado School of Mines Experimental

Mine Site, Idaho Springs, Colorado," USGS Open File Report 83-235, 48 pp.

Killoran, L.K., 1992. "Cross Well Acoustic Tomography to Locate Abandoned Underground Mines and Subsidence Failure," Proc 11th Intl Conf on Ground Control in Mining, Wollongong, NSW, Australia, Jul, pp. 499-505.

Lytle, R.J. and M.R. Portnoff, 1982. "Cross-Borehole Seismic Probing to Locate High-Contrast Anomalies," Rept UCID-19247, Lawrence Livermore Laboratory, Livermore, CA, Feb, 58 pp.

Peters, W.R., T.E. Owen, and R.E. Thill, 1985. "A New Seismic Probe for Coal Seam Hazard Detection," Society of Mining Engineers AIME Fall Meeting, Albuquerque, NM, Preprint 85-312, 7 pp.

Schneider, G.J. and W.R. Peters, 1987. "The Location of an Underground Opening with an Acoustic Cross Borehole Logging System and Tomographic Signal Processing," Proc 2nd Intl Symp on Borehole Geophysics for Minerals, Geotechnical, and Groundwater Applications, Golden, CO, Oct, pp. 251-255.

U.S. Army Corp of Engineers, 1988. "Idaho Springs Tunnel Detection Test Facility," 15 pp.

Wattrus, N.J., 1984. Two-Dimensional Velocity Anomaly Reconstruction by Seismic Tomography, Univ Microfilms Intl, Ann Arbor, MI, 245 pp.

Wong, J., N. Bregman, G. West, and P. Hurley, 1987. "Cross-Hole Seismic Scanning and Tomography," Geophysics: The Leading Edge of Exploration, Jan, pp. 37-41.

CROSS-HOLE TOMOGRAPHY USING IMPROVED BORN INVERSION

Jung-Hye Kim, Sang-Gi Kim, and Jung-Woong Ra

Department of Electrical Engineering
Korea Advanced Institute of Science and Technology
373-1, Kusung-dong, Yuseong-gu, Taejeon, 305-701, Korea

ABSTRACT

Crosshole tomography for imaging a dielectric cylinder using improved Born inversion is shown. It extends the validity of the Born inversion about 10 times where its criterion is defined by the size of the object multiplied by the square root of the relative dielectric constant minus one. The reconstructed images using the conventional Born and improved Born in the cross-hole geometry are compared.

INTRODUCTION

Conventional diffraction tomography is based upon the Born approximation, where the total field inside the object is substituted by the incident field by assuming that the object medium constants (i.e. dielectric constant for the electromagnetic wave) are close to that of the background medium[1]-[3]. Its validity is well known[4] and is given by $k|\sqrt{\epsilon} - 1|D < \pi$, where k is the wave number in the background medium, ϵ is the dielectric constant of the object relative to the background medium, and D is the maximum dimension of the object.

In order to apply this technique to finding an air tunnel of about 2 m diameter in the granite rock, one is limited to use the electromagnetic field in the frequency range up to about 100MHz due to its severe attenuation. By taking the relative dielectric constant of the granite as 9, the criterion of the Born approximation for the tunnel, $k|\sqrt{\epsilon} - 1|D = 2.67\pi$ for 100MHz, is violated by exceeding its limit π . High frequency signal is needed to obtain the object resolution of about 2 m in the x -direction in the forward cross-hole diffraction tomography scheme shown in Figure 1.

The realistic cross-hole tomographic measurements are limited to the sensor positions only in the straight vertical boreholes, as in Figure 1. This limited view angles distort the reconstructed image much more along the x -axis than that of the y -axis[5]. One may improve the limitation of the Born inversion about 10 times by using the wide-band multifrequencies to measure the object size and correcting the sectionized reconstructed image size via the concept of the projection function[6]. This improved Born inversion is then expected to give improvement also to the distortion due to the limited view angles in the cross-hole tomogram.

Improved Born Inversion in the Cross-hole Tomography

For the simplicity, no variation in the z -direction (cylindrical object and line sensors) in Figure 1, is assumed. The scattered field u^s may be obtained by using Born approximation[2] as

$$u^s(\rho_t, \rho_s) \simeq -j \frac{k}{8\pi} \frac{e^{-jk(\rho_t + \rho_s)}}{\sqrt{\rho_s \rho_t}} \int \int_S d\rho' [\epsilon(\rho') - 1] e^{-j(\mathbf{k}^i - \mathbf{k}^s) \cdot \rho'} \quad (1)$$

Where ρ_t and ρ_s are the transmitter and receiver points, respectively, ρ' is the points inside the object, \mathbf{k}^i and \mathbf{k}^s are the wave vectors designating the propagation directions of the incident and scattered fields, respectively as in Figure 1, and its magnitude is the wave number in the background medium, $|\mathbf{k}^i| = |\mathbf{k}^s| = k$.

One may assume that ρ_t and ρ_s satisfy the far field criterion of the cylindrical object and the directions of the vectors \mathbf{k}^i and \mathbf{k}^s are approximated by those of $-\rho_t$ and ρ_s , respectively, pointing to the center of the object (origin of the coordinate). By introducing a rotated rectangular coordinate system (ξ, η) , where the ξ -axis is chosen along the direction of the difference vector $\mathbf{k}^i - \mathbf{k}^s = \boldsymbol{\kappa}$, one may rewrite the integral in eq.(1) by the normalized scattered field u_N^s as

$$u_N^s(\boldsymbol{\kappa}) \simeq \int_{-\infty}^{\infty} d\xi p_{\kappa}(\xi) e^{-j\kappa\xi}, \quad (2)$$

where p_{κ} is the projection function defined by

$$p_{\kappa}(\xi) = \int_{-\infty}^{\infty} d\eta [\epsilon(\xi, \eta) - 1] \quad (3)$$

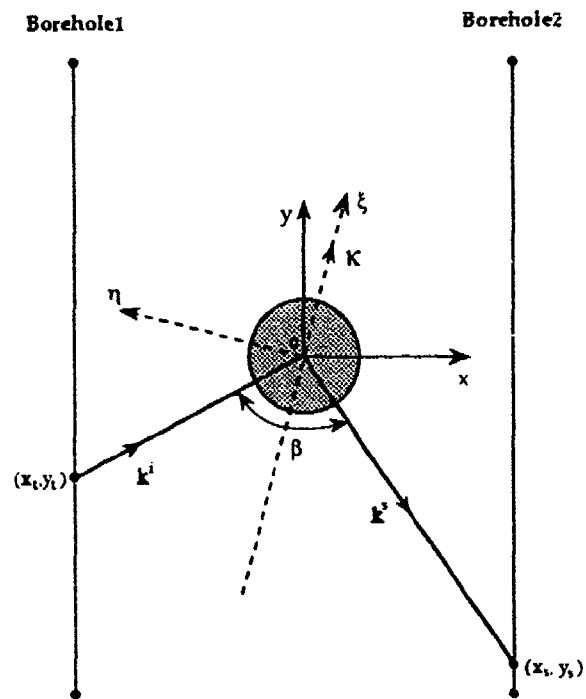


Figure 1. Cross Borehole Tomographic Configuration

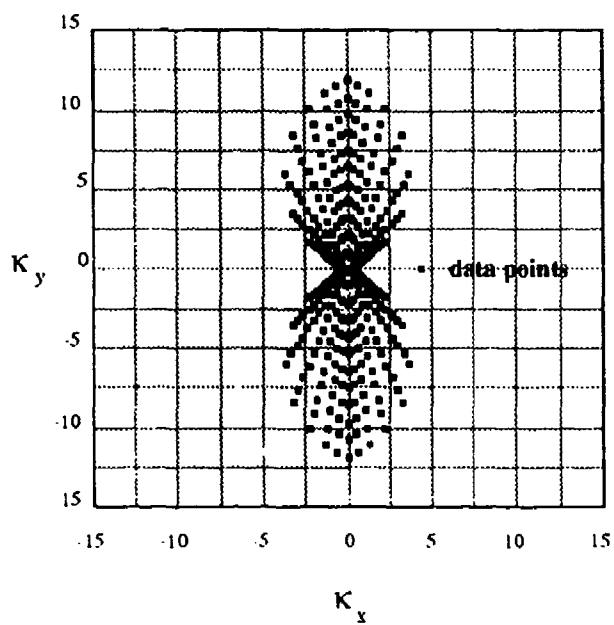


Figure 2. Data Points in the Spectral Domain of Cross Borehole Measurement

integrated along the η -direction for each values of ξ at those measurement points ρ_t and ρ_s , which is substituted by the difference vector κ . The normalization factor in front of the integral in eq. (1) is a function of k or κ via

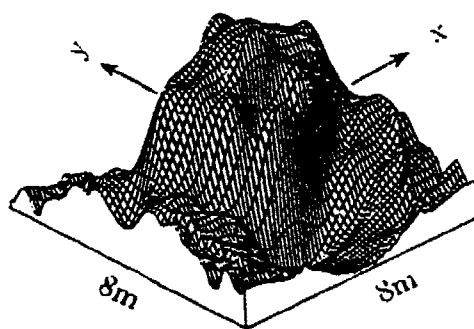
$$\kappa = 2k \cos(\beta/2), \quad (4)$$

where β is the inner product angle of vectors k^t and k^s as in Figure 1.

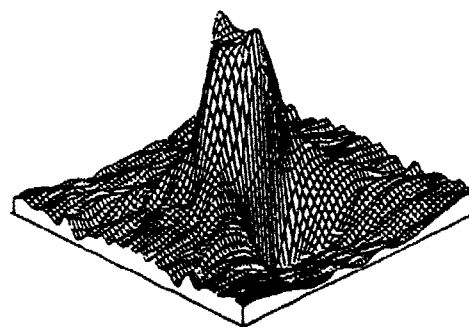
The object may be reconstructed by taking the inverse Fourier transformation of $u_N^*(\kappa)$ in the spectral domain and its back-projection[2]. Since the measurement points are limited to the borehole geometry, the data points obtainable in the spectral domain is limited to the inside of the ellipses in the κ -plane in Figure 2. When the measurement points ρ_t and ρ_s are fixed the corresponding data points along a straight line in the direction of the vector κ are generated by changing frequencies which makes the magnitude of k varying. Since the boreholes are vertical and no backscattering is allowed, the vector κ along the x -axis is impossible to get for this cross-borehole geometry, as shown in Figure 2.

The resolution ΔL of the reconstructed object may be obtained from the Fourier transform relationship and the data points in the spectral domain as $(\Delta\kappa)(\Delta L) < \pi$, where $\Delta\kappa$ is the total length of the available data points in the κ domain in the interested direction of the resolution. From Figure 2, one expects better resolution along the y -direction than the x -direction.

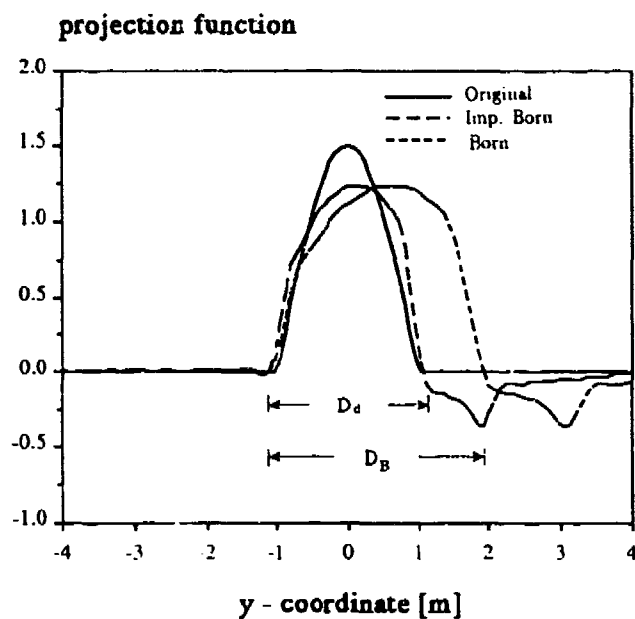
The conventional diffraction tomography obtained from the cross-hole measurement (as shown in Figure 1) is shown in Figure 3(a) where the object is a homogeneous dielectric circular cylinder of its relative dielectric constant 2.5 and diameter 2 m. The Born criterion for this example at the maximum frequency, $k|\sqrt{\epsilon} - 1|D = 2.45\pi$ exceeds π , where the used frequencies are from 1MHz to 100MHz by 101 equal intervals. The reconstructed image shows 4 peaked shoulders surrounding the original cylinder and poor resolution along the x -axis, as expected. Calculated model has the depth of and the distance between the boreholes 60 meters and 30 meters, respectively. Increments in the receiver points are taken to be 1.2 m, which yields 50 measurement points in the borehole. Total of 4 transmitter points in two boreholes multiplied by 50 receiver points give total of 200 measurement and the total data points accounting



(a)

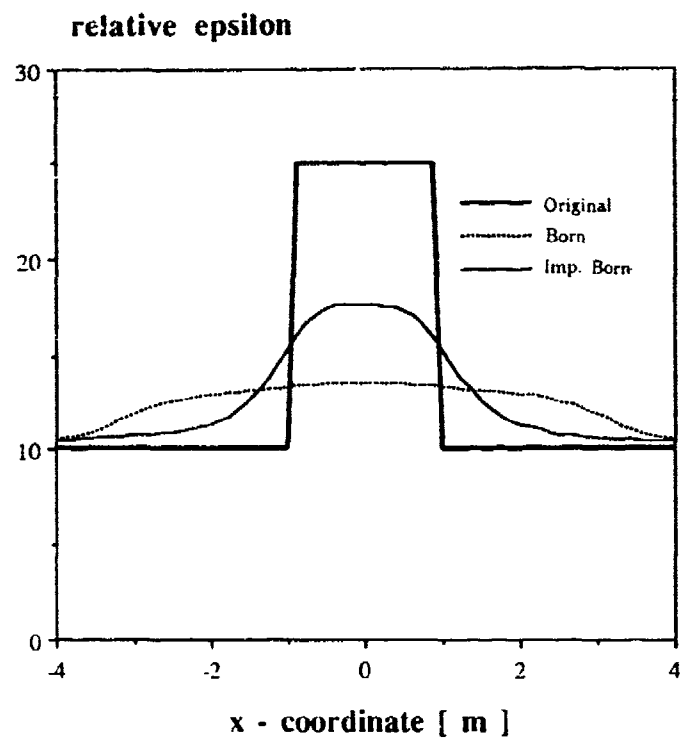


(b)

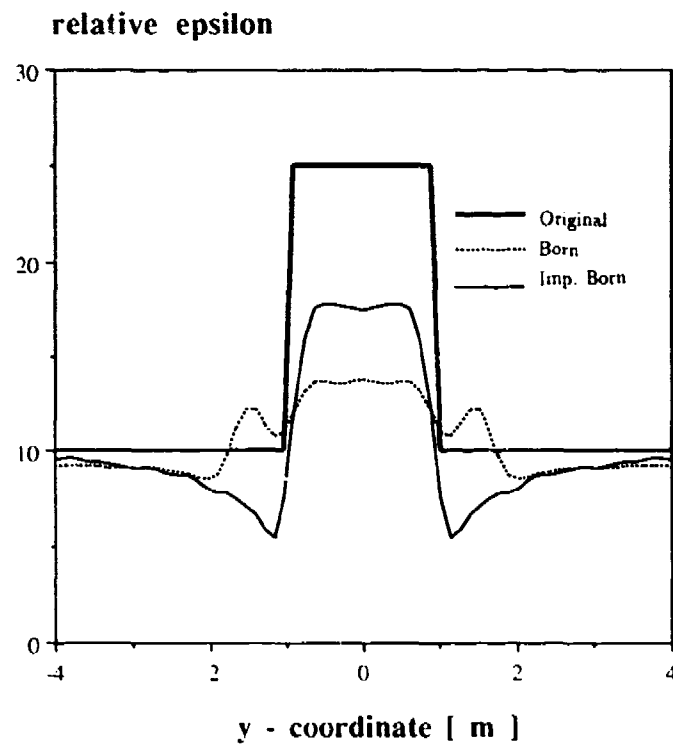


(c)

Figure 3. For a Homogeneous Dielectric Circular Cylinder of $\epsilon_r=2.5$ and $D=2m$, (a) Reconstructed Image of the Conventional Born, (b) Reconstructed Image of the Improved Born, and (c) Reconstructed Projection Function of Conventional Born (- - - - -); Improved Born (- - - - -), and the Original (———).



(a)



(b)

Figure 4. Cross Sectional Profile of Born (.....), Improved Born (———), and the Original (———) along the (a) x -axis and (b) y -axis.

101 frequencies becomes 20200 points.

In order to use equal interval back-projection algorithm from the computerized tomography[2], one may interpolate the measured data points into 64 angular intervals in the κ -plane which satisfies the sampling criteria for the 2 meters cylinder with the shortest wavelength 1.1 m corresponding to 100MHz for the background medium of $\epsilon = 10$.

Extended size of the reconstructed image may be reasoned to the nature of the Born approximation since the optical path length is increased by the factor of $\sqrt{\epsilon}$ compared with the background medium[6]. By using multi-frequency signals, the size of the object may be detected and the reconstructed projection function which extends larger than the real projection function may be corrected as shown in Figure 3(c). From this corrected projection function one may obtain the improved Born reconstruction shown in Figure 3(b).

Improved Born inversion is compared with the conventional Born inversion in the cross sectional reconstruction of the dielectric profile in Figure 4(a) and (b). In terms of the cross sectional shape, this improvement is about 10 times of the conventional Born criterion and this method may be used to the imaging of the high contrast object such as an air tunnel in the granite medium.

References

- [1] S. X. Pan and A. C. Kak, 1983, "A Computational Study of Reconstruction Algorithms for Diffraction Tomography: Interpolation Versus Filtered Back Propagation," IEEE Trans. Acoust., Speech, Signal Proc., Vol. ASSP-31, No. 5, Oct., pp. 1262-1275.
- [2] T. H. Chu and N. H. Farhat, 1988, "Frequency-swept Microwave Imaging of Dielectric Objects," IEEE Trans. Microwave Theory Tech., Vol. MTT-36, No. 3, pp. 489-493.
- [3] A. J. Devaney, 1983, "A Computer Simulation Study of Diffraction Tomography," IEEE Trans. Biomed. Eng., BME-30, No. 7, July, pp. 377-386.

- [4] M. Slaney, A. C. Kak, and L. E. Larsen, 1984, "Limitations of Imaging with First-Order Diffraction Tomography," IEEE Trans. Microwave Theory Tech., Vol. MTT-32, No. 8, Aug., pp. 860-874.
- [5] C. Q. Lan, K. K. Xu, and Glen Wade, 1990, "Limited Angle Diffraction Tomography and Its Applications to Planar Scanning Systems," IEEE Trans. Med. Imag. June.
- [6] S. G. Kim, K. W. Suh, and J. W. Ra, 1992, "Improved Born Inversion for Frequency-Swept Microwave Imaging of Dielectric Cylinder," Microwave and Optical Tech. Lett., Vol. 5, June, pp. 340-343.

Velocity, Attenuation, Dispersion and Diffraction Hole-to-Hole Radar Processing

by

Gary R. Olhoeft
U.S. Geological Survey
P.O. Box 25046 DFC MS964
Denver, CO 80225-0046

Computer programs have been developed to automatically process hole-to-hole radar data without operator intervention. One version of the program takes the PEMSS (Pulsed Electromagnetic Search System; Owen, 1981) raw ground penetrating radar data, PEMSS II calibration data (if available), borehole deviation logs, and borehole 3D survey coordinates to produce:

- 1) apparent velocity, attenuation and dispersion logs versus depth for each offset,
 - 2) self-consistency test error estimates,
 - 3) raypath inversion to locate the principle anomaly,
 - 4) multipath and diffraction analyses to size the anomaly (assuming a cylindrical air-filled void),
 - 5) tomographs of apparent velocity, attenuation and dispersion in the plane between the boreholes to show surrounding geology,
- and 6) three-dimensional perspective views of the tomographs to show geometry.

In order to accomplish this, first arrivals must be automatically picked. Several different first arrival pickers are used to handle noisy and distorted data, with the consensus (weighted with the location of the previous pick) chosen as the first arrival wavelet to process. Next, the datasets are subjected to a variety of self-consistency tests to determine the impact of errors on further tomographic processing or modeling. The largest errors occur from inadequate knowledge of the location of the logging tools in three dimensional space. Small corrections (meter-scale) can be inferred from the datasets themselves, larger errors require re-collection of the data. Then processing and modeling are performed, and lastly, several interpretive plots are generated. The raypath inversion accurately locates the depth and height of the tunnel (assuming straight ray paths), but exaggerates the width from the limited angular coverage during data acquisition. The diffraction and multipath modeling accurately determines the height of the tunnel (assuming an air-filled cylindrical void). The tomography confirms the character of the anomaly as an air-filled tunnel with velocity, attenuation and dispersion high compared to the surrounding rock and also provides geological context for the location of the tunnel between the borehole pair.

Presented to Fourth Tunnel Detection Symposium on Subsurface Exploration Technology, Colorado School of Mines, Golden, CO, April 26-29, 1993.

Velocity, Attenuation, Dispersion and Diffraction Hole-to-Hole Radar Processing

by Gary R. Olhoeft

Introduction

The acquisition of large amounts of hole-to-hole radar data on a production basis requires automatic processing and interpretation methods. The PEMS GRO 10 program (discussed in this paper and in use since April, 1990) allows completely automatic and unattended processing of PEMSS I and PEMSS II (Pulsed Electromagnetic Search System)(Owen, 1981) data. PEMSS data processing (Kemerait and others, 1988; Olhoeft, 1988) and modeling (Greenfield, 1988; Moran, 1989) have been the subject of several papers in this and previous tunnel detection symposia.

The PEMS GRO 10 program has built in safeguards to test the quality of data before processing. Inconsistent data can be processed, but with misleading or erroneous results. The program was designed to process a multiple sequence of data sets, flagging and labelling those with errors, and processing the good datasets to completion. Relatively unskilled personnel can keep data flowing into the system.

Data Acquisition

Hole-to-hole radar data are acquired by logging a pair of boreholes repeatedly. The transmitter is placed in one hole and the receiver in the other hole. Depths are recorded relative to the center of the transmitter tool. Both tools are simultaneously moved slowly and continuously during logging with a vertical depth offset between the transmitter and receiver. Several logging runs at different offsets are performed: typically -10, -5, 0, +5 and +10 meters (receiver relative to transmitter). A separate field crew acquires the hole survey location information and hole deviation logs.

Errors and Inconsistencies

In order to process hole-to-hole radar data (Olhoeft, 1988), the location of the holes must be known in three dimensional space (with surveys of the top of the holes at ground surface and borehole deviation surveys with depth). Inaccuracies in the knowledge of the positions of the holes and of the radar transmitter and receiver logging tools in the holes during data acquisition are the most significant errors in the entire data acquisition process. These errors propagate through data processing and modeling to produce artifacts in the final output that can lead to misleading or erroneous interpretation. Other sources of error include missing data, duplicate data (such as identical deviation logs for two different holes), clipped data, instrument error, excessive noise, and so forth. After the first arrivals are picked, a self-consistency test is performed on the entire data set to determine its overall quality before proceeding with tomography and modeling.

Data Processing and Modeling

The data are parameterized as described in Olhoeft (1988). A first arrival picker uses the consensus of a variety of methods to find the first arriving wavelet. The raypath distance between transmitter and receiver divided by the arrival time of the wavelet yields velocity. The reciprocal of the product of raypath distance times first arrival wavelet amplitude is apparent attenuation. Calibrated attenuation requires correction for the antenna patterns (which are unknown). The peak-to-peak broadening of the wavelet shape is used as an apparent dispersion (a measure of frequency dependence in velocity and attenuation). Calibrated dispersion requires wideband processing and correction for frequency dependent system characteristics (which are unknown).

To determine the quality and consistency of the entire dataset, the first arrival times are used with the given survey and deviation coordinates to perform a consistency test. The square of the ratio of the speed of light in vacuum to the velocity in the ground is the relative dielectric permittivity. For each offset between transmitter and receiver, the apparent relative permittivity is plotted versus the probe perturbation from its nominal position. The apparent relative permittivity is computed using first arrival time and raypath distance for the perturbed receiver tool position. A set of curves such as shown in Figure 1 for five offsets is generated. These curves are averages for the entire hole-pair dataset. If the dataset is consistent and there are no errors in instrument timing nor knowledge of the tool positions, the five curves should intersect at probe deviation equal to zero and the relative dielectric permittivity of the medium. In practice, some error occurs, so there is a spread in the intersections of the five curves. This spread is an indication of the quality of the overall dataset. In Figure 1, a box is drawn around the intersection showing ± 0.5 units error in permittivity and ± 0.5 meter error in position. The curve just skirting the lower edge of the box is the zero offset level run (transmitter and receiver run at same depth), not intersecting the remaining curves, and indicative of a timing error in that run. The entire dataset is marginally acceptable for further processing. In rock with large natural variations in electrical properties, it may be necessary to perform this test piecewise over uniform lithological sections or to use modal statistical analysis instead of the averages for the entire dataset.

For each offset between transmitter and receiver, a set of data is produced (similar to wireline logs) consisting of tool separation, hole-to-hole velocity, apparent attenuation and apparent dispersion, each versus depth. The left half of Figure 2 illustrates the zero offset set of such data for one hole pair. A summary (as the product of velocity times dispersion versus depth) of the multiple offsets is shown in the upper right part of Figure 2. The lines connecting the most significant anomaly in each offset are used in the lower right part of Figure 2 to locate the anomaly by raypath inversion between the two holes. The outer ellipse represents the locus of the possible centers for the anomaly, while the inner ellipse represents the probable size of the anomaly.

The offset data are then run through a filtered back projection algorithm (Olhoeft, 1988, and references therein) to produce velocity, apparent attenuation and apparent dispersion tomographs as shown in Figure 3. The plus surrounded by two ellipses is the raypath inversion from Figure 2. Note the borehole deviation on the right edge of each panel. Everything is plotted relative to the transmitter hole (on the left edge of each panel). An air filled mined tunnel appears as a velocity high (red contours) as the speed of light is higher in air than in rock. It appears as an attenuation high from scattering of energy at the tunnel walls (and possibly from enhanced electrical conductivity in the crack halo around the tunnel, Pusch, 1989). It appears as a dispersion high from the distortion of the wavelet caused by

frequency dependent scattering (the tunnel is about the size of the radar wavelength in the rock; Olhoeft, 1988) or from constructive and destructive multipath interference.

The approximate location of the center of the anomaly from raypath inversion is then used to find the maximum anomaly in the zero offset level run data. In Figure 4, on the left half of the plot are shown a portion of the level run data centered on the maximum anomaly. Assuming a circular cross-section, air-filled void, the right half of Figure 4 is an attempt to model the electromagnetic waves around, through and scattered from the tunnel. The yellow color represents waves through the rock with no apparent effect from the tunnel. The red color shows where the waves go through the tunnel and recombine with waves that leak around the tunnel, producing multipath constructive and destructive interference. The green color traces out the complex parabola from diffracted waves, scattered off the tunnel walls. Such full waveform diffraction modeling improves the resolution of the size and shape of the void by up to an order of magnitude. If such diffractions are evident in all of the offset data, diffraction tomography (Witten and King, 1988) may be performed. However, diffraction tomography is typically possible in only a few percent of the data. Either there are too many diffractions and they can't be clearly sorted out, or there are few diffractions to be exploited. Figure 4 shows an example of negligible diffractions. The tunnel is still visible in the data, but the resolution-enhancing improvement possible with diffraction tomography cannot be exploited in this data set. Diffraction modeling only provides a limit to the size of the tunnel. Figures 5 through 8 illustrate a clear example of hole-to-hole radar data for a similar sized tunnel in similar geological material, but causing strong diffractions. The factors determining the presence or absence of strong diffractions have not been investigated. However, they are probably related to changes in the rough walled faceting of the tunnels as the diffractions have been observed to come and go along the length of the same tunnel in the same material, and with differing transmitter-receiver offsets (or radar viewing angles of the tunnel).

Discussion

All of the figures in this paper were produced automatically and without operator interaction. Figures 1 to 4 are an uncalibrated PEMMS I set from one tunnel site, and Figures 5 to 8 are a calibrated PEMSS II set from a second tunnel site. Calibrated refers to the accuracy of the time base and knowledge of the location of time zero. Greater drift in the PEMSS I time base produces higher inconsistency in PEMSS I data than in PEMSS II data. Also, much of the archival PEMSS I data was not calibrated to test the time base and locate time zero (by measuring the travel time through air with the transmitter and receiver at known separation). The surveying, deviation and PEMSS data were placed into a database accessible to the PEMS GRO 10 program, and the program executed. All of the data were automatically processed and plotted as shown. Accompanying datasets which contained inconsistencies or missing components were flagged for operator attention. The raypath inversion accurately locates the depth and height of the tunnel (assuming straight ray paths), but exaggerates the width from the limited angular coverage during data acquisition. The diffraction and multipath modeling accurately determines the height of the tunnel (assuming an air-filled cylindrical void). The tomography confirms the character of the anomaly as an air-filled tunnel with velocity, attenuation and dispersion high compared to the surrounding rock, and they also provide geological context for the location of the tunnel between the borehole pair (in other words, the homogeneity of the rock surrounding the tunnel).

Finally, three-dimensional perspective views of the tomograms are presented to show the true spatial relationships between the tunnel and surrounding geology, with the ability to zoom in and out, and to tilt and rotate the 3D views on the graphics display of a workstation (see example in Wright and others, 1993).

Acknowledgement

This work was funded by the U. S. Army Belvoir Research, Development and Engineering Center, Ft. Belvoir, Virginia.

References

- Greenfield, R. J., 1988, Modeling of electromagnetic propagation between boreholes: in Third Technical Symposium on Tunnel Detection Proceedings, Jan. 12-15, 1988, Colorado School of Mines, Golden, CO, p. 156-172.
- Kemerait, R. C., Griffin, J. N., Meade, J. L., Kraft, G. D. and Pound, G. W., 1988, Signal processing applied to tunnel detection by borehole radar: in Third Technical Symposium on Tunnel Detection Proceedings, Jan. 12-15, 1988, Colorado School of Mines, Golden, CO, p. 593-615.
- Moran, M., 1989, Time domain analysis of electromagnetic scattering for a three dimensional tunnel in the presence of a vertically oriented electric dipole: MSc thesis, Dept. of Geosciences, Pennsylvania State Univ., State College, PA, var. pag.
- Olhoeft, G. R., 1988, Interpretation of hole-to-hole radar measurements: in Third Technical Symposium on Tunnel Detection Proceedings, Jan. 12-15, 1988, Colorado School of Mines, Golden, CO, p. 616-629.
- Owen, T. R., 1981, Cavity detection using VHF hole-to-hole electromagnetic techniques: Second Tunnel Detection Symposium, Colorado School of Mines, Golden, CO, July 21-23, 1981, U. S. Army MERADCOM, Ft. Belvoir, VA, p. 126-141.
- Pusch, R., 1989, Influence of various excavation techniques on the structure and physical properties of "near-field" rock around large boreholes: Svensk Karnbranslehantering AB (Swedish Nuclear Fuel and Waste Management Co.) Technical Report 89-32, Stockholm, Sweden, 57p.
- Witten, A. J. and King, W. C., 1988, Geophysical diffraction tomography for imaging isolated subsurface inclusions: in Third Technical Symposium on Tunnel Detection Proceedings, Jan. 12-15, 1988, Colorado School of Mines, Golden, CO, p. 227-241.
- Wright, D. L., Olhoeft, G. R., Grover, T. P., and Bradley, J. A., 1993, High-speed digital radar systems and applications to subsurface exploration: Fourth Tunnel Detection Symposium on Subsurface Exploration Technology, Colorado School of Mines, Golden, CO, April 26-29, 1993, this volume.

Figure Captions

Figure 1

Self-consistency test of the dataset for Figures 1 to 4. The apparent relative dielectric permittivity is plotted versus perturbed receiver probe position for each of the five transmitter-receiver depth offsets (expressed as probe deviation from its nominal position). All the curves should intersect at a point above deviation zero and at the true relative permittivity of the medium in the absence of errors. The box is ± 0.5 dielectric units by ± 0.5 meters in size, outlining the acceptable locus of spread in the intersection of the curves. The relative dielectric permittivity is 6.06 ± 0.27 .

Figure 2

The left half of this figure shows the velocity, apparent attenuation and apparent dispersion logs for the level run at this site. The upper right quarter of the figures shows the velocity-dispersion product for the five offsets. The lower right portion of the plot shows the ray path inversion of the largest anomaly in the upper right set of offsets. The outer ellipse is the possible location of the center of the anomaly and the inner ellipse is its probable size.

Figure 3

The velocity, apparent attenuation and apparent dispersion tomographs for the site in Figures 1, 2 and 4. In each case, the spectrum blue through red is low to high, and the plus surrounded by ellipses is the raypath inversion from the previous figure.

Figure 4

The left half is the original data and the right half is the diffraction and multipath model. The yellow coded curves represent the radiowaves travelling through the rock with no influence from the tunnel. The red coded curves represent the waves travelling through the tunnel and combining constructively and destructively with the waves leaking around the tunnel. The green coded curves are the waves diffracting off of the tunnel.

Figures 5 to 8 are the same as Figures 1 to 4, though for a different tunnel at another site exhibiting strong diffraction events.

/3074/D/DT_7TDT_9L01 19.3 meters maximum separation
DT_7 is 16.7 meters from and 0.1 meters below DT_9

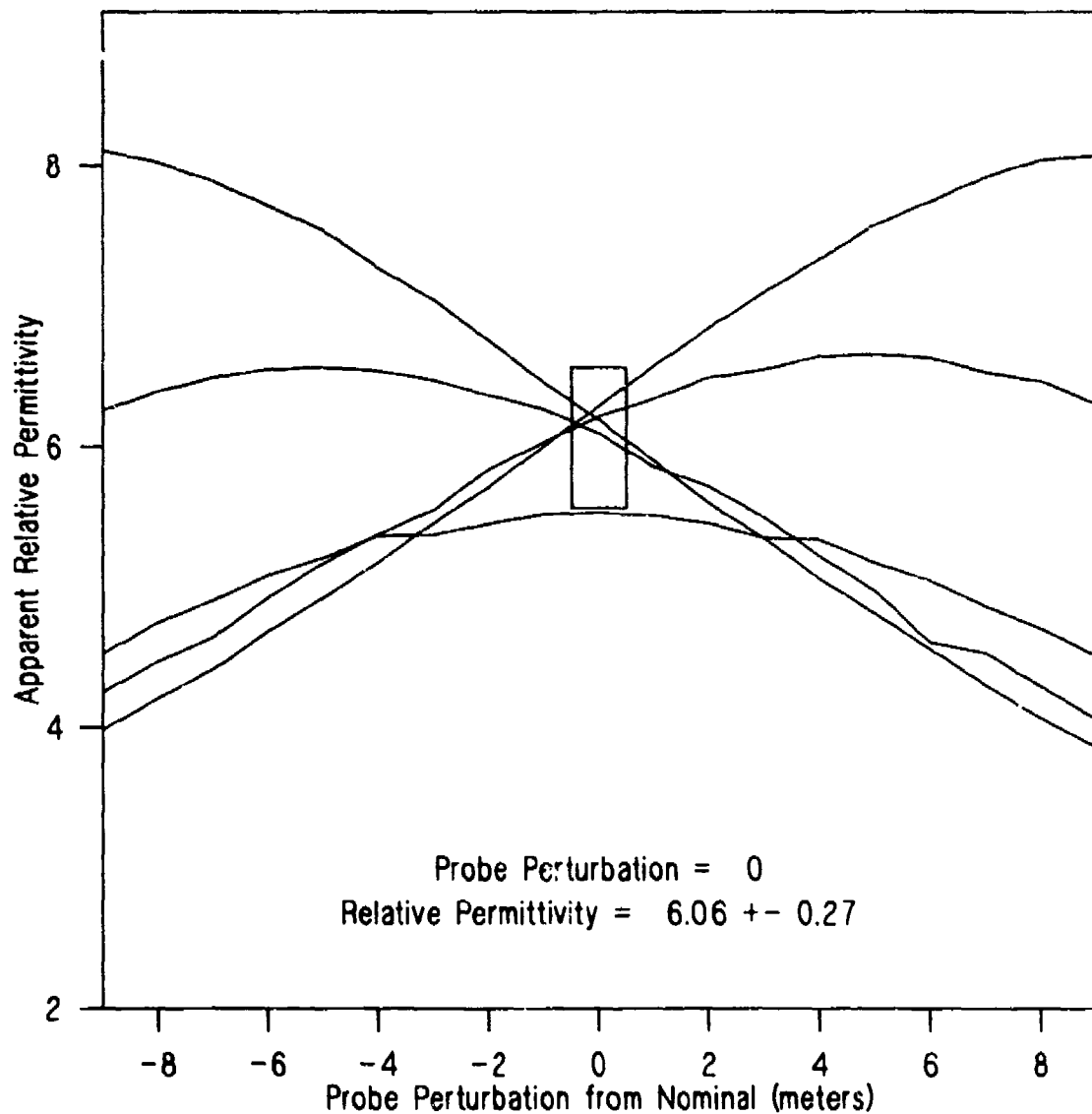


Figure 1

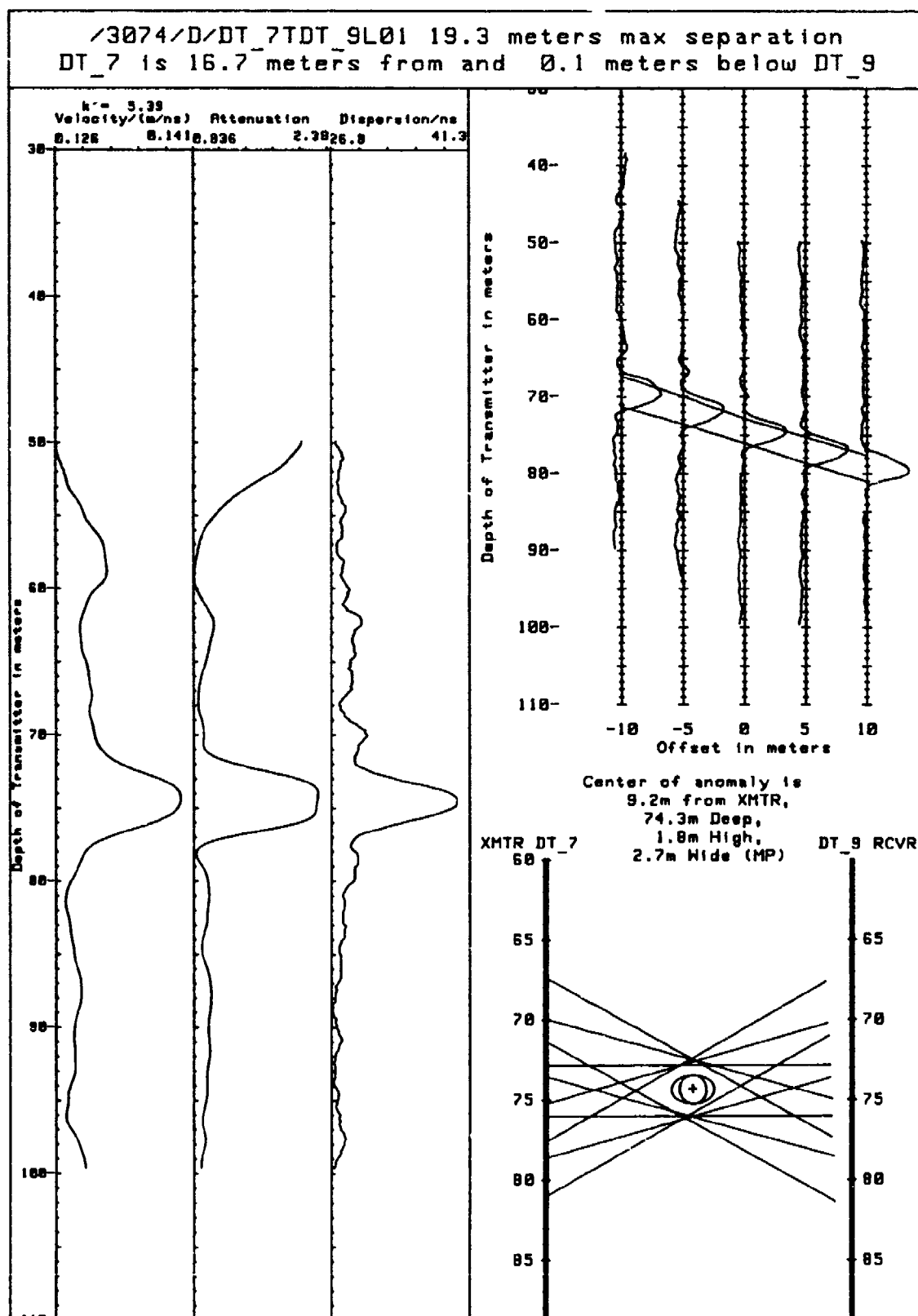


Figure 2

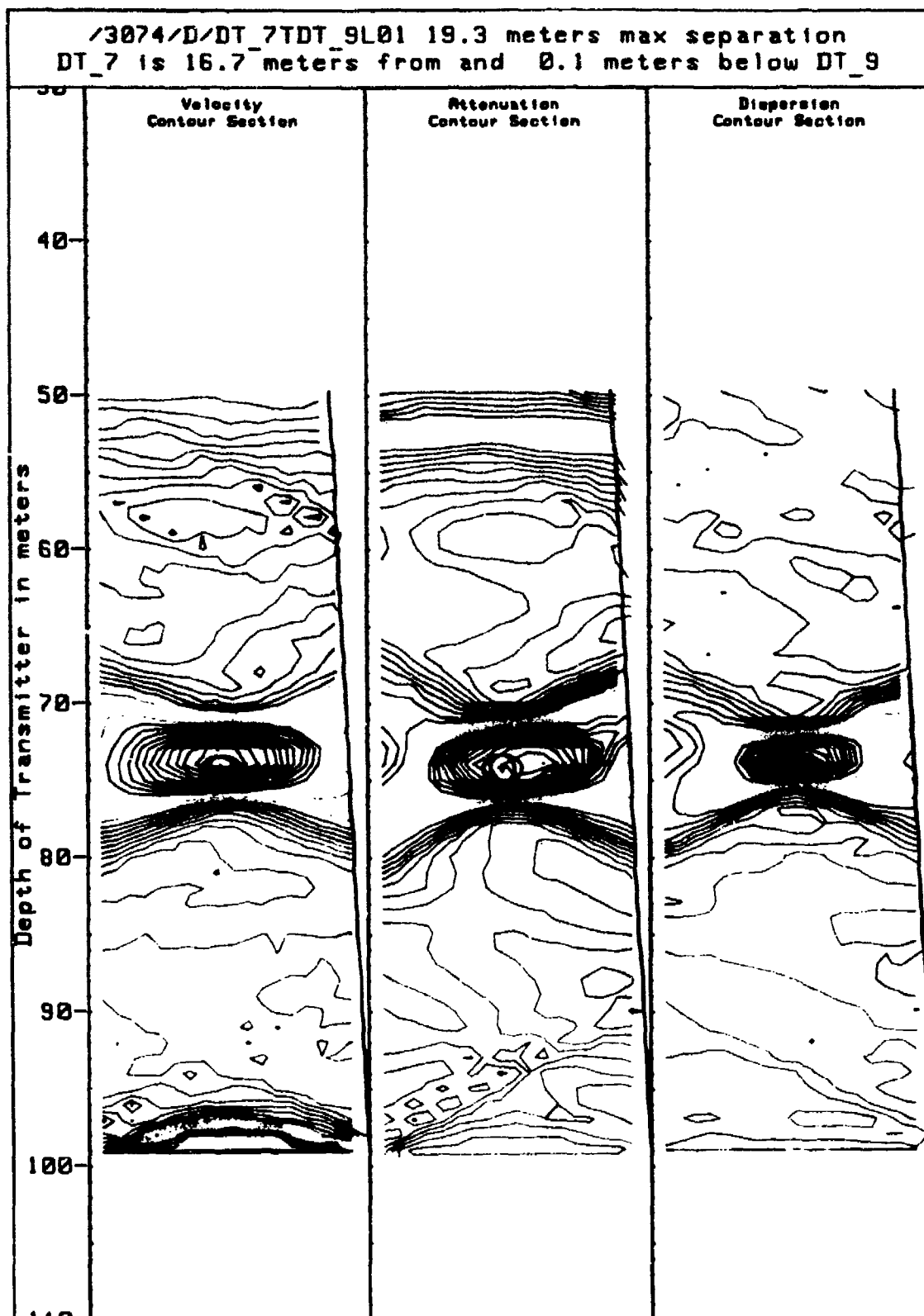


Figure 3

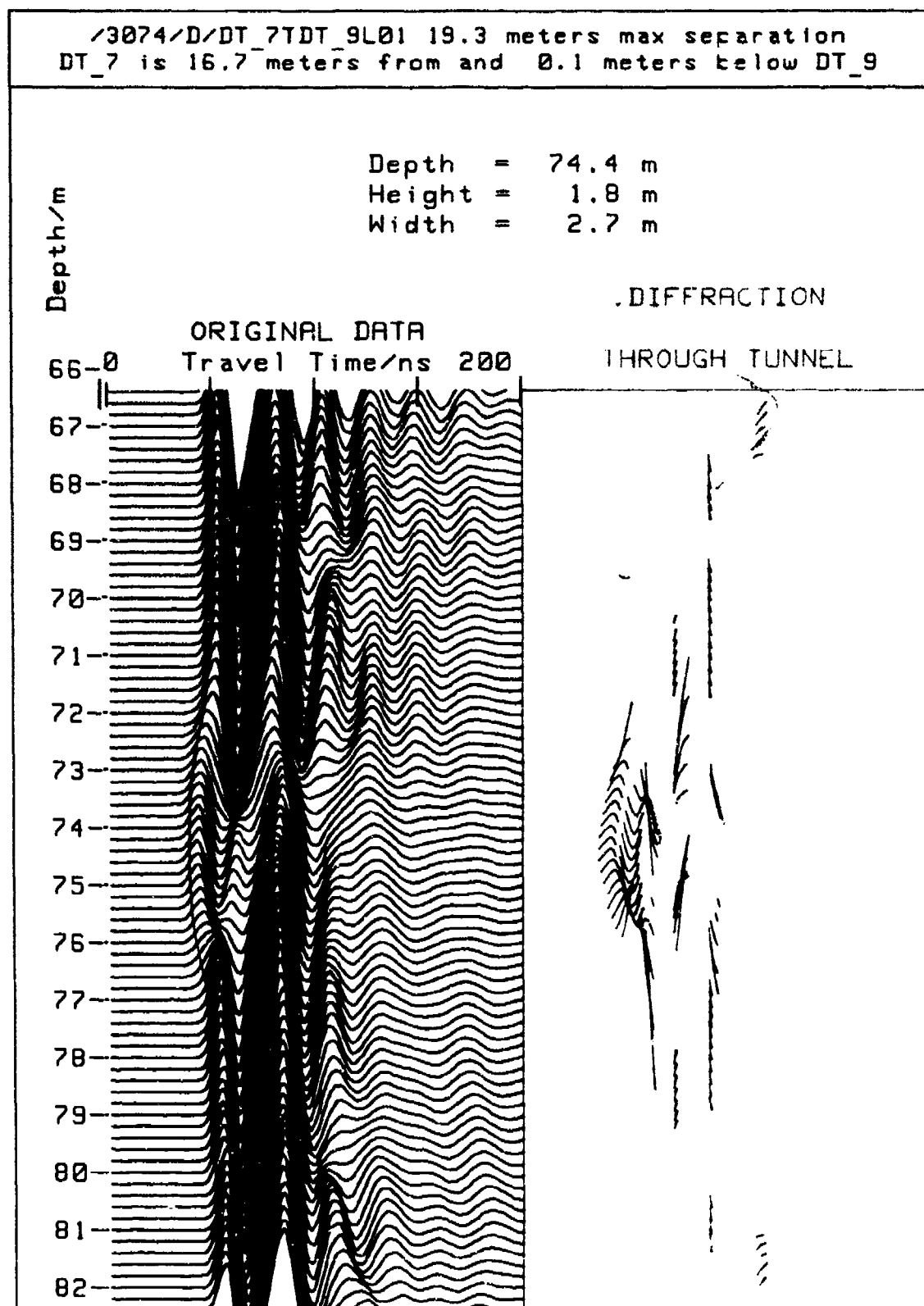


Figure 4

/0381/1/801441T8014_SL01 11.0 meters max separation
801441 is 9.4 meters from and 0.2 meters above 8014_5

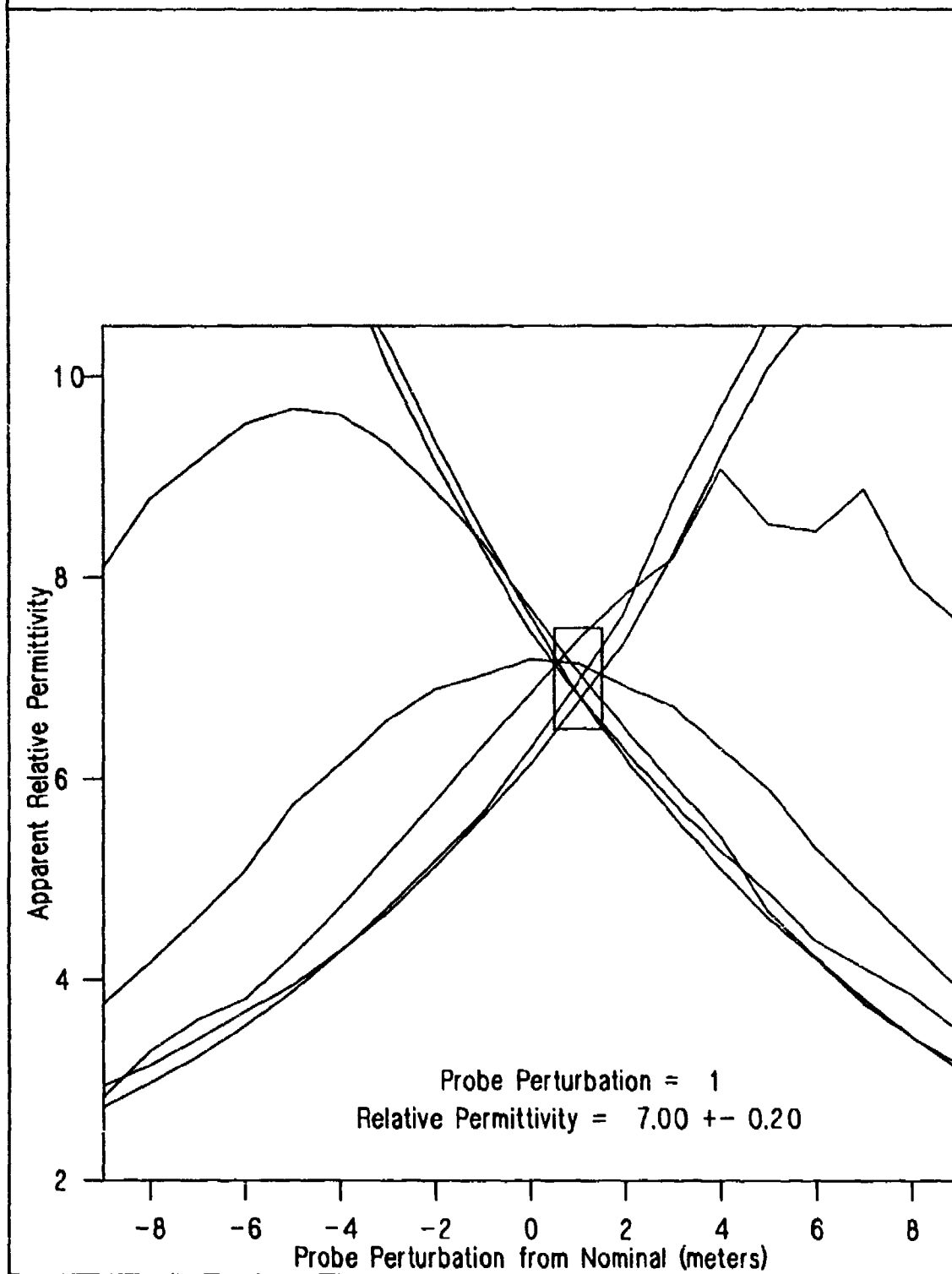


Figure 5

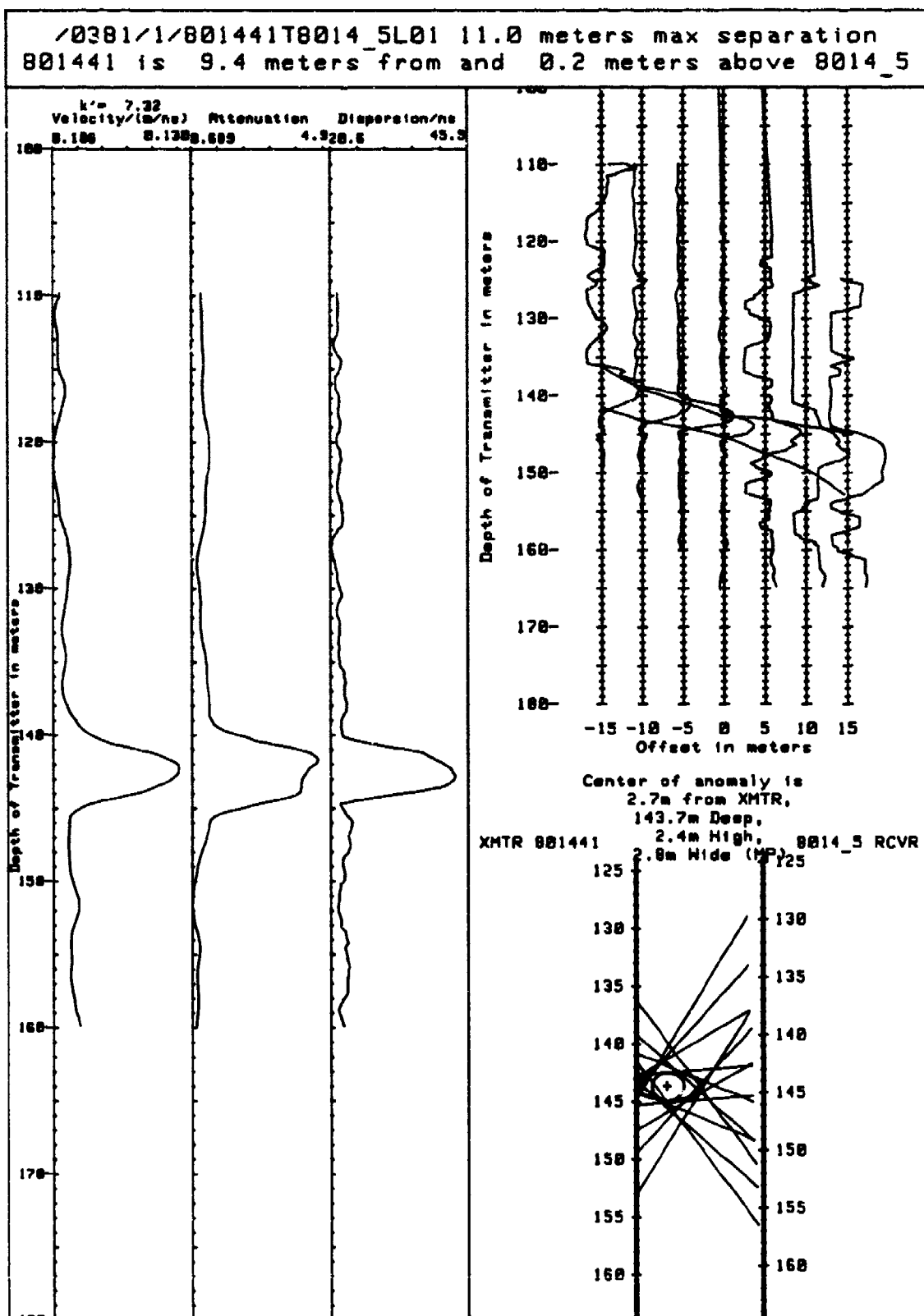


Figure 6

/0381/1/801441T8014_5L01 11.0 meters max separation
 801441 is 9.4 meters from and 0.2 meters above 8014_5

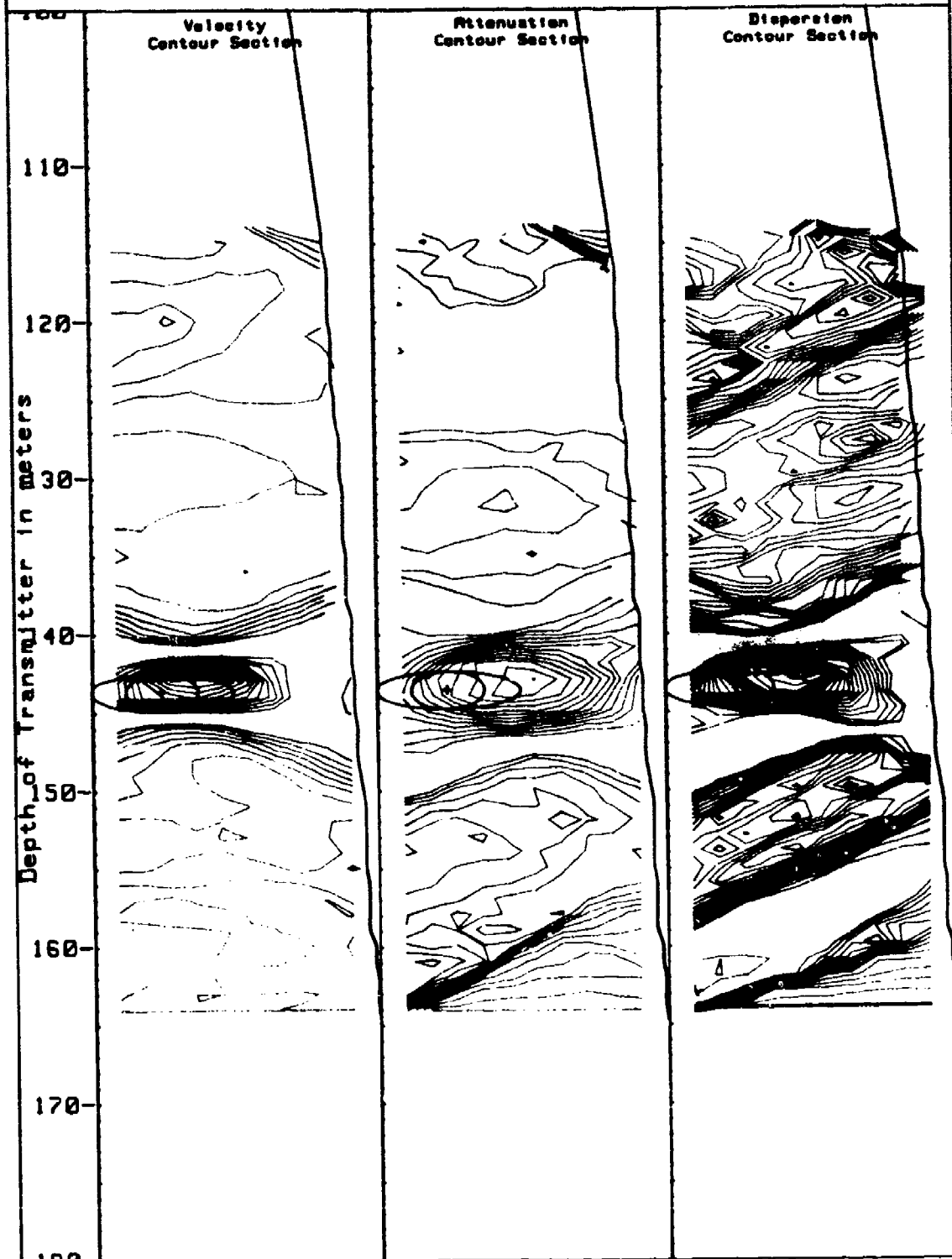


Figure 7

/0381/1/801441T8014_SL01 11.0 meters max separation
801441 is 9.4 meters from and 0.2 meters above 8014_5

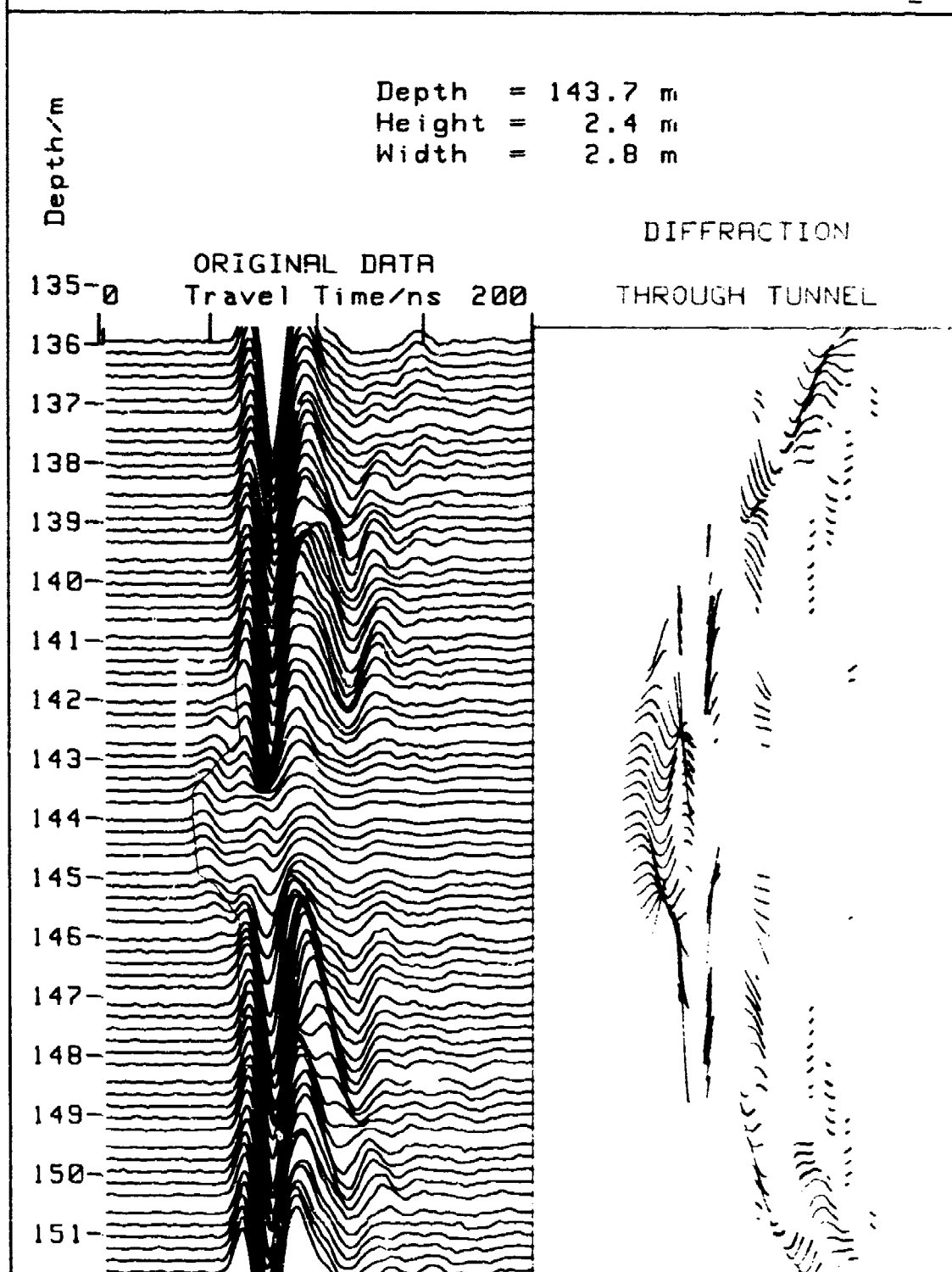


Figure 8

CROSS-BOREHOLE MEASUREMENT OF DIPOLE ARRAY PATTERNS IN A DISSIPATIVE MEDIUM: A LABORATORY SCALE MODEL STUDY

Irene C. Peden and Robert Kipp
Electromagnetics and Remote Sensing Laboratory
University of Washington
Seattle, WA

INTRODUCTION

The cross-borehole measurement technique at VHF frequencies typically employs winched, single transmitting and receiving dipoles in various offset configurations to detect a buried target whose vertical position is estimated from the pattern of forward scatter. The characteristic tunnel signature displays double nulls whose position in the receiver borehole is a function of frequency and degree of offset. Signal-to-noise ratio and clutter from random scatterers in the host medium are practical limitations to target detection that can be modified by means of synthetic collinear arrays whose electric fields are determined as a function of vertical position from the measured amplitude and phase of a single dipole element as it moves in the borehole.

This paper compares the results of laboratory scale model measurements and simple synthetic antenna array techniques. Calculations are based on the thin bare dipole in a low-loss host medium. Maintaining a magnitude and phase reference between the transmitter and receiver allows single-element coherent measurements to be recorded at selected collinear array element locations, and the results added to form focused beams. Such synthetic arrays neither suffer pattern degradation through mutual coupling among elements, nor require the use of hardware in the borehole to shift phase or adjust amplitudes. Element weightings are implemented numerically, resulting in better accuracy than would be provided by a physical array, and requiring much less effort. They can be applied at a later time, and numerous configurations and design schemes can be produced from a single data set. As the number of synthetic array elements increases, irregularities due to unwanted reflections from nearby objects, whether natural or man-made, tend to disappear, and some of the practical problems such as inadequate signal-to-clutter ratio and weakened signals due to attenuation along the propagation path are at least partially overcome. An example is provided to illustrate the improvement that can be achieved in locating a buried dielectric ellipsoid in the model.

THEORETICAL MODELS

The full-scale borehole antenna problem in the frequency domain is one of a dipole antenna immediately surrounded by air or another dielectric, and embedded in rock or earth that can be described as a lossy dielectric medium with specific constitutive parameters that are functions of frequency. In the neighborhood of the antenna itself, the physical configuration is that of a sheathed, or insulated dipole. The range of possible electromagnetic parameters for both sheath

and host medium is wide, and may lead to a difficult analytical problem. However, the rock medium of interest to the application that has brought this group together qualifies as a low loss dielectric in the VHF band (30 - 300 MHz.), with measured dielectric and loss parameters of $\epsilon_r = 9$ and $\sigma = 0.002 \text{ S/m}$ * at 300 MHz. It follows that the loss tangent ($\tan \delta = \sigma/\omega\epsilon$) is 0.079 at 50 MHz, if ϵ_r and σ are assumed constant over the band. We have verified that in the range of electromagnetic parameters at issue here, the bare and insulated dipole results differ only slightly so long as the borehole-to-antenna radius is less than 10, a condition that is typical in practice. The mismatch in intrinsic impedances at the interface of borehole and sheath is small enough to justify the assumption that the sheath can be neglected and the problem treated as that of a bare dipole in a low loss material medium. The reader is referred to the literature on antennas in matter for more detailed information.

The cross-borehole geometry illustrated in Figure 1 indicates that the measurable field quantity of interest is the vertical component of the received electric field measured along a vertical path, i.e. $E_z(z)$. This is not a radiation pattern $E_\theta(\theta)$ measured at constant radius. For convenience, however, $E_z(z)$ will be referred to herein as the pattern. The half-power beamwidth HPBW is defined in terms of $E_z(z)$ as well, and is thus narrower than the conventionally defined HPBW, since the z component of $E_\theta(\theta)$ decreases with offset angle along the vertical receiver path.

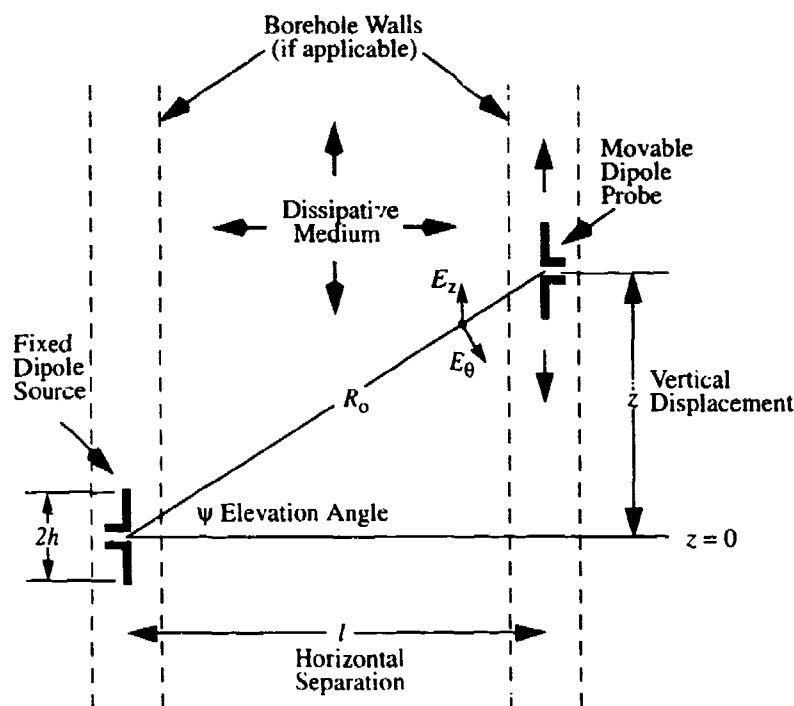


Fig. 1. Geometry for measuring the z -component of the electric field from a vertical dipole in a dissipative medium.

*. Courtesy of the U.S. Army

Using the simplified approximate dipole current distribution,

$$I(z) = \sin \beta (h - |z|)$$

we have verified that it suffices for calculating $E_z(z)$ in this low loss case. The computations were done by integrating the current over the length of the dipole in 0.02335 wavelength segments. The narrower shape of the buried dipole $E_z(z)$ curve of Figure 2 over that of free space is due to absorption in the host medium over the longer distances associated with increasing elevation angles. This simple current distribution provides the same calculated $E_z(z)$ as that of more complicated expressions, so long as the dielectrics are low loss and the dipole is not longer than a half-wavelength. For reasons related to the properties of the laboratory scale model to be described, the calculations presented in this paper are based upon a host medium having $\epsilon_r = 3.2$, and $\tan \delta = 0.026$ at 3 GHz.

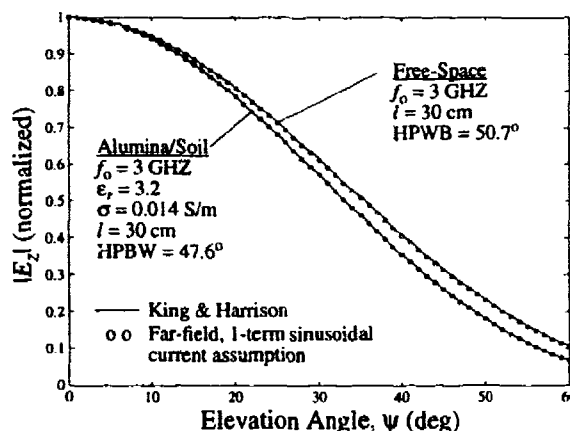


Fig. 2. Vertical component of the electric field radiated by a half-wave dipole computed by two different methods and under free-space and scale model conditions.

Additional calculations have verified the intuitive expectation that absorption causes the pattern to narrow with increasing distance between transmitting and receiving boreholes, and with increasing loss in the host medium.

LABORATORY SCALE MODEL

Physical Description

The schematic of Figure 1 was translated into the microwave band scale model of Figure 3, operating at 3 GHz and incorporating a slightly lossy powder medium whose dielectric and loss properties are identified above, 2-1/8" polyvinyl chloride tube boreholes with inner diameters of 5.44 cm, and instrumentation that will be described. The configuration was contained in a cylin-

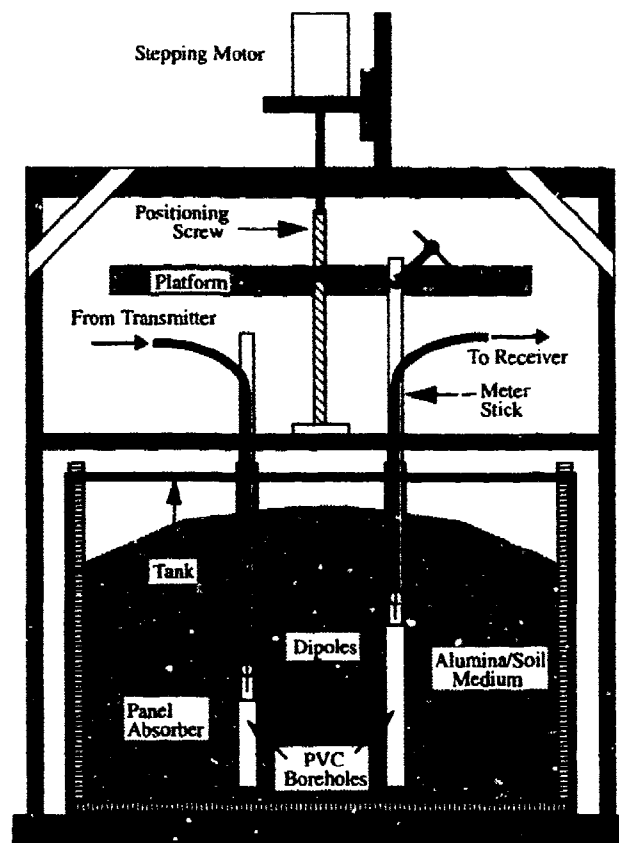


Fig. 3. Scale model cross-borehole probing set-up.

drical aluminum tank 137.2 cm diameter, lined with microwave absorbing material. Reflection from the walls and bottom of the tank were not completely eliminated, and there were additional reflections from the powder/air interface. These were imperfections from the modeling point of view. However, they proved useful for inferring the advantages of the synthetic array approach to improving signal-to-clutter effects in the measured results.

Antennas

The vertical dipoles deployed in the boreholes were constructed specifically for this project. Measurements were taken with capacitively loaded short dipoles acting as both source and field probes; Figure 4 is illustrative. The capacitive loading plates were made from thin PC board and were provided to enhance field strength. There is no other effect on the pattern so long as the antennas are less than a half wavelength in the medium. The plates were placed offset on the leads to reduce the space required, to a degree that permitted them to be inserted in the boreholes. The loading plates provide for possible cross-polarized fields, but it was determined experimentally that such field components are at least 10 dB below the intended field for angles up to 50° away from broadside.

The dipoles were fed by 0.141" semi-rigid coaxial lines, requiring baluns to prevent the flow of

current on the outside of the cables and consequent interference with the desired results. The baluns were of the bazooka or folded coaxial cable type, designed to be a quarter wavelength long at 3 GHz, with an external coaxial section that was short-circuited at the point of attachment and open-circuited at the end near the leads. Figure 4a illustrates the configuration in a PVC tube of a pair of dipoles used to verify the two-element synthetic array results, whereas Figure 4b shows a source and receiving probe pair as they would be oriented in the transmitting and receiving boreholes respectively. The field probe *B1* was 1.81 cm in length, whereas the two-element array dipoles *B2* and *B3* were 2.0 cm. long A number of free-space pattern measurements verified that these antennas operated as expected.

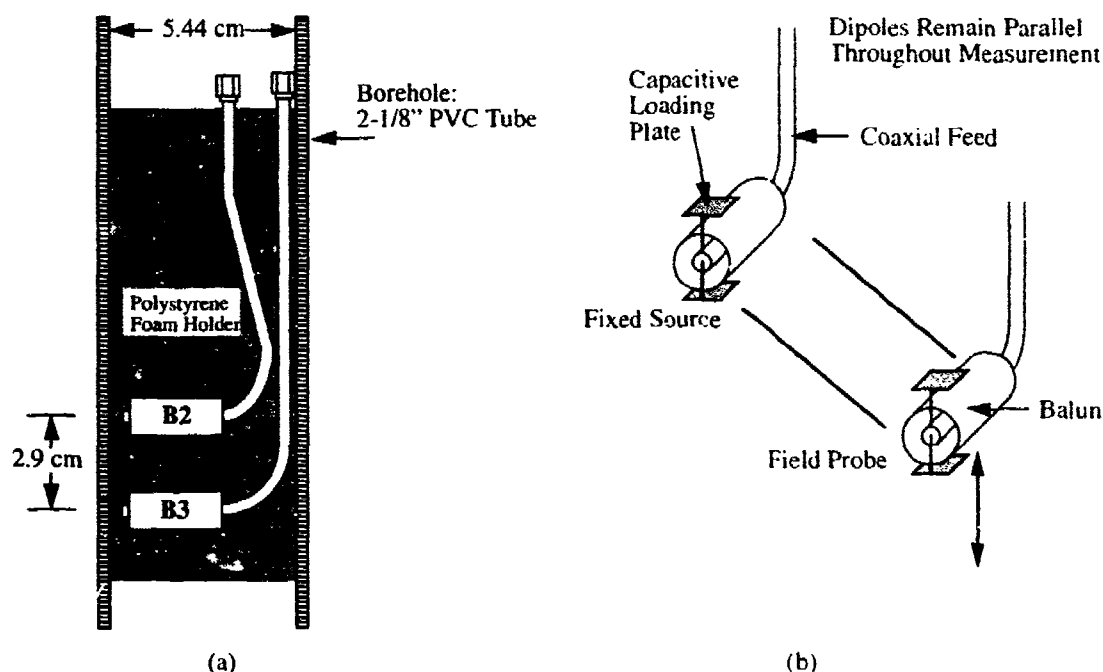


Fig. 4. Capacitively loaded short dipoles: a) deployed as a two-element array, b) relative orientation of source and field probe in model.

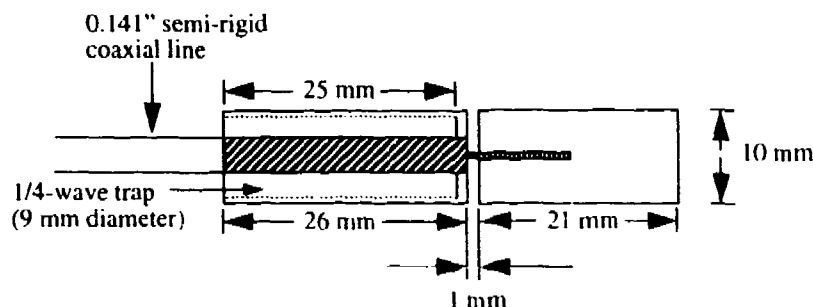


Fig. 5. Half-wave sleeve dipole.

Half-wave sleeve-dipoles as shown in Figure 5 were constructed for the target detection studies. The sleeve for each was made by drilling a 9 mm diameter hole in 10 mm brass tubing at the top of the upper leg to a depth of 25 mm. This provided an open circuit at 3 GHz, limiting pattern distortion. The upper and lower legs of the dipoles were 26 mm and 21 mm long, respectively.

The antennas were attached to wooden meter sticks, and the top edge of the tank employed as a reference. Position in the boreholes could be determined to within 3 mm. The meter sticks were attached to a platform set on a positioning screw driven by a stepping motor. Resolution was within 0.5 mm for measurement runs consistently made in a single motion from bottom to top of the range of travel in the boreholes. There was no measurable distortion due to shifting of feed cables or connectors.

Instrumentation

An HP-8510B Vector Network Analyzer served to generate and detect the S-band signals, permitting c-w transmission measurements over a wide frequency range. An HP-8340 Synthesized Sweeper, HP-8511 Frequency Converter Test Set, and HP-11691D Directional Coupler were attached by control links and transmission lines to the network analyzer. The instrument contains references that permit relative phase to be recorded, as well as magnitude. An HP-9000/200 computer directed operation of the network analyzer, positioned the field probe and collected measured data, storing it for later manipulation.

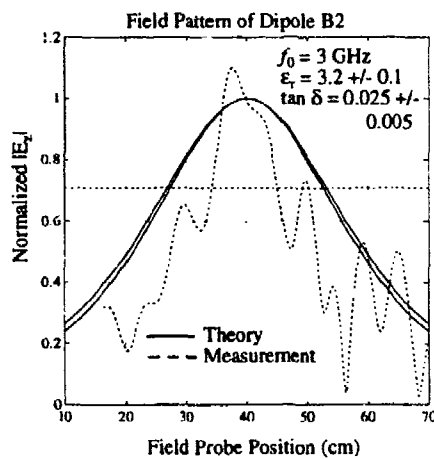
When two transmitting dipoles were used as a physical two-element array, additional instrumentation included a 10 dB directional coupler and adjustable phase-shifter for permitting arbitrary selection of the relative phase between the two array elements. Microwave isolators were inserted between the splitter outputs and the dipoles and their feeds, so that the dipoles could not upset network performance. The variable attenuator placed a limit on the useful frequency range of the system, permitting operation only between 2.6 and 3.95 GHz. This constraint was not important to the study.

MEASURED RESULTS

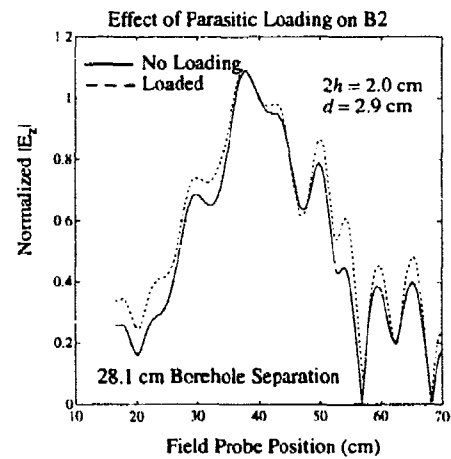
Two-Element Array

Figure 6 is indicative of the effect of reflections from the tank walls on measured patterns $E_z(z)$. In Fig. 6a we see the measured and theoretical patterns of one of the source probe alone; the two theoretical curves bound the range of possible curves given the uncertainties in the constitutive parameters of the host medium. It was determined from the time-gating feature of the network analyzer that reflections from the tank wall dominate in disturbing the pattern, unless or until the probe approaches the bottom of the tank. The 28 cm borehole separation would correspond to 14 meters full scale at 60 MHz. A similar measurement, not shown, was made for dipole B3 and found to be nearly identical. When two physical elements are deployed together in a collinear array, there is mutual coupling between them. Figure 6b illustrates the effect of B3 on B2 when one is excited and the other placed in proximity but not excited. The distance between dipole centers, λ , is 2.9 cm. Figure 6c shows the broadside pattern for the two-element array in three different modalities, i.e. calculated, measured directly, and synthesized from the measured amplitude and phase of the single, parasitically loaded element at different locations in the borehole. The

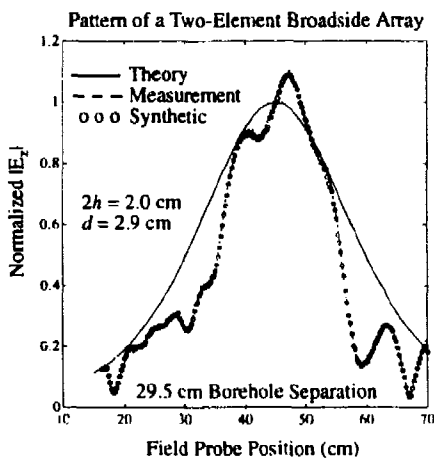
theoretical field $E_z(z)$ was calculated on the basis of a 29.5 cm. borehole separation, and 2.9 separation between the centers of two collinearly located 2 cm. dipoles. Parameters assumed for the host medium were $\epsilon_r = 3.2$ and $\tan \delta = 0.025$. The dashed trace is the measured pattern of the array when B3, located 46.45 cm below the tank edge, has its magnitude and phase adjusted experimentally to compensate for departures from the theoretical ideal introduced by the power-splitter network. For the array synthesis calculation, the same adjustments were made and point-by-point phasor addition employed. Figure 6d illustrates the synthetic two-element array pattern obtained from measured data using B2 first at 40 cm. and then at 37.1 cm below the tank edge



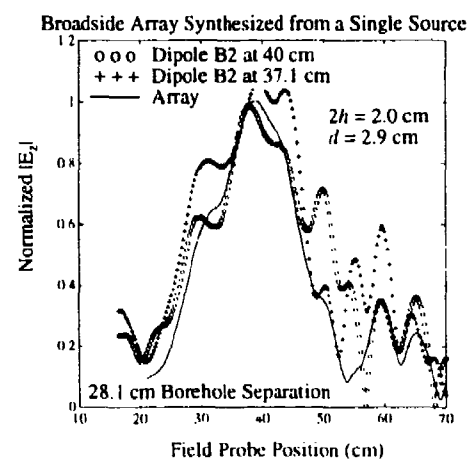
(a)



(b)



(c)



(d)

Fig. 6. Antenna patterns of a) a single source, b) a parasitically loaded source, c) a two-element array with mutual coupling, and d) a synthetic two-element array.

with $B3$ not present in the tank. As before, $B1$ served as the receiving field probe. Although irregularities due to reflections are still present, it is clear that the maximum field strength occurs closer to its expected location, and the level of fluctuation is reduced with respect to Figure 6c.

It should be pointed out that other array features can be synthesized from the same data set, i.e. difference patterns and different angular orientations of the position of the main lobe, by numerically shifting the relative phase between elements.

Four-and Six-Element Array

As before, all measurements of $E_z(z)$ are based on a source location 40 cm below the top of the tank. The estimated uncertainty in position of either dipole is 3 mm. Variance in the signal level is estimated at 0.03 dB. Figure 7 compares the theoretical and measured patterns of the single element with those obtained by synthetic array calculation for 4 such collinear elements with their centers spaced 3 cm. apart. Magnitude and phase of E_z were measured at 0.254-cm increments along the borehole axis. Each point in the array pattern is a combination of four measurements separated by 12 intervals, or 3.08 cm. The ordinates are the signal voltages measured by the network analyzer, normalized at the point of maximum amplitude. The HPBW of the single-element pattern is found to be approximately 70% of the predicted value, an effect that is attributed to the boreholes which are neglected in the theoretical, bare dipole model. A plausibility argument for

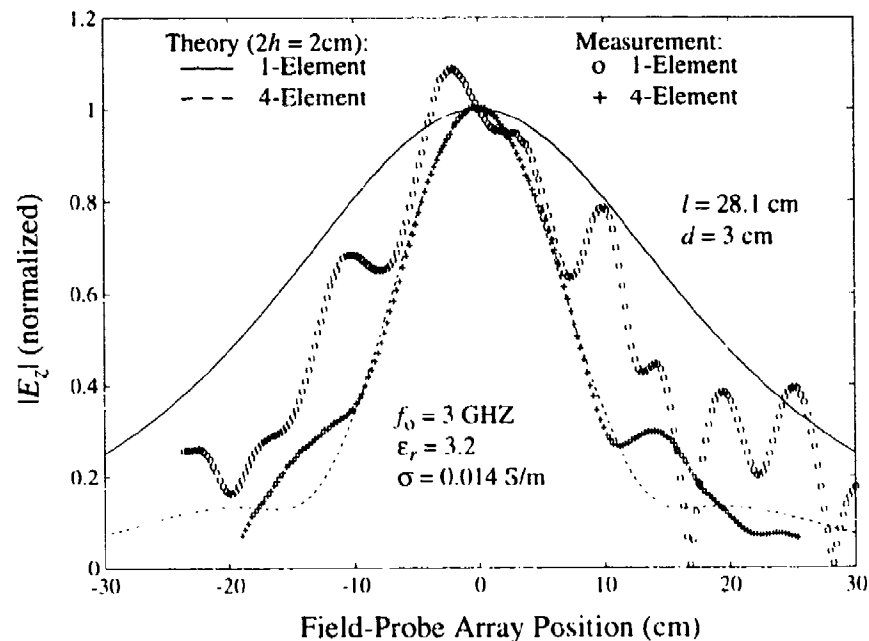


Fig. 7. Theoretical and measured patterns with a single-element and a synthetic four-element field-probe array.

this effect can be constructed using the planar and ray-theory model of Figure 8. The effect was investigated experimentally as well, by making measurements with empty and powder-filled boreholes. Results were in agreement with the plausibility argument.

Synthetic 4- and 6-element broadside array patterns are illustrated in Figure 9, where it is seen that the array factor, which is not affected by reflections or other scattered signals, now dominates over the element factor, which is heavily influenced by these anomalies. A broadside array improves target detection and ranging accuracy in the cross-borehole environment by vertically focusing the energy between transmitter and receiver. At the same time, the angular extent of the null areas is increased, limiting clutter from illumination of anomalous scatterers in those regions of the space, whether these are the tank walls in a laboratory scale model, or various kinds of fractures, inclusions, etc. in a real rock or soil medium. The price for these advantages over the single dipole is the requirement for measured phase as well as amplitude

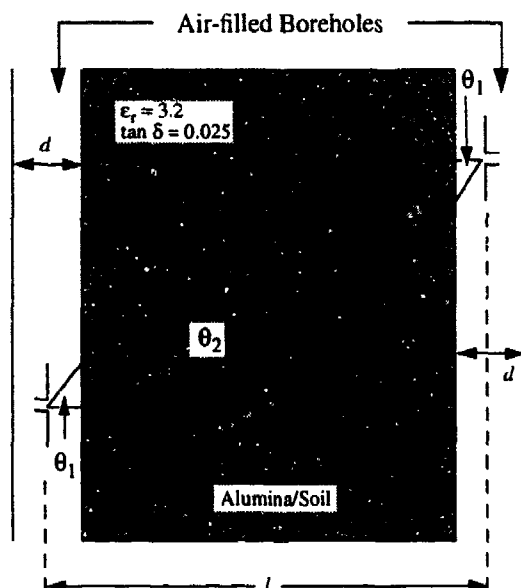


Fig. 8. 2-D geometry for applying ray-tracing to predict the effect of large boreholes.

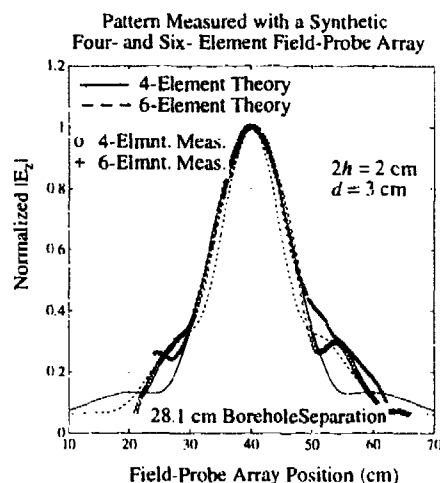


Fig. 9. Synthetic 4- and 6-element field-probe array.

Other synthetic array configurations can be constructed from the same data sets by changing the weighting functions associated with amplitude and phase of the single element in different physical locations in the borehole. For example, Figures 10 and 11 represent difference and steered-beam patterns, respectively. The difference pattern might have some advantages in improving an estimate of tunnel location after preliminary detection, whereas some vertical scanning is possible in the steered beam case. It was determined experimentally that calculations could predict the angular location of the maximum within 3° over an angular extent of $\pm 20^\circ$ in the six-element array case.

To investigate the relevance of the synthetic array concept to target detection, a polyfoam ellip-

soid whose dimensions are shown in Figure 12, was inserted into the scale model as indicated, providing a low contrast target. The ellipsoid serves as a reasonable three-dimensional model of a tunnel buried in a lossy material medium, as has been shown in other work. The half-wave sleeve dipoles were used for this measurement. The transmitting and receiving antennas were moved

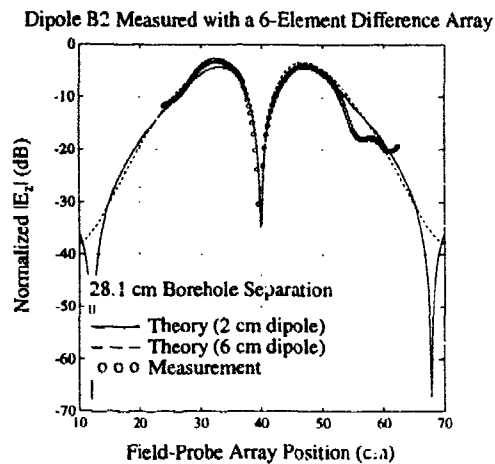


Fig. 10 Comparison of theoretical and experimental patterns of dipole B2 measured with a 6-element difference array.

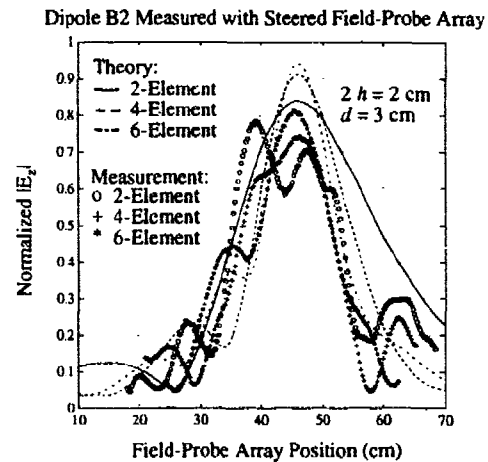


Fig. 11. Comparison of theoretical and experimental patterns of dipole B2 measured with a 6-element steered array.

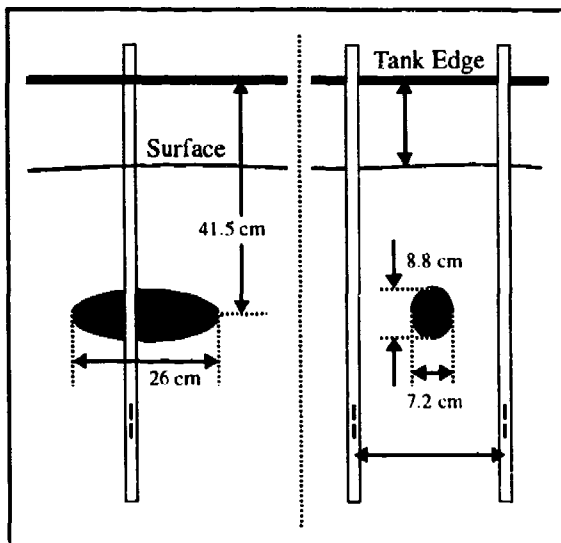
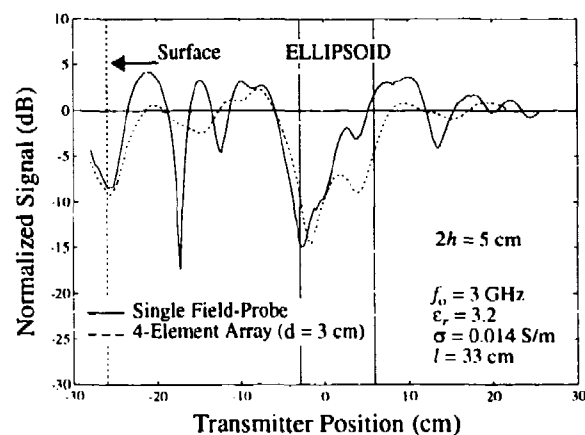


Fig. 12. Example of improved target detection with a synthetic array. Figure shows ellipsoid target placement and comparison of transmission profiles with a single receiver and a four-element receiving array.



together past the ellipsoid. A four-element array was synthesized in the receiver borehole by combining measurements made with -1.5 cm, 0 cm, and +1.5 cm vertical offsets between the two antennas. This scheme permitted reconstruction of the ray paths for a physical array with 3 cm. spacing and no mutual couplings among elements. Although perfect double nulls in the pattern are not achieved in either case, the target location is considerably easier to observe when the collinear array result is used.

CONCLUSIONS

Simple signal processing in the form of synthetic collinear antenna array techniques can be used to enhance the capability of a single dipole to locate a tunnel or other subsurface dielectric target in the cross-borehole configuration. Both amplitude and phase measurements are required to be made in the frequency domain. Use of c-w or stepped-frequency subsurface radar is implied by this requirement. As the number of synthetic array elements increases, the array factor becomes dominant over the element pattern, and irregularities due to reflections from unwanted scattering surfaces in the host medium, whether natural or man-made, tend to disappear. Some of the practical problems such as inadequate signal-to-clutter ratio and weakened signals due to attenuation along the propagation path are partially overcome, and location of the vertical position of a subsurface target can be more clearly revealed by the array than is the case when a single dipole element is used.

REFERENCES

- Cook, J.C., 1975, Radar Transparencies of Mine and Tunnel Rocks, *Geophysics*, Vol. 40, No. 5, pp. 865-885.
- Elliott, R.S., 1981, *Antenna Theory and Design*, Prentice-Hall, Englewood Cliffs, N.J.
- King, R.W.P., and Harrison, C.W., Jr., 1969, *Antennas and Waves: A Modern Approach*, MIT Press, Cambridge, MA.
- King, R.W.P., Smith, G.L., Owens, M. and Wu, T.T., 1981, *Antennas in Matter: Fundamentals, Theory and Application*, MIT Press, Cambridge, MA.
- Kipp, R., 1990, *Cross-Borehole Measurement of Dipole Patterns in a Dissipative Medium Using a Laboratory Scale Model*, unpublished Masters thesis, University of Washington.
- Lee, T.K., Kim, S.Y., and Ra, J.A., 1988, Resonant Scattering of CW Electromagnetic Waves by an Underground Tunnel of Circular Cross-Section, *Proceedings of the Third Technical Symposium on Tunnel Detection*, pp. 104-122.
- Peden, I.C., Kipp, R., and Allestad, J., 1992, A Scale-Model Study of Down-Hole VHF Dipole Arrays with Application to Subsurface Exploration, *IEEE Transactions on Geoscience and Remote Sensing*, Vol. 30, No. 5, pp. 885-891.
- Schneider, J.B., Brew, J., and Peden, I.C., 1991, Electromagnetic Detection of Buried Dielectric Targets, *IEEE Transactions on Geoscience and Remote Sensing*, Vol. 29, No. 4, pp. 555-562.

Cross-borehole Seismic Tomographs of Tunnels

R.D. Rechtien
The University of Missouri at Rolla
Rolla, Missouri

R.F. Ballard
U.S. Army Corps of Engineers
Vicksburg, Mississippi

ABSTRACT

Velocity and amplitude tomograms are presented for two 2 m diameter tunnels. Delay time anomalies associated with 2 m diameter tunnels are less than 0.1 ms, depending on transmitter-tunnel-receiver distances. These time delays are manifested in tomograms as slowness variations on the order of 10 to 15%. Amplitude anomalies associated with the tunnel are on the order of -12 dB, depending on transmitter-tunnel-receiver distances.

For host environments with gentle velocity variations the tunnel is evident in velocity tomograms for transmitter-receiver distances of 25 m. Whereas amplitude tomograms, even in host environments with strong velocity variations, are evident to much larger separations and at wide angular variations of the vertical acquisition plane relative to the tunnel axis.

INTRODUCTION

During the spring and summer of 1990 extensive cross-borehole seismic studies were conducted over two known tunnels within the demilitarized zone separating North and South Korea. At the time of these studies definitive cross-borehole tunnel diffraction data for small diameter tunnels was, essentially, non-existent, or at least unknown in the literature. In addition, high-frequency borehole sources and borehole acquisition systems were in process of being developed. One such system, referred to as the Borehole Imaging and Tomographic System (BITS), was developed jointly by the Waterways Experiment Station (WES) and the University of Missouri for the specific purpose of tunnel detection. This work was sponsored by the Combat Engineering Directorate, U.S. Army Belvoir Research, Development, and Engineering Center.

The studies conducted in Korea, therefore, had two objectives. The primary objective was the acquisition of an extensive suite of definitive tunnel diffraction data, from which application limitations and/or detection system requirements could be obtained. The secondary objective was the evaluation of BITS relative to target resolution. This paper presents some of the results of these studies.

FIELD STUDY

BITS System Description

The seismic energy source used during data acquisition was an electric-arc discharge device. Construction and performance aspects of this instrument, as well as a functional description of the data acquisition system, are given by Rechten et al. (1993). The dominant frequency of the primary waveform generated by this device is in the neighborhood of 1.5 kHz, depending on borehole coupling and source-receiver distance, with a half-power bandwidth exceeding 1 kHz. The seismic field was sensed with wide-band hydrophones having 32 dB downhole preamplifiers. Received signals were passed through high-pass filters set at 1 kHz (-3 dB point, -25 dB per octave) and anti-alias, low-pass filters set at 7 kHz (-0.1 dB point, -94 dB per octave). These data were digitized with a 16-bit A/D converter at a sample interval of 10 μ s.

Data Acquisition Procedure

In all cases reported here source and receiver boreholes were chosen such that the tunnel under investigation was located at depth somewhere in between. Data acquisition would begin by lowering the transmitter and receiver within their respective boreholes to a depth well below the tunnel. After reception of the signal from the transmitter, each instrument was raised 0.2 m in their respective boreholes. This data acquisition cycle was repeated until both source and receiver were at a depth well above the tunnel, resulting in a seismic section.

Seven seismic sections were obtained for each borehole pair. These sections differed by the vertical angle of illumination of the target. This angle was set for each section gather by offsetting the source starting depth relative to the receiver starting depth. These offsets were chosen to achieve illumination angles of -45, -30, -15, 0, +15, +30, and +45 degrees.

Geologic Settings

The tunnels selected for investigation are commonly referred to as Tunnel #2 and Tunnel #3.

Tunnel #2 is located in rugged, mountainous terrain which has about 250 m of relief. The site and surrounding 2 km area is on an exposed pluton, the composition of which ranges from granodiorite to granite. A man-made tunnel penetrates the pluton approximately 81 m beneath the ground surface. This tunnel, which is accessible for visual examination, is fenced on either side by a series of boreholes that provide unique opportunities for experimental investigations.

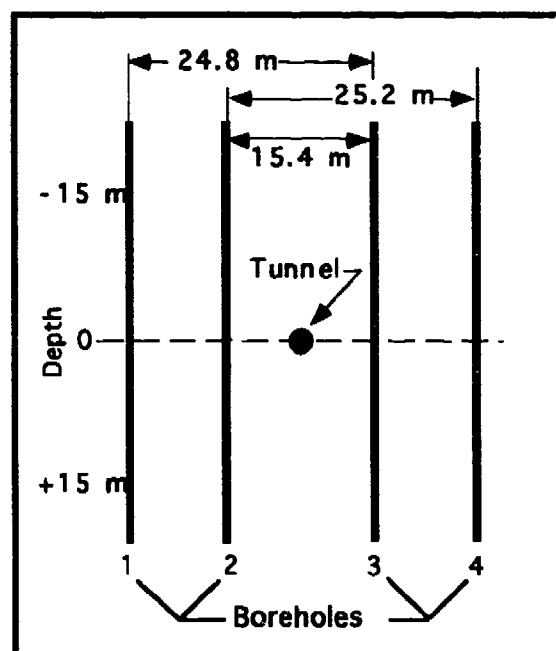


Figure 1. Tunnel #3 Test Configuration

Tunnel #3 is located beneath a region with moderate surface relief. At the location of the

test site the tunnel penetrates granite approximately 70 m beneath the ground surface. This tunnel is also accessible for visual examination.

Geometry of Survey

The test configuration employed at Tunnel #3 is shown in Figure 1. Four boreholes, two on either side of tunnel, were used for data acquisition. The set of four boreholes defined a plane perpendicular to the axis of the tunnel. The relative horizontal separations of these boreholes are given in this figure.

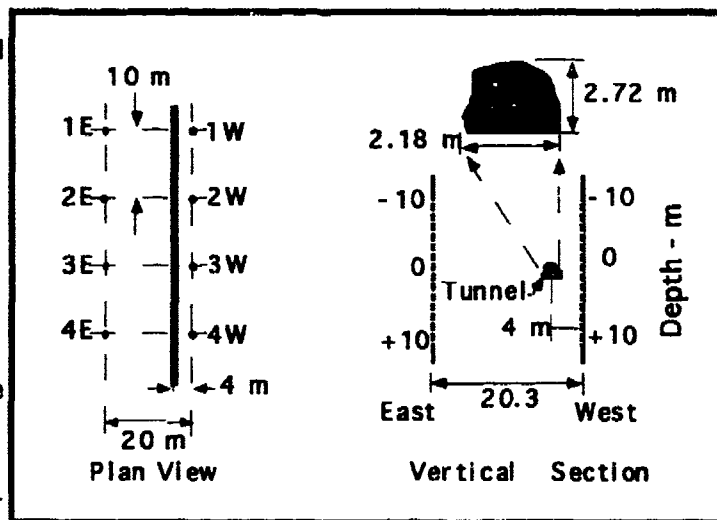


Figure 2. Tunnel #2 Test Configuration

The general test configuration employed at Tunnel #2 is shown in Figure 2. In plan view, the borehole pattern formed a fence on either side of the tunnel. The eastern set of boreholes was approximately 16 m from the tunnel, while the western set was approximately 4 m from the tunnel. In the north-south direction the boreholes were separated approximately 10 m.

A typical vertical section is also given in this figure. The center of the tunnel was located approximately 4 m to the east of the receiver borehole. The geometric shape of the tunnel, which at any given position was determined to a large degree by existing joint patterns, is illustrated. The tunnel was approximately 2.7 m in width and 2.2 m in height.

Acquired data

A typical zero vertical offset (0 degree illumination angle) seismic section obtained at Tunnel #3 is shown in Figure 3. These data are presented in an amplitude normalized format; the amplitude of each trace was normalized to the amplitude value of the first positive peak. Amplitude variation of first arrivals is illustrated in Figure 3 as attenuation in dB relative to the maximum value of the data set comprised of first positive peak amplitudes. These data were acquired with the transmitter in Borehole #2 and the receiver in Borehole #3. Using the first arrival times and attenuation of this data section, along with

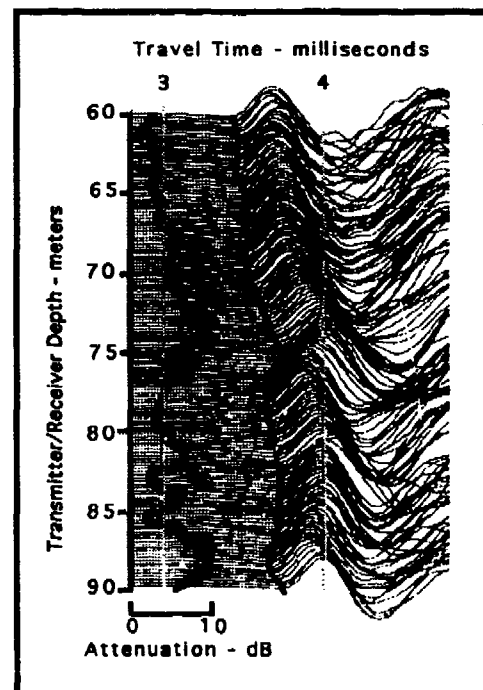


Figure 3. Zero-vertical offset data.

corresponding values from the other 6 sections for non-zero illumination angles, time and amplitude tomograms were generated for this borehole pair. The tomographic algorithm used was a modified version of BOMTOM produced by Tweeton (1988). BOMTOM uses the simultaneous iterative reconstruction technique (SIRT) employing straight ray paths. Consequently, time delays associated with extended travel paths around the tunnel are manifested within the tomogram as regions of slow velocity with values just slightly less than the host background velocity. Attenuation tomograms, similarly, manifest regions of absorption within the rock in near proximity to the tunnel boundary. Thus velocity and attenuation anomalies are not really associated with transport of energy through the tunnel proper.

In Figure 4 we present Tunnel #3 velocity and amplitude tomograms for the borehole pair (2,3). The transmitter (T) is located in Borehole 2 and the receiver (R) in Borehole 3.

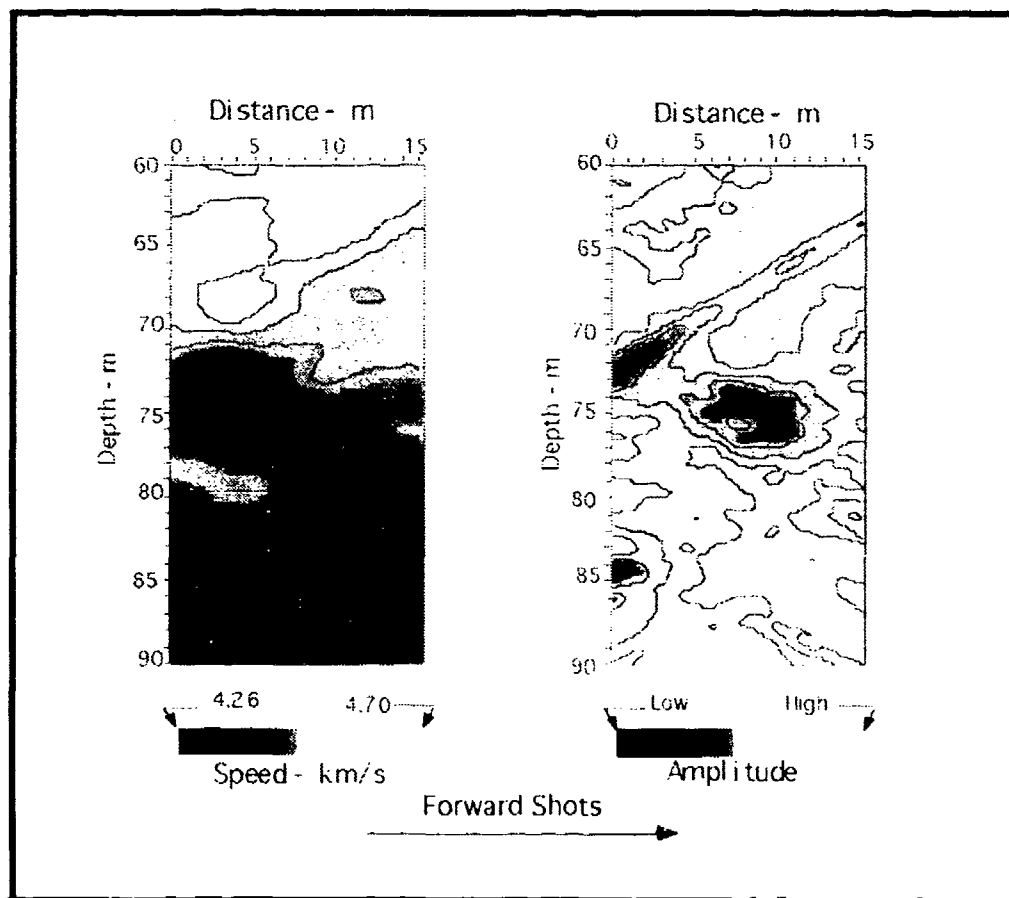


Figure 4. Velocity and amplitude tomogram for borehole pair (2,3)

In this figure the tunnel is manifested in the velocity tomogram as a low velocity zone at 4.26 km/s at a depth of 75 meters. The amplitude tomogram, on the other hand, shows a high attenuation zone above and to the right of the tunnel. This attenuation zone is probably a manifestation of the stress relief around the tunnel roof.

By interchange of the instruments within the two boreholes, we test the assumption of reciprocity. In Figure 5 we present velocity tomograms for forward and reverse shot patterns in Boreholes 2 and 3. In Figure 6 we also present amplitude tomograms to further examine the question of reciprocity.

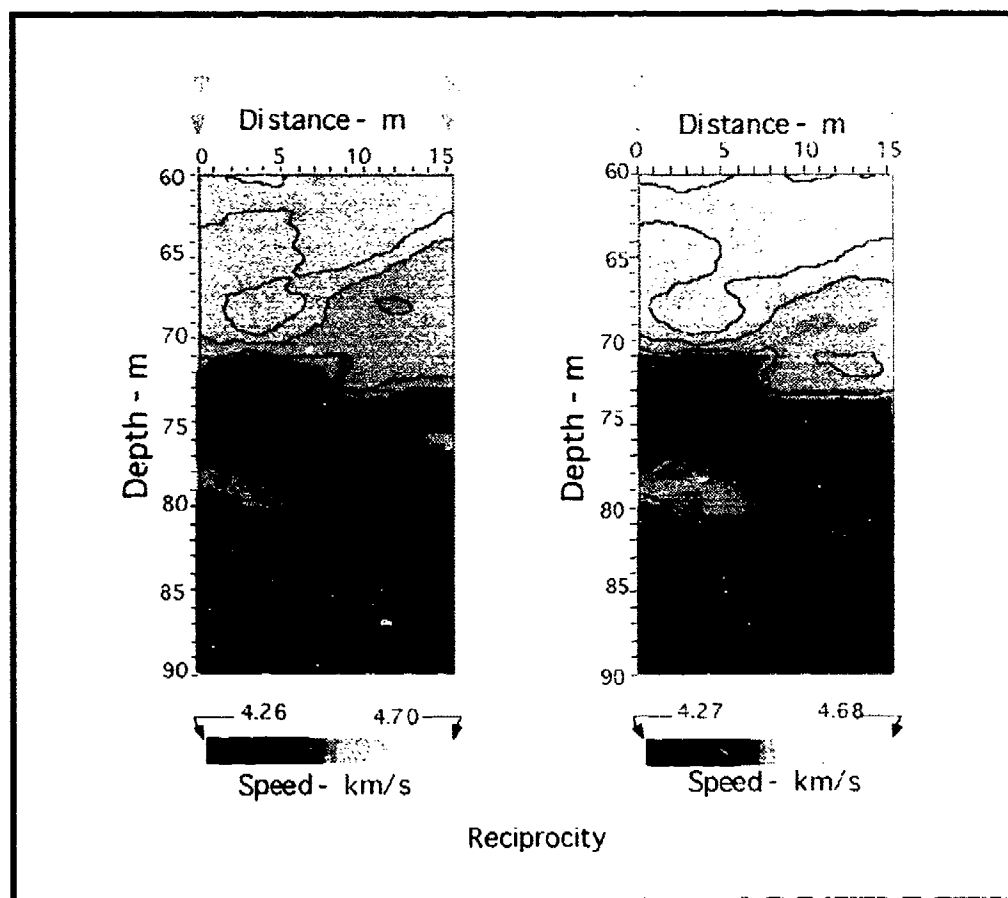


Figure 5. Travel time reciprocity.

In reference to Figure 5, the forward and reverse tomograms are remarkably similar, thus verifying the concept of travel time reciprocity. Note the velocity variation throughout the entire section is at most 440 mps. Relative to the background average of 4.48 km/s, the maximum velocity variation is only about 10%. This maximum variation is associated with delay paths around the tunnel.

In reference to the amplitude tomograms of Figure 6, the attenuation zones coincident with the stress relief/fracture halo about the tunnel are fairly well replicated. The tomograms show, however, that source coupling at certain weak, or soft, points of the borehole wall create attenuation anomalies in the near vicinity of the borehole that are not reciprocated. Such zones can be seen in the vicinity of the transmitter borehole at 83 m in the left tomogram and at 73 and 85 m in the right tomogram.

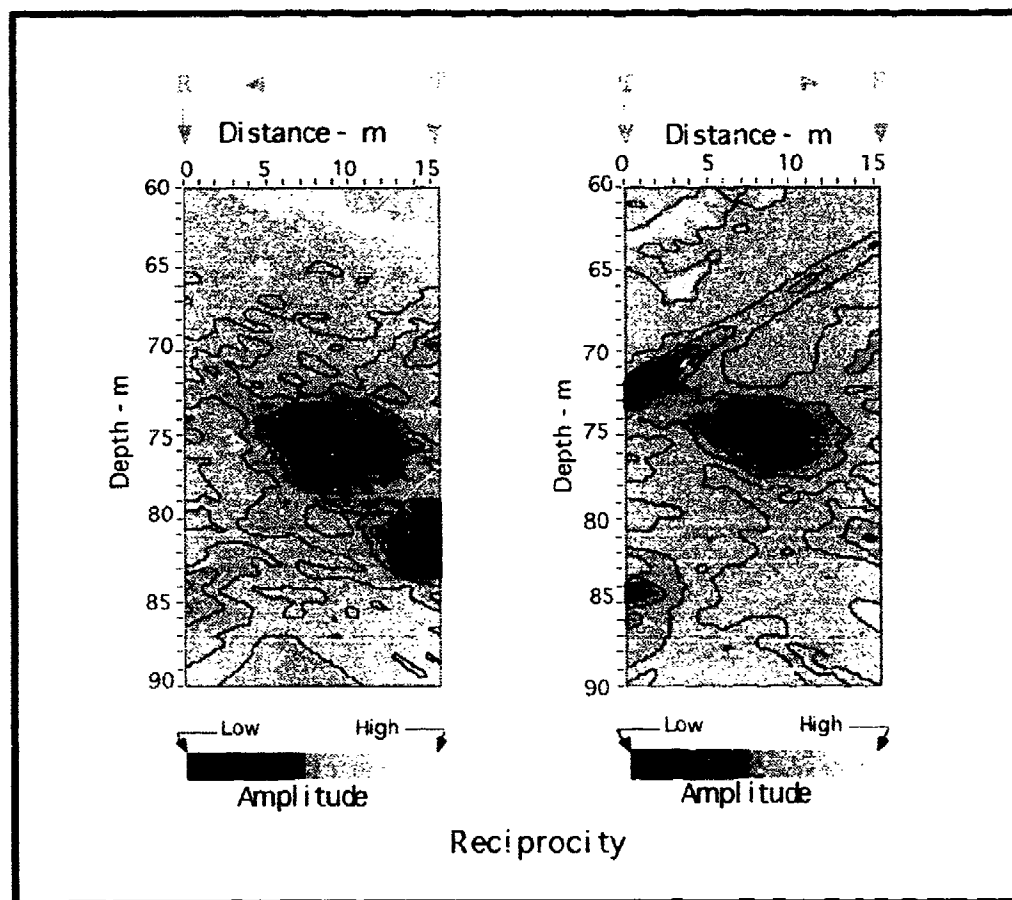


Figure 6. Amplitude reciprocity

Figures 7 and 8 show, respectively, the velocity and amplitude tomograms for different borehole separations. In each of these figures the transmitter (T) was located within Borehole 3, while one receiver (R) was in Borehole 1 and the other in Borehole 2. The data for these two tomographic panels was acquired simultaneously. The panels themselves overlap; the right panel occupies the same space as the right three-fifths of the left panel.

Both velocity tomographs in Figure 7 show the low velocity zones due to the presence of the tunnel. One can notice in the bottom left hand corner of the left tomogram a 45 degree region of low velocity. This region had been introduced into the image because of inadequate coverage of one of the 45 degree illumination section sweeps. The presence of this low velocity zone in the tomogram severely distorts the colorbar, or shade bar, and manipulation of shading was performed to render the two images color, or shade, compatible. The velocity variations due to the tunnel for the larger borehole separation is significantly smaller than for the shorter distance.

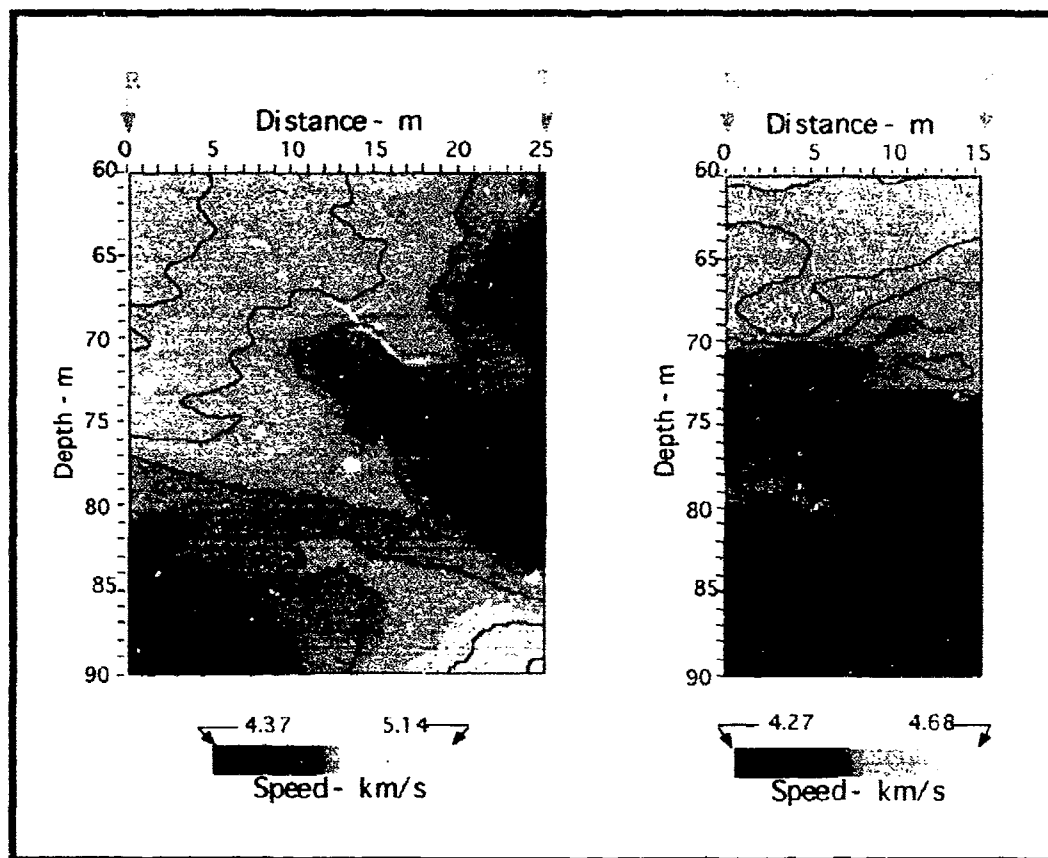


Figure 7. Velocity tomograms. Transmitter in Borehole 3; receivers in Boreholes 1 and 2.

In the amplitude tomograms of Figure 8 we have excellent agreement of the high attenuation zones due both to the presence of the tunnel and the near borehole environment. The result of inadequate coverage in the 45 degree illumination run is also reflected in the left tomogram as a tight closed contour oriented at 45 degrees.

At Tunnel # 3 eight tomographic data sets, corresponding to combinations of the 4 boreholes illustrated in Figure 1, were acquired. The limited results that we have presented in this paper is typical of the total body of data acquired at this site. The velocity structure of the host medium was relatively uniform, and travel time tunnel anomalies were generally evident in the raw field records. In general, reciprocity of tunnel anomalies was excellent; amplitude tunnel anomalies accurately tracked over the entire range of borehole separation distances; and velocity anomalies indicative of the tunnel were clearly observed at borehole separations of 25 m. However, the velocity anomalies attenuated rapidly with borehole separation distance and the practical limit for time delay tomography, focused on a 2 m target, is probably 20 m. Amplitude tomography for 2 m targets should be useful to much larger borehole separation distances.

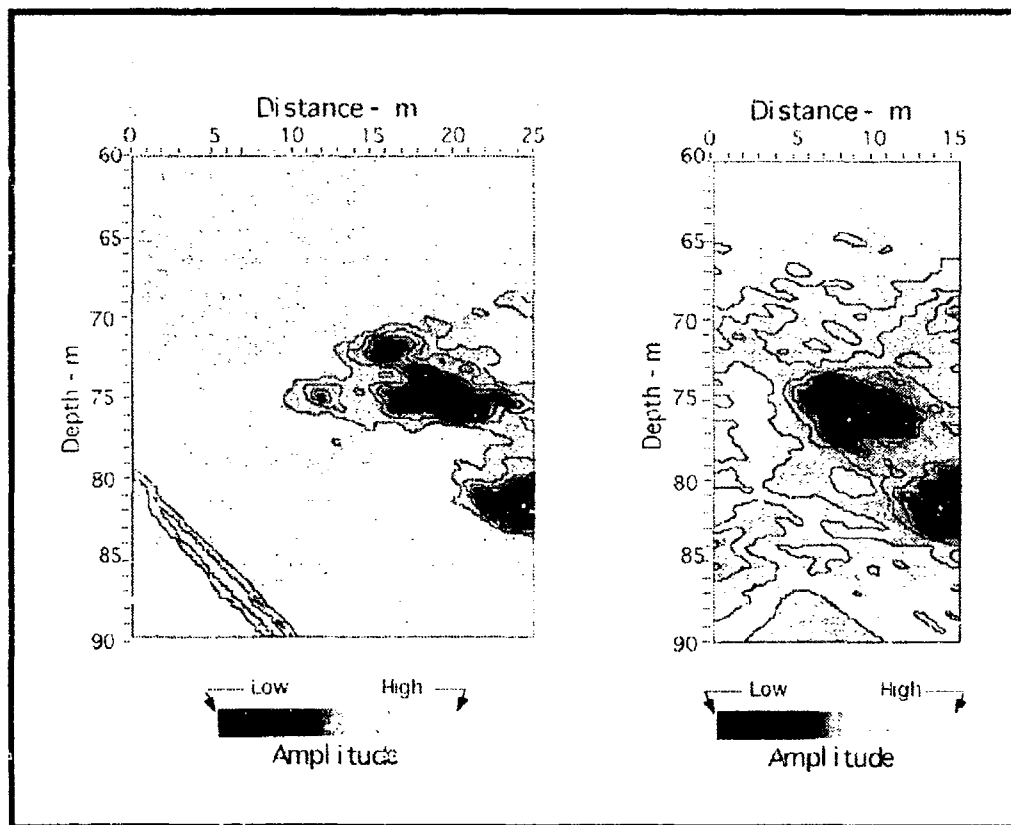


Figure 8. Amplitude tomograms. Transmitter in Borehole 3; receivers in Boreholes 1 and 2.

Turning our attention now to Tunnel #2, we present in Figure 9 velocity and amplitude tomographs for a vertical section (panel) oriented at 90 degrees to the tunnel axis. Referring to Figure 2, the transmitter was located in Borehole 1E and the receiver in Borehole 1W. Due to the limited depth of Borehole 1E the tomogram is also limited in vertical extent to 20 m.

In reference to Figure 9 the tunnel is again manifested in the velocity tomogram on the left as a low speed zone with speed variation of about 10 % of background. The velocity anomaly plots exactly at the known tunnel location. The low amplitude anomaly in the tomogram on the right again centers at a position slightly above the tunnel. In Figure 10 the same amplitude tomogram of Figure 9 is reproduced along with an amplitude tomogram obtained by offsetting the orientation of the vertical plane relative to the tunnel axis. During the acquisition process the

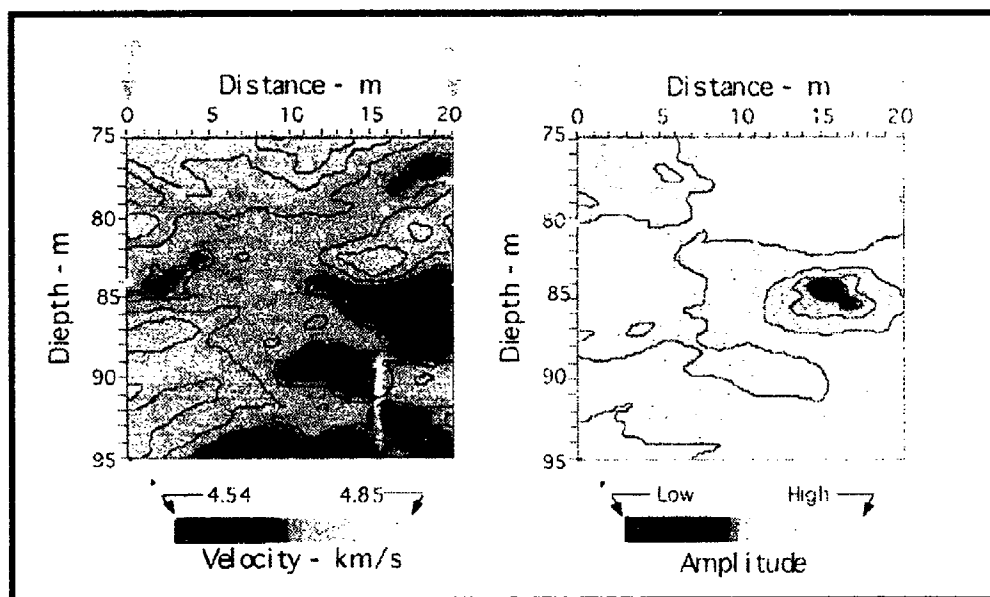


Figure 9. Velocity and amplitude tomographs at Tunnel #2. Vertical section oriented at 90 degrees to tunnel axis.

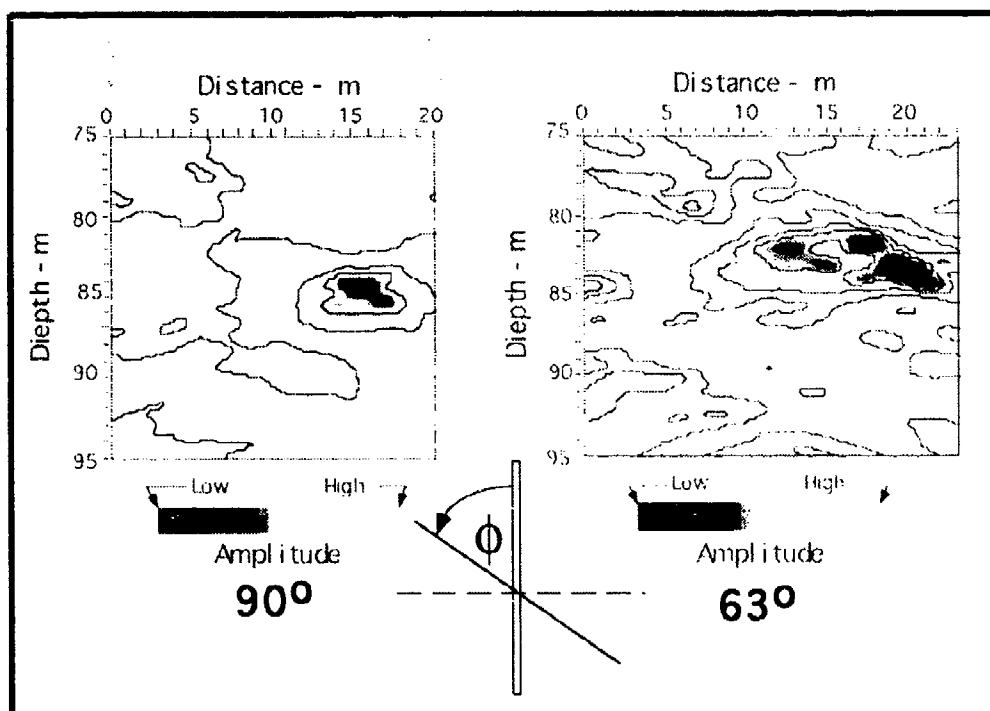


Figure 10. Amplitude tomographs for two angular orientation of the vertical plane relative to the tunnel axis.

transmitter was located in Borehole 1E while the receiver was in Borehole 2W. Thus the vertical plane of energy transmission was oriented at an angle of 63 degrees to the tunnel axis. In this tomogram the amplitude anomaly is again quite strong but appears to be slightly displaced upward relative to the anomaly of the 90 degree panel. Moreover, a second anomaly appears slightly higher and to the left. We must remember, however, that these anomalies are associated with stress relief/fracture zones principally in the roof of the tunnel and can have an infinite variety of shapes.

In general, amplitude tomographs at Tunnel #2 consistently exhibited strong amplitude anomalies for angular orientations of the panel (relative to the axis of the tunnel) ranging from 90 to 33 degrees. Velocity tomographs, however, didn't fair quite so well.

Figure 11 shows a typical zero vertical offset section at a right angle to the tunnel axis. The first arrival time varies 0.8 ms over short vertical distances in the record. Tunnel anomalies are only around .1 ms. Consequently, tunnel anomalies are lost in the section "noise". The section from which the velocity tomogram of Figure 9 was derived was exceptionally uniform relative to velocity variation and resembled the data from Tunnel 3 where good velocity topographic results were obtained. However, the data of Figure 9 represents the only data set in all that was recorded at Tunnel #2 that yielded good tunnel velocity anomalies.

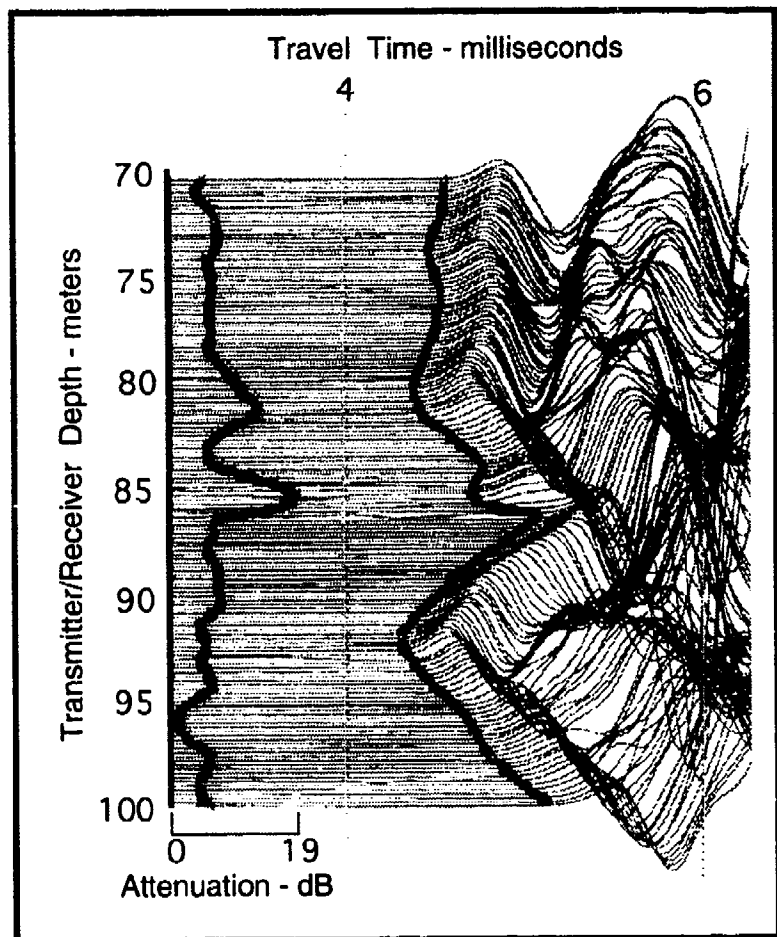


Figure 11. Typical Tunnel #2 Zero-vertical offset section.

Again in reference to Figure 11, although the velocity variations are strong throughout the section, the amplitude, or attenuation, is well behaved. This result was generally true of all the data, resulting in good amplitude tomographic results.

CONCLUSIONS

Tunnel signatures are only evident in raw field records when the host medium is exceptionally uniform in velocity. Otherwise, data must be view through the process of

tomographic reconstruction, or some other imaging process, in order to arrive at conclusions with some level of confidence. The results of this study show that velocity tomograms are only successful if the medium is relatively uniform in speed. Thus one can conclude that if you can see the anomaly in the raw field record than the velocity tomogram will also be successful. One can also conclude that if the tunnel anomaly is not evident in the raw field record then the probability of observing it in the velocity tomogram is small.

Amplitude tunnel anomalies are also not all that evident in raw field records due to the occurrence of other regions of high attenuation in the host medium. These regions can generally be found in the vicinity of the borehole, and the high attenuation results from poor transmitter-borehole coupling. If the tunnel is at some distance from such regions, amplitude tomography will successfully separate overlapping attenuation anomalies in the raw field record to their proper spatial locations in the tomograph. Consequently, amplitude tomography applied to tunnel detection was quite successful in this study.

ACKNOWLEDGMENTS

This research was supported by the USAE Waterways Experiment Station, Vicksburg, MS, and the Physical Security Equipment Division's Geophysics Team headed by Mr. Ray Dennis at the US Army Belvoir Research, Development and Engineering Center, Ft. Belvoir, VA. We also express our appreciation to the US Eighth Army Tunnel Neutralization Team, Seoul, Korea for their technical and logistical support of our extended field activities. Permission was granted by the Chief of Engineers to publish this information. The view of the authors do not purport to reflect the position of the Department of the Army or the Department of Defense.

REFERENCES

- Rechtien, R.D., Hambacker, K.L., and Ballard, Jr., R. F., 1993, "A High-Frequency Sparker Source for the Borehole Environment", Geophysics, Vol. 58, No. 5, May
- Tweeton, D. R., 1988, "A Tomographic Computer Program with Constraints to Improve Reconstructions for Monitoring In Situ Mining Leachate" USBM RI9159, Washington, D.C.

Diffraction Tomographic Signal Processing Algorithms for Tunnel Detection

Alan J. Witten
Oak Ridge National Laboratory
Oak Ridge, TN 37831-6200
Alon Schatzberg and Anthony J. Devaney
A.J. Devaney Associates
355 Boylston Street
Boston, MA 02116

ABSTRACT

Signal processing algorithms have been developed for wave based imaging using diffraction tomography. The basis for this image reconstruction procedure is the *generalized projection slice theorem* (GPST) which, for homogeneous waves, is an analytic relationship between the spatial Fourier transform of the acquired data and the spatial Fourier transform of the spatial profile (object function) of the object being imaged. Imaging within geophysical diffraction tomography when only homogeneous waves are considered can then be accomplished by inversion of the GPST using standard numerical techniques. In an attenuating background medium or when eddy currents or static fields are considered, a generalized GPST can be derived that involves both real and complex spatial frequencies. In this case, direct Fourier inversion is not possible because of the presence of the complex frequencies. Although direct inversion and, hence, complete imaging is not possible for such cases, the generalized GPST's can be used to analytically shift the location of data templates matched to specified targets and these templates can, in turn, be correlated with acquired data to detect and estimate the location of the specified targets. Since GPST's are used directly in the detection problem, there is no need to numerically invert the integral transform of the object function. For this reason, target detection can be accomplished in a computationally efficient manner independent of the type of measurement or background geologic conditions. A number of GPST's are derived and the use of GPST's for both imaging and detection of subsurface voids is demonstrated in several recent applications.

INTRODUCTION

The capability to image or detect subsurface voids is important in problems concerning abandoned mine safety, the environmental and geotechnical impacts of karst, archaeological exploration, and determination of the existence and location of tunnels. The tunnel detection problem has applications in national defense as well as in counter narcotics and counter terrorism. One signal processing algorithm that has been applied to the imaging of tunnels is geophysical diffraction tomography (GDT) (Devaney, 1984). GDT is a generalization of the more commonly used straight ray tomographic methods to the longer wave lengths employed in geophysical investigations. In GDT, the wave equation is used to *backpropagate* the data and thereby map the spatial variations in wave speed. In a more recent development, GDT has been combined with a statistical estimator, maximum likelihood estimation, to address the specific problem of target detection and location estimation. These types of signal processing algorithms have become known as diffraction tomographic maximum likelihood estimators (DTMLE) (Devaney and Tsihrintzis, 1991). GDT and DTMLE have been applied to cross borehole radar data collected in the Korean DMZ to both image and detect tunnels (Witten, 1991).

This paper provides an overview of the theory of GDT and DTMLE as it applies to scalar waves and fields in monostatic and bistatic measurement geometries. Also presented are excerpts from several case studies in which GDT (DTMLE) signal processing algorithms have been applied to subsurface void imaging (detection). At a site in Israel's northern Negev desert, images were reconstructed of a system of subterranean rooms and connecting tunnels inhabited by a stone age civilization. Results are also provided that demonstrate the application of a DTMLE algorithm that considers orthogonally polarized radar waves to exploit the high aspect ratio of tunnels. This algorithm also considers evanescent wave modes to increase the spatial resolution. It is shown here that, by the application of this algorithm to ground penetrating radar data acquired over a known shallow tunnel, evanescent waves can be used to obtain sufficient resolution to detect the tunnel at frequencies so low that tunnel detection could not be accomplished otherwise.

THE UNIFIED FORWARD FORMULATION

In this section, the forward problem is considered with the goal being the development of a family of relationships that can serve as the basis for imaging and detection of buried features. For the geophysical tools considered here, the measured quantity, ϕ , is governed by the general partial differential equation

$$\nabla \cdot [A \nabla \phi] - B \frac{\partial \phi}{\partial t} - C \frac{\partial^2 \phi}{\partial t^2} = f(\mathbf{x}, t), \quad (1)$$

where the time independent coefficients A , B , and C are defined, by tool, in Table 1; and f is a spatially and temporally varying source. For simplicity, this governing equation is

Technique	A	B	C	O(x)
waves (seismic, radar)	1	0	$(1 - O(x))/c_0^2$	$1 - (c_0^2/c^2(x))$
EMI	$(1 - O(x))/\sigma_0$	μ_0	0	$1 - (\sigma_0/\sigma(x))$
resistivity	$(1 - O(x))/\sigma_0$	0	0	$1 - (\sigma_0/\sigma(x))$
magnetometry	$\mu_0(1 - O(x))$	0	0	$-\mu_0/\mu(x)$

Table 1: Definition of the coefficients in the governing equation.

taken to be scalar and two dimensional (a vertical cross-section). The generalization to three dimensions and for a vector governing equation is straight forward but beyond the scope of this paper. The material properties used in Table 1 are defined as follows: c is the wave speed (seismic or electromagnetic), σ is the conductivity, and μ is the magnetic permeability. In all cases, the x argument implies that this quantity is spatially variable and the subscript zero denotes a constant background value. In the case of waves, $c(x)$ is an absolute wave speed while, for the conductivity and permeability $\sigma(x)$ and $\mu(x)$ are taken to be perturbations about their respective background values.

For the transient methods, waves and electromagnetic induction (EMI), it will be more convenient to consider the forward problem in the frequency, ω , domain rather than the time domain. For this reason, the temporal Fourier transform

$$\tilde{\phi} = \begin{cases} \int dt e^{i\omega t} \phi & \text{for waves and EMI} \\ \phi & \text{for resistivity and magnetometry} \end{cases} \quad (2)$$

is introduced and the total measured quantity is taken to be the superposition of the unperturbed quantity, ϕ_0 , associated with $O(x) = 0$ and a scattered quantity, ϕ_s , associated with $O(x) \neq 0$. We refer to $O(x)$ as the "object function." This quantity is defined in terms of the material parameters in Table 1. Taking ϕ_s and $O(x)$ to both be small and of the same magnitude, performing a temporal Fourier transform, and linearizing Eq. (1) yields the two governing equations

$$\nabla^2 \tilde{\phi}_0 + k^2 \tilde{\phi}_0 = \tilde{f}(x, \omega) \quad (3)$$

and

$$\nabla^2 \tilde{\phi}_s + k^2 \tilde{\phi}_s = \begin{cases} k^2 O(x) \tilde{\phi}_0 & \text{for waves, where } k = \frac{\omega^2}{c_0^2} \\ \nabla \cdot [O(x) \nabla \tilde{\phi}_0] & \text{for EMI, where } k^2 = -i\mu_0 \sigma_0 \omega \\ \nabla \cdot [O(x) \nabla \tilde{\phi}_0] & \text{for resistivity and magnetometry, where } k = 0, \end{cases} \quad (4)$$

where f is the source function. The final form of the non-measurement configuration specific forward formulation is obtained by rewriting Eq. (4) in the integral equation form

$$\tilde{\phi}_s(\mathbf{r}) = -\frac{1}{4\pi} \int d\xi G(\mathbf{r} - \xi) \begin{cases} k^2 O(\xi) \tilde{\phi}_0 & \text{for waves} \\ \nabla \cdot [O(\xi) \nabla \tilde{\phi}_0] & \text{for EMI, resistivity, and magnetometry,} \end{cases} \quad (5)$$

where G is the Green's function for the scalar Helmholtz equation.

The remainder of the derivation is specific to the measurement configuration employed. The forward problem is considered for two commonly utilized measurement geometries in subsequent subsections.

The Bistatic Geometry

The bistatic geometry, as defined here, is a measurement system in which sources and receivers are independently positioned at a uniform spacing along lines having arbitrary orientations with respect to some reference coordinate system (Fig. 1). The source and receiver lines are defined by their outward normal unit vectors \mathbf{n} and \mathbf{m} , respectively. The

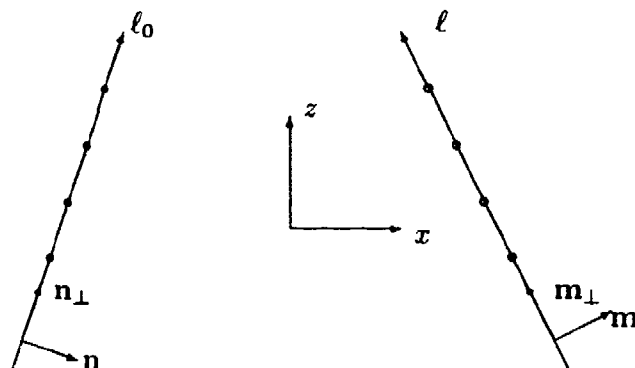


Figure 1: Illustration of the bistatic measurement geometry. The sources are indicated by •'s and the receivers are indicated by o's.

unit vectors \mathbf{n} and \mathbf{m} define an arbitrary bistatic geometry. For the case of cross-hole measurements, $\mathbf{n} = \mathbf{m} = (1, 0)$; for offset vertical seismic profiling (VSP), $\mathbf{n} = (0, -1)$ and $\mathbf{m} = (1, 0)$; and for a surface reflection geometry, $\mathbf{m} = -\mathbf{n} = (0, 1)$.

The final form of the forward bistatic relationship is obtained by introducing the Weyl expansions for the incident wave (field), $\hat{\phi}_0$, assuming sources distributed along a line \mathbf{r}_0 with outward normal \mathbf{n}

$$\hat{\phi}_0(\boldsymbol{\xi}) = \frac{i}{4\pi} \int \frac{d\alpha_0}{\sqrt{k^2 - \alpha_0^2}} \hat{f}(\alpha_0, \omega) e^{i(\sqrt{k^2 - \alpha_0^2} \mathbf{n} + \alpha_0 \mathbf{n}_\perp) \cdot (\boldsymbol{\xi} - \mathbf{r}_0)}, \quad (6)$$

where \hat{f} is the spatial Fourier transform of f and for the Green's function based on receivers

deployed along a line with outward normal \mathbf{m}^1

$$G(\mathbf{r}) = i \int \frac{d\alpha}{\sqrt{k^2 - \alpha^2}} e^{i(\sqrt{k^2 - \alpha^2} \mathbf{m} + \alpha \mathbf{m}_\perp) \cdot \mathbf{r}} \quad (7)$$

Substituting Eqs. (6) and (7) into Eq. (5), defining the reduced data $\hat{\phi}_s$ to be $\tilde{\phi}_s$ Fourier transformed with respect to source $\ell_0 = \mathbf{n}_\perp \cdot \mathbf{r}_0$ and receiver $\ell = \mathbf{m}_\perp \cdot \mathbf{r}$ locations

$$\hat{\phi}_s(\kappa, \kappa_0) = \int d\ell \int d\ell_0 e^{-i(\kappa\ell - \kappa_0\ell_0)} \tilde{\phi}_s \quad (8)$$

and applying this integral transform to Eq. (5) yields

$$\hat{\phi}_s(\kappa, \kappa_0) = \frac{\pi \hat{f}}{\gamma \gamma_0} e^{i(\gamma \mathbf{m} \cdot \mathbf{r} - \gamma_0 \mathbf{n} \cdot \mathbf{r}_0)} \int d\xi e^{-i\mathbf{K} \cdot \xi} \begin{cases} k^2 O(\xi) & \text{for waves} \\ -[k^2 + \mathbf{K} \cdot \mathbf{K}_0] O(\xi) & \text{for EMI, resistivity} \\ & \text{and magnetometry,} \end{cases} \quad (9)$$

where

$$\mathbf{K} = \gamma \mathbf{m} + \kappa \mathbf{m}_\perp - \gamma_0 \mathbf{n} - \kappa_0 \mathbf{n}_\perp, \quad (10)$$

$$\mathbf{K}_0 = \gamma_0 \mathbf{n} + \kappa_0 \mathbf{n}_\perp, \quad (11)$$

$\gamma = \sqrt{k^2 - \kappa^2}$, and $\gamma_0 = \sqrt{k^2 - \kappa_0^2}$. It should be noted that Eq. (9) is appropriate for waves, EMI, and resistivity. For magnetometry, however, the bistatic geometry applies only to the receiver position. A modified definition of Eq. (8) is needed where this integral transform is with respect to ℓ only and similar modifications to \mathbf{K} and \mathbf{K}_0 are also needed where $\mathbf{K} = \gamma \mathbf{m} + \kappa \mathbf{m}_\perp$ and $\mathbf{K}_0 = \nabla \tilde{\phi}_0 = \mathbf{B}_0$ where \mathbf{B}_0 is a vector defining the local magnitude and direction of the earth's magnetic field. The final modifications needed for the magnetometry interpretation of Eq. (9) is that γ_0 is taken to be zero in the exponential term and $1/2\pi$ in the denominator.

Eq. (9) represents the desired result for the forward formulation relating the reduced data to an integral transform of the object function $O(\mathbf{x})$. This form is quite similar to the *generalized projection slice theorem* (GPST) that serves as the basis for diffraction tomography (DT). It should be noted, however, that in the traditional DT concept, the GPST was based on a spatial Fourier transform of O . In the general relationship presented in Eq. (9), this integral transform is only Fourier in the case of homogeneous waves $|\kappa|, |\kappa_0| \leq k$.

The Monostatic Geometry

In this study, a monostatic geometry is defined to be a coincident source/receiver pair moved in unison along the ground surface $\mathbf{r} = (\ell, 0)$ with the support of O lying in the half-plane $z \leq 0$. This geometry is typical of ground penetrating radar (GPR) and some

¹A receiver aperture comparable to the source aperture \hat{f} in Eq. (6) can be introduced into the Green's function. For simplicity, this aperture function has been taken as unity (point receivers) here.

forms of EMI where the two coils are sufficiently close together to be considered coincident. The main difficulty in dealing with this geometry is that the unperturbed wave or field is represented by $G(\xi - \mathbf{r})$ and the Green's function for the Helmholtz equation is represented by $G(\mathbf{r} - \xi)$ so that the integral transform defined by Eq. (8) can no longer be used to deconvolve the double Weyl expansion produced by the product $G(\mathbf{r} - \xi)G(\mathbf{x} - \mathbf{r}) = G^2(\mathbf{r} - \xi)$. For this reason, the approach used for a bistatic geometry cannot be used in a monostatic geometry and it becomes necessary to seek a Weyl expansion of G^2 .

Unfortunately, an exact expansion for G^2 has not been found; however, if the target depth is at least $|z_0|$ such that $k|z_0|$ is greater than one, an approximate Weyl expansion can be derived by performing the integration over α or α_0 by stationary phase. This leaves only a single integral in the expansion of G^2 that can be eliminated by Fourier transforming with respect to ℓ . This yields the monostatic form of the GPST

$$\hat{\psi}_s(\kappa) = \frac{ike^{i\pi/4}}{4\sqrt{2\pi}\gamma} \int d\xi \frac{O(\xi)}{\sqrt{|\eta|}} e^{-i(\kappa\xi + \gamma\eta)}, \quad (12)$$

where $\gamma = \sqrt{4k^2 - \kappa^2}$ and $\xi = (\xi, \eta)$. It is obvious that Eq. (12) is valid for radar applications provided that the ratio of target depth to wave length is at least unity. For EMI, however, the wave lengths used are typically huge compared to the depths of interest. Therefore, Eq. (12) is unsuitable for EMI.

IMAGING AND DETECTION

The relationships developed in the previous sections, subsequently referred to as GPST's, can serve as the basis for imaging and detection of subsurface features. As discussed in the subsequent subsection, these GPST's are not directly applicable to imaging with all tools considered, however, they can be used for all tools in the detection problem.

Imaging

For homogeneous waves, Eqs. (9) and (12) relate a quantity that can be extracted from measurements, $\hat{\phi}_s$, to a two-dimensional Fourier transform of O . It is, therefore, straight forward to reconstruct images of O by inverting the indicated Fourier transform.

In the bistatic geometry, \mathbf{K} is commonly considered to be a function of θ and κ , where it is recognized that the mapping of ℓ_0 into κ_0 is a synthetic aperture step simulating plane wave view angles θ such that $\mathbf{K}_0 = k \cos \theta \mathbf{n} + k \sin \theta \mathbf{n}_\perp$. The two-dimensional integration over \mathbf{K} can be cast as a sum over view angles θ and an integration over κ .

In the monostatic geometry, there is only the single parameter κ so that here it is necessary to exploit source bandwidth and express \mathbf{K} as a function of ω , where $\omega = c_0 k$. The Fourier inversion of Eq. (12) is then implemented as an integration over κ and a sum over frequencies.

The application of this imaging procedure is limited to cases where \mathbf{K} is real and the integral transform given by the GPST's is a multi-dimensional Fourier transform. Only in such cases (homogeneous waves) can this transform be inverted by standard numerical techniques.

Detection

The detection of a known target can be formulated based on the cost function

$$F_c(\mathbf{x}_0) = \int d\ell |\tilde{\phi}_s(\ell) - \tilde{\phi}'_s(\ell; \mathbf{x}_0)|^2, \quad (13)$$

where $\tilde{\phi}'_s$ is the data model for the known target centered at \mathbf{x}_0 . Although shown as only an integration over ℓ , Eq. (13) can also be integrated over ℓ_0 or summed over ω , as appropriate, and the most probable target location is taken to be the \mathbf{x}_0 that minimizes F_c over all data.

Although Eq. (13) can be used directly for target detection and location estimation, it has computational and storage requirements, associated with the need to compute the "data templates" $\tilde{\phi}'_s$, that could be prohibitive. An alternative procedure, referred to as diffraction tomography maximum likelihood estimation (DTMLE), is given here that eliminates the need to generate a large number of data templates. The DTMLE algorithm is implemented in the wave number, κ , domain rather than the space domain, ℓ , and Parseval's Theorem is used to express the integration over ℓ in Eq. (13) as an integration over κ of the Fourier transforms of the functions under the integral. This gives

$$F_c(\mathbf{x}_0) = \int d\kappa [\hat{\phi}_s \hat{\phi}_s^* - 2\hat{\phi}_s \hat{\phi}'_s{}^* + \hat{\phi}'_s \hat{\phi}'_s{}^*], \quad (14)$$

where the square in Eq. (13) has been expanded and the superscripted asterisk denotes complex conjugation. The $\hat{\phi}_s \hat{\phi}_s^*$ term is the square of the data which is independent of \mathbf{x}_0 , the postulated target location, and a constant after integration. Therefore, this term is neglected. The GPST's, Eqs. (9) and (13), can be used to represent $\hat{\phi}'_s$ and $\hat{\phi}'_s{}^*$ where the shift rule for Fourier transforms can be used to represent O centered at \mathbf{x}_0 in terms of O centered at some reference location, O_0 ,

$$\hat{O}(\mathbf{K}; \mathbf{x}_0) = \hat{O}_0(\mathbf{K}) e^{-i\mathbf{K} \cdot \mathbf{x}_0}, \quad (15)$$

where the reference location here is taken to be the origin. Introducing these changes into Eq. (14) and changing signs yields

$$F_L(\mathbf{x}_0) = \int d\kappa [2K \hat{\phi}_s \hat{O}_0^* e^{-i\mathbf{K} \cdot \mathbf{x}_0} - K K^* \hat{O}_0 \hat{O}_0^* e^{-i(\mathbf{K} + \mathbf{K}^*) \cdot \mathbf{x}_0}], \quad (16)$$

where F_L is referred to as the ambiguity function or, in the case of noisy data, the log

likelihood function,

$$K = \begin{cases} \frac{\pi f}{\gamma \gamma_0} e^{i(\gamma \mathbf{m} \cdot \mathbf{r} - \gamma_0 \mathbf{n} \cdot \mathbf{r}_0)} k^2 & \text{for bistatic waves} \\ -\frac{\pi f}{\gamma \gamma_0} e^{i(\gamma \mathbf{m} \cdot \mathbf{r} - \gamma_0 \mathbf{n} \cdot \mathbf{r}_0)} [k^2 + \mathbf{K} \cdot \mathbf{K}_0] & \text{for bistatic EMI, resistivity, and magnetometry} \\ i k e^{i\pi/4} / 4 \sqrt{2\pi\gamma|\eta|} & \text{for the monostatic geometry,} \end{cases} \quad (17)$$

and, by virtue of the introduced sign change, the most probable target location is the \mathbf{x}_0 that maximizes F_L . Although not explicitly represented, Eq. (16) can have an outer summation over view angle θ , frequency ω , or both.

Equation (16) achieves the desired result in that it provides a mechanism for target detection requiring the specification of only a single data template O_0 . This template represents target characteristics including shape, orientation, and material properties at a single reference location. Templates associated with all other possible locations \mathbf{x}_0 are analytically incorporated by the phase shift $\exp(-i\mathbf{K} \cdot \mathbf{x}_0)$. The first term on the right hand side of Eq. (16) is the correlation of the data with the data template while the second term is an energy correction that, in the case of \mathbf{K} real, is independent of \mathbf{x}_0 .

Equation (16) can be considered a parameter estimation problem where the two- (or, alternatively, three-) dimensional parameter space \mathbf{x}_0 is searched for the specific \mathbf{x}_0 that maximizes F_L . This procedure can be extended to a parameter space of higher dimensionality where additional parameters O_0^i , representing different targets or a single target of different orientations, are introduced and this space of additional parameters is searched to estimate target characteristics as well as target location.

Several concluding comments are in order concerning the DTMLE algorithm. First, since it employs *a priori* information (the specification of the target characteristics), less information is needed for detecting than for imaging. This allows its implementation with less acquired data and, specifically, it can be applied to magnetometry data where imaging is precluded since information can only be obtained for a single view and frequency. Furthermore, the DTMLE algorithm exploits the forward integral transform defined in the GPST's and, consequently, can be applied to all geophysical tools.

RESULTS

The results of the application of the imaging and detecting algorithms described above are presented in this section. In all examples, "images" are over vertical cross-sections. For the imaging applications, the quantity displayed is a physical one, O , while for the detection applications this quantity is a statistical one, the log likelihood function F_L . All images are presented as gray scales, with darker shades of gray associated with increasing values of O or F_L . The interpretation of these images are that, for imaging applications, darker gray scales correspond to increasing values of wave speed. For the detection applications, darker shades of gray correspond to increasing probability that the specified target occurs at a particular location.

Figure 2 is an image derived from offset vertical seismic profiling measurements made at a prehistoric archaeological site in Israel. This example is of particular relevance to

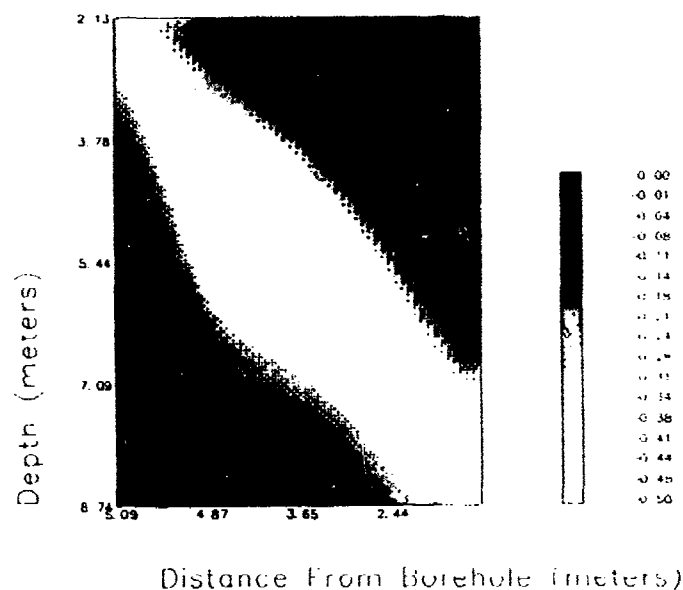


Figure 2: Image of a vertical cross-section through a prehistoric room and tunnel complex.

tunnel detection since the targets of interest here are sequences of subterranean rooms and connecting tunnels that were inhabited about 6,500 years ago. Figure 2 shows one example of the spatial variations of O obtained over one of many vertical cross-sections through a suspect complex. It is important to note that these targets do not consist of voids, but rather, are completely filled with unconsolidated material as a result of the actions of depositional forces over the six millennium since their abandonment. These features are characterized by lower sound speeds (negative O) than background, therefore, a plotting contrast emphasizing negative values of O is used. A room is evident in the center of this image with a tunnel, presumably leading to another room beyond the imaged region, extending diagonally downward and to the right away from the room. The background sound speed in the host soil at this site is about 500 meters per second and the reconstructed sound speed within the room-tunnel complex is 400 meters per second.

Figure 3 is an image of O over a vertical cross-section reconstructed from 100 MHz. GPR data acquired at a cemetery. These data were acquired using the monostatic measurement geometry. The black and dark gray masses in the upper right of this image are slices through two adjacent coffins. The "ringing" (alternating contrast highs and lows) about these features are associated with phase uncertainty and are attributable to limited antenna bandwidth.

The remainder of the results presented here are for detection applications. Figures 4 and 5 are images of the log likelihood function based on seismic and GPR data, respec-

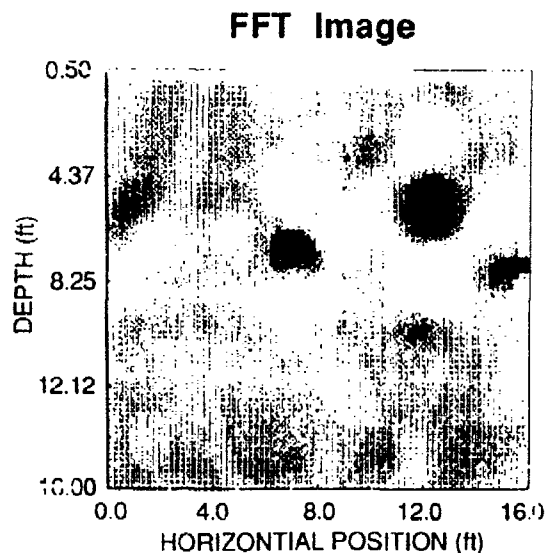


Figure 3: GPR image of two coffins [Source: Witten et. al., 1993a].

tively, over a known tunnel. For the seismic study, a bistatic reflection mode was utilized with geophones placed at 0.91 m (3 ft.) intervals along a line approximately normal to the tunnel axis. A Betsy seisgun source was used and this source was "fired" at three foot intervals between geophone locations. Data from all source positions was summed to synthesize a vertically-propagating plane wave and the resulting stacked data was processed at a frequency of 40 Hz. The tunnel position is indicated in Fig. 4 as the black area in the center of the image. Figure 5 is the corresponding image of the log likelihood function derived from 25 MHz. GPR data exploiting evanescent waves. Again, the tunnel location appears as the black area in the center of the image. At 25 MHz., the tunnel could not be detected by inspection of the acquired data or by the application of DTMLE within the homogeneous wave regime. The difference in tunnel depth estimates between Figs. 4 and 5 are a result of GPR measurements being made along a road while the seismics measurements were made in an approximately 12 foot deep ditch that parallels the road. In both images, depths are given relative to the elevation of the measurement line.

CONCLUSIONS

Signal processing algorithms have been developed for imaging and target detection for applications to data acquired with many commonly used geophysical methods. The algorithms are computationally efficient and are capable of processing data in real time with an 80486-based personal computer. For subsurface void detection, imaging algorithms for

TUNNEL LIKELIHOOD FUNCTION

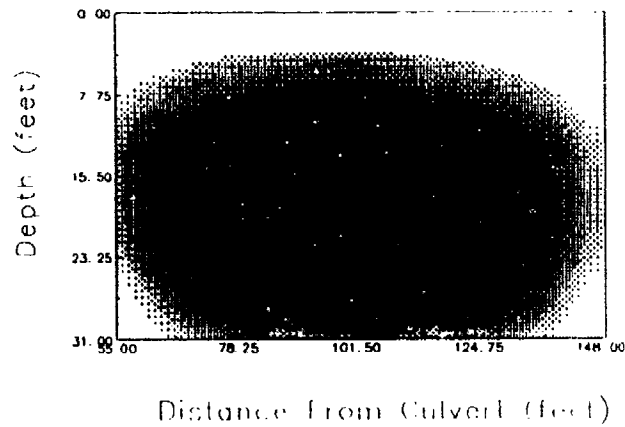


Figure 4: Cross-sectional image of the log likelihood function for seismic data acquired above a shallow tunnel.

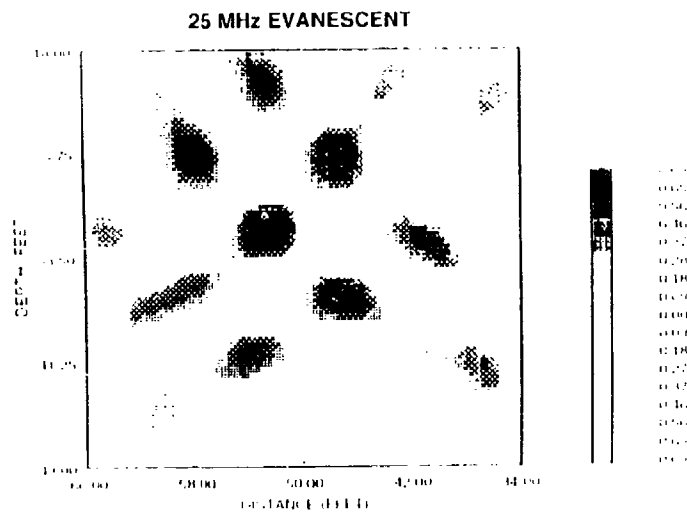


Figure 5: Cross-sectional image of the log likelihood function for GPR data acquired over a shallow tunnel [Source: Witten et. al., 1993b].

acoustic offset vertical seismic profiling and cross-hole radar have produced excellent results. Detection algorithms applied to cross-hole radar, monostatic ground penetrating radar, and seismic reflection have provided similarly good results.

REFERENCES

- Devaney, A.J., 1984, "Geophysical Diffraction Tomography," IEEE Trans. Geosci. and Remote Sensing, Vol. GE-22, p. 3.
- Devaney, A.J. and G.A. Tsihrintzis, 1991, "Maximum Likelihood Estimation of Object Location in Diffraction Tomography," IEEE Trans. Signal Processing, Vol. 39, p. 672.
- Witten, A.J., 1991, "The Application of a Maximum Likelihood Estimator to Tunnel Detection," Inverse Problems, Vol. 7, p. L49.
- Witten, A.J., Molyneux, J.E., and J. Nyquist, 1993a, "Ground Penetrating Radar Tomography: Algorithms and Case Studies," submitted to IEEE Trans. Geosci. and Remote Sensing.
- Witten, A.J., Devaney, A.J., and A. Schatzberg, 1993b, "Enhanced Signal Processing Algorithms for Tunnel Detection," Oak Ridge K-25 Site Report No. K/NSP-108, Oak Ridge, TN.

TUNNEL IMAGING EMPLOYING PSEUDO-ATTENUATION OF HIGH-FREQUENCY SEISMIC WAVES

J. Wong
JODEX Applied Geoscience Limited
Calgary, Alberta, Canada

J. Wright and L. Block
U.S. Bureau of Reclamation
Denver, Colorado

ABSTRACT

Pseudo-attenuation seismic tomograms were generated to image tunnels at the Fort Belvoir/CSM Test Tunnel in Idaho Springs and at selected sites in South Korea. Use of the CORRSEIS Borehole Seismic System allowed for rapid data collection with intense spatial sampling, and resulted in seismic signals with frequencies of about 3.5 to 5.5 kHz. Borehole geophysical data, especially variable density sonic logs, were essential for accurate interpretation of the crosshole tomograms. Modifications to the original CORRSEIS System, including upgraded transmitters, electrically-powered winches, and shielded receiver strings provided for efficient data acquisition and excellent data quality. Tomographic imaging was done using a straight-ray iterative back-projection algorithm. A total of twenty-nine crosshole panels were imaged incorporating in excess of 90,000 seismograms. Two separate tunnels were successfully imaged by the pseudo-attenuation tomograms.

INTRODUCTION

In crosshole scanning for seismic tomography, seismograms are recorded with a seismic source or transmitter fixed at a given depth in one borehole while a detector occupies a series of adjacent locations in a second borehole. This procedure generates a seismic fan, defined by a series of lines joining the detector locations to the source (see Figure 1). Each line is called a raypath, and represents the path along which a seismic wave travels from the source to reach the detector. The characteristics of the seismogram associated with a particular raypath depends on the seismic properties of the materials along that path. When many other fans are produced with the source located at different depths, the result is a dense network of raypaths criss-crossing the area between the boreholes. The section of ground between the two boreholes being scanned in this way is called a panel.

The rationale for scanning a section of rock or soil as depicted in Figure 1 is quite simple. If the rock is relatively homogeneous, then both the travel times and amplitudes of the seismic arrivals will be relatively systematic and predictable. Suppose, however, that an open cavity such as a tunnel is located in the rock. There is a significant difference in the elastic and acoustic properties of the rock compared to those of the air in the tunnel. Seismic waves travelling through the rock are blocked or scattered when they encounter the rock-air interface. They cannot travel directly through the tunnel because there is no rock to support the vibrations

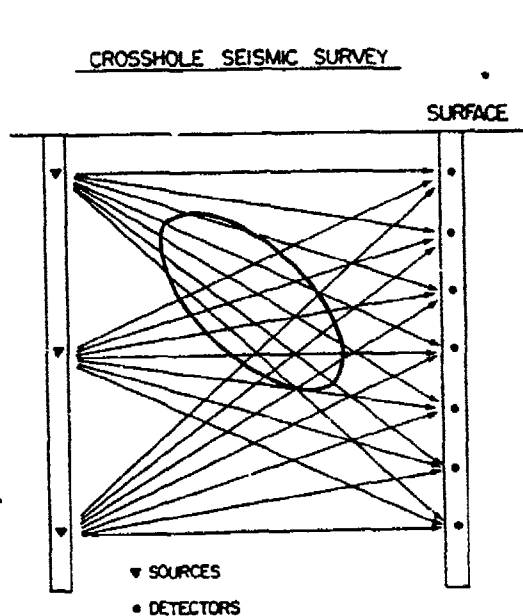


Figure 1: Field procedure for crosshole seismic scanning.

Rack Velocity = 5.8 km/sec.
Tunnel Diameter = 2 meters.

Distance AC = 10.20 meters,
Distance ABC = 10.20 meters,
Delay around tunnel = .04 msec.

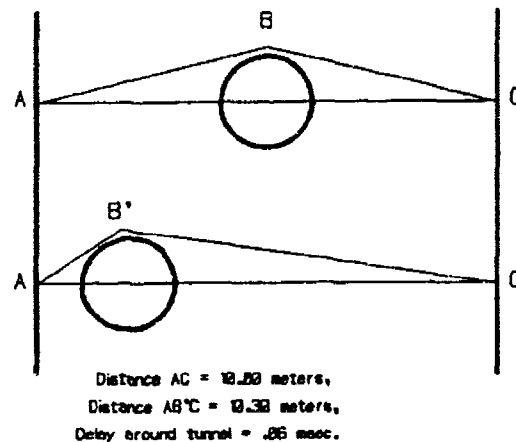


Figure 2: Travel-time delays due to a tunnel.

and consequently must diffract around and take a longer path. If the tunnel is sufficiently large in size, the seismic waves will lose much of their coherence and amplitude. Gathers of crosshole seismograms will reveal the tunnel by the presence of time delays and low-amplitude anomalies in first arrivals. Not only will the existence of the tunnel be revealed, but also, under favorable conditions, its location within the rock section can be determined when information from a detailed seismic scan is available. An effective way of analyzing the highly redundant information from a seismic scan containing hundreds or even thousands of raypaths is to use tomographic imaging (Wong et al., 1983, 1987; McMechan, 1983; Peterson et al., 1985).

A tunnel "sufficiently large in size" means it has a diameter or cross-section of at least one or two seismic wavelengths, which in turn means that the seismic waves used to detect the tunnel must be of high enough frequency. For example, if the P-wave velocity of the rock is 5 km/sec, and the tunnel diameter is 2 meters, then the required seismic wavelengths (at most 1 to 2 meters) dictate that the frequency of the seismic waves must be in the range 2.5 to 5 kHz or higher. Frequencies which are lower will be less effective for detecting the tunnel.

If the seismic waves meet these frequency requirements, cross-borehole seismograms should indicate, through unexpected variations in arrival times and amplitudes, the existence of the tunnel even though it may not be intersected by either borehole. Experimental studies (Wong, 1992; Schneider, 1991) and theoretical considerations (Rectien et al., 1991) concerning the use of high-frequency seismic waves to detect tunnels indicate that seismic

amplitudes are more sensitive than arrival times to the presence of a tunnel. An estimate of the extra travel-time delay caused by a tunnel in a typical situation can be made by referring to the upper diagram of Figure 2. A tunnel 2 meters in diameter is situated between two boreholes 10 meters apart in rock with a P-wave velocity of 5.0 km/sec. A seismic source located at Point A sends a seismic pulse towards a detector at Point C. When no tunnel is present the time taken for the pulse to traverse the distance AC is 2.00 msec. When a tunnel is present at the center of the panel, the seismic energy must follow the path ABC around the tunnel in order to arrive at the detector. The length of this path can be calculated to be 10.20 meters. The travel time will be 2.04 msec., so that the extra delay in the travel time when the seismic pulse must go around the tunnel will be only .04 msec.

If the tunnel is close to either one of the source or detector boreholes, the delay will be somewhat larger. In the case depicted by the lower diagram of Figure 2, the tunnel center is only two meters away from the source borehole. To arrive at the detector located at C, the seismic pulse must follow the path AB'C (total length 10.30 meters) around the tunnel, and the P wave arrival will be delayed by .06 msec. in comparison with the direct path AC. Such small delays caused by the tunnel would be even less if the distance between the boreholes were to increase, and may be only marginally larger than uncertainties in time-picking and delays caused by normal variations in rock properties. By contrast, field studies have shown that the presence of a tunnel on the direct path AC can decrease the amplitudes of the first arrivals in high-frequency seismograms by factors of 6 to 20. Thus, low-amplitude anomalies would seem to be a much more robust indicator of tunnel presence, especially when the hole-to-hole separations are more than 5 or 6 times the tunnel size.

In practice, first-arrival times picked on real seismograms may have tunnel delays significantly larger than those estimated above. The diffracted or scattered arrivals following the paths ABC or AB'C will have very small amplitudes. The first motion deflections (either up-breaks or down-breaks) on the corresponding seismograms may be so small that they are difficult to discern above background noise. In this case, time-picks may be made not on the true first motion, but on later cycles of the seismic coda. Such "cycle-skipping" will result in travel-time anomalies which correlate with seismic traces having low-amplitude first arrivals. In addition, when the tunnel is close to one of the boreholes, the first discernible cycles of the seismogram coda may be due to a converted wave. In calculating the arrival time delay along the path AB'C, it was assumed that the velocity along the entire path was that of the P wave. However, in reality, radiation pattern and near-field considerations may mean that the most of the seismic energy reaching the intermediate point B' from the source point A travels not as a P wave, but as a slower but much more energetic mode such as a surface wave propagating along the surface of the tunnel. Motion of the surface wave near point B' then generates a P wave which travels to the detector following the path B'C. In this case, the extra delay can be estimated very roughly by supposing that the slow surface wave travels along a quarter of the tunnel circumference. If the surface wave velocity is 3 km/sec, the extra delay is about .33 msec when compared with the direct P-wave travel time along AC in the absence of the tunnel. Finally, a tunnel may have larger delays associated with it because it is surrounded by a low-velocity halo consisting of rock cracked and broken by stress relief. The halo may extend two or more meters beyond the surface

of the tunnel and increase its effective size insofar as seismic transmission is concerned.

Tomographic imaging of seismic velocities has been widely studied and thoroughly presented in the literature (see, for example, Peterson et al., 1985). Tomographic images based on the amplitudes of seismic arrivals is much less common, mostly because seismic sources with repeatable output energy which can be controlled and tracked are not readily available. However, when such a source is available, imaging based on arrival amplitudes is highly desirable because, as we have already seen, the amplitudes can be more sensitive to tunnel presence. In the Appendix, we present the principles and assumptions used in reconstructing images of apparent attenuation from first arrival amplitudes. Since amplitudes are affected by scattering, focusing and de-focusing caused by refraction, and reflections from seismic boundaries as well as dissipation due to classical anelastic attenuation (micro-frictional losses), images of apparent attenuation will include the effects from all these phenomena, and so we call them pseudo-attenuation tomograms.

INSTRUMENTATION

Data acquisition was done using the CORRSEIS Borehole Seismic System, a system specifically designed for rapid and efficient recording of crosshole seismograms. The key components of the system are a high-power piezoelectric vibrator source, a receiver string of high-sensitivity hydrophones spaced at .62-meter (2-foot) intervals, and a high-speed AT-compatible computer. The vibrator and hydrophones require water-filled boreholes in order to operate. Using this equipment, digital seismograms 25 msec. long with sampling times of .05 msec. were recorded at rates of 500 to 700 per hour.

Two important features of the CORRSEIS System are responsible for its effectiveness as a high-resolution tool for detecting and locating small geological targets such as tunnels. The first is the high-frequency nature of the seismic energy it generates. Detection and location of features such as fractures and tunnels with sizes on the order of 2 to 3 meters (6 to 10 feet) require seismic wavelengths of at most 1 to 2 meters (3 to 6 feet). For granitic rocks with P-wave velocities on the order of 5 to 6 km/sec (15,000 to 19,000 ft/sec), such short wavelengths mean that the frequencies of the seismic waves must be 2 to 5 kHz or higher. The CORRSEIS System has been designed to generate and record seismic energy at exactly these frequencies.

The second advanced feature of the CORRSEIS System is its use of a cross-correlation technique to record seismograms. The source is driven by a continuous-wave periodic pseudo-noise waveform known as a pseudo-random binary sequence (PRBS). Associated seismic vibrations, generated by the source and detected by sensors after propagating through rocks, are cross-correlated with the original PRBS to obtain impulsive seismograms. This procedure produces seismograms with large gains in signal-to-noise ratios. Peak power generated by the source can thus be kept low enough to avoid damage to expensive boreholes, and yet high-quality seismograms can still be recorded even through lossy rocks. The cross-correlation technique with the controlled CORRSEIS source generates seismograms with highly repeatable amplitudes which are particularly suitable for pseudo-attenuation imaging.

FIELDWORK AND PROCESSING

Crosshole seismic scanning was done at two tunnel sites to acquire data for testing pseudo-attenuation imaging as a method of tunnel detection. The first site was the Upper Pad Area at the Belvoir Test Tunnel in Idaho Springs, Colorado, involving the boreholes shown in Figure 3. The rock here is highly fractured at many depths, and the zones of interest centered around the known tunnel at an elevation of about 7882 feet are unsaturated. These two factors make acquisition of cross-borehole seismic data very difficult. Nonetheless, using the CORRSEIS System with its signal enhancement features, five panels were scanned successfully, with over 10,000 seismograms being recorded in a period of six days in April 1992. Of these traces, about 6,500 were of good enough quality so that first arrival time-picks and amplitude estimates could be made to be used for imaging P-wave velocities and pseudo-attenuations in a straight-ray iterative back-projection algorithm. Amplitude estimates were made by taking the Fourier transform of tapered 2 msec. windows following the time picks and averaging the spectral densities in the 3 to 6 kHz frequency band. The pseudo-attenuation tomograms for four panels AC, CB, DE, and CE are presented as grey-scale plots on Figure 7 to illustrate the theme of this paper (the letters identifying the panels refer to the bounding boreholes on Figure 3). On these images, high-attenuation anomalies corresponding to fractures or cavities appear as dark features.

During the Idaho Springs survey, a number of equipment problems were identified and subsequently corrected before undertaking scanning at the second site in South Korea. The major equipment improvements included electrically-powered winches, shielded armored cables, more robust vibrator design, and high-pressure waterproof connectors.

In October, 1992, the upgraded CORRSEIS System was used in South Korea to do seismic scanning across four panels at the Tunnel 3 Site (see Figure 8). The results confirmed the belief that tunnels could be detected using high-frequency crosshole seismic data in geological environments typical of the DMZ. The equipment was then taken to two other sites in the DMZ to do reconnaissance and detailed searches for suspected tunnels across twenty panels. Over a period of fifteen days in the field, over 95,000 seismograms were recorded. Of these, over 85,000 were used to provide first arrival travel-time and amplitude data for P-wave velocity and pseudo-attenuation imaging within the 24 separate panels. Only the attenuation results for the four panels at the Tunnel 3 Site are presented in this paper (Figure 11).

A small spatial sampling interval in the seismic scans is essential for detecting a relatively small target such as a 2-meter diameter tunnel. As many raypaths connecting source and detector locations as practical must be generated to impinge on or intersect the tunnel. This will ensure that the tunnel will be clearly defined when imaging via tomographic reconstruction is done. The scans both at Idaho Springs and in Korea were done in such a way so that the spacing between adjacent source locations was .31 meters (1 foot), and the separation between adjacent detector locations were .62 meters (2 feet). Maximum depth offsets between the source and receiver varied with the panel widths in order to generate as many raypaths as possible with angles (+/-) 45 degrees or greater relative to the horizontal. These steep ray angles are needed to better localize the lateral position of the tunnel within the final tomogram.

RESULTS: BELVOIR TEST TUNNEL

Scanning of the Upper Pad Area of the Belvoir Test Tunnel Site for seismic tomography was done between the boreholes shown on Figure 3. The raypath diagrams in Figure 4 represent schematically the scanning patterns for Panel DE, which intersects the tunnel, and Panel CE, which does not. There are about 1300 rays in each of these scans. The depicted position of the tunnel in Panel DE is approximate. The tunnel cross-section is about 2.5 meters high by 2.5 meters wide.

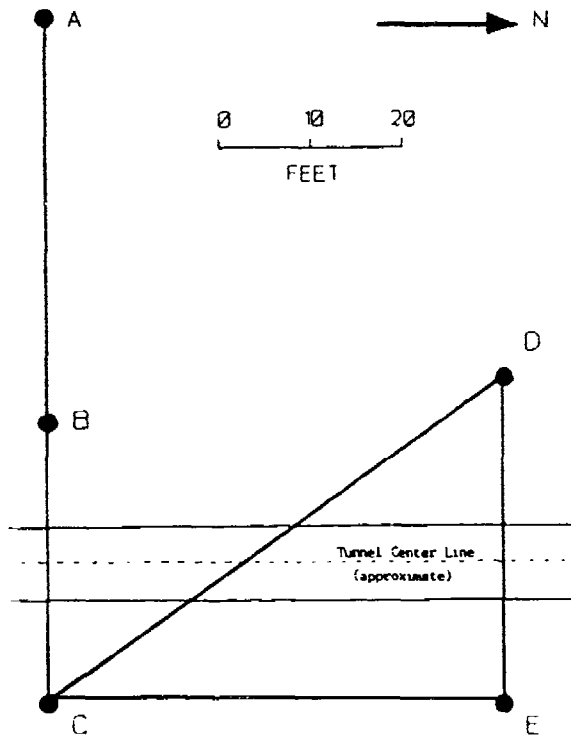


Figure 3: Plan map of borehole locations, Belvoir Tunnel Site.

BELVOIR TUNNEL SITE (IDARO SPRINGS) SEISMIC TOMOGRAPHY SURVEY:
ELEVATION RAYPATH DIAGRAM: EVERY SECOND RAY SHOWN.

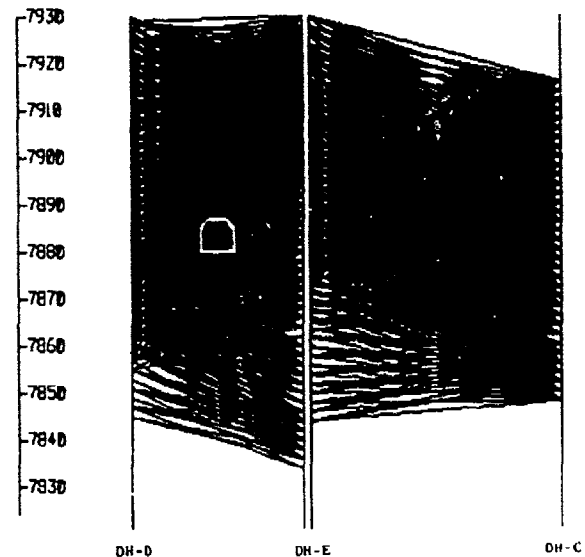


Figure 4: Scanning patterns for Panels DE and CE.

Sonic variable density logs (VDL's) between the elevations of 7940 and 7820 feet for the five boreholes A, B, C, D, and E are shown in Figure 5. On these logs, disruptions in the variable density patterns and transit time deflections to the right indicate poor rock conditions. In many cases, they correspond to fracture intersections in the boreholes. Figure 6 shows the common elevation gathers (CEG) for the four panels at the Belvoir Tunnel Site (each seismogram in the gathers has equal source and detector elevations). The traces are plotted with a constant gain factor, so that trace-to-trace variations of the amplitudes of the seismic signals can be easily perceived. The CEG plot for each panel contains only a small fraction of the number of traces used for tomographic imaging, but it indicates many of the main seismic characteristics of the panel. Muting of electrical crosstalk between the transmitter and receivers has been applied to the CEG plots (the crosstalk problem has since been solved by the use of shielded armored cables and better preamplifier design).

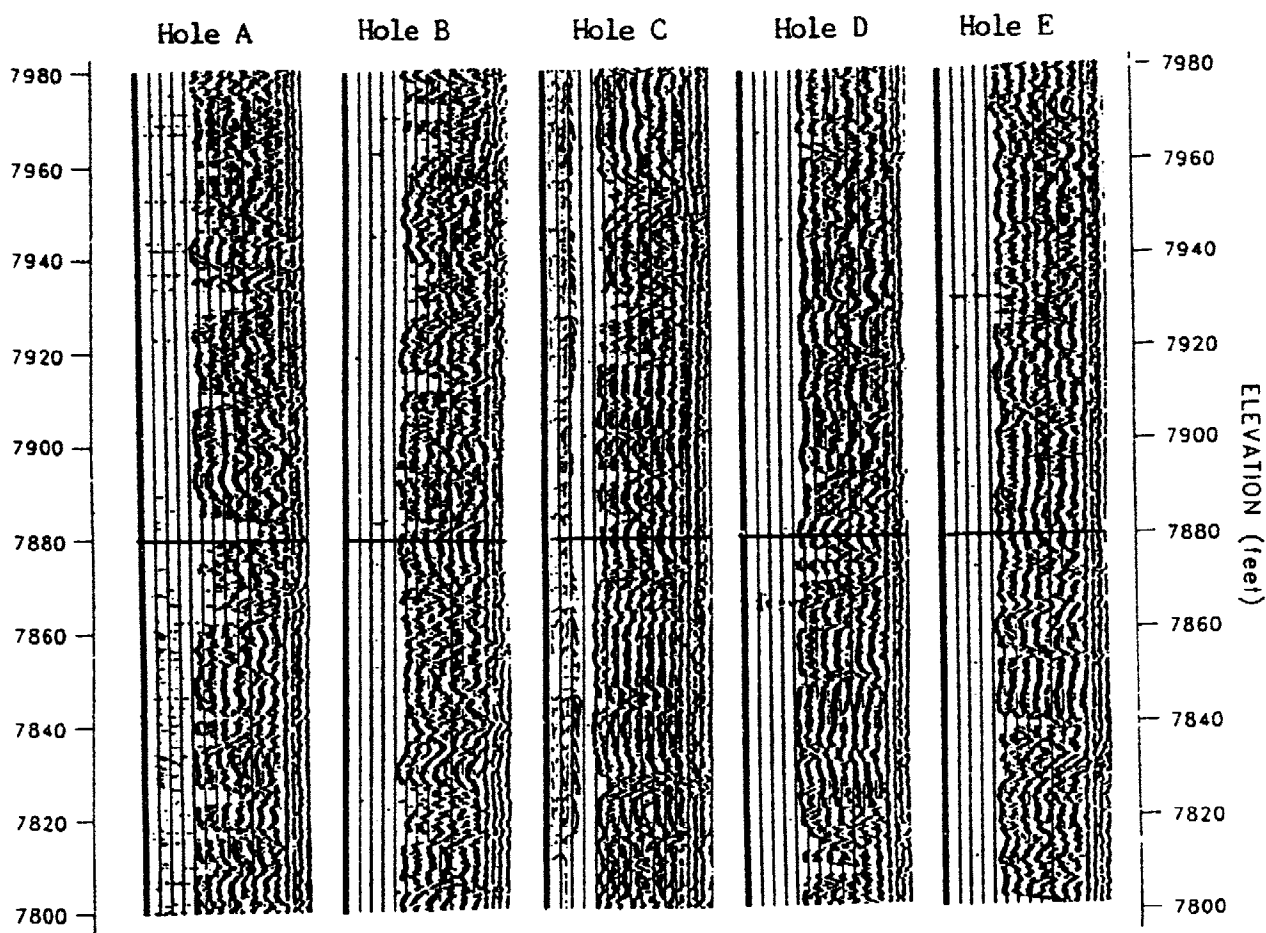


Figure 5: Sonic variable density logs (VDL's) for Belvoir Tunnel Site.

Average P-wave velocities for the rock at the Belvoir Test Tunnel Site can be calculated using the arrival times observed on Figure 6 and the hole-to-hole separations determined by borehole deviation surveys. The average velocities range from about 13,000 feet/sec in highly-fractured zones to over 19,000 feet/sec in the deeper portions of the holes.

Panel AC is about 75 feet wide, and sonic VDL's indicate that the rock encountered in Borehole A is very badly fractured. Consequently, the overall quality of seismic data from this panel is only fair (see Figure 6). Note the low amplitudes and lower frequencies of the seismograms at elevations just below 7885 feet. On the pseudo-attenuation tomogram for Panel AC (Figure 7), the tunnel is coincident with a broad high-attenuation zone adjacent to Hole C near Elevation 7880. However, if its location were not known, it may be difficult to infer the existence of the tunnel from the tomogram because of masking by the high-attenuation zones caused by intense fracturing. High-attenuation features on this panel tend to elongate in a subhorizontal direction. This is due to the limited angular aperture of the scan, which has very few rays with angles more than 40 degrees relative to the horizontal (see Figure 1).

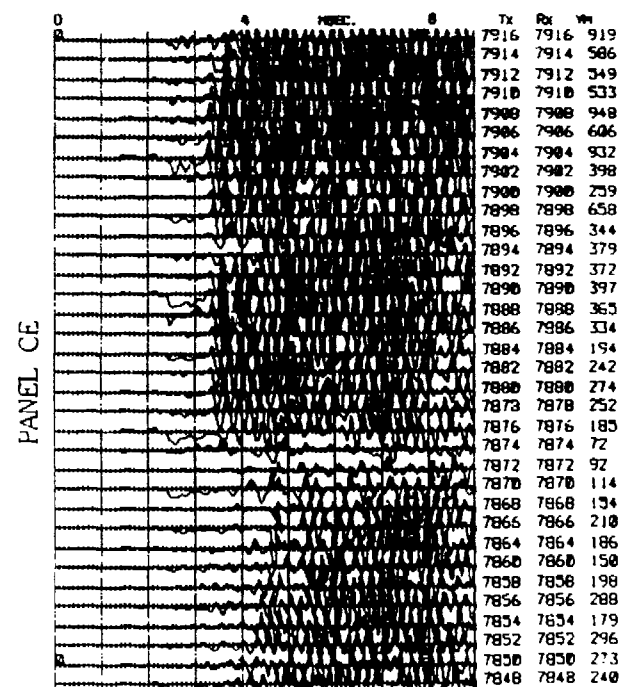
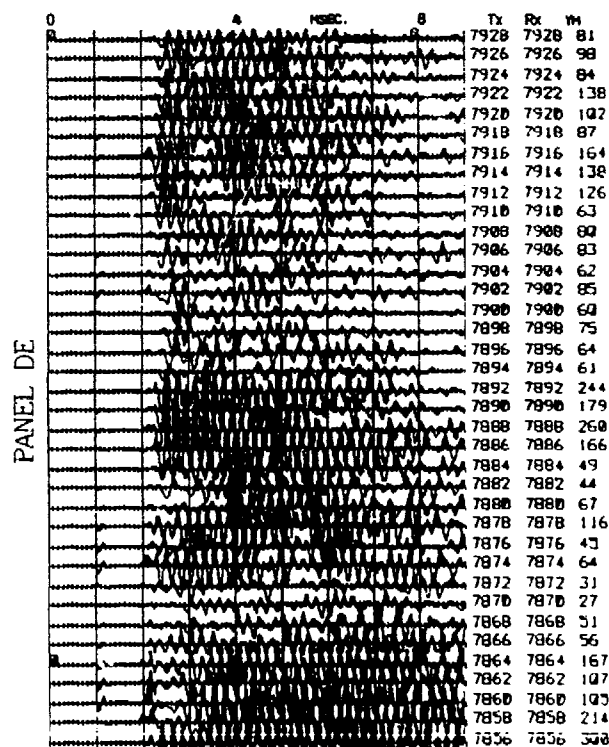
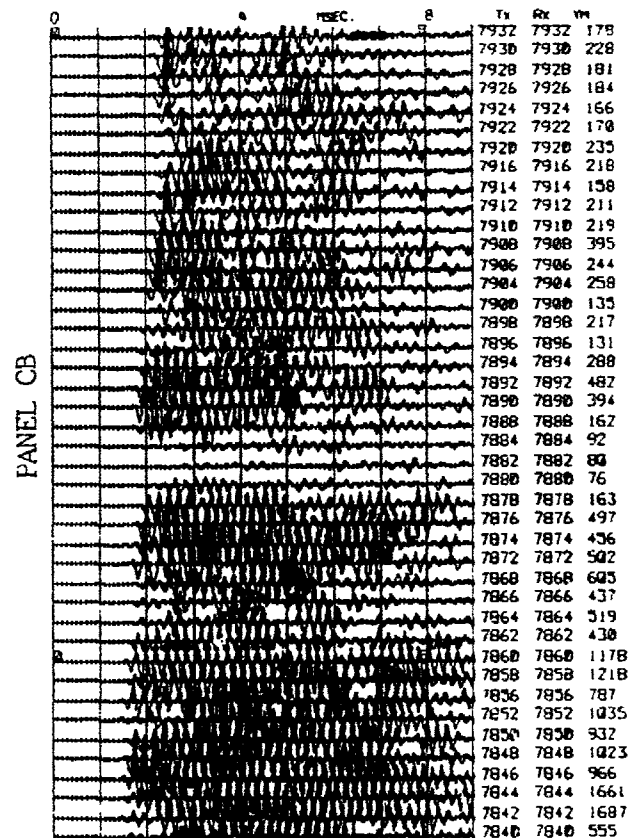
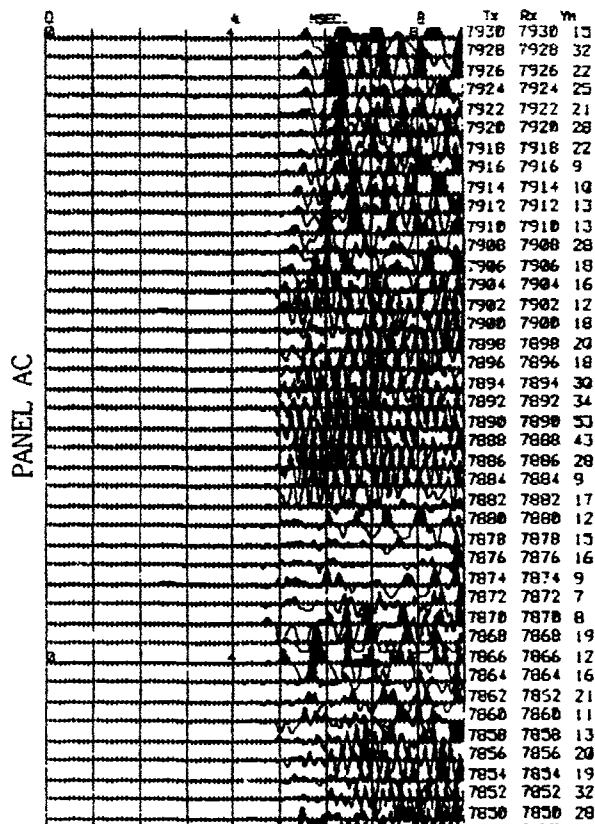


Figure 6: Common Elevation Gathers for Belvoir Tunnel Site (fixed gain plots).
Tx and Rx headings refer to source and detector depths in feet;
Ym heading refers to the maximum amplitude of the trace.

Panel CB is about 31 feet wide, and a good number of the seismic rays in this panel have angles of over 50 degrees relative to the horizontal. Though sonic VDL's show fracturing in both holes B and C, it appears to be much less intense than in Hole A. Consequently, the seismic data quality for Panel BC is better, as can be seen in the CEG plot in Figure 6. Note the very clear low-amplitude zone centered about the tunnel elevation near 7882 feet.

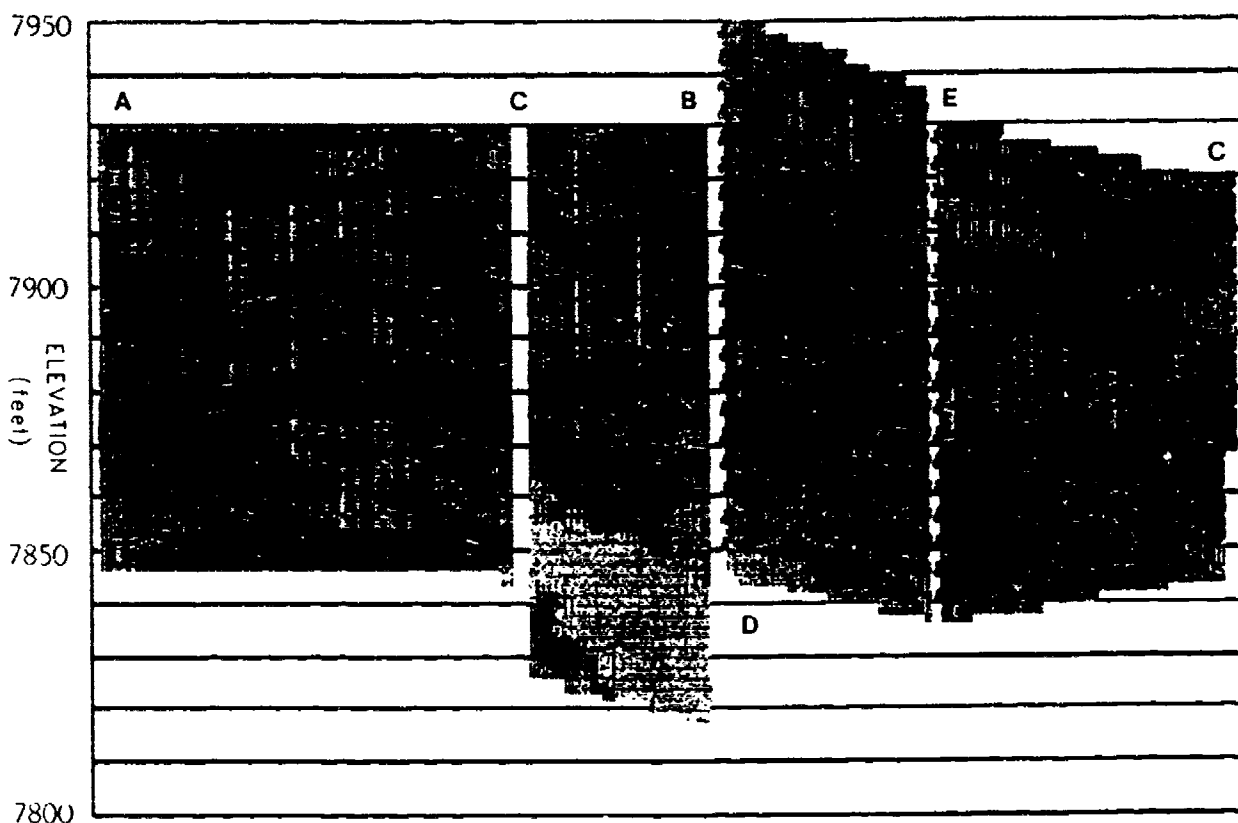


Figure 7 : Pseudo-attenuation tomograms for Belvoir Tunnel Site.

The pseudo-attenuation tomogram for Panel CB on Figure 7 shows that a well-formed high-attenuation anomaly is coincident with the tunnel. There appears to be little interference from high-attenuation zones caused by fracturing. The high-attenuation features along Hole B appear to be associated with fracture intersections indicated by the sonic VDL. Because of less masking by geological features, better data quality, and the increased angular aperture of the seismic scan, the Panel CB tomogram is a better result than the Panel AC tomogram in terms of imaging the known tunnel.

Panel DE is about 34 feet wide. The steepest seismic rays in this panel have angles near 50 degrees relative to the horizontal. In the elevation range under study, the sonic VDL's show moderate fracturing encountered by Holes D and slight fracturing in Hole E. The seismic data quality for Panel DE as observed on the CEG plot is reasonably good. A clear low-amplitude zone is seen near the tunnel elevation at 7880 feet. Low-amplitude traces are also present at about 7905 and 7870 feet.

The pseudo-attenuation tomogram for Panel DE shows a high-attenuation anomaly where the tunnel should be. Two other strong anomalies appear right next to Hole E above and below the tunnel anomaly. There are no corresponding features on the sonic VDL for Hole E, so they may be off-hole fractures, or they may be imaging artifacts. If the tunnel were not known to exist at this elevation, differentiating the tunnel anomaly from the geological anomalies would not be straightforward.

Panel CE is about 50 feet wide, and the steepest seismic rays in this panel are about 50 degrees. Near the tunnel elevation, the sonic VDL's show moderate fracturing encountered by Hole C and only slight fracturing in Hole E. The seismic data quality for Panel DE is good (Figure 6). A clear low-amplitude zone is seen at elevations 7870 to 7875, beneath the tunnel elevation near 7882 feet.

The pseudo-attenuation tomogram for Panel CE shows no attenuation anomaly at the tunnel elevation (7882 feet). This is expected, as Panel CE does not intersect the tunnel. Beneath Elevation 7875, a number of moderately high attenuation features are observed next to Holes C and E. These are not accompanied by any obvious VDL anomalies, so they may be off-hole fractures.

RESULTS: TUNNEL 3 SITE, SOUTH KOREA

Figure 8 is a plan map showing the boreholes spanning Panels A, B, C, and D at the Tunnel 3 Site in South Korea. The four panels were scanned in order to determine whether or not the CORRSEIS System was able to detect a known tunnel. Panels A, B, and C shared a common transmitter hole (DT-14). Panel D is some 100 meters to the north-west of Panel A. Tunnel 3 has a cross-section of about 2.5 meters high by 2.5 meters wide, and intersects Panels A, B, and C at a depth of about 60 meters. The tunnel intersection on Panel D occurs at a depth of about 75 meters.

In general, the seismic data collected in Korea was excellent. The data quality was much better than observed at the Belvoir Test Tunnel Site in Idaho Springs. The rock investigated in the Korean survey appeared to be much less fractured than the rock at the Idaho Springs site, and furthermore it was fully saturated with water. The seismic fan or common receiver gather of seismograms shown in Figure 9 is typical of the Korean data. In this gather, the receiver is fixed at a depth of 51.2 meters in Hole DT-15 while the source is moved along Hole Dt-14 in .62-meter (2-foot) increments. Each trace in the gather has been normalized by its maximum amplitude. Note the strong tube wave originating at a depth of 44.8 meters in the source borehole (DT-14).

The high signal-to-noise ratios of the field data can be seen on the seismic fan of Figure 9 as well as on the common depth gathers (CDG) for the four panels on Figure 10. The fixed-gain CDG plots on Figure 10 show those traces for which the source and detector depths are the same. Note the low-amplitude traces at depths near 60 meters for Panels A, B, and C, and at depths near 75 meters for Panel D. These low-amplitude seismograms appear to be indicative of the tunnel presence. The pseudo-attenuation tomograms for Panels A to D are shown in Figure 11. Reliable sonic VDL's were not available for the boreholes at this site.

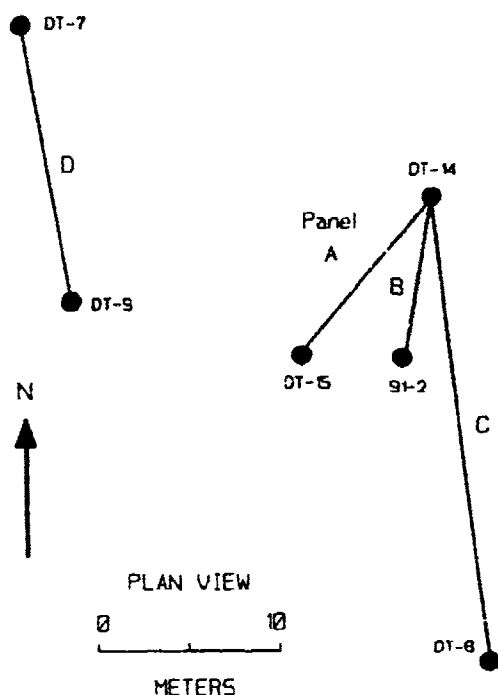


Figure 8: Plan map of borehole locations, Tunnel 3 Site.

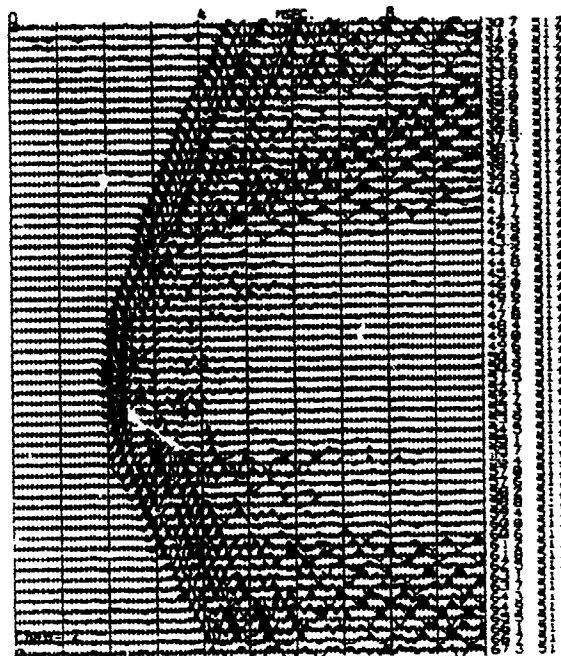
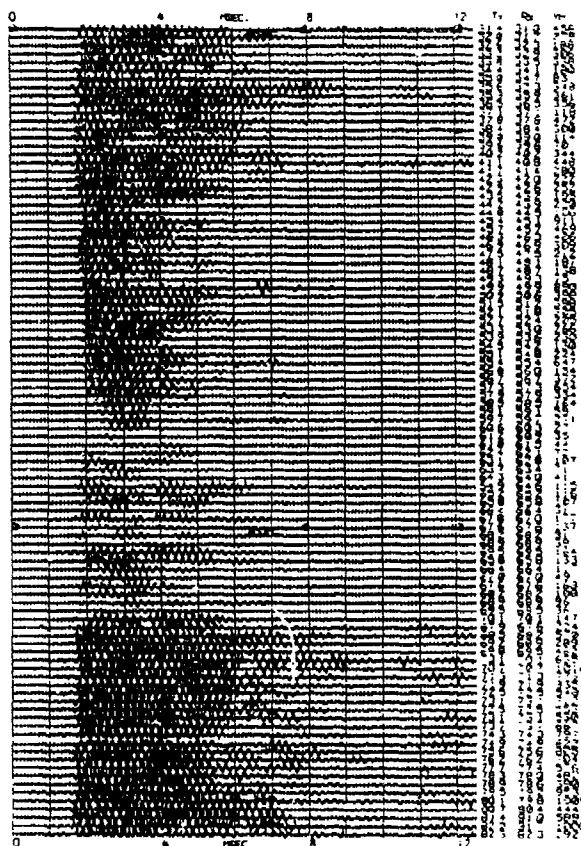


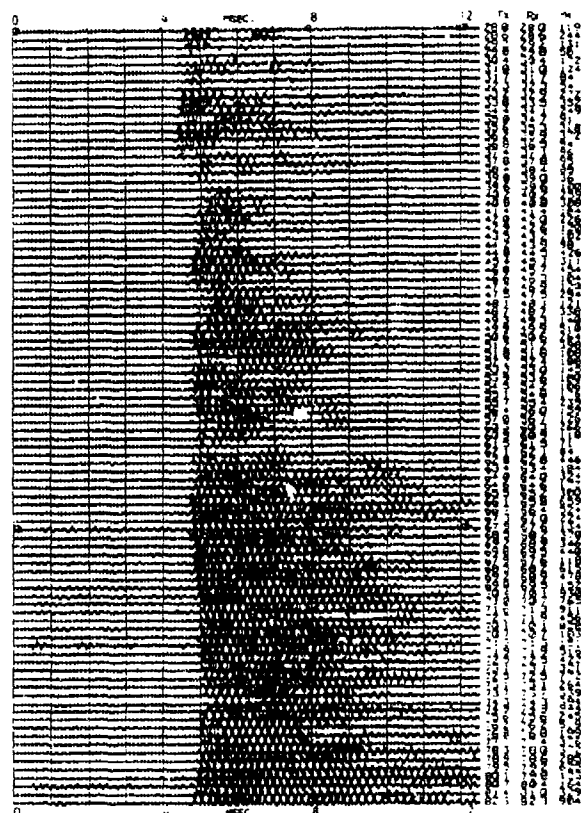
Figure 9: Common Receiver Gather, Tunnel 3 Site Panel A.

Examination of the CDG seismograms on Figure 10 reveals that for Panels A, B, C, and D, all of which intersect a known tunnel, low-amplitude first arrivals occur at depths near the tunnel. On Panels A and B, which are about 10 meters wide, the low-amplitude zones at depths of 57 to 62 meters are especially striking. On Panels C and D, which are about 25 and 17 meters wide, the low-amplitude anomalies are less well-defined, but are still readily discernible at depths near 60 and 74 meters, respectively. Distinctly slower travel-times can be seen for Panels A and B at the tunnel depths, but for Panels C and D, the arrivals are not perceptibly delayed at the tunnel depths. The clarity of the tunnel-related amplitude and travel-time anomalies in Panel C has been compromised by a gap in the seismic coverage right near the tunnel. The gap was caused by operator error during data acquisition.

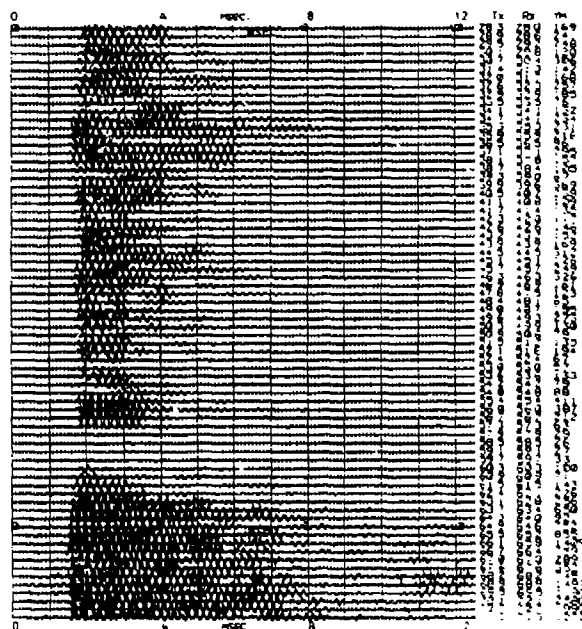
From the arrival times on the CDG plots and the panel widths, the P-wave velocities of the host rock at the Tunnel 3 Site can be estimated to be from 5.0 to 5.6 km/s. The energy of the CDG traces on Figure 10 is concentrated in the frequency band between 1.5 kHz and 6 kHz. The dominant frequencies are more narrowly constrained to the 3.5 to 5.5 kHz range. For velocities of about 5.2 km/s, the corresponding dominant wavelengths are .9 to 1.5 meters. These are short enough that they should adequately resolve a tunnel with a 2 meter by 2 meter cross-section.



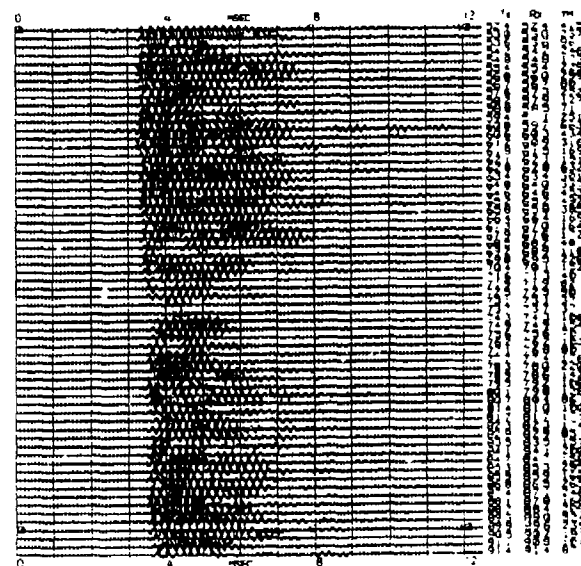
Panel A



Panel C



Panel B



Panel D

Figure 10: Common Depth Gathers for Korea Tunnel 3 Site (fixed gain plots).
Tx and Rx headings refer to source and detector depths in meters;
Ym heading refers to the maximum amplitude of the trace.

Figure 11 displays the grey-scale attenuation tomograms for the four panels at the Tunnel 3 Site. The aspect ratio (ratio of horizontal to vertical scales) is approximately 1:1. High-attenuation anomalies appear as dark features on the tomograms near the expected tunnel depth.

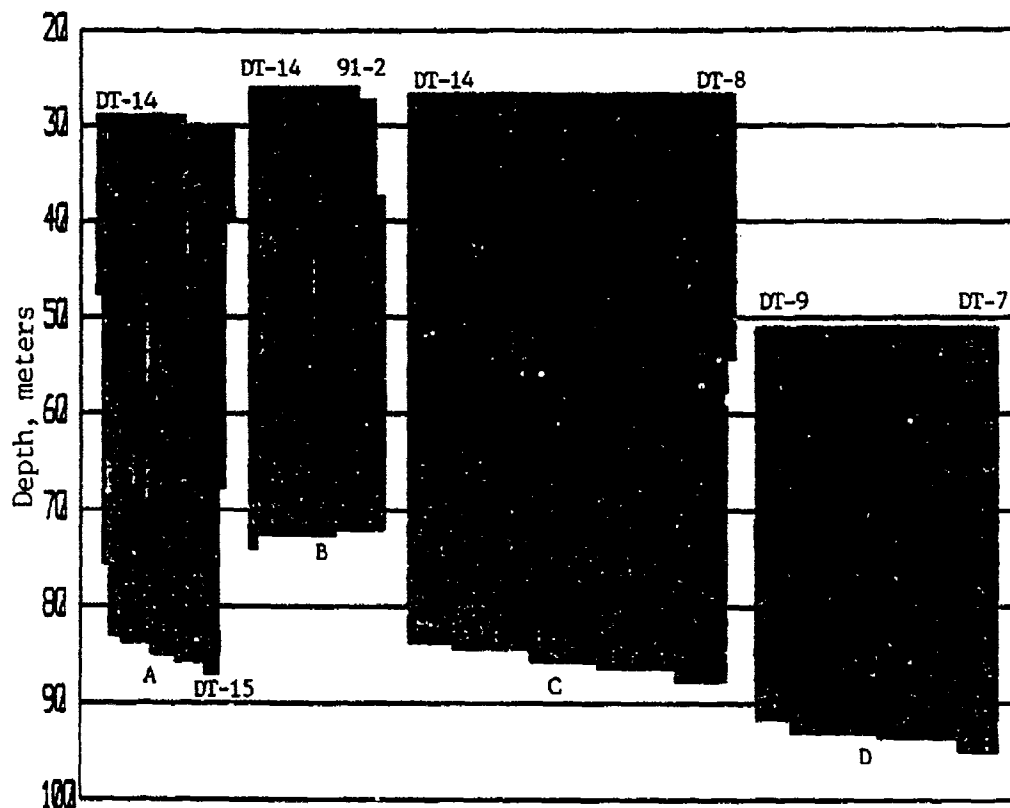


Figure 11 : Pseudo-attenuation tomograms for Tunnel 3 Site.

On Panels A and B, the anomalies seem to indicate that the tunnel is closer to Boreholes DT-15 and 91-02. Indeed, Borehole 91-02 appears to be close to intersecting the tunnel. For each of these panels, the short hole-to-hole spacing and the proximity of the tunnel to one borehole accounts for the clear travel time delays on Figure 10 associated with it. The attenuation tomogram for Panel A seems to indicate a zone of fractured or poor quality rock below the tunnel and extending down toward DT-15.

On Panel C, anomalies due to the tunnel are expected at depths near 59 meters. There are a number of small features on the attenuation tomogram with moderately high attenuation values, but none of these anomalies is not a very good image of a tunnel. The previously mentioned gap in the seismic coverage right near the tunnel depth has caused a critical deficiency in the data needed to create a proper image. The plane of Panel C cuts the tunnel at a significant angle, and this probably has also affected the clarity of the image. Above 50 meters, attenuation anomalies indicate zones of high seismic loss, perhaps caused by weathering, strong fracturing, or changes in saturation and/or lithology.

The common depth seismograms for panel D (Figure 10) have low amplitudes at depths near 74 meters where the tunnel should be. There is a corresponding high-attenuation anomaly on the pseudo-attenuation tomogram (Figure 11). Although the panel width of 17 meters is relatively large compared to the tunnel size, the effect of the tunnel on the crosshole seismic amplitudes appears to be large enough to cause a clear high-attenuation feature on the resulting tomogram.

DISCUSSION

Concerns may be raised about the fact that the above tomograms were created using the assumption of straight raypaths across the rock sections. A better approximation may be to use curved raypaths which bend according to Snell's Law in a host rock with seismic velocities which vary with position. We believe that if the velocity gradients in the host medium are no more than about 15 percent over distances of two or three wavelengths, the straight-raypath assumption is a good enough approximation for imaging a tunnel. To support this statement, we compare straight-ray and curved ray tomograms.

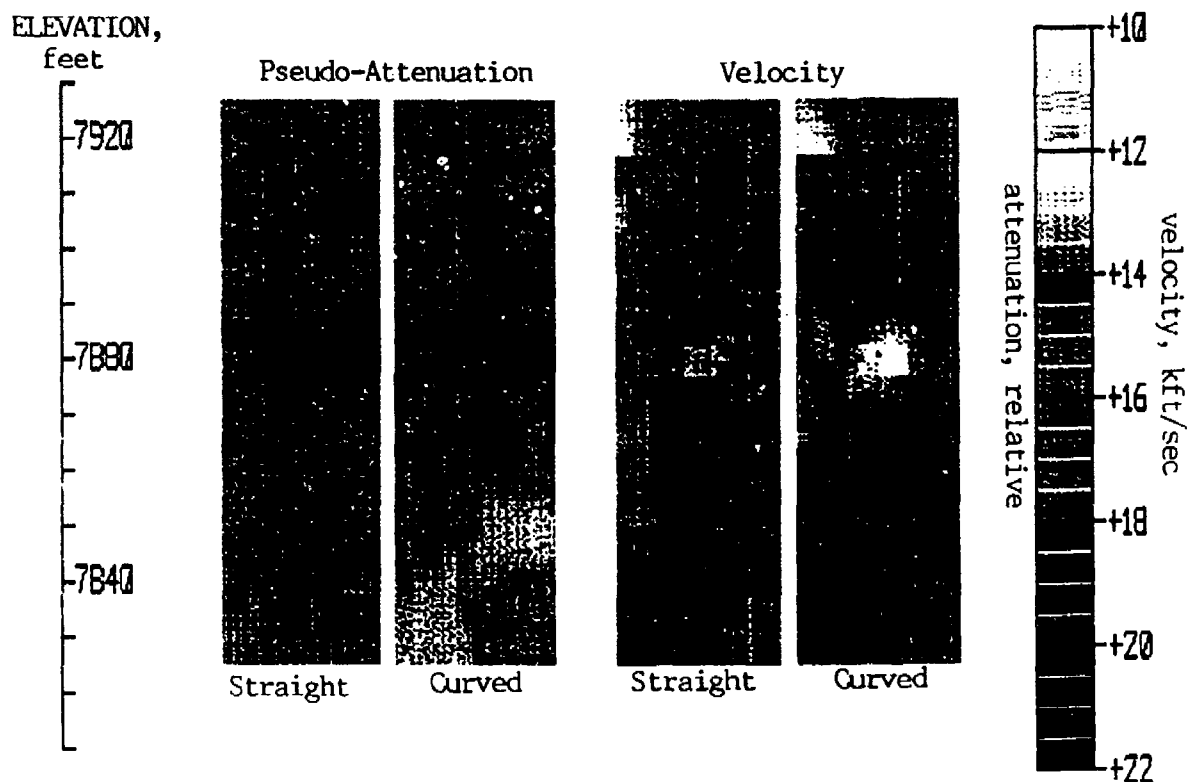


Figure 12 : Comparison of straight-ray and curved ray tomograms, Panel CB, Belvoir Tunnel Site.

We have re-calculated P-wave pseudo-attenuation and velocity tomograms for Panel CB at the Belvoir Tunnel Site using both straight rays and curved rays. The results are presented on Figure 12. The same grey scales are used for both the straight-ray and the curved-ray tomograms. The tunnel appears as

a dark (high-attenuation) feature on the attenuation tomograms and a light (low-velocity) feature on the velocity tomograms. The dimensions of the tunnel anomalies at Elevation 7882 feet are somewhat larger on the curved-ray images. In addition, the deviations of tunnel anomaly values from the host rock values, for both attenuation and velocity, are about 25 to 50 percent higher on the curved-ray images. However, if a more sensitive grey scale is used to display the straight-ray tomograms, the tunnel anomalies on the straight-ray and the curved ray tomograms would be very similar in appearance. They are also similar to the back-projection results shown on Figure 7.

The tomograms on Figure 12 were computed with a modified SIRT algorithm. In the traditional SIRT algorithm, the residuals are distributed along the ray paths such that the sum of the squared changes in the slownesses (or attenuations) are minimized (Dines and Lytle, 1979). In the modified algorithm, the residuals are distributed along the ray paths such that the sum of the squared spatial first velocity (or attenuation) derivatives are minimized. This method has been used for inversion of earthquake data to stabilize full least squares inversions (Sambridge, 1990; Block et al., 1993). It reduces artifacts when incorporated into the SIRT algorithm. Curved ray tracing was performed using the method of Saito (1989), in which wavefronts are computed throughout the model using Huygen's principle of secondary sources and the ray path with the smallest travel time is then computed.

Initial velocity and attenuation values were found by inverting the data for homogeneous models. Values of 16.22 kft/s and 0.61 dB/ft were obtained for the initial homogeneous velocity and attenuation models, respectively. The horizontal pixel width for the tomographic inversion was 2 ft. The vertical pixel width was 2 ft in the central part of the tomograms (7852 - 7908 ft elevation), and was 4 ft in the upper and lower sections where the ray coverage was less dense. Twenty-five iterations were performed. The rms travel time residuals decreased by 32%, from 0.42 msec to 0.285 msec. The rms log amplitude decreased by 56%, from 9.23 dB to 4.10 dB.

APPENDIX: CALCULATION OF PSEUDO-ATTENUATION TOMOGRAMS

Attenuation analysis of borehole-to-borehole seismic data is based on an equation which relates a function of the seismic amplitude to a line integral of apparent attenuation through the panel. We develop this equation taking into account amplitude variations due to the radiation pattern of the source (that is, amplitudes of seismic waves from a source in a fluid-filled borehole depends on the direction). For a cylindrical source shorter than a wavelength in a borehole filled with fluid, the pressure amplitude normal to the rock-fluid interface at the detector borehole A_r is

$$A_r = A_0 * F(\theta) * \exp(-a*r)/r, \quad (1)$$

$$F(\theta) = (1 - 2*[V_s/V_p * \cos(\theta)]^2) * \sin(\theta) \quad (\text{Heelan, 1953})$$

where A_0 is the radiation strength, $F(\theta)$ is the angular dependence or radiation pattern, a is the attenuation coefficient, r is the distance between the source and detector, V_s and V_p are the shear and pressure wave velocities of the elastic medium, and θ is the angle between the source borehole axis and the straight line joining the source and detector (see Fig. A1 with $\theta_1 = \theta_2 = \theta$).

This equation is valid only for homogeneous isotropic media; it does not account for the anisotropic effects discussed by Saito, 1991, and Williamson et al., 1993. We will nevertheless assume its validity for real seismic data in real geology and use it as the basis for pseudo-attenuation tomography.

If attenuation is not constant along the raypath joining the source and detector, Equation 1 becomes

$$A_r = A_0 * F(\theta) * \exp (- \int a(x,y) * dl) / r \quad (2)$$

The attenuation $a(x,y)$ is now a function of position, and the line integral is along a given raypath.

From Equation 2, we may write

$$\int a(x,y) * dl = \log_e [(A_0/A_r) * (F(\theta)/r)] ,$$

or, expressing the right-hand side in decibels,

$$\int a(x,y) * dl = 20 \log_{10} [(A_0/A_r) * (F(\theta)/r)] \text{ dB.} \quad (3)$$

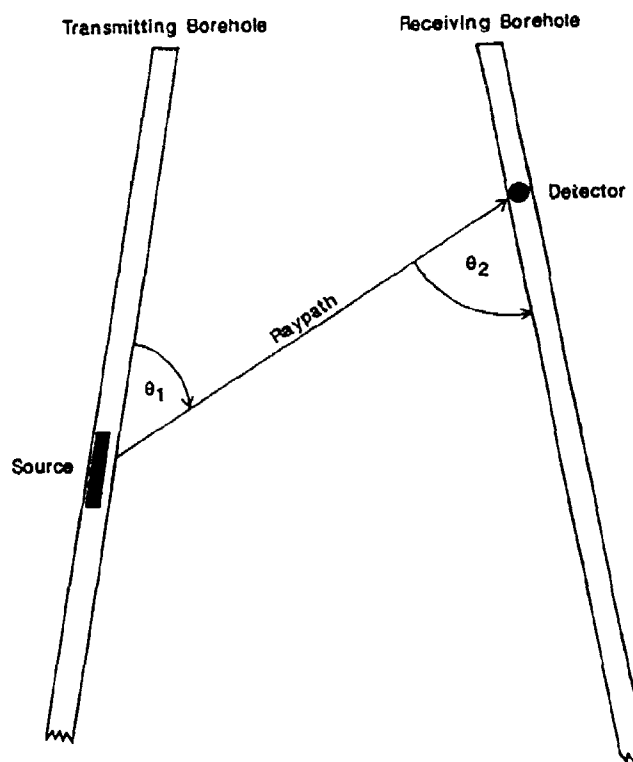


Figure A1 : Schematic diagram showing the angles θ_1 and θ_2 in the radiation pattern. If the boreholes are parallel, then $\theta_1 = \theta_2 = \theta$.

Letting $D = 20 \cdot \log_{10} [(A_0/A_r) \cdot (F(\theta)/r)]$, and dividing the panel into a grid of rectangular pixels with the attenuation $a(x,y)$ assumed to be constant within each pixel, the line integral becomes a sum. Thus,

$$\sum_k l_{km} a_k = D_m \quad (4)$$

where m refers to the m -th ray and k refers to the k -th pixel. D_m is the measured quantity A_r for the m -th ray (i.e., the P-wave amplitude) as modified in equation 3, l_{km} is the length of the m -th ray within the k -th pixel; a_k is the value of attenuation in the k -th pixel.

Equation 4 has the same form as the standard equation which relates travel times with seismic slownesses and is the basis of most tomographic reconstruction algorithms. Hence, tomograms of both seismic attenuation and slowness can be reconstructed using the same iterative algebraic and back-projection algorithms.

Two complications exist in reconstructing seismic attenuation from cross-borehole amplitude data: the need to estimate the radiation strength A_0 , and the need to apply a correction for the radiation pattern. Theoretically, A_0 is the amplitude measured by the seismic system with the source and detector separated by a unit distance (i.e., one foot, one meter, etc.) in the absence of attenuation and radiation pattern effects. A_0 depends on the source strength, the detector sensitivity, and the efficiency in the transfer of pressure wave energy in a fluid-filled borehole to elastic waves in the solid medium. Although the source strength and detector sensitivity are reasonably well-known, the transfer efficiency will vary as the elastic properties of the solid medium in the borehole vary. It may be difficult to quantify the change in efficiency as, for example, the source moves from the unsaturated zone into the saturated zone in a soil column. Thus, A_0 cannot be measured directly, and must be estimated. Errors in the estimation of A_0 will lead to quantitative errors in the resulting attenuation tomogram. For example, if A_0 is estimated to be too large by a factor of two, then all the tomographic values will be too large by about $6/S$ dB/meter, where S is the hole-to-hole distance in meters. Fortunately, such a (nearly) constant shift in attenuation does not affect the significance of large variations within the tomogram. High values of attenuation will still be associated with more lossy soil or rock, while low values will be indicative of more competent materials.

The radiation pattern $F(\theta)$ in Equation 1 applies only if the source and detector boreholes are parallel. If they are not, then $F(\theta)$ must be replaced by $F(\theta_1, \theta_2)$:

$$F(\theta_1, \theta_2) = (1 - 2 \cdot [V_s/V_p \cdot \cos(\theta_1)]^2) \cdot \sin(\theta_2) \quad (5)$$

where θ_1 is the angle between the borehole wall at the source location and the straight line joining the source and detector, and θ_2 is the angle between the borehole wall at the detector location and the same straight line (Figure A1). If the angle θ_1 and θ_2 as well as the velocity ratio V_s/V_p must be estimated because directly observed values are not available, the radiation pattern correction to amplitudes may contain a systematic error. It could also happen that the medium between the boreholes is so different from being elastic, homogeneous, and isotropic that the theoretical radiation pattern of Equation 1 or 5 is grossly inappropriate.

As long as the errors in the correction for radiation pattern are not too large, their effects on the final attenuation tomogram will be similar to that caused by errors in estimating the radiation strength A_0 . All the values of tomographic attenuation will be shifted by a nearly constant amount. The attenuation values lose some accuracy in an absolute sense, and quantitative comparisons between different panels may not be possible. However, large variations within a single tomogram retain geological significance.

A comparison of measured P-wave arrival amplitudes with Heelan's theoretical prediction is shown in Figure A2. For vertical parallel boreholes, the angular dependence may be written in terms of the source-detector distance r , the hole-to-hole separation x , and the vertical offset z between the source (or transmitter Tx) and the detector (or receiver Rx):

$$\sin(\theta) = x/r, \quad \cos(\theta) = z/r$$

Thus, setting the attenuation a in Equation 1 to be zero, we have

$$A_r = A_0/r * (1 - 2*[V_s/V_p * z/r]^2) * x/r \quad (6)$$

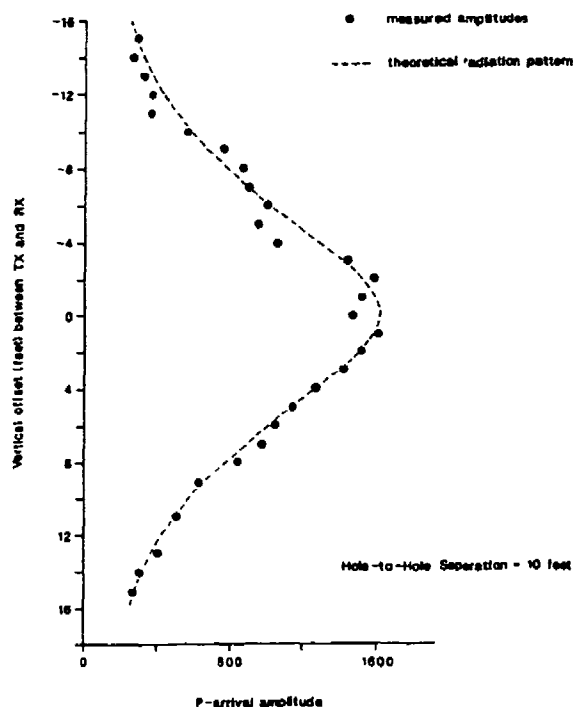


Figure A2 : Comparison of measured P-arrival amplitudes with the radiation pattern predicted by Heelan, 1953.

The measured amplitudes in Figure A2 were obtained at a damsite in Wyoming with the CORSEIS System operating in two boreholes drilled 10 feet apart in soil-crete (concrete mixed in place with soil). The measured amplitudes in general follow the predicted radiation pattern with the parameter A_0 set equal to 1600 and the V_s/V_p ratio set equal to .52. Deviations from the theoretical curve are caused by variations in the quality of the soil-crete.

REFERENCES

- Block, L. V., Cheng, C. H., Fehler, M. C., and Phillips, W. S., 1993. Seismic imaging using microearthquakes induced by hydraulic fracturing, *Geophysics*, in press.
- Dines, K. A., and Lytle, R. J., 1979. Computerized geophysical tomography, *Proceedings of the IEEE*, 67, pp. 1065-1073.
- Heelan, P.A., 1953. Radiation of a cylindrical source of finite length, *Geophysics*, Vol. 18, pp. 685-696.
- Peterson, J.E., B.N.P. Paulsson, and T.V. McEvilly, 1985. Application of algebraic reconstruction techniques to crosshole seismic data, *Geophysics*, vol. 50, pp. 1566-1580.
- Rectien, R.D., R.J. Greenfield, and R.F. Ballard, 1991. Tunnel signature prediction for a crosshole seismic survey, *Expanded Abstracts, SEG 61st Annual International Meeting*, pp. 518-521.
- Saito, H., 1989. Travel times and ray paths of first arriving seismic waves: a computation method based on Huygens' principle, *Expanded Abstracts, SEG 59th Annual International Meeting*, pp. 244-247.
- Saito, H., 1991. Anisotropic travelttime tomography at the Buckhorn Test Facility in Illinois, *Expanded Abstracts, SEG 61st Annual International Meeting*, pp. 123-126.
- Sambridge, M. S., 1990. Non-linear arrival time inversion: constraining velocity anomalies by seeking smooth models in 3-D, *Geophys. J. Int.*, 102, pp. 653-677.
- Schneider, W.A., and A.H. Balch, 1991. Tomographic inversion as a tunnel detection tool: a three-dimensional physical modeling feasibility study, *Expanded Abstracts, SEG 61st Annual International Meeting*, pp. 656-659.
- Williamson, P.R., M.S. Sams, and M.H. Worthington, 1993. Crosshole imaging in anisotropic media, *The Leading Edge*, vol.12, pp. 19-23.
- Wong, J., 1992. Cross-borehole seismic tomography survey: Belvoir Tunnel Test Site, Idaho Springs, Colorado, Final Report to the U.S. Bureau of Reclamation, Department of the Interior, Contract No. 1425-2-CR-81-18500.
- Wong, J., N.D. Bregman, G.F. West and P.A. Hurley, 1987. Crosshole seismic scanning and tomography, *The Leading Edge*, vol. 6, pp. 36-41.
- Wong, J., G.F. West, and P.A. Hurley, 1983. Crosshole seismology and seismic imaging in crystalline rocks, *Geophysical Research Letters*, vol. 10, pp. 686-689.

Session 5

Models

EFFORTS TO GENERATE GUIDED S-WAVES IN ROCK

J. M. Descour and R. J. Miller

Earth Mechanics Institute
Colorado School of Mines
Golden, Colorado 80401

ABSTRACT

A sudden release of a load applied between the opposite sides of an underground mine tunnel was proven to generate an explicit S-wave response in the rock in directions perpendicular to the load orientation. The duration of generated waveforms and/or their wavelength appeared related to the dimension of the tunnel, and to the elastic constants of the rock. In general, a stress distribution associated with oriented shear stress concentration along tunnels or boreholes appear to have a guiding effect on S-waves generated when a sudden stress release occurs. The presented phenomenon has a significant potential for improving detection of underground tunnels and anomalies of acoustic impedance in rock.

INTRODUCTION

Due to energy dispersion, the levels of seismic waves reflected from underground tunnels are typically very low compared to waves reflected from practically two-dimensional geologic strata. The data processing techniques presently in use for extracting reflected seismic waves from the "background noise" are very sophisticated, with no immediate prospect for a significant breakthrough in their efficiency. However, a considerable improvement appears possible by increasing the strength of waves *reflected* from tunnels through developing a technique to generate guided, and therefore stronger *incident* seismic waves. Also, the guided waves approach has a potential to significantly improve detection of tunnels between boreholes. The investigation in progress conducted at the Colorado School of Mines (CSM) produced promising results for S-waves.

BACKGROUND INFORMATION

The investigation was conducted at the geophysical Test Bed at the Colorado School of Mines Experimental Mine in Idaho Springs, Colorado. The mine operates/maintains the system of tunnels for educational and research purposes. Formerly the access tunnels of an approximately 100-year-old silver mine, the tunnels were developed by blasting in the gneissic rock. The layout of the tunnels is presented in figure 1.

The investigation concentrated on the directional characteristics of the seismic response to a sudden release of load applied between the two opposite points of the

tunnel's profile. The loading and release cycle was produced by the expandable hydraulic prop (fig.2), equipped with an instantaneous load release mechanism. When the load reached a predetermined range, an instantaneous load release in the prop triggered an elastic response in the rock. A pressure transducer connected to the hydraulic system measured the pressure change following the load release (fig.3). A carriage on rubber wheels was used to move the prop manually to different locations in the mine. The suspension of the prop allowed its rotation to the desired angle. The prop was activated subsequently at five locations underground, and at one location in the ventilation tunnel approximately 65m above the array and 10m below the surface (fig.1). At the underground locations the prop was activated either in the vertical position, or interchangeably in the vertical and horizontal positions. At the point above the array the prop was activated only in the horizontal position.

The seismic response to the stress release was monitored by an array of seven accelerometers. The accelerometers were coupled to the rock in 4-cm boreholes 30-cm to 120-cm deep. Six accelerometers were located in boreholes drilled from underground tunnels, and one was installed in a borehole drilled from the surface (fig.1).

Seismic signals detected by accelerometers were recorded by the digital data acquisition system. Each recording interval was triggered by the signal from the pressure transducer following the load release in the prop.

For all prop locations except one, the accelerometers underground were oriented to detect vertical components of motion, and the surface accelerometer was oriented horizontally and approximately 56 degree east-of-north (fig.1). For the prop at point S3 the orientation of each accelerometer was changed subsequently from vertical, to horizontal along the borehole, to horizontal perpendicular to the borehole. The prop was activated a minimum of three times in the vertical orientation, and subsequently in the horizontal orientation, for each accelerometer orientation. The records from each orientation of an individual accelerometer were normalized based on the pressure records from the prop. This approach allowed the three dimensional analysis of the ground motion at each accelerometer location.

RESULTS OF INVESTIGATION

The waveforms for a specific location and orientation of the prop were practically identical regardless of how many times the prop was activated (fig.4). The differences in their dynamics were proportional to the load differences at the moment of the load release (fig.5).

There were significant differences between waveforms from individual accelerometer locations for vertical and horizontal orientation of the prop. For the vertical prop orientation, the waveforms at all underground detection points (from 3m to over 120m from the prop), were characteristic of strong S-waves, and practically no P-waves (fig.6). An accelerometer at the surface location, approximately 120m above the prop detected both waves. For the horizontal orientation of the prop, S-waves dominated in directions

perpendicular to the loading direction (including the surface accelerometer), while P-waves appeared to prevail along the direction of loading (fig.7). The wave modes were identified based on the average group velocity of wave propagation in the CSM Experimental Mine, on the order of 5800m/s for P-waves, and 3000m/s for S-waves (Carmichael, 1989 & lab ultrasonic data)

Based on the velocity analysis for S-waves in directions perpendicular to the direction of loading, the velocity was the highest in proximity to the prop (load application/release), with the tendency to decrease exponentially with distance (fig.8). The opposite relationship with distance from the source was detected for the inverse of the dominant frequency (dominant wave period) for S-waves (fig.9). By combining both results using the distance as a parameter, a practically linear relationship was obtained between the average velocity of S-waves and the log dominant period (fig.10). The slope of this relationship appears the same for different prop locations in the mine. The dominant wave period at the source could be evaluated by the extrapolation of the period values toward the source (fig. 9). For the period at the source, the velocity at the source could be read from figure 10. The product of both the velocity and the dominant wave period at the source, on the order of 2m, should be proportional to the average diameter of the elastic stress envelope generated in the rock by the prop. For the conditions at the CSM Experimental Mine the stress envelope appeared to follow the profile of the tunnel.

Based on the three-dimensional analysis, the ground motion caused by S-waves appears to retain a significant component of the original orientation of the load at the source (fig.11). The deviation may be related to the dispersion of seismic waves caused by convolution with the anomalies in the rock (e.g.: joint systems, lamination).

The results obtained for the prop activated in the underground locations appeared indicative of a guided S-wave effect produced by the rapid (short wave) load changes in the practically stationary loading system generated by the prop.

Subsequently, the prop was installed in the ventilation tunnel, approximately 65m above the underground array, to test the feasibility of sending strong S-waves from the surface down. The waveforms in figure 12 were detected from the prop activated in the ventilation tunnel, and provided strong evidence for a guided S-wave effect. The waveforms were dominated by S-waves with the most explicit S-wavelets detected at point 2, the closest point to the vertical plane of symmetry perpendicular to the prop.

CONCLUSIONS

Considering the relatively uniform characteristics of the gneissic rock in the CSM Experimental Mine, the effect of guided S-waves could not be attributed to the presence of any wave-guiding rock layer.

Because of the symmetry of the loading system with respect to the profile of the tunnel, a significant part of the stress distribution produced by the system at each location appeared to resemble the pure shear stress in rock (Ohert et al, 1967). Those conditions

differ from the traditional S-wave sources where lack of symmetry appears responsible for significant P-wave components, and an asymmetry in the directional radiation characteristics (Waters, 1978).

The elastic stress anomaly formed in the rock by a relatively slow shear loading prior to the load release appears to result in a consequential guiding effect along the plain of symmetry perpendicular to the direction of loading. This phenomenon should be directly applicable for generating guided S-waves in boreholes. However, it does not appear feasible for practical applications to generate this type of stress anomaly from the surface. For surface conditions, a combination of low and high frequency horizontal loads applied in a symmetrical arrangement (a set of dipoles), with the proper shift in phase between the low and high frequency stimulation may generate similar wave guiding effect. The investigation in this approach will continue.

REFERENCES

1. Waters, K. H., 1978, "Reflection Seismology. A Tool for Energy Resource Exploration," Wiley, 377 pp.
2. Obert, L., and W. I. Duvall, 1967, "Rock Mechanics and the Design of Structures in Rock," Wiley, 650 pp.
3. Carmichael, R. S., 1989, "Practical Handbook of Physical Properties of Rocks and Minerals," CRC Press Inc., 741 pp.

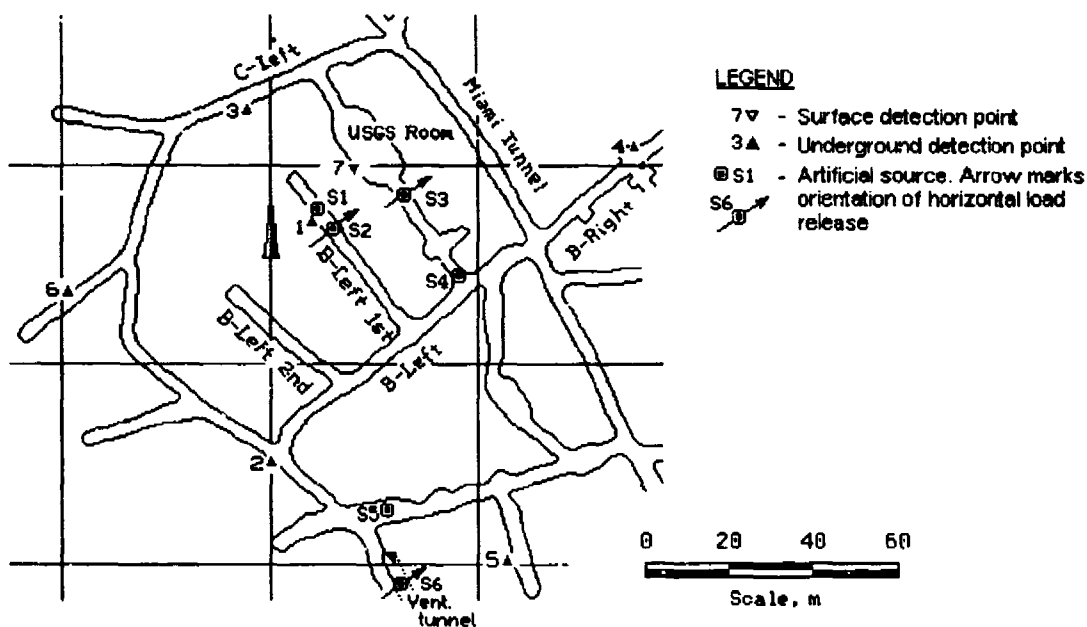


Figure 1. - Layout of tunnels, configuration of microseismic array, and locations of artificial source (prop) in the CSM Experimental Mine.

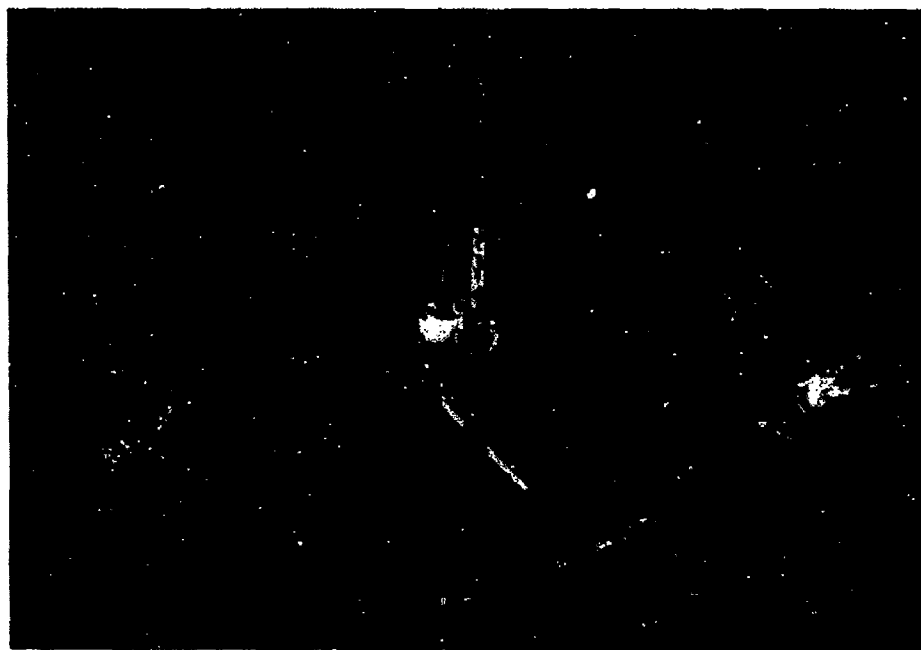


Figure 2. - The prop installed at point S2 for horizontal load release.

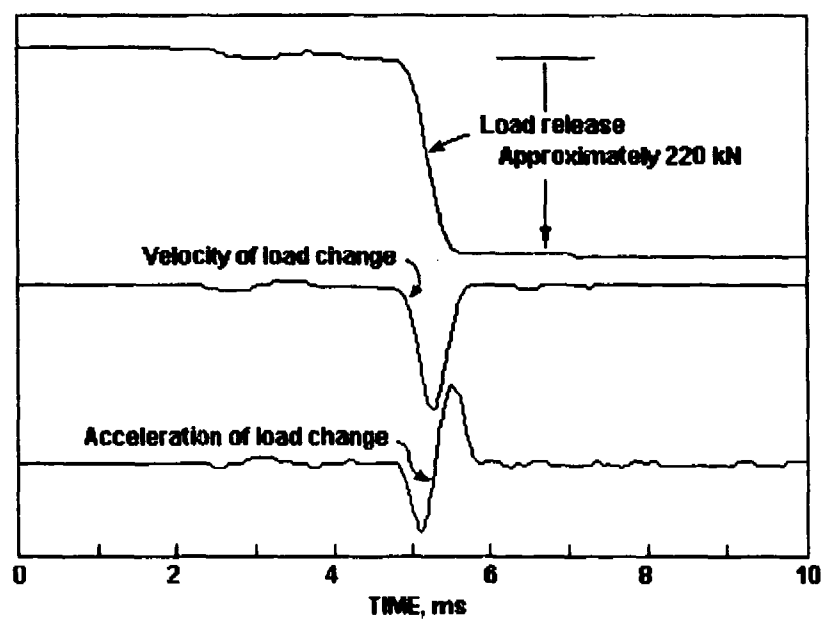


Figure 3.- Record of hydraulic pressure change in the prop (top), and the velocity (middle) and acceleration (bottom) of the change.

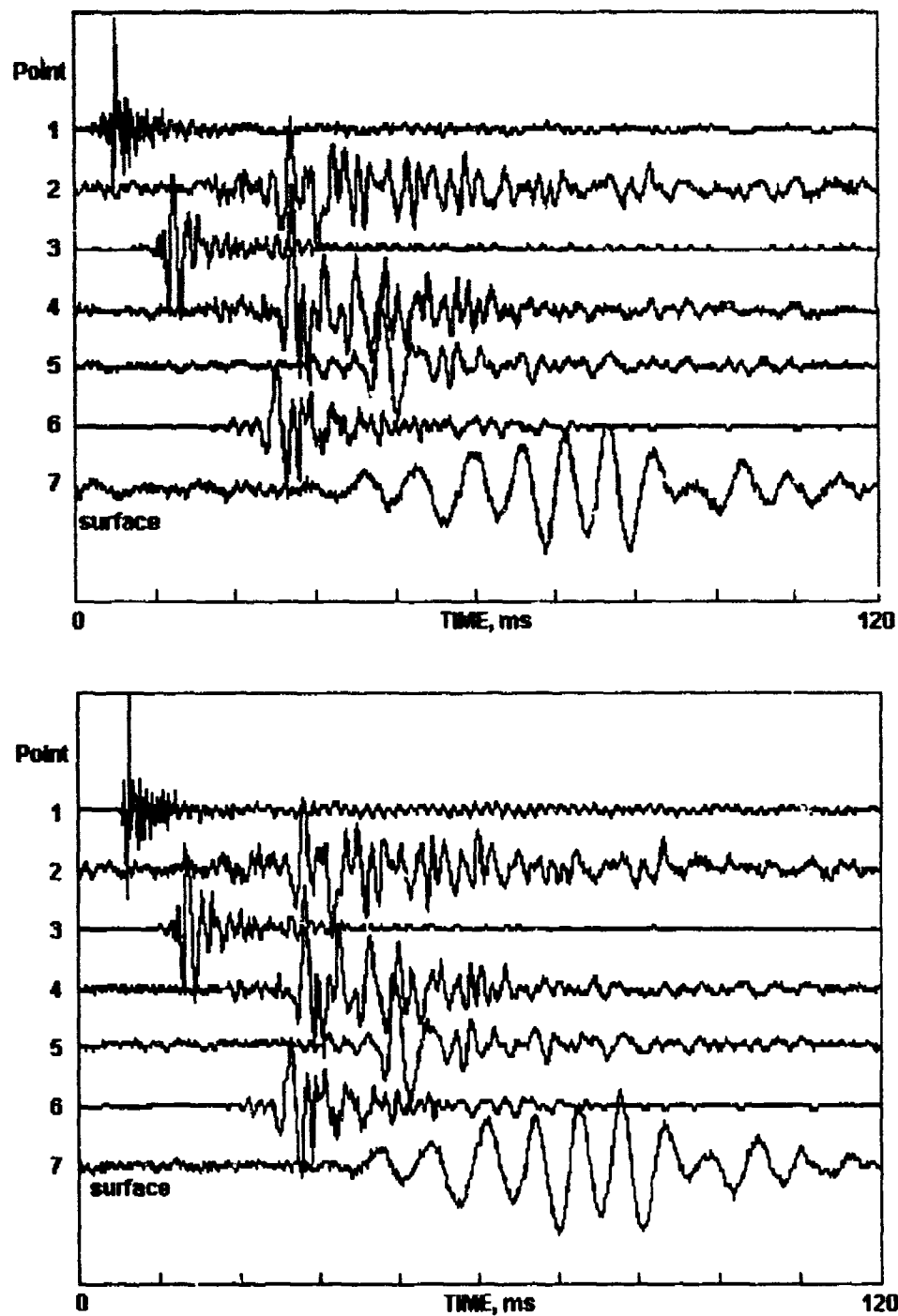
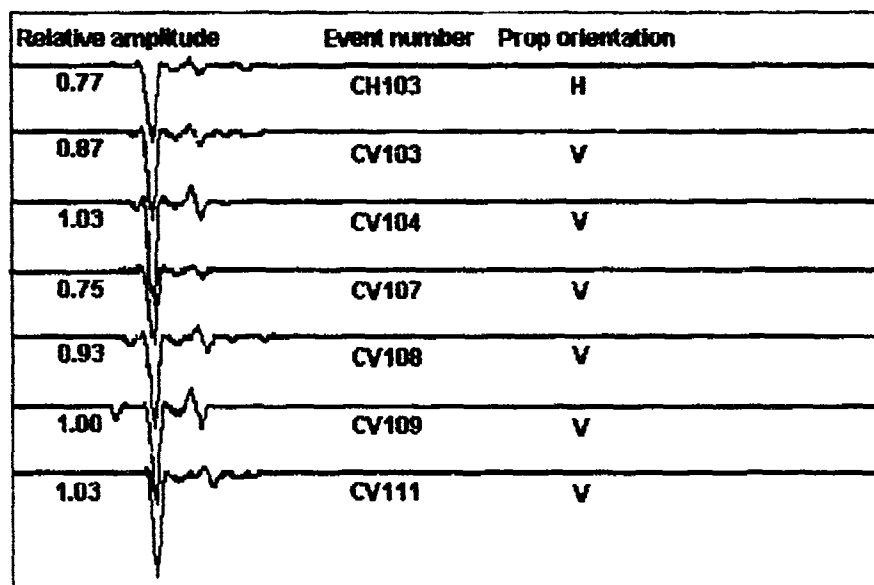


Figure 4. - Two sets of waveforms for two separate vertical discharges of the prop at point S1. Note an explicit match between both sets, confirming a significant repeatability of the source.

A



B

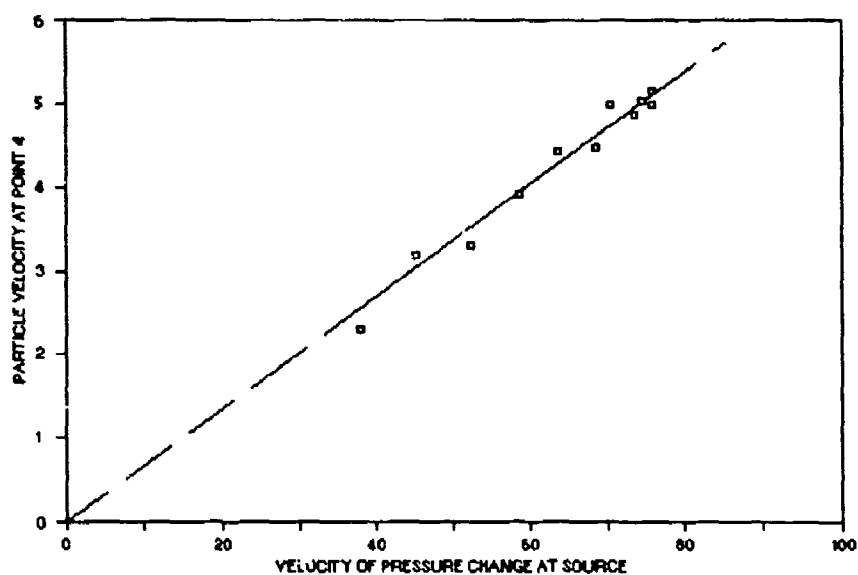


Figure 5. - The peak velocity of the pressure discharge (**A**) provided an effective measure of the energy released by each prop discharge (**B**), regardless of the orientation of the prop. Data at **B** from detection point 4 and for vertical prop discharge at S3.

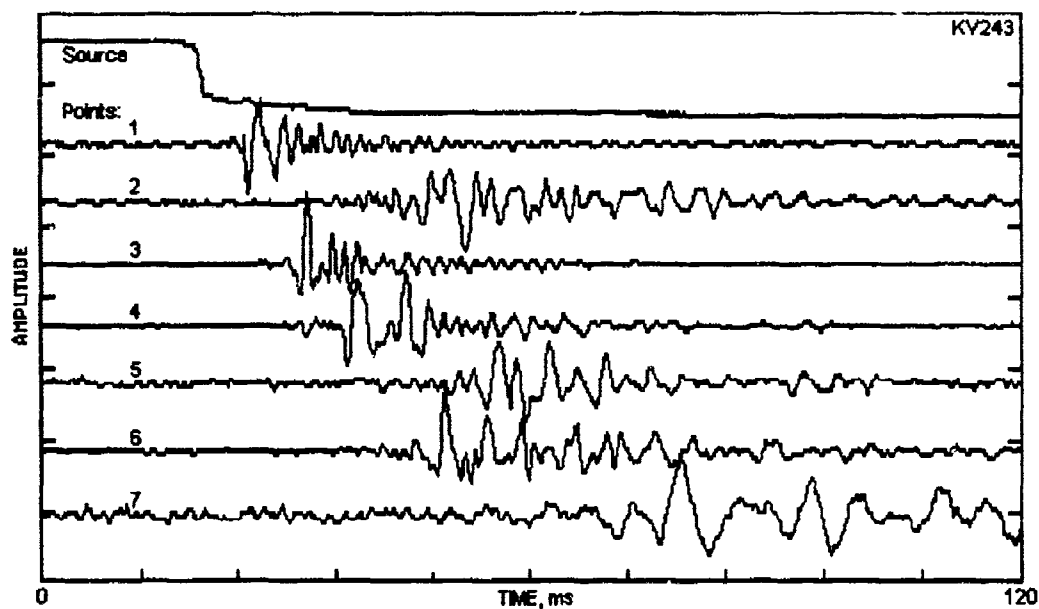


Figure 6. - Waveforms for vertical prop discharge at point S3. Note S-waves dominating at horizontal array underground, and significant P-waves detected at point 7 above the prop.

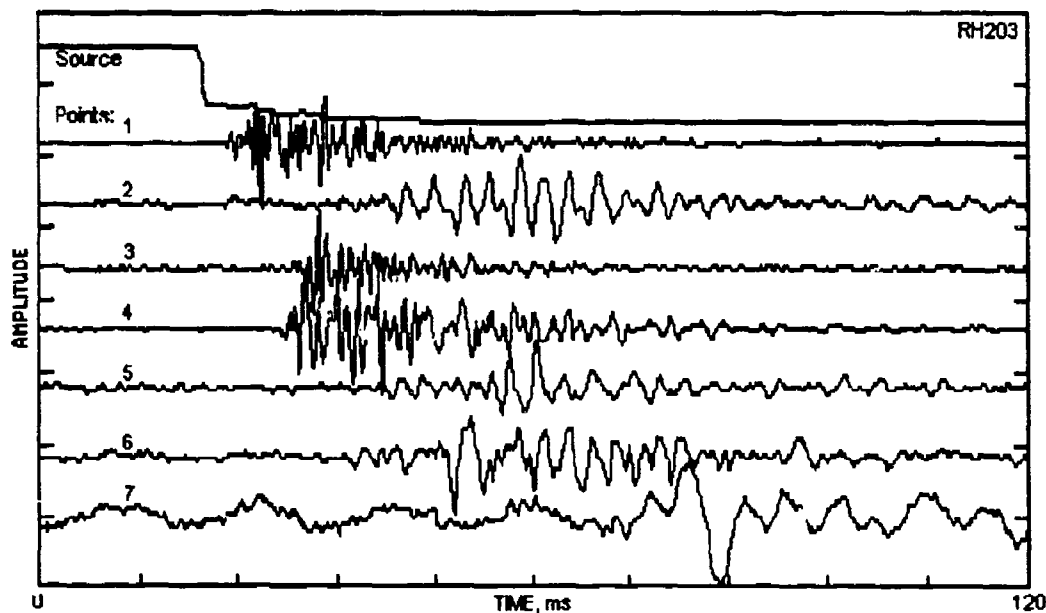


Figure 7. - Waveforms for horizontal prop discharge at point S3. Note the levels of P-waves depending on location of sensors with respect to the direction of discharge.

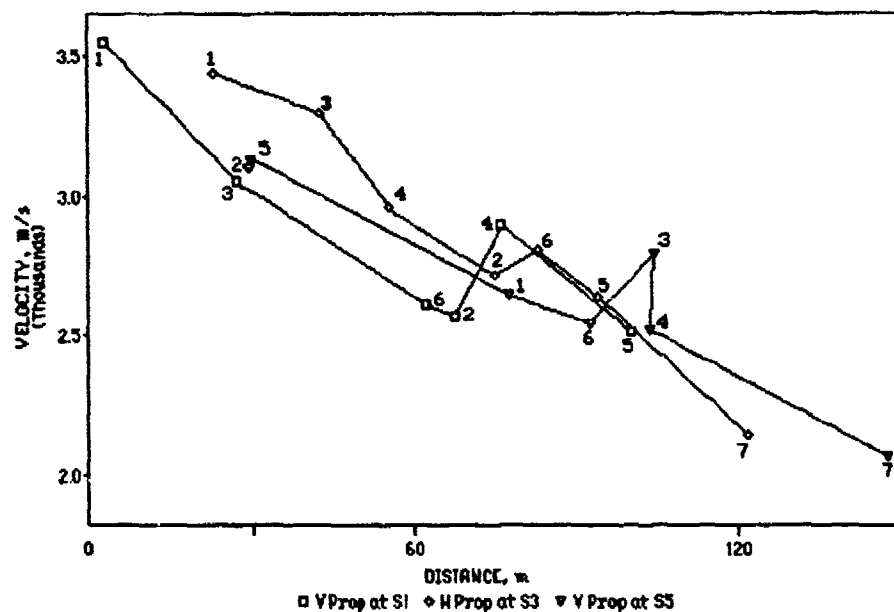


Figure 8. - Typical group velocity changes for S-waves with distance. Data from vertical prop discharges at points S1, S3, and S5.

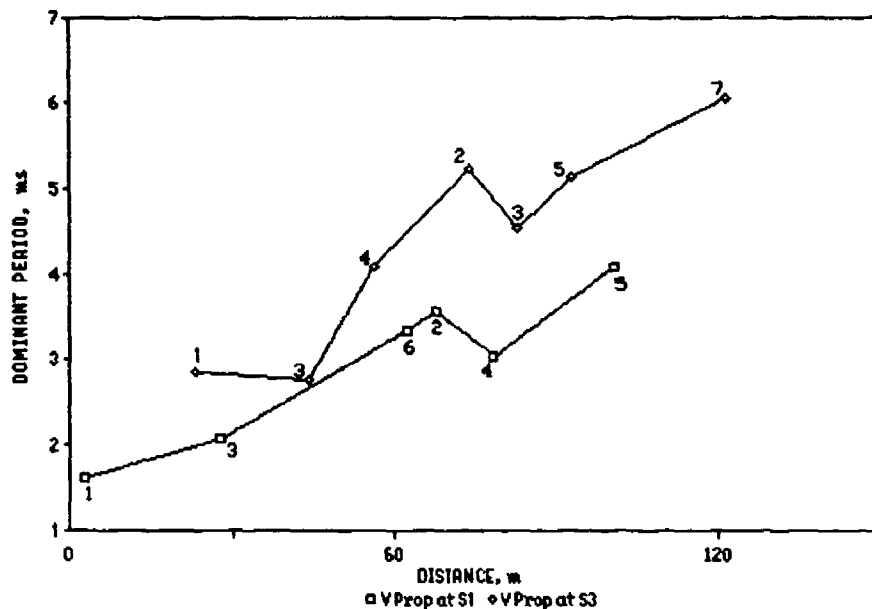


Figure 9. - Typical changes for dominant wave period (inverse of frequency) for S-waves with distance. Data for vertical prop discharges at points S1 and S3.

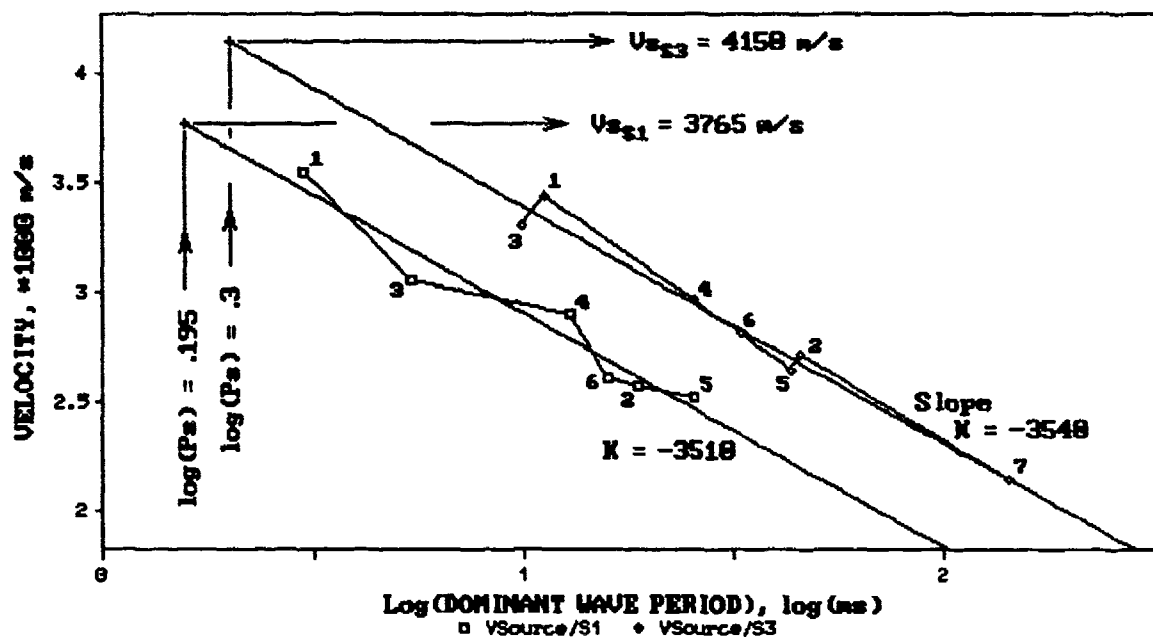


Figure 10. - Relationship between group velocity, and dominant wave period (inverse of frequency) for S-waves detected for the vertical prop discharges at points S1 and S3. The differences appear related to the size of the tunnel at the prop location.

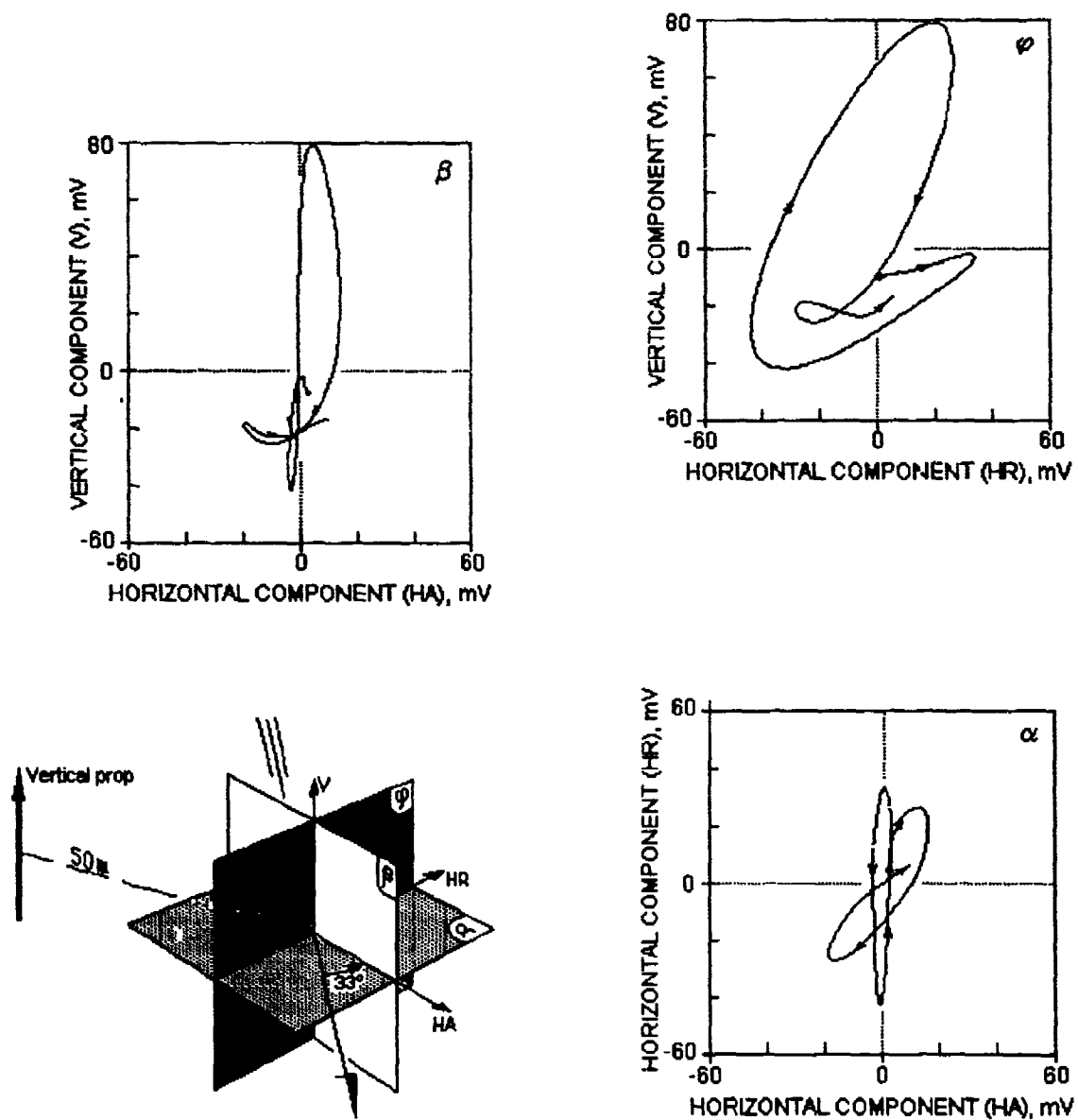


Figure 11. - Two-dimensional projections (a, b, c) of ground motions produced at detection point 3 by the S-wave response to the vertical prop discharge at point S3. Orientation of coordinates: HA - north 33-degree west; HR - south 57-degree west; V - up.

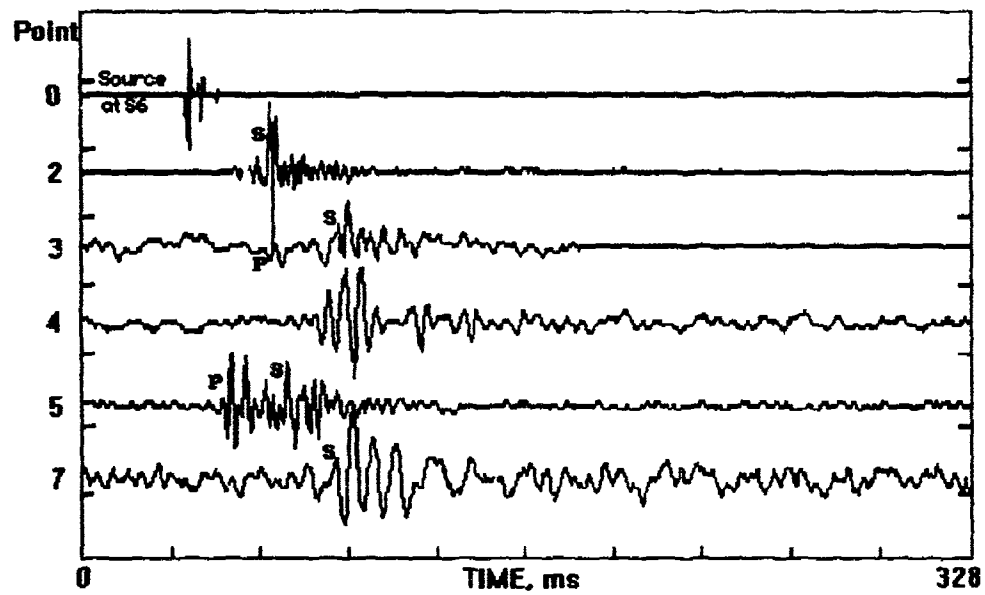


Figure 12. - Waveforms detected for horizontal prop discharge at the ventilation tunnel (point S6). Note an explicit S-wave response at point 2 underground, and a significant P-wave response at point 5 situated approximately 45-degree of vertical with respect to the source.

DEVELOPMENT OF A WIDE-BAND AMPLITUDE AND PHASE MEASUREMENT SYSTEM FOR UNDERGROUND IMAGING

Tae-Sook Ha, Jung-Sang Yun, Jin-Seob Kang, and Jung-Woong Ra

Department of Electrical Engineering

Korea Advanced Institute of Science and Technology

373-1, Kusung-dong, Yuseong-gu, Taejeon, Korea

ABSTRACT

A continuous electromagnetic wave system is developed to measure the amplitude and phase of the diffracted field in the cross-borehole of its depth of 500 meters in the frequency range up to 150 MHz. From the in-situ measurement values, it shows the detectability of the air tunnel and the possibility of producing incoherent multi-frequency tomogram of high contrast object.

INTRODUCTION

Deep dormant underground tunnel may be detected by using pulse[1] or continuous electromagnetic wave[2,3]. Continuous electromagnetic wave system measures the forward diffraction pattern scattered by the air tunnel and only the amplitude pattern has been utilized in the cross-borehole radar[3]. Although the laboratory measurement of the phase delays across an air-filled cylinder in the scale-down cross-borehole similitude experiment exhibited a resonance feature in the phase as well as in the amplitude[4], in-situ measurement of phase delays has not been reported. This is mainly due to a very long coaxial cable to operate in the borehole of 500 meters deep. A Radiowave Geo-Vision System (Ra-Geovis) has been developed to measure the amplitude and the phase of the diffracted field as a continuous electromagnetic wave cross-borehole radar.

Outline of the Ra-Geovis System

A network analyzer is used to measure the amplitude and the phase of the received signal in the frequency range up to 150 MHz. Typical operating amplitude and phase errors are 0.45 dB and 2.5 degrees at the signal level of -90 to -100 dB and -60 to -70 dB compared with the reference signal, respectively. In order to feed the transmitted power to the radiating antenna in the borehole of its depth of about 500 meter via coaxial cable, a radio wave power amplifier of 200 watts output power is used to cover the 500 meter cable attenuation of about 17 dB at 50 MHz. A low noise amplifier is fabricated and used in the receiving antenna to detect up to -150 dBm signal, where about 60 dB attenuation occurs between the boreholes of 20 meters apart as a free space divergence loss(-48 dB) and the medium loss(-12 dB).

Two (transmitting and receiving) cable drums are needed to control the positions of the antennas in the borehole and they are closely installed in the field shelter. Large transmitting power is directly coupled to the receiving cable in the drum which makes the measurement of the very low received signal detected in the receiving antenna impossible. One may, however, convert the frequency of the received signal in order to isolate the direct coupling between the cables and reconvert to the original received frequency to measure the amplitude as well as the phase by the network analyzer.

Sytem dynamic range of the Ra-Geovis is measured as more than 180 dB where the radiated power from the transmitting antenna is about 33 dB at 50 MHz and -150 dBm signal is detectable at the receiving antenna. System measurement errors of amplitude and phase are ± 1 dB and ± 2.5 degree in dynamic range, respectively.

In-Situ Measurements

An artificial tunnel of about 2 meters in its diameter in the depth of about 75 meters from the surface is detected. The distance between two boreholes is 10 meters and this tunnel is located in the water-saturated granite medium. Measured amplitude and phase patterns versus the borehole depth are shown in Figure 1 and 2, respectively, for various frequencies from 30 MHz to 65 MHz. One may find resonance phenomena at the depth of the tunnel via the interference fringes of the single dip

changing into the double dips as the frequency increase in the depth lower then 81 meter and higher then 70 meters where there is no tunnel, as shown in figure 1.

The phase in figure 2. changes rather abruptly at about boundaries of the tunnel by about 180 degrees, which it keeps almost constant values in the other depth. The phase jump of 360 degrees in figure 2. may be noted as no change in its phase.

These pattern may be generated from the theoretical analysis of the field diffraction by the tripizodal air cavity.[4] Because of the asymmetry in the cross section, double dips are asymmetry depending on frequencies. Phase jumps are concave for either lower frequencies then null frequency of lower boundary or upper frequency then null frequency of upper boundary or 180 degrees twice either upward or downward for the inn-between frequencies of the null frequencies of the upper and the lower null.[4]

From the measured amplitude values, one may reconstruct an incoherent multi-frequency tomogram shown in figure 3. Ten different frequencies from 30 MHz to 65 MHz are used with one parallel and four off-set angle (15, 30, 45 and 60 degrees) measurements in every 0.1 meter increment antenna position. Logarithm of the different frequency amplitudes are added to produce the average amplitude values which are back-projected to obtain this tomogram. At the depth of about 74 meters, low amplitude areas (up to green) are clearly shown but the artifact areas of blue colours are also shown.

Conclusion

A continous electromagnetic wave system capable of measuring the amplitude and phase in the deep cross-borehole mode has been developed. This system is shown to produce an incoherent multi-frequency tomogram for high contrast objects and diffraction tomogram.[5] One may also utilize this system for the pulsed electromagnetic response by superposing multi-frequency response.

References

- [1] Duff, R. 1988, "Short pulse hole-to-hole electromagnetic tunnel detection system and signal processing development," Proceedings of the Third Technical

Symposium on Tunnel Detection, Golden, Colorado, Jan.

- [2] Lytle, R. J., Laine, E. F., Lager, D. L., and Davis, D. T., 1979, "Cross-borehole Electromagnetic Probing to Locate High-contrast Anomalies," Geophysics, Vol. 44, No. 10, pp. 1667-1676.
- [3] Lee, T. K., Park, S. O., Kim, S. Y., and Ra, J. W., 1989, "Near-field Diffraction Pattern by an Underground Void of Circular Cylinder," Microwave and Optical Technology Letters, Vol. 2, No. 5, pp. 179-183.
- [4] Lee, T. K., Kang, J. S. and Ra, J. W., 1993, "Near-field diffraction pattern by a tripezoidal cylinder air cavity," Proceedings of the Fourth Technical Symposium on Tunnel Detection, Golden, Colorado, April. this volume
- [5] Kim, J. H. ,Kim, S. G. and Ra, J. W., 1993, "Cross-hole tomography using improved Born inversion," Proceedings of the Fourth Technical Symposium on Tunnel Detection, Golden, Colorado, April. this volume

KAIST MICROWAVE LAB. : Mar. 25 1993

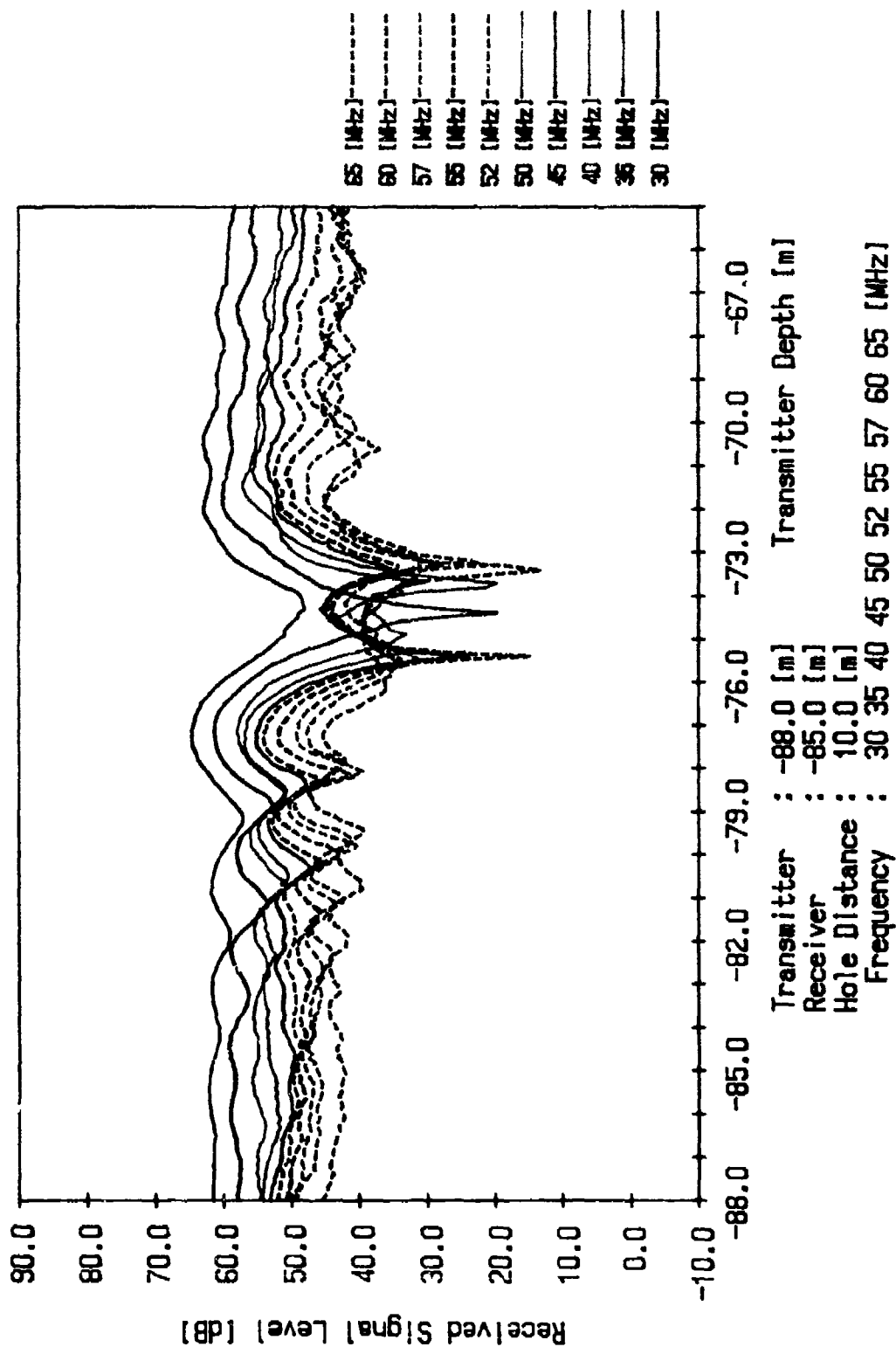


Figure 1. Measured Amplitude Pattern Diffracted by an Air Tunnel in a Granite.

KAIST MICROWAVE LAB. : Mar. 25 1993

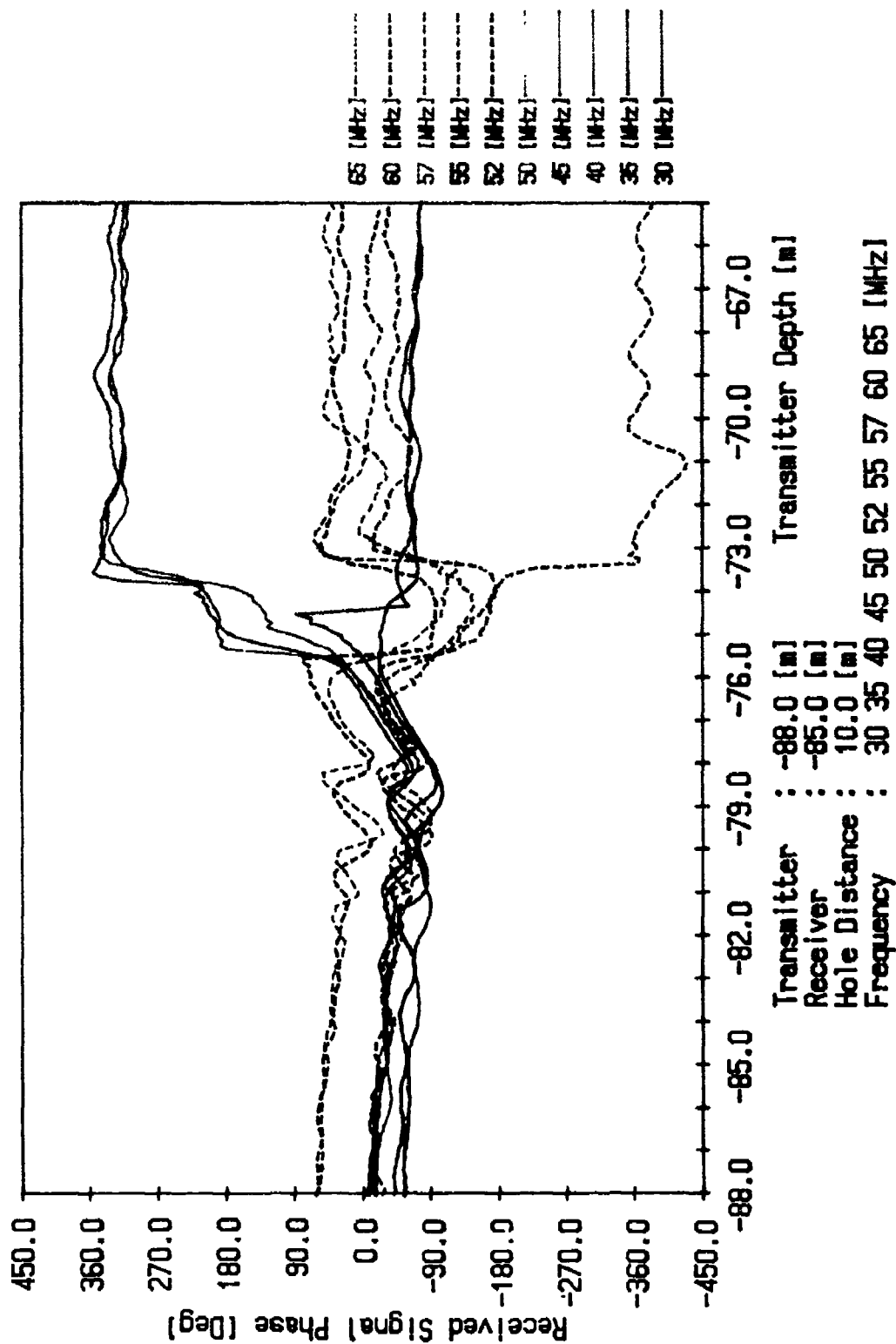
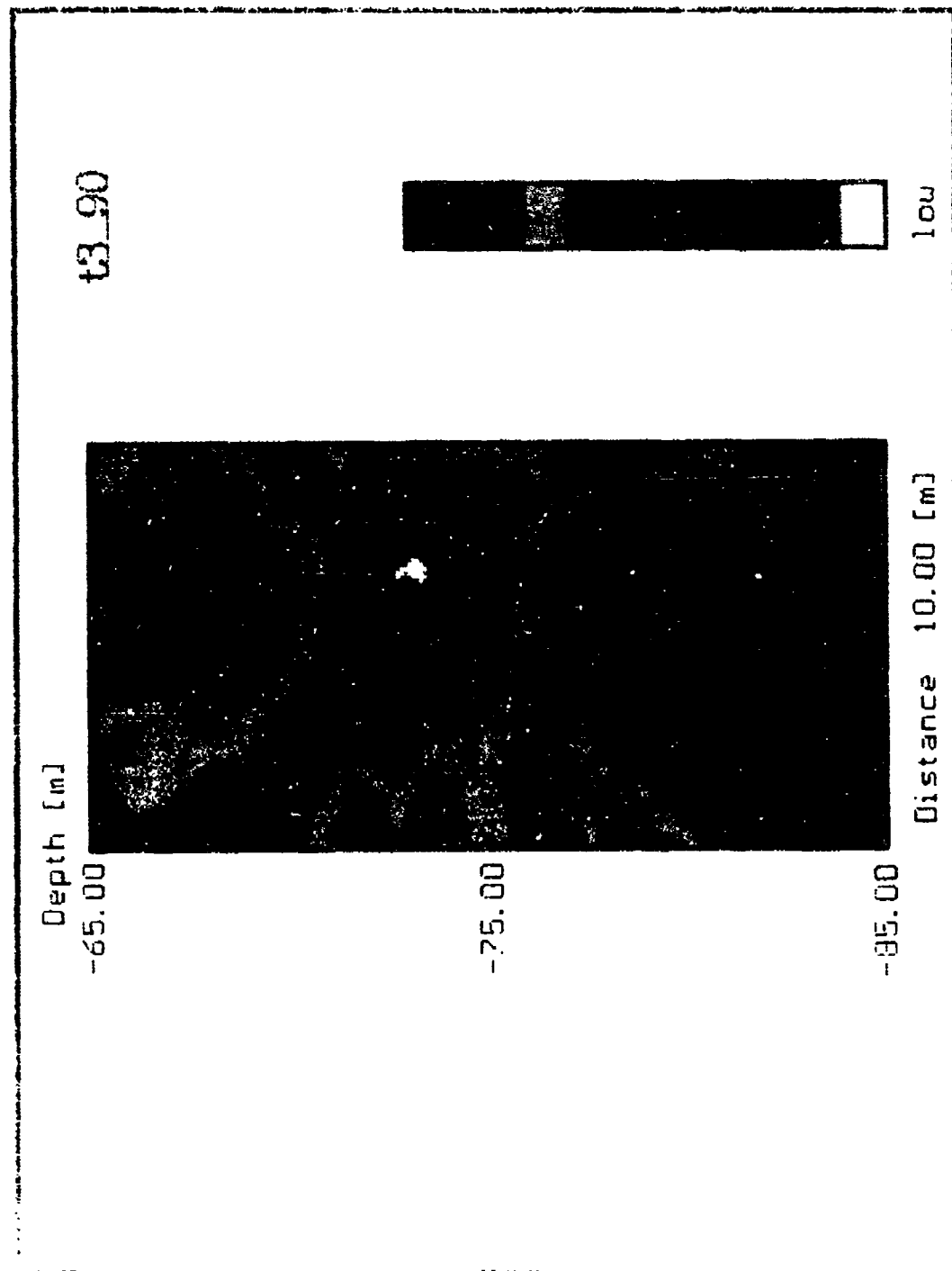


Figure 2. Measured Phase Pattern Diffracted by an Air Tunnel in a Granite.

KAIST MICROWAVE LAB : Mar 26 1993



HOLE DISTANCE : 10[m]
FREQUENCY : 30, 35, 40, 45, 50, 52, 55, 57, 60, 65[MHz]
VIEW ANGLE : 0, 15, 30, 45, 60[Deg]

Figure 3. Incoherent Multi-Frequency Tomogram.

**FORWARD MODELING OF ELECTROMAGNETIC WAVE PROPAGATION IN LAYERED
MEDIA: IMPLICATIONS FOR CROSS-BOREHOLE RADIO-WAVE DETECTION OF
VOIDS IN COAL MEASURE ROCKS**

Mike Jackson
Twin Cities Research Center, U.S. Bureau of Mines

Eric Wedepohl
South African Chamber of Mines Research Organization

Mike Friedel and Ken Hauser
Twin Cities Research Center, U.S. Bureau of Mines

ABSTRACT

The U. S. Bureau of Mines, in collaboration with the South African Chamber of Mines Research Organization, has carried out field experiments and forward numerical modeling, to evaluate the effectiveness of cross-borehole radio-wave surveys for detection and characterization of abandoned coal mine workings. The results show that in narrow coal seams, interference effects associated with reflection become important, and may mask the transmission and diffraction signatures of mining voids. In-seam data acquisition, when practical, helps to avoid these problems. Cross-borehole tomography is predicted to be successful when the geometrical configuration and electrical properties are such that radio wavelengths are comparable to or smaller than void dimensions and bed thicknesses.

INTRODUCTION

Subsurface imaging methods using seismic or electromagnetic waves may utilize 1) the directly-transmitted, 2) the reflected, or 3) the scattered (diffracted) wave field. Transmission tomography (Dynes and Lytle, 1979; Worthington, 1984) has been successfully applied to numerous mining-related problems (Thill et al., 1992; Friedel et al., 1992; Young and Maxwell, 1986). Diffraction tomography (Devaney, 1984) is less commonly used due to the difficulties associated with extracting the scattered component from the total wave field, but offers superior resolution when these difficulties can be overcome (Lo et al, 1988). Tomographic studies in coal beds are commonly carried out using in-seam waves (Wattrus, 1984; Shope, 1987; Stolarczyk, 1990; Dennen and Stroud, 1991), but cross-borehole tomography presents particular challenges (Menke, 1984; Ivansson, 1986; Bregman et al., 1989).

In a collaborative effort with the South African Chamber of Mines Research Organization (COMRO), the Bureau of Mines has collected and analyzed a set of cross-borehole radio-wave amplitude

data, and carried out numerical forward modeling of radio wave propagation through coal measure strata. The two principal objectives of the study were: 1) to determine the conditions under which cross-hole radio-wave transmission tomography is an effective means of locating and characterizing abandoned coal mine workings, and 2) to determine whether the scattered wave field from a mining void could be adequately identified in a cross-borehole setting.

Data were obtained using COMRO's transmitting and receiving apparatus at the Randallson Mine in eastern Ohio. This mine has been inactive for a number of years, and reliable maps of the underground workings are not available. New mining operations in the vicinity (Fairfield Coal Co.) are concerned about potential hazards related to the abandoned workings. A series of holes was drilled by Fairfield at the Randallson site (Fig. 1); one of them (H30) encountered a void in the 1-meter thick coal layer, at a depth of approximately 16

meters. Cross-borehole data were collected using boreholes H29 and H31, in which solid coal was encountered (Fig. 1).

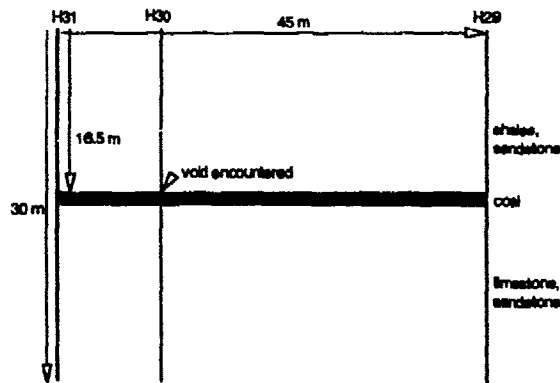


Figure 1. Borehole geometry and generalized stratigraphy at Fairfield site.

ROCK PROPERTIES

Laboratory measurements of the electrical properties of representative hand specimens showed that the coal has a much higher resistivity than the other rock types (i.e., it is more transparent to electromagnetic wave energy); limestone and sandstone were least resistive, and shales had intermediate values (Table 1). Calculations using the measured values of resistivity and dielectric constant at a frequency of 4.4 MHz indicate propagation velocities ranging from 6.6×10^7 m/s in the sandstone and limestone to 1.1×10^8 m/s in the coal, with corresponding radio wavelengths ranging from about 15 m to approximately 25 m. Calculated attenuation rates vary considerably, from 0.03 dB/m in the coal to 1 dB/m in the limestone.

Resistivities determined in the laboratory decrease with increasing frequency. At 23 MHz, the approximate resistivities of the coal, shale, and sandstone/limestone samples were 2000, 150, and 100 Ohm-m, respectively. The reduced resistivity values result in lower calculated velocities, which together with the higher frequency lead to significantly smaller wavelengths than those at

Table 1. Summary of Electrical Properties (4.4 MHz)

Sample #	Rock Type	ρ	k	α	v	λ
17	coal	22000	7	0.03	113	25.8
18	coal	21000	8	0.03	107	24.4
21	shale	1700	10	0.30	92	21.3
22	shale	2000	10	0.25	94	20.9
19	sandstone	485	18	0.80	69	15.7
20	sandstone	550	18	0.71	70	16.0
24	limestone	375	20	1.00	66	15.1

ρ : resistivity, Ohm-m

k: dielectric constant (ϵ/ϵ_0)

α : attenuation, dB/m

v: phase velocity, 10^6 m/s

λ : wavelength, m

4.4 MHz. The calculated wavelengths at 29 MHz are comparable to the coal seam thickness and expected void size at the field site, and should therefore provide adequate resolution. However, the calculated attenuation rates are much higher at 29 MHz, and penetration ranges are diminished accordingly.

FIELD DATA

The apparatus for measurements made in the field consisted of two vertical electric dipole antennas, each 4 meters in length; a continuous transmitter with operating frequencies from 2 to 30 MHz and a power output of approximately 2 W; and a sensitive receiver. Field profile measurements were conducted by placing the receiving antenna at a particular depth in one of the boreholes, moving the transmitting antenna up or down the other borehole in one-meter steps, and noting the amplitude received at each step. These amplitude measurements were recorded (in dB relative to 1 mV) at five different frequencies for each source and receiver position: 4, 7, 18, 23, and 29 MHz. Twenty five profiles were measured in this way, yielding amplitude measurements along approximately 500 ray paths for each of the five frequencies.

Figure 2 shows some representative amplitude data for individual receiver positions. Several features of the data are noteworthy. First, amplitudes were too low to measure for some source and receiver locations, particularly in the lower half of the boreholes (where the lithology is dominated by more conductive

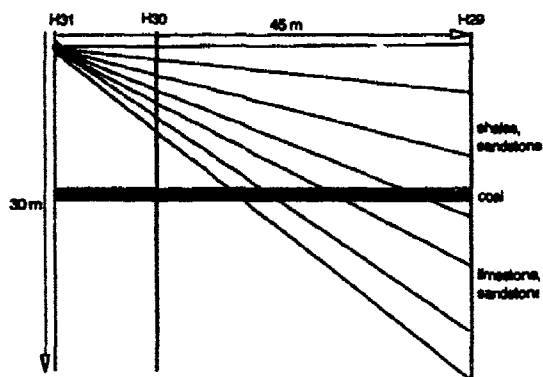


Figure 2a. Profile 1 data acquisition geometry. Receiver at 2 meters depth in H31.

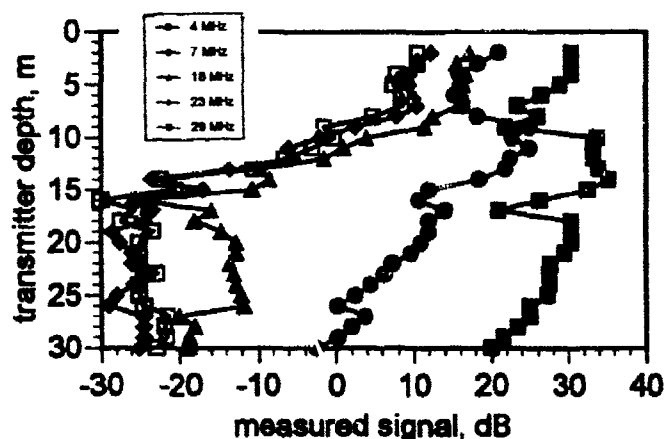


Figure 2b. Measured amplitude profiles for the five frequencies.

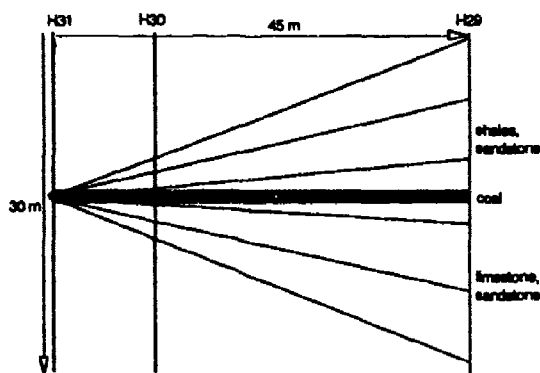


Figure 2c. Profile 2: receiving antenna at 16.5 m depth, centered in coal seam.

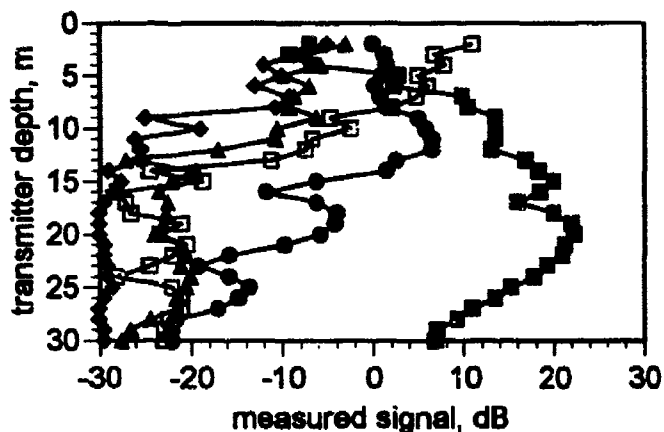


Figure 2d. Measured amplitudes for profile 2.

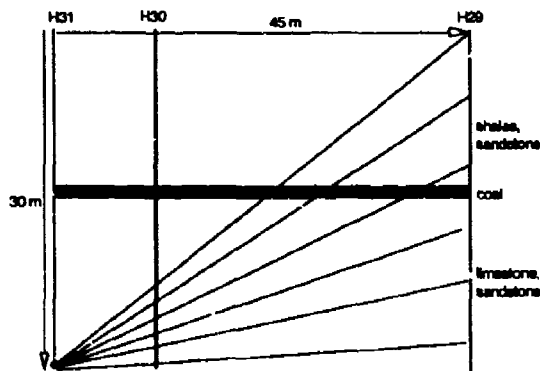


Figure 2e. Profile 3.

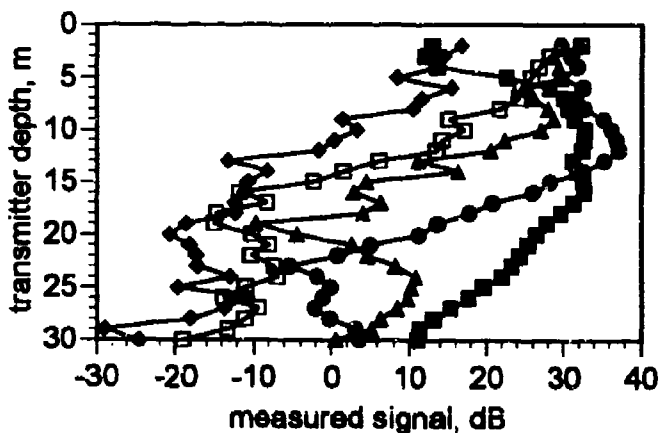


Figure 2f. Measured amplitudes for profile 3.

sandstones and limestones), and particularly at the higher frequencies. This may be interpreted in terms of stronger attenuation in the more conductive lower layers and at higher frequencies. Second, although the coal is highly resistive, amplitudes measured in the vicinity of the coal tended to be anomalously low (depth interval approximately 16 to 18 m). This is a surprising result, and may indicate ineffective antenna-to-seam coupling, since the antenna length is much larger than the seam thickness. Third, there are sharp local minima in the amplitude profiles at other depths, varying with frequency.

Data reduction prior to tomographic analysis involved corrections for the angular dependence of radiated energy, for receiving antenna angular sensitivity, and for amplitude reduction due to spherical spreading of the electromagnetic waves. Transmission tomograms were calculated for each frequency using an iterative straight-ray reconstruction technique (Tweeton and Jackson, 1992) and a grid of 20 x 20 cells, with a uniform starting model. Fifteen iterations generally reduced the root-mean-square residual to less than half that of the starting model. However, the resulting images of the attenuation distribution generally bore little resemblance to the expected horizontally layered structure. The likely cause for the disparity is the fact that the tomographic inversions neglected interference effects involving refraction, reflection and diffraction, which are probably significant in view of the strong contrasts in electrical properties (Table 1). In particular, diffraction from the void combines with stratigraphically-controlled reflection and refraction to produce secondary phases that interfere with directly transmitted energy. In order to evaluate the importance of these effects, a series of numerical forward models were computed using software developed by COMRO.

FORWARD MODELING

FORMOD uses a volume-integral method to calculate amplitude profiles for a homogenous half-space model with embedded anomalies. The software assumes a fixed transmitter oriented perpendicular to the survey plane; therefore the transmitter is treated as a point source, with radiation independent of direction. Note that in the forward modeling, the electric fields are therefore horizontally polarized, whereas in the field data they are vertical. Calculations were performed for two frequencies, 7 and 23 MHz, corresponding to wavelengths of approximately 12 and 4 meters, respectively, in the homogeneous material. Figure 3 shows the effects of exponential attenuation and spherical spreading in a uniform medium with a dielectric constant of 12 ($k=\epsilon/\epsilon_0=12$), relative magnetic permeability of 1 ($\mu=\mu_0$), and electrical resistivity ρ of 500 Ohm-m, typical of the values measured on laboratory specimens. These properties may be denoted by the ordered triple (12, 1, 500), and this notation will be used for the

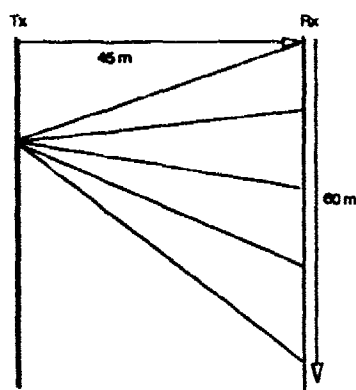


Figure 3a. Forward model, no anomalies.

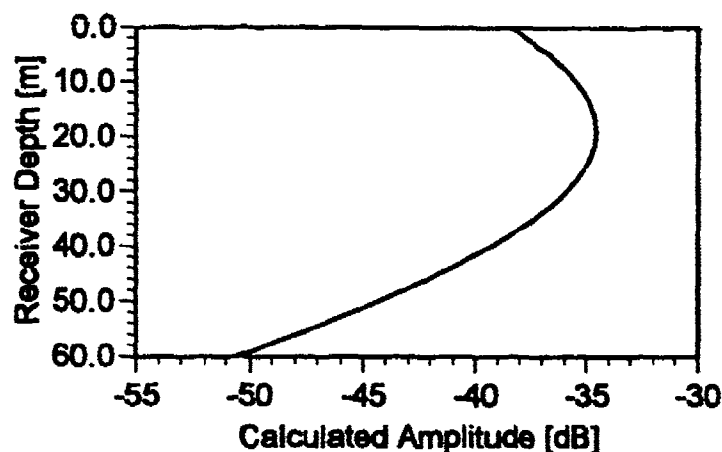


Figure 3b. Calculated amplitude profile, 7 MHz.

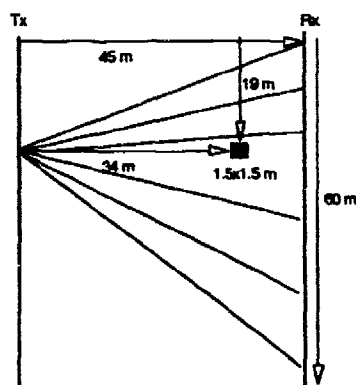


Figure 4a. Model with 1.5 m void near receiving borehole.

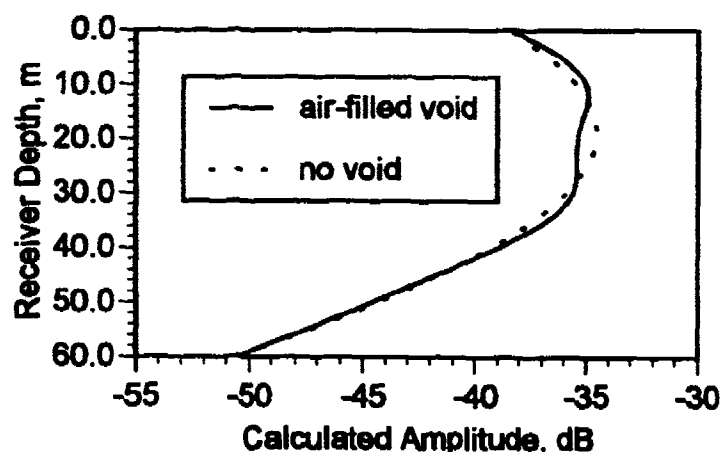


Figure 4b. Calculated amplitude profile, 7 MHz, air-filled void.

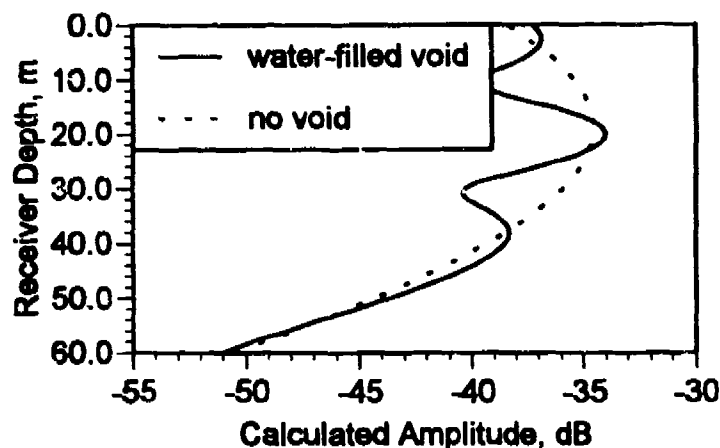


Figure 4c. Calculated amplitude profile, 7 MHz, water-filled void.

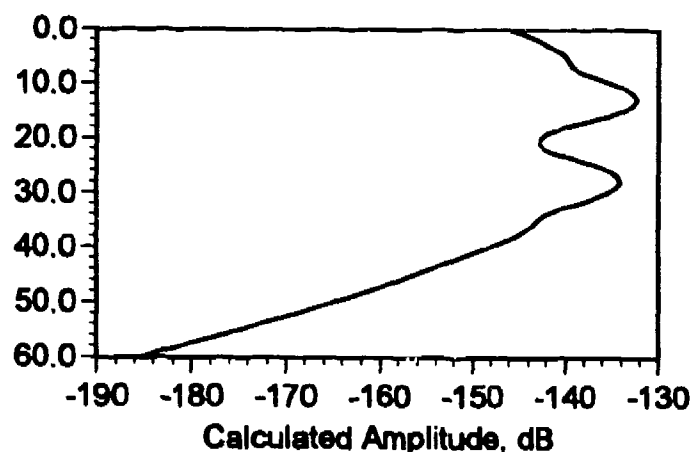


Figure 4d. Calculated amplitude profile, 23 MHz, air-filled void.

remainder of this report.

Figure 4 illustrates diffraction effects at 7 MHz associated with a small anomaly near the receiver hole. Two cases are considered: a highly resistive air-filled void (1, 1, 10^7), and a relatively conductive water-filled void (70, 1, 250), both in relatively resistive coal. Note that the anomaly projects as a local minimum amplitude for an air-filled void (Fig. 4b), but as a peak for a water-filled void (Fig. 4c). These results are opposite to those expected for straight-ray transmission, i.e., minimum amplitudes at the depth of a conductive water-filled void and peak amplitudes for an air-filled void. At 23 MHz, the diffraction maxima and minima are more closely spaced, as expected (Fig 4d). The effects of diffraction are less readily recognizable when the void is located near the transmitter hole (Figure 5). The field data in Figure 2 show some indications of similar diffraction patterns, with local minima and maxima that shift location at different frequencies.

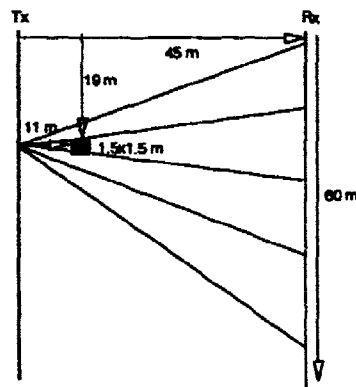


Figure 5a. Model with void near transmitting borehole.

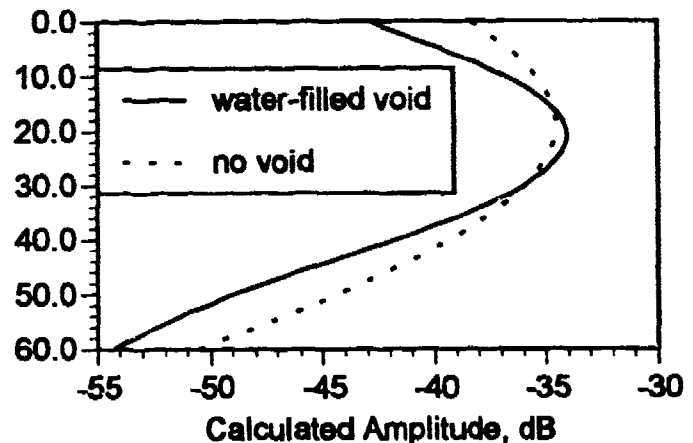


Figure 5b. Calculated amplitude profile, 7 MHz.

Figure 6 illustrates the influence of a continuous, resistive coal layer, with a thickness of 1 m, at a frequency of 7 MHz. Surprisingly, there is an amplitude minimum calculated at the depth of the coal, despite the fact that the coal is much less attenuating than the other rock types. Note that this result mimics a conspicuous feature of the field data described above. The diminished amplitude may indicate that the frequency is below the cutoff for the coal seam to act as a wave guide. The cutoff frequency corresponds to a wavelength approximately equal to twice the seam thickness (Shope, 1987). At 7 MHz, the wavelength in the coal is approximately 16 m, much greater than the seam thickness.

Figure 7a shows the sensitivity of the calculated amplitude profiles to the coal thickness, at 7 MHz. At depths well above or below the coal, amplitudes are increased by the presence of the coal layer, roughly in proportion to the coal thickness. This

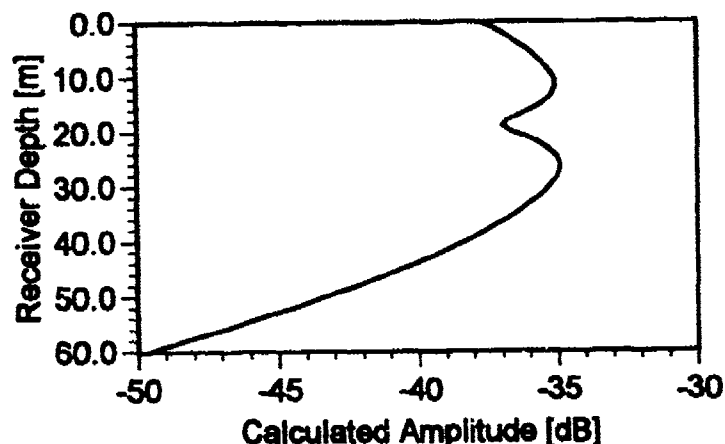
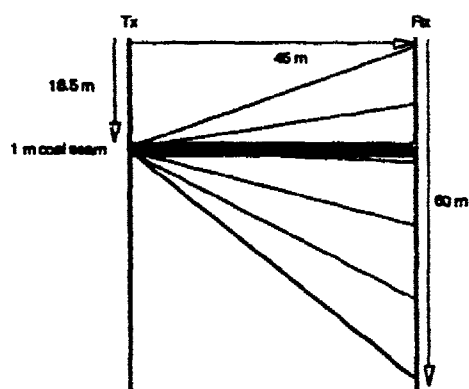


Figure 6a. Model with 1-m resistive coal layer at 19 m depth.

Figure 6b. Calculated amplitude profile for 7 MHz.

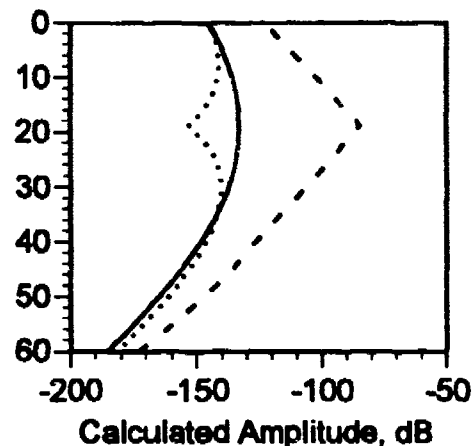
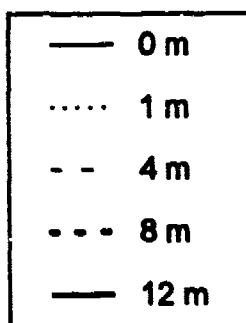
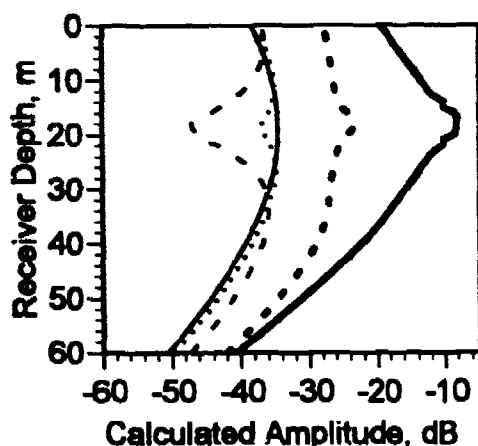


Figure 7a. Calculated amplitude profiles for different seam thicknesses, 7 MHz.

Figure 7b. Calculated amplitude profiles for different seam thicknesses, 23 MHz.

results from diminished attenuation for the part of the ray path through the coal. For horizontal ray paths at depths near that of the coal, amplitudes are decreased for thin layers and increased for thick ones. The transition occurs at a thickness equal to about one half of the wavelength in the coal (i.e., at a seam thickness of approximately 8 m). At 23 MHz, the transition from negative to positive amplitude anomalies occurs at a seam thickness of less than 4 m (Fig 7b). These results are consistent with calculations showing that the cutoff frequency for normal-mode propagation coincides with a wavelength of twice the seam thickness (Shope, 1987). At higher frequencies (shorter wavelengths), the seam acts as a dielectric wave guide (Shope, 1987).

Next we consider a simplified layered representation of the Ohio site and model its electromagnetic behavior. In general, the upper 15 to 20 meters at the site are shaly; the lower part contains more sandstones and limestones (Fig 1). Using the laboratory values of electrical properties for these rock types (Table 1) yields the site model of Figure 8a. Synthetic amplitude profiles for transmitter depths of 15 and 25 meters are shown in Figures 8b and 8c respectively. There are some surprising complexities in the profiles, given the simple structure of the model. When the transmitter is located at 15 meters depth, above the lower-velocity, more highly attenuating sandstone-limestone layer, the amplitude maximum is not at the transmitter depth (as in Figure 3), but is displaced upwards by 7 or 8 meters (Figure 8b). This can be interpreted in simple ray-optical terms as resulting from destructively interfering reflections off the slower layer, with a 180-degree phase shift on reflection, diminishing the amplitude of the direct arrivals just above the sandstone. Amplitudes within the sandstone (depth interval 20 to 28 m) are generally reduced, due to stronger attenuation there. When the transmitter is located in the sandstone interval (Fig 8c), there is a complex amplitude pattern, with a sharp

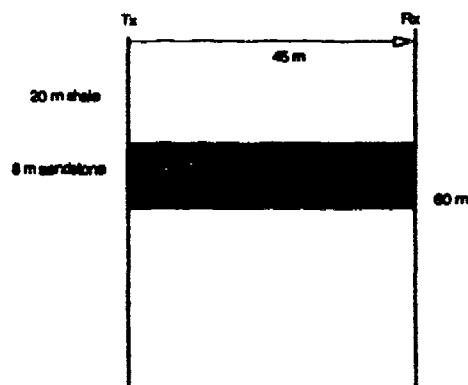


Figure 8a. Simplified layered model of Ohio site.

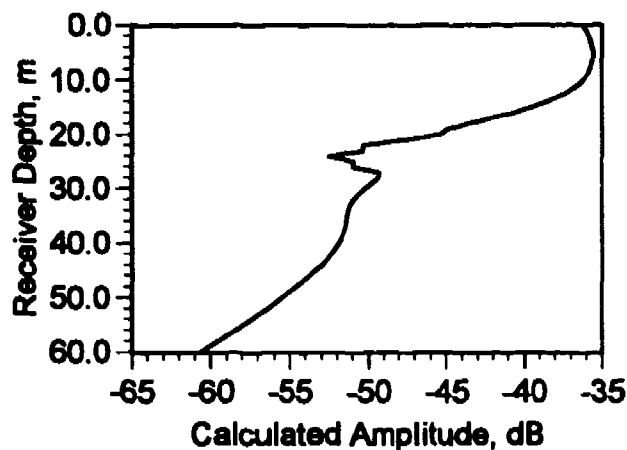


Figure 8b. Calculated amplitude profile, 7 MHz, transmitter depth 15 m.

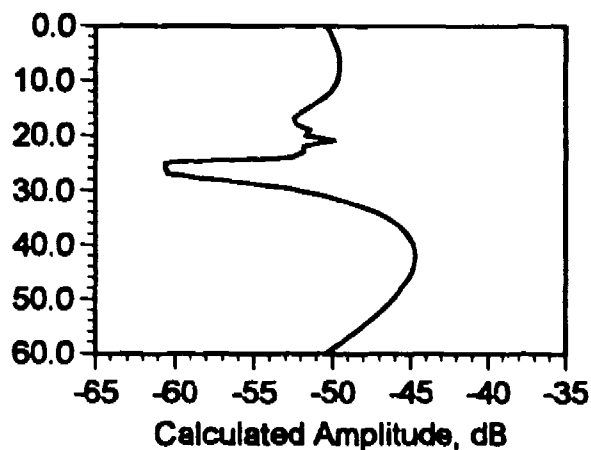


Figure 8c. Calculated amplitude profile, 7 MHz, transmitter depth 25 m.

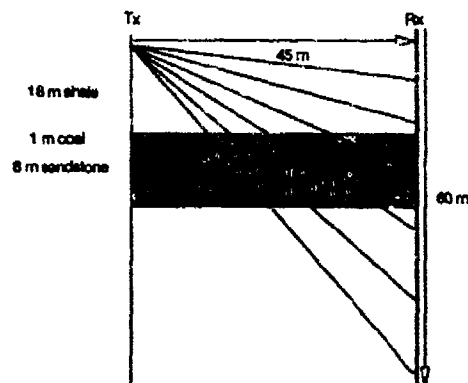


Figure 9a. Layered model with 1-m coal seam and void. Transmitter depth 2 m.

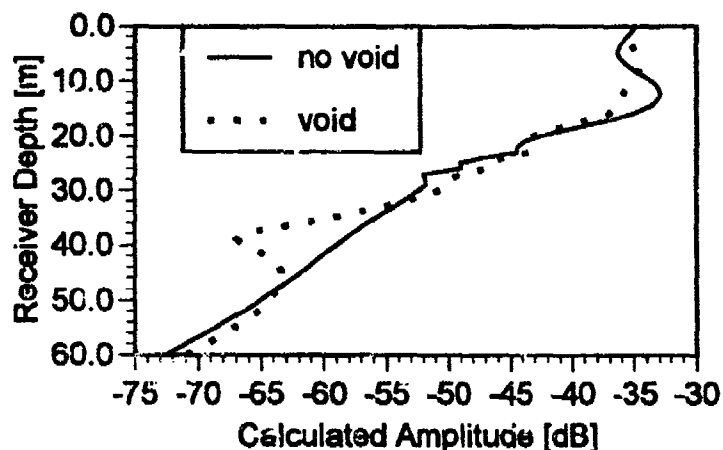


Figure 9b. Calculated amplitude profile, 7 MHz.

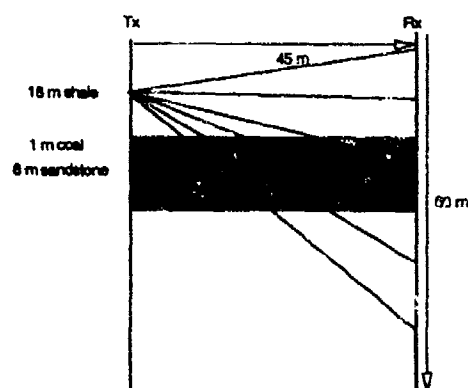


Figure 9c. Layered model with 1-m coal seam and void. Transmitter depth 10 m.

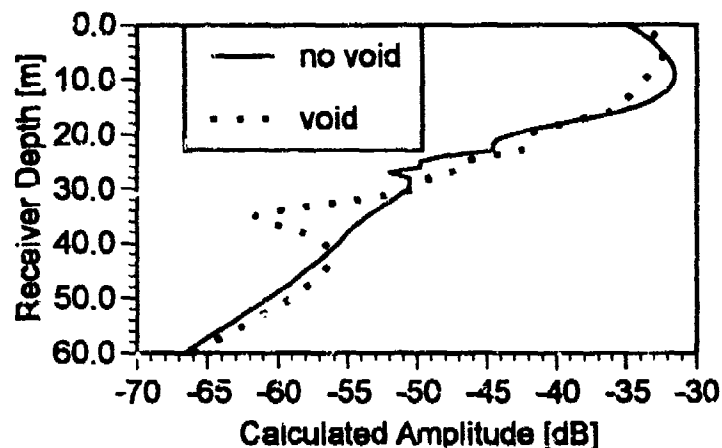


Figure 9d. Calculated amplitude profile, 7 MHz.

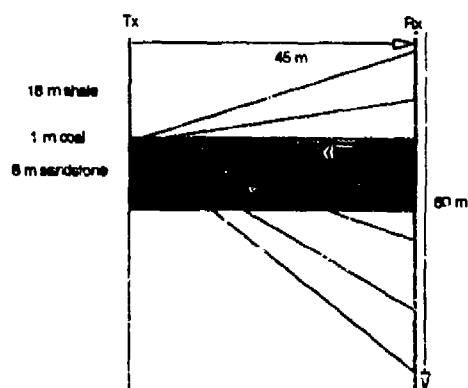


Figure 9e. Layered model with 1-m coal seam and void. Transmitter depth 19 m.

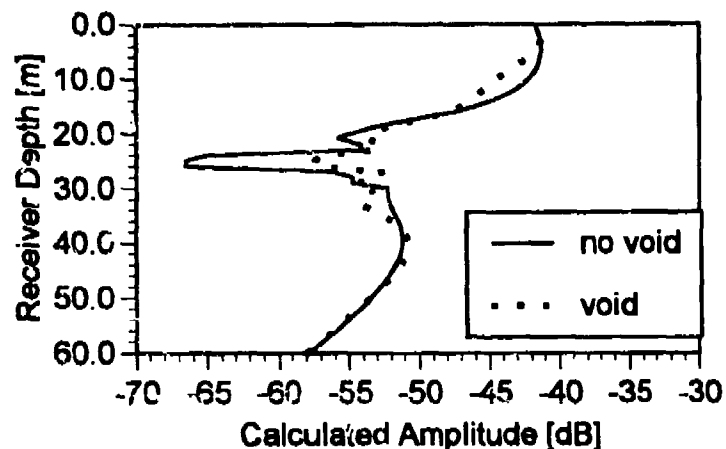


Figure 9f. Calculated amplitude profile, 7 MHz.

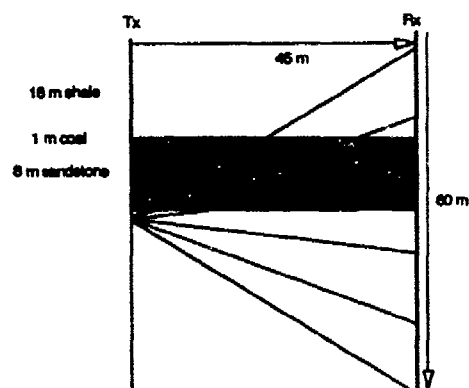


Figure 9g. Layered model with 1-m coal seam and void. Transmitter depth 30 m.

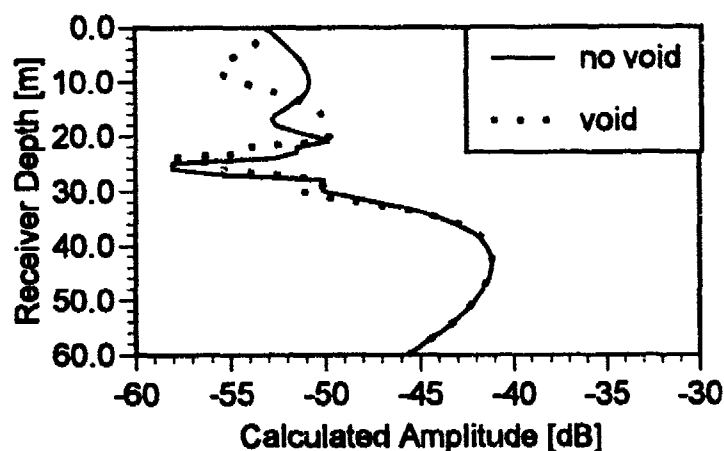


Figure 9h. Calculated amplitude profile, 7 MHz.

minimum and a local maximum in the lower and upper parts of the layer, respectively.

Figure 9 illustrates the calculated amplitude profiles when a one-meter coal layer (depth interval 18-19) is added to the model of Figure 8, with and without a one-meter wide water-filled void near (11 meters from) the receiving borehole. For each transmitter depth, there is a strong localized difference between the void and no-void models, which can be considered the void signature. Two significant features may be observed. First, the presence of the void results in larger amplitudes for a source depth of 19 m (within the coal), but decreased amplitudes for the other source depths; in other words the void projects as a positive or a negative anomaly depending on transmitter depth. Second, the amplitude anomaly does not occur at the depth where the void projects onto the receiving borehole: assuming straight ray paths, the void would project to respective depths of approximately 23, 21, 19, and 15 meters for the four transmitter depths, whereas the amplitude signatures appear at respective depths of approximately 39, 35, 25, and 8 meters. This displacement is probably related, at least in part, to diffraction effects from the relatively low-velocity sandstone/limestone layer.

DISCUSSION

The strong diffraction effects modeled above indicate that inversion of cross-borehole radio-wave amplitude data must account for these effects in order to produce accurate tomographic images. A rock mass anomaly (either a discrete body or a continuous layer with contrasting electrical properties) may project as either a positive or a negative amplitude anomaly (or even as no anomaly), depending on its size, shape, and location. Further, the location

of the amplitude anomaly may not correspond with the straight-ray projection of a physical anomaly. For these reasons, tomographic inversions based on straight-ray transmission may yield erroneous results. These effects can generally be expected in cross-borehole data from horizontally stratified rocks, particularly when the layer thickness is a small fraction of the borehole separation. This study has demonstrated that accurate inversion of cross-borehole data from stratified rock masses, such as coal measure rocks, is a difficult problem requiring the incorporation of diffraction effects.

The use of an in-seam source and receiver geometry avoids many of these complications, particularly when the source frequency is chosen to generate guided waves (Shope, 1987; Stolarczyk, 1990). However, obtaining in-seam data from the surface requires either a large number of boreholes or directional in-seam drilling; both of these approaches carry large costs and present logistical difficulties for data collection.

Diffraction tomography (Devaney, 1984) has been shown to produce higher-resolution images of isolated anomalies in a uniform background than can be obtained by conventional transmission tomography (Lo et al., 1987). In principle, diffraction tomography is well suited to the void detection problem. However in practice, it requires identification and quantification of the diffracted wave field within the total wave field, which may be quite complex in cross-borehole investigations. Detailed forward modeling as carried out above may be used to help identify void signatures in cross-borehole data, and enable the application of diffraction tomographic methods. Where possible, in-seam data acquisition should provide a simpler basis for diffraction tomography, with isolated anomalies in a relatively homogeneous background.

The combination of large borehole separation, small void size, and attenuating strata make the field site of this study unsuitable for transmission tomography. For this approach to succeed, the radio wavelength should be comparable to or less than the size of the target, thus requiring relatively high frequencies. However, the attenuation rates at the higher frequencies prevented their use at the available borehole separation. In cases where the voids are larger, borehole separation is smaller, or attenuation rates are lower, transmission tomography should be an effective means of locating voids.

CONCLUSIONS

A number of important effects complicate void detection by cross-borehole radio-wave surveys in layered rocks. Diffraction from a void can cause it to project as either a positive or negative amplitude anomaly in the receiving borehole, regardless of whether the void is conductive (water-filled) or resistive (air-filled). This leads to serious errors in reconstructions based on transmission tomography. Simple layering (with sharp boundaries

and strong physical contrasts) produces complicated diffraction effects that depend on layer thickness, borehole separation, wave frequency, and source and receiver locations. For in-seam measurements, the signal can be tuned to generate guided waves in a particular layer, avoiding many of these complications. However for cross-borehole experiments, the wave energy must travel along and across all layers.

The primary conclusion of this study is that sites such as the Fairfield coal site are inherently unsuitable for void detection by transmission tomography, because 1) the seam thickness and void sizes are quite small, requiring short wavelengths and high frequencies for adequate resolution, 2) the rock mass is conductive enough that the necessary frequencies are strongly attenuated, and 3) the electrical contrasts between layers produce significant interference effects. Cross-borehole radio-wave transmission tomography can be expected to be successful at sites where the expected void sizes are larger, and the rock mass is more resistive and more homogeneous. In addition, alternative methods, such as in-seam data collection, and/or inversion by the methods of diffraction tomography, promise to overcome the difficulties identified in this study.

REFERENCES

- Bregman, N. D., R. C. Bailey, and C. H. Chapman. Crosshole seismic tomography, *Geophysics*, v. 54, pp. 200-215, 1989.
- Dennen, R. S. and W. P. Stroud, Radar hazard detection in a coal structure, *Mining Engineering*, 413-418, 1991.
- Devaney, A. J., Geophysical diffraction tomography, *IEEE Trans. Geosci. Remote Sensing*, 22, 3-13, 1984.
- Dines, K. A., and R. J. Lytle. Computerized geophysical tomography, *Proceedings of the Institute of Electrical and Electronics Engineers*, v. 67, pp. 1065-1073, 1979.
- Friedel, M. J., D. R. Tweeton, M. J. Jackson, J. A. Jessop, and S. Billington. Mining applications of seismic tomography, *Society of Exploration Geophysicists 62nd Annual Meeting*, 1992.
- Ivansson, S. Seismic borehole tomography - theory and computational methods, *Proceedings of the Institute of Electrical and Electronics Engineers*, v. 74, p. 328-338, 1986.
- Lo, T., M.N. Toksöz, S. Xu, and R. Wu, Ultrasonic laboratory tests of geophysical tomographic reconstruction, *Geophysics*, 53, 947-956, 1988.
- Menke, W. The resolving power of cross-borehole tomography,

- Geophysical Research Letters*, v. 11, p. 105-108, 1984.
- Peterson, J. E., B. N. P. Paulson, and T. V. McEvilly. Applications of algebraic reconstruction techniques to crosshole seismic data, *Geophysics*, v. 50, p. 1566-1580, 1985.
- Shope, S. M., Electromagnetic Coal Seam Tomography, PhD. thesis, PA St. Univ., University Park, PA, 293 pp., 1987.
- Stolarczyk, L. G., Radio imaging in seam waveguides, in Ward, S. H. ed., *Geotechnical and Environmental Geophysics*, Volume III, 187-209, 1990.
- Thill, R. E., D. R. Tweeton, J. A. Jessop, and K. S. Roessler, Developments in seismic tomography for minesite investigation, *Proceedings of the 33rd U.S. Symposium on Rock Mechanics*, J. R. Tillerson and W. R. Wawersik, eds., Balkema, Rotterdam, 1093-1102, 1992.
- Tweeton, D. R., and M. J. Jackson, Seismic tomography and related computer programs for locating fractured zones during deposit evaluation, *Proceedings of the Engineering Foundation Conference on In-Situ Recovery of Minerals*, Santa Barbara CA, 1992.
- Tweeton, D.R., C. L. Cumerlato, J. C. Hanson and H. L. Kuhlman. Field Tests of Geophysical Techniques for Predicting and Monitoring Leach Solution Flow during In Situ Mining. *Geoexploration*, v. 28, pp. 251-268, 1991.
- Wattrus, N. J. *Two-Dimensional Velocity Anomaly Reconstruction By Seismic Tomography*. PhD thesis, University of Minnesota, Minneapolis, 1984.
- Worthington, M. H. An introduction to geophysical tomography, *First Break*, v. 2, p. 20-26, 1984.
- Young, R.P. and S.C. Maxwell. 1992, Seismic Characterization of a Highly Stressed Rock Mass Using Tomographic Imaging and Induced Seismicity, *Journal of Geophys. Res.*, Vol. 97, No. B9, pp. 12,361-12,373.

NEAR-FIELD DIFFRACTION PATTERN BY A TRAPEZOIDAL CYLINDRICAL AIR CAVITY

Taek-Kyung Lee

Department of Avionics Engineering

Hankuk Aviation University

200-1, Hwajon-dong, Koyang, Kyonggi-do, Korea

Jin-Seob Kang and Jung-Woong Ra

Department of Electrical Engineering

Korea Advanced Institute of Science and Technology

373-1, Kusung-dong, Yuseong-gu, Taejeon, Korea

ABSTRACT

Diffraction patterns of the electromagnetic field scattered by a cylindrical air cavity of a trapezoidal cross-section embedded in a dielectric medium is analyzed for the detection of geological anomalies. For the excitation wavelength comparable to the dimension of the cavity, strong asymmetric double dips in the amplitude pattern occur at the locations corresponding to the upper and the lower boundaries of the trapezoidal cylindrical cavity. By selecting proper signal frequency, the analysis shows that the dips become nulls in the near-field region. For the cylindrical cavity of asymmetric cross-section, null frequencies corresponding to the upper and lower boundaries of the cavity are different. These characters are useful in locating high contrast geological anomalies of cylindrical cavity such as underground tunnel.

INTRODUCTION

In locating high-contrast geological anomalies such as underground cylindrical cavity, the cross-borehole continuous wave electromagnetic probing (Lytle, et al., 1979) is superior to the geophysical tomography methods (Dines and Lytle, 1979) because the single frequency signal is free from the dispersion of the host medium which gives greater system dynamic range, and effects of refraction and diffraction

by the cavity for the tomogram are far beyond the correction level (Slaney, et al., 1984). If the signal wavelength in the host medium is about the size of the cylindrical cavity, double dips in the amplitude pattern of the received signal appear at two locations corresponding to the top and the bottom boundaries of the empty cavity. For a circular cylindrical cavity, these double dips of the total field for certain signal frequencies become double nulls in the near-field region (Lee, et al., 1989).

In order to see the effects of different cross-section, diffraction pattern by a trapezoidal cylindrical air cavity of the asymmetric cross section is analyzed by the boundary element method (Yashiro and Ohkawa, 1985) in the near field region. Due to the asymmetry of the cavity cross-section, asymmetric double dips occur at the locations corresponding to the upper and the lower boundaries of the cavity. In the near-field region, these dips are shown to become nulls where the scattered field is equal to the incident field with its phase reversed. It is shown also that the phase of the total field jumps by 180° at the null point while it is less than 180° at the dip point. Frequencies giving nulls at the upper and the lower boundaries are different since it is asymmetric.

Formulation

When an E-polarized monochromatic plane wave u^i propagation in the positive x direction is incident upon a trapezoidal cylindrical air cavity in a homogeneous dielectric medium of its relative dielectric constant ϵ_r , as shown in Figure 1, the total field u in the $x = x_0$ plane outside the cavity may be written as

$$u(\rho) = u^i(\rho) + u^s(\rho),$$

where the incident plane wave is

$$u^i(\rho) = e^{-jkx}.$$

The scattered field u^s may be obtained from the boundary fields on the cylinder(s) as

$$u^s(\rho) = - \int_S [G(|\rho - \rho'|) \frac{\partial}{\partial n} u(\rho') - u(\rho') \frac{\partial}{\partial n} G(|\rho - \rho'|)] dS',$$

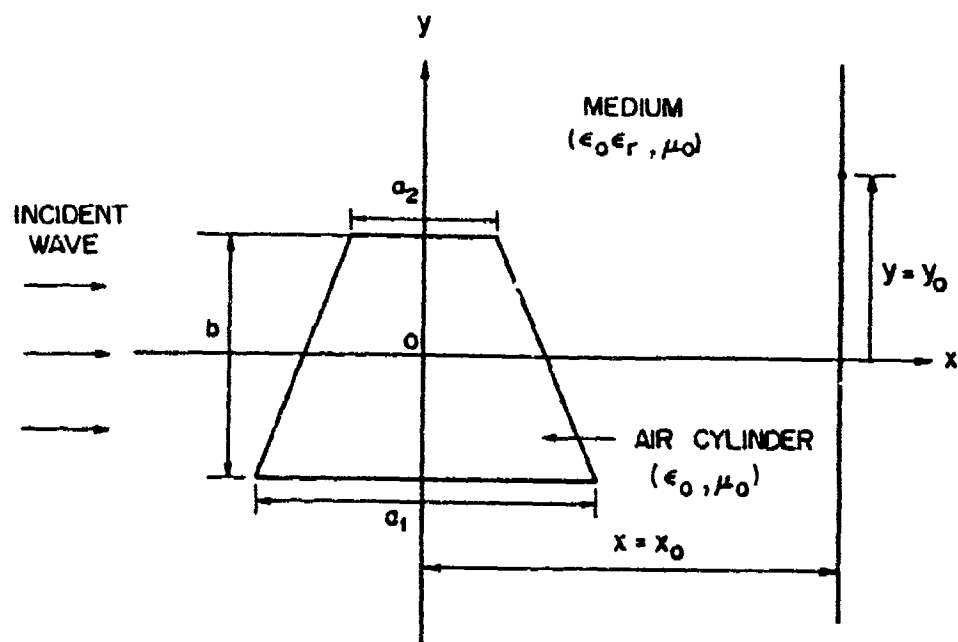


Figure 1. Two Dimensional Scattering by a Trapezoidal Cylindrical Air Cavity in a Homogeneous Dielectric Medium.

where \mathbf{n} is the unit outward normal vector, and $G(|\boldsymbol{\rho} - \boldsymbol{\rho}'|) = -\frac{i}{4}H_0^{(2)}(k|\boldsymbol{\rho} - \boldsymbol{\rho}'|)$ is the 2-dimensional free space Green's function of the host medium region. The field u and its normal derivative on the boundary of the cavity are obtained by the boundary element method using the linear basis function.

Asymmetric Field Patterns

Field patterns diffracted by the cylindrical cavity of the trapezoidal cross-section, which is shown as in Figure 1, are calculated by employing the boundary element method. For numerical calculations, the dimensions of the cavity a_1 , a_2 , and b are chosen to be 2.5 m, 1.5m, and 2 m, respectively, and ϵ_r of the host medium to be 2. The amplitude of the incident wave is chosen to be unity and the signal frequency to be from 90 MHz to 300 MHz.

A typical asymmetric double dip pattern of the total field for the frequency of 138 MHz and the distance of $x_0 = 4.5$ m is shown in Figure 2. Amplitude and phase variation of the corresponding scattered field is shown in the bottom of the figure. Two dips occur at $y = y_{p1}$ and y_{p2} , where the phase of the scattered field differs by 180° from that of the incident field and the amplitudes of the scattered field are slightly different from that of the incident field. In Figure 2, the difference of the amplitude of the scattered field from that of the incident field at $y = y_{p1}$ is smaller than that at y_{p2} and the resulting amplitude pattern of the total field becomes asymmetric. Asymmetric double dips are caused by the asymmetric cross-section of the cavity but occur at the locations corresponding to the upper and the lower boundaries of the cavity.

In the near field region, these dips may become nulls for certain signal frequencies where the scattered field is equal to the incident field with its phase reversed and the phase of the total field jumps 180° at these null points. Amplitude and phase pattern of the total field for the frequency of 140.83 MHz, where the dip corresponding to the lower boundary becomes the null at $x_0 = 4.5$ m, are shown in Figure 3. At the dip point corresponding to the upper boundary, the phase of the total field abruptly changes about 180° .

Null Frequencies

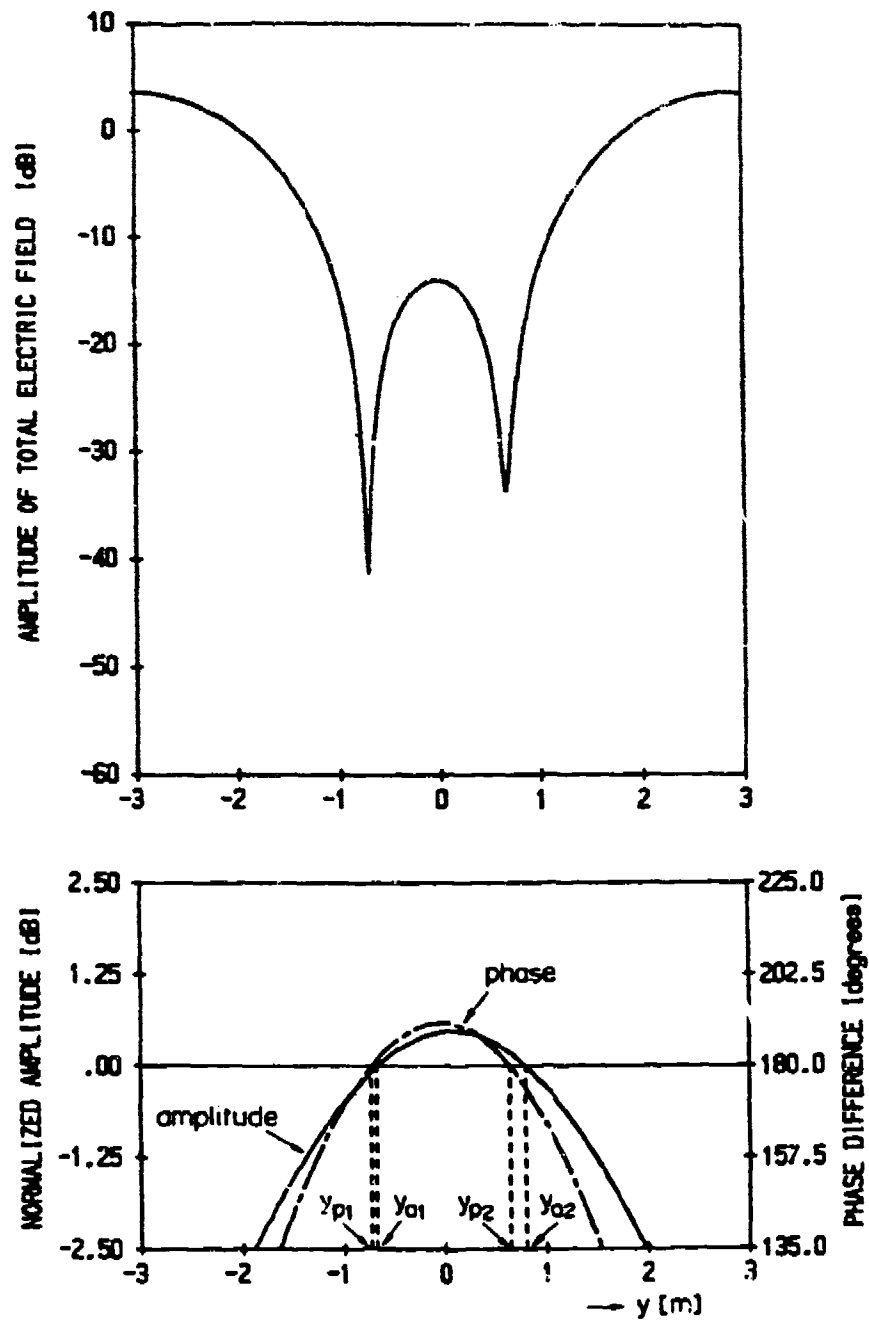


Figure 2. Amplitude Pattern of the Total Field (top) and the Amplitude and Phase Pattern of the Scattered Field Normalized by the Incident Field (bottom) for 138 MHz and $x_0 = 4.5$ m.

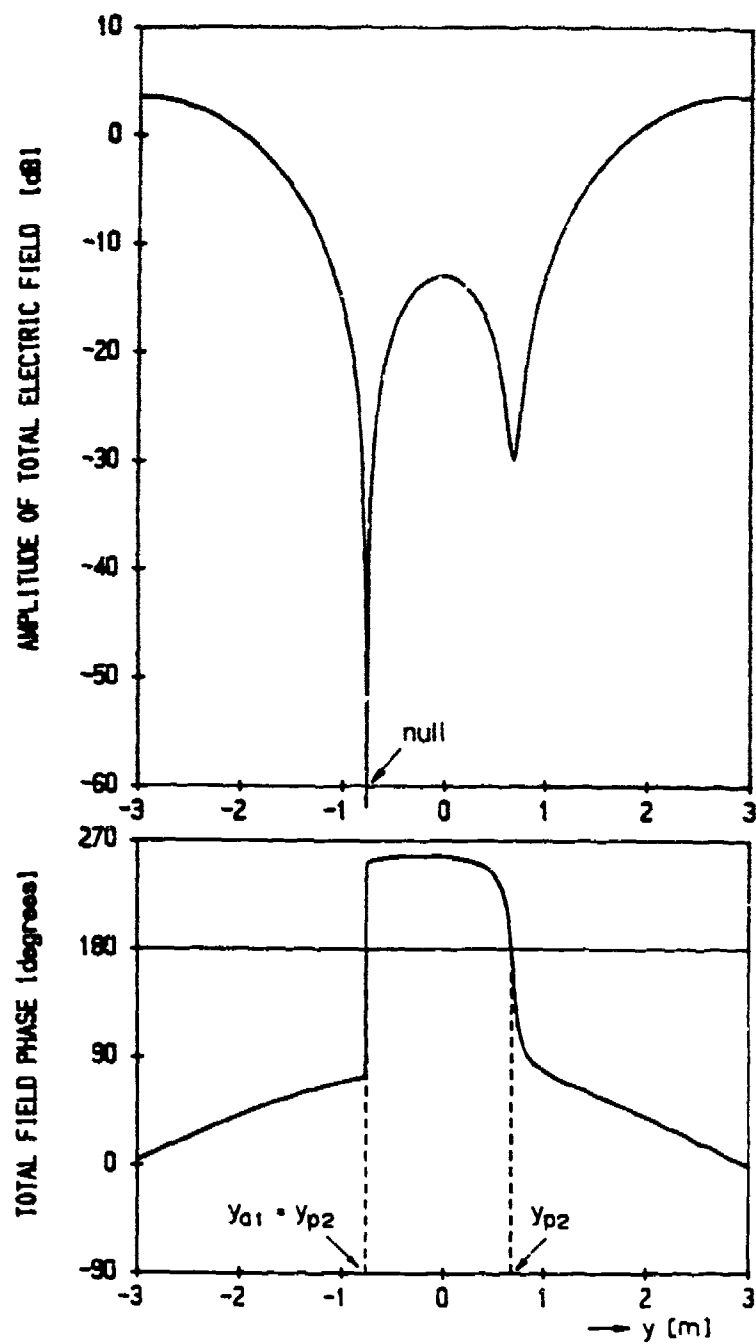


Figure 3. Amplitude Pattern (top) and Phase Pattern (bottom) of the Total Field for 140.83 MHz and $x_0 = 4.5$ m.

For the asymmetric cross-section of the cavity, null frequencies corresponding to the upper and lower boundaries are different. One may find out the signal frequencies where the null occurs by plotting y_a and y_p versus frequency as shown in Figure 4, for $x_o = 4.5$ m. For the frequencies of 133.55 MHz and 224.82 MHz, the upper null occurs by making $y_{a2} = y_{p2}$. Lower null occurs at $y_{a1} = y_{p1}$ for the frequencies of 140.83 MHz and 197.44 MHz. Calculated result shows that the dip pattern of the total field changes as the frequencies cross the null frequencies. The upper dips are stronger than the lower dips either for the frequencies lower than 133.55 MHz (Figure 5) or higher than 224.82 MHz. For the frequencies from 140.83 MHz to 197.44 MHz, the lower dips are stronger than the upper dips, as shown in Figure 6. The phase jumps about 180° in a concave way for the frequencies lower than 133.55 MHz and a convex way in the frequencies from 140.83 MHz to 197.44 MHz as in Figure 5 and 6, respectively. In the frequencies from 133.55 MHz to 140.83 MHz, however, phase jumps of about 180° occur twice downward, as shown in Figure 7.

CONCLUSION

Diffraction patterns by the trapezoidal cylindrical cavity are analyzed in order to see the effects of asymmetric cross-section in the near field region. Amplitude and phase variations of the scattered field are calculated to show how the dips and nulls are formed in the total field pattern. It provides an effective tool in locating high-contrast underground anomalies without complicated data processing.

References

- [1] Dines, K. A. and Lytle, R. J., 1979, "Computerized Geophysical Tomography," Proceedings of the IEEE, Vol. 67, pp. 471-480.
- [2] Lee, T. K., Park, S. O., Kim, S. Y., and Ra, J. W., 1989, "Near-field Diffraction Pattern by an Underground Void of Circular Cylinder," Microwave and Optical Technology Letters, Vol. 2, No. 5, pp. 179-183.

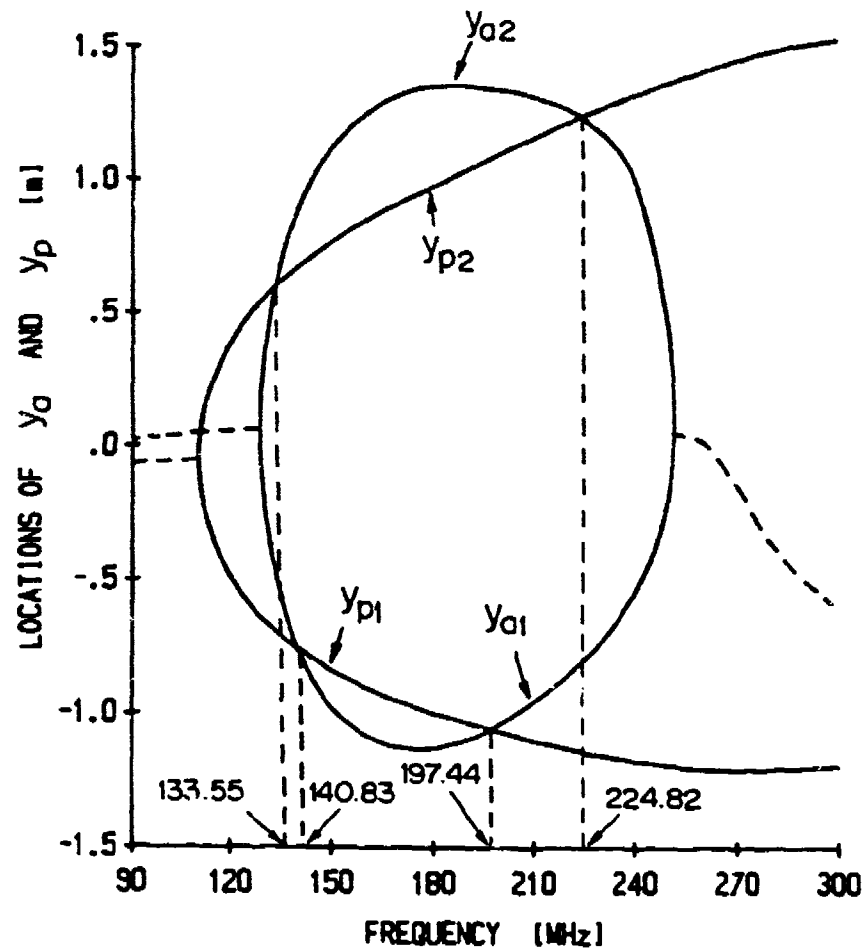


Figure 4. Loci of y_a and y_p as a Function of the Frequency from 90 MHz to 300 MHz for $x_o = 4.5$ m.

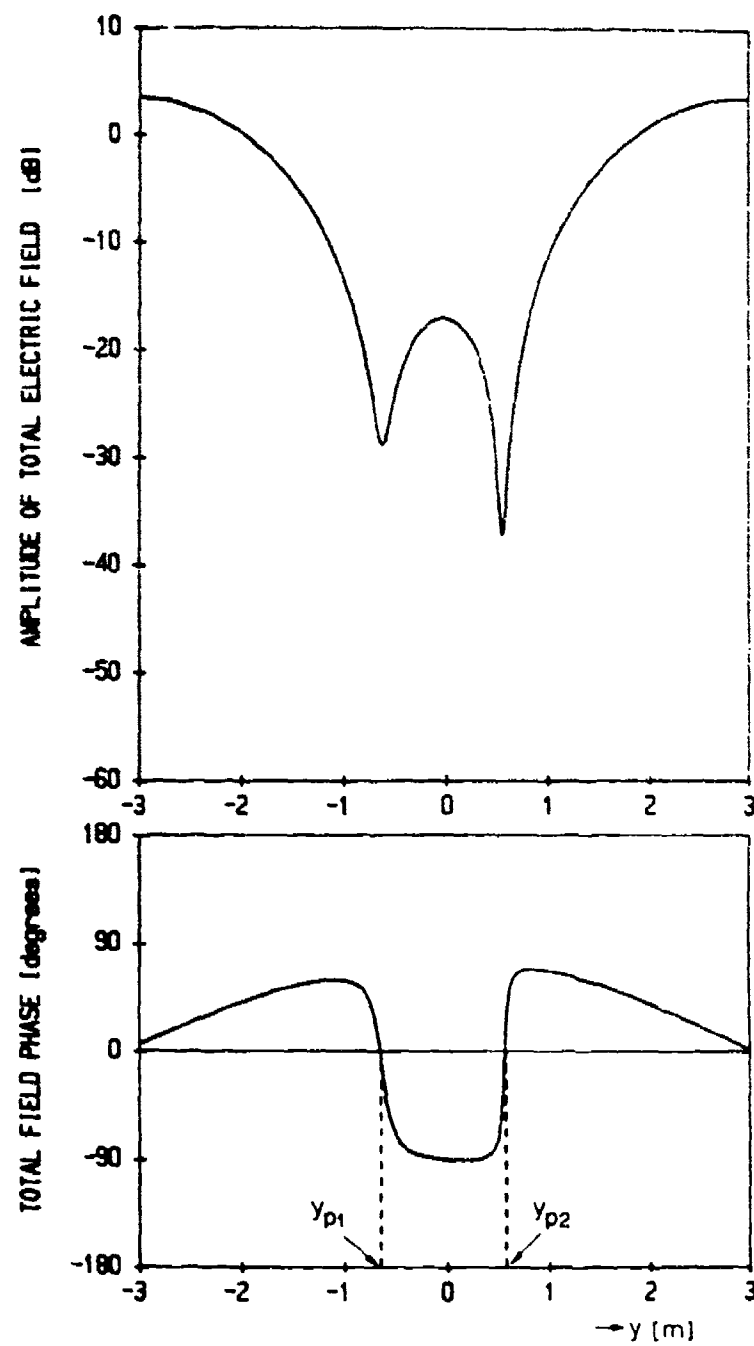


Figure 5. Asymmetric Amplitude (top) and Phase (bottom) Patterns of the Total Field for $x_0 = 4.5$ m and 131 MHz.

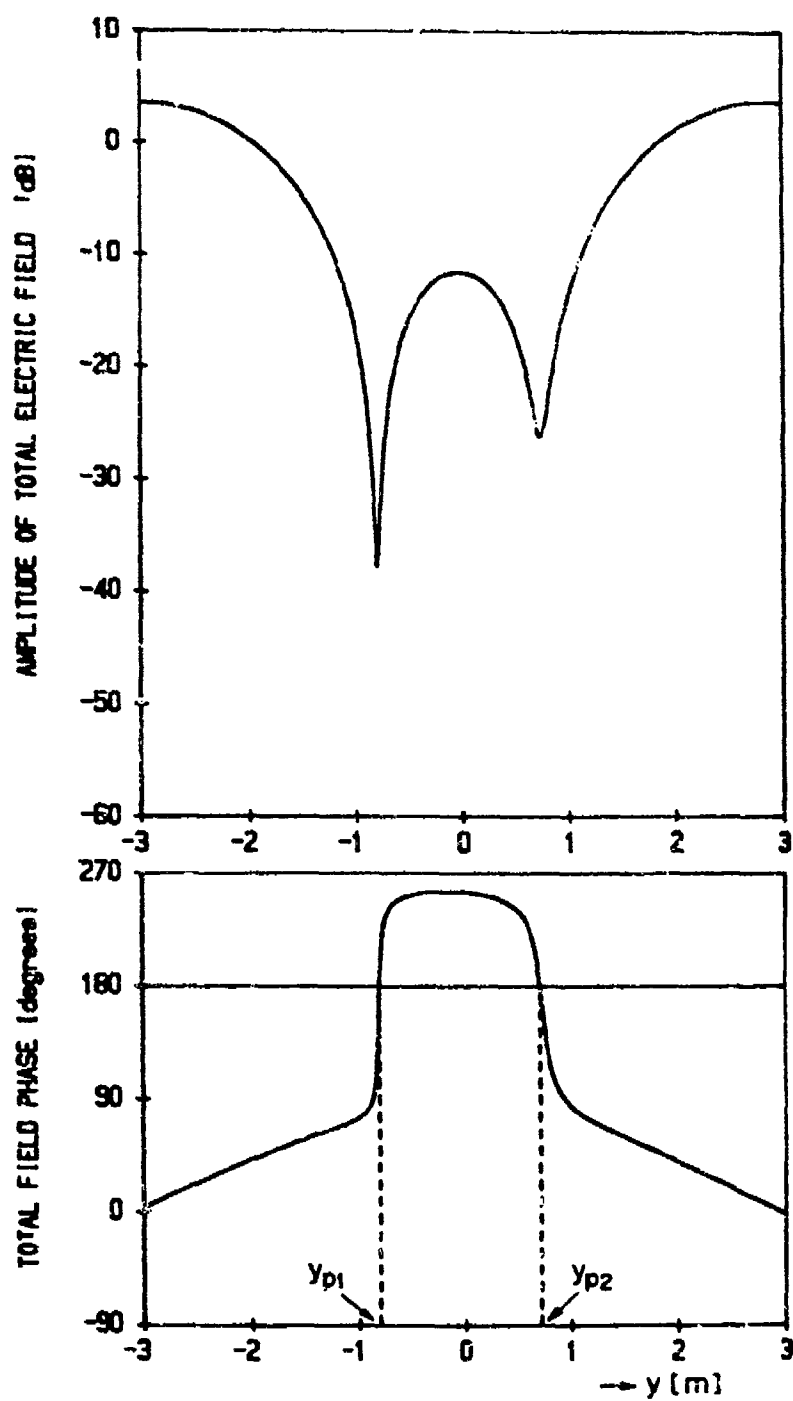


Figure 6. Asymmetric Amplitude (top) and Phase (bottom) Patterns of the Total Field for $r_c = 4.5$ m and 145 MHz.

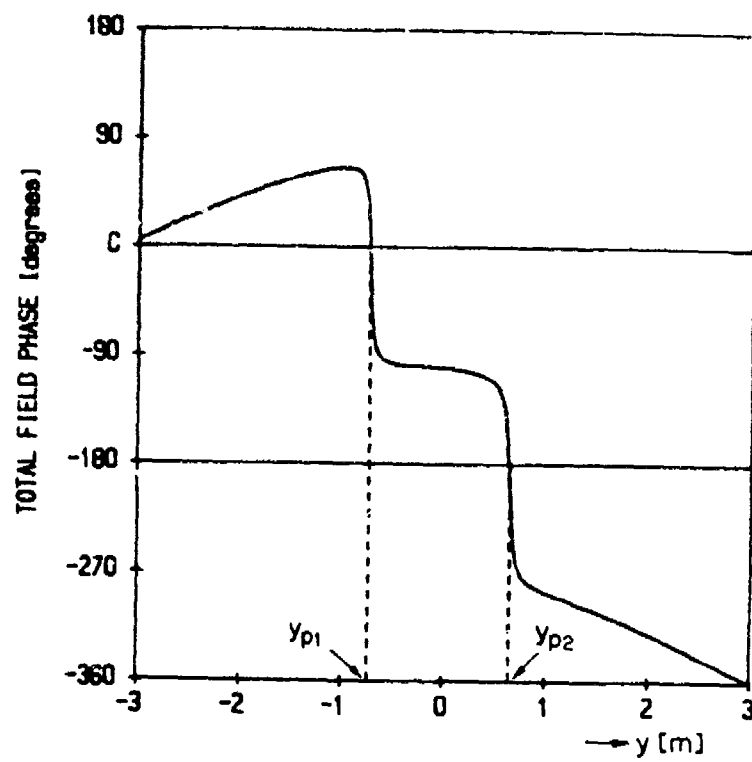


Figure 7. Asymmetric Phase Pattern of the Total Field for $x_0 = 4.5$ m and 137 MHz.

- [3] Lytle, R. J., Laine, E. F., Lager, D. L., and Davis, D. T., 1979, "Cross-borehole Electromagnetic Probing to Locate High-contrast Anomalies," Geophysics, Vol. 44, No. 10, pp. 1667-1676.
- [4] Slaney, M., Kak, A. C., and Larsen, L. E., 1984, "Limitations of Imaging with First Order Diffraction Tomography," IEEE Transactions on Microwave Theory and Techniques, Vol. MTT-32, pp. 860-874.
- [5] Yashiro, K. and Ohkawa, S., 1985, "Boundary Element Method for Electromagnetic Scattering from Cylinders," IEEE Transactions on Microwave Theory and Techniques, Vol. MTT-33, pp. 771-778.

LABORATORY INVESTIGATIONS OF THE SEISMO-ELECTRIC EFFECT

C.K. Skokan and D. Chi

Colorado School of Mines Department of Geophysics
Golden, Colorado

ABSTRACT

Electric polarization can occur in rock as a result of a pressure difference caused by a seismic wave. Mathematically, this seismo-electric effect is a function of frequency, permeability, porosity, and fluid resistivity. Laboratory studies have concluded that seismic and electrical measurements that correlate can be made. Laboratory results, along with a field test, demonstrate that this method could be used in conjunction with more standard electrical and seismic techniques. Monitoring of the seismo-electric effect can produce additional information on subsurface activity, either natural or man-made, such as tunneling.

INTRODUCTION

The seismo-electric effect is observed as the development of a potential between two points in a rock which has been subjected to elastic deformation. There are various causes of this potential which include movement of charged particles in the earth's magnetic field caused by earthquakes, the piezo-electric effect, and electro-kinetic phenomena. For this study, the electro-kinetic phenomena of electro-osmosis and streaming potential will be considered. Electro-osmosis results from the movement of fluid in a solid framework when an electric field is applied. Streaming potential, the inverse of electro-osmosis, is the development of an electric field when pressure changes cause movement of fluid.

In rocks, the electro-kinetic phenomena depend upon the development of a Helmholtz double electric layer. This layer occurs in one of two ways:

- 1) when fresh water comes into contact with a rock, there can be preferential adsorption of some ions in the pore fluid.
- 2) some adsorbed ions on the rock pore surface can pass into a mobile state.

The greatest potential difference established is called electrochemical potential (ϵ) as described in the Nernst formula:

$$\epsilon = (RT/nF) \ln(a_1/a_2)$$

where a_1 and a_2 are the activities of the ions in solution, $R = 8.314$ joules, $F = 96,500$ coulombs, T is absolute temperature, and n is the valency (Pirson, 1950, p. 88).

Because of electrostatic attraction between rock and fluid, another potential termed zeta potential (ζ) is developed. This is the potential within the moveable fluid. Figure 1 illustrates these various potentials.

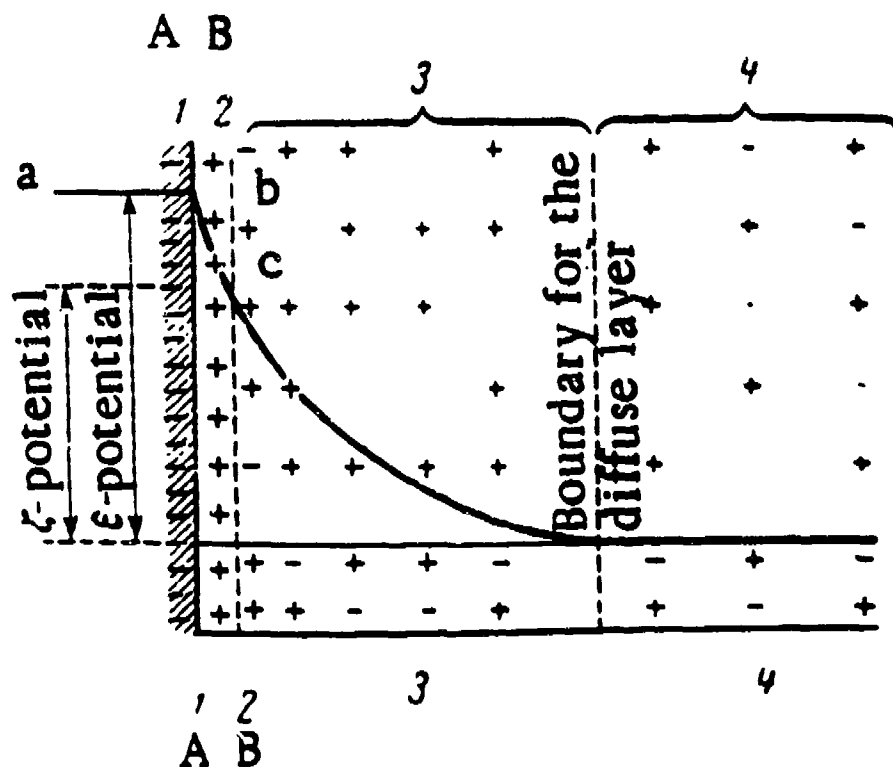


Figure 1. Electric double layer. 1-1) negatively charged solid surface; 2-2) immobile layer of positive ions; 3-3) solid phase; 4-4) free solution; a) level of potential in the solid phase; b-c) drop in potential in the immobile part of the electrical double layer; c-d) drop in potential in the mobile part of the electric double layer; d-e) level of the potential in the free solution; A-A) interface between the mobile and immobile fluid; B-B) boundary between the mobile and immobile fluid. (after Parkhomenko)

These values can now be incorporated into the mathematics of the seismo-electric effect beginning with Helmholtz equation which describes fluid flow in a pore:

$$v = \frac{\epsilon \zeta I}{4 \pi \eta \sigma}$$

where v is the rate of fluid flow; ϵ is the dielectric constant; σ is the fluid conductivity; ζ is the zeta potential; I is current and η is viscosity of the fluid (Parkhomenko, 1971, p. 180 - 1). Smoluchowski is responsible for extending this equation to apply to porous rocks. When a pressure change ΔP is applied, the expression becomes:

$$U = \frac{\epsilon \zeta \Delta \phi}{4 \pi \eta \sigma}$$

This is the equation commonly found in the literature (Chandler, 1981, p. 118; Ogilvy, et. al., 1969, p. 38; Parkomenko, 1971, p. 181) which describes streaming potential, the inverse of electro-osmosis. Here, U is the streaming potential.

Frenkel (1944) has computed the electric field caused by seismic waves as:

$$E = \frac{4 \epsilon \zeta}{\pi \sigma r^2} \bar{v}$$

where \bar{v} is average velocity and πr^2 is the pore area. Parkhomenko (1971, p. 187) refined the value for average velocity by replacing it with v_2 (rate of movement of the liquid phase) and v_1 (rate of movement of the solid phase):

$$v_2 - v_1 = i \frac{f \chi}{\eta} \gamma v_0 \left(\frac{k_0}{\rho} \frac{\beta}{\beta'} \frac{1}{v_0^2} - 1 \right) \Delta V,$$

where f is the frequency of oscillation, χ is permeability; η is the viscosity of the fluid phase, γ is effective fluid density and equal to $k\rho$; ρ is fluid density; k_0 is compressibility of fluid, v_0 is longitudinal wave speed; ΔV is relative change in volume of rock; k_1 is compressibility of the solid phase; α is a mechanical property such that:

$$\beta = 1 / (k(1+\alpha))$$

and

$$\beta' = 1 + (\beta - 1) \frac{k_0}{k_1} \cdot$$

Combining the equations of Frenkel and Parkhomenko gives:

$$E = i \frac{4\epsilon \zeta \times f^2}{\pi \sigma \tau^2 \eta} k\rho \left[\frac{k_0}{\rho} \frac{\beta}{\beta'} \frac{1}{v_0^2} - 1 \right] u$$

provided, $\Delta v = du/dx = i g u$ and $g = f/v_0$ where u is movement of particles. The i indicates a phase relationship. The result of these equations is that there is a linear relationship between electric field and permeability if other factors are constant. Also, measurement of both seismic and electric signals in order to identify the seismo-electric effect can yield information about porosity, fluid content or changes in resistivity or velocity. That makes this measurement a valuable tool to be used in conjunction with more well-established seismic or electrical geophysical methods.

LABORATORY EXPERIMENTS

In the laboratory, seismo-electric effects have been measured on synthetic sandstones of known porosities and permeabilities. In order to prepare the samples, they were cleaned and injected with a fluid of known resistivity. The sample was then placed in the testing circuit (see figure 2) and subjected to an impulsive seismic source by a dropped weight. An electric signal was recorded from two electrode bands placed at either end of the sample. A seismic signal was recorded by using a pressure transducer. Both of these signals were amplified and then recorded on a Nicolet digital oscilloscope.

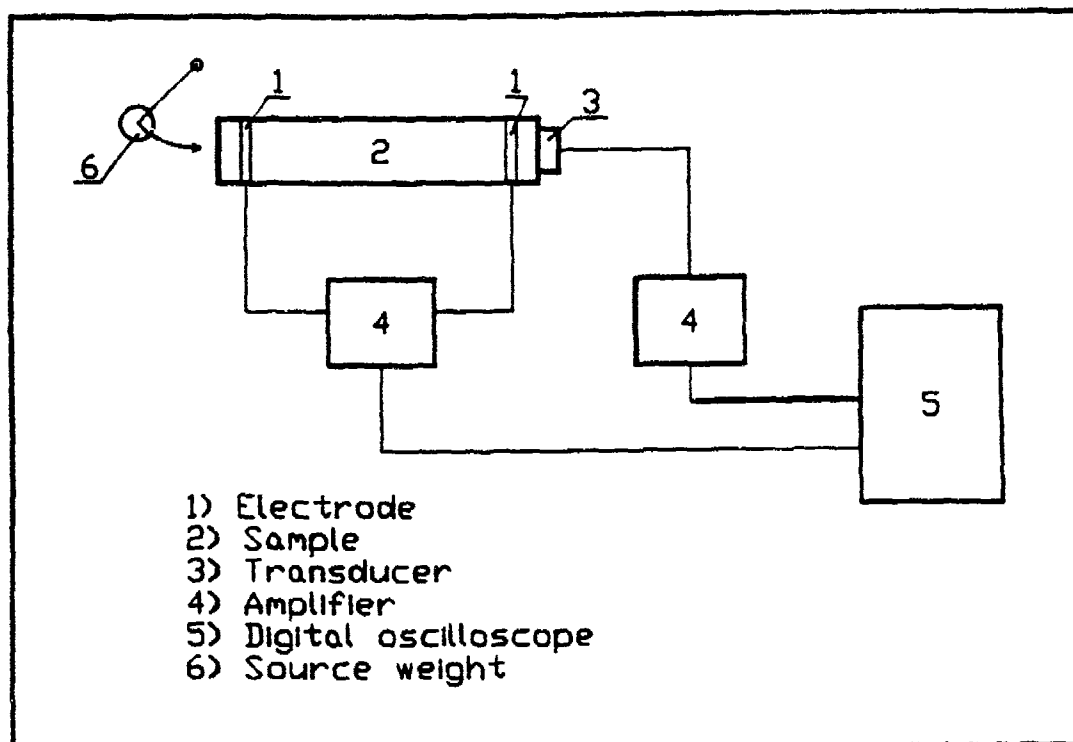


Figure 2. Laboratory set-up for seismo-electric measurements.

Figure 3 shows the result of the measured seismic and electric traces from a sample saturated with a mixture of water and oil. These data were then qualitatively analyzed in order to compare the measured results with the theoretical predictions for seismo-electricity (Chi, 1990). The frequency spectra for the electric and seismic signals were computed (Figures 4a & 4b). There appears to be comparable signals over some frequency ranges but not all ranges. For example, signals between 100 and 200 Hz appear to correlate well. However, signals at 1000 Hz. do not correlate. Some of the differences were attributed to the different frequency responses of the specific transducers and electrodes used in the measuring system and to noise in the laboratory. The phase shift described by the theoretical equation is also observed. In conclusion, some, but not all of the signals appear to satisfy the seismo-electric theory. A calibrated source and system of measurements could help to better define which portion of the signal is true seismo-electric data and is the next logical step in this research.

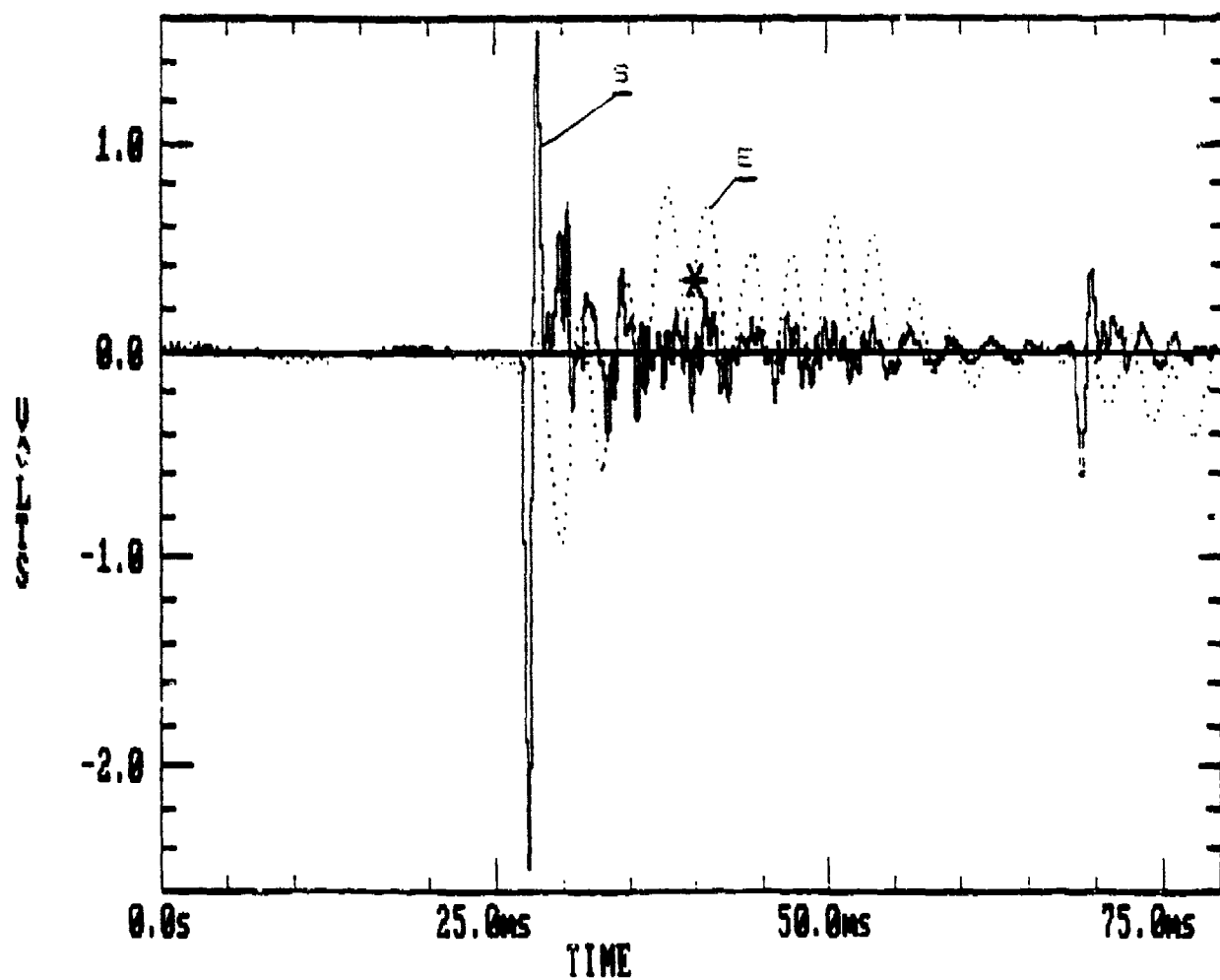
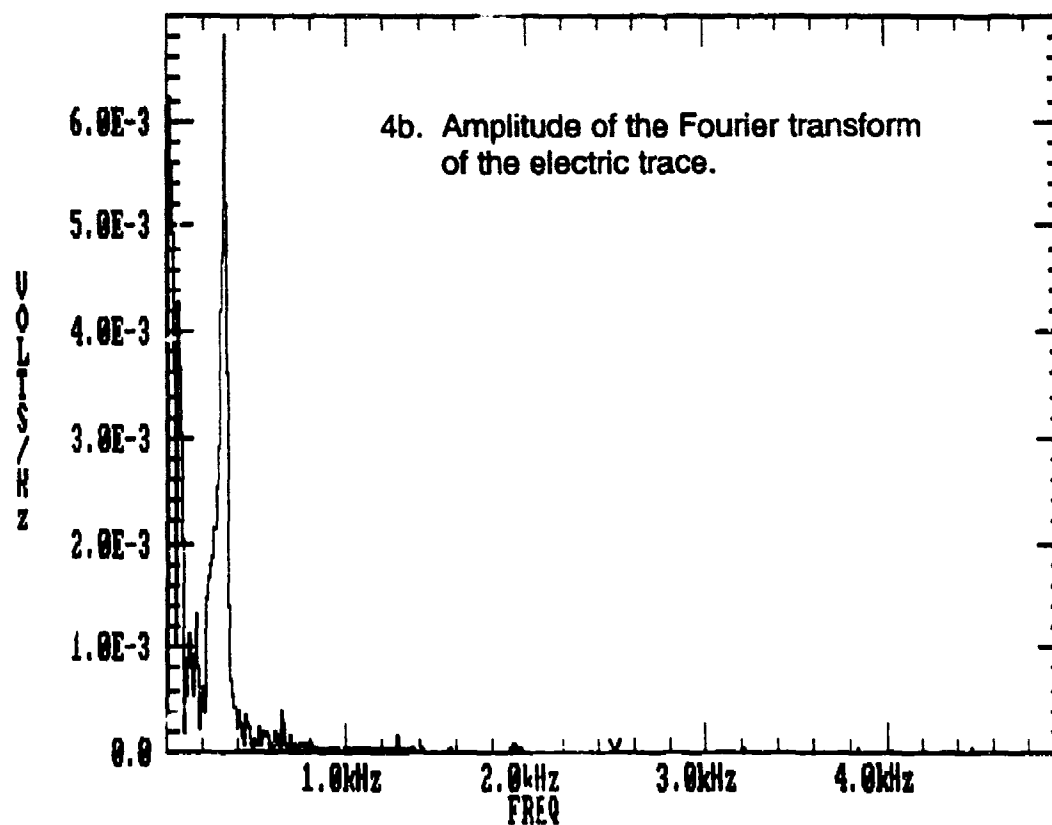
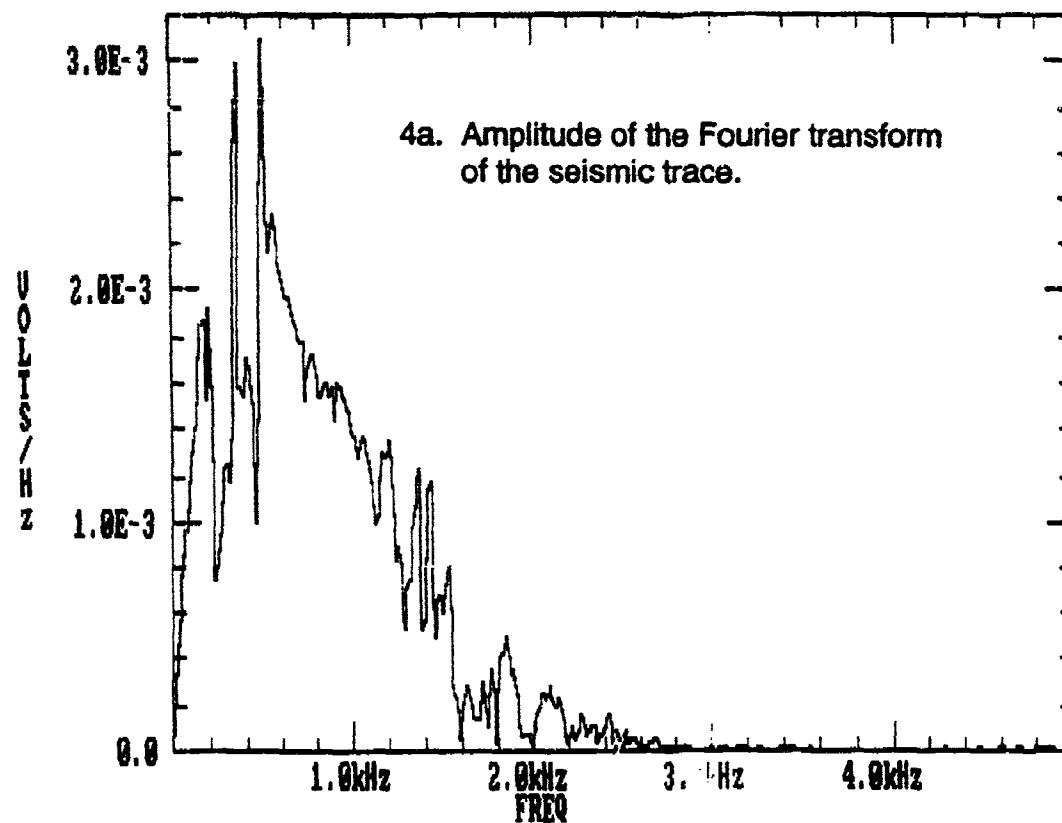


Figure 3. Seismic signal (S) and electric signal (E) from an impulsive source in a sample saturated with oil and water. Note that the amplitude of this signal has been amplified by a factor of 10,000.



Figures 4a and 4b. The Fourier transform of the seismic and electric signals from the oil and water saturated laboratory sample. A sampling rate of 10 KHz. was used.

Next, the experiment was moved to the field to see if signals could be received outside of the laboratory environment (Chi, 1990). A site was chosen where the surface soil was water-saturated in order to maximize the signal strength. The electric signal was measured with two non-polarizing electrodes placed at a 1 foot spacing; a standard reflection seismic geophone and seismic source were placed at one electrode. A hammer striking a metal plate produced the seismic signal. The resulting information is seen on figure 5. Fourier transforms were again calculated for frequency analysis and correlation (Figures 6a & 6b). As in the laboratory example, correlation for some frequencies is evident and the predicted phase shift appears. As before, the system was not calibrated and therefore only qualitative interpretations are possible. Correlating signals at 40 and 80 Hz. are encouraging. Again, the frequency responses of the two receiving systems for the seismic and electric signals were different so it is not possible to compare all frequencies. Because small signals are possible to measure in both the laboratory and in the field, a research program aimed at calibration of a system is recommended.

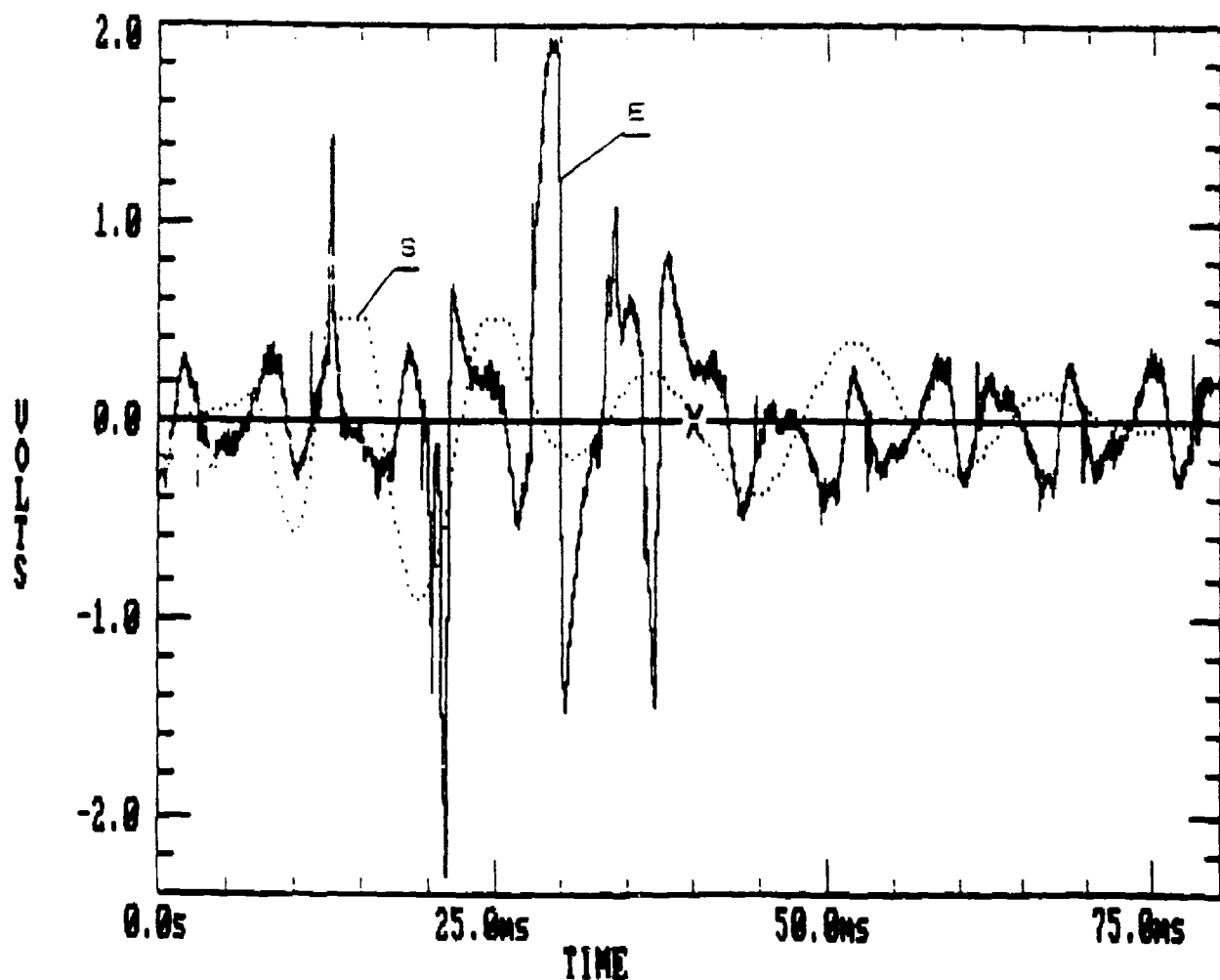
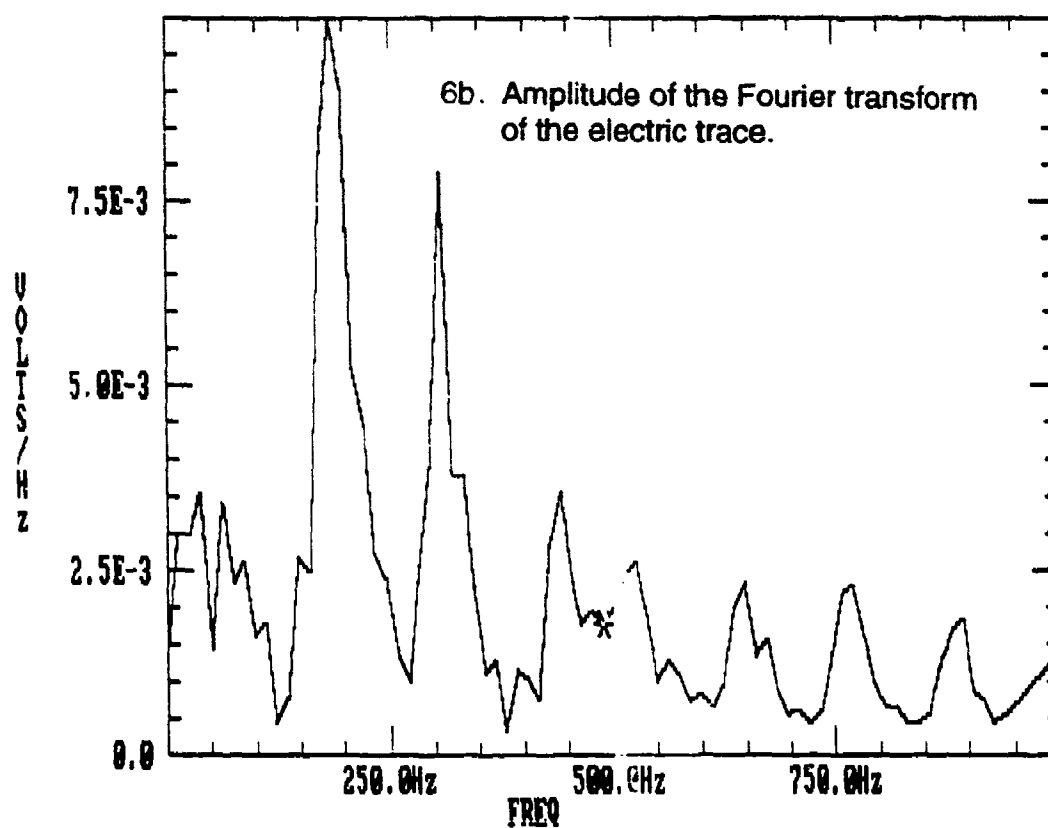
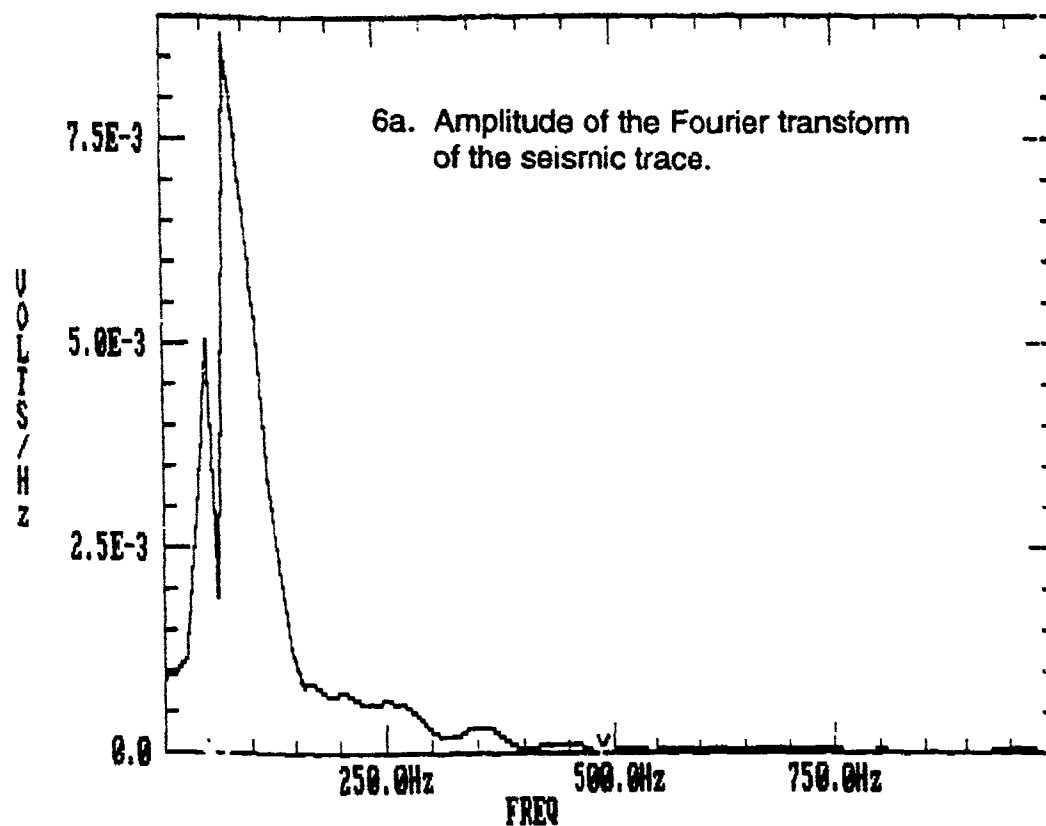


Figure 5. Seismic signal (S) and electric signal (E) from a hammer source in a water-saturated-soil field experiment with an amplification of 10,000.



Figures 6a and 6b. The Fourier transform of the seismic and electric signals from a hammer source in a water-saturated-soil field experiment . A sampling rate of 10 kHz. was used.

SUMMARY AND FUTURE DEVELOPMENT

The seismo-electric effect can be represented mathematically. Laboratory measurements show that the practice and theory are not inconsistent. These laboratory measurements were not made in a calibrated setting and therefore can be interpreted in a qualitative manner only. It is also possible to make laboratory and field measurements and receive an electric signal which, in part, correlates with a seismic signal. The seismo-electric method will not replace more conventional seismic and electrical surveys or monitoring systems but can give an additional dimension of information. For example, the seismo-electric method is the only method which is sensitive to permeability. This method may prove to be a valuable additional tool which could be used to monitor subsurface activity, either natural or man-made. More research in the calibration and field application of this technique must be undertaken before its use can be more fully understood.

REFERENCES

- Chandler, R., 1981, Transient streaming potential measurements on fluid-saturated porous structures: an experimental verification of Biot's slow wave in the quasi-static limit: *J. Acoust. Soc. Am.*, Vol. 70 (1), p. 116 - 121.
- Chi, Dong, 1990, Seismoelectric Effect: CSM Masters Thesis T-3886.
- Frenkel, J., 1944, On the theory of seismic and seismoelectric phenomena in a moist soil: *Jour. of Physics*, Vol. 8, No. 4.
- Ogilvy, A. A., Ayed, M. A., Bogoslovsky, V. A., 1969, Geophysical studies of water leakages from reservoirs: *Geop. Pros.*, Vol. 17, p. 36-62.
- Parkhomenko, E., 1971, *Electrification Phenomena in Rocks* (translated from Russian by G. V. Keller): Plenum Press, New York.
- Pirson, S., 1950, *Electric logging: a study of the self potential curve in elements of oil reservoir engineering*: McGraw-Hill.
- Skokan, C. K., and Andersen, H. T., 1988, Use of the seismoelectric effect to directly detect permeability at the WIPP site: Sandia National Laboratory Report.

**GRADIOMETER ANTENNAS FOR DETECTION OF TUNNELS
BY SCATTERED ELECTROMAGNETIC WAVES**

**LARRY G. STOLARCZYK
RINTECH, INC., RATON, NM 87740**

AND

**JIM ALLEN
CHEM-NUCLEAR GEOTECH INC.,
GRAND JUNCTION, CO. 81502**

ABSTRACT

Theoretical analyses and field demonstration tests have shown that low frequency scattered secondary electromagnetic (EM) waves can be detected in the rock mass surrounding a shallow or deeply buried tunnel which contains electrical conductors. Gradiometer antennas suppress the slow varying primary EM wave but respond to the rapid spatial variations of the tunnel-generated secondary EM wave. The unique signature (spatial response pattern) of the gradiometer antenna, together with its enhanced tunnel signal to geologic noise ratio greatly improve reliability of tunnel detection in the interpretation problem. This, together with the lower signal attenuation rate in the rock mass, increases the radius of detection. Theoretical analyses by Hill (1990) considered theoretical wave propagation issues relating to experimental tests. The tests were conducted at the San Xavier Mine near Tucson, Arizona in 1990. At the San Xavier Mine, a response from rails in a shallow adit were detected with a gradiometer antenna on the surface when the rail was excited at 102.5 kHz by a vertical magnetic dipole antenna near the portal. This paper describes the close agreement between Hill's theoretical formulation and field test results.

1. INTRODUCTION

Theoretical research by Hill (1,2) and field demonstration results show that shallow and deeply buried tunnels with electrical conductors can be detected with low frequency EM waves. Low frequency EM waves are useful because the scattering cross-section of the buried conductor increases with decreasing frequency (3). The radius of detection increases because the attenuation rate is relatively low in the low frequency band. The magnitude of the scattered secondary wave depends on the amplitude of current induced in the conductor. The amplitude of current is proportional to magnitude of the primary EM wave electric field component that is polarized with the axial direction of the conductor. The magnitude of the scattered wave is oftentimes between one and two orders of magnitude less than the primary wave. Tunnel detection strongly depends upon the suppression of the primary wave.

In past field demonstration work (4), large physical separation distances between the down-the-hole transmitting and receiving antennas provided natural suppression of the primary wave below the threshold sensitivity level of the companion receiver. The detection of a secondary EM wave confirmed the existence of a nearby electrical conductor. It is also possible to suppress the primary wave by using a receiving antenna that is polarized orthogonally to the primary field. A gradiometer antenna can also suppress the primary wave and receive the secondary wave. This paper describes crosshole and hole-to-surface gradiometer field tests performed at the San Xavier Mine near Tucson, Arizona.

2. SUPPRESSION OF PRIMARY WAVE FIELDS

Methods of detecting clandestine tunnels using electromagnetic waves are illustrated in Figure 1.

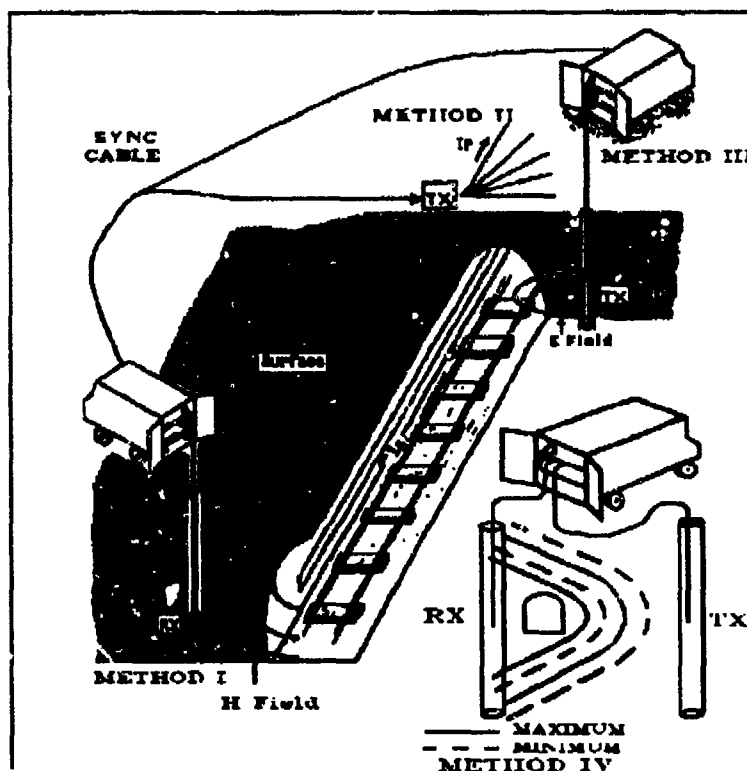


Figure 1 Cut away view illustrating suite of "long and short wavelength scattering limit" tunnel detection methods.

The primary electromagnetic (EM) wave field components of the surface grounded dipole (Method II) and the down-the-hole vertical magnetic dipole (VMD) antennas (Method III) induce secondary current flow in the target conductor. The current depends upon the magnitude of the primary electric field component that is tangential to the conductor. For uniform illumination of the

target conductor, the induced current is given by

$$I_s = \frac{2\pi E_p}{i\mu\omega \ln(ka)} \quad (1)$$

where E_p = the magnitude of the primary electric field that is tangential to the electrical conductor,

μ = the magnetic permeability of the surrounding rock mass,

$\omega = 2\pi f_0$ and f_0 is the operating frequency in Hz.,

$i = \sqrt{-1}$,

$k = \beta - i\alpha$ is the complex wave number. β is the phase constant in radians per meter and α is the attenuation rate in nepers per meter,

and, a = the radius of the conductor.

Equation (1) suggests that the current increases with the magnitude of the primary field component (E_p). It also increases as frequency (ω) is decreased.

Method I employs a down-the-hole receiver to detect current flow in electrical conductors. The current flow may be induced by electrical noise generated in the tunnel electrical power system (switching transients and motor start-up current) or by terrestrial EM wave coupling into the earth. The magnitude of the primary surface wave decays with depth into the earth as $e^{-\alpha}$. The current flow in the conductors produces a secondary EM field that cylindrically decays with the inverse square root of distance (r) from the conductor. Burrow (5) shows that in the cylindrical coordinate system (ρ, ϕ, z), EM field components are represented by

$$H_s = -\phi \left[\frac{iI_s k}{4} \right] H_1^{(2)}(k\rho) \quad (2)$$

$$\text{and } E_s = -\mathbf{z} \left[\frac{\omega\mu I}{4} \right] H_0^{(2)}(k\rho) \quad (3)$$

where ϕ , \mathbf{z} are unit vectors,

$H_0^{(2)}$, $H_1^{(2)}$ are Hankle functions of the second kind (order 0 and 1),

and ρ is the radial distance in meters to the measurement point.

At radial distances that are large compared with the skin depth, the asymptotic formula of the Hankle function leads to simplified expressions:

$$H_s \approx \phi \frac{I_s}{2} \frac{ik}{2\pi\rho}^{1/2} e^{-ik\rho} \quad (4)$$

$$\text{and } E_s \approx -\frac{\omega\mu I_s}{2} \frac{i}{2\pi k\rho}^{1/2} e^{-ik\rho}. \quad (5)$$

The cylindrically spreading ($\rho^{-1/2}$) fields become increasingly more like a plane wave as the radial distance from the conductor increases. That is, the E to H field ratio become $\omega\mu k$, which is the plane wave impedance η of the surrounding rock mass. Near the conductor, the fields are cylindrical. A gradiometer antenna is designed to measure the gradient of the cylindrical spreading EM wave. The reception of secondary EM waves in the rock mass surrounding the tunnel confirm the existence of nearby electrical conductors.

Recently, Hill (1,2) theoretically investigated the "long wavelength scattering limit" Methods I, II and III of tunnel detection. Hill's contribution considered the practical fact that tunnel conductors have finite length and conductivity. Equation 1 considered the perfect case of infinite length and conductivity of the tunnel conductor. The perfect conductor was assumed to be in the field of a uniform plane wave. The assumptions used in the development of Equation 1 lead to an overly optimistic induced current expectation. Hill also considered the fact that the distance between drill holes may be constrained by the surface features of the tunnel site. This could lead to the condition that the magnitude of the primary wave was greater than the secondary wave, preventing detection of the tunnel. Method III in Figure 1 deploys a down-the-hole vertical magnetic dipole (VMD) radiating antenna. It is used to induce current flow in the target conductor. The secondary EM fields produced by the current flow in the conductor are measured by the companion down-the-hole receiver. Because the primary E field of the VMD antenna illuminates the underground conductor with a toroidal (non-uniform) E-field pattern, induced transmission line mode currents flow in the conductor. Monofilar and bifilar modes of current flow give rise to standing waves on finite length electrical conductors. For uniform plane wave illumination assumed in Equation 1, strong monofilar mode current flows is induced in the conductors. Transmission line mode current, together with the fact that the E field magnitude vanishes at zero frequency, causes the Method III tunnel detection process to have significant frequency dependance.

The Method III VMD antenna E field is given by

$$E_r = \frac{i\omega\mu_0 M_1}{4\pi} \left[\frac{-1}{(kr)^2} + \frac{1}{i(kr)} \right] e^{-ikr} \sin \theta \text{ volt per meter} \quad (6)$$

where r is the radial distance from the VMD antenna,

and M_1 is the magnetic moment of the radiating dipole in amperes turn square-meter.

The E field vanishes at zero frequency because both ω & k vanish at zero frequency.

Hill found that with a non-uniform VMD E Field, the magnitude of the transmission line mode current standing wave reached a maximum value in the 300 to 500 kHz frequency band. The magnitude of the standing wave current versus distance is illustrated in Figure 2.

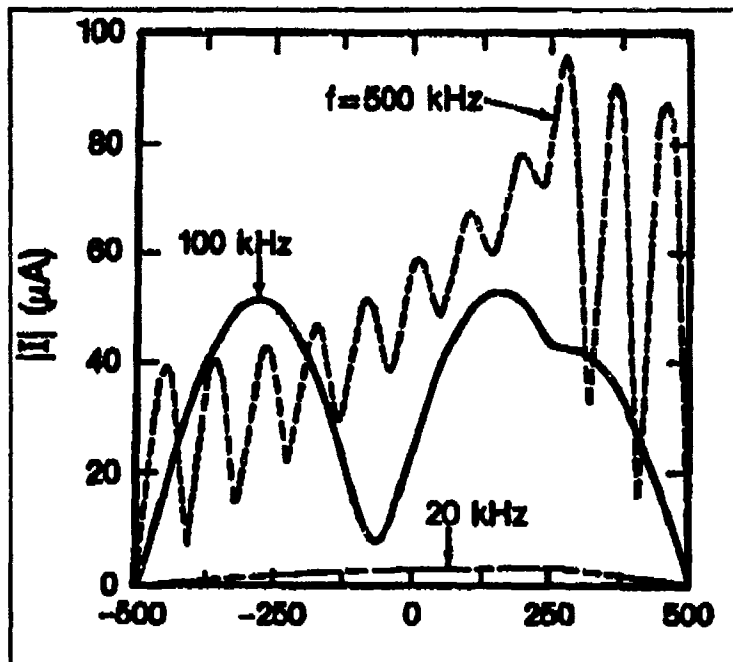


Figure 2 Standing waves expected on a 1,000 meter single conductor waveguide along the Z axis (after Hill 1988). (The VMD antenna is located at +250 meters.)

The VMD antenna is located at 250 m, and 15 m away from the conductor (at the same elevation as the conductor in the rock mass). Induced current flow produces secondary EM waves in the surrounding rock. Method II and III receiving antennas respond to

the vertical (Y) component of the primary and secondary wave. Tunnel detection requires that the magnitude of the secondary field be greater than the magnitude of the primary field.

Suppression of the primary Y field component can be accomplished by increasing the rock path separation distance between the radiating and receiving antennas such that the primary wave is extinguished on the direct rock path. The induced current travels on the conductor at a much lower attenuation rate. Suppression can also be accomplished with a gradiometer antenna.

The gradiometer antenna is designed with two identical receiving elements that are electrically connected to produce opposite but equal electromotive force (emf) output voltages in responding to a plane wave field. The equivalent circuit of a gradiometer antenna is illustrated in Figure 3.

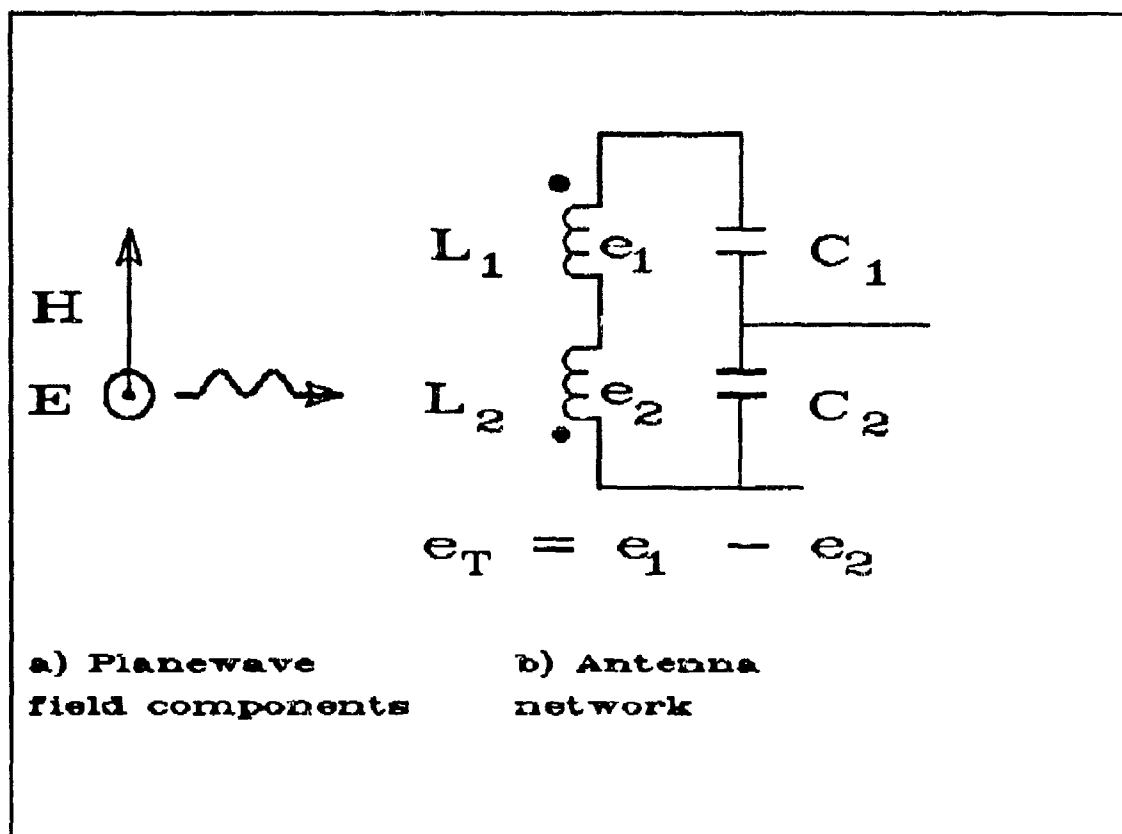


Figure 3 Equivalent network of a gradiometer antenna switched to the primary wave "suppression" mode.

The gradiometer antenna elements are composed of two ferrite rod antennas with identical inductance (L) values. The capacitors are used to resonate the circuit at the operating frequency (ω) and provide matching impedance to the emf voltage measuring receiver. The ferrite rod antennas are physically separated so that the mutual inductance is essentially zero. In this case, the total inductance (L_t) of the antenna circuit is:

$$L_t = L_1 + L_2 = 2L. \quad (7)$$

The polarity (indicated by dot symbols) of either ferrite rod antenna can be reversed and the total inductance remains unchanged. Therefore, the resonant frequency does not change when the polarity of any antenna coil is reversed. When the antennas are interconnected as shown in Figure 3, the "suppression" gradiometer mode antenna output emf voltage is given by:

$$e_t = e_1 - e_2 \quad (8)$$

When the polarity of one of the antennas is reversed, the "add" mode antenna output EMF voltage is given by:

$$e_t = e_1 + e_2. \quad (9)$$

In the vicinity of a target conductor, the "suppressed" mode gradiometer antenna responds to only the gradient of the conductor magnetic field. Since the primary wave produces equal but opposite voltages, the gradiometer output voltage sums to zero.

The response of the gradiometer antenna is illustrated in Figure 4.

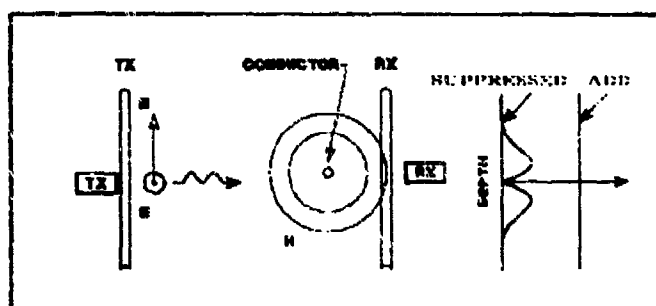


Figure 4 Vertical plane between drill holes illustrating the gradiometer antenna response.

When the radiating and receiving antennas are used in a crosshole direct ray scan between drill holes, the "add" mode emf voltage would always be greater than the "suppressed" mode emf voltage. The "suppressed" emf voltage would be a minimum value and phase shifts by 180° at the depth of the tunnel. In the suppressed voltage mode, equal magnitude maximum values would be found above and below the tunnel.

3. METHOD III CROSSHOLE GRADIOMETER TESTS AT THE SAN XAVIER MINE

The stratigraphic cross section of the San Xavier Mine test site is illustrated in Figure 5.

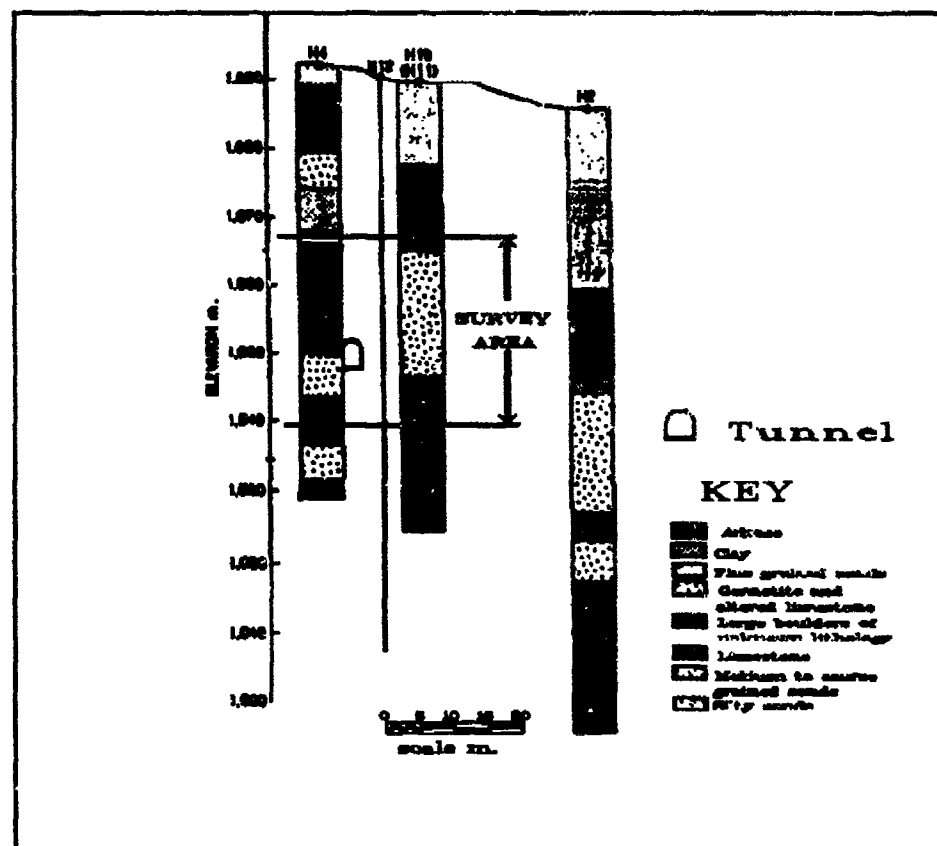


Figure 5 Stratigraphic cross section drill holes at San Xavier Mine.

A grounded conductor was placed in the tunnel at a depth of 146 feet. The tests were designed to measure the primary wave suppression and secondary (scattered) wave response. Primary wave suppression is the difference between the "add" mode and "suppressed" antenna output emf voltages. The secondary response would be measured in the "suppressed" mode. The suppressed mode direct ray scan was expected to produce a "null" in the output voltage at tunnel depth. The tests were designed to determine the dependence of null depth on gradiometer antenna element separation distance. The antenna element separation distance of 2, 5 and 10 m were used in the test. The 2m test data is illustrated in Figure 6.

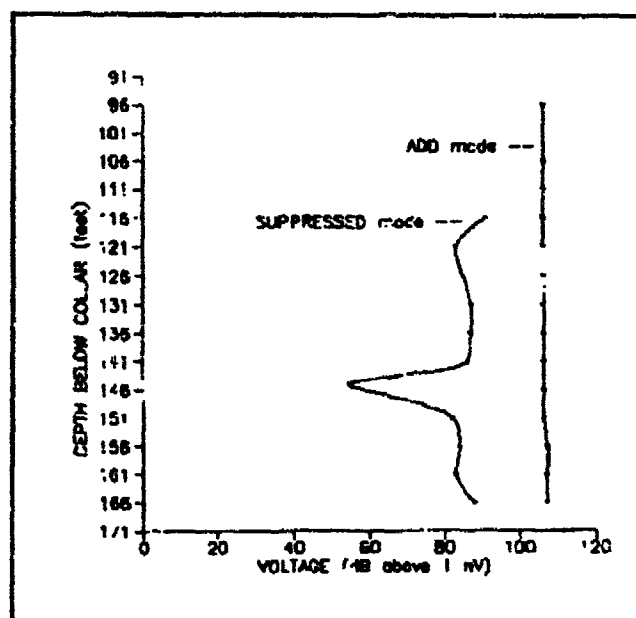


Figure 6 102.5 kHz gradiometer "add" and "suppressed" mode output voltage versus depth from the collar.

In the "suppressed" mode, the minimum output voltage occurred at the conductor depth of 146 ft. The radiating and receiving antennas were lowered in increments of 0.1 ft to find the minimum value. The minimum occurred at a depth of 145.6 ft. The 5 m element separation distance minimum was 54.8 dB re 1 nV. The 10 m element separation distance minimum was 64 dB re 1 nV.

The "null" location is very sharp. It occurs in less than 1 ft of down-the-hole distance.

4. SURFACE GRADIOMETER ANTENNA RESPONSE

The detection of shallow buried tunnels was demonstrated with a gradiometer receiving antenna on the surface. The instrument configuration is illustrated in Figure 7.

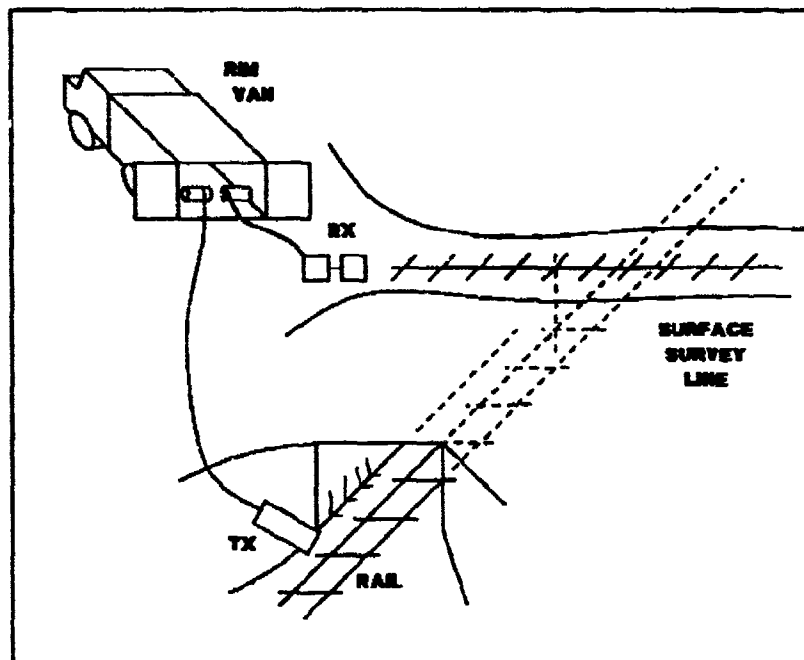


Figure 7 Detection of shallow buried tunnels with Modified Method II.

The radiating antenna was located at the adit of the San Xavier Mine, near a train track which entered the mine. A gradiometer traverse line was established on the surface. The magnitude and phase of the gradiometer output emf voltage is presented in Figure 8.

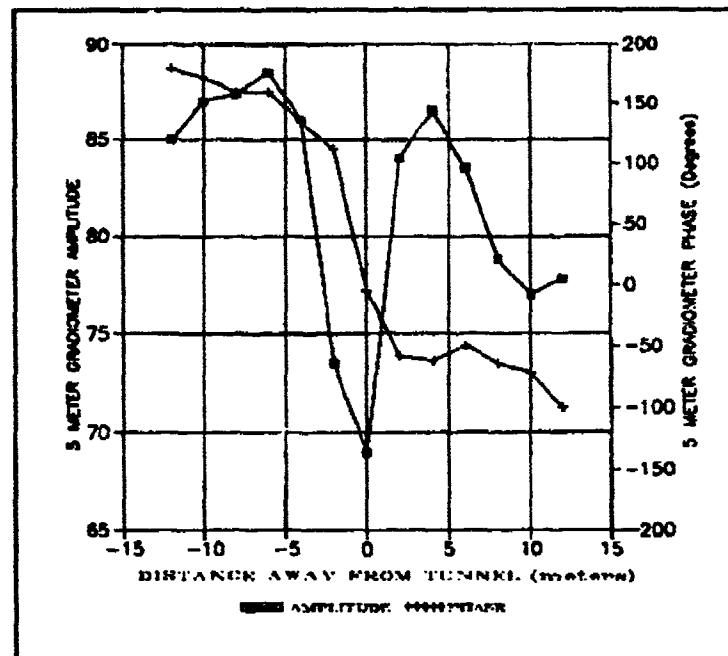


Figure 8 Measured magnitude and phase of the gradiometer "suppression" mode output signal versus distance along the surface survey line (102.5 kHz).

The gradiometer antenna emf output voltage exhibits a sharp dip (null) in the magnitude response directly above the tunnel. The dip occurs where the measured phase rapidly changes. The gradiometer output voltage decreases from 87 dB re 1 μ V to 69 dB re 1 μ V - A 18 dB null in the measured data. The sharp dip and phase shift appears to be a reliable tunnel signature because the scattered secondary wave from geologic anomalies produces increased gradiometer emf output voltage.

5. CONCLUSIONS

A gradiometer receiving antenna enhances the detection of conductors in tunnels using EM methods. Shallow buried tunnels were detected with the gradiometer antenna. The gradiometer antenna suppresses the primary wave by more than 20 dB and permits detection of the secondary wave in the presence of a strong primary field. A cross-hole scan detected a target conductor by exhibiting a very sharp null at the tunnel depth. The null was approximately 14 dB.

The gradiometer was also used in a surface reconnaissance scan. A radiating VMD antenna was placed near conductors that entered the adit. The gradiometer null of 18 dB occurred directly over the tunnel. In both tests, the phase shift approaches 180 electrical degrees at the depth of the tunnel.

Bibliography List

1. Hill, D. A., Nearfield and Farfield Excitation of a Long Conductor in a Lossy Medium. Report NISTIR 3954 National Institute of Standards and Technology, Boulder, Co.; 1990.
2. Hill, D. A., Electromagnetic Detection of Long Conduits in Tunnels, Third Technical Symposium on Tunnel Detection Proceedings, Jan. 12-16, 1988, Golden, Co.
3. Morse P. and Feshback H., Methods of Theoretical Physics, McGraw Hill, New York; 1957.
4. Stolarczyk, L.G., Long Feature Tunnel Detection Methodologies using Phase Coherent Electromagnetic Instrumentation, Thier Technical Symposium on Tunnel Detection Proceedings, Jan., 12-16, 1988, Golden, Co.
5. Burrows, M.L., Elf Communications Antennas, Peter Peregrins Ltd., Southgate House Stevenage, England, 1978.

DECISION AIDS FOR SUBSURFACE EXPLORATION

J.R. Weisinger

Applied Decision Analysis
2710 Sand Hill Road
Menlo Park, CA 94025

ABSTRACT

This paper describes a Bayesian decision framework for evaluating and optimizing the search for subsurface anomalies. The methodology has three main components: a physical model that reflects the geological uncertainty and the available information on the "target" location, a sensor model that includes the detection effectiveness, and a decision model. This approach can be used to design and evaluate search plans, to compare the impact of alternative sensor components on overall search effectiveness, and to assess data worth in the design of a site investigation program.

INTRODUCTION

Consider the following two-dimensional model for tunnel search. There is a region with area A under which an opponent has constructed a series of tunnels. Based on our best estimates of the time and technical resources available to our opponent, we feel that the area of these tunnels is A_T --that is, the portion of the region having a tunnel directly beneath it has a total area A_T . However, we are uncertain about how these tunnels may be distributed throughout the region. A new passive sensor is available that can allow us to investigate k points within the region. If a tunnel lies beneath one of these points, the sensor will detect it with probability 1. However, the range of this sensor is very small. So, we will assume that if there is not a tunnel beneath any of the k points, no detection will occur. There will be no false alarms.

What is the optimal placement of our k search points within the region? (Here an optimal strategy maximizes the probability that a tunnel is detected at one or more of the k points.)

Before discussing the optimal strategy, we can evaluate one straightforward search plan--random guessing. If each search point is drawn from a uniform distribution over the region, then each point has a probability of $a = A_T/A$ of detecting a tunnel. So, random guessing offers a probability

$$P = 1 - (1 - a)^k$$

of obtaining at least one detection. In fact, it is a result on geometric games that if our opponent proceeds optimally then no search strategy offers a higher probability of detection than P . (See Ruckle [1983].) In other words, we can never do better than random guessing in our selection of search points.

Initially, this can be a disturbing example. Although we are assuming a perfect sensor (probability of detection 1 and no false alarms) and perfect knowledge about the amount of tunneling present (the known area A_T), search planning is effectively impossible. The difficulties in this example arise from our unwillingness to introduce additional assumptions about the size, shape, or distribution of the targets. Search planning requires a model that combines information on the target, the sensor, and the environment. When one of these components is missing, planning is reduced to guesswork.

The purpose of this paper is to describe a Bayesian decision framework for evaluating and optimizing the search for subsurface anomalies. This framework will be illustrated through two examples:

- The first example is the search for tunnels. Search theory is a well developed discipline. (See the overview provided at the Third Technical Symposium on Tunnel Detection by LTC V.M. Bettencourt [1988].) However, much of this theory models the target as a point mass. The decision model that we describe reflects the physical dimensions of the tunnels and as a result accounts for spatial correlation in evaluating candidate search plans.
- The second example is a sampling model for toxic waste inspections. The problem here is to select inspection points within a potentially contaminated region. Sequential (multiple stage) sampling is allowed in this formulation. As in the tunnel search example spatial correlation is an important issue.

SEARCH THEORY OVERVIEW

Search theory had its beginning during World War II in the work of the Navy's Anti-Submarine Warfare Operations Research Group (ASWORG). The results of this work were collected in the 1946 report, Search and Screening (Koopman [1946]). The four and one-half decades since Koopman's initial work have seen the growth of a substantial body of work in search theory. Benkoski, Monticino, and Weisinger [1991] provides an overview of the current state of this field.

Some examples. Since its introduction during World War II, search theory has been applied successfully to a variety of problems. Examples include:

- **Thresher search.** On April 10, 1963, the U.S. nuclear submarine Thresher was lost while conducting her second day of sea trials. Search theory was employed to integrate information on the location of the lost submarine--and the remains were discovered. (See Richardson, Stone, and Andrews [1971].)
- **Mediterranean H-bomb search.** In 1966, the United States lost an H-bomb in the Mediterranean. Multiple scenarios were evaluated using search theory--and the bomb was recovered.
- **Scorpion search.** In 1968, the U.S. nuclear submarine Scorpion was lost--and as in the Thresher operation, search theory was employed to find the remains. (See Richardson and Stone [1971].)
- **Search and rescue.** During the 1970's, the U.S. Coast Guard developed a computer-based system for planning their search and rescue operations. This system which employs search theory has been used repeatedly to find persons lost at sea. (See Richardson and Dicensa [1980].)
- **Mining operations.** Search theory has been used to evaluate the potential of planned mining operations. An example is the search for polymetallic nodules on the ocean floor. (See Mangel [1983] and several of the articles in Haley and Stone [1980].)
- **Satellite search.** The U.S. Air Force has employed search theory to direct the operation of a series of ground-based, electro-optical telescopes in the search for lost satellites. (See Richardson and Weisinger [1984].)

Uses of search theory. In each of the examples above, search theory was applied to assist in finding a lost object. However, the specific motivation for employing

search theory varied from application to application. Typically, search theory is used to address the following problems:

- Integrating past search. Often when search theory is applied a series of unsuccessful searches have already been conducted. The key issue in these situations is to sum up the past efforts and to determine the most likely target locations in light of these efforts. Search theory is able to combine initial target information with both positive information (detections that do not completely localize the target) and negative information (unsuccessful search) to generate a posterior probability distribution for the target location.
- Planning future search. Significant research has been conducted on the construction of optimal search plans. Here the objective being optimized may be the probability of detection, the expected time/cost until a detection is obtained, or the expected number of targets detected. Stationary target problems were the first to be addressed in the literature. (See Koopman [1946].) In 1980, Brown demonstrated how a moving target problem can be reduced to a series of stationary target problems. (See Brown [1980]). This observation greatly expanded the class of search problems that can be effectively solved.
- Evaluating new sensors. Suppose that a collection of new sensors could be obtained to assist in a search operation. How can the search planner evaluate these sensors and select those that are most effective? One approach is to apply search theory and to plan a series of optimal searches with and without the new sensors. This provides a bottomline measure for the impact of the new sensors on the overall search effectiveness.
- Measuring the value of information. Additional information is often available to the search planner--at a cost. For example, an in-depth geological survey of the search region could be undertaken to assist the search operations. How can the search planner determine the potential value of this new information? One approach is to formulate several scenarios for the results of the information gathering effort. Optimal search plans can be constructed and evaluated for each alternative. These evaluations provide a basis for measuring the impact of the new information.
- Generating rules for starting/stopping search. When is it worthwhile to begin a search? When should the searcher just give up? A search planner often has to prioritize potential search operations. Planning and evaluating optimal searches offers a framework for such a prioritization. After a search has been initiated, one of the most difficult questions is when to stop. By

evaluating the past search, the planner can determine the probability that a target is present given that no detections have been obtained. If this probability is sufficiently high, then further investigations can be suspended.

The elements of a search problem. There are three basic elements present in any search problem:

- **Target information.** As the example in the introduction illustrates, a target model is critical for effective search planning. This model can reflect assumptions about the size, shape or location of the target. In most of the search theory literature, the target is modelled as a point mass. This assumption reduces the target model to a probability distribution on the target location. An example of a target location distribution can be found in Bettencourt [1988]. Target location distributions are often constructed by asking experts to describe a series of plausible scenarios. As an example, suppose that a ship has been lost at sea. After interviewing on-site personnel, we might generate three scenarios: the ship sunk close to its last reported position, the ship has drifted northward with the current from its last reported position, and an unidentified sighting earlier in the day by an aircraft might be the missing ship. Each of these scenarios can be quantified as a probability distribution on the target location--and an overall target location distribution can be formed by taking a weighted average of the three scenarios.
- **Detection function.** The detection function relates the amount of search effort placed in an area to the probability of detecting the target. This probability will depend on both the sensor being employed and the environment in which the search is being conducted. As an example, suppose that we plan to fly aircraft over the region in which the ship was lost and to attempt to obtain a visual detection. Engel and Weisinger [1988] describe the development of a "detection lobe model" for visual detection. This detection function starts with a physical model for the operation of the human eye. Based on controlled experiments conducted by the U.S. Coast Guard, this detection function estimates key parameters to determine the influence of environment factors such as the meteorological visibility on search success.
- **Constraints on effort.** Typically, the search planner has a limited amount of search effort or time available to conduct the operation. There are a variety of ways in which these constraints might be expressed: the total search effort is limited, the rate at which the search can be conducted is limited (there is only one search unit that must move from site to site), or the cost of

the search is limited (and the cost of search varies throughout the search region). In the example of the lost ship, search effort might be expressed in "swept area". Given the speed of the aircraft and the width of the swath that can be visually searched, the search planner can quantify the limitations on the available effort.

Search decision aids. Computer-based search decision aids have been constructed for a variety of search problems. An example is the CASP system employed by the U.S. Coast Guard to plan search and rescue operations. (See Richardson and Discenza [1980].) Some of these systems use Monte Carlo techniques; others are "analytic" (non-Monte Carlo). In order to provide an overview of the operation of one of these systems, we focus here on the Monte Carlo approach.

The search decision aid begins by drawing a collection of potential target locations. These draws are based on the target scenarios described above. So, each target draw can be viewed as a plausible explanation for the condition of the lost object. The decision aid establishes a "target state record" for each draw. At a minimum, this record will include the location of the draw and the "weight" of the draw. Initially, all draws receive an equal weight--given by one over the number of draws. If the target can adopt several states that will impact its detectability, then values for these states will also be included in the target state vector. As time progresses, the decision aid may need to update the locations of the target draws to account for target motion. Since our primary concern is tunnel search, we will ignore this possibility.

Now suppose that a candidate search plan is to be evaluated. We will assume that this candidate satisfies the constraints on search effort. Given this plan, the detection function allows us to determine the probability that each of the target draws will be detected. Taking the weighted average of these detection probabilities (using the weights in the target state records) yields the probability of detection for the plan.

In addition to evaluating plans, the search decision aid can provide a graphic image of the current state of knowledge about the target location. Before conducting search, the density of the target draws reflect this knowledge. So, a prior target location map can be developed by dividing the search region into cells and counting the number of draws in each cell. After conducting unsuccessful search a similar map can be constructed--if we update the weights in the target state records. The updated weights are given by Bayes' Theorem. This theorem indicates that the new weight of a draw is proportional to the old weight times the probability that the candidate search plan will not detect this draw. (This probability of non-detection is just one minus the probability generated by the detection function.) Now the posterior target location map can be constructed by adding the weights of the target draws within each cell.

UNIQUE ASPECTS OF TUNNEL SEARCH

Developing a search decision aid for subsurface anomalies involves two unique features not included in the discussion above: the shape and size of the target and the impact of the geology.

Shape and size. Search theory normally models the target as a point mass. In the case of lost submarines, people at sea, or satellites, this is a reasonable approximation. However, the length dimension of a tunnel makes this model inappropriate for tunnel search. In particular, a point mass model for tunnels would ignore the interaction among search efforts at different locations. As an example, failure to detect a tunnel with a line of boreholes (and some passive sensor) indicates not only that a tunnel is unlikely to run directly beneath this line, but that it is unlikely that any tunnel running perpendicular to this line is located nearby.

The Monte Carlo decision aid described above could be adapted to the tunnel search problem by drawing entire candidate tunnels--rather than single points. In other words, each target state record would be extended to include a description of an entire tunnel path. (This is similar to generating a sample path for a stochastic process.) These Monte Carlo tunnels could be based on the following information:

- Likely starting points. A probability distribution can be established on likely starting points for tunnels. For example, abandoned mining sites might be viewed as plausible points for initiating tunnel construction.
- Tunnel statistics. Statistics from tunnels that have been discovered can be collected. This information can be combined with the input of mining experts to describe the likely distribution of tunnel characteristics--including length, depth, and the number of direction changes.
- Geological features. The geology of a region can dictate the likely position of tunnels. For example, tunnels may follow joint planes. This information can be quantified in a "vector field" describing likely directions for a tunnel to progress.

"Tunnel draws" could now be generated by drawing a starting position and then moving in a random direction--as dictated by the distribution on tunnel statistics and the impact of the geological features. Once these target state records have been established, candidate search plans can be evaluated as before.

Geological features. The environment can have a strong impact on both the target model and the detection function. Most of the applications reported in the search literature were conducted in the air or underwater. Typically, these search models attempt to divide the environment into homogeneous subregions. As an example, consider the original application of search theory--anti-submarine warfare (ASW). The most common means for locating a submerged submarine is acoustic detection. ASW search models divide the region of search into homogeneous water masses. Detection capability within a subregion is then characterized by an acoustic propagation loss curve.

An analogous model for geological features needs to be developed for tunnel search. Common approaches to determining strata boundaries include trend surface analysis, Fourier methods, and kriging. Hunter and Mann [1992] includes an overview of these techniques. However, in the final analysis, the only basis upon which strata can be interpolated is a clear understanding of the geological processes leading to their formation.

SAMPLING FOR TOXIC WASTE

Search theory provides a Bayesian framework for allocating resources. In the context of tunnel search, the development of a search decision aid faces some unique problems in modeling the geology of the search region. A related and increasing important problem involves sampling for toxic waste. Like the tunnel search problem, this involves the allocation of resources and depends on a model for the geology of the region. To conclude our discussion of decision aids, we describe the Sample Plan Evaluator. This is a Bayesian decision aid developed for the Los Alamos National Laboratory (LANL) to compare the performance of proposed sampling plans for the investigation of potentially contaminated sites.

Problem statement. A list of sites at LANL have been designated as potentially contaminated with toxic waste. Managers at LANL have been charged with reviewing these sites--and if appropriate initiating a clean-up effort. Prior to making these decisions, the managers have the option of conducting a series of sampling experiments at any of the sites. These experiments will provide more precise information on the level of contaminant at the sampled sites. Both clean-up and sampling efforts are expensive--although these expenses are small when compared with the potential consequences of declaring a contaminated site clean. At which sites should the sampling experiments be undertaken--and what is the probability of an incorrect evaluation of a site?

The elements of the sampling problem. As in the search problem, there are three key elements:

- "Target" information. Here the target is the toxic waste. Records on the previous use of each site provide prior information on the level and location of the contamination. Discussions with experts provide a series of scenarios on the evolution of the contaminant over time. For example, a stream that once flowed through the area may have provided a mechanism for spreading the contaminant beyond its original location.
- Detection function. Surface and subsurface sampling forms the search portion of this problem. Each sample is tested for the contaminant--with some measurement error. A key part of this model is the assumed spatial correlation in the contamination. This allows the sampling model to extend the point estimates of the contaminant to overall estimates on the level of contamination.
- "Search" constraints. Cost and the availability test equipment form constraints on the sampling plans.

The sampling model. In the search decision aid, a probability distribution is maintained on the target location. In the sampling model, a probability distribution is maintained on the overall level of contamination in the region. A threshold on this overall contamination has been established. Sites above this threshold must be cleaned up; those below are regarded as safe. The probability distribution on the overall level of contamination allows us to compute the probability that a clean-up/no clean-up decision is correct. More precisely, if we decide not to clean up, then the probability of an incorrect decision is equal to the probability that the contaminant is above the designated threshold. Similarly, if we decide to clean up.

Sampling provides information on the level of contamination. Based on our model for the spatial correlation of the toxic, we can apply Bayes' Theorem to compute a posterior distribution on the level of contamination given the sampling results. However, there is one main difference between this updating procedure and the search problem. In search, there are two possible outcomes: detection or non-detection. When evaluating potential search plans, this simplifies the application of Bayes' Theorem. In the sampling problem, there are a spectrum of outcomes corresponding to the contaminant levels that can be reported in the sample. So, candidate sampling plans must be evaluated in view of the probabilities of these possible outcomes.

SUMMARY

Search theory provides a Bayesian framework for planning effective search operations. This theory has been applied successfully to a variety of applications ranging from ASW to search and rescue. In these applications, search theory has been able to perform several functions including the integration of past search, the planning of future search, and the evaluation of new sensors. Most of these applications have involved the development of a computer-based search decision aid. The tunnel search problem offers unique challenges in modeling the target and the environment. However, plausible approaches to both of these difficulties appear to be available. In fact, a related problem in the sampling for toxic waste has been addressed within a similar Bayesian framework.

REFERENCES

- Benkoski, S.J., Monticino, M.G., and Weisinger, J.R., 1991, "A Survey of the Search Theory Literature", Naval Research Logistics, Vol. 38, pp. 469-494.
- Bettencourt, LTC V.M., 1988, "A Theoretically Based Evaluation of the Korean Tunnel Search", Proceedings of the Third Technical Symposium on Tunnel Detection.
- Brown, S.S., 1980, "Optimal Search for a Moving Target in Discrete Time and Space", Operations Research, Vol. 28, pp. 1275-1289.
- Engel, D.D. and Weisinger, J.R., 1988, "Estimating Visual Detection Performance At Sea", Operations Research, Vol. 36, pp. 651-659.
- Haley, K.B. and Stone, L.D., 1980, Search Theory and Applications, Plenum, New York.
- Hunter, R.L. and Mann, C.J., 1992, Techniques for Determining Probabilities of Geological Events and Processes, Oxford University Press.
- Koopman, B.O., 1946, Search and Screening, OEG Report No. 56, The Summary Reports Group of the Columbia University Division of War Research. (Available from the Center for Naval Analyses.)
- Mangel, M., 1983, "Optimal Search for the Mining of Underwater Mineral Resources", SIAM Journal of Applied Mathematics, Vol. 43, pp. 99-106.

Richardson, H.R. and Discenza, J.H., 1980, "The United States Coast Guard Computer-Assisted Search Planning System (CASP)", Naval Research Logistics Quarterly, Vol. 27, pp. 659-680.

Richardson, H.R. and Stone, L.D., 1971, "Operations Analysis During the Underwater Search for Scorpion", Naval Research Logistics Quarterly, Vol. 18, pp. 141-157.

Richardson, H.R., Stone, L.D., and Andrews, F.A., 1971, Manual for the Operations Analysis of Deep Ocean Search, Prepared for the Supervisor of Salvage, Naval Ship Systems Command.

Richardson, H.R. and Weisinger, J.R., 1984, "The Search for Lost Satellites", Proceedings of the 7th MIT/ONR Workshop on C³ Systems.

Ruckle, W.H., 1983, Geometric Games and Their Applications, Pitman Advanced Publishing Program, London.

Session 6
Other Methods

THE APPLICATION OF COAL AND ROCK THICKNESS MEASUREMENT TECHNOLOGY TO TUNNEL DETECTION

Robert L. Chufo

U.S. Bureau of Mines
Pittsburgh Research Center
Pittsburgh, PA 15236

ABSTRACT

The technology for a new class of spectral, spatial sensors has been developed by the U.S. Bureau of Mines for the guidance of automated mining machines. The sensor can accurately determine the thickness and dielectric constant of coal and rock and locate the interfaces in multilayer media. The noncontacting electromagnetic technique uses spatial modulation created by moving a simple sensor antenna in a direction along each axis to be measured while the complex reflection coefficient is measured at multiple frequencies over a two-to-one bandwidth. The antenna motion imparts spatial modulation to the data that, through signal processing, solves the problem of media, target, and antenna dispersion. The system, including the dipole antenna, is calibrated by making a measurement of a reflecting metal surface. Knowledge of the dielectric constant of the media is not necessary because the electrical properties of the media are determined automatically along with the distance measurement. The signal processing technique avoids the use of radio frequency absorbing material to deal with multipath problems and the effects of nearby signal distorting structures. In addition to a summary of the system theory and measurement architecture, field test results and application examples will be presented. Preliminary tests at nonoptimum frequencies have detected tunnels at a depth of 3 ft. Application of this technology at lower frequencies and where a larger antenna is acceptable along with changes in the spatial and spectral integration parameters, is being pursued by the U.S. Bureau of Mines for application to the general problem of "seeing into the earth."

INTRODUCTION

Ground penetration radar technology has to deal with two fundamental problems: penetration and focus. Low-frequency electromagnetic waves penetrate the media but do not clearly image small objects. When the transmitted energy does penetrate the media, the returning signal appears to be scrambled and out of focus. The problem is caused by dispersion. Media dispersion coupled with antenna and target dispersion cause problems too complex to resolve in the time domain. It is much easier to solve these problems in the frequency domain. The theory supporting the U.S. Bureau of Mines Radar Coal Thickness Sensor technology is in the frequency domain but the signal processing architecture uses both

frequency domain and time domain signal processing. In the future, all the signal processing will be in the frequency domain. A time domain graphics plot of the transformed frequency domain data is provided to visualize the reflected signal.

The Bureau's thickness measurement technique uses a continuous-wave (CW) signal with a single antenna for simultaneously transmitting and receiving. The antenna is moved perpendicular to the surface whose layers are being investigated. The antenna movement is in 32 discrete steps over a distance of 16 in. At each step, CW signals are transmitted in 401 increments from 600 to 1,600 MHz. The amplitude and phase of the reflected signal are recorded. When the antenna has completed its motion, all of the recorded data are analyzed by a computer. The result of the analysis shows the location and thickness of layers of material with different dielectric constants. The boundaries between air and coal, coal and shale, etc., can be measured with an accuracy of 1 in to a depth of at least 10 ft. Field experience with the sensor has provided the confidence to envision that this sensor technology can be a general solution that will satisfy other underground imaging and thickness measurement requirements. These requirements include the detection of tunnels and the detection of mining hazards such as water-filled voids and fractures that may be particularly dangerous to the mining process. [The present technology has been implemented as a one-dimensional (1-D) sensor]. However, the theory for developing this same concept into a 2-D and 3-D imaging sensor has been developed and will be implemented and field tested.

ACKNOWLEDGMENT

The author acknowledges the contributions of Boeing Defense and Space Group in supplying material for this paper under U.S. Bureau of Mines contract No. HO398009, Development of a Radar Coal Thickness Sensor. Walter J. Johnson, now with WALTECH Holography, was the Principal Investigator. Raymond J. Helinski, Electronic Technician, U.S. Bureau of Mines, assisted in installing and modifying the software at the Pittsburgh Research Center and in the data collection during both surface and underground testing.

DESIGN APPROACH

Equipment

Early in this development effort it was decided that the thickness measurement scheme would be developed in software that could control off-the-shelf radio frequency (RF) test equipment. This approach was taken to insure that no resources were devoted to the expense of hardware design and development and the associated development risk. Consequently, the program effort went into the development and validation of software to gather and process the measurement data. The antenna is a simple dipole with a polarized screen reflector and matching balun. The antenna positioner (fig. 1) that moves the antenna to produce the spatial modulation is constructed entirely of common hardware store PVC tubing. A stepper

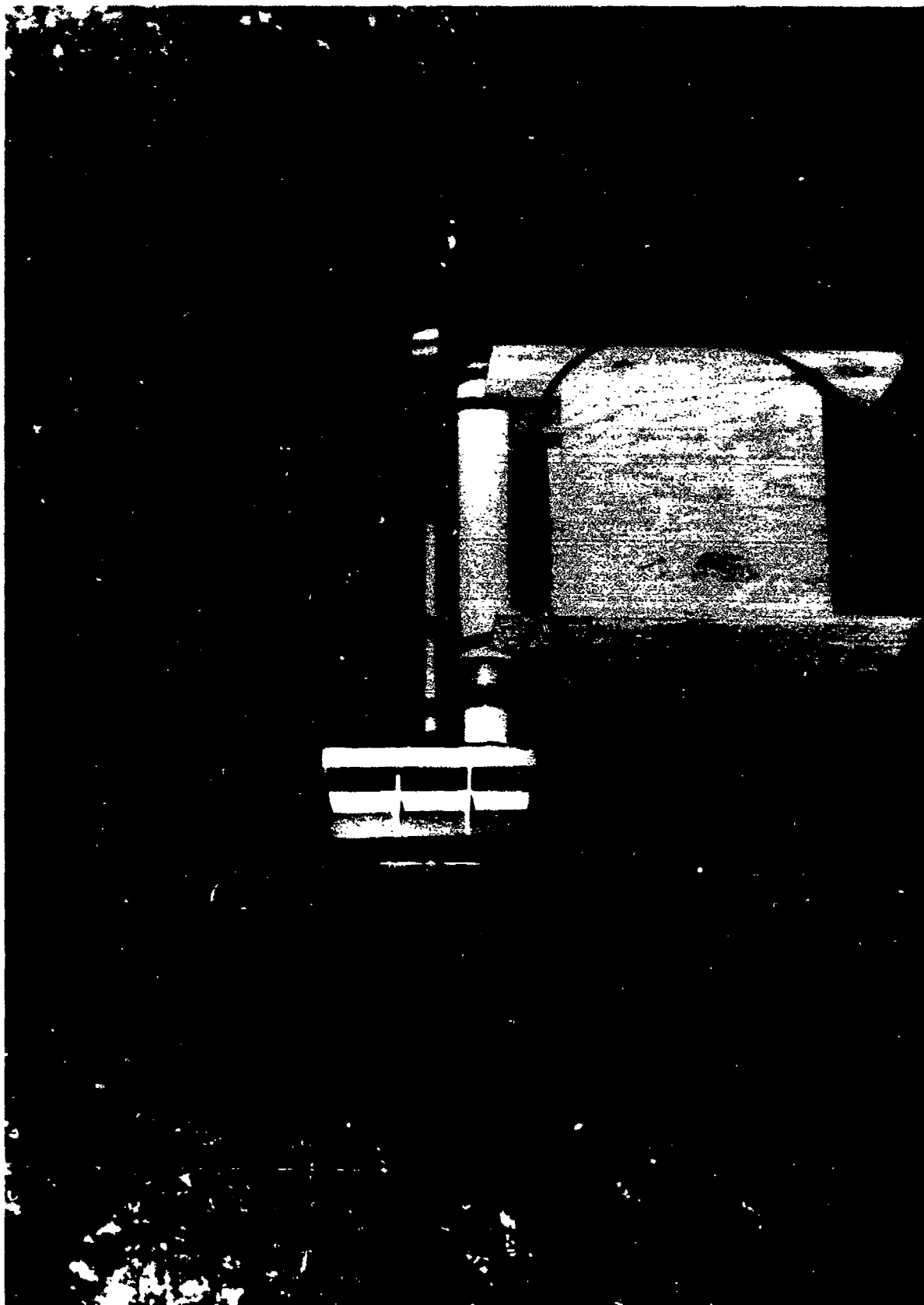


FIGURE 1. - The antenna and positioner

motor is enclosed in the base of the positioner and drives a nonmetallic screw to position the antenna with sub-millimeter accuracy. The positioner assembly includes limit switches that interrupt the data collection software if antenna positions beyond the range of travel are entered into the computer data statements. Originally it was thought that the antenna positioner should be constructed of nonmetallic components, and with the exception of the stepper motor at the far end of the assembly and the small limit switches, the positioner is nonmetallic.

The instrumentation (fig. 2) used is a HP8753 network analyzer,¹ a HP R/382 68040-based computer controller, and a general purpose IEEE488 bus controller for driving the stepper motor. A fiber optic IEEE488 data link is used when it is desired to locate the control computer in a sheltered location away from rock falls and the mining machinery. The computer code is written in Rocky Mountain Basic (RMB).

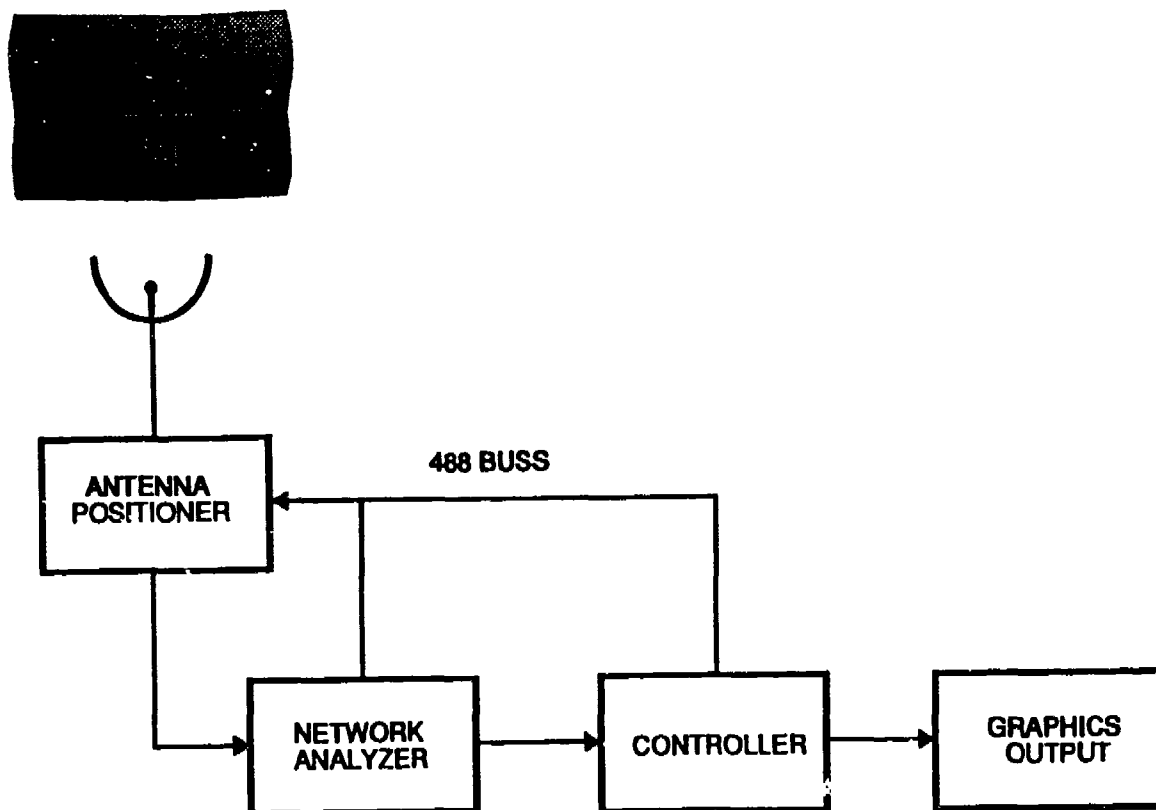


FIGURE 2. - Instrumentation

¹Reference to specific products does not imply endorsement by the U.S. Bureau of Mines.

Theoretical Summary

The problems of designing an electromagnetic coal thickness sensor can best be defined by utilizing a sensor model created from 1-D spherical-wave-scattering matrix theory. This is based on plane-wave scattering matrix theory (Kerns 1981). By separating surface reflections from single-layered media reflections, laboratory and field testing confirmed the validity of the model. Also, by having a model based on fundamentals, a wide range of design architectures can be used.

Several theoretical modeling approaches were pursued over the course of this research project. The merits of a bistatic antenna configuration with antenna motion parallel to the coal face, was explored to some length. In the bistatic configuration, all four S parameters [i.e., the reflection coefficient at each antenna (S_{11} and S_{22}), the forward and reverse transmission between the several antennas (S_{12} and S_{21}), along with their polarizations] were measured. However, the monostatic configuration with its single antenna moving on an axis perpendicular to the coal face provided an adequate signal-to-noise ratio (SNR) while avoiding the multiple reflection problems of using more than one antenna. This choice was a classic example of trading SNR for hardware simplicity.

A complete and rigorous theoretical discussion of the implementation of the several design architectures developed during the course of this research is lengthy and beyond the scope of this paper. Chufo and Johnson, 1991, cover the original development of this technology in more detail. However, in the interest of presenting the reader with a summary understanding of the complexity of the mathematics involved, the following information on the data reduction architecture, called the Quick Reduction Method, is presented.

Fig. 3a shows a single antenna interacting with a dielectric half space. In order to integrate through the boundary, we characterize the boundary as four parameters of a scattering matrix (1) that are all experimentally measurable.

$$\begin{bmatrix} b_0 \\ b_1 \end{bmatrix} = \begin{bmatrix} S_{00} & S_{01} \\ S_{10} & S_{11} \end{bmatrix} \begin{bmatrix} a_0 \\ a_1 \end{bmatrix} \quad (1)$$

Because the mathematical equations are in the frequency domain and the antenna interactions with the half-space are so difficult to visualize without a time variable, we have formalized a frequency domain diagram (fig. 3b) that looks like a time space diagram. This frequency domain diagram is called the Monochromatic Phase Space Diagram (MSPD).

We assume the boundary is a single point in space with four nodes, with two incident voltage waves and two reflected waves emerging from the nodes (fig. 3b). In between the

four nodes are four transfer functions (S parameters of the matrix) which transfer the voltage waves to the other nodes. All four antenna nodes are collocated in space but not phase.

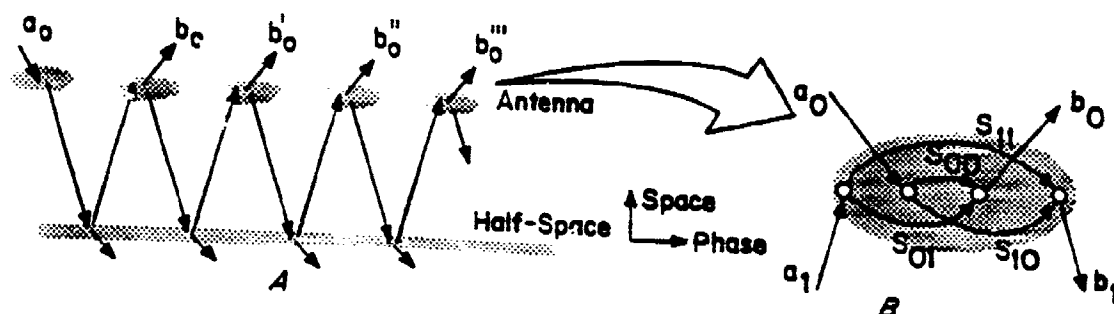


FIGURE 3. - Antenna as a scatterer (a) and as a scattering matrix (b)

Considering the reflections from the antenna and half-space in fig. 3a we can write:

$$M_{11} = \frac{b_0 + b'_0 + b''_0 + b'''_0 + \dots}{a_0} \quad (2)$$

This summation starts with a transmitted wave a_0 and with no outside interference (i.e., $a_1 = 0$).

For a single target we can write:

$$M_{00} = \frac{a_0 S_{00} + a_0 S_{10} S_{12} R_1 + a_0 S_{10} S_{01} R_1^2 S_{11} + \dots}{a_0} \quad (3)$$

and if we define a feedback term F_1 :

$$F_1 = 1 + S_{11} R_1 + (S_{11} R_1)^2 + \dots = \frac{1}{1 - S_{11} R_1} \quad (4)$$

This results in the general form of the monostatic model of:

$$\frac{M_{11} - S_{00}}{S_{01}S_{10}} = \sum_{n=1}^{\infty} \left[R_n^{-1} - S_{11} \right]^{-1} \quad (5)$$

Considering two-target multipath in the case of a single antenna with a reflector looking into a dielectric half-space, and considering that signals can have a double-bounce from the antenna as a passive scatterer (i.e., the first bounce is from the half-space to the antenna reflector and does not intercept the antenna), before returning to the receiver and generalizing about the two targets, we can write:

$$\frac{M_{11} - S_{00}}{S_{10}S_{01}} = \sum R F + 2 \sum R F F + \sum R'' F'' \quad (6)$$

The left hand side of equation 6 does not show the second order multipath terms. An important element of this measurement technique is the signal modulation produced by the antenna motion. By integrating over space, we can decorrelate the multipath term. Since the spatial integration is coherent with the coal target but not coherent with any other spatial distances, the multipath will become zero sum or at least small compared with the surface reflection.

Then considering that all the summation terms contain at least one $T_{232}\Gamma_3$ term, the expression can be rewritten as:

$$\frac{M_{11} - S_{00}}{S_{10}S_{01}} = T_{232}\Gamma_3 [\sum R'' F] \quad (7)$$

or

$$\Gamma_3 = \frac{M_{11} - S_{00}}{T_{232}S_{10}S_{01}} [\sum R'' F]^{-1} \quad (8)$$

This equation becomes the basis of the Ratio Reduction Method: that the ratio of unknown reflection to the calibrated reflection will cancel translation, reflection, and part of the series.

A calibration test setup similar to a mine test can be made with:

$$\Gamma_3^{cal} = \frac{M_{11}^{cal} - S_{00}}{T_{232}^{cal}S_{10}S_{01}} [\sum R'' F]_{cal}^{-1} \quad (9)$$

The unknown data will have the similar form of:

$$\Gamma_3^{data} = \frac{M_{11}^{data} - S_{00}}{T_{232}^{data} S_{10} S_{01}} [\Sigma R \cdot F]_{data}^{-1} \quad (10)$$

Assuming that Γ_3^{cal} is a perfect metal plate reflector and $T_{232}^{cal} = T_{232}^{data}$, then:

$$\Gamma_3 = \frac{M_{11}^{data} - S_{00}}{M_{11}^{cal} - S_{00}} \left[\frac{[\Sigma R \cdot F]_{cal}}{[\Sigma R \cdot F]_{data}} \right] \quad (11)$$

The $R \cdot F$ ratio term contains all the second order terms, and assuming the calibration test setup geometry is close to the mine test geometry, then this term is unity and drops out of the equation.

Underground testing of this concept for both coal roof and rib measurements as well as surface tests of sandstone and granite samples have confirmed that the assumptions made are of sufficient validity to enable spot thickness measurements to be made to within 1-in accuracy. As the technique is further developed it is expected that even greater accuracy and measurement confidence levels will be obtained for a running series of measurements made from a mining machine moving along the coal roof, floor, or rib.

SOFTWARE

The software has been written in the form of three linked programs (fig. 4). The first program named "SCRIPT" initializes the antenna positioner (spatial modulator) and the network analyzer. A file name and comments describing the conditions of the test are included for future reference and data cataloging.

The first antenna position is set and the amplitude and phase of the reflected signal are measured and stored for 401 frequency steps. The positioner is then incremented by one step and the frequency again stepped through the same range. This is repeated for all 32 antenna positions. This procedure produces a file of the spatial and spectral data that can be processed by several methods to obtain the thickness, dielectric constant, and loss in decibels per meter of each layer of the target material.

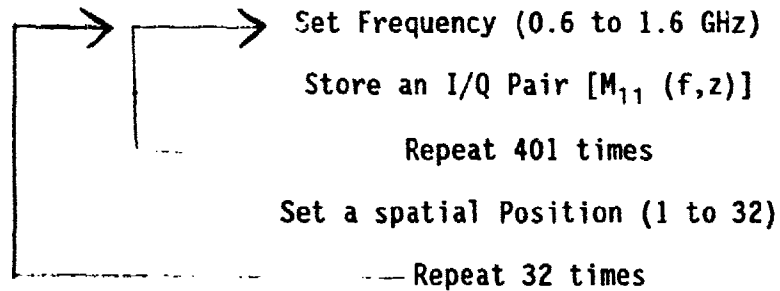
The second program named "GAMMA" retrieves the metal plate calibration data and computes the antenna reflection dispersion coefficient for each frequency. Then the antenna dispersion is subtracted from the calibration data and stored.

SOFTWARE ARCHITECTURE

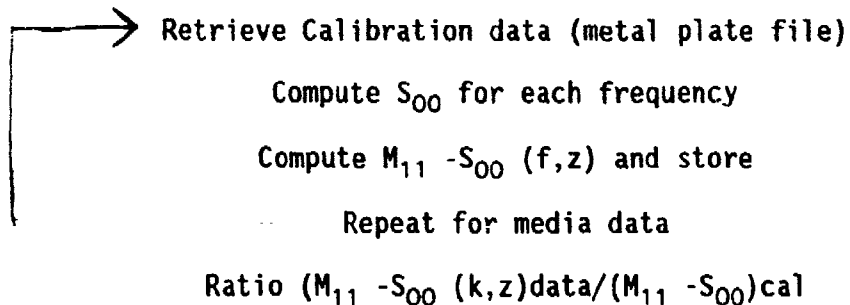
Setup the spatial modulator & network analyzer

run SCRIPT

Enter file name and test description



run GAMMA (Ratio Reduction Method)



run BUFF2DFT

compute spatial integration

Compute first reflection

If roof, compute thickness and dielectric

Find second peak

If wall, compute thickness and dielectric

Transform into the time domain

Plot amplitude vs time

FIGURE 4. - Software architecture

The same procedure is done for the target data. The ratio of the two results gives the reflection coefficient as a function of frequency and distance, and compensates for the gain of the antenna, and removes the rest of the dispersion and some of the higher order effects.

The third program named "BUFF2DFT" is a computation of the spatial integration and takes an average of all the I's and Q's (the in-phase quadrature phase components). A single I and Q pair is obtained for each frequency and a fourier transform is performed to convert the data to the time domain. The first peak, the coal surface, is used as a reference for the computation of the distance to the remaining dielectric interfaces. These data are then plotted against time to provide a visual representation of the reflections from each surface. It is expected that a 60 dB SNR referenced to a perfect metal reflector can be maintained. Power levels greater than the present 0 dBm have been tried in the field but the present level or less is more than adequate. The most sensitive and expensive parameter to implement is the system bandwidth. Varying the number of antenna positions or the total range of antenna travel has less effect on measurement accuracy than system bandwidth.

FIELD TESTS

The initial purpose of this research was to develop a coal and rock thickness sensor of sufficient accuracy to provide vertical and horizontal guidance of both room-and-pillar and highwall mining machines. In order to validate the theory developed for thickness measurement, extensive underground and surface mine testing was conducted over a period of 2 years in mines with a variety of geological and environmental conditions. Test areas of both freshly mined and aged coal from 3 in to 60 in thick were measured. The areas measured ranged from very dry to extremely wet with water dripping from the roof test area. The wet coal did not affect the thickness measurement. Coal seams with clay and metal vein intrusions of iron pyrite could be imaged and the distance from the coal surface to the intrusion could be accurately measured. Surface roughness and cleating was not a problem. The average thickness of rough cleated surfaces was measured accurately. Accurate measurements were obtained even when water filled the cracks between the cleats.

Figures 5 through 9 are examples of thickness measurements made on mine roof coal, mine rib coal, granite, sandstone, and salt. On the vertical axis, the plot shows the amplitude of the reflected signal in decibels; time in nanoseconds is shown on the horizontal axis. The large peak on the vertical axis represents the reflection from the first interface. Signals plotted to the left of the large peak represent discontinuities internal to the measurement equipment and between the antenna and the first surface. These reflections are reduced to at least 30 dB below the first interface reflection by the calibration and spatial integration scheme. Peaks to the right of the first reflection are reflections from discontinuities internal to the media being measured. The printout on the left lists the calculated real part of the dielectric constant, the loss in decibels per meter, and the thickness of the target material. Measurements have identified both the thickness of the coal and the thickness of the next layer, usually shale, above the coal roof. At the L-band frequencies

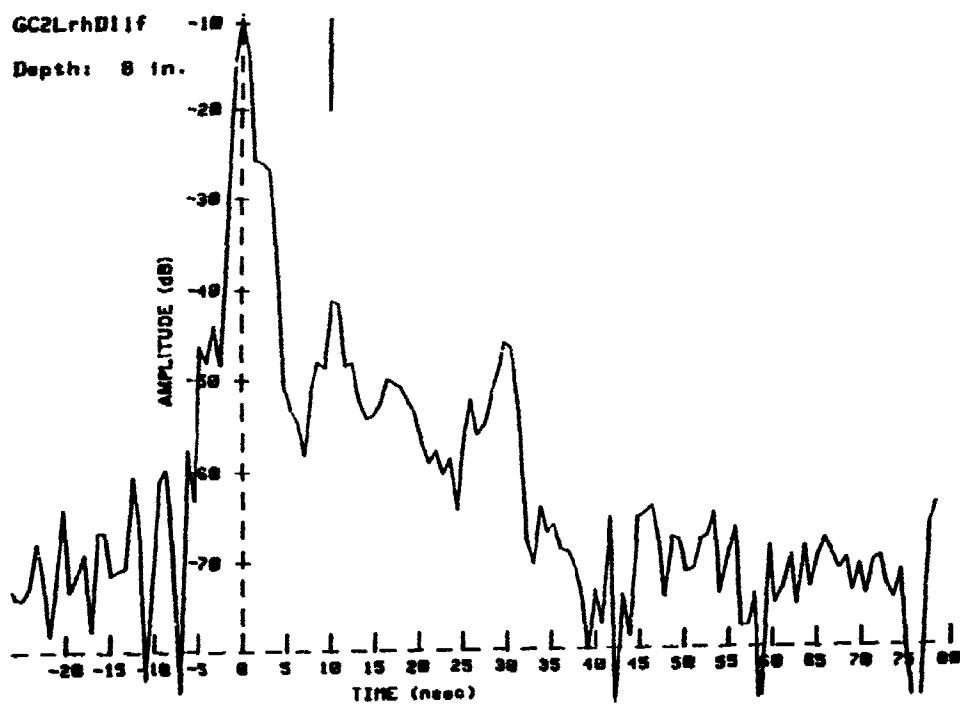


FIGURE 5. - Roof coal thickness

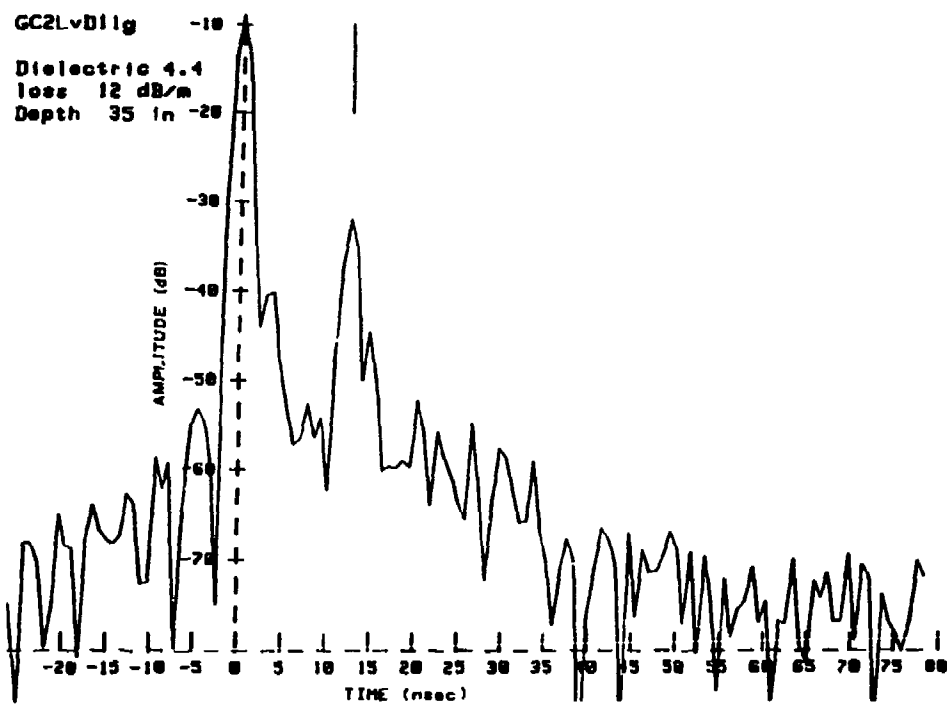


FIGURE 6 - Rib thickness

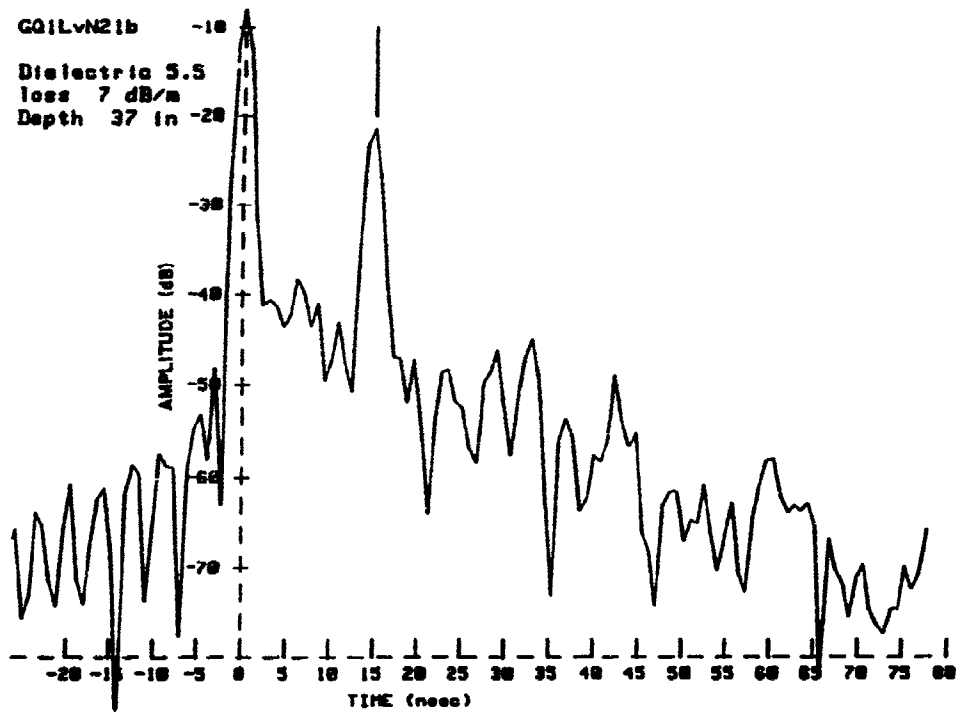


FIGURE 7. - Granite block thickness

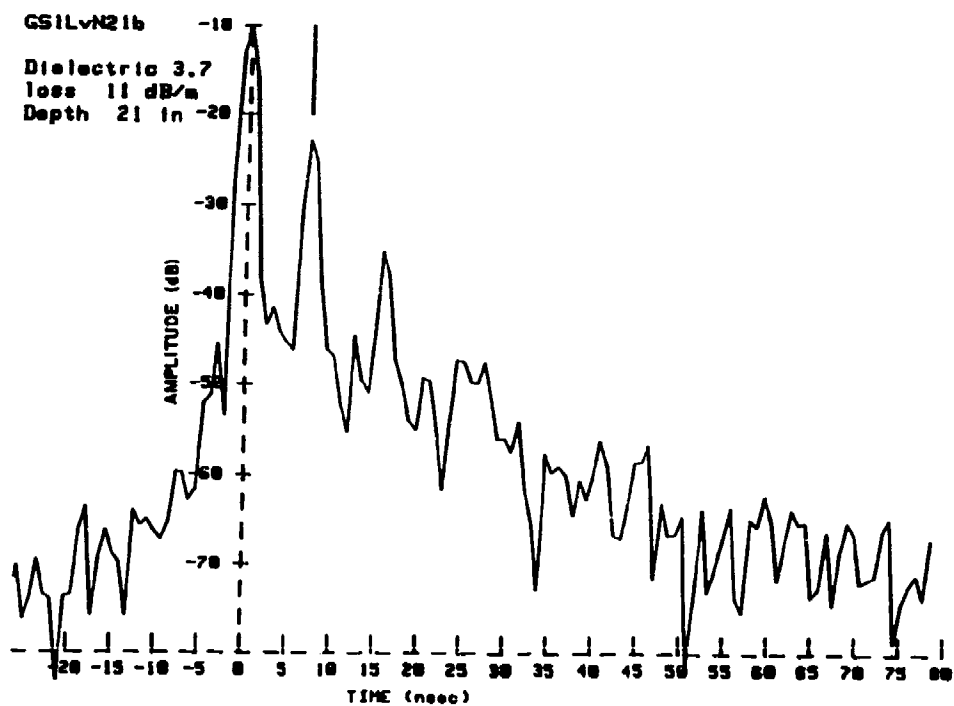


FIGURE 8. - Sandstone block thickness

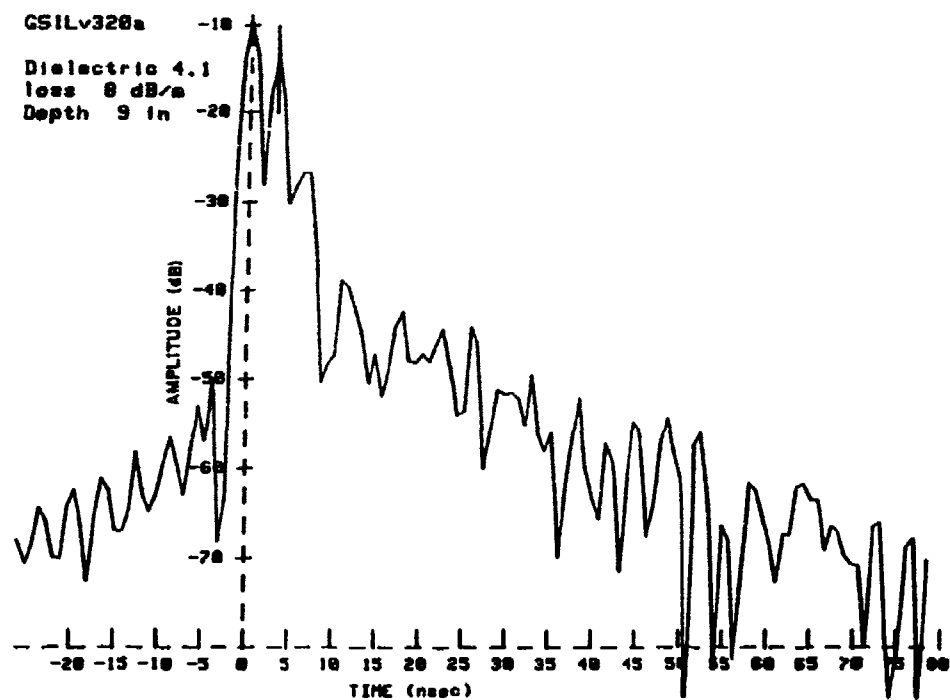


FIGURE 9. - Sas. blk. & thickness

presently used, the depth of penetration is usually about 10 ft. Future roof thickness measurement research will attempt to provide a direct readout of the thickness of each layer of geological material within the penetration range of the signal. At the present time the power level of the transmitted signal is 0 dBm (1 MW). This signal level or less is adequate to produce a good SNR for the return signal measurement and increased power levels are not necessary. Both the hardware and software will operate from 300 kHz to 3,000 MHz.

Similar results are obtained when the sensor is used to measure the thickness of concrete or asphalt paving. Multiple layers of paving can be detected and the thickness of each layer measured.

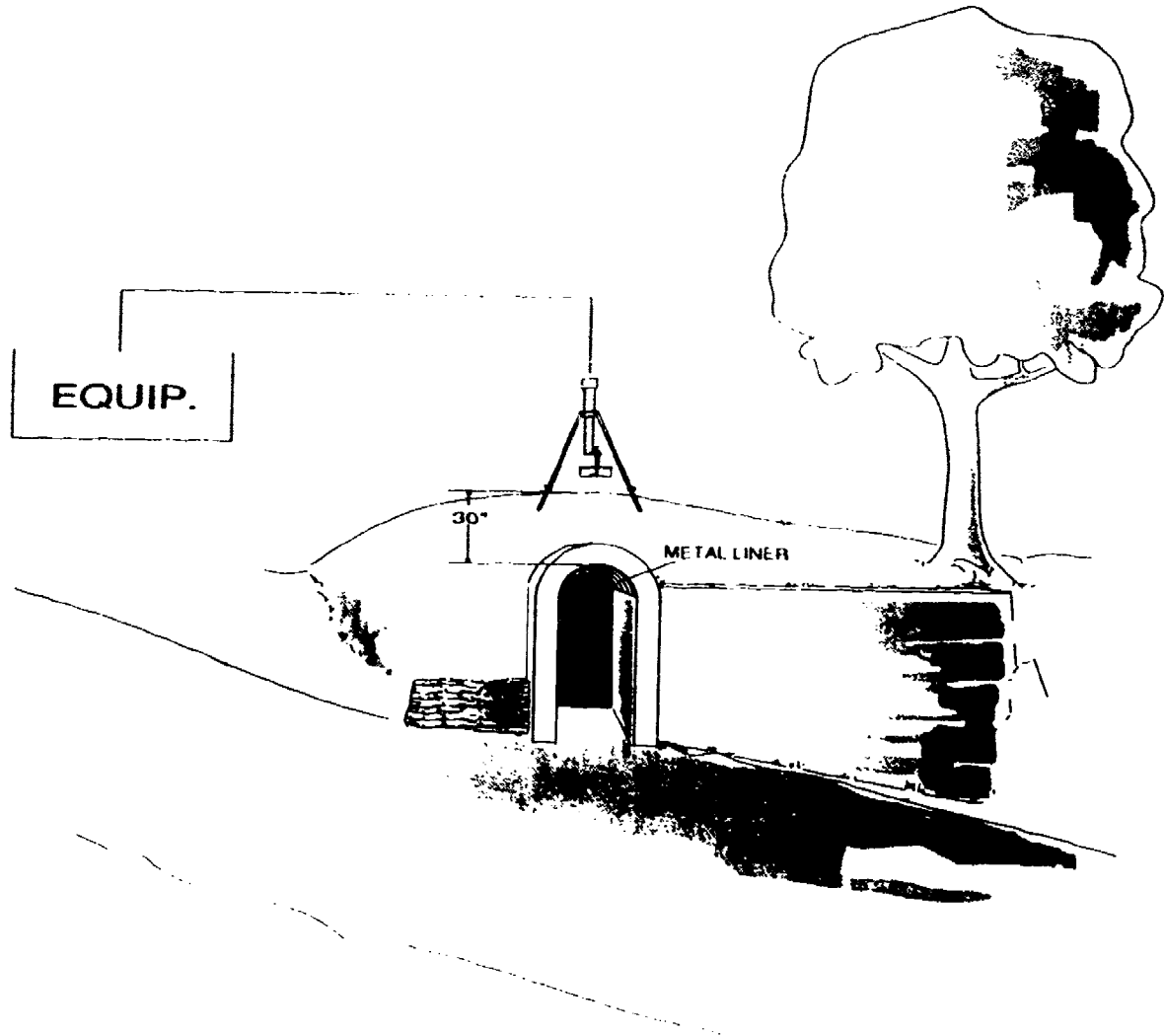


FIGURE 10. - Test site and equipment location

Figure 10 shows the site layout and equipment location of a depth measurement test made on a tunnel located on the grounds of the Pittsburgh Research Center. Figure 11

shows the first results of this test. No effort was made to change the thickness sensor parameters from those used in mine roof and rib thickness measurement applications. The same equipment used in the previously described tests was used for a "quick look" at what was thought to be a tunnel constructed of a corrugated metal form covered with several inches of concrete. At first it appeared that the incorrect depth was obtained but upon probing the surface with a metal rod to measure the actual tunnel depth, it was found that the concrete only existed at the visible tunnel portal and not under the earthen overburden.

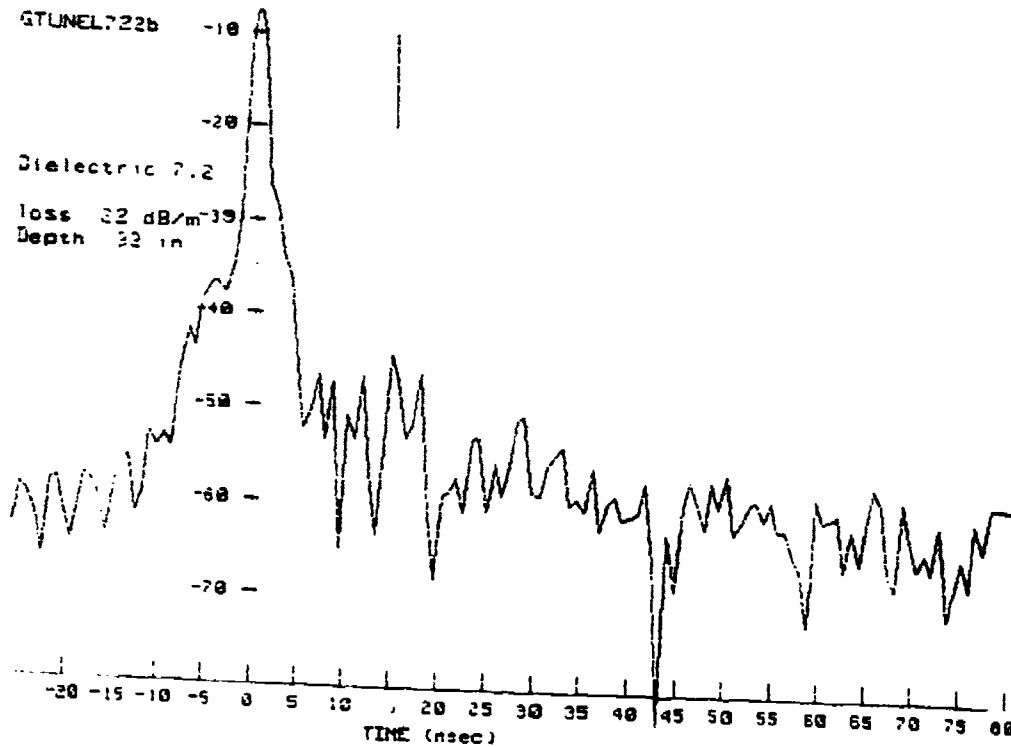


FIGURE 11. - Tunnel depth

While this one test is far from conclusive, it does offer the encouragement to pursue the problem of tunnel detection and add it to the list of potential spatial-spectral sensor applications. A lower frequency antenna will be constructed so that, at the next opportunity, an effort can be made to begin optimizing the software parameters to best fit the tunnel detection application. In addition, the system will use a two- or three-axes antenna positioner to provide the detail of a 2-D or 3-D image.

FUTURE PLANS

At this time, an electronics package has been designed that will replace the off-the-shelf test equipment that has been used on the tests described in this paper. This second-generation effort will result in a small portable instrument that will greatly ease the problems associated with transporting the laboratory test equipment to the various test sites and into and out of operating underground and surface coal mines. The sensor package, including the antenna, will be packaged so that it can be installed on an operating highwall mining machine to measure the thickness of the coal rib separating the active cut from the previous cut. This information will be used for automated machine guidance so that a rib thickness of 3 ft to 5 ft can be maintained for roof support. The actual thickness maintained will be determined by the conditions at each mine site.

This first generation sensor will measure multilayer targets in 1-D with a spatial modulator that moves the antenna on an axis perpendicular to the target. The same electronic package will also be used in future sensors to produce a 2-D or 3-D image of the target. The antenna positioner in this case will move the antenna in the necessary two or three dimensions as required to scan the target.

The present development is focused on the design of a low-cost electronics package to replace the function of the laboratory network analyzer. The frequency synthesizer included in the new analyzer package will cover a two- or three-to-one bandwidth with sub-microsecond coherent switching between programmed frequency steps. The success of the system depends on the accuracy and speed of the frequency synthesizer, the data processing speed and data acquisition, and transmission rate. For low-frequency ground probing applications, it is now possible to construct an all-digital programmable receiver and transmitter at low cost.

CONCLUSIONS

An electromagnetic, noncontacting thickness sensor has been designed, constructed, and field tested. The results are of sufficient accuracy (1 in for coal and rock 3 in to 60 in thick) to justify continuing with the engineering work necessary to develop a practical sensor that can be mounted on mining machines for the determination of roof, floor, and rib thickness. The equipment can operate in the presence of nearby and adjacent metal structures and will be packaged as a portable instrument that can be used for other applications for measuring the thickness of rock and concrete, locating reinforcement rods in concrete structures, and measuring the size and depth of tunnels. The technology when fully developed appears to be usable as a general solution to the problem of locating and imaging underground artifacts.

REFERENCES

- Kerns, D. M., June 1981, "Plane-Wave Scattering-Matrix Theory of Antennas and Antenna-Antenna Interactions," Nat. Bur. Stand., NBS Monogram 162.
- Chufo, R. L., and W. J. Johnson, 1991, "A Radar Coal Thickness Sensor." Conf. Proceedings of the 1991 IEEE Industry Applications Society Annual Meeting, Dearborn, MI.

NOMENCLATURE

A	Area of a spatial modulation spiral area
a	Vectorial spectrum for E of incident field
a₀	Incident wave-amplitude in antenna feed transmission line
b	Vectorial spectrum for E of scattered or radiated field
b₀	Emergent wave-amplitude in antenna feed transmission line
c	Constant (2.718281828)
f	Frequency
j	Imaginary number ($j^2 = -1$)
k	Wave number ($2\pi/\lambda$, free space)
M₁₁	Measured input reflection coefficient
R	Recursive reflection terms
S	Scattering matrix parameter
S₀₀	Antenna reflecting characteristic into coax cable
S₀₁, S₀₂	Antenna receiving characteristic from free space to coax
S₁₀, S₂₀	Antenna transmitting characteristic from coax to free space
S₁₁	Antenna reflecting characteristic from space to space
T	Vector spatial delay with diffraction
t	Time
v	Velocity
Z	Distance of antenna to dielectric
Z₀	Characteristic impedance
λ	Wave length
Γ	Reflection coefficient
θ e^{-jkz}	Spatial delay factor

GRADIOMETER ANTENNAS FOR TUNNEL DETECTION

David A. Hill

Electromagnetic Fields Division
National Institute of Standards and Technology
Boulder, CO 80303

ABSTRACT

The use of gradiometer antennas for detection of long conductors and detection of empty tunnels is analyzed. For reception in vertical boreholes, the gradiometer consists of two vertical electric or magnetic dipoles with a vertical separation. Both sum and difference responses are useful, but the difference response has the potential advantage of suppressing the primary field and making the scattered field easier to detect. The difference response is most effective in suppressing the primary field for a parallel scan where the transmitting antenna and receiving gradiometer are always at the same height. Gradiometers are most advantageous at low frequencies where the scattered field is small compared to the primary field.

INTRODUCTION

A common problem in electromagnetic detection of tunnels or other subsurface objects is that the scattered field is small compared to the primary field and is therefore difficult to detect. This problem occurs for detection of both empty tunnels and tunnels containing conductors. Several methods have been used to attempt to suppress the primary field: (1) the use of a large separation between transmitting and receiving antennas in the detection of long conductors at low frequencies [1,2], (2) the use of a receiving antenna that is polarized orthogonally to the primary field [3,4], and (3) the use of a gradiometer receiving antenna [5].

This paper will consider the gradiometer method, and further details are given in [6]. Stolarczyk [5] has performed low-frequency measurements with a gradiometer antenna, and the suppression of the primary field was encouraging. In this report, the theoretical basis of the gradiometer method will be studied. We cover the application of the method to tunnels containing long conductors and to empty (air-filled) tunnels.

MAGNETIC DIPOLE EXCITATION OF LONG CONDUCTORS

Formulation

The geometry for excitation of a long conductor by a vertical magnetic dipole is shown in figure 1. An infinitely long conductor of outer radius b is centered on the z axis. A transmitting vertical (y -directed) magnetic

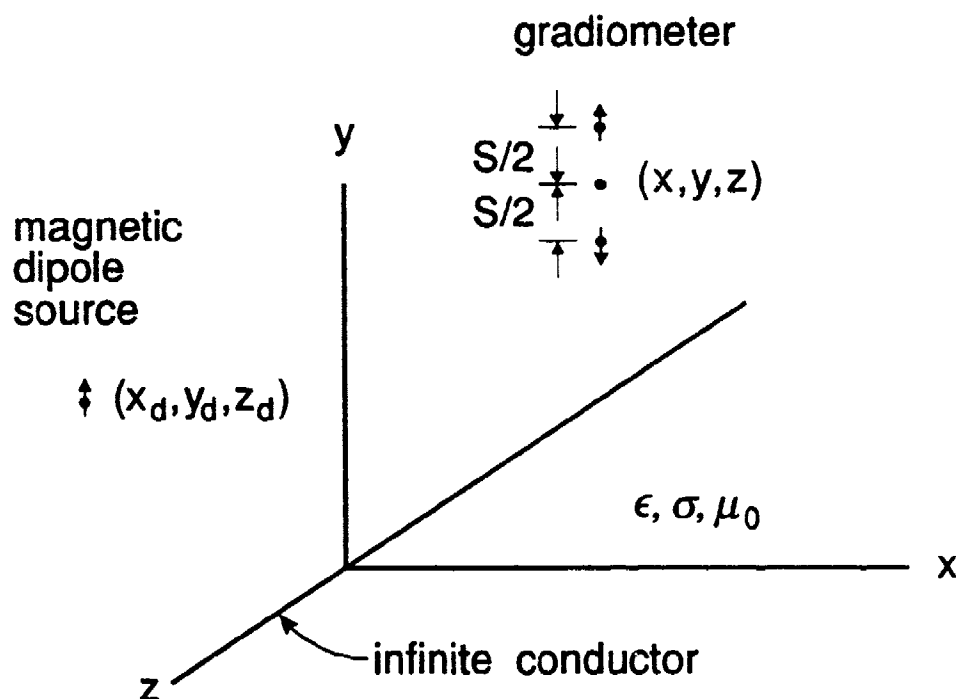


Figure 1. Geometry for an infinitely long conductor excited by a vertical magnetic dipole. The gradiometer receiver consists of two vertical magnetic dipoles separated by a distance s .

dipole of magnetic moment IA is located at (x_d, y_d, z_d) . A gradiometer receiving antenna is centered at (x, y, z) and will be described mathematically in eqs (6) and (7). The earth has permittivity ϵ , conductivity σ , and free-space magnetic permeability μ_0 . We assume that the magnetic dipole source and the conductor are located at a sufficient depth that the air-earth interface can be neglected.

A vertical magnetic dipole antenna is well suited to detection of horizontal conductors in tunnels because it radiates a horizontal electric field which will excite axial currents in horizontal conductors. A practical vertical magnetic dipole that will fit in boreholes has been constructed using a solenoidal winding on a ferrite core [5]. The gradiometer receiving antenna can be constructed using a pair of such antennas.

The electric and magnetic fields can be derived in terms of a y -directed magnetic Hertz vector, and the derivation is given in [1]. For a vertical magnetic gradiometer receiving antenna, only the vertical magnetic field H_y is required. It can be written as the sum of the primary field H_y^d due to the dipole and the secondary field H_y^c due to the conductor:

$$H_y = H_y^d + H_y^c. \quad (1)$$

The primary field is given by [1]

$$H_y^d = \frac{IA}{4\pi r_d} e^{-jkr_d} \left\{ k^2 \left[1 - \frac{(y-y_d)^2}{r_d^2} \right] + \frac{jkr_d + 1}{r_d^2} \left[\frac{3(y-y_d)^2}{r_d^2} - 1 \right] \right\}, \quad (2)$$

where $k = \omega[\mu_0(\epsilon - j\sigma/\omega)]^{1/2}$ and $r_d = [(x-x_d)^2 + (y-y_d)^2 + (z-z_d)^2]^{1/2}$.

The time dependence is $\exp(j\omega t)$. In general all terms in eq (2) need to be retained.

The secondary magnetic field due to the conductor is [1]

$$H_y^c = \frac{x}{2\pi\rho} \int_{-\infty}^{\infty} \hat{I}(\lambda) v K_1(v\rho) e^{-j\lambda z} d\lambda, \quad (3)$$

where $\rho = (x^2 + y^2)^{1/2}$, $v = (\lambda^2 - k^2)^{1/2}$, and K_1 is the first-order modified Bessel function of the second kind. $\hat{I}(\lambda)$ is the spatial transform of the conductor current and is given by [1]

$$\hat{I}(\lambda) = \frac{IA}{2\pi} \left[\frac{x_d k^2 K_1(v\rho_{d0})}{\rho_{d0} v D(\lambda)} \right], \quad (4)$$

where $\rho_{d0} = (x_d^2 + y_d^2)^{1/2}$, $D(\lambda) = K_0(vb) + \frac{2\pi(\sigma + j\omega\epsilon)}{v^2} Z_s(\lambda)$, and $Z_s(\lambda)$ is the axial impedance (series impedance per unit length) of the conductor.

A good model for a conductor in a tunnel is shown in figure 2. It consists of a metal cylinder of radius a surrounded by an insulating region of outer radius b . The metal has conductivity σ_m and magnetic permeability μ_m , and the insulation has permittivity ϵ_i and free-space permeability μ_0 . The axial impedance of this model is [1]

$$Z_s(\lambda) = Z_m + \frac{\lambda^2 - k_i^2}{2\pi j\omega\epsilon_i} \ln(b/a), \quad (5)$$

$$\text{where } Z_m = \frac{1}{2\pi a} \left(\frac{j\omega\mu_m}{\sigma_m} \right)^{1/2} \frac{I_0(jk_m a)}{I_1(jk_m a)},$$

$$jk_m = (j\omega\mu_m\sigma_m)^{1/2}, \quad k_i = \omega(\mu_0\epsilon_i)^{1/2},$$

and I_0 and I_1 are modified Bessel functions of the first kind. If we set $b = a$, then $Z_s(\lambda) = Z_m$, and we have a grounded metal conductor (such as a

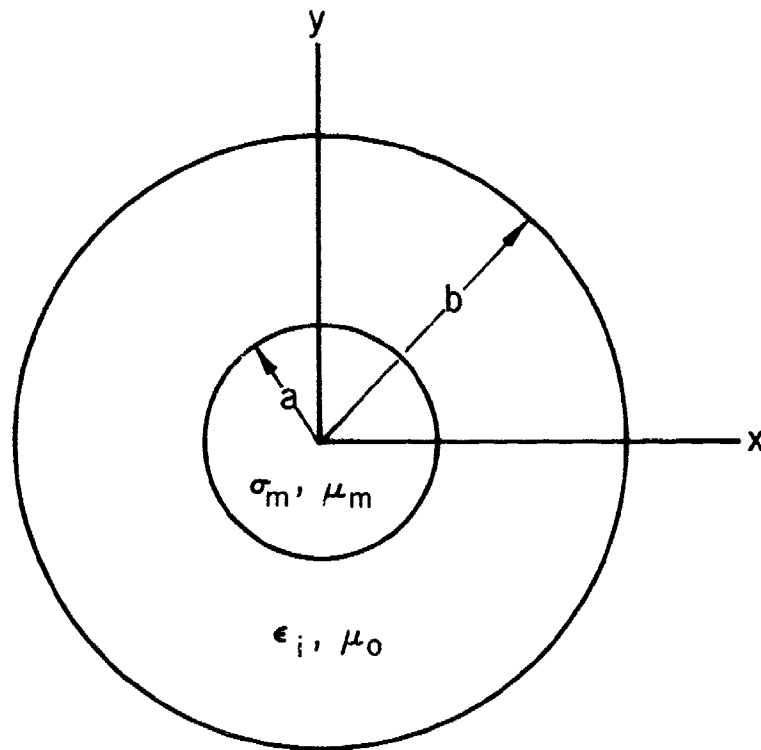


Figure 2. Geometry for an insulated conductor.

rail in a tunnel). If we set ϵ_i equal to the free-space permittivity ϵ_0 , then we can model a conductor (such as a power line) suspended in an air-filled tunnel at a distance $b - a$ from the tunnel wall.

When magnetic field reception is with a pair of magnetic dipole antennas as in figure 1, two outputs (sum and difference) are possible, and Stolarczyk [5] has recorded both as a function of height y . The sum output is proportional to the sum $H_{y\Sigma}$ of the vertical magnetic field at the two dipole heights:

$$H_{y\Sigma}(y) = H_y(y + s/2) + H_y(y - s/2). \quad (6)$$

In eq (6), we show only the y dependence because both terms are a function of the same x and z coordinates. In a vertical borehole scan, only the y coordinate is varied while x and z are held constant. In a similar manner, the difference output is proportional to the difference $H_{y\Delta}$ of the vertical magnetic field at the two dipole heights:

$$H_{y\Delta}(y) = H_y(y + s/2) - H_y(y - s/2). \quad (7)$$

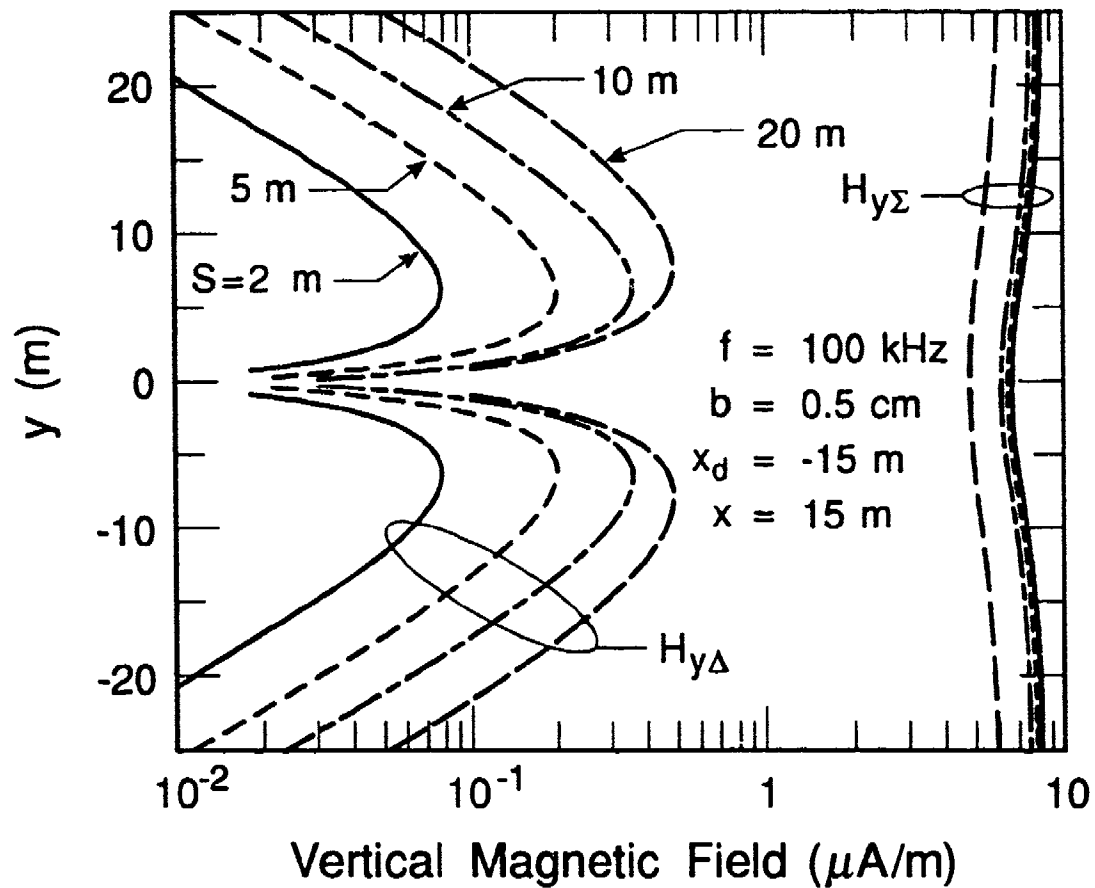


Figure 3. Magnitude of magnetic field gradiometer responses for different values of dipole separation s .

If s is small, then $H_{y\Delta}$ is given approximately by

$$H_{y\Delta}(y) \approx s \hat{y} \cdot \nabla H(y), \quad (8)$$

where \hat{y} is a unit vector. Thus $H_{y\Delta}$ is proportional to the y component of the gradient of the magnetic field when s is small, and the pair of magnetic dipoles in the difference mode is called a gradiometer. Under the same condition, $H_{y\Sigma}$ is given approximately by twice the value of $H_y(y)$:

$$H_{y\Sigma}(y) \approx 2 H_y(y). \quad (9)$$

For the cases discussed in the following sections, s is not necessarily small, and eqs (6) and (7) are used to generate the numerical results.

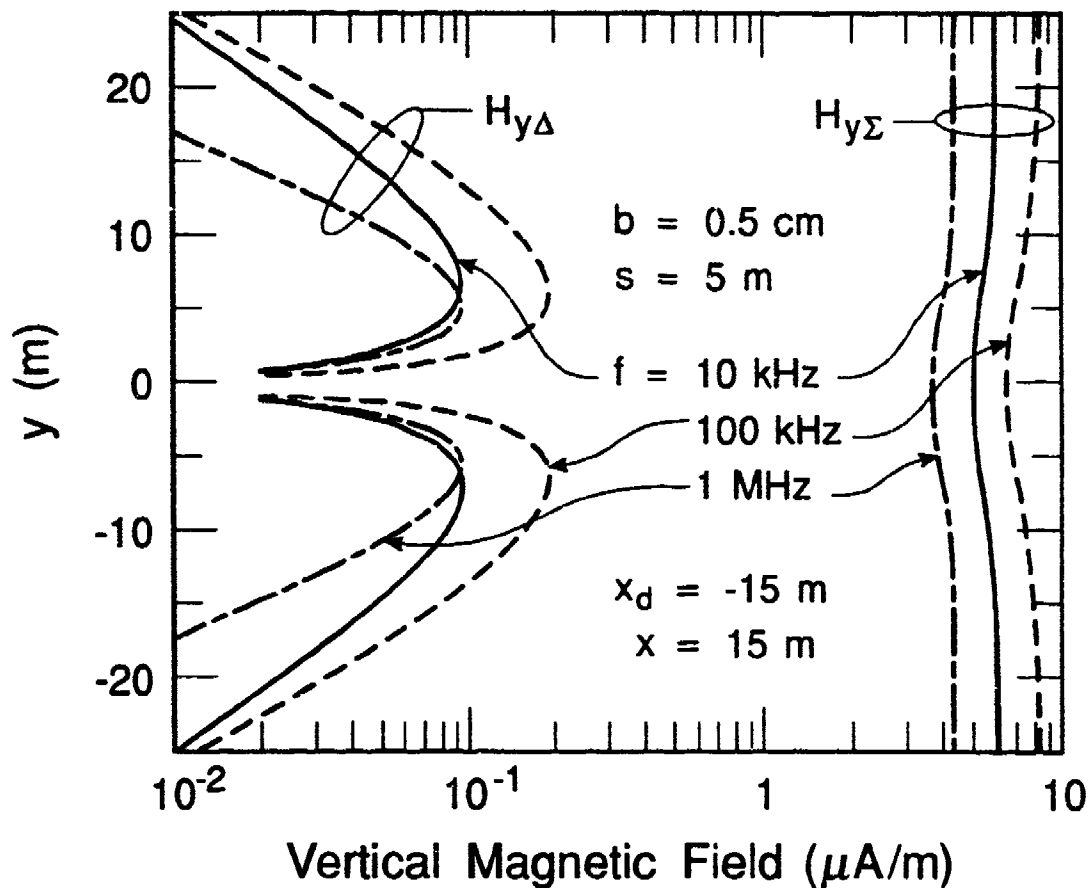


Figure 4. Magnitude of magnetic field gradiometer responses for various frequencies.

Parallel Scan

In a parallel scan, as opposed to a full tomography scan [7,8], the source dipole and receiving gradiometer are moved vertically together, and the heights are equal ($y = y_d$). The advantage of this geometry is that the primary field is cancelled in the difference mode of the gradiometer, and $H_{y\Delta}$ reduces to

$$H_{y\Delta}(y) = [H_y^c(y + s/2) - H_y^c(y - s/2)]|_{y_d=y}. \quad (10)$$

Thus the gradiometer in the difference mode responds only to the field scattered by the conductor. In the sum mode, the primary field components add to produce the following result for $H_{y\Sigma}$:

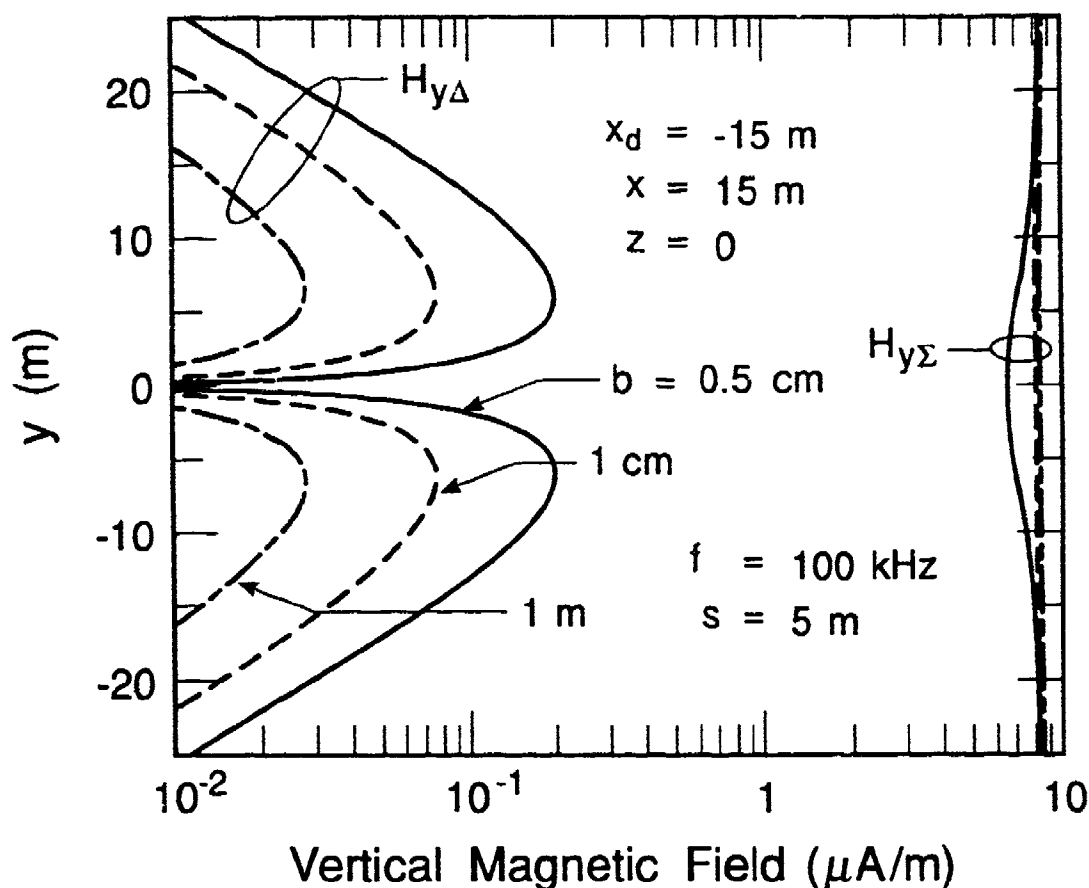


Figure 5. Magnitude of magnetic field gradiometer responses for various values of insulation radius b .

$$H_{y\Sigma}(y) = [2 H_y^d(y + s/2) + H_y^c(y + s/2) + H_y^c(y - s/2)]|_{y_d=y}. \quad (11)$$

If the primary dipole field H_y^d dominates the secondary conductor field H_y^c , then $H_{y\Sigma}$ is nearly independent of y .

A computer program was written to evaluate $H_{y\Sigma}$ and $H_{y\Delta}$ from eqs (1)-(5), (10), and (11). The λ integration in (3) was evaluated by FFT. In all of the numerical results, we use the following values for the source, conductor, and earth parameters: $IA = 1 \text{ A}\cdot\text{m}^2$, $z_d = 0$, $a = 0.5 \text{ cm}$, $\sigma_m = 5.7 \times 10^7 \text{ S/m}$, $\mu_m/\mu_0 = 1$, $\epsilon_i/\epsilon_0 = 1$, $\epsilon/\epsilon_0 = 10$, and $\sigma = 5 \times 10^{-3} \text{ S/m}$.

In figures 3 and 4, the magnitudes of $H_{y\Sigma}$ and $H_{y\Delta}$ are shown as a function of y for a conductor midway between the two boreholes ($x = -x_d = 15$

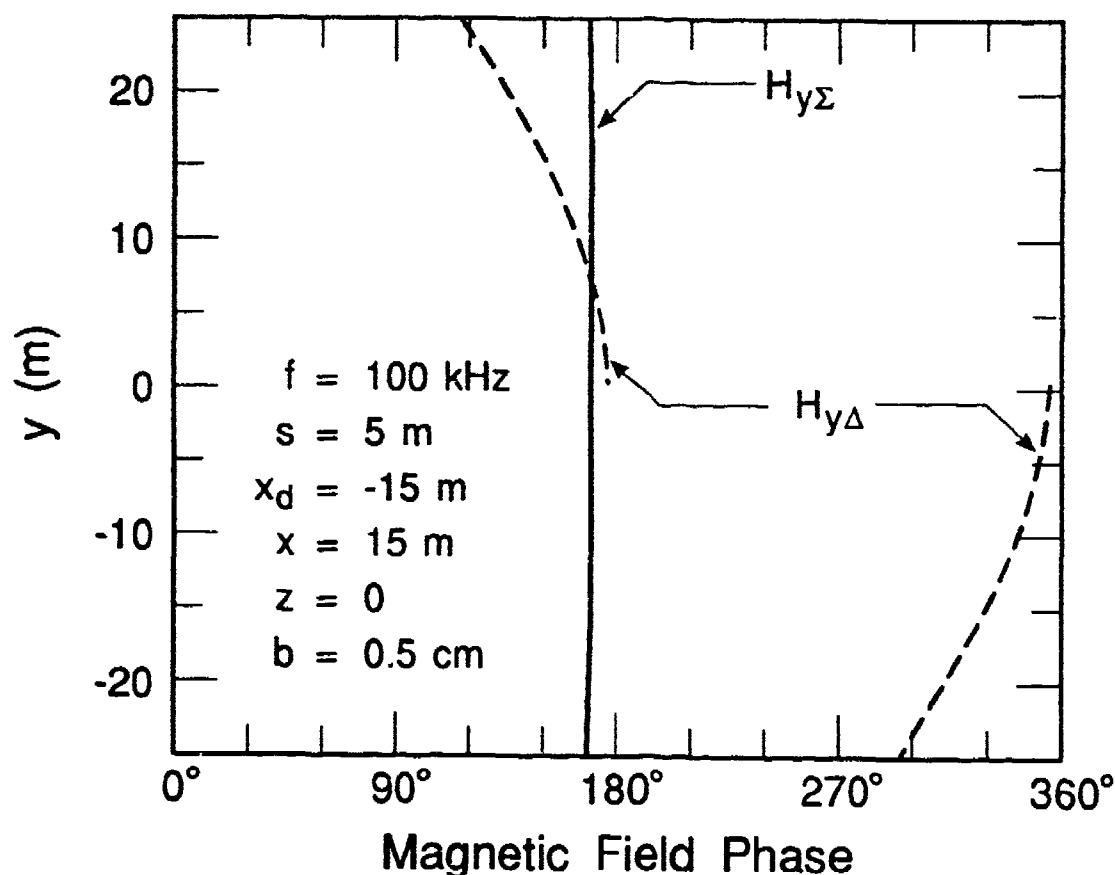


Figure 6. Phase of magnetic field gradiometer responses.

m and $z = 0$). The insulation radius b is set equal to a to model a grounded conductor. In figure 3, the gradiometer separation parameter s is varied from 2 to 20 m. The sum response is only weakly dependent on s , but the difference response has a higher peak value for larger values of s . However, further calculations for values of s larger than 20 m showed a decline in peak value. A perfect null is obtained at $y = 0$, and this null should be easier to detect than the small dip in the sum response. In figure 4, the responses are shown for various frequencies. A frequency of 1 MHz is too high because of increased attenuation in the rock, and a frequency of 10 kHz is too low because of reduced scattering from the conductor. A frequency on the order of 100 kHz is probably optimum for the typical distances involved (30 m borehole separation).

In figure 5, the effect of the insulation radius b is shown. The scattered field is weaker for larger values of b because the current induced on the conductor [1] is smaller than for the grounded case ($b = a$) shown in figure 3. However the difference response still has its characteristic null at $y = 0$.

Another quantity of interest is the phase of either $H_{y\Sigma}$ or $H_{y\Delta}$ [5]. Figure 6 shows phase results for the same parameters as in figure 3. The

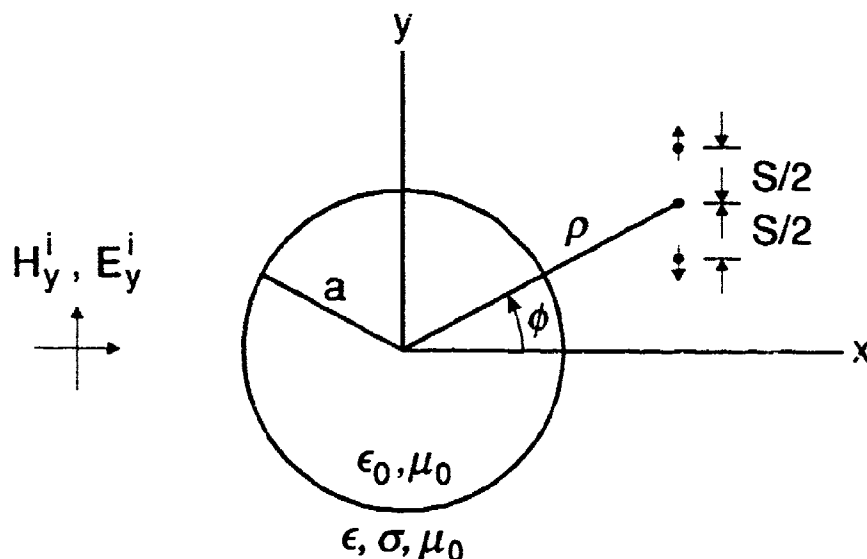


Figure 7. Geometry for a plane wave incident on an empty, circular tunnel. The gradiometer consists of two vertical electric or magnetic dipoles.

phase of $H_{y\Sigma}$ is nearly constant versus y , but the phase of $H_{y\Delta}$ has a 180° jump at $y = 0$, the location of the null. This rapid phase shift is another possible indicator of the conductor location.

PLANE WAVE EXCITATION OF EMPTY CIRCULAR TUNNELS

Formulation

In this section, we consider a circular tunnel model as shown in figure 7. The tunnel of radius a (not to be confused with conductor radius a of section 2) is air filled with permittivity ϵ_0 and permeability μ_0 . As in the previous section, the surrounding rock has permittivity ϵ , conductivity σ , and permeability μ_0 .

For detection of air-filled tunnels, both polarizations are of interest. For simplicity we consider a plane-wave source rather than a vertical magnetic or electric dipole. The incident plane wave is propagating in the x direction and has either E_z or H_z polarization:

$$E_z^i = E_0 \exp(-jkx) \text{ or } H_z^i = H_0 \exp(-jkx). \quad (12)$$

The total fields for the two polarizations are the sum of the incident and scattered fields:

$$E_z = E_z^i + E_z^s \text{ or } H_z = H_z^i + H_z^s. \quad (13)$$

The scattered field for E_z polarization is [9-11]

$$E_z^s = E_0 \sum_{m=0}^{\infty} \epsilon_m (-j)^m a_m H_m^{(2)}(k\rho) \cos(m\phi), \quad (14)$$

$$\text{where } a_m = - \frac{k_0 J'_m(k_0 a) J_m(ka) - k J_m(k_0 a) J'_m(ka)}{k_0 J'_m(k_0 a) H_m^{(2)}(ka) - k J_m(k_0 a) H_m^{(2)'}(ka)},$$

$$\epsilon_m = \begin{cases} 1, & m = 0 \\ 2, & m \neq 0 \end{cases}, \quad k_0 = \omega(\mu_0 \epsilon_0)^{1/2}.$$

k is given by eq (2), J_m is the m th-order Bessel Function, and $H_m^{(2)}$ is the m th order Hankel function of the second kind. The scattered field for H_z polarization is

$$H_z^s = H_0 \sum_{m=0}^{\infty} \epsilon_m (-j)^m b_m H_m^{(2)}(k\rho) \cos(m\phi), \quad (15)$$

$$\text{where } b_m = - \frac{k J'_m(k_0 a) J_m(ka) - k_0 J_m(k_0 a) J'_m(ka)}{k J'_m(k_0 a) H_m^{(2)}(ka) - k_0 J_m(k_0 a) H_m^{(2)'}(ka)}.$$

For reception in boreholes, we are interested in the vertical (y -directed) components of the fields. The y components can be obtained from the z components from Maxwell's curl equations. For E_z polarization, the H_y component is given by

$$H_y = \frac{1}{j\omega\mu_0} \frac{\partial E_z}{\partial x}. \quad (16)$$

For H_z polarization, the E_y component is given by

$$E_y = \frac{-1}{\sigma + j\omega\epsilon} \frac{\partial H_z}{\partial x}. \quad (17)$$

By substituting eqs (12)-(15) into eqs (16) and (17) and carrying out the differentiation, we can obtain explicit expressions for H_y and E_y . Convenient normalizations for numerical results are

$$E_0 = -\eta \text{ and } H_0 = 1/\eta, \quad (18)$$

where $\eta = [\mu_0/(\sigma + j\omega\epsilon)]^{1/2}$.

Then the incident fields are the same for the two polarizations, and H_y and E_y can be written

$$\begin{pmatrix} H_y \\ E_y \end{pmatrix} = e^{-jkx} + \begin{pmatrix} H_y^s \\ E_y^s \end{pmatrix}, \quad (19)$$

$$\begin{aligned} \text{where } \begin{pmatrix} H_y^s \\ E_y^s \end{pmatrix} = -\frac{1}{jk} \sum_{m=0}^{\infty} \begin{pmatrix} a_m \\ b_m \end{pmatrix} \epsilon_m (-j)^m \left[\frac{m \sin \phi}{\rho} H_m^{(2)}(k\rho) \sin(m\phi) \right. \\ \left. + k \cos \phi H_m^{(2)}(k\rho) \cos(m\phi) \right]. \end{aligned} \quad (20)$$

Thus, the only difference between the two polarizations is in the scattering coefficient: a_m is associated with H_y^s and b_m is associated with E_y^s . A computer program was written to handle both polarizations simultaneously. Convergence of the m summation in eq (20) is fairly rapid so long as $|k|a$ is not too large.

Scattered Field

Before performing a numerical evaluation of the scattered fields, it is useful to examine the low-frequency behavior. When $k_0 a$ and $|k|a$ are small, the Bessel functions in a_m and b_m can be replaced by their small argument expansions [6]. For E_z polarization, the leading scattering coefficient is

$$a_0 \approx (j\pi/4) (k^2 - k_0^2) a^2. \quad (21)$$

Then the leading term in H_y^s is

$$H_y^s \approx -(\pi/4) (k^2 - k_0^2) a^2 \cos \phi H_0^{(2)}(k\rho). \quad (22)$$

The $(k^2 - k_0^2) a^2$ dependence in eq (22) indicates that the scattering from an electrically small, empty tunnel is very weak. This is quite different from

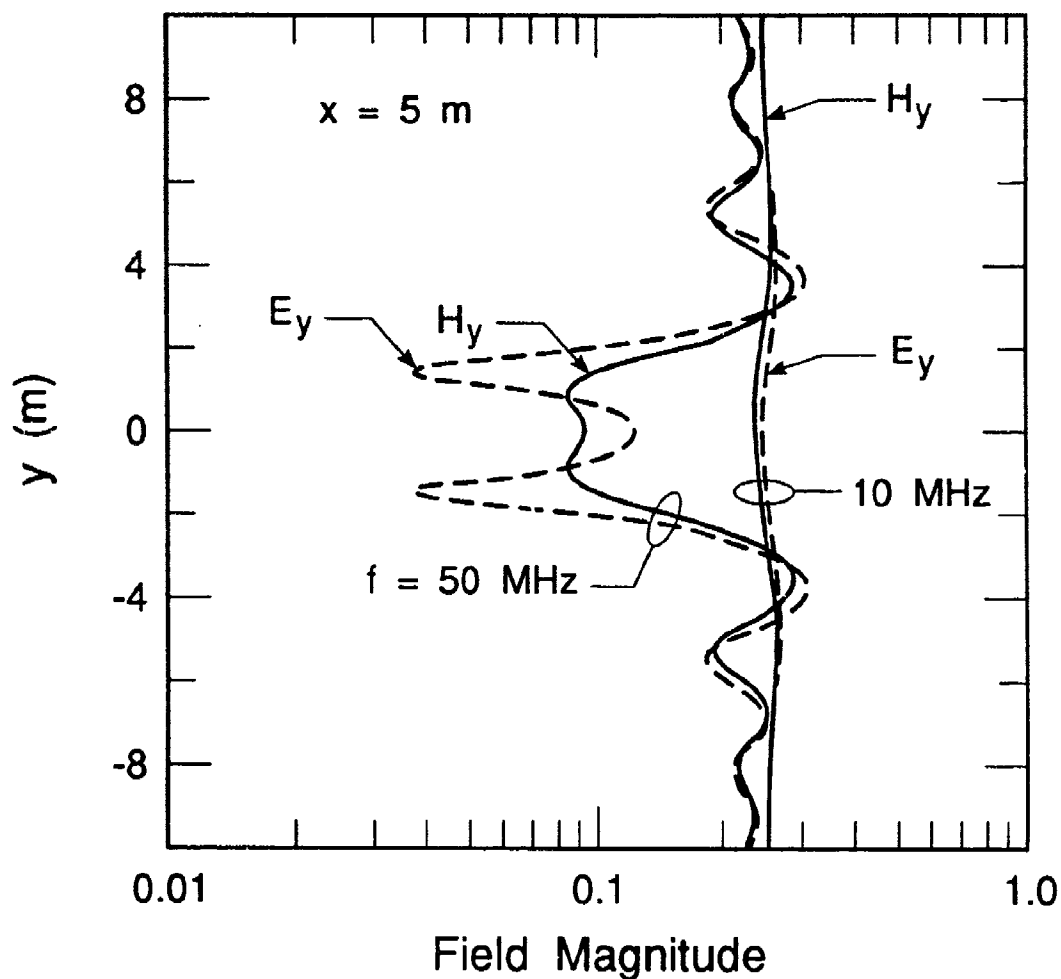


Figure 8. Field magnitudes on the shadow side of an empty tunnel.

E_z scattering from an electrically small, highly conducting cylinder where the scattering is strong [12].

For H_z scattering, the leading scattering coefficient is

$$b_1 \approx (j\pi/4) (k^2 - k_0^2) a^2, \quad (23)$$

which is equal to a_0 in eq (21). The leading term in E_y^s is

$$E_y^s \approx (j\pi/2) (k^2 - k_0^2) a^2 \left[\frac{\sin^2 \phi}{k\rho} H_1^{(2)}(k\rho) + \cos^2 \phi H_1^{(2)}(k\rho) \right]. \quad (24)$$

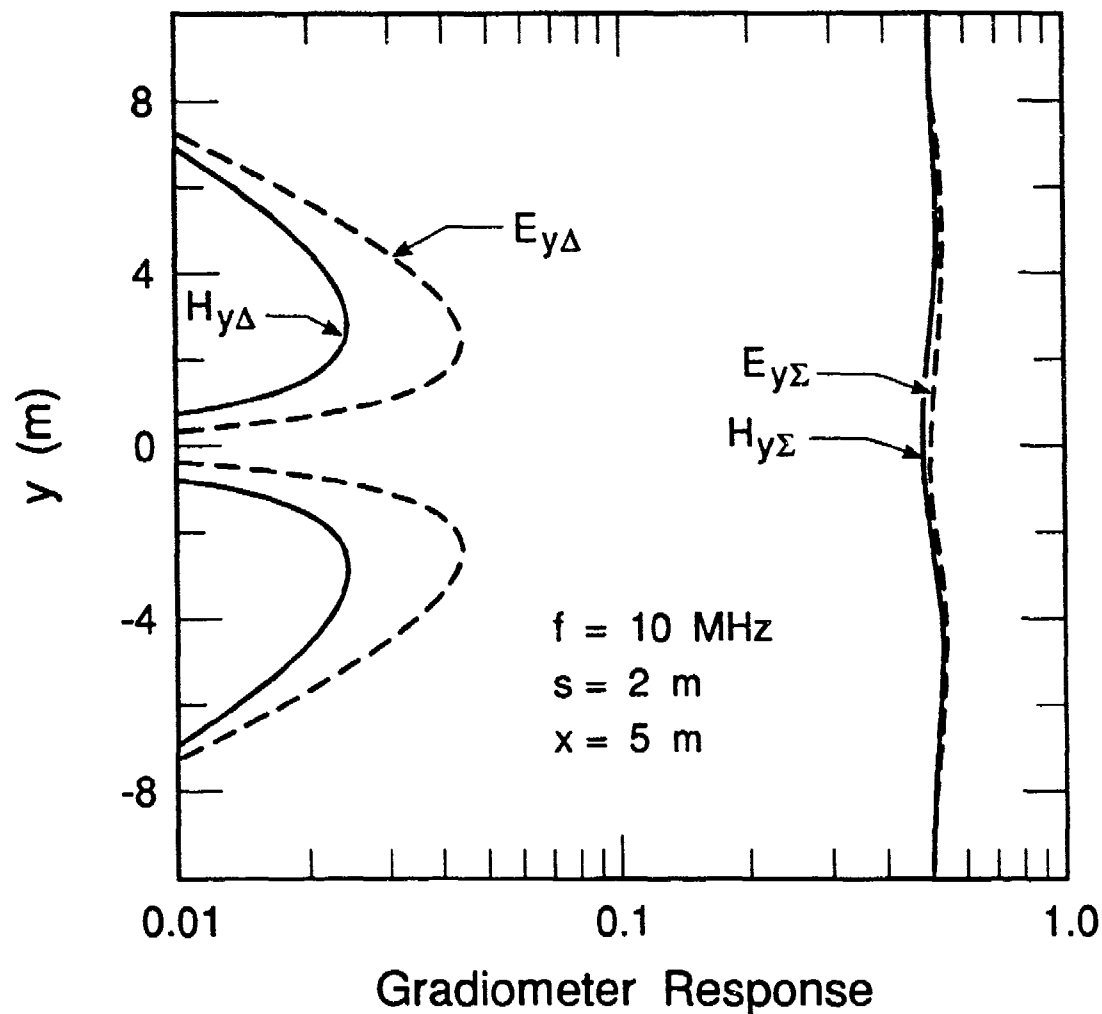


Figure 9. Magnitude of gradiometer responses on the shadow side of an empty tunnel at 10 MHz.

The computer program was found to agree with eqs (22) and (24) for sufficiently low frequencies.

For all of the numerical results for the empty tunnel, we choose the following parameters: $a = 1 \text{ m}$, $\epsilon/\epsilon_0 = 10$, and $\sigma = 5 \times 10^{-3} \text{ S/m}$. The numerical results in figures 8-11 are normalized to the incident field at $x = 0$. In figure 8, we show the magnitudes of the y components of the total fields as a function of y at $x = 5 \text{ m}$. At 10 MHz, the scattered field is weak, and the total field is nearly constant at the incident field value of $\exp(-jkx)$. At 50 MHz, the circumference of the tunnel is approximately equal to a free-space wavelength, and the scattering is fairly strong. The two dips in the total field (for both polarizations) have been discussed by other authors [9,13] in tunnel detection applications. Further calculations

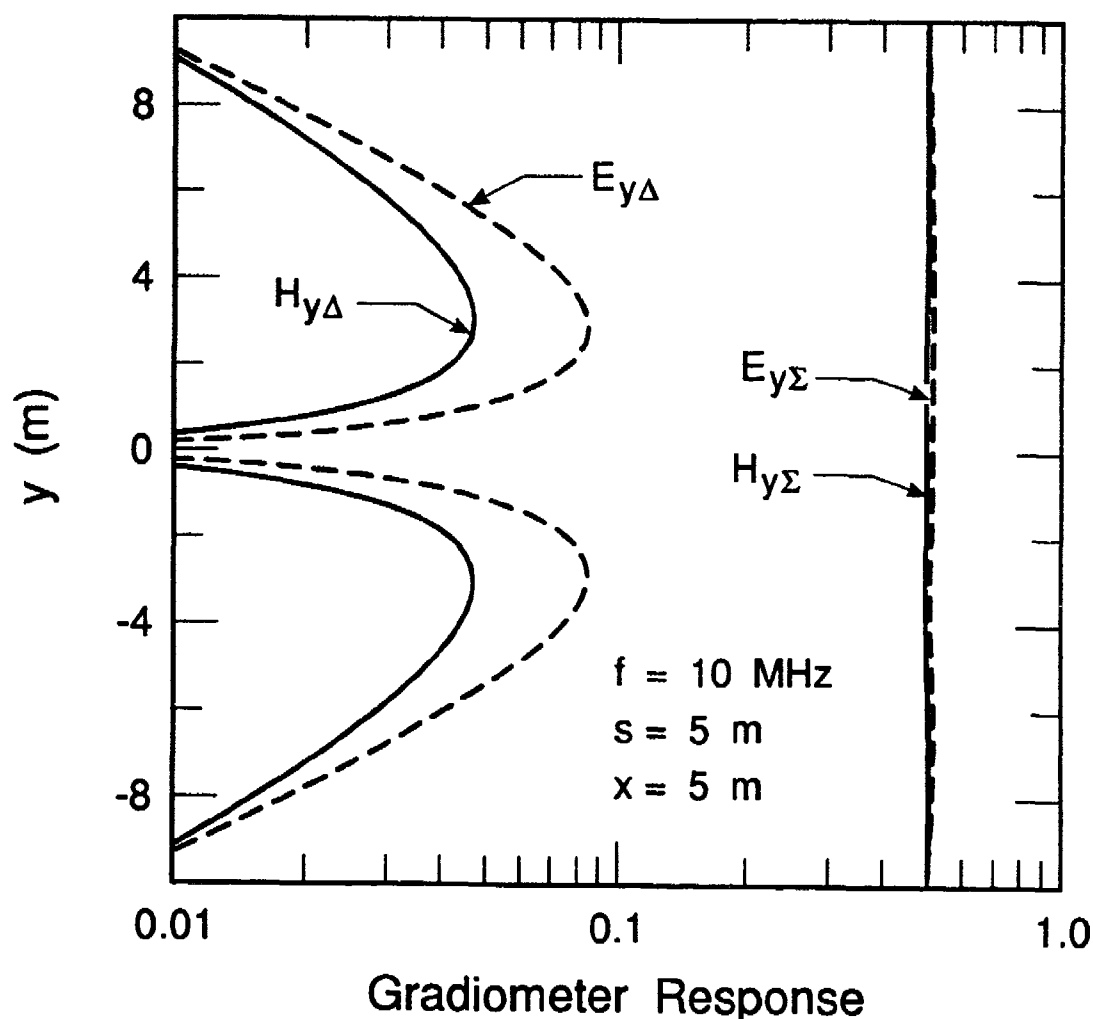


Figure 10. Magnitude of gradiometer responses on the shadow side of an empty tunnel for a larger dipole separation s .

show strong scattering for most frequencies above 50 MHz, but weak scattering for frequencies below about 20 MHz.

Calculations for larger values of x show weaker scattered fields and more nearly constant total fields. This model is not well suited to analyzing the far-field (large x) behavior of the total field because the plane-wave incident field has no spreading loss while the scattered field has inverse square root distance spreading loss. A better model for examining the far-field behavior would have either a line source or a dipole source. In these cases the incident field and scattered field would have the same spreading loss.

Gradiometer Response

Since the field scattered from an empty tunnel at low frequencies is weak compared to the primary field, we again examine the possibility of

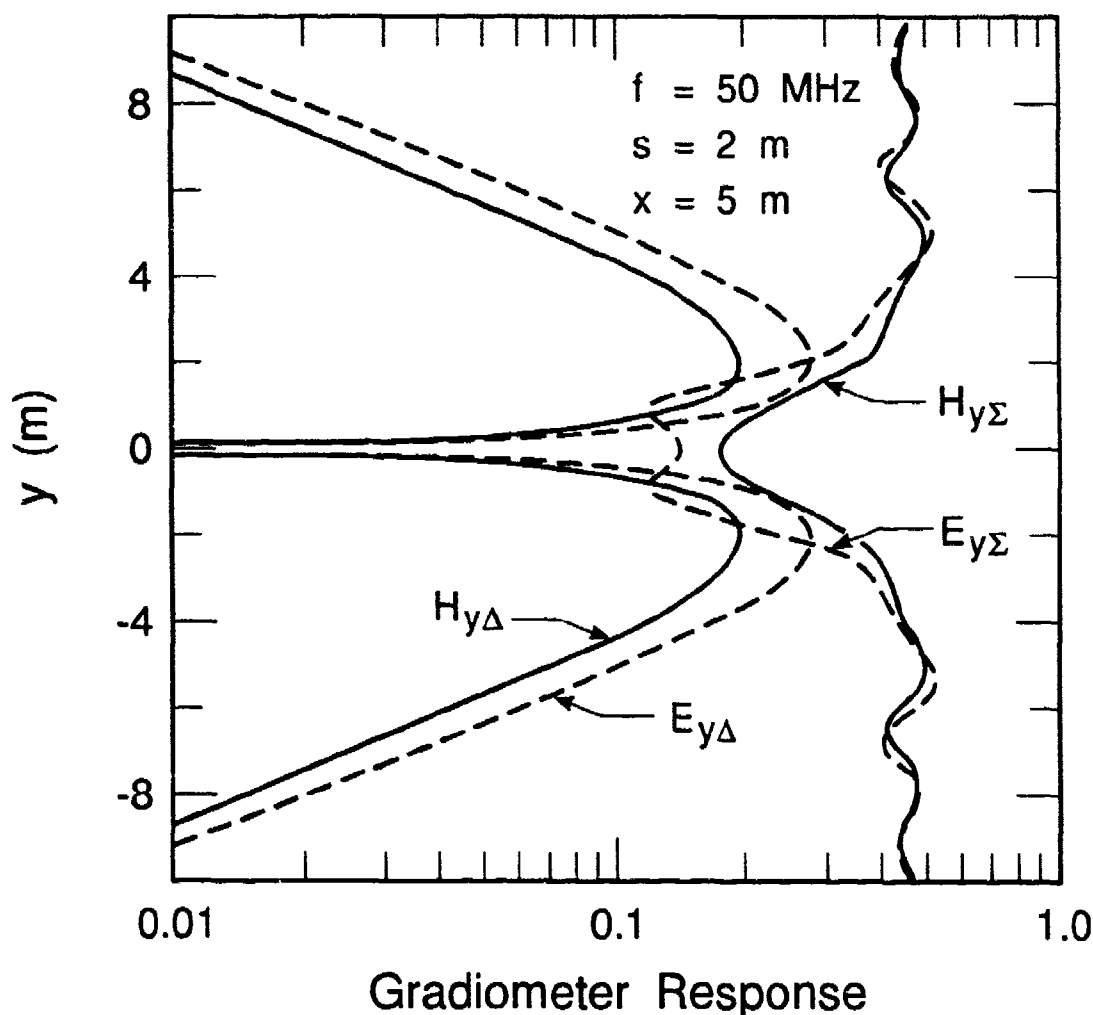


Figure 11. Magnitude of gradiometer responses on the shadow side of an empty tunnel at 50 MHz.

using a gradiometer receiving antenna to suppress the primary field. For E_z polarization, H_y is the vertical field component that can be received most easily in a borehole. The gradiometer antenna for this case has already been described, and the sum and difference responses are proportional to $H_{y\Sigma}$ and $H_{y\Delta}$ as given in eqs (6) and (7).

For H_z polarization, E_y is the vertical component that can be received in a vertical borehole. In this case the two receiving antennas shown in figure 7 are vertical electric dipoles. The sum and difference responses are proportional to $E_{y\Sigma}$ and $E_{y\Delta}$ which are given by

$$E_{y\Sigma}(y) = E_y(y + s/2) + E_y(y - s/2) \quad (25)$$

$$\text{and } E_{y\Delta}(y) = E_y(y + s/2) - E_y(y - s/2). \quad (26)$$

In figures 9 and 10, we show the gradiometer responses at 10 MHz for $s = 2$ m and 5 m. In both cases the sum response shows little variation with y , but the difference response shows the characteristic null at $y = 0$. The peak values are greater for $s = 5$ m. Also, the H_z polarization (vertical E_y) produces a stronger scattered field and difference response. This is consistent with scattered field calculations by others.

Figure 11 shows gradiometer responses at 50 MHz. Here the scattered field is strong enough that both the sum and difference responses show enough y variation to indicate the tunnel height. For such cases with strong scattering, it is not clear whether the gradiometer provides a significant advantage over a single dipole antenna.

CONCLUSIONS

The analytical and numerical results indicate that a gradiometer receiving antenna is useful in suppressing the primary field and allowing the field scattered by an empty tunnel or a conductor in a tunnel to be observed in the absence of the primary field. The typical gradiometer response has a null at the height of the tunnel due to symmetry and symmetrical peaks above and below. These features occur most prominently with a parallel scan, rather than with a diagonal scan where the primary field is not completely nulled out.

The best frequencies for detection of long conductors are in the vicinity of 100 kHz, and this is unchanged from earlier results with single dipole receivers [1,2]. The spacing between the two vertical dipole receivers that form the gradiometer is not critical, but too small a spacing reduces the received difference to too low a level. Too large a spacing broadens the distance between the two peaks and degrades the vertical resolution. Spacings on the order of 2 to 10 m yield good results.

For detection of empty tunnels, either vertical or horizontal polarization can be used. Thus the source and gradiometer can use either vertical electric or vertical magnetic dipoles in boreholes. Stronger scattering is obtained for vertical polarization using vertical electric dipoles. Frequencies of 50 MHz or higher yield strong scattering that should be detectable with either a single antenna or a gradiometer. When strong scattering is obtained, it is not as clear whether a gradiometer receiver has a significant advantage over a single dipole receiver. However, there is always some advantage because the sum response is approximately the same as the response of a single dipole and the difference response provides additional information. If lower frequencies on the order of 10 MHz are used, gradiometers are useful in suppressing the primary field and allowing the weak scattered field to be detected. Normally the reason for using lower frequencies is to increase range.

Further study of several issues involving gradiometer antennas would be useful. The idealized theoretical scans for gradiometers show a perfect

null with symmetrical peaks above and below, but preliminary measurements [5] do not show such deep nulls. Models with less symmetry, such as noncircular tunnels [14] or tunnels with multiple conductors, could be studied to determine asymmetry effects on gradiometers. Imperfect alignment and spacings of the gradiometer dipoles could degrade the null, and these effects could be studied. We assumed a plane-wave source in the empty tunnel analysis, but a more realistic source (such as a vertical dipole) would be useful in predicting the proper field decay with distance. Earth layering or inhomogenieties could also be studied to obtain an estimate of the effects of geologic noise [15-18] on gradiometer response. The gradiometers studied here utilize the vertical variation of the vertical field component, but other variations and field components could also be useful in improving the ratio of the received scattered field to primary field if other receiving geometries could be employed in boreholes.

ACKNOWLEDGMENTS

This research was supported by the U.S. Army Belvoir RD&E Center. I thank Larry Stolarczyk for helpful discussions.

REFERENCES

- [1] Hill, D.A. Magnetic dipole excitation of a long conductor in a lossy medium. IEEE Trans. Geosci. Rem. Sens., GE-26: 720-725; 1988.
- [2] Hill, D.A. Magnetic dipole excitation of an insulated conductor of finite length. IEEE Trans. Geosci. Rem. Sens., GE-28: 289-294; 1990.
- [3] Bollen, R.L. Tunnel detection by low-frequency magnetic-field emissions and the controlled source audio magneto telluric techniques. SRI International: January 1989.
- [4] Hill, D.A. Near-field and far-field excitation of a long conductor in a lossy medium. Nat. Inst. Stand. Tech. (U.S.) NISTIR 3954; 1990.
- [5] Stolarczyk, L.G. Evaluation of RIM system II instruments, data acquisition methods, and data processing algorithms for detection of shallow and deeply buried tunnels with and without electrical conductors. Stolar Inc.: May 1991.
- [6] Hill, D.A. Gradiometer antennas for tunnel detection. Nat. Inst. Stand. Tech. (U.S.) NISTIR 3990; 1992.
- [7] Shope, S.; Greenfield, R.J. Electromagnetic cross-hole tomography for tunnel detection. Third Technical Symposium on Tunnel Detection. Golden, CO: January 12-15, 1988.
- [8] Frank, M.S.; Balanis, C.A. Electromagnetic tomography in tunnel detection. Third Technical Symposium on Tunnel Detection. Golden, CO: January 12-15, 1988.

- [9] Lee, T.K.; Kim, S.Y.; Ra, J.W. Resonant scattering of cw electromagnetic wave by an underground tunnel of circular cross-section. Third Technical Symposium on Tunnel Detection. Golden, CO: January 12-15, 1988.
- [10] Jones, D.S. The Theory of Electromagnetism. Oxford: Pergamon Press, 1964.
- [11] Van de Hulst, H.C. Light Scattering by Small Particles. New York: Wiley; 1957.
- [12] Harrington, R.F. Time-Harmonic Electromagnetic Fields. New York: McGraw-Hill; 1961.
- [13] Lee, T.K.; Park, S.O.; Ra, J.W. Near-field diffraction pattern by an underground void of circular cylinder. Microwave Opt. Tech. Let., 2: 179-183; 1989.
- [14] Lytle, R.J.; Laine, E.F.; Lager, D.L.; Davis, D.T. Cross-borehole electromagnetic probing to locate high-contrast anomalies. Geophys., 44: 1667-1676; 1979.
- [15] Hill, D.A.; Wait, J.R. Theoretical noise and propagation models for through-the-earth communication. National Telecommunications and Information Administration; May 1992.
- [16] Eaton, P.A.; Hohmann, G.W. An evaluation of electromagnetic methods in the presence of geologic noise. Geophys., 52: 1106-1126; 1987.
- [17] Greenfield, R. Borehole radar clutter. National Radio Science Meeting; Boulder, CO; January 4-6, 1989.
- [18] Hill, D.A. Clutter models for subsurface electromagnetic applications. Nat. Inst. Stand. Tech. (U.S.) NISTIR 89-3909; 1989.

**Tunnel Detection without the use of boreholes:
What are our capabilities and what improvements can be made?**

Robert C. Kemerait

ENSCO Inc.

Abstract

For the past decade, we have been involved in tunnel and subsurface void detection research. Originally, this research was primarily conducted using data collected from GPR borehole data collection systems such as the PEMSS system. However, data collected using only surface techniques can be effectively used to resolve some tunnel and void detection problems.

In this paper, we will discuss our experience with tunnel and void detection field data collection exercises where boreholes were not available. Our focus will be on the following three items:

- Problems encountered/results obtained when detecting tunnels in tuff, clay and shist, and limestone with sandstone and/or Hawthorne clay overburden,
- Representative results from each of these tests, and
- Identification of the eminent changes in software and hardware and the improvements expected from these changes.

The subject field exercises have been conducted with an enhanced SIR 8, SIR10, and Synthetic Pulse Prototype GPR systems. These tests were performed at the University of Arizona Test Tunnel, a gold tunnel in Dahlonega Georgia, Bat Cave and Wilson Cave near Gainesville, Florida and the Metro tunnels near the Anacostia Station in Washington DC.

The exercises covered a wide range of tunnel sizes, depths, and configurations; geology of the overburden material; and physical access for the survey. The results obtained from the analysis of the collected data are combined with details on specific survey parameters including antenna selection, time-range window determination, gain settings, bistatic and monostatic antenna configurations, and cable selection.

Finally, our plans for software enhancement and development of a new synthetic pulse system are discussed.

Introduction

The detection of tunnels is an extremely important issue for several different problem areas. Probably the most experience has been gained from the Korean tunnel project which has been underway for two decades¹. Here, the likelihood is that any tunnel to be discovered will be quite deep and in hardrock. Since the depths tend to be hundreds of meters, the use of a surface survey, such as ground penetrating radar, is not feasible in detecting and locating such deep tunnels. Thus, boreholes with the associated data processing for a given number of offsets have been the primary procedure. In contrast, there are suspected tunnels which are equally important to detect and locate which are considerably shallower and can possibly be detected from the surface.

There are a number of applications where a rather large void or tunnel would be dug within 15 to 20 meters of the surface. In such circumstances, it may not be necessary to put down numerous boreholes in order to detect and locate such tunnels; however, the use of boreholes is a costly and time-consuming process which should be employed only as a last resort. For the shallow tunnels (arbitrarily defined as those with depths less than one hundred feet), our greatest fear is that attenuation in the overburden is to the point that a tunnel's reflected signal cannot be observed for a reasonable dynamic range; i.e., 100 dB. We have had success in detecting tunnels at depths of approximately 50 feet with a simple monostatic surface scan, (see Figures 1 and 2). In this case, the tunnel was located in a schist-type material with several feet of clay as overburden. The antenna, which was used in the monostatic mode, was 120 MHz; this antenna was also used as the receiver in the associated transmission test. The transmitter was 300 MHz and was used for convenience rather than by design.

This same antenna arrangement (300 MHz transmitter and 120 MHz receiver) was employed during our investigations of two caves in limestone near Gainesville, Florida. The first cave, Wilson Cave, was in limestone but with approximately fifteen feet of Hawthorne clay as an overburden. The second cave, Bat Cave, was similar but with no clay overburden; in fact, the limestone protrudes to the surface in some cases. Results of the Bat Cave investigations are given in Figures 8 and 9.

Finally, we will present some results from our surveys over the Anacostia Metro station near Washington, DC. Here, we attempted to locate a pair of tunnels beneath approximately 50 feet in clay using the 80 MHz antennae in a bistatic mode.

These investigations indicate that detecting and locating sizable voids down to fifty feet is feasible in many materials; however, one needs to be aware of the optimum parameter settings and signal processing required in order to achieve these depths..

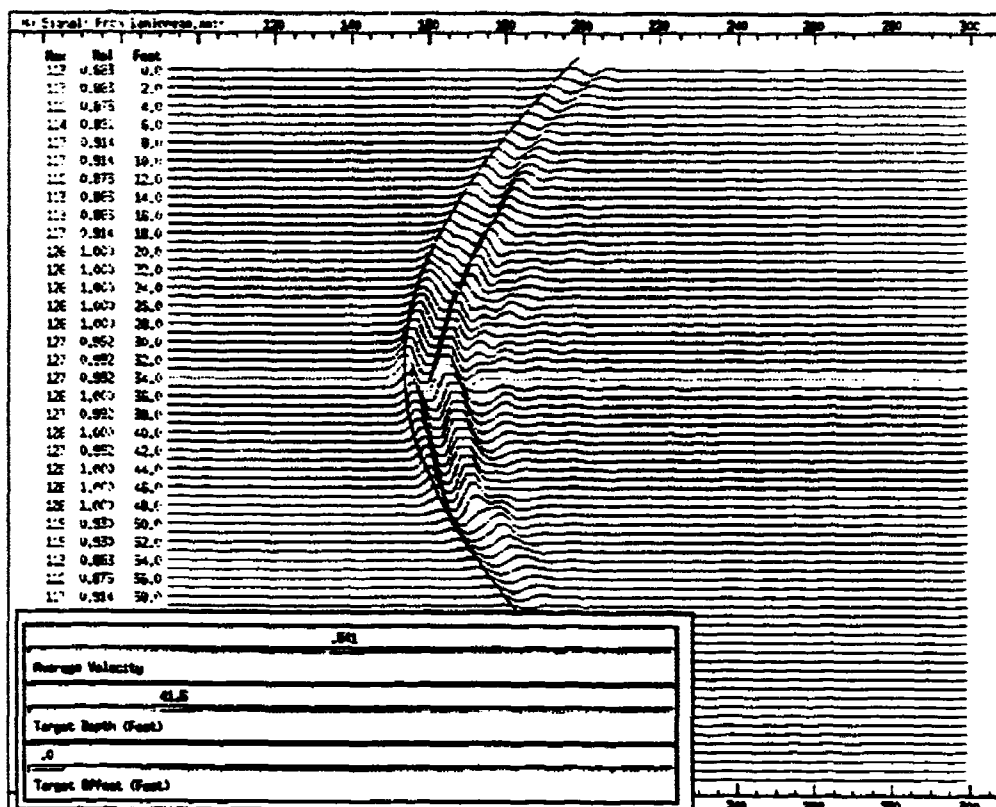


Figure 1: Transmission test at the Dahlonega Test Site.
Tunnel is approximately 42 feet deep or below the surface.

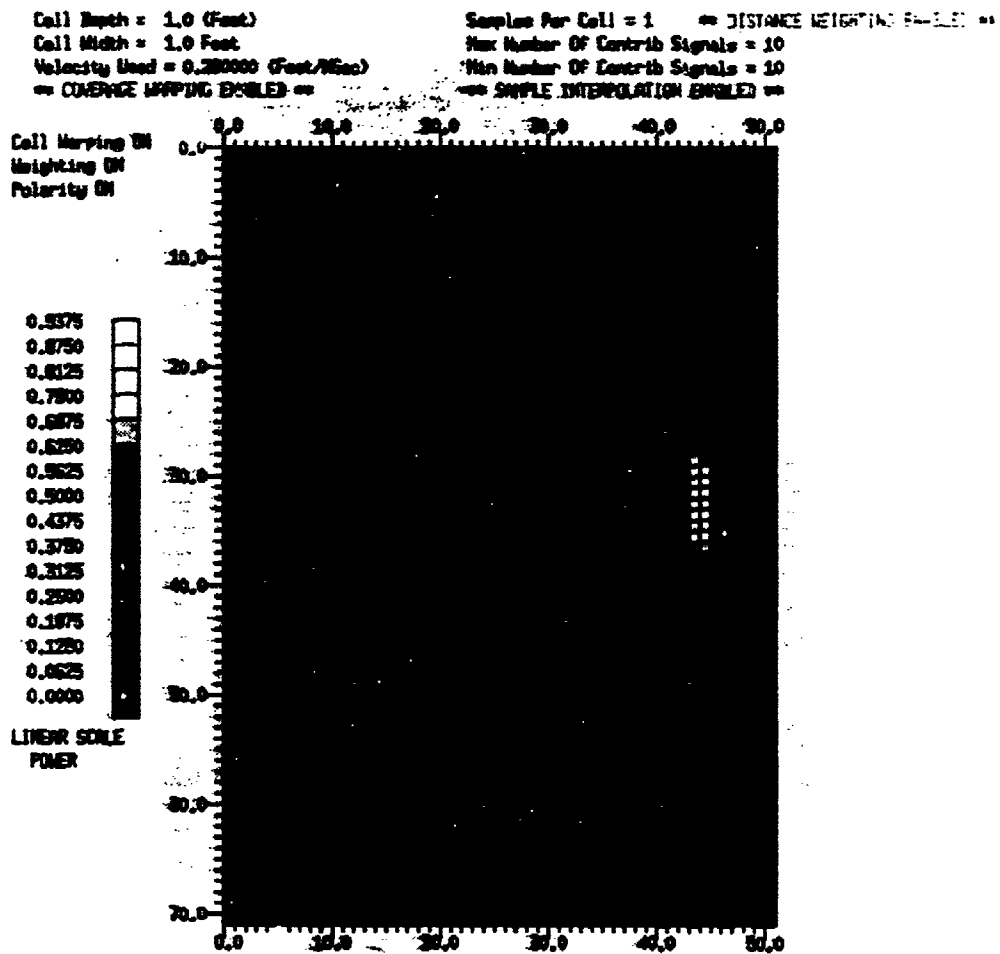


Figure 2: Reflection (monostatic) results. Same tunnel as Figure 1.

Survey Considerations

Most of our discussions in this section relate to our experience with the SIR-8 system; however, we are seeing similar "problems" with the SIR-10. We have used similar cables on both systems and many of the problems are associated with the cables.

The two way travel time would be in the 300-500 nano-second range for a tunnel that is 50 feet below the surface. Assuming the 500 nano-second scale is selected, the half-range ramp gain starts at 250 nano-seconds, complimented by the overall gain and the agc. The next sequence of figures illustrates the complications (artifacts) encountered when large gain settings are achieved. Figure 3 shows the raw (stacked) results from the transmission test. Since the signals were quite large, actually clipped at the closest point of approach, the gains were set in the medium range.

The results given in Figure 4 are for the monostatic reflection test with the time scale set to 750 nano-seconds and the gains the same as in the transmission test. We notice an artifact near 210 nano-seconds. The results given in Figure 5 are also for the monostatic reflection test but with a 500 nano-second time window and considerably more agc and mid-range gains. The obvious large artifact now appears near 330 nano-seconds; however, the time delays around 250 nano-seconds are relatively undisturbed and have much more gain than those times in Figure 4. We would not have known this setting to be possible had we not known the tunnel depth and associated velocity, i.e., the transmission results in Figure 3. Figures 6 and 7 illustrate how these artifacts can easily be reduced by subtracting the mean of the data. Figure 6 relates to Figure 4 and

Figure 7 relates to Figure 5. The procedure is to now to inspect/process Figures 6 and/or 7 in order to determine if and where a tunnel exists.

From this set of figures, we observe that the detection of tunnels at depths of 50 to 100 feet may be possible, but the operator will need to stress the system to the point where data collection and interpretation are very difficult. He will probably have to make multiple traverses in order to determine which part of the data is real and which part is system artifact.

Site ID: DAHLONEGA SITE 3 Test ID: 09/02/90 TEST 2 Type: 300T120R
Gather: 40

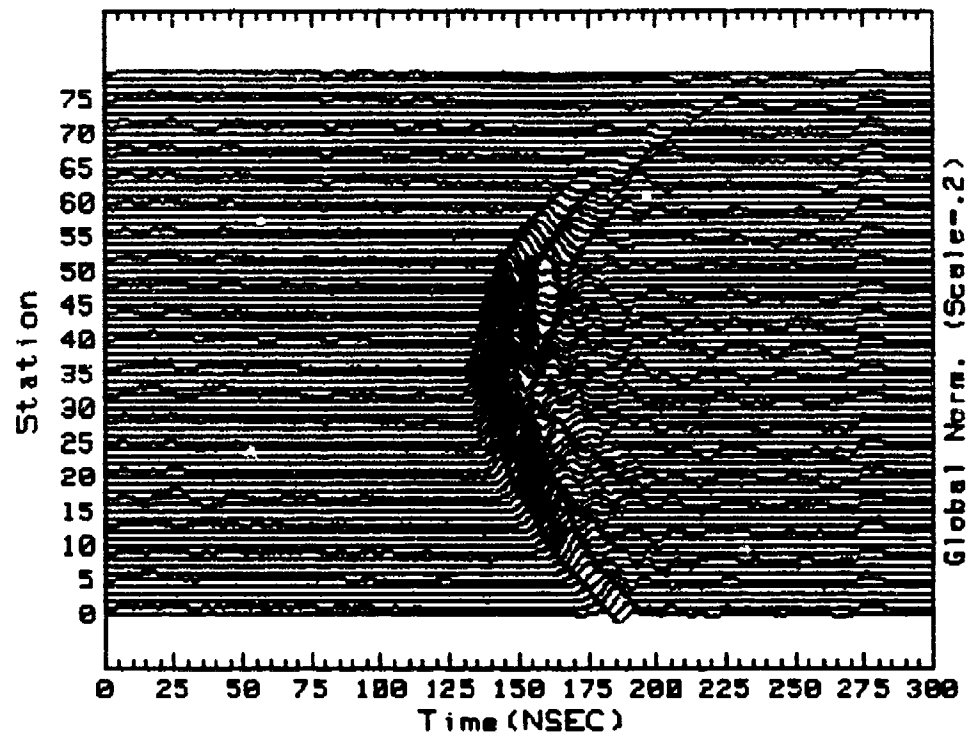


Figure 3: Transmission results repeated for 42 foot deep tunnel.

Site ID: DAHLONEGA SITE 3 Test ID: 09/02/90 TEST 6 Type: SURF 120
Gather: 40

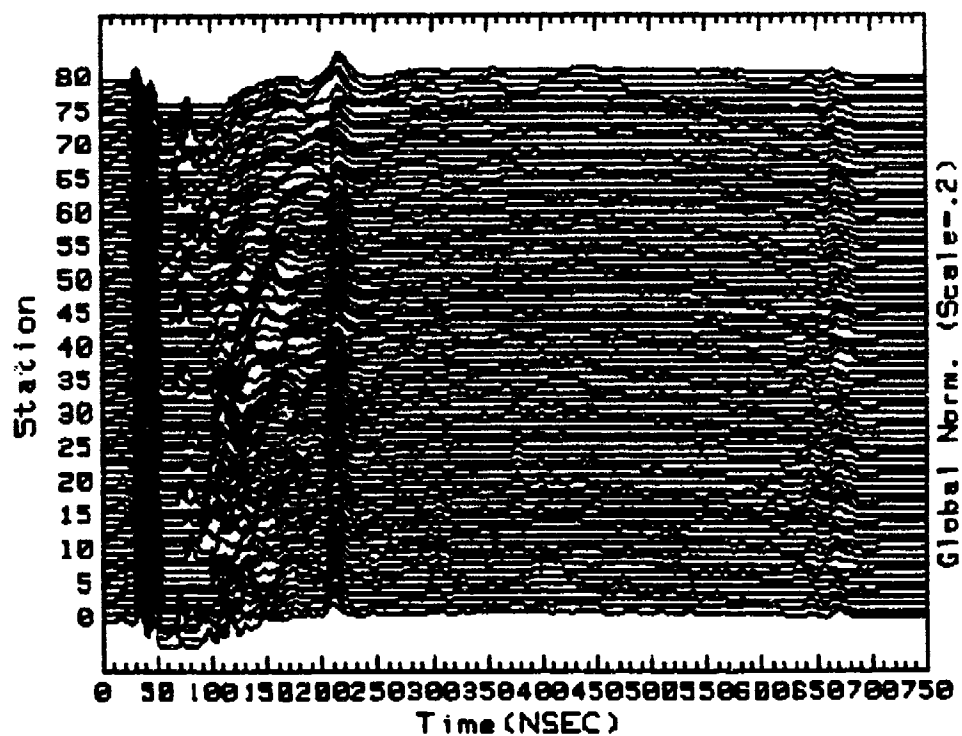


Figure 4: Monostatic reflection results for longer time window and low-to-moderate gain settings.

Site ID: DAHLONEGA SITE 3 Test ID: 09/02/90 TEST 1 Type: SURF 120
Gather: 40

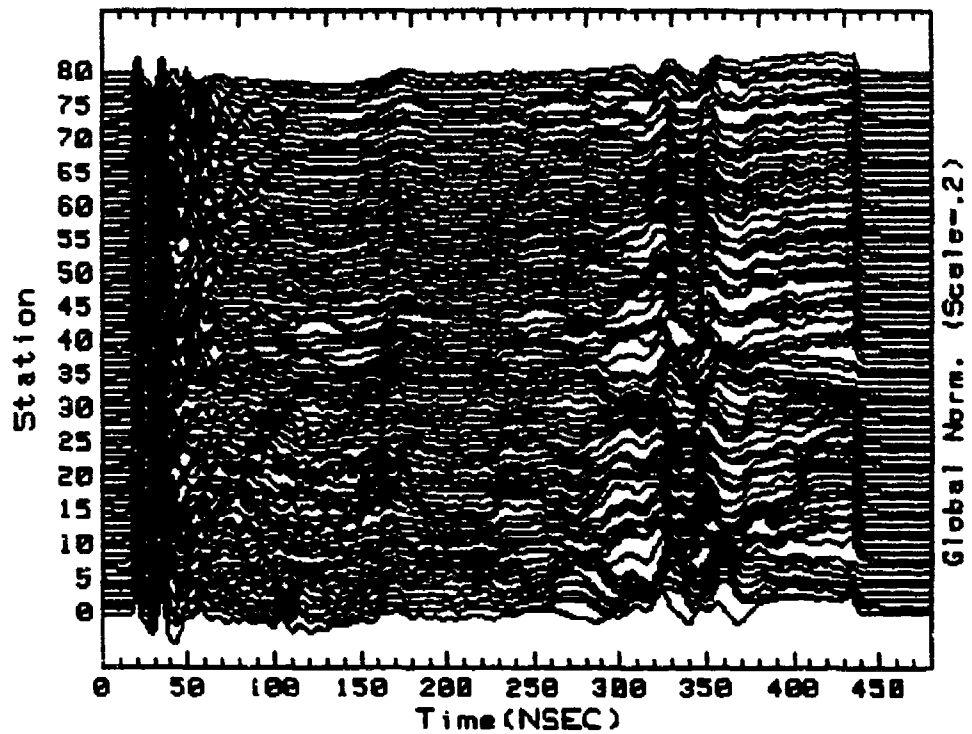


Figure 5: Monostatic reflection results for shorter time window and high gain settings

Site ID: DAHLONEGA SITE 3 Test ID: 09/02/90 TEST 6 Type: SURF 120
Gather: 40

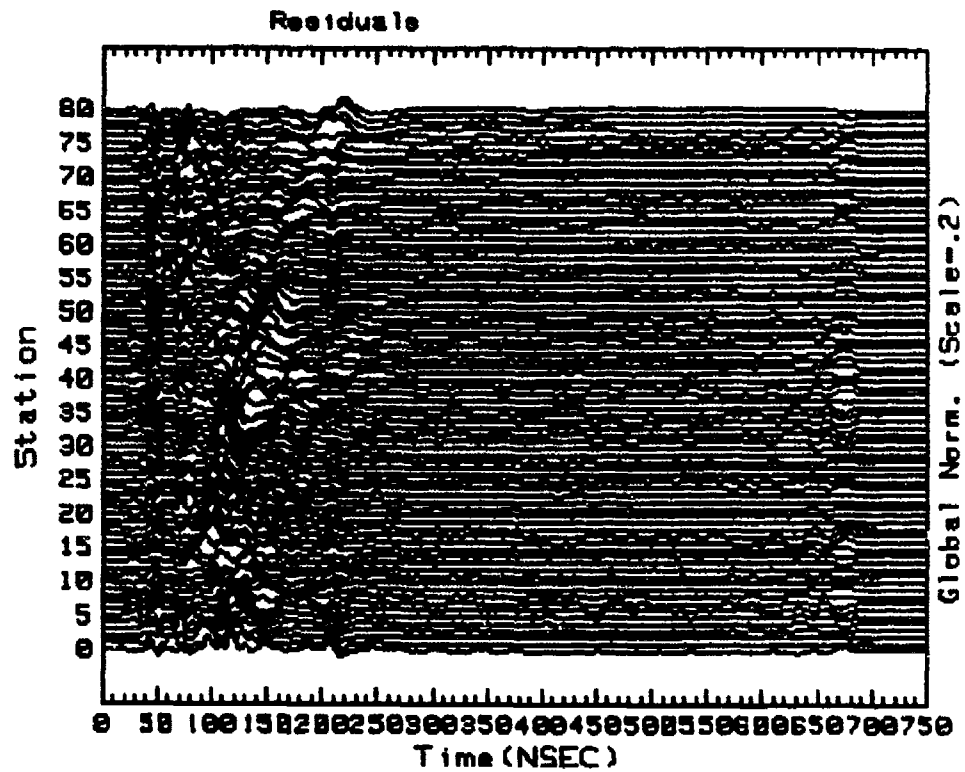


Figure 6: Monostatic survey with average background removed.
(Relates to Figure 4)

Site ID: DAHLONEGA SITE 3 Test ID: 09/02/90 TEST 1 Type: SURF 120
Gather: 40

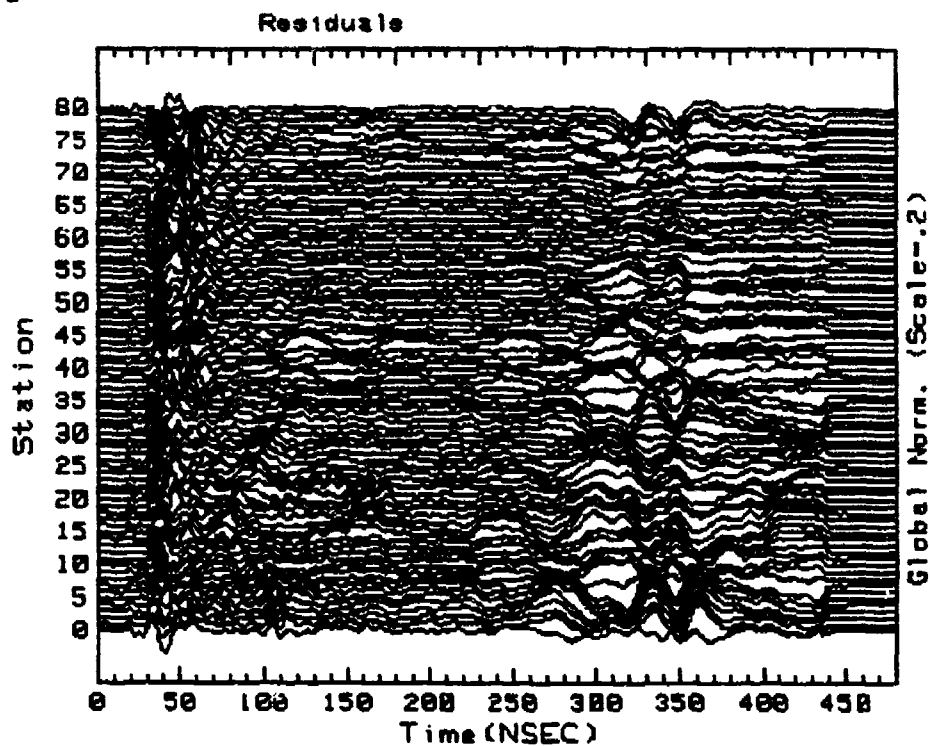


Figure 7: Monostatic survey with average background removed.
(Relates to Figure 5)

Data Considerations

In the borehole-to-borehole tomography situation, we expect to observe several well documented features to show up when the data are collected across a tunnel. The most prominent (assuming the tunnel is airfilled) is the early arrival due to the speedup in velocity through the tunnel. Additional features include the hyperbolic moveout wings exhibited in the data taken above and below the tunnel, and thirdly, that feature which has been referred to as dispersion. This last feature is presumed to be destructive/constructive interference as the rays pass through the tunnel. Thus, a set of discriminants has been developed for discriminating between tunnels and natural phenomena by utilizing these features from several sets of borehole offset data.

When this offset data obtained from a pair of boreholes is not available, one must modify the above set of features to be used on surface scan data. We believe that the data from a bistatic survey will potentially provide better features than a monostatic survey. There is more flexibility because the transmitter and receiver can be separated at different distances and the survey repeated as well as keeping one antenna stationary (i.e., over the suspected tunnel) and moving the other across the suspected tunnel. (Also, for several antennae configurations the bistatic configuration allows for higher power transmitters.)

Regardless, the primary discriminant for a small (1 meter by 2 meter) tunnel becomes the typical hyperbolic moveout. Since this survey configuration does not allow for the transmission through the tunnel, more importance must be placed on secondary features which were not as important in the Korean project. These secondary features are the interference phenomena which can be emphasized by cepstral processing and

refraction phenomena where the data is taken at angles considerably different from the normal 90° to the tunnel axis which is strived for.

We have taken several sets of preliminary data which show promise and developed several additional discriminants; however, we will have a much more definitive discriminant set when our Dahlonaga test facility is completed in the summer of 1993. Figures 8 and 9 illustrate the differences in taking monostatic and bistatic data from an underground air-filled cave from which we are developing discriminants.

Site ID: BAT CAVE
Gather: 45

Test ID: 11/9/91 TEST 2

Type: SURFACE

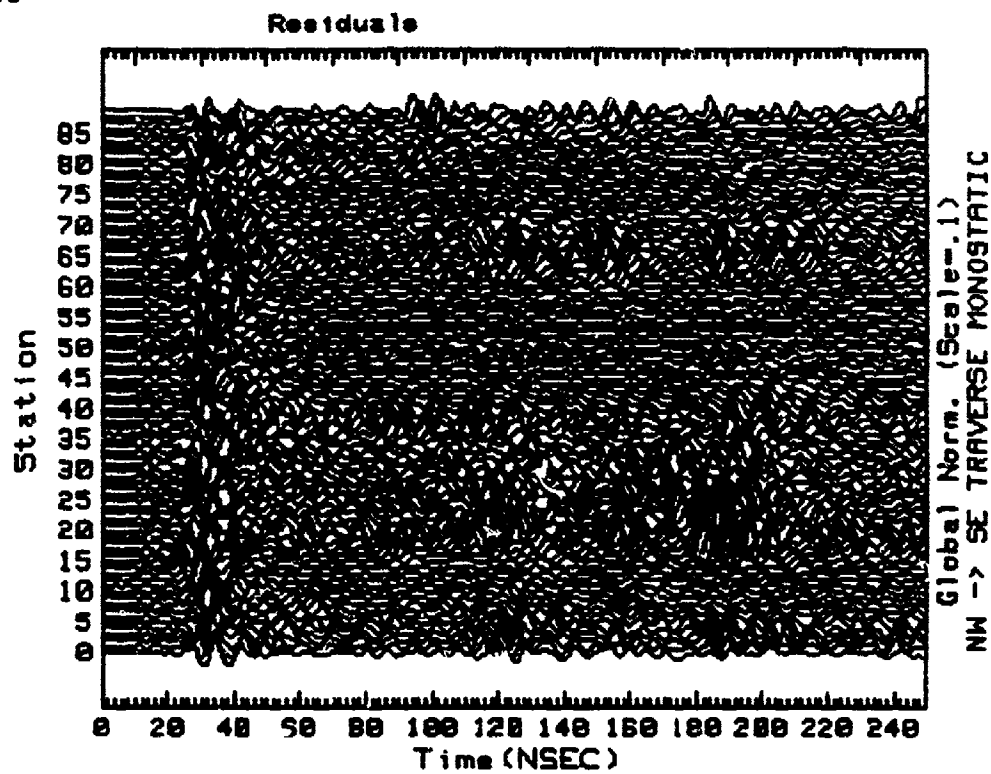


Figure 8: Monostatic traverse over an underground cave.

Site ID: BAT CAVE T2 Test ID: 11/9/91 TEST 5 Type: SURFACE
Gather: 40

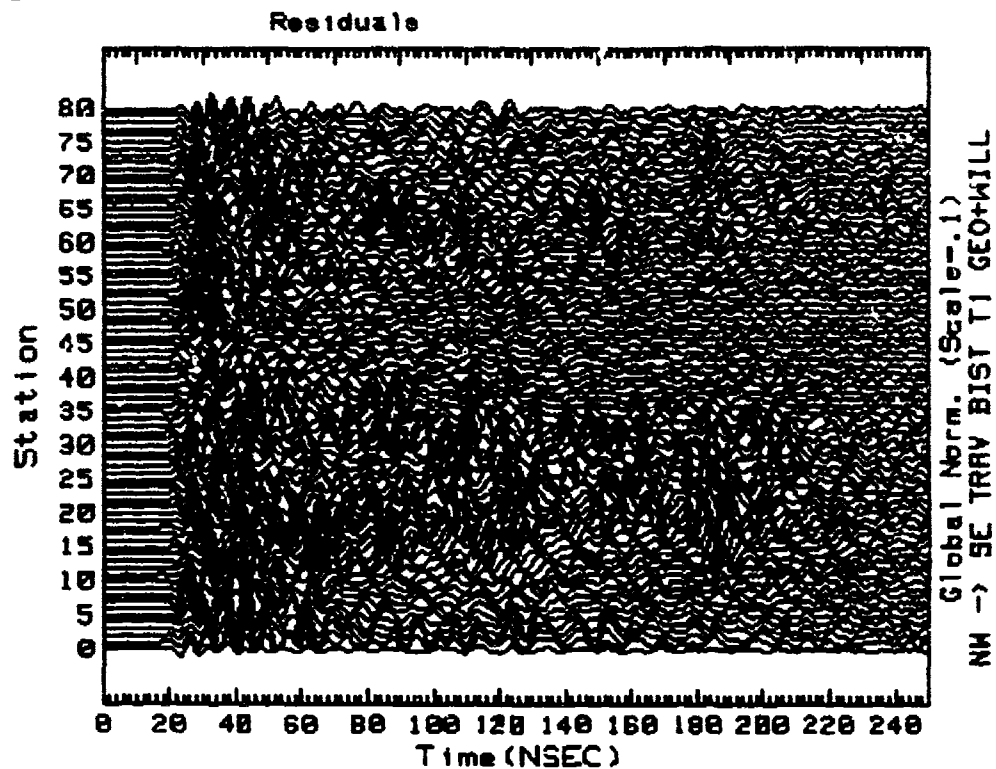


Figure 9: Bistatic traverse over the same cave as in Figure 8.

Conclusions

The use of boreholes considerably enhances the potential for detecting tunnels. By using ground penetrating radar in the transmission mode, we do not have to rely on reflection coefficients and travel paths of twice as long or even substantially longer. Also, the borehole concept allows for better identification since the tunnel can be illuminated from many more angles.

Since, in many situations where intrusive investigations are not possible, we have to rely only on surface surveys, the question is what can we expect as far as tunnel detection and identification. We would expect a maximum tunnel depth of one hundred feet in a rather ideal situation and considerable less as the overburden attenuation increases. We should be able to counteract the attenuation to a small degree by utilizing the synthetic pulse concept², increasing the transmitted power, averaging the data, hardware (antennae) improvements and the more effective use of signal processing³. The combination of all of these will have a limited effect on the depth of penetration, perhaps optimistically, by a factor of two.

We believe that the identification problem can be further enhanced to a limited degree, procedurally, by collecting multiple sets of data with the appropriate antennae and by employing monostatic as well as bistatic surveys.

References

1. Olhoeft, G. R., 1988, "Interpretation of hole-to-hole Radar Measurements", pp. 616-629, Third Technical Symposium on Tunnel Detection, Jan. 12-15, Golden CO.
2. Kemerait, R.C. and J.N. Griffin, 1988, "Synthetic Pulse Radar", pp. 570-592, Third Technical Symposium on Tunnel Detection, Jan. 12-15, Golden CO.
3. Kemerait R.C. et al., 1988, "Signal Processing Applied to Tunnel Detection by Borehole Radar", pp. 593-615 Third Technical Symposium on Tunnel Detection, Jan. 12-15, Golden CO..

ELECTROMAGNETIC DETECTION OF BURIED DIELECTRIC TARGETS IN LOW LOSS MEDIA

Irene C. Peden, John B. Schneider and John Brew

ABSTRACT

The cross-borehole tunnel detection problem is represented in terms of an eccentric dielectric ellipsoid that is illuminated by a vertical dipole and immersed in a medium whose electromagnetic properties at VHF are those of a lossy dielectric. The T-matrix method is utilized for studying the scattering properties of this target for the three-dimensional theoretical portion of the study. Results are compared with those of a two-dimensional obtained by the method of moments. Additional comparisons are made with measured data from a laboratory scale model that is described. With the pulse shape assumed to be Gaussian, the T-matrix results obtained in the frequency domain are then transformed into the time-domain utilizing the Fourier transform, a procedure that is not completely general but which the spectral shape of the PEMSS II pulse makes allowable for the problem at hand. It is found that significant diagnostic features of the PEMSS II field data are preserved.

INTRODUCTION

Scattering from three-dimensional subsurface objects has been studied in both the frequency and time domains using the T-matrix method, with the target represented as a dielectric ellipsoid and the source as an electric dipole. Rotations of this non-axially symmetric target with respect to the source can be accommodated by the method, with results that illustrate the importance of using non-symmetric representations for the scatterer rather than those having axial symmetry, such as prolate spheroids. Other results demonstrate that a method based on polarization of the forward scattered field may provide a more robust diagnostic of target location in cross-borehole investigations than one that uses only a single field component. Results from the analytic model compare favorably with those obtained from an experiment based on a laboratory scale model of a subsurface tunnel detection problem that is also described.

The field scattered from a buried dielectric ellipsoid illuminated by a transient pulse is then determined. Although the T-matrix method itself is a resonance-region, frequency-domain technique, it is shown that it applies to problems in which the energy in the pulse is restricted to several decades in the frequency domain. The pulse, which simulates one used in the PEMSS VHF subsurface radar, is radiated from an electric dipole in a vertical borehole surrounded by a low loss rock medium. The scattered pulse is obtained by first calculating the components in the spectral description of the transmitting antenna current. The T-matrix method is then used to determine the system transfer function. This, in turn, gives the scattered energy in terms of the antenna current. An inverse Fourier transform yields the temporal scattered field. Results are compared to those obtained from a field experiment in which a deeply buried empty tunnel embedded in granite was illuminated by a dipole source. The hyperbolic wings that serve as a diagnostic of tunnel location, and the expected earlier arrival time of energy that has propagated through the air-filled tunnel, are found to be features of the calculated results for the ellipsoid as well.

ANALYTICAL MODEL

Methodology

The T-matrix extended boundary condition method was selected for this cross-borehole study. This technique provides the opportunity to model the source as an arbitrarily-oriented dipole and the target as a three-dimensional object. It is primarily a resonance region technique, and thus serves as a good match to the illuminating pulse of the PEMSS II VHF subsurface radar, whose radiated energy is contained largely in the resonance region for scattering objects with dimensions of the order of 2 m. in granite. This restriction on spectral width permits the time domain scattering problem to be studied with the use of Fourier transforms.

The transition-, or T-matrix directly relates the incident electric field to the scattered field. The reader is referred to the bibliography for references that provide details of the formulation. Briefly, an integral equation is written for the incident electric field and the total electric fields on the surface of the scatterer utilizing the vector wave equation, the vector Green's theorem and the dyadic Green's function. In a similar manner, the scattered field E^s is also expressed in terms of the unknown surface fields through an integral equation. The surface fields can be obtained by solving the integral equation relating them to E^i , and then used to obtain the scattered fields. To solve the integral equations, all the field quantities, as well as the dyadic function, are expressed as series expansions of vector spherical harmonics, where the appropriate representation is dependent on the location of the observation point with respect to the scattering surface. Two matrix equations are obtained and the surface fields eliminated between them. The resulting matrix, which directly relates the scattered fields to the incident field, is the T-matrix.

Tunnel Representation

The T-matrix method, as employed here, requires the target to be of finite extent. For purposes of this three-dimensional study, a dielectric ellipsoid was selected as representative of an air- or water-filled tunnel. The cross section can be adjusted for best fit to a domed top tunnel, as illustrated in Figure 1; the length or eccentricity of the ellipsoid can be chosen so that the actual locations of the endpoints are masked by loss in the host medium, thereby rendering the target essentially infinite for purposes of the study. The ellipsoid is a non-axially symmetric scatterer whose orientation with respect to the source may be varied by means of a rotation operator, simulating variations in the angle of the tunnel floor or axis with respect to the orientation of the source dipole, or equivalently, deviations from vertical in the borehole axis with respect to the tunnel. Unlike axially symmetric scatterers, the ellipsoid has a preferred scattering direction, qualifying it as a useful general model. At the same time, it has a symmetry of its own that can be exploited in calculating the T-matrix elements. The lossy dielectric host medium acts as a low pass filter, smoothing out rough edges, sharp corners, etc. on the surface of a tunnel being represented, lending further validity to the model.

Description of the Problem

An air- or water-filled dome-topped tunnel with a 2 meter cross section is assumed so deeply buried in a granite medium that scattering effects of the air-earth interface can be neglected. Vertical boreholes are located on either side of the tunnel, with the tunnel axis approximately perpendicular to the plane of the boreholes. An electrically short vertical dipole

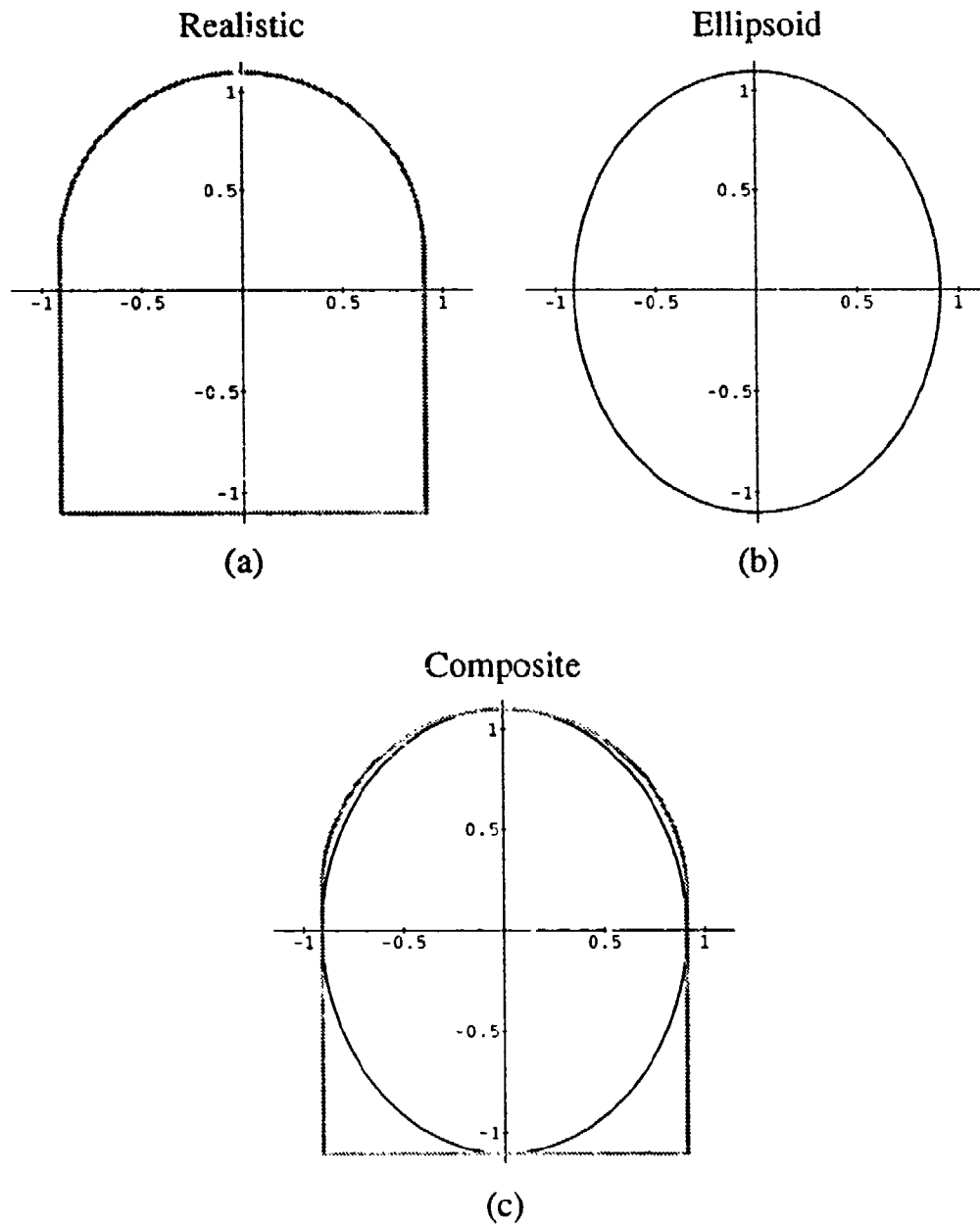


Figure 1. Elliptical Model of Tunnel Cross Section
(a) True Shape (b) Ellipse (c) Composite View

antenna in one of the boreholes serves as a source of illumination; its vertical position in the borehole with respect to the tunnel is variable. A combination of incident and forward-scattered electric fields can be received at any point along a vertical path in the second borehole. The host medium is granite with a relative dielectric constant $\epsilon_r = 9$, $\mu_r = 1$, and conductivity $\sigma = 0.002$ S/m.* It is assumed that these parameters are constant over the VHF band (30 - 300 MHz), yielding a range of loss tangents δ between 0.0133 and 0.133. Low loss dielectric approximations for propagation constants, etc. can be justified over this loss tangent range.

CALCULATED RESULTS

An infinitely long dome-top tunnel is represented to good approximation by an eccentric ellipsoid 6.6-m long, 2.2-m high and 1.82-m wide whose volume equals that of a spheroid having the same length and a 2.2-m diameter. It is centered between boreholes 8 m apart, and is surrounded by a medium having the constitutive parameters identified above.

Figure 2 is illustrative of the forward-scattered vertical electric field obtained by the T-matrix method at 60 MHz. The transmitter and receiver have the same height in the curve identified as #1. Maintaining a constant vertical offset between the two antennas, curves #2 and #3 are obtained with the receiver 14° above and below the transmitter, respectively. Horizontal offsets in the figure are used for clarity in the presentation. The double nulls of #1 are due to diffraction effects at the top and bottom of the ellipsoid; the nulls are 3.6 m apart, providing a rough measure of the 2.2 m tunnel height, and a better measure of the location of its center. The latter can be improved by adding and averaging the center locations suggested by #2 and #3. The result of three such trials places the centroid of the scatterer within 20 cm of its actual location.

Figure 3 presents the results for the total vertical electric field calculated at 30 MHz along a vertical path simulating a receiver borehole when the tunnel is air- or water-filled.

The consequences of scatterer rotation are considered next, using the same ellipsoidal target model, depths and borehole locations, and assuming an air-filled tunnel. Calculations are made at a frequency of 60 MHz. Adopting the nomenclature used for ships or aircraft, rotating the target about its longitudinal axis, i.e. normal to the plane containing the borehole axes, is referred to as roll, a rotation that would have no effect on the received scattered fields of an axially symmetric object. The results for angular variations of 0°, 30°, 60°, and 90° are shown in figure 4, where significant change as a function of angle is observed. This result confirms that there is a preferred scattering direction for this non-symmetric target. Several features of figure 4 can be explained by assuming that the scatterer contains an induced dipole. Note that the focus of the energy is "down" in the 30° and 60° cases, and that the primary difference between the 0° and 90° figures is that the magnitude of 4d is smaller than that of 4a, reflecting the fact that in the 90° case the shorter cross-section dimension is brought into vertical alignment with the source, inducing a weaker dipole in the scatterer. The roll calculation is representative of situations in which the borehole axis drifts off vertical, or equivalently, the vertical orientation of the tunnel becomes offset.

Results of the pitch and yaw calculations are not shown. Differences in the received scattered fields over the span of the principal lobe and first nulls are confined to variations in

*Courtesy of the U.S. Army

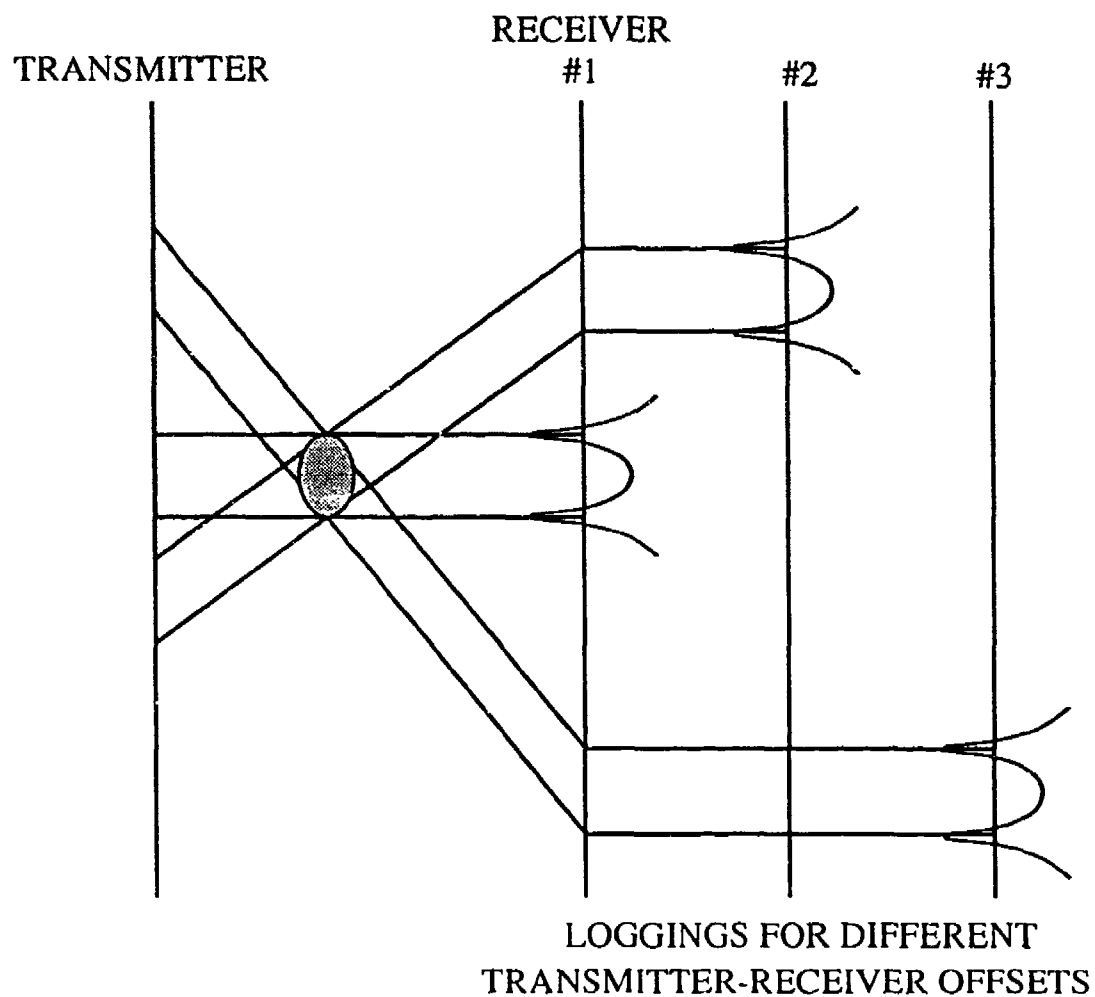


Figure 2. Ellipsoidal Tunnel Signature
Magnitude of Received Vertical Electric Field

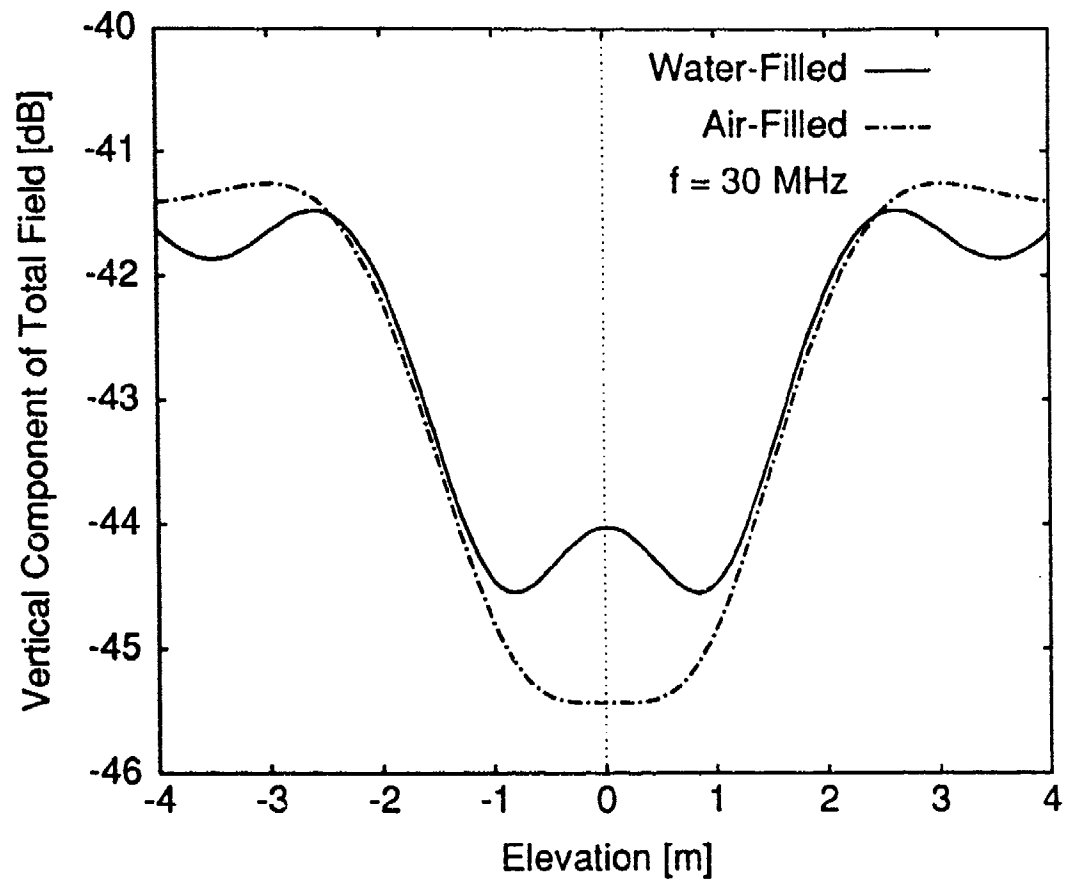


Figure 3. Calculated Vertical Electric Field in Receiver Borehole as a Function of Elevation at 30 MHz
Comparison of Air and Water Targets

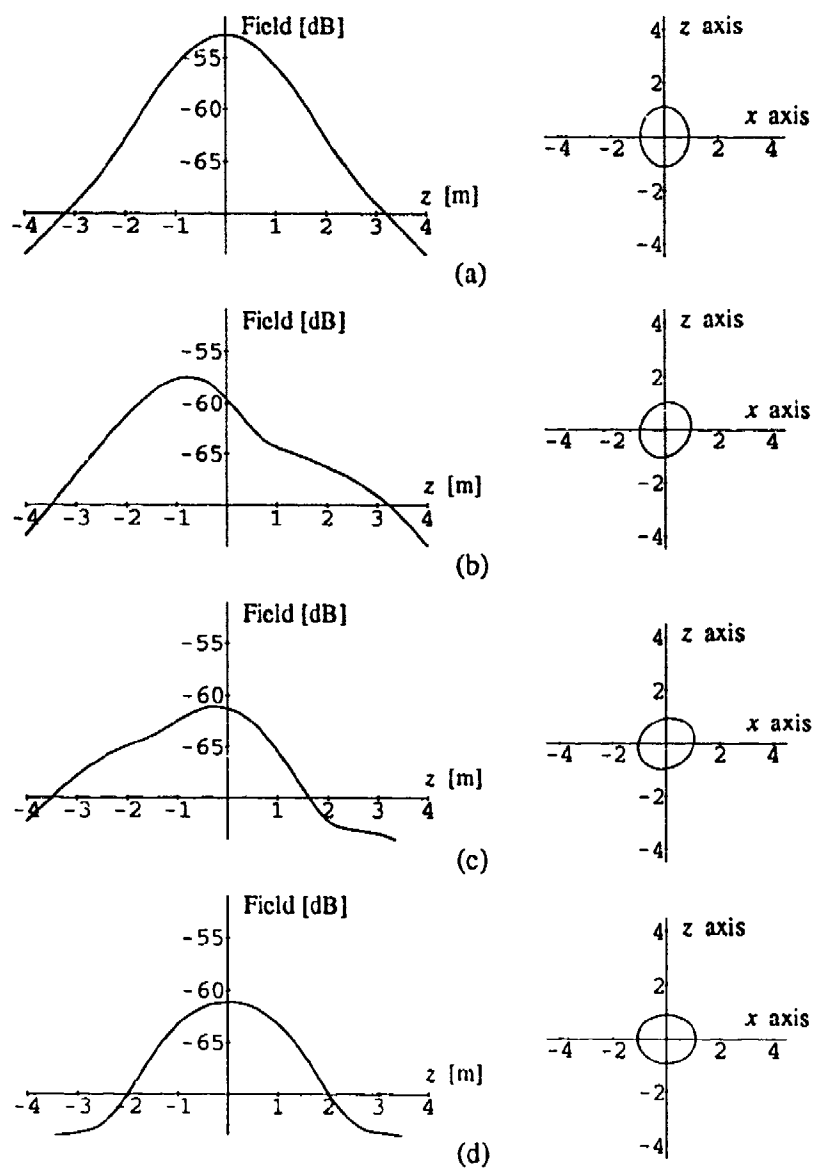


Figure 4. Received Vertical Electric Field for Four Different Angles of Rotation (Roll) Around the Longitudinal Axis of the Ellipsoid

magnitude or of distance between pattern nulls, consistent with the concept of an induced dipole within the dielectric ellipsoid. Variations in pitch angle correspond to angles of incline in the tunnel floor with respect to the normal to the plane of the boreholes. The longer cross-sectional dimension of the ellipsoid remains vertical under this rotation. Slight differences occur in the magnitude of the scattered field over pitch angles of $\pm 10^\circ$, which correspond roughly to $z = \pm 3$ m. When a larger vertical segment of the borehole is considered, the expected result is that increasing the pitch angle increases the value of the scattered field in off-center vertical directions. The yaw rotation leaves the vertical and horizontal orientations of the ellipsoid unaffected, while moving one endpoint closer to and the other away from the receiver borehole. For this reason, large angular values affect the validity of the model. Maintained within $\pm 8^\circ$, however, it is found that increasing the angle increases the magnitude of the vertical electric field within 4 m of $z = 0$. This rotation would occur in field work when the longitudinal axis of a tunnel is not perpendicular to the plane containing the boreholes.

The deep null in the magnitude of the horizontal component of the received scattered electric field opposite the center of the ellipsoid is seen in figure 5 to be insensitive to roll. Given both the vertical and horizontal components of the received electric field, it should be possible in theory to be relatively confident about the vertical location of the center of a tunnel, so long as the transmitting and receiving dipoles are parallel. There are practical problems associated with measurement of the horizontal electric field in a borehole of small diameter, since a horizontal loop antenna that might fit the space would have a small area, requiring a large number of turns. Some of the difficulties associated with the use of loop antennas in boreholes can be found in the literature.

MODEL VALIDATION

Comparison with Two-Dimensional Theoretical Model

It is assumed for this phase of the study that the tunnel is infinitely long and has an elliptical or circular cross-section, with no variations along the tunnel axis. The problem then becomes two-dimensional, requiring a two-dimensional source of vertically polarized illumination. This is taken to be a magnetic line source parallel to the longitudinal axis of the tunnel. As before, the air-ground interface is presumed to contribute negligibly to the forward scattered fields in the receiving borehole. The well-known method of moments is employed, and the cross-section of the scatterer partitioned into cells small enough that the field is essentially uniform over any one of them. The total field in each cell is calculated, the scattered field due to each obtained, and the superposition theorem invoked for the composite scattered field at a desired receiving borehole location.

The two- and three-dimensional calculated results were compared with some related experimental results in order to provide a validity check. A laboratory model that will be described below was used for this purpose. The problem was scaled in physical dimension and frequency, and the dielectric and loss properties of the host medium adjusted to fit those of the laboratory configuration. The latter are $\epsilon_r = 3.2$ and $\sigma = 0.0167$ S/m at 2.0 GHz. The two-dimensional scatterer for the method of moments calculation is an air-filled cylinder with a diameter of 8.5 cm. The three-dimensional scatterer for the T-matrix comparison is a spheroid whose cross-section at the widest dimension is a circle of 8.5 cm. diameter, and whose longest dimension is 25.5 cm, an aspect ratio of 3:1. the boreholes are assumed to be 17 cm on

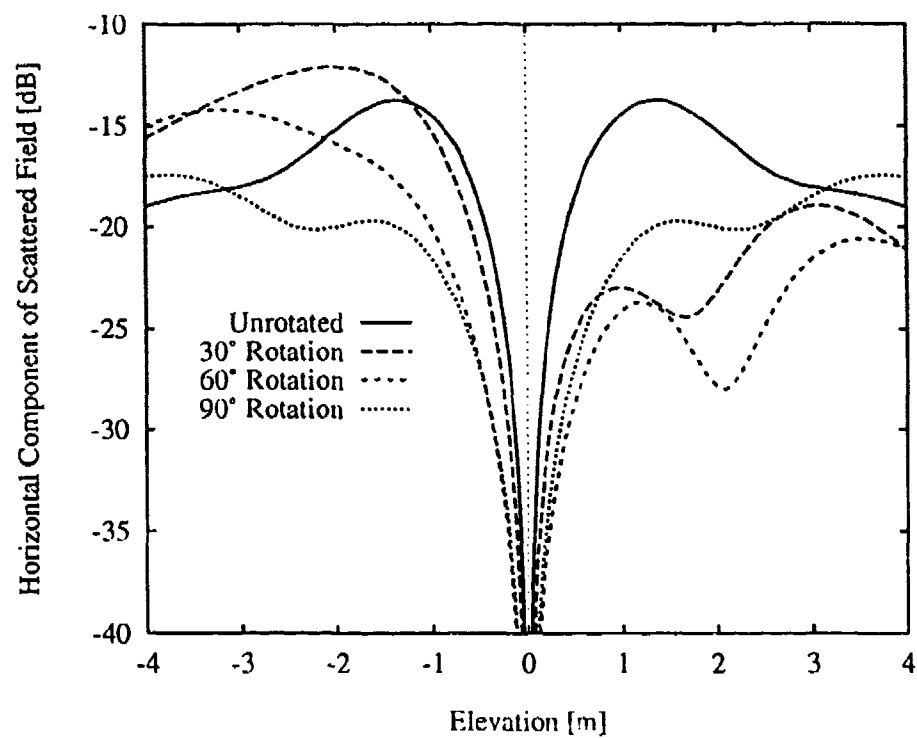


Figure 5. Received Horizontal Scattered Electric Field for Four Different Angles of Rotation (Roll) Around the Longitudinal Axis of the Ellipsoid

either side of the tunnel. Figure 6 shows the received signals when the transmitter and receiver are moved simultaneously from 40 cm below the center of the target to 40 cm above. A major difference between the two curves, which are otherwise quite similar, is the absence in the two-dimensional result of the strong central "peak" observed in the T-matrix result. The double-null diagnostic feature is present in both results, albeit the linear distance between nulls is a closer representation of the actual target height in the two-dimensional case. The pitch and yaw results for the more general ellipsoid could only be obtained by the T-matrix, 3-dimensional approach. In addition, it was found that the two-dimensional results do not display the sensitivity to frequency seen in the T-matrix case.

Comparison with Laboratory Scale Model Results

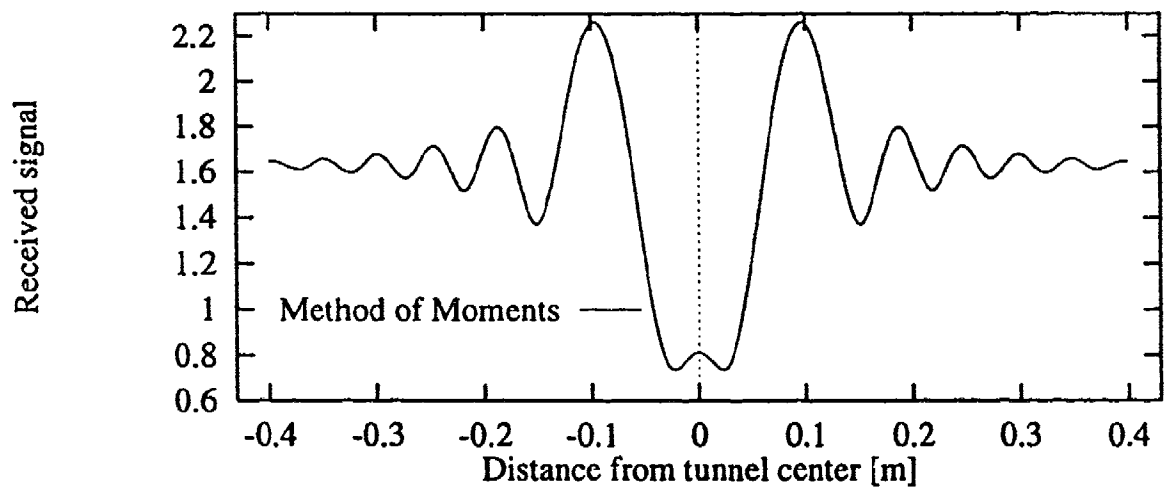
The experimental set-up is illustrated in Figure 7. A mixture of 93% alumina and 7% potting soil, by volume, served as the host medium. Initially, its relative permittivity ϵ_r measured 5.3, but drying of the soil caused it to stabilize at 3.2, the value used for the above calculations. The lower relative permittivity of the model host medium results in a lower contrast scattering problem than that of the actual air-filled tunnel embedded in granite. The powder was contained in a circular aluminum tank 137.2 cm in diameter, lined with microwave absorbing material. The target was a hollow cylindrical cardboard tube 8.5 cm in diameter and boreholes were simulated by PVC tubes located symmetrically at 17 cm on either side of the "tunnel". Metal sleeves were placed over the plastic tubes at and somewhat below the surface to restrict propagation to a completely subsurface path between boreholes, preventing the up-over-and-down mode associated with shallowly buried targets. Sleeve dipole antennas were constructed for use as transmitting and receiving probes. Radiation pattern measurements ensured that they served effectively as infinitesimal electric dipoles.

Cross-borehole electric fields in the simulated receiving borehole were measured using an HP 8510B network analyzer to obtain the transmission parameter S_{21} over the S-band frequency range 2 - 4 GHz. Positioning of the transmitting and receiving probes was controlled by a stepping motor that was in turn controlled by a personal computer. The computer also controlled data acquisition through the network analyzer, and archived and manipulated the data. Experimental and calculated results at 2.74 GHz are shown in figure 8. Exaggeration of one of the nulls and partial suppression of the other in the scale model case was determined to be due to internal reflections primarily associated with the air-powder interface; this was verified using the time-domain gating feature of the HP 8510B.

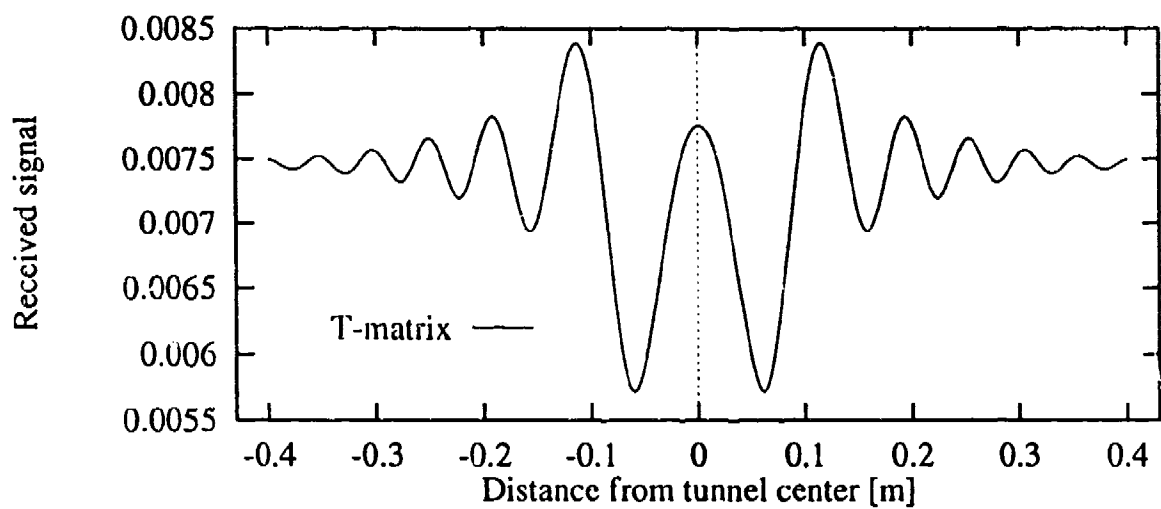
It should be emphasized that the laboratory scale model was constructed as an independent representation of the full-scale tunnel detection problem, rather than as a dedicated vehicle for analytical model validation. Thus, each approach has its own strengths and weaknesses as a tractable approximation, and perfect agreement was not expected.

ADDITIONAL LABORATORY MODEL RESULTS

As part of an independent experimental investigation of the tunnel detection problem, a Styrofoam ellipsoid was constructed for use as a scatterer in the laboratory scale model. It had major and minor cross section axes of 8.5 and 7.65 cm respectively, and was 27 cm in length. Subsequent to system calibration procedures, measurements of the amplitude of S_{21} were made as a function of both depth and frequency over the 2 - 4 GHz range. The results were plotted and color-coded such that deep nulls in the received vertical electric field are represented as dark



(a)



(b)

Figure 6. Received Signal Calculated by (a) Method of Moments Technique and (b) T-Matrix Technique

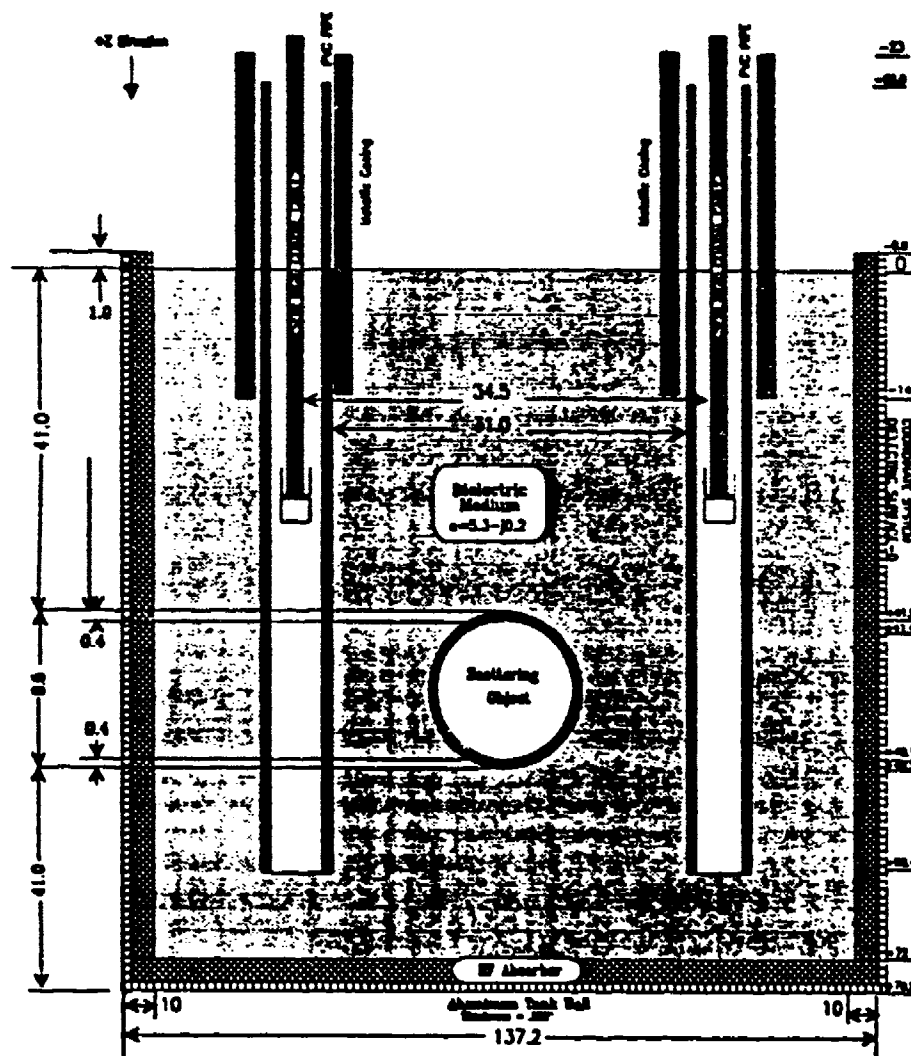


Figure 5.3: Cross-sectional view of the tank used in the scale model.

Figure 7. Cross-Section View of the Measuring Tank Used In Laboratory Scale Model

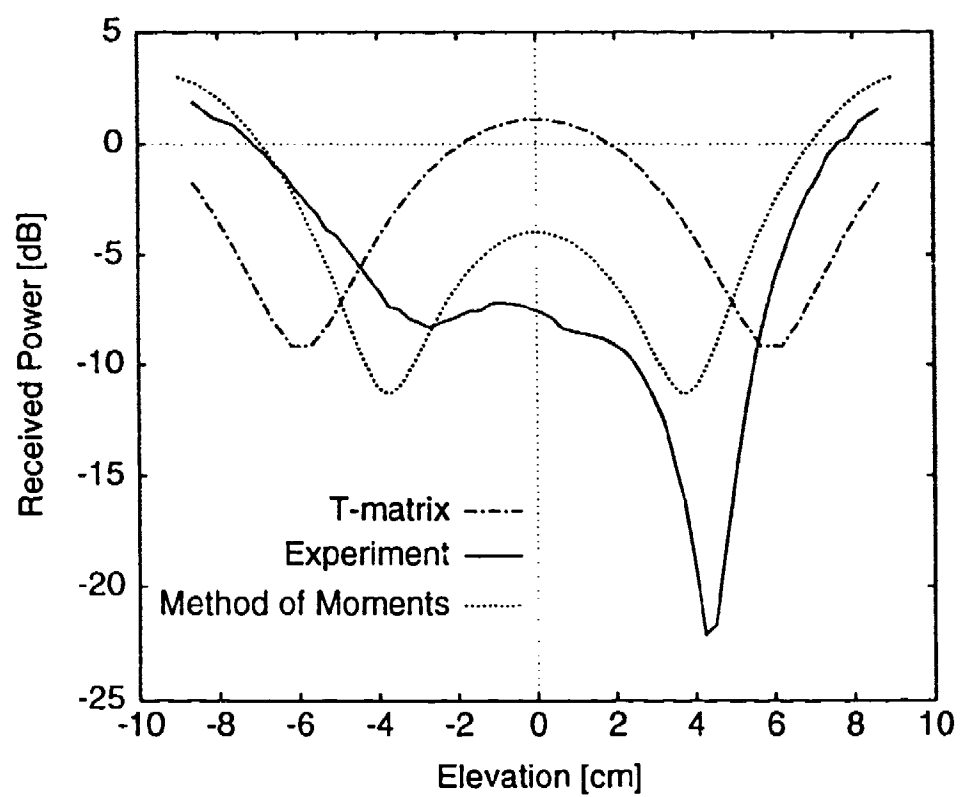


Figure 8. Comparison of Results from the Analytic and Scale Models at 2.64 GHz

areas on the resulting figure, a black-and-white version of which is included here as figure 9. It is concluded that frequency-domain measurements of the amplitude of received electric fields are reasonably good indicators of the vertical location of the target, even in a low-contrast situation.

TIME DOMAIN CALCULATION

The PEMSS radar pulse can be closely approximated by assuming the antenna current $i(t)$ to be a 40 MHz sinusoid weighted by a Gaussian envelope, and passed through a low Q bandpass filter. This is a purely heuristic description that agrees well with the observed radiated pulse. When $t \geq 0$ we have:

$$i(t) = \sin(\omega_c t) e^{-(t-d)^2 / \tau^2}$$

where $d = 12\Delta$ is an offset, $\omega_c = 2\pi 40 \times 10^6$ rad/s and $\tau = 1.25 \mu s$ is a time constant. The time $\Delta = 1.953125 \mu s$ is the interval used for sample spacing in the time domain. Chosen for convenience in performing the Fourier transforms, Δ corresponds to a sampling interval of 2 MHz in the frequency domain, where $\omega_0 = 2\pi 20 \times 10^6$ rad/s. When $I(\omega)$, the Fourier transform of $i(t)$, is multiplied by the transfer function $B(\omega)$ of the bandpass filter, a product $I(\omega)B(\omega)$ is obtained that represents the current on the transmitting dipole. Although purely heuristic, it shows good agreement with the observed radiated pulse. $I(\omega)$ is obtained by taking a 256-point FFT of $i(t)$ with a sample spacing of Δ . Multiplied by the appropriate T-matrix, $I(\omega)B(\omega)$ yields a spectral description of the scattered field. The T-matrix is essentially the transfer function for the transmitting antenna, the host medium, and the scatterer. The T-matrix multiplied by the transfer function of a dipole gives the spectral components of the incident pulse. The transfer function obtained from the T-matrix is $T(\omega)$, and the dipole transfer function is $D(\omega)$. The expressions are:

$$B(\omega) = \frac{\omega^2}{-\omega^2 - i\omega\omega_0 / 1.2 + \omega_0^2}$$

$$D_\theta(\omega) = -i\omega\mu \frac{1}{4\pi r} \left(1 - \frac{1}{\gamma r} + \frac{1}{\gamma^2 r^2}\right) \sin(\theta) e^{\gamma r}$$

where $\gamma = i\omega\sqrt{\mu\epsilon}$ is the propagation constant.

Calculated vertical electric fields in this paper will be limited to cases in which the transmitter and receiver are lowered simultaneously in the borehole, maintaining the angle θ at 90° . The constitutive parameters were identified in connection with the analytical model.

The spectrum of the radiated pulse must be truncated, for reasons associated with the properties of the T-matrix. The matrices become more and more poorly conditioned as the frequency increases, becoming inaccurate above 72MHz in the case at hand. The limitation, imposed by practical considerations such as finite numeric precision and finite memory, is equivalent to bandlimiting the scattered pulse. However, the majority of the energy in the PEMSS pulse lies below this cutoff frequency. Figure 10 shows that the temporal representations are not strongly affected. The "ringing" in the bandlimited pulse is an artifact of the truncation. Any persistent or anticausal fluctuations seen in the scattered pulse are

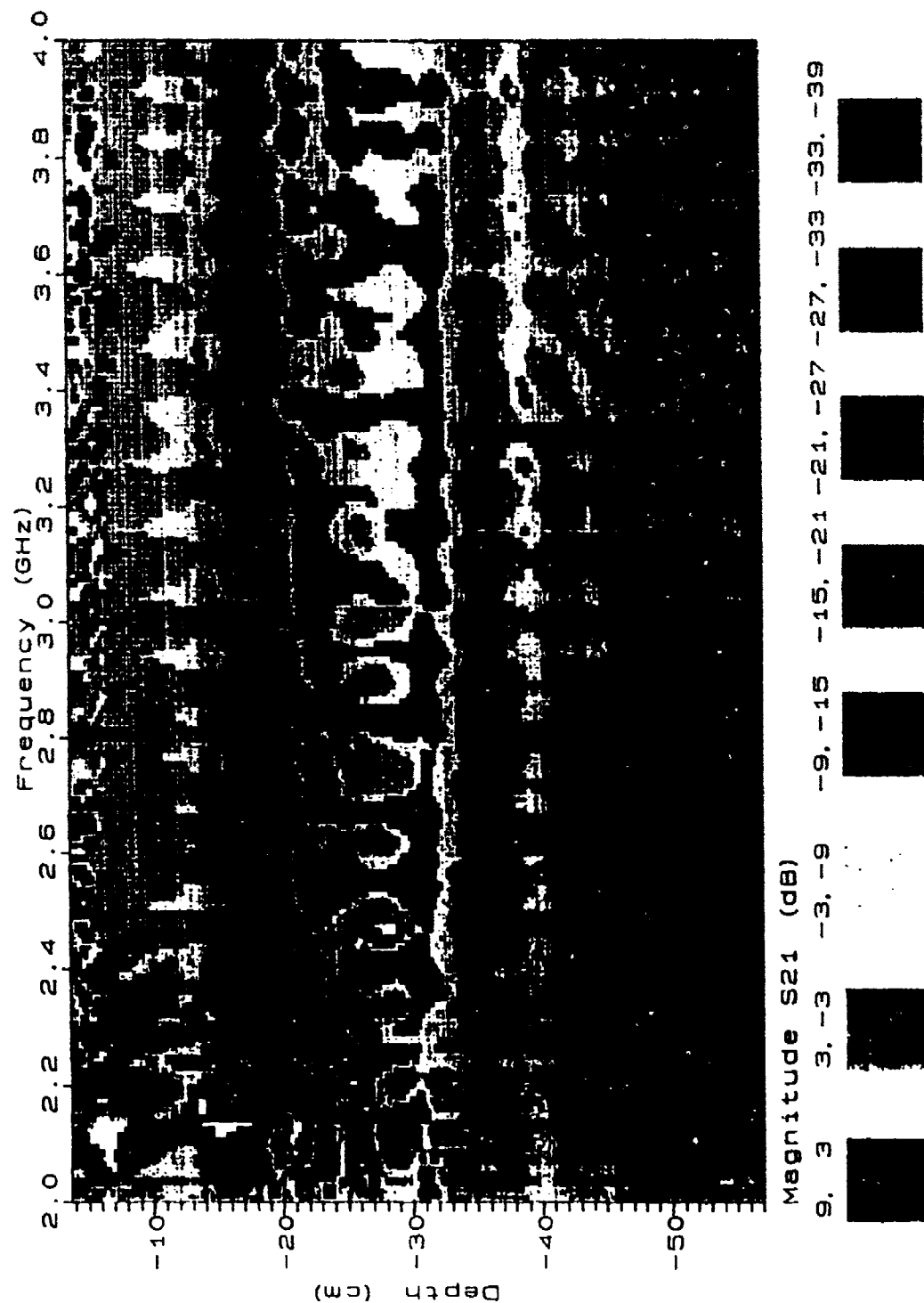
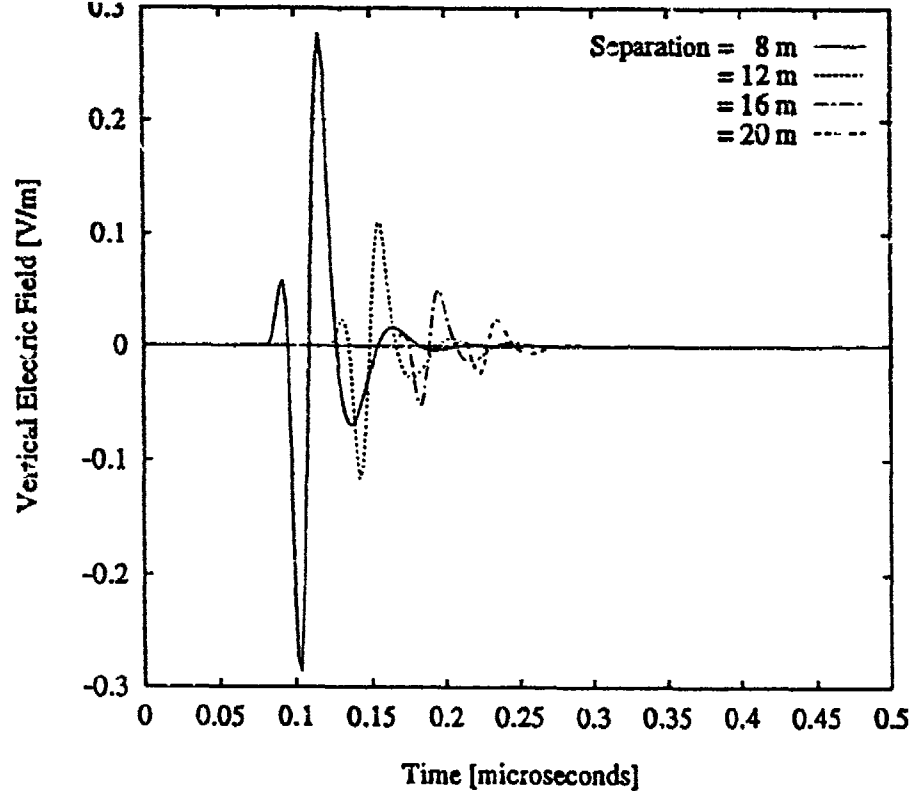
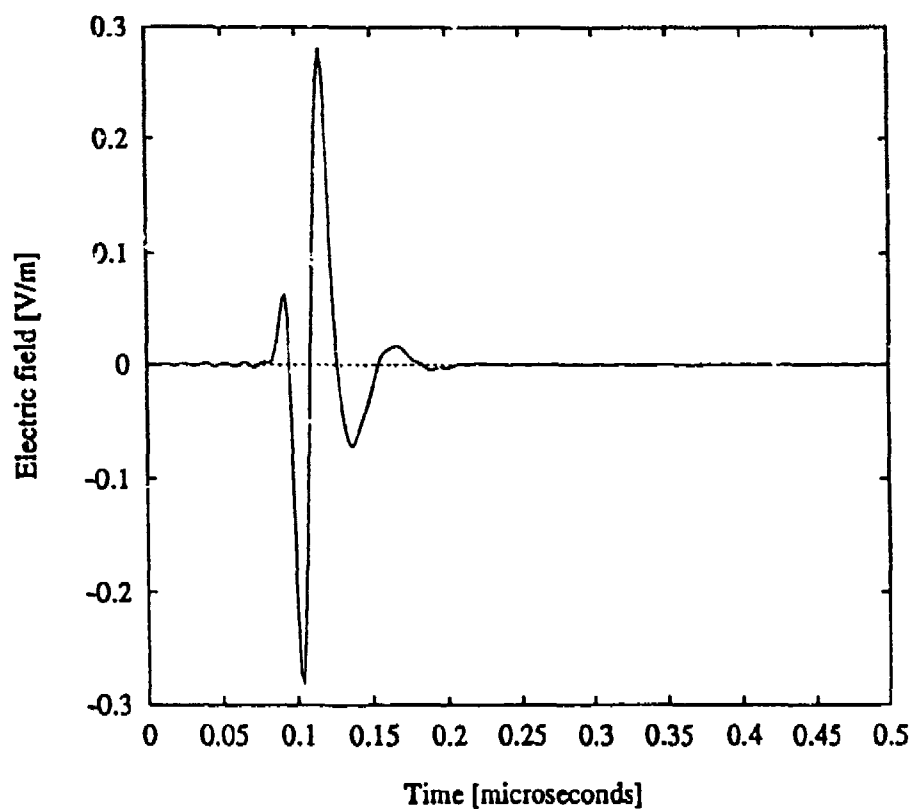


Figure 9. Received Vertical Electric Field Measured in Scale Model as a Function of Position and Frequency: Dielectric Ellipsoid Target



10 (a)



10 (b)

Figure 10. Vertical Component of Radiated Pulse as a Function of Time
 (a) At Four Positions Away From the Dipole and
 (b) Frequencies Above 72 MHz Removed

effects of a limited number of harmonics. The magnitude and phase of the antenna current are multiplied by the weighting function $-k^2\eta/6\pi$, where η is the intrinsic impedance $\sqrt{\mu/\epsilon}$ and $k = \omega\sqrt{\mu\epsilon}$. The scattered field is obtained when the weighting function multiplies $I(\omega)B(\omega)$. Addition of the incident pulse to the scattered field yields the total field.

Figure 11 illustrates two perspectives of the vertical component of the scattered pulse at the receiver borehole location as a function of time and elevation. The ellipsoid is horizontally centered between boreholes 20 cm apart. When the antennas are at the depth of the center of the ellipsoid, their position is designated $z = 0$. The calculation covers the time span $0.16 \mu s < t < 0.32 \mu s$. Numeric noise, seen as ringing before and after the arrival of the pulse, is visible in the figure. The magnitude of the scattered field decreases with distance from the target, as would be expected on the basis of increased loss along the propagation path. Other contributing factors to this effect are the finite size of the ellipsoid and the fact that the receiving dipole measures only the vertical component of a scattered field whose vertical component is decreasing with distance from the target.

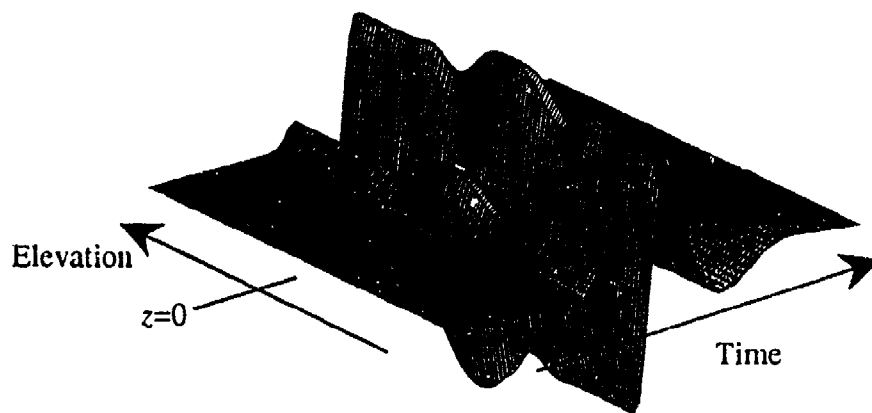
The total field, or sum of the incident and scattered components, is seen in Figure 12. As distance from the target increases, the incident field becomes dominant. Points of constructive and destructive interference are evident with the former occurring in the vicinity of zero elevation, and the latter at approximately ± 3 m of elevation. The scattered field is visible as a small ripple arriving after the direct field for nonzero elevations, providing a pattern similar to a hyperbola which is an important diagnostic of the "tunnel" location. In the vicinity of zero elevation, it is seen that some energy arrives ahead of the incident pulse due to its faster speed of propagation through the air-filled target. This is another diagnostic of scatterer location and composition.

Results are compared in figure 13 with field data obtained from the PEMSS II radar for a 2 m cross-section air-filled tunnel deeply buried in granite. The borehole spacing was 20 m. The approximate target location is indicated on the vertical axis. The hyperbolic wings and earlier arrival of the leading edges of the pulses in the tunnel vicinity are clearly visible, confirming that these indicators of tunnel location are well simulated by the theoretical model that is the subject of this study.

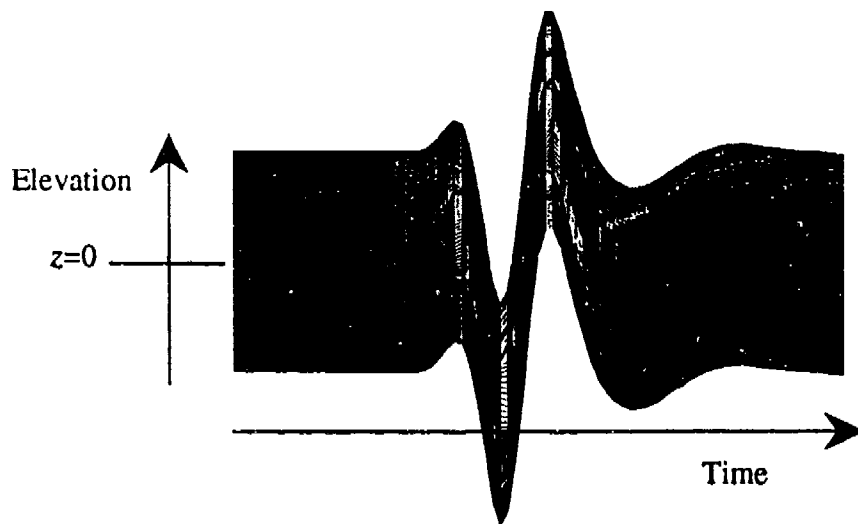
CONCLUSIONS

It is concluded that the cross-borehole tunnel detection problem can be usefully studied in the frequency domain utilizing an ellipsoidal tunnel, a dipole source of radiation, and the T-matrix method. When the ellipsoidal target is illuminated by a transient pulse with the spectral characteristics of the PEMSS II VHF subsurface radar system, the T-matrix method coupled with the Fourier transform technique permits the time domain characteristics of the received field to be obtained. Significant features of these results compare well with those observed in measured field data.

Irene C. Peden and John Brew are with the University of Washington, Seattle, WA
John B. Schneider is with Washington State University, Pullman, WA



(a)



(b)

Figure 11. Two Views of the Sum of Direct and Scattered Pulses From an Ellipsoid: 8 m Segment of Receiver Borehole at 8 m Borehole Separation

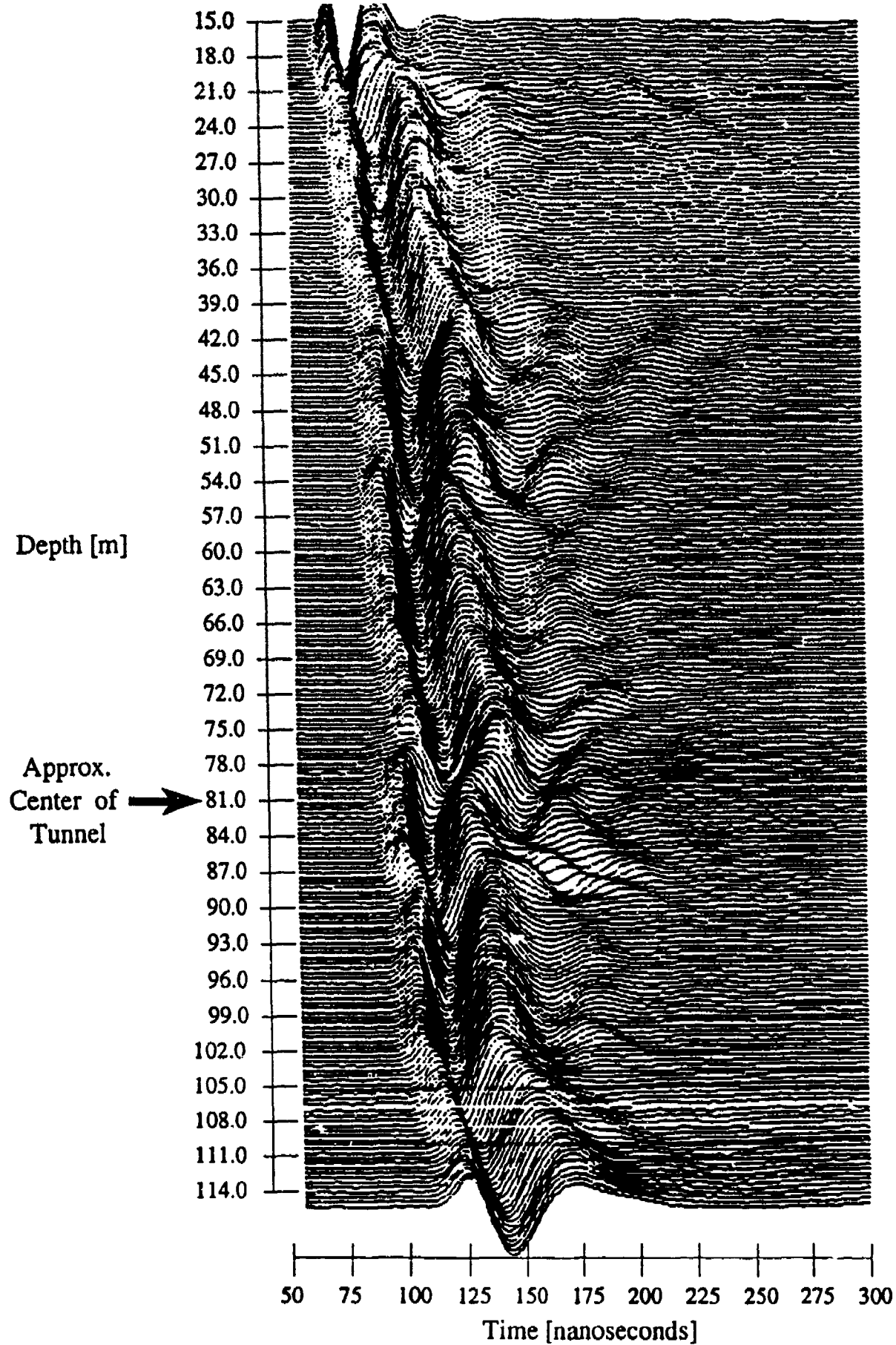


Figure 12: PEMSS II Data for 20 m Borehole Separation

REFERENCES

- Barber, P. and Yeh, C., 1975, "Scattering of Electromagnetic Waves by Arbitrary Shaped Dielectric Bodies", Applied Optics, Vol. 14, No. 12, pp. 2864-2872.
- Greenfield, R., 1988, "Modeling of Electromagnetic Propagation Between Boreholes", Proceedings of the 3rd Technical Symposium on Tunnel Detection.
- Karlsson, A., and Kristensson, G., 1983 "Electromagnetic Scattering From Subterranean Obstacles in a Stratified Ground", Radio Science, Vol. 18, No. 3, pp. 345-356.
- Kristensson, G. and Strom, S., 1979, "The T-matrix Approach to Scattering from Buried Inhomogeneities", Acoustic, Electromagnetic, and Elastic Wave Scattering - Focus on the T-Matrix Approach, Pergamon Press, New York, N.Y., pp. 135-167.
- Kristensson, G. and Strom, S., 1982, "Electromagnetic Scattering from Geophysical Targets by Means of the T-Matrix Approach: A Review of Some Recent Results", Radio Science, Vol. 17, No. 5, pp. 903-912.
- Lytle, R.J., Laine, E.F., Lager, D.L., and Davis, D.T., 1979, "Cross-borehole Electromagnetic Probing to Locate High-Contrast Anomalies", Geophysics, Vol. 44, No. 10, pp. 1667-1676.
- Olhoeft, G.R., 1988, "Modeling of Electromagnetic Propagation Between Boreholes", Proceedings of the 3rd Technical Symposium on Tunnel Detection.
- Owen, T.E. and Shuler, S.A., 1980, "Subsurface Void Detection Using Surface Resistivity and Borehole Electromagnetic Techniques", Technical Progress Abstracts and Biographies, 50th Annual International Meeting and Exposition, Society of Exploration Geophysicists.
- Richmond, J.H., 1966, "TE-Wave Scattering by a Dielectric Cylinder of Arbitrary Cross-Section Shape", IEEE Transactions on Antennas and Propagation, Vol. AP-14, No. 4, pp. 460-464.
- Sato, M. and Thierback, R., 1991, "Analysis of a Borehole Radar in Cross-Hole Mode", IEEE Transactions on Geoscience and Remote Sensing, Vol. 29, No. 6, pp. 899-904.
- Schneider, J.B. and Peden, I.C., 1988, "Differential Cross Section of a Dielectric Ellipsoid by the T-Matrix, Extended Boundary Condition Method", IEEE Transactions on Antennas and Propagation, Vol. AP-36, No. 9, pp. 1317-1321.
- Schneider, J.B., Brew, J. and Peden, I.C., 1991, "Electromagnetic Detection of Buried Dielectric Targets", IEEE Transactions on Geoscience and Remote Sensing, Vol. 29, No. 4, pp. 555-562.

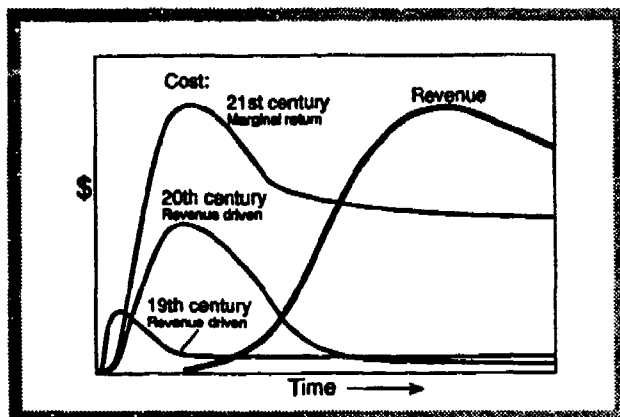
Considerations for Geophysical Survey Design and Data Interpretation

P.R. Romig and D. Wilson

Colorado School of Mines
Golden, CO 80401
April 28, 1993

The Difference Between Traditional Exploration and Site Characterization

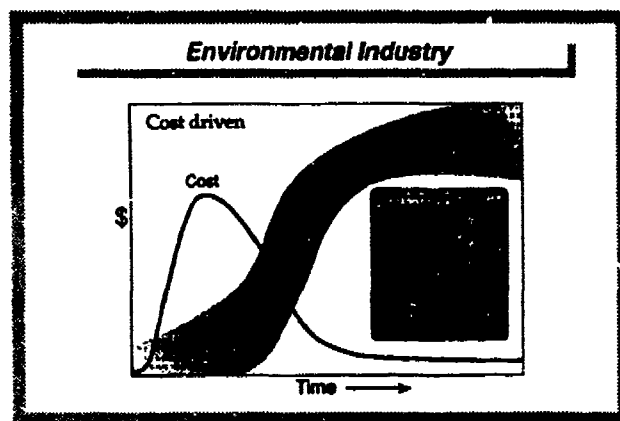
One of the impediments to progress in geophysical site characterization is that the applied geophysics industry has been dominated by oil exploration. Resource-exploration tools and techniques are not necessarily suitable for near-surface geophysical applications because of the fundamental differences in the economic structures of these two industries.



The days of the individual prospector were the epitome of what we might call a "revenue-driven industry." The only investment required was a pick and shovel, a grubstake, and the blood and sweat of the prospector. The lucky ones found the mother lode and became rich. This prospect of riches drove them and dominated all other aspects of their life.

Before long, the resources that could be found by scratching on the surface of the earth had been developed, and it became necessary to look inside the earth. About the same time, electronic instruments were invented. Together these gave birth to the science of geophysical exploration.

Although this drove up the cost of finding oil, the basic economics remained unchanged. It still was possible to be wrong 85% of the time (i.e. drill half a dozen dry wildcats for every discovery well) then pay for the mistakes and get rich when the seventh hole brought in a gusher. The industry was a lot like a lottery: risks were high, but the more tickets you bought, the better your chance of getting rich.



Engineering geophysics is at the other extreme. No-one will get rich (or even make much money) selling the toxic waste they pump out of the ground. The industry is entirely cost-driven; the primary objective is to fulfill contractual requirements on schedule and under budget. More importantly, it is a zero-risk business: one hole drilled in the wrong place at a hazardous-waste dump (for example) can bankrupt everyone involved, and bad decisions can send managers and engineers to jail.

Earth Science Industry Projections		
Former Resource	Future Resource	Environmental
Mineral Resource	Cost Source	Resource Cost
Oil-Industry	Transport	Chemical
Superfund Sites	Regulation	Chemical
Regulation	Regulation	Cost
Snake Oil	Marketing	Marketing
High Risk	Management	High Risk
Expert Client	Knowledgeable Client	Knowledgeable Client

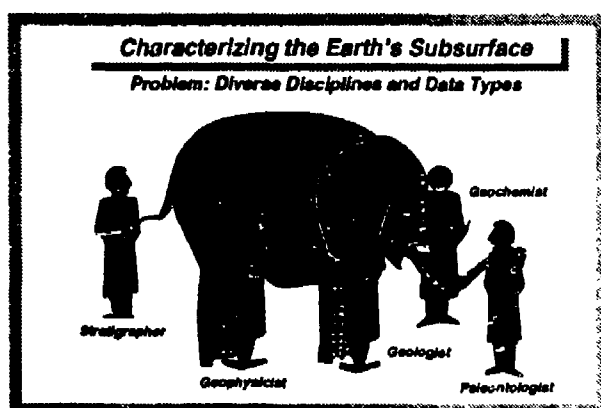
This figure summarizes a few of the cultural differences between the two industries. For example, in the oil industry of yore, it was

traditional for jobs to go to the contracting companies that had the best reputations; cost was a secondary issue. Most jobs in engineering geophysics, on the other hand, are awarded on the basis of the lowest bid. Among other things, this raises the question of how the client can be assured that the lowest bidder is competent. Until these differences are recognized and some of the fundamental problems addressed, scientific research will not have the impact that it should.

In both the resource and engineering industries, the trend is actually toward the middle. The resource industries are becoming marginal-return businesses, and as we are better able to quantify the "revenue equivalent of societal cost avoidance" associated with better engineering, engineering geophysics also will become more like a marginal-return business. The middle column in this figure indicates what some of the characteristics of both industries will become as they evolve.

Research Issues Related to Human Problems

For geophysical site and material characterization to achieve its full potential, scientific advances must be accompanied by a better understanding of and solutions to some of the basic language and cultural problems that divide geophysicists and engineers.

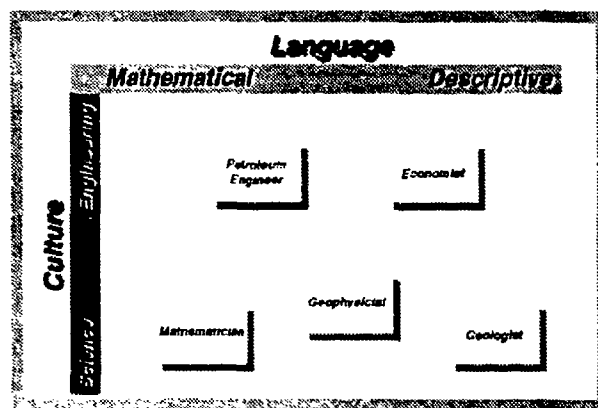


One wide-spread problem is the communication gap that results from specialization. All too often, we are like the fable of the blind man and the elephant; each of us has grown accustomed to working on our

own part of a project without interacting with those from other disciplines working on other parts. As a result, we have developed specialized jargon that helps protect our status as experts but prevents effective teamwork.

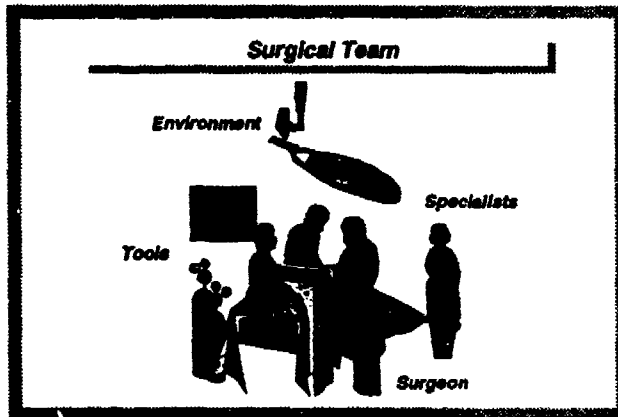


Another major problem that is especially pronounced in applied geophysics is that much of our decision making is intuitive. If, for example, we ask a seismic interpreter how they decided on certain details in interpreting a seismic section, too often their response is simply "experience" or "judgement". Our inability to validate and defend decisions is a primary reason that clients often don't trust our conclusions.



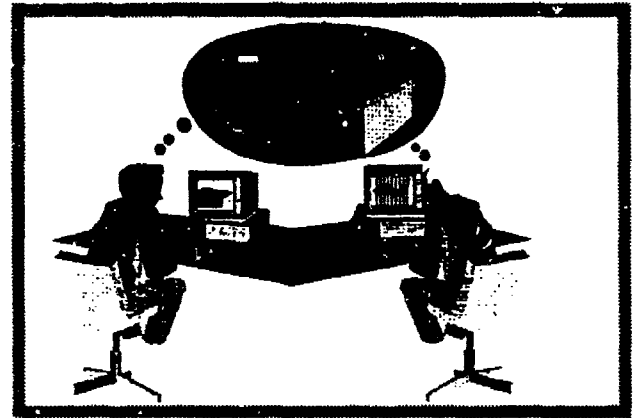
In summary, there are important language and cultural barriers that must be overcome before we can make much progress. The language barrier is obvious to anyone who has tried to deal with the acronyms and specialized terms of another discipline. The cultural barriers are not as obvious, but they exist because we have not made enough

effort to codify and document those thought process so that we can defend and validate key decisions.

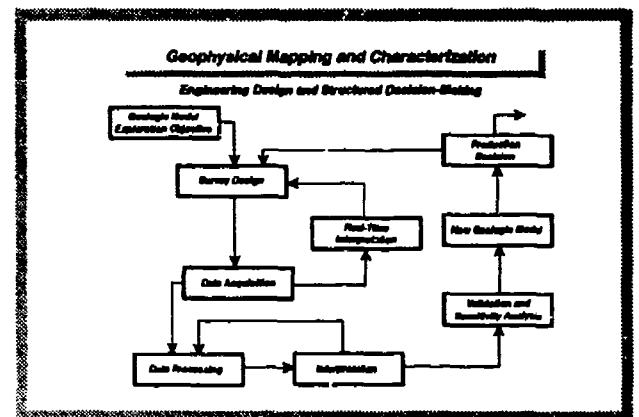


The objective, of course, is to break down those language and cultural barriers so that geophysicists and engineers can work together effectively on multi-disciplinary, problem-solving teams. To work toward that end, we do not need to start from the beginning; there are models in other industries that we can adapt to meet our needs. Perhaps the best model is a surgical team. The problem is very similar: diagnose the problem using non-invasive mapping; make decisions on the basis of incomplete and noisy data, and then operate.

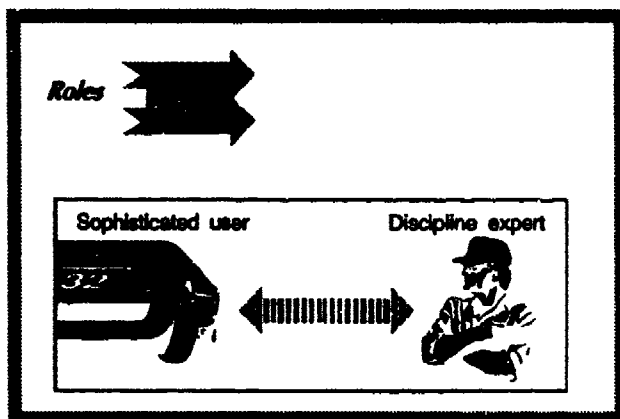
If we study the keys to success of a surgical team, we find there are four factors. The environment (the sterile operating room with support equipment), the specialized tools, and the highly-educated specialists that have been trained to operate in a team as a well-oiled machine are obvious. Less obvious but perhaps most important is the surgeon - the leader that has both the innate qualities and the broad-based training that will allow them to assimilate information from all of the specialties and then make the critical decisions about where to cut. Our challenge is to adapt this understanding of the surgical team to the needs of the engineering profession.



An obvious solution to the language problem is to not use language. The interactive computer software that is available today can let us begin to communicate in the form of images rather than words, and the international networking capabilities allow us to work together effectively even if we are physically thousands of miles apart. We have the tools available for breaking down both language and distance barriers if we are willing to take advantage of them.

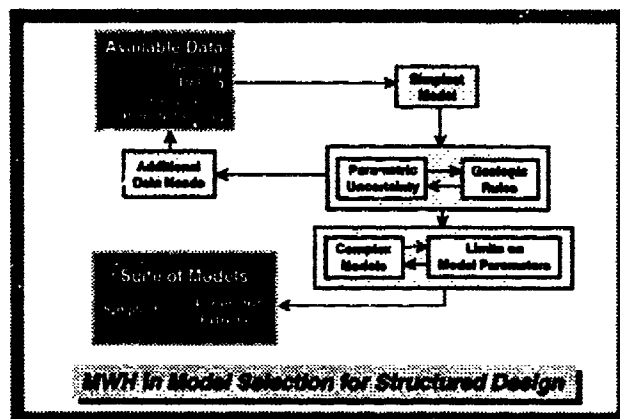


A step toward eliminating the cultural barriers is to begin to codify and document decision making processes, thereby eliminating the intuitive aspects that so often seem like magic. This also will allow us to quantify uncertainties in our interpretations and recommendations. If we can explain how we arrived at a decision, then our client is more likely to accept and act on that decision. If we can quantify uncertainty, our client will be more confident that they can defend their actions in court.

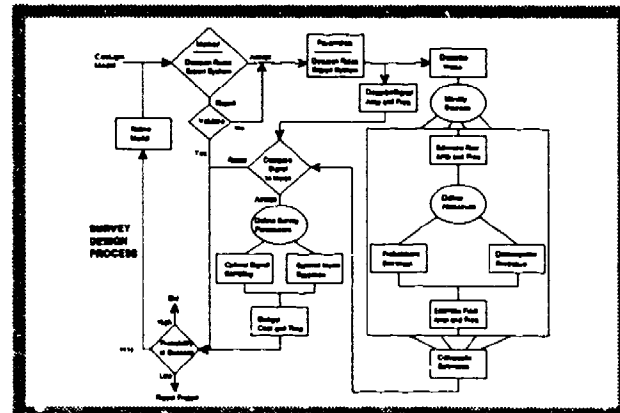


To document decision-making processes effectively, we must understand the two kinds of roles that we all play at various times in a project: the sophisticated user and the domain expert. For example, a car driver is a sophisticated user, while the mechanic is a domain expert. Establishing a high level of trust between the two depends on the driver knowing something about how an engine works and the mechanic understanding the driving habits of the driver.

The same principle applies to the relationship of engineers and scientists on a site-characterization project. Just as a hydrologist might be a sophisticated user of seismic data in one part of the project, so the seismologist might be a sophisticated user of a hydrological flow model during a different phase. If we understand the differences between these two roles we can do a better job of developing tools and techniques that will contribute to more-effective teamwork.

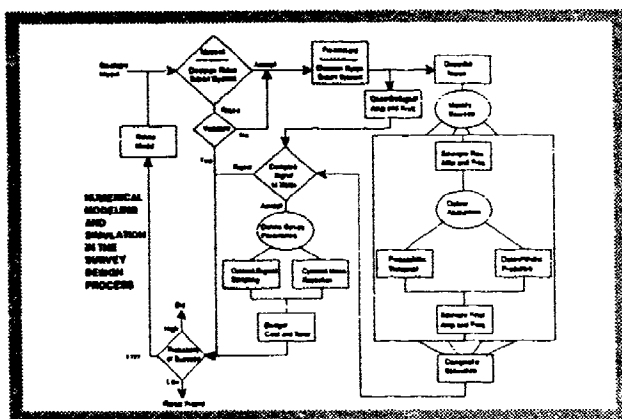


The first step in the exploration process shown earlier was the seemingly-trivial step of collecting all available information about the site. However, I suspect we all are familiar with situations where that was not done. Codifying the decision-making process helps emphasize the point that rigorous survey design depends on having access to everything that is known about the site and assembling it into a best-fit geologic model for the site.

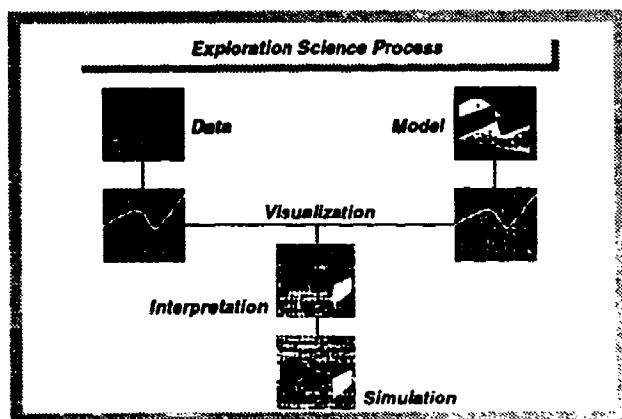


The next step in the process, survey design, is an iterative process that continues throughout the life of the project. As more data become available, we must constantly check the current suite of models against the current survey design. This addresses another important point: quality assurance. The traditional cookbook approach usually fails largely because every site is unique, and no cookbook can anticipate all possible situations. If, however, decision-making processes can be codified and

certified, we can allow us to reach conclusions or answers that are unique to a site in a controlled process that can be defended in court.



Codification of decision-making processes also can help identify research needs. For example, a rigorous design process clarifies the need for generic rules (in the upper left corner of the diagram) and rigorous, quantitative modelling and simulation software (the gray boxes indicate where such software would be applicable).

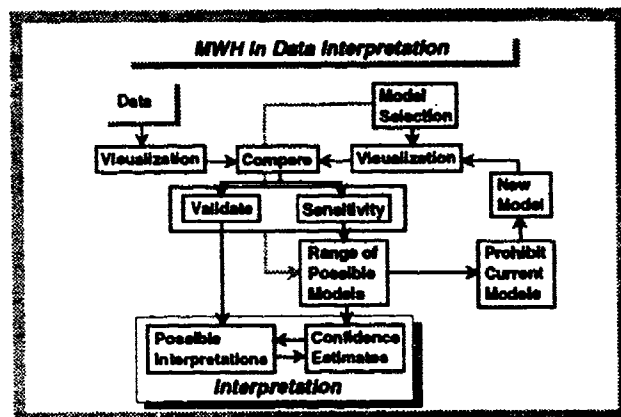


In addition to codifying procedures, we also can document thought processes. For example, if we analyze how a geophysicist interprets seismic data, we realize that there are four steps:

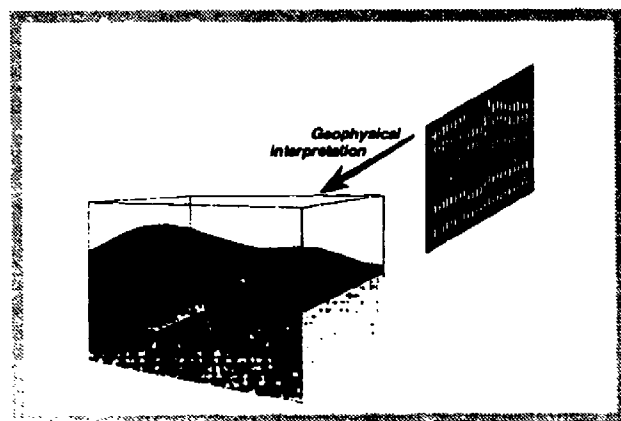
- 1) Process the data to produce a graphical visualization.
- 2) Generate hypothetical models based on experience and education, then convert it to a graphical visualization in the same format as the data visualization.
- 3) When the data visualization and the model

visualization match within an acceptable level of uncertainty, then we have an interpretation.

4) The interpretation is validated, and a sensitivity analysis is done with numerical simulation..

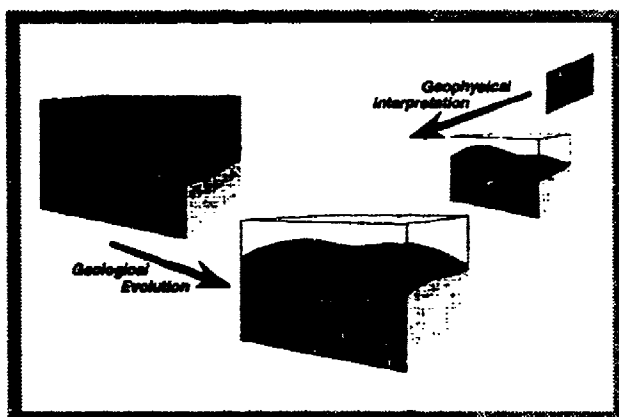


Normally, the thought process we just described is done intuitively, and the visualization is done mentally. However it's possible to analyze this thought process in detail and develop a rigorous decision-making structure which will ensure that the full range of possible interpretations are included in the final report. In this figure, the thought process we just discussed is contained in the upper part of the figure. The remainder describes a formal process by which we can ensure that all possible solutions are considered.

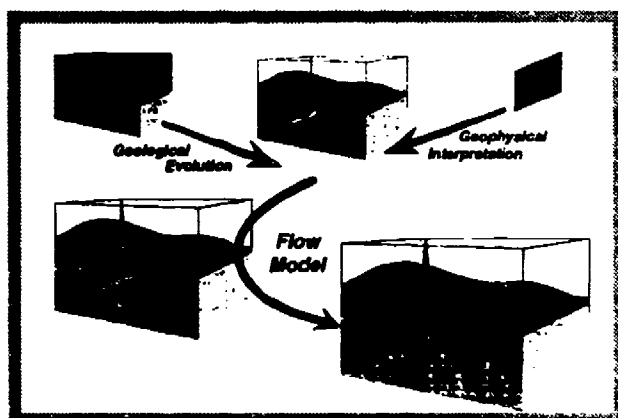


I've just used the phrase "all possible models" several times. It is important that we understand the idea conveyed by that phrase. Many geophysicists think their objective is to produce the "best-fit" model from a set of seismic data. In fact, the parameters of that model are always uncertain, and

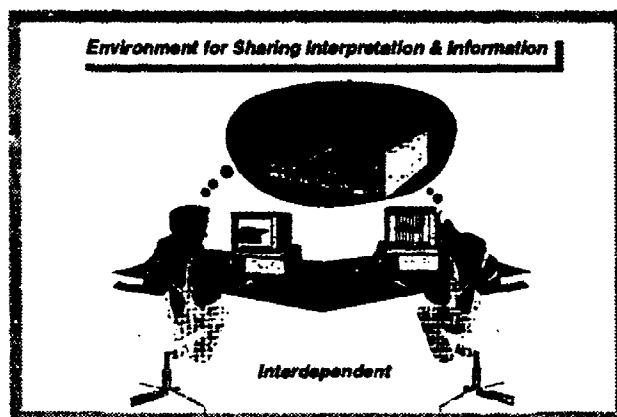
there is actually a wide range of models that will fit within the uncertainty inherent in the data.



Geologists have their own ways of inferring the subsurface structure of a site. Because of uncertainties in both types of data, if a geologist and a geophysicist each produces a single, deterministic model, we can virtually guarantee that the two interpretations will not be the same. Resolving the differences often falls to a manager who bases his decision on his subjective opinion about who he trusts most, but such judgments are not acceptable in a zero-risk business.



Our ultimate objective is to produce a unified model. We can do that only if each participant - in this case, the geologist, geophysicist and hydrologist - develop statistical interpretations that use distributions for the parameters rather than single numbers. This is another important research agenda if site characterization is to move forward.



Today, we can consider radical new ways of practicing our profession because of the new technologies becoming available. The rapidly-increasing computing power of work stations and the communications capability provided by robust networks will allow us to develop interdependent teams of geoengineers, each working within their own specialty, but linked together in a common conceptual and numeric model. This approach will allow all of us to begin working in a common engineering culture: using integrated information and structured decision-making to solve problems and provide answers in which uncertainties and risks are defined and quantified and which are subject to practical constraints on the availability of time and money.

Summary

Because of fundamental economic differences between oil exploration and engineering geophysics, the tools and techniques of the former are not necessarily appropriate for the latter. The key to good engineering geophysics is teamwork, but to develop effective teams, we must develop new tools and techniques for overcoming the language and cultural barriers between the different earth science and engineering disciplines. Graphic visualization and high-speed networks will help overcome the language barriers, and a better understanding of the engineering concepts of engineering design and structured decision-making will help overcome the cultural barriers. To

accomplish the latter will require the development of better modeling and simulation tools, ultimately leading to the geological equivalent of CAD packages. Finally, we must move from deterministic interpretations to statistical models in order to achieve a unified model that will allow all of the disciplines to work together.

RESISTIVITY CHANGES OVER TIME RELATED TO MODELED FLUID FLOW IN ROOM-Q OF THE WASTE ISOLATION PILOT PLANT

M. G. Truskowski and H. T. Andersen

Department of Geophysics
Colorado School of Mines
Golden, Colorado 80401

ABSTRACT

The Waste Isolation Pilot Plant (WIPP Site) is located in southeastern New Mexico about 35 miles east of the town of Carlsbad. The purpose of the WIPP Site is to evaluate the storage of transuranic waste in mine excavations within the layered Salado salt formation. Room-Q is a horizontal cylindrical room that was excavated and sealed to measure brine influx. The Colorado School of Mines installed a stationary, permanent DC resistivity grid in Room-Q in late 1989 and following electrode stabilization, the grid has been read periodically since then. The experimental nature of the WIPP site provides an excellent opportunity to evaluate the physical properties of underground excavations in various stages of development. The material properties of both the tunnel fill and the surrounding rocks influence how the tunnel is detected by electrical geophysical methods. Fluid content and hydraulic properties of the formation influence the bulk material properties of the tunnel.

A fluid flow model of Room-Q was constructed using the MODFLOW modeling program. The profile-oriented model incorporated geologic information from underground mapping and hydraulic parameters available from limited borehole permeability testing in Room-Q. Electrical geophysical data gathered in the room from January to March, 1990, were correlated with modeled fluid flow for the same length of time and a similar overall trend was observed. The introduction of minor geological heterogeneities produced an improved fit. A correlation was found to exist between the change in resistance over time and the change in fluid content within the unsaturated fracture porosity zone surrounding the room.

INTRODUCTION

The Waste Isolation Pilot Plant (WIPP) is located in Southeastern New Mexico between the towns of Carlsbad and Hobbs. Its purpose is to test the feasibility of using such a facility as a repository for transuranic wastes. The storage area and an experimental area are excavated within the Salado layered salt formation at a depth of 2150 feet below the ground surface. Within the experimental area, numerous measurements and tests have been performed to determine the hydraulic characteristics of the formation and the overall bulk material electrical properties of the excavations.

In late 1989 the Colorado School of Mines installed electrodes in a horizontal cylindrical room, known as Room-Q, in an attempt to measure rock deformation within the room as well as fluid influx. This electrode array has been monitored periodically since January of 1990, which allowed a period of stabilization for the electrodes. The purpose of this survey was to monitor the increased fracture density comprising the damaged rock zone due to the excavation of the room, as is commonly observed in mining operations, and to monitor the fluid flow into this newly created unsaturated zone.

The electrical properties are of interest since the probability of success in detecting a tunnel using electrical geophysical methods is influenced by the type and magnitude of the anomaly observed. The nature of the anomaly is determined by the contrast of the electrical properties of the tunnel with the undisturbed formation properties. The type of electrical anomaly a tunnel creates can change over the life of the tunnel, appearing as a resistant zone relative to the surrounding rock while the deformation zone and the tunnel are unsaturated. Later in the life of the tunnel, it can appear as a conductive anomaly as the damaged rock zone and possibly the tunnel fill with fluid. Although a room in the WIPP underground is highly unlikely to become fluid filled the concepts developed for the saturation of the damaged rock zone can be extrapolated to this case.

In addition to the electrode array in Room-Q, three boreholes were used to measure hydraulic conductivity in the formations surrounding the room. These data and geologic information from the interior of the room were used to construct a groundwater flow model which has been correlated to the change in the electrical geophysical measurements over time. As a low resistivity fluid flows into an unsaturated zone within a high resistivity rock matrix, a change in the bulk electrical properties of the rock should take place. The question that presents itself is how we describe this phenomenon mathematically. This paper begins to quantify the factors influencing the resistivity measurements, with future analysis of these data yielding a further understanding of these relationships.

SITE DESCRIPTION

The WIPP underground is located in the Permian Salado formation 2150 feet below the ground surface. This formation is composed of layers of halite and polyhalite with argillaceous impurities and thin interbedded clay layers. Several distinctive layers within the formation have been designated as "marker beds" due to their persistence throughout the mine. (figure 1)

The lithologic units are described as:

- | | |
|--------|--|
| Unit 6 | Halite, trace of polyhalite |
| Unit 5 | Clear halite, trace of argillaceous material |
| Unit 4 | Argillaceous halite, traces of polyhalite, clay and silt |
| Unit 3 | Halite, trace of polyhalite |

Unit 2	Argillaceous halite, argillaceous laminations
Unit 1	Halite, light reddish orange, trace polyhalite
Unit 0	Halite, argillaceous laminations

Room-Q is a horizontal cylindrical room with a diameter of nine and a half feet which was excavated as a test room to be sealed and measure the magnitude of brine inflow. Excavation was completed in July, 1989. Three boreholes were drilled in the room, one into the back or roof, one into the floor, and one into the right rib or wall. Hydraulic conductivities were measured in these boreholes, beginning at eight feet from the room and taken periodically up to 24 feet from the room. Lithological descriptions were made at each measurement point making it possible to estimate hydraulic conductivity values for lithologically similar units within the room where direct measurements were not taken.

It can be hypothesized that two stages of change occurred subsequent to the excavation of the room. During the first stage, which is relatively short in duration, the rock immediately surrounding the room develops greater porosity due to the fracturing and deformation. This type of deformation or disturbed rock zone is due to changes in the underground stress-strain regime and can be observed in most mining operations. Since this zone develops quickly, the volume of water contained in this volume of rock remains nearly the same while the available porosity increases, resulting in a decreased water saturation and thus an unsaturated zone. The second stage of change is the resaturating of this zone by flow from the surrounding formation.

Both of the processes described above should result in changes in the bulk electrical properties of the rock immediately surrounding the test room. Crystalline salt in the WIPP underground has a resistivity of approximately 700 ohm-m while the brine has a resistivity of 0.1 to 1.0 ohm-m. (Pfeifer, 1987) Knowing this we can surmise that the Phase 1 deformation should result in an increase in bulk resistivity while the resaturation of Phase 2 should result in resistivity decrease.

SURVEY DESIGN

Two electrode arrays were installed in Room-Q, each consisting of a single source electrode and numerous receiver electrodes. The receiver electrodes are arranged in "rings" of sixteen electrodes which cover 270 degrees of the room's interior surface, there are 24 such rings in each of the two arrays. (figure 2) This design results in a total of nearly 800 electrodes which must be reliably monitored on a regular basis, from the exterior of a sealed room. The current source for this survey also must be located outside of the sealed room.

The acquisition system used to record the Room-Q data consists of cabling similar to that used in seismic operations to accommodate the large number of electrodes or channels and a switching box with the data being either recorded manually

or directly to a personal computer. Due to the special requirements and hazards of the underground environment the cables were specially made for this purpose and attached to cable heads installed in the bulkhead door. The switching box allowed the rapid recording of a large number of measurements in a relatively short period of time.

DATA ANALYSIS

In most conventional DC electrical surveys the self potential (SP) level remains relatively constant and is related to the lithology of the area. Because the electrodes in this survey are stationary, this should be of no concern. Unfortunately the equipment being operated in the underground, such as the hoisting mechanisms, drilling, and mechanized scaling, has a profound effect on the background SP level, requiring that it be measured each time the electrode array is recorded. A measurement is then made with the source electrode active. The current source is a pair of 12 volt dry cell batteries which provides a current of about 40 milliamps.

The SP is subtracted from the voltage reading to normalize the measurements for the variations in mine activity and provide a meaningful comparison of measurements from different times. This normalized voltage is then divided by the source current to yield resistance according to Ohm's law. Resistances for each electrode position can then be mapped to indicate the trends for each time. Maps are also constructed by subtracting measurements from two different dates yielding a map of the resistance change over time. This type of map for January through March 1990 is shown in figure 3.

FLUID FLOW MODELING

The period during which the measurements in Room-Q were made by CSM was six months following the excavation of the room and is considered to be in the second Phase of change for the bulk rock properties. Thus a fluid flow model was used to simulate the probable physical phenomena causing the observed change in resistance over time. The USGS program MODFLOW was chosen to fulfill this purpose. MODFLOW is a grid centered finite difference groundwater modeling program which uses a modular approach allowing various components of a model to be represented.

Input data for the fluid flow model consisted of the lithological information from mapping of the interior of Room-Q, hydraulic conductivity measurements made in the radial boreholes, and a grid to represent the spatial configuration of the room. Profile oriented slices one meter thick corresponding in location with the electrode rings of Room-Q were used to model the room in two dimensions. The model extends a minimum of two radii from the center of the room and is discretized using variable size rectilinear blocks to approximate the circular shape of the room (figures 4-6). The smallest height rows are no thicker than the thinnest observed lithologic units. Since the

three measurement boreholes did not intersect all of the units of interest, it was assumed that those of similar lithology as those measured possessed the same saturated hydraulic conductivity.

The fluid flow was simulated for a period of sixty days which roughly corresponds to the period of time which elapsed between the first two resistance measurements. In order to operate MODFLOW, which assumes flat lying layered media in areal view, in a profile orientation it is necessary to assume that the formation of interest is confined and to use transmissivities rather than conductivities (Anderson, 1992). However, since the assumed thickness of the profile slice is one meter, the transmissivity and the hydraulic conductivity are numerically equivalent. The assumption of a confined aquifer is not unreasonable given the depth of the WIPP underground and the water levels observed in surface boreholes in the area.

Boundary conditions which need to be defined in this model consist of the interior of the room, the surface of the room, and the interlayer interactions. Grid nodes comprising the interior void of the room were considered to be inactive, as they do not participate in the flow field. Drain nodes were used to simulate the flow into the room through the nodes making up the room's interior surface which is treated as a seepage face. The vertical transmissivity between lithologic layers is considered negligible, with the dominant flow being horizontal along the layers.

CALIBRATION

Calibration of the model parameters was achieved using the total observed brine flow volume for the room and the change in resistance over time observations. Drain conductances were initially made equal to the hydraulic conductivity of the surrounding strata and then adjusted proportionally to yield a reasonable total fluid flow volume for the room. The resulting lower drain conductances were reasonable since the zone is unsaturated. These numbers should increase as the zone resaturates, since unsaturated hydraulic conductivities are a function of formation moisture content.

To calibrate for the changes in resistance with time, the flow rates from the initial model were plotted versus the negative change in resistance (figures 7-9). This was done since the reinvansion of fluid into the unsaturated zone should result in a decrease in the resistance with time. Three rings, numbers three, ten, and seventeen, were chosen for calibration. This comparison was favorable as an overall trend, but each ring had areas in which the fit could be improved. Calibration was accomplished by minor alterations in the hydraulic conductivity of layers not encountered by the test boreholes. The changes made in the conductivities were within a reasonable range considering the measured values. The changes in hydraulic conductivity corresponded to one persistent layer and a few intermittent layers of lower hydraulic conductivity, and a zone underlying the floor of increased hydraulic conductivity which probably corresponds to buckling of the floor, as is often seen in mine excavations.

MATHEMATICAL RELATIONSHIPS

In order to fully understand the meaning of the resistance changes over time it is appropriate to develop mathematical relationships between these measurements and physical rock properties. The simplest way to relate the change in resistance with time to fluid flow is plot one versus the other. From the time interval used in this set of models the relationship appears to be linear in nature, resulting in an equation of the form:

$$\frac{dr}{dt} = \frac{C_1 Q}{K} + C_2$$

The general relationship is shown here for one case of the model, however the constants C_1 and C_2 are undefined. Further, it is not known if these coefficients are constants in all cases or if they are time or space dependent functions.

To further understand the observed phenomena one can refer to Archie's formulas (Archie, 1942):

$$F = \frac{R_o}{R_w} = a\phi^{-m}$$

$$\frac{R_o}{R_t} = S_w^n$$

R_o = saturated formation resistivity

R_w = formation water resistivity

R_t = true formation resistivity

a = proportionality constant

m = cementation factor

n = saturation exponent

S_w = water saturation

ϕ = porosity

These equations can then be rearranged and set equal to one another yielding a single expression relating resistivity and water saturation:

$$R_t = a \frac{R_w}{\phi^m} S_w^{-n}$$

If the definition of water saturation is substituted in this equation:

$$S_w = \frac{\theta_w}{\phi}$$

where:

$$\theta_w = \text{moisture content}$$

$$R_t = \frac{aR_w \theta_w^{-n}}{\phi^{m-n}}$$

the resulting equation is in terms of the quantities that vary during the two different phases of deformation and resaturation, porosity and moisture content. Unfortunately there are still poorly constrained coefficients in this expression in a , m , and n and the resistivity term is not time varying. The second concern is easily remedied by taking the derivative of the expression with respect to time, also allowing the development of equations relating to the two different time phases.

Stage 1:

Development of Increased Porosity

$$\frac{dR_t}{dt} = aR_w \theta_w^{-n} \frac{d}{dt} (\phi^{-(m-n)})$$

Stage 2:

Brine Influx

$$\frac{dR_t}{dt} = \frac{aR_w}{\phi^{m-n}} \frac{d\theta_w^{-n}}{dt}$$

Since the zone surrounding the room is assumed to be unsaturated during the second stage, Richard's equation (Richard, 1931) can be introduced and substituted in the above expression, introducing additional physical rock properties such as hydraulic conductivity and matric potential as a function of moisture content.

$$\frac{\partial \theta}{\partial t} = -\nabla \cdot (-K(\theta) \cdot \nabla (-\psi(\theta) + z))$$

$$\frac{\partial \theta}{\partial t} = -\nabla q$$

$$\frac{dR_t}{dt} = \frac{aR_w}{\phi^{m-n}} [-\nabla q]^{-n}$$

This final expression once again relates the change in resistivity with respect to time to fluid flow however now some of the coefficients have physical significance and can be given realistic bounds.

FURTHER RESEARCH

Additional work is continuing on this project, with the primary emphasis on definition of the mathematical parameters, bounding those with physical significance and introducing additional measurements taken in Room-Q, such as relative humidity and pore pressure. Better definition of the behavior of both the rock and the electrical geophysical data during the development of the increased porosity zone are needed. Verification of this behavior is not possible with the present electrode array due to its late emplacement, but this work can help to predict the behavior in any future excavations.

REFERENCES

- Anderson and Woessner, Applied Groundwater Modeling, Academic Press, 1992, p. 176.
- Archie, G.E., 1942, The electrical resistivity log as an aid in determining some reservoir characteristics, Trans. A.I.M.E., 146, 54-62.
- Pfeifer, M.C., 1987, Multicomponent Underground DC Resistivity Study at the Waste Isolation Pilot Plant, Southeast New Mexico: MS Thesis T3372, Colorado School of Mines.
- Richards, L.A., 1931, Capillary conduction of liquids through porous medium, Physics, v. 1, p.318-33.

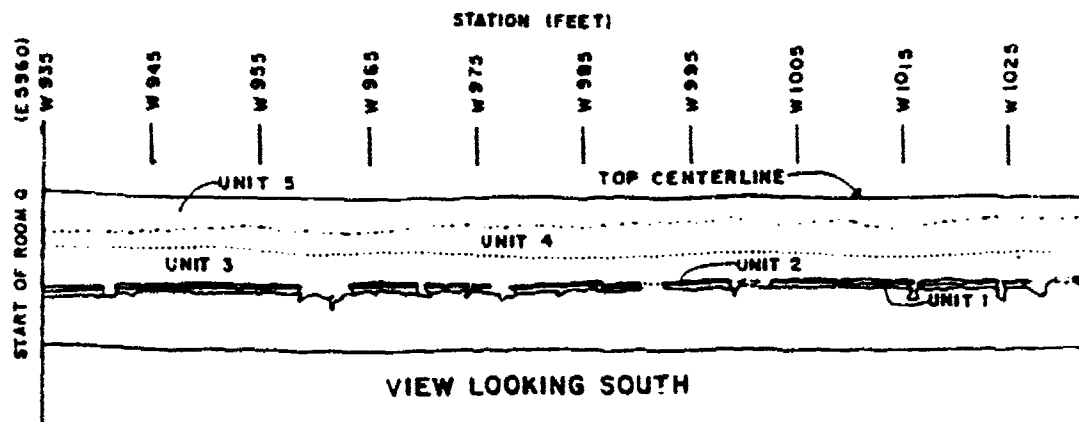


Figure 1

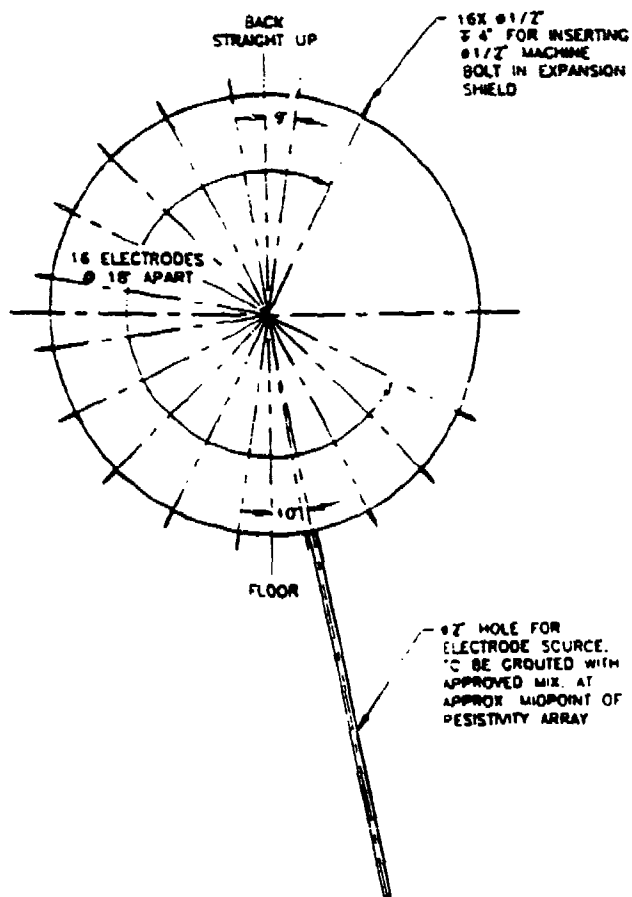


Figure 2

Room-Q: Changes in resistance 1/11 to 3/7 1990.

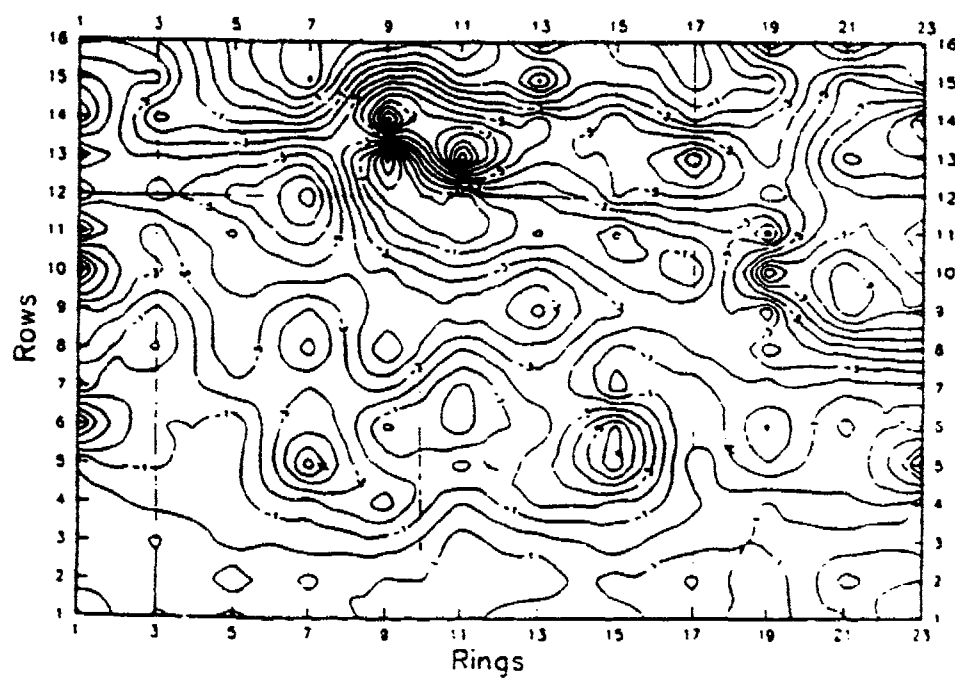
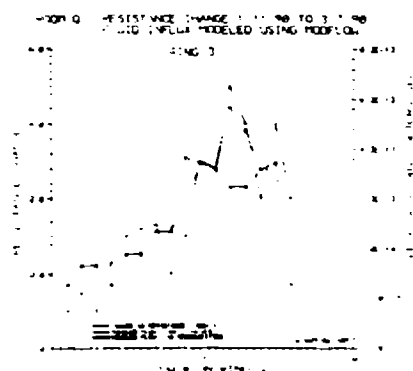
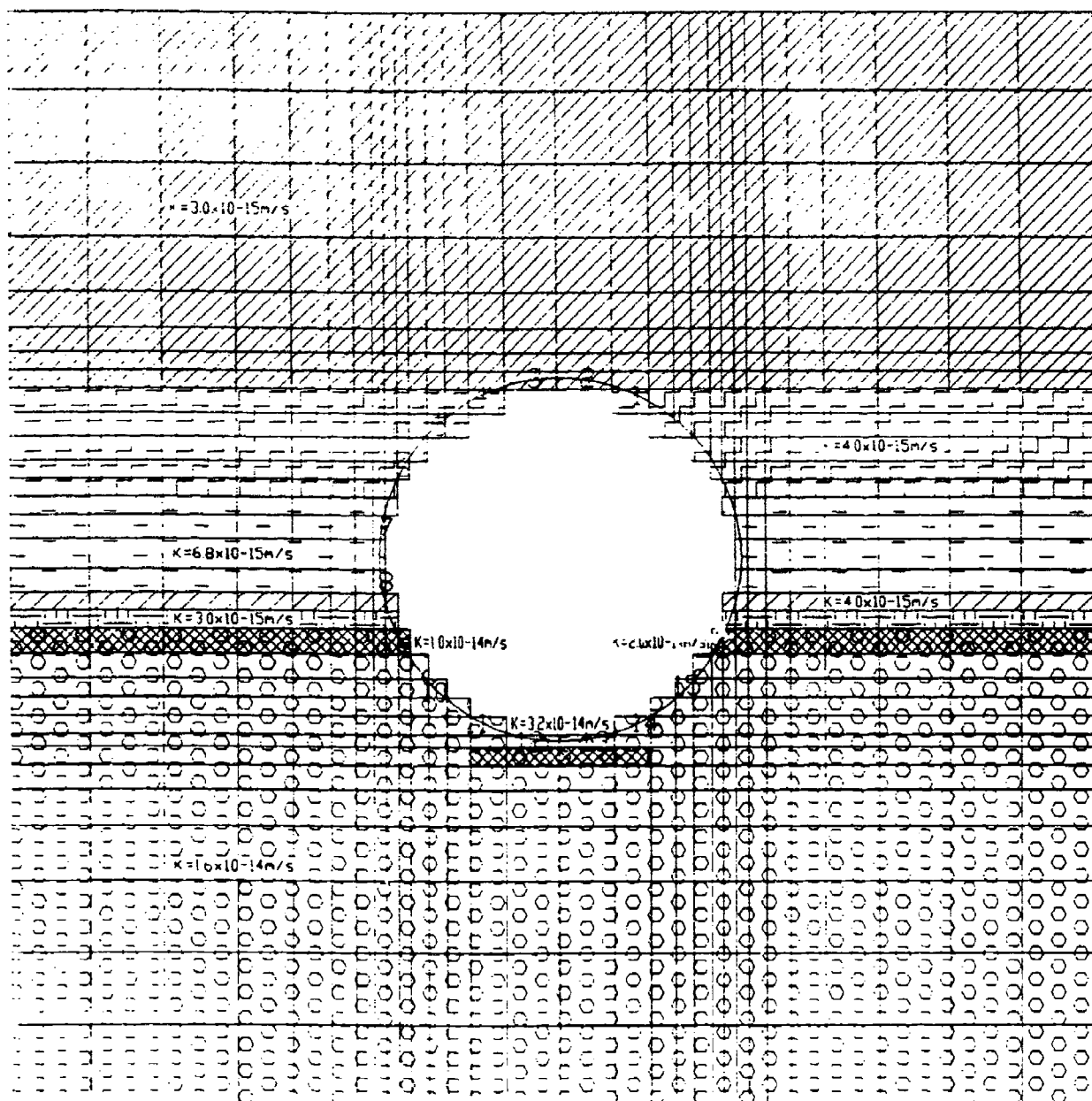


Figure 3

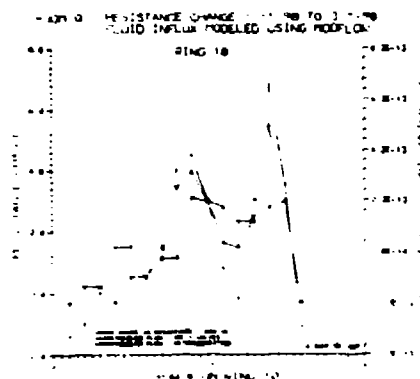
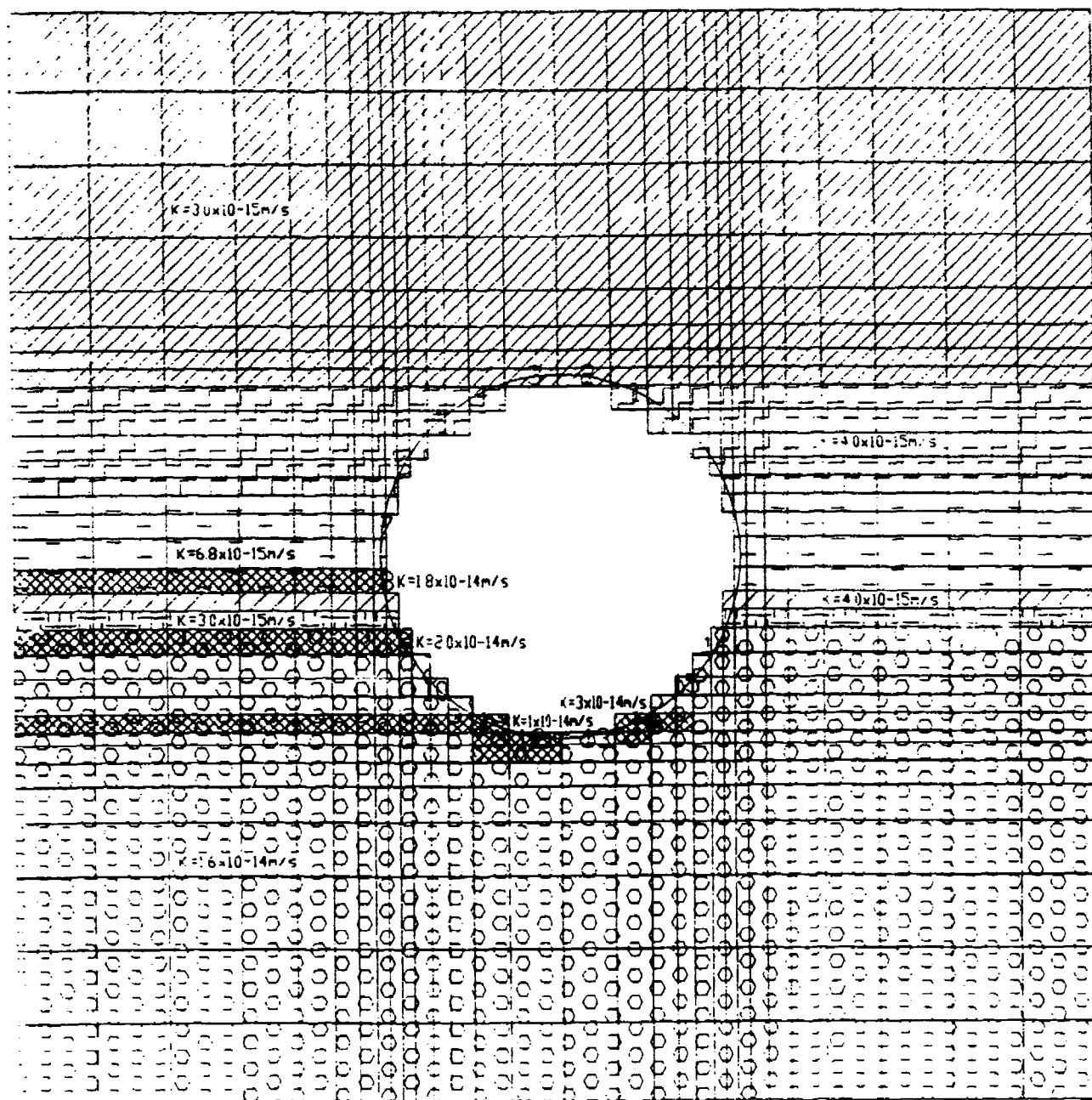
WIPP Site: Room Q MODFLOW Model - Ring 3



- | | |
|--------|-----------------|
| Unit 0 | Unit 4 |
| Unit 1 | Unit 5 |
| Unit 2 | Heterogeneities |
| Unit 3 | |

Figure 4

WIPP Site: Room Q MODFLOW Model – Ring 10



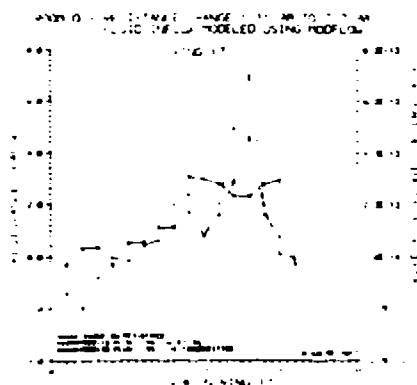
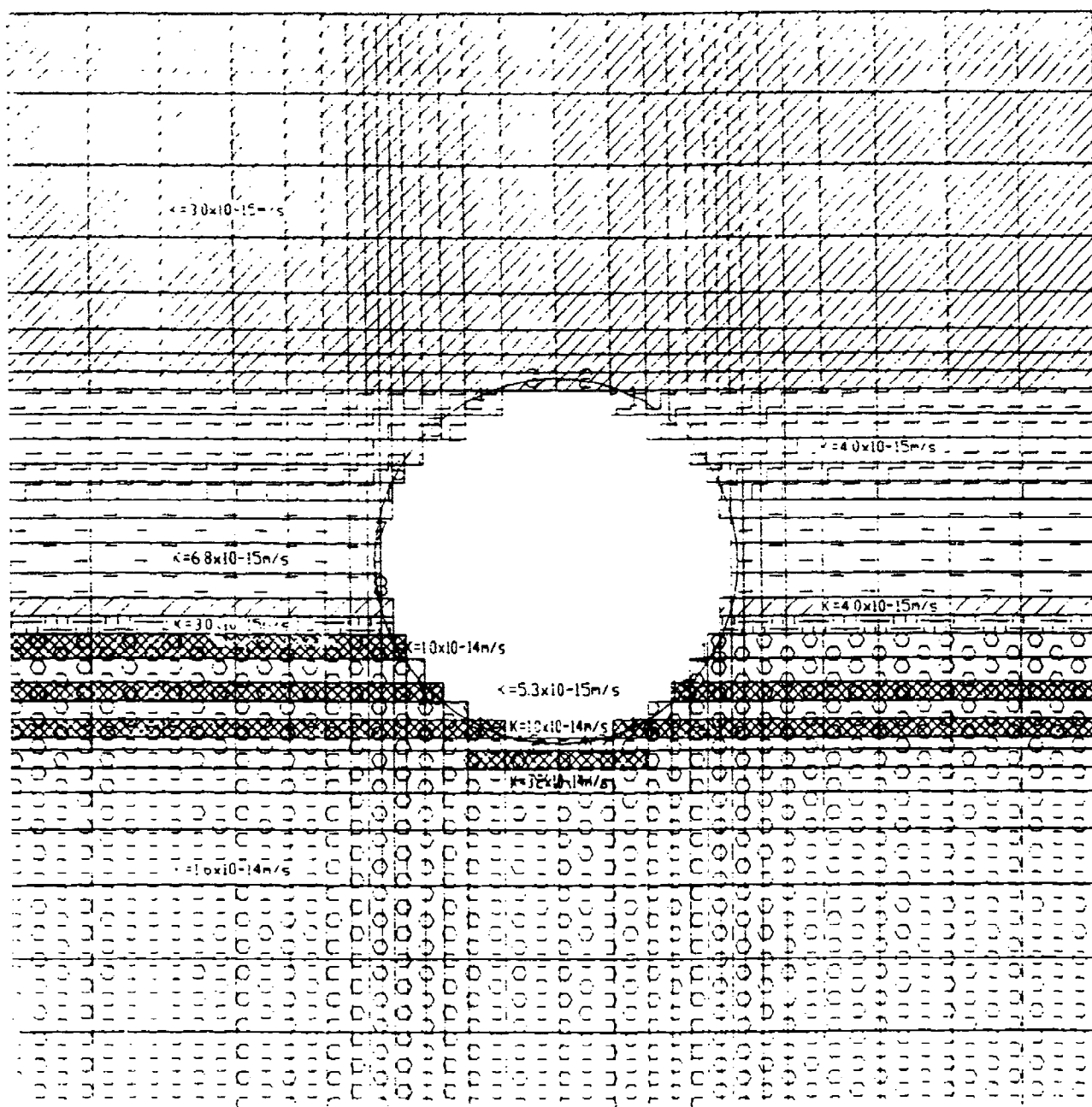
Unit 0
Unit 1
Unit 2
Unit 3

Unit 4
Unit 5
Heterogeneities

Figure 5

MGT 18 Sept 92

WIPP Site: Room Q MODFLOW Model - Ring 17



- | | | | |
|--|--------|--|-----------------|
| | Unit 0 | | Unit 4 |
| | Unit 1 | | Unit 5 |
| | Unit 2 | | Heterogeneities |
| | Unit 3 | | |

Figure 6

MGT. 18 Sept 92

ROOM 0 - RESISTANCE CHANGE 1/11/90 TO 3/7/90
 FLUID INJECTION MODELED USING MODFLOW

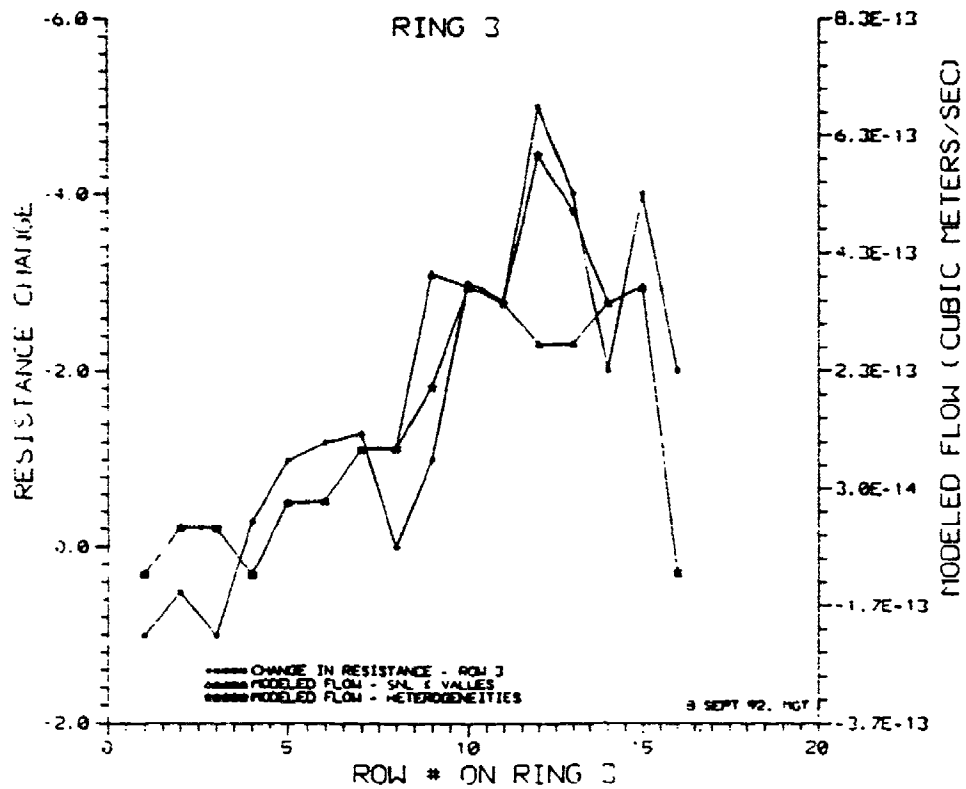


Figure 7

ROOM 0 - RESISTANCE CHANGE 1/11/90 TO 3/7/90
FLUID INFLUX MODELED USING MODFLOW

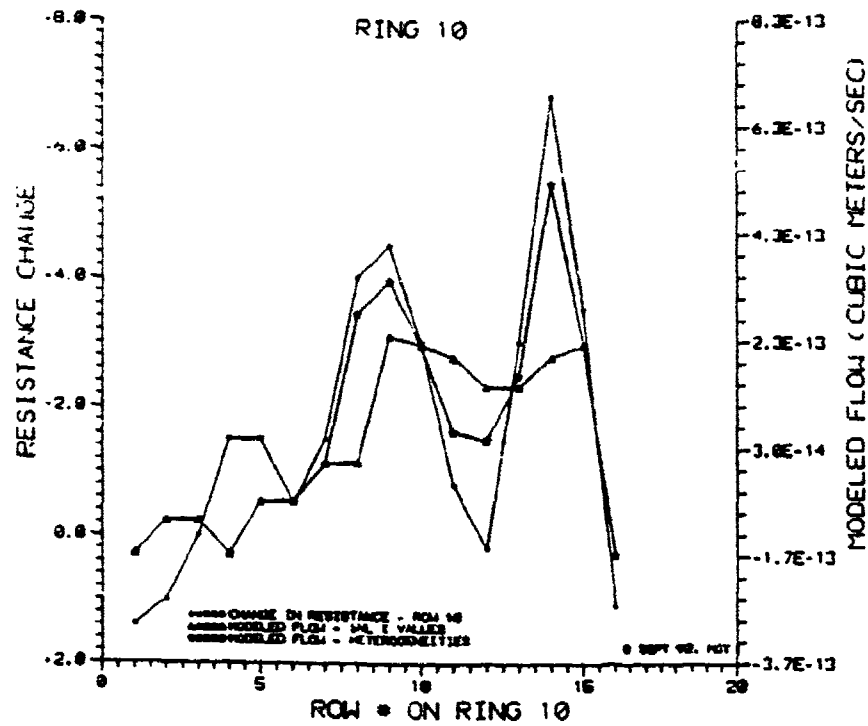


Figure 8

ROOM 0 - RESISTANCE CHANGE 1/11/90 TO 3/7/90
FLUID INFLUX MODELED USING MODFLOW

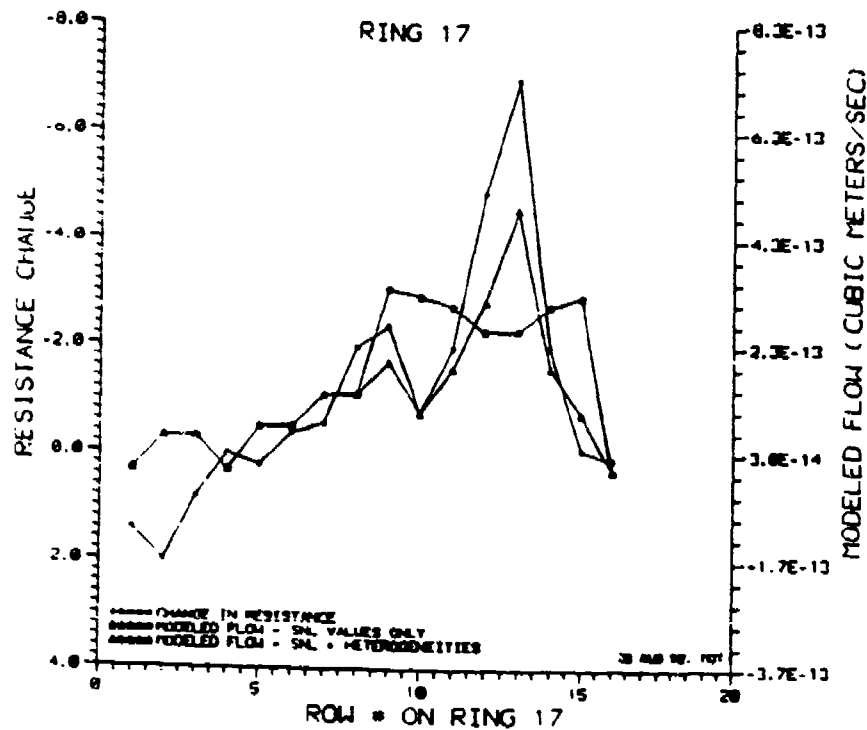


Figure 9

**DETECTION OF DEEPLY
BURIED TUNNELS
WITH ELECTRICAL CONDUCTORS**

BY

**LARRY G. STOLARCZYK
RIMTECH, INC.
RATON, NM 87740**

**JIM ALLEN
CHEM-NUCLEAR GEOTECH, INC.
GRAND JUNCTION, CO 81503**

ABSTRACT

Deeply buried tunnels which contain electrical conductors can be detected with low frequency electromagnetic waves. These conductors may be the utilities used to keep clandestine tunnels and bunkers in the ready state. A 600 ft. long horizontal electric dipole antenna on the surface causes a radio wave to propagate into the earth. The primary electric field component that is polarized with the buried conductor induces current flow. Induced current flow creates a scattered secondary EM wave in the rock mass surrounding the tunnel. A down-the-hole or surface instrumentation configuration can be used to detect secondary EM wave energy near the conductor. In this method, reception of a secondary wave signal confirms the existence of the conductor. Theoretical analyses of the method by Hill (1988, 1990) addressed feasibility issues. One of the issues relates to the separation distance required to absorb the primary wave energy on the path between the radiating to receiving antennas. Another was the maximum radius of detection and its dependence on operating frequency and electrical conductivity of the rock mass. Experimental field tests were conducted at the Oracle Ridge Mine near Tucson, Arizona. The test results compared favorably with the theoretical expectation. The grounded surface dipole with 679 milliamperes of current induced 668 microamperes of current in the tunnel conductor. The conductor was buried in 500 ft. of limestone rock ($\sigma=0.001$ S/m). A lateral tunnel in the rock mass was used to measure the magnitude of the secondary wave up to 200 ft. from the conductor. Measured data predicted a radius of detection of 1300 ft. for the geologic conditions at the test site.

1. INTRODUCTION

The detection of deeply buried tunnels and bunkers with electric power/telephone cable, air/hydro pipe and rail is important in physical security and modern warfare. Clandestine tunnels can be developed from existing mine working or beneath mountains to enable access to sensitive installations. In Korea, tunnels have been used to threaten the security of the South Korean Government. In the gulf war, Iraq used subsurface bunkers to shield assets from detection and destruction by coalition forces. Maintaining tunnels and bunkers in a readiness state requires ventilation and installed utilities. If these utility conductors are long enough they can be detected by low frequency electromagnetic waves.

In this paper, we describe an electromagnetic (EM) wave field experiment that was carried out to investigate feasibility issues related to detection of deeply buried electrical conductors. There are many interesting technical issues that arise in feasibility consideration. A practical instrumentation configuration that can be deployed in field operations must be considered. Detection requires theoretical modeling of the instrument configuration to determine effect of physical and geologic factors on the radius of detection. Uniform or non-uniform illumination of the conductor induces different guided wave modes that impact the detection method. The radius of detection depends on electrical conductivity of the overlying rock mass. The primary wave must be suppressed below that of the secondary wave.

The detection of deeply buried conductors is based upon the long wavelength scattering limit described in mathematical physics (1). The scattering cross section of a thin electrical conductor increases at lower frequency. The electric field component of the EM wave that is tangential to the axial direction of the conductor induces current. Current flow produces a scattered "secondary" EM wave that can be detected. Detection is based upon the reception of the scattered field in the rock mass surrounding the target or on the surface. Non-uniform illumination causes both minofilar and bifilar current modes to propagate on the utilities. The bifilar mode attenuation rate is less and provides greater detection distance along the conductor. Technical issues are related to questions about frequency for maximum radius of detection, effects of electrical parameters of the overburden, the ratio of the primary to secondary wave at the detection location, and optimum configuration of instrumentation.

A field experiment to evaluate these issues was carried out at Oracle Ridge Mine located on the Eastern escarpment of Mount Leamon near Tucson, Arizona. Analytical modeling by Hill (2) was completed prior to the field work. This enabled planning of the experiment to address theoretical, as well as practical, issues.

2. THE ORACLE RIDGE MINE

The Oracle Ridge Mine is ideal for evaluating technology to detect deeply buried active tunnels. The transmitting (radiating) to receiving antenna separation distances can be varied to assess suppression of the primary wave at various measurement locations. When the separation distance is sufficient, induced current flow produces a secondary EM wave with a magnitude greater than the primary wave. To obtain valid field test data, surface electrical conductors near the transmitting antenna should not couple test signals into the target tunnel conductors. This problem could not be easily alleviated during previous tests at the Colorado School of Mines (CSM) test site.

The Oracle Ridge Mine is located on the eastern escarpment of the Catalina Mountains near Tucson, Arizona. Drifts have been developed into limestone host rock. Laboratory measurements of host rock core samples found the electrical conductivity (σ) to be 1 mS/m at 100 kHz. The test site is also suitable for evaluating the feasibility of deploying RIM instrumentation and data acquisition methods in rugged terrain.

The planview drawing of the Oracle Ridge Mine illustrates the topology of the surface, surface access roads (dashed line) and drifts (solid lines).

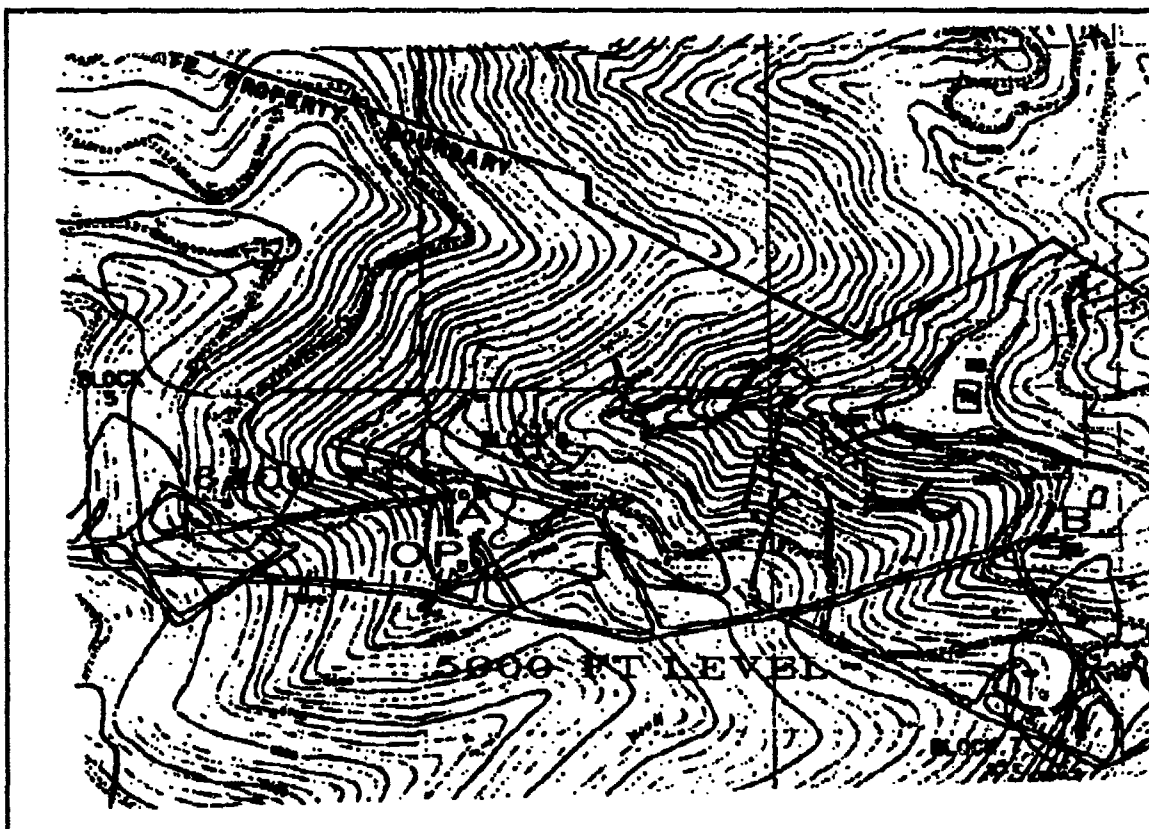


Figure 1 Planview of the Oracle Ridge Mine.

The 6400 ft. (above sea level) adit is illustrated by the A symbol near the center of the planview illustration. A similar adit (B symbol) on the right side of the illustration has been developed at the 5900 ft. elevation. Level surfaces at each adit provide clearings for an electric power generation station, warehouse, and office buildings. Drifts from the adits lead to highly mineralized ore zones in the limestone host rock.

The main west 5900 ft. level drift extends from right to left across the planview illustration. A second 5900 ft. level drift heads downward in the illustration to a lower working level in Block 7. The Block 7 drift continues from the working level and crosses under the main west roadway. The 6400 ft. level drift approximately parallels the 5900 ft. drift. It extends left from the orepass (OP) symbol.

The Oracle Ridge Mine has been developed on two different levels. The lower level has been designated as the tunnel target in this work. The upper level and its service area were used for deployment of the Method II grounded dipole antennas.

Diesel electric generating stations at each adit provides power for each level of the mine. Separate power systems prevent direct transmission of radio signals between the 5900 and 6400 ft. level drifts. A high pressure pipe exits the mine at each level. The pipe was disconnected at the adit for our tests to prevent transmission of radio signals between level drifts. An orepass has been developed from the main west 6400 ft. level adit to intersect the main west 5900 ft. level drift. The orepass and test configuration are illustrated in Figure 2.

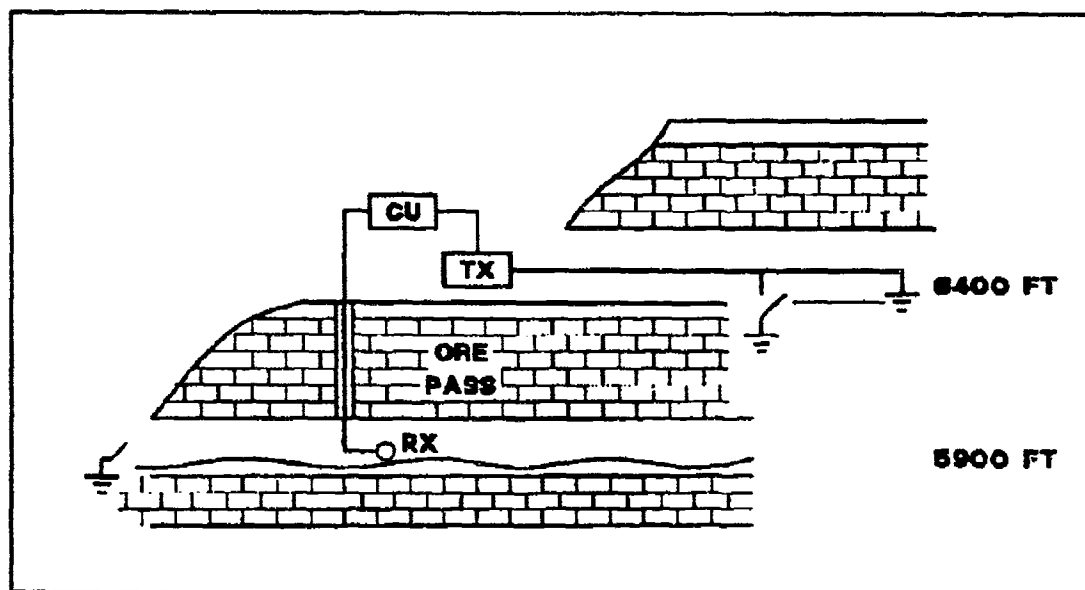


Figure 2 Orepass and method II instrumentation.

An insulated 16 Gauge conductor was installed in the main west 5900 ft. level drift. The insulated conductor extended 1700 ft. from the adit to the orepass. It extended past the orepass for a distance of 800 ft. A switch at the 5900 ft. level adit was used to ground the outby end of the conductor. The inby end of the cable was permanently grounded to a roof bolt.

A test plan was developed to evaluate Method II, and Modified Method II at the Oracle Ridge test sites. Method II deployed a grounded dipole antenna on the surface to induce current flow in the target conductors on the 5900 ft. level. The feasibility of detecting a deeply buried tunnel from an upper tunnel drift was an important objective of the test plan. The feasibility was to be determined by installing the grounded dipole antenna in the 6400 ft. level drift and measuring the current induced in the 5900 ft level target conductor. The dipole included a grounding switch that was located 228 m (750 ft.) inby the 6400 ft. level adit. This location is directly over the end of the 5900 ft. level target conductor. The headings of the 5900 and 6400 ft. level drifts are

approximately parallel and separated by approximately 500 ft. of limestone. The induced current in the target conductor would be expected to be maximum for the parallel orientation of the grounded dipole axis and 5900 ft. level tunnel headings. To confirm this, a grounded dipole antenna was also deployed on the adit service area. The 106 m (150 ft.) grounded dipole could be deployed in a "fan" configuration on the adit service area. The headings were restricted by service area access roads, a loadout facility, shop, and ore pile to angles of +60°, +5° and -20° with respect to the target tunnel heading.

During the Method II tests, the RIM System II receiver was lowered down the orepass to the 5900 ft. level drift. The receiving antenna was then carried in the drift to predetermined measuring stations. Measuring stations were marked at 15.2 m (50 ft.) intervals from the orepass towards the adit. The target conductor current flow at each frequency was measured using the transfer impedance method of measuring conductor current with the receiving antenna. At measuring station 250, a lateral crosscut drift enabled the measurement of the y component (vertical) of the magnetic field at 15.2 m (50 ft.) distance intervals from the target conductor.

Prior to the tests, the transfer impedance of the antenna was determined in the laboratory.

TABLE A
TRANSFER IMPEDANCE

FREQUENCY	IMPEDANCE
KHz	OHMS
57.5	3.98
102.5	3.55
302.5	7.05
522.5	5.63

The transfer impedance is the ratio of the receiving antenna output electromotive force (emf) voltage to the current flowing in the target conductor. The induced current is computed from the measured voltage by dividing the measured voltage by the impedance given in Table A.

3. FREQUENCY RESPONSE OF THE TARGET CONDUCTOR

In the first test, the induced current in the target conductor was measured with the transfer impedance measurement technique at measuring stations 0, 50, 100, 150, 200 and 250 in the 5900 ft. drift. In the second test, the y component of the magnetic field was measured in a lateral (cross-cut) drift that intersected the 5900 ft. main drift at station 250. The cross-cut measuring stations were designated A, B, C, D and E. Measuring station E was at the end of the cross-cut drift, 200 ft. away from the conductor.

At measuring stations A, B, C, D, and E, the receiving antenna output voltage is recorded in dB above one nanovolt. The induced current measured in the target conductor at each test frequency is graphically presented in Figure 3.

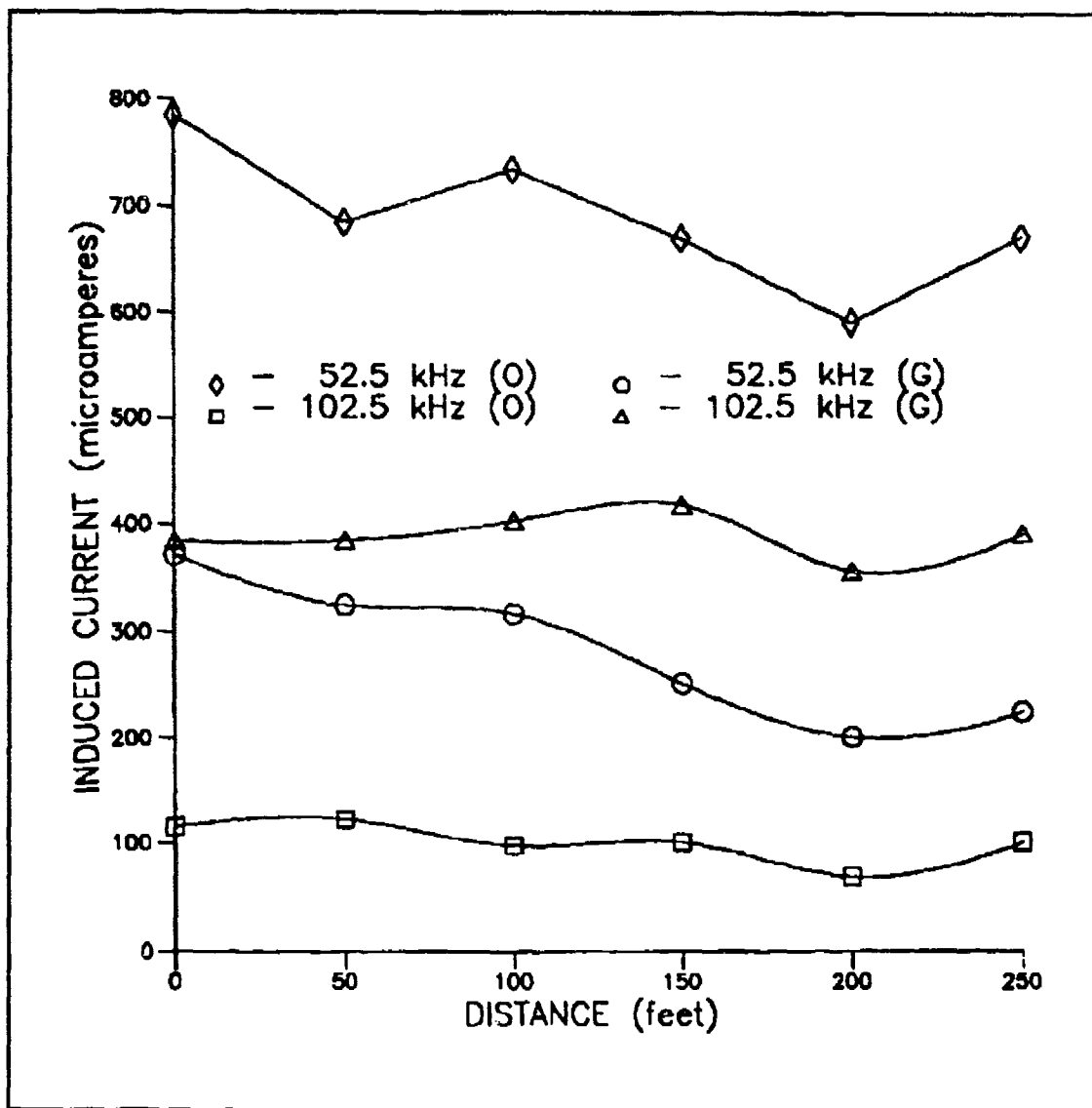


Figure 3 - Measured induced current versus distance along buried conductor; adit end open (O) or grounded (G).

The test data shows that the induced current decreases with frequency. At measuring station 250, the magnitude of the induced current is 668 micro amperes. The magnitude of the current flowing in the grounded dipole antenna is 679 milliamperes. The current ratio is $20 \log 679/.668 = 60.1$ dB. At 522.5 kHz, the induced current decreases to 10 microamperes. The current ratio is $20 \log 679/0.01 = 97$ dB. The 52.5 to 522.5 kHz induced current difference

is 37 dB. Hill's work suggests that the difference should be approximately 30 dB.

At 52.5 kHz, the magnitude of the induced current decreases when the adit end of the target conductor was in a grounded condition. At 102.5 kHz, the current increases when the adit end was in a grounded condition. The data suggests that a current standing wave exists along the line. This is due to the finite length of the target conductor. The test results show that strong current can be induced in the target conductors that are buried 500 ft. below the Method II grounded dipole antenna.

The y component of the magnetic field was measured in the lateral cross cut drift at measuring stations 250. The measured value represents the magnetic field that would be measured in a simulated receiver drillhole when the drillhole is 0, 50, 100, 150 and 200 ft. from the target conductor. The receiving antenna output voltage is presented in Table B.

TABLE B
RECEIVING ANTENNA OUTPUT
VOLTAGE VERSUS LATERAL DISTANCE
FROM THE TARGET CONDUCTOR
(dB re 1 nanovolt)

DISTANCE IN FT.	FREQUENCY IN KHz							
	52.5		102.5		302.5		522.5	
	ADIT		CONDUCTOR		GROUNDING		CONDITIONS	
	O	G	O	G	O	G	O	G
0	106	102	-	-	-	88.1	-	64
50	89	85	-	-	-	83.2	-	68
100	86	86	-	-	-	90.0	-	71
150	88	88	-	-	-	69.3	-	57
200	95	95	-	-	-	84.3	-	56

The measured data suggests that the 52.5 kHz frequency induces the largest current in the target conductor. The measured signal level increases to 95 dB re 1nV at measuring station 200(E). The planview map of the 5900 ft. level drift in Figure 1 shows that the crosscut veers toward the orepass. The primary wave dominates the secondary wave at the 200 ft. location.

4. DETERMINING TARGET TUNNEL HEADING FROM METHOD II PAN MEASUREMENTS

The 6400 ft. level service area was used to deploy the Method II grounded dipole search antenna configuration illustrated in Figure 2. The receiving antenna was located in the 5900 ft. level drift at measuring station 0. The receiving antenna output voltage was measured as the axis of the surface grounded dipole antenna was rotated with respect to the tunnel heading. The measured data

is presented in Table C.

TABLE C
TARGET TUNNEL HEADING
SEARCH AT 52.5 kHz

ANGULAR DEVIATION BETWEEN DIPOLE ANTENNA AND 5900 FT. LEVEL DRIFT IN DEGREES	MEASURED SIGNAL LEVEL IN dB RE 1 nV.
+60°	82.5
+ 5°	102
- 20	102

The measured signal level increased when the grounded dipole was aligned with the target conductor.

A loop antenna was also deployed on the surface. The diameter of the loop was approximately 45.7 m (150 ft.). The received signal level was 60 dB re 1 nV. The grounded dipole antenna response was 22 dB better than the loop antenna response.

5. INDUCED TARGET CONDUCTOR CURRENT VERSUS VMD TRANSMITTER ELEVATION

A transmitting vertical magnetic dipole (VMD) antenna was used to induce current flow in the underground conductor. The receiving antenna in the 6900 ft. drift was used to measure the induced conductor current produced by a VMD antenna in the orepass. The induced current was measured for VMD antenna elevation of 25, 50, 100, and 125 ft. above the conductor.

TABLE D
INDUCED LINE CURRENT (Microamperes)
VERSUS RADIATING VMD ELEVATION
ABOVE TARGET CONDUCTOR

ELEVATION IN FT.	FREQUENCY IN kHz			
	52.5	102.5	302.5	522.5
125	1.7	11	4.5	1.0
100	1.9	13	9	2.0
75	2.7	14	9	1.7
50	3.9	14	8	8
25	1.7	9	56	40
0	18	44.6	142	99

When the radiating VMD antenna was at the elevation of the 5900 ft. level drift conductor (0 ft), the maximum induced current occurred at the 302.5 kHz frequency. In the previous Colorado School of Mines Method III tests, a radiating VMD also induced maximum current at 302.5 kHz (3). When the measured current decreases to less than 10 microamperes, the measured signal to

noise ratio is low. The measured signal is near the noise level induced by the mine electrical power system.

6. METHOD III RADIUS OF DETECTION

The down-the-hole VMD antenna was located 15 meters from the target conductor at measuring station 0. The down-the-hole receiver was located 500 ft. outby and in a crosscut. The second crosscut outby drift is illustrated in Figure 1. Measuring stations were established at 20 ft., 70 ft. and 120 ft. from the conductor. The receiving antenna output voltage is presented in Table E.

TABLE E
MEASURED SIGNAL LEVEL IN dB re 1 nV
VERSUS LATERAL DISTANCE
FROM THE TARGET CONDUCTOR

LATERAL DISTANCE IN FT.	FREQUENCY IN KHz							
	52.5		102.5		302.5		522.5	
	ADIT CONDUCTOR GROUND							
	CONDITION							
	O	G	O	G	O	G	O	G
20	66	51	68	73	75	73	64	65
70	56	47	60	63	65	64	56	56
120	53	45	55	59	59	57	46	47

The data suggests that the target conductor response reaches a maximum value near 302.5 kHz.

The data presented in Table E can be used to estimate the maximum conductor signal range. The antenna output voltage versus distance from the conductor is in Figure 4.

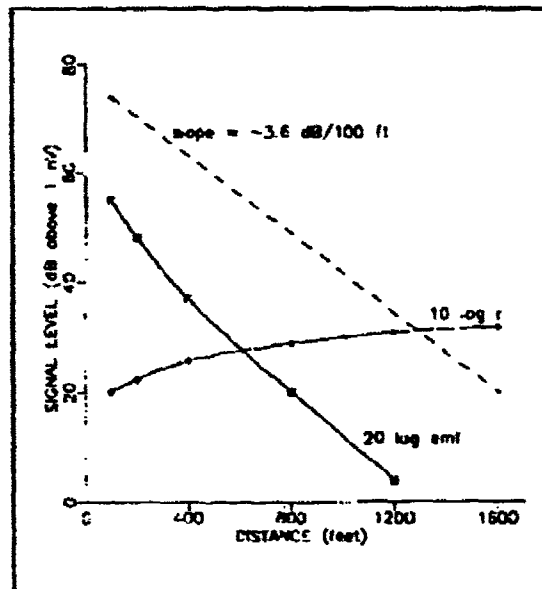


Figure 4 Antenna output voltage versus distance from the conductor (52.k kHz).

The antenna output voltage (emf) is given by

$$20 \log \text{emf} = 20 \log c - \alpha \rho - 10 \log \rho \quad (11)$$

where $20 \log c$ is the RIM System II coupling factor,

and, $10 \log \rho$ is the cylindrical spreading factor.

The conductor to rock mass EM coupling factor is approximately 77 dB above 1 nanovolt. This is the approximate antenna output voltage when the antenna is located near the target conductor. The long dashed curve is represented by

$$20 \log \text{emf} + 10 \log \rho = 20 \log c - \alpha \rho.$$

The right side of the equation is recognized as a linear function versus distance from the conductor. The linear function has Y axis intercept $20 \log c$ with negative slope. The slope is the attenuation rate of the radio wave in the host rock. The solid curve illustrates the antenna output voltage $20 \log \text{emf}$. The maximum range occurs when the $20 \log \text{emf}$ curve intersects the X axis. At 50 kHz, the maximum detection distance from the conductor is approximately 396 m (1300 ft).

7. CONCLUSION

Field evaluation of the instrumentation configuration and data processing algorithms has demonstrated that deeply buried tunnels can be detected with a grounded dipole antenna on the surface (or in an upper tunnel) and a companion down-the-hole receiving antenna. The grounded dipole induced approximately 668 microamperes of current in the target conductor. The frequency response of the target conductor reached a maximum near 50 kHz. The rock path distance to the conductor was approximately 152m (500 ft.). The estimated receiving distance from the target conductor was 396m (1300 ft.). The radius of detection is 548m (1800 ft.) in low conductivity rock mass.

BIBLIOGRAPHY LIST

- (1) Morse, P. and Feshbach H., Methods of Theoretical Physics, McGraw Hill, New York: 1957.
- (2) Hill, David A., Nearfield and Farfield Excitation of a Long Conductor in a Lossy Medium. Report NISTR 3954 National Institute of Standards and Technology, Boulder, CO, 1990.
- (3) Stolarczyk, L.G., Long Feature Tunnel Detection Methodologies using Phase Coherent Electromagnetic Instrumentation, Third Technical Symposium on Tunnel Detection Proceedings, Golden, CO, 1988.

Session 7

Case Studies

Surface Geophysical Methods Applied to the Detection of Shallow Tunnels and Buried Objects

J. W. Allen

Chem-Nuclear Geotech, Inc.
Geophysical Programs
P.O. Box 14000
Grand Junction, Colorado 81502

ABSTRACT

Surface geophysical methods have proven effective for the detection of shallow tunnels and buried objects when applied with a well-planned, synergistic (integrated) methodology. The incorporation of information from intelligence sources, geologic assessments, historical reviews, computer modeling, and multiple geophysical survey methods provides the maximum probability of success. Responses from multiple survey methods define specific characteristics of anomaly sources. These characteristics provide a means of differentiating a bona fide target from geologic or cultural features when compared with modeled signatures of the suspected target.

Magnetic sensors can detect ferromagnetic materials used in tunnel construction; analyses of these data indicate the depth and path of the tunnel. The intrinsic parameters of observed electromagnetic anomalies and the surface patterns of instrument responses provide additional indications of tunnel-related conductors. These methods have successfully differentiated the responses from materials used in tunnel construction and operational support systems from those generated by surface features such as fences and buildings and from near-surface underground structures and utility lines. Migrated seismic compressional waves (*P*-waves) collected by the common-midpoint method have provided clear and unique anomaly patterns that can be associated with known tunnels. Ground-penetrating radar, magnetic, and electromagnetic methods have been effective in mapping underground features such as trench boundaries, utility lines, underground storage tanks, and shallow-depth caches constructed of various materials.

A 10-kilometer long, 4-meter high by 3-meter wide irrigation tunnel near Montrose, Colorado, served as a test site for the evaluation of multiple surface geophysical methods for the detection of a shallow tunnel in a well-characterized environment. Magnetic, electromagnetic, electrical, seismic, and gravity methods have all been tested for tunnel depths varying from 14 to 24 meters. Reflection seismic, time-domain electromagnetic, and gravity methods provided the most convincing data for detecting and locating the tunnel.

INTRODUCTION

During the last two decades, the need has increased for better methods to detect and locate shallow tunnels and buried objects. Military and law enforcement agencies are the primary users of the emerging technologies directed at these requirements. Geophysical methods developed

primarily for mineral exploration and engineering applications have been modified to detect smaller targets (e.g., objects, tunnels, utilities, geologic formations) at shallower depths and to provide more precise information on the locations and characteristics of the detected targets. A synergistic (integrated) methodology, using data from multiple geophysical methods, has proven effective for detecting shallow tunnels and buried caches in several different geological environments.

SYNERGISTIC METHODOLOGY

"Synergistic" is an adjective which describes the effect of multiple factors working simultaneously to produce a result that is greater than the sum of their individual efforts. Synergistic methodology, as defined here, combines all available information to detect and locate shallow tunnels and buried objects. Intelligence information, historical reviews, and computer modeling complement and supplement data collected by multiple geophysical survey methods.

Intelligence

Information from intelligence sources is a vital element in synergistic methodology. It often suggests an area to begin geophysical surveys, narrows the scope of reconnaissance surveys, and may even pinpoint a specific location for detailed surveys. Information about a target's location and construction may suggest the type of response characteristics (signatures) to expect from the various geophysical methods.

In the final analysis and interpretation of geophysical data, intelligence information may lend more importance to subtle responses from a specific location and may be a major factor in concluding that a specific target exists at that location. Conversely, false information may color the interpretation of subtle responses, lead to an overemphasis of the importance of certain features, and ultimately result in false conclusions about the existence of a suspected target at a specific location.

Historical Review

A review of available geological and historical records about a survey area may provide information that is useful in planning and conducting geophysical surveys. These records include U.S. Geological Survey maps and reports, city utility maps (current and historic), water-well drilling records, title insurance company records, fire insurance company records (often containing excellent map archives), and other public records that show past land ownership and usage. Some of these records may provide descriptions of former structures with remnant features that may affect survey data. For example, abandoned mines, old septic tanks, drain systems, and underground storage tanks may not exhibit surface expressions or be shown on contemporary maps but may produce a dramatic response during geophysical surveys. If not recognized for what they are, such features could easily lead to false conclusions about the presence of a suspected target. Interviews with "old-timers" or nearby residents often can reveal additional useful information not available from public sources.

Modeling

Computer modeling of specific target characteristics in specific environments is used to predict the expected responses in the data. The modeled response can be used to predict the probable success of the search method, given that those conditions actually exist. If the model shows the magnitude of the expected response to be on the order of typical geophysical background variations (noise), then the probability of success is low. Conversely, if the expected response is one or two orders of magnitude greater than the noise, the probability of detecting the target is high.

Geophysical Survey Methods

Geophysical survey methods used to search for shallow tunnels and buried objects typically respond to contrasts in physical properties of the target and target environment. Methods used in the search for shallow tunnels and buried objects include total field and gradient magnetic, induction electromagnetic (IEM), very low frequency electromagnetic (VLF-EM), time-domain electromagnetic (TDEM), ground-penetrating radar (GPR), resistivity/induced polarization, microgravity, and seismic refraction/reflection surveys. For deep tunnels, passive seismic and electromagnetic listening systems, cross-borehole radar, and active seismic imaging systems have been effectively used.

Survey instruments are usually battery-powered, highly portable, and easily operated by one or two persons. Data are typically recorded in solid-state memory for later readout and processing by portable computer. Some sophisticated systems process the data as acquired and present results in the field in real time. A broad variety of computer software is available for processing and displaying data in profile, contour, and 3-dimensional surface formats.

Synergistic methodology associates the responses of several different survey methods to determine different characteristics of the target and its environment. For example, a magnetic response can indicate the presence of ferrous materials, while an inphase IEM response can indicate a metallic conductor. If both responses show a long linear feature when contoured, we may infer that the target is a steel pipe. If the long, linear inphase IEM response is present and the magnetic response is not, we may infer a nonmagnetic electrical conductor, such as a copper wire. A gravity low can indicate the presence of a cavity or tunnel. When this information is coupled with the results of other geophysical surveys, we may deduce a great deal more about the source of the anomaly.

The character of the individual responses (or signatures) often provides additional information; for instance, a convex surface such as a pipe, wire, or tank will generate a characteristic parabolic signature on GPR. With proper recording of antenna position as the response is generated, a simple relation between the time scale and the surface position can be used to calculate depth to the target (Geophysical Survey Systems, Inc.). If this information is coupled with the previously described magnetic and IEM responses, we can infer the probable kind of target and its depth. The depth to a magnetic source can be estimated from the shape and amplitude of the anomaly it produces, using the half-width rules given by Breiner (1973).

REAL-WORLD EXAMPLES

Shallow Tunnels

Surface geophysical methods have been used to locate shallow tunnels at depths ranging from 1 to 24 meters (m). Such depths are typical for short, hand-excavated tunnels that may be used for breaching security fences or barricades, penetrating basements or underground vaults, smuggling materials beneath international borders, or a number of other clandestine activities.

Shallow Clandestine Tunnel—A shallow clandestine tunnel, hand excavated in alluvial sands with interbedded clays and caliche, was located using elements of synergistic methodology. The tunnel is approximately 90 m in length with depth to centerline ranging from 8.5 to 11.5 m. It is approximately 1 m wide by 1.5 m high and is lined with precast concrete roof and floor members and cast-in-place concrete sidewall members. In addition to the reinforcing steel which created a magnetic response, it contained electrical conductors which made a good electromagnetic target. Surveys, using multiple-surface geophysical methods, were conducted in the area of the suspected tunnel to support previously collected intelligence information. Site conditions, and the need to maintain operational security, limited both the quantity and quality of the data collected and prohibited the use of a grid of multiple, parallel survey lines that is useful in detecting the long linear response features that diagnose a tunnel.

Figure 1 shows magnetic data from a survey line perpendicular to the tunnel axis. The shape and amplitude of the total field anomaly agree very closely with a computer model of the tunnel. Using the half-width rule, the apparent depth scaled from the total field anomaly is 8.4 m, which is approximately the depth to the rebar-reinforced tunnel top. Figure 2 is a plot of VLF-EM wave-tilt data collected during the same survey. Note that the center of the tilt anomaly correlates closely with the crossing of the tunnel as expected for a buried conductor.

Conversely, IEM, resistivity, seismic, and GPR surveys at the site did not provide diagnostic data that suggested the presence a tunnel.

Gunnison Tunnel—The Gunnison Tunnel, located approximately 10 kilometers east of Montrose, Colorado, carries water from the Black Canyon of the Gunnison River to the Uncompahgre Valley for irrigation purposes. It was constructed by the Bureau of Reclamation during the period 1906 to 1912. The tunnel is 9,324 m long and has a nominal cross section 3.3 m wide by 4 m high. Some segments are of unlined natural rock while others are lined with concrete. The western end of the tunnel, which lies in alluvial clays, sands, and gravels, is lined with concrete and provides an excellent test site for shallow tunnel detection methodologies. The surface is nearly flat with overburden that gently slopes to provide depths to the tunnel ranging from about 12 to 75 m. Surface access is excellent, and several parallel survey lines were established over the tunnel axis to test a variety of surface geophysical methods. During one phase of the tests, a 1,200-m-long telephone cable was installed in the tunnel to simulate power or communications system conductors.

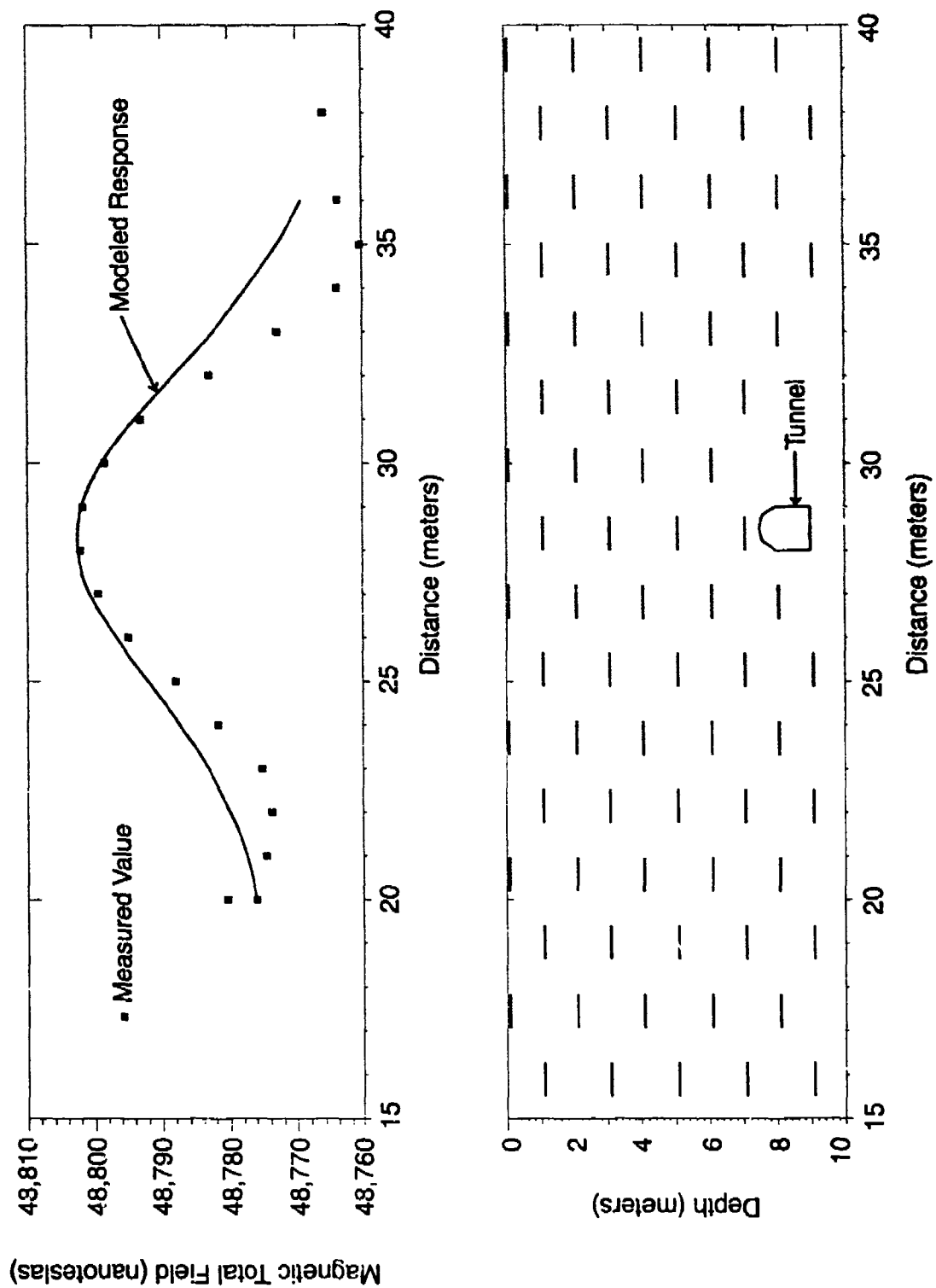


Figure 1. Total Field Magnetic Anomaly Over Shallow Tunnel

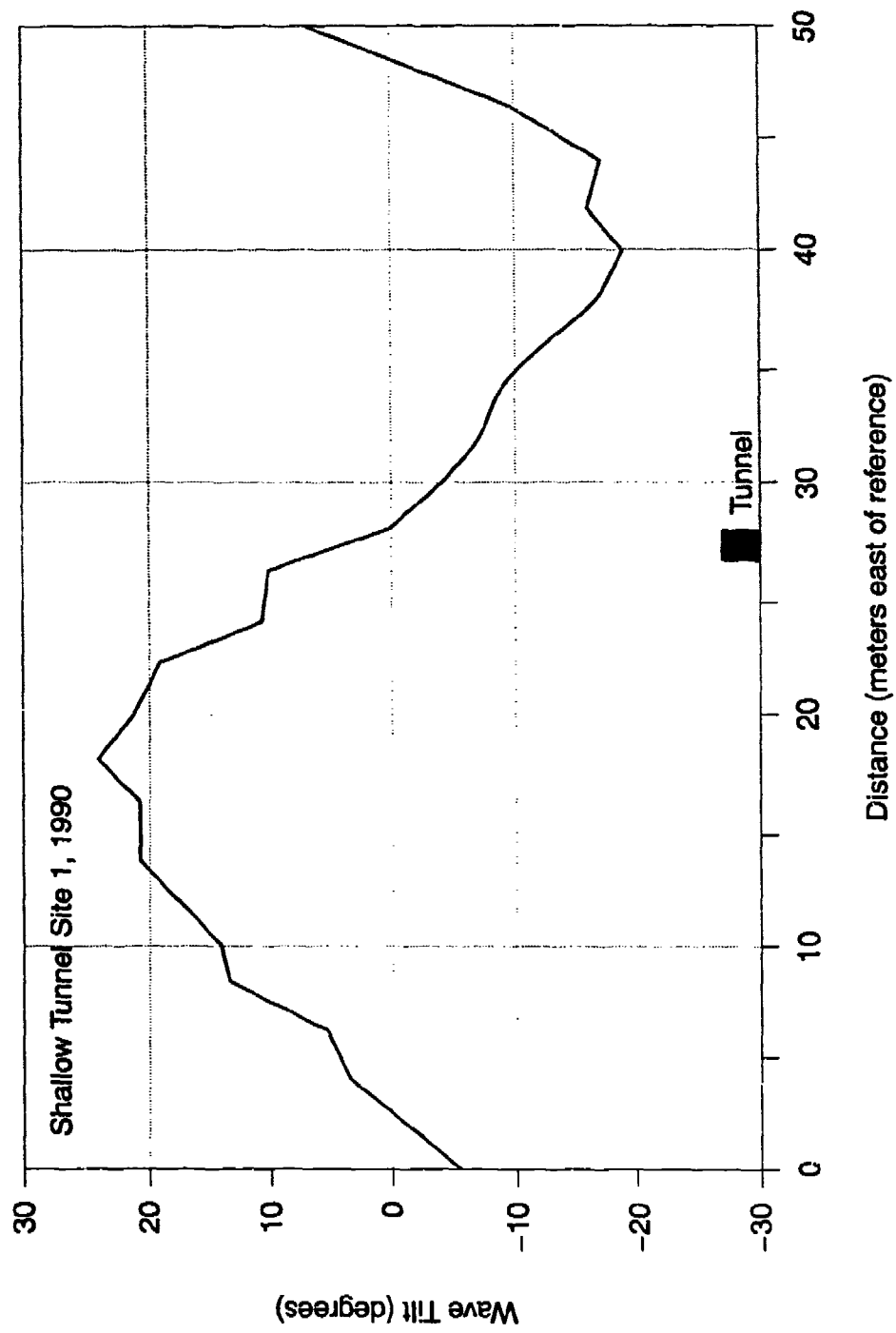


Figure 2. VLF-EM Wave-Tilt Anomaly Over Shallow Tunnel

Geophysical surveys were conducted with commercially available instruments to evaluate surface geophysical methods believed to be appropriate for the detection of shallow tunnels. Electrical, magnetic, electromagnetic, seismic, and gravity methods were evaluated for three different tunnel conditions. They were bare tunnel, tunnel with open-ended conductor, and tunnel with conductor grounded at both ends.

The results of these surveys demonstrated that the detection of this tunnel, which is at a depth more than 3.5 times its diameter, is a difficult task. Only three geophysical methods produced data that were interpreted as "clearly tunnel-related." These methods were TDEM, gravity, and seismic. Of the three, TDEM produced the most dramatic response and is the obvious method to use when searching for a tunnel believed to contain electrical conductors. A TDEM survey with no conductors present in the tunnel showed a near-surface response at the location of a shallow, metal drainage pipe and a very small response over the tunnel location. Figure 3 is a plot of the received TDEM signal for the bare tunnel, the tunnel with an open wire installed, and the tunnel with a grounded wire installed. Note the greatly enhanced responses for the cases with the wire in the tunnel. The open wire showed the most significant increase, indicating it had the most current induced in it. David Hill (1988) has shown that this condition can occur on open-ended transmission lines within an air-filled tunnel.

The seismic method produced the best indication for the bare tunnel but is slower and more labor-intensive than the TDEM method. A common-midpoint, reflection seismic survey provided one of the most dramatic responses to the tunnel. Stacked and filtered data from this survey are shown in wiggle-trace format in Figure 4. Ground roll and direct arrival (refraction) events were muted for clarity. Migration (which places reflected events closer to their actual subsurface locations) of these data produced the more easily interpreted result shown in Figure 5.

Gravity data were collected for tunnel depths of 14 and 24 m, using two different state-of-the-art gravity systems. The data for the 14-m depth are shown in Figure 6, together with a computer-modeled response for a realistic physical model of the tunnel and its environment at the survey line nearest the western portal. The measured data points are shown by the small squares. Curve A (solid line) is the modeled response for the air-filled tunnel in a homogeneous material with a density of 2.5 g/cm^3 . Curve B (dashed line) is the modeled response for the physical model shown in the bottom half of the figure. The body labeled "FILL ROCK" simulates the crystalline tunnel spoil which is exposed along the edge of a filled-in arroyo at the location of line 1. Note that the portion of the response that is attributable to the geologic structure overshadows that from the tunnel alone. Data from the survey over the tunnel with a depth of 24 m showed even greater influence from geologic factors.

From these data, it is apparent that the gravity method is heavily influenced by geologic structure and is probably not effective for locating tunnels at depths of more than about 2 times their diameter. The gravity method is also very slow, as it requires exacting setup and measurement procedures and precise elevation measurements for every measurement station.

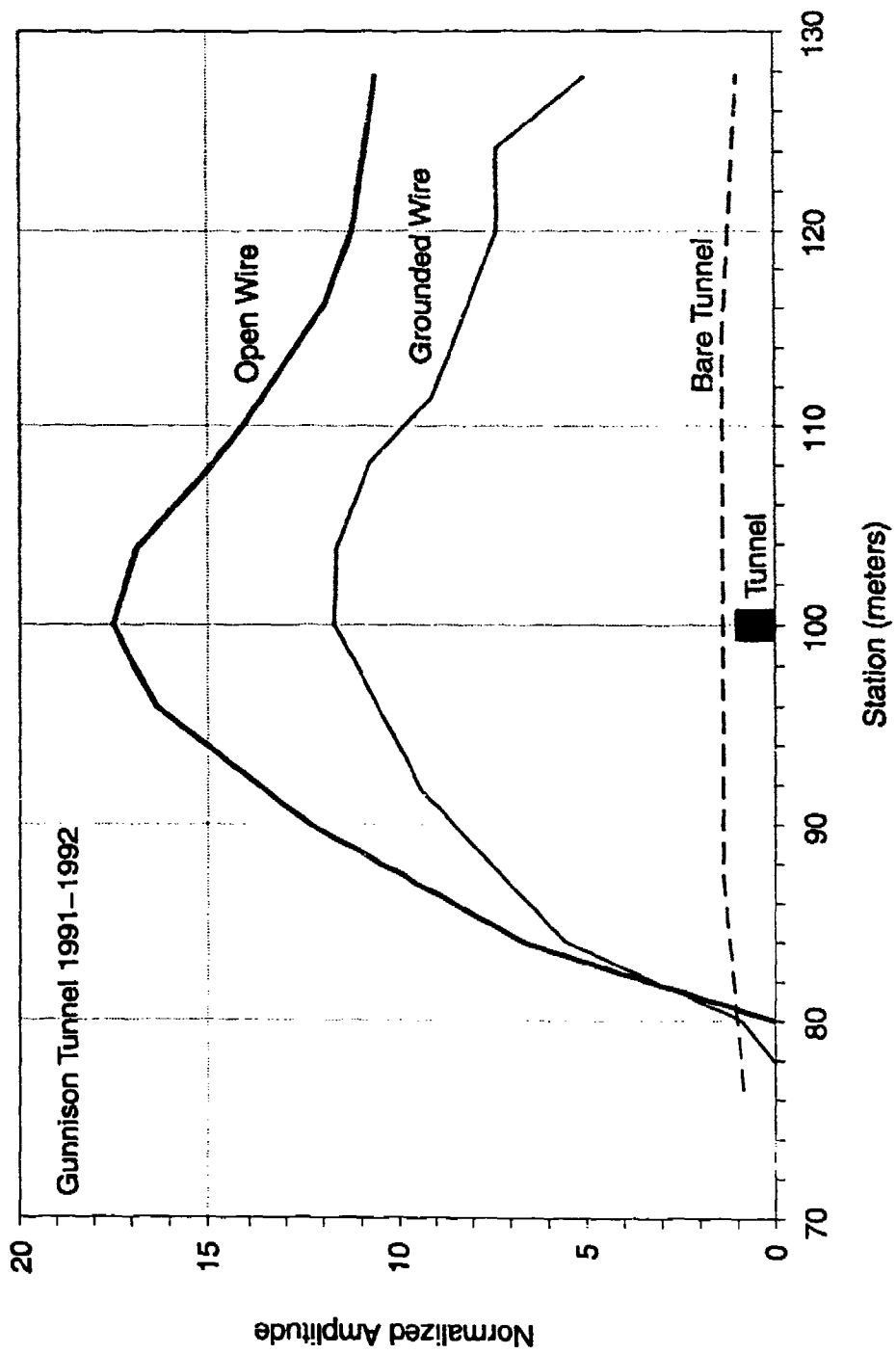


Figure 3. TDEM Survey Over Bare Tunnel and Tunnel with Open and Grounded Wires

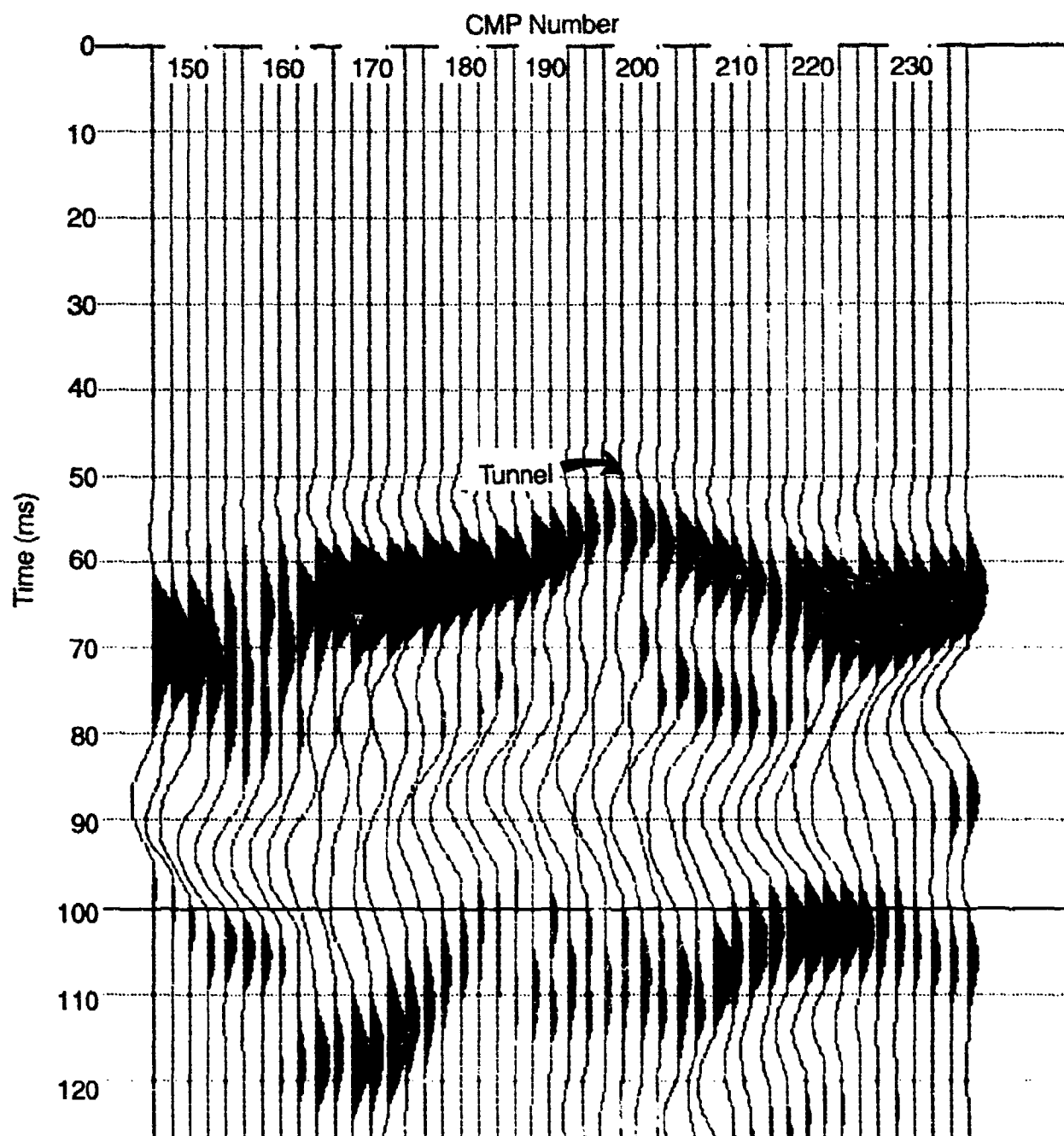


Figure 4. Wiggle-Trace Presentation of Common-Midpoint (CMP) Reflection Seismic Data

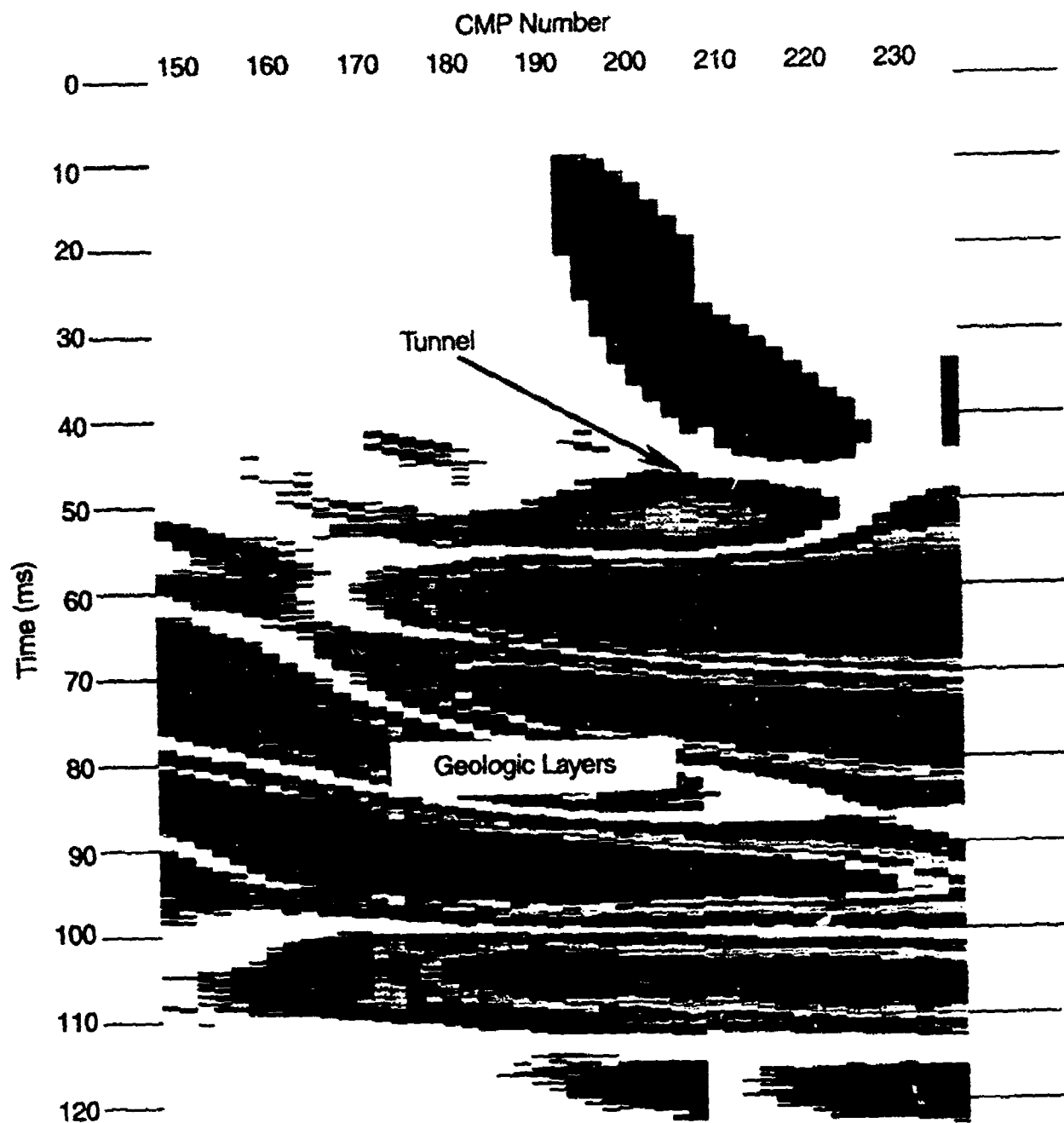


Figure 5. Migrated Common-Midpoint (CMP) Seismic Reflection Survey Results

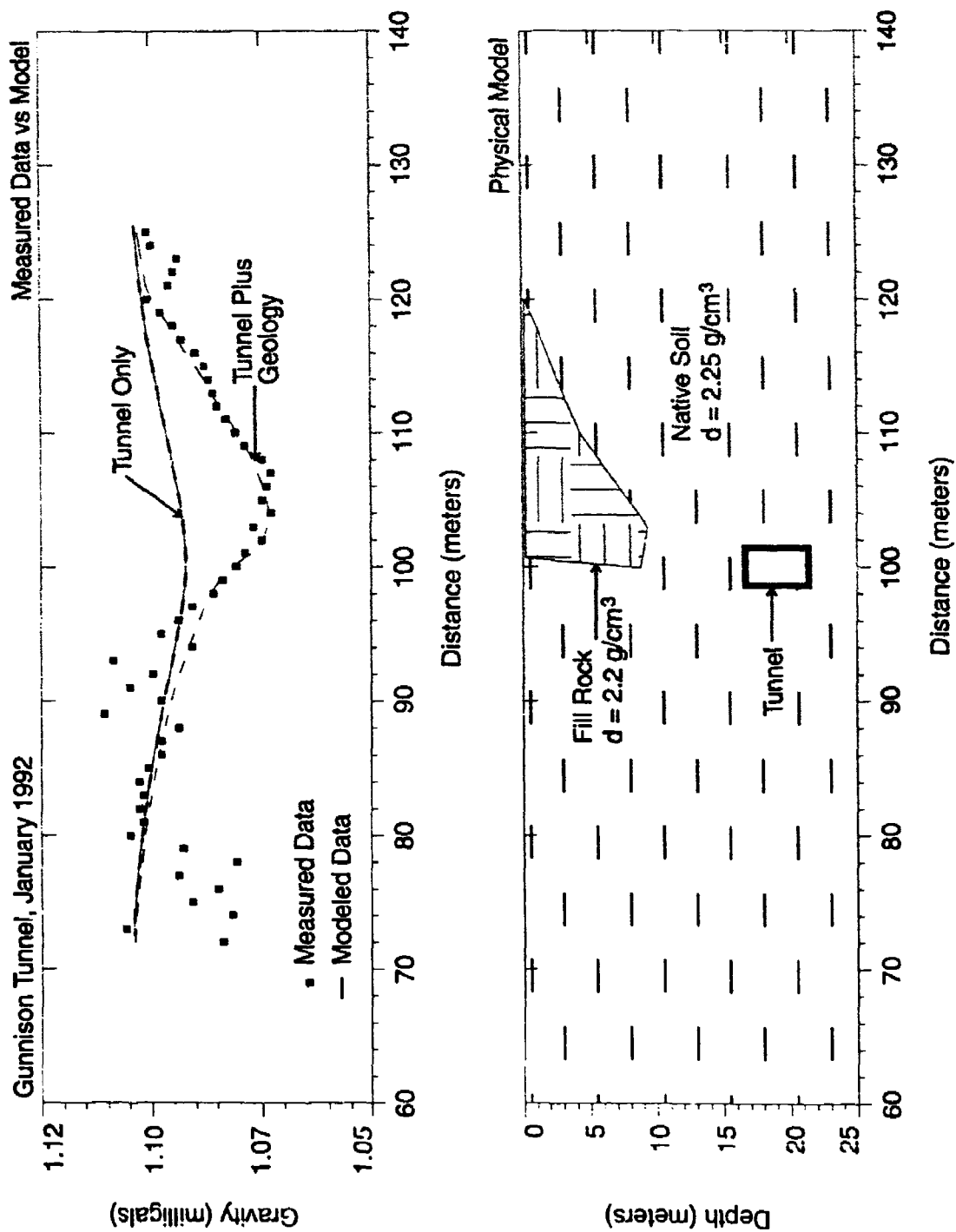


Figure 6. Gravity Data and Model for Gunnison Tunnel Site Line 1

The electrical resistivity method produced a possible tunnel-related response but was not thoroughly tested because of scheduling and access constraints. The electrical method is believed, however, to be viable for the detection of a shallow bare tunnel.

None of the magnetic surveys conducted at the Gunnison Tunnel site produced anomalies that can be interpreted as resulting from the tunnel. The tunnel, which was constructed in the early 1900s, does not appear to be heavily reinforced with steel. Magnetic surveys over the filled area on line 1 showed a contrast between the native soil and the arroyo fill material but did not show an anomaly from the tunnel. Magnetic surveys along lines over the nonfilled area showed only small variations resulting from geologic features and a large response at the location of a 2-m-deep metal drainage pipe which crosses the survey area.

VLF-EM surveys, which were conducted concurrently with the magnetic surveys, did not show any significant responses from the tunnel, but did show responses over the drainage pipe. Figure 7 is a plot of the VLF-EM wave tilt over the tunnel for an open wire and for a grounded wire in the tunnel. Note that the expected enhancement of the response from the conductor in the tunnel (centered at station 100) did not occur. There is a dramatic response at station 48 from the buried metal drain pipe at a depth of 2 m. Factors such as the moderately high soil conductivity (40 mS/m), the 24-m depth, and the large responses from the drain pipe and geological features could be responsible for preventing detection of the conductor by standard VLF-EM methods. Figure 8 is an expanded portion of this survey to demonstrate the classic anomaly recorded over the buried pipe. Note that the field strength (total field) reaches a maximum directly over the conductor and that the inphase, quadrature, and tilt components pass through zero directly over the conductor.

Buried Objects

Surface geophysical methods also can be used to detect and map a variety of buried objects. Magnetic, IEM, and GPR surveys can be very effective in detecting metallic objects. Resistivity/induced polarization, GPR, and seismic methods can be used to detect nonmetallic objects.

Concrete Vault—A 4-ft diameter by 4-ft high cylindrical concrete vault was buried under 1 ft of soil to provide a test target for a variety of geophysical methods. The vault was constructed entirely of nonmetallic materials to make it more difficult to detect. This target was readily detected by GPR, gravity, and seismic methods. Figure 9 shows the results of a 500-MHz GPR scan over the empty vault. The vault signature stands out clearly near the center of the figure.

Figure 10 shows data from a microgravity survey over the empty vault. The resulting gravity profile (squares) compares favorably with that predicted by computer modeling (solid line).

Metal Drum—A single, empty 55-gallon metal drum covered with 3 ft of river-bottom sand/gravel and cobbles was a challenging target to locate precisely but was detected by magnetic, IEM, and GPR methods. Figure 11 is a contour plot from a flux-gate magnetic gradiometer survey. A borehole that was augered at the center of the "bull's-eye" contour pattern contacted the drum, confirming the accuracy of the survey.

Gunnison Tunnel Line 4, 1991-1992
24.0 kHz VLF-EM

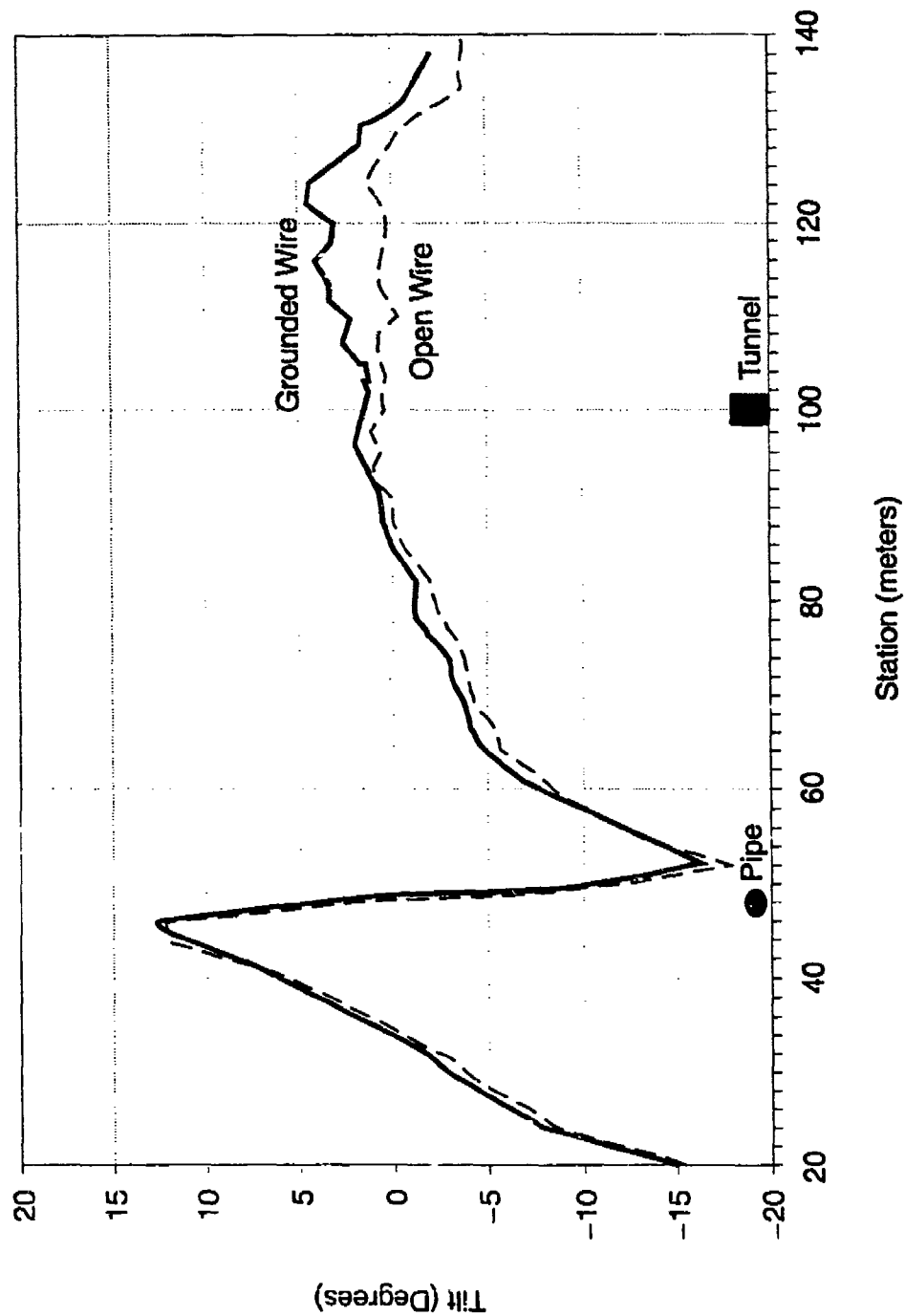


Figure 7. VLF-EM Wave Tilt Over Tunnel with Open and Grounded Wire

Gunnison Tunnel Line 4, 1991-1992
24.0 kHz VLF-EM

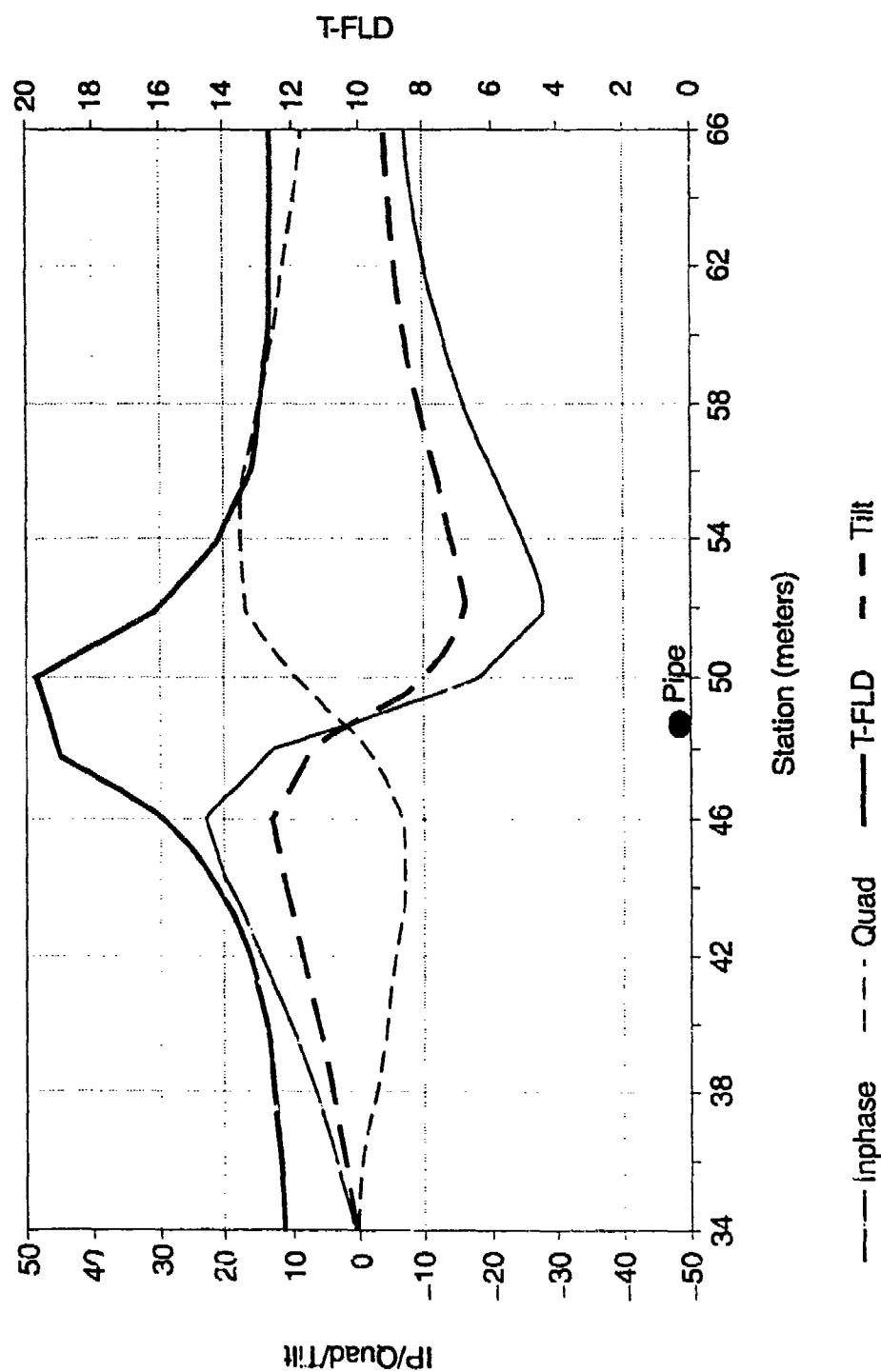


Figure 8. VLF-EM Response Over Buried Metal Drainage Pipe

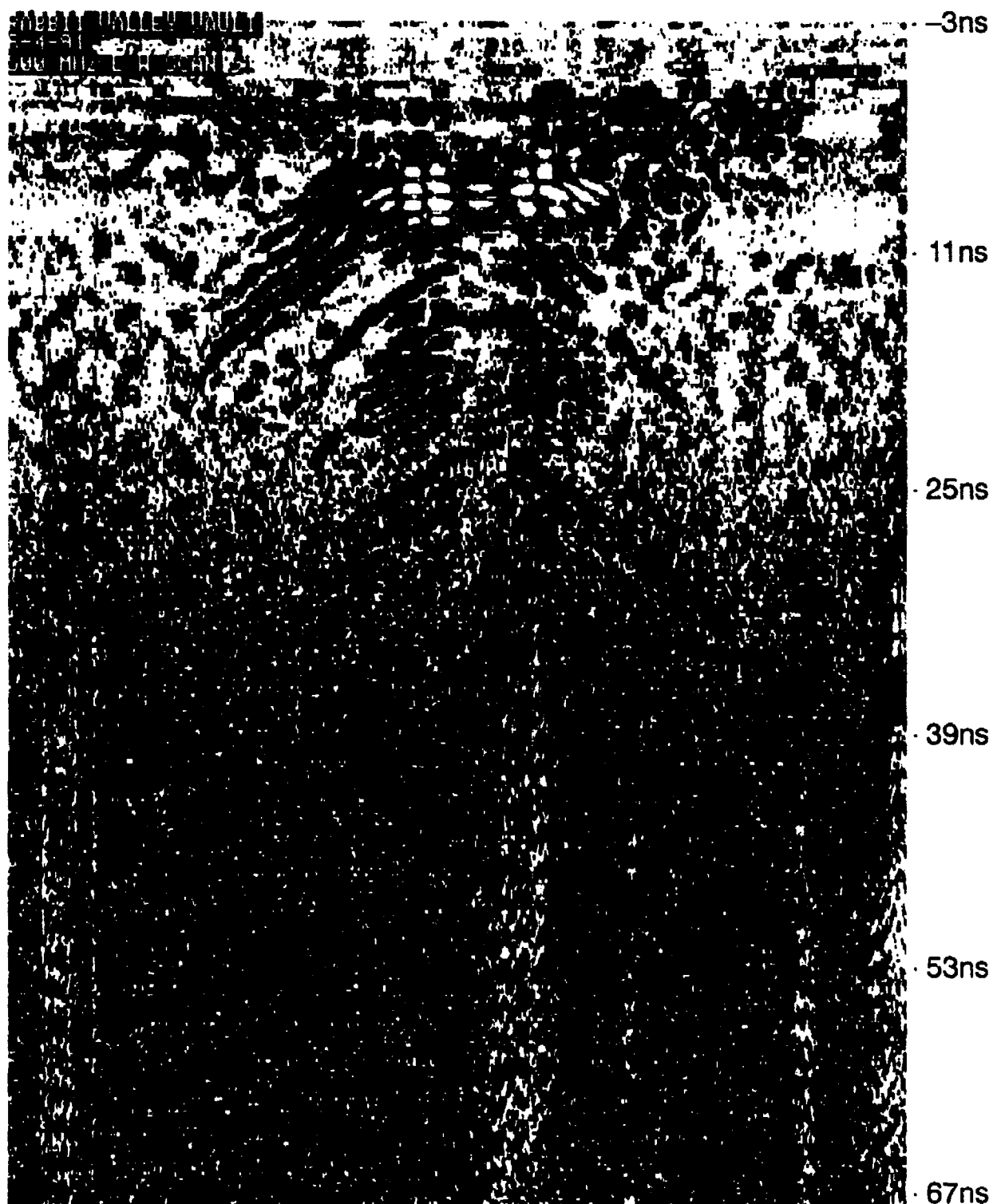


Figure 9. 500-MHz GPR Scan Over Empty Concrete Vault

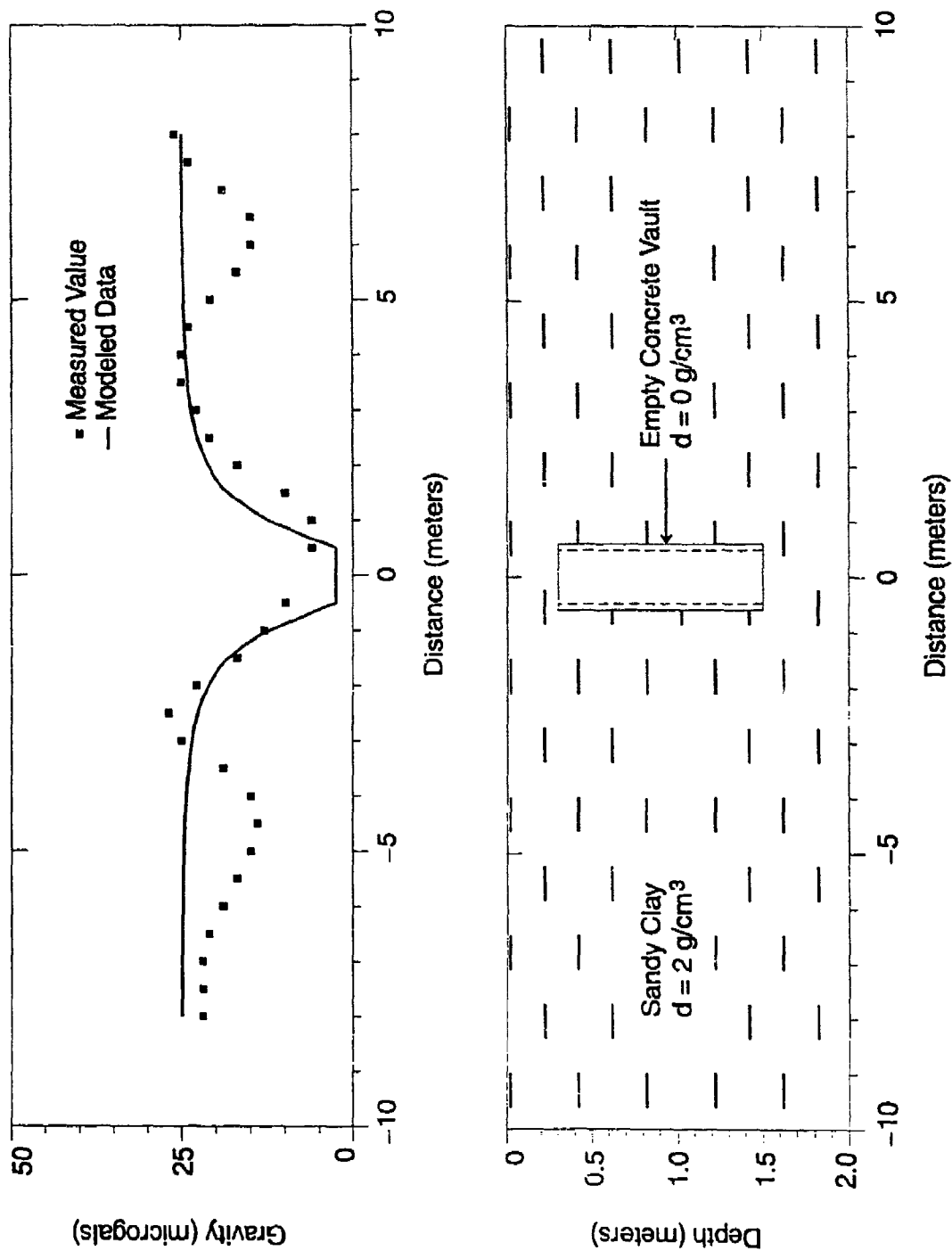


Figure 10. Result of Microgravity Survey Over Empty Vault

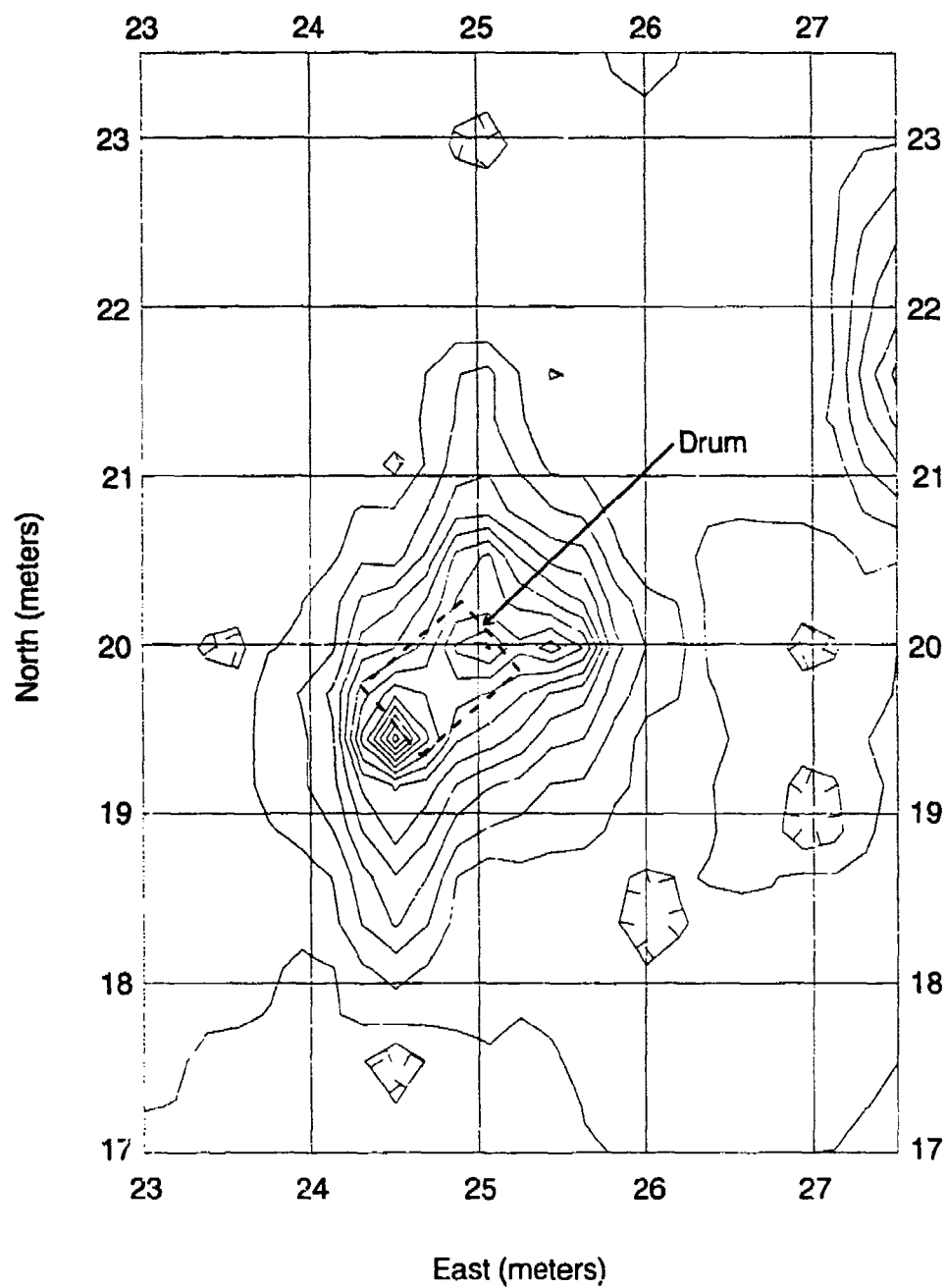


Figure 11. Contour Plot of Flux-Gate Magnetic Gradiometer Survey Over Buried 55-Gallon Drum

PVC Pipe Cache—A 2-ft long piece of 6-inch-diameter PVC pipe was filled with paper to simulate currency, capped, and buried 2 ft under several different soil types to simulate a “money cache.” When buried under a lawn with wet clay soil, the cache was not detectable by GPR. It was, however, detectable by GPR when buried under sand/gravel fill and under sandy natural soil. Figure 12 is an example of the GPR signature from a 500-MHz scan taken perpendicular to the axis of the pipe when covered with 2 ft of sandy natural soil. Note the parabolic signature that is characteristic of a convex surface or point source.

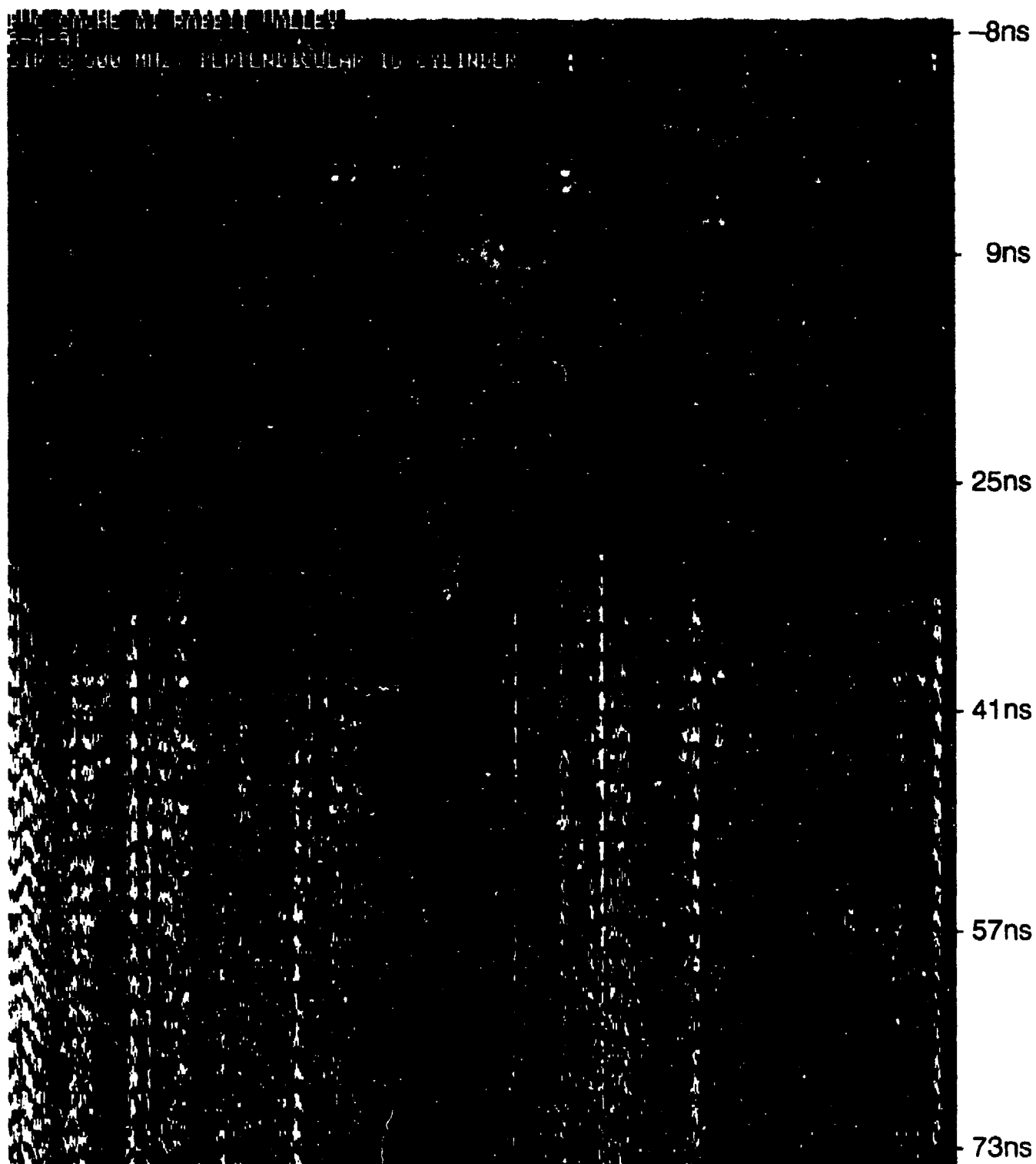


Figure 12. 500-MHz GPR Scan Over PVC Pipe Cache Buried in Sandy Natural Soil

CONCLUSIONS

Surface geophysical methods have been successfully used to detect a variety of buried objects and clandestine tunnels in a variety of geological environments. Carefully planned synergistic methodology combining intelligence information, historical data, computer modeling of suspected target characteristics, and multiple geophysical survey methods has proven to be very effective. No single survey technique has proven to be universally effective.

ACKNOWLEDGMENTS

The work reported in this paper was sponsored by the U.S. Army, Belvoir Research, Development and Engineering Center, Fort Belvoir, Virginia. Work was performed by Chem-Nuclear Geotech, Inc., operating contractor for the U.S. Department of Energy Grand Junction Projects Office, under DOE contract No. DE-AC04-86ID12584. Mr. Ray Dennis, Tunnel Neutralization Team Support Program Manager, provided direction and encouragement. Mr. Larry Ball, Department of Energy Special Programs Manager, provided program guidance and support.

Finally, special thanks go to Messrs. Dickerson, Hasbrouck, Mac Lean, Schwenk, Snyder, Spencer, and Steele of Chem-Nuclear Geotech, Inc., for their help and professional guidance in collecting and interpreting the data.

REFERENCES

- Geophysical Survey Systems, Inc., *Operations Manual, Subsurface Interface Radar, SIR System-3*, pp. B6-B10, Hudson, New Hampshire.
- Breiner, S., 1973. *Applications Manual for Portable Magnetometers*, pp. 28-31, geoMetrics, Sunnyvale, California.
- Hill, D. A., 1988. *Magnetic Dipole Excitation of an Insulated Conductor of Finite Length*, Third Technical Symposium on Tunnel Detection, Golden, Colorado, January 12-15, 1988.

**EXPLORATION CASE HISTORY AND ENGINEERING GEOLOGY
OF "TUNNEL-4", NORTHERN PUNCHBOWL SECTOR,
KOREAN DEMILITARIZED ZONE**

By

**C. P. Cameron
The University of Southern Mississippi
Hattiesburg, MS**

".....One of the first principles of underground warfare is that operations should be carried on with as little sound as possible, so as not to reveal the position of the mines to the enemy....."

".....The noise of the operations was so great, however, that both armies had fairly definite information about the operations of their opponents. In general, the plan was ill-conceived and led to no decisive results....."

- From accounts of the underground war in the hardrock terranes of the Vosges Mountains in "The Use of Geology on the Western Front" USGS Professional Paper 128D, September, 1920 by Alfred H. Brooks

Paper prepared for:

**Fourth Tunnel Detection Symposium on
Subsurface Exploration Technology
Colorado School of Mines
Golden, Colorado**

April 26-29, 1993

ABSTRACT

The Punchbowl is a large topographic basin whose steep northern rim forms part of the southern boundary of the Korean Demilitarized Zone (DMZ) in the rugged Taebaek Mountains of east-central Korea. The potential of this terrain to host clandestine infiltration tunnels of tactical or strategic significance was highlighted by Intelligence studies. Stubbornly determined pursuit of objectives by the Republic of Korea Army Tunnel Detection Section (ROKA-TDS), and the Eighth US Army Tunnel Neutralization Team (EUSA-TNT), resulted in a series of exploration programs which combined percussion drilling and cross-hole geophysics, supported in their latter stages by engineering site geological characterization including core drilling and fracture analysis.

In December, 1989, a coherent crosshole electromagnetic anomaly with a signature indicative of an air filled cavity was recorded by the Korean Advanced Institute for Science and Technology (KAIST) Continuous Wave System in boreholes drilled to follow-up earlier Intelligence studies. The anomaly, detected at a depth of 145 meters, was confirmed as a probable air-filled cavity by the Pulsed Electromagnetic Search System (PEMSS). Natural air filled cavities at this depth were precluded by geological considerations (massive homogeneous granodiorite) and borehole water level elevations. Target evaluation drilling followed and, on 24 December at 0130 hours, a drill bit penetrated "Tunnel-4". EUSA-TNT deployed a borehole television camera that provided clear images of artifacts of human tunnel construction activity. Two and one-half months later Korean engineers, using a Wirth 3-meter TBM (tunnel boring machine), gained entrance to the tunnel and confirmed its nature and purpose.

Subsequent mapping and surveying of the tunnel revealed that the tunnel penetrated approximately 1.1 kilometers into the Republic of Korea from the point where it crossed the Military Demarcation Line (MDL). The tunnel was constructed both in intrusive granodiorite, (similar to that hosting Tunnel-2 and Tunnel-3), and in Precambrian gneisses. Tunnel-4 slopes up to the south at an average grade of 2.3%, ranging from a low of 0.91% to a high of 3.5%. The survey data suggests that the tunnel may contain an invert near its entrance in North Korea. The average dimensions of the tunnel (1.6m x 1.6m) are somewhat smaller than other discovered hardrock tunnels in the DMZ. The tunnel was constructed by drill and blast methods in both the granitic intrusive and precambrian gneiss rock masses. The rock mass rating (Fair-Poor) of the gneisses is significantly less than that of the homogeneous granite (Good-Excellent), but apparently this did not substantially impede tunnel construction; nor did the 8 meter wide fault zone (at the granite gneiss contact) which was negotiated with a minimum of remediation and timbering. Muck removal was accomplished using carts on narrow-gauge rails. This operation was facilitated by side-wall (east) galleries 12-15 meters in length and up to 3m wide located every 150-200 meters along the tunnel.

INTRODUCTION

The Punchbowl is aptly named. It is a large topographic basin whose steep northern rim forms part of the southern boundary of the Korean Demilitarized Zone (DMZ) in the rugged Taebak Mountains of east-central Korea (Figures 1 and 3). Almost circular in plan, the basin has a uniform diameter of about 7.5 kilometers. The floor of the basin has elevations in the 4-500 meter (MSL) range. Summit elevations along the dramatic western and northern rim are in the range 1000-1242 meters, while those of the gentler eastern and southern rims attain elevations of 800-1000 meters. The Punchbowl gained worldwide attention and a prominent place in military history during the latter stages of the Korean War as its high points (especially Kach'il Bong) on the northwest rim were major objectives of "Operation Touchdown"; a campaign that assured that the final lines of demarcation being negotiate at Panmunjon would not follow the original border violated at the 38th parallel. The battle for the Punchbowl was followed by costly victories at similar steep ridges and promitories 9 kilometers to the immediate west (Bloody Ridge, Heartbreak Ridge), and at the Kim 'il Sung Ridge (Baesaksan) a further 9 kilometers in the same direction. With these victories United Nations and ROK forces secured the strategic high ground controlling north-south access routes from the Soyang-Gang to the Pukhan-Gang; and stabilized the northern border of the Republic of South Korea at its current DMZ position.

The objective of this paper is to provide brief summaries of the exploration activities which led to the discovery, confirmation, and entry of Tunnel-4, and to comment on salient aspects of the tunnel's geology and engineering. As such this paper compliments that of George et.al. (1993, this volume), which treats the role of cross-borehole radar in the discovery.

EXPLORATION CASE HISTORY

The potential for the Punchbowl terrain to host clandestine North Korean Peoples Army (NKPA) tunnels was highlighted by allied Intelligence studies during the 1970's. The effectiveness of these early efforts in neutralizing the tunnel threat on the northwest rim of the Punchbowl can be demonstrated from a study of the historic pattern of exploration drilling in the immediate area (see Figure 2-A). The first boreholes drilled in the Punchbowl, K79-1, K79-2, and K79-3, were drilled on a narrow winding road that was in existence for many years as the only low elevation vehicular access on the northwest rim. These boreholes effectively straddled the trend of the tunnel. Drilling in 1980 then filled in the pattern and "fenced-off" the suspect axis. The following facts should be taken into consideration when evaluating the record of events at this site.

- a. A portion of the drilling road is within line of sight from high points (e.g. Hill 1052) along the DMZ in North Korea.
- b. K-1-14 (1980) was drilled directly on trend and only approximately 12-13

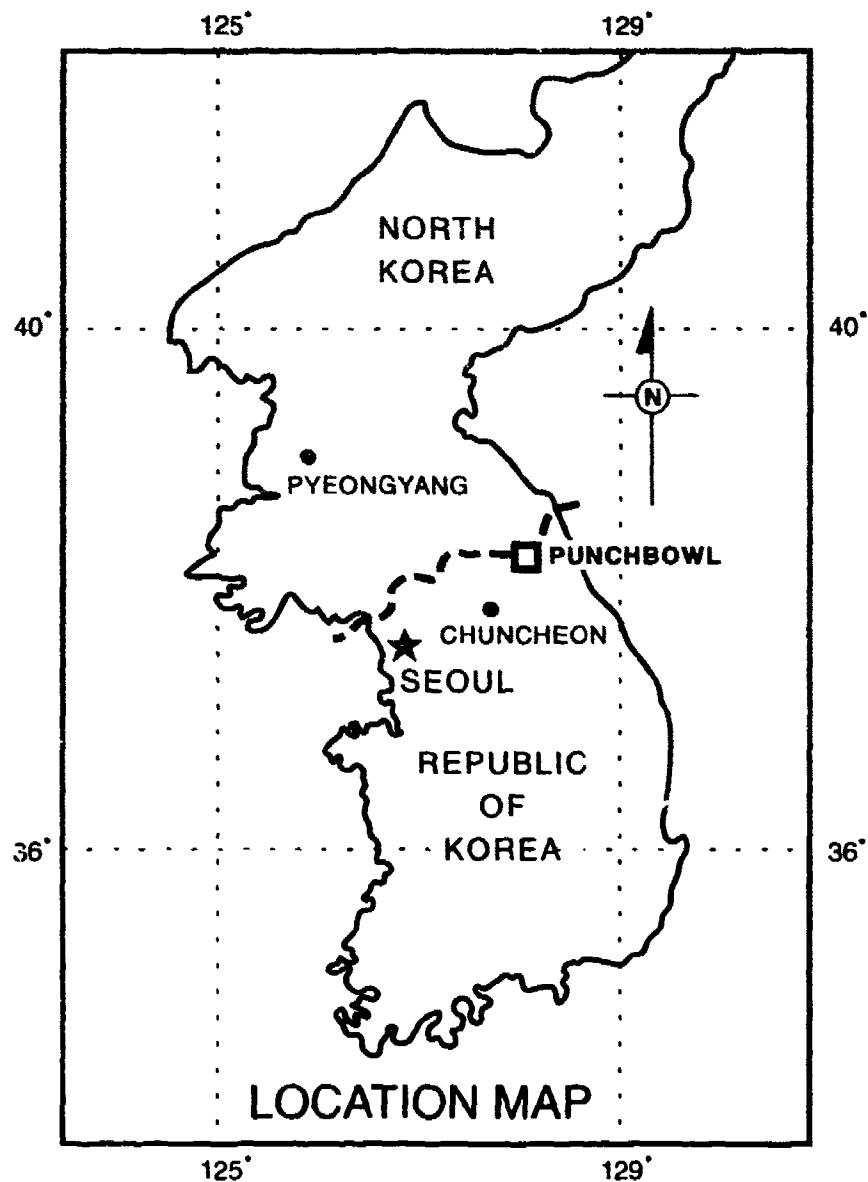


Figure 1. Location Map of the Korean Peninsula showing The Punchbowl situated in the eastern sector of the Peninsula. This region is dominated by the Taebaeksan, a rugged, steeply dissected mountain range which parallels the eastern coast of Korea. From Seoul and Chuncheon the Punchbowl is linked to the local population centers of Yang-ku and Inje by modern sealed roads; enabling tourists to visit Tunnel-4 and the lovely plaza, theater, museum, and monuments erected at the Countertunnel-4 entrance. A small mine train installed in the main tunnel transports the lucky visitor on a short round trip under the southern portion of the DMZ to the vicinity of the MDL.

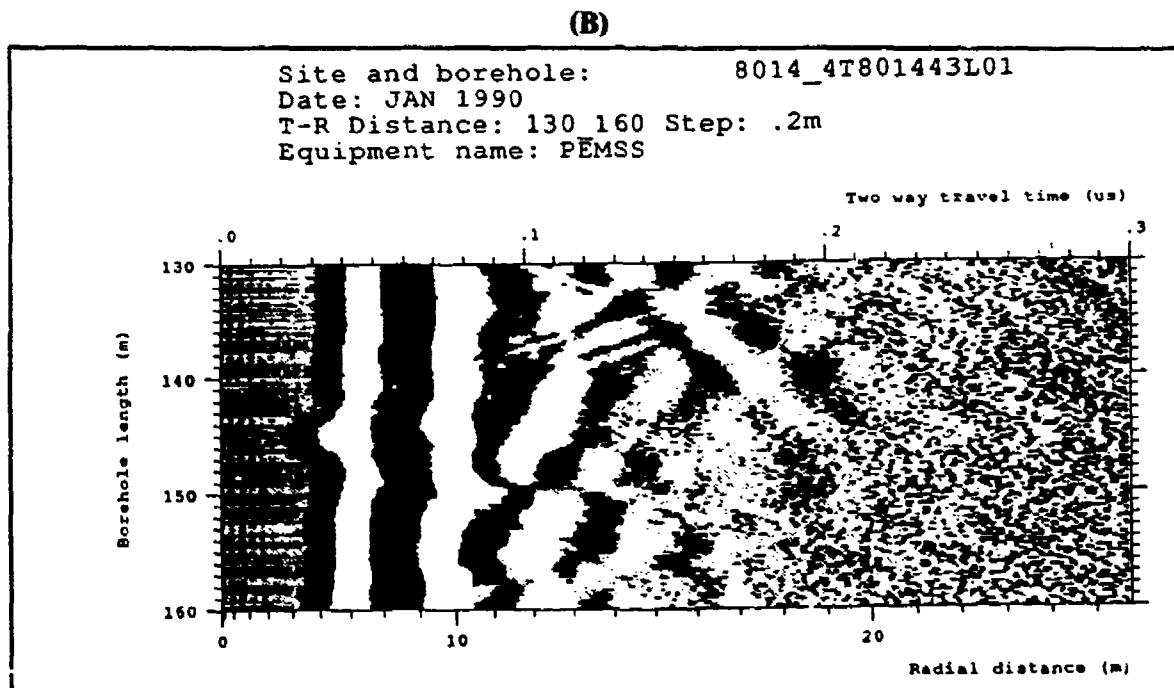
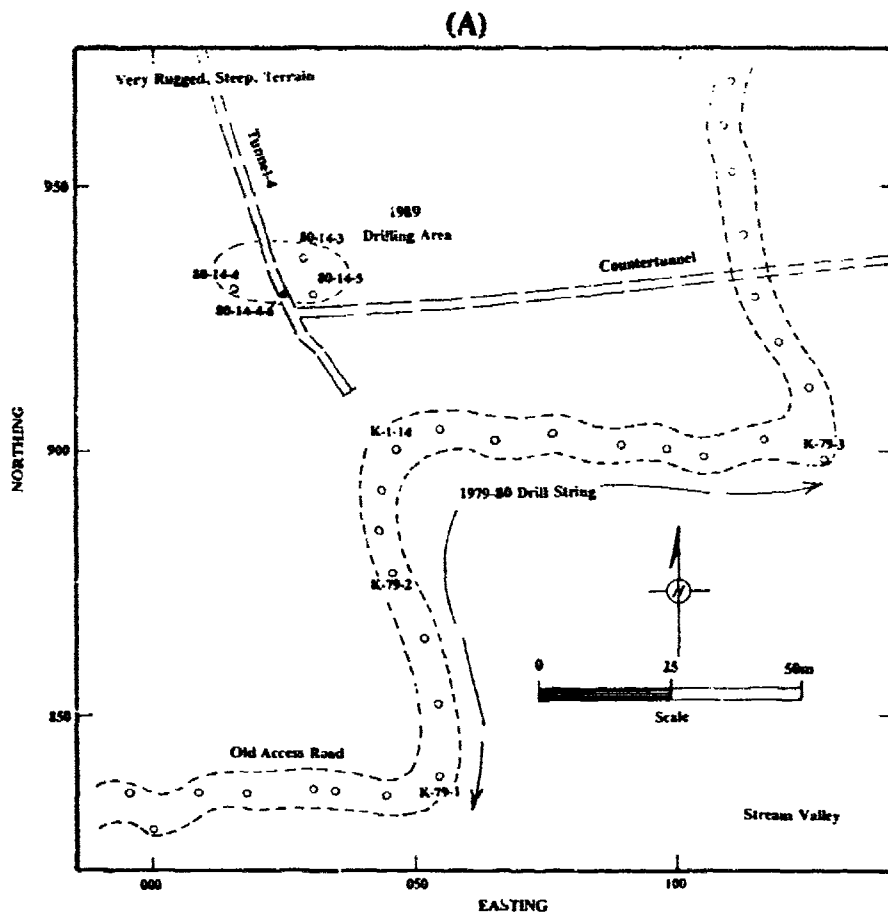


Figure 2. (A) Borehole Location Map of the Fourth Tunnel Area. (B) PEMSS Data Record (Filtered) for Borehole Pair 80-14-4 to 80-14-3, Level Run.

meters southeast of the end of the tunnel.

c. The terrain immediately which flanks the original drill road is very steep; particularly up-slope to the northwest.

d. The tunnel bearing shifts about 7° counterclockwise (to a more easterly direction) in its final 25 meters; and its gradient steepens sharply to about 4%.

From these observations one might draw the following conclusions, albeit that they are at this time still somewhat speculative:

1. The NKPA responsible for the construction of this tunnel somehow had knowledge of the ROKA borehole placement and drilling; and "saw" or anticipated that the drills were being ordered into position(s) directly "on-axis" with their tunnel; and/or,
2. The NKPA personnel underground constructing the tunnel actually heard the startling sound of drills nearby searching for them; and/or,
3. The capture of NKPA Third Tunnel in 1978 resulted in a significant shift in NKPA thinking with respect to the advisability of further construction of tactical tunnels under the DMZ.

Whatever the reason for the NKPA stopping their tunnel where and when they did, the aforementioned shift in direction of the tunnel over its last 25 meters or so is interesting and worthy of further discussion; particularly since underground mapping established that the directional shift was not occasioned by a change in rock quality or condition. Two possibilities are suggested. The first is that the tunnel was swinging to its breakout position; probably about 300 meters to the southeast; and commencing to develop two or more splayed branches. The second is that the NKPA were trying to avoid the straddling effect of the 1979 boreholes. The latter possibility requires that the NKPA had the drill site under observation.

Stubbornly determined pursuit of objectives by the Republic of Korea Army Tunnel Detection Section (ROKA-TDS), and the Eighth US Army Tunnel Neutralization Team (EUSA-TNT), resulted in a series of exploration programs which combined percussion drilling and cross-hole geophysics. The drilling program commenced in the Spring of 1989 was also supported by engineering site geological characterization including core drilling and fracture analysis. The success of this program, now a matter of historical record, was highlighted by the following key operational events:

1. In December, 1989, a coherent cross-hole electromagnetic anomaly with a signature indicative of an air filled cavity was recorded by the Korean Advanced Institute for Science and Technology (KAIST) Continuous Wave System in boreholes drilled to follow-up earlier Intelligence studies.

2. The anomaly, detected at a depth of 145 meters, was confirmed as a probable air-filled cavity by the Pulsed Electromagnetic Search System (PEMSS).

3. Natural air filled cavities at this depth were precluded by geological considerations (massive homogeneous granodiorite) and borehole water level elevations.

4. Target evaluation drilling followed and, on 24 December at 0130 hours, a drill bit penetrated "Tunnel-4".

5. EUSA-TNT deployed a borehole television camera that provided clear images of artifacts of human tunnel construction activity, (jackleg drill rod scars on the tunnel walls, rail ties, etc).

6. Two and one-half months later Korean engineers, using a Wirth 3-meter TBM (tunnel boring machine), gained entrance to the tunnel and confirmed its nature and purpose. The borehole TV once again played a significant role in that it was able to provide continuous coverage of the tunnel as the TBM broke through.

7. Inspection and clearing of the tunnel was accomplished by a ROKA reconnaissance team who suffered the loss of their mine-sniffing dog when he triggered a hidden mine under shallow water pooled in the vicinity of the MDL.

GEOLOGY

General Setting.

Accounts of the historical geology of central Korea document a 2.8 billion year record, often incomplete, of repeated cycles of sedimentation, metamorphism, orogeny, and igneous intrusion. The interested reader is referred to the treatise, "Geology of Korea" (ed. Lee Dai-Sung, Geological Society of Korea, 1987), for thorough and well-referenced summary of the geological evolution of the Korean Peninsula.

The Punchbowl area is underlain by Kyonggi Metamorphic Basement Complex (early Precambrian) gneiss and migmatite (mixed metamorphic and partially melted phases) which were uplifted during the diapiric intrusion of a Bulguksa or Daebo granitic stock (Late Cretaceous or Jurassic respectively); resulting in the creation and/or reactivation of a ring and radial fault pattern. The roof of the stock was stripped by erosion and/or crypto-volcanic venting of the intrusive mass. Apparently, the intrusive granite, being more prone to weathering and erosion by virtue of its composition, mode of emplacement, and crystallization history, preferentially eroded to create a bowl-like topographic basin rimmed by the resistant Precambrian gneiss. An alternate interpretation of the Punchbowl is that it represents an impact structure. This interpretation lacks evidence (other than compelling terrain features) at present; and requires acquisition of radiometric age dates and certain petrographic data to attain credibility.

What ever the origin of the Punchbowl, regional geological analysis suggest that the entire area, including terranes across the MDL in North Korea, is underlain by granites below elevations of 3-400 meters (MSL). Details of the geology of the northern half of the Punchbowl are illustrated on the geologic map and cross sections illustrated in Figures 3 and 4, both of which include the longitudinal section of Tunnel - 4. The geology of Tunnel-4 and Countertunnel - 4 is illustrated in Figures 5 (A) and 5(B).

Lithology and Structure

Kyonggi Gneiss Complex. Kyonggi Gneiss Complex rocks rimming the Punch Bowl are in contact with intrusive "Punchbowl Granite" at elevations above 900 - 1000 meters along the western, northwestern, and northern rims; and variable elevations in the range 550-900 meters along the northeastern and eastern rims. These rocks comprise a suite of high-grade (probably amphibolite and upper amphibolite facies) paragneiss and orthogneiss. Cameron, (1990), mapped the northern Punchbowl in 1989 and developed the following classification scheme for field mapping and descriptions at detailed scales in the study area:

a. Foliated porphyroblastic and banded paragneiss. Typically comprising a quartz-feldspar-biotite-garnet (hornblende) paragenesis, this is common rock in the study area and , volumetrically, probably makes up 50-80 percent of the percent of the paragneiss section at any given location along the western and northern Punchbowl rims.

b. Migmatites. Commonly, quartzose and quartzo- feldspathic gneisses are intimately associated with amphibolitic and mafic varieties; the resulting admixed assemblage forming a classic migmatite ("mixed rock") terrane. The migmatites are commonly characterized by fine banding or lamination (lit-par-lit fabrics).

c. Granitic Orthogneiss. These rocks are generally non- foliated, lineated, porphyroblastic (2cm-12cm porphyroblasts), crystalline gneisses with a biotite-garnet-plagioclase mineralogy. The plagioclase is commonly gray and twined with possibly a high anorthite content. Partial melting of calcareous metasediments could produce such a mineral assemblage. These rocks form an extensive outcrop belt along the eastern side of the Punchbowl.

The gneiss exhibits a considerable range of textures (from very coarse to medium-grained). An equally diverse suite of fabrics includes large-scale banding, lit-par-lit (Fr. "Leaf-by- Leaf") structure, augen phyroblasts, boudinage (indicating extensional strains during folding), ptigmatic folding and veining (indicative of contractions during similar events). Strong lineation characterizes the orthogneiss which forms the terrane along the eastern rim of the Punch Bowl. Where affected by faulting and shearing the gneiss is commonly phyllonitized, mylonitized, or cataclastized (terms which denote smearing, granulation, crushing, mineral alteration and recrystallization, in zones of maximum stress and rock mass displacements).

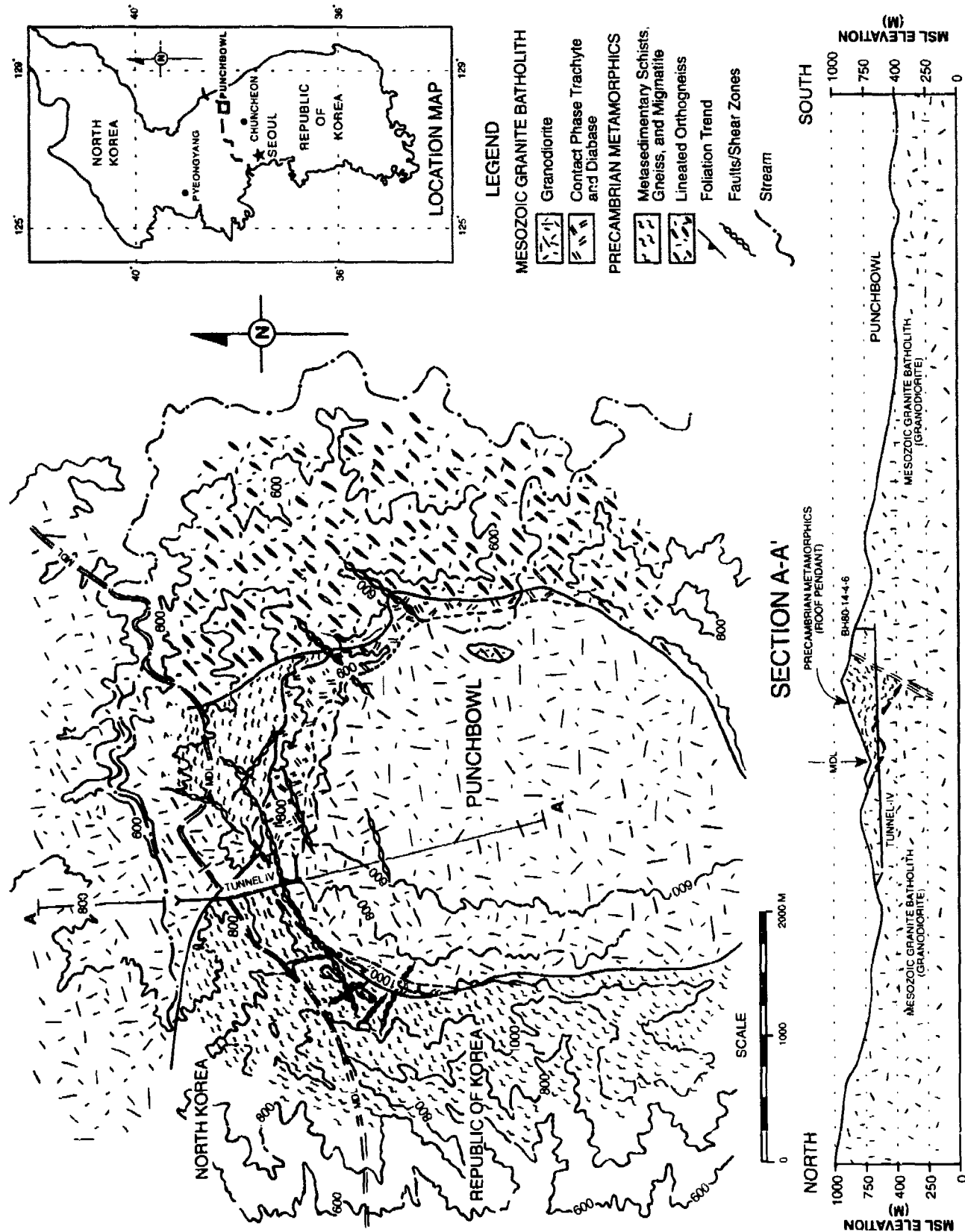


FIGURE 3. GEOLOGIC MAP - PUNCHBOWL AREA

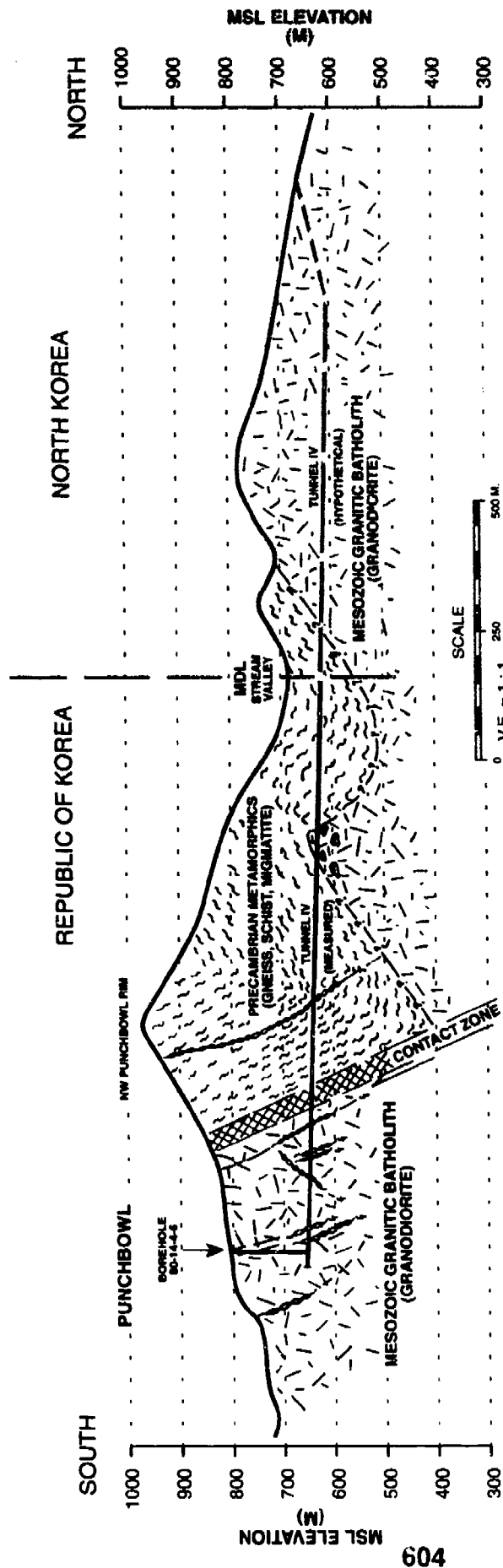
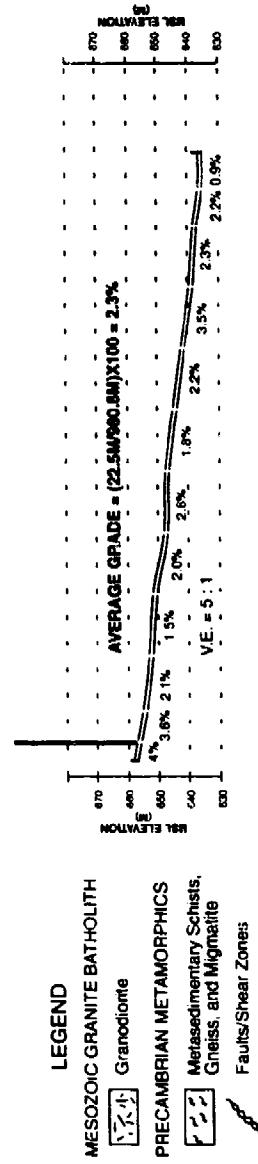
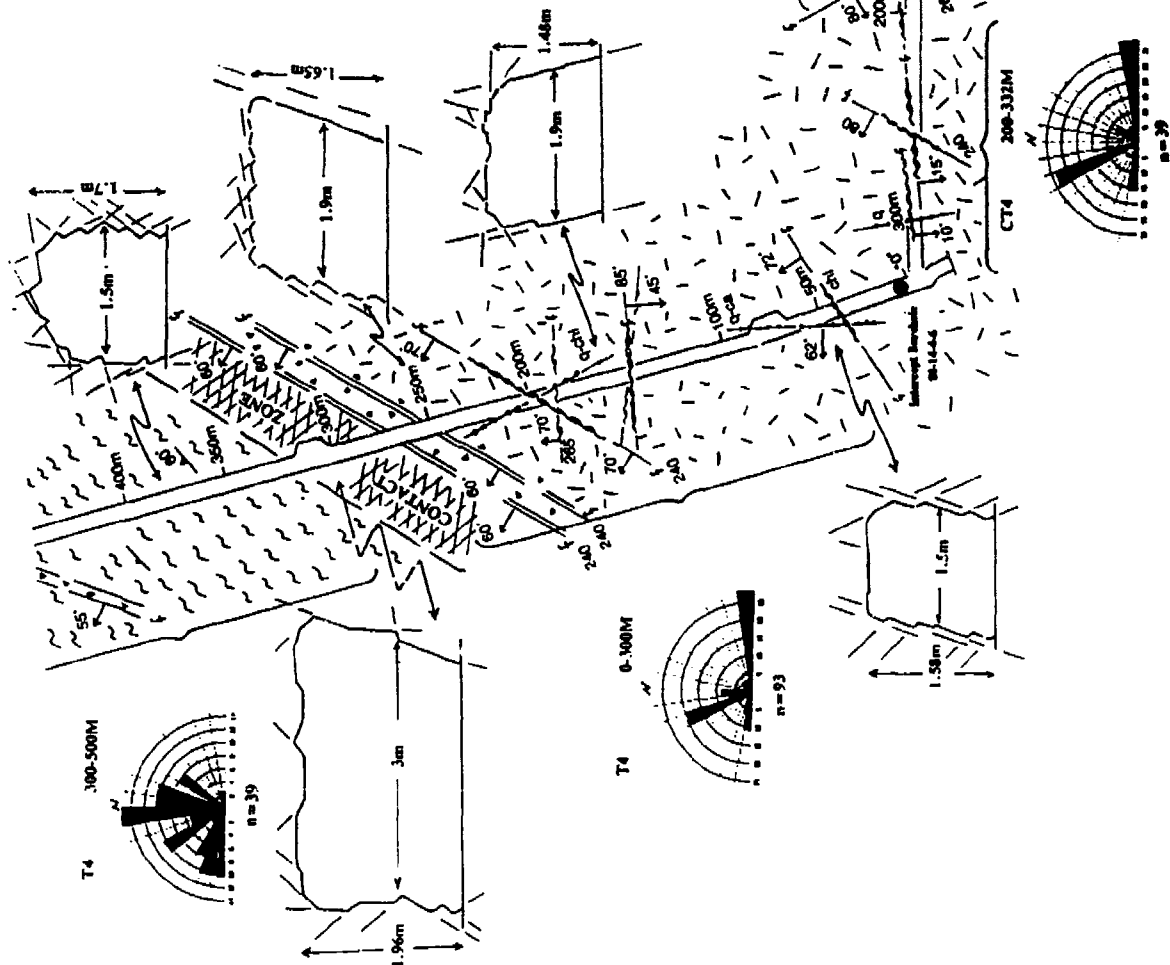
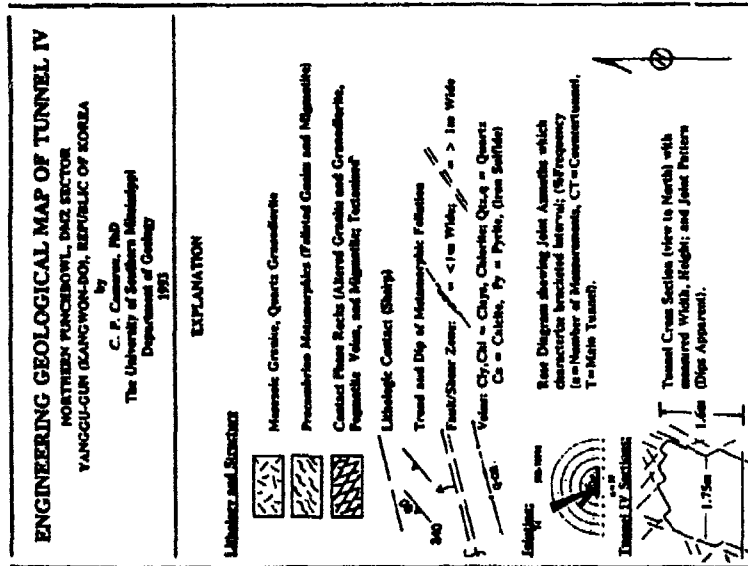


FIGURE 4.
TOPOGRAPHIC AND
GEOLOGIC PROFILE
TUNNEL IV

NORTHERN PUNCHBOWL, DMZ SECTOR
 YANGGU-GUN (KANGWON-DO), REPUBLIC OF KOREA
 C.P. CAMERON, USM
 MAY, 1991





SCALE
 (Note: Tunnel width amplified; see cross sections)

Figure 5(A). Engineering Geological Map of the southern part of Tunnel-4

ENGINEERING GEOLOGICAL MAP OF TUNNEL IV

NORTHERN PUNCHBOWL, DMZ SECTOR
YANGGUGUN (KANGWON-DO), REPUBLIC OF KOREA

by
C. P. Cameron, PhD
The University of Southern Mississippi
Department of Geology
1993

EXPLANATION

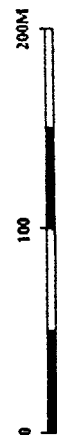
Lithology and Structures

- Mesozoic Granite, Quartz Granodiorite
- Precambrian Metamorphics (Foliated Gneiss and Migmatite)
- Contact Phase Rocks (Altered Granite and Granodiorite, Pegmatite Veins, and Migmatite; Tectonized)
- Lithologic Contact (Sharp)
- Trend and Dip of Metamorphic Foliation
- Fault/Shear Zone: $\leq 1m$ Wide; $\geq 1m$ Wide
- Veins: Cly, Chl = Clays, Chlorite; Qtz, q = Quartz
Ca = Calcite, Py = Pyrite, (Iron Sulfide)

Rose Diagram showing Joint Azimuths which characterize bracketed interval; (% Frequency (n = Number of Measurements, CT = Countertunnel, T = Main Tunnel).

Tunnel IV Sections:

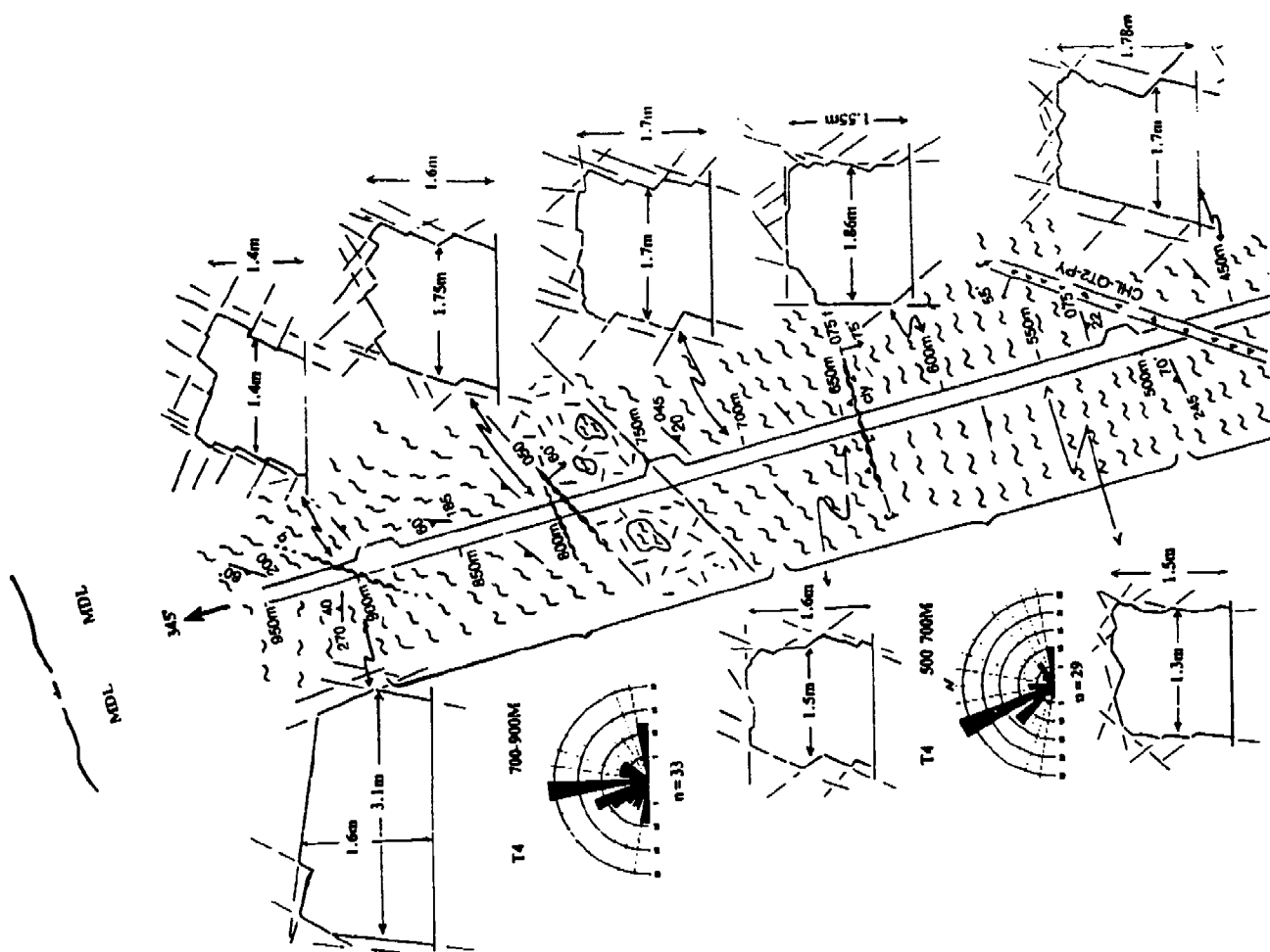
Tunnel Cross Section (view to North) with measured Width, Height, and Joint Pattern (Dips Apparent).



SCALE

(Note: Tunnel width amplified; see cross sections)

Figure 5(B).



Cameron's (1990) analysis of foliation orientations along the northern and northwestern Punch Bowl rim revealed that short wave length - low amplitude folding along NNE-SSW and N-S plunging fold axes is common in the paragneisses. Foliation dips vary widely; from low to very steep with pronounced steepening and even overturning of fold limbs in zones disrupted by faulting. In these fault zones the noses of the folds are commonly "sheared out" by axial plane faults which trend ENE-SSW, or are "cut-off" by ENE trending faults. This structural style is very common along the steep and broken ridges between the Punchbowl and the Pukhan-Gang. At least one episode involving longitudinal strain in an uplifted and buckled layer of Kyonggi gneisses resulted in the development of concentric fold structures. These folds were apparently superimposed on earlier fold structures but this is difficult to document in the immediate study area. The strong compressive strains perpendicular to layering predicted by this model are manifested in steep "strike" joint sets, severe internal deformation attributed to flexural slip along foliation planes or layers, small sub-parallel tension fissures ("gashes"), and slaty cleavages observed near some fold hinges. Late strain increments led to the development of small thrust faults whose planes may have been involved in the folding. Finally, the intrusion of the "Punch Bowl Granite" activated and/or reactivated high-angle reverse and normal faults which form a ring and radial pattern around the margin of the stock.

Where the gneiss is affected by faulting, a gouge zone of variable thickness (0.3-3.5 meters), occasionally accompanied by sheared leucocratic dike rocks or cataclastized gneiss, is generally present, (Figure 12). The latter situation is particularly characteristic in fault zones which control the margin of intrusive Punchbowl Granite. The lithological and mineralogical composition of the gouge is a function of the mineral composition of the rocks disrupted by the fault zone, and of the chemistry of the groundwater which has episodically entered the fault zone and interacted with the affected lithologies.

Foliation, joint, and fault planes were measured at over 100 surface outcrop stations in the northern Punchbowl, as well as at intervals along Tunnel-4. The latter are shown in (Appendix A). Analysis of this data clearly indicates that the trend of a substantial number of faults, shears, veins and dikes which transect the gneiss complex, is controlled by the trend of the foliation in the metamorphics. In most of the northern Punchbowl this trend is N5-15E with moderate-steep dips. Quite the opposite is true of the intrusive Punchbowl Granite terrane. The predominant fault trend in the granites appears to parallel that of a major joint set which strikes N70-90E. This trend is also present in the metamorphics but to a lesser degree than in the granites.

Failure along foliation planes in the metamorphics was probably aided by zones of graphite and chlorite whose low shear strength facilitates their behavior as fault plane "lubricants". In summary, faults which offset the gneiss complex commonly have phyllonitic gouge zones composed of finely crushed, smeared, and macerated rock fragments, sericite, chlorite and/or biotite, other clays and occasionally graphite. In some cases, pinch-and-swell quartz veins with true thicknesses of up to 1.0 meters occupy phyllonitic fault zones. Some of the gneisses are recrystallized where brecciated

by faulting; the breccias healed by an intricate network of small quartz "stringer veins" (generally less than one centimeter in width). Cameron (1990) documents core studies immediately adjacent (to the northeast) of Tunnel-4 which revealed broken healed breccias in the faulted intrusive contact bounding the gneisses and the Punchbowl Granite (exposed at 300-315 meters north of the countertunnel intercept in Tunnel-4). These breccias were ruptured and sheared-out by fault re-activation, possibly during emplacement of the "Punchbowl Granite" to its present structural level.

Punchbowl Granite. The term "Punchbowl Granite" was used by Cameron, (1989) to define the massive, jointed, medium-coarse grained, biotite-hornblende granite and granodiorite pluton which forms the lower slopes and floor of the Punch Bowl. Larger intrusive granite masses occupy terranes to both the north and south and apparently connect, via petrogenetic continuity or intrusive-fault contact, with the Punchbowl Granite at depth. The large intrusive mass to the south and west occupies most of the ample, wide valley which trends north and east from Yanggu. Only a narrow ridge of Kyonggi Gneiss separates this mass from the Punchbowl Granite. The large intrusive mass to the north of the Punch Bowl, in North Korea, is similarly separated from the "Punch Bowl Granite" by a ridge of gneisses which outcrop at elevations in the 700-1200 meter range.

The intrusion of the Punchbowl Granite and (perhaps) the granitic intrusive masses to the north and south, may be part of the Bulguksa Event, a late Cretaceous orogenic pulse which was characterized by widespread explosive volcanism, crypto-volcanic activity, and granitic intrusion. The Punchbowl Granite is comprised of two recognizable petrological phases, although sometimes their relationship is blurred and transitional in the field:

a. A main intrusive phase comprised of medium and coarse-grained leucocratic, gray, biotite-hornblende granodiorite and subordinate granite. Where observed in Countertunnel - 4 the granodiorite contains common (and occasionally abundant) mafic, rounded, fine-grained xenoliths commonly 10-40 cm in diameter.

b. A marginal contact phase, also intrusive, comprised of fine-medium grained hornblende granodiorite and trachyte, and dark hornblende-biotite-pyroxene diabase and diorite. The latter appear to occur as sills and dikes marginal to the main intrusive phase.

As revealed in surface and subsurface mapping portions of the northwestern and northern margins of the "Punch Bowl Granite" are fault-controlled. It is notable that faulting combined with erosion apparently controls the elevation and position of the Punchbowl Granite as it trends into North Korea through the topographic saddle that splits the northern rim. This is the only locale in the study area where outcrop continuity of the Kyonggi Gneiss Complex along the rim is broken by the Punchbowl Granite.

Tunnel - 4 Construction Features and Rock Mass Properties

Mapping and surveying of Tunnel - 4 revealed that the tunnel penetrated approximately 1.1 kilometers into the Republic of Korea from the point where it crossed the Military Demarcation Line (MDL). As is illustrated in Figures 3, 4, and 5, the tunnel was constructed both in intrusive granodiorite, (similar to that hosting Tunnel-2 and Tunnel-3), and in Precambrian gneiss and migmatite.

Tunnel-4 slopes up to the south at an average grade of 2.3%, ranging from a low of 0.91% to a high of 3.5%, (see Figure 4). The survey data suggests that the tunnel may contain an invert near its entrance in North Korea. However, this suggestion is tenuous at best and should be used with due caution. The elevation control at Borehole 80-14-4-6 is based on PADS, a vehicle-mounted automatic survey system used generally for artillery surveying. The PADS system uses a different geodetic datum than that on which the 1:25,000 map sheet of the area is contoured. The latter was used to estimate the elevation of the suspect entrance in North Korea. Previous experience has demonstrated that PADS elevations can differ by 20-30 meters from those estimated from the contoured map sheets. Furthermore, it can be easily demonstrated that the map sheets themselves often have errors which can amount to 20-40 meters. Discrepancies of this magnitude could, over the distance of the tunnel, significantly affect the longitudinal configuration and remove the need to draw an invert near the entrance.

Visual aspects of Tunnel-4 are shown in the accompanying photo figures. The average dimensions of the tunnel (1.6m x 1.6m) are somewhat smaller than other discovered hardrock tunnel in the DMZ. The tunnel was constructed by drill and blast methods in both the Mesozoic granitic intrusive and Precambrian gneiss rock masses. These rocks are hard and very hard (compressive strengths in the 20-30,000 psi range). Most discontinuities are wide-moderately wide joint planes which have rough, interlocking asperities, and are filled or partially filled with clays and quartz-calcite veinlets. The ground-water condition is generally wet-dripping, and occasionally flowing at fault contacts or where discontinuity fillings are washed out. It should be noted that the groundwater condition is highly variable; very much dependent on local precipitation and seasonal variations.

The rock mass rating, estimated using methods developed by Bieniawski, (1979, 1989), and Gonzalez de Vallejo, (1983), is "Fair-Poor" in the gneisses; significantly less than in the homogeneous granite (Good-Excellent). However, the rock quality and condition in the metamorphics did not substantially impede tunnel construction; nor did the 50 meter wide intrusive-fault zone at the granite/gneiss contact. This zone was negotiated without remediation and timbering. A significant 8 meter wide fault severely disrupts the metamorphic section at about 480 meters along the tunnel. Although the rock mass is very altered and ostensibly lacks quality, the zone was crossed and supported with a minimum of timbering and remediation. Tunnel stability was aided by the fact that the fault zones are occupied by broken rocks with substantial build-ups of the alteration clay mineral chlorite in the matrix of the rock mass. While soft and

prone to failure by shear, the chlorite served to seal permeability in these zones. Water inflow is minimal except in very local situations at the fault contact(s).

A steep, wide-spaced, joint set which trends NNW follows the general bearing of the tunnel. As is shown on the Tunnel Cross Sections (Figure 5) these joints form even, unbroken walls in many cases, a factor which lends stability to a tunnel of small dimension.

Muck removal was accomplished using carts on narrow-gauge rails. This operation was facilitated by side-wall (east) galleries 12-15 meters in length and up to 3m wide located every 150-200 meters along the tunnel. Loaded rail carts were sidetracked into the galleries, allowing empty carts to access the working face.

CONCLUSIONS

- o The discovery of Tunnel - 4 demonstrated the effectiveness of Continuous Wave (CW) and pulsed electromagnetic search systems (PEMSS) in the location and definition of deep hardrock tunnels. Confirmation of human construction activity by borehole television camera was a resounding technical success, as was the TBM counter-tunneling operation.
- o Tunnel - 4 is 2.1 kilometers long from its suspect entrance and undergoes several (small) clockwise shifts in bearing relative to true north. The tunnel slopes up to the south at an average grade of 2.3% (0.91% - 3.5%) and may contain an invert near its entrance in North Korea.
- o Although it was once again observed that, "Tunnels are most easily found where they are most easily constructed", Tunnel-4 was constructed through both granitic and metamorphic rock masses, (unlike previously discovered DMZ tunnels which are hosted entirely in the former lithology).
- o The average dimension of Tunnel-4 (1.6 m x 1.6 m) is less than that of other discovered DMZ tunnels; however, Tunnel - 4 contains more sidewall galleries (where the width doubles) to facilitate muck removal.
- o The fact that the rock mass rating in the metamorphics (Fair - Poor) is significantly less than that of the granite (Good - Excellent) apparently did not substantially affect tunnel construction activity which was conducted by drill and blast methods with a minimum of timbering. In a manner very analogous to the situation at Tunnel-2, the walls of Tunnel - 4, are frequently formed by a steep, easterly dipping, north-northwesterly trending master joint set. This structural feature enhances rock mass quality and substantially reduces support requirements.
- o Rock mass rating and classification schemes currently in use may yield overly

pessimistic results with respect to construction difficulty and support requirements for tunnels less than two meters in diameter.

BIBLIOGRAPHY

Bieniawski, Z. T., 1975, "The Point-Load Test in Geotechnical Practice," Engineering Geology, vol.9, pp.1-11.

_____, 1979, "Tunnel Design by Rock Mass Classifications," Technical Report GL-79-19, US Army Engineer Waterways Experiment Station, Vicksburg, Miss.

_____, 1989, Engineering Rock Mass Classifications, John Wiley and Sons, New York, 251 pp.

Cameron, C. P., 1988, "Geological Reconnaissance; Kach'il-Bong Sector, Northern Punch Bowl, Yanggu-Gun, Kangwon-Do, Republic of Korea", Memorandum, EUSA-TNT-(J2), Yongsan Army Garrison, Seoul, Republic of Korea, 18 pp.

_____, 1990, "Geology of the Northern Punchbowl", Technical (Draft) Report, EUSA-TNT-J2, Yongsan Army Garrison, Seoul, Republic of Korea, and the US Army Engineer Waterways Experiment Station, Vicksburg, MS, 40 pp.

Deere, D. U., 1964, "Technical Description of Rock Cores for Engineering Purposes," Rock Mechanics and Engineering Geology, Vol.1, No.1, pp. 17-22.

_____, Hendron, A. J., Patton, F. D., and Cording, E. J., 1966, "Design of Surface and Near-Surface Construction in Rock," Proceedings, Eighth Rock Mechanics Symposium, Minneapolis, Minn.

_____, Merritt, A. H., and Coon, R. F., 1969, "Engineering Classification of In-Situ Rock", Technical Report No. AFWL-TR-67- 144, Air Force Weapons Laboratory, Kirtland Air Force Base, NM.

Gonzalez de Vallejo, L. I., 1983., "A New Rock Classification System for Underground Assessment Using Surface Data." Proc. Int. Symp. Eng. Geol. Underground Const., LNEC, Lisbon, Vol.1, pp. 1185-1194.

Kang, P. J., 1984, "A study on Remote Sensing Application for the Tectonic Framework of the Korean Peninsula," Ph.D. Thesis, Korea University.

Kim, H. S., and Na K. C., 1987, "Part IV: Igneous Activity", in The Geology of Korea, Lee Dai-Sung (Editor). The Kyohak-Sa Publishing Co., Seoul, pp. 289-344.

Kim, O. J., 1970., "Geology and Tectonics of the Mid-Central Region of South Korea," Jour. Korean Inst. Mining Geol., Vol.2, pp.73-90.

Kim, O. J., 1973, "The Stratigraphy and Geologic Structure of the Metamorphic Complex in the Northwestern Area of the Kyonggi Massif," Jour. Korean Inst. Mining Geol., Vol.6, pp. 201-218.

Lee, Dai-Sung (Ed.), 1987, The Geology of Korea, 1st Ed., The Kychak-Sa Publishing Co., Seoul, 514 pp.

Murphy, W. L., 1985, "Geotechnical Descriptions of Rock and Rock Masses," Technical Report GL-35-3, US Army Engineer Waterways Experiment Station, Vicksburg, Miss.

Republic of Korea Ministry of Construction - Korea Water Resources Development Corporation, (1971), "Reconnaissance Report, Water Resources Study, Han River Basin - Chapter 2: Geology".

Sang H. O., and Hee, Y. C., 1984, "Geological Evolution and Tectonic Classification of Korea," Korean Institute of Energy Resources Report 86-7, pp.35-90.

ACKNOWLEDGEMENTS

This work is part of the operations and research conducted under the Tunnel Detection Program of the United States Army. Funding for this mission is provided by the U.S. Army Belvoir Research, Development, and Engineering Center (BRDEC). The author's participation is funded by a Broad Agency Grant Contract (DACA39-90-K-0029) from the US Army Engineer Waterways Experiment Station (WES). Sincere appreciation is extend to Mr. Ray Dennis (BRDEC) and to Mr. Bob Ballard (WES) for their long-term support and encouragement during the course of this work.

This work would not have been possible without the enthusiastic cooperation of the EUSA-TNT, the ROKA-TDD, and the ROKA 21st Division. Particular appreciation is extended to SPC Chris Hacker who assisted the author in all phases of the surface mapping and field work; and to SFC Mike Joos, Sgt John Britton, and Sgt John Rodgers, whose hard work in conducting the Tunnel-4 topographic survey was both inspiring and invaluable.

The views expressed herein do not purport to reflect the views nor the position of the Department of the Army or the Department of Defense.

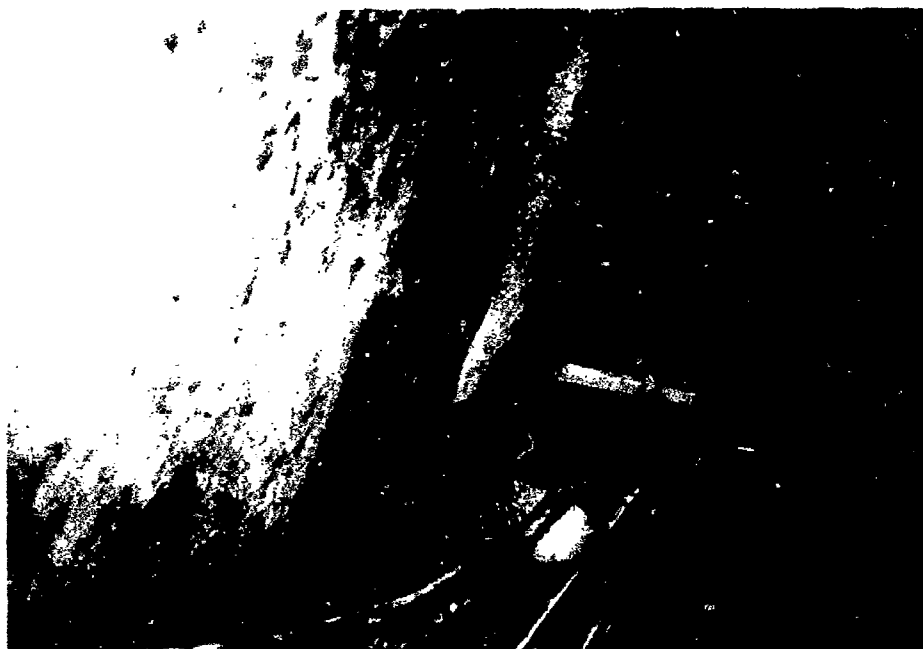


Figure 6. (Top) Large westerly dipping joint planes form slab-like walls of Tunnel-4 where it is hosted in the Punchbowl granite 50-100 meters north of the Countertunnel intercept. (Bottom) An east wall gallery doubles the width of Tunnel-4 300 meters north of the Countertunnel intercept.

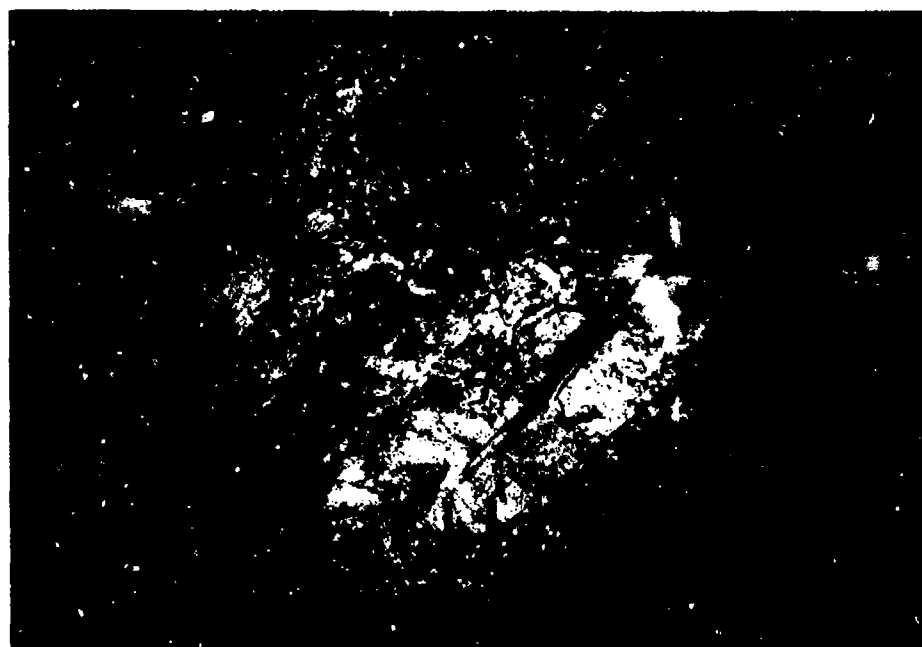
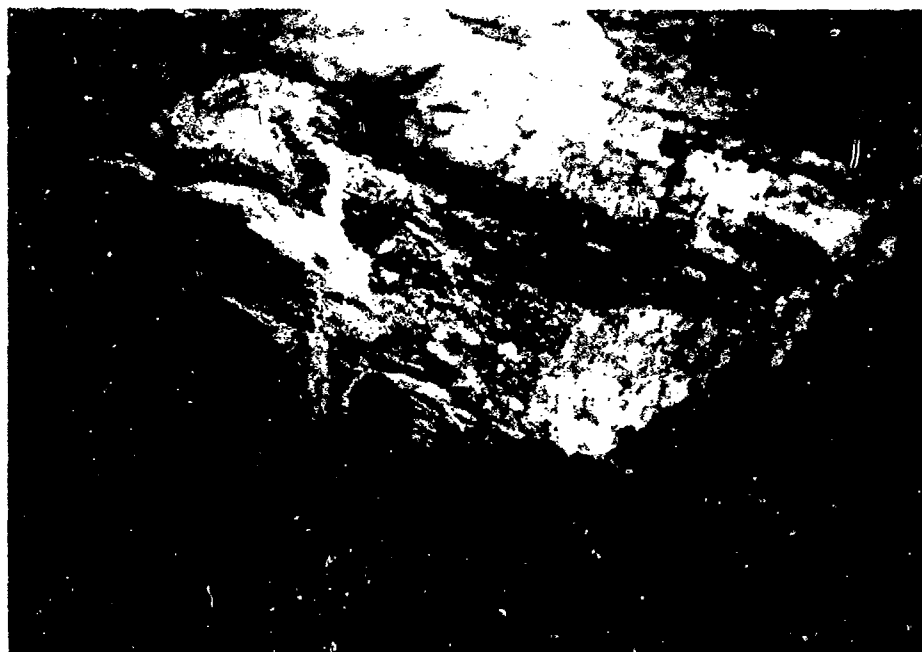


Figure 7. (Top) Moderately-dipping banded gneisses and migmatites forming the walls of Tunnel-4 just north of their contact with the Punchbowl granite at 312-315 meters. (Bottom) the same metamorphic rock mass exhibits a wet and flowing groundwater condition where joint fillings have been washed out of open apertures.

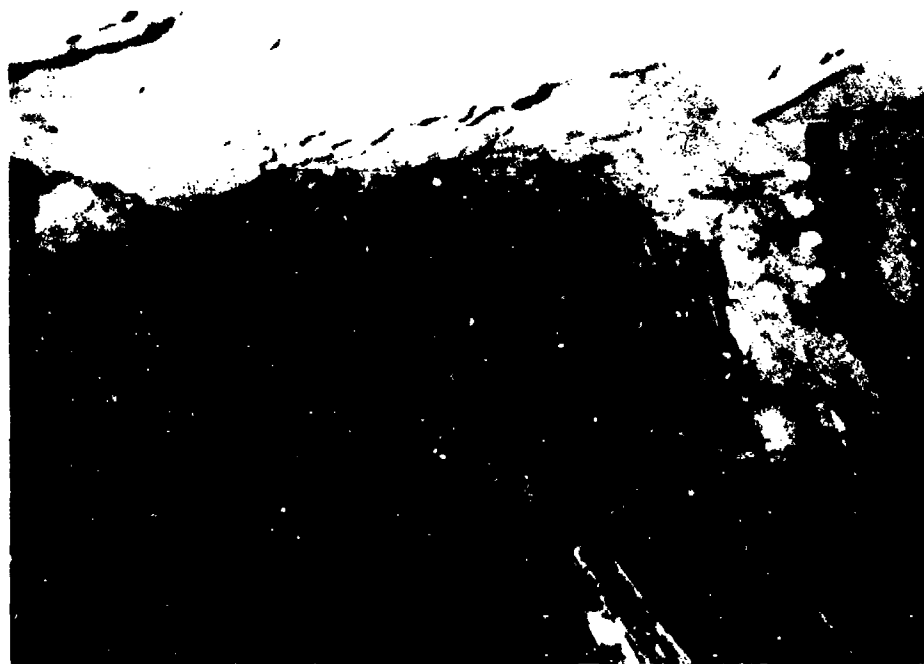
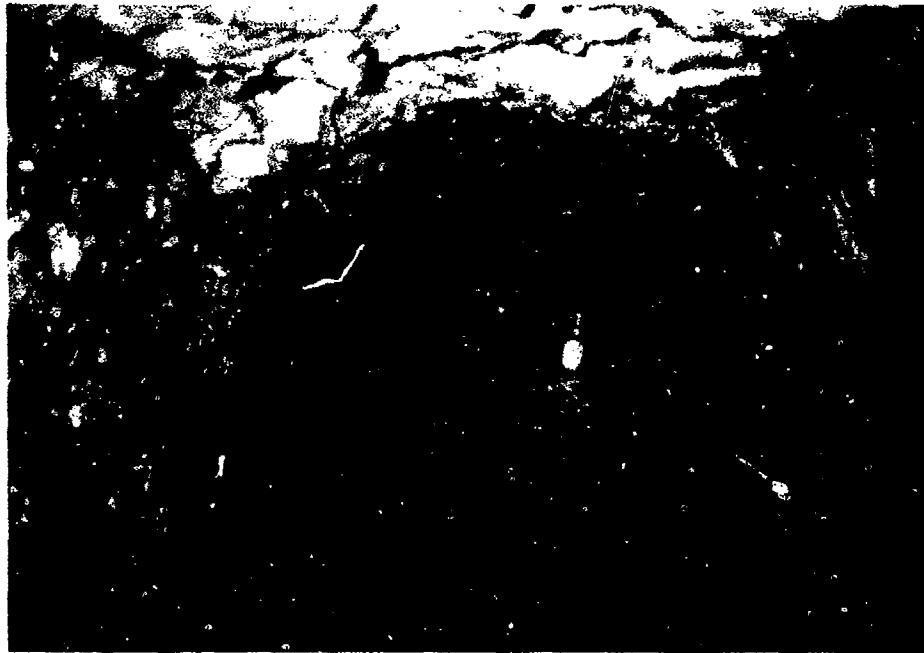


Figure 8. (Top and Bottom) These views to the south along Tunnel-4 (at about 650 meters north of the countertunnel intercept) demonstrate that increased fracture density in the metamorphics generally lends rough aspect to the walls of the tunnel. Note the log rail ties and the "hanging" insulators for four electrical wires left by the NKPA.



Figure 9. (Top) Quartz-calcite veining is common in the metamorphics where the rock mass has been disturbed by shearing or faulting. (Bottom) This south-facing view at about 900 meters along the tunnel shows that the metamorphic rock mass is squeezing in somewhat to produce a diameter of approximately 1.4m x 1.4m.

GEOPHYSICAL TECHNIQUES APPLIED TO CAVITY DETECTION AT THE WHARF MINE, LEAD, SOUTH DAKOTA

K.L. Hauser and M.J. Friedel

**U.S. Bureau of Mines - Twin Cities Research Center
Minneapolis, Minnesota**

ABSTRACT

Subsurface cavity detection in advance of surface mining operations is an issue of great concern in today's mining community. Potential hazards exist for both mining personnel and equipment. Because of this concern, the U. S. Bureau of Mines has undertaken research to determine the ability of several geophysical techniques to both detect and delineate known subsurface cavities and attendant features. The field investigation site, a surface gold mine near Lead, SD, hosts numerous examples of these target cavities. The location of these cavities, which encompass a variety of sizes, shapes, and depths, was determined in advance by drilling. This region of the Black Hills has been extensively mined by a variety of methods since 1875, resulting in many abandoned mine passageways. Most of the earlier workings were poorly mapped. The work discussed here included a closely spaced microgravity survey, a magnetic gradiometer recording over the same sites, and a dipole-dipole resistivity profile which crossed the targets in a manner that was determined by field conditions. The variation in depth and size of the targets has provided information about both the viability and limitations of these techniques in this geologic environment. All the methods responded to some targets, while other targets were more difficult to map with specific techniques. This fact reinforces the need for an integration of several methods to be employed in cavity detection studies.

INTRODUCTION

The need for a suite of reliable methods to be employed in the detection of subsurface cavities is well known and widespread. It has been observed that the ability to remotely detect these features has military, economic, health and safety, and environmental implications (Dobecki, 1988). There have been a wide range of successes and failures in the approach to this problem, and perhaps the only statement which can be made with certainty is that there exists no single technique which will address all situations at all times. Therefore, an integration of several geophysical sensing methods seems to be the most prudent approach to the problem (Friedel and Hanson, 1990, and Militzer, et al, 1979). Complexities in detecting voids arise due to variable target depth, changes in fill

material (water, mud, air, etc.), differences in size and orientation of the targets, and the nature of the host rock as compared to the void (Thill, et al, 1992). Another observation (Benson, 1977) is that all the geophysical methods may work well under a certain set of conditions, but the same technique might fail when employed in a different field situation. To be sure, subsurface cavity detection continues to be a diverse, complex, and challenging problem (Butler, 1977).

A particularly hazardous situation arises when surface mining operations commence over pre-existing subsurface workings. These workings are often poorly mapped (Friedel, et al, 1990), and occasionally are completely unmapped. The mining industry has traditionally employed exploratory drilling in an attempt to determine the location of these cavities prior to the emplacement of heavy equipment and personnel. Drilling programs of this magnitude are expensive, time consuming, and sometimes ineffective, depending upon the drill pattern being employed. The objective of this investigation is to identify easily applied surface geophysical sensing methods that may be used to help reduce drilling costs by guiding the drilling program to specific target areas. In this way, cost savings may be realized without compromising mine safety and productivity. Drilling as a detection method will continue to be a significant part of the pre-mine safety assessment, and it is critical because it provides the only available source of ground truth.

The impetus for this study came from the South Dakota Gold Producers's Meeting in April, 1992, where one of the many topics discussed was that of the cavity detection problem in Black Hills gold mining operations. This area has been heavily mined by a variety of techniques since the 1870's (Paterson, et al, 1988). The result is a network of underground workings which exist throughout the region, presenting an ongoing health and safety concern for mining operators on a daily basis. Wharf Resources, Inc. of Lead, South Dakota, demonstrated it's commitment to the mitigation of this problem by both promoting and partially funding this project.

The selection of methods to be tested in this survey was largely based on the level of success during previously reported applications, but was tempered by theoretical and site specific aspects as well. For example, the magnetic method has not always been effective in locating solution cavities in limestone rock, but the iron content of the glauconitic sandstone unit in this area suggested a need for further testing of the technique. Measurement of the vertical gradient of the magnetic field tends to minimize regional anomalies and increase local resolution (Hinze, 1988). The minimal amount of data reduction involved, and the rapid rate of data acquisition, makes this an attractive method.

Microgravity has a long history of successful applications to this problem (Butler, 1977, and Butler, 1984). Instruments with the sensitivity required for measurements of density contrast at the microgal level have been available since the 1960's. As these instruments have advanced, they have been tested in many engineering problems and in a variety of

geologic environments. Today, this method may be the most dependable cavity detection scheme available. At the same time, it is costly and requires a large amount of time for data acquisition and data reduction.

Certain resistivity methods also have a history of successful applications to the cavity detection problem (Militzer, et al, 1979). It has been stated (Bristow, 1966) that voids are detectable at depths of up to 100 feet, depending upon size and fill material, using resistivity techniques. However, the response from a cavity in a non-uniform rock mass to different measurements is highly variable, and the results of a single geophysical method may be misleading. Therefore, by integrating several methods, the mapping of voids from surface measurements can be accomplished with a higher degree of confidence. The problem of non-uniqueness, or the inability to uniquely correlate the causative body with an observed response, can be minimized with the use of multiple methods, and the range of possible interpretations can be constrained.

The blasting procedure employed at the investigation site has resulted in back-filling of many target cavities. Holes are drilled from the surface to a depth of 23 feet and blasted, and then 20 foot benches are removed. As a result, voids lower in the geologic section are usually filled with some of the collapsing material, and the upper three feet of the new bench is typically fractured or rubblized.

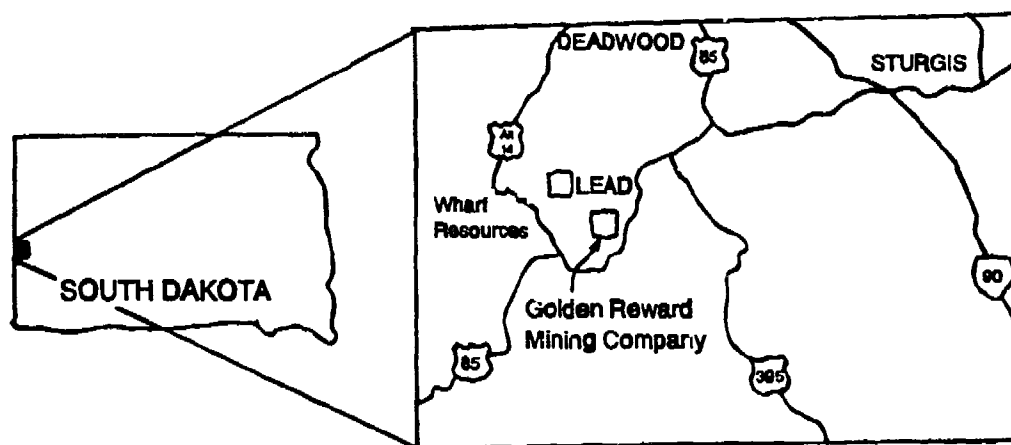


Figure 1. Location map.

Data acquisition began at the field site in late September, 1992, and lasted for one week. A location map of the area is provided in Figure 1. During that time, the three surface geophysical sensing methods were tested across known cavities in the Vulcan Pit of the Wharf Mine. In addition to concern over the detection capabilities of these methods, attention was also given to the time required for the acquisition, data reduction, and interpretation of each data set. All factors will play a role in determining how easily one or all of these methods might be incorporated into the daily operation of the mine. This

logistical information is summarized in appendix A.

GENERAL GEOPHYSICAL PRINCIPLES

Microgravity

Microgravity has been applied to the cavity detection problem since the late 1960's (Neumann, 1977), and has possibly been the most successful method employed. To be effective, the sensitivity required of microgravity instruments must be on the order of microgals (parts per billion = ugal), since targets often express themselves as low density anomalies in the 5-10 ugal range. To achieve this level of sensitivity, and thus resolution, extreme care must be given to the acquisition phase of the microgravity survey. Experience has shown that a 0.3 cm error in surveyed station elevation can result in a 1 ugal error in the station gravity reading (Brown, 1992). The size of an anomaly depends upon depth of burial, size of the targets, and the density contrast between the host rock and the cavity. A common occurrence in abandoned mine workings is that some collapse of the roof structure (chimneying) has occurred over time. This is a progressive migration of the feature upwards in response to stress relief in the overburden. This cracking and fracturing of the overlying strata will enhance the anomaly, and may increase the detectability by increasing the overall density contrast in the rock mass above the cavity. In theory, a large enough compromise in the integrity of the overlying strata should give a measurable signature. It is actually the lateral change in rock density that is measured through profiling (LaFehr, et al, 1980), and the density contrast between host rock and void space inclusions can commonly be detected at the ugal level. Cavities that have been filled by water or secondary geologic material also show a density contrast with the surrounding rock, but since the contrast is smaller than an air-filled opening, these features are subtle and more difficult to detect.

The microgravity data was acquired using the Super G, a modified LaCoste and Romberg Model G gravity meter which was supplied by Edcon, Inc. (¹). This system features automatic data logging using a laptop computer, automatic tide correction, hands-on operator selection of reading period, and a graphical display of both the tide-corrected station gravity readings and meter leveling values. Meter temperature, tide correction, electrostatic positioning force, observation time, beam position, level values, and tide-corrected gravity readings are digitally recorded for each station.

Resistivity

Resistivity techniques have also been applied to the cavity detection problem, but in general have been less consistent in mapping voids than the microgravity method. In

¹Reference to specific products or companies does not imply endorsement by the U.S. Bureau of Mines.

conventional resistivity methods, electric current is imparted to the ground via two electrodes, and a resulting potential (voltage) difference is measured across another pair of electrodes. Knowledge of the input amperage, the resulting voltage, and the spatial geometry of the electrode arrays (dipoles) gives an estimate of the apparent resistivity of the subsurface. Changes in apparent resistivity can be measured in both a lateral and vertical sense, depending upon the field procedure adopted. In theory, current flow tends to be away from high resistivity material (Owen and Suhler, 1980). An air-filled void would present such a feature (Peters and Burdick, 1983), and would be indicated graphically as a high resistivity anomaly. Water-filled cavities and those filled by secondary geologic materials will be expressed as resistivity anomalies of varying magnitudes because of the extreme variability in the resistivity of these fill materials (Mooney, 1980).

Resistivity measurements were collected in the dipole-dipole mode using a Model 2390 Signal Enhancement Earth Resistivity System made by Bison Instruments, Inc. The system consists of a separate transmitter and receiver. The transmitter emits a synchronous, repetitive square waveform. The signal enhancement feature employs a stacking algorithm which allows increased sensitivity and depth of investigation in the presence of electrical and geologic noise.

Magnetic Gradiometry

Although the magnetic field of the earth is highly complex and variable, it tends to be stable on a local scale. Sophisticated techniques and methods for studying and gaining useful information from the magnetic field have been developed and enhanced over time (Breiner, 1973). The magnetic method has been previously tested (Butler, 1983) to assess its ability to detect cavities. Theory suggests that lines of magnetic flux will be distorted by the existence of subsurface cavities (if the host rock is magnetic), and that this distortion should be detectable as an anomalous excursion in the magnetic readings. Vertical gradient measurements at each station are accomplished by taking two readings at a fixed vertical separation. The difference in the total field measurements by each magnetometer, divided by the magnetometer separation, is the vertical gradient at the half way point between the two sensors. In a similar way, horizontal sensors can be used to measure the horizontal gradient of the magnetic field. Operation in the gradiometer mode diminishes the need for data reduction, since diurnal variations need not be removed from the data. In addition, gradiometer measurements of the type discussed here are known to emphasize anomalies from shallow sources (Dobrin, 1976), and shallow targets detected by surface means were the focus of this research.

Magnetic gradiometry data was collected using the G-856 Memory-Mag Proton Precession Magnetometer system made by EG&G Geometrics. It consists of two proton precession magnetometers situated on a vertical staff, with both the height and vertical separation of the two sensors controlled by the operator. It is a hand carried,

weatherproof, and portable unit which can store over 1000 readings. For each station, the line number, Julian day, sequential reading number, time of day, and the total magnetic field in gammas are recorded.

FIELD PROCEDURES

Seven geophysical lines were established at the test site, with line endpoints surveyed by Wharf Resources (Figure 2). Line 1 was the longest, and ran parallel to the muck face. The station spacing (measurement interval) along this line was one meter. Line 3 began at station 119 on line 1, and extended out 81 meters at approximately a 50 degree angle to line 1. The station spacing on this line was also one meter. Lines 2, 4, 5, 6, and 7 were then oriented parallel to line 3 in a manner that would form a grid which was coincident with a drilling pattern completed by the mine crew. The drill pattern provided ground truth information regarding the location of open and backfilled cavities versus solid rock in the survey area. The holes were drilled on a four meter grid, and the survey stations for lines 2, 4, 5, 6, and 7 were therefore separated by four meters. It should be noted that for line 3, magnetic stations increase in number from the muck face out toward the open pit area, but for the

VULCAN PIT/WHARF MINE

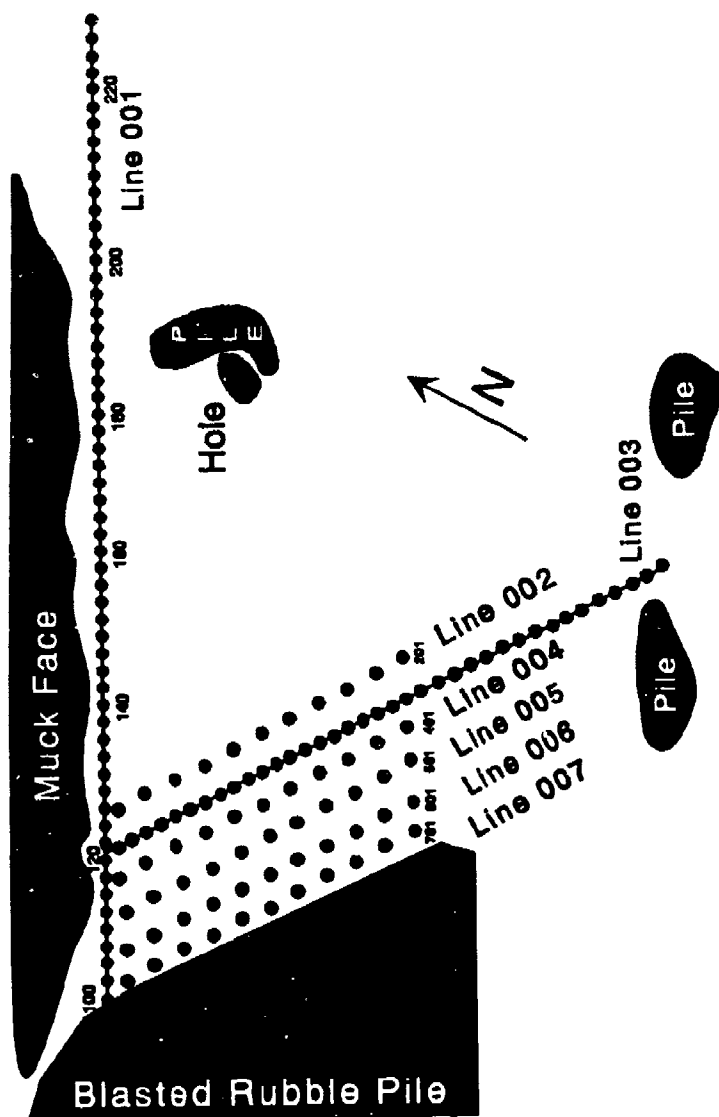


Figure 2. Site/Line location map.

gravity stations on line 3, station numbers increase from the pit area toward the muck face, in order to conform with lines 2, 4, 5, 6, and 7.

Microgravity

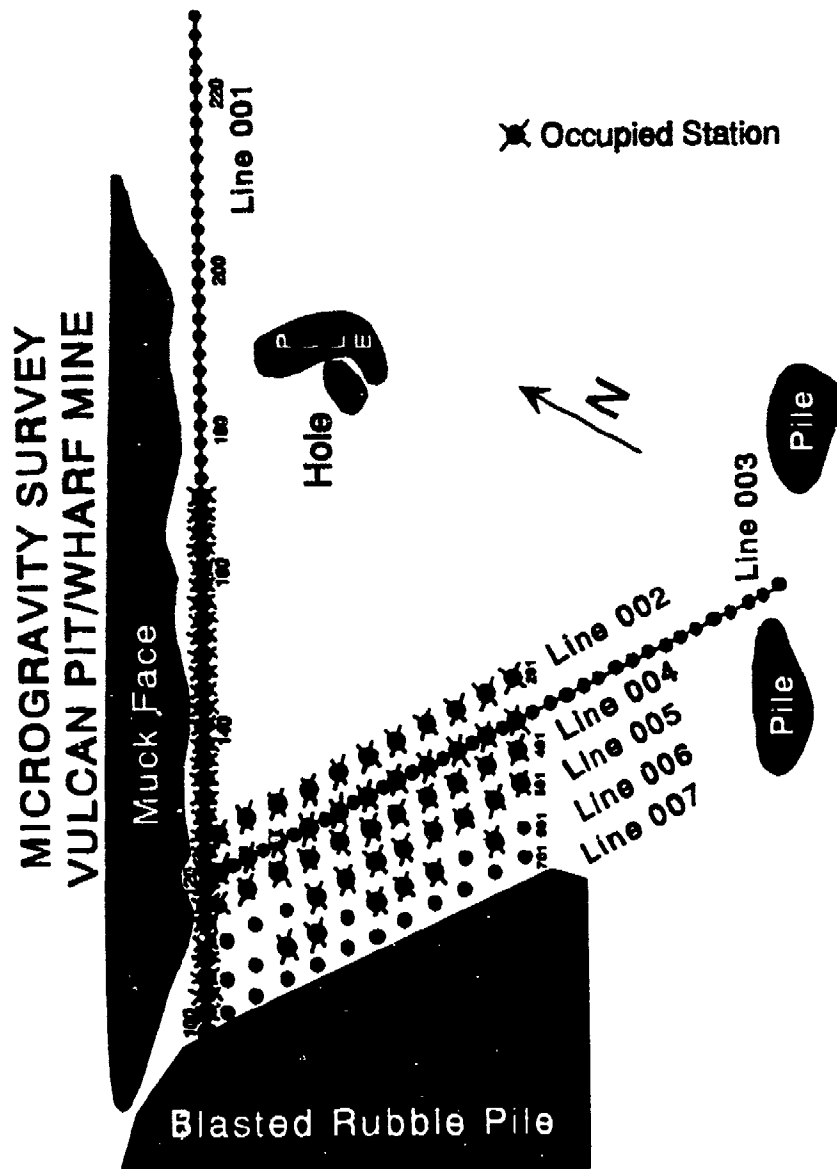


Figure 3. Microgravity station locations.

Microgravity data were collected along selected parts of lines 1, 2, 3, 4, 5, and 6. The stations for which microgravity data were recorded are documented in Figure 3. Gravity data were recorded on line 1, from station 100 through station 169. Due to time constraints, it was impossible to occupy every station, and it was deemed better to occupy every other station in areas without documented voids. Station 134 was used as the base station for line 1, in order to record data necessary for instrument drift corrections. Measurements were taken at all 11 stations on each of lines 2 and 3. The first 11 stations of line 4 and the first 8 stations of line 5 were recorded. On line 6, stations 2, 4, 5, 6, 8, and 9 were recorded. Station 605 on line 6 was used as the base for drift corrections in the gridded area. In total, 99 gravity

stations were recorded.

Resistivity

Resistivity data were collected along line 1 from station 112 through station 157, as shown in Figure 4. The data plotted in this paper were collected using the dipole-dipole electrode array with an 'a' spacing of 2 meters, and $N=1...8$.

Magnetic Gradiometry

Due to the speed and relative ease of operation of this system, all stations in the survey area were recorded.

DATA REDUCTION AND INTERPRETATION

Microgravity

Data reduction was simplified by the fact that most of the data were collected in open, flat areas, and that the muck face was a constant linear feature with respect to line 1. A correction for instrument drift and tidal effects was applied by using the base station information supplied from

station 134 on line 1, and station 605 for all other lines. Because of the limited areal extent of the survey area, no latitude correction was applied. There was some effect due to the blasted rubble pile at the southwest end of line 1, which was removed by application of linear regression techniques. Measured values were free-air and Bouguer slab corrected to arrive at simple Bouguer values (see Dobrin, 1976).

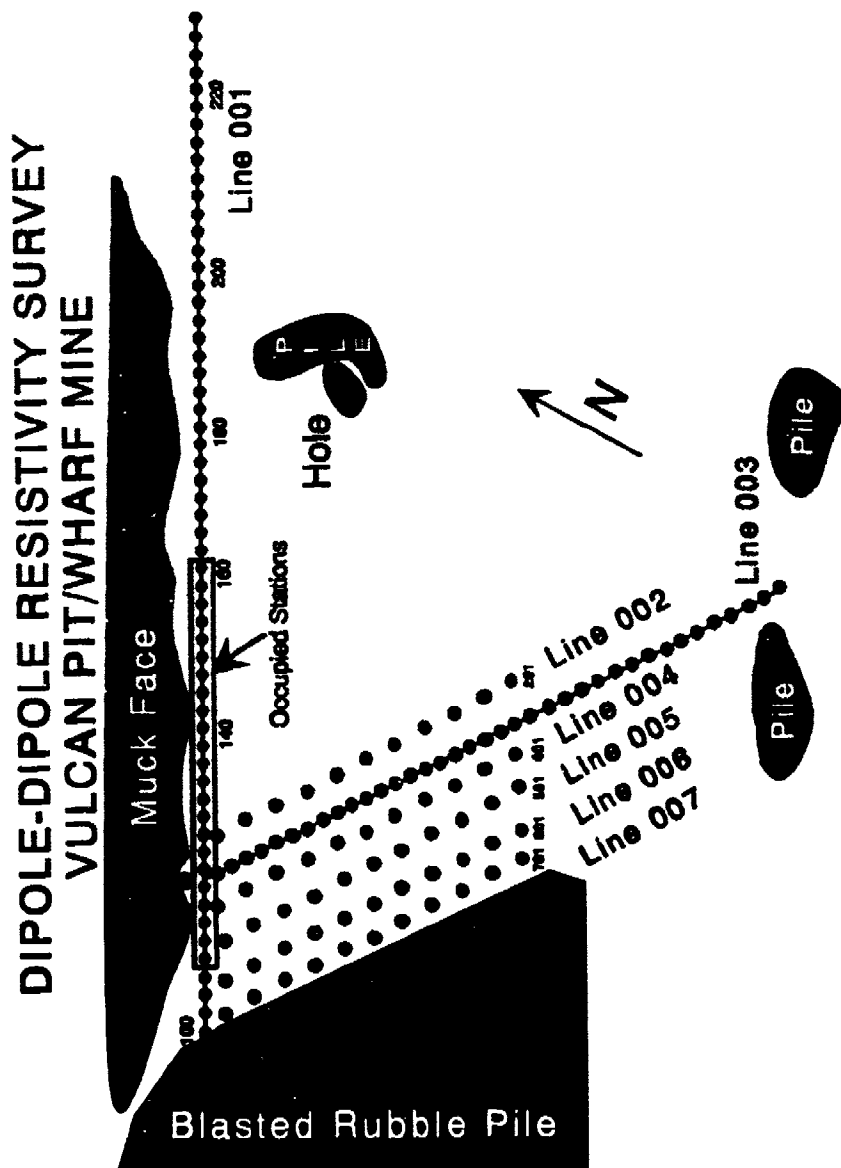


Figure 4. Resistivity profile.



625

gravity profiles from lines 3 and 5. The locations of known cavities can be correlated with profile minima in each figure. Figure 6 is a contoured map of the gravity data from the gridded area, with a known crossing drift highlighted. Comparison of figures 5a,b and 6 to the abandoned mine passageway map (Figure 7) provides good correlation between known voids and void locations inferred from the gravity data.

The gravity profile for line 1 is shown in Figure 8. There is a 50 ugal anomaly centered near station 152, which is attributed to a mine passageway. This passageway was also detected using resistivity (Figure 9) and magnetic methods (Figure 13) between stations 145 and 160.

A known drift crosses perpendicular to line 1 at about station 166, and is observed on both the gravity profile and the magnetic gradiometer profile for line 1. There is also good agreement between the magnetic, resistivity, and gravity profiles regarding the feature at station 115. Station 132 clearly shows anomalies on the gravity,

resistivity, and magnetic profiles, and an anomaly is indicated by all three methods at station 142. Other features occur at stations 106, 120, and 125. The feature at station 106 was a cavity which was open to the surface and can readily be seen in the gradiometer profile. There was no resistivity data recorded at this location.

Resistivity

Data were recorded only on line 1, and only between stations 112 and 159 due to time constraints. Both magnetic and microgravity data were also collected on this section of line 1, making it the most completely covered line in the project. Figure 9 is an apparent resistivity versus depth pseudosection of this portion of line 1. A pseudosection conveys

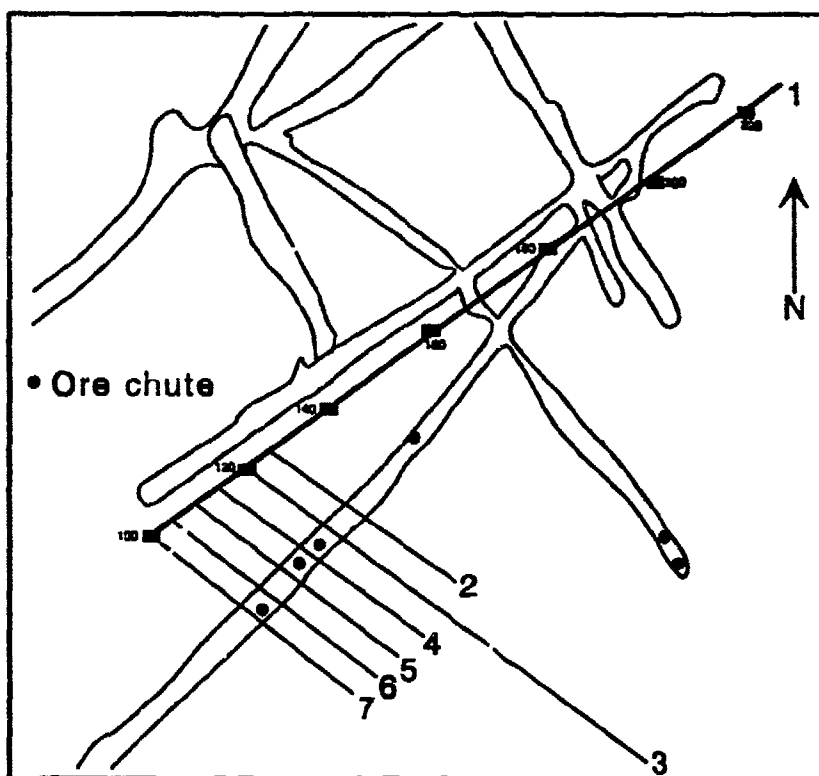


Figure 7. Abandoned mine passageway map, with geophysical lines superimposed.

the variation of apparent resistivity with location and gives an apparent depth of

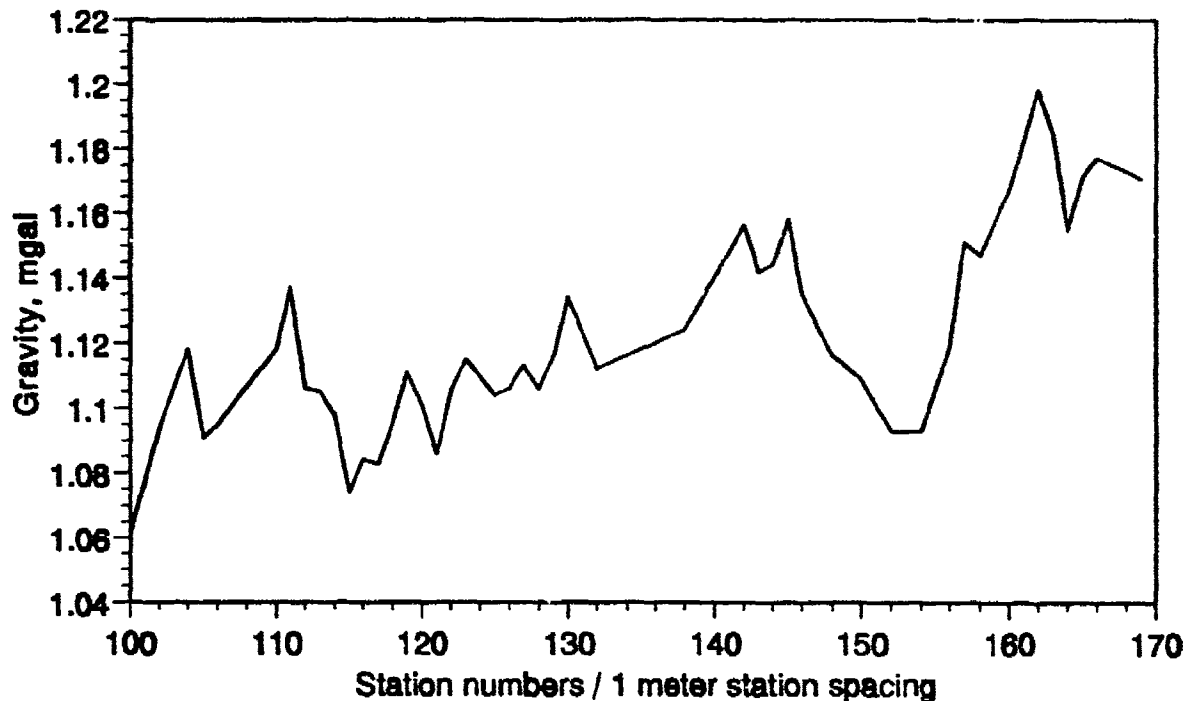


Figure 8. Microgravity profile for line 1.

penetration (Sheriff, 1982). Note that the true depth of a target is often difficult to determine from resistivity data because the data are strongly influenced by the electrical properties of the entire region under investigation.

There are several highly resistive features which stand out in this figure. Only the features with resistivity values greater than 225 ohm-meters are plotted. A suite of plots at different threshold ohm-meter levels was used to determine that the background resistivity of the glauconitic sandstone host rock is between 135-155 ohm-meters, and higher resistivity responses are taken to indicate potential cavities. The most striking anomaly occurs between stations 145 and 159. Documentation from drilling, as well as conversations with drillers, indicate an area of back-filled voids extending from station 145 to 160. Lesser anomalies are centered on stations 141, 127, 133, and 115 through 118. With the exception of the anomaly centered on station 118, these anomalies compare favorably with voids documented by drilling. Although there was no void documented by drilling at station 118, there is a striking feature on the magnetic gradiometer profile at this same point (Figure 13). It is possible that there are fractured zones in the near surface due to the bench blasting method used during the mining operation, and fractured zones or a series of small cracks can often produce the same overall resistivity response as a

void (Burdick, et al, 1986). This fracturing phenomena has been known to make resistivity anomalies appear higher (more shallow) in the section than they really are, which appears to be the case here.

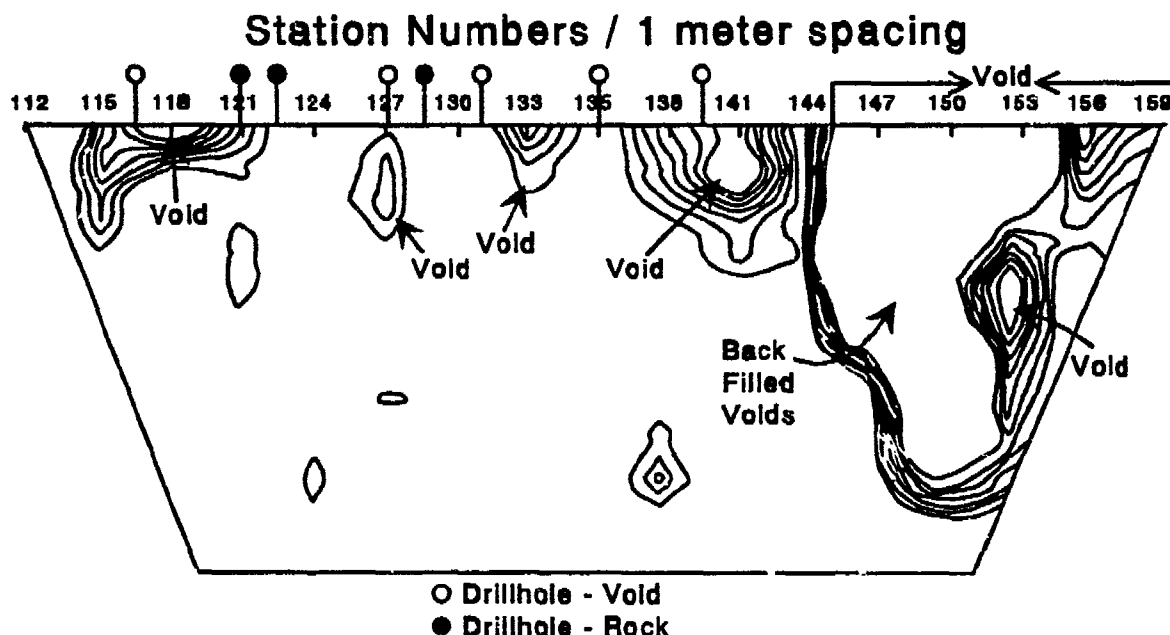


Figure 9. Resistivity pseudosection for selected portion of line 1.

Magnetic Gradiometry

The initial results of the magnetic interpretation were encouraging. The magnetic survey over line 3 showed a distinct decrease in the field strength that was coincident with the area of known back-filled void's. This can be seen in Figure 10, between stations 310 and 335. These low values were originally thought to be the expression of subsurface cavities, but further investigation uncovered other explanations. These ~ 25 gamma/meter anomalies could also be attributed to noise, or a variety of other factors.

Upon further inspection, it was determined that this 'low' was actually the negative lobe of a typical magnetic dipole anomaly (see Figure 11). Examination of the gradiometer profile for line 5 (Figure 12d) shows a large positive anomaly, centered around station 506, with a magnitude of over 100 gammas/meter. This is the kind of expression that might be expected over a point-source metallic/magnetic object, such as an ore cart or other hardware. The gradiometer profiles for lines 2, 3, 4, and 5 are plotted in Figures 12a,b,c,d. Figures 11 and 12 reveal that the low values for line 3 (Figure 10) are not necessarily related to the known voids in the gridded area for two reasons. The negative lobe would not be expected from a void, and the magnitude of the anomaly on line 5 is

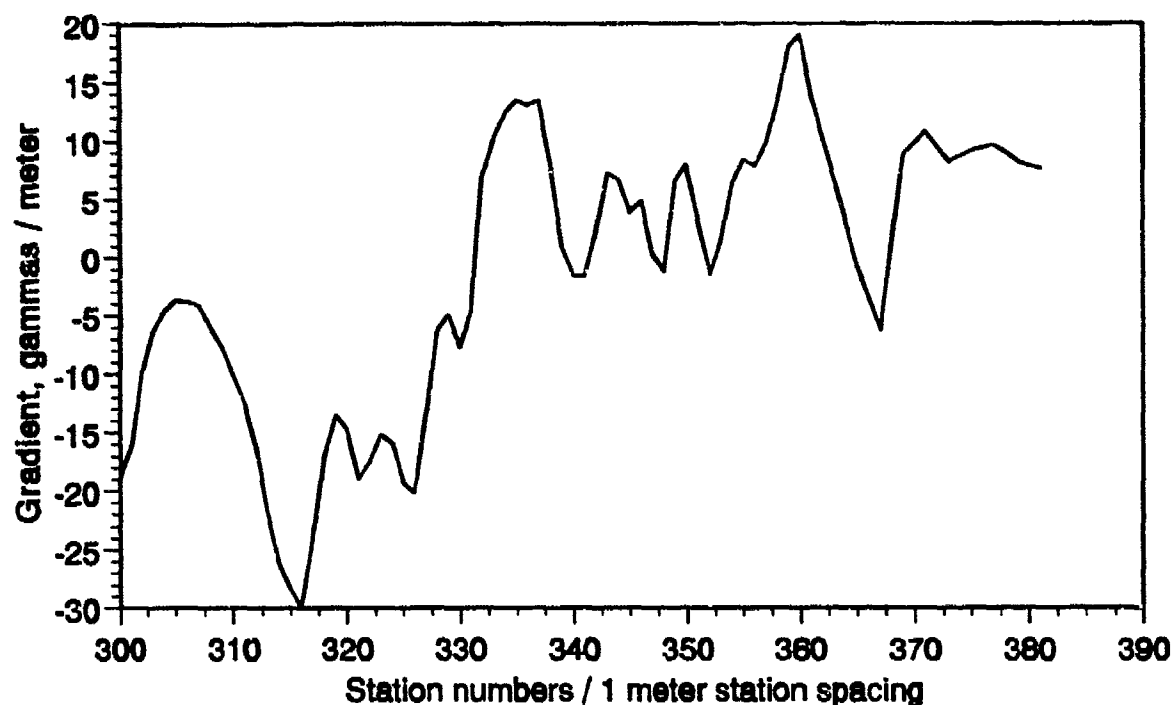


Figure 10. Magnetic Gradiometer profile for line 3.

much too high. It appears that a magnetic object has been left behind in the old workings below the gridded area. The map of the old passageways (see Figure 7) indicates two

ore chutes in this area. It is speculated that an ore cart has been left in the passageway. Use of graphical interpretation methods (Peter's method, etc), and computer modeling indicate that this object is at a depth of 20-35 feet below the surface. A ground penetrating radar survey was conducted over the same lines one week after the completion of this field work and indicates a depth to the underground passageway, and hence to attendant metallic objects, to be 30-35 feet (Roggenthen, 1992).

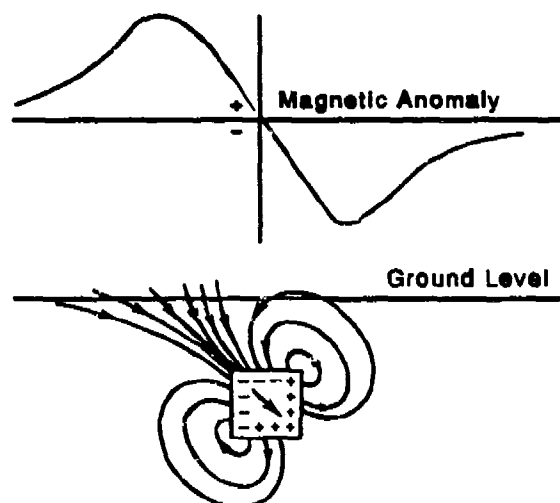


Figure 11. Magnetic response of dipolar anomaly (after Dobrin, 1976).

The gradient profile for line 1, along the muck face, shows high amplitude

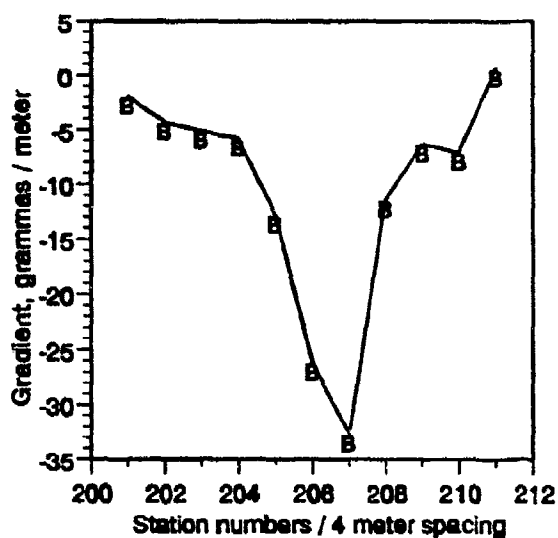


Figure 12a. Magnetic gradiometer profile for line 2.

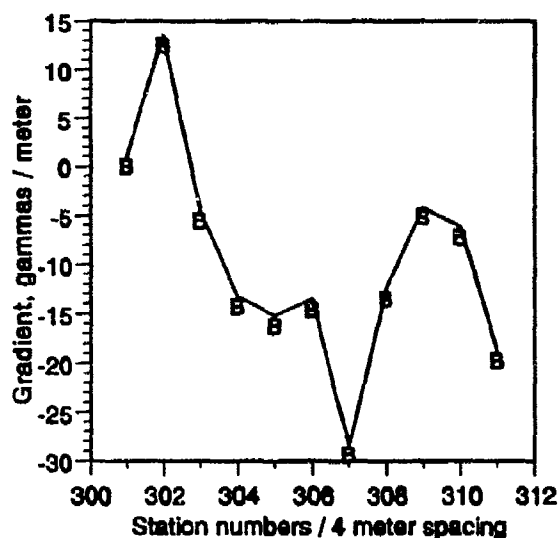


Figure 12b. Magnetic gradiometer profile for line 3.

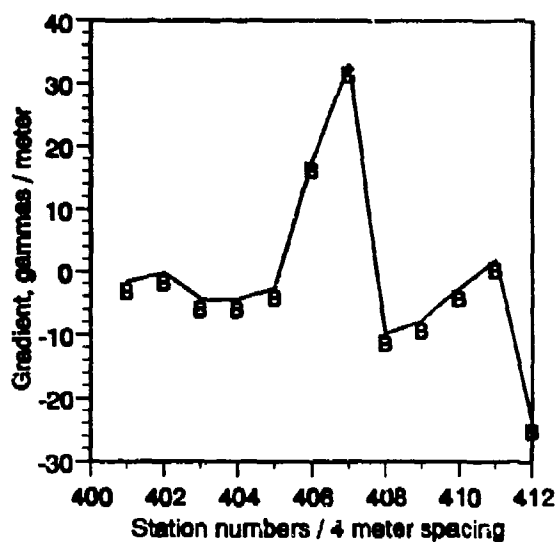


Figure 12c. Magnetic gradiometer profile for line 4.

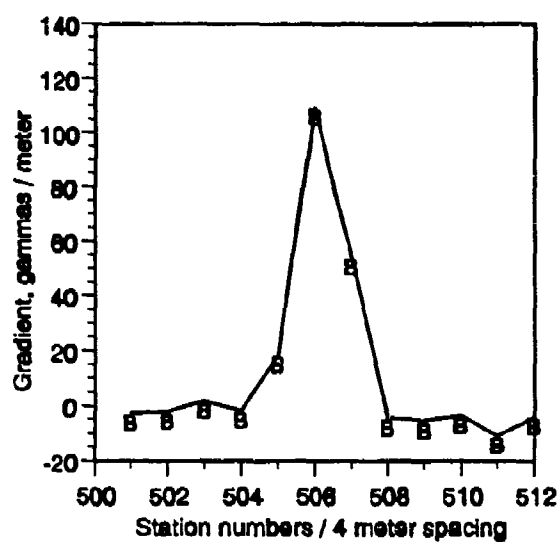


Figure 12d. Magnetic gradiometer profile for line 5.

anomalies at stations 180, 150, and 115 (Figure 13). It is likely that the anomaly at station 180 is due to a metallic object in the subsurface, based on the magnitude of the response and the close proximity of a crossing drift in this area. There is another

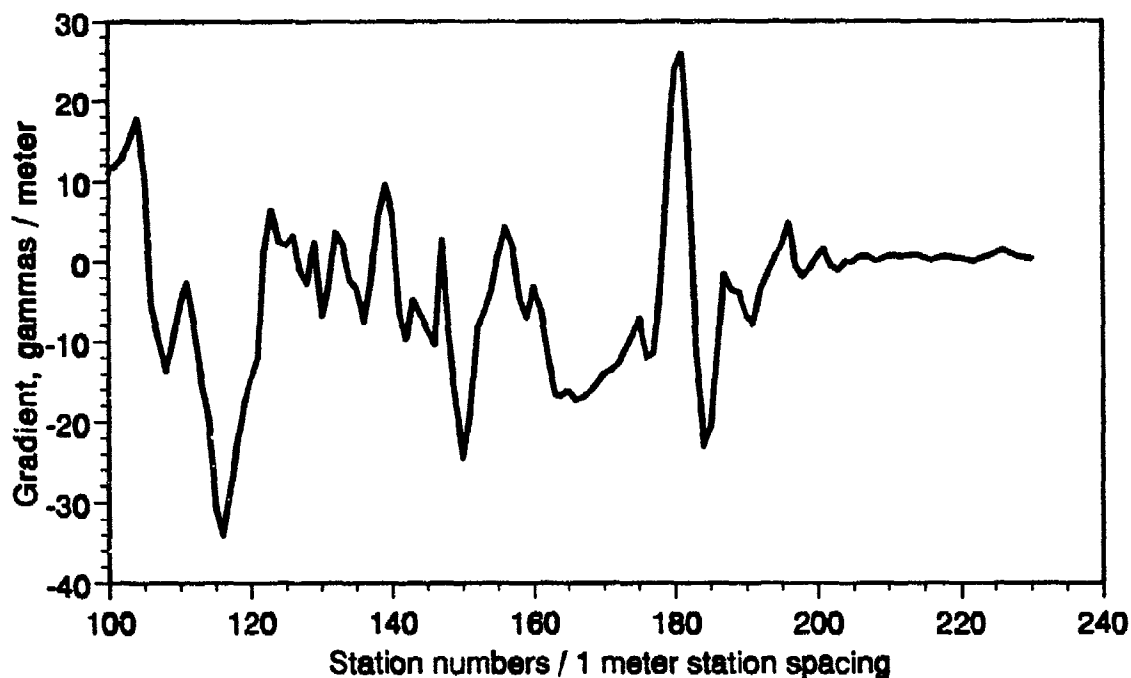


Figure 13. Magnetic gradiometer profile for line 1.

crossing drift located near station 165, but this anomaly does not have the same high amplitude expression. Similarly, there is a known area of back-filled voids between stations 145 and 160, and there is no high amplitude spike associated with this region. It is possible that these anomalies are voids which contain no metallic objects to distort the magnetic response. The large, dual-peaked anomaly between stations 105 and 118 is attributed to the fact that there was a caved void exposed at the surface between stations 106 and 109, expressed as a five foot diameter hole which angled under the muck face. The secondary positive peak at station 110 may be the result of a smaller or deeper metallic inclusion.

The magnitude of the local anomaly has essentially overwhelmed the lower intensity expression of the voids the authors hoped to map, and attempts to remove the effect were unsuccessful. However, the presence of magnetic objects in the subsurface may be advantageous in some cases. A void may be easily detectable through the magnetic signature of metallic objects left behind after previous mining operations were abandoned. Alternatively, the signature of the mine cavities may not be strong enough to be detected reliably in this area using this method, particularly in the presence of strong localized magnetic anomalies produced by ore carts, railroad tracks, tools, and other hardware left behind by former operations in the subsurface. The ambiguity of these magnetic

interpretations serves to underscore the need for the utilization and integration of several geophysical methods in cavity detection.

CONCLUSIONS

Line 1 was the only line to which all three methods were applied, and the data reveal that the integration of methods has worked well in delineating subsurface cavities. The interpretation of this suite of data compares favorably to both the drill information and the abandoned mine passageway map (Figure 7).

In the gridded area, where no resistivity data were recorded, the gravity data indicate a trend of anomalies which is coincident with a drift. This drift is also indicated on the mine passageway map (Figure 7) and was confirmed by drilling. Magnetic data from the gridded area were strongly affected by a dipolar anomaly, suspected to be a magnetic object left behind in the drift. This magnetic data also illustrates the need for closely spaced information, and it shows how easily the data may be misinterpreted when only viewed selectively.

The results shown in Figure 14 suggest that these methods work well as cavity detection agents in this geologic environment. The microgravity technique responded well to areas of low density associated with known subsurface cavities. The resistivity data delineated several areas of high resistivity associated with voids and back-filled voids, and it correlated well with the microgravity results. The magnetic data are more difficult to assess. Areas of low vertical gradient along line 1 suggest that the technique is responding to a lack of iron grains in the void areas as compared to the surrounding glauconitic sandstone. The magnetic data in the gridded area seem to respond more to metallic objects left behind in the older underground workings, but also demonstrates that the workings may be mapped with this technique on the basis of these inclusions. The GPR survey mentioned previously showed generally good agreement with the interpretation presented here. The data show a linearly trending drift which indicates that a geologic structure was followed through this area.

The rapid field acquisition time of the magnetic technique is such that it is very attractive to the mining community. However, resolution of the method and the potential interference from outside sources, indicate that it is not a stand-alone technique. Both the microgravity and resistivity methods appear to be well suited for detecting subsurface cavities in this geologic setting, but the time needed to acquire these data may be prohibitive for production oriented mining operations. There are microgravity and resistivity instruments available at much higher cost which could dramatically reduce the acquisition and interpretation time for these surveys, and may make them more readily adaptable for mining applications. For future research considerations, a less ambitious layout encompassing all three methods would provide a more complete study than a large survey area with intermittent coverage by one or two of the techniques.

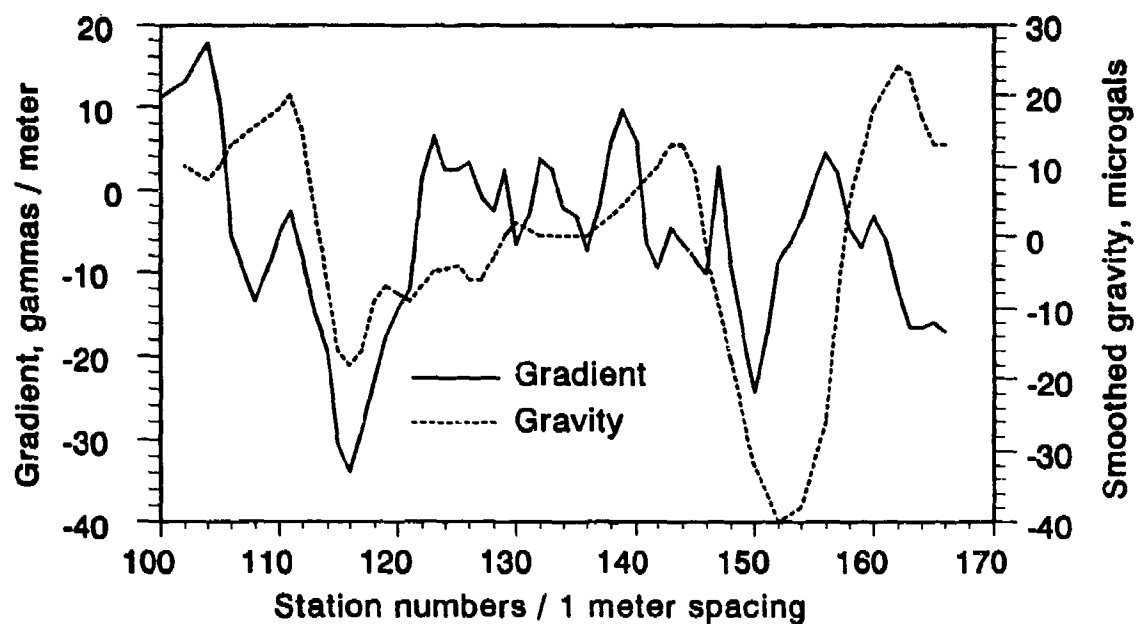
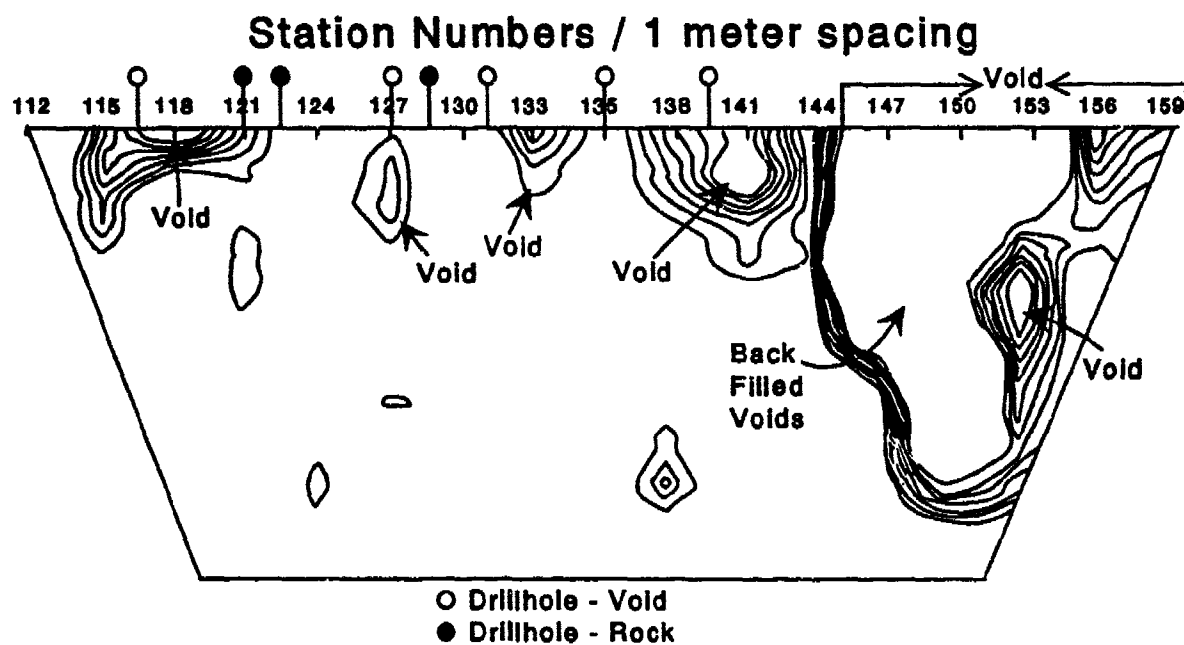


Figure 14. Data plotted from all three methods for selected portion of line 1.

APPENDIX A PRODUCTION RATES

Prior to acquisition, seven geophysical lines were established for the survey. Line layout required about seven hours.

Production rates for data acquisition:

- * Microgravity acquisition was interrupted once by the effect of a distant earthquake, and twice by minor equipment problems. In all, 139 stations were recorded, resulting in 99 data points (there were 40 reoccupations). This averaged to just over six stations per hour, and the exercise took 22 hours not including down time.
- * Resistivity data were collected along line 1 between stations 112 and 159, using a dipole-dipole arrangement, an 'a' spacing of 2 meters, and N values of 1-8. This took two full days.
- * Magnetic data were recorded for every station (268) in a two hour period.

Production rates for data processing:

- * Microgravity data were reduced, edited, and plotted in various forms in about ten hours.
- * Resistivity data were entered, edited, and plotted as a contoured pseudosection in about four hours.
- * Magnetic data were downloaded from the magnetometer, organized into files by line, and plotted as individual profiles and a contour map in about eight hours.

ACKNOWLEDGEMENTS

Special thanks to Mr. Tom Loomis and his associates at Wharf Resources and to Mr. Larry Brown of Edcon for being constant sources of help and cooperation.

REFERENCES

- Benson, R.C., 1977, "An Overview of Cavity Detection," Symposium on Detection of Subsurface Cavities, Vicksburg, Mississippi, pgs 44-79.
- Breiner, S., 1973, "Applications Manual for Portable Magnetometers," copyright 1973 by GeoMetrics, Sunnyvale, California, 58pp.

Brown, L., 1992, Edcon, Inc., Personal communication.

Bristow, C., 1966, "A New Graphical Resistivity Technique for Detecting Air-filled Cavities," *Studies in Speleology*, Vol.1, Part 4, pgs 204-227.

Burdick, R.G., Snyder, L.E., and Kimbrough, W.F., 1986, "A Method for Locating Abandoned Mines," U.S. Bureau of Mines RI # 9050.

Butler, D.K., 1977, "Geophysics Versus the Cavity Detection Problem," *Symposium on Detection of Subsurface Cavities*, Vicksburg, Mississippi, pgs 27-43.

Butler, D.K., 1983, "Cavity Detection and Delineation Research, Report 1, Microgravimetric and Magnetic Surveys, Medford Cave Site, Florida: Tech. Rep. GL-83-1," U.S. Army Engineer Waterways Experiment Station, CE, Vicksburg, Mississippi.

Butler, D.K., 1984, "Microgravimetric and Gravity Gradient Techniques for Detection of Subsurface Cavities" *Geophysics*, Vol.49, No.7, pgs 1084-1096.

Dobecki, T.L., 1988, "A Rapid Seismic Technique for Detecting Subsurface Voids and Unmapped Mine Workings," *Symposium on the Application of Geophysics to Engineering and Environmental Problems*, Golden, Colorado, pgs 666-690.

Dobrin, M.B., 1976, "Introduction to Geophysical Prospecting," McGraw-Hill Publishers, 3rd Edition, 630 pp.

Friedel, M.J., and Hanson, J.C., 1990, "Integrated Geophysical Approach to Abandoned Mine Detection," *Proceedings: 12th Annual NAAML P Conference*, Breckenridge, Colorado.

Friedel, M.J., Jessop, J.A., Thill, R.E., and Veith, D.L., 1990, "Electromagnetic Investigation of Abandoned Mines in the Galena, KS, Area," U.S. Bureau of Mines Report of Investigations #9303.

Hinze, W.J., 1988, "Gravity and Magnetic Methods Applied to Engineering and Environmental Problems," *Symposium on the Application of Geophysics to Engineering and Environmental Problems* Golden, Colorado, pgs 1-107.

LaFehr, T.R., Laurin, P.J., and Black, A., 1980, "Tunnel Detection by Surface and Borehole Gravity Methods," in *proceedings, U.S. Department of Defense Seminar on Tunnel Detection*, Idaho, pgs 224-246.

Militzer, H., Rosler, R., and Losch, W., 1979, "Theoretical and Experimental Investigations for Cavity Research With Geoelectrical Resistivity Methods," *Geophysical Prospecting*, Vol.27, pgs 640-652.

Mooney, H.M., 1980, "Handbook of Engineering Geophysics, Volume Two: Electrical Resistivity," copyright 1980 by Harold M. Mooney for Bison Instruments, Minneapolis, Minnesota.

Neumann, R., 1977, "Microgravity Method Applied to the Detection of Cavities," *Symposium on Detection of Subsurface Cavities*, Vicksburg, Mississippi, pgs 142-160.

Owen, T.E., and Suhler, S.A., 1980, "Subsurface Void Detection Using Surface Resistivity and Borehole Electromagnetic Techniques," Paper # E-7, International SEG Meeting, 50th Anniversary Meeting, Houston, Texas, 1980, pgs 2-23.

Paterson, C.J., Lisenbee, A.L., and Redden, J.A., 1988, "Gold Deposits in the Black Hills, South Dakota" *Wyoming Geological Association Guidebook*, 39th Field Conference, pgs 295-303.

Peters, W.R., and Burdick, R.G., 1983, "Use of an Automatic Resistivity System For Detecting Abandoned Mine Workings," *Mining Engineering*, January, 1983, pgs 55-59.

Roggenthen, W.M., 1992, South Dakota School of Mines and Technology, Personal Communication.

Sheriff, R.E., 1982, "Encyclopedic Dictionary of Exploration Geophysics," SEG Publication, 8th printing.

Thill, R.E., Friedel, M.J., Jessop, J.A., and Jackson, M.J., 1992, "Integrated Geophysics and Geotomography for Ground Control Applications," Unpublished U.S. Bureau of Mines Report.

STEALTH TUNNELING USING TRENCHLESS TECHNOLOGY

**TIMOTHY R. COSS
MICROTUNNELING, INC.
BOULDER, COLORADO
303/444-2650**

ABSTRACT

Stealth Tunneling using Trenchless Technology developed for civil applications has the potential for use as a "quiet" tunneling method in support of clandestine access to restricted areas. Excavation techniques such as boring, jacking and fluid assist can be applied in a manner so as to reduce the seismic signature associated with their operation. This paper will discuss the newest technique available in the area of Trenchless Technology, Microtunneling, its capabilities and restrictions, and its potential application to Stealth Tunneling. Characteristics of the systems that may aid in the detection of the resulting tunnels, both during and after construction will be identified as well.

INTRODUCTION

Tunnels throughout history have played important rolls in wartime and peacetime alike. For the first time in history, length, depth, water table, ground conditions and accuracy are only considerations for the type of equipment readily available to do tunnels of 12" to 12 ft. in diameter.

Microtunneling has grown by leaps and bounds since its introduction to the US in the mid 1980's. So much has been learned and it's still in its infancy. To better understand its possible unique applications, an understanding of its mechanics are in order.

TRENCHLESS TECHNOLOGY: AN OVERVIEW

The US Trenchless Technology Industry has grown tremendously during recent years. Trenchless Technology can be defined as that group of methods or techniques which allows the repair, replacement or installation of buried utilities without the opening of a trench from the surface. Major developments have taken place within the last fifteen years.

Today the list would seem to be endless with all the different types of trenchless methods and their sub-methods. Volumes have been written on them all. It is not the intent of this paper to review all of them, just one, Microtunneling, a newcomer that by its very nature lends itself to some very interesting possibilities. Listed below and broken down into two categories, "Man Entry" and "Non-Man Entry" are the various forms of trenchless excavation methods available today.

Covert tunnels haven't waited for microtunneling to come of age, but they have applauded its debut.

Many of the types listed below will, for one reason or another, be better for specific assignments than others. The trick is to understand them all and select the best.

I. Non-Man Entry

A. Horizontal Earth Boring

- 1. Auger Boring**
 - a. Track Type**
 - b. Cradle Type**
- 2. Composition Method**
 - a. Push Rod Method**
 - b. Rotary Method**
 - c. Percussion Method**
- 3. Pipe Ramming Method**
- 4. Slurry Method**
 - a. Water Jetting**
 - b. Slurry Boring**
- 5. Microtunneling Method**
 - a. Slurry Method**
 - b. Auger Method**
- 6. Directional Method**
 - a. Directional Drilling**
 - b. Mini-directional Drilling**
 - 1. Fluid Cutting**
 - 2. Mechanical Cutting**

II. Man Entry

A. Pipe Jacking and Utility Tunneling

1. Hand Mining
2. Open Face Shield
3. Tunnel Boring Machine
4. Road Header Method
5. New Austrian Tunneling Method

MICROTUNNELING METHODS

The term microtunneling is used to describe methods of horizontal boring which are highly sophisticated. Micro-TBMs are laser guided, remotely controlled and permit accurate monitoring and adjusting of the alignment and grade as the work proceeds so that the pipe can be installed on precise line and grade. These methods are generally for lines that are less than or equal to 36 inches (900 mm). However, the same term and equipment is used for much larger sizes. Basically, they are non-personnel entry tunnel boring machines.

The microtunneling method for the installation of pipes is being widely used all over the world for virtually all types of soils. The method was developed in Japan during the 1970's. There are over thirty major manufacturers of microtunneling machines in the world. However, the majority are in Japan. Only three manufacturers are marketing in the United States. Currently no U.S. firm manufactures microtunneling equipment. The method is capable of installing pipes even in rock formations, up to 150 feet (45 meters) below the ground surface, and below the ground water table up to 2000 feet in length from shaft to shaft.

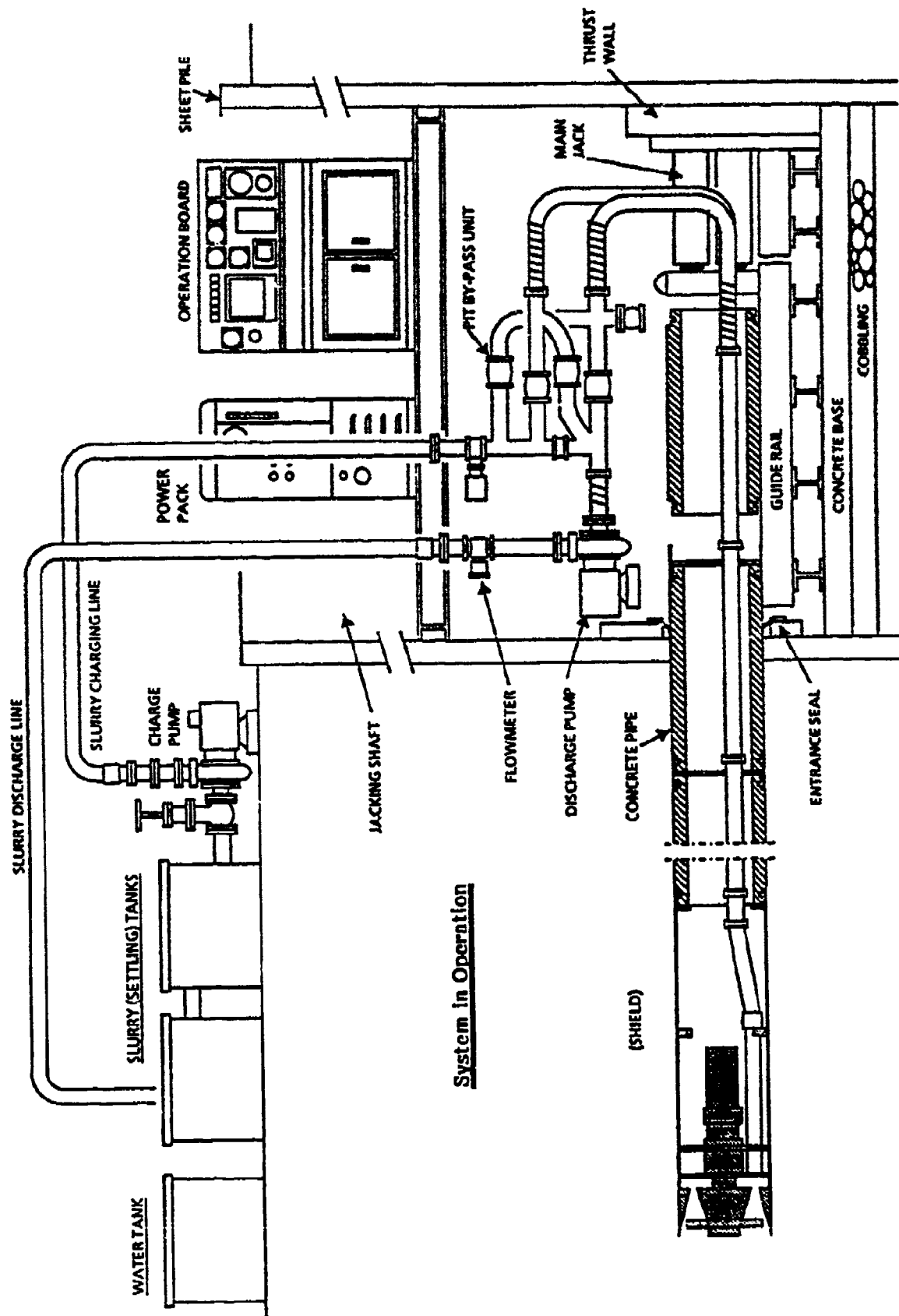
This method is uniquely suited for the installation of sewer lines where a high degree of accuracy is required.

Based on the mode of operation, the microtunneling method can be subdivided into the following two major groups:

- (1) Slurry Method
- (2) Auger Method

SLURRY METHOD

The slurry method involves jacking of pipe from the jacking pit and simultaneous cutting of soil at the face of the tunnel by a cutting head. The tunnel is supported at the face mechanically and/or by pressurized slurry. The spoil is removed hydraulically in the form of a slurry. The conveying fluid is simultaneously used to counteract hydrostatic forces created by ground water pressure as well as spoil removal.



System in Operation

METHOD DESCRIPTION

The soil is cut mechanically at the face by a cutting head. The design of cutting the head depends on the type of soil or rock expected to be encountered. The material cut at the face is removed by hydraulic action. The material enters the boring head through inlet openings and is then placed in suspension in the slurry chamber which is sealed by the boring head at the front end and a bulkhead at the rear. The slurry chamber is integrated in a circuit designed to handle water or bentonite slurry.

The microtunneling boring machine is made up of two articulated units, i.e., steering head and follower. The shield is steered by two to four steering cylinders which are actuated from a remote monitoring and control panel. The problems of soil stabilization at the face, soil excavation mechanics, and slurry hydraulics must be considered at all times by the operator. The soil properties and the ground water characteristics must be carefully considered. Measures should be taken so that soil uplifts and settlements at the surface are avoided. The forces that act on the tunnel face are the soil pressure, ground water pressure, boring head contact pressure, and the pressure of supporting and conveying in the suspension chamber.

The existing soil pressure is counter balanced by maintaining controlled pressure applied on the boring head at the tunnel face. This means that the pressure acting on the cutting head is set somewhat higher than the active soil pressure to avoid a cave-in at the tunnel face which may result in settlement at the surface. However, the pressure should be lower than the passive soil pressure to prevent uplift at the ground surface. Special equipment is employed to determine the soil pressure at the face. This data is transmitted to the control system which allows automatic maintenance of equilibrium pressure.

Different machines have different methods of maintaining the counterbalance. One of the methods of applying and maintaining pressure is by advancing or retracting the boring head and by opening or closing the cutting head soil inlets. If during the tunneling operation, the pressure on the cutting head exceeds the counterbalance, the cutting head automatically widens the soil inlets and advances slightly so that the equilibrium between soil pressure and cutting head pressure is restored. The pressure is maintained as required during the jacking operation.

In some machines, the earth counterbalance is provided by slurry pressures and flow rates. These machines work on the closed face mechanism. The cutting head is sealed off from the rest of the machine. There is one slurry inlet and one slurry outlet into and from the cutting head. Each is equipped with a valve. The flow rates through these valves can be controlled from the control panel. If during the tunneling operation, the pressure on the cutting head exceeds the counterbalance pressure, the rate of inflow is increased till the counterbalance pressure equals the pressure on the cutting head. In the other case when the counterbalance pressure exceeds the pressure on the cutting head, the outflow is increased until balance is achieved. The microtunneling machine can do this automatically within limits. When slurry lines are required to be removed, the pressure is balanced and both valves are closed so that the cutting head is sealed.

It is also possible to control the pressures manually. The advantage of automatic control of pressure equilibrium is that it makes the operation very safe and efficient in practically all types of soils with or without the impact of ground water. The size of the soil inlets in the cutting head governs the maximum size of aggregate the machine is capable of handling. The latest models of

machines are equipped with cutting heads which crush boulders to a size the equipment is capable of handling. If a cutting head with large openings is used, a bulkhead is provided immediately behind the cutting head to counteract the soil pressure. In this case, the excavated material is moved through an opening that is hydraulically controlled by a door. The gap of the door depends on the desired counterbalance pressure. This opening also prevents the oversized aggregates from entering the hydraulic conveying unit.

As a general rule, a separate shield is required for each nominal size of pipe.

EQUIPMENT DESCRIPTION

The equipment required for the installation of pipes by the microtunneling method includes the following:

1. Tunneling machine or tunneling shield
2. Main jacking station
3. Slurry conveying system and required pumps
4. Earth pressure counterbalance system
5. Slurry separation and/or sedimentation system
6. Laser guidance system for controlling alignment
7. Operator control panel for monitoring alignment, flow rates and pressures
8. Pipe lubrication system.

The tunneling shield is equipped with a boring head. Different manufacturers use different types of cutting heads for different types of soils. The rear of the tunneling machine is equipped with various pressure gauges or sensors and the laser target. These are continuously monitored by a remote TV camera or a sensitized board which transmits these readings to the operator at the control panel.

AUGER METHOD

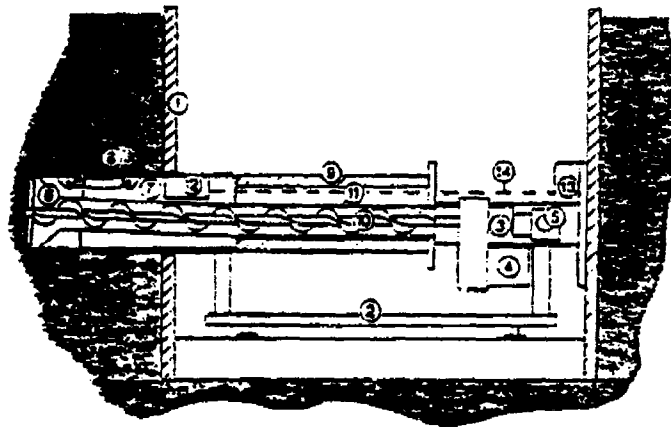
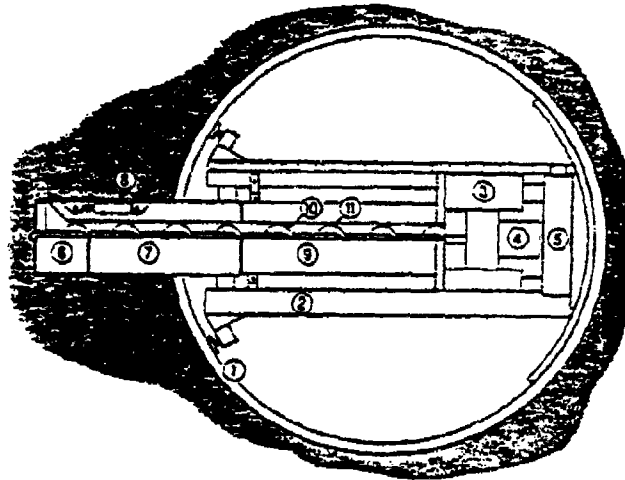
The auger method involves jacking pipe with simultaneous soil cutting at the face by a boring head and continuous soil removal by means of a continuous flight auger. The steering is accomplished by having an articulated steering head in the tunneling machine. The steering head is capable of being deflected in all directions by intermediately positioned steering cylinders. The auger runs in a separate guiding pipe.

METHOD DESCRIPTION

The soil is cut at the face of the machine by a cutting head. The design of the cutting head varies with manufacturer and depends on the type of soil expected to be encountered. The soil cut at the face is conveyed to the starting pit by an auger where it is collected in a container for final disposal. The conveyor screw and the boring head can be driven by a common or separate drive unit which is positioned in the starting pit.

System layout

- ① Jacking shaft
- ② Guide rails
- ③ Jacks
- ④ Auger drive
- ⑤ Back pressure plate
- ⑥ Steering head
- ⑦ Equipment housing
- ⑧ Steering jack
- ⑨ Product pipe
- ⑩ Auger flight
- ⑪ Auger casing
- ⑫ Lazer target
- ⑬ Lazer
- ⑭ Lazer beam



Auger Type Microtunneling Machine Layout Detail

The tunneling machine is made up of two articulated units, the steering head and the follower. These two units can be deflected in relation to each other and in all directions by intermediately positioned steering cylinders. All machine monitors and controls are located at an operator's console.

The auger method can be used in ground water bearing soil to a limited extent. In wet flowing conditions, the open system design of the conveying unit allows ground water to flow from the tunnel face to the starting pit. This method necessitates the use of a system lock to maintain the pressure difference between the atmosphere and at the tunnel face. The simplest method of sealing and supporting ground water at the face of a tunnel is by the injection of compressed air in the area of the boring and steering head. Another method is to seal the conveying unit in the boring head area and at the end of the conveyer screw string by means of supplementary mechanical devices. The hydraulic or pneumatic pressurizing permits counteracting the static ground water pressure at the tunnel face to avoid cave-in at the tunnel face.

The various steps involved in the installation of pipe by this method are described below:

1. The first step involves the installation of the microtunneling machine in the starting pit.
2. After installing the microtunneling machine in the starting pit, the conveyer screw string end is sealed by a pressure lock. Then the conveyer screw string, with boring head extended and open, is pressurized to counteract the ground water pressure at the tunnel face. The system locks differ in design with manufacturer but all have a direct bearing on the ultimate removal of the soil cut at the face.
3. After build up of counterpressure, the jacks are activated and the pipe is jacked forward by cutting at the face and simultaneous removal of spoil by augers. The excavated spoil collects in a collection chamber.
4. After a section of pipe has been jacked, the tunnel face has to be sealed before another section of pipe can be installed to prevent inrush of water and caving in of the soil. For this, the boring head is retracted so that it is in contact with the steering head and all the soil inlets in the boring head are kept closed so as to make it watertight and airtight.
5. After the boring head is sealed against the tunnel face the pressure lock at the starting pit is released to facilitate the removal of spoil collected in the collection chamber and the installation of another section of jacking pipe and conveyer screw.
6. After another section of jacking pipe is set up, steps 2 thru 5 are repeated until the target pit is reached. All through the operation, a laser beam gives readings on the alignment of the bore head and in case the bore head is out of line, corrections can be made by activating the required jacks of the steering head.
7. Once the boring and steering head has exited the target pit, it is removed from the target pit and the augers are withdrawn from inside the pipe leaving the pipe in place.

The conveyer screw pitch and diameter determine the maximum cobble size which can be handled by the system. This is usually 2.75 inches (70mm) for normal auger methods. Special boring heads can be used to crush the boulders to a size acceptable by the conveyer system. Crushing is accomplished by having special bits or by a crusher at the rear of the boring head or a combination of both.

EQUIPMENT DESCRIPTION

The equipment required for the installation of pipes by this method includes the following:

1. Tunneling machine or tunneling shield
2. Main jacking station
3. Screw conveyer system and motors
4. Pressure locking arrangement
5. Spoil collection chamber
6. Laser guidance system for controlling alignment
7. Operator control panel for monitoring alignment, pressures and boring rate
8. Pipe lubrication system.

The tunneling shield is equipped with a boring head. The design of the boring head depends on the type of soil expected to be encountered. As a general rule, a separate shield is required for each nominal size of pipe.

MAIN CHARACTERISTICS

1. **Type of Pipe Installed:** Any type of smooth jacking pipe with continuous outside diameter which is capable of resisting the compressive forces that arise from jacking the pipe into the ground can be installed by the microtunneling method. The most common types of pipes are steel, reinforced concrete, fiberglass, ductile iron, vitrified clay, and PVC.
2. **Pipe Size Range:** The size of pipe that can be installed by this method ranges from 10 inches (250 mm) to 40 inches (1000 mm) for auger method and 10 inches (250 mm) to 120 inches (3000 mm) for slurry systems.
3. **Bore Span:** The system is capable of installing pipes up to 2000 feet within specified tolerance. In case of high frictional resistance, intermediate jacking stations may be required for sizes greater than 36 inches (900 mm) in slurry systems.
4. **Disturbance to the ground:** There is virtually no disturbance to the ground surface. The pressures are automatically controlled to counteract the soil and water pressures eliminating chances of ground subsidence or heaving.
5. **Area Requirements:** The method requires a primary jacking pit. In addition, the site should allow adequate room for slurry tanks, loading and hauling spoil, storage of jacking pipes, operation of equipment, and for the placement of the operator's remote control booth.
6. **Operative Skill Requirements:** The equipment is a high technology system and requires a high degree of skill. The operator must be able to interpret the readings on the various gauges correctly and must be able to handle the various situations that develop in the field.
7. **Accuracy:** The method is capable of installing pipes to a high degree of precision. Hence these are mainly used for the installation of sewer lines where a high degree of precision is required. The laser system for controlling the alignment permits systems to be installed to an accuracy of ± 1 inch (25 mm).

8. **Recommended Ground Conditions:** The method is capable of installing pipes in a wide variety of soils from soft soils to hard clays. The equipment is also capable of handling boulders up to 30% of the nominal diameter of the pipe. It has been observed that the auger method is particularly suitable for cohesive soils. The latest designed slurry machines have cutter heads that do very well in solid rock. Water table is no problem for the slurry machines.

MAJOR ADVANTAGES

The method is capable of installing pipes to extremely accurate line and grade tolerances. It has the capability of performing in very difficult ground conditions without expensive dewatering systems and/or compressed air. Lines can be installed at a greater depth without a drastic effect on the cost. The depth factor becomes increasingly important as congestion is increased. Safety is enhanced as men are not required to enter trenches or tunnels. The finished product (carrier) pipe can be jacked directly without the need of a separate casing pipe.

MAJOR DISADVANTAGES

The capital cost in equipment is high. However, on projects where these methods have been competitively bid against other tunneling methods, the unit price costs have been in line. Some micro-TBM systems have difficulty in soil with boulders.

SOME INTERESTING STORIES

My father, a Marine during W.W.II, told me stories about the "silent enemy" on the islands of the south Pacific. "If they weren't tied to the trees, they were in the tunnels." In Iwo Jima alone there were 26 km of tunnels found at the War's end.

During the early 70's, while stationed in Japan, I was amazed by the stories of all the tunnels dug by the Japanese during the War. The tunnels between Yokota AB and Tachikawa AB were used to ferry aircraft back and forth. The American housing complex now called Green Park, in Tokyo, previously a Mitsubishi engine facility, had tunnels in the basement leading to all the surrounding assembly points and air fields. These were sealed off in the 50's after the unfortunate deaths of several U.S. dependent children.

But tunnels played an important part in history long before the war. In fact, there is evidence they were instrumental as far back as biblical times. Remember the story of Jericho.

Jericho was a fortress strategically located protecting the territory west of the Jordan from invasions from the east. It was surrounded by two parallel walls made of sun-dried brick which were bridged at intervals, and houses were built on the walls at these points. Biblical records of this event are substantially sustained by discoveries in excavations. The outer wall collapsed outwardly; the inner wall fell into the area between the two walls and on the ruins of the outer

wall. Masses of burned brick, cracked stones, charred timbers and ashes reveal the fact that an intense fire accompanied the destruction of the city.

Consider the possibility that a tunnel dug under Jericho's walls was supported by massive oak timbers, placed there during the excavation. As the Israelites marched around Jericho for seven days blowing their horns, Israel's first covert tunnel was underway.

The diversion of this constant ceremony and its noise gave Joshua's "Corps of Engineers" enough time to complete its job. A realistic time frame even with manual excavation. On the seventh day the timbers were set on fire and "the walls came tumbling down."

SOME POSSIBILITIES

Think of the possibilities of microtunneling in the 60's under the Berlin Wall into the basement of a building in the East. This month Crowder Construction of North Carolina microtunnelled into the basement of a hospital in Winston-Salem to tie into the buildings existing sewer system.

Think of the possibilities of tunneling several thousand feet behind enemy lines under rivers or lakes. In 1989-90 in Staten Island, New York, a stone thrown from the ocean, E.E. Cruz & Co., Inc. of Holmdel, New Jersey, tunneled 100 feet deep, pushed 1600 feet in one drive, under 60 feet of water head a 63" OD Pipe to within 1" of target.

Think of the possibilities of tunneling under the desert floor next to an impossible oil well fire! Imagine being 50 feet deep and within 1" of the oil pipe. A special pipe behind the tunnel machine is opened and two men install a wet tap into the oil pipe and shut down the flow.

Think of the possibilities at military installations around the world. The capability of installing access shafts and tunnels for the movement of people or materials to places outside the walls.

Think of the possibilities of accessing the middle of a river, lake or ocean from a thousand feet away to rendezvous with submarines or divers.

Think of the possibilities of installing utility lines under our military bases without excavation, or fuel and water lines at a naval base from one side of the bay to the other.

Think of the bridge over the river which has been destroyed or discovered by the enemy. Now, think of the tunnel that's cheaper to build, can't be bombed, and is virtually undetectable.

Think of the possibility of tunneling under a nuclear reactor trying to control a melt down by supplying cooling water to its core.

Think of the possibility of the entrepreneur who finds his way into the vault at the Denver Mint, starting 2000 feet away in the parking lot of a nearby Burger King.

Think of all the possibilities. This list could go on and on. Its length is only limited by one's imagination to solutions for a given problem. Microtunneling is not a panacea, it is merely another door to open in one's search for the best solution. Joshua found the right door for his problem.

Borehole Radar Tunnel Detection at Gjøvik, Norway

F.N. Kong, H. Westerdahl and T.L. By

**Norwegian Geotechnical Institute
Oslo, Norway**

ABSTRACT

Tomographic tests were performed both before and after the driving of a $10 \times 10\text{m}^2$ tunnel in conjunction with the excavation of the Gjøvik Olympic Mountain Hall for the 1994 Winter Olympic Games. Test results indicate that the NGI georadar system functions well in the performance of borehole tomography measurements. The tomographic image obtained clearly shows the location and dimension of the tunnel.

INTRODUCTION

The Gjøvik Ice Hockey stadium for the 17th Winter Olympic games to be held in Norway in 1994 is now successfully completed. With a span of 61m, a height of 25m and a length of 91m, the cavern that houses the stadium is by far the largest man-made underground cavern for public use in existence today (Bhasin and Løset, 1992)

Numerous research projects were scheduled to take place during the excavation of the cavern (SINTEF, 1991). Among these, the project "Tunnel detection using borehole radar" was to investigate the capability and effectiveness of the NGI Georadar system for tomographic tests made both before and after a tunnel (ca. 10m in diameter and 35m below the surface) was driven. The main results of the tests are reported below.

MEASUREMENT LAYOUT AND NGI RADAR SYSTEM

The layout used for the tests is shown in Figure 1. The two vertical boreholes were drilled 25m apart to a depth of 50m. At each transmitter position, measurements were taken at 22 receiver positions from 49m to 7m depth with a step distance of 2m. There was a total number of 22 transmitter positions, also from 49m to 7m depth.

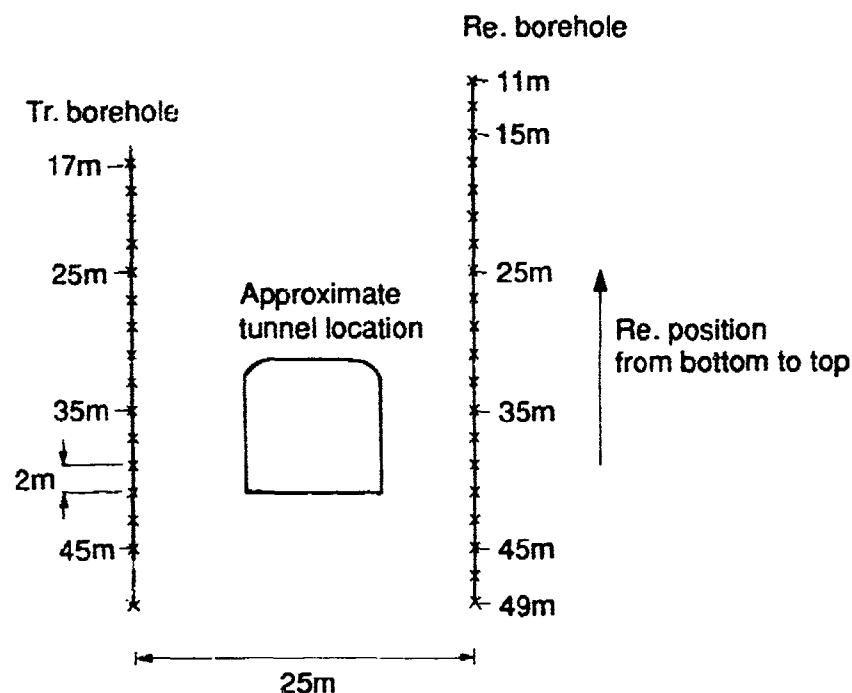


Fig. 1 Measurement layout.

The NGI georadar system uses step frequency signals instead of impulse signals as most commercial georadar systems use. A network analyser (HP 8753) is used as the signal generator and receiver. During measurement, 201 frequency samples covering the desired signal bandwidth are generated in sequence. The magnitudes and phases of the echo are received, also sequentially, by the network analyser and recorded by the data acquisition computer. A time domain signal can then be obtained by performing Fast Fourier Transform (FFT) to the received spectrum. The power level generated by the network analyser is from -5 to 20 dB mW and the receiver noise level is -100 dB mW. Considering that the maximum input to the receiver is 20 dB mW, the receiver has a dynamic range > 120 dB. Other main features and applications of the NGI georadar system are more specifically described in By et al., 1992; Kong et al., 1990; Kong et al., 1992 and Westerdahl et al., 1992.

Wire dipole antennas were used for the borehole test. The antenna length was set to 2.5m, corresponding to a resonance frequency of 50 MHz in the air and 20 MHz in the rock material, given that the dielectric constant of $\epsilon = 6$. A pair of 100m cables was used to connect the antennas to the transmitter and receiver.

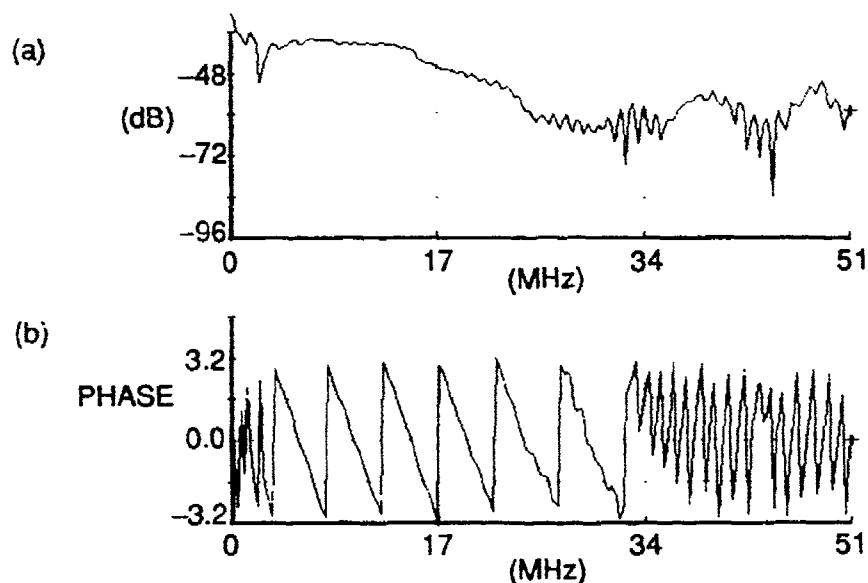


Fig. 2 Received spectrum while both Tr. and Re. antenna at same depth.

Figures 2 a and b show the spectrum magnitude and phase of the received signal, respectively, while both transmitter and receiver antennas are located at 35m depth within the corresponding boreholes before the tunnel was driven. The phase curve (Figure 2b) indicates that the usable frequency band is about 3 MHz - 34 MHz; the antenna is thus good for a wide frequency band. The spectrum magnitude curve (Figure 2a) shows that the signal received is much stronger than the system's noise floor (-100 dB mW). The system's remaining dynamic range can therefore be used for detection at a greater distance or detection with a shorter wavelength. According to the information in Figure 2, the NGI system can accurately measure both phase and magnitude spectrums, providing the basis for a tomography inversion operation.

TEST RESULTS AND TOMOGRAPHIC IMAGE

The received time-domain waveforms measured before the tunnel was driven are presented in Figure 3. Figure 3a shows the waveforms for 22 receiver positions, while the transmitter antenna was located at 25m depth. The horizontal axis of the figure shows the trace number. Trace No. 1 is for the receiver position at 49m depth, trace No. 2 is for the receiver position at 47m depth, and so on to trace No. 22 at 7m depth. The vertical axis shows the distance between the transmitting antenna and the receiver antenna

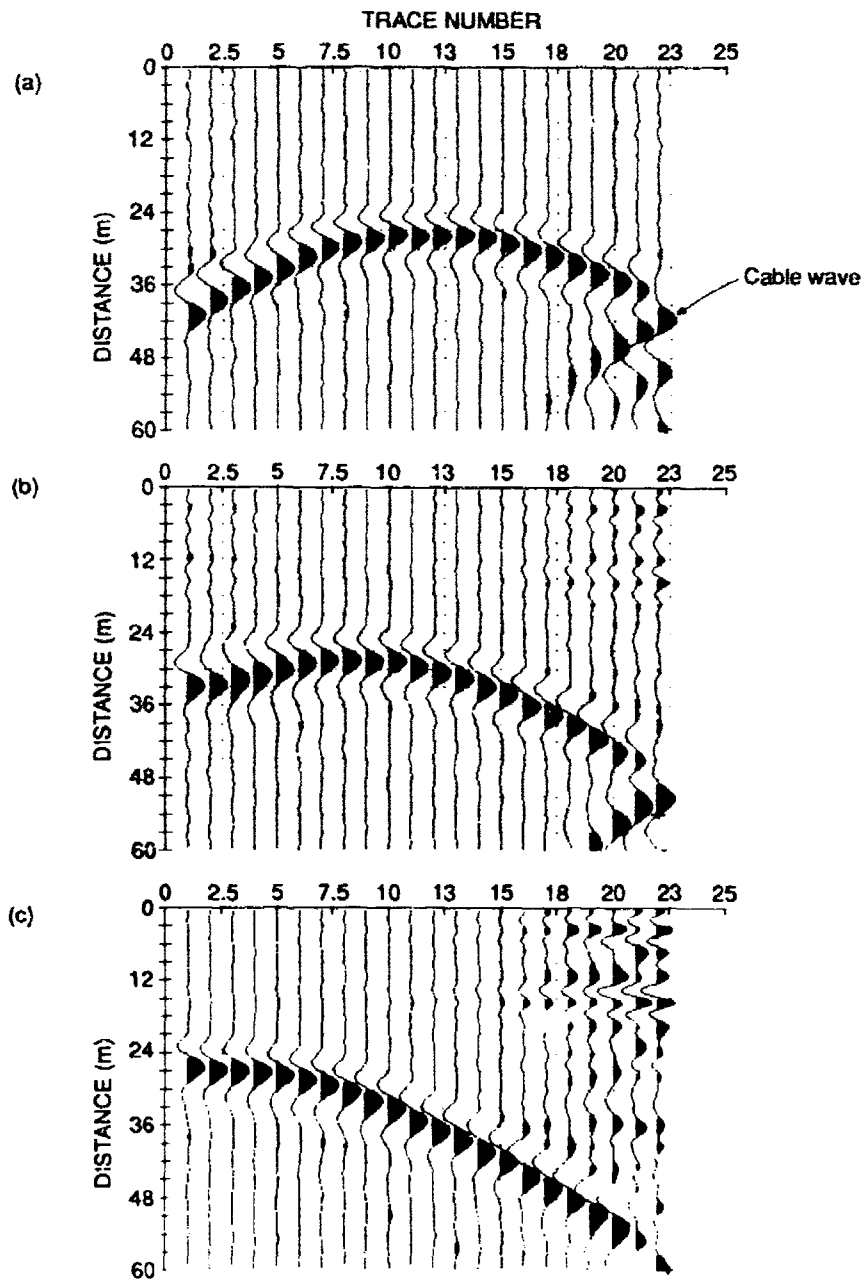


Fig. 3 Measurement before tunnel was driven.

a) Tr. position ~ 25m, b) Tr. position - 35m, c) Tr. position - 45m.

(an estimated wave speed of 12.5 cm/ns was used). Figure 3b and c correspond for a positioning of the transmitting antenna at 35m and 45m depth, respectively.

The time-domain waveforms shown in Figure 3 were obtained by performing FFT on the raw measured spectra. A Hann window was introduced in this process, but apart from this, no additional signal processing is introduced.

The figures show that the received signals are clean and have a good "impulsive" shape. Each waveform shown is normalised by its maximum value. The magnitudes, or the maximum values, of the time-domain waveforms are shown in Figure 4. From an examination of the arrivals and magnitudes of the waveforms, the rock mass can be inferred to be rather homogenous. The dielectric constant is $\epsilon \approx 6$ and the attenuation is about 0.7 dB/m for the centre frequency signal.

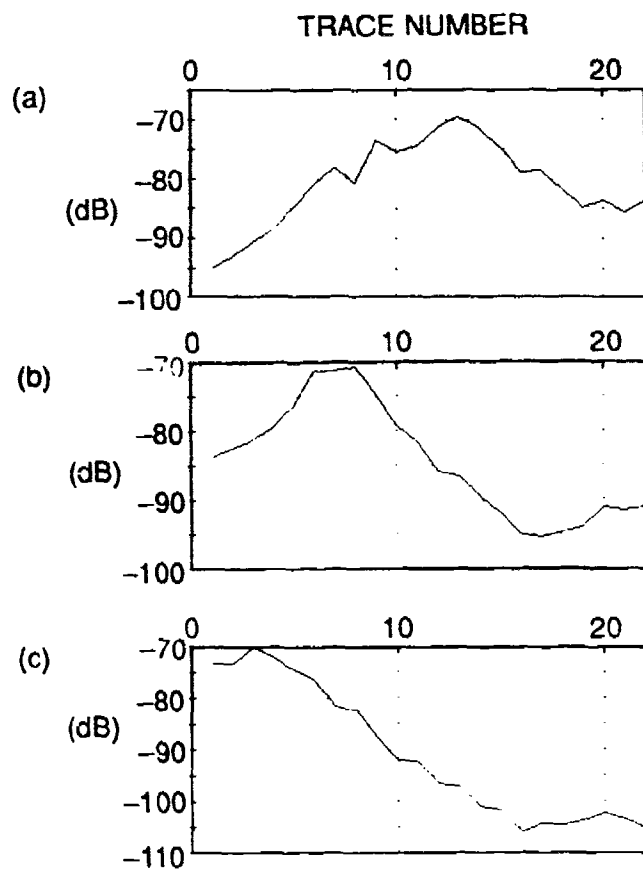


Fig. 4 Magnitudes of waveforms shown in Fig. 3

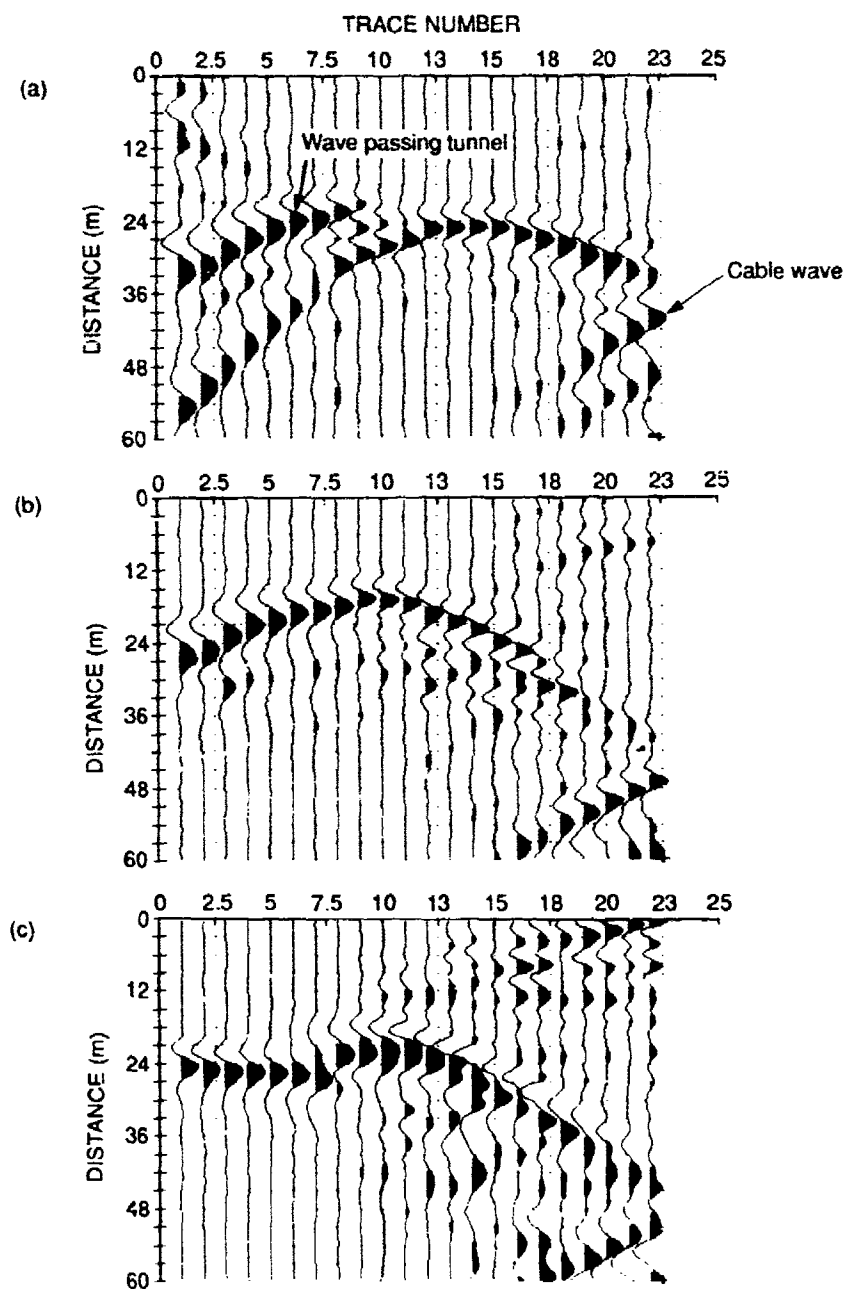


Fig. 5 Measurement after tunnel was driven.
 a) Tr. position – 25m, b) Tr. position – 35m, c) Tr. position – 45m.

Figure 5 shows the measurement results from testing after the tunnel was driven for transmitter positions at 25m, 35m and 45m depth.

In comparing Figure 5 with Figure 3, note that while the transmitter antenna is at 25m depth for the first 9 receiver locations (49m to 33m depth), the wave speed is obviously faster than that in the rock mass. When the transmitter antenna is placed at 45m depth, starting at trace 7 (receiver position: 37m depth), the wave speed becomes faster than in the rock mass. It is here that the wave paths pass across the tunnel air body. There is also a transition zone (e.g., trace Nos 10, 11, and 12 in Figure 5a), where part of the wave energy passes inside the tunnel and part of the wave energy passes outside the tunnel. Once past this transitional zone, the main wave energy travels inside the rock mass (e.g., trace Nos 13, 14 and so on in Figure 5a). One noticeable feature of Figure 5a is that there are two peaks in the waveforms for trace Nos 1 - 10. These later peaks are probably from waves which have travelled around the tunnel boundary to arrive at the receiver.

Based on the measurement results shown in Figure 5, a propagation model assumption for this strong scatter case is used as follows:

- The time arrival is defined as where the waveform maximum occurs in the time domain.
- The wave path is not a ray, but a beam. The beam width can be defined by, e.g., the Fresnel diffraction plate theory. Here we use the following formula to define the wave beam width:

$$B = \sqrt{\frac{\lambda d}{2}}$$

where B is the beam width, and d is the distance between the transmitter and the receiver. The above formula is derived according to the geometry defined in Figure 6.

- When the main energy in the beam passes through the air body of a tunnel, the travel time of the wave will become shorter than if there had been no tunnel.
- When the wave beam passes across the tunnel boundary, part of the energy travels through the body of tunnel air and part of the energy travels through the rock mass. The waveform received is thus the interference between these two waves.

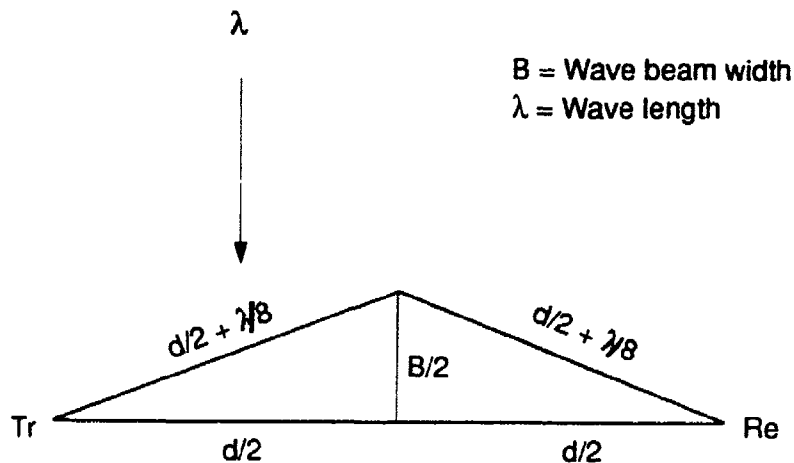


Fig. 6 Definition of wave beam width.

In this model, the "wave rays" are replaced by "wave beams". However, it can be imagined that as long as we can avoid using the beams which pass across the tunnel boundary (e.g., trace No. 7 in Figure 5c, trace Nos 16, 17 and 18 in Figure 5b and trace Nos 9, 10 and 11 in Figure 5a), the tomographic inverse based on the geometrical optics (and using only the time arrival information) can still give a good result. We have performed such an inversion, and the tomographic image is shown in Figure 7. The figure shows that the tunnel dimension and location are clearly defined. The vertical location and dimension of the tunnel are accurately determined. However, the horizontal dimension is wider than the real tunnel dimension.

CONCLUSIONS

The NGI georadar system functions well for performing borehole tomographic measurement.

Tomographic inversion based on geometrical optics can be used for tunnel detection using only the time arrival information, as long as the tunnel dimension is not very much smaller than the beam width which has been defined in the text.

Speed of the electromagnetic waves

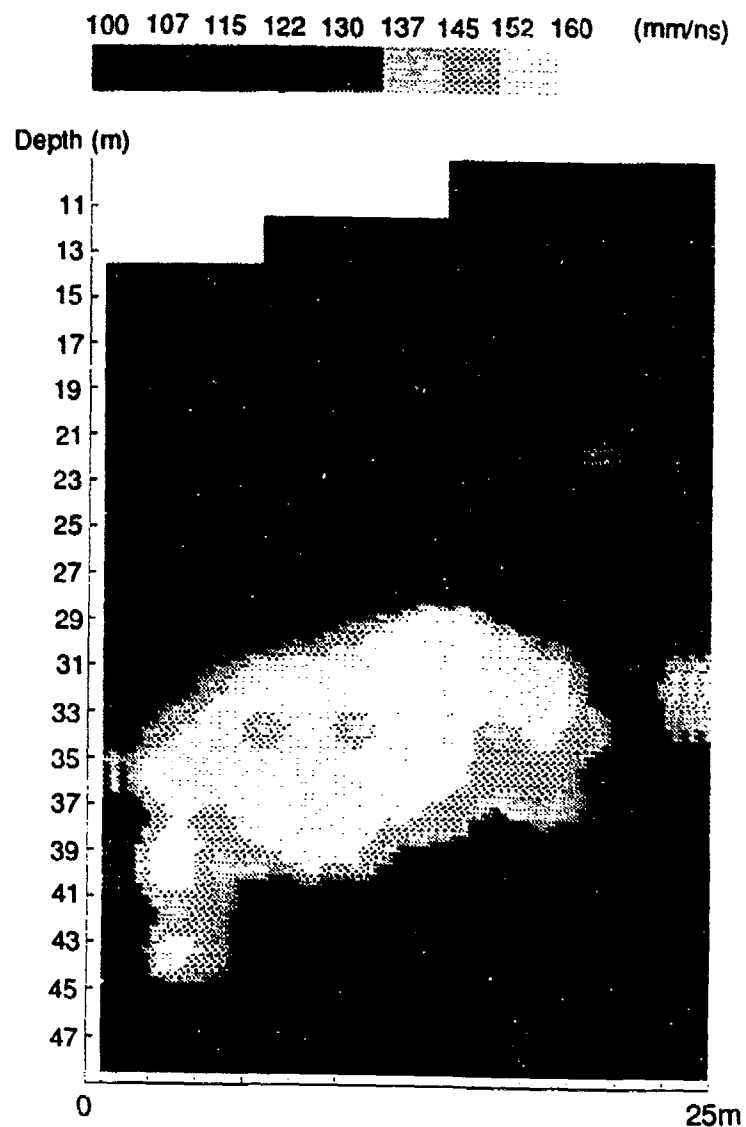


Fig. 7 Tomographic image of Gjøvic tunnel.
Dark areas show homogenous rock mass.
Light area indicates the tunnel location.

REFERENCES

- Bhasin, R. and F. Løset, 1992, "Norway's Olympic Cavern", *Civil Engineering*, December 1992.
- By, T.L., F.N. Kong and H. Westerdahl, 1992, "Geo-radar Development at the Norwegian Geotechnical Institute (NGI)", Fourth International Conference on Ground Penetrating Radar, Rovaniemi, Finland, Special Paper 16, pp 21-28.
- Kong, F.N. and T.L. By, 1990, "Ground penetrating radar using a frequency sweeping signal", Third International Conference on Ground Penetrating Radar, Denver, USA, May 1990.
- Kong, F.N., J. Kristiansen and T.L. By, 1992, "A Radar Investigation of Pyramids", Fourth International Conference on Ground Penetrating Radar, Rovaniemi, Finland, Special Paper 16, pp 345-349.
- SINTEF, 1991, "Rock Cavern Stadium: A Research Evaluation of the Gjøvik Olympic Mountain Hall", Report Summaries, STF15 A92013.
- Westerdahl, H., R. Austvik and F.N. Kong, 1992, "Geo-radar in Tunnelling - The Tunnel Radar", Fourth International Conference on Ground Penetrating Radar, Rovaniemi, Finland, Special Paper 16, pp 41-45.

MINING THROUGH UNDERGROUND WORKINGS AT
WHARF RESOURCES' OPEN PIT GOLD MINE,
BLACK HILLS, SOUTH DAKOTA, USA

A. D. Hammond and T. A. Loomis

Wharf Resources, Lead, South Dakota

ABSTRACT

Since 1983, Wharf Resources has operated an open-pit/heap leach gold mine in the Black Hills of South Dakota. The mine is located in the historic Bald Mountain Mining District, site of extensive gold mining activities between 1877 and 1959. The area was mined using underground methods which included room and pillar and shrinkage stoping in the Cambrian Deadwood Formation. During the course of the present open-pit operation, numerous surface collapses and shallow stopes have been and are being encountered, creating a need for accurate detection methods.

The current stope detection practice at Wharf Resources consists of drilling deeper blast holes in suspected areas within a production blasting pattern with the objective of locating and collapsing the cavities before heavy equipment is allowed to enter the area.

In addition to the current procedures, Wharf is pursuing geophysical methods for the identification of underground workings. Ground penetrating radar, resistivity, magnetic and gravimetric methods have been tested at the Wharf Mine by private, academic, and government research institutes, making it a valuable test ground for the application of geophysics in the detection of underground workings at an active open pit.

This paper describes the current stope detection practices used at the Wharf Mine.

INTRODUCTION

Wharf Resources operates an open pit, heap leach gold mine in the Black Hills of South Dakota. Ore is mined by conventional truck/shovel methods in multiple 6 m (20 ft) benches. Much of the active area contains historic underground mine workings and presents both engineering difficulties and safety hazards. Wharf currently employs an aggressive program to define the extent and location of the underground workings. Production drill rigs are used to delineate the voids in combination with historic maps. Specialty

maps showing void locations, collapsed features, safe haulage routes, and a hazard control team help create the safest working environment possible.

Wharf is also testing additional geophysical methods of void detection such as ground penetrating radar, gravity survey, resistivity, and magnetic methods.

GENERAL INFORMATION

The Wharf Mine is located 9 km west/southwest of Lead, South Dakota (Fig. 1), in the historic Bald Mountain Mining District of the northern Black Hills. Rapid City is the nearest major transportation center and is located approximately 120 km, by road, southeast of the mine site.

The Black Hills is an asymmetrical domal mountain range. The range is approximately 148 km long in the north-south direction and 102 km wide. Elevations vary from 1,070 m above sea level to over 2,130 m. The mine site is located at approximately 1,890 m above sea level.

The topography of the Black Hills is largely controlled by the geologic setting. A band of upturned Paleozoic and Mesozoic sedimentary units ring a core consisting of metamorphic rocks and Precambrian intrusives. The resulting topography consists of elongated valleys and ridges in the sediments and rugged pinnacles in the core.

The Bald Mountain Mining District lies in an area of gently rounded hills cut by two principal drainages. Squaw Creek drains to the north and Annie Creek drains to the southwest. Both are intermittent in the mine area.

Annual average precipitation in Lead is 710 mm with most precipitation coming between April and September.

HISTORICAL SUMMARY

The Bald Mountain Mining District includes both the Portland and Ruby Basin Districts of earlier literature. Production from the Bald Mountain Mining District is estimated at 43,945 kg (1,412,900 troy oz) of gold and 134,610 kg (4,327,900 troy oz) of silver between 1877 and 1959. During this time, gold ore was mined from extensive underground workings. The property, which lies mostly within the Portland District, is now controlled by Wharf Resources.

The first claims in the district were located near the town of Trojan, within the Portland District, in 1877. The development of the district proceeded rapidly and many small underground operations were producing ore by 1910. Between that date and 1928, the majority of the properties were consolidated into two major companies, the Bald Mountain Mining Company and the Golden Reward Consolidated Mining and Milling Company.

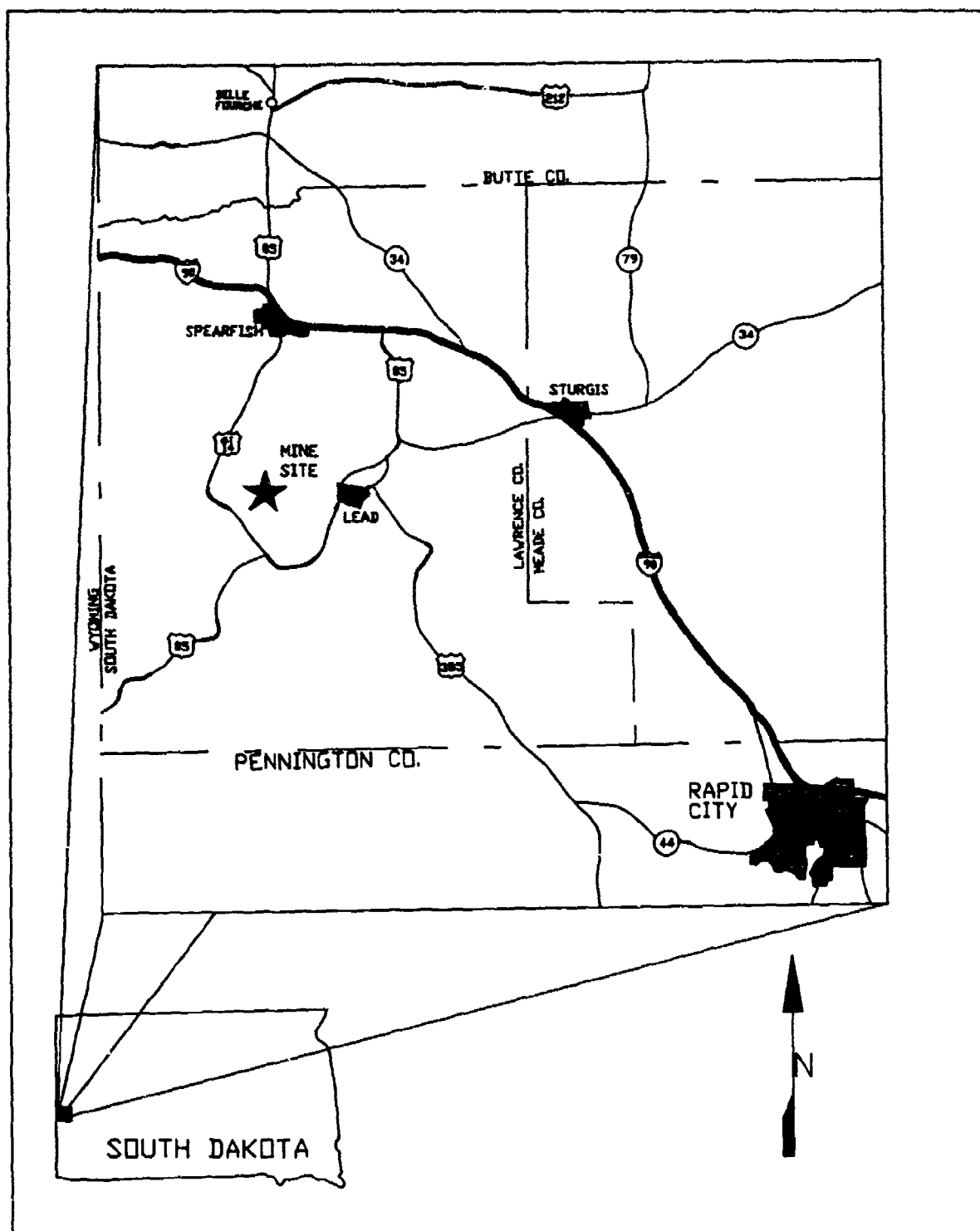


Figure 1. Location of the Bald Mountain Mining District and the Wharf Mine

Tertiary age intrusives at Wharf occur as dikes and sills in both the Deadwood Formation and the overlying Winnipeg Formation. The intrusive rocks found at Wharf are predominantly monzonite and phonolite porphyry. The major igneous ore host at Wharf is a 70-85 m thick monzonite porphyry sill. The sill is emplaced within the middle member of the Deadwood Formation and is continuous throughout most of the pit area. The underground workings in the pit area are found above the monzonite porphyry sill within Deadwood Formation.

Ore localization in the Deadwood Formation is primarily controlled by N-NE trending, sub-vertical fractures. Ore zones are best developed as replacement deposits adjacent to the fractures. The fractures, locally referred to as "verticals", are continuous through the Deadwood Formation up to 760 m along strike. Mineralized widths vary from 1 to 30 meters. In areas of closely-spaced fractures, extensive, disseminated deposits occur (Loomis & Alexander, 1990). Underground workings were developed along the high-grade verticals (Fig. 2).

The Deadwood Formation is oxidized throughout the pit area and weathered at the surface to illitic and montmorillonitic clays. Weathered zones typically contain a high degree of moisture. Ore zones typically contain a high siliceous content with abundant iron oxides and secondary clays.

DESCRIPTION OF UNDERGROUND WORKINGS

The ore in the upper contact unit of the Deadwood Formation was mined by the room and pillar method (Fig. 3). This method facilitated the extraction of ore in the flat-lying blanket type deposits. Timber was occasionally used to support highly fractured ground in wide stopes and to insure against sloughing along haulage ways. Shrinkage stoping was used to mine narrow ore bodies along the "vertical" trends (Fig. 4). This mining method is basically an overhand stoping system in which a portion of the broken ore accumulates until the stope is completed. The underground mines in the Bald Mountain District were described by Miller (1962).

"Intermediate Contact ore bodies were mined by shrinkage and open-overhand stoping methods. Ore bodies of small cross section were mined by open-overhand methods from the development drift level. Shrinkage was used to mine layered ore bodies. The standard procedure in development of the stopes was to drive a 7 by 7 ft drift along the vertical, at the bottom of the ore. Timbered raises were then driven, usually at the extremities of the ore body to the top of the mineralized zone. Where shrinkage was warranted, chute raises were installed, spaced at 22 feet center to center."

From mining experience at Wharf, the average width varied between 1.8 and 2.4 m (6-8 ft) in the shrinkage stopes. Room and pillar stopes overlies shrinkage stopes in many places, posing additional safety hazards. Typical

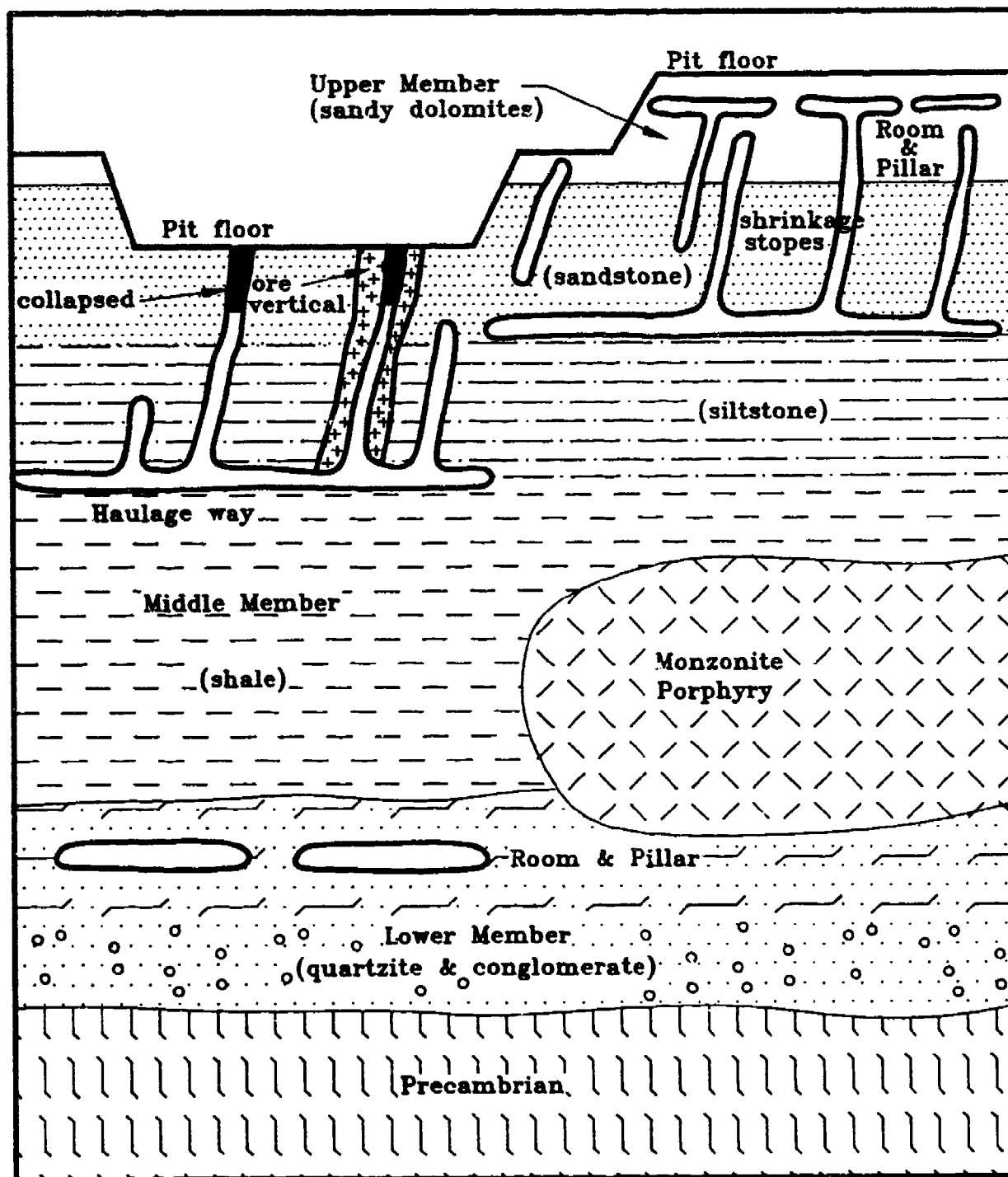


Figure 2. Deadwood Formation showing areas of stope development.

room and pillar stopes are often collapsed easily during routine blasting operations. However, shrinkage stopes, because of the narrow width, may bridge off after a blast, creating an unsafe condition. Present ore trends typically follow shrinkage stopes, which may be up to 45 m (150 ft) deep.

Historic underground workings maps are available from the previous underground mining operation and have been incorporated as part of Wharf's routine grade control practices by digitizing into AUTOCAD software.

CURRENT OPERATIONAL PROCEDURE FOR MANAGING STOPE AREAS

In recognition of the potential safety hazards in a stoped area, a Hazard Control Team (HCT) has been implemented at the Wharf operation. This team consists of select engineers, a safety coordinator, pit foremen, and management. The team meets weekly to discuss the drilling and mucking operations.

The following outline summarizes the procedure followed by the HCT in the implementation of the plan to identify stope areas.

1. Stope delineation

The stope delineation program is carried out by drilling in suspected void areas. The grade control engineer overlays a pre-engineered blast hole pattern over the historic stope maps. He identifies the blast holes that would intersect a stope hazard and marks them in the field with a blue flag. The grade control engineer notifies the drill/blast foreman that the area is ready for drilling (Fig. 5). In areas of question, every fifth row of the blast hole pattern is marked with blue flags for further assurance.

2. Verification

The drill/blast foreman will verify the holes staked by the grade control engineer. The HCT conducts a weekly field safety audit to ensure proper implementation of the plan. A continuous flow in communications at all levels is essential to the successful implementation of this plan.

3. Drilling

The stope delineation holes marked with the blue flags are drilled to a depth of 15 m (50 ft). Should a stope delineation hole encounter no stope or backfill, the driller annotates the depth of the hole and either "NS" for no stope or "BF" for backfill on the flag.

Should a stope delineation hole encounter a void, the driller immediately pulls pipe and backs away from the hole in the same direction as he approached. The driller then measures the depth of the void and annotates the depth to back and floor, along with

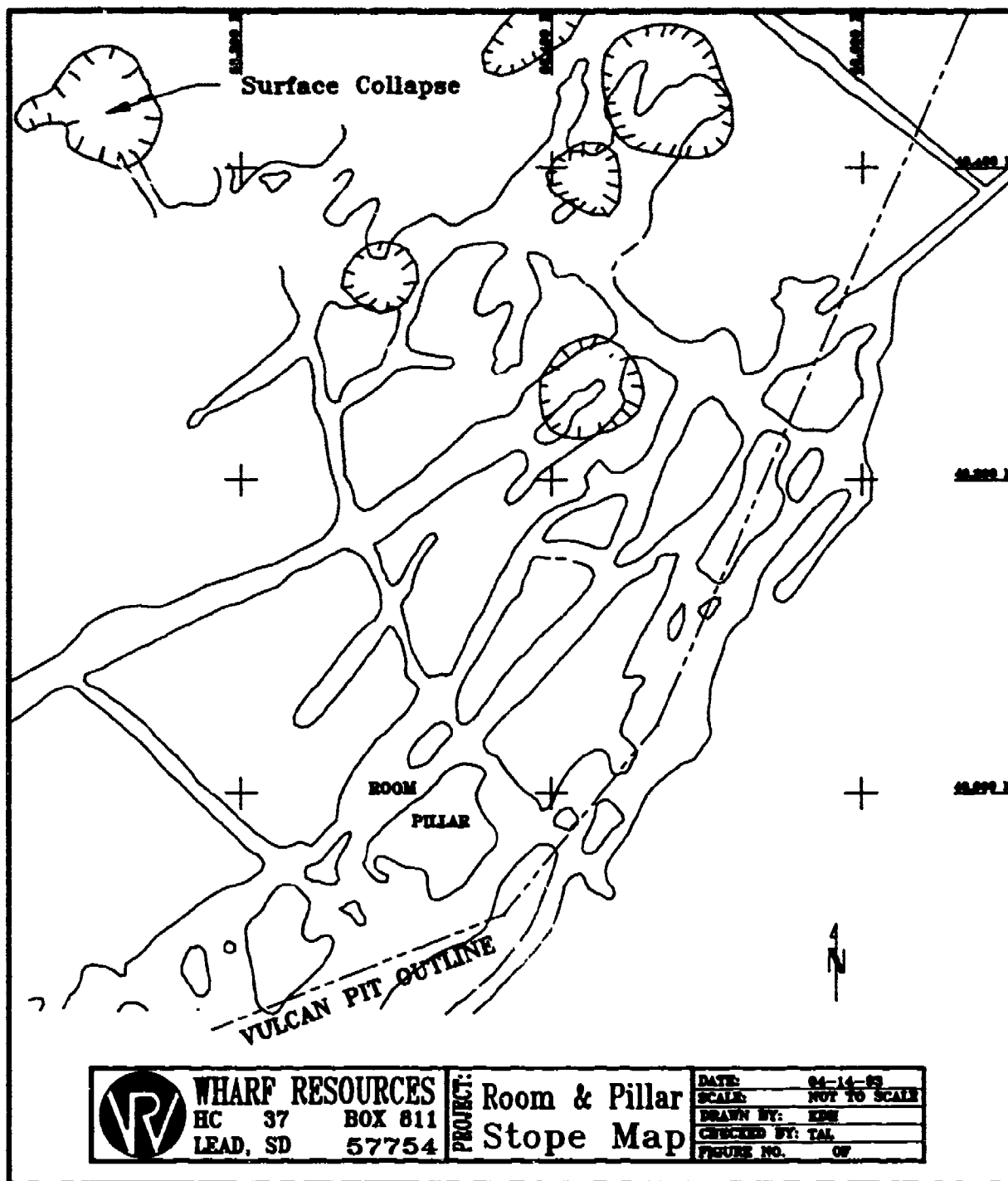


Figure 3. Typical room and pillar stopes.

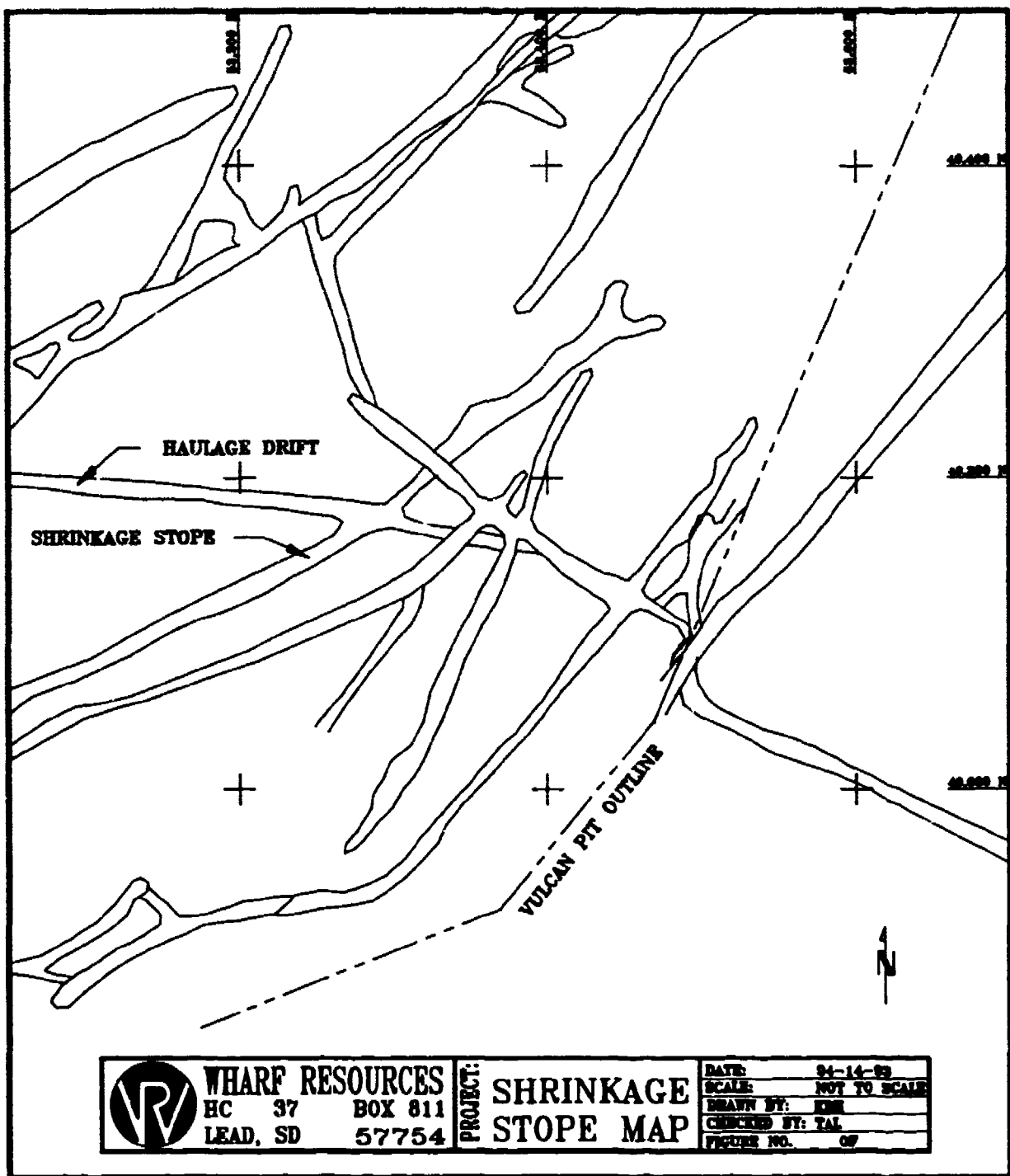


Figure 4. Typical shrinkage stopes.

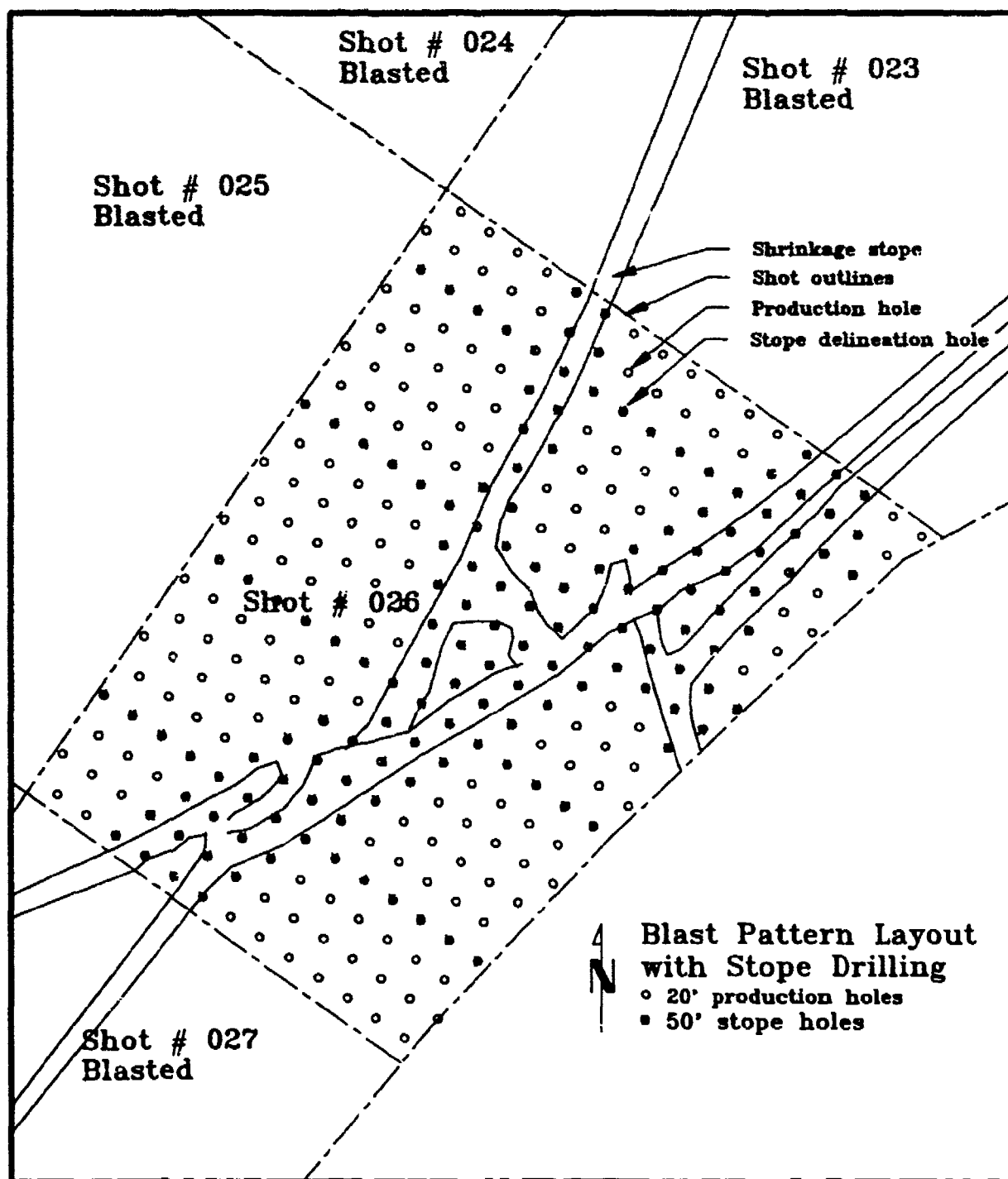


Figure 5. Blasting pattern with stope delineation holes.

the word "VOID" or "STOP". The location of the hole is then transferred to a map posted in the foremen's office.

For safety reasons, stope delineation drilling is not scheduled unless two people are present in the immediate area.

4. Blasting

When a shot which contains voids is blasted, the drill/blast foreman ensures that the voids have been collapsed. Wharf's current policy is to collapse voids with the use of blasting whenever possible.

As a precaution, sufficient time (approximately 12 hours) must be allowed for the settling of backfill before the area is walked upon.

5. Handling of voids following blasting

Following blasting, depressions or collapses will sometimes appear where blasted material has filled or partially filled voids. In cases such as this, the depression or collapse is barricaded off and backfilled with the appropriate material. The surveyors will take note of this area and plot it on the dig maps.

The safety coordinator will place a sign alerting for the presence of voids, and only authorized personnel are allowed in.

6. Mining

Areas of known stopes and suspected trends are shown on maps posted in the foremen's office and on dig maps provided to the equipment operators. Outlines will be denoted with a red marker and will be staked in the field with red "CAUTION" flags and fluorescent green lath.

If, during mucking, voids are opened, the above-mentioned procedures for backfilling should be followed. Further delineation drilling may be necessary before backfilling.

The major stope trends marked in the field are to be mucked perpendicular to the trend. A berm is to be constructed on the major stope trends to designate the stope hazard and direct all traffic to or from the muck face.

7. General responsibilities

It is the responsibility of everyone involved to insure caution and general awareness when operating in potentially hazardous areas. A smooth flow of communication is essential at all levels.

Wharf's policy is to encourage participants to communicate new ideas and suggestions to create a safe work environment.

In the event of a stope collapse involving personnel or equipment, emergency procedures have been developed and are incorporated in Wharf's Emergency Procedure Manual. The Surface Mine Rescue Team (SMRT) will be called upon immediately following notification.

8. Individual Responsibilities

- ♦ Grade Control Engineer: responsible for the overall stope management program, specifically stope delineation, safe haulage definitions, map updates, chairing hazard control meetings, and assuring proper flow of communication.
- ♦ Blasting Foreman: responsible for implementing the stope delineation program. Also responsible for record keeping of void depth.
- ♦ Pit Foreman: responsible for mucking around stopes, berm placement for safe haul routes, and backfilling voids.
- ♦ Safety Coordinator: responsible as a member of the HCT which oversees the general safety procedures in stope areas.
- ♦ Chief Surveyor: responsible for assuring that all major trends and collapses are properly flagged and maintained. Also responsible for timely surveying of shot patterns for the Grade Control Engineer.

CONCLUSION

Wharf Resources is actively seeking new methods to improve its stope delineation program, for which numerous private and government agencies were contacted. Among them, the U.S. Bureau of Mines and the South Dakota School of Mines and Technology have carried out tests at the mine site using ground penetrating radar, microgravity, resistivity, and magnetic techniques which are being evaluated and will be presented at this conference by those parties.

The authors hope that this presentation will raise awareness of the potential hazard encountered by surface mines in areas that have been mined by underground methods and help other mine operations facing similar problems. The authors believe this is an excellent forum to exchange ideas and promote discussion and research on this topic.

ACKNOWLEDGMENTS

The authors wish to acknowledge the management of Wharf Resources for its continuous support in this matter, Dr. W. M. Roggenthen of the South Dakota School of Mines and Technology, and K. L. Hauser and M. J. Friedel of the U.S. Bureau of Mines, for their interest and participation.

REFERENCES

Miller, P.A. "A Study of the Bald Mountain Mining Area, Lawrence County, South Dakota", Engineer of Mines thesis, South Dakota School of Mines and Technology, 1962.

Noble, J.A., 1952, "Evaluation of Criteria for the Forcible Intrusion of Magma," Journal of Geology, Vol. 60, pp. 34-57.

Shapiro, L.H., and Gries, J.P., 1970, "Ore Deposits in Rocks of Paleozoic and Tertiary Age of the Northern Black Hills, South Dakota," U.S. Geological Survey Open-File Report 70-300, 235 p.

Erown, B. W., 1954, "A Study of Northern Black Hills Tertiary Petrogenic Province with Notes on the Geomorphology Involved," Unpub. Ph.D. Thesis, Univ. of Nebraska.

SME Mining Engineering Handbook, AIME, 1973, Volume 1, pp. 9-11; 9-14.

Loomis, T. A. and Alexander, D. L., 1990 "Geology of the Foley Ridge Gold Mine", proceedings from the Fourth Western Regional Conference on Precious Metals and the Environment, Lead, SD, 1990.

APPENDIX A
AUTHOR INDEX

INDEX TO AUTHORS

- Alleman, T.J. - 21
Allen, J. - 437,563,577
Andersen, H.T. - 181,547
Balch, A.H. - 187
Ballard, Jr., R.F. - 133,335
Beasley, Jr., G.C. - 199
Block, L. - 359
Bradley, J.A. - 277
Brew, J. - 519
By, T.L. - 651
Cameron, C.P. - 21,47,597
Chi, D. - 427
Chignell, R.J. - 67
Chufo, R.L. - 463
Cisar, D. - 209
Coss, T.R. - 639
Descour, J.M. - 97,381
Devaney, A.J. - 347
Dickerson, J. - 209
Duff, B.M. - 223
Friedel, M. - 401,619
Greenfield, R.J. - 73,117,133,261
Grover, T.P. - 277
Ha, T-S. - 393
Hammond, A.D. - 661
Hauser, K. - 401,619
Hill, D.A. - 481
Jackson, M. - 401
Kang, J-S. - 393,415
Karazincir, M.H. - 187
Kernerait, R.C. - 499
Killoran, L.K. - 293
Kim, J-H. - 301
Kim, S-G. - 301
Kim, S-Y. - 255
Kipp, R. - 323
Koester, J. - 117
Kong, F.N. - 651
Lee, T-K. - 415
Lewis, R.D. - 117
Loomis, T.A. - 661
Mac Lean, H.D. - 21
Miller, R.J. - 381
Mitchell, K.D. - 47
Moran, M.L. - 73
Munson, R.D. - 293
Novotny, T. - 209
Olhoeft, G.R. - 277,309
Peden, I.C. - 323,519
Ra, J-W. - 255,301,393,415
Rechtien, R.D. - 133,335
Rich, T.T. - 293
Roggenthen, W.M. - 87
Romig, P.R. - 1,539
Ruskey, F. - 5,11,149
Schatzberg, A. - 347
Schneider, J.B. - 519
Shin, K.C. - 47
Silva, W. - 149
Skokan, C.K. - 181,427
Stark, C. - 149
Stolarczyk, L.G. - 437,563
Sykora, D. - 117
Truskowski, M.G. - 547
Walker, B.W. - 47
Wedepohl, E. - 401
Weisinger, J.R. - 449
Westerdahl, H. - 651
Wilson, D. - 539
Witten, A.J. - 347
Wong, J. - 359
Wright, D.L. - 277
Wright, J. - 359
Yun, J-S. - 393
Zook, B.J. - 223

APPENDIX B
SYMPOSIUM ATTENDEES

SYMPOSIUM ATTENDEES

J. W. Allen
Principal Scientist
RUST Geotech Inc.
P. O. Box 14000
Grand Junction, CO 81502-5504

H. T. (Andy) Andersen
Colorado School of Mines
Geophysics Department
Golden, CO 80401

James Warren Andrews
Mining Engineer
U.S. Dept. of Labor
MSHA/SHTC
P. O. Box 25367 DFC
Lakewood, CO 80225

A. H. Balch
Professor
Colorado School of Mines
Golden, CO 80401

Yves Barbin
Research
CNRS Service d'Aeronomie
BP3
Verrieres F91371
France

Gerald B. Battey
1SG, U.S. Army
EUSA-TNT (J2)
PSC 303, Box 26
APO AP 96204-0112

George Beasley
Staff Systems Engineer
ENSCO Inc.
445 Pineda Ct.
Melbourne, FL 32940

Robert W. Bruhn
Staff Consultant
GAI Consultants Inc.
570 Beatty Road
Monroeville, PA 15146

Dick Burdick
Vick President
Rimrock Geophysics
2301 Nelson Ct.
Lakewood, CO 80215

Thurlow Caffey
SMTS
Sandia National Lab
Dept. 6114
P.O. Box 5800
Albuquerque, NM 87185

Chris Cameron
Associate Professor
Dept. of Geology, USM
Box 5044
Hattiesburg, MS 39401

Richard J. Chignell
EMRAD Ltd.
Surrey Tech Centre
40 Occam Road
Guildford GU2 544
England

R. Chojnacki
Geophysicist
Ferrovant Inc.
1916 Garfield
Laramie, WY 82070

Robert L. Chufo
Electrical Engineer
U.S. Bureau of Mines
Cochrans Mill Road
Pittsburgh, PA 15236

SYMPOSIUM ATTENDEES

Darrin Cisar
Computer Consultant
RUST Geotech Inc.
P. O. Box 14000
Grand Junction, CO 81502-5504

Allen H. Cogbill
Technical Staff Member
Los Alamos National Lab
Box 1663, Mail Stop F659
Los Alamos, NM 87545

Dave Cowling
Professor
Louisiana Tech University
P. O. Box 10348
Ruston, LA 71272-0046

Raymond F. Dennis
Ldr, Geophysics Team
Belvoir Research Dev. & Engrg Ctr.
ATTN: SATBE-JIG
Fort Belvoir, VA 22060-5818

Jozef Descour
Research Associate
Colorado School of Mines
Earth Mechanics Institute
Golden, CO 80401

Bob Duff
Director
Southwest Research Inst.
P. O. Drawer 28510
San Antonio, TX 78228-0510

Seymour Edelberg
Senior Staff
M.I.T. Lincoln Laboratory
244 Wood Street
Lexington, MA 02173

C. L. Edwards
Group Leader
Los Alamos Scientific Lab.
2344 36th
Los Alamos, NM 87545

Karl J. Ellefsen
Geophysicist
U.S. Geological Survey
MS 964, Box 25046
Denver, CO 80225

Dave Emilia
RUST Geotech Inc.
P. O. Box 14000
Grand Junction, CO 81502-5504

Richard A. Fenster
TSM Engineer
Los Alamos National Lab
316 Greenfield
Las Vegas, NV 89107

Frederick Followill
Geophysicst
Lawrence Livermore Natl. Lab.
P. O. Box 808, L-208
Livermore, CA 94551

Valentin Freilikher
Bar - Ilan University
Ramat - Gan 52900
Israel

Hal A. Gardner
Energy & Minerals Geologist
L.D.S. Church-Nat. Resources
50 E. North Temple St.
Salt Lake City, UT 84150

D.C. George
Senior Geophysicist
RUST Geotech Inc.
P. O. Box 14000
Grand Junction, CO 81502-5504

Greg Glazner
National Speleological Society
7689 W. Frost Drive
Littleton, CO 80123

Roy J. Greenfield
Professor
Penn. State University
Geophysics Department
441 Deike Building
University Park, PA 16892

Gerry Grisak
VP Hydrogeology
INTERA Inc.
6850 Austin Center Blvd.
Suite 300
Austin, TX 78731

SYMPOSIUM ATTENDEES

Zhan Guosheng
Graduate Student
Mackay School of Mines
University of Nevada, Reno
1775 Evans Ave. #406
Reno, NV 89512

Tony Hammond
Planning Engineer
Wharf Resources
HC 37, Box 811
Lead, SD 57754

Sid L. Hansen
Mining Engineer
U.S. Department of Labor
MSHA/SHTC
P.O. Box 25367 - DFC
Denver, CO 80225-0367

James C. Hasbrouck
Senior Staff Scientist
RUST Geotech Inc.
P. O. Box 14000
Grand Junction, CO 81502-5504

Ken Houser
Research Geophysicist
US Bureau of Mines
Twin Cities Research Ctr.
5629 Minnehaha Ave. South
Minneapolis, MN 55417

David A. Hill
NIST
325 Broadway
Boulder, CO 80303

Jeff Hynes
Senior Engineer Geol.
Colorado Geological Survey
1313 Sherman St. #715
Denver, CO 80203

Mike Jackson
Geophysicist
US Bureau of Mines
5629 Minnehaha Ave. South
Minneapolis, MN 55417

Eric P. Johnson
Group Leader
Southwest Research Institute
6220 Culebra Road
San Antonio, TX 78228

Chan-Tae Jung
Col ROKA
HQ EUSA USFK J-2 TNT
PSC 303, Box 26
APO AP 96204-0112

Bob Kemerait
Vice President
ENSCO Inc.
445 Pineda Ct.
Melbourne, FL 32940

Linda Killoran
U.S. Bureau of Mines
Building 20
Denver Federal Center
Denver, CO 80225

Young Dae Kim
Col ROKA
HQ EUSA USFK J-2 TNT
PSC 303, Box 26
APO AP 96204-0112

Peter Krumhansl
Staff Scientist
BBN Systems and Technologies
70 Fawcett Street
Cambridge, MA 02238

Robert Leary
Technical Consultant
Self Employed/Cons. to DNA
6908 Presley Road
Lanham, MD 20706

Melvin Lepper
Phys Scientist
U.S. Bureau of Mines
Bldg. 20
Denver Federal Center
Denver, CO 80225

SYMPOSIUM ATTENDEES

Richard D. Lewis
Research Geophysicist
US Army Corps of Engineers
3909 Halls Ferry Road
Vicksburg, MS 39180

Dave List
Geophysicist
RIMtech
9056 Marshall Court
Westminster, CO 80030

Tom Loomis
Mine Geologist
Wharf Resources
HC 37, Box 811
Lead, SD 57754

Hugh D. MacLean
Geophysicist
RUST Geotech Inc.
P. O. Box 14000
Grand Junction, CO 21502-5504

John Meloy
Sr. Research Engineer
SRI International
333 Ravenswood Ave.
Menlo Park, CA 94025

Glenn Miller
Consulting geologist
Glenn Miller Geological Cons.
6236 W. Grand River
Brighton, MI 48116

Russell J. Miller
Professor
Colorado School of Mines
Mining Engineering Dept.
Golden, CO 80401

W. Michael Miller
Consultant
Self Employed/Cons to DNA
15391 Autumn Lane
Dumfries, Va 22026

Nolan Mitchell
Geologist
USACE - MRD Laboratory
420 South 18th Street
Omaha, NE 68102

Mark L. Moran
Geophysicist
USA Cold Regions Res. & Eng.
72 Lyme Road
Hanover, NH 03755-1290

Robert Munson
Geophysicist
U.S. Bureau of Mines
Building 20
Denver, CO 80228

V.J. Murphy
Chief Consultant
ARCHAEO Consultants Ltd.
89 Traincroft
Medford, MA 02155

Jerome S. Nelson
Owner/Consultant
Jerry S. Nelson Consultant
7315 Hill Road
Granite Bay, CA 95746

Gary Olhoeft
Res. Geophysicist
U.S. Geological Survey
MS 964, P.O. Box 25146
Denver Federal Center
Denver, CO 80225-0046

Sergio B. Paradas
Geophysics Engineer
Comercio y Administracion #29
Mexico 04360
Mexico

SYMPOSIUM ATTENDEES

Irene C. Peden
Director
National Science Foundation
Div. of Elec. & Comm. Systems
1800 G Street, NW
Room 1151
Washington, DC 20550

D. Lee Petersen
Senior Engineer
CNA Consulting Engineers
2800 University Ave. SE
Minneapolis, MN 55414

Claude E. (Pete) Petrone
Mgr., Photo Special Projects
National Geographic Society
1145 17th St., NW
Washington, DC 20036

Thomas L. Pratt
Geophysicist
U.S. Geological Survey
MS 966
Denver Federal Center
Denver, CO 80225

Jung-Woong Ra
Professor
Korea Advanced Inst. Sci. & Tech.
373-1, Kusong-Dong
Yousong-gu
Taejon 305-701
Rep. of Korea

Richard D. Rechtein
Professor of Geophysics
University of Missouri
Dept./Geology & Geophysics
Rolla, MO 65401

Harold J. Rider, Jr.
Captain (Intel. Officer)
U.S. Army
EUSA-TNT (J2)
PSC 303, Box 26
APO AP 96204-0112

Louis Roemer
Department Head
Louisiana Tech University
P.O. Box 10348
Ruston, LA 71272-0046

Bill Roggenthen
Professor
SD School of Mines & Tech.
Rapid City, SD 57751

Cathy Rogland
Geophysicist
Spectrum ESI
712 W. 26th Street
San Pedro, CA 90731

Phil Romig
Professor
Colorado School of Mines
Geophysics Department
Golden, CO 80401

Gene Roseth
SMTS
Sandia National Labs
Dept. 6114, Box 5800
Albuquerque, NM 87185

Frank Ruskey
Research Geophysicist
18 Yosemite Drive
Cherokee Village, AR 72529

Thomas F. Schreier
Engineer
P. O. Box 771507
Houston, TX 77215-1507

SYMPOSIUM ATTENDEES

Weon-Hum Shim (ROKA)
HQ EUSA USFK J-2 TNT
PSC 303, Box 26
APO AP 96204-0112

Keumcheul Shin
Sr. Computer Programmer
EUSA-TNT (J2)
PSC 303, Box 26
APO AP 96205

Walter Silva
Senior Seismologist
Pacific Engineering & Analysis
311 Pomona Avenue
El Cerrito, CA 94530

Catherine Skokan
Associate Professor
Colorado School of Mines
Dept. of Geophysics
Golden, CO 80401

James Snodgrass
Geophysicist
U.S. Bureau of Mines
Denver Research Ctr.
P. O. Box 25086
Bldg. 20, Federal Ctr.
Denver, CO 80225

Robert M. Steele
Dir./Verification Technology
ENSCO Inc.
5400 Port Royal Road
Springfield, VA 22151-2312

W. Doug Steele
Manager, TNT Support Program
RUST Geotech Inc.
P. O. Box 14000
Grand Junction, CO 81502

Larry G. Stolarczyk
VP for Res. & Dev.
RIMtech Inc.
1030 Clayton Road
P. O. Box 428
Raton, NM 87740

Baek-Soo Suh
Assistant Professor
Colorado School of Mines
Golden, CO 80401

Toru Takahashi
Research Geophysicist
OYO Corporation
ERL, MIT, E34-408
42 Carleton Street
Cambridge, MA 02142

Peter H. Thompson
Geologist
Defense Nuclear Agency
Field Command
Nevada Operations Office
P. O. Box 98539
Las Vegas, NV 89193-8539

Melinda Truskowski
Colorado School of Mines
Geophysics Department
Golden, CO 80401

John Warburton
Dir. Business Development
ENSCO Inc.
445 Pineda Ct.
Melbourne, FL 32940

James Weisinger
Applied Decision Analysis Inc.
2710 Sand Hill Road
Menlo Park, CA 94025

Earle Williams
Geophysical Engineer
U.S. Bureau of Mines
P.O. Box 25086
Denver Federal Center
Denver, CO 80225

SYMPOSIUM ATTENDEES

Jim Wilson
Staff Engineer
ENSCO Inc.
445 Pineda Ct.
Melbourne, FL 32940

Skip Withrow
5404 S. Walden Street
Aurora, CO 80015

Alan Witten
Group Leader
Oak Ridge National Lab.
P. O. Box 2008, MS 6200
Oak Ridge, TN 37831-6200

J. Wong
President
JODEX Applied Geoscience Ltd.
12140 Lake Waterton Cres. SE
Calgary, AB T2J 2M7
Canada

David L. Wright
Electronics Engineer
U.S. Geological Survey
MS 964
Box 25046, Federal Center
Lakewood, CO 80225

Jerry Wright
Geophysicist
U.S. Bureau of Reclamation
P. O. Box 25007
MC D-3611
Denver, CO 80225

R. Kent Young
Geophysics Team
Belvoir Research Dev & Engrg Ctr.
ATTN: SATBE-JIG
Fort Belvoir, VA 22060-5818

Li-He Zou
Professor
Louisiana Tech University
P. O. Box 10348
Ruston, LA 71272-0046

Albert R. Zushin
Chief, Phys Sec Equip Div
Belvoir Research Dev & Engrg Ctr
ATTN: SATBE-JI
Fort Belvoir, VA 22060-5818

APPENDIX C
BRDEC NEWS RELEASE
ON
BRAC 93

Date: 15 Mar 93 11:42:43 EST
From: jmorales @ BELVOIR-EMH4.ARMY.MIL
Subject: IMPACT OF BRAC '93 ON BRDEC (News Release)

FOR IMMEDIATE RELEASE

15 March 1993

BRDEC hit hard on BRAC '93 Recommendations

by Joe Morales

DOD recommended on March 12 the disestablishment of the Belvoir Research, Development and Engineering Center (BRDEC) as part of their 1993 base realignment and closure (BRAC '93) package.

BRDEC is one of the 122 smaller bases and activities on the recommended list, submitted to the Base Closure and realignment Commission, that also includes the closing of 31 major military installations and the realignment of 12 others.

As required by law, the commission will review the list before forwarding it to the President on or before July 1. The President then has two weeks to either accept or reject the list. If he rejects it, the commission will have 30 days to submit a new list. If he accepts it, it will then go to Congress to either approve or disapprove it in its entirety. They cannot modify it. If Congress does not disapprove it within 45 days, it will then automatically become law.

The recommended disestablishment of BRDEC includes --

- Relocation of five Business Areas to the Tank Automotive RD&E Center (TARDEC) at Detroit Arsenal, Mich. They are: Supply, Bridging, Countermobility, Water Purification and Fuels and Lubricants. Approximately 165 positions.

- Transferring command and control of six Business Areas to the Night Vision Electro-Optics Directorate of the Communications and electronics SD&E Center (CRDEC), Fort Belvoir, Va. They are: Physical Security, Battlefield Deception, Electric Power, Remote Mine Detection and Neutralization, Environmental Control and Low-cost/Low-observable. Approximately 370 positions.

- Eliminating of the following five Business Areas: Tunnel Detection, Marine Craft, Topographic Equipment, Support Equipment and Construction Equipment. Approximately 290 positions.

Army officials state that the BRDEC realignment will have minimal impact on the local economy in and around Fort Belvoir. Their study shows that the projected employment loss is less than one percent of the employment base in the Washington, D.C. - Maryland area.

BRDEC dates back to 1870 when it was first established as the Army Engineer Board at Willets Point, NY. In 1921, it moved to Fort Belvoir and was renamed the Army Board on Engineer Equipment. Since then, it has been in continuous operation at Fort Belvoir under six different names. The present name, BRDEC, was adopted in 1985.

The Center has always played a major RD&D role for combat engineer equipment and logistics equipment in support of our military forces. The latest contributions include support to our troops deployed during Desert Storm and Operation Restore Hope in Somalia.